



# **PHYSICAL CHEMISTRY 2016**

*13<sup>th</sup> International Conference on  
Fundamental and Applied Aspects of  
Physical Chemistry*

*Proceedings  
Volume I*

**BELGRADE**  
**September 26 - 30, 2016**





# **PHYSICAL CHEMISTRY 2016**

*13<sup>th</sup> International Conference on  
Fundamental and Applied Aspects of  
Physical Chemistry*

*Proceedings  
Volume I*

**BELGRADE**  
**September 26-30, 2016**

**ISBN 978-86-82475-34-7**

**Title:** Physical Chemistry 2016 (Proceedings)

**Editors:** Željko Čupić and Slobodan Anić

**Published by:** Society of Physical Chemists of Serbia, Studentski trg 12-16, 11158, Belgrade, Serbia.

**Publisher:** Society of Physical Chemists of Serbia

**For Publisher:** S. Anić, President of Society of Physical Chemists of Serbia

**Printed by:** "Jovan", Printing and Publishing Company; 200 Copies.

**Number of pages:** 6+502; Format B5; printing finished in September 2016

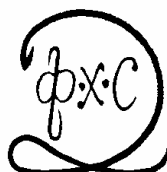
Text and Layout: "Jovan"

Neither this book nor any part may be reproduced or transmitted in any form or by any means, including photocopying, or by any information storage and retrieval system, without permission in writing from the publisher.

*200 - Copy printing*

## CONTENT

<i>Volume I</i>	
<i>Organizer</i>	IV
<i>Comittes</i>	V
<i>Sponsors</i>	VI
<i>Plenary Lecture</i>	1
<i>Spectroscopy, Molecular Structure, Physical Chemistry of Plasma</i>	47
<i>Kinetics, Catalysis</i>	183
<i>Nonlinear Dynamics, Oscillatory Reactions, Chaos</i>	267
<i>Electrochemistry</i>	355
<i>Biophysical Chemistry, EPR Investigations of bio-systems, Photochemistry, Radiation Chemistry</i>	409



# **PHYSICAL CHEMISTRY 2016**

*13<sup>th</sup> International Conference on  
Fundamental and Applied Aspects of  
Physical Chemistry*

*Organized by*

*The Society of Physical Chemists of  
Serbia*

*in co-operation with*

*Institute of Catalysis Bulgarian Academy of Sciences*

*and*

*Boriskov Institute of Catalysis Siberian Branch of  
Russian Academy of Sciences*

*and*

*University of Belgrade, Serbia:*

*Faculty of Physical Chemistry*

*Institute of Chemistry, Technology and Metallurgy*

*Vinča Institute of Nuclear Sciences*

*Faculty of Pharmacy*

*Institute of General and Physical Chemistry, Belgrade, Serbia*

### **International Organizing Committee**

- Chairman:** S. Anić (Serbia)  
**Vice-chairman:** M. Gabrovska (Bulgaria)  
A. A. Vedyagin (Russia)  
S. N. Blagojević (Serbia)  
**Members:** N. Cvjetičanin (Serbia), S. M. Blagojević (Serbia), M. Daković (Serbia), J. Dimitrić-Marković (Serbia), T. Grozdić (Serbia), Lj. Ignjatović (Serbia), D. Jovanović (Serbia), J. Jovanović (Serbia), M. Kuzmanović (Serbia), D. Marković (Serbia), B. Milosavljević (USA), M. Mojović (Serbia), N. Ostrovski (Serbia), N. Pejić (Serbia), M. Petković (Serbia), A. Popović-Bjelić (Serbia), B. Simonović (Serbia), D. Stanisavljev (Serbia), M. Stanković (Serbia), Z. Šaponjić (Serbia), B. Šljukić (Serbia), G. Tasić (Serbia), N. Vukelić (Serbia), V. Vukojević (Sweden)

### **International Scientific Committee**

- Chairman:** Ž. Čupić (Serbia)  
**Vice-chairmans:** V. N. Parmon (Russia)  
S. Rakovsky (Bulgaria)  
B. Adnađević (Serbia)  
**Members:** S. Anić (Serbia), A. Antić-Jovanović (Serbia), G. Bačić (Serbia), R. Cervellati (Italy), G. Ćirić-Marjanović (Serbia), A. Cricenti (Italy), V. Dondur (Serbia), S. D. Furrow (USA), L. Gábor (Hungary), Vilmos Gáspár (Hungary), K. Hedrih (Serbia), M. Jeremić (Serbia), E. Kiš (Serbia), Lj. Kolar-Anić (Serbia), U. Kortz (Germany), T. Kowalska (Poland), V. Kuntić (Serbia), Z. Marković (Serbia), S. Mentus (Serbia), K. Novaković (UK), B. Novakovski (Poland), T. Parac Vogt (Belgium), M. Perić (Serbia), M. Plavšić (Serbia), G. Schmitz (Belgium), I. Schreiber (Czech Republic), P. Ševčík (Slovakia), N. Stepanov (Russia), M. Trtica (Serbia), V. Vasić (Serbia), D. Veselinović (Serbia), Á. Tóth (Hungary)

### **Local Executive Committee**

- Chairman:** S. N. Blagojević  
**Vice-chairmans:** A. Ivanović-Šašić  
A. Stoiljković  
**Members:** M. Ajduković, P. Banković, N. Bošnjaković, I. N. Bubanja, D. Dimić, A. Dobrota, J. Dostanić, A. Ignjatović, S. Jovanović, Z. Jovanović, A. Jović, N. Jović-Jovičić, D. Lončarević, M. Kragović, J. Krstić, S. Maćešić, J. Maksimović, V. Marković, D. Milenković, M. Milovanović, B. Nedić-Vasiljević, M. Pagnacco, A. Pavićević, N. Potkonjak, D. Ranković, M. Ristić, B. Stanković, A. Stanojević

## SPONSORS

Ministry of Education, Science and Technological Development  
University of Belgrade, Belgrade  
Institute of General and Physical Chemistry, Belgrade  
PRIMALAB d.o.o., Serbia

*PL - Plenary lecture*



## TRIPLE MR SPECTRAL IMAGING: CHALLENGING THEORIES OF SHIFT AND RELAXATION

K. L. N. A. Finney, N. J. Rogers, P. Kanthi Senanayake and D. Parker

*Department of Chemistry, Durham University, Durham, DH1 3LE, UK*

### ABSTRACT

MR is a powerful tool for non-invasive imaging with high spatial resolution, although it suffers from low sensitivity. Recent developments with PARASHIFT agents, i.e paramagnetic lanthanide probes bearing a reporter group that can be detected directly by chemical shift imaging,[1,2] allow probe detection against a negligible background, with the possibility of simultaneous dual or triple imaging. In such systems, the reporter group (i.e. tert-butyl) needs to be integrated into the complex so that the chosen lanthanide will shift the resonance far away from water and fat signals to allow selective excitation and imaging (Fig.1). The paramagnetic enhanced relaxation of the signal can also be optimised to allow fast acquisition times, improving sensitivity.

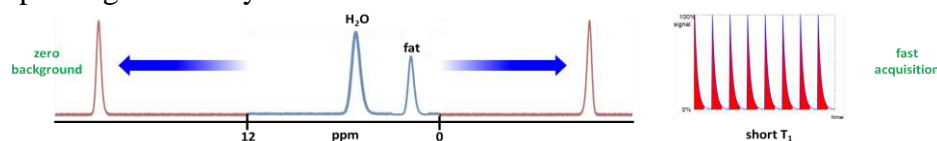


**Figure 1.** Paramagnetically shifted probe <sup>1</sup>Bu <sup>1</sup>H NMR signals relax rapidly, allowing fast acquisition

In the series of lanthanide complexes with L<sup>1</sup> vs L<sup>2</sup>, (Tb, Dy, Ho, Er, Tm, Yb), the relaxation rates for Er and Tm were faster at low field than the Tb and Dy analogues,[3] challenging the validity of many of the assumptions inherent in Bloch-Redfield-Wangsness theory.[4] Both T and dual pH/T-sensitive probes have been made (pK<sub>a</sub> 6.7; 0.1 M NaCl), and the differing pH and T sensitivity of their chemical shifts allows triple imaging encoding anatomical information, pH and T using Tm ( $\delta_{\text{H}}$  +75) and Dy ( $\delta_{\text{H}}$  -78 ppm) complexes of L<sup>1</sup> (Fig 2.).

The design of future paramagnetic shift (PARASHIFT) agents for MR imaging, requires probe functionalisation to allow clearance-specific, targeted and/or ‘smart’ imaging [6]. The progress towards these findings supports the notion that more accurate theories of both paramagnetic relaxation [4] and pseudocontact shift [5] are required.

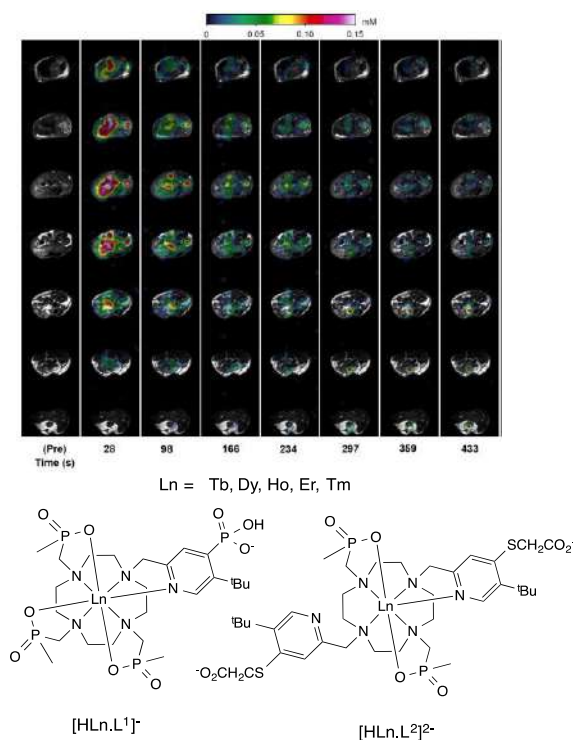


**Figure 2.** Dual  $^1\text{H}$ - $^1\text{H}$  image showing location of the probe complex in MRI ‘slice’ images of a mouse (7T, 307K)

### Acknowledgement

We thank the ERC and EPSRC for support.

### REFERENCES

- [1] P. Harvey, A. M. Blamire, J. I. Wilson, K-L NA Finney, A. M. Funk, P. K. Senanayake, D. Parker, *Chem. Sci.*, 2013, **4**, 4251.
- [2] E. De Luca, P. Harvey, K. H. Chalmers, A. Mishra, P. K. Senanayake, J. I. Wilson, M. Botta, M. Fekete, A. M. Blamire, D. Parker, *J. Biol. Inorg. Chem.*, 2014, **42**, 15610.
- [3] AM Funk, P Harvey, K-L NA Finney, MA Fox, AM Kenwright, NJ Rogers, PK Senanayake, D Parker, *PCCP*, 2015, **17**, 16507.
- [4] A. M. Funk, P. H. Fries, P. Harvey, A. M. Kenwright, D. Parker, *J. Phys. Chem. A.*, 2013, **117**, 905; N. J. Rogers, K-L. N. A. Finney, P. K. Senanayake, D. Parker, *PCCP*, 2016, **18**, 4370.
- [5] A. M. Funk, P. Harvey, K-L N. A. Finney, A. M. Kenwright, E. R. Neil, N. J. Rogers, P. K. Senanayake, D. Parker, *Chem. Sci.* 2015, **6**, 1655.
- [6] P. K. Senanayake, N. J. Rogers, P. Harvey, K-L N. A. Finney, A. M. Funk, J. I. Wilson, R. Maxwell, A. M. Blamire, D. Parker, *Magn. Reson. Med.*, 2016, in press, DOI 10.1002/mrm. 26185.

**FLUORESCENCE CORRELATION SPECTROSCOPY.  
A QUANTITATIVE METHOD WITH SINGLE-  
MOLECULE SENSITIVITY AND ITS APPLICATION IN  
BIOMEDICAL RESEARCH**

V. Vukojević

*Karolinska Institute, Department of Clinical Neuroscience,  
Center for Molecular Medicine CMM L8:01, 17176 Stockholm, Sweden  
(vladana.vukojevic@ki.se)*

**ABSTRACT**

Fluorescence Correlation Spectroscopy (FCS), a quantitative analytical method that analyses spontaneous fluctuations around an equilibrium stationary state to provide information about macroscopic properties of the investigated system, is used in biomedical research to measure the concentration, diffusion coefficients and binding constants of molecules in solution and in live cells. This lecture describes the basic theoretical principles underlying FCS, demonstrates some typical applications in life sciences using examples from our own work and shows recent advances in the use of FCS for the development of quantitative confocal fluorescence microscopy imaging without scanning, a development that allows the study of spatio-temporal integration of fast reaction-diffusion processes in live cells.

**INTRODUCTION**

Fluorescence Correlation Spectroscopy (FCS) is a quantitative analytical method that derives information about macroscopic properties of the investigated system, such as the concentration, diffusion coefficients and chemical binding constants, based on the analysis of spontaneous fluctuations around equilibrium stationary states or nonequilibrium steady states [1-5]. The theoretical principles underlying FCS, which originate in the field of equilibrium fluctuation analysis, were experimentally verified in the early 1970-ties, when the method was successfully applied for in solution studies of the kinetics of chemical interactions, translational and rotational diffusion [6–10]. However, early FCS measurements required relatively high laser-intensities and long signal acquisition times, which caused fluorescence loss due to photobleaching and thereby complicated the measurements and the subsequent data analysis. A more widespread application of FCS became possible only 20 years later, when the

introduction of several important technical improvements made it possible to overcome these difficulties. Most notably, by using the optical arrangement of a confocal microscope it was possible to generate a well-defined observation volume element (OVE) that is sufficiently small to enable the observation of a small number of molecules at a time. In addition, the use of ultra-sensitive and fast avalanche photodiode (APD) detectors enabled the detection of fluctuations in molecular numbers with high sensitivity and high temporal resolution. [11,12] These innovations have significantly improved the signal-to-noise ratio (SNR) and enabled quantitative FCS measurements with single-molecule detection sensitivity in complex solutions, consisting of molecular species that differ in concentration, brightness and/or size, and in live cells (Fig. 1). Building on these innovations, second and third generations of versatile instruments that combine FCS with confocal laser scanning microscopy (CLSM) were developed, [13,14] paving the way for a more widespread use of FCS in biomedical research.

### **BASIC BACKGROUND ON FCS**

Schematic presentation of the simplest and most commonly available single-point FCS system realized through coupling to an inverted CLSM microscope is given in Fig. 1A. To induce fluorescence, the sample is illuminated by incident light delivered by a continuous wave (cw) laser. The laser beam is reflected by the main dichroic mirror and sharply focused by the objective into the sample. Fluorescence and scattered light from the sample are collected through the same objective, separated at the main dichroic mirror that reflects the elastically scattered light, and, after passing through a dichroic filter, which further narrows spectrally the collected light, fluorescence is transmitted to the detector. The volume from which fluorescence is detected is further reduced by a pinhole, *i.e.* a confocal aperture in the image plane, which rejects stray and out of focus light. In this way, fluorescence is detected from a minute OVE that is about  $2 \cdot 10 \times 10^{-19} \text{ m}^3$  large. The small size of the OVE is crucial for reaching single-molecule sensitivity and for quantitative analysis, as it decreases the duration of fluorescence fluctuations due to molecular movement, thereby allowing the acquisition of more fluctuations per time interval, *i.e.* shorter signal acquisition times; and minimizes the background by reducing the contribution from sample auto-fluorescence and from Raman scattered light from water molecules. Fluorescence is transmitted to the single-photon avalanche photodiode (APD) detector, which responds with an electrical pulse to each detected photon, and fluctuations in fluorescence intensity are recorded over time (Fig. 1C, top).

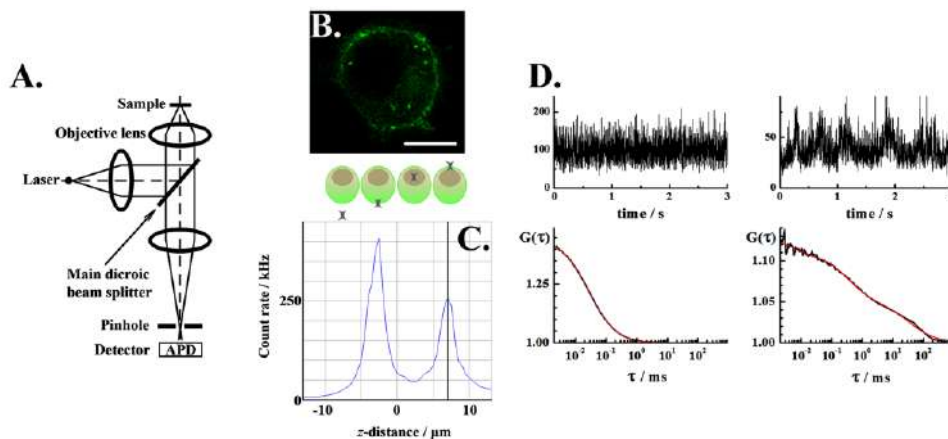


**Figure 1. Fluorescence Correlation Spectroscopy (FCS).** **A.** Schematic drawing of a classical single-point FCS/CLSM setup. **B.** Confocal image of a single PC12 cell stably transformed to express the mu-opioid receptor fused with the enhanced Green Fluorescent Protein (MOP-eGFP; green), acquired using an APD detector. Scale bar 5  $\mu\text{m}$ . **C.** Fluorescence intensity distribution across a single PC12 cell expressing MOP-eGFP determined by a linear scan in the axial direction ( $z$ -scan). The first and second maximums indicate the position of the basal and apical plasma membrane, respectively, as schematically depicted in the middle panel. **D.** Fluorescence intensity fluctuations (top) and corresponding autocorrelation curves (bottom) recorded in a standard solution of rhodamine 6G (Rh6G) in water (left) and on the apical plasma membrane of a single PC12 cell expressing MOP-eGFP (right). Rh6G and eGFP fluorescence was excited using the 488 nm line of an Ar/ArKr laser. The main dichroic beam splitter HFT KP 700/488 was used to separate the incident and emitted light, which was further spectrally selected using a band pass filter (BP 505–530 nm) in front of the APD detector. Autocorrelation analysis showed that the average number of Rh6G molecules in the OVE was 2.3 (left), whereas the average number of observed MOPeGFP molecules is 9.2 (right). The number of detected photons per molecule and second in Rh6G aqueous solution was  $\text{CPM}_{\text{Rh6G}} = 41.9$  kHz, yielding a virtually noise-less autocorrelation curve (black) that is well fitted with the autocorrelation function for free 3D diffusion and singlet/triplet transition of a single component (eq.2, red). In contrast, the eGFP brightness is an order of magnitude lower,  $\text{CPM}_{\text{MOPeGFP}} = 3.8$  kHz. The experimental autocorrelation curve is complex, showing several characteristic times. Image modified from [15].

To analyse and interpret the sampled time series, statistical methods of data analysis are applied. This is, most often done by temporal autocorrelation analysis, but other methods of data analysis can also be applied [1]. In temporal autocorrelation analysis, we first derive the intensity autocorrelation function normalized to the mean intensity squared:

$$G(\tau) = \frac{\langle F(t) \cdot F(t+\tau) \rangle}{\langle F(t) \rangle^2} = 1 + \frac{\langle \delta F(t) \cdot \delta F(t+\tau) \rangle}{\langle F(t) \rangle^2} \quad (1)$$

where  $F(t)$  and  $F(t+\tau)$  are fluorescence intensities at time  $t$  and at a later time  $t+\tau$ , respectively;  $\langle F(t) \rangle$  is the mean fluorescence intensity over the measured time; and  $\delta F(t) = F(t) - \langle F(t) \rangle$  and  $\delta F(t+\tau) = F(t+\tau) - \langle F(t) \rangle$  are the fluctuations in fluorescence intensity at time  $t$  and at a later time  $t+\tau$ , respectively. By dividing the intensity correlation function (the numerator in eq. 1) with the mean fluorescence intensity squared (the denominator in eq. 1), the normalized autocorrelation function  $G(\tau)$  is obtained that is independent of the absorption and quantum yield of the fluorophore, the detection efficiency of the instrumental setup and the laser power.

By performing temporal autocorrelation analysis of fluorescence intensity fluctuations, we essentially ask what is the probability to observe a photon at a time point  $t+\tau$  if a photon was detected at time  $t$ ? Obviously, in an FCS experiment, where photons are emitted by molecules residing in the OVE, the shorter the time lag  $\tau$ , the higher is this probability. As the time lag increases, the fluctuations in fluorescence intensity become uncorrelated and the intensity correlation function decreases. Thus, the normalized autocorrelation function  $G(\tau)$  is a decreasing function of the time lag  $\tau$  (Fig. 1D, bottom), and the rate of correlation decay is related to phenomenological parameters that describe the dynamic processes in the system through which the fluorescence intensity fluctuations arise. Moreover, different dynamic processes, such as diffusion and chemical reactions, yield different correlation functions and the underlying processes can be distinguished by analyzing the experimentally recorded autocorrelation curves. This is typically done by fitting the experimentally derived autocorrelation curves with theoretically derived autocorrelation functions [1,4], exemplified here by eq.2 and eq.3:

$$G(\tau) = 1 + \frac{1}{N} \cdot \frac{1}{\left(1 + \frac{\tau}{\tau_D}\right) \sqrt{1 + \frac{w_{xy}^2}{w_z^2} \frac{\tau}{\tau_D}}} \cdot \left[1 + \frac{T}{1-T} \exp\left(-\frac{\tau}{\tau_T}\right)\right] \quad (2)$$

$$G(\tau) = 1 + \frac{1}{N} \cdot \left( \frac{1-y}{\left(1 + \frac{\tau}{\tau_{D1}}\right) \sqrt{1 + \frac{w_{xy}^2}{w_z^2} \frac{\tau}{\tau_{D1}}}} + \frac{y}{\left(1 + \frac{\tau}{\tau_{D2}}\right)} \right) \quad (3)$$

In eq. 2, which represents an autocorrelation function derived for free three-dimensional (3D) diffusion of a single molecular species and triplet formation,  $N$  is the average number of molecules in the OVE determined from the amplitude of the autocorrelation curve at  $\tau = 0$ ;  $T$  is the average equilibrium fraction of molecules in the triplet state;  $\tau_T$  is the triplet correlation time that is related to the rate constants for intersystem crossing and the triplet decay;  $w_{xy}$  and  $w_z$  are, respectively, the radial (perpendicular to the direction of light propagation) and axial (in the direction of light propagation) distance of the focused laser beam at which the collected fluorescence intensity has dropped by a factor of  $e^2$  compared to its peak value in the center;  $\tau_D$  is the diffusion time. In eq. 3, which describes free 3D diffusion of an unbound ligand and two-dimensional (2D) diffusion of the ligand bound in a ligand-receptor complex at the plasma membrane,  $\tau_{D1}$  and  $\tau_{D2}$  are diffusion times of the unbound and bound ligand, respectively, and  $y$  is the fraction of the ligand that is bound to the receptor.

Even though the autocorrelation functions that describe different dynamic processes are mathematically distinct, as can be seen from the expression in eq. 2 and eq. 3, the experimentally derived autocorrelation curves may still be difficult to analyze unequivocally, unless additional experiments are performed. For example, the relative contributions of diffusion *versus* chemical reaction can be efficiently tested by varying the size of the OVE. Whilst rates of chemical reactions are independent of the OVE size, the characteristic diffusion time  $\tau_D$  is not, and will vary in accordance with the relation  $\tau_D = w_{xy}^2 / 4D$ , where  $D$  is the diffusion coefficient. Likewise, the chemical relaxation times of a second order chemical reaction are functions of the mean concentrations of the reactants, and the characteristic decay time of the corresponding autocorrelation curve will change when the concentration of the reactants is changed [1,5].

Thus, although the measured fluctuations are utterly stochastic by themselves, their average rate of relaxation to the equilibrium value is not stochastic but rather constrained by macroscopic properties of the investigated system. It is exactly this interrelation that makes it possible to apply fluctuation's analysis to obtain information about macroscopic

properties of the investigated system and measure local diffusion coefficients, concentration, apparent hydrodynamic radius, kinetic rate constants and equilibrium binding/dissociation constants.

### QUANTITATIVE STUDY OF SYNTHETIC HOX TRANSCRIPTION FACTOR–DNA INTERACTIONS IN LIVE CELLS

An example from our own work, where we measured differences in wild type *versus* mutant transcription factor binding to chromatin in live salivary glands *ex vivo* is shown in Fig. 2 [16].

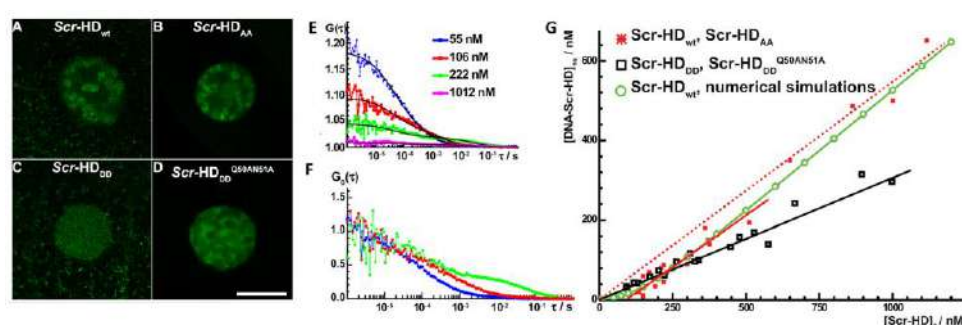


**Figure 2.** Differences in binding between different genetic variants of the synthetic transcription factor Scr-HD to chromatin studied *ex vivo* in live salivary glands of *Drosophila melanogaster* third instar larvae. **(A.–D.)** Polytene nuclei expressing different variants of the synthetic transcription factor Scr-HD: Scr-HD<sub>wt</sub> (A), Scr-HD<sub>AA</sub> (B) Scr-HD<sub>DD</sub> (C) or Scr-HD<sub>DD</sub><sup>Q50AN51A</sup> (D). **E.** Gradual increase of Scr-HD<sub>wt</sub> concentration in live salivary gland cells recorded by FCS after exposing the larvae to heat shock (15 min at 37 °C). **F.** Normalized autocorrelation curves showing changes in Scr-HD<sub>wt</sub> dynamics as a function of its concentration. All FCS measurements were performed at the same location in the same cell. **G.** Extent of synthetic transcription factor Scr-HD binding to chromatin studied experimentally (symbols) and emulated by numerical simulations (lines). FCS analysis in live cells reveals that the extent of Scr-HD binding to chromatin is different for the different genetic variants examined and characterized by different underlying kinetics. Image modified from [16].

By advancing the detection sensitivity of CLSM [14], we could visualize differences in the spatial distribution of wild type and mutant variants of the synthetic transcription factor Scr-HD (Fig. 2 A-D) in cells expressing low, physiologically relevant concentrations of the transcription factor measured by FCS to be: [Scr-HD<sub>wt</sub>] = 105 nM, [Scr-HD<sub>AA</sub>] = 157 nM, [Scr-HD<sub>DD</sub>] =

66 nM and  $[\text{Scr-HD}^{DD}]^{Q50AN51A} = 220$  nM. By FCS, we were able to discern free 3D diffusion of Scr-HD molecules (Fig. 2E and F, fast decaying component), from the significantly slower mobility of Scr-HD molecules whose movement was stalled by interactions with the chromatin (Fig. 2E and 2F, slowly decaying component). Moreover, we could also characterize the specific and nonspecific Scr-HD interactions with the DNA, and estimate their corresponding dissociation constants ( $K_d$ ) *ex vivo*: the dissociation constant for nonspecific DNA – Scr-HD complexes was estimated to be  $K_{d,ns}^{\text{Scr-HD}^{DD}} = (80 \pm 50)$   $\mu\text{M}$  and  $K_{d,ns}^{\text{Scr-HD}^{wt}} = (25 \pm 15)$   $\mu\text{M}$ , whereas it was  $K_{d,s}^{\text{Scr-HD}^{wt}} = (7 \pm 5)$  nM for specific complexes. Our results suggested that the synthetic Scr-HD transcription factors find their specific target sites primarily by multiple association/dissociation events, the rapidity of which is largely owed to electrostatic interactions. Based on these new findings, we could propose a model mechanism and could emulate the kinetics of Scr-HD interactions with DNA in live cells using numerical simulations (Fig. 2G) [16].

### MASSIVELY PARALLEL FLUORESCENCE CORRELATION SPECTROSCOPY FOR IMAGING OF FAST DYNAMIC PROCESSES IN LIVE CELLS

One principal limitation of classical single-point FCS is limited overview, *i.e.* the capacity to provide quantitative information in the minute OVE only. Hence, to acquire quantitative information from several locations in a cell using the conventional single-point FCS setup, FCS measurements need to be performed successively, which is not suitable for the study of fast dynamical processes. To overcome this limitation and enable quantitative studies of fast dynamical processes across the specimen, we have developed a new instrumental system for quantitative confocal fluorescence microscopy imaging of dynamical systems without scanning *via* massively parallel FCS measurements [17]. In this system, a Diffractive Optical Element (DOE) and a matrix single-photon avalanche photodiode (SPAD) camera are used to achieve massively parallel confocal arrangement [17] and probe the kinetic landscape of the synthetic Scr-HD transcription factor binding to DNA in live cells in 1024 (32×32) OVE simultaneously (Fig. 3). Our study reveals that the nuclear dynamics of the synthetic transcription factor Scr-HD is complex and exhibits a changing landscape of interactions that is difficult to characterize by probing one OVE at a time (Fig. 3) [18].

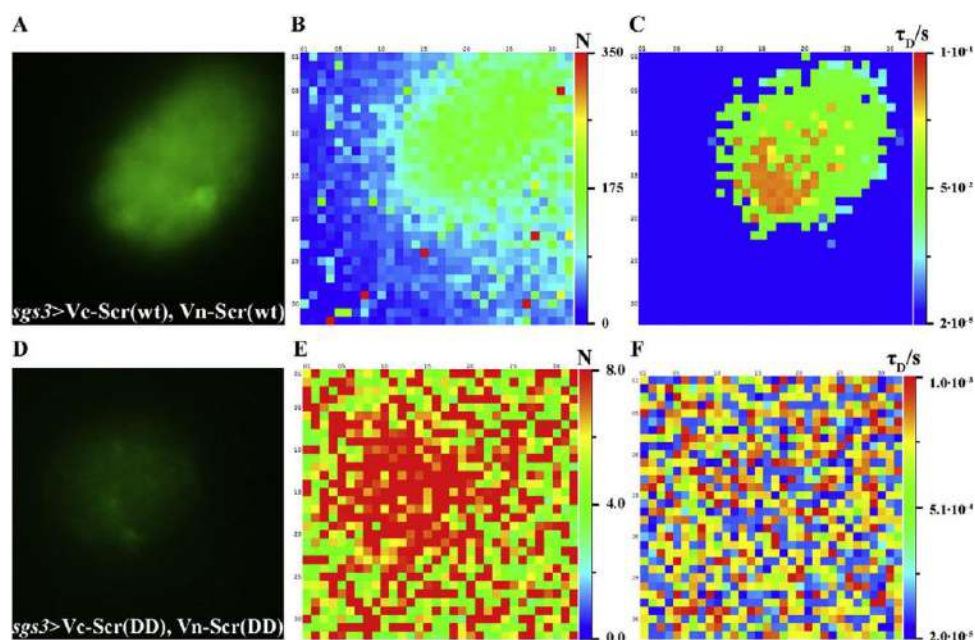


**Figure 3.** Spatial distribution of molecular numbers and mobility of wild-type and constitutively inactive Scr-HD transcription factor dimers visualized by bimolecular fluorescence complementation (BiFC) and quantitatively characterized by mpFCS. (A.-C.) Scr-HD<sub>wt</sub> dimers visualized. (D.-F.) Scr-HD<sub>DD</sub> showing no dimerization. Image modified from [18].

Using bimolecular fluorescence complementation (BiFC), we show that Scr-HD forms dimers that strongly associate with its specific *fork head* binding site (*fh250*) in live salivary gland cell nuclei (Fig. 3A-C). In contrast, dimers of the constitutively inactive, phosphomimicking variant of Scr, Scr-HD<sub>DD</sub>, show weak, non-specific DNA-binding (Fig. 3D-F). mpFCS revealed that Scr-HD dimers are predominantly formed on the DNA and are equally abundant at the chromosomes and the introduced multimeric *fh250* binding-site (Fig. 3B), but differ significantly in mobility (Fig. 3C), possibly reflecting transient binding with different affinities on the DNA.

This dataset indicates that mpFCS is a suitable method for the simultaneous recording of molecular mobility and concentration over a larger area. Therefore, it is possible to study differences in these parameters in live cells with high spatio-temporal resolution. The high temporal resolution of mpFCS is expected to allow quantification and dynamics of faster processes, such as calcium signaling and neuronal transmission, simultaneously and across larger areas.

**Acknowledgement**

Support from The Knut and Alice Wallenberg Foundation (grant KAW 2011.0218), The Swedish Research Council (VR 2012-2595), Foundation for Strategic Research (SBE13-0115), The Foundation Olle Engkvist Byggmästare and The Rajko and Maj Đermanović Fund, is gratefully acknowledged.

**REFERENCES**

- [1] E. L. Elson, Brief introduction to fluorescence correlation spectroscopy. *Methods Enzymol.* 2013, **518**, 11-41.
- [2] J. Ries, P. Schwille, Fluorescence correlation spectroscopy. *Bioessays* 2012, **34**, 361-368.
- [3] P. Schwille, E. Haustein, Fluorescence correlation spectroscopy, an introduction to its concepts and applications. *Biophysics Textbook Online* 2004 1-33 <https://www.biophysics.org/Portals/1/PDFs/Education/schwille.pdf>.
- [4] V. Vukojević, A. Pramanik, T. Yakovleva, R. Rigler, L. Terenius, G. Bakalkin, Study of molecular events in cells by fluorescence correlation spectroscopy, *Cell. Mol. Life Sci.* 2005, **62**, 535-550.
- [5] E. L. Elson, Fluorescence correlation spectroscopy measures molecular transport in cells, *Traffic*, 2001, **2**, 789-796.
- [6] D. Magde, W. W. Webb, E. Elson, Thermodynamic fluctuations in a reacting system-measurement by fluorescence correlation spectroscopy. *Phys. Rev. Lett.* 1972, **29**, 705-708.
- [7] M. Ehrenberg, R. Rigler, Polarized fluorescence and rotational Brownian motion, *Chem. Phys. Lett.* 1972, **14**, 539-544.
- [8] E. L. Elson, D. Magde, Fluorescence correlation spectroscopy. I. Conceptual basis and theory, *Biopolymers* 1974, **13**, 1-27.
- [9] M. Ehrenberg, R. Rigler, Rotational brownian motion and fluorescence intensity fluctuations. *Chem. Phys.* 1974, **4**, 390-401.
- [10] D. E. Koppel, Statistical accuracy in fluorescence correlation spectroscopy, *Phys. Rev. A* 1974, **10**, 1938-1945.
- [11] R. Rigler, -. Mets, J. Widengren, P. Kask, Fluorescence correlation spectroscopy with high count rate and low background: analysis of translational diffusion. *Eur. Biophys. J.* 1993, **22**, 169-175.
- [12] M. Eigen, R. Rigler, Sorting single molecules: application to diagnostics and evolutionary biotechnology. *Proc. Natl. Acad. Sci. USA* 1994, **91**, 5740-5747.

- [13] K. Weisshart, V. Jüngel, S. J. Briddon, The LSM 510 META ConfoCor 2 system: An integrated imaging and spectroscopic platform for single-molecule detection. *Curr. Pharm. Biotechnol.* 2004, **5**, 135-154.
- [14] V. Vukojević, M. Heidkamp, Y. Ming, B. Johansson, L. Terenius, R. Rigler, Quantitative single-molecule imaging by confocal laser scanning microscopy. *Proc. Natl. Acad. Sci. USA* 2008, **105**, 18176-18181.
- [15] T. Jovanović-Talisman, V. Vukojević, Super-resolution fluorescence imaging and correlation spectroscopy: principles and examples of application. *J. Serb. Chem. Soc.* 2013, **78**, 1671–1688.
- [16] V. Vukojević, D. K. Papadopoulos, L. Terenius, W. J. Gehring, R. Rigler, Quantitative study of synthetic Hox transcription factor–DNA interactions in live cells. *Proc Natl Acad Sci USA* 2010, **107**, 4087-4092.
- [17] M. Vitali, D. Bronzi, A. J. Krmpot, S. Nikolić, F-J.Schmitt, C. Junghans, S. Tisa, T. Friedrich, V. Vukojević, L. Terenius, F. Zappa, R. Rigler, A single-photon avalanche camera for fluorescence lifetime imaging microscopy and correlation spectroscopy. *IEEE J. Sel. Top. Quantum Electron.* 2014, **20**, 344-353.
- [18] D. K. Papadopoulos, A. J. Krmpot, S. N. Nikolić, R. Krautz, L. Terenius, P. Tomancak, R. Rigler R, W. J. Gehring, V. Vukojević, Probing the kinetic landscape of Hox transcription factor-DNA binding in live cells by massively parallel Fluorescence Correlation Spectroscopy. *Mech. Dev.* 2015, pii: S0925-4773(15)30029-0.

## BIOMEDICAL APPLICATIONS BY INFRARED SCANNING NEAR-FIELD OPTICAL MICROSCOPY

A. Cricenti<sup>1</sup>, M. Luce<sup>1</sup>, M. Ortenzi<sup>1</sup>, M.R.F. Siggel-King<sup>2</sup>, T. Craig<sup>2</sup>, J. Ingham<sup>2</sup>, D. S. Martin<sup>2</sup> and P. Weightman<sup>2</sup>

<sup>1</sup>*Istituto di Struttura della Materia (ISM-CNR), via del Fosso del Cavaliere 100, 00133 Rome, Italy(antonio.cricenti@ism.cnr.it)*

<sup>2</sup>*Department of Physics, University of Liverpool, Liverpool L69 7ZE, United Kingdom*

### ABSTRACT

We present a fully implemented Infrared Scanning Near-field Optical Microscopy in spectroscopic mode for tissue imaging and early cancer diagnostics. The experiments have been performed on oesophageal tissue and have shown that the setup can operate at nanometer resolution and has been able to distinguish between healthy and malignant tissues, thus demonstrating the potential of the technique for yielding a diagnostic for oesophageal cancer and other kind of cancer.

### INTRODUCTION

Scanning near-field optical microscopy (SNOM) is a sensitive and flexible technique that achieves an enhanced optical resolution through the very close placement of the sensing element to the object to be imaged. Conventional spectroscopy is often not enough sensitive and spatially resolved to detect specific elements or domains in a sample. The need of imaging objects on increasingly finer scales and spatially localize specific molecules, brought to the combination of infrared, visible and Raman spectroscopy with scanning near-field microscopy, giving rise to a powerful nanospectroscopic tool used to perform simultaneous topographical measurements and optical/chemical characterizations with subwavelength resolution, overcoming the diffraction limit of light. Infrared (IR) spectroscopy is a potentially powerful tool for identifying the chemistry of biologically active molecules in cells [1]. However, practical implementation of intracellular IR imaging has been problematic because of the diffraction limit of conventional infrared microscopy, which gives a spatial resolution not better than a few microns. The advent of SNOM [2] has augmented the usefulness of IR spectroscopy at a microscopic level. In fact, by coupling a SNOM with a tunable IR source (usually a laser in this

region) it is possible to overcome the diffraction limit also in the infrared region [3-4].

Tunability of the laser is extremely important since the biochemical cellular compounds have their own vibrational “fingerprints” in the absorption of light: in fact, their frequencies lie in the mid-infrared wavelengths from 3  $\mu\text{m}$  to about 11 $\mu\text{m}$  (spectral range between 3300  $\text{cm}^{-1}$  and 900  $\text{cm}^{-1}$ ). In particular the following wavelengths are particularly interesting for determining the inner chemical composition of a cell:

$\lambda = 3.04 \mu\text{m}$  (CH stretch band)

$\lambda = 3.4 \mu\text{m}$  ( $\text{CH}_2$  asymmetric stretch band)

$\lambda = 6.1 \mu\text{m}$  (Amide C=O stretch band)

$\lambda = 6.45 \mu\text{m}$  (Reflection of Sulphur, key component of amino-acids)

$\lambda = 6.95 \mu\text{m}$  (Sulfide cell growth medium stretch band)

$\lambda = 7.6 \mu\text{m}$  ( $\text{CH}_3$  stretch band)

$\lambda = 8.05 \mu\text{m}$  (Phosphate stretch band)

In this way, once found the optimal wavelengths corresponding to the distribution of functional groups within a cell, it is possible to map the distribution of functional groups (proteins, lipids and nucleic acids) inside a single cell with a nanometric resolution and to see possible chemical differences between perturbed and unperturbed cells.

The potential of IR spectroscopy to characterise cancerous tissues has long been recognised and studies of various cancers by many groups have established that regions of malignant tissue can be easily identified on the basis of its IR spectrum [5]. The oesophageal adenocarcinoma, the cancer with the fastest rise in incidence in the Western world, requires an instrument providing specific chemical images at sub-cellular level of oesophagus tissue. Oesophageal adenocarcinoma develops in some patients who have a precursor condition called Barrett's oesophagus in which the epithelial cells of the distal oesophagus acquire a columnar rather than squamous morphology as a result of chronic gastro-oesophageal reflux disease.

We present a study of Barrett's oesophagus by Infrared Scanning Near-field Optical Microscopy in spectroscopic mode. The SNOM can operate at nanometer resolution and has been able to distinguish between healthy and malignant tissues.

## EXPERIMENTAL

The SNOM employed in this work was developed on the IR Free Electron Laser (FEL) at Vanderbilt (USA) and established on the IR FEL on the ALICE energy recovery linear accelerator at Daresbury (UK) [6]. Figure 1 shows the experimental setup: IR photons from the unfocused FEL beam are

directed by a mirror onto the sample surface at a  $\sim 85^\circ$  angle to the surface normal. Reflected photons are detected through a narrow-point optical fiber tip mounted on a SNOM module, which also measures shear-force (topographic) images. During a scan, reflected IR light is picked up through the fiber and is detected by a photoconductive detector.

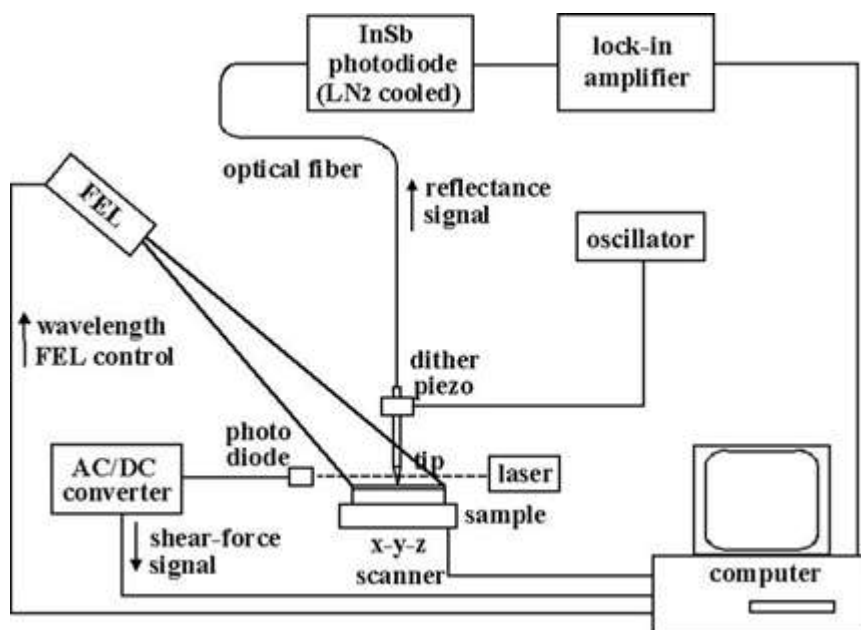


**Figure 1.** Schematic diagram of the experimental setup.

Topographical and optical images were taken simultaneously, with the FEL illuminating the specimen over a broad area ( $\sim 1$  mm spot diameter) and the SNOM probe collecting the reflected light. The scanning tip is a specially prepared IR-transmitting Chalcogenide glass fibre, where one end was either etched or cleaved forming an aperture of  $0.1\text{--}1\ \mu\text{m}$  in diameter through which the light is collected. The wavelength of light from the FEL was selected by changing the undulator gap and was operating at a macro-pulse repetition rate of 10 Hz, which limits, and determines, the rate of data collection. The IR light from the FEL was transported to the experimental area via an evacuated beamline and exited the beamline through a KBr window. The intensity of the FEL radiation was attenuated using a set of polarisers and focussed onto the sample. A CaF<sub>2</sub> beam-splitter enables the FEL radiation to be split so that approximately 80% went to the SNOM and 20% was used as a reference signal. The reference signal was monitored with a single-element pyro detector. The spectral resolution of the FEL has been

measured to be  $0.13 \mu\text{m}$  ( $\sim 20 \text{ cm}^{-1}$ ) FWHM at  $\lambda = 8 \mu\text{m}$ , which whilst broader than the typical resolution obtained by FTIR, is adequate to resolve the distribution of significant spectral resonances. The results reported in this paper used wavelengths of  $8.05 \mu\text{m}$  and  $7.3 \mu\text{m}$ , which are associated with DNA and protein/glycoprotein respectively and  $7.0 \mu\text{m}$ , which is not strongly associated with any particular biomolecule [[7]]. These wavelengths were confirmed by FTIR and ATR measurements on model compounds of DNA (Calf Thymus), glycoprotein (Mucin from Sigma Aldrich), and protein (human serum albumin from Sigma). A single IR-FEL macro-pulse is used for each pixel of the images.

Oesophageal biopsy samples were obtained from patients with Barrett's oesophagus (with no histological evidence of dysplasia) and from patients with Barrett's associated oesophageal adenocarcinoma. These were fixed in 10% formalin and embedded in paraffin wax. Serial  $5 \mu\text{m}$  sections from each paraffin block were subsequently cut using a microtome, mounted on calcium fluoride discs and dewaxed using xylene shortly before being assessed in the SNOM.

## RESULTS AND DISCUSSION



**Figure 2.** Monitor picture of the Chalcogenide fiber (on top on monitor) and of the biopsy sample (full area of monitor).

The SNOM microscope was operating with a videocamera that allowed the tip to be positioned in special area of the sample: figure 2 shows the biopsy sample together with the chalcogenide fiber.

A topographical image of 350 micron is then taken to check the observed area: figure 3 is an image of a control sample where it is possible to see the different parts of the sample. In the image white colour are the highest protrusions while dark areas represents depressions on the samples: Z-variations are of the order of several microns through the image.

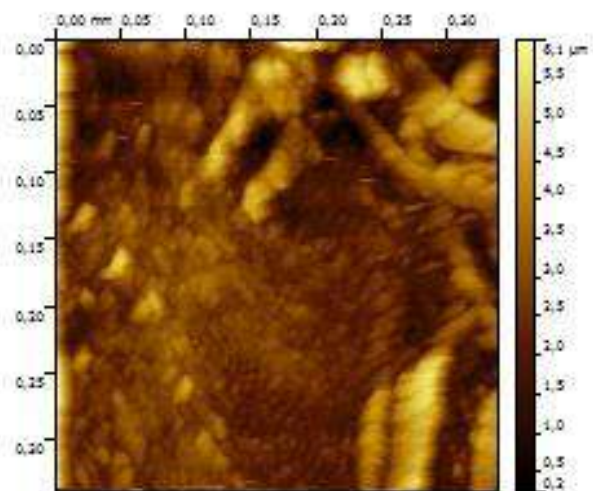


**Figure 3.** Topographical image ( $350 \mu\text{m} \times 350 \mu\text{m}$ ) of a non-cancerous biopsy sample.

Finally, the optical fibre has been driven in particular areas of the oesophageal tissue and topographical and optical images have been collected simultaneously at different wavelengths. In particular, SNOM images were collected at wavelengths of  $7.0 \mu\text{m}$  (no strong biomarker),  $7.3 \mu\text{m}$  (protein/glycoprotein), and  $8.05 \mu\text{m}$  (DNA).

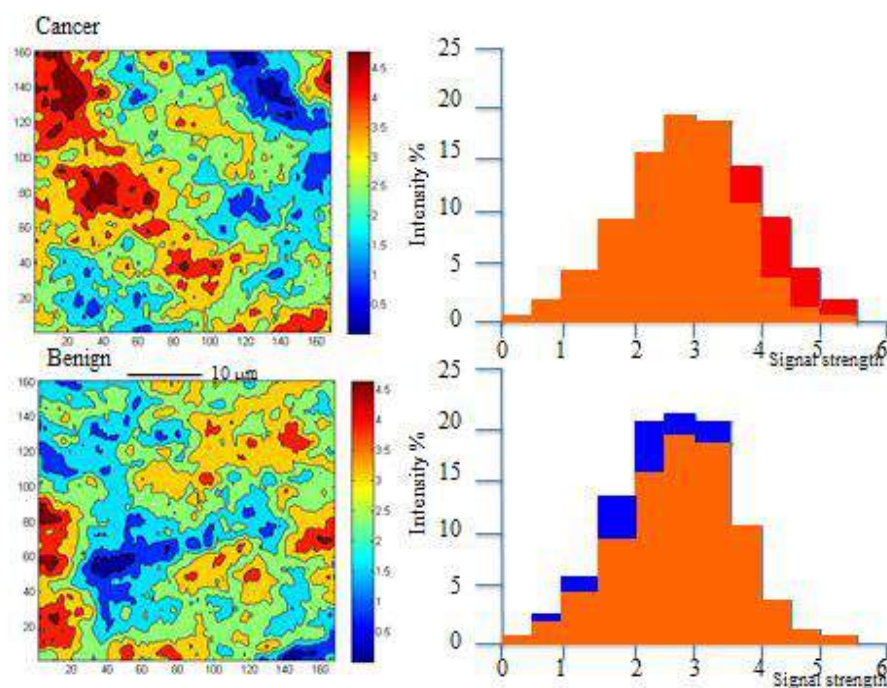
Infrared high resolution SNOM images of  $40 \mu\text{m} \times 40 \mu\text{m}$  areas of cancerous and non-cancerous Barrett's specimens were collected at  $0.2 \mu\text{m}$  intervals. The area is large enough to image several cells and resolve their nuclei, however the microtomed samples do not necessarily provide clear topological features which can be related to the SNOM images. Although these areas are too small to be representative of the diverse range of tissue types that can be observed within the oesophagus, they do serve to demonstrate the potential of the technique to obtain chemical information, relevant to cancer research, at high spatial resolution.

Figure 4. shows  $40 \mu\text{m} \times 40 \mu\text{m}$  optical SNOM images for two samples, labelled Cancer and Benign: the colour maps show the location of intense

DNA (red), intense protein/glycoprotein (blue) and of strong overlap of DNA and protein/glycoprotein (orange).

The raw data has been 4-point Gaussian smoothed and, for visual purposes, the contrast enhanced. Previous work [7,8] has shown that cancerous tissue is associated with a significant (60%) increase in overall DNA content. As clearly visible, Cancer sample shows a large spread of intense signal from DNA whereas Benign sample shows a lower overall density of DNA, which is more dispersed and exhibits more localised centres.

In cancer sample strong signals from DNA are spread over areas of  $\sim 20 \mu\text{m}^2$ , whilst in benign sample the largest equivalent area is  $< 10 \mu\text{m}^2$  and the others are significantly smaller.



**Figure 4.** IR-SNOM image maps showing the location of intense DNA (red), intense protein/glycoprotein (blue) and of strong overlap of DNA and protein/glycoprotein (orange).

The images also show that there is a tendency for DNA and protein/glycoprotein to be closely associated in the cancerous material. These visual observations lead us to correctly distinguish between

cancerous and benign specimen. This figure shows the potential of the SNOM technique to reveal chemical information on a subcellular scale.

## CONCLUSION

This combination of InfraRed radiation and Scanning Near-field Optical Microscopy, in its spectroscopic mode, on oesophageal adenocarcinoma have shown that the system can operate at nanometer resolution and has been able to distinguish between healthy and malignant tissues [9]. This approach can be an important tool for tissue imaging and early cancer diagnostics. It is expected to produce a major advance in imaging of malignant tissues [10], leading to the development of portable diagnostic devices for hospital use for various types of cancer. It is also planned to utilise the powerful combination of high spatial resolution and chemical specificity of the mentioned methodologies to study the key components, responsible for cancer formation.

## Acknowledgement

This work was supported by the Cockcroft Institute via the STFC core grant ST/G008248/1 and STFC's Daresbury Laboratory via its ASTeC centre and ALICE operations team.

## REFERENCES

- [1] G. L. Carr, P. Dumas, C. J. Hirshmuyl and G. P. Williams, *Nuovo Cimento Soc. Fis. Ital. D*, 1998, **20**, 375-395, and references therein.
- [2] *Near Field Optics*, ed. D. W. Pohl and D. Courjon, Kluwer Academic Press, 1992, NATO ASI Series vol. **262**.
- [3] A. Cricenti, R. Generosi, M. Luce, P. Perfetti, G. Margaritondo, D. Talley, J. S. Sanghera, I. D. Aggarwal and N. H. Tolk. *Phys. Chem. Chem. Phys.*, 2002, **4**, 2738-2741.
- [4] A. Cricenti, R. Generosi, M. Luce, P. Perfetti, G. Margaritondo, D. Talley, J. S. Sanghera, I. D. Aggarwal, N. H. Tolk, A. Congiu-Castellano, M. A. Rizzo and D. W. Piston, *Biophysical Journal*, 2003, **85**, 1-6.
- [5] M.J. Baker, E. Gazi, M.D. Brown, J.H. Shanks, P. Gardner and N.W. Clarke. *B. J. Cancer*, 2008, **99**, 1859-1866.
- [6] A. Cricenti, M. Luce, N.H. Tolk, G. Margaritondo, *Nanosci. Nanotechnol. Lett.*, 2011, **3**, 913-921.
- [7] L. Quaroni and A.G. Casson *Analyst*, 2009, **134**, 1240-1246.

- 
- [8] T. D. Wang, G. Triadafilopoulos, J. M. Crawford, L. R. Dixon, T. Bhandari, P. Sahbaie, S. Friedland, R. Soetikno, and C.H. Contag *PNAS*, 2007, **104**, 15864-15869.
- [9] A. D. Smith, M.R.F. Siggel-King, G. M. Holder, A. Cricenti, M. Luce, P. Harrison, D. S. Martin, M. Surman, T. Craig, S. D. Barrett, A. Wolski, D. J. Dunning, N. R. Thompson, Y. Saveliev, D. M. Pritchard, A. Varro, S. Chattopadhyay, P. Weightman, *Applied Physics Letters*, 2013, **102**, 053701-4.
- [10] D.E. Halliwell, C. L. M. Morais, K. M. G. Lima, J. Trevisan, M.R.F. Siggel-King, T. Craig, J. Ingham, D. S. Martin, K.A. Heys, M. Kyrgiou, A. Mitra, E. Paraskevaidis, G. Theophilou, P. L. Martin-Hirsch, A. Cricenti, M. Luce, P. Weightman, F. L. Martin, *Nature Scientific Reports*, 2016, **6**, 29494 1-10.

## POLYXOMETALATES AS ARTIFICIAL ENZYMES

K. Stroobants, A. Sap, H. G. Ly Thi, T. Quanten and T. N. Parac-Vogt\*

*Department of Chemistry, KU Leuven, 3001 Leuven, Belgium  
tatjana.vogt@kuleuven.be*

Selective hydrolysis of proteins is an important procedure in numerous biochemical applications. Based on the non-covalent, electrostatic interaction between negatively charged polyoxometalates (POMs) and positive surface domains of proteins<sup>1</sup>, we recently introduced a conceptually new approach in the development of artificial proteases by using POMs as ligands for Lewis acid metal ions. In our approach the POM acts as a ligand for the Zr(IV)ion, and due to its three-dimensional shape and negative charge it also induces the selectivity that is necessary for a controlled fragmentation of the polyamide backbone (Fig 1). Zr(IV)-substituted POMs were proven to be catalytically active towards the hydrolysis of the highly inert amide bond in dipeptides and oligopeptides.<sup>2</sup> More importantly, these POMs were shown to display unprecedented hydrolytic activity towards insulin chain B, lysozyme, myoglobin and albumin proteins.<sup>3</sup> The hydrolysis occurs at peptide bonds which are located either at clearly defined positive patches that are able to accommodate the POM ligand, or on the interface of positive surface zones containing negatively charged Asp or Glu residues that allow for additional anchoring of Zr(IV). A range of biophysical and spectroscopic techniques has been applied in order to elucidate the molecular interactions between POMs and proteins under investigation.

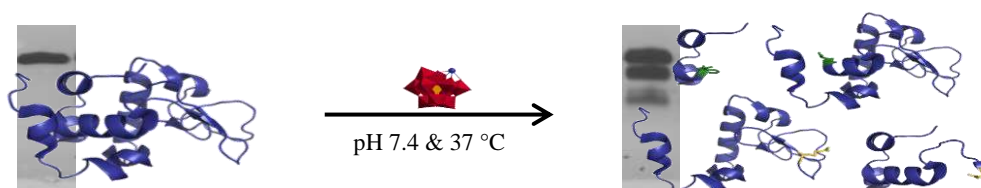


**Figure 1.** Selective Hydrolysis of Hen Egg White Lysozyme by Keggin type  $[\text{Zr}(\text{PW}_{11}\text{O}_{39})_2]^{10-}$  polyoxometalate complex.

**REFERENCES**

- [1] Goovaerts V., Stroobants K., Absillis G., Parac-Vogt T.N., *Phys. Chem. Chem. Phys.*, 2013, **15**, 18378. b) V. Goovaerts, K. Stroobants, G. Absillis, T. N. Parac-Vogt J. *Inorg. Biochem.* 2015, DOI:10.1016/j.jinorgbio.2015.03.015. c) Stroobants, K., Saadallah, D., Bruylants, G.; Parac-Vogt, T. N. *Phys. Chem. Chem. Phys.*, 2014, **16**, 21778.
- [2] a) Absillis G., Parac-Vogt T. N., *Inorg. Chem.*, 2012, **51**, 9902. b) Ly H.G.T., Absillis G., Parac-Vogt T.N., *Dalton Trans.*, 2013, **42**, 10929. c) Ly H.G.T., Mihaylov T. Absillis G., Pierloot K, Parac-Vogt T.N., *Inorg. Chem.*, 2015, **54**, 11477.
- [3] a) Stroobants K., Moelants E., Ly H.G.T., Proost P., Bartik K., Parac-Vogt T.N., *Chem. Eur. J.*, 2013, **19**, 2848. b) Stroobants K., Goovaerts V., Absillis G., Moelants E., Proost P., Parac-Vogt T.N., *Chem. Eur. J.*, 2014, **20**, 9567. c) Stroobants K., Absillis G., Moelants E., Proost P., Parac-Vogt T.N., *Chem. Eur. J.* 2014, **20**, 3894. d) Sap A, Absillis G., Parac-Vogt T.N, *Dalton Trans.* 2015, **44**, 1539. e) Ly, H. G. T.; Absillis, G.; Janssens, R.; Proost, P.; Parac-Vogt, T. N. *Angew. Chem. Int. Ed.* 2015, **54**, 7391. f) Sap. A. De Zitter E., Van Meervelt L., Parac-Vogt T.N., *Chem. Eur. J.* 2015, **21**, 11692. g) Quanten T., Shestakova P., Van Den Bulck, D., Kirschhock, C., Parac-Vogt, T. N., *Chem. Eur. J.*, 2016, **22**, 3775.

## NANOFABRICATION AND SPECTROSCOPY OF PLASMONIC NANOCONES

M. Fleischer<sup>1,2</sup>

<sup>1</sup>*University of Tübingen, Institute for Applied Physics, Auf der Morgenstelle 10, 72076 Tübingen, Germany (monika.fleischer@uni-tuebingen.de).*

<sup>2</sup>*Center for Light-Matter-Interaction, Sensors and Analytics, University of Tübingen, Auf der Morgenstelle 15, 72076 Tübingen, Germany.*

### ABSTRACT

Top-down nanofabrication is employed for the fabrication of optical antennas with conical shapes. Different nano-lithographic techniques are demonstrated. Plasmonic nanocones offer narrow, high near-field intensity hotspots near their tip apex. The geometry-dependent plasmon resonances, linear and non-linear optical properties of the nanocones are investigated. Procedures for selectively coupling few or single nano-emitters to these tips are shown. Emission enhancement and lifetime reductions are observed in the resulting hybrid structures.

### INTRODUCTION

Plasmonic nanostructures that act as optical nanoantennas for visible light offer interesting opportunities for locally concentrating and enhancing the electric near-field of an incident light wave, or of spectrally tuning the antenna characteristics via their size, shape and material.

These properties are increasingly employed for the development of high-resolution optical microscopy and spectroscopy. Using various nanofabrication techniques, suitable antenna structures can be prepared for surface-enhanced Raman spectroscopy, optical near-field scanning probes, or nano-optical (bio-)sensors [1].

By coupling the antenna structures to a second component in hybrid configurations, such as quantum dots, fluorescent molecules, or organic thin-films, the antennas can be employed to modify the absorption and emission characteristics of these objects. Key challenges in this context are the optimization of the antenna properties in view of the envisaged application, as well as achieving selective coupling of the nano-emitters [2].

Here, different techniques for the fabrication of conical plasmonic nanostructures will be shown. The linear and nonlinear optical properties of the nanocones are investigated. The nanocones are combined with semiconductor quantum dots to form hybrid antenna-emitter-structures.

## EXPERIMENTAL

Two different approaches based on electron beam lithography are applied for the fabrication of metallic nanocones, especially from gold or silver.

In the first approach a substrate, e.g. glass with a thin layer of indium tin oxide (ITO), is spin-coated with electron beam resist. The resist is exposed and developed to form a regular nanohole pattern. A metal film is evaporated on top of this pattern. During the evaporation the nanoholes are slowly closing up due to lateral deposition. This leads to the formation of tapered conical metal nanostructures inside the nanoholes. After lift-off, the resist and the metal film on top are removed, and arrays of nanocones remain on the surface.

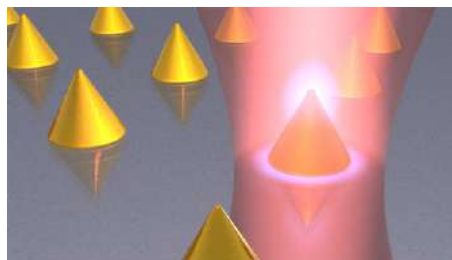


**Figure 1.** Schematic illustration of gold nanocones investigated by confocal microscopy [courtesy of D.A. Gollmer].

In the second approach, a continuous gold film of the thickness of the envisaged nanocone height is deposited on the substrate. The gold is spin-coated with electron beam resist, and a nanohole array is patterned by electron beam lithography. Aluminum oxide is deposited to form an array of nanodiscs as a hard mask on top of the gold. Both the mask and the unprotected gold are etched down by argon ion milling. In the process, gold nanostructures with sloped side-walls are forming. The etching is continued until the mask is removed and an array of gold nanocones remains.

In an additional step, the final nanocones are embedded in a resist layer that is only slightly thicker than the cone height. The top few nanometers of the cones are exposed by back-etching of the resist. Linker molecules are attached to the gold, and the sample is immersed in a solution containing semiconductor quantum dots, which are dispersed on the resist surface and the protruding cone tips. After removal of the resist, a statistical distribution between zero and few quantum dots remains fixed to the nanocone tips.

The pure plasmonic nanocones as well as the hybrid nanocone-emitter-structures are investigated by white-light dark-field scattering spectroscopy, extinction spectroscopy, confocal microscopy and spectroscopy, and lifetime measurements.

## RESULTS AND DISCUSSION

Gold and silver nanocones with dimensions on the order of 100 nm and different geometrical parameters are fabricated. Numerical simulations show that their plasmon resonance wavelengths can be shifted across the whole

visible spectrum by tuning the size and aspect ratio [3]. In simulations and experiments, tip modes (excitation parallel to the cone axis, near-field enhancement near the apex) and base modes (excitation parallel to the substrate surface, near-field enhancement at the base edges) can be distinguished, depending on the polarization of the excitation field. The plasmon modes are analysed via dark-field scattering spectroscopy and angle-dependent extinction spectroscopy. The luminescence intensity of the cones under excitation with differently polarized higher order vector beams is recorded, investigating the linear optical properties for continuous wave excitation as well as non-linear optical properties under illumination with a femtosecond laser, for which the nanocones exhibit second harmonic generation [4].

The hybrid nanoantenna-emitter-structures of gold nanocones decorated with few or single quantum dots are evaluated with respect to their emission properties [5]. The quantum dots coupled to the nanocones show higher average emission intensities and more frequent on-times in their blinking statistics than quantum dots on glass. The quantum dot emission wavelength is slightly modified through the nanocone resonance. Lifetime measurements indicate a drastic reduction of the lifetime upon coupling to the nanocone antennas by almost two orders of magnitude [6].

## **CONCLUSION**

Electron beam lithography of hole-masks with subsequent metal deposition as well as etch-mask transfer are demonstrated to yield sharp-tipped plasmonic nanocones. The cones have interesting properties for spectroscopic applications, since strong and highly localized electric near-fields can be created near their apex upon illumination. The plasmonic modes and the linear and non-linear optical response of gold nanocones with different geometrical parameters are investigated and numerically simulated. Combining gold nanocones with semiconductor quantum dots is shown to result in strongly modified emission properties of the quantum dots.

## ***Acknowledgement***

This work was performed in the context of the COST Action MP1302 Nanospectroscopy.

**REFERENCES**

- [1] Horrér, K. Krieg, K. Freudenberger, S. Rau, L. Leidner, G. Gauglitz, D. P. Kern, M. Fleischer, *Anal. Bioanal. Chem.*, 2015, **407**(27), 8225-8231.
- [2] C. Schäfer, D. P. Kern, M. Fleischer, *Lab Chip*, 2015, **15**, 1066-1071.
- [3] C. Schäfer, D. A. Gollmer, A. Horrér, J. Fulmes, A. Weber-Bargioni, S. Cabrini, P. J. Schuck, D. P. Kern, M. Fleischer, *Nanoscale*, 2013, **5**, 7861-7866.
- [4] P. Reichenbach, A. Horneber, D. A. Gollmer, A. Hille, J. Mihaljevic, C. Schäfer, D. P. Kern, A. J. Meixner, D. Zhang, M. Fleischer, *L. Eng. Opt. Express*, 2014, **22**(13), 15484-15501.
- [5] J. Fulmes, R. Jäger, A. Bräuer, C. Schäfer, S. Jäger, D. A. Gollmer, A. Horrér, E. Nadler, T. Chassé, D. Zhang, A. J. Meixner, D. P. Kern, M. Fleischer, *Nanoscale*, 2015, **7**, 14691-14696.
- [6] A. J. Meixner, R. Jäger, S. Jäger, A. Bräuer, K. Scherzinger, J. Fulmes, S. zur Oven Krockhaus, D. A. Gollmer, D. P. Kern, M. Fleischer, *Faraday Discussions*, 2015, **184**, 321-337.

## FIRST PRINCIPLES INSIGHTS IN GRAPHENE FUNCTIONALIZATION FOR ENERGY CONVERSION APPLICATIONS

I. A. Pašti<sup>1</sup>, A. S. Dobrota<sup>1</sup>, N. M. Gavrilov<sup>1</sup>, S. Gutić<sup>2</sup>,  
N. V. Skorodumova<sup>3,4</sup> and S. V. Mentus<sup>1,5</sup>

<sup>1</sup> *University of Belgrade, Faculty of Physical Chemistry, Studentski trg 12-16, 11158 Belgrade, Serbia. (igor@ffh.bg.ac.rs)*

<sup>2</sup> *Department of chemistry, Faculty of Science, Zmaja od Bosne 33-35, Sarajevo, Bosnia and Hercegovina*

<sup>3</sup> *Department of Physics and Astronomy, Uppsala University, Box 516, 751 20 Uppsala, Sweden*

<sup>4</sup> *Department of Materials Science and Engineering, School of Industrial Engineering and Management, KTH – Royal Institute of Technology, Brinellvägen 23, 100 44 Stockholm, Sweden*

<sup>5</sup> *Serbian Academy of Sciences and Arts, Knez Mihailova 35, 11000 Belgrade, Serbia*

### ABSTRACT

Developing new materials with specific properties is of crucial importance for the growing energy-related problems. Graphene is currently in the focus of the Materials Science community due to its fascinating and unique properties. Pristine graphene interacts weakly with species of interest for applications in electrochemical energy conversion systems. However, the presence of various defects and functional groups affects the electronic and chemical properties of graphene and boosts its performance for various applications. In this contribution we provide an overview of our recent theoretical results on graphene functionalization for energy conversion applications. First we show the existence of general reactivity trends for oxygen-functionalized graphene and then turn to the charge/metal ion storage capabilities of oxygen-functionalized graphene. We have shown that the charge/metal ion storage capabilities depend strongly on the type and the concentration of oxygen functional groups.

### INTRODUCTION

With the increasing world population and energy demand, energy conversion and storage have become issues of crucial importance, especially for mobile applications. Electrochemical cells for energy conversion and storage include fuel cells, batteries, and electrochemical capacitors. The

realization of high performance in such devices requires the development of novel materials. Due to its unique and extraordinary properties, graphene is a good candidate for the future energy-related applications.

Graphene [1] is a single layer of carbon atoms organized in a 2D honeycomb lattice. This zero-gap semiconductor is now in the centre of the advanced technologies due to its exceptional properties [2], such as high mechanical stiffness, good thermal conductivity and exceptional charge carrier mobility [3]. Based on these properties, graphene has found possible applications in many fields, including gas sensors [4], electronics [5], and energy storage [6,7]. Atomic-scale defects in graphene alter its physical and chemical properties and allow optimization of the material for targeted applications [8].

The mentioned electrochemical energy sources are based on various mechanisms of energy storage and conversion - from electrocatalytic reactions and pseudo-faradaic processes to purely adsorptive processes. Computational methods have proved to be powerful tools for investigating crucial steps of catalytic cycles and revealing the key characteristics of a catalyst, while providing insights for the design of materials with superior catalytic activity [9].

In this contribution we provide an overview of our recent theoretical graphene-related research with the focus on the application of functionalized graphene-based materials in the field of energy conversion.

## COMPUTATIONAL DETAILS

The calculations were based on DFT within the generalized gradient approximation employing Perdew–Burke–Ernzerhof exchange correlation functional [10], using ultrasoft pseudopotentials as implemented in the PWscf code of Quantum ESPRESSO distribution [11]. The core of the present research lies in the investigation of the interactions of different species with functionalized graphene. The interaction of different chemical species with functionalized graphene models was quantified in terms of the adsorption energies ( $E_{\text{ads}}$ ), defined as:

$$E_{\text{ads}}(\text{X}) = E_{\text{subs+X}} - (E_{\text{subs}} + E_{\text{X,isol}}) \quad (1)$$

where  $E_{\text{subs+X}}$ ,  $E_{\text{subs}}$  and  $E_{\text{X,isol}}$  stand for the total energies of the substrate with adsorbed chemical specie X (such as H, Pt, or alkali metal atoms, depending on the specific field of interest), of the bare substrate and of an isolated specie X. 3D charge difference plots ( $\Delta\rho$ ) were made based on the equation:

$$\Delta\rho = \rho_{\text{subs+X}} - (\rho_{\text{subs-X}} + \rho_{\text{X}}) \quad (2)$$

where  $\rho_{\text{subs+X}}$ ,  $\rho_{\text{subs-X}}$  and  $\rho_{\text{X}}$  stand for the ground state charge densities of the system with adsorbed X, the system without X (frozen geometry) and of isolated X.

## RESULTS AND DISCUSSION

In the forthcoming sections we overview some of the results we have obtained regarding graphene functionalization and its energy-related applications. First we address general reactivity trends of oxygen-functionalized graphene, and then consider graphene functionalization for its application in metal-ion batteries and electrochemical capacitors.

### a) General trends in the reactivity of the oxygen-functionalized graphene basal plane

We have analysed the adsorption of H, OH, Cl and Pt on three models of graphene functionalized by epoxy and hydroxyl groups [12]. The basal plane of oxidized graphene exhibits enhanced chemisorption properties towards H, OH and Pt, due to the deformation of the basal plane, resulting in the formation of surface dangling bonds, further tuned by specific oxygen functional groups. On the other hand, the affinity towards Cl is decreased. Clear scaling relations between the adsorption energies of different adsorbates have been revealed, which brings a possibility of using a single adsorbate to obtain a general picture of the reactivity of the oxidized graphene's basal plane [12]. The electronic states of carbon atoms located up to 2 eV below the Fermi level ( $E_{\text{F}}$ ) are found to be responsible for the chemical bonding of the investigated adsorbates to the basal plane. We have confirmed that the adsorption energy of hydrogen atoms scales with the number of states found in the energy window located between  $-2$  and  $0$  eV vs.  $E_{\text{F}}$  (Fig. 1), indicating that the adsorption will be stronger if there are more electronic states close to the Fermi level.

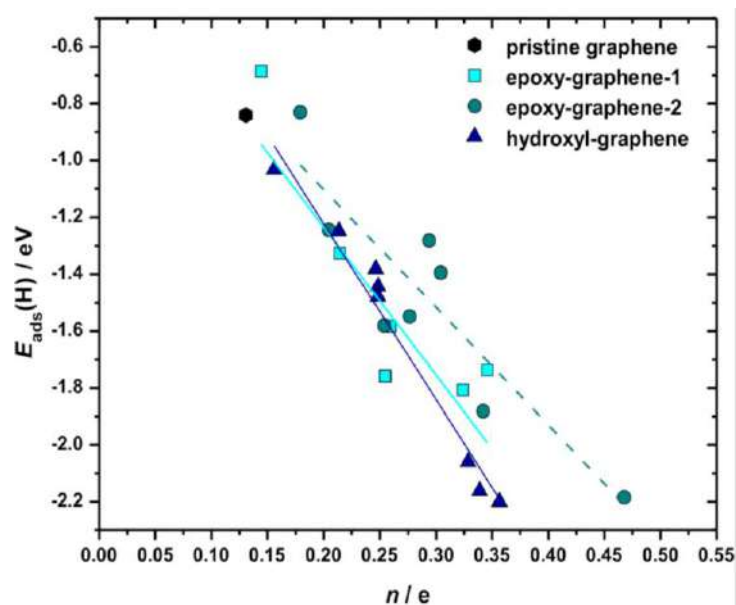


**Figure 1.** Correlation between  $E_{\text{ads}}(\text{H})$  and the number of states found between  $-2$  eV and  $E_F$  for three models of oxidized graphene.

### b) Oxidized graphene as an electrode material for charge storage applications – DFT insights

In our recent study [13] we have found that the epoxy groups are redox active, which can provide a mechanism for the metal ion storage on O-functionalized graphene: alkali metal atoms transfer their valence electron to oxidized graphene, resulting in purely ionic bonding, and +1 valence state of the metal. Isolated hydroxyl groups, however, upon the interaction with alkali metal atoms result in MOH as a by-product (Fig. 2). The strength of the interaction of these functionalized graphene surfaces is much larger compared to that with pristine graphene. The type and content of O-groups on graphene should be carefully chosen to maximize the charge storage capabilities: the oxidation level needs to be high enough, to provide high storage capability via present O-functional groups, but at the same time, low enough, to avoid performance loss caused by the reduced conductivity. Moreover, we have observed that the chemical environment of the oxygen-functional groups, such as epoxy-group, can significantly affect the interaction with alkali metal atoms, and ultimately energy storage capabilities of functionalized graphene (Fig. 3).

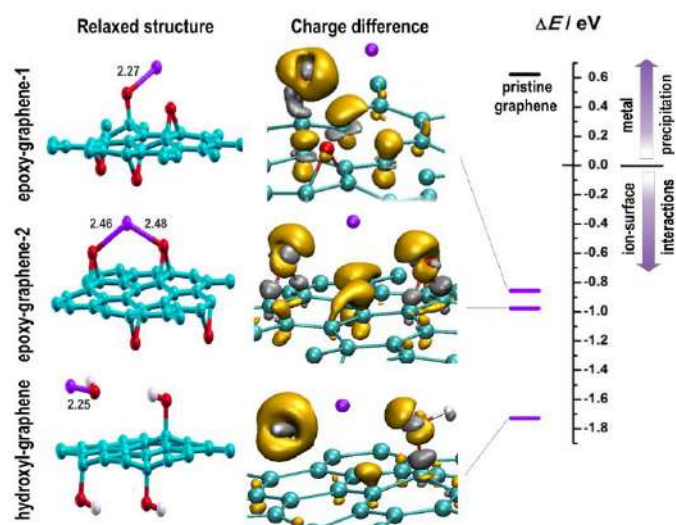


**Figure 2.** Relaxed structures, charge difference plots, and Na adsorption energies with respect to free metal phase ( $\Delta E$ ) for three models of rGO. Yellow isosurfaces indicate charge gain, while gray isosurfaces indicate charge loss. Isosurface values are  $\pm 0.0033 \text{ e \AA}^{-1}$ .

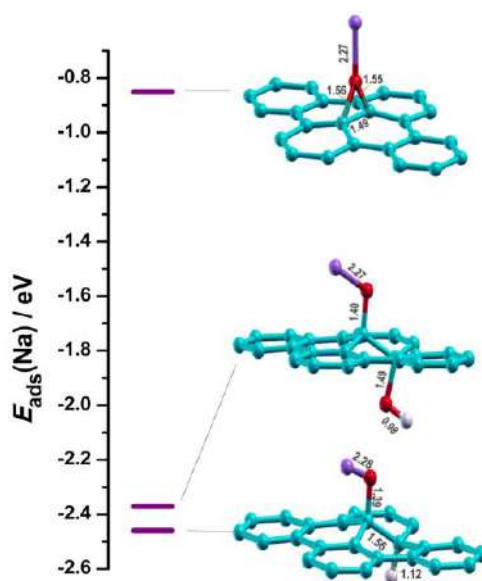


**Figure 3.** Na atom adsorption energy on epoxy-functionalized graphene depending on the chemical environment of the epoxy group.

While the first calculations suggested that OH groups should be avoided in order to prevent separation of metal-hydroxide phase [13], but there are some direct experimental observations of the reversible interaction of  $\text{Li}^+$  ions with hydroxyl groups on graphene [14]. This issue was further investigated in a combined theoretical and experimental study [15], in which alkali metals interaction with  $n\text{OH}$ -graphene systems were probed ( $n = 1-5$ ). OH groups exhibit a clustering tendency on the graphene basal plane, driven by minimal  $\pi$  cloud disruption and maximal hydrogen bonding between neighbouring OH groups. This clustering of OH groups was found to prevent irreversible reduction of the substrate through MOH or  $\text{H}_2\text{O}$  formation, as with the addition of each OH group, integral OH adsorption energy decreases. The analysis of charge redistribution has showed that the alkali metal's valence  $s$  electron causes weakening of charge depletion in the region of C–OH and O–H bonds, while both OH groups and certain domain of the  $\pi$  electronic system is involved in charge storage (Fig. 4).

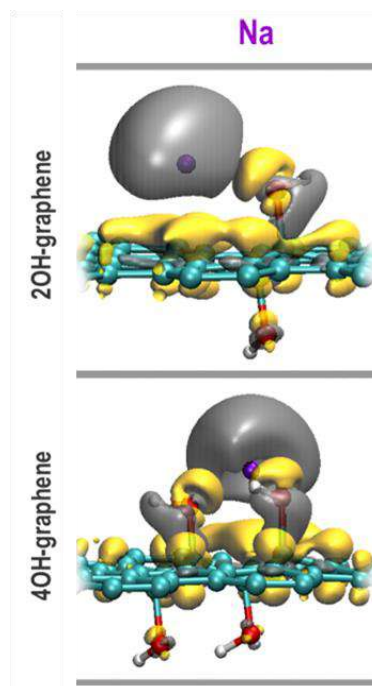


**Figure 4.** Charge redistribution analysis of Na adsorption on OH functionalized graphene in the case where OH clustering takes place. Dark domains indicate charge depletion.

## CONCLUSION

In this contribution we have overviewed our recent theoretical findings related to graphene functionalization for energy conversion application. In specific we have demonstrated the existence of the general reactivity trends in the case of O-functionalized graphene and further analyzed the interactions of differently O-functionalized graphene with alkali metal atoms. The later is specifically connected to the fields of metal-ion batteries and electrochemical capacitors. We have showed that it is possible to tune charge storage capabilities of O-functionalized graphene and that the charge storage capacity depends on the type and the concentration of the oxygen functional groups. It should be noted that presented research barely touches many possible fields of application of functionalized graphene and that there

is a constantly growing interest in this field as theoretical methods can provide very accurate information on the physical and chemical properties of functionalized graphene.

### *Acknowledgement*

This work was supported by the Swedish Research Links initiative of the Swedish Research Council (348-2012-6196). Computational resources are provided by the Swedish National Infrastructure for Computing (SNIC). I. A. P., A. S. D., N. M. G., and S. V. M. acknowledge the support provided by the Serbian Ministry of Educations, Science and Technological Development through the project III45014. Partial financial support is also provided through the NATO multi-year Science for Peace Project EAP.SFPP 984925 - "DURAPEM - Novel Materials for Durable Proton Exchange Membrane Fuel Cells".

### **REFERENCES**

- [1] K.S. Novoselov, A. K. Geim, S. V. Morozov, D. Jiang, Y. Zhang, S. A. Dubonos, I. V. Grigorieva, A.A. Firsov, *Science*, 2004, **306** (5696), 666-669.
- [2] A. K. Geim, K. S. Novoselov, *Nature Mater.*, 2007, **6**( 3), 183-191.
- [3] M. Orlita, C. Faugeras, P. Plochocka, P. Neugebauer, G. Martinez, D. K. Maude, A. L. Barra, M. Sprinkle, C. Berger, W.A. de Heer, M. Potemski, *Phys. Rev. Lett.*, 2008, **101**(26), 267601.
- [4] J. D. Fowler, M. J. Allen, V. C. Tung, Y. Yang, R.B. Kaner, B.H. Weiller, *ACS Nano*, 2009, **3** (2), 301-306.
- [5] J. U. Park, S. Nam, M. S. Lee, C. M. Lieber, *Nature Mater.*, 2012, **11** (2), 120-125.
- [6] M. D. Stoller, S. Park, Y. Zhu, J. An, R. S. Ruoff, *Nano Lett.* **8** (10), 3498-3502,
- [7] C. Wang, D. Li, C.O. Too, G. G. Wallace, *Chem. Mater.*, 2009, **21** (13), 2604-2606.
- [8] A. Hashimoto, K. Suenaga, A. Gloter, K. Urita, S. Iijima, *Nature*, 2004, **430** (7002), 870-873.
- [9] I. A. Pažiti, N. V. Skorodumova, S. V. Mentus, *React. Kinet. Mech. Cat.*, 2015, **115** (1), 5-32.
- [10] J. P. Perdew, K. Burke, M. Ernzerhof, *Phys. Rev. Lett.*, 1996, **77** (18), 3865–3868.
- [11] P. Giannozzi, S. Baroni, N. Bonini, M. Calandra, R. Car, C. Cavazzoni, D. Ceresoli, G. L. Chiarotti, M. Cococcioni, I. Dabo, A. D. Corso, S. Fabris, G. Fratesi, S. de Gironcoli, R. Gebauer, U. Gerstmann, C. Gougoussis, A. Kokalj, M. Lazzeri, L. Martin-Samos,

- N. Marzari, F. Mauri, R. Mazzarello, S. Paolini, A. Pasquarello, L. Paulatto, C. Sbraccia, S. Scandolo, G. Sclauzero, A.P. Seitsonen, A. Smogunov, P. Umari, R. M. Wentzcovitch, *J. Phys.: Condens. Matter*, 2009, **21** (39), 395502.
- [12] A. S. Dobrota, I. A. Pažiti, S. V. Mentus, N. V. Skorodumova, *Phys. Chem. Chem. Phys.*, 2015, **18** (9), 6580-6586.
- [13] A. S. Dobrota, I. A. Pažiti, N. V. Skorodumova, *Electrochim. Acta* 2015, **176**, 1092–1099.
- [14] S. H. Ha, Y.S. Jeong, Y. J. Lee, *ACS Appl. Mater. Interfaces*, 2013, **5**, 12295-12303.
- [15] A. S. Dobrota, S. Gutić, A. Kalijadis, M. Baljuzović, S. V. Mentus, N. V. Skorodumova, I. A. Pažiti, *RSC Adv.*, 2016, **6**, 57910 -57919.

## DYNAMICAL INSTABILITIES IN ELECTROCHEMICAL SYSTEMS

V.Gáspár<sup>1</sup> and I. Z. Kiss<sup>2</sup>

<sup>1</sup>*Department of Physical Chemistry, University of Debrecen  
4002 Debrecen, P.O Box 400, Hungary  
(gaspar.vilmos@science.unideb.hu)*

<sup>2</sup>*Department of Chemistry, Saint Louis University  
3501 Laclede Ave., St. Louis, MO 63103, USA*

### ABSTRACT

Electrochemical cells often exhibit instabilities that can result in temporal current/potential oscillations of reaction rate over the electrode surface. The complexity arises from the interplay of nonlinear chemical reactions and various physical processes. In this plenary lecture, the characterization, description, and control of different temporal phenomena are reviewed based mainly on our long series of experiments performed during the last twenty years by systematically studying the dynamics of the anodic electro-dissolution of a rotating copper disk electrode in phosphoric acid electrolyte.

We start with a theoretical introduction to the origin and classification of dynamical instabilities in electrochemical systems, and follow by the characterization of nonlinear phenomena occurring at different experimental conditions by varying the rotation rate, external resistance, temperature, etc. Basic experimental methods and data processing algorithms are discussed briefly. We then overview the results on the investigation of bistability, oscillations, chaos, and multirhythmicity in the studied electrochemical system. We close with a short outlook toward practical applications.

The lecture is based on the following two publications:

- [1] Kiss, I.; Nagy, T.; Gáspár, V.: *Dynamical Instabilities in Electrochemical Processes*, Handbook of Solid State Electrochemistry, 2011, **2**, 125-178. ISBN-10: 3-527-32638-3..
- [2] Nagy, T.; Verner, E.; Gáspár, V.; Kori, H.; Kiss, I.: Delayed feedback induced multirhythmicity in the oscillatory electro-dissolution of copper, *Chaos: An Interdisciplinary Journal of Nonlinear Science*, 2015, Art. No. 064608

## UNIVERSAL METHOD ACROSS DIFFERENT AREA OF SCIENCES AND TRANSIENT OF KNOWLEDGE FLOWS

Katica R. (Stevanović) Hedrih<sup>1,2</sup>

<sup>1</sup>*Department of Mechanics, Mathematical Institute Serbian Academy of Sciences and Arts, Belgrade, Serbia.*

<sup>2</sup>*Faculty of Mechanical Engineering, University of Niš, Serbia  
e-mails: khedrih@sbb.rs, khedrih@eunet.rs.*

### ABSTRACT

Under the author's use of Petrović's "Elements of mathematical phenomenology", especially qualitative and mathematical analogy, new analogous models and phenomena in dynamics of physically disparate nature systems and between them of mechanical, physic-chemical, electrical and biodynamical oscillators are pointed out.

Use these results, author plan to present an optimal method for multidisciplinary research and education not only in special an area of science, but in other disparate area of science for education, not only for students, but also for scientific researchers. Numerous examples will be presented for illustration of the method of optimal and most effective power of research coupling models and methods across all, "for first look" pure disparate area of sciences. Also series of analogous theorems about energy in fractional order discrete and multi-deformable body systems and chain mechanical, electrical and biodynamical oscillators will be presented.

Advances to theory of collision between bodies and its generalization (use Petrović's theory) to the collision between two rolling rigid bodies will be presented.

The basic idea given by Mikhailo Petrović and elaborated in his two books entitled: Elements of mathematical phenomenology and Phenomenological mappings is applied here on one physic-chemical reaction system and a rheonomic nonlinear mechanical system. In particular, in both nonlinear systems the local dynamic nonlinear phenomena around stationary states are analyzed by the phenomenological approximate mappings.

**KEYWORDS:** Mikhail Petrović's theory, mathematical phenomenology, linear and nonlinear phenomena, stationary states, trigger of coupled singularities, qualitative and mathematical analogy, physically disparate systems, universal method across different area of sciences, transient of knowledge flow.

## INTRODUCTION

Nonlinear Dynamics (see Reference [1]) reaches across the whole range of scientific research and study, and is applied in fields as diverse as mechanics, complete interdisciplinary area of physics, chemistry, physical chemistry, mechanical, electrical and civil engineering, technology, biology, biogenetics, economics and medicine. Phenomenological mapping and mathematical analogy (see Reference [2]) are very important for transfer knowledge and new scientific research results from one area of science through other disparate area of sciences. For that reason is very important that scientists understand each other in use different key words and terms as well as notations in presenting new knowledge about nonlinear phenomena and new methods for investigation and research in different area of sciences. In cited References [1,2], it was pointed out that for understanding between researchers working in different area of sciences and disparate area of sciences is very important to have a universal dictionary of basic terms with list of different named of phenomena and properties descriptions as well as mathematical descriptions. For example, in Reference [1], a short list of main basic terms and nonlinear phenomena in the form of a general dictionary, containing main keywords with corresponding definitions and mathematical descriptions through presentation a number of dynamical system models as abstraction of real nonlinear dynamics is presented. Also, a number of the methods applied in nonlinear dynamics research are presented.

In reference [2], phenomenological approximate mapping as a universal method of nonlinear dynamics is presented. The basic idea given by Mihailo Petrović and as a complete theory, elaborated in his two books entitled: *Elements of mathematical phenomenology* [3] and *Phenomenological mappings* [4], is applied in the Reference [2] on one physic-chemical reaction system and a mechanical system. In particular, in both nonlinear systems the local dynamic nonlinear phenomena around stationary states are analyzed by the phenomenological approximate mappings. A general table with phenomenological linear and nonlinear approximate mappings around singular states was presented. For details see also References [5,6]. Under the author's use of Petrović's elements of mathematical phenomenology, especially mathematical analogy (see References [7-20]), new results are obtained and published. Use these results, author plan to present an optimal method for education not only in area of mechanics, but in other disparate area of science for education, but not only for education of the students, but also for scientific researchers.

In present literature no numerous known fully described examples with analogous models with physically disparate matire. Some more known is electro-mechanical analogy between mechanical and electrical oscillators. But in scientific literature are numerous new scientific results and examples of models and dynamics for which will be possible to indicate as pairs for illustration of the method of optimal and most effective power of education as well as future research. Starting by logical analogy and qualitative analogy and, also using structural and mathematical analogies as elements of mathematical phenomenology and phenomenological precise or approximate mappings in analysis of kinetic parameters of disparate nature system dynamics, new technology of complex general educations appear, as very economic method for education with possibility that student can logical power for transfer known knowledge from one to other not earlier known area of study or education.

#### **MIHAILO PETROVIĆ'S THEORY: ELEMENTS OF MATHEMATICAL PHENOMENOLOGY**

Complete theory under the title: "*Elements of Mathematical Phenomenology*" [3], from 1911, is published on 789 pages and title "*Phenomenological Mappings*" [4], issued in 1933 on 33 pages, contain fundamental and basic ides, which from time to time appear in current scientific publications. These cited Petrović's publications contain general theory of Elements of Mathematical Phenomenology and Phenomenological Mappings, but both books were published in Serbian and no visible from other world languages. A short presentation of this book was in France, but not in integral form [5]. Now, let's present some basic parts of the published theory: Elements of Mathematical Phenomenology. We list only key elements and titles and sub-titles, for obtaining general view of numerous ideas and organization of this fundamental book or theory. For this Petrović's Elements of Mathematical Phenomenology, Milutin Milanković (author of world known famous Canon of Sun insulation) and one of three important Serbian, and also, world scientists (first is Tesla Nikola –Unit "Tesla" and second Mihaio Pupin, Rector of Columbia University in New York) evaluate this book as some important in Petrović's scientific results, but understandable only for two persons, both Serbian scientist in this period, and no readable for other world scientists because is published in Serbian Language.

Introducing part is titled: Some elements of multi-dimensional geometry, and then in first subsection take into presentation Elements for descriptions of phenomena and their mechanisms. These elements are elements for schematically and analytical descriptions. Second part is titles: Coupling

between mechanisms and manifestation of phenomena in which present: Basic differential equations for description of simple and complex phenomena. In next sections general transformations of differential equations are presented. Third part is dedicated to transformation of equations for phenomenon in holonomic systems, and fourth part is dedicated to potential phenomena. In this part, the systems of Appell's and Lagrange's equations are presented and analyzed. Third section is under the subtitle: The immediate consequence of phenomenological differential equations, in which it is presented, stationary phases of phenomena. In next section, Petrović present proper theory of the viva forces and their phenomenological consequences. This subsection is very important for new quality that Petrović point out proper separation in its proper approaches and differences from pure geometrical and introducing approach in dynamics of systems, usually no understandable for pure mathematicians. This is very important part and point of view to geometry and dynamics.

In next section action of discontinuous causes is presented. In the fourth section studies the events of occurrence as a result of its composition mechanisms are presented. The head of the headlines are: Quantitative and qualitative images of appearances (phenomenons).

Fifth part is under the title: The composition and patterns of phenomenological mechanisms, within which combinations and distribution role in the mechanisms of emergence and activation activity in the mechanisms of occurrence are studied. The sixth chapter is entitled: Phenomenological analogies which include following heads: Mathematical analogies and qualitative analogy.

Mihailo Petrović [6,18] is one of three doctoral students of world known scientist Julius Henri Poincare.

In author cited References logical and structural analogies are additionally defined. These four types of analogies: logical, qualitative, structural and mathematical analogies are optimal and power scientific tools for education students and researchers across different area of sciences and especially across Theoretical and applied mechanics: Theory of elasticity, kinematics, dynamics, and theory of oscillations, fluid mechanics. Also, using analogous models of physically disparate dynamical systems is possible to optimize education across different area of science as it is qualitative and mathematical analogies between mechanical oscillators and electrical circuit's oscillators.

### EXAMPLES OF DIFFERENT TYPES OF THE ANALOGIES

Comparing three publications: Mihailo Petrović's theory: Mathematical Phenomenology[3] first published 1911, Roger Penrose: The Emperor's New Mind, concerning Computers, Minds and the Laws of Physics [25], published by Oxford University Press in 1985/ 1990 and James Gleick, Chaos: Making a new Sciences, published by Penguin BOOKS, in 1987/1988 we can identify numerous analogous phenomena and dynamics in physically disparate nature systems, but presented by different tools, mathematical and computer graphics depending of period of publishing and level of knowledge. These three cited books contain analogous examples of analogous nonlinear phenomena existing in disparate nature nonlinear dynamical system. It is not difficult to identify analogous elements of mathematical phenomenology. All these examples are useful for large-scale education of the students in nonlinear dynamics.

In References [7-20] numerous examples of analogous models and dynamic of mechanical and electrical systems useful in process of education in Theoretical and Applied Mechanics are presented. A chooses of these are:

\* Mathematical analogies between vector models in local area of stress state, strain state of the point in stressed and deformed deformable body as well as with vector model of the mass inertia moment state at point of rigid body, used mass inertia moment vectors coupled for pole and axis;

\* Mathematical analogies between theorems of linear momentum conservation and theorem of angular momentum conservation and other kinetic parameters between collision of two bodies in translational motions and collision between two rolling bodies in pre- and post-collision kinetic states.

### EXAMPLE OF ANALOGY BETWEEN NONLINEAR DYNAMICS OF A PHYSICO-CHEMICAL OSCILLATOR AND A MECHANICAL RHEONOMIC OSCILLATOR

Let us consider nonlinear dynamics of two concentrations  $a$  and  $b$  of species A and B with a cubic autocatalytic reaction in an open reactor (Continuous Stirred Tank Reactor - CSTR) presented in Reference [21] and analysed in Reference [2]):  $A + 2B \rightarrow 3B$  ( $v = kab^2$ ). The time evolution of the concentrations of species A and B denoted by  $a$  and  $b$ , are described by the following first order nonlinear differential equations (for detail see References: [22] and [2]):

$$\frac{da}{dt} = k_f(a_o - a) - kab^2, \quad \frac{db}{dt} = k_f(b_o - b) + kab^2 \quad (1)$$

where  $a_0$  and  $b_0$  are constants as a consequence of permanent inflow of them and outflow of surplus of reaction mixture. Hence, the volume of reaction mixture in stationary state is also constant.

In the stationary states  $\frac{da}{dt}=0$  and  $\frac{db}{dt}=0$ . From these conditions it is possible to obtain one linear algebra equations and one nonlinear algebra cubic equation in the following form:

$$(a_o - a_s) + (b_o - b_s) = 0, \quad a_s^3 - 2pa_s^2 + qa_s - \beta a_o = 0 \quad (2)$$

where the following denotations are introduced:

$$p = [a_o + b_o], \quad q = \left[ \frac{k_f}{k} + (a_o + b_o)^2 \right], \quad \beta = \frac{k_f}{k} \quad (3)$$

Cubic equation from (2), in general case, posses three roots, which can be denoted by  $a_s$ ,  $s = 1, 2, 3$ . Taking into account linear algebra equation from (2) there is corresponding pair of stationary state concentrations  $a_s, b_s = (a_o - a_s) + b_o$ ,  $s = 1, 2, 3$ . These pairs of roots  $a_s$ , and  $b_s = (a_o - a_s) + b_o$ ,  $s = 1, 2, 3$  present three possible stationary states or singular points considered nonlinear reaction system described by the first order nonlinear differential equations (1). From the first order nonlinear differential equations (1), taking into account that  $a_0$  and  $b_0$  are constants, integration give:

$$[(a+b) - (a_o + b_o)] = [(a(t_0) + b(t_0)) - (a_o + b_o)] e^{-k_f [(a+b) - (a_o + b_o)] (t-t_0)} \quad (4)$$

where  $a(t_0)$  and  $b(t_0)$  are initial concentrations of species A and B. If we take at initial moments  $t_0 = 0$ , that  $a_o$  and  $b_o$  are concentrations of species A and B,  $a(t_0) = a(0) = a_o$  and  $b(t_0) = b(0) = b_o$ , then we obtain that  $(a+b) = (a_o + b_o) = (a_s + b_s)$ ,  $s = 1, 2, 3$  if cubic algebra equation posses three real roots. This relation is valid at initial state, at stationary states and at arbitrary states for special case that initial values of concentrations  $a = a(t)$  and  $b = b(t)$  of species A and B are  $a(t_0) = a(0) = a_o$  and  $b(t_0) = b(0) = b_o$ . Depending of values of parameters  $k_f$ ,  $k$ ,  $a_o$  and  $b_o$  three stationary states will appear and coexist all together. They will appear or disappear in related bifurcation points. From this point of view,  $k_f$ ,  $k$ ,  $a_o$  or  $b_o$  are bifurcation parameter. From expression (4) we can write  $b = (a_o + b_o) - a - [(a_o + b_o) - (a(0) + b(0))] e^{-k_f t}$  and introducing in first nonlinear differential equation (1), after denotation

$$k_{f0} = k_f + k(a_o + b_o)^2; \quad k_{01} = k(a_o + b_o)[(a_o + b_o) - (a(0) + b(0))]$$

$$k_{02} = k[(a_o + b_o) - (a(0) + b(0))]^2; k_o = k(a_o + b_o); k_{oo} = k[(a_o + b_o) - (a(0) + b(0))]$$

we obtain:

$$b = \frac{1}{k} \langle k_o - ka - k_{oo} e^{-k_f t} \rangle$$

$$\frac{da}{dt} = k_f a_o - a \langle k_{f0} - 2k_{o1} e^{-k_f t} + k_{o2}^2 e^{-2k_f t} \rangle + 2a^2 \langle k_o + k_{oo} e^{-k_f t} \rangle - ka^3 \quad (5)$$

$$\frac{db}{dt} = \frac{k_{oo} k_f}{k} e^{-k_f t} - k_f a_o + a \langle k_{f0} - 2k_{o1} e^{-k_f t} + k_{o2}^2 e^{-2k_f t} \rangle - 2a^2 \langle k_o + k_{oo} e^{-k_f t} \rangle + ka^3$$

Also, it is possible to obtain the following rheonomic nonlinear differential equation in the form:

$$\frac{d^2 a}{dt^2} + \frac{da}{dt} \langle 3ka^2 - 4a(k_o + k_{oo} e^{-k_f t}) + k_{f0} + 2k_{o1} e^{-k_f t} + k_{o2} e^{-2k_f t} \rangle + 2k_f a \langle k_{o1} e^{-k_f t} - k_{o2} e^{-2k_f t} \rangle + 2a^2 k_f k_{oo} e^{-k_f t} = 0 \quad (6)$$

Previous rheonomic nonlinear differential equation correspond to mathematical description of a rheonomic nonlinear forced oscillator with one degree of freedom with dissipative rheonomic and nonlinear force and spring with rheonomic coefficient of linear rigidity and also nonlinear rheonomic rigidity, depending nonlinear of spring elongation and time.

We can conclude an analogy between nonlinear phenomena in nonlinear dynamics of two concentrations  $a$  and  $b$  of species A and B with a cubic autocatalytic reaction in an open reactor (Continuous Stirred Tank Reactor - CSTR) described by autonomous system of nonlinear differential equations (1) and nonlinear dynamics of a rheonomic nonlinear oscillator with one degree of freedom under dissipative rheonomic and nonlinear force and rheonomic nonlinear spring with rheonomic coefficient of linear and nonlinear rigidity with restitution force depending nonlinear of spring elongation and time described by rheonomic nonlinear differential equation (6). Taking into account rheonomic nonlinear differential equation (6) with additional first relation from (5) is possible after transformation obtain autonomous system of nonlinear differential equation (1). Then, if we take  $a$  and  $b$ , as phase coordinates of rheonomic nonlinear mechanical oscillator, in this phase plane is possible to use all scientific results obtained as nonlinear phenomena in nonlinear dynamics of two concentration in open reactor for analysis nonlinear phenomena of rheonomic nonlinear mechanical oscillator in phase plane  $(a, b)$ .

## CONCLUSION

On the basis of the elements of mathematical phenomenology, scientific results in World research progress, is possible to classify in the few numbers

of the following two groups: \* elements of mathematical phenomenology on the basis of non-linear phenomena in different area of sciences and identification of general methods applicable, as mathematical tools, in investigation of non-linear dynamics in different area of sciences; and \* elements of phenomenological precise or approximate mappings on the basis of investigation series of similar types of nonlinear phenomena in global or local area of system dynamics using qualitative, structural or mathematical analogies and similarities. Presented approach is an optimal method for education in the Theoretical and Applied Mechanics, and also in other area of education and research.

### *Acknowledgement*

This work was supported by the Ministry for Science of the Republic of Serbia (Grant No. ON174001) through Mathematical Institute SANU Belgrade and FME University of Niš.

### REFERENCES

- [1] K. Hedrih (Stevanović), Proceedings of 11th International Conference of fundamental and Applied Aspects of Physical Chemistry, PHYSICAL CHEMISTRY 2012, Belgrade. 24-28 September 2012, **I**, 13-33.
- [2] K. Hedrih (Stevanović), Proceedings of the 12<sup>th</sup> International Conference on Fundamental and Applied Aspects of Physical Chemistry, Editors A. Antić-Jovanović and S. Anić, Belgrade, September 22-26, 2014, **I** 328-335.
- [3] M. Petrović, Elementi matematičke fenomenologije (Elements of mathematical phenomenology), Srpska kraljevska akademija, Beograd, 1911, 789 (in Serbian)
- [4] M. Petrović, Fenomenološko preslikavanje (Phenomenological mapp), Srpska kraljevska akademija, Beograd, 1933. str. 33.
- [5] M. Petrović, Mecanismes communs aux phenomenes disparates, Paris 1921.
- [6] M. Petrović, (1868-1943), [http://en.wikipedia.org/wiki/Mihailo\\_Petrovi%C4%87](http://en.wikipedia.org/wiki/Mihailo_Petrovi%C4%87)
- [7] K. Hedrih (Stevanović), (2015), Elements of mathematical phenomenology: I. Mathematical and qualitative analogies, Труды МАИ. Выпуск №84, pp. 42 (1-42).
- [8] K. Hedrih (Stevanović), (2015), Elements of mathematical phenomenology:II. Phenomenological approximate mappings, Труды МАИ. Выпуск №84, pp. 29 (1- 29).
- [9] K. Hedrih (Stevanović), Theoretical and Applied Mechanics, 2014, **41** (S1), 43-61.
- [10] K. Hedrih (Stevanović), International Journal of Structural Stability and Dynamics, 2013, **13** (7), 1340007
- [11] K. Hedrih (Stevanović), (2001), Vector Method of the Heavy Rotor Kinetic Parameter Analysis and Nonlinear Dynamics, University of Niš 2001, Monograph, p. 252. (in English).

- [12]K. Hedrih (Stevanović), The eleventh world congress in Mechanism and machine Sciences, IFToMM, Proceedings, China Machine press, Tianjin, China, April 1-4, 2004, **2**, 1475-1479.
- [13]K. Hedrih (Stevanović), , The 5th International Congress of Serbian Society of Mechanics. Arandjelovac, Proceedings Published by Serbian Society of Mechanics and Faculty of Technical Sciences, Novi Sad, June 15-17, 2015, pp. 98-98. pp. 1-4.
- [14]K. Hedrih (Stevanović), (2005), Chaotic Dynamics and Control of Systems and Processes in Mechanics (Eds: G. Rega, and F. Vestroni), IUTAM Book, in Series Solid Mechanics and Its Applications, Edited by G.M.L. Gladwell, Springer, 2005, 37-45.
- [15]Preface: Elements of mathematical phenomenology and phenomenological mapping in non-linear dynamics, Edited by Katica R. (Stevanovic) Hedrih, Ivan Kosenko, Pavel Krasilnikov and Pol D. Spanos, Special Issue of International Journal of Non-Linear, Mechanics, 2015, **73**, 1-128
- [16]Katica (Stevanović) Hedrih, Mechatronics and control, colloquium in honour of the 65th birthday of prof. Nenad D. Pavlović and prof. Tomislav Petrović, The 3<sup>rd</sup> International conference mechanical engineering in xxi century, proceeding, September 17 - 18, Niš, Faculty of mechanical engineering University of Niš, 2015, 313-318.
- [17]K. Hedrih (Stevanović), A. N Hedrih , Journal of Vibration and Control, 2016, **22**, 18-36,
- [18]K. Hedrih (Stevanović), Beseda o Mihailu Petroviću i fascinantnoj nelinearnoj dinamici, Srpski matematičari, Maj mesec matematike -- Srpski matematičari , Naucni skup maj 2012, Srpska akademija nauka I umetnosi, Univerzitet u Beogradu, Zavod za izdavanje udžbenike, Beograd 2015, 29-64.
- [19]K. Hedrih (Stevanović), A. Ivanović-Šašić, J. Simonović, Lj. Kolar-Anić, Ž. Čupić, Scientific Technical Review, 2015, **65** (3), 27-38.
- [20]K. Hedrih (Stevanović), J. Simonović, A. Ivanović-Šašić, Lj. Kolar-Anić, Ž. Čupić, Scientific Technical Review, 2015, **65** (3), 37-45.
- [21]Lj. Kolar-Anić, Ž . Čupić, V. Vukojević, S, Anić, S., Dinamika nelinearnih procesa, Fakultet za fizičku hemiju, Univerzitet u Beogradu, Beograd 2011.
- [22]S. Maćešić , Ž. Čupić, S. Anić, Lj. Kolar-Anić, International Journal of non-linear mechanics, 2015, **73**, 25-30.
- [23]Yu. A. Mitropolyskiy, (1955), Nestashionamie proshesi v nelineyeynih sistemah, AN USSR, Kiev. (in Russian)
- [24]Gleick James, Chaos, Making a new Sciences, Penguin BOOKS,1987/1988.
- [25]Penrose Roger, The Emperor's New Mind, concerning Computers, Minds and the Laws of Physics, Oxford University Press 1985/ 1990.

*B - Spectroscopy,  
Molecular Structure,  
Physical Chemistry of Plasma*



## THE ANALYTICAL CAPABILITY OF LASER INDUCED BREAKDOWN SPECTROSCOPY (LIBS) BASED ON TEA CO<sub>2</sub> LASER SYSTEM

J. Savović<sup>1</sup>, S. Živković<sup>1</sup>, M. Momčilović<sup>1</sup>, M. Trtica<sup>1</sup>, M. Stoiljković<sup>1</sup>  
and M. Kuzmanović<sup>2</sup>

<sup>1</sup> *University of Belgrade, Institute of Nuclear Sciences Vinca,  
Mike Alasa 12-14, 11001 Belgrade, Serbia. (lelas@vin.bg.ac.rs)*

<sup>2</sup> *University of Belgrade, Faculty of Physical Chemistry,  
Studentski trg 12-16, 11001 Belgrade, Serbia.*

### ABSTRACT

This paper gives an overview of analytical capabilities of the laser induced breakdown spectroscopy (LIBS) system, based on Transversely-Excited Atmospheric pressure (TEA) CO<sub>2</sub> laser, and time-integrated, spatially-resolved detection, for the analysis of solid materials. The developed LIBS system is unique, and differs from the commonly used systems in two respects. The first one is the laser used as an energy source for plasma generation, and the second one is the applied non-gated detection scheme. Various types of materials were analyzed, from metals to biological samples, under different experimental conditions. The obtained results were critically evaluated and compared to the results obtained using commercially available LIBS that comprises Nd:YAG laser and time-gated detection. It was concluded that when it comes to detectability, precision and sensitivity, this simple and cost effective LIBS system may be regarded highly competitive to standard LIBS systems.

### INTRODUCTION

LIBS is a contemporary optical emission spectroscopy method that uses the optical signal from laser-generated plasma to study elemental composition of a sample. In this technique, laser radiation interacts with the material causing its ablation, vaporization, ionization and, at sufficiently high power densities, creation of plasma of the irradiated material. In plasma, the species are excited to emit element specific radiation which is analyzed by the spectrometer. Using the information provided by emission spectra, both qualitative and quantitative analysis could be performed. In a review article by Hahn and Omenetto [1], unique features of LIBS were summarized in one sentence: "Suffice it to say that LIBS, in principle, can directly address and simultaneously detect all neutral and ion spectral features of all atomic

and molecular species of all elements present in any type of sample and its surrounding environment using a single laser shot". In 2004, LIBS was promoted as the future superstar of atomic spectrometric methods [2], and twelve years later we may see that LIBS has been successfully applied in a variety of fields ranging from cultural heritage to space explorations [3].

Contrary to qualitative, quantitative LIBS analysis is not an easy task and has been considered the "Achilles heel" of the technique [4]. One of the main difficulties for a precise and accurate quantitative analysis by LIBS is due to matrix effects, to which laser induced plasmas can be very sensitive. For quantitative analysis of solids, the sample matrix must closely match the matrix of the standards, and appropriate standards are often difficult to obtain. Thus, further improvements of LIBS technique require new instrumental and analytical approaches in order to overcome problems connected with matrix effects and calibration issues, as well as research aimed at lowering the limit of detection, and improved precision and accuracy of measurements.

### **CHARACTERISTICS OF LIBS SYSTEM BASED ON TEA CO<sub>2</sub> LASER**

Analytical performance of LIBS depends on many experimental parameters, the most important being laser characteristics (power, wavelength, pulse length, beam profile), ambient gas and its pressure, geometric setup and time of observation. As a consequence, optimization of experimental conditions is needed for each particular application. Although different experimental configurations are reported in the literature, a nanosecond Q-switched solid-state Nd:YAG laser is most often for LIBS [5]. Thus, a "conventional" LIBS comprises of three basic components, Nd:YAG laser, a monochromator coupled with an Intensified Charge Coupled Device (ICCD) and a pulse generator to synchronize the plasma production and the emission spectra acquisition. In that sense, TEA-CO<sub>2</sub> LIBS system may be regarded as "unconventional" because of the laser used for plasma generation, and also because time-integrated spatially resolved detection was used for acquisition of emission spectra.

#### Laser characteristics

The laser source for LIBS was a commercial version of the TEA CO<sub>2</sub> laser system developed at the VINCA Institute of Nuclear Sciences. Pulsed TEA CO<sub>2</sub> laser emits radiation at 10.6 μm, with an output peak power typically in the order of megawatts. The laser-optical pulse has a gain-switched spike, followed by a slowly decaying tail. The full width at half-maximum

(FWHM) of the spike is about 100 ns, and the tail about 2  $\mu\text{s}$ , Fig. 1. About 35% of the total irradiated laser energy is consisted in the initial spike.

Compared to the most commonly used solid state laser Nd:YAG, TEA CO<sub>2</sub> laser has lower photon energy and longer pulse duration ( $\sim 0.12$  eV, 100 ns for TEA CO<sub>2</sub> compared to  $\sim 1.17$  eV, 10 ns for Nd:YAG). As a consequence, differences regarding the ablation process, plasma parameters and plasma expansion dynamics are to be expected. The advantage of Nd:YAG laser compared to CO<sub>2</sub> laser is higher mass ablation rate per pulse [6]. However, longer wavelength of CO<sub>2</sub> laser, and specific temporal profile of the pulse (ns peak followed by  $\mu\text{s}$  tail), may produce a plume with better properties for analytical applications [7,8].

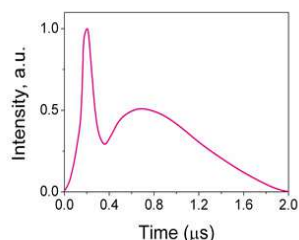


**Figure 1.** Temporal profile of TEA CO<sub>2</sub> laser pulse.

### Detection scheme

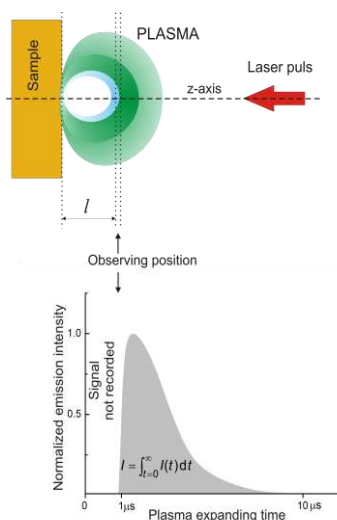


**Figure 2.** Schematic representation of time-integrated, spatially-resolved detection of plasma emission.

Laser-induced plasma is transient in nature, i.e., characteristic plasma parameters (like emission intensity, electron number density, electron temperature, etc.) evolve in space and time. In LIBS applications, a key objective is to reduce the spectral continuum background intensity compared to the discrete line signal intensity. Usually, to achieve this goal, temporal gating of the emission signal is used, which utilizes the fact that different decay rates characterize the continuum emission and atomic emission processes. Therefore, temporal resolution is used for optimizing the signal-to-noise and signal-to-background ratio, which are a function of delay and integration times.

In our LIBS system temporal resolution was replaced with spatial resolution, Fig.2. Obviously, the two approaches are correlated, because the plasma reaches a given distance above the analyzed surface with a certain time delay. A time-integrated space-resolved laser induced plasma spectroscopy (TISR-LIPS)

utilizes the fact that intense continuum emission is mostly emitted from a region close to the sample surface, while in further-out regions of the plasma the continuum emission is largely reduced [9]. The obvious advantage of this method is reduced complexity of the detection system and its cost (eliminating the need for expensive time-gated detectors). Characteristics of TEA CO<sub>2</sub> laser pulse (wavelength and pulse duration) are favorable for non-gated detection of spectral lines. The leading edge of the CO<sub>2</sub> laser pulse creates plasma, while the remaining part of the pulse (tail) interacts with the plume through the *inverse Bremsstrahlung*, IB. The rate of IB absorption ( $\alpha_{IB}$ ) is strongly dependent on laser wavelength  $\lambda$  ( $\alpha_{IB} \sim \lambda^3$ ), which means that laser-plasma interaction is much stronger in the case of CO<sub>2</sub> laser than the Nd:YAG laser [10]. Efficient IB absorption reheats the plasma. Long wavelengths are efficiently absorbed by the plume causing an additional plasma excitation and expansion, which increase the LIBS signal through enhancement of emission lines. Consequently, in low density regions far from the target surface, spatial discrimination between line and continuum emission is improved, and line broadening reduced. In addition, the dimensions and lifetime of plasma increase with pulse duration. The plasma takes longer to decay and hence, the emission lasts longer.

### ELEMENTAL ANALYSIS OF SOLIDS BY TISR-LIPS BASED ON TEA CO<sub>2</sub> LASER

Analytical capability of the plasma induced by IR TEA CO<sub>2</sub> laser pulses was evaluated for three different types of solids, metals and alloys, geochemical, and biological material.

#### Metals and alloys

TEA CO<sub>2</sub> laser based LIBS was applied for elemental analysis of metals and alloys (Cu, brass, bronze, Ti, Al alloys) [9,11-13]. Due to high reflectivity of the metals in mid-IR region, generation of metal target plasma, with low intensities of TEA CO<sub>2</sub> laser pulses was relatively difficult to obtain. Most metals have high melting, as well as normal boiling temperature, thus heating of the metal surface by IR laser pulse was the most critical stage for plasma generation. In the case of copper, the situation was even more complicated, because copper has high diffusivity and thermal

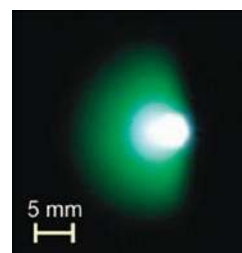


**Figure 3.** Cu plasma produced by focused CO<sub>2</sub> laser beam at air pressure of 0.1 mbar.

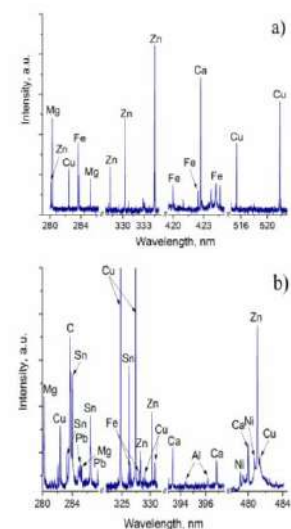


**Figure 4.** LIBS spectra of (a) brass and (b) bronze

optimum air pressure for target plasma formation was 0.1 mbar.

In Fig. 3, image of the Cu-plasma produced by focused CO<sub>2</sub> laser beam (laser fluence 8.6 J cm<sup>-2</sup>, intensity 30 MW cm<sup>-2</sup>) is shown. The plasma had a semi-spherical shape with two clearly visible, spatially separated regions usually denoted as primary and secondary plasma).

For all investigated metal samples, spectra consisted of sharp spectral lines (Fig. 4) and relatively large signal to background and signal to noise ratios were obtained. For Cu and Cu based alloys, estimated limits of detection (LODs) of trace element were in the range of 10 ppm, i.e. of the same order as obtained with standard LIBS. In addition, TEA CO<sub>2</sub> laser radiation induced negligible damage on the investigated samples, which is important if this LIBS system is to be applied for the analysis of cultural heritage objects.

Another example is quantitative

conductivity, so the heat deposited on the surface spreads rapidly into the bulk. At high pressures, plasma generated by ns-pulse was always accompanied by simultaneous formation of the gas breakdown plasma. However, the threshold for plasma formation was significantly reduced by increasing the target absorptivity (by increasing the surface roughness) and reducing the pressure. Lowering of the air pressure reduces the extent of gas breakdown, enabling better laser-target coupling because of a less plasma shielding. Better heating of the copper surface by IR laser pulse was achieved, and thus ablation was increased. Below 10 mbar, the spectrum consisted only of copper emission lines, which means that the plasma was ignited in a vapor without initiation of a gas breakdown. The

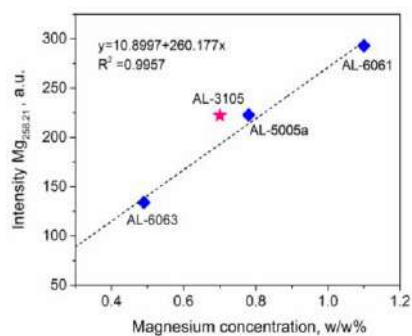


**Figure 5.** Calibration curve for Mg in Al-alloys.

analysis of metal samples. TISR-LIPS based on TEA CO<sub>2</sub> laser was applied to determination of Mg in Al-alloys under reduced air pressure. A calibration curve for Mg was constructed using certified aluminium alloy samples Fig. 5. A linear relationship between LIBS signal and analyte concentration was obtained, and used for determination of Mg in a control sample. Results were compared with the results obtained using standard analytical technique, inductively coupled plasma emission spectroscopy (ICP), and excellent agreement between LIBS and ICP results was obtained.

### Geological samples

A TEA CO<sub>2</sub> laser based LIBS system was applied for the analysis of basalt samples under simulated Martian atmospheric conditions (CO<sub>2</sub> gas, pressure 9 mbar) [8]. Photograph of the plasma induced by pulsed TEA CO<sub>2</sub> laser radiation (peak intensity 56 MW cm<sup>-2</sup>) in front of the basalt surface is shown in Fig. 6. The plasma emission was strong for relatively long period of time, and the propagation length was relatively large (25-30 mm). Fig. 7a shows spectra obtained for selected wavelength regions. Sixteen elements present in the sample (Al, Ba, Ca, Cr, Cu, Fe, K, Mg, Mn, Na, Ni, Si, Sr, Ti, V, and Zr) were identified. The estimated limits of detection were comparable to those reported in the literature, Fig. 7b [14,15].

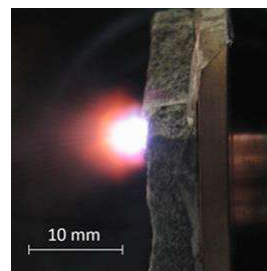


**Figure 6.** Plasma induced over basalt.

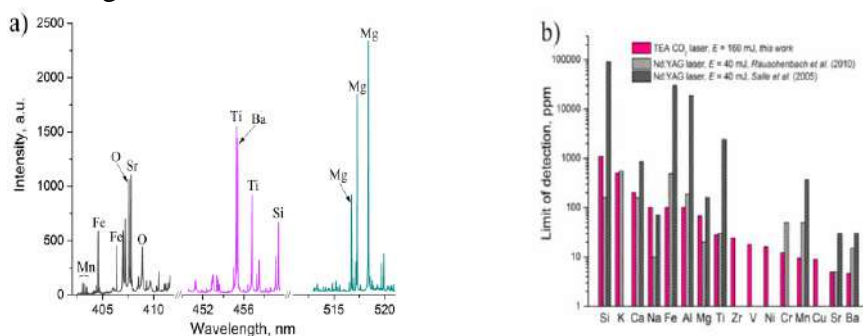


**Figure 7.**a) LIBS spectrum of basalt in a narrow spectral window. b) Comparison of LODs obtained with TEA CO<sub>2</sub> and Nd:YAG lasers.

### Biological samples

The vast majority of LIBS applications deal with compact solid samples (homogeneous or structured) while analysis of powdered samples is less utilized. Compared to the analysis of compact solid samples, quantitative LIBS analysis of powdered samples is more easily achieved because of the possibility to prepare synthetic matrix-matching calibration standards.

TEA CO<sub>2</sub> laser based LIBS technique has been applied to the qualitative and quantitative analysis of macro and micro elements in commercial food supplement *Spirulina*. *Spirulina* is an edible photosynthetic multicellular cyanobacterium (blue-green algae) produced on a large scale to be used for animal and human nutrition, for pharmaceutical, biochemical and fertilizer products.

Results of qualitative analysis were compared to those obtained using a commercial LIBS system based on pulsed Nd:YAG. In general, 5 to 10 times higher analyte signals were measured in Nd:YAG plasma. Nevertheless, higher intensity of background continuum and background noise caused deterioration in the signal quality. Although of lower intensity, better resolved and sharper emission lines were obtained in CO<sub>2</sub> plasma. This may be attributed to relatively slow heating of the plasma (through absorption of the long lasting tail of the laser pulse), causing a larger and less-dense plasma plume and, therefore, less broadened lines. For quantitative analysis of metal content in *Spirulina*, laboratory produced matrix-matching calibration standards were used. Linear calibration curves were obtained for Ba (Fig. 9), Fe, Mg, Mn and Sr, with regression coefficients exceeding 0.92 and precision between 1.9 % (Ba) and 8.6 % (Sr). The estimated limits of detection were in the 0.1 ppm to 7 ppm concentration range, comparable to those reported in the literature.

## CONCLUSION

Laser induced breakdown spectroscopy based on TEA CO<sub>2</sub> laser has been applied to elemental analysis of metals, geological and biological samples. A unique laser characteristics, the most important being the laser wavelength (10.6 μm) and the long lasting pulse tail (~2 μs), allowed successful application of time-integrated spatially resolved detection system for acquisition of emission spectra. Taking all into consideration: low-cost detection system; well-resolved, sharp spectral lines; minimal destructivity; good sensitivity; LODs in the ppm range, typical for LIBS, it can be concluded that the proposed LIBS system may be a suitable alternative to conventional LIBS that comprises Nd:YAG laser and time-gated detection.

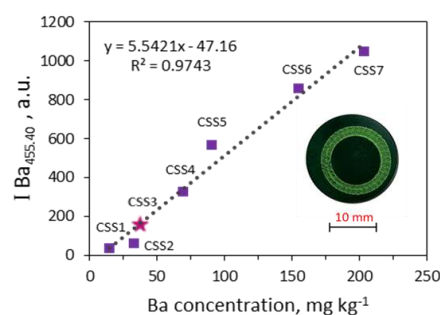


**Figure 8.** Calibration curve for Ba. Inset shows *Spirulina* sample pellet with clearly visible laser produced damages.

**Acknowledgement**

This work was supported by the Ministry of Education, Science and Technological Development of Republic of Serbia (Project No. 172019).

**REFERENCES**

- [1] D.W. Hahn, N. Omenetto, *Applied Spectroscopy*, 2012, **66**, 347–419.
- [2] J. D. Winefordner, I. B. Gornushkin, T. Correll, E. Gibb, B. W. Smith, N. Omenetto, *Journal of Analytical Atomic Spectrometry*, 2004, **19**, 1061-1083.
- [3] R. Gaudiuso, M. Dell’Aglia, O. DePascale, G.S. Senesi, A. De Giacomo, *Sensors*, 2010, **10**, 7434–7468.
- [4] D.W. Hahn, N. Omenetto, *Applied Spectroscopy*, 2010, **64**, 335A-336A.
- [5] K.Y. Yamamoto, D. A. Cremers, L.E. Foster, M.P. Davies, R. D. Harris, *Applied Spectroscopy*, 2005, **59**, 1082-1097.
- [6] D. Campos, S. S. Harilal, A. Hassanein, *Journal of Applied Physics*, 2010, **108**, 113305-1/7–113305-7.
- [7] A. Khumaeni, Z.S. Lie, H. Niki, Y.I. Lee, K. Kurihara, M. Wakasugi, T. Takahashi, K. Kagawa, *Applied Optics*, 2012, **51**, B121–B129.
- [8] J. Savovic, M. Stoiljkovic, M. Kuzmanovic, M. Momcilovic, J. Ciganovic, D. Rankovic, S. Zivkovic, M. Trtica, *Spectrochimica Acta B*, 2016, **118**, 127–136.
- [9] M. Momcilovic, M. Kuzmanovic, D. Rankovic, J. Ciganovic, M. Stoiljkovic, J. Savovic, M. Trtica, *Applied Spectroscopy*, 2015, **69**, 419-429.
- [10] D. Campos, S. S. Harilal, A. Hassanein, *Journal of Applied Physics*, 2010, **108**, 113305-1 –113305-7.
- [11] M. Momčilović, M. Trtica, J. Ciganović, J. Savović, J. Stašić, M. Kuzmanović, *Applied Surface Science*, 2013, **270**, 486-494.
- [12] M. Momcilovic, J. Ciganovic, D. Rankovic, U. Jovanovic, M. Stoiljkovic, J. Savovic, M. Trtica, *Journal of the Serbian Chemical Society*, 2015, **80**, 1-9.
- [13] M. Kuzmanovic, M. Momcilovic, J. Ciganovic, D. Rankovic, J. Savovic, D. Milovanovic, M. Stoiljkovic, M.S. Pavlovic, M. Trtica, *Physica Scripta*, 2014, **T162**, 014011 (4pp).
- [14] B. Salle, D.A. Cremers, S. Maurice, R.C. Wiens, P. Fichet, *Spectrochimica Acta B*, 2005, **60**, 805-815.
- [15] I. Rauschenbach, V. Lazic, S.G. Pavlov, H.-W. Hübers, E.K. Jessberger, *Spectrochimica Acta B* 2008, **63**, 1205-1215.

## MODELING THE STABILITY OF METAL COMPLEXES WITH AROMATIC LIGANDS USING GRAPH-THEORETICAL METHOD

N. Raos and A. Miličević

*Institute for Medical Research and Occupational Health, Ksaverska c. 2,  
P.O.B. 291, 10001 Zagreb, Croatia*

### ABSTRACT

Models for the prediction of stability constants of coordination compounds based of the valence connectivity index  ${}^3\chi^v$  do not treat interactions with aromatic compounds explicitly, but in spite of this by introducing specific interactions (“bonds”) it is possible to overcome original imperfections of the models. In this contribution we presented our results on complexes of amino acids, tetrapeptides and heterocyclic aromatic ligands.

### INTRODUCTION

There are the two most important problems in applying graph-theoretical methods in QSAR and QSPR analysis [1-5]. The first is to choose an appropriate graph-theoretical index (as a molecular descriptor) among the hundreds developed. The second problem is to write a proper structural (constitutional) formula of the studied molecule. The first problem is well known and researchers usually use all available indices to choose the best or best ones. The second problem is, however, specific for coordination compounds. Namely, the structures of these compounds are not strictly defined, especially in solution, where a number of molecular species with the same molecular formula could be proposed. Potentiometric methods gave, besides stability constants, only stoichiometry of the studied complexes and spectroscopic techniques are not capable to elucidate a detailed structure of the complex in solution.

Such a state of art moved us to develop graph-theoretical models aimed specifically to coordination compounds [6,7]. Finding valence index of the 3<sup>rd</sup> order,  ${}^3\chi^v$ , the best for the modeling the stability constants of metal complexes [8,9], we decided to use it exclusively, but to vary constitutional formula from which the index is derived. In our first systematic paper on copper(II) complexes with amino acids and diamines [10], we check  ${}^3\chi^v$  index derived from three kinds of formulas; from the constitutional formula of the ligand (L), from the formula of complex (ML or ML<sub>2</sub>), and from hydrated complex (ML<sup>aq</sup>, ML<sub>2</sub><sup>aq</sup>), assuming binding of two water

molecules to copper(II) mono-complex (cn=4) and bis-complex (cn=6). The mentioned formulas gave the results of cross validation (live-one-out procedure) in order  $S.E._{cv}(L) > S.E._{cv}(ML) > S.E._{cv}(ML^{aq})$ . Such results clearly demonstrated the validity of our method, namely that the results are dependent on the real structure of the molecular species present in solution; more realistic formula gave better results. Such an approach gave its best assuming that all complexes in the set do not bind the same number of water molecules [11-13].

But there was another problem facing the proper structural formula of these complexes. We namely noticed “anomalous” behavior of complexes having donor atoms in the side chains of ligands, or simply having long side chains. For these compounds we proposed additional ligand coordination. From this assumption we derived a new graph representation leading to a new  ${}^3\chi^v$  set, denoted as  ${}^3\chi^v(ML^{cor})$  [10]. With this set a substantially better agreement between theory and experiment was achieved. Such a representation was used in the developed model for the amino-acid complexes [12] and for modeling copper(II) and nickel(II) complexes with fructose-amino acid adducts [14].

#### ***Aromatic compounds as secondary ligands***

In our systematic research aimed at development QSPR models based on  ${}^3\chi^v$  for prediction of stability constants of coordination compounds we studied many systems, like copper(II) chelates with amino acids and their derivatives [11,13,15], amino-acidato complexes with bivalent transition metals [16], complexes of lanthanides with carboxylic [17] and amino acids [18], peptide complexes [19-22], *etc.* Many ligands in the sets were aromatic, but the aromatic moieties of these compounds do not participate directly in coordination.

This is particularly notable in copper(II) complexes with aromatic amino acids, phenylalanine and its hydroxyl derivative, tyrosine [10]. The model with additional coordination ( $ML^{cor}$ ,  $ML_2^{cor}$ ) yielded substantially better results than other models (Figure 1).

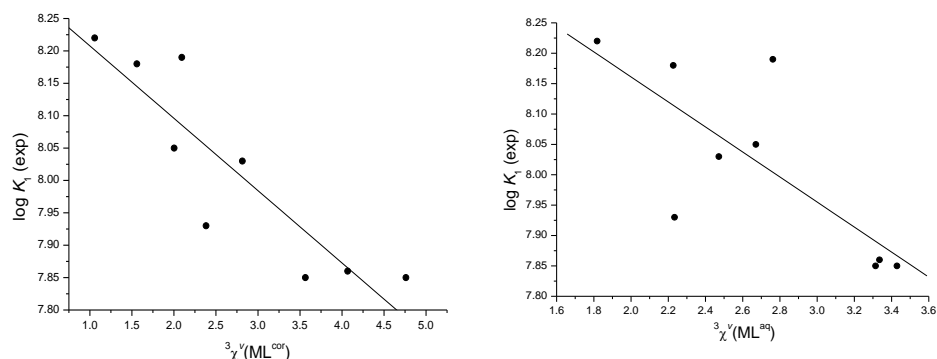


**Figure 1.** Linear regressions of  $\log K_1$  on  ${}^3\chi^v$  (calculated from  $ML^{cor}$  and  $ML^{aq}$  graph representations) for Cu(II) mono-complexes of naturally occurring amino acids.

The rationale for binding of –OH group of tyrosine is obvious, but not so for the aromatic ring of phenylalanine (which was modelled as binding of its 4' C-atom to copper). However, there are experimental indications that aromatic rings of both ligands interact with copper(II) atom [23,24]. Thus the theoretical calculations, without the direct reference to structure, confirmed in a way the experimental findings. The results of even better quality were obtained proposing that copper(II) mono-complexes with phenylalanine and tyrosine were coordinated with three instead of two water molecules, but in their bis-complexes no water is assumed to be bonded to the central atom [11]. Rationale for this supposition was found in the hypothesis that side chains in mono-complexes interact with water molecules in apical position, stabilizing the complex, but in bis-complexes aromatic rings interact with each other (stacking interactions), making apical position unfavorable for binding of water molecule.

#### ***Aromatic compounds as primary ligands***

At first it seems that the involvement of aromatic ring in the *primary* binding to metal, *i.e.* by including it in the chelate ring, has no special effect on complex stability. This conclusion came from the prediction of stability of ten copper(II) bis-complexes with thioflavin- and clioquinol-like molecules relevant to Alzheimer's disease [25]. Our results correlated very well with the results of DFT method, and a slight discrepancy has been observed only for thia-ligands. However, the effect of bulkiness of aromatic ligands was observed in copper(II) *N*-salicylidene-aminoacidato complexes [26]. Namely, in contrast to complexes of the mentioned ligands with other divalent metals ( $Ni^{2+}$ ,  $Zn^{2+}$ ), which gave fairly agreement ( $S.E._{cv} = 0.08 -$

0.17 for  $\log K_1$ ), copper(II) yielded  $S.E._{cv} = 0.37$  for  $\log K_1$ . Results were, however, improved when different number of coordinated water was proposed and salicylidene glycine ligand was excluded from regression ( $S.E._{cv} = 0.02$ ). Rationale for such a modeling was found in the plasticity of copper(II) coordination, which enables binding of various number of ligand water molecules and formation of many forms of coordination polyhedron.

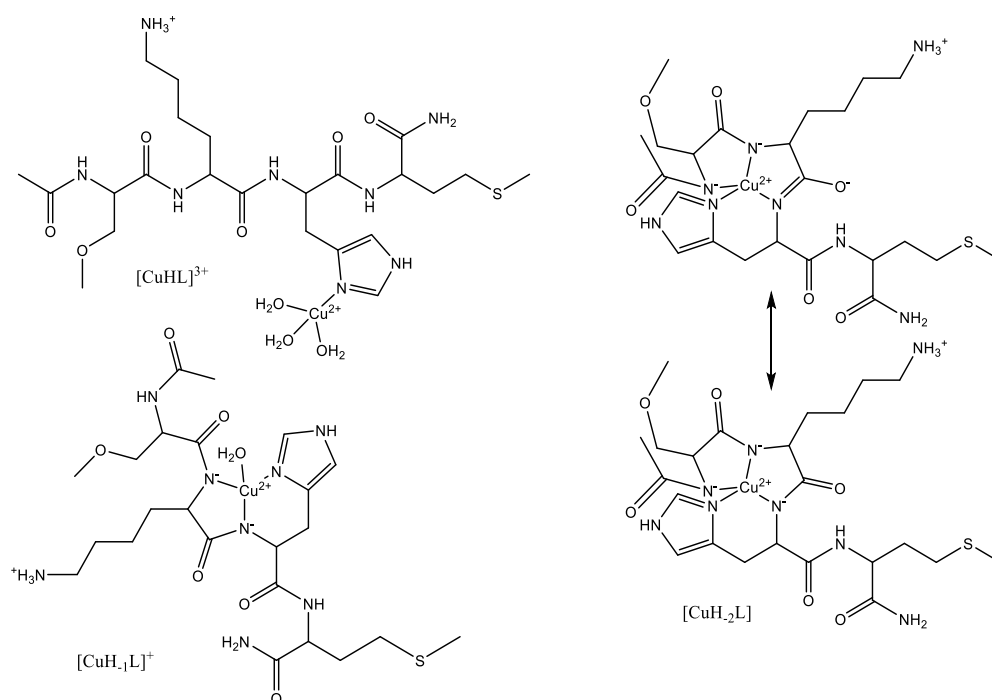


**Figure 2.** Constitutional formulas of 1N, 3N, and 4N copper(II) complexes with Ac-S(OMe)KHM-NH<sub>2</sub>.

Specific problem with the aromaticity was observed in the modeling of copper(II) complexes with tetrapeptides containing histidyl residue [27]. These ligands may form monodentate,  $[CuHL]^{3+}$ , 1N, tridentate,  $[CuH_1L]^+$ , 3N, and tetradentate,  $[CuH_2L]$ , 4N, complexes (Figure 2). At first very poor results were obtained for all peptides ( $S.E._{cv} = 0.75-0.98$ ). In this first attempt we assumed the  $Cu-N^--C=O$  bonding for 4N, the same as in 1N and 3N complexes. However, by introducing an alternative, resonant structure,  $Cu=N=C-O^-$ , for 4N complexes we obtained quite satisfactory results ( $S.E._{cv} = 0.05 - 0.22$ ).

## CONCLUSION

Graph-theoretical indices lack in general proper theoretical foundations; despite various attempts to explain them in terms of usual chemical concepts like molecular volumes and surface areas [28,29], it is not yet explained why they are successful, and especially why some topological indices are advantageous over the others. Such a state of art led to “emerging hostility toward chemical graph theory”, which some scientists view as scientifically unfounded and “primitive” [30]. Bearing this in mind it cannot be expected that graph-theoretical methods should treat aromaticity in a specific way, by introducing special models or methods to deal with it. However, this contribution points to the fact that in the case of coordination compounds three effects of aromatic ligands are to be expected and accordingly solved by graph-theoretical models: (1) steric interactions among ligands, (2) interactions with central atom leading to different coordination, and (3) formation of resonant structure with dislocated electrons (“bonds”) of coordination polyhedron.

## REFERENCES

- [1] E. V. Babaev, in: *Chemical Topology: Introduction and Fundamentals*, D. Bonchev, R. Rouvray (Eds.), Gordon and Breach, Reading, 1999, pp. 167-264.
- [2] Z. Mihalić, N. Trinajstić, *J. Chem. Educ.* 1992, **69**, 701-712.
- [3] H. Bögel, J. Dettmann, M. Randić, *Croat. Chem. Acta*, 1997, **70**, 827-840.
- [4] L. Pogliani, *Chem. Rev.*, 2000, **100**, 3827-3849.
- [5] S. Bajaja, S. Sami, A. K. Madan, *Croat. Chem. Acta*, 2005, **78**, 165-174.
- [6] N. Raos, A. Miličević, *Arh. Hig. Rada Toksikol.*, 2009, **60**, 123-128.
- [7] N. Raos, A. Miličević, in: *Handbook of Inorganic Chemistry Research*, D. A. Morrison (Ed.), Nova Science Publishers, Inc., New York, 2010, pp. 267-294.
- [8] B. Grgas, S. Nikolić, N. Paulić, N. Raos, *Croat. Chem. Acta*, 1999, **72**, 885-895.
- [9] S. Nikolić, N. Raos, *Croat. Chem. Acta*, 2001, **74**, 621-631.
- [10] A. Miličević, N. Raos, *Polyhedron*, 2006, **25**, 2800-2808.
- [11] A. Miličević, N. Raos, in: *Topics in Chemical Graph Theory*, Univ. Kragujevac, Kragujevac, Serbia, 2014, pp. 193-204.
- [12] A. Miličević, N. Raos, *J. Phys. Chem.*, 2008, **112**, 7745-7749.
- [13] A. Miličević, N. Raos, *Chin. J. Chem.*, 2011, **29**, 1800-1804.
- [14] A. Miličević, N. Raos, *Croat. Chem. Acta*, 2007, **80**, 557-563.
- [15] N. Raos, G. Branica, A. Miličević, *Croat. Chem. Acta*, 2008, **81**, 511-518.
- [16] A. Miličević, G. Branica, N. Raos, *Molecules*, 2011, **16**, 1103-1112.
- [17] A. Miličević, N. Raos, *Chem. Phys. Lett.*, 2012, **528**, 63-57.
- [18] A. Miličević, N. Raos, *Acta Chim. Slov.*, 2014, **61**, 904-908.
- [19] A. Miličević, N. Raos, *Polyhedron*, 2008, **27**, 887-892.
- [20] A. Miličević, N. Raos, *J. Coord. Chem.*, 2014, **67**, 623-629.

- [21] A. Miličević, N. Raos, *Bull. Chem. Soc. Jpn.*,2015, **88**, 490-495.
- [22] A. Miličević, N. Raos, *Arh. Hig. Rada Toksikol.*,2015, **66**, 165-170.
- [23] S. H. Laurie, *Amino acids, peptides and proteins*, Comprehensive Coordination Chemistry, Vol. 1, Pergamon Press, Oxford, 1987.
- [24] T. Sugimori, H. Masuda, N. Ohata, K. Koiwai, A. Odani, O. Yamauchi, *Inorg. Chem.*,1997, **36**, 576-583.
- [25] A. Miličević, N. Raos, *Arh. Hig. Rada Toksikol.*,2013, **64**, 539-545.
- [26] A. Miličević, N. Raos, *Cent. Eur. J. Chem.*,2014, **12**, 74-79.
- [27] A. Miličević, N. Raos, *Int. J. Chem. Modell.*,2014, **6**, 301-309.
- [28] N. Raos, *Croat. Chem. Acta*,2003 **76**, 81-85.
- [29] E. Estrada, *J. Phys. Chem. A*,2004, **108**, 5468-5473.
- [30] M. Randić, *MATCH Commun. Math. Comput. Chem.*,2008, **59**, 5-124.

## REACTIVITY OF MONO-SILICON ANALOGUE OF VINYL ANIONS AGAINST TO CARBON MONOXIDE

C. B. Yildiz

*Department of Chemistry, Faculty of Arts and Sciences, University of Aksaray, Aksaray, Turkey. (cemburakyildiz@aksaray.edu.tr)*

### ABSTRACT

Density functional theory (B3LYP) calculations with 6-311++G(d,p) basis set in the solvent of tetrahydrofuran (THF) elucidated the first possible reaction mechanism for activation of carbon monoxide by mono-silicon analogue of vinyl anion **1**. The reaction between **1** and CO can form C=C=O moiety **3** with the barrier of 31.8 kJ/mol after formation of pre-complex **2**. The energy barrier to arrive at the structure **5** via **TS3** is calculated to be relatively high with the energy of 135.2 kJ/mol. However, the first step is found to be highly exergonic and this energy can compensate the required barrier for **TS3**. Furthermore, we believe that the experimental conditions (bulky substituents and counter ion) could reduce the related energy barriers. Moreover,

### INTRODUCTION

Activation of small molecules such as harmful gases is a helpful reputation *for being feedstock* for organic compounds. Especially, the activation of carbon monoxide (CO) experiences is having considerable attention in the context of the limited availability of fossil hydrocarbons [1]. The Fischer-Tropsch process, a predominant method, is for the generation of hydrocarbons from CO + H<sub>2</sub> in the presence of catalyst [2]. Additionally, several studies were employed to homogeneous transition metal complexes to achieve complete cleavage of the CO triple bond [3]. Numerous methods have been improved to sequester CO by such as metal-organic frameworks (MOFs) or low-valent main-group compounds as an alternative.

Recently, a few main-group systems have been shown to activate carbon monoxide stoichiometrically [4-6]. For instance, the reactivity of CO against to NHC stabilized B≡B triple bond (as a main group compound) to form bis(boralactone) was reported by Braunschweig and his co-workers [4]. Then, the formation of functionalized cyclic silenes from direct carbonylation of cyclotrisilenes was disclosed by the collaboration of Scheschkewitz and Sekiguchi [5]. In a very recent study, the first complete

reductive cleavage of C–O triple bond of carbon monoxide with using a lithium disilene in the absence of catalyst was discovered by the group of Scheschkewitz (Figure 1) [6].

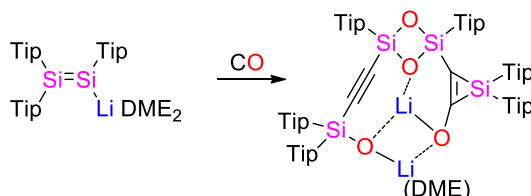


**Figure 1.** Reductive coupling of CO by disilene (Tip=2,4,6-*i*Pr<sub>3</sub>C<sub>6</sub>H<sub>3</sub>).

Likewise, it is necessary to be performed systematic theoretical study on unknown mono-silicon analogues of vinyl anions to penetrate their structures, properties, and reactions. With this motivation, we have performed DFT calculations on the reactivity of a heavier vinyl anion against to carbon monoxide (CO).

## EXPERIMENTAL

All the calculations were performed with the Gaussian 09W suite of program [7]. In order to optimize the title structures on their potential energy surface, B3LYP theory was employed. The 6-311++G(d,p) was chosen as basis set. Solvent effects with (Tetrahydrofuran) were also included at the B3LYP/6-311++G(d,p) level with using the polarizable continuum model (PCM) [8,9]. The optimized structures were determined as a minimum (no imaginary frequency) or transition state. The relative  $\Delta G$  energies are given in kJ/mol. The Intrinsic Reaction Coordinate (IRC) procedure was carried out for the identification of the connectivity of stationary points.

## RESULTS AND DISCUSSION

Disilenes, silicon analogue of vinyl anions, are well-suited from transfer a Si–Si double bond moiety to a broad variety of organic and inorganic substrates [10]. In a very recent study, full cleavage of CO with lithium disilene under ambient conditions was achieved by Scheschkewitz et. al. [6]. The mechanism of the reaction was also investigated by DFT method with using simplified system (Methyl groups instead of Tip Groups). With this incentive, we decided to investigate behaviour of mono silicon analogue of vinyl anion against to carbon monoxide. We have started with optimizing pre-complex **2** which is 36.0 kJ/mol higher in energy than **1**+CO. Then, the

required energy to form **3** is determined to be 31.8 kJ/mol. The formation of C=C=O moiety, similar to ketenylidenes, sufficiently stabilize structure **3** with the energy of 207.2 kJ/mol as compared to **2**. At this point, single bond rotation between Si and C atoms occurs via **TS2** with the barrier of 23.4 kJ/mol. This step generates the intermediate **4** which then undergoes cyclization step for **5** via **TS3** (Figure 2). Although the required energy barrier to **TS3** is found to be high with 135.2 kJ/mol for a reaction at room temperature, the highly exergonic first step can compensate the barrier of **TS3**.

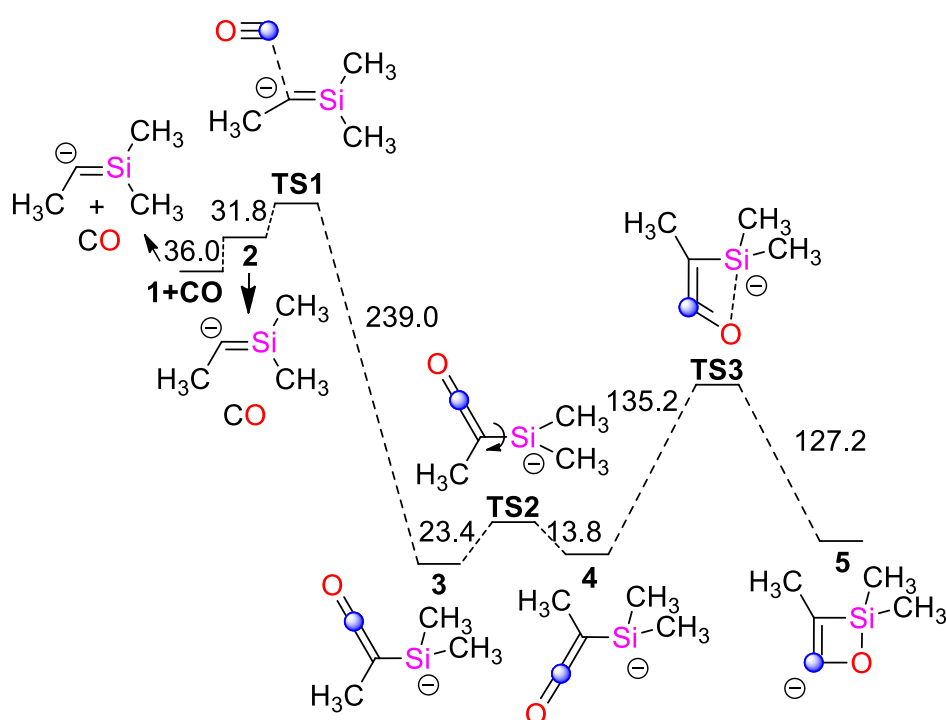


**Figure 2.** The proposed mechanism for the reaction of CO with mono-silicon analogue of vinyl anion (**1**) at the B3LYP/6-311++G(d,p) level (Solvent = THF).

## CONCLUSION

In summary, mono silicon effect on the activation of carbon monoxide by vinyl anions were investigated. The required energy for the first step (**TS1**) is found to be 31.8 kJ/mol at B3LYP/6-311++G(d,p) level of theory (Solvent = THF). The final compound (**5**) was found 189.6 kJ/mol

more stable than pre-complex of **2**. We hope the results would be very helpful for further experimental and theoretical investigations on the CO reactivity by heavier vinyl anions.

## REFERENCES

- [1] V. Macho, M. Kralik, L. Komora, *Pet. Coal.*, 1997, **39**, 6–12
- [2] F. Fischer, H. Tropsch, *Brennstoff-Chemie.*, 1926, **7**, 97–104.
- [3] D. R. Neithamer, R. E. LaPointe, R. A. Wheeler, D. S. Richeson, G. D. Van Duyne, P. T. Wolczanski, *J. Am. Chem. Soc.*, 1989, **111**, 9056.
- [4] H. Braunschweig, T. Dellermann, R. D. Dewhurst, W. C. Ewing, K. Hammond, J. O. C. Jimenez-Halla, T. Kramer, I. Krumm-nacher, J. Mies, A. K. Phukan, A. Vargas, *Nat. Chem.* 2013, **5**, 1025–1028.
- [5] M. J. Cowley, Y. Ohmori, V. Huch, M. Ichinohe, A. Sekiguchi, D. Scheschkewitz, *Angew. Chem. Int. Ed.* 2013, **52**, 13247–13250; *Angew. Chem.* 2013, **125**, 13489–13492.
- [6] M. Majumdar, I. Omlor, C. B. Yildiz, A. Azizoglu, V. Huch, D. Scheschkewitz, *Angew. Chem. Int. Ed.*, 2015, **54**, 8746–8750.
- [7] Gaussian 09, revision A02. Gaussian Inc, Wallingford, 2009.
- [8] V. Barone, M. Cossi, *J. Phys. Chem. A*, 1998, **102**, 1995.
- [9] B. Mennucci, J. Tomasi, *J. Chem. Phys.*, 1997, **106**, 5151.
- [10] D. Scheschkewitz, *Angew. Chem.* 2004, **116**, 3025–3028; *Angew. Chem. Int. Ed.* 2004, **43**, 2965–2967.

## HYDROGEN ATOM TRANSFER MECHANISM IN CHLOROGENIC ACID

S. D. Marković and J. Tošović

*University of Kragujevac, Faculty of Science,  
12 Radoja Domanovića, 34000 Kragujevac, Serbia. (mark@kg.ac.rs)*

### ABSTRACT

The reactions of hydroxyl radical with chlorogenic acid in the positions 3' and 4' were investigated using the M06-2X/6-311++G(d,p) level of theory in conjunction with the CPCM solvation model. The research was performed to simulate reactions in three media of different polarity: benzene, ethanol, and water. These results confirm our previous finding that the HAT mechanism is virtually independent of the solvent polarity. All the reactions are notably exothermic and exergonic. The reaction in the 3' position requires lower activation energies, but the radical product of the reaction in the 4' position is more stable in all three solvents. Taking into account that activation energies are low for both reaction centres, it turns out that the 3' and 4' positions are competitive in the radical scavenging reactions of chlorogenic acid.

### INTRODUCTION

Phenolic acids form an important class of polyphenols. These compounds are widely spread in the human diet, and show potential biological functions, such as anti-inflammatory, antiallergic, anticarcinogenic, antimicrobial, antiviral, and antioxidative [1]. Antioxidative activity of phenolic compounds can be realised via three major mechanistic pathways: HAT (Hydrogen Atom Transfer), SPLET (Sequential Proton Loss Electron Transfer), and SET-PT (Single Electron Transfer – Proton Transfer) [2-4].

In our recent work [5] a comparative study of the antioxidative activities of caffeoylquinic and caffeic acids was performed by focusing on the thermodynamics of the three antioxidative mechanisms. It was suggested that the major reaction pathway for all the investigated compounds is HAT mechanism in nonpolar solvents, while HAT and SPLET are competitive mechanisms in polar media. In the present paper our interest is focused on kinetic investigation of the HAT mechanism of chlorogenic acid (5-O-caffeoylquinic acid, **5CQA**).

## EXPERIMENTAL

All calculations were performed with the Gaussian 09 software package [6] using the M06-2X/6-311++G(d,p) theoretical model. The influence of the solvents (benzene, ethanol, and water) was approximated by the CPCM solvation model. The geometries of all species under investigation in the three solvents were achieved by optimisations without any symmetry constraints, and frequency calculations were also included.

Transition states (TS) for the 3' and 4' pathways in all three solvents were revealed. The intrinsic reaction coordinates, from the transition states down to the two lower energy structures, were traced to verify that each saddle point is linked with the corresponding reactant complex (RC) and product complex (PC). The obtained geometries were verified to be minima (no imaginary frequencies), or maxima (one imaginary frequency) on the potential energy surface. The calculated relative enthalpies and Gibbs energies refer to 298 K and 101325 Pa.

## RESULTS AND DISCUSSION

The HAT mechanism was examined by simulating the reaction of **5CQA** with hydroxyl radical:  $5\text{CQA} + \cdot\text{OH} \rightarrow 5\text{CQA}^{\cdot} + \text{H}_2\text{O}$ . This radical was selected for its biological relevance. A **5CQA** molecule has two phenolic groups suitable for radical scavenging reactions: 3' and 4' (Fig. 1.). It is apparent that in the presented transition state simultaneous cleavage of the O-H bond of the hydroxyl group and formation of the  $\text{H}_2\text{O}$  molecule occur, followed with the C3'-O3' bond shortening.

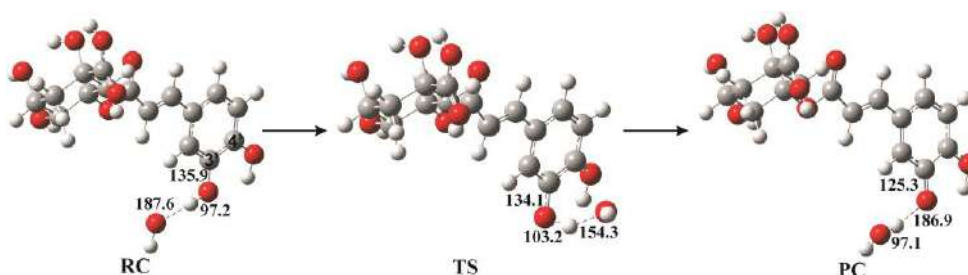


**Figure 1.** Participants in the reaction of hydroxyl radical with chlorogenic acid in the position 3' in water. **RC**, **TS**, and **PC** stand for the reactant complex, transition state, and product complex, respectively.

The relevant relative enthalpies and Gibbs energies for the reactions in both positions were calculated, and collected in Table 1. One can observe that, in the case of the reactant complexes, the relative enthalpy values are

negative, whereas the relative Gibbs energy values are positive. This occurrence is a consequence of the fact that the entropy of a reactant complex is decreased in comparison to the corresponding separated reactants, due to the increased amount of order (Fig. 2.).

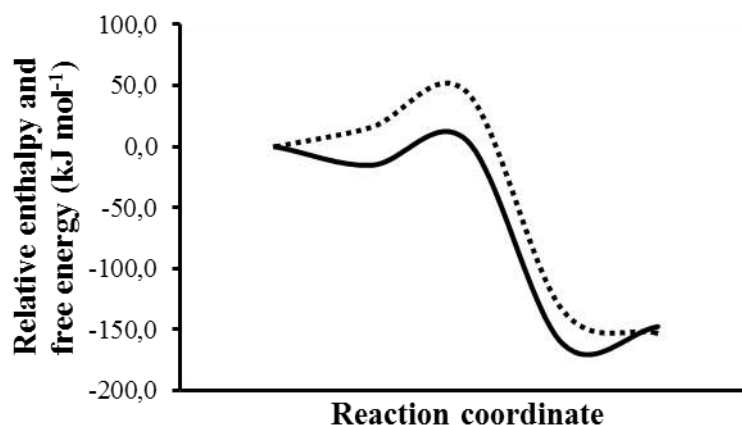


**Figure 2.** Enthalpy (solid line) and Gibbs energy (dashed line) change in the reaction of hydroxyl radical with chlorogenic acid in the position 3' in water.

**Table 1.** Relative enthalpies (regular) and Gibbs energies (*italic*) in  $\text{kJ mol}^{-1}$  related to the reactions of hydroxyl radical with chlorogenic acid in the positions 3' and 4' in three media. The reactions were calculated relative to the energies of separated reactants.  $\Delta^\ddagger H_a$  and  $\Delta^\ddagger G_a$  stand for activation enthalpy and activation Gibbs energy.

	Benzene		Ethanol		Water	
	3'	4'	3'	4'	3'	4'
RC	-17.7	-15.5	-15.5	-12.9	-15.3	-12.8
	<i>15.0</i>	<i>15.3</i>	<i>15.6</i>	<i>17.3</i>	<i>15.8</i>	<i>16.9</i>
TS	0.5	4.6	5.1	8.4	5.1	8.6
	<i>41.5</i>	<i>45.5</i>	<i>44.3</i>	<i>47.7</i>	<i>44.9</i>	<i>47.7</i>
PC	-179.2	-187.8	-161.6	-182.5	-161.3	-182.1
	<i>-147.2</i>	<i>-152.1</i>	<i>-133.3</i>	<i>-149.1</i>	<i>-133.7</i>	<i>-148.6</i>
P	-146.2	-156.0	-147.4	-157.0	-147.5	-157.1
	<i>-150.7</i>	<i>-160.5</i>	<i>-152.8</i>	<i>-161.9</i>	<i>-153.0</i>	<i>-162.0</i>
$\Delta^\ddagger H_a$	18.2	20.1	20.6	21.3	20.5	21.4
$\Delta^\ddagger G_a$	26.6	30.2	28.7	30.4	29.1	30.8

If either enthalpy or Gibbs energy is considered, the values for each reaction participant are almost identical for polar solvents, and very similar to those for benzene. The values for the activation enthalpies and Gibbs

energies, as well as for reaction enthalpies and Gibbs energies, are mutually very similar for all three solvents. These results confirm our previous finding that the HAT mechanism is virtually independent of the solvent polarity. All reactions are notably exothermic and exergonic. The reaction in the 3' position requires lower activation energies, but the radical product of the reaction in the 4' position is more stable in all three solvents. Taking into account that both reaction centres require low activation energies, it turns out that the 3' and 4' positions are competitive in the radical scavenging reactions of chlorogenic acid.

### CONCLUSION

In our recent paper [5] we found that the 4' position is more favourable than 3' position, irrespectively of either the reaction mechanism or solvent polarity. This finding was based on the thermodynamic investigation. Taking into account that the reactions in the 3' position are more endothermic than those in the 4' position, but slightly, it was concluded that activation energies, i.e. reaction kinetics, could be determining factor. The present mechanistic study shows that the reaction in the 3' position requires lower activation energies, but the radical product of the reaction in the 4' position is more stable in all three solvents, implying that the two reaction centres are competitive in the radical scavenging reactions.

### *Acknowledgement*

This work was supported by the Ministry of Science and Technological Development of the Republic of Serbia (project no. 172016).

### REFERENCES

- [1] T. Jayasena, A. Poljak, G. Smythe, N. Braid, G. Münch, P. Sachdev, *Ageing Res. Rev.*, 2013, **12**, 867–883.
- [2] J. S. Wright, E. R. Johnson, G. A. DiLabio, *J. Am. Chem. Soc.*, 2001, **123**, 1173-1183.
- [3] E. Klein, V. Lukeš, M. Ilčin, *M. Chem. Phys.*, 2007, **336**, 51-57.
- [4] G. Litwinienko, K. U. Ingold, *Accounts Chem. Res.*, 2007, **40**, 222-230.
- [5] S. Marković, J. Tošović, *Food Chem.*, 2016, **210**, 585-592.
- [6] Gaussian 09. Revision C.01. Wallingford: Gaussian, Inc., 2010.

## EXAMINATION OF ANTIOXIDANT ACTIVITY OF THREE DIHYDROXYBENZOIC ACIDS

S. D. Marković<sup>1</sup>, J. Đorović<sup>2</sup>, Z. Petrović<sup>1</sup> and A. Amić<sup>3</sup>

<sup>1</sup> Faculty of Science, University of Kragujevac, Radoja Domanovića 12, 34000 Kragujevac, Serbia. (e-mail: mark@kg.ac.rs)

<sup>2</sup> Bioengineering Research and Development Center, Prvoslava Stojanovića 6, 34000 Kragujevac, Serbia.

<sup>3</sup> Department of Biology, The Josip Juraj Strossmayer University, Cara Hadrijana 8a, HR-31000 Osijek, Croatia.

### ABSTRACT

In the present study the M05-2X/6-311++G(d,p) model is used to evaluate scavenging potency of 2,3-, 2,6-, and 3,4-dihydroxybenzoic acids (DHBAs). Reaction enthalpies related to the scavenging mechanisms of the studied species were calculated in water and benzene. Hydrogen atom transfer is a preferred reaction pathway in benzene, while sequential proton loss electron transfer is a predominant reaction pathway in polar solvent, water, for all the studied compounds.

### INTRODUCTION

Phenolic acids represents important class of phenolic compounds which are widely distributed in the plant world, being an integral part of the human diet. Naturally occurring phenolic acids, with common basic skeleton, are divided into two large groups: hydroxycinnamic and hydroxybenzoic acids [1]. Phenolic acids exist in almost all vegetables, fruits, and grains. They are rarely found as free molecules in nature, more often they are found in plants in the form of esters, ethers, and acetals, or as structural components of cellulose, hemicellulose, proteins and lignin [2]. Free-radical scavenging ability of 3,4-DHBA inhibits chemical carcinogenesis and protects against hydroperoxide-induced toxicity [3]. 2,3-DHBA is also a human metabolite found in plasma and a biological marker for the detection and quantification of OH radicals.

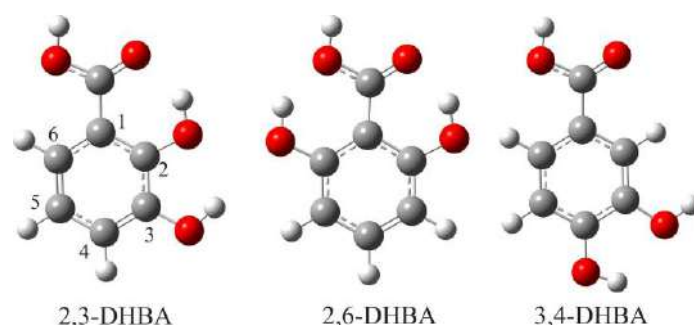


**Figure 1.** The most stable structures of the studied dihydroxybenzoic acids

Scavenging properties of phenolic acids are related to their ability to transfer hydrogen atom to a free radical species. It has been suggested that antioxidant ability of phenolic acids is greatly influenced by the number and relative position of OH groups in the ring. In the radical scavenging mechanisms reactive radical species are inactivated by accepting hydrogen atom from hydroxyl group of phenolic acid. This transfer can be visualized through at least three general mechanisms characteristic to all phenolic compounds: hydrogen atom transfer (HAT, Eq. 1), sequential proton loss electron transfer (SPLET, Eq. 2), and single electron transfer followed by proton transfer (SET-PT, Eq. 3) [5].



These mechanisms are described by thermodynamic parameters: bond dissociation enthalpy (BDE) related to Eq. (1), proton affinity (PA) related to Eq. (2.1), electron transfer enthalpy (ETE), ionization potential (IP) related to Eq. (3.1), proton dissociation enthalpy (PDE) related to Eq. (3.2). They can be determined from the total enthalpies of individual species:

$$\text{BDE} = H(\text{Ph-O}^\bullet) + H(\text{H}^\bullet) - H(\text{Ph-OH}) \quad (4)$$

$$\text{IP} = H(\text{Ph-OH}^{\bullet+}) + H(\text{e}^-) - H(\text{Ph-OH}) \quad (5.1)$$

$$\text{PDE} = H(\text{Ph-O}^\bullet) + H(\text{H}^+) - H(\text{Ph-OH}^{\bullet+}) \quad (5.2)$$

$$\text{PA} = H(\text{Ph-O}^-) + H(\text{H}^+) - H(\text{Ph-OH}) \quad (6.1)$$

$$\text{ETE} = H(\text{Ph-O}^\bullet) + H(\text{e}^-) - H(\text{Ph-O}^-) \quad (6.2)$$

Preferred mechanism of antioxidant activity of phenols can be estimated from the BDE, IP, and PA values. The lowest of the three values shows thermodynamically most favorable mechanism.

The aim of the present paper is to estimate antioxidant capacity of several dihydroxybenzoic acids (DHBAs): 2,3-, 2,6- and 3,4-DHBA (Fig. 1).

## METHODS

The equilibrium geometries of investigated DHBAs and corresponding radicals, radical cations, and anions were fully optimized by the hybrid density functional method (M05-2X), developed by the Truhlar group [4] and 6-311+d,p) basis set, implemented in the Gaussian 09 package. Vibrational frequencies were computed: no imaginary frequencies were obtained. The SMD solvation model was applied to approximate the influence of water and benzene as solvents, i.e. to mimic polar and nonpolar solutions.

## RESULTS AND DISCUSSION

All DHBAs are planar molecules with internal hydrogen bonds. The NBO analysis of DHBs revealed the stabilizing donor-acceptor interactions between the lone pairs on oxygens and proximate antibonding O-H orbitals. In Table 1 the thermodynamic data regarding all three DHBAs are collected.

**Table 1:** M052X/6-311++G(d,p) calculated parameters of antioxidant mechanisms for DHBAs in  $\text{kJ mol}^{-1}$  in water and benzene

		WATER					BENZENE				
		HAT		SET-PT		SPLET	HAT		SET-PT		SPLET
		BDE	IP	PDE	PA	ETE	BDE	IP	PDE	PA	ETE
<b>DHBAs</b>		518					664				
	<b>2O</b>	369		32	132	419	377		122	425	361
	<b>3O</b>	362		25	145	405	366		111	436	347
		521					665				
	<b>2O</b>	391		51	149	423	403		147	450	362
	<b>6O</b>	380		39	137	424	381		125	426	365
		533					684				
	<b>3O</b>	361		9	130	412	346		71	403	352
	<b>4O</b>	364		12	119	426	347		73	385	371

From the thermodynamic data (Table 1), it is clear that the IP values are high for all DHBAs in both solvents. That means SET-PT is not a plausible mechanism for these conditions. On the other hand, PA values of DHBAOH groups are significantly lower than the corresponding BDE values, indicating that SPLET mechanism is the most probable reaction pathway in polar solvent. The calculated BDE values of DHBAs are lower than the corresponding PA values in benzene. That means HAT mechanism is a probable reaction path in nonpolar solvent.

Further analysis of thermodynamic values in Table 1 indicates that, based on the values of BDE and PA, 3,4-DHBA is stronger antioxidant than other two DHBAs in benzene as well as in water.

### CONCLUSION

Antioxidant activity of 2,3-, 2,6- and 3,4-dihydroxybenzoic acids was examined by analysing thermodynamic properties of the parent molecules, corresponding radicals, radical cations and anions. From the obtained results it can be concluded that HAT mechanism is dominant in non-polar solvent while SPLET mechanism is prevailing reaction path in polar solvent. It should be pointed out that according to the obtained results 3,4-DHBA is probably the strongest antioxidant among the studied compounds.

### *Acknowledgement*

This work was partially supported by the Ministry of Science and Technological Development of the Republic of Serbia (Grant nos 172016 and 174028), and bilateral project Serbia-Croatia 2016-2017.

### REFERENCES

- [1] K. Herrmann, Crit. Rev. Food Sci. Nutr., 1989, **28**, 315-347.
- [2] M.F. Andreasen, L.P. Christensen, A.S. Meyer, A. Hansen, J. Agric. Food Chem., 2000, **48**, 2837-2842.
- [3] W. DeGraff, L.S. Myers Jr., J. Mitchell, S. Hahn, Int. J. Oncol., 2003, **23**, 159-163.
- [4] Y. Zhao, D.G. Truhlar, Theor. Chem. Acc., 2008, **120**, 215-241.
- [5] G. Litwinienko, K.U. Ingold, Acc. Chem. Res., 2007, **40**, 222-230.

## BENCHMARK STUDY FOR 2-BUTENE PARALLEL INTERACTIONS

M. Zarić<sup>1</sup>, B. Bugarski<sup>2</sup>, V. Pavelkić<sup>1</sup>, M. Pantović<sup>1</sup>, J. Stojanović<sup>1</sup>, M. Pavlović<sup>1</sup> and M. Kijevčanin<sup>2</sup>

<sup>1</sup>*University of Belgrade, Institute of Chemistry, Technology and Metallurgy, Njegoševa 12, 11000 Belgrade, Serbia. (milana.zaric@ihtm.bg.ac.rs)*

<sup>2</sup>*Faculty of Technology and Metallurgy, University of Belgrade, Karnegijeva 4, 11000 Belgrade, Serbia*

### ABSTRACT

The interactions in model systems of unsaturated molecules with *cis*- and *trans*-double bonds were studied using quantum chemical calculations. We present benchmark study of *cis*- and *trans*-2-butene dimer model systems with various methods and different basis sets. Root Mean Square Deviation (RMSD) values are represented and results showed that the best agreement with CCSD(T)/CBS values has B3LYP-D3 method with cc-pVTZ basis set, with the lowest RMSD value of 0.032.

### INTRODUCTION

Non-covalent interactions of molecules with double bonds are important and have been studied with great interest [1-5]. Presence of double bonds can affect the properties and behavior of various systems and processes [6]. For example, molecules with double bonds, like fatty acids, have a significant role in living organisms, effecting on human health [7]. Most of the studies on non-covalent interaction of molecules with double bonds have been done on ethene (ethylene) molecule. Interactions in ethene dimer, as the simplest model system with double bonds, have been studied using different quantum chemical methods [2-5].

In previous study, in order to find differences in interactions of *cis*- and *trans*-unsaturated molecules, *cis*- and *trans*-2-butene have been studied, as the smallest model system [8]. Potential differences in interactions of model systems was performed using high level quantum chemical methods including very accurate CCSD(T) at complete basis set (CBS) approximation [9].

In the previous work we compared a few methods for two *cis*-2-butene dimers, while in this work detailed benchmark study using MP2 and several DFT-D methods, with various basis sets, on model systems of all five 2-

butene dimers (Figure 1), has been performed in order to find the best method and basis set for interactions of these molecules.

### METHODOLOGY

The benchmark study was performed using MP2, BLYP-D3, M05-D3, M052X-D3, M06-D3, M06HF-D3, B3LYP-D3, BP86, TPSS, and PBE1PBE methods and the four basis sets (cc-pVDZ, cc-pVTZ, aug-cc-pVDZ and 6-31++G\*\*) for each method.

The geometries of interactions of *cis*- and *trans*-2-butene used for the calculations in this work were obtained in previous work, as minima on potential curves [8]. The potential energy curves were

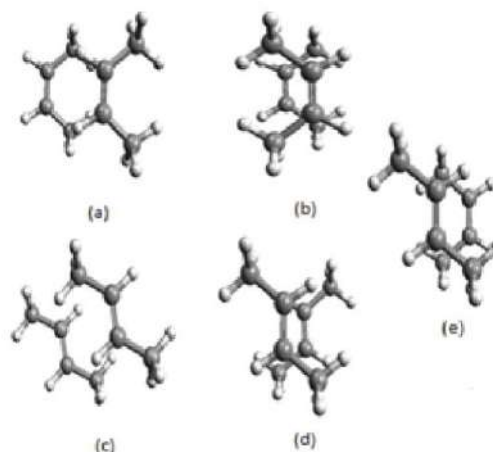


**Figure 1.** Model systems used in benchmark study

calculated by keeping monomer geometries rigid and varying the offset,  $r$  (parallel displacement) and normal distance between the planes of the two molecules,  $R$  [8]. Offset is the distance between double bond centre in one molecule and the projection of the double bond centre of the other molecule on the plane of the first molecule. The monomer geometries were optimized using MP2 method, while the potential curves were calculated using M052X-D3 method with cc-pVDZ basis set [8]. All calculations on interaction energies in 2-butene dimers have been performed in Gaussian 09 (version D.01) [10].

### RESULTS AND DISCUSSION

We have performed detailed benchmark study using ten methods, and four basis sets for each of the methods, by comparing calculated interaction energies at various level of theory with CCSD(T)/CBS energies, since CCSD(T)/CBS method is considered golden standard in quantum chemistry. The benchmark study was performed using five possible geometries for interactions in *cis*- and *trans*-2-butene dimers shown on Figure 1: (a) *cis*-2-butene dimer with parallel orientation ( $r=2.4$ ,  $R=3.3$ ), (b) *cis*-2-butene dimer with anti-parallel orientation ( $r=1.0$ ,  $R=3.7$ ), (c) *trans*-2-butene dimer with parallel orientation ( $r=2.3$ ,  $R=3.3$ ), (d) *trans*-2-butene dimer with anti-parallel orientation ( $r=0.8$ ,  $R=3.6$ ) and (e) *cis*-2-butene / *trans*-2-butene ( $r=1.4$ ,  $R=3.7$ ).

The results show that influence of the basis set is the largest on MP2 method, while on DFT-D methods it is much smaller. It was shown that the MP2, M06HF-D3, B3LYP-D3 methods underestimate interaction energies in comparison to values of CCSD(T)/CBS interaction energies.

**Table 1.** RMSD values for each methods with various basis sets (without(-) and with dispersion correction (D3) in kcal/mol

Methods	Basis sets							
	cc-pVDZ		cc-pVTZ		aug-cc-pVDZ		6-31++G**	
	-	D3	-	D3	-	D3	-	D3
MP2		1.34		0.245		0.071		0.805
BLYP	2.91	0.139	2.45	0.187	2.39	0.137	2.68	0.058
M05	1.64	0.263	1.56	0.349	1.43	0.483	1.36	0.553
M052X	1.06	0.095	0.86	0.103	0.66	0.303	0.70	0.269
M06	1.03	0.283	0.75	0.565	0.29	1.03	0.11	1.22
M06HF	1.13	0.255	1.16	0.287	0.71	0.190	0.52	0.353
B3LYP	4.00	0.103	3.89	0.032	3.91	0.052	3.99	0.105
BP86	4.64	0.258	4.47	0.388	4.40	0.418	4.56	0.352
TPSS	3.65	0.188	3.59	0.228	3.52	0.248	3.62	0.222
PBE1PBE	2.84	0.185	2.71	0.278	2.64	0.298	2.71	0.302

In Table 1 the data for Root Mean Square Deviation, RMSD, for each theory level are shown. It is shown that dispersion correction has influence on the interaction energy and have a much better agreement with CCSD(T) values. RMSD values are much lower with dispersion correction then without. However, one can notice that results without correction are better for Minnesota functionals, while dispersion is very important for other functionals. When considering the data with dispersion correction only a few levels have very large errors, above 1.0 kcal/mol.

The best level of theory for *cis*- and *trans*-2-butene dimers is B3LYP-D3/cc-pVTZ with RMSD value of 0.032, the second best is B3LYP-D3/aug-cc-pVDZ basis set with RMSD value of 0.052. Five levels of theory (B3LYP-D3/cc-pVTZ, B3LYP-D3/aug-cc-pVDZ, BLYP-D3/6-31++G\*\*, MP2/aug-cc-pVDZ and M052X/cc-pVDZ) have RMSD values below 0.1, indicating that all these level sare very reliable for calculations on 2-butene dimers.

After obtained the best level of theory (B3LYP-D3/cc-pVTZ), we recalculated the potential curves using B3LYP-D3/cc-pVTZ. The

geometries at potential curves minima did not changed much, offset and normal distance are almost the same. The energies of new potential curves are somewhat more stable(up to 0.32kcal/mol).

## CONCLUSION

Benchmarking study of *cis*- and *trans*-2-butene dimers was performed with various methods and basis sets. The study used ten methods and four basis sets for each of the method. The best method is B3LYP-D3 with cc-pVTZ basis set, where value of RMSD is 0.032. Five of 40 levels of theory, that we tested, have RMSD values below 0.1, indicating that these methods are good in reproducing interaction energies.

## Acknowledgement

This work was supported by the Education, Science and Technology Development, Republic of Serbia Projects no. OI172063 and III46010.

## REFERENCES

- [1] J. Rezač, K. E. Riley, P. Hobza, *J. Chem. Theory Comput*, 2011, **7**, 2427-2438.
- [2] S. Boehm, O. Exner, *J. Mol. Struct.: Theochem*, 2004, **682**, 171–177.
- [3] Y. Cao M. W. Wong, *J. Mol. Model.*, 2014, 2185
- [4] R. A. King, *Mol. Phys.*, 2009, **107**, 789–795.
- [5] Tsuzuki S, Uchimaru T, Mikami M, Tanabe K, *Chem. Phys. Lett.*, 1996, **252**, 206–210.
- [6] W Gao, D. Cui, *J. Am. Chem. Soc.*, 2008, **130**, 4984-4991., B. Wang, D. Cui, K. Lv, *Macromolecules*, 2008, **41**, 1983-1988.
- [7] M.B. Katan, P.L. Zock, R.P. Mensink, *Annu. Rev. Nutr.*, 1995, **15**, 473–493., R.R. Mensink, P.L. Zock, M.B. Katan, G. Hornstra, *J. Lipid Res.*, 1992, **33**, 1493–1501.
- [8] M. Zarić, B. Bugarski, M. Kijevčanin, *Chem. Phys. Chem*, 2015, **17**, 317-324.
- [9] I. D. Mackie, G. A. DiLabio, *J. Chem. Phys.*, 2011, **135**, 134318.
- [10] M. J. Frisch et al., *Gaussian 09, Revision D.01*, Gaussian, Inc., Wallingford CT, 2013.

## THEORETICAL EXAMINATION OF ORGANO-CATALYZED STEREOSELECTIVE DIELS-ALDER REACTION

B. P. Bondžić<sup>1</sup>, M. Stojanović<sup>1</sup> and A. Rašović<sup>1</sup>

<sup>1</sup>University of Belgrade, Institute of Chemistry, Technology and Metallurgy, Njegoševa 12, 11000 Belgrade, Serbia. (bbondzic@chem.bg.ac.rs)

### ABSTRACT

Theoretical study on the stereo selective Diels-Alder reaction has been performed on the model system consisting of a diene and a  $\alpha$ -halo substituted acroleine. DFT calculations revealed origin of selectivity of these reactions. Steric and electronic effects worked cooperatively to determine the outcome of the reaction.

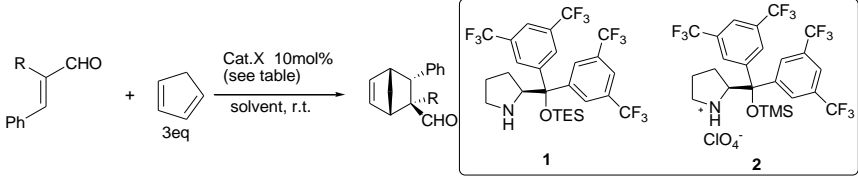
### INTRODUCTION

The Diels-Alder reaction [1] of  $\alpha$ -substituted acrolein derivatives proceeds in the presence of trifluoroacetic acid salt of trifluoromethyl substituted diarylprolinol silyl ether to afford *exo*-isomer with excellent diastereoselectivity, in sharp contrast from the reaction of the unsubstituted acroleins which give only moderate selectivities under the same reaction conditions. Aim of this study was to determine all the factors that influence such a difference in the chemical behavior of these compounds.

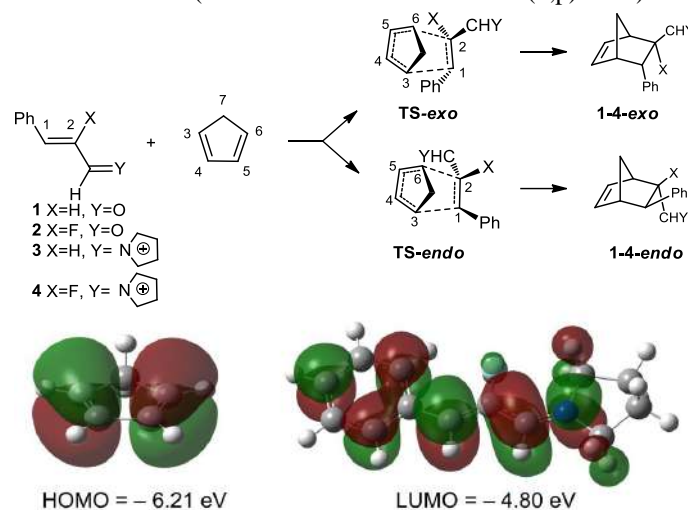
### RESULTS AND DISCUSSION

Organocatalyzed reaction of  $\alpha$ -F substituted acroleine was compared to the reaction of unsubstituted parent compound (Table 1). The rate of the reaction of  $\alpha$ -fluoro cinnam aldehyde is significantly lower compared to nonfluorinated cinnamaldehyde. Fluorine atom attached to the double bond decreases reactivity of dienophile in the Diels-Alder reaction [2]. On the other hand, diastereoselectivities are much better in the case of  $\alpha$ -fluoro cinnamaldehyde and are in the range of 99/1 while in the nonfluorinated substrate *exo/endo* ratio is approximately 4/1.

Starting from our experimental result, DFT calculations were performed in order to provide a further understanding of the observed *exo/endo* selectivity, and the contribution of fluorine atom on it. TS energies of organocatalyzed D-A reaction were compared to TS energies of uncatalyzed D-A reaction (Scheme 1).

**Table 1.** Reaction differences for fluorinated and nonfluorinated compounds


	Catalyst 1				Catalyst 2			
R	solvent	Time/h	Yield(%)	Dr	solvent	Time(h)	Yield(%)	Dr
H	toluene	26	quant	85/15	H <sub>2</sub> O	7	93	80/20
F	toluene	36	77	99/1	H <sub>2</sub> O	30	87	99/1

**Scheme 1.** Transition States and Products of *exo/endo*-Diels-Alder Reaction<sup>a</sup> (calculated on B3LYP/6311+G(d,p) level)

<sup>a</sup> The interacting cyclopentadiene HOMO and dienophile **4** LUMO are also shown as calculated on B3LYP/6311+G(d,p) level.

Energy profile, of the conventional (thermal) D-A reaction and the D-A reaction catalyzed by pyrrolidine as a model catalyst, as expected, shows drastically lower TS energies of the latter. There is a decrease of the cycloaddition activation energy ( $E_{act}$ ) of the substrate **3** and **4** (11.8 – 14.5 kcalmol<sup>-1</sup>) versus **1** and **2** (19.2 – 20.0 kcalmol<sup>-1</sup>).

FMO theory [3] has been applied to calculate LUMO energies and orbital coefficients of the **1-4** dienophile (Table 2).  $p_z$  orbital coefficients of C<sub>1</sub> and C<sub>2</sub> atoms, *i.e.* their differences, suggest increased character of asynchronicity. Decrease of absolute  $p_z$  orbital coefficients of the C<sub>1</sub> and C<sub>2</sub> atoms suggests that the fluorine substituent has an electron-donating effect rather than a withdrawing one.

**Table 2.** Calculated LUMO energies,  $p_z$  orbital coefficients (absolute value) of the double bond carbon atoms, double bond lengths and bond orders (BO) of dienophile **1-4**, at B3LYP/6311+G(d,p) level.

LUMO (eV)	-2.53	-2.67	-4.63	-4.80
$p_z$ LUMO C <sub>1</sub> /C <sub>2</sub>	0.764 / 0.562	0.710 / 0.504	0.835 / 0.313	0.782 / 0.253
d <sub>1-2</sub> (Å)	1.349	1.346	1.365	1.362
BO <sub>1-2</sub> <sup>a</sup>	1.294	1.299	1.220	1.232

Based on the analysis of the structural parameters of the optimized transition state structures **TS-1** - **TS-4**, presented in Table 3, it can be concluded that the *endo* transition state in each case occurs a little bit later on the reaction coordinate compared to the *exo* cyclization mode.

**Table 3.** Calculated bond lengths and bond orders of the forming bonds and charge transfer (CT) between subunits in TSs.

	TS-1 - <i>exo</i>	TS-1- <i>endo</i>	TS-2- <i>exo</i>	TS-2- <i>endo</i>	TS-3- <i>exo</i>	TS-3- <i>endo</i>	TS-4- <i>exo</i>	TS-4- <i>endo</i>
d <sub>1-3</sub> /d <sub>2-6</sub> (Å)	2.08/ 2.31	2.10/ 2.26	1.98/2.47	2.03/2.34	1.89/ 2.85	1.83/ 2.75	1.90/ 3.02	1.83/ 2.90
BO <sub>1-3</sub> /BO <sub>2-6</sub>	0.37/ 0.25	0.36/0.28	0.43/0.19	0.40/ 0.25	0.51/ 0.07	0.56/ 0.10	0.49/ 0.05	0.55/ 0.07
d <sub>1-2</sub> (Å)	1.419	1.420	1.419	1.423	1.439	1.451	1.429	1.446
BO <sub>1-2</sub>	1.139	1.136	1.154	1.150	1.061	1.034	1.096	1.065
CT (e)	0.188	0.179	0.205	0.197	0.465	0.487	0.454	0.514

In order to clarify the origin of the *exo/endo* selectivity, natural bond orbital (NBO) analyses on the transition states were performed (Table 4).

**Table 4.** Steric, electrical and donor-acceptor contributions (kcalmol<sup>-1</sup>) for the energy interaction in TSs, calculated using NBO analysis.

	TS-1- <i>exo</i>	TS-1- <i>endo</i>	TS-2- <i>exo</i>	TS-2- <i>endo</i>	TS-3- <i>exo</i>	TS-3- <i>endo</i>	TS-4- <i>exo</i>	TS-4- <i>endo</i>
$\Delta E_{steric}(endo-exo)$	5.51		2.80		33.52		36.23	
$\Delta E_{elec}(endo-exo)$	-3.09		-4.76		-2.98		1.26	
$\Delta E_{NL}(endo-exo)$	-3.10		0.12		-36.08		-45.04	

**TS-4-endo** is maximally steric destabilized (~36 kcalmol<sup>-1</sup>) which is consistent with the maximum of the *exo* preference. However, **Ts-2-endo** is almost twice less steric destabilized than **TS-1-endo** but requires more energy of distortion which supports the interpretation that the *exo* preference

of the reaction, with respect to the F atom, has not only the steric but also an electronic origin [4].

### CONCLUSION

The present study offers following conclusions: (1) FMO analysis of **1-4** dienophiles indicates lower reactivity of  $\alpha$ -fluoro derivatives **2** and **4**. The increase in the electron density of the central C=C bond is the consequence of electron donating character of the fluorine atom. (2) The presence of  $\alpha$ -F atom and the iminium ion in the dienophile have a cooperative effect on the stereoselectivity of the D-A reaction. (3) The *endo*-transition state in each case occurs a little bit later on the reaction coordinate (4) electrostatic interactions between the fluorine substituent in the  $\alpha$ -position of the dienophile and cyclopentadiene determine the stereoselectivity rather than simple steric interactions.

### Acknowledgement

This work was supported by the Ministry for Science of the Republic of Serbia (Grant no. 172020).

### REFERENCES

- [1] (a) E. Corey, J. Angew., Chem., Int. Ed. 2002, **41**, 1650. (b) K. C. Nicolaou, S. Snyder, T.A. Montagnon, G. Vassilikogiannakis, Angew. Chem., Int. Ed. 2002, **41**, 1668.
- [2] (a) J. A. Snell, A. Kuppermann, J. Chem. Phys. 1979, **71**, 4703- 4715. (b) J. K. Olthoff, J. A. Tossell, J. H. Moore, J. Chem. Phys. 1985, **83**, 5627-5634.
- [3] K. N. Houk, J. Am. Chem. Soc. 1973, **95**, 4092
- [4] G. K. Schenter, E. D. Glendening, J. Phys. Chem. 1996, **100**, 17152-17156.

## DIRECTION AND MECHANISM OF $\pi$ -ELECTRON DELOCALIZATION IN $\beta$ -SULFIDO- $\alpha,\beta$ -UNSATURATED ESTERS AND THEIR OXIDATION PRODUCTS

Z. Džambaski<sup>1</sup>, B. P. Bondžić<sup>1</sup>, J. Aleksić<sup>1</sup> and M. Baranac-Stojanović<sup>2</sup>

<sup>1</sup>University of Belgrade, Institute of Chemistry, Technology and Metallurgy,  
Njegoševa 12, 11000 Belgrade, Serbia. (zdzambas@chem.bg.ac.rs)

<sup>2</sup>Faculty of Chemistry, University of Belgrade, Studentski trg 12-16, 11000  
Belgrade, Serbia

### ABSTRACT

The strength of the Don-C=C-Acc  $\pi$ -electron flow, the *push-pull* effect, in the title sulfides and sulfoxides has been quantified theoretically on the basis of  $\pi^*/\pi$  occupation quotient and C=C bond length. Surprisingly, the two parameters changed little upon transformation to Acc'-C=C-Acc system, by sulfur oxidation to SO<sub>2</sub>. A careful analysis of donor-acceptor interactions in all molecules studied, revealed, the yet not described, backward  $\pi$ -electron flow from Acc to the C=C  $\pi$ -electron system. This type of electron delocalization should enhance the strength of the *push-pull* effect in *push-pull* systems.

### INTRODUCTION

Sulfur-containing compounds, such as sulfides and their oxidation products, sulfoxides and sulfones, play an important role in our lives, since they are involved in cell metabolism and used as drugs [1]. If a sulfide sulfur atom is connected to a double bond, containing an electron-acceptor (Acc) at its other end, a *push-pull* system **I** arises (Figure 1). It is characterized by the  $\pi$ -electron flow from donor to acceptor part, occurring via the C=C double bond (resonance structures **II** and **III**). As a consequence, *push-pull* systems are highly polarized molecules, exhibiting interesting physical properties and chemical reactivity [2,3].

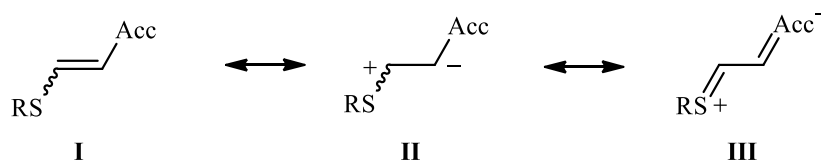


**Figure 1.** *Push-pull* alkenes containing sulfide moiety.



3.2 kcal/mol. The  $\pi_{C=C} \rightarrow \pi^*_{C=O}$  electron donation is less affected. The corresponding values are reduced from 18.4-19.4 kcal/mol to 15.4-16.9 kcal/mol. Quite unexpectedly, removal of the sulfur lone pair in sulfoxides **2**, by their oxidation to sulfones **3**, had a little effect on the C=C bond lengths and  $\pi^*/\pi$  quotient in *E* isomers, and almost no effect in *Z* isomers (Table 1). An inspection of electron occupancy of  $\pi^*_{C=C}$  orbital shows that it still receives electron density, even though the Don group has been transformed into the Acc' group, SO<sub>2</sub>. This observation prompted us to carefully examine energies associated with donor-acceptor interactions. As the data in Table 1. show, there is an electron *donation* from the *acceptor* group into the  $\pi$ -electron system of the C=C double bond, more pronounced in *Z* than in *E* sulfones.

**Table 1.** Occupation numbers of  $\pi$  and  $\pi^*$  orbitals of the C=C double bond, their quotient ( $\pi^*/\pi$ ), C=C double bond length (Å) and energies of donor-acceptor interactions (kcal/mol) in compounds **1-3** (a: R = CH<sub>2</sub>CO<sub>2</sub>Et; b: R = Ph; c: R = Et).

		$\pi$	$\pi^*$	$\pi^*/\pi$	$d_{C=C}$	$\begin{matrix} n_s \\ \rightarrow \pi^*_C \\ C \end{matrix}$	$\begin{matrix} \pi_{CC} \rightarrow \\ \pi^*_{CO} \end{matrix}$	$\begin{matrix} \pi_{CO} \rightarrow \\ \pi^*_{CC} \end{matrix}$
	<i>E</i> - <b>1a</b>	1.904	0.156	0.082	1.341	23.0	18.4	3.5
	<i>E</i> - <b>1b</b>	1.901	0.164	0.086	1.341	22.2	18.6	3.4
	<i>E</i> - <b>1c</b>	1.900	0.171	0.090	1.342	25.3	19.0	3.4
	<i>Z</i> - <b>1a</b>	1.898	0.182	0.096	1.346	26.2	19.4	4.0
	<i>Z</i> - <b>1b</b>	1.900	0.193	0.102	1.347	26.4	19.1	4.1
	<i>Z</i> - <b>1c</b>	1.899	0.198	0.104	1.348	28.4	19.1	4.1
	<i>E</i> - <b>2a</b>	1.916	0.078	0.040	1.330	3.0	15.4	3.9
	<i>E</i> - <b>2b</b>	1.914	0.077	0.040	1.329	3.2	15.8	3.8
	<i>E</i> - <b>2c</b>	1.915	0.082	0.043	1.330	3.2	15.8	3.9
	<i>Z</i> - <b>2a</b>	1.912	0.069	0.036	1.334	2.1	16.4	4.0
	<i>Z</i> - <b>2b</b>	1.910	0.071	0.037	1.333	1.3	16.4	4.0
	<i>Z</i> - <b>2c</b>	1.911	0.073	0.038	1.335	2.2	16.9	4.0
	<i>E</i> - <b>3a</b>	1.916	0.044	0.023	1.328	/	14.0	4.1
	<i>E</i> - <b>3b</b>	1.912	0.049	0.026	1.328	/	14.7	4.0
	<i>E</i> - <b>3c</b>	1.916	0.043	0.023	1.328	/	14.4	4.0
	<i>Z</i> - <b>3a</b>	1.926	0.064	0.033	1.332	/	13.5	4.9
	<i>Z</i> - <b>3b</b>	1.924	0.062	0.032	1.332	/	13.6	4.7
	<i>Z</i> - <b>3c</b>	1.925	0.064	0.033	1.332	/	13.6	4.8

Also, the  $\pi_{C=C}$  orbital donates its electron density not only to  $\pi^*_{C=O}$ , but also to  $\sigma^*_{S-O}$ , more so in *Z* ( $\sim 4.5$  kcal/mol) than in *E* isomers ( $\sim 2.3$  kcal/mol, not shown in the table). As a consequence, there is a little, or almost no change of  $\pi^*/\pi$  values and C=C bond lengths upon going from **2** to **3**. Further examination of donor-acceptor interactions showed that the backward  $\pi$ -electron flow from Acc to the C=C double bond contributes to the *push-pull* effect in *push-pull* systems **1** and **2**, as well.

The remote substituent, RS, shows a slight influence on the extent of the Don-C=C-Acc interactions only in sulfides **1**, the *push-pull* activity decreasing in the order Et > Ph > CH<sub>2</sub>CO<sub>2</sub>Et.

## CONCLUSION

A theoretical study of the  $\pi$ -electron delocalization in the title compounds has revealed that, in addition to one-directional Don  $\rightarrow$  Acc electron flow via the C=C bond, classically associated to *push-pull* systems, there exists the backward Acc  $\rightarrow$  C=C bond  $\pi$ -electron donation, contributing to the *push-pull* effect in sulfides and sulfoxides. The same was found for sulfones, which represent Acc'-C=C-Acc system.

## Acknowledgement

This work was supported by the Ministry of Education, Science and Technological Development of the Republic of Serbia (Grant No. 172020).

## REFERENCES

- [1] Kalir, H. H. Kalir, in: *The Chemistry of Sulphur-Containing Functional Groups*, (Ed.: S. Patai, Z. Rappoport), Wiley - VCH, 1993, 957-973.
- [2] J. Sandström, *Top. Stereochem.* 1983, **14**, 83-181.
- [3] E. Kleinpeter, *J. Serb. Chem. Soc.*, 2006, **71**, 1-17.
- [4] A. D. Becke, *J. Chem. Phys.*, 1993, **98**, 5648-5652; C. Lee, W. Yang, R. G. Parr, *Phys. Rev. B: Condens. Matter Mater. Phys.*, 1988, **37**, 785-789.
- [5] J. B. Foresman, A. Frisch, *Exploring Chemistry with Electronic Structure Methods*, Gaussian, Inc., 1996.
- [6] R. Ditchfield, *Mol. Phys.*, 1974, **27**, 789-807; K. Wolinski, J. F. Hinton, P. Pulay, *J. Am. Chem. Soc.*, 1990, **112**, 8251-8260.
- [7] E. Kleinpeter, S. Klod, W.-D. Rudolf, *J. Org. Chem.*, 2004, **69**, 4317-4329.
- [8] E. D. Glendening, C. R. Landis, F. Weinhold, *Wiley Interdiscip. Rev.: Comput. Mol. Sci.*, 2012, **2**, 1-42.
- [9] M. J. Frisch et al., *Gaussian 09 (Revision D.01)*, Gaussian Inc.: Wallingford, CT, 2013.

## EXPERIMENTAL AND THEORETICAL VIBRATIONAL SPECTRA OF SIDERIDIOL ISOLATED FROM *SIDERITIS* SPECIES

T.Kılıç<sup>1</sup>, Z. Özer Sağır<sup>2</sup>, S. Çarıkçı<sup>3</sup> and A. A. Azizoğlu<sup>3</sup>

<sup>1</sup>Balıkesir University, Necatibey Education Faculty, Department of Science Educations, 10100, Balıkesir. Turkey. (tkilic@balikesir.edu.tr)

<sup>2</sup>Balıkesir University, Altınoluk Vocational School, Medicinal and Aromatical Plants Program, 10870, Edremit, Balıkesir. Turkey.

<sup>3</sup>Balıkesir University, Faculty of Sciences and Arts, Department of Chemistry, Campus of Çağış, 10145- Balıkesir, Turkey.

### ABSTRACT

Sideridiol (*ent*-7 $\alpha$ ,18 $\beta$ -dihidroksikaur-15-en) one of the *ent*-kaurene diterpenoid, is isolated from the genus *Sideritis* L. belongs to the family of Lamiaceae. The vibrational frequencies of sideridiol in the ground state have been calculated using the Density Functional Theory (DFT) method with the 6-31G(d) and 6 31+G(d,p) basis sets. The calculated vibrational frequencies have been compared with that of obtained experimental IR spectrum.

### INTRODUCTION

As a member of the Lamiaceae plant family the *Sideritis* genus is represented by about 150 species in the world [1]. The therapeutic use of *Sideritis* species is mentioned firstly Dioscorides book written in the 1st century; "Da Materia Medica"[2]. This genus widely used in the treatment of gastrointestinal disorders, cough, the common cold and as a diuretic, and are commonly used as an herbal tea in folk medicine in Turkey [3]. The chemical components found in *Sideritis* genus include terpenes, flavonoids, iridoids, coumarins, lignanes and sterols, among others. Diterpenes and flavonoids occur in almost every species and are the main compounds responsible for the observed in vivo and in vitro pharmacological activities [2]. Sideridiol (1) is an *ent*-kaurene diterpene, the most frequently found in *Sideritis* species. It has the antifeedant [4], antioxidant, anticholinesterase [5], antibacterial and antifungal activity [6].

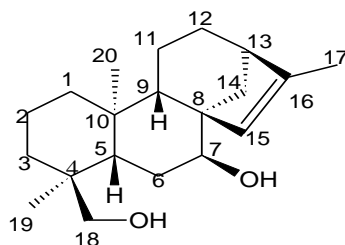


**Figure 1.** Structure and atom numbering scheme of sideridiol.

## EXPERIMENTAL

Sideridiol having the *ent*-kaurene skeleton can be isolated from different species of *Sideritis* such as *S. akmanii*, *S. argyrea*, *S. condensata*, *S. congesta*, *S. dichotoma*, *S. erythrantha*, *S. huber-morathii*, *S. libanotica*, *S. perfoliata*, *S. sipylea*, *S. stricta* and *S. trojana* [7]. Infrared spectrum was obtained using a PerkinElmer Spectrum Version 10.02.00. The molecular structure of the title molecule in the ground state (in vacuo) was optimized using Density Functional Theory (DFT) with the 6-31G(d) and 6-31+G(d,p) basis sets. All of the calculations reported in this study have been performed using the Gaussian 09 code [8].

## RESULTS AND DISCUSSION

We have calculated the theoretical vibrational spectra of sideridiol using B3LYP and X3LYP levels with 6-31G(d) and 6-31+G(d,p) basis sets. Theoretical and experimental results of title compound are shown in Table 1. The vibrational analysis of sideridiol is performed on the basis of the characteristic vibrations of methyl groups, OH groups and C=C group. The symmetric C=C stretching frequencies observed at  $1656\text{ cm}^{-1}$  are theoretically predicted at between  $1705\text{ cm}^{-1}$  and  $1726\text{ cm}^{-1}$ . The free OH group in the region  $3700\text{--}3580\text{ cm}^{-1}$ , whereas the existence of intermolecular hydrogen bond formation can lower the O-H stretching frequency to the  $3550\text{--}3200\text{ cm}^{-1}$  region with increase in intensity and broadness [9]. The OH vibration is observed to  $3759$  and  $3864\text{ cm}^{-1}$  in experimental IR spektrum. This bands calculated  $3710\text{--}3854\text{ cm}^{-1}$ . Methyl vibrations are generally occur in the range  $(2900\text{--}3000)\text{ cm}^{-1}$ . The bands observed in the range  $(3013\text{--}3160)\text{ cm}^{-1}$  using DFT are assigned to asymmetrical stretching methyl vibrations. The correlation values are found to be 0,9966 and 0,9966 for B3LYP and X3LYP with the 6- 31G(d) basis set and 0,9986 and 0,9987 for B3LYP and X3LYP with 6-31+G(d,p) respectively. So that X3LYP level with 6-31+G(d,p) basis set is the best method.

**Table 1.** Selected experimental and theoretical vibrational wavenumbers of Sideridiol

Exp.	B3LYP/6-31G(d)	B3LYP/6-31+G(d,p)	X3LYP/6-31G(d)	X3LYP/6-31+G(d,p)	Approximate description
	390,46	339,03	393,9	351,18	<b>O-H</b> rocking (C7)
	347,76	333,17	349,23	334,70	<b>O-H</b> rocking (C18)
	870,95	850,17	873,21	865,20	<b>H-C=C</b> rocking
	990,07	979,99	992,50	982,30	<b>H<sub>2</sub>C-OH</b> rocking
	1012,14	1001,22	1014,69	1022,23	C=C- <b>CH<sub>3</sub></b> rocking
	1030,91	1020,11	1033,00	1043,62	
	1075,80	1058,33	1079,73	1062,37	<b>C-O</b> symmetrical stretch (C18)
	1102,08	1088,45	959,90	1092,36	<b>C-O</b> symmetrical stretch (C7)
	1286,95	1192,04	1289,54	1135,91	<b>H-C=C</b> rocking
1357,34	1314,24	1302,07	1317,01	1304,62	<b>CH<sub>2</sub>-OH</b> twisting (C18)
1381,58	1389,43	1371,73	1384,46	1366,66	<b>H-C-OH</b> rocking (C7)
	1398,85	1380,65	1392,08	1374,29	
1441,81	1440,86	1415,90	1442,58	1417,88	C=C- <b>CH<sub>3</sub></b> wagging
	1448,03	1426,76	1450,51	1429,41	CH <sub>3</sub> wagging
	1463,76	1437,87	1466,20	1440,02	<b>CH<sub>2</sub>-OH</b> wagging
	1508,62	1482,45	1510,09	1483,64	
	1518,24	1489,91	1519,78	1491,23	C=C- <b>CH<sub>3</sub></b> scissoring
	1519,97	1490,89	1520,64	1492,21	
	1528,21	1503,46	1533,68	1504,86	CH <sub>2</sub> scissoring
	1551,06	1521,22	1552,86	1526,64	<b>CH<sub>2</sub>-OH</b> scissoring (C18)
	1555,52	1531,56	1556,92	1532,89	CH <sub>3</sub> scissoring
1656,35	1720,92	1705,59	1726,48	1710,74	C=C symmetrical stretch
	2986,87	2991,24	2992,43	2996,12	<b>H-C-OH</b> symmetrical stretch (C7)
	3001	3001,79	3006,48	3006,44	<b>H<sub>2</sub>C-OH</b> symmetrical stretch (C18)
2944,78	3022,41	3013,76	3027,39	3017,86	C=C- <b>CH<sub>3</sub></b> symmetrical stretch
2994,42	3032,31	3038,36	3038,03	3043,20	<b>CH<sub>2</sub>-OH</b> (C-18) asymmetrical stretch
	3088,68	3081,03	3093,35	3051,90	CH <sub>2</sub> (C6) asymmetrical stretch
3055,99	3116,22	3108,46	3121,54	3112,78	C=C- <b>CH<sub>3</sub></b> asymmetrical stretch
	3155,83	3136,45	3160,43	3128,34	CH <sub>3</sub> asymmetrical stretch
	3219,74	3212,96	3224,24	3216,57	<b>H-C=C</b> symmetrical stretch
3759,45	3710,84	3793,49	3716,64	3799,31	O-H symmetrical stretch (C7)
3864,01	3759,52	3845,38	3768,04	3854,34	O-H symmetrical stretch (C18)

## CONCLUSION

In this study, we have calculated the geometric parameters and vibrational frequencies of sideridiol by using DFT (B3LYP and X3LYP) methods with 6-31G(d) and 6-31+G(d,p) basis sets. The theoretical vibrational analysis of sideridiol has also been performed for the first time. The calculated vibrational frequencies have been compared with that obtained from the experimental IR spectrum. As a result, experimental fundamentals are found to have slightly a better correlation for X3LYP level with 6 31+G(d,p) basis set than others.

## Acknowledgement

This work was partially supported by TUBITAK (Grant no. 105T430 and Grant no. 113Z710).

## REFERENCES

- [1] Aslan, T. Kılıç, A.C. Goren, G. Topçu, *Industrial Crops and Products*, 2006, **23**, 171-176.
- [2] E. González-Burgos, M.E. Carretero, M.P. Gómez-Serranillos, *Journal of Ethnopharmacology*, 2011, **135**, 209-225.
- [3] A. Güvenç, Y. Okada, E. Küpeli Akkol, H. Duman, T. Okuyama, I. Çalış, *Food Chemistry*, 2010, **118**, 686-692.
- [4] M.L. Bondi, M. Bruno, F. Piozzi, K. Husnu Can Baser, M. S.J. Simmonds, *Biochemical Systematics and Ecology*, 2000, **28**, 299-303.
- [5] G. Topçu, A. Ertas, M. Öztürk, D. Dinçel, T. Kılıç, B. Halfon, *Phytochemistry Letters*, 2011, **4**, 436-439.
- [6] T. Kilic, *Molecules*, 2006, **11**, 257-262.
- [7] B.M. Fraga, *Phytochemistry*, 2012, **76**, 7-24.
- [8] Gaussian 09. Revision A02, Gaussian, Inc., Pittsburgh.
- [9] A. Azizoglu, Z. Zuer and T. Kilic, *Collect. Czech. Chem. Comm.*, 2011, **76**, 95-114.

## THEORETICAL STUDIES ON MOLECULAR STRUCTURE AND NMR SPECTRA OF SIDEROXOL ISOLATED FROM *SIDERITIS* SPECIES

T.Kılıç<sup>1</sup>, Z. Özer Sağır<sup>2</sup>, S. Çarıkçı<sup>3</sup> and A. A. Azizoğlu<sup>3</sup>

<sup>1</sup>*Balıkesir University, Necatibey Education Faculty, Department of Science  
Educations, 10100, Balıkesir. Turkey. (tkilic@balikesir.edu.tr)*

<sup>2</sup>*Balıkesir University, Altınoluk Vocational School, Medicinal and  
Aromatical Plants Program, 10870, Edremit, Balıkesir. Turkey.*

<sup>3</sup>*Balıkesir University, Faculty of Sciences and Arts, Department of  
Chemistry, Campus of Çağış, 10145- Balıkesir, Turkey.*

### ABSTRACT

The molecular geometry and gauge including atomic orbital (GIAO) <sup>1</sup>H and <sup>13</sup>C NMR chemical shift values of sideroxol have been calculated using the Hartree–Fock (HF) and Density Functional Theory (DFT) methods with the 6-31G(d) and 6-31+G(d,p) basis sets, and compared with the experimental data. The optimized geometrical parameters obtained by theoretical calculations are in good conformity with XRD data. Also <sup>1</sup>H and <sup>13</sup>C NMR chemical shifts of sideroxol were compared with experimental values, which yield good agreement between the observed and calculated values.

### INTRODUCTION

Sideroxol (*ent*-7 $\alpha$ ,18-dihidroksi-15 $\beta$ ,16 $\beta$ -epoksikauran), one of the *ent*-kaurene diterpenoid, is isolated from the genus *Sideritis* L. belongs to the family of Lamiaceae (Labiatae) [1]. *Sideritis* species are widely distributed in Turkey with 44 species (55 taxa) mainly in Marmara and Aegean regions. They are widespread used against gastrointestinal disorders, such as stomach ache, indigestion and flatulence, to alleviate the symptoms of common colds including fever, flu, sore throat and bronchitis as well as a tonic and diuretic remedy [2]. Sideroxol (Fig.1) is an important compound that has the antifeedant [3], antioxidant, anticholinesterase [4], antibacterial and antifungal activity [5].

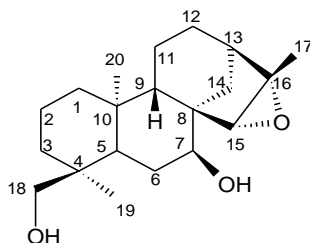


**Figure 1.** Structure and atom numbering scheme of sideroxol.

The effects of the structural features on the physico-chemical properties and on the bioactivity of these compounds were investigated in numerous experimental and theoretical studies. Density Functional Theory (DFT), have become the dominant computational tools for dealing with organic molecules, isolated from plants. NMR spectroscopy constitutes an extremely useful tool for the determination of molecular electronic structure and structural information [6].

### EXPERIMENTAL

Sideroxol having the *ent*-kaurene skeleton can be isolated from different species of *Sideritis* such as *S. arguta*, *S. leptoclada*, *S. akmanii*, *S. gulendami*, *S. condensata*, *S. rubiflora*, *S. congesta*, *S. dichotoma*, *S. ozturkii* and *S. stricta* [7]. All the calculations are performed by using GAUSSIAN 09W program [8]. The geometry data of title molecule was taken from X-ray structure [9]. The molecular structure of the title molecule was optimized using Hartree-Fock (HF) and Density Functional Theory (DFT) with the 6-31G(d) and 6-31+G(d,p) basis sets.

### RESULTS AND DISCUSSION

The optimized geometric parameters (bond length and angles) by DFT and HF methods with 6-31G(d) and 6-31+G(d,p) basis sets are listed in Table 1 and compared with the experimental crystal geometry for the title compound ( $C_{20}H_{32}O_3$ ). For instance, the correlation coefficient values ( $R^2$ ) between experimental and theoretical bond lengths are found to be 0.9648, 0.9649, 0.9545, 0.9558, 0.9586 and 0.9588 for B3LYP, HF, M05 levels with 6-31+G(d,p) and 6-31G(d) basis sets respectively. It can be deduced that the B3LYP level with 6-31G(d) basis set is the best method. After the optimization of the title compound,  $^1H$  and  $^{13}C$  NMR chemical shifts were calculated. Sideroxol shows 20 different carbon atoms, which is consistent with the structure of the molecule.

**Table 1.** Experimental and Optimized structural parameters of Sideroxol.

Bond lengths (Å)	Exp.	HF/6-31G(d)	HF/6-31+G(d,p)	B3LYP/6-31G(d)	B3LYP/6-31+G(d,p)	M05/6-31G(d)	M05/6-31+G(d,p)
O18-C18	1.428	1.409	1.410	1.432	1.436	1.418	1.422
O7-C7	1.465	1.413	1.414	1.435	1.439	1.422	1.426
O-C15	1.467	1.412	1.414	1.442	1.446	1.419	1.422
O-C16	1.467	1.414	1.415	1.448	1.450	1.425	1.426
C15-C16	1.478	1.450	1.451	1.469	1.470	1.458	1.459
O18-H	0.988	0.947	0.942	0.969	0.965	0.963	0.959
O7-H	0.958	0.948	0.944	0.972	0.968	0.966	0.962
C18-H18a	0.940	1.086	1.086	1.100	1.099	1.099	1.098
C18-H18b	0.976	1.088	1.088	1.101	1.099	1.099	1.098
Bond angles (°)							
C18-O18-H	117.25	109.39	110.16	107.85	108.91	107.87	109.02
C7-O7-H	119.54	110.20	110.91	108.39	109.40	108.56	109.64
H18a-C18-O18	110.43	109.77	109.57	110.09	109.62	110.13	109.65
H18b-C18-O18	108.95	109.97	109.84	110.24	110.04	110.28	110.05
H7-C7-O7	109.34	108.47	108.31	108.28	108.03	108.46	108.11
C15-O-C16	60.47	61.73	61.72	61.11	61.02	61.70	61.63
C16-C15-O	59.76	59.20	59.17	59.64	59.64	59.33	59.32
C15-C16-O	59.77	59.06	59.10	59.24	59.34	58.97	59.04
C17-C16-O	115.06	115.29	115.28	115.36	15.36	115.72	115.71
Dihedral angles (°)							
C19-C4-C18-O18	-179.82	-168.09	-180.64	-167.19	-168.14	-167.68	-168.32
C8-C7-O7-H	-174.53	-149.59	-152.50	-140.40	-145.79	-143.70	-147.12
C6-C7-O7-H	-61.58	-27.27	-29.96	-18.06	-23.13	-21.23	-24.32
C14-C8-C15-O	37.82	38.62	38.61	38.60	38.67	38.26	38.28
C14-C13-C16-O	-37.57	-36.42	-36.49	-36.64	-36.86	-36.00	-36.19
C17-C16-C15-O	100.93	100.59	100.56	100.86	100.83	101.19	101.12
C8-C15-C16-C17	-153.87	-152.72	-152.79	-151.67	-151.71	-151.26	-151.34
C4-C18-O18-H	-177.46	-166.01	-163.82	-168.20	-164.09	-167.04	-163.83

Experimental  $^{13}\text{C}$  NMR spectrum peaks which appear at 71.31 and 71.23 ppm belong to the (C7) and (C18), theirs computed values are in the range of 60.37–64.22 and 60.08–63.3 ppm respectively. Also  $^1\text{H}$  NMR spectrum provides information about the number of different types of protons. The  $^1\text{H}$  NMR chemical shift values (with respect to TMS) have been calculated to be -0.35–3.75 ppm with HF level, -0.21–4.25 ppm with B3LYP level, -0.5–4.19 ppm with the M05 level. Meanwhile, the O-H signal was obtained as 0.14–1.18 (C7) and -0.5–0.45 (C18) ppm theoretically. The H7 signals was observed as 4.79 ppm, this signal was computed as 3.28–3.70 ppm by HF and DFT theories with the 6-31G (d) basis set, and 3.74–4.25 ppm with the 6-31+G(d,p) basis set. B3LYP level with 6-31G(d) basis set is the best

method for  $^{13}\text{C}$  and  $^1\text{H}$  NMR. The correlation values for proton and carbon chemical shifts are 0.9726 and 0.9759 with B3LYP/6-31G(d).

## CONCLUSION

In this study, we have calculated the geometric parameters and chemical shifts of *ent*-kaurane diterpenoid Sideroxol (Fig. 1) by using DFT and HF methods with 6-31G(d) and 6-31+G(d,p) basis sets. In general, all bond lengths and bond angles computed herein show good agreement with experimental findings. As a result, calculated bond lengths and angles at B3LYP/6-31G(d) method show much better agreement than other methods. Moreover,  $^1\text{H}$  and  $^{13}\text{C}$  NMR chemical shifts have been compared with experimental values. The experimental chemical shift values of all the carbon and hydrogen atoms are in good agreement with the theoretical values. In particular the computational results at the B3LYP/6-31G(d) method have shown better fit to experimental predictions than others in evaluating  $^1\text{H}$  NMR and  $^{13}\text{C}$  NMR chemical shifts.

## Acknowledgement

This work was partially supported by TUBITAK (Grant no. 105T430 and Grant no. 113Z710).

## REFERENCES

- [1] S. Çarıkçı, T. Kılıç, A. Azizoglu and G. Topçu, Rec. Nat. Prod., 2012, **6**, 101-109
- [2] S. Çıtak, Z. Özer Sağır, S. Çarıkçı, T. Kılıç and A. Azizoglu, Rev. Roum. Chim., 2014, **59**, 227-234.
- [3] M.L. Bondi, M. Bruno, F. Piozzi, K. Husnu Can Baser, M. S.J. Simmonds, Biochemical Systematics and Ecology, 2000, **28**, 299-303.
- [4] G. Topçu, A. Ertas, M. Öztürk, D. Dinçel, T. Kiliç, B. Halfon, Phytochemistry Letters, 2011, **4**, 436-439.
- [5] T. Kiliç, Molecules, 2006, **11**, 257-262.
- [6] C.B. Yıldız, Z. Ozer Sagır, T. Kılıç and A. Azizoglu, Studia Ubb Chemia, Lix, 2014, **2**, 17-32.
- [7] B.M. Fraga, Phytochemistry, 2012, **76**, 7-24.
- [8] Gaussian 09. Revision A02, Gaussian, Inc., Pittsburgh.
- [9] T. Kiliç, Y.K. Yildiz, G. Topçu, A.C. Goren, M. Ay, S.G. Bodge, W.H. Watson, J. Chem. Crystallogr, 2005, **35**, 647-650.

## SLOW AND LOW YIELD *N*-ALKYLATION OF 3-(2-PHENYLHYDRAZONO)INDOLIN-2-ONE, COMPARED TO THAT OF 1*H*-INDOLE-2,3-DIONE; REASONS BY THEORETICAL INVESTIGATION

A. R.Nekoei

*Department of Chemistry, Shiraz University of Technology, Shiraz, 71555-313, Iran (nekoei@sutech.ac.ir)*

### ABSTRACT

Synthetic strategies of an important derivative of isatin's Schiff bases, which have been reported to possess important pharmaceutical activities, are focused in the present study. Although the nitrogen atom in isatin molecule is experimentally known as a strong nucleophile, it has been shown that this character vanishes in its phenylhydrazono derivative reactions. According to our DFT and NBO investigation, turning a lone pair of atom N to a  $\pi$ -bond in the anion of phenylhydrazono derivative of isatin is the main reason for its slow and low yield *N*-alkylation.

### INTRODUCTION

Isatin (*1H*-indole-2,3-dione) is an endogenous heterocyclic molecule which has significant properties and also presents in tissues of mammals such as human [1-3]. Possessing a wide range of biological activities leads to the publication of numerous articles and books about isatin and its derivatives, especially its Schiff bases. Some of these activities are antifungal, antibacterial, antiviral, antiallergic and anticonvulsant activities [4-9]. They have also been frequently used as precursors for the manufacture of other heterocyclic compounds [10]. Furthermore, isatin and its derivatives are employed as initiator for synthesis of some pharmaceutical compounds.

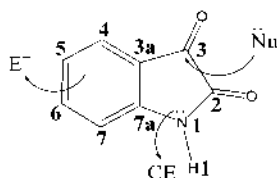
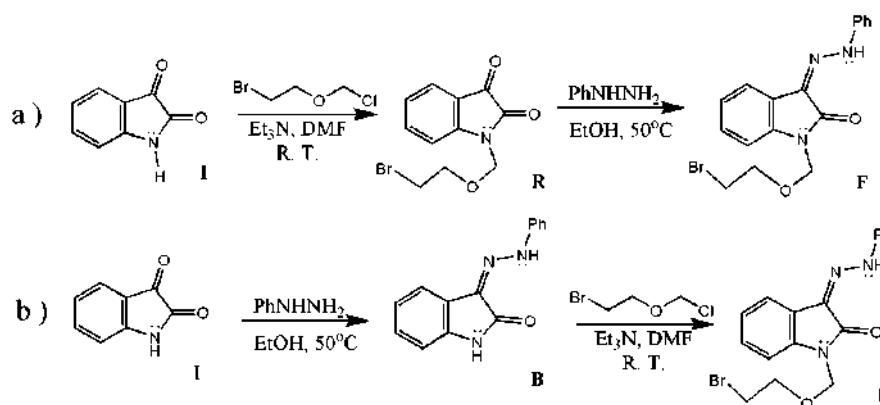


**Figure 1.** Different reaction sites of isatin(CE: carbon electrophile) and its atom numbering scheme

According to the experimental observation [10, 11], as shown in Fig. 1, isatin mainly reacts at three sites, including electrophilic aromatic substitution at C5, *N*-alkylation at N1, and carbonyl reaction at C3.

According to the experiment [12], as it is apparent in Scheme 1, two procedures have been proposed for synthesis of 3-(2-phenylhydrazono)-1-((2-bromoethoxy) methyl) indolin-2-one (compound **F**, an important derivative of isatin in pharmaceutical chemistry) from isatin (compound **I**).



**Scheme 1.** Proposed reaction pathways for synthesis of compound **F** from isatin

The first pathway (a) is the direct condensation of isatin in the presence of base  $\text{Et}_3\text{N}$  with 2-bromoethoxymethyl chloride (RX as electrophile for *N*-alkylation) that gave acyclic nucleoside 1-((2-bromoethoxy)methyl)indoline-2,3-dione (compound **R**). To convert the compound **R** to its phenylhydrazone analogue (**F**), phenylhydrazine solution in EtOH is subsequently used [12].

The second pathway (b) to obtain compound **F** is direct condensation of compound **B** (3-(2-phenylhydrazono) indolin-2-one, PHIO), which have been obtained from reaction between **I** and phenylhydrazine solution in EtOH, with 2-bromoethoxymethyl chloride [12]; but it gave very poor yield of **F** [12]. Since the RX used is very strong electrophile, which even reacts with water vapor of breath out, reason of the poor yield of this reaction could be of interest and are discussed in this paper. It is noteworthy that some previous studies suggest this could be attributed to the formation of intramolecular hydrogen bonding in the lactim form of compound **B** (see Fig. 2), in which there is no adjacent H atom to the atom N1, and so the nucleophilic power of N1 diminishes [12].

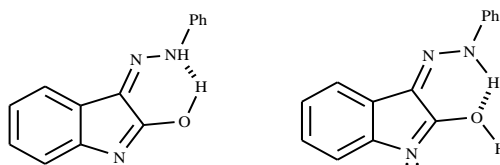


**Figure 2.** Possible lactim forms for compound **B** and its intramolecular hydrogen bond

## METHODOLOGY

All computations in the present work have been carried out using Gaussian 09 software package at B3LYP level of DFT quantum mechanical method with 6-31G(d,p), 6-311G(d,p) and 6-311++G(d,p) basis sets. Also, GenNBO 5.0 and GaussView 5.0 programs have been employed for natural bond orbital (NBO) and structural analysis at the same method and basis sets.

## RESULTS AND DISCUSSION

All five possible tautomeric classes of PHIO (each have several conformers) and three tautomeric forms of satin have been fully analysed for conformational search and computational relative stabilities. According to the results at all used DFT levels, the presence of lactim tautomers of **I** and **B** (in which the atom H1 is not bonded to N1, with relative energies for their most stable conformations of about 14 and 18 kcal/mol, respectively) is improbable at room temperature. Therefore the H1 engaged in IHB as the reason for vanishing the nucleophilic character of N1 was rejected.

Based on the NBO analyses, reactants **I** and **B** show no remarkable differences in orbital hybridization, occupancy and interaction, Wiberg bond orders, and natural charges at N1. Therefore, because we are sure from experimental observation that the *N*-alkylation of **I** and **B** in the presence of base is quite different in speed and yield, in the next step, we assumed a two-step reaction in which **I** and **B** first convert to their anion analogues as nucleophiles for reaction with RX. Therefore we performed optimization and NBO analyses for **I** and **B** anions, and their results have been compared with each other and also with their neutral forms. The most interesting result, which was not predictable from the molecular structure, is that **I**<sup>-</sup> has two free electron lone pairs on N1, first in sp<sup>1.83</sup> hybridized orbital with occupancy of 1.93, second in pure p orbital with occupancy of 1.4, while there is just one lone pair in sp<sup>1.90</sup> hybridized orbital in **B**<sup>-</sup> with occupancy of 1.93. More investigation showed that second lone pair turns to a π-bond in **B**<sup>-</sup>, which could be the main reason of diminishing nucleophilic character of N1 in this anion. Also, natural atomic charge analyses showed that the most

negative site of  $\mathbf{B}^-$  is the oxygen atom of C2=O carbonyl group with charge of -0.725, while in  $\mathbf{I}^-$ , N1 atom with charge of -0.679 is the most negative site. This result also confirms the mentioned reason for the questioned observation. Donor-acceptor orbital interactions, evaluated by second order perturbation theory, also confirm the mentioned conclusion.

Also, since the two-step reaction reasonably explains the experimental observation, while one-step reaction leads to no acceptable answer for the problem, we suggest that this *N*-alkylation is a two-step reaction.

### CONCLUSION

The main reason for slow and low yield *N*-alkylation of phenylhydrazono derivative of isatin, using RX as electrophile in the presence of base, is attributed to the N1 nucleophilic character vanishing, due to turning of an electron lone pair of atom N1 to a  $\pi$ -bond in the anion of the compound formed in a two-step reaction in the presence of the base.

### REFERENCES

- [1] R.D. Souza, A. Chattree, *Chem. Sci.*, 2014, **4** (1), 208-212.
- [2] N. Igosheva, S. Matta, V. Glover, *Physiol. Behav.*, 2004, **80** (5), 665-668.
- [3] N. Usami, K. Kitahara, S. Ishikura, M. Nagano, S. Sakai, A. Hara, *FEBS J.*, 2001, **268** (22), 5755-5763.
- [4] S. Ali, M. Alam, *J. Pharm. Pract. Res.*, 1994, **17** (2), 131-133.
- [5] A. Jarrahpour, D. Khalili, E. De Clerc, C. Salmi, J. M. Brunel, *Molecules*, 2007, **12** (8), 1720-1730.
- [6] S. K. Sridhar, M. Saravanan, A. Ramesh, *Eur. J. Med. Chem.*, 2001, **36** (7), 615-625.
- [7] S. N. Pandeya, S. Smitha, M. Jyoti, S. K. Sridhar, *Acta Pharm.*, 2005, **55** (1), 27-46.
- [8] N. Nami, M. Hosseinzadeh, *Heterocycl. Commun.*, 2007, **13** (6), 403-406.
- [9] A. Bacchi, M. Carcelli, P. Pelagatti, G. Pelizzi, M. C. Rodriguez-Arguelles, D. Rogolino, C. Solinas, D. F. Zani, *J. Inorg. Biochem.*, 2005, **99** (2), 397-408.
- [10] J. F. Da Silva, S. J. Garden, A. C. Pinto, *J. Braz. Chem. Soc.*, 2001, **12** (3), 273-324.
- [11] M. F. Ibrahim, A. A. A. Al-Karewi, S. N. Khattab, E. A. Hamed, A. El-Faham, *Asian J. Chem.*, 2014, **26** (23), 8029-8038.
- [12] M. N. Soltani Rad, Ph.D Thesis, Shiraz University, Shiraz, 2004.

## CHEMOSELECTIVE ALKYLATION OF $\beta$ - ENAMINOESTERES WITH ETHYL PROPIOLATE: EXPERIMENTAL AND THEORETICAL STUDY

M. Stojanović<sup>1</sup>, J. Aleksić,<sup>1</sup> Z. Džambaski<sup>1</sup> and M. Baranac-Stojanović<sup>2</sup>

<sup>1</sup>*Center for Chemistry, Institute of Chemistry, Technology and Metallurgy, University of Belgrade, Njegoševa 12, P.O. Box 473, 11000 Belgrade, Serbia*

<sup>2</sup>*Faculty of Chemistry, University of Belgrade, Studentski trg 12-16, P.O. Box 153, 11000 Belgrade, Serbia*

### ABSTRACT

An efficient and chemo selective synthesis of highly functionalized  $\delta$ -dienaminoester and *N,N*-bis( $\beta$ -enaminoester) is achieved under neutral and basic conditions, starting from benzylamine and ethyl propiolate. The origin of chemo selectivity of the Michael-type addition of intermediate  $\beta$ -enaminoester to ethyl propiolate is investigated using DFT study.

### INTRODUCTION

The addition of amines to electron deficient acetylenes has been the subject of a number of studies since the sixties of the last century.[1] This aza-Michael-type reaction is one of the most suitable and most commonly used methods for obtaining the special type of enamines having electron-withdrawing group on the other terminus of C=C bond -  $\beta$ -enaminones. This type of compounds also belong to the group of the so-called *push-pull* olefins, which contain one or two electron-donor groups at one end and one or two electron-acceptor groups at the other end of the double bond.[2] Due to electronic interactions between donor and acceptor groups, across the central C=C double bond, it becomes polarized with a partial single bond character affecting its bond order, bond length and energy of rotation (Figure 1.).

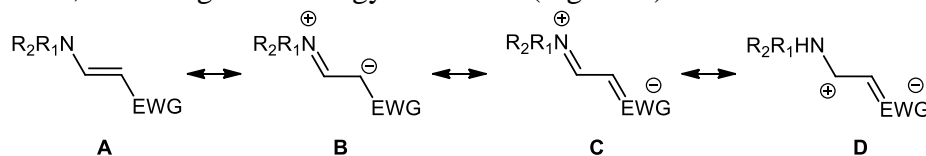


**Figure 1.** Resonance structures of enaminones.

A direct consequence of this electronic structure is specific chemical behavior: these compounds have interesting amphiphilic reactivity, that is the double bond possesses both nucleophilic and electrophilic sites

(structures **B** and **D**, Figure 1.) However, it should be noted that their nucleophilicity is lower than that for conventional enamines and electrophilicity is smaller than for classical Michael's acceptors bearing only electron-withdrawing groups. Enamin ones are versatile building blocks and have a wide range of synthetic applications, such as in the preparations of heterocycles, including alkaloids,  $\alpha$ - and  $\beta$ -amino acids, peptides, and other synthetically relevant compounds.[3] Our study of the reaction of  $\beta$ -amino acrilates with excess of ethyl propiolate gave us new insight into the reactivity of these compounds.

## RESULTS AND DISCUSSION

It is well known that the addition of propiolate to either primary or secondary amines in the cold generally results in the formation of  $\beta$ -enaminoester **1** (Figure 2). However, heating a primary amine with excess of propiolate results in the formation of  $\delta$ -dienaminoesters **2**, evidently by C-alkylation of initially formed enamino ester **1**. [4] There are several nucleophilic centers in enamino esters **1**, including the  $\alpha$ -carbon atom, the oxygen atom, and the amino group. Compounds of structure **2** has recently been used as substrates for further cyclizations to 1,2-dihidropyridines, 1,4-dihidropyridines, 2-pyridinones, pyrroles.[5] Herein we report that complementary chemoselectivity of enamino esters with the amino group as a nucleophilic center can be achieved. In the presence of a base, such as triethyl amine, potassium *tert*-butoxide and cesium carbonate, a primary amine, i.e. benzyl amine, reacts with excess of ethyl propiolate producing exclusively *N,N*-disubstituted product **3** ( $R_1$ =Bn,  $R_2$ =Et) which was characterized on the basis of HRMS and 2D NMR techniques. After a series of screenings,  $\text{Cs}_2\text{CO}_3$  was identified as the most efficient base for this reaction, in which desired product **3** ( $R_1$ =Bn,  $R_2$ =Et) was isolated in 74% yield, after a reaction time of 10' in refluxing  $\text{CH}_3\text{CN}$ .

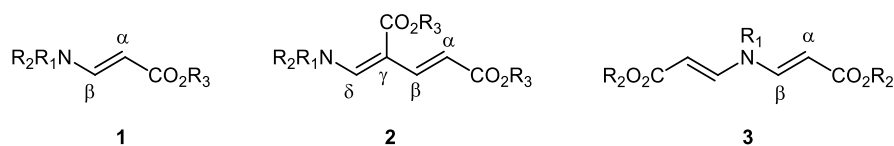


**Figure 2.**  $\beta$ -Enaminoester **1** and its alkylation products **2** and **3**.

The question to which we intend to give an answer is whether deprotonation of enamine moiety inverts the relative nucleophilicity of the two reactive centers. For this purpose, MO calculations were done.

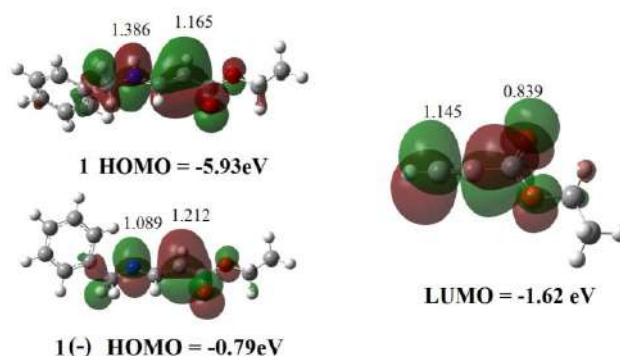


**Figure 3.** Frontier molecular orbitals of enamino ester **1** ( $R_1$ =Bn,  $R_2$ =H,  $R_3$ =Et), deprotonated **1(-)**, ethyl propiolate and orbital coefficients of the most reactive centers.

Unlike the case of the neutral **1** ( $R_1$ =Bn,  $R_2$ =H,  $R_3$ =Et), the HOMO-LUMO interaction for deprotonated enamino ester **1(-)** and ethyl propiolate becomes exothermic and  $C_\alpha$  orbital coefficient of **1(-)** is greater than that of nitrogen (Figure 3). Condensed Fukui indices were used in order to assess which atoms have the highest nucleophilic and electrophilic character. Figure 4 shows the highest Fukui indices for atoms in compound **1** ( $R_1$ =Bn,  $R_2$ =H,  $R_3$ =Et) (nucleophilic  $f^-$ ), deprotonated structure **1(-)** (nucleophilic  $f^-$ ) and ethyl propiolate (electrophilic  $f^+$ ). Fukui functions are calculated as the change in the gross orbital population for each atom in the original electron density and the population of that same atom when the total electron count has increased,  $f^+$ , (or decreased,  $f^-$ ) by one unit.

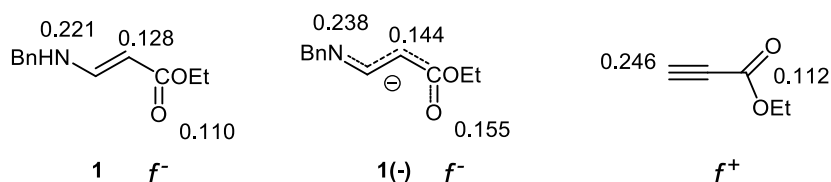


**Figure 4.** Highest atomic Fukui indices of compounds **1** ( $R_1$ =Bn,  $R_2$ =H,  $R_3$ =Et), **1(-)** and ethyl propiolate calculated at the B3LYP/6-311++G(2d,2p)//B3LYP 6-31+G(d,p) level using Natural Population Analysis.

Deprotonation leads to an increase in reactivity indices of  $C_\alpha$  and nitrogen in almost identical amount. Thus, nitrogen remained almost twice reactive than carbon, which is not consistent with exclusive formation of C-alkylated product **2** ( $R_1$ =Bn,  $R_2$ =H,  $R_3$ =Et), under neutral conditions. Thus, the most probable explanation is that, under neutral conditions the thermodynamically more stable

product **2** is formed, while under basic conditions a kinetic control favours **3** ( $R_1=Bn$ ,  $R_2=Et$ ), by alkylation at the most nucleophilic site. As Figure 5 shows, among the two regioisomers, **2** is more stable than **3**, more probably due to the higher electronic delocalization, which can be seen from the  $\pi^*/\pi$  occupation quotient of the C=C double bonds in **1-3**.

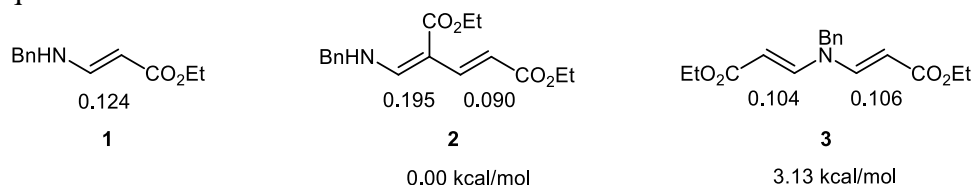


**Figure 5.** Relative free energies and C=C double bond occupation quotient  $\pi^*/\pi$  calculated at the B3LYP/6-311++G(d,p)//B3LYP 6-31G(d) level using NBO Analysis.

## CONCLUSION

With the aid of quantum chemical calculations, the origin of chemo selectivity in the reaction of enamine ester **1** ( $R_1=Bn$ ,  $R_2=H$ ,  $R_3=Et$ ) with ethyl propiolate, under neutral and basic conditions, was shown to arise from thermodynamic vs. kinetic control, respectively.

## Acknowledgments

This work was supported by Ministry of Education, Science and Technological Development of Republic of , project No. 172020.

## REFERENCES

- [1] C. H. McMullen, C. J. M. Stirling, *J. Chem. Soc. B* 1966, 1217; (b) E. Winterfeldt, H. Preuss, *Chem. Ber.* 1966, **99**, 450; (c) R. Huisgen, K. Herbig, A. Siegl, H. Huber, *Chem. Ber.* 1966, **99**, 2526
- [2] E. Kleinpeter, *J. Serb. Chem. Soc.*, 2006, 71, 1
- [3] for reviews see: B. Stanovnik, J. Svete, *Chem. Rev.* 2004, **104**, 2433; A.-Z. A. Elassar, A. A. El-Khair, *Tetrahedron* 2003, **59**, 8463; P. Lue, J. V. Greenhill *Adv. Heterocycl. Chem.* 1996, **67**, 207
- [4] (a) W. Bottomley, *Tetrahedron Lett.* 1967, **8**, 1997; (b) W. Bottomley, J. N. Philips, J. G. Wilson, *Tetrahedron Lett.* 1967, **8**, 2957; (c) M. A. Khan, H. Adams, *Tetrahedron Lett.* 1999, **40**, 5389
- [5] (a) C. Challa, M. John, R. S. Lankalapalli, *Tetrahedron lett.* 2013, **54**, 3810; (b) T. Sirijindalert, K. Hansuthirakul, P. Rashatasakhon, M. Sukwattanasinitt, A. Ajavakon, *Tetrahedron* 2010, **66**, 5161; (c) J. Adams, A. Hardin, F. Vounatsos, *J. Org. Chem.* 2006, **71**, 9895; (d) C. Agami, L. Dechoux, S. Hebbe, *Synlett* 2001, 1440.

**CONFORMATIONAL ANALYSIS AND *PUSH-PULL*  
EFFECT OF DIETHYL 4-  
((PHENYLAMINO)METHYLENE)PENT-2-ENEDIOATE**

J. Aleksić<sup>1</sup>, M. Stojanović<sup>1</sup>, Z. Džambaski<sup>1</sup> and M. Baranac-Stojanović<sup>2</sup>

<sup>1</sup> *University of Belgrade, ICTM-Center for Chemistry, Njegoševa 12, 11000  
Belgrade, Serbia(jovanat@chem.bg.ac.rs)*

<sup>2</sup> *University of Belgrade, Faculty of Chemistry, Studentski trg 12-16, 11000  
Belgrade, Serbia*

**ABSTRACT**

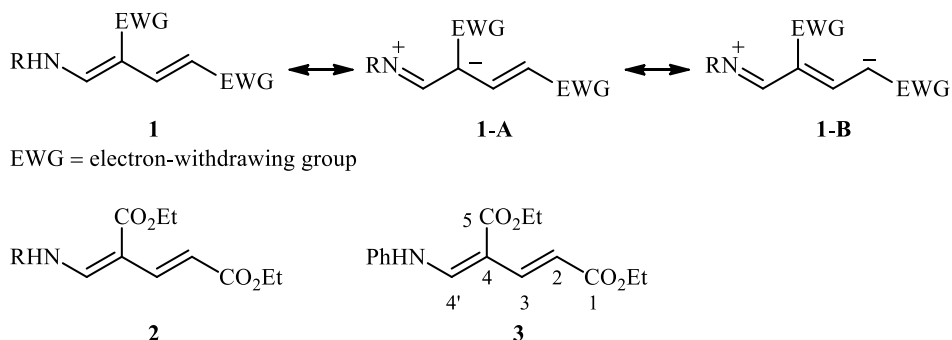
Experimental and theoretical studies showed that the title compound exists as an equilibrium of four conformers in chloroform solution, all having the *E* and *Z* configuration around the C2C3 and C4C4' double bonds, respectively, and the *s-cis* conformation in the  $\alpha,\beta$ -unsaturated C4C5 ester moiety. The most populated conformer also attains the *s-cis* arrangement in the other  $\alpha,\beta$ -unsaturated C1C2 ester fragment and *s-trans* conformation in the conjugated diene part. The strength of the *push-pull* effect of the C4C4' double bond exceeds that of the C2C3 double bond.

**INTRODUCTION**

Conjugated dienes and their derivatives are widely spread structural motifs that are present in a great number of natural products and pharmaceuticals. Due to the unique reactivity of conjugated  $\pi$  bonds, they are also versatile precursors for the synthesis of biologically and industrially important compounds. The highly functionalized conjugated dienes of the type **1**, however, are rarely mentioned in the literature and data on their physical and chemical behaviour are rather scarce [1,2]. Owing to the presence of electron-donor(s) at one end of the double bond and electron-acceptor(s) at the other, **1** also belongs to the class of the so-called *push-pull* alkenes/polyenes [3], which are highly polarized molecules due to the charge delocalization, as represented by the dipolar resonance structures **1-A** and **1-B**.

In just a few reports, conjugated *push-pull* dienes **2** were obtained by the one-pot sequential reaction of a primary amine with ethyl propiolate [2,4,5]. No data on their conformational behaviour, nor on the strength of their *push-pull* effect are currently available. For this reason, we have carried out a systematic experimental and theoretical conformational analysis of compound **3**, which we synthesized by the highly regioselective reaction of aniline with ethyl propiolate [6]. We have also quantified the

*push-pull* effect of the two double bonds by means of the  $\pi^*/\pi$  occupation quotient [3], based on NBO method [7], and chemical shift difference of the two olefinic carbon atoms [3].



## EXPERIMENTAL

The NMR spectra of compound **3** were recorded on a Bruker Ultrashield Advance III ( $^1\text{H}$  at 500.26 MHz,  $^{13}\text{C}$  at 125.79 MHz) in  $\text{CDCl}_3$  as a solvent. Computational studies were done at the B3LYP/6-31+G(d,p) level [8,9]. All optimized structures were characterized as minima by the absence of imaginary frequencies. The NMR chemical shifts were computed by using the GIAO method [10]. Solvent effects were included by using the IEFPCM model, solvent chloroform [11]. All calculations were done by using the Gaussian 09 program package [12].

## RESULTS AND DISCUSSION

The title compound **3** possesses six degrees of configurational/conformational flexibility, each having two stereoisomeric arrangements. This leads to 64 possible conformations (excluding conformational variations around the C–O ester bond, which is known to attain *Z* conformation). These could be reduced to only four (Figure 1.), on the basis of 1D and 2D NMR spectral data. The most diagnostic ones were the following: 1) The low-field signal of the *NH* at 10.76 ppm indicating an intramolecular hydrogen bonding, that is the *Z* configuration around the  $\text{C4}=\text{C4}'$  double bond and a favourable hydrogen-bonded *s-cis* conformation around the  $\text{C4}-\text{C5}$  single bond, 2) the high value of  $^3J_{\text{H2H3}} = 15.5$  Hz, which is consistent with the *E* stereochemistry around the  $\text{C2}=\text{C3}$  double bond, and 3) the NOE couplings between the  $\text{H3}$  and  $\text{H4}'$ , and somewhat less intensive between the  $\text{H2}$  and  $\text{H4}'$ , indicating the presence of both *s-cis* and *s-trans* arrangements around the  $\text{C3}-\text{C4}$  single bond. What had left unknown was the conformation around the  $\text{C1}-\text{C2}$  single bond and mole fractions of the four conformers. Thus, the structures **3a-d** were optimized at the B3LYP/6-

31+G(d,p) level, in the gas phase, followed by their re-optimizations in chloroform. Frequency calculations provided Gibbs free energies at 298 K, which were basis for an assessment of mole fractions of **3a-d**, all given in Figure 1.

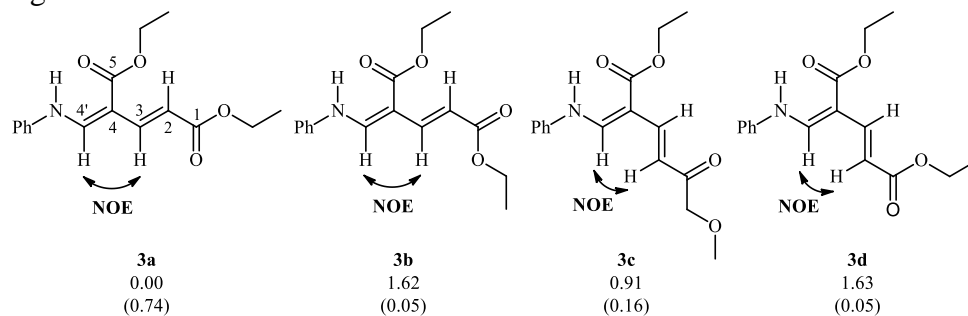


**Figure 1.** The four conformations of **3**, their calculated relative free energies (kcal/mol) and mole fractions (given in brackets).

Table 1. lists experimental and calculated  $^{13}\text{C}$  NMR chemical shifts of the four olefinic carbon atoms, their difference and  $\pi^*/\pi$  values. There is an excellent agreement between experimental and calculated average chemical shifts, the latter based on the calculated mole fractions of conformers **3a-d**. The highest deviation from experimental data is observed for the C2 atom and amounts 5.2 ppm (difference between experimental and calculated average value in the table).

**Table 1.** Experimental and calculated (B3LYP/6-31+G(d,p)) NMR chemical shifts of olefinic carbon atoms in  $\text{CDCl}_3$  ( $\delta/\text{ppm}$ ), their difference ( $\Delta\delta/\text{ppm}$ ) and occupation quotient  $\pi^*/\pi$ .

Structure	$\delta$				$\Delta\delta$		$\pi^*/\pi$	
	C2	C3	C4	C4'	C2C3	C4C4'	C2C3	C4C4'
exp.	112.6	143.9	100.1	149.3	31.3	49.2		
<b>3a</b>	109.0	140.7	99.4	148.4	31.7	49.0	0.09	0.19
<b>3b</b>	110.4	141.8	99.2	147.3	31.4	48.1	0.09	0.19
calc. <b>3c</b>	100.8	139.9	97.6	138.0	39.1	40.4	0.09	0.19
<b>3d</b>	102.1	138.6	96.6	140.3	36.5	43.7	0.09	0.19
<b>av<sup>a</sup></b>	107.4	140.5	99.0	146.3	33.1	47.3		

<sup>a</sup> Based on calculated mole fractions of **3a-d**.

The  $\Delta\delta$  and  $\pi^*/\pi$  data reveal that the C4=C4' double bond shows greater *push-pull* effect than the C2=C3 double bond. This can be rationalized by considering the former as having one donor (NH) and two acceptor groups (CO<sub>2</sub>Et, CH=CHCO<sub>2</sub>Et), and the latter one significantly weaker donor (NHCH=CHCO<sub>2</sub>Et moiety), due to the NH/C3=C2 separation and electron-withdrawing ester group, and one acceptor group (CO<sub>2</sub>Et).

## CONCLUSION

Combination of experimental and theoretical studies enabled us to analyze conformational behaviour of the title compound, which exists in equilibrium of four conformers, **3a** being the most populated one (74%), followed by **3c** (16%). The *push-pull* effect of the trisubstituted C4=C4' double bond is stronger than that of the C2=C3 double bond, the latter receiving considerably less electron density from the donor part, and losing less electron density owing to the presence of only one acceptor at its other end.

## Acknowledgement

This work was supported by the Ministry of education, science and technological development of the Republic of Serbia(Grant no. 172020).

## REFERENCES

- [1] Y. Zhao, F. Zhang, W. Yao, C. Wang, Y. Liu, Y. Li, Eur. J. Org. Chem., 2015, **2015**, 7984-7991.
- [2] J. Adams, A. Hardin, F. Vounatsos, J. Org. Chem., 2006, **71**, 9895-9898.
- [3] E. Kleinpeter, J. Serb. Chem. Soc., 2006, **71**, 1-17.
- [4] C. Challa, M. John, R. S. Lankalapalli, Tetrahedron Lett., 2013, **54**, 3810-3812.
- [5] W. Bottomley, Tetrahedron Lett., 1967, **8**, 1997-1999.
- [6] J. Aleksić, M. Stojanović, M. Baranac-Stojanović, not reported data.
- [7] E. D. Glendening, C. R. Landis, F. Weinhold, Wiley Interdiscip. Rev.: Comput. Mol. Sci., 2012, **2**, 1-42.
- [8] A. D. Becke, J. Chem. Phys., 1993, **98**, 5648-5652; C. Lee, W. Yang, R. G. Parr, Phys. Rev. B: Condens. Matter Mater. Phys., 1988, **37**, 785- 789.
- [9] J. B. Foresman, A. Frisch, Exploring Chemistry with Electronic Structure Methods, Gaussian, Inc., 1996.
- [10] R. Ditchfield, Mol. Phys., 1974, **27**, 789-807; K. Wolinski, J. F. Hinton, P. Pulay, J. Am. Chem. Soc., 1990, **112**, 8251-8260.
- [11] J. Tomasi, B. Mennucci, R. Cammi, Chem. Rev., 2005, **105**, 2999-3093.
- [12] M. J. Frisch et al., Gaussian 09 (Revision D.01), Gaussian Inc.: Wallingford, CT, 2013.

## THEORETICAL AND EXPERIMENTAL EVALUATION OF $K_2Br^+$ AND $K_3Br^+$ CLUSTERS' IONIZATION ENERGIES

F. Veljković<sup>1</sup>, M. Mitić<sup>2</sup>, M. Milovanović<sup>2</sup>, S. Jerosimić<sup>2</sup>, D. Drakulić<sup>3</sup> and  
S. Veličković<sup>1</sup>

<sup>1</sup>University of Belgrade, VINČA Institute of Nuclear Sciences, Department of  
Physical Chemistry, P. O. Box 522, 11001 Belgrade, Serbia.

<sup>2</sup>University of Belgrade, Faculty of Physical Chemistry, Studentski trg 12-  
16, P.O. Box 47, 11158 Belgrade, Serbia.

<sup>3</sup>University of Belgrade, VINČA Institute of Nuclear Sciences, Department of  
molecular biology and endocrinology, P. O. Box 522, 11001 Belgrade,  
Serbia., (filipveljkovic@vinca.rs)

### ABSTRACT

In current study, a non-stoichiometric bromine-doped potassium  $K_2Br^+$  and  $K_3Br^+$  clusters are generated by combining a Knudsen effusion cell as a chemical reactor with thermal or surface ionization, and selected by a magnetic sector mass spectrometer. Furthermore, their ionization energies (IEs) are calculated for the first time using B3LYP/9-ve PP(K),cc-pVTZ-PP(Br) level of theory. Herein, presented results indicate that experimentally obtained IEs by Ionov equation,  $4.10 \pm 0.20$  eV for  $K_2Br^+$ , and  $4.03 \pm 0.20$  eV for  $K_3Br^+$ , are in consistence with their theoretically determined IEs.

### INTRODUCTION

In the past decades, clusters, groups of constituents (atoms, molecules) connected with bounds of different strength, become increasingly attractive research field given that their formation and properties enable to investigate the gradual development of matter from the atom to the bulk. A clusters consisting of an alkali metal combined with more electronegative element exhibit unique physical and chemical phenomena, which are of both fundamental and technological significance. The very small bromine-doped potassium clusters violate stoichiometry based on the octet rule is the reason why such systems are called hyperpotassium or, more generally, hypervalent clusters.

Experimentally,  $K_2Br^+$  cluster was detected the in vapor of KBr salt, using the Knudsen effusion method in the temperature range from 700 K to 890 K [1]. Further, this cluster was produced by electrospray ionization (ESI) [2]. The ionization energy (IE) of  $K_2Br^+$  cluster was determined in our

previous experiments using a triple thermal or surface ionization source, confirming that this cluster belongs to the “superalkali” species, since its IE of  $3.95 \pm 0.1$  eV is lower than the IE of  $K^+$  [3].

Given that there is lack of experimental and theoretical evidence for existence of  $K_3Br^+$  cluster while  $K_2Br^+$  was obtained by different source of ionization, current study was undertaken to theoretically and experimentally evaluate IE of these clusters using Ionov equation and different source of ionization, respectively.

### EXPERIMENTAL

The experimental method has been previously described [4]. Briefly, the rhenium (Re) filament was placed in the centre of the Knudsen effusion cell's base. The sample, KBr salt, was pressed as a ring and placed on the inner wall of the Knudsen effusion cell. The ions emitted from the surface of Re filament were extracted to a mass analyzer, a 12-inch radius,  $90^\circ$  magnetic sector. To determine IE of the clusters produced, the ion currents of  $K_nBr^+$  ( $n = 2, 3$ ) clusters were measured using  $K^+$  ion for calibration as a function of the Re filament temperature. Furthermore, the IE of the clusters were calculated by the Ionov equation:

$$\ln(I(K^+)/I(\text{cluster}^+)) = (IE(\text{cluster}^+) - IE(K^+))/kT.$$

Using 4.34 eV as the IE of  $K^+$ , and the values of the slopes of the plots  $\ln(I(K^+)/I(\text{cluster}^+)) = 1/T$  by this equation, the IE of clusters were obtained.

Theoretical calculations for the IE of  $K_2Br^+$  and  $K_3Br^+$  clusters were done on the CCSD(T)/9-ve PP(K),cc-pVTZ-PP(Br)//B3LYP/9-ve PP(K),cc-pVTZ-PP(Br) level of theory.

### RESULTS AND DISCUSSION

In this work  $K_2Br^+$  and  $K_3Br^+$  clusters were detected the in vapor of KBr salt, using the Knudsen effusion method in the temperature range from 1150 to 1350 °K. The mass spectrum of the ionic beam  $K_nBr$  ( $n=2$  and 3) is presented in Figure 1.

In order to determined of the IE the natural logarithm of the ion intensities for  $K_nBr^+$  ( $n = 2, 3$ ) are plotted in Figure 2 as a function of the inverse of Re filament temperature ( $1/T$ ).

The ground electronic state structures of the lowest isomers of the neutral and charged  $K_nBr$  ( $n = 2, 3$ ) clusters calculated at the B3LYP/9-ve PP(K),cc-pVTZ-PP(Br) level of theory is presented in Figure 2 [5], [6].

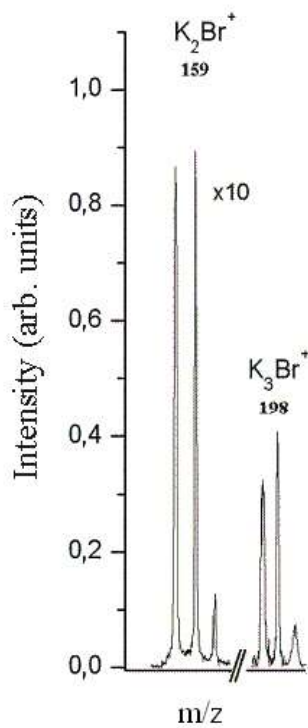


**Figure 1.** The mass spectrum of  $K_n Br^+$  ( $n = 2, 3$ ) cluster ions.

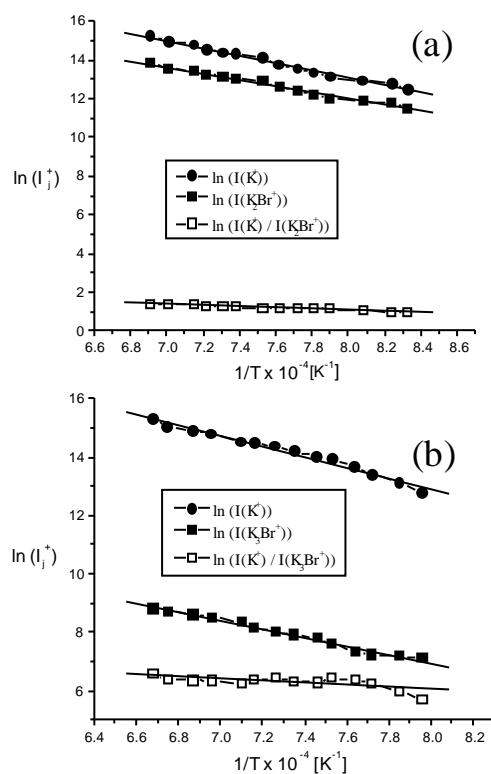


**Figure 2.** Plots of  $\ln I_i^+$  ( $I_i^+$  - ion current of clusters) versus  $1/T$  for (a)  $K_2 Br^+$  and (b)  $K_3 Br^+$  clusters.

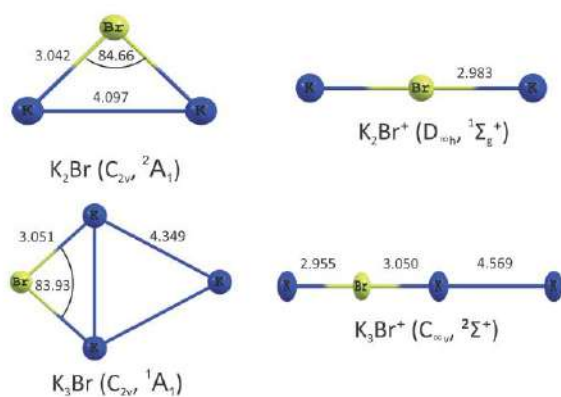


**Figure 3.** The ground electronic state structures of the lowest isomers of the neutral and charged  $K_n Br$  ( $n = 2, 3$ ) clusters calculated at the B3LYP/9-ve PP(K),cc-pVTZ-PP(Br) level of theory. Bond lengths are in Å, angles in degrees.

As presented in Table 1, the experimentally obtained IE of  $K_nBr^+$  and calculated IEs are in agreement within experimental uncertainties.

**Table 1.** Experimentally obtained and *ab initio* calculated adiabatic (aIE) and vertical (vIE) ionization energies (in eV) of neutral  $K_2Br^+$  and  $K_3Br^+$  in the  $^2A_1$  and  $^1A_1$  ground electronic states, respectively.

Species	aIE	vIE	Exp.
$K_2Br^+$ ( $C_{2v}$ , $^2A_1$ )	3.31	3.96	$4.10 \pm 0.20$
$K_3Br^+$ ( $C_{2v}$ , $^1A_1$ )	3.76	4.28	$4.03 \pm 0.20$

Since the IE of investigated clusters are lower than the IE of the potassium atom, the experimental setup presented in this paper provides a convenient way for generate “superalkali” clusters of the type  $K_nBr^+$ .

## CONCLUSION

Being in accordance with theoretically obtained data for  $K_2Br^+$  and  $K_3Br^+$  clusters IE, the obtained experimental results showed that modified Knudsen effusion cell, a chemical reactor combined with thermal or surface ionization, is a suitable method for generation of investigated clusters.

## Acknowledgement

This work was supported by the Ministry of Education, Science and Technological development of the Republic of Serbia (Project No. 172019 and 172040).

## REFERENCES

- [1] M. F. Butman, A. A. Smirnov, L. S. Kudin, Z. A. Munir. J. Mater. Synth. Process., 2000, **8**, 55.
- [2] A. T. Blades, M. Pesahe, U. H. Verkerk, P. Kebarale J. Am. Chem. Soc., 2004, **126**, 11995.
- [3] S. R. Veličković, F. M. Veljković, A. A. Perić-Grujić, B. B. Radak, F. M. Veljković. Rapid Commun. Mass Spectrom., 2011, **25**, 2327.
- [4] F. M. Veljković, J. B. Djustebek, M. V. Veljković, S. R. Veličković, A. A. Perić-Grujić. Rapid Commun. Mass Spectrom., 2012, **26**, 1761.
- [5] Lim, I. S., Schwerdtfeger, P., Söhnel, T., Stoll, H. The Journal of chemical physics, 2005, **122**, 134307.
- [6] Peterson, K. A., Figgen, D., Goll, E., Stoll, H., and Dolg, M. The Journal of Chemical Physics, 2003, **119**, 11113.

## DFT STUDY ON THE RING-OPENING OF GERMACYCLOPROPYLIDENOIDS TO GERMAALLENES

A. Azizoglu<sup>1</sup> and C. B. Yildiz<sup>2</sup>

<sup>1</sup>Laboratory of Computational Chemistry, Department of Chemistry,  
University of Balıkesir, TR-10145 Balıkesir, Turkey  
([azizoglu@balikesir.edu.tr](mailto:azizoglu@balikesir.edu.tr))

<sup>2</sup>Department of Chemistry, Faculty of Arts and Sciences, University of  
Aksaray, Aksaray, Turkey.

### ABSTRACT

Density functional theory (WB97XD) quantum mechanical calculations elucidated the ring-opening reactions of germacyclopropylidenoids germaallenes via Doering-Moore-Skattebøl method. The ring-opening of **1** to **3** can proceed in a stepwise fashion with the intermediacy of a free germacyclopropylidene (**2**). Here, a high-energy barrier needs to be overcome in order to open the germacyclopropylidene ring and to generate **3**. On the contrary, the ring-opening of **4** to **5** can occur in a concerted fashion. Moreover, halogen effect (X = F, Cl, Br) on the energetic of the reaction was also investigated. Thus the most favourable halogene determined to be Bromine with the lowest energy barriers 11.6 kcal/mol and 4.1 kcal/mol for **1** and **4**, respectively.

### INTRODUCTION

Germynes, the heavy analogs of carbenes, are one of the most often occurring key intermediates in reactions of organogermanium compounds [1,2]. Similar to carbenoid and silylenoid, germynoid is the complex formed between free germylene and inorganic salt. In principle, reactions of germynoids are similar to silylenoids. The first experimental study on the germynoids has been reported by Gasspar et al. in 1991. It was postulated that a kind of germynoid might be the intermediate in the reaction of dichlorodimethylgermane with substituted butadiene [3]. The first theoretical study on the structural isomers of germacyclopropylidenoids, cyclic analogues of germynoids, was reported by Azizoglu et al [4]. It is indicated that germacyclopropylidenoids might have two stationary structures, germanoidal (**G**) and inverted (**I**).

Likewise, it is necessary to be performed systematic theoretical study on germacyclopropylidenoids to penetrate their structures, properties, and

reactions. With this motivation, we have performed DFT calculations on the ring–opening mechanism of germacyclopropylidenoids to germaallenes.

## EXPERIMENTAL

All the calculations were performed with Gaussian 09W suite of program [5]. In order to optimize the title structures on their potential energy surface, DFT/WB97XD theory was employed. The 6–31+G(d,p) was chosen as a basis set. The optimized structures were determined by the characterization of their Hessian matrix as a minimum (no imaginary frequency) or transition state. The relative  $\Delta G$  energies are given in kcal/mol. The Intrinsic Reaction Coordinate (IRC) procedure was carried out for the identification of the connectivity of stationary points.

## RESULTS AND DISCUSSION

Initially, all structures were optimized using the Gaussian 09 suite of programs at the WB97XD/6–31+G(d,p) level. For the ring–opening reactions of germacyclopropylidenoids to germaallenes, two pathways can be considered: the reaction may either proceed stepwise or in a concerted fashion.

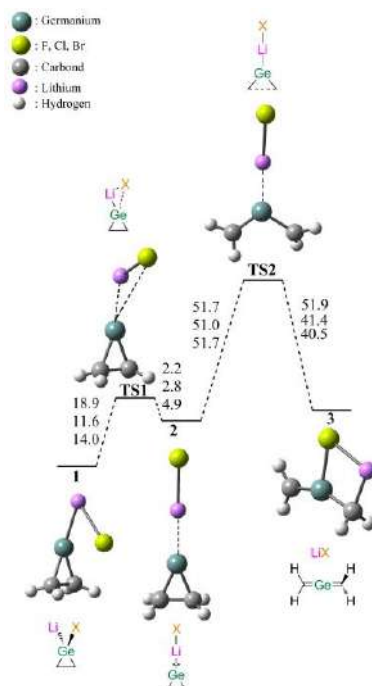


**Figure 1.** The Calculated reaction path at the WB97XD/6–31+G(d,p) level for the stepwise ring–opening of **1** to **3**. (Energy values for F, Cl, and Br, respectively).

The energy profile for the stepwise ring-opening of **1** is shown in Figure 1. The elimination of LiX from **1** is the first step of stepwise ring-opening, and it starts readily with the transition state **TS1**. The lowest energy barrier is found to be 11.6 kcal/mol with Br bounded structure. In the second step, the three-membered ring collapses to the **3** by overcoming a very high activation energy barrier (**TS2**), 51.7 kcal/mol for Br at WB97XD/6-31+G(d,p) level of theory. In this case, the formation of 2-germaallene is determined to be endergonic with the energy of 19.3 kcal/mol (X = Br). For this reason, the reaction is not spontaneous at room temperature. Furthermore, concerted mechanism does not play any role for the ring-opening of **1**.

The formation of 1-germaallene can be computed only as a concerted process (**TS3**), where the isomerization of a germanoid to a germaallene may occur readily without the intermediacy of a free germylene (Figure 2). Moreover, the calculated reaction barrier for the concerted ring-opening of **4** to 1-germaallene (**5**) is found to be very low, 4.1 kcal/mol (X = Br), but in this case the reaction is moderately exothermic, by 46.2 kcal/mol at the WB97XD/6-31+G(d,p) level.

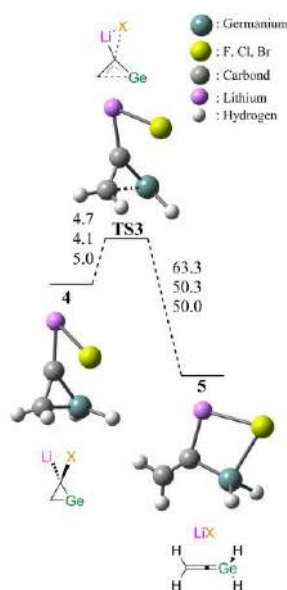


**Figure 2.** The Calculated reaction path at the WB97XD/6-31+G(d,p) level for the concerted ring-opening of **4** to **5**. (Energy values for F, Cl, and Br, respectively).

## CONCLUSION

In summary, the halogen effect ( $X = F, Cl, Br$ ) on the ring-opening reaction of **1** and **4** to 2-germaallene and 1-germaallene were investigated, respectively. The ring-opening of **1** to the complex 2-germaallene (**3**) can occur in a stepwise fashion with the intermediacy of a free germacyclopropylidene, whereas the ring-opening of **4** to the complex 1-germaallene (**5**) can proceed in a concerted fashion. The lowest energy barrier was found for the Br bonded structures. Moreover, the ring-opening reaction of **1** is endergonic by 19.3 kcal/mol, while that of **4** is highly exergonic, by 46.2 kcal/mol. Thus, the ring-opening reaction for **4** is thermodynamically more favourable than the ring-opening of **1** with halogen ( $X = Br$ ).

## Acknowledgement

This work was partially supported by the Scientific and Technological Research Council of Turkey (Grant No: TUBITAK TBAG-212T049).

## REFERENCES

- [1] J. Satge, M. Massil, P. Riviere, J. Organomet. Chem. 1973, **56**, 1–39.
- [2] Y. Mizuhata, T. Sasamori, N. Tokitoh, Chem. Rev., 2009, **109**, 3479–3511.
- [3] D. Lei, P. Gaspar, Polyhedron, 1991, **10**, 1221–1225.
- [4] C.B. Yildiz, A. Azizoglu, Comput. Theor. Chem., 2013, **1023**, 24–28.
- [5] M.J. Frisch, et al., Gaussian 09W Revision D.01, Gaussian, Inc., Pittsburgh, 2009.

## STUDY ON THE STRUCTURE AND VIBRATIONAL SPECTRA OF ISATOIC ANHYDRIDE AND *N*-METHYL ISATOIC ANHYDRIDE USING HF AND DFT: COMPARISON TO EXPERIMENTAL DATA

A. Azizoglu

*Laboratory of Computational Chemistry, Department of Chemistry,  
University of Balikesir, TR-10145 Balikesir, Turkey  
(azizoglu@balikesir.edu.tr)*

### ABSTRACT

Structural and spectral characteristics of isatoic anhydride and *N*-methyl isatoic anhydride have been studied by vibrational spectroscopy and quantum chemical methods. Hartree Fock (HF) and Density functional theory (DFT) calculations for potential energy curve, optimized geometries and vibrational spectra have been carried out using the 6-31G(d) and 6-31+G(d,p) basis sets. Based on these results, we have discussed the correlation between the vibrational modes and the crystalline structure of the most stable form of isatoic anhydride and *N*-methyl isatoic anhydride. A complete analysis of the experimental infrared and Raman spectra has been reported on the basis of wave number of the vibrational bands and potential energy distribution. The infrared spectra of title molecules based on DFT calculations show reasonable agreement with the experimental results. The calculated HOMO and LUMO energies shows that charge transfer occur within the molecule.

### INTRODUCTION

Isatoic anhydride is an extremely versatile compound [1]. Due to the ease of its reactions with electrophiles or nucleophiles, its derivatives have found wide application in the manufacture of agricultural chemicals, dyes, pigments, flavors, fragrances, pharmaceuticals, and various industrial chemicals useful as UV light absorbers, blowing agents, flame-proofing agents, corrosion inhibitors, dry bleaches, disinfectants, and sanitizing agents [2,3].

Vibrational spectroscopic methods are especially important for characterization of organic compounds because hydrogen-bonding patterns and other weak interactions differ among forms and the functional groups affected will display shifts in the energy of the vibrational modes

The current study presents the results of computational chemistry to provide an understanding of the spectroscopic characteristics of isatoic anhydride and N-methylisatoic anhydride. IR spectroscopic studies along with HOMO and LUMO analysis have been used to elucidate information regarding charge transfer within the molecule.

### EXPERIMENTAL

The calculations of geometrical parameters in the ground state were performed using the Gaussian 03 suite of programs at the HF and DFT/M06 levels with both the 6-31G(d) and 6-31G+(d,p) basis sets [4]. Initial geometry was generated by Gaussview 3.0 program. The optimized structures were determined by the characterization of their Hessian matrix as a minimum (no imaginary frequency) or transition state. The energies reported herein include the zero-point vibrational energy (ZPVE) corrections.

### RESULTS AND DISCUSSION

In Fig. 1 the numbering of the atoms is shown. We can see from the resulting equilibrium geometries that the isatoic anhydride is planar molecule. The benzene ring in these compounds becomes a bit distorted with C–C bond distances between 1.387 Å and 1.413 Å and the bond angles between 117.2° and 123.0°. In the N-methyl substituted molecule, N-methylisatoic anhydride the methyl group orient itself in such a way that the hydrogen atom of the methyl group which is nearest to the oxygen atom lies in the plane of the ring. This fact can be explained by the formation of a C–H...O intramolecular interaction, which further stabilizes this molecular conformation.

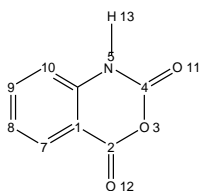


**Figure 1.** Atom numbering scheme for isatoic anhydride. The position 5 in the anhydride can be either H or CH<sub>3</sub>.

On an absolute scale, it is well known that experimental results of infrared spectroscopy are usually lower than the corresponding computational quantities due to the combination of electron correlation effects and basis set deficiencies [5]. The experimental and theoretical FT-IR spectra are presented in Figure 2.

The theoretical calculations predict 45 vibrations from 63-3885  $\text{cm}^{-1}$ , the exact limits being dependent on the method of calculation. The vibrational analysis of isatoic anhydride is performed on the basis of the characteristic vibrations of carbonyl group, N-H group, C=N group and C=C group. There is also a good agreement between the experimental and the computed vibrational frequencies.

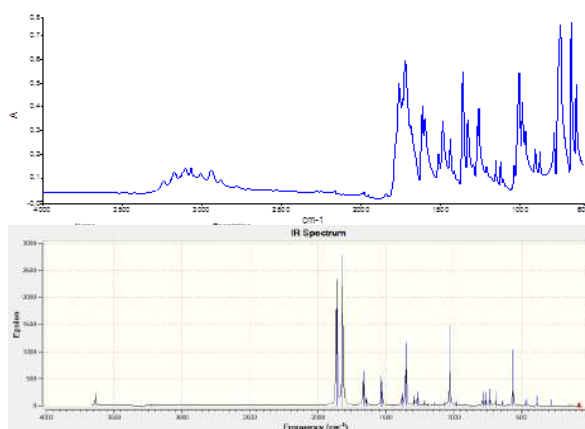


**Figure 2.** Visualization of experimental (above) and theoretical (below at RM06/6-31G(d) level) IR spectra of isatoic anhydride.

The frontier molecular orbitals, which are called HOMO (Highest Occupied Molecular Orbital) and LUMO (Lowest Unoccupied Molecular Orbital) are most important orbitals in molecular systems [6]. Figure 3 indicates the distribution and energy levels of the HOMO and LUMO orbitals calculated at B3LYP/6-31G(d) level for isatoic anhydride *N*-methyl isatoic anhydride. As seen from Fig. 3, HOMO is mainly on the benzene part of title compound, whereas LUMO is substantially localized on the carbonyl group. Electrons in the HOMO-1 are also delocalized through the molecule. The value of energy separations between HOMO and LUMO are 0.178 eV and 0.175 eV for isatoic anhydride and *N*-methyl isatoic anhydride, respectively. This small HOMO-LUMO gap means low excitation energies for many of excited states and low chemical hardness.

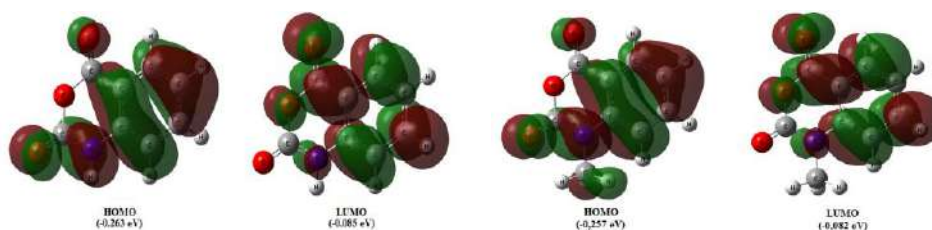


**Figure 3.** Molecular orbital surfaces and energies (in parentheses, eV) for the HOMO (left) and LUMO (right) of the isatoic anhydride (top) and *N*-methylisatoic anhydride (bottom) computed at M06/6-31G(d) level

### CONCLUSION

In this study, vibrational spectroscopy and density functional theoretical calculation have been applied to the structural and spectroscopic investigation of isatoic anhydride and *N*-methylisatoic anhydride. The equilibrium geometries and harmonic vibrational wavenumbers of all the 45 normal modes of the molecule were determined and analyzed with HF and DFT level of theory. The LUMO as an electron acceptor represents the ability to obtain an electron, and HOMO represents the ability to donate an electron. Moreover, a lower HOMO–LUMO energy gap explains the fact that eventual charge transfer interaction is taking place within the molecule.

### Acknowledgement

This work was supported by Balikesir University Research Grant No.: BAP 2016/156. The author also would like to thank TUBITAK (Grant No. TBAG-212T049) for financial support.

### REFERENCES

- [1] G. M. Coppola, *Synthesis*, 1980, **1980**, 505-536.
- [2] M. A. R. Matos, M. S. Miranda, V. M. F. Morais, J. F. Liebman, *Org . Biomol. Chem.*, 2003, **1**, 2566 – 2571.
- [3] T. Kappe, W. Stadlbauer in: *Adv. Heterocyclic Chem.*, **28**, A. R. Katritzky, J. Boulton (Eds.), Academic Press, London, 1981.
- [4] M.J. Frisch, et al., *Gaussian 09W Revision D.01*, Gaussian, Inc., Pittsburgh, 2009.
- [5] A. Azizoglu, Z. Özer, T. Kilic, *Collect. Czech. Chem. Commun.*, 2011, **76**, 95-114.
- [6] I. Fleming, *Frontier Orbitals and Organic Chemical Reactions*, Wiley, London, 1976.

## ELECTRONIC AND STRUCTURAL ANALYSIS OF AVOBENZONE BY MEANS OF QUANTUM CHEMICAL CALCULATIONS

M. Kojić

*University of Belgrade, Faculty of Physical Chemistry,  
Studentski trg 12-16, 11000 Belgrade, Serbia (kojicmarko91@gmail.com)*

### ABSTRACT

We report the ground-state equilibrium structures and vertical electronic singlet and triplet excitation spectra of the enol and keto tautomers of the avobenzene (4-tert-butyl-4'-methoxydibenzoylmethane, AB) derivative – 4-methoxydibenzoylmethane (DBM), calculated at the B3LYP, CAM-B3LYP, M06-2X, PBE0/TZVP level of theory. A comparative analysis of results obtained with different functionals, presented in this work, show that B3LYP level of computation provides the best agreements with experimental data.

### INTRODUCTION

Avobenzene is one of the most widely used UVA filters in cosmetic sunscreens [1]. AB is a  $\beta$ -dicarbonyl compound liable to keto-enol tautomerization. Many theoretical and experimental studies of AB derivatives provided evidences that in the ground state chelated enol form is favored due to the intramolecular hydrogen bond. It has been shown that enol form has absorption bands in the UVA (around 355 nm) region due to the  $\pi$ - $\pi^*$  transition of the chelated quasi-aromatic system. On the other hand, the keto tautomer absorbs in the UVC range around 265nm. Photochemical experiments have shown that photodegradation and complete loss of UV protection of AB is the consequence of the enol tautomerization to the keto form, under irradiation [2-4]. In this contribution we optimized the nuclear arrangements and calculated vertical electronic excitation energies to the first three singlet and triplet electronic states of the enol and keto tautomers in the gas phase. Due to the computational feasibility we excluded tert-butyl group from AB and studied 4-methoxydibenzoylmethane. Also, in order to make our study more reliable we performed density functional theory (DFT) calculations with a different type of functionals. All calculations were performed with TURBOMOLE program package [5] (DFT-B3LYP, M06-2X and PBE0 functionals) and with the Gaussian package [6] (at the CAM-B3LYP level of theory). For all calculations we used TZVP basis set.

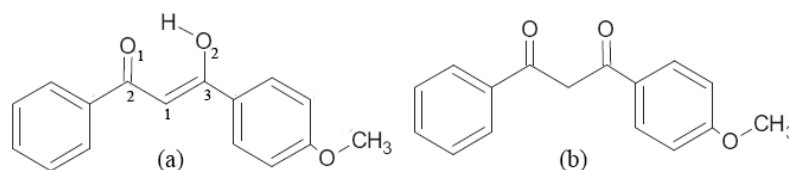


**Figure 1.** Atom labeling and the tautomers considered in this work: (a) enol and (b) keto.

## RESULTS AND DISCUSSION

Calculated bond lengths of enol and keto tautomers in the gas phase are collected in Tables 1-2. Comparison of the bond lengths of enol tautomer obtained with different methods revealed that the maximum bond length change occurs for the intramolecular  $\text{H}\cdots\text{O}_1$  hydrogen bond, while other bond lengths are found to be very similar. B3LYP and CAM-B3LYP hydrogen bond lengths are found to be elongated for 0.11 Å and 0.10 Å compared to the  $\text{H}\cdots\text{O}_1$  bond length obtained with M06-2X functional. The PBE0 optimized  $\text{H}\cdots\text{O}_1$  bond distance is elongated for 0.04 Å relative to the M06-2X  $\text{H}\cdots\text{O}_1$  bond, while compared to the B3LYP and CAM-B3LYP this bond is shorter for 0.07 Å and 0.06 Å, respectively. The best match with experimentally obtained hydrogen bond length (1.59 Å) was found for B3LYP  $\text{H}\cdots\text{O}_1$  bond [7].

**Table 1.** Calculated bond lengths for the enol tautomer of DBM (values in Å).

Bond length	B3LYP	CAM-B3LYP	M06-2X	PBE0
$\text{C}_2\text{-O}_1$	1.26	1.25	1.25	1.25
$\text{C}_3\text{-O}_2$	1.33	1.32	1.31	1.31
$\text{C}_1\text{-C}_2$	1.43	1.43	1.43	1.43
$\text{C}_1\text{-C}_3$	1.38	1.37	1.38	1.38
$\text{H}\cdots\text{O}_1$	1.56	1.55	1.45	1.49
$\text{H-O}_2$	1.02	1.01	1.02	1.03

For keto tautomer, calculated bond distances at the different level of theory was found to be almost the same. The biggest bond length change occurs for the B3LYP  $\text{C}_1\text{-C}_3$  bond, which is elongated for 0.02 Å compared to the corresponding PBE0 and M06-2X values. The biggest difference in matching bond lengths of enol and keto tautomer was found for  $\text{C}_1\text{-C}_3$  bond, which is elongated by  $\approx 0.15$  Å in keto tautomer. Vertical excitation energies of singlets and triplet states, oscillator strengths and excitation transitions of enol and keto tautomers at the ground state geometries are

presented in Tables 3-4. For enol tautomer, we find that  $S_1$  state has  $\pi \rightarrow \pi^*$  character and comes from HOMO  $\rightarrow$  LUMO orbital excitation.

**Table 2.** Calculated bond lengths for the keto tautomer of DBM (values in Å).

Bond length	B3LYP	CAM-B3LYP	M06-2X	PBE0
C <sub>2</sub> -O <sub>1</sub>	1.22	1.21	1.21	1.21
C <sub>3</sub> -O <sub>2</sub>	1.22	1.21	1.21	1.21
C <sub>1</sub> -C <sub>2</sub>	1.54	1.53	1.52	1.52
C <sub>1</sub> -C <sub>3</sub>	1.54	1.53	1.52	1.53

Energy required for this transition, computed at the B3LYP level, is lower than those obtained with CAM-B3LYP, M06-2X and PBE0 level, and amounts 3.66 eV, this is in good agreement with experimental result which is 3.48 eV [3].  $T_1$  state results mostly from HOMO  $\rightarrow$  LUMO and HOMO  $\rightarrow$  LUMO+1 excitation and exhibits  $\pi \rightarrow \pi^*$  character. B3LYP excitation energy to  $T_1$  state was found to be 2.56 eV which is somewhat lower than corresponding CAM-B3LYP, M06-2X and PBE0 values. For the keto tautomer we found that bright state is the third excited state, which originates from HOMO  $\rightarrow$  LUMO ( $\pi \rightarrow \pi^*$ ) transition. Computed at the B3LYP level, excitation energy to the  $S_3$  state was determined to be 3.98 eV which is significantly lower than corresponding values computed with other functionals. In addition, this energy is relatively in good agreement with one experimentally obtained, which value is 4.68 eV [3].  $T_1$  state results from HOMO  $\rightarrow$  LUMO ( $\pi \rightarrow \pi^*$ ) transition. As in the previous cases B3LYP excitation energy is lower than corresponding CAM-B3LYP, M06-2X and PBE0 values, and amounts 3.05 eV.

**Table 3.** Vertical excitation spectrum of enol tautomer at the ground-state geometry.

	Transition	Oscillator strength	Energy /eV		
			Calculated	Experimental [3]	CAM- B3LYP [8]
B3LYP	$S_0 \rightarrow S_1$	0.80307	<b>3.66</b>	3.48	3.70
	$S_0 \rightarrow T_1$	0	2.56		
CAM-B3LYP	$S_0 \rightarrow S_1$	0.9195	<b>4.09</b>		
	$S_0 \rightarrow T_1$	0	2.66		
M06-2X	$S_0 \rightarrow S_1$	0.93827	<b>4.16</b>		
	$S_0 \rightarrow T_1$	0	2.91		
PBE0	$S_0 \rightarrow S_1$	0.84955	<b>3.78</b>		
	$S_0 \rightarrow T_1$	0	2.57		

**Table 4.** Vertical excitation spectrum of keto tautomer at the ground-state geometry.

	Transition	Oscillator strength	Energy /eV		
			Calculated	Experimental [3]	CAM-B3LYP [8]
B3LYP	$S_0 \rightarrow S_3$	0.99552	<b>3.98</b>	4.68	4.48
	$S_0 \rightarrow T_1$	0	3.05		
CAM-B3LYP	$S_0 \rightarrow S_3$	0.43021	<b>4.80</b>		
	$S_0 \rightarrow T_1$	0	3.11		
M06-2X	$S_0 \rightarrow S_3$	0.83022	<b>4.86</b>		
	$S_0 \rightarrow T_1$	0	3.50		
PBE0	$S_0 \rightarrow S_3$	0.84955	<b>4.21</b>		
	$S_0 \rightarrow T_1$	0	3.06		

## CONCLUSION

The present paper report and discuss optimized structural parameters and vertical electronic excitation energies of enol and keto tautomers of Avobenzene derivative - DBM. Comparison of results calculated at the different levels of theory show that the best agreement with experimental data is accomplished using B3LYP functional

## Acknowledgement

The authors acknowledge the Ministry of Education and Science of Serbia for the financial support (Contract No. 172040).

## REFERENCES

- [1] N. A. Shaath, Photochem. Photobiol. Sci., 2010, **9**, 464–469.
- [2] G. Mturi and B. S. Martincigh, J. Photochem. Photobiol. A, 2008, **200**, 410–420.
- [3] M. Yamaji and M. Kida, J. Phys. Chem. A, 2013, **117**, 1946–1951.
- [4] A. Cantrell and D. J. McGarvey, J. Photochem. Photobiol. B, 2001, **64**, 117–122.
- [5] TURBOMOLE V7.0 2015, a development of University of Karlsruhe and Forschungszentrum Karlsruhe GmbH, 1989-2007, TURBOMOLE GmbH, since 2007; available from <http://www.turbomole.com>.
- [6] M. J. Frisch, et al., Gaussian 09 Revision D.01, Gaussian Inc. Wallingford, CT2009.
- [7] N.V. Belova, H. Oberhammer, G.V. Girichev, Struct. Chem. 2011, **22**, 269–277.
- [8] L. Pinto da Silva, P. J. O. Ferreira, D. J. R. Duarte, M. S. Miranda, and J. C. G. Esteves da Silva, Phys. Chem. A, 2014, **118**, 1511-1518.

**THE STUDIES OF THE PUSH-PULL EFFECT OF  
SELECTED 2-ALKYLIDENE-4-OXOTHIAZOLIDINES  
UNDER DIFFERENT SOLVENT CONDITIONS:  
EXPERIMENTAL AND COMPUTATIONAL APPROACH**

A. Rašović<sup>1</sup>, V. A. Blagojević<sup>2</sup> and B. Bondžić<sup>1</sup>

<sup>1</sup>Center for Chemistry ICTM, University of Belgrade, Studentski trg 16,  
P. O. Box 473, 11000 Belgrade, Serbia (arasovic@chem.bg.ac.rs)

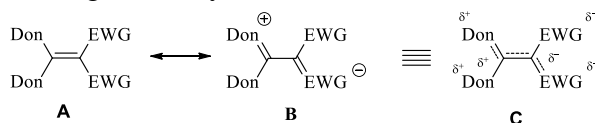
<sup>2</sup>Institute of Technical Sciences, Serbian Academy of Sciences and Arts,  
Knez Mihailova 35/IV, P.O. Box 377, 11000 Belgrade, Serbia

**ABSTRACT**

The correlation studies between the calculated and experimentally determined barriers to rotation around the C=C double bond have been done for the selected 2-alkylidene-4-oxothiazolidine derivatives **1-3**. Aiming to provide the complete picture of the efficiency of the using the  $\Delta G^\ddagger$  to quantify their *push-pull* effect the computations of their rotational barriers were performed in the same solvents which were employing under experimental conditions. In this regard, for these compounds the calculated and experimentally determined barriers to rotation greatly corroborate.

**INTRODUCTION**

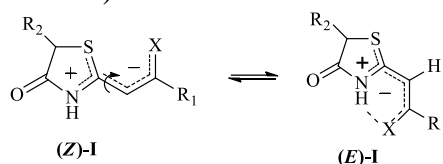
*Push-pull* alkenes can be depicted by the general formula **A** where **Don** represents electron-donating groups and **EWG** electron-withdrawing groups (Scheme 1). As a result, donor-acceptor electronic interactions occurring via the C=C double bond, the so called *push-pull* effect, the barrier to rotation around this bond is significantly reduced.



**Scheme 1.**

In the case of our stereodefined *push-pull* thiazolidine derivatives **I** these interactions occurring between two electron-donors (-NH and -S-) and one electron-acceptor ( $R_1CX$ ;  $R_1 = \text{Ph, OEt, NH}_2, \text{NHPh}$ ;  $X = \text{O or S}$ ) are presented by the fragment in Scheme 2. Consequently, as we showed previously [1], the facile *Z/E* configurational isomerization, whose direction is dictated by the solvent polarity, takes place spontaneously at room

temperature (Scheme 2). As a result of the forming the stable solvent-solute intermolecular interactions, as well as the breaking the intramolecular hydrogen bond in (*E*)-**I**, the polar solvents shift the equilibrium to the (*Z*)-**I**. On the other hand, in the nonpolar solvents the intramolecular hydrogen bonding is favored and in such conditions (*E*)-**I** isomer becomes the dominant species (Scheme 2).



**Scheme 2.**

Barriers to rotation around the C=C double bond ought to be discussed in terms of their free energy of activation. However, for the majority of the compounds, only  $\Delta G^\ddagger$  obtained at the temperature of coalescence are available which limits the validity of comparing their values, even if they are obtained at the same or similar temperatures [2].

On the other side, contrary to the bulk literature data, our previously published data concerning the rotational barriers around the C=C double bond of the **1-3** were determined by the monitoring of their stereodynamic behavior using the integration of the clearly distinguished signals assigned to the vinyl protons of the *Z* and *E* counterparts at the broad temperature range [1].

## EXPERIMENTAL AND COMPUTATIONAL DETAILS

The detail experimental protocols associated with the monitoring of the stereodynamic behavior of the studied compounds **1-3** ( $R_1 = \text{Ph}$ ,  $R_2 = \text{CH}_2\text{COOEt}$ ,  $X = \text{O}$ , **1**;  $R_1 = \text{OEt}$ ,  $R_2 = -\text{CHCOOEt}$ ,  $X = \text{O}$ , **2**;  $R_1 = \text{NH}_2$ ,  $R_2 = \text{CH}_2\text{COOEt}$ ,  $X = \text{S}$ , **3**; Scheme 2), have been already reported by us [1].

Geometry optimization and frequency analysis of *Z* and *E* isomers of studied compounds was conducted at the M06-2X/6-311G\*\* level [3], using the Gaussian 09 program package. Transition state structures were determined using Synchronous Transit-Guided Quasi-Newton method [4] at the M06-2X/6-311G\*\* level. To account for solvent effects, the structures of the three derivatives, **1-3**, were re-optimized in chloroform and dimethylsulfoxide along with their **TS**, using the continuum solvation COSMO model (conductor-like screening model) [5]. All transition state structures were characterized by an imaginary frequency, the vibrational mode of which corresponded to the rotation around the C(2)–C(2') bond. The calculated and experimentally determined barriers to rotation for (*Z*)-**1**,

(2*E*,5*Z*)-**2** and (*E*)-**3** showed an excellent correlation with correlation coefficient 0.996 (Fig. 1).

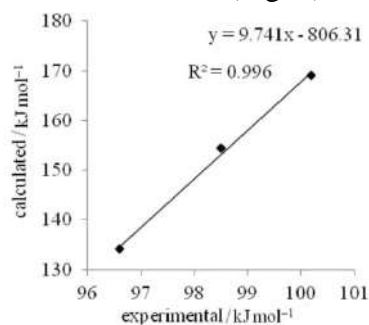
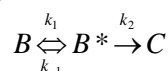


**Figure 1.** Correlation between calculated and experimental barriers to rotation for compounds **1-3**.

## RESULTS AND DISCUSSION

Based on all the relevant kinetic data, that is, the Arrhenius parameters (apparent activation energy  $E_a$  and frequency factor  $A$ ) and activation parameters ( $\Delta S^\ddagger$ ,  $\Delta H^\ddagger$  and  $\Delta G^\ddagger$ ) for the configurational isomerization mechanism of the **1-3**, (*E*)-**I**  $\rightleftharpoons$  (*Z*)-**I**, has been established the first order kinetics, as follows:



As continuation of the extending our knowledge about this reaction mechanism, as well as the strength of the *push-pull* effect of the investigated compounds, we did computations as noted above. That was primarily related to the solvent impact on the barrier to rotation around the C=C double bond, and closely connected to this, on the efficiency of the application of the  $\Delta G^\ddagger$  to quantify the *push-pull* effect of the 2-alkylidene-4-oxothiazolidines under different solvent conditions.

Generally, the solvation of the polar rotational transition state affects both the entropy and enthalpy data and so Gibbs free energy data as a balance of the total change. In this sense, whether they are polar or nonpolar, solvents decrease both the  $\Delta H^\ddagger$  and  $\Delta S^\ddagger$  values because of the more polar **TS** (due to the full charge separation) is more solvated than the less polar **GS**.

This fact fully corroborates with the  $\Delta G^\ddagger$ ,  $\Delta H^\ddagger$  and  $\Delta S^\ddagger$  values experimentally determined for thiazolidine derivatives **1-3** which are for comparison purpose included in Table 1, along with the computed  $\Delta G^\ddagger$  and  $\Delta H^\ddagger$  data. Thus, as we expected, the studied isomerization of (*Z*)-**1** required a higher ordering in the weakly polar CDCl<sub>3</sub> molecules at the moment **TS** is reached, so as to stabilize the **TS** as efficiently as possible. This reduces both the  $\Delta S^\ddagger$  and  $\Delta H^\ddagger$  (entry 1). By contrast, polar DMSO-*d*<sub>6</sub> stabilizes **TS** of the (2*E*,5*Z*)-**2** and (*E*)-**3** with less molecular ordering, resulting in higher entropy and enthalpy values (entries 3 and 5).

Although, an excellent correlation between the computed and experimentally determined  $\Delta G^\ddagger$  values was obtained, the calculated barriers to rotation overestimate the experimental ones. This fact can be rationalized by taking into account that effects of solute-solute and solute-solvent direct interactions were not completely considered by the theoretical calculations.

Similarly, the experimentally obtained negative entropy values, which can be associated with ordering of solvent molecules, were not taken into account in computations resulting in the calculated  $\Delta H^\ddagger$  and  $\Delta G^\ddagger$  values almost identical, or differ slightly. Thus, in theoretical calculations, the impact of the solvation effects on the kinetics of this isomeric equilibrium was not observed via entropy factor, but quantified only by the change of enthalpy.

**Table 1.** Experimentally being determined selected activation parameters ( $\Delta G^\ddagger$  and  $\Delta H^\ddagger$  in kJ/mol;  $\Delta S^\ddagger$  in Jmol<sup>-1</sup>K<sup>-1</sup>; T = 298 K) and calculated barriers to rotation ( $\Delta G^\ddagger$  and  $\Delta H^\ddagger$  in kJ/mol) for configurational isomerization of compounds **1-3**.

entry	compound	solvent	isomerization direction	$\Delta G^\ddagger_{\text{exp}}^a$	$\Delta H^\ddagger_{\text{exp}}^a$	$\Delta S^\ddagger_{\text{exp}}^a$	$\Delta G^\ddagger_{\text{calc}}^b$	$\Delta H^\ddagger_{\text{calc}}^b$
1	1	chloroform	Z → E	98.5	39.3	-198.7	154.4	155.1
2	1	DMSO- <i>d</i> <sub>6</sub>	E → Z	/	/	/	146.4	147.0
3	2	DMSO- <i>d</i> <sub>6</sub>	E → Z	100.2	80.9	-64.7	169.1	168.5
4	2	chloroform	Z → E	/	/	/	173.4	167.3
5	3	DMSO- <i>d</i> <sub>6</sub>	E → Z	96.6	57.8	-130.2	134.1	132.5
6	3	chloroform	Z → E	/	/	/	132.7	129.7

<sup>a</sup>From ref. 1. <sup>b</sup>This work.

## CONCLUSION

In conclusion, all the calculated values show the correct trend in decreasing rotational barriers, **3** > **1** > **2**, as do experimental ones. This also means that the *push-pull* effect is not affected by the solvent (at least the two solvents studied) and the direction of isomerization.

## Acknowledgement

This work was supported by the Ministry of Education, Science and Technological Development of the Republic of Serbia (project ID: 172020).

## REFERENCES

- [1] Rašović, D. M. Minić, M. Baranac-Stojanović, V. A. Blagojević and R. Marković, Proceedings of the 12<sup>th</sup> International Conference on Fundamental and Applied Aspects of Physical Chemistry, September 22-26, Belgrade, Physical Chemistry, 2014, **1**, 200-203, and references therein.
- [2] J. Sandström, *Top. Stereochem.*, 1983, **14**, 83-181.
- [3] Y. Zhao and D. G. Truhlar, *Theor. Chem. Acc.*, 2008, **120**, 215-241.
- [4] C. Peng and H. B. Schlegel, *Israel J. of Chem.*, 1993, **33**, 449-454.
- [5] A. Klamt and G. Schüürmann, *J. Chem. Soc., Perkin Trans.*, 1993 **2**, 799-805.

## CORRELATION BETWEEN THE C=C BOND LENGTHS AND ITS ROTATIONAL BARRIERS: EN ROUTE TO QUANTIFY THE PUSH-PULL EFFECT OF 2-ALKYLIDENE-4-OXOTHIAZOLIDINES

A. Rašović<sup>1</sup>, V. A. Blagojević<sup>2</sup> and D. M. Minić<sup>3</sup>

<sup>1</sup>Center for Chemistry ICTM, University of Belgrade, Studentski trg 16,  
P. O. Box 473, 11000 Belgrade, Serbia (arasovic@chem.bg.ac.rs)

<sup>2</sup>Institute of Technical Sciences, Serbian Academy of Sciences and Arts,  
Knez Mihailova 35/IV, P.O. Box 377, 11000 Belgrade, Serbia

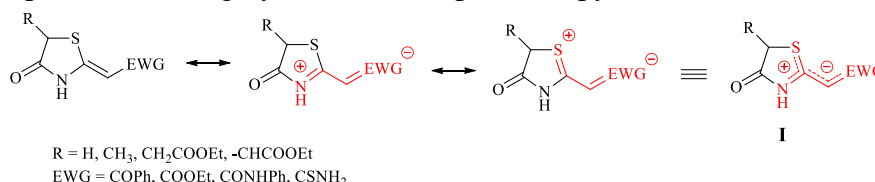
<sup>3</sup>State University in Novi Pazar, Vuka Karadžića bb, 36300, Novi Pazar, Serbia

### ABSTRACT

Our previous report, which is also published in this Edition of papers, shows that barrier to rotations proved to be a good indicator of the strength of the *push-pull* character of the 2-alkylidene-4-oxothiazolidines. Therefore, this work represents the continuation of our efforts, giving us further answers concerning the evaluation of the effectiveness of the  $\Delta G^\ddagger$  employment for that purpose. Viewed in this light, the theoretical calculations of rotational barriers, performed herein for eight selected derivatives **1-3**, excellently correlate with the calculated C=C bond lengths and corroborate the applicability of  $\Delta G^\ddagger$  for estimation of their *push-pull* effect.

### INTRODUCTION

The *push-pull* effect of the 2-alkylidene-4-oxothiazolidines, occurring as a result of the  $\pi$ -electron transfer between two electron-donors (-NH and -S-) and one electron-withdrawing group (EWG; Scheme 1) and, such as, readily apparent by the restricted rotations about the central partial C=C double bond was the subject of our previous papers[1,2]. These thorough studies were performed using dynamic NMR spectroscopy.



**Scheme 1.**

Bearing in mind the importance of the *push-pull* effect as the driving force that determines the physico-chemical properties and reactivity of the 2-

alkylidene-4-oxothiazolidines in the versatile reactions that, as we showed, led to the synthesis of the functionally important heterocyclic compounds [3], in this paper we continue the study of the effectiveness of deployment of rotational barriers as a potential significant parameter for its quantification. Guided in that direction, the knowledge which we gained from the achieved grate agreement between the experimentally determined and calculated barriers to rotations around the C=C double bond [2] served us as the starting point for our further investigations in this work.

### COMPUTATIONAL DETAILS

Geometry optimization and frequency analysis of *Z* and *E* isomers of studied compounds was conducted at the M06-2X/6-311G (d, p) DFT method, using the Gaussian 09 program package. Transition state (TS) structures were determined using Synchronous Transit-Guided Quasi-Newton method at the M06-2X/6-311G (d, p) level. All transition state structures were characterized by an imaginary frequency, the vibrational mode of which corresponded to the rotation around the C(2)–C(2') bond [2]. As shown in Fig. 1, by the correlation of the calculated barriers to rotation with the C=C bond lengths of the ground state (GS) structures **1-3**, has obtained a good linear relationship with correlation coefficients 0.917 and 0.924, for both, the *E* → *Z* and *Z* → *E* isomerization direction, respectively (Table 1).

### RESULTS AND DISCUSSION

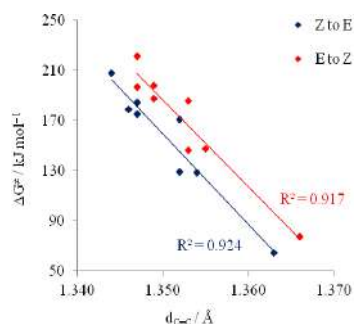


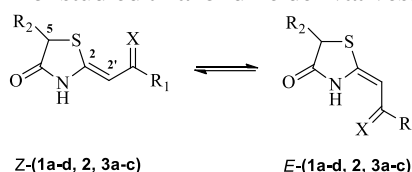
**Figure 1.** Correlation between the calculated barriers to rotation ( $\Delta G^\ddagger$ ) and the C=C bond lengths of GS structures.

→*Z* isomerizations encounter higher barriers than for the reverse ones. This can be easily rationalized by the lower energy of *E* isomers due to their stabilization by intramolecular hydrogen bond, which exceeds the one

Taking into account that for selected thiazolidine derivatives **1-3** the gas-phase calculated  $\Delta H^\ddagger$  and  $\Delta G^\ddagger$  values of the *E* → *Z* and *Z* → *E* isomerizations did not differ by more than 7 kJ/mol and the fact that they showed the same trend, only  $\Delta G^\ddagger$  values are presented in Table 1, along with the calculated C(2)=C(2') bond lengths in their ground and transition state structures. Additionally, the  $\Delta G^\ddagger$  values span a broad range of ~144 kJ/mol, being the lowest for **3a** and the highest for **2** (entries 6 and 5, respectively) and for *E*

coming from the non-bonded 1,5-S<sub>ring</sub>...O(S)<sub>substituent</sub> interactions. Another important conclusion, which can be made on the basis of data in the Table 1, is that R<sub>1</sub>CX substituents can be ordered according to their electron-accepting ability as follows: CSpH > CSNH<sub>2</sub> ≈ CSNH(CH<sub>2</sub>)<sub>2</sub>Ph > COPh > CO<sub>2</sub>Et > CONH(CH<sub>2</sub>)<sub>2</sub>Ph > CONHPh. This established trend supports our understanding of electronic properties of substituents and also corroborates with our previously reported trend, which was obtained on the basis of the occupation quotient values [4].

**Table 1.** Calculated C(2)=C(2') bond lengths (Å) in GS and TS and barriers to rotation ( $\Delta G^\ddagger$ , kJ/mol) around the C=C double bond for studied thiazolidine derivatives.



entry	compound	R <sub>1</sub>	R <sub>2</sub>	$\Delta G^\ddagger$		d <sub>C-C</sub> (GS)		d <sub>C-C</sub> (TS)
				Z → E	E → Z	E isomer	Z isomer	
1	1a (X = O)	Ph	CH <sub>2</sub> COOEt	171.5	186.1	1.353	1.352	1.427
2	1b (X = O)	NHPh	CH <sub>2</sub> COOEt	185.0	198.6	1.349	1.347	1.424
3	1c (X = O)	NH(CH <sub>2</sub> ) <sub>2</sub> Ph	H	179.3	196.8	1.347	1.346	1.425
4	1d (X = O)	OEt	CH <sub>2</sub> COOEt	175.8	187.6	1.349	1.347	1.428
5	2 (X = O)	OEt	=CHCOOEt	207.9	221.6	1.347	1.344	1.424
6	3a (X = S)	Ph	CH <sub>3</sub>	64.5	77.8	1.366	1.363	1.503
7	3b (X = S)	NH <sub>2</sub>	CH <sub>2</sub> COOEt	128.6	147.8	1.355	1.354	1.445
8	3c (X = S)	NH(CH <sub>2</sub> ) <sub>2</sub> Ph	H	129.5	146.3	1.353	1.352	1.440

By careful analysis of the data concerning the barriers to rotations of the derivative **2** we can conclude that the remote effect of the substituent attached at position C(5) of the thiazolidine ring places them to be the highest. Actually, barriers in **2** are affected by the two effects, acting in opposite directions: the C(2') ester group withdraws  $\pi$  electrons from the C(2)=C(2') double bond and decreases the barrier, while the C(5)=C(5')CO<sub>2</sub>Et moiety withdraws electron density from the ring sulfur atom, thus reducing its ability to donate the lone pair to the C(2)=C(2') double bond which increases the barrier.

In the ground state of both Z and E isomers, 4-oxothiazolidine ring and exocyclic carbon atom of the double bond with its C=X substituent are in the same plane. When R<sub>1</sub> part of R<sub>1</sub>CX is NHPh (**1b**), OEt (**1d**) and NH<sub>2</sub>

(**3b**), whole EWG is in the plane with the ring. When  $R_1 = \text{Ph}$ , as in **1a** ( $R_1\text{CX} = \text{COPh}$ ) and **3a** ( $R_1\text{CX} = \text{CSPH}$ ), the fully planar thiazolidine/double bond/CO(S) moiety and the phenyl ring form an angle of  $\sim 16^\circ$  and  $\sim 40^\circ$ , respectively, due to steric hindrance between the Ph and the CX part. In the case of  $R_1 = \text{NH}(\text{CH}_2)_2\text{Ph}$ , a fully planar structure was obtained for **3c** ( $R_1\text{CX} = \text{CSNH}(\text{CH}_2)_2\text{Ph}$ ). However, in the case of **1c** ( $R_1\text{CX} = \text{CONH}(\text{CH}_2)_2\text{Ph}$ ), the conformation around the  $\text{H}_2\text{CH}_2\text{C}-\text{C}_{\text{Ar}}$  bond is such that the phenyl ring and the neighbouring C–C bond form an angle of  $\sim 80^\circ$ . The C(5) substituent ( $\text{CH}_2\text{CO}_2\text{Et}$ ) is out of plane when attached at the  $\text{sp}^3$ -hybridized carbon atom. In the case of **2**, possessing another exocyclic C=C double bond at the C(5) position, the structure is fully planar.

## CONCLUSION

In conclusion, the C=C bond lengths correlated with rotational barriers provide a reliable information about the strength of the *push–pull* effect, as had been previously proven in the case of their correlation with the quotient of the occupation numbers. Thus, the relative magnitudes of barriers to rotation can give us information about the changes in the *push–pull* character of studied and related compounds.

## Acknowledgment

This work was supported by the Ministry of Education, Science and Technological Development of the Republic of Serbia (project ID: 172020).

## REFERENCES

- [1] Rašović, D. M. Minić, M. Baranac-Stojanović, V. A. Blagojević and R. Marković, *Proceedings of the 12<sup>th</sup> International Conference on Fundamental and Applied Aspects of Physical Chemistry, September 22-26, Belgrade, Physical Chemistry*, 2014, **1**, 200-203, and references therein.
- [2] A. Rašović, V. A. Blagojević, B. Bondžić and D. M. Minić, The studies of the *push–pull* effect of selected 2-alkylidene-4-oxothiazolidines under different solvent conditions: Experimental and computational approach, *Proceedings of the 13<sup>th</sup> International Conference on Fundamental and Applied Aspects of Physical Chemistry, September 26-30, Belgrade, Physical Chemistry*, 2016, and references therein.
- [3] M. Stojanović, Z. Džambaski, B. Bondžić, J. Aleksić and M. Baranac-Stojanović, *Curr. Org. Chem.*, 2014, **18**, 1108-1148.
- [4] M. Baranac-Stojanović, U. Klumünzer, R. Marković and E. Kleinpeter, *Tetrahedron*, 2010, **66**, 8958-8967.

## VIBRATIONAL SPECTROSCOPIC ANALYSIS OF KAEMPFEROL: A COMBINED EXPERIMENTAL AND THEORETICAL STUDY

D. Milenković<sup>1</sup>, Z. Marković<sup>2</sup>, S. Jeremić<sup>2</sup>, D. Dimić<sup>3</sup> and  
J. Dimitrić Marković<sup>3</sup>

<sup>1</sup>*Bioengineering Research and Development Center, Prvoslava Stojanovića  
6, 34000 Kragujevac, Republic of Serbia. (e-mail: deki82@kg.ac.rs)*

<sup>2</sup>*Department of Chemical-Technological Sciences, State University of Novi  
Pazar, Vuka Karadžića bb, 36300 Novi Pazar, Republic of Serbia.*

<sup>3</sup>*Faculty of Physical Chemistry, University of Belgrade, Studentski trg 12-  
16, 11000 Belgrade, Republic of Serbia.*

### ABSTRACT

Theoretically predicted vibrational wave numbers of kaempferol were compared with available IR and Raman experimental data obtained in the 4000 to 400 cm<sup>-1</sup> range. Assignments of the experimentally obtained normal vibrational modes were done by the density functional theory using the B3LYP-D3 functional in combination with the 6-311+G(d,p) basis set implemented in the Gaussian 09 package. The optimized geometry of kaempferol, in the gas-phase was used to predict the IR and Raman spectra. The complete vibrational assignments of wave numbers were made on the basis of potential energy distribution (PED). The results of the calculations, which were applied to simulated spectra of kaempferol, showed an excellent agreement with the experimental spectra.

### INTRODUCTION

Flavonoids are natural polyphenolic compounds reported to exert a wide range of positive health effects mainly arising from their antioxidant ability. Kaempferol (3,5,7-trihydroxy-2-(4-hydroxyphenyl)-4H-chromen-4-one) is a natural flavonoid that can be found mainly in broccoli, tea, kale, ginkgo, cabbage, endive, leek, beans, tomato, strawberries, grapes and many medical herbs used in traditional medicine [1]. It is known as a strong antioxidant which helps to prevent arteriosclerosis by inhibiting the oxidation of low density lipoprotein and the formation of platelets in the blood. By inhibiting angiogenesis *in vitro* and/or *in vivo* it may reduce the risk of developing some types of cancer, including pancreatic cancer, lung cancer, gastric cancer and ovarian cancer in post-menopausal women [1].

The present study comprises *in vitro* experimental (IR and Raman) and theoretical approaches in analysis of kaempferol structure. The applied combination of the experimental vibrational spectroscopic methods and theoretical calculations could be generally applied in analyzing the structural changes of naturally occurring flavonoids under physiologically relevant conditions, providing insight into the mechanism of their bioactivity.

## EXPERIMENTAL

### IR and Raman spectra

The IR spectra were recorded on a Thermo Nicolet 6700 FT-IR Spectrometers with ATR and DTGS TEC detector. The Raman spectra were recorded on Thermo Scientific DXR Raman microscope. The spectra were excited with a diode pumped solid state high-brightness 532 nm laser. Both spectra were recorded in the middle IR region, 4000-400  $\text{cm}^{-1}$ . The spectra were directly from the pure powder samples.

### DFT calculations

The structure of most stable conformation of kaempferol (Fig.1) is defined using B3LYP-D3 [2] local density functional method in combination with 6-311+G (d, p) basis as implemented in the Gaussian 09 package [3]. In order to find the most stable rotamer of kaempferol, all rotamers are designed. All of the conformations are obtained by combining antiperiplanar and synperiplanar arrangements of hydrogen atoms of the OH groups as well as rotation around the dihedral angle O1-C2-C1'-C2', which defines the coplanarity of C and B rings. All geometry minima are optimized without any geometric restrictions. The structures obtained in this way were verified by normal mode analysis to be minimum on the potential energy surface. No imaginary frequencies were obtained. The calculated wavenumbers were scaled with scaling factor of 0.9873 in order to get better match between calculated and experimental wavenumber values. The vibrational modes were assigned on the basis of PED analysis using VEDA [4] software.

## RESULTS AND DISCUSSION

### Conformational analysis

From the optimized molecular structure of the kaempferol, it is found that torsion angle,  $\tau$ , defined by the C3-C2-C1'-C2' atoms is  $\sim 180^\circ$ . Thus, as expected, investigated molecule is a planar with the facilitated electron delocalization between the B and C rings.

### IR and Raman spectra analysis

The observed and calculated infrared and Raman spectra of kaempferol and scaled band positions, wavenumbers, along with the corresponding assignments for first 66 vibrational modes (of the total 87) appearing in the 4000 to 400  $\text{cm}^{-1}$  region, are calculated. The experimentally obtained and scaled theoretical frequencies, IR intensities, and Raman activities, PEDs and mode of description are also calculated.

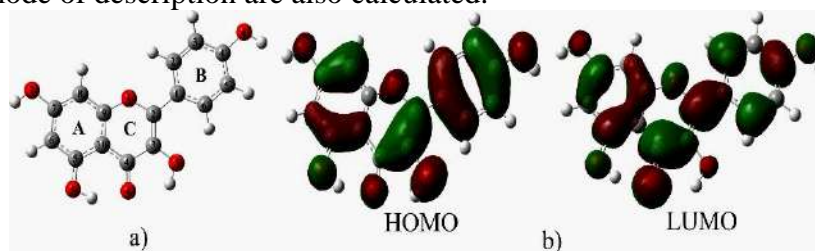


**Figure 1.** The optimized structure and numbering of kaempferol: a) HOMO and LUMO orbitals of kaempferol b)

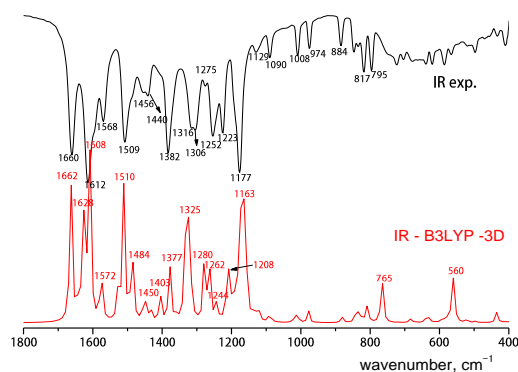


**Figure 2.** Experimental and theoretical IR spectrum of kaempferol

The most distinct bands in the IR spectrum of kaempferol are those in high frequency region (4000–2000  $\text{cm}^{-1}$ ) assigned to different modes of OH vibrations. This region is dominated by very massive and intense band. Taking into account the polyhydroxylated structure of kaempferol the intense band positioned at 3420  $\text{cm}^{-1}$  could be taken as possible absorption for (O5–H5---O4) hydrogen bond. This is also the result confirmed by the calculations which predict hydrogen bonding. The high frequency region is also very characteristic to CH stretching modes (3206  $\text{cm}^{-1}$ ). In the 4000–3000  $\text{cm}^{-1}$  region of the experimental Raman spectrum there are no bands easily assignable to O–H and C–H stretching modes.

The majority of the intense bands both in kaempferol IR and Raman spectra are to be found in the 1800-500  $\text{cm}^{-1}$  wavenumber region (Fig. 2).

The DFT wavenumbers are adjusted by a scaling factor of 0.9873. The scaling factor is determined by means of the least squares method, on the basis of the experimental data for the IR spectrum. The low frequency region involves combination of the C=O stretching ( $1660_{(\text{IR})}$  and  $1612_{(\text{IR})}$   $\text{cm}^{-1}$ ;  $1660_{(\text{R})}$  and  $1607_{(\text{R})}$   $\text{cm}^{-1}$ )(modes  $\nu_{77}$  and  $\nu_{74}$ ), C2=C3 stretching ( $1660_{(\text{IR})}$  and  $1568_{(\text{IR})}$   $\text{cm}^{-1}$ ;  $1660_{(\text{R})}$  and  $1561_{(\text{R})}$   $\text{cm}^{-1}$ )(modes  $\nu_{77}$  and  $\nu_{72}$ ) and C–C stretching ( $1660_{(\text{IR})}$ ,  $1612_{(\text{IR})}$ ,  $1568_{(\text{IR})}$ ,  $1509_{(\text{IR})}$   $\text{cm}^{-1}$ ;  $1660_{(\text{R})}$ ,  $1607_{(\text{R})}$ ,  $1561_{(\text{R})}$ ,  $1509_{(\text{R})}$   $\text{cm}^{-1}$ )(modes  $\nu_{77}$ ,  $\nu_{74}$ ,  $\nu_{72}$  and  $\nu_{70}$ ). The bands between 1500 and 1000  $\text{cm}^{-1}$  mostly involve C–C stretching, O–C stretching and in-plane C–C–H, C–O–H, C–C–O and C–C–C bending vibrations of the rings. The most intense bands in this region belong to  $\nu_{65}$ ,  $\nu_{62}$ ,  $\nu_{61}$ ,  $\nu_{58}$ ,  $\nu_{57}$  and  $\nu_{53}$  IR modes and only to  $\nu_{55}$  Raman mode. Bands appearing below 1000  $\text{cm}^{-1}$ , medium to low intensity, are assigned to bending modes (C–C–O, C–C–C, C–O–H, H–C–C and C–O–C) of all three rings and also to the combination of various in plane (C–C–C–H, H–C–C–H, C–C–C–C, C–C–O–C) and out of plane (O–C–C–C and C–C–O–C) modes.

## CONCLUSION

The results of the applied B3LYP-D3/6-311+G(d,p) density functional method in determination of the spectroscopic and electronic features of kaempferol point to a planar molecule, characterized by facilitated electron delocalization between the B-ring and the C-ring. Spectral assignments, done on the basis of a best-fit comparison between the experimentally obtained and theoretically calculated IR and Raman spectra, match quite well, indicating DFT calculations as a very accurate source of normal mode assignments.

## Acknowledgement

Authors acknowledge the Ministry of Education, Science and Technological Development of the Republic of Serbia (Grants No. 172015, and 174028).

## REFERENCES

- [1] J.M. Calderón-Montaña, E. Burgos-Morón, C. Pérez-Guerrero, M. López-Lázaro, *Mini. Rev. Med. Chem.* 2011, **11**, 298–344.
- [2] S. Grimme, J. Antony, S. Ehrlich, H. Krieg, *J. Chem. Phys.* 2010, **132**, 154104.
- [3] M. J. Frisch, G. W. Trucks, H. B. Schlegel, et al. *Gaussian 09*, Revision C.01, Gaussian, Inc., Wallingford, CT, USA. 2010.
- [4] M. H. Jamroz, *Vibrational Energy Distribution Analysis VEDA 4*, Warsaw, 2004.

## DAMAGES CAUSED BY THE PRESENCE OF 5-URACILYL RADICAL IN SHORT, DOUBLE-STRANDED DNA: ONIOM CALCULATIONS

S. Makurat<sup>1</sup>, L. Chomicz-Mańska<sup>1</sup>

<sup>1</sup> *University of Gdańsk, Faculty of Chemistry, Biological Sensitizers Laboratory, Wita Stwosza 63, 80-308 Gdańsk, Poland (samantamakurat@gmail.com)*

### ABSTRACT

Modified nucleosides with the increased electron affinity like widely studied 5-bromo-2'-deoxyuridine (5-BrdU), are able to be incorporated into double stranded DNA helix, sensitizing it to ionizing radiation in an aqueous solution. Attachment of electron (one of the main product of water radiolysis) to DNA modified with 5-BrdU leads to the production of nucleobase radical, which is believed to induce hydrogen abstraction from the sugar moiety, followed by a further DNA damage. In the current project the degradation processes of 21 base-pair, double-stranded DNA containing 2'-deoxyuridine-5'-radical (5-dU•) were investigated with the use of QM/MM methodology. The obtained results allowed us to elucidate chemical mechanisms leading to DNA strand breaks and abasic sites.

### INTRODUCTION

Modified nucleosides, such as 5-bromo-2'-deoxyuridine can be phosphorylated and incorporated to cellular DNA, due to their similarity to the native thymidine, where they can act as radiosensitizers. Owing to the increased electron affinity of modified nucleosides, they react with hydrated electrons produced during water radiolysis (indirect effect of irradiation) forming a substituent (bromine) anion and reactive nucleobase radical (5-dU•) [1,2].

5-dU• radical can be stabilized by hydrogen atom abstraction from the own or neighboring sugar moiety. Such produced radical localized in sugar-phosphate chain can further lead to potentially lethal DNA lesions [3]. While the first step of damage to the modified DNA – nucleobase radical production – seems to be well understood, the following degradation steps – hydrogen abstraction and its consequences, require further studies [4].

To understand the nature of radiodamage observed in the modified DNA we performed the QM/MM calculations for chosen degradation paths (Fig. 1)

using as a model the 21 base-pair, double stranded, 5-dU• labeled DNA, surrounded with water molecules.

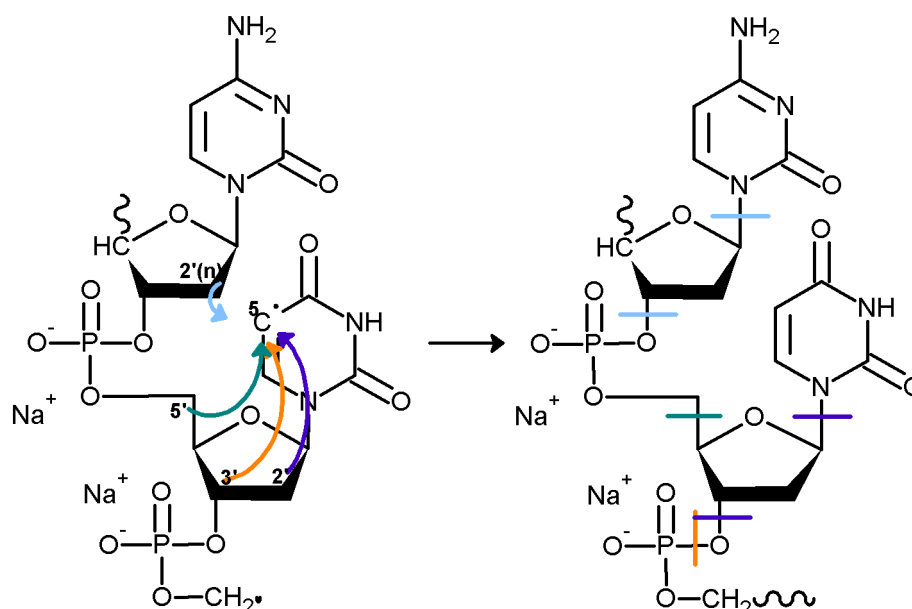


**Figure 1.** Schematic representation of the reactions modelled in the current study. The primary 2'-deoxyuridine-5-radical (**5-dU•**) abstracts hydrogen atom from the own or neighboring sugar, which may result in SSBs, or abasic sites. Hydrogen atom transfers (left) and possible DNA lesions (right) are marked with colored arrows or lines, respectively.

## COMPUTATIONAL

The X3DNA obtained structure of 21 base-pair, double stranded B-DNA with the uracil radical as the 11th base was equilibrated over 200ns (AMBER99SB force field with the PARMBSC0 refinement of the AMBER Force Field for Nucleic Acids) in a cuboid box (60x60x110Å) filled with TIP3P rigid water model and Na<sup>+</sup>, Cl<sup>-</sup> ions used to neutralize the system (in concentration of 0.154 mM). These calculations was performed with the GROMACS molecular dynamics package.

After MD equilibration the excess water (over 10 Å) was cut off and the possible pathways of DNA damage were studied with the QM/MM hybrid method, implemented in the Gaussian09 program. We performed two-layer ONIOM calculations. High level model contained central dinucleotide, including 5-dU• and C5'-site neighboring 2'-deoxycytidine with two sodium ions, neutralizing and stabilizing dinucleotide's phosphates. The low

level was built of the rest of the B-DNA helix surrounded with the remaining water molecules and anions. For the model system, shown in Fig. 1, both the wB97XD and M06-2X functionals with the 6-31++G(d,p) basis set were used for comparison, while for the real system (low level) the Amber96 force field was employed.

## RESULTS AND DISCUSSION

We obtained the free energy profiles of two main degradation steps: (1) hydrogen atom transfer from the 2', 3' or 5' positions of the own sugar or from the 2'(n) position of neighbouring sugar to the 2'-deoxyuridine-5'-radical (5-dU•), resulting in the sugar• type radicals (see left panel of Fig. 1); and (2) further damaging processes, resulting in a single strand break (SSB) or abasic sites (see right panel of Fig. 1). These profiles suggest that in the first step, in most cases favourable (since the sugar-centred radical is thermodynamically much more stable than the 5-dU• one), the hydrogen atom transfer kinetic barriers are about 10 kcal/mol and. Still, the damage on the proposed pathways is not that easy as the subsequent step is connected with much higher barriers and seems to not always be thermodynamically favoured.

## CONCLUSION

The present findings are similar to the results obtained in our previous project, where 2'-deoxyadenosine-8-radical (8-dA•) was investigated in a similar context. However, in the case of 8-dA•, the most favorable degradation path leads to 5'-8-cycloadenosine product, while the cyclization process is not possible for pyrimidines. Moreover, the current results are in good agreement with the previous DFT studies on a smaller model – 2'-deoxyuridine-5-yl 3',5'-diphosphate radical [5], although the ONIOM kinetic barriers occurred to be somewhat higher. These quantitative differences can be explained by the limited flexibility of B-DNA double helix, stabilized by the *explicite* water and salt environment, in comparison to the relatively flexible single nucleotide studied in ref. 5.

### *Acknowledgement*

This work was supported by the Polish National Science Centre under Grant No. 2014/14/A/ST4/00405 (J.R.) and BMN grant No. 538-8227-B056-16 (S.M).

**REFERENCES**

- [1] D. S. Shewach, T. S. Lawrence in: Deoxynucleoside Analogs in Cancer Therapy, J. P. Godefridus, J. P. (Ed.), Humana Press Inc., Totowa, NJ, 2006, 289-329.
- [2] E. H. Szybalska, W. Szybalski. Genetics of human cell lines, IV. DNA-mediated heritable transformation of a biochemical trait, Proc. Natl. Acad. Sci. U. S. A., 1926, **48**.12, 2026-2034.
- [3] J. Rak, L. Chomicz, J. Wiczak, K. Westphal, M. Zdrowowicz, P. Wityk, M. Żyndul, S. Makurat, Ł. Golon, Mechanisms of Damage to DNA Labeled with Electrophilic Nucleobases Induced by Ionizing or UV Radiation, J. Phys. Chem. B, 2015, **119**.26, 8227-8238.
- [4] L. Chomicz, J. Rak, P. Storniak, Electron-induced elimination of the bromide anion from brominated nucleobases. A computational study, J. Phys. Chem. B, 2012, **116**.19, 5612-5619.
- [5] Ł. Golon, L. Chomicz, J. Rak, Electron-induced single strand break in the nucleotide of 5-and 6-bromouridine. A DFT study, Chem. Phys. Lett., 2014, **612**, 289-294.

## HALOGEN AND SOLVENT EFFECT ON THE ADDITION REACTION OF SILACYCLOPROPYLIDENE TO ETHYLENE

C. B. Yildiz<sup>1</sup> and A. Azizoglu<sup>2</sup>

<sup>1</sup>*Department of Chemistry, Faculty of Arts and Sciences, University of Aksaray, Aksaray, Turkey. (cemburakyildiz@aksaray.edu.tr)*

<sup>2</sup>*Laboratory of Computational Chemistry, Department of Chemistry, University of Balikesir, TR-10145 Balikesir, Turkey*

### ABSTRACT

The addition reactions of halo-silacyclopropylidenoids ( $C_2H_4SiXLi$ ,  $X = F, Cl, Br$ ) to ethylene have been investigated separately at the B3LYP/6-311+G(d,p) level of theory. The calculations depict that addition of silacyclopropylidenoids to ethylene occurs via stepwise mechanisms. The required initial energy barriers for the conversion of silacyclopropylidenoids to silaspiropentanes were determined to be 77.4 kJ/mol, 9.6 kJ/mol, and 9.2 kJ/mol for F, Cl, and Br, respectively. The gas phase calculations show that the reactions are not spontaneous at room temperature. However, solvent (THF) included systems indicate that the formations of silaspiropentanes ( $X = Br$  and  $Cl$ ) are spontaneous at room temperature.

### INTRODUCTION

Silylenoids are key intermediates in organosilicon reactions [1–6]. As stable species, preparations of silylenoids are very hard due to their highly reactive nature. In 1995, Tamao and Kawachi [6] detected the existence of the first silylenoid and studied its chemical properties. From the literature, it appears that although several reports and discussions on experimental and theoretical studies of cyclopropylidenoids can be found, [7,8], only a few scientific studies on silacyclopropylidenoids, which are cyclic analogues of silylenoids, have been reported so far [9–11]. More recently, we have carried out a series of DFT calculations on the formation and rearrangement of silaspiropentane from addition of lithium-bromosilacyclopropylidenoid to ethylene [11].

In the present paper, we wish to provide the first computational study of the halogene ( $X = F, Cl, Br$ ) and solvent effects on the addition reaction of silacyclopropylidenoids to ethylene.

## EXPERIMENTAL

All the calculations were performed with Gaussian 09W suite of program [12]. In order to optimize the title structures on their potential energy surface, B3LYP theory was employed. The 6-311+G(d,p) was chosen as basis set. The optimized structures were determined as a minimum (no imaginary frequency) or transition state. The relative  $\Delta G$  energies are given in kJ/mol. The Intrinsic Reaction Coordinate (IRC) procedure was carried out for the identification of the connectivity of stationary points. The single point frequency calculations in THF (Tetrahydrofuran) have been done for the optimized structures with using polarized continuum model (PCM) solvation model to estimate solvent effect on the energetic of the reactions.

## RESULTS AND DISCUSSION

Previous calculation has shown that **1Br** addition to ethylene has stepwise manner via **TS1** and **TS2** with the energy barriers of 94.6 kJ/mol and 90.4 kJ/mol at B3LYP/6-31+G(d,p) level of theory [11]. On the other hand, the barrier to arrive at **TS1F** and **TS2F** are calculated to be relatively lower with the energy of 77.4 kJ/mol and 46.4 kJ/mol at B3LYP/6-311+G(d,p) level of theory, respectively (Figure 1.). Moreover, the formation of **3F** was found to be highly endergonic with 72.3 kJ/mol.

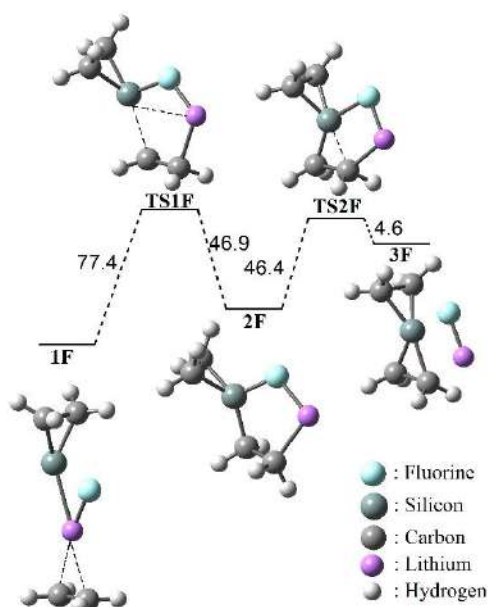


**Figure 1.** Addition reaction mechanism of **1F** to ethylene.

Despite of **1F**, the addition mechanisms of **1Cl** and **1Br** to ethylene have three steps. The required energy barriers to **TS1X–3X** (X = Cl, Br) are determined to be very similar (Figure 2 and 3). The results indicate that formations of **4Cl** and **4Br** are endergonic with the energies of 23.8 kJ/mol and 27.3 kJ/mol, respectively. Thus the gas phase calculations at room temperature suggest that the reactions are not spontaneous.

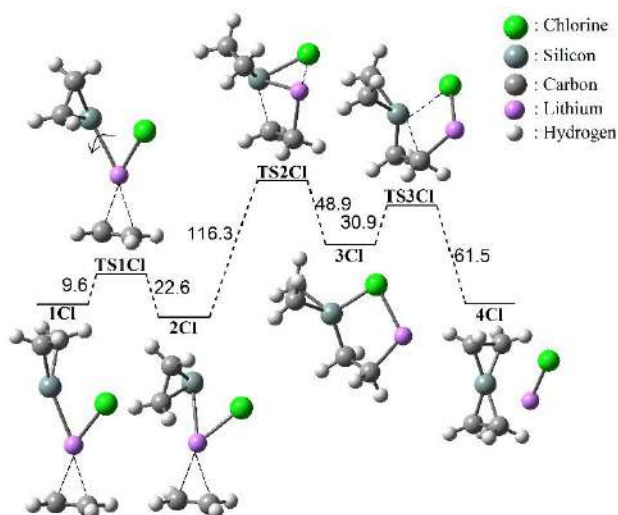


**Figure 2.** Addition reaction mechanism of **1Cl** to ethylene.

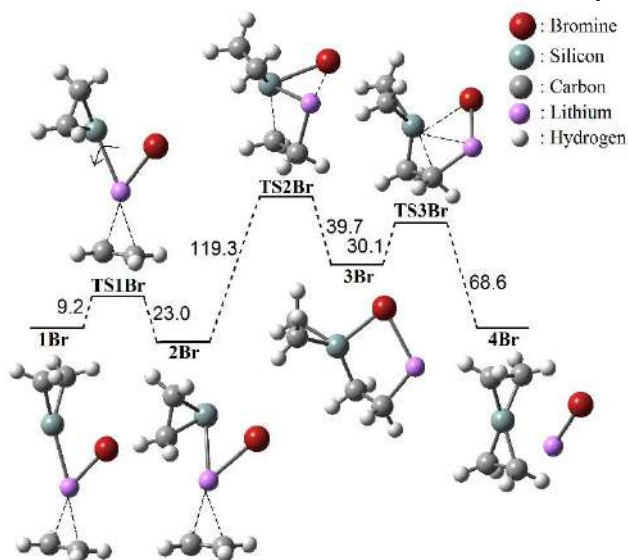


**Figure 3.** Addition reaction mechanism of **1Br** to ethylene.

**Table 1.** The solvent effect on the energetic of the reactions at B3LYP/6-311+G(d,p) level of theory (Solvent = THF).

	<b>1X to TS1X</b>	<b>TS1X to 2X</b>	<b>2X to TS2X</b>	<b>TS2X to 3X</b>	<b>3X to TS3X</b>	<b>TS3X to 4X</b>
<b>X= F</b>	+50.6	-54.0	+21.7	+0.4	-	-
<b>X= Cl</b>	+14.6	-28.4	+96.2	-61.1	+27.6	-66.5
<b>X= Br</b>	+12.9	-28.0	+100.0	-56.1	+23.0	-64.8

To obtain more insights on the energetic of the mechanisms, we have performed implicit solvation models with PCM method using tetrahydrofuran (THF) as solvent. The single point calculations estimate that formations of **4Cl** and **4Br** are spontaneous in THF at room temperature (Table 1).

## CONCLUSION

The energetic of the addition reactions are compared and the contributing of the halogens to the stability of the structures is simply discussed. Moreover, we have investigated solvent effect on the formation of silaspiropentanes. To create an implicit solvation model, single point calculations have been carried out for the optimized structures at the B3LYP/6-311+G(d,p) level of theory, with inclusion of the polarized continuum model (PCM) and THF as solvent. The solvated models were found to be spontaneous at room temperature for **1Br** and **1Cl** additions.

## Acknowledgement

This work was partially supported by Aksaray University (BAP-2016024).

## REFERENCES

- [1] P. Gaspar, R. West, *The Chemistry of Organic Silicon Compounds*. Wiley, New York, 1998.
- [2] V. Y. Lee, A. Sekiguchi, *Inorg. Chem.* 2011, **50**, 12303–12314.
- [3] T. Clark, P. R. Schleyer, *J. Organomet. Chem.* 1980, **191**, 347–353.
- [4] D. C. Feng, S. Y. Feng, C. H. Deng, *Chem. J. Chin. Univ.* 1996, **17**, 1108–1111.
- [5] M. Zhang, W. Li, O. O. Cheng J, *J. Mol. Model.* 2015, **21**, 202–207.
- [6] K. Tamao, A. Kawachi, *Angew. Chem. Int. Edit.* 1995, **34**, 818–820
- [7] C. B. Yildiz, A. Azizoglu, *J. Phys. Org. Chem.* 2016, **29**, 63–68.
- [8] A. Azizoglu, O. Demirkol, T. Kilic, Y. K. Yildiz, *Tetrahedron*, 2007, **63**, 2409–2413.
- [9] A. Azizoglu, C. B. Yildiz, *Organometallics*, 2010, **29**, 6739–6743.
- [10] A. Azizoglu, C. B. Yildiz, *J. Organomet. Chem.* 2012, **715**, 19–25.
- [11] C. B. Yildiz, A. Azizoglu, *J. Mol. Mod.* 2016, Accepted.
- [12] Gaussian 09, revision A02. Gaussian Inc, Wallingford, 2009.

## CONFORMATIONAL AND VIBRATIONAL ANALYSIS OF 3-METHOXYTYRAMINE

D. Dimić<sup>1</sup>, D. Milenković<sup>2</sup>, Z. Marković<sup>3</sup> and J. Dimitrić Marković<sup>1</sup>

<sup>1</sup>*Faculty of Physical Chemistry, University of Belgrade, Studentski trg 12-16, 11000 Belgrade, Republic of Serbia (ddimic@ffh.bg.ac.rs).*

<sup>2</sup>*Bioengineering Research and Development Center, Prvoslava Stojanovića 6, 34000 Kragujevac, Republic of Serbia.*

<sup>3</sup>*Department of Chemical-Technological Sciences, State University of Novi Pazar, VukaKaradžića bb, 36300 Novi Pazar, Republic of Serbia.*

### ABSTRACT

Conformations and vibrational spectra of 3-methoxytyramine (3-MT), a metabolite of dopamine, have been investigated by density functional theory, at B3LYP/6-311++G(d,p) level, implemented in Gaussian Program package. From crystallographic data, by the conformational search, the most stable conformations were determined in gas phase. The most stable conformer, with emphasis on the specific interactions (hydrogen bonds and N–H $\cdots\pi$ ) stabilizing the structure, is discussed. Experimental IR and Raman spectra, recorded in the region 4000–400 cm<sup>-1</sup>, have been assigned based on the potential energy distribution (PED).

### INTRODUCTION

3-methoxytyramine (3-MT) is a major extracellular metabolite of dopamine, produced via catechol-O-methyltransferase from parent molecule. This molecule acts as neuromodulator that can be involved in movement control. Its elevated concentrations may indicate mental disorders, brain and carcinoid tumors' development [1]. Unlike the other metabolites of dopamine, for example homovanillic acid and 3,4-dihydroxyphenylacetic acid, 3-MT has not been investigated by the means of theoretical methods and results of those being compared to experimental spectra and crystallographic data. In present study, the theoretical vibrational spectra are compared to experimental (IR and Raman), after the detailed conformational analysis.

### THEORETICAL AND EXPERIMENTAL METHODS

All of the calculations have been performed with the Gaussian 09 program package [2]. Density functional theory (DFT) with B3LYP functional in conjunction with 6-311++G(d,p) basis set, has been employed for the conformational search of the most stable conformer of 3-MT. Vibrational

frequencies, computed in harmonic approximation, verified that the minimum of potential energy surface was found. The calculated frequencies were scaled based on the least square method, with scaling factor of 0.9800 in order to obtain better reproduction of experimental spectra. The assignment of vibrational modes was done based on PED analysis implemented in VEDA [3] software. Natural bond Orbital analysis was performed in order to investigate possible stabilization interactions.

## RESULTS AND DISCUSSION

### Conformational analysis

3-methoxytyramine 3-MT (Figure 1.) consists of aliphatic 2-aminoethyl chain and aromatic ring with hydroxyl and methoxy substituents. For the present study the protonated form of molecule was chosen, because 3-MT hydrochloride was used for experiments. The conformational search was as following: three possible orientations of substituents were selected – hydroxyl and methoxy substituents oriented in the same direction with methoxy group pointing to hydroxyl (a), with hydroxyl group pointing to methoxy (b), and with substituents pointing in opposite directions (c). For these orientations, the rotation around dihedral angles  $\alpha$  and  $\beta$  was performed and minima of the potential energy curve taken as starting structures for optimization.



**Figure 1.**  
Structure of 3-MT

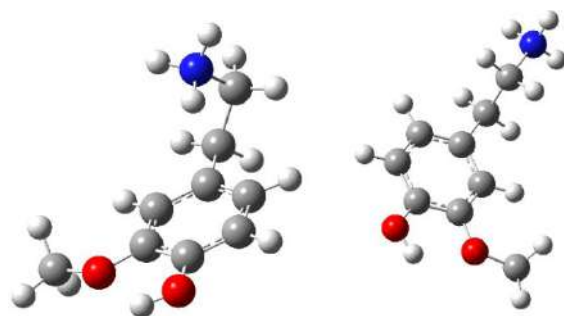


**Figure 2.** Optimized structures of 3-MT (*1-1* left; *2-1* – right)  
a) *1-1* and b) *2-1*

There was the total of 12 structures. Based on differences in energy and enthalpy, two conformers, that were the most stable, were chosen (Figure 2), and named *1-1* and *2-1*. In the most stable conformers hydroxyl and methoxy substituents are oriented in the same direction, leading to the formation of an intramolecular  $\text{OH}\cdots\text{O}-\text{CH}_3$  hydrogen bond. The energy difference was 20.51 kJ/mol with *1-1* being more stable, but when enthalpy is concerned structure

**2-I** is more stable for 13.86 kJ/mol, which is very ambiguous about the real conformation of 3-MT.

Structure **1-I** resembles the most stable conformer of dopamine from reference of Lagutschenkov[4] and this structure is additionally stabilized by the presence of weak intermolecular bond between N-H group of aliphatic chain and aromatic ring  $\pi$  system.

The stabilization energy for this conformer is only 2 kJ/mol as predicted by NBO. These interactions are broken if solvent model for water is used, and more stable conformer is **1-I'** for only 0.29 kJ/mol. Structure **2-I** is found in crystallographic structure of some salts of 3-MT, due to strong interactions with surrounding molecules through amino group.

### Vibrational analysis

The total of 72 vibrational modes were calculated and scaled, in the region between 4000 and 400 $\text{cm}^{-1}$ , of which 60 are assigned based on PED analysis. As this is a low symmetry molecule, the most of modes are present in both spectra. The correlation between experimental and theoretical spectra was higher than 0.99. The comparative representation of experimental and theoretical IR and Raman spectra (R) are shown in Figure 3.

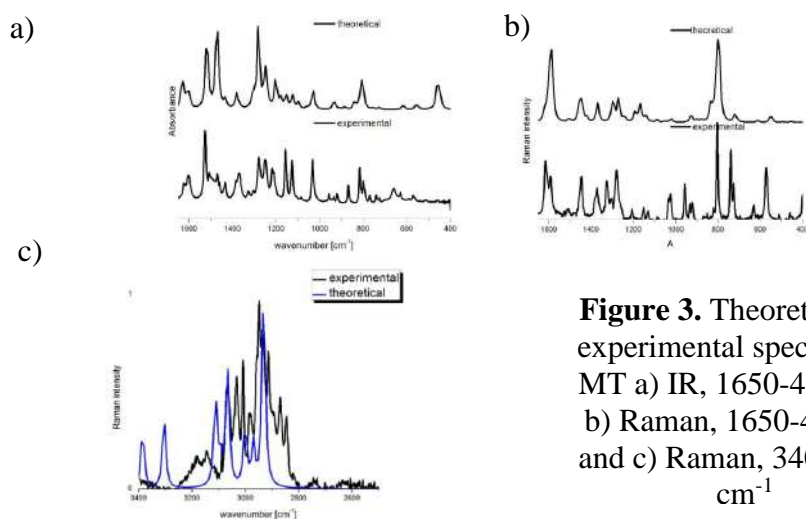


**Figure 3.** Theoretical and experimental spectra of 3-MT a) IR, 1650-400  $\text{cm}^{-1}$ , b) Raman, 1650-400 $\text{cm}^{-1}$  and c) Raman, 3400-2500  $\text{cm}^{-1}$

In high frequency region (4000-2000 $\text{cm}^{-1}$ ) the most prominent peak is assigned to N-H stretching vibration of aliphatic chain, along with C-H stretching mode of aromatic ring and aliphatic chain (3440-2940  $\text{cm}^{-1}$ ). The mid frequency region (1700-100  $\text{cm}^{-1}$ ) comprises of medium to strong and very strong bands at 1603, 1279, 1249, 1160, 1032  $\text{cm}^{-1}$  (IR) and 1616, 1593, 1279 and 1025  $\text{cm}^{-1}$  (R) assigned to C-C and C-O stretching vibrations of aromatic ring and aliphatic chain, along with weak vibrations

of the same type at 1433, 1385, 1085  $\text{cm}^{-1}$  (IR) and 1150 and 1083  $\text{cm}^{-1}$ (R). In the region between 1500 and 1000  $\text{cm}^{-1}$  there are bending H–C–C, C–C–C, H–C–H, H–C–N and H–O–C modes appearing as weak intensity bands at 1623, 1506, 1471, 1458, 1304  $\text{cm}^{-1}$  (IR) and 1508, 1303, 1206 and 1131  $\text{cm}^{-1}$ (R). Below 1000  $\text{cm}^{-1}$ , the observed bands go from strong to medium, and are assigned to OC, CC and NC stretching modes (1032 and 799  $\text{cm}^{-1}$ (IR) and 1025 and 803  $\text{cm}^{-1}$ (R)). The torsion modes, composed of mixed vibrations of type C–C–C–C, H–C–C–C, C–C–C–O, H–O–C–C and C–C–O–C are positioned at 816, 724, 571, 460 and 457  $\text{cm}^{-1}$ (IR) and 821, 725, 571 and 454  $\text{cm}^{-1}$ (R) mostly as low intensity bands.

### CONCLUSION

The conformational search for the most stable structure of 3-MT was performed at B3LYP/6-311++G(d, p) level. Formation of hydrogen bond between O–H and O–CH<sub>3</sub> additionally stabilizes structure **1-I**, along with N–H interactions with  $\pi$  system, thus making the discussed structure the most stable in gas phase, although these interactions are broken in polar solvent. For the comparison, structure **2-I** was chosen because it resembles structure from crystallographic data. Experimental vibrational spectra were assigned based on the best-fit comparison between experimental and theoretical spectra, with correlation of higher than 0.99, thus proving that structure of 3-MT describes well structure in solid state and solution.

### Acknowledgement

Authors acknowledge the Ministry of Education, Science and Technological Development of the Republic of Serbia (Grants No. 172015, 174028 and 172040).

### REFERENCES

- [1] Fitzgerald, J. C. & Plun-Favreau, H. Emerging pathways in genetic Parkinson's disease: Autosomal-recessive genes in Parkinson's disease - A common pathway? *FEBS J.* **275**, 5758–5766 (2008).
- [2] M. J. Frisch, G. W. Trucks, H. B. Schlegel, et al. Gaussian 09, Revision C. 01, Gaussian Inc. Wallingford, CT, USA, 2010.
- [3] M. H. Jamroz, Vibrational Energy Distribution Analysis VEDA 4, Warsaw, 2004.
- [4] Lagutschenkov, A., Langer, J., Berden, G., Oomens, J. & Dopfer, O. Infrared spectra of protonated neurotransmitters: dopamine. *Phys. Chem. Chem. Phys.*, **13**, 2815–23 (2011).

## THE ELECTRON NUMBER DENSITY OF ARGON-OXYGEN ATMOSPHERIC PRESSURE PLASMA

D. P. Ranković<sup>1</sup>, M. M. Kuzmanović<sup>1</sup> and J. J. Savović<sup>2</sup>

<sup>1</sup>*Faculty of Physical Chemistry, University of Belgrade, P.O. BOX 276,  
11001 Belgrade, Serbia (dragan@ffh.bg.ac.rs)*

<sup>2</sup>*Institute of Nuclear Sciences Vinca, University of Belgrade, P.O. BOX 522,  
11001 Belgrade, Serbia*

### ABSTRACT

The studied plasma source was a wall stabilized direct current arc burning in argon at atmospheric pressure, originally designed for elemental spectrochemical analysis. The influence of oxygen addition (1 - 20 %) on the electron density of mixed gas plasma was investigated for two initial plasma compositions, i.e. argon gas with water aerosol and argon with water aerosol containing 0.5 % KCl. The electron number densities were calculated from the measured *Stark* profiles of H $\beta$  spectral line. The results have shown that the addition of oxygen has weak influence on electron number density in the studied central plasma zones. Similar trends were observed regardless of the presence or absence of easily ionized element (potassium).

### INTRODUCTION

A direct current (DC) argon arc is an atmospheric-pressure plasma source that has several important operational characteristics in common with inductively coupled plasma (ICP): argon as the main gas, similar values of temperature and electron number density, and analyte introduction in the form of aerosol. The detection power of this device is comparable with ICP devices, especially for analysis of heavy metals in aqueous solutions. The addition of easily ionisable elements or molecular gases to argon plasma is a common spectrochemical practice, applied to improve excitation conditions of the source, or to minimize matrix effects [1]. Our previous studies of argon-nitrogen plasma have shown that the addition of molecular gas may improve the analytical performance of DC arc source [2,3]. The aim of the present research is to test the applicability of another molecular gas, oxygen, for the same purpose. This paper describes the effects of various proportions of added oxygen on electron number density ( $n_e$ ) in argon DC arc burning in atmospheric pressure. As an air constituent, oxygen diffuses into the open-

air plasma, thus, our results may be of interest for other atmospheric plasma sources as well.

### EXPERIMENTAL

The excitation source under study is an arc specifically designed for spectrochemical analysis. A detailed description of U-shaped direct current (DC) argon stabilized arc was given in our previous papers [2,3]. The oxygen was added to two initial plasma gas compositions, argon gas with water aerosol, and argon gas with water aerosol containing 0.5% KCl. The addition of oxygen gas was carried out by increasing the flow rate of the O<sub>2</sub> and decreasing that of Ar, so that the total flow rate of the mixed gas was kept constant at 2.7 dm<sup>3</sup>min<sup>-1</sup>, which is the optimal flow for plasma operating in pure argon. An appropriate amount of oxygen, in the range from 1 to 20 %, was gradually added. The effect of the addition of oxygen on electron number density at the arc axis was investigated for three arc currents 5, 7 and 9 A. Also, radially resolved electron density profiles were obtained for the arc current of 7A, a current that is commonly used in spectrochemical applications of this source.

Our prime goal was to measure changes of the electron number density ( $n_e$ ) caused by the addition of oxygen to the argon plasma. Among the various methods available for this purpose, measurement of the half widths of the *Stark* broadened *Balmer*- H<sub>β</sub> spectral line (486.13 nm) was chosen for two reasons. Firstly, the method is independent on local thermodynamic equilibrium assumption (LTE). Secondly, hydrogen exhibits a linear *Stark* effect that is readily measured even at densities lower than 10<sup>21</sup>/m<sup>3</sup>. Another accurate method for determination of  $n_e$  (that is also independent on LTE assumption), the absolute measurement of the continuum emission, was a rather complicated task for mixed gas plasma. For evaluation of  $n_e$  a program proposed by *Zikic et al* [4] was used. The program enables evaluation of electron number densities by comparing the experimentally obtained emission profiles of H<sub>β</sub> with the theoretically calculated ones.

### RESULTS AND DISCUSSION

For our working conditions (atmospheric pressure, not too high values of electron number densities and temperature), the most important cause of hydrogen spectral lines broadening was *Stark* broadening (full width at half maximum, FWHM between 5·10<sup>-2</sup> and 3·10<sup>-1</sup> nm), while instrumental and *Doppler* widths were much smaller (FWHM < 10<sup>-2</sup> nm). The accuracy of the electron density determination was estimated to be 5 – 7%. Addition of oxygen to the argon plasma with an aqueous aerosol (with or without KCl)

caused negligible changes in the electron number density at the arc axis, for all investigated arc currents (Figure 1).

Moving away from the arc axis, small changes in radial distribution of electron number density could be observed (Figure 2). The largest change (increase) of  $n_e$  was observed in the zone 0.5 mm to 1 mm from the arc axis. At greater distances from the arc axis,  $n_e$  is somewhat higher than in the plasma without oxygen, but does not depend on the concentration of added oxygen. In the presence of potassium, density of electrons in the plasma core was smaller

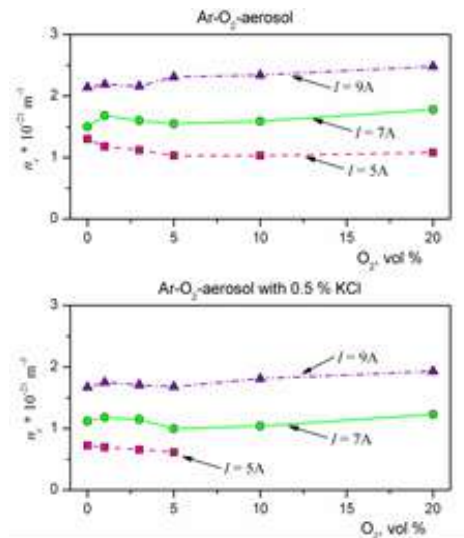


**Figure 1.** The influence of oxygen gas addition on electron number densities at the arc axis, for different arc currents.

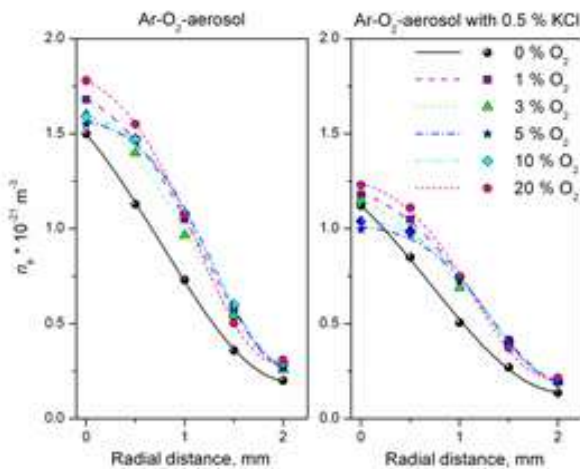


**Figure 2.** The influence of oxygen gas addition on radial distribution of electron number density in argon arc plasma operating at 7 A.

compared to the plasma without KCl, however, the added oxygen had a same effect on  $n_e$ . DC argon arc plasma is characterized by a large electron number density and temperature gradients in radial direction. The addition of oxygen may influence the energy transport through the discharge causing the changes of the fundamental plasma properties ( $n_e$ , electron and gas temperature), the bulk plasma characteristics (thermodynamic functions and transport coefficients, diffusion coefficient, viscosity, thermal and electrical conductivity) and radiation properties of the plasma. In the present case, these changes are found to have minor influence on plasma parameters in the arc core.

Dissociation of oxygen contributes to a local increase in thermal conductivity of plasma through the heat transferred as chemical enthalpy of molecules. However, the largest effect is expected in plasma zones where the temperature corresponds to the dissociation temperature of molecular oxygen, which is around 3500 K, and for the studied argon arc, this zone is at the plasma periphery. Consequently, the presence of oxygen will reduce the temperature gradient in the peripheral plasma zones which will indirectly induce small changes of the plasma parameters in the arc core. At the same time, due to high temperature, and relatively low dissociation energy of O<sub>2</sub> (5.2 eV), a dissociation degree of oxygen in the arc core is probably high. If that is the case, mixtures of oxygen and argon would behave as a mixture of two atomic gases, which could explain the small effect of oxygen on the electron number density of the arc core.

### CONCLUSION

Influence of different oxygen contents (1 % to 20 %) on the electron number density in atmospheric pressure argon DC arc has been studied. The results have shown that the changes in oxygen content slightly influence the changes in electron number density through changes in plasma temperature and thermal conductivity. The presence of easily ionized element lowers electron number densities in the central plasma zones of argon plasma, but the effect of oxygen on  $n_e$  is the same as for mixed gas plasma without potassium.

### *Acknowledgement*

This work was supported by the Ministry of Education and Science of the Republic Serbia, project No. 172019.

### REFERENCES

- [1] C. Tendero, C. Tixier, P. Tristant, J. Desmaison, P. Leprince, *Spectrochim Acta B*, 2006, **61**, 2-30.
- [2] D. Ranković, M. Kuzmanović, J. Savović, M.S. Pavlović, M. Stoiljković, M. Momčilović, *J. Phys. D. Appl. Phys.*, 2010, **43**, 335202
- [3] D.P. Ranković, M.M. Kuzmanović, M.S.Pavlović, M.Stoiljković and J.J. Savović, *Plasma Chem. Plasma P.*, 2015, **35**(6), 1071-1095.
- [4] R. Žikić, M.A. Gigosos, M. Ivković, M.A. Gonzalez and N.A. Konjević, *Spectrochim Acta B*, 2002, **57**, 987–998.

## EFFECTS OF ATMOSPHERIC PRESSURE ARGON PLASMA ON 2-((4-HYDROXYPHENYL) DIAZENIL)BENZENE-1,3,5-TRIOLE MOLECULE

M. Tanişli<sup>1</sup>, E. Taşal<sup>2</sup> and S. Pat<sup>2</sup>

<sup>1</sup>Anadolu University, Science Faculty, Department of Physics, 26470 Eskişehir, Turkey.

<sup>2</sup>Eskişehir Osmangazi University, Department of Physics, 26040 Eskişehir, Turkey.

### ABSTRACT

An interesting application of the atmospheric pressure plasma is decomposing of the long chemical chain molecules 2-((4-Hydroxyphenyl)Diazenil)Benzene-1,3,5-Triol. These molecules are very harmful and danger for the ecological life. Fourier transform infrared spectrometry (FT-IR) and UV-Vis spectrophotometry tools were used to characterization of the molecules after the plasma applications to molecule in ethanol and methanol solution. Characterizations for solutions prepared with ethanol and methanol solvents of 2-((4-Hidroksifenil)Diazenil)Benzene-1,3,5-Triol molecule have been analysed after applying (*duration*: 3 minutes) the atmospheric pressure plasma jet. After the plasma treatment, photo products were produced at  $1455.9\text{ cm}^{-1}$  and  $1453.94\text{ cm}^{-1}$ . These are strong stretching peaks of  $9\text{C}-8\text{N}-7\text{N}=6\text{C}$  of molecules in ethanol and methanol solutions. Moreover, other photoproducts were produced at  $1624.84\text{ cm}^{-1}$  and  $1645.92\text{ cm}^{-1}$ , corresponds to  $3\text{C}=15\text{O}$  stretching peaks. Finally, obtained new molecules contains  $9\text{C}-8\text{N}-7\text{N}=6\text{C}$  inspire of the  $9\text{C}-8\text{N}=7\text{N}-6\text{C}$ .

### INTRODUCTION

Atmospheric pressure plasma may be more popular research subject about material and surface treatment. Atmospheric pressure plasma is used to degradation of the chemical bond and re-order of the chemical bonds in molecules chains. Atmospheric pressure plasma can change the surface free energy in some applications. Plasma jets operating with noble gases such as argon, neon... can be classified into four ways, i.e. dielectric-free electrode jets, dielectric barrier discharge jets, dielectric barrier discharge-like jets and single electrode jets. Dielectric barrier discharges (DBD) actuating with either sinusoidal signals or pulsed high voltages are the most common atmospheric pressure system currently in use and the dielectric prevents the

formation of high temperature arcs. The atmospheric pressure dielectric barrier discharges are very important in many fields of industry, such as large scale of ozone generation, surface polymerization, exhaust gas treatment plasma using spray droplets, sterilization of surfaces and cavities, inactivation of microorganisms, medicines, pollution control, deposition of thin film. A device was developed to generate a non-equilibrium atmospheric-pressure plasma jet at low temperature and supplied by a high-voltage pulsed power source [1].

Azo dyes are used to industrial dye product. Using rate of the AZO dye is approximately 65%. They are very popular because of the photoisomerization process and optical storage, liquid crystal, molecular motors and etc. Isomerization process are due to  $\pi$ - $\pi^*$  and  $n$ - $\pi^*$  electronic transitions. These two transitions are very important for the determination of the colour of the dyes. Azo dyes are used to photocatalytic materials. Solvents are important for the chemical process and analyses. Vibration spectroscopic analysis and peak assignments were realized to determine new molecule structure after the obtained plasma treatments. Finally, AZO molecules chemical bond properties were changed [2-7].

## EXPERIMENTAL

The chemical structure of molecule was represented in Figure. 1a and 1b. Chemical formula is  $C_{12}H_{10}N_2O_4$ . Mass of the molecules is 246.06. Molecular weight is 246.22. Elemental analysis ratio of AZO molecule includes carbon of 58.54, hydrogen of 4.09, and nitrogen of 11.38 and oxygen of 25.99.

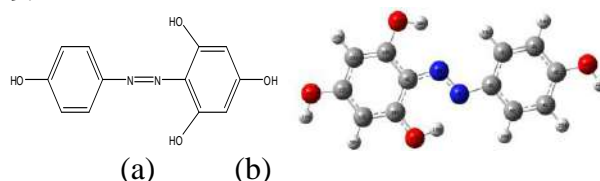


**Figure 1.** a) Chemical drawing, b) Chemical structure of the AZO 2-((4-Hydroxyphenyl)Diazenyl)Benzen-1,3,5-Triol Molecule

The power supply provides 10kHz-25kHz frequency, and 4kV-20kV input voltage adjustments. 24 kHz frequency and 12 kV input voltage with ac power supply have been selected and the flow rate is fixed to 3.0 l/min. Application distance has also been preferred as 2 cm. Pure Ar plasma was generated in the discharge tube. High purity Ar gas was used for the all experiments. Plasma treatment duration is strictly adjusted to 3 mins. UV-Vis were also recorded on a 4802 Unico UV-Vis double beam spectrophotometer (Fig.2).

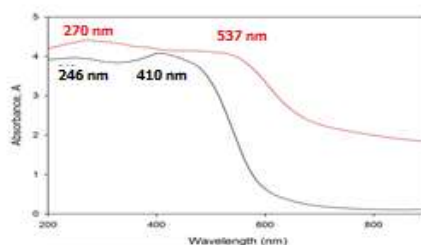


**Figure 2.** UV spectra of molecule dissolved in methanol before and after APPT

FT-IR spectra were obtained with a Jasco FT/IR-300 E spectrophotometer using the KBr pellet technique in the range 4000-400 $\text{cm}^{-1}$ . The FT-IR spectra of molecule are presented in Figs. (3 and 4).

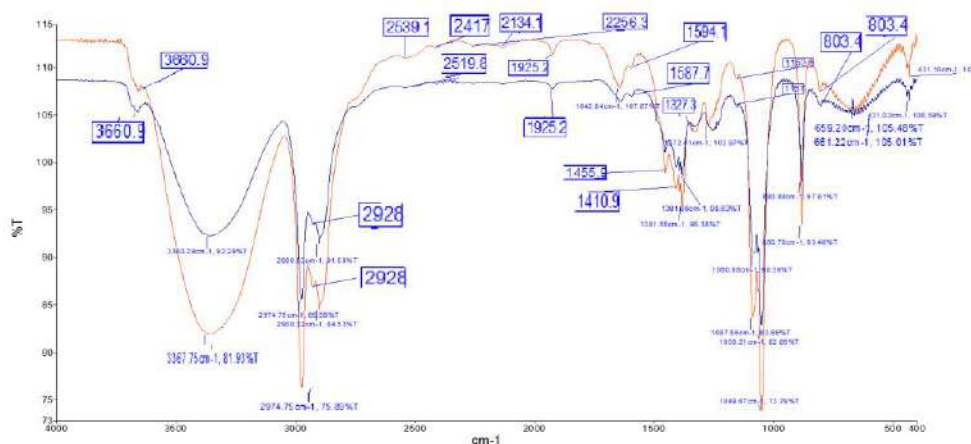


**Figure 3.** FT-IR spectra of molecule dissolved in ethanol before and after APPT



**Figure 4.** FT-IR spectra of molecule dissolved in methanol before and after APPT

## CONCLUSION

AZO dye molecules are very popular because of the photo-isomerization process and optical storage, liquid crystal, molecular motors and etc. They are used to photocatalytic materials. We present a new decomposing method for the molecules. Atmospheric pressure jet was specially designed for the decomposing of the molecule. We present a new fast and effective molecule degradation method. This method is atmospheric pressure plasma treatment (APPT) with Argon gas. APPT can be a most popular method for the surface and chemical methods. Here, APPT was applied to industrial dye molecule of 2-((4-Hydroxyphenyl)Diazenil)Benzene-1,3,5-Triol. After the APPT treatment, chemical bonds types were changed. Especially, molecular bridge of molecule was seriously affected. One bond of this bridge was moved to another interatomic region. Moreover, new vibrations peaks were seen from the FT-IR analysis. APPT was applied to 3 mins. Two-photo products were obtained after the APPT. Finally, new photoproduct are defined as  $9C=8N-7N=6C$  at  $1455.9\text{ cm}^{-1}$  and  $3C=15O$  at  $1624.84\text{ cm}^{-1}$  stretching peaks.

## Acknowledgement

This work was partially supported by the Anadolu University (Grand no: 1605F408) and Eskişehir Osmangazi University.

## REFERENCES

- [1] S. Pat, M. Z Balbag, M. I. Cenik, N. Ekem, S. Okur, G. Musa, R. Vladiou, *Optoelectronic and Advanced Materials*, 2007 **10** (3), 663-664.
- [2] E. Taşal, Y Sıdır, İ. Sıdır, H. Berber, T. Güngör, (Project Manager Assoc. Prof. Dr. Erol Taşal), Project No: 200819015, 2008-2011, Eskişehir Osmangazi University, Turkey.
- [3] Y. Sıdır, İ. Sıdır, E. Taşal, E. Ermiş, *Spectrochimica Acta Part A: Molecular and Biomolecular*, 2011, **78**, 640–647).
- [4] Y. Sıdır, İ. Sıdır, H. Berber, E. Taşal, *Journal of Molecular Liquids*, 2011, **162**, 148–154.
- [5] Y. Sıdır, İ. Sıdır, H. Berber, E. Taşal, *Journal of Molecular Liquids*, 2013, **178**, 127–136.
- [6] Y. Gülseven, E. Taşal, İ. Sıdır, T. Güngör, H. Berber, C. Öğretir, *Int. J. Hydrogen Energy*, 2009, **34**, 5255-5259.
- [7] Y. Gülseven, E. Taşal, İ. Sıdır, T. Güngör, H. Berber, C. Öğretir, *Int. J. Hydrogen Energy*, 2009, **34**, 5267–5273.

## IR SPECTROSCOPIC FINDING OF WATER COMPLEXES WITH ORGANIC COMPOUNDS IN LOW TEMPERATURE FILMS AND KBr MATRIX

I. Grinvald, I. Kalagaev, A. Petuchov, I. Vorotyntsev,  
I. Spirin and R. Kapustin

*R.A. Alekseev State Technical University  
Minin str. 24, 603950 Nizhniy Novgorod, Russia. (grinwald@mts-nn.ru)*

### ABSTRACT

It was established that in low temperature films and KBr matrix water complexes with benzene, furan, thiophene, bromoform and methylene dichloride can form. The mechanism of intermolecular interaction in these systems depends on the nature of the organic partner. The  $n$ -, or  $\pi$ -donors transfer the electronic density on the shifted proton of water cluster, whereas the methane halides form intermediates *via* hydrogen bond between active proton of organic compounds and water oxygen.

### INTRODUCTION

Water plays an important and often unclear role in many organic reactions. It is able to form complexes with interacting molecules due to the formation of hydrogen bond or as a nucleophilic agent, having electron pair on the oxygen atom. The water adducts were fixed for many inorganic species in gas and condensed phase, whereas for organic compounds they were observed seldom, although the possibility of their existence was predicted by quantum chemical calculations. Some time ago we published the IR spectroscopic data indicating on the formation of water complexes with organic compounds in the liquid and solid phase [1, 2].

The general approach to the interpretation of IR data was suggested in [1-2]. It is based on the idea that the compounds, having an electronic pair, can interact with hydrated shifted hydrogen atom of water cluster, i.e. with the, so called, hydronium ion. The IR manifestation of similar interaction has been shown as a considerable shift of hydronium ion stretching band, observed in free water cluster at 2350-2300  $\text{cm}^{-1}$ . Thus the complex formation in this case may be accompanied by arising of new absorption in the middle IR range due to the shifting of the hydronium ion stretching band to lower frequencies.

In the case of molecules with active proton the complex formation of these ones with water should be going on under the interaction of the active proton with an electronic pair of water oxygen. Therefore we might expect

the changes in high frequencies region, where OH stretching bands of water shown to be, because the bending vibration of water, locating at  $1650\text{-}1600\text{ cm}^{-1}$  in solid phase, is weakly sensitive to intermolecular binding.

In the presented work we have discussed the IR spectroscopic finding of water intermediates with a few organic molecules, namely, furan, thiophene, bromoform and methylene dichloride in low temperatures films ( $t=130\text{-}100\text{K}$ ) and benzene in KBr matrix at ambient temperature. Such a collection of compounds can manifest the different types of intermolecular interactions between organic molecules and water: furan and thiophene have an active electronic pair at the hetero atom, benzene is a  $\pi$ -donor, bromoform and methylene dichloride are the typical CH - acids.

### EXPERIMENTAL

For the preparation of low temperature films the unit, which scheme is shown in the Figure 1, was used. The low temperature shell (9) is vacuumed by pumping installation (11) and cooled by liquid nitrogen in open cycle. The shell is situated into IR spectrometer (12). The organic sample is evaporated from volume (13) and fills the shell by the valves (2, 5, 6). The water vapour fills the shell by the flow of nitrogen gas passing through water layer. The temperature control was provided by digital controller (14) and pressure control by manometers (7, 8). The investigated films were obtained by the condensation of water and organic samples vapour on the NaCl window cooled up to  $130\text{-}100\text{K}$ .

The method of sample preparation in KBr matrix was described in detail in [2]. Briefly, KBr powder saturated by water vapour is mixed in a definite ratio with a liquid sample and is pressed in a pallet. Then its spectrum is recorded by standard technique.

The spectra were recorded by the Fourier spectrometer Shimadzu IRAffinity-1 in  $4000\text{-}600\text{ cm}^{-1}$  interval with resolution  $2\text{ cm}^{-1}$  and 50 scans.

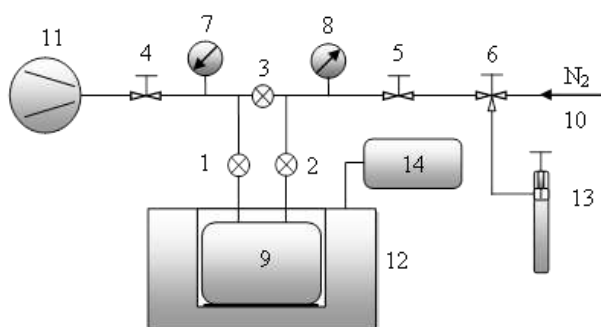


**Figure 1.**  
The scheme of the  
unit for low  
temperature films  
preparation.

## RESULTS AND DISCUSSION

In the spectra of condensate of water and furan mixture (1:1) the new bands at 1551 and 1266  $\text{cm}^{-1}$ , which are lacking in low temperatures films of initial components, were observed (in Figure 2, left side, they are indicated by asterisk). These bands have expected shifts in low temperature films, containing heavy water.

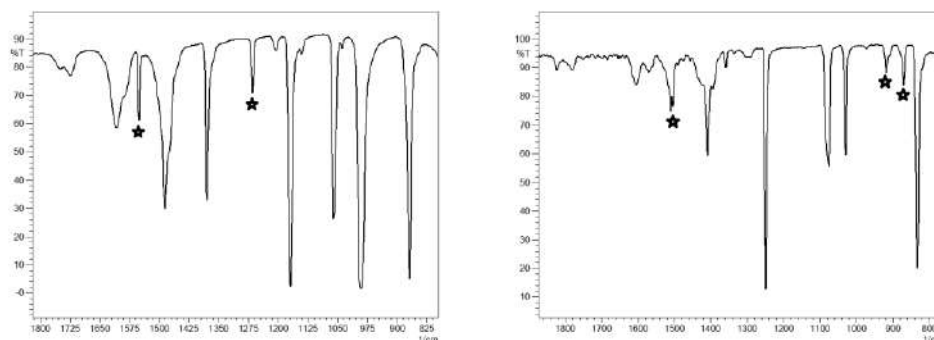


**Figure 2.** The spectra of low temperature films of water and furan (left side), water and thiophene (right side) mixtures (1:1) at 130K.

Therefore they can be assigned to the water adduct with organic molecules. It is reasonable to assume that the binding of water and organic partner arises by the most appropriate interaction between shifted hydrogen atom ( $\text{H}^*$ ) of water and lone pair of hetero atom in furan. The scheme of similar transformation can be presented in a following way:



This approach leads to the conclusion that the found new bands belong to the stretching (high frequency mode) and bending vibration (low frequencies mode) of hydronium molecule bounded with furan.

The new bands in the low temperature films of water and thiophene mixture (1:1) at 1506 (doublet), 918 and 870  $\text{cm}^{-1}$  were observed (in Figure 2, right side, they are indicated by asterisk). For the heavy water mixture they have predicted shift to lower frequencies. Analogically to previous case these bands can be assigned to stretching and bending vibration of the hydronium ion intermediate with thiophene.

The spectra of benzene/water mixture in the KBr matrix at the ratio of the initial components (benzene/water) 3:1, 1:1 and 1:3 were recorded. In the first case the spectrum exhibits the band at 1740  $\text{cm}^{-1}$ , which disappears at the increase of the water concentration in the mixture, whereas a band at 1458  $\text{cm}^{-1}$  appears, and its intensity increases with the growth of water concentration. Besides, in the last case, a new band at 1380  $\text{cm}^{-1}$  is detected.

In the spectrum of the mixture containing heavy water, two new bands appear at 1072 ( $\nu\text{H}/\nu\text{D}=1.36$ ) and 1022  $\text{cm}^{-1}$  ( $\nu\text{H}/\nu\text{D}=1.35$ ). Therefore the found new bands were assigned to vibrations of the hydronium ion in associates with the benzene molecule (see the interpretation for furan and thiophene complexes as well).

We have observed for bromoform and methylene dichloride films, containing water, for mixture water/methane halide in ratio of components 3:1 (see Figure 3, b) at 100K, the new bands (relatively 1:1 mixture, see Figure 3, a) in high frequencies range only (in Figure 3 they are indicated by asterisk). It becomes quite clear, if we take into account that the most possible interaction of water with organic molecules should be provided by binding of water oxygen and proton of methane halide. Similar interaction leads to the bands shift of OH stretching, because the HOH bending mode is weakly sensitive to complex formation.

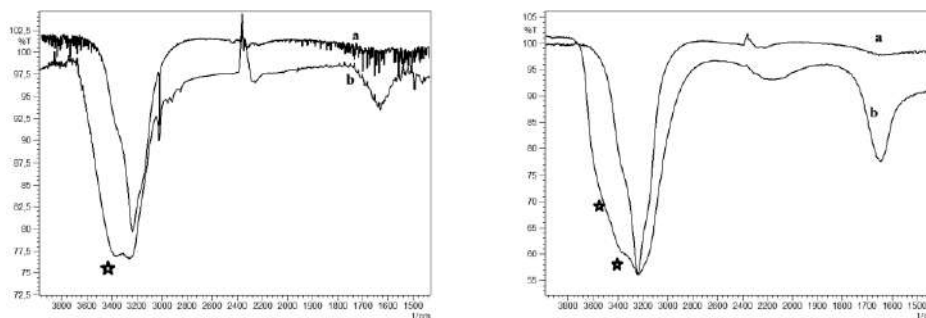


**Figure 3.** The spectra of water/methane halide mixtures: for bromoform, left side and methylene dichloride, right side (a-1:1 mixture, b-3:1 mixture).

## CONCLUSION

It was established by IR technique that water can form complexes with organic molecules at various ratios of components both in low temperature films and KBr matrix at ambient temperature.

## Acknowledgement

This work was supported by the Russian Foundation of Basic research, grant no. 14-08-00898-a.

## REFERENCES

- [1] I.I.Greenwald, I.Yu. Kalagaev, Tetrahedron letters, 2010, **51**, 2610-2612.
- [2] I. I. Grinvald, I. Yu. Kalagaev, A. N. Artemov, E. A. Sutyagina, and I. A. Spirin, Russian Chemical Bulletin, International Edition, 2014, **63**, 1-4.

## PREPARATION AND FTIR CHARACTERIZATION OF CHOLINE CHLORIDE-BASED DEEP EUTECTIC SOLVENTS WITH THIOUREA AND DIMETHYLUREA

D. Z. Troter<sup>1</sup>, M. Z. Zlatković<sup>1</sup>, B. S. Đorđević<sup>1</sup>, D. R. Đokić-Stojanović<sup>2</sup>  
S. S. Konstantinović<sup>1</sup>, Z. B. Todorović<sup>1</sup>, and V. B. Veljković<sup>1</sup>

<sup>1</sup> *University of Niš, Faculty of Technology, Bulevar oslobođenja 124, 16000 Leskovac, Serbia (drtroter@gmail.com).*

<sup>2</sup> *Zdravlje Actavis, Vljakova 199, 16000 Leskovac, Serbia.*

### ABSTRACT

Deep eutectic solvents (DESs) are environmentally-friendly, easy to be prepared and tested for various applications. Two choline chloride-based DESs with thiourea and dimethylurea as hydrogen bond donors (in 1:2 molar ratios) were prepared. The functional groups of these mixtures were analyzed by Fourier transform infrared (FTIR) spectroscopy. Thiourea is in its thiol form when forming the DES, while dimethylurea does the same in its imidic acid form.

### INTRODUCTION

Deep eutectic solvents (DESs) have been referred as promising alternative to conventional ionic liquids (ILs). In comparison with ILs, DESs are cheaper and easier to be prepared, less toxic and have shown to be biodegradable [1-3], which makes them referred as green solvents. These eutectic mixtures are usually made by combining a substituted quaternary ammonium salt (for example choline chloride) and a complexing agent (usually a hydrogen bond donor), resulting a compound with lower melting point [1,4]. When complexing agent interacts with the anion, its effective size is increased, leading to decreased interaction between anion and cation, so freezing point depression of the mixture occurs. Choline chloride (2-hydroxy-ethyltrimethyl-ammonium chloride, ChCl) is a quaternary ammonium salt, consisted from a choline cation and chloride anion, often used in preparation of DESs. Thiourea is a white crystalline solid, both naturally occurring and synthetic. Dimethylurea appears as a colorless-to-white crystalline powder.

The main aim of the present paper was to prepare two choline chloride-based DESs with thiourea and dimethylurea as hydrogen bond donors (in 1:2 molar ratio) and to analyze the functional groups of these mixtures by

Fourier transform infrared (FTIR) spectroscopy, in order to explain the interactions of the molecules and the stability of these mixtures.

## EXPERIMENTAL

### Chemicals

Choline chloride (Sigma Aldrich,  $\geq 98.0\%$ ), thiourea (99.5%, ZorkaŠabac, Serbia) and 1,3-dimethylurea (Sigma Aldrich,  $\geq 98\%$ ) were used as purchased, without purification.

### Instruments

The FTIR spectra were recorded on a Michaelson Bomen MB-series spectrophotometer, using the KBr pellet (1.5 mg/150 mg) technique, in the area of  $4000\text{--}400\text{ cm}^{-1}$  wave length, and  $2\text{ cm}^{-1}$  resolution. The mixture is vacuumed, pressed under the pressure of 200 MPa, in order to form thin, permeable pastilles. The spectra were recorded on the room temperature, after the formation of pastilles.

### Preparation of DESs

ChCl was combined with thiourea or dimethylurea as hydrogen bond donors at 1:2 molar ratio of ChCl to hydrogen bond donor in a round-bottomed flask. The flask was placed on a rotary evaporator at 348.15 K for 1 h, until a homogeneous and transparent liquid was formed. DESs were stored in a well closed glass bottles in a desiccator containing  $\text{CaCl}_2$ . ChCl:thiourea and ChCl:dimethylurea are liquids, viscous, homogeneous, and colorless, turning into white solid upon cooling.

## RESULTS AND DISCUSSION

The spectra of choline chloride (Figure 1) shows a very strong and broad band at  $3406\text{ cm}^{-1}$ , which is assigned to  $\nu(\text{OH})$  stretching vibration. The shape of band indicates the presence of (most likely) intramolecular hydrogen bond, since choline chloride possesses both hydrogen bonding donors and acceptors. The existence of hydrogen bonds is also confirmed by the weak peak at  $2846\text{ cm}^{-1}$  [5]. The band at  $3247\text{ cm}^{-1}$  is assigned to the  $\nu(\text{NH}_3^+)$  vibrations, typical seen in case of charged amine derivatives, and the appropriate deformation vibration  $\delta(\text{NH}_3^+)$  is positioned at  $1660\text{ cm}^{-1}$  [6]. The spectra of choline chloride DESs with thiourea and dimethylurea show a strong and broad band at  $\sim 3400\text{ cm}^{-1}$  which, as in choline chloride spectra, belongs to hydrogen bonded hydroxyl functional group.

An FTIR spectrum of thiourea (Figure 1.) has asymmetrical and symmetrical stretching vibrations  $\nu_{\text{as}}(\text{NH}_2) + \nu_{\text{s}}(\text{NH}_2)$  at  $3380$  and  $3273\text{ cm}^{-1}$ , and N-C=S I, N-C=S II and N-C=S III bands at  $1436$ ,  $1399$  and  $1084\text{ cm}^{-1}$ , which is consistent with its thiol form, carbamimidothioic acid [7].

The slightly shift of amine deformational vibrations ( $\Delta\nu = 11 \text{ cm}^{-1}$ ) also suggests interaction through these functional groups between choline and thiourea.

An FTIR spectrum of dimethylurea (Figure 1) clearly shows a stretching vibration at  $3345 \text{ cm}^{-1}$ , which corresponds to secondary  $\nu(\text{NH})$  group. Bands at  $2344 \text{ cm}^{-1}$  and  $1837 \text{ cm}^{-1}$  belong to stretching  $\nu(\text{C}=\text{NH}^+)$  and deformation  $\delta(\text{C}=\text{NH}^+)$  vibrations, which prove the imidic acid form of dimethylurea, *(Z)-N,N'*-dimethylcarbamimidic acid. The band which belongs to stretching  $\nu(\text{OH})$  vibration is widely broad at  $3378 \text{ cm}^{-1}$  and covers all the amine vibrations' belonging bands.  $\nu(\text{C}-\text{O})$  vibration in DES is slightly moved for  $\Delta\nu = 11 \text{ cm}^{-1}$  in spectrum of DES, probably due to choline-dimethylurea interaction.

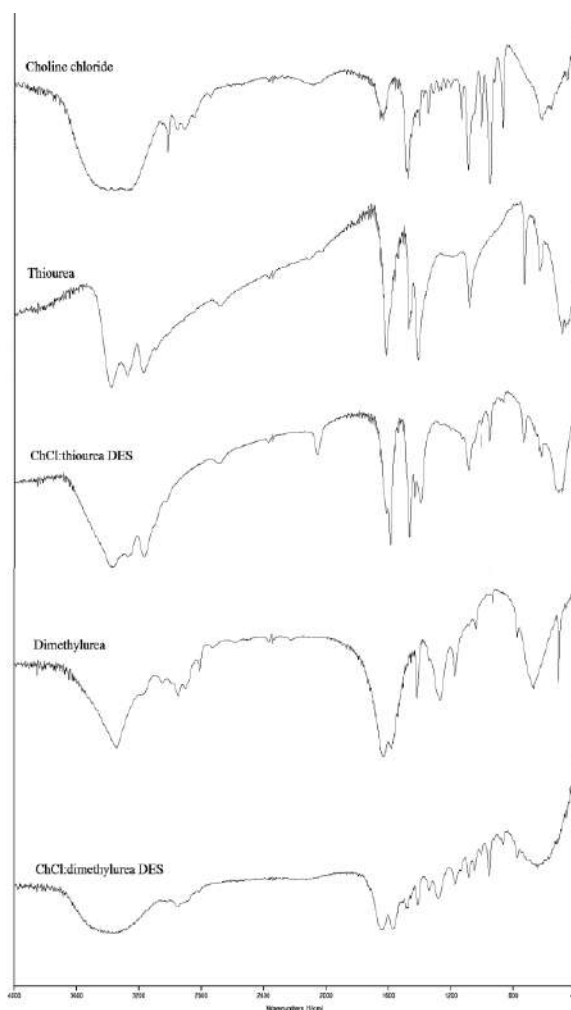


**Figure 1.** FTIR spectra of choline chloride, thiourea, ChCl:thiourea DES, dimethylurea and ChCl:dimethylurea DES.

## CONCLUSION

It was established that there are interactions among the components of the binary mixtures of choline chloride and thiourea or dimethylurea, leading to the formation of deep eutectic mixtures. Thiourea in its thiol form forms the DES with choline chloride, while dimethylurea does the same in its imidic acid form. These deep eutectic mixtures can be promising alternatives to

classical ionic liquids, because of the easy synthesis, availability and biodegradability of the components.

### *Acknowledgments*

This work has been funded by the Ministry of Education, Science and Technological Development of the Republic of Serbia (Project III 45001).

### **REFERENCES**

- [1] P. Abbott, D. Boothby, G. Capper, D. L. Davies, R. K. Rasheed, *Journal of the American Chemical Society*, 2004, **126**, 9142-9147.
- [2] M. Avalos, R. Babiano, P. Cintas, J. L. Jimenez, J. C. Palacios, *Angewandte Chemie International Edition*, 2006, **45**, 3904-3908.
- [3] H. G. Morrison, C. C. Sun, S. Neervannan, *International Journal of Pharmaceutics*, 2009, **378**, 136-139.
- [4] D. Z. Troter, Z. B. Todorović, D. R. Đokić-Stojanović, O. S. Stamenković, V. B. Veljković, *Renewable and Sustainable Energy Reviews*, 2016, **61**, 473-500.
- [5] H. Wang, Y. Jia, X. Wang, J. Ma, Y. Jing, *Journal of the Chilean Chemical Society*, 2012, **57**, 1208-1212.
- [6] V. M. Parikh, *Absorption spectroscopy of organic molecules*, Addison Wesley Publishing Company, 1974, pp.258.
- [7] C. N. R. Rao, R. Venkataraghavan, *Spectrochimica Acta*, 1962, **18**, 541-547.

## GENERATION OF Au<sub>2</sub>Cl<sub>2n+1</sub> (n = 1-3) CLUSTER IONS BY LASER DESORPTION/IONIZATION MASS SPECTROMETRY

B. Rajčić<sup>1</sup>, T. Pantić<sup>1</sup>, S. B. Dimitrijević<sup>2</sup>, S. P. Dimitrijević<sup>2</sup>,  
F. Veljković<sup>1</sup>, M. Petković<sup>1</sup> and S. Veličković<sup>1</sup>

<sup>1</sup> University of Belgrade, VINČA Institute of Nuclear Sciences, P. O. Box 522, Belgrade, Serbia, (filipveljkovic@vinca.rs).

<sup>2</sup> Mining and Metallurgy Institute Bor, Zeleni bulevar 35, 19210 Bor, Serbia.

### ABSTRACT

Gold chloride clusters were generated from an aqueous solution of gold-hydrochloric acid deposited onto the target plate using laser desorption/ionization (LDI) on a commercial matrix assisted laser desorption/ionization – time of flight (MALDI-TOF) mass spectrometric instrument. In our experimental conditions negative mode of LDI mass spectra provided the most valuable informations. The mass peaks at m/z about 339, 499, 571, 641, were assigned to AuCl<sub>4</sub><sup>-</sup>, Au<sub>2</sub>Cl<sub>3</sub><sup>-</sup>, Au<sub>2</sub>Cl<sub>5</sub><sup>-</sup>, Au<sub>2</sub>Cl<sub>7</sub><sup>-</sup> cluster ions, respectively. The Au<sub>2</sub>Cl<sub>5</sub><sup>-</sup> and Au<sub>2</sub>Cl<sub>7</sub><sup>-</sup> clusters are detected for the first time in this work. This research showed that LDI MS, thanks to its easy experimental procedure, a soft ionization technique which may be a useful characterization tool in the chemistry of heterogeneous gold clusters.

### INTRODUCTION

Investigations of homogeneous and heterogeneous clusters of gold are important for their potential application in different areas such as catalysis, optics, medicaments, and environmental sciences [1-4]. For specific technological and scientific requests, it is necessary to examine the structure and stability of these clusters as the function of their composition and size. Generally, mass spectrometric methods allow both the examination of conditions for obtaining various types of metal clusters, and the investigation of their electronic and geometric properties. In the past two decades, several mass spectrometric techniques have been used to study homogeneous gold clusters, and most of these techniques were based on the evaporation of metals by heating, or using laser ablation and ion-bombardment. For example, laser desorption Fourier-transform ion cyclotron resonance (LD FT-ICR) mass spectrometry was used as a simple method for generating large gold cluster ions, Au<sub>n</sub><sup>+/-</sup> [5]. Mass distributions

of negative cluster ions of gold  $(\text{Au})_n^-$  obtained by the bombardment of metal sheets with Xe ions were examined up to cluster size  $n = 250$  [6].

Research of the structures of gold halides clusters is important because it provides insight into the extent of aurophilic interactions which are intermediates between van der Waals' forces and covalent bonding. Previous studies have shown that  $\text{Au}_2\text{Cl}_3^+$ ,  $\text{Au}_2\text{Cl}_4^+$ , and  $\text{Au}_2\text{Cl}_6^+$  clusters can be obtained by the evaporated  $\text{HAuCl}_4$  at 100–120°C, and these species were detected in the conventional way through electron impact ionization (EI) [7]. Also, mononuclear cluster types  $[\text{AuCl}_2]^+(\text{H}_2\text{O})_n$  ( $n = 0-4$ ),  $[\text{AuOHCl}]^+(\text{H}_2\text{O})_n$  ( $n = 0-1$ ) and  $[\text{AuCl}_2]^+(\text{HCl})_2(\text{H}_2\text{O})_n$  ( $n = 0-4$ ), and dinuclear cluster types  $[\text{Au}_2\text{Cl}_{5-x}(\text{OH})_x]^+(\text{H}_2\text{O})_n$  ( $x = 0-1$ ) have been detected in electrospray ionization mass spectra of aqueous  $\text{AuCl}_3$  [8].

In this work, we have investigated the conditions for the application of LDI TOF mass spectrometry for the generation of gold chloride clusters from an aqueous solution of gold-hydrochloric acid.

## EXPERIMENTAL

LDI mass spectra were obtained using the commercial MALDI-TOF mass spectrometer (Voyager-DE PRO, AB Sciex, USA) equipped with a 20 Hz pulsed nitrogen laser (337 nm) and with delayed extraction. A stainless steel target was used as the MALDI substrate on which the samples are deposited. The accelerating voltage used was 19 kV. The mass spectra were collected using both positive and negative ion modes and both linear and reflector modes. Data Explorer software 4.9 includes a suite of tools and processing options that allow you to graphically and interactively manipulate mass spectral data (for example, determine elemental composition, theoretical isotope distributions, resolution, signal-to-noise ratio, and fragment ions). No matrices were used for this sample preparation. A small volume (0.5  $\mu\text{l}$ ) of an aqueous  $\text{HAuCl}_4$  solution, concentration 2.5 g  $\text{Au}/\text{dm}^3$ , was applied onto the sample plate and left to dry at room temperature.

## RESULTS AND DISCUSSION

In our experimental conditions the positive mode LDI mass spectra did not contain the peaks of Au-Cl clusters. The positive mode spectra did confirm the identity of the  $\text{Au}_n^+$  ( $n = 1-3$ ) clusters, however these clusters have already been detected. For that reason, positive mode of LDI mass spectrumis neither presented no further discussed.

An example of a mass spectrum for aqueous solution of gold-hydrochloric acid obtained in the reflector negative mode is shown in Fig. 1.

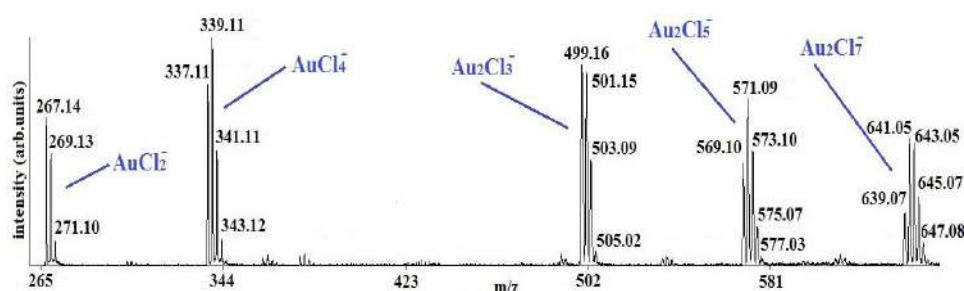


**Figure 1.** Reflector negative ion LDI-TOF mass spectrum of HAuCl<sub>4</sub>. The spectrum represents the average of 300 laser shots with laser intensity of 1800 a.u.

For the confirmation of the identity of signals detected, we have compared experimental and theoretical values of gold chloride clusters generated via LDI TOF mass spectrometry, in Table 1. The experimental values have a very good agreement with theoretical values of  $m/z$  ratio, which confirms the identity of signals detectable in the LDI spectra.

**Table 1.** Experimental values of Au<sub>2</sub>Cl<sub>2n+1</sub> (n = 1-3) generated via laser desorption/ionization-time of flight mass spectrometry (theoretical isotope distributions were taken from Data Explorer software 4.9)

Cluster	Experimental m/z	Theoretical m/z	Relative intensity of isotopes (%)	Cluster	Experimental m/z	Theoretical m/z	Relative intensity of isotopes (%)
Au <sub>2</sub> Cl <sub>3</sub> <sup>-</sup>	499.16	498.84	100	Au <sub>2</sub> Cl <sub>7</sub> <sup>-</sup>	639.07	638.72	44
	501.15	500.84	97		641.05	640.71	100
	503.09	502.84	31		643.05	642.71	97
	505.02	504.83	3		645.07	644.71	52
Au <sub>2</sub> Cl <sub>5</sub> <sup>-</sup>	569.10	568.78	62		647.08	646.70	17
	571.09	570.77	100				
	573.10	572.77	65				
	575.07	574.77	21				
	577.03	576.77	3				

These data show that negative ion of cluster Au<sub>2</sub>Cl<sub>3</sub><sup>-</sup> is the dominant dinuclear gold cluster, in which gold exists as the monovalent (Au<sup>I</sup>) ion, while Au<sub>2</sub>Cl<sub>5</sub><sup>-</sup> cluster contains monovalent (Au<sup>I</sup>) and trivalent (Au<sup>III</sup>) ions, and Au<sub>2</sub>Cl<sub>7</sub><sup>-</sup> cluster contains two trivalent (Au<sup>III</sup>) ions. It should be observed

that in the EI mass spectra only positively charged clusters, such as  $\text{Au}_2\text{Cl}_3^+$ ,  $\text{Au}_2\text{Cl}_4^+$ , and  $\text{Au}_2\text{Cl}_6^+$  (with different oxidation state of gold than above mentioned) have been detected after  $\text{HAuCl}_4$  has evaporated at a small rate ( $\sim 3\text{--}5$  K/min) [7]. In our case, heating of the sample ( $\text{HAuCl}_4$ ) in the ionization chamber was very fast, because desorption/ionization process is determined by the energy density supplied to the sample by the laser pulse. In the LDI mass spectrum (Fig. 1) only negatively charged clusters were detected. This indicates that heating rate of the sample may affect on stability, composition, and size of dinuclear gold chloride clusters.

## CONCLUSION

Here, the laser desorption/ionization – time of flight (LDI-TOF) mass spectra of aqueous solution of gold-hydrochloric acid have been investigated. Mass spectra were acquired in both linear and reflector positive/negative modes. However, the best resolution of isotope peaks of  $\text{Au}_2\text{Cl}_{2n+1}$  ( $n = 1\text{--}3$ ) clusters were obtained in reflector negative ion mode. Some of the clusters were found for the first time whose isotope peaks were in very good correlation with theoretical values.

## Acknowledgement

This work was supported by the Ministry of Education, Science and Technological development of the Republic of Serbia (Project No. 172019).

## REFERENCES

- [1] Sanchez, S. Abbet, U. Heiz, W.D. Schneider, H. Hakkinen, R.N. Barnett, U. Landman, *J. Phys. Chem. A*, 1999, **103**, 9573–9578.
- [2] M. Gaudry, J. Lerme, E. Cottancin, M. Pellarin, J.L. Vialle, M. Broyer, B. Prevel, M. Treilleux, P. Melinon, *Phys. Rev. B*, 2001, **64**, 085407.
- [3] S. Saito, S. Hiyamuta, M. Kurasaki, T. Saito, T. Hosokawa, H. Fujita, K. Yoshida, *Chem. Biol. Interact.*, 2002, **140**(3), 265-278.
- [4] S. Dimitrijević, M. Rajčić-Vujasinović, S. Alagić, V. Grekulović, V. Trujić, *Electrochimica acta*, 2013, **104**, 330-336
- [5] H.S. Kim, T.D. Wood, A.G. Marshall, J. Lee, *Chem. Phys. Letters*, 1994, **224**, 589-594.
- [6] I. Katakuse, T. Ichihara, Y. Fujita, T. Matsuo, T. Sakurai, H. Matsuda, *Int. Jour. of Mass Spectr. and Ion Proc.*, 1986, **74**, 33-41.
- [7] V.I. Karataev, *Techn. Phys. Letters*, 2008, **34**, 1082-1084.
- [8] K.H. Lemke, *Phys. Chem. Chem. Phys.*, 2014, **16**, 7813-7822.

## UV-Vis SPECTRAL DETERMINATION OF CURCUMINOIDS

O. Kovačević<sup>1</sup>, S. Zlatanović<sup>1</sup>, B. Kovačević<sup>1</sup>  
and S. Gorjanović<sup>1</sup>

<sup>1</sup>*University of Belgrade, Institute of General and Physical Chemistry,  
szlatanovic@gmail.com  
Studentski trg 12-16, P.O. Box 45, 11158 Belgrade 118, Serbia*

### ABSTRACT

The Joint Expert Committee on Food Additives published a procedure for the determination of curcumin based on absorbance at  $\lambda_{\max}$  (425 nm). According to the procedure, the content of coloring matters, ie. curcuminoids in ethanolic solutions of commercially available curcumin have been determined in this study. The UV-Vis spectrum of analyzed samples has been recorded in range from 220 to 600 nm. The improvement of accuracy has been achieved by obtaining data from calibration curves. The results obtained have been found to be in accordance with manufacturers' specifications. The relation between absorbance at about 427 nm (attributed to curcumin) and 262 nm (attributed to substituted phenolic nuclei within the molecules of curcumin) has been considered. The obtained relation  $A(\sim 427 \text{ nm})/A(\sim 262 \text{ nm})$  is  $4.3 \pm 0.2$ . Lower values of the before mentioned relation indicate a degradation of curcumin.

### INTRODUCTION

Curcumin, obtained by the extraction from the root of *Curcuma longa*, is a natural mixture of curcuminoids, which belong to a group of phenolic substances, with three major curcuminoid: curcumin (1,7-Bis-(4-hydroxy-3-methoxyphenyl)-1,6-heptadiene-3,5-dione), demethoxycurcumin, and bis-demethoxycurcumin [1,2]. In the UV-Vis spectral region, curcumin has a characteristic absorption in the area of 300-500 nm, with a maximum of absorption at about 430 nm [1-4]. The position of this peak was found to be dependent on the difference in the proportion of curcuminoids in their mixture and influenced by the kind of the solvent and pH of the solution [1]. The Joint Expert Committee on Food Additives (2001) published a procedure for UV-Vis spectroscopic determination of curcumin [2]. There are only a few articles dealing with UV-Vis spectroscopic determination of the curcumin content, but none of them deal with the above-mentioned JECFA procedure (2001) [3,4]. On the other hand, there are numerous

reported on HPLC determination of the curcumin content based on UV Vis detection of the absorbance at 262 nm, attributed to substituted phenolic groups within curcumin, or at about 427 nm[3].

The aim of this study is to show the possibilities of simple UV-Vis method for the determination of curcumin according by applying JECFA procedure (2001). Particular attention has been paid to ratio of absorbance at 427 and at 262 nm. Until now, this ratio has been neglected in literature.

### EXPERIMENTAL

Curcumin - Fluka, Lot: 1355475, Assay  $\geq 95.0$  % (TLC), Curcumin - Merck, Lot: S7101854 537, Assay (acidimetric)  $\geq 90.0$  %, Curcumin - Sigma, Lot: # SLBN 7214V, Assay  $> 65.0$  % (HPLC), ethyl alcohol (ethanolum denat) HeMos, Belgrade. The pH readings were obtained using colour-fixed indicator sticks, Macherey-Nagel, pH-Fix 0-14.

The total content of colouring matters (curcuminoids) has been determined by JECFA procedure (2001). The first solution has been prepared by dissolution of 0.08 g of the curcumin sample in a 200-mL ethanol. A solution for recording has been prepared by dissolution of 1.0 mL of the first solution into a 100 mL ethanol. Absorbance (A) at 427 nm has been measured in a 1-cm cell. The total colouring matters content (TC) of the sample has been calculated using the following equation Eq1:  $TC (\%) = (A \times 200 \times 100) / (W \times 1607)$ , where A = absorbance of sample, W = weight of sample (g), and 1607 = specific absorbance of the curcumin standard in ethanol.

Absorption spectra were recorded using Thermo, type Evolution 600, UV-Vis at the interval of 220-800 nm, with bandwidth of 4.0 nm, scan speed of 60 nm/min, data interval of 0.2 nm, and with Helma quartz cuvette of 1 cm.

### RESULTS AND DISCUSSION

Commercial samples of Merck, Fluka and Sigma curcumin were labeled as K1, K2 and K3, respectively. In accordance with the procedure which was given by JECFA (2001) to determine the total content of colouring matters (curcuminoids) (TC), UV-Vis spectra of the samples K1, K2 and K3, were recorded. Spectra absorption maximum has been found to be positioned at 427.2 nm (denoted as  $A_2$ ) as shown in Fig. 1. Corresponding absorbance values have been used to calculate the value of TC in accordance with Eq1 (Tab. 1). In order to improve determination accuracy, instead of one point measurement, four point calibration curves have been made for each sample.

**Table 1.** Absorbance  $A_1$  at 262.2 nm,  $A_2$  at 427.2 nm,  $A_{2g}$  value corresponding to value calculated from graf (Fig. 2) and the total content of colouring matters (curcuminoids) (TC) in curcumin samples K1, K2 and K3.

Sample	K1	K2	K3
$C_x 10^{-3}$ (g/L)	4.34	4.44	4.06
$A_{262.2}$	0.141	0.170	0.140
$A_{427.7}$	0.633	0.707	0.598
$A_{2g}$	0.630	0.694	0.603
$A_{427.7}/A_{262.2}$	4.49	4.16	4.27
$A_{2g}/A_{262.2}$	4.47	4.08	4.31
TC (%)	90.8	99.1	91.7
TCg (%)	90.3	97.3	92.2

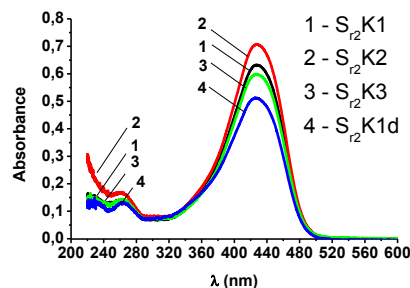


**Figure 1.** UV-Vis spectra of curcumin samples K1, K2, K3, and K1(d) for solution of K1 recorded 16 days after the solution was made.

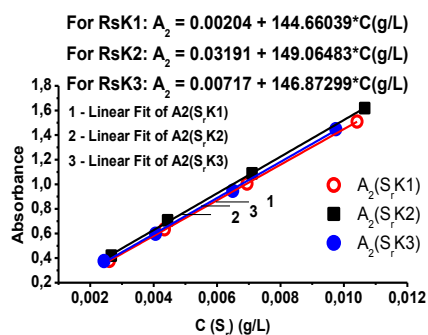


**Figure 2.** Relation  $A_2 = f[C(S_r)]$ , for samples K1, K2, and K3.

Calibration curves showing the dependence of  $A_2 = f(C)$  are given in Fig. 2. According to the obtained calibration straight lines, absorbances which correspond to concentrations present in K1, K2 and K3 have been calculated ( $A_{2g}$ , see Tab. 1). The  $A_{2g}$  values have been used to calculate the TC values in accordance with Eq1 (TCg values, Tab. 1). The results of the analysis have been found to be in accordance with manufacturers' specifications. However, the content of curcumin present in sample K3 has been found much higher than expected. Manufacturer declaration cited the minimum value of curcumin content is above 65%, while the content determined in this study is 92.2%.

Curcumin degradation has been noticed after 16 days of solution storage at room temperature. Its degradation products belong to phenolics [1]. Fig. 1 shows the spectrum recorded 16 days after the solution of sample K1 was made (spectrum  $S_{r2}K1d$ ). The total content of curcumin in solution after

storage of 16 days has been found reduced in comparison to fresh solution for 17% (Tab. 1). In the spectrum S<sub>r2</sub>K1d, the absorbance at 262.2 nm (denoted as A<sub>1</sub>), remains at the same order of magnitude as in the spectrum of freshly made solution of sample K1 (see Tab. 1). In the spectrum of partly degraded curcumin, the value of relation A<sub>2</sub>(~427 nm)/A<sub>1</sub>(~262 nm) = 3.88 is below the corresponding values in the spectra of freshly made curcumin solutions where A<sub>2</sub>/A<sub>1</sub> = 4.3 ± 0.2 ( Tab. 1).

### CONCLUSION

The fast, simple, and accurate UV-Vis method for the determination of the total content of coloring matters (curcuminoids) based on the procedure published by JECFA (2001) has been improved. In this study, more accurate determination of curcumin content has been achieved by introduction of calibration curves. This procedure is not time consuming. Spectra of investigated samples indicate: i) absorption of substituted phenolic nuclei within the molecules of curcumin and in the degradation products at 262 nm is in the same order of magnitude and ii) the values of the ratio A<sub>2</sub>(~427 nm)/A<sub>1</sub>(~262 nm) in the spectra of freshly made curcumin solutions are in range 4.3 ± 0.2, while values below indicate the degradation of curcumin.

### Acknowledgement

This work was partially supported by the Ministry of Education, Science and Technological Development of the Republic of Serbia, under the Project No TR-31055 and TR-31093.

### REFERENCES

- [1] P.-Hoon Bong, Bull. Korean Chem. Soc. 2000, **21**, 81-86.
- [2] Joint FAO/WHO Expert Committee on Food Additives, 57<sup>th</sup> session, Rome, Italy, 5-14 June, 2001, Compendium of food additive specifications, Addendum **9**, 21-23.
- [3] A. Rohman, International Food Research Journal, 2012, **19**, 19-27
- [4] K. Sharma, S. S. Agrawal, M. Gupta, International Journal of Drug Development and Research, 2012, **4**, 375-380.

## CURCUMIN AUTOXIDATION IN ALKALINE SOLUTION FOLLOWED BY UV-Vis

O. Kovacević, S. Zlatanović, B. Kovacević and S. Gorjanović

*University of Belgrade, Institute of General and Physical Chemistry,  
Studentski trg 12-16, P.O. Box 45, 11158 Belgrade 118, Serbia,  
szlatanovic@gmail.com*

### ABSTRACT

Autoxidation of curcumin in EtOH water solutions (40 vol %) set at pH 8 and 10 by addition of NaOH was followed in the spectral range from 220 to 800 nm. Autoxidation of curcumin in these solutions was to be found slower in comparison to literature data. After 46 h of beginning of curcumin decomposition, UV Vis spectra indicate the existence of new intermediate structures which could lead to the formation of bicyclopentadiones.

### INTRODUCTION

Curcumin is a natural mixture of curcuminoids. The most important ones are curcumin, demethoxycurcumin, and *bis*-demethoxycurcumin [1,2,3]. Curcumin (1,7-Bis-(4-hydroxy-3-methoxyphenyl)-1,6-heptadiene-3,5-dione) was found to be active against human diseases such as diabetes, obesity, neurologic and psychiatric disorders, cancer etc. [1,2,3]. Curcumin is soluble in acetone, dichloromethane, methanol, ethanol and 2-propanol [1,2]. It is insoluble in water at acidic and neutral pH but soluble in alkaline water solutions. However, after dissolving in alkaline environment, it experiences rapid decomposition. Many reports on curcumin stability at different pH have been published [3-6]. In 0.1 M phosphate buffer (pH 7.2), vanillin, ferulic acid and feruloyl methane were identified as minor degradation products and a major product was bicyclopentadione, with a molecular formula of  $C_{21}H_{20}O_8$  and mass of 401.12 g/mol, formed by cyclization and oxygenation of the heptadienone carbon chain of curcumin [5,6]. Gordon et al (2015) have established optimal conditions for chromatographic and spectroscopic analysis of curcumin intermediates. They have reported UV-Vis spectra of curcumin degradation products as well as a reaction mechanism of curcumin decomposition [6].

In this study, autoxidation of curcumin in the alkaline solution EtOH-water (60 : 40 vol %) has been investigated spectrophotometrically in the spectral range 220-800 nm. In these solutions, autoxidation of curcumin is found to

be slower than reported in literature. In order to avoid the influence of phosphate anion the starting condition has been adjusted by NaOH addition.

### EXPERIMENTAL

Curcumin was from Merck, Ethyl alcohol (ethanolum denat) and sodium hydroxide were from HeMos. The pH readings were obtained using colour-fixed indicator sticks, Macherey-Nagel, pH-Fix 0-14. 0.25 mL of curcumin solution (0.04g in 100 mL EtOH) was mixed with 14.75 EtOH and water was added to 25 mL. pH was adjusted with NaOH.

Absorption spectra were recorded using Thermo, type Evolution 600, UV-Vis at the interval of 220-800 nm, with bandwidth of 4.0 nm, scan speed of 60 nm/min, data interval of 0.2 nm, and **with** Helma quartz cuvette of 1 cm.

### RESULTS AND DISCUSSION

Changes in curcumin solutions at pH 8 and 10, denoted as S8 and S10 respectively, have been followed spectrophotometrically in 220-800 nm spectral range. Five minutes after solution of curcumin was made the spectrum shown in Figure 1 was recorded. Absorption maxima at 220, 265 i 520 nm (spectrum 1) corresponds to initial transformation of curcumin initiated by the hydrogen atom abstraction from one of the phenolic hydroxyl groups [2,5,6]. Spectra 2 - 7 reflect the changes related to autoxidation of curcumin after 30 to 380 min. Degradation of initially transformed curcumin follows the absorption intensity at 520 nm fall, with a maximum movement to 460 nm. At the same time, intensity of the first peak at 220 increases and moves bathochromically to the position of 230 nm, intensity of the second peak at 265 nm increases but retains the position, while a new peak whose absorbance at 350 increases over time appeared. All these changes indicate emergence of degradation products phase. Spectra of curcumin solution at S10 are identical (not shown). Also, kinetics of curcumin autoxidation at pH 8 and 10 is similar. According to maxima positions, products of curcumin autoxidation are related to spiroepoxy cyclopentadiones and vinyl ether cyclopentadiones, whose adsorption maxima, according to Gordon et al, were at 263 nm and 360 nm, respectively [6]. Based on reported spectra of chromatographically divided products of curcumin degradation [6], maximum at 230 could be attributed to vinyl ether cyclopentadiones. Maximum at 280 nm has not been noticed in recorded spectra (Fig. 1). Also, according to Gordon et al two maxima at 230 and 280 nm could be ascribed to bicyclopentadione [6]. Spiroepoxy cyclopentadiones and vinyl ether cyclopentadiones were supposed to be intermediates in the autoxidation of curcumin, during bicyclopentadiones

formation. It is worth to note that spiroepoxy cyclopentadiones was the earliest intermediate [6]. Spectra of autooxidation curcumin solution at pH 8 and 10 indicates simultaneous formation of spiroepoxy i vinyether cyclopentadiones. Considering that maximum at 280 has not been visible even after 46 h, formation of bicyclopentadione does not occur. Spectra shown in Fig.1. indicate the slower autooxidation of curcumin at pH 8 and 10 (solution S8 and S10) than reported before in literature, where after 7 h intermediate disappeared while bicyclopentadione was appeared [6]. It is questionable whether the presence of alcohol inhibits this mechanism, or if the absence of phosphate anion, or even some ingredient present in the initial curcumin sample (90% purity) affects this significant retardation of curcumin degradation mechanism and formation of new structures .

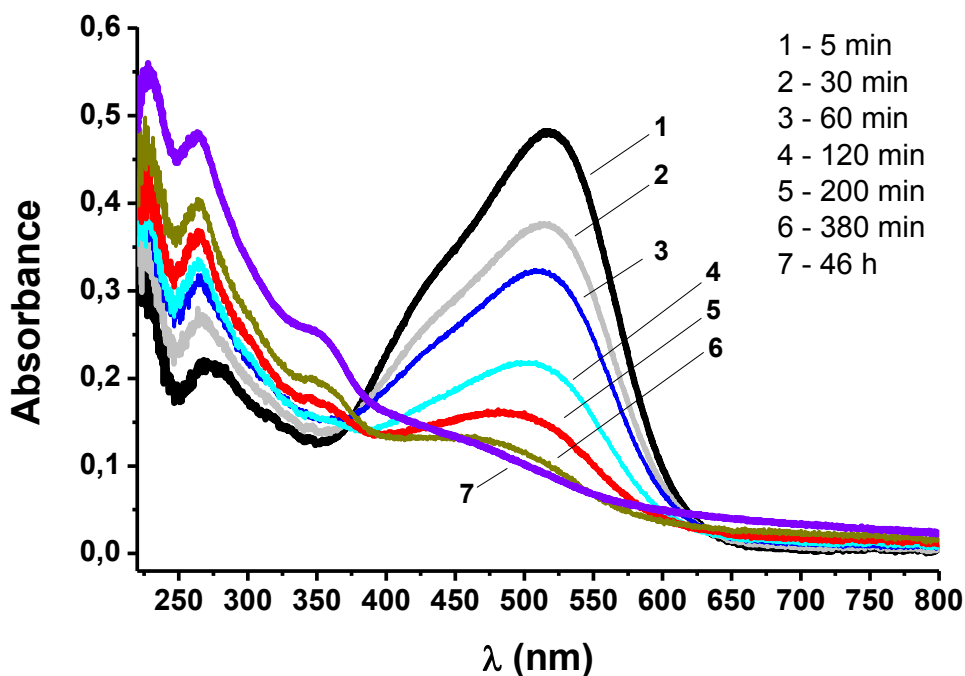


**Figure 1.** UV-Vis spectra of curcumin in solution (pH= 8); time dependence of autooxidation

### CONCLUSION

UV-Vis spectra of curcumin in ethanol - water (40 vol %) solution, adjusted with NaOH at pH=8 and pH=10, indicate a significant retardation of autooxidation of curcumin, in relation to literature data. Reasons for such behavior of curcumin solutions remain to be established. UV-Vis spectra

corresponding to the 46th hour of the start of curcumin decomposition indicate the existence of new structures; these intermediates could possibly lead to the formation of bicyclopentadione.

### ***Acknowledgement***

This work was partially supported by the Ministry of Education, Science and Technological Development of the Republic of Serbia, under the Project No TR-31055 and No 172018.

### **REFERENCES**

- [1] M. Heger, R. F. van Golen, M. Broekgaarden, and M. C. Michel, *Pharmacological Reviews*, 2014, **66**, 222–307.
- [2] L. Shen, H.-F. Ji, *Spectrochimica Acta Part A*, 2007, **67**, 619–623.
- [3] S. D. Kumavat, Y. S. Chaudhari, P. Borole, P. Mishra, K. Shenghani, P. Duvvuri, *International Journal of Pharmacy Review & Research*, 2013, **3**, 50-55.
- [4] Y. J. Wang, M. H Pan, A. L. Cheng, L. I. Lin, Y. S. Ho, C.Y. Hsieh, J. K. Lin, *Journal of Pharmaceutical and Biomedical Analysis*, 1997, **15**, 1867–1876.
- [5] M. Griesser, V. Pistis, T. Suzuki, N. Tejera, D. A. Pratt, and C. Schneider, *The Journal Of Biological Chemistry*, 2011, **286**, 1114–1124.
- [6] O. N. Gordon, P. B. Luis, H. O. Sintim, and C. Schneider, *The Journal Of Biological Chemistry*, 2015, **290**, 4817–4828.

## ON THE ROLE OF THE SOLVENT IN THE FORMATION OF SURFACE LAYER OF COPOLYMERS

J. Kostina<sup>1</sup>, Yu. Bogdanova<sup>2</sup>, E. Chernikova<sup>2</sup> and A. Plutalova<sup>2</sup>

<sup>1</sup>*A.V. Topchiev Institute of Petrochemical Synthesis RAS,  
Leninsky prospect, 29, 119071, Moscow, Russia, (julia@ips.ac.ru)*  
<sup>2</sup>*Moscow Lomonosov State University, Leninskie Gory, 1/3, 119991,  
Moscow, Russia*

### ABSTRACT

In this work a correlation is suggested between the conformational characteristics of the elementary unit, determined by ATR-FTIR spectroscopy data, and components of the surface free energy which were calculated on the base of the contact angles. The effect of the solvent nature on the conformational structure of macromolecules and surface properties of the copolymer films was shown for styrene and *n*-butyl acrylate copolymers with varied composition and predetermined microstructure. It was found that the microstructure of the polymer chain predetermined by synthesis governs the surface properties of polymer films at low contents of one of the comonomers. It was demonstrated that by changing the nature of the solvent used for film casting it is possible to control the conformational structure of the elementary unit thus enriching the film surface with polar or non-polar groups.

### INTRODUCTION

Effect of non-covalent interactions (dipole-dipole or complexes with hydrogen bonds) on the conformational structure of the elementary unit of macromolecule and applicability of Fourier transform infrared spectroscopy to detect these changes were described in detail in the paper [1]. In this paper a correlation between the change spectral characteristics (relative intensity) of several absorption bands in the ATR-FTIR spectra of films and components of the free surface energy was established for the first time for the films of polynorbornenes synthesized by metathesis polymerization cast from the solutions in different solvents.

In other words, the solvent forms a new conformational structure of the polymer chain through the non-covalent interaction with functional groups of the polymer. This conformational structure remains in the film after solvent evaporation and desorption determining the packaging of macromolecules and thus affecting on the macro parameters of polymer films. We assume that the changes on the conformational level initiated by

various solvents manifest themselves at the macroscopic level and the common patterns between the change in conformation structure of the macromolecule and the components of the specific free surface energy of the films could be found. The polar component of the specific free surface energy of the polymer depends on the presence of polar groups on the surface. The dispersion component of the surface free energy is related to the density of the surface layers.

## EXPERIMENTAL

The binary copolymers of styrene and *n*-butyl acrylate (nBA) of various composition and chain microstructure obtained via a controlled radical polymerization and conventional radical polymerization (compositionally heterogeneous, random **RC**) have been studied (Table 1).

Their synthesis and characterization is described in detail in [2]. Polymer films were prepared by casting of 1 wt.% solutions in toluene or acetone on KBr pellets with subsequent drying during 2 h at ambient conditions. The ATR-FTIR-spectra were recorded using IR-microscope Hyperion2000, conjugated with vacuum IR-spectrometer IFS 66v/s (Bruker).

For surface energy characteristics measurement, Owens-Wendt-Kaelble approach was used (test liquids were water and diiodomethane) [4]. Contact angles of test liquids were measured by sessile drop technique with accuracy of 1 degree. The accuracy of  $\gamma_{SV}$  value determination was  $1 \text{ mJ}\cdot\text{m}^{-2}$ .

To take into account the possible influence of the polarization of C=O bonds on the corresponding bands intensity in ATR spectra, the ATR spectra were recorded with polarizer and without polarizer (0 and 90 degrees with respect to the polarizer plane).

## RESULTS AND DISCUSSION

Analytical absorption bands for analysis were selected so that the relative deviation of the average values (between the intensity of the spectrum recorded without a polarizer and in two mutually perpendicular polarization

**Table 1.** Characteristics of (co)polymers:  $F_s$  – styrene mole fraction in copolymer,  $M_n$  – number average molecular weight,  $PDI$  – polydispersity index\*

Sample	$F_s$ , %	$M_n \times 10^{-3}$	$PDI$
PS	100	25.8	1.20
RC-60a	60	14500	1.24
RC-60b	60	230900	2.32
BC-60	60	21000	1.46
GC-30	30	353.9	1.93
RC-30	30	16.6	1.25
GC-10	10	25.8	1.21
RC-10	10	19.6	1.18
PnBA	0	36.8	1.53

planes,  $P=0.95$ ) does not exceed 10%. The absorption bands of CH deformation vibrations in mono-substituted aromatic ring ( $\delta_{\text{CH}}$  at  $757\text{ cm}^{-1}$ ) and the absorption bands of CO valence vibration ( $\nu_{\text{C=O}}$  at  $1730\text{ cm}^{-1}$ ) and their ratio  $A_{1730}/A_{757}$  were selected. For samples with low concentration of styrene component only gradient copolymer with small polydispersity index is sensitive to the change of the solvent. The points of the dispersive component of specific free surface energy and structural characterization differ dramatically for the films formed from different solvent (fig.1).

If the content of the styrene component increases to 30% the difference between samples with different microstructures and films prehistory becomes less pronounced. When the content of the styrene component is above 50%, the copolymer with a random microstructure and a large PDI is more sensitive to the influence of the solvent type on the dispersion component, which is connected with packaging. If we compare the copolymers points movement on diagram with the values of the polar ( $\gamma^{\text{p}_{\text{SV}}}$ ) and the dispersive ( $\gamma^{\text{d}_{\text{SV}}}$ ) components of specific free surface energy (Table 2) we can see that for the RC-10 films the polar component cannot be calculated, and these samples have the most dense packaging, which means that the films surface is enriched with styrene groups. For GC-10 film which was cast from acetone solution we see the same picture. And for the film cast from toluene we see loosening of packaging and sufficiently high value of polar component, i.e. the surface is enriched with butyl acrylate groups. For a block copolymer (BC-60) the surface of the film cast from toluene is enriched with butyl acrylate groups. And the surface of a film cast from acetone is enriched with styrene groups, enabling dense packaging.

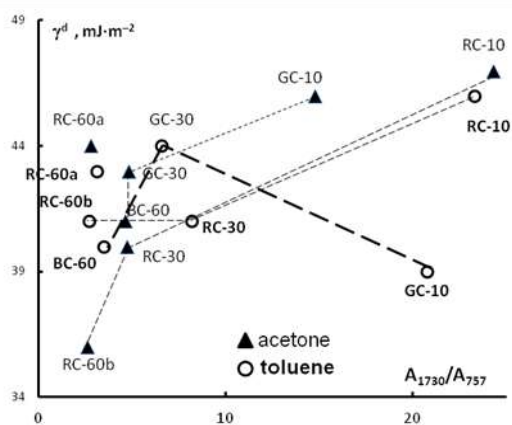


**Figure 1.** Dependence of the dispersion component of the specific free surface energy on the intensity of the characteristic absorption bands ratio.

**Table 1.** PS/PNBA films polar ( $\gamma^p_{sv}$ ) and dispersive ( $\gamma^d_{sv}$ ) components of surface energy

Samples	Solvent	$\gamma_{sv}^d, \text{mJ}\cdot\text{m}^{-2}$			
		<i>toluene</i>	<i>acetone</i>	<i>toluene</i>	<i>acetone</i>
PS		45	42	1	2
RC-60b		41	36	3	<i>close to zero</i>
BC-60		40	41	10	2
RC-30		42	40	1	1
GC-30		44	43	<i>close to zero</i>	2
RC-10		46	47	<i>close to zero</i>	<i>close to zero</i>
GC-10		39	46	7	<i>close to zero</i>
PNBA		40	39	9	8

## CONCLUSION

In this work we have shown the possibility to “pull” into the surface layer the required functional groups of copolymers simply by replacing the solvent. Polymer materials with different properties can be prepared from the same polymer. Using this approach, one can control the structure of the surface layer of copolymers with a predetermined microstructure. The conformational structure of elementary unit is an important parameter which must be considered when dealing with the copolymers with determined microstructure. The greatest effect of the “gentle” influence of solvent on the conformational structure of the elementary unit and morphological structure of the polymer chain is observed for small content of one of comonomers.

## Acknowledgement

This work was supported by Russian Foundation of Basic Research, project 14-03-00142.

## REFERENCES

- [1] J. Kostina, G. Bondarenko, M. Gringolts, A. Rodionov, O. Rusakova, A. Alentiev, A. Yakimanskii, Yu. Bogdanova, V. Gerasimov, *Polym. Int.*, 2013, **62**, 1566 – 1574.
- [2] E. V. Chernikova, V. V. Yulusov, E. S. Garina, Yu. V. Kostina, G. N. Bondarenko and A.Yu. Nikolaev, *Polym. Sci., B*, 2013, **55** (3–4), 176 – 186.
- [3] Yu.G. Bogdanova, J.V. Kostina, V.D. Dolzhikova, E.V. Chernikova, A.V. Plutalova, *Russ. J. of Phys. Chem. A*, 2015, **89**(13), 2466–2472.
- [4] J. Vojtechovska, L. Kvitek, *Acta Univ. Palacki. Olomuc., Fac. Rerum Natur., Chemica*, 2005, **44**, 25 – 48.

**STRUCTURE REARRANGEMENTS AT THERMAL  
TREATMENT OF FILMS BASED ON  
POLY(ETHYLENE GLYCOL), POLY(ETHYLENE  
OXIDE) AND METHACRYLIC ACID - METHYL  
METHACRYLATE COPOLYMER**

L. Vdovikh<sup>1</sup>, J. Kostina<sup>1</sup>, Yu. Korolev<sup>1</sup>, S. Antonov<sup>1</sup> and Yu. Bogdanova<sup>2</sup>

<sup>1</sup>*A.V.Topchiev Institute of Petrochemical Synthesis, RAS*

*29, Leninsky prosp., Moscow 119991, Russia (vdovih@ips.ac.ru)*

<sup>2</sup>*Moscow Lomonosov State University, Leninskie Gory, 1/3, 119991,  
Moscow, Russia*

**ABSTRACT**

Formation of an interpolymer complex in mixtures of poly(ethylene oxide), methacrylic acid - methyl methacrylate copolymer and poly(ethylene glycol) and rearrangements at heating in this system was studied by means of DSC, X-ray diffraction, FTIR and contact angles measurement. It was demonstrated that the interpolymer complex is formed in dry films prepared from the ethanol solution after heating above PEO melting point. This results in some changes in conformations of PEO chains which may explain some increase of hydrophobicity of the film surface after heat treatment.

**INTRODUCTION**

Interpolymer complexes (IPCs) represent a specific type of substances formed by polymers having complementary functional groups and stabilized by H-bonds or electrostatic interactions between these groups. In spite of the fact that the energy of single bond can be quite low (e.g. in case of H-bonds), the overall strength of bonding of two polymer molecules in a IPC is high enough due to their length. That is why IPCs are usually insoluble in various solvents, or at least their solubility is very low. At heating the H-bonds network may deteriorate which leads to dissociation of the IPC.

Usually IPC are prepared from solution by mixing the solutions of the complementary polymers which is followed by the IPC precipitation.

It was demonstrated however [1] that in some cases IPCs can be formed in polymer melts. Furthermore, using low molecular weight or oligomeric plasticizers it is possible to tailor their mechanical properties so that they satisfy the Dalquist's criterion of tack [2] thus obtaining materials that can be used as hydrophilic pressure-sensitive adhesives [1]. In such adhesives

IPCs play an important role restricting their dissolution in water or other solvents and providing their integrity.

This work is focused on the study of formation of an IPC in mixtures of poly(ethylene oxide), methacrylic acid - methyl methacrylate copolymer and poly(ethylene glycol) and rearrangements at heating in this system.

## EXPERIMENTAL

In our work we used:

- Polyox WSR N 750 poly(ethylene oxide) (PEO) provided by Dow Home, with molecular weight 300000 Da;
- Lutrol E-400 polyethylene glycol (PEG) provided by BASF, with molecular weight 400 Da.
- Eudragit L100 (Eu L) methacrylic acid - methyl methacrylate copolymer provided by Evonik Industries AG with 1:1 molar ratio of comonomers and 135000 Da molecular weight.

The films of the compositions were prepared by mixing of the ethanol solutions of initial components followed by solution casting and then drying at ambient conditions for 24 hrs. Some of the films were then exposed to elevated temperature (60°C) for 3 hrs (heat treatment).

DSC measurements were performed using TA 2920 calorimeter with heating/cooling rates of 20°C/min. X-ray diffraction data were obtained in the reflection mode by means of DRON-3 diffractometer (CuK $\alpha$  - radiation).

Fourier transform infrared spectroscopy (FTIR - spectroscopy) was performed in the thermostatic cell on a substrate of the optical Si (chip) in transmission mode. Attenuated Total Reflectance (ATR - spectroscopy) data were obtained using the germanium crystal in reflection regime.

Contact angles were measured by sessile drop method at 20°C with accuracy of  $\pm 1$  degree at advancing ( $\theta_a$ ) and receding ( $\theta_r$ ) conditions [1]. Surface energy of films ( $\gamma_{sv}$ ), its dispersive ( $\gamma_{sv}^d$ ) and polar ( $\gamma_{sv}^p$ ) components were calculated by Owens-Wendt-Kaelble approach using  $\theta_a$  of two probe liquids (H<sub>2</sub>O, CH<sub>2</sub>I<sub>2</sub>) [3].

## RESULTS AND DISCUSSION

DSC thermograms of binary PEO – Eu L blends (Fig. 1) demonstrate that even small amounts of Eu L (at ratio PEO to Eu 10:1) suppress significantly PEO crystallinity. At equimolar ratio the PEO melting peak is completely absent. PEG has very low influence on the position and area of the melting peak.

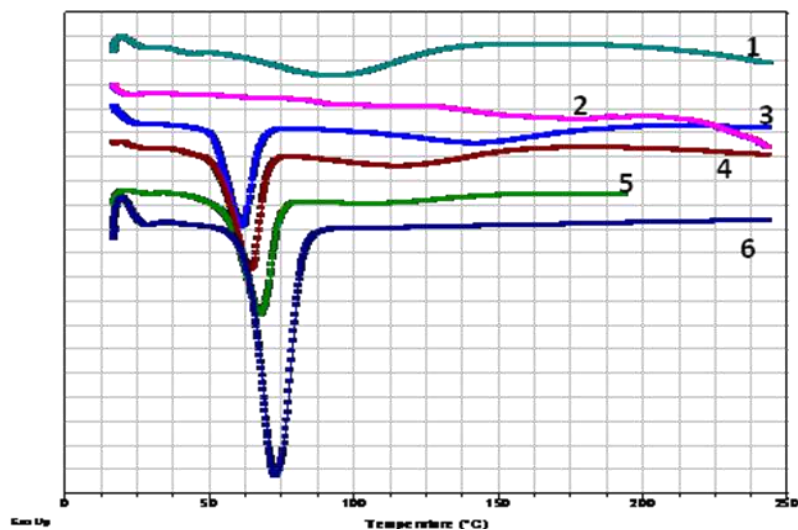


**Figure 1.** DSC thermograms of PEO – PEG - Eu L films at heating. 1 - PEO:Eu L=1:1, 25% PEG; 2 - PEO:Eu L=1:1, 0% PEG; 3 – PEO:Eu L=10:1, 50% PEG; 4 - PEO:Eu L=10:1, 25% PEG; 5 - PEO:Eu L=10 : 1, 0% PEG; 6 - PEO

X-Ray diffraction data confirm these findings(Fig.2).

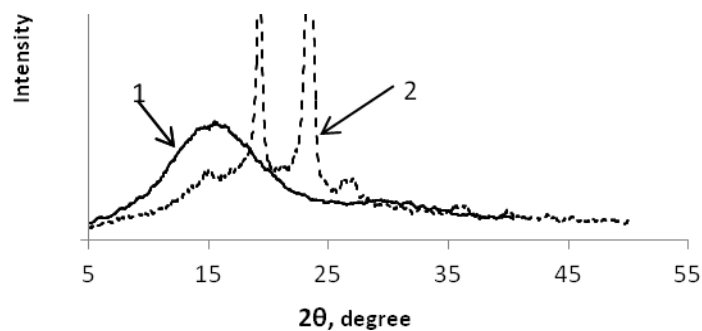


**Figure 2.** X-Ray diffraction data for binary PEO – Eu L blends. 1 – PEO:Eu L=1:1, 2 - PEO:Eu L=10:1

FTIR data (Fig. 3) indicate some changes in conformations of PEO chains which may explain some increase of hydrophobicity of the films surface after heat treatment (Table 1).

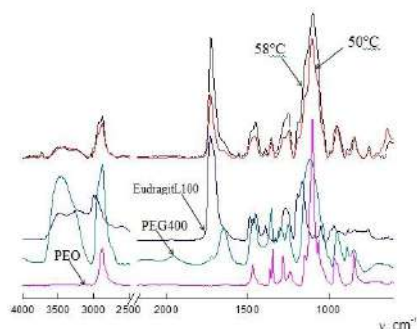


**Figure 3.** FTIR spectra of pure components and PEO:Eu L: PEG blend with 1.5:1.0:3.8 components ratio at temperatures close to PEO melting point.

**Table 1.** Surface characteristics of samples

PEO:Eu L: PEG ratio	Heat treatment	$\theta_a$ , degree		$\theta_r$ , degree	$\Delta\theta$ , degree	$\gamma^{d}_{sv}$ , $\text{mJ}\cdot\text{m}^{-2}$	$\gamma^{p}_{sv}$ , $\text{mJ}\cdot\text{m}^{-2}$	$\gamma_{sv}$ , $\text{mJ}\cdot\text{m}^{-2}$
		H <sub>2</sub> O	CH <sub>2</sub> I <sub>2</sub>					
1:1:1	No	51	28	50	1	35	20	55
1.5:1.0:3.8	No	84	22	42	42	46	2	48
1:1:1	Yes	70	51	40	30	30	11	41
1.5:1.0:3.8	Yes	63	30	41	22	37	12	49

## CONCLUSION

It was established that formation of an IPC can proceed at heating of dry films obtained from mixtures of poly(ethylene oxide), methacrylic acid - methyl methacrylate copolymer and poly(ethylene glycol). The formation of complex is accompanied by PEO crystallization suppression and some hydrophobization of the film surface initiated by changes of microstructure of PEO chains.

## REFERENCES

- [1] M.M. Feldstein, G.W. Cleary, P. Singh. Hydrophilic Adhesives. In: I. Benedek, M.M. Feldstein (Editors), Technology of Pressure-Sensitive Adhesives and Products (Handbook of Pressure-Sensitive Adhesives and Products), CRC - Taylor & Francis, Boca Raton, London, New York, 2009, Chapter 7, pp. 7-1 - 7-80
- [2] Dahlquist CA. Pressure-sensitive adhesives. In: Patrick RL, editor. Treatise on adhesion and adhesives. Vol. 2, Materials. New York (NY): Marcel Dekker; 1969. p. 219–260.
- [3] J. Kloubek, Adv. Colloid Interface Sci, 1992, **38**, 99–142.

*C - Kinetics, Catalysis*



## RENEWABLE RESOURCES FOR ENERGY AND CHEMICALS PRODUCTION

S. Damyanova and J. M. C. Bueno

*Institute of Catalysis, Bulgarian Academy of Sciences, 1113 Sofia, Bulgaria*

### ABSTRACT

The need to reduce greenhouse gases emissions and the shortages expected in the near future in the supply of fossil hydrocarbons as an energy source and resource for the synthesis of chemicals has generated substantial interest in developing of alternative routes for energy and chemicals production, especially from renewable feed stocks. Biomass is one of the most prospective renewable resources because in most of the cases is clean, carbon neutral and widely available. Hydrogen produced from renewable resources is identified as an ideal energy carrier to support sustainable energy development since its combustion does not produce any emissions of carbon dioxide but only water. The demand for hydrogen in the next decade is expected to grow substantially due to its wide application in the fuel cells technologies. As a result, there is a growing interest in the search of effective alternatives to produce renewable hydrogen cleanly and safely.

Among the various feed stock for hydrogen production, the biomass derived ethanol is very attractive because of its relatively high hydrogen content, availability, non-toxicity, and storage and handling safety. The ethanol steam reforming to hydrogen has received special attention due to the associated environmental benefits. However, it is not an industrial process yet due to the difficulties of the reaction, such as the lack of catalyst's stability caused by carbon accumulation and structural changes (oxidation, sintering).

On the other hand, the rapid development of the bioethanol market has been also accompanied by a growing interest in its use as renewable feedstock for the manufacture of bio-based chemicals (green chemistry). Moreover, bioethanol was recently identified as one of the potential top bio-based raw materials for the chemical industry.

For successfully industrial application of bioethanol conversion to hydrogen or other chemical products the research efforts were focused on development of a new generation of active and stable catalysts that play a crucial role in the reactivity toward ethanol conversion to hydrogen and chemicals. The active catalyst should maximize product selectivity and inhibit coke formation.

The attention was paid on the different reaction pathways of ethanol reforming to hydrogen as a function of metallic composition (regarding electronic properties) by modifying Ni-based catalysts with Co addition, focusing on the structural properties. On the other hand, Cu-based catalysts supported on zirconia with different morphologies were used for ethanol conversion to ethylacetate formation.

***Acknowledgment***

The author share gratefully acknowledged to FAPESP and DFNI E02/16/14.

## STUDY OF MgO TRANSFORMATION INTO MgF<sub>2</sub> IN THE PRESENCE OF CF<sub>2</sub>Cl<sub>2</sub>

A. A. Vedyagin, A. F. Bedilo, I. V. Mishakov and E. I. Shuvarakova

*Boreskov Institute of Catalysis SB RAS, Novosibirsk 630090, Russia*

### ABSTRACT

Alkaline-earth metal oxide aerogels prepared by sol–gel method followed by autoclave drying are nanocrystalline mesoporous materials with high reactivity. The reaction of MgO aerogels with CF<sub>2</sub>Cl<sub>2</sub> was shown to take place after a long induction period. It was found that addition of vanadium had a promoting effect on this reaction accelerating the formation of the active sites on the surface of the nanoparticles. A good correlation was observed between the rate of the CF<sub>2</sub>Cl<sub>2</sub> destructive sorption and the concentration of weak electron-acceptor sites characterized by EPR technique using perylene as a spin probe.

### INTRODUCTION

Inorganic aerogels can be prepared via sol-gel process followed by drying under supercritical conditions when the liquid-vapor interface is eliminated. Nanocrystalline MgO aerogels have high surface areas, small crystallite sizes, enhanced adsorption properties and have been used as destructive adsorbents and in various catalytic applications [1, 2]. In this communication we will review our main results obtained for CF<sub>2</sub>Cl<sub>2</sub> destructive sorption on AP-MgO, which is characterized by unusual long induction period, the effect of vanadium on it and characterization of electron-acceptor sites during this solid-state reaction.

### RESULTS AND DISCUSSION

Nanocrystalline magnesium oxide synthesized by modified aerogel method (AP-MgO) with the surface area about 400 m<sup>2</sup>/g was used in the study. The detailed synthesis procedure was described in [1, 2]. VO<sub>x</sub>·MgO aerogels were prepared by a similar method following a previously reported procedure with vanadium (V) triisopropoxide oxide added to the freshly prepared Mg(OH)<sub>2</sub> gel in desired proportion [3].

Dehydration of Mg(OH)<sub>2</sub> aerogels is typically carried out by heating in vacuum to 500°C or higher temperatures. The AP-MgO samples after heat treatment at 500°C consist of 1-5 nm crystallites arranged into chains

forming a very porous secondary structure [1, 2]. The abundance of pores of different sizes gives AP-MgO large accessible surface area.

Dehydration of V-Mg(OH)<sub>x</sub> hydroxide aerogels in a flow reactor with intense air flow and slow heating yielded nanoscale AP-VO<sub>x</sub>/MgO mixed oxides with the surface area exceeding 400 m<sup>2</sup>/g [3]. The XRD analysis of VO<sub>x</sub>/MgO samples with different vanadium concentrations showed the presence of nanocrystalline MgO phase with the average crystallite size 5-6 nm together with some Mg(OH)<sub>2</sub>. It is remarkable that no vanadium oxide or magnesium vanadate phase was observed even in the sample with vanadium concentration as high as 26%.

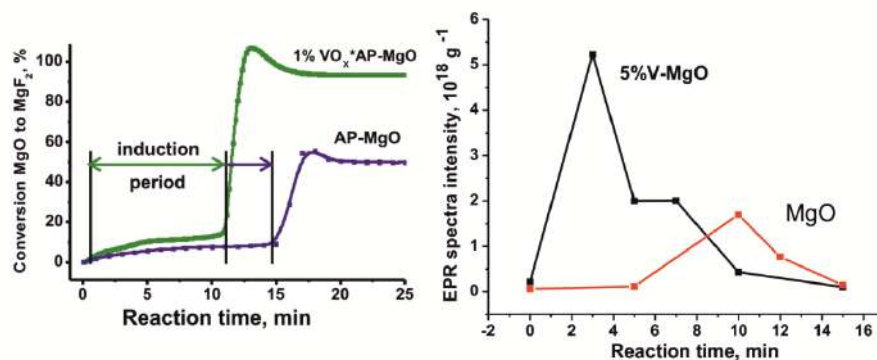
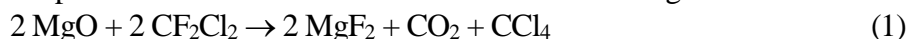


**Figure 1.** Weight gain during CF<sub>2</sub>Cl<sub>2</sub> reaction at 350°C with aerogel MgO and 1% VO<sub>x</sub>·MgO samples (left) and dependence of the intensities of EPR spectra observed after perylene adsorption from toluene solution on aerogel MgO and 5% V<sub>2</sub>O<sub>5</sub>/MgO on time of their reaction with CF<sub>2</sub>Cl<sub>2</sub> (right).

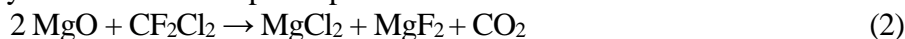
CF<sub>2</sub>Cl<sub>2</sub> was found to react with aerogel MgO at 325°C or higher temperatures to give a significant gain of the sample weight as evidenced by kinetic curves presented in Fig. 1 [4]. The presence of an obvious induction period, after which an intense gain of the sample weight starts, is the most distinctive and interesting feature of the kinetic curves. Its duration depends on the reaction temperature and the used experimental setup.

The addition of just 1% vanadium results in a substantial increase of the MgO reactivity in the solid-state exchange of the oxygen atoms for halogens (Fig. 1) [5]. The rate of MgO interaction with CF<sub>2</sub>Cl<sub>2</sub> is also much higher in the presence of vanadium (12%/min for MgO and 41%/min for 1% VO<sub>x</sub>·MgO). Most likely, such acceleration is related to the fact that vanadium acts as a catalytic intermediate in the solid-state exchange of the oxygen atoms for fluorine and chlorine. Deeper conversion of the vanadium-doped sample is also notable.

Very low but steady conversion of  $\text{CF}_2\text{Cl}_2$  to  $\text{CO}_2$  and  $\text{CCl}_4$  formed in approximately equal molar amounts was observed during the induction period before the beginning of the active stage. Such reaction should be accompanied by the  $\text{MgO}$  conversion to  $\text{MgF}_2$  according to reaction (1). This reaction is mostly limited to the surface and its rate begins to increase towards the end of the induction period. Some chlorine atoms are retained on the  $\text{MgO}$  surface as well.



After the end of the induction period the halocarbon conversion quickly increases in less than a minute. Sometimes the ratio of released  $\text{CO}_2$  and  $\text{CCl}_4$  is changed, so that the peaks of their release may not match. The overall bulk reaction after the end of the induction period seems to be the sum of separate reactions (2) and (3). Magnesium chloride is formed as an intermediate, which usually does not form a separate phase.



The obtained data for the reaction with  $\text{CF}_2\text{Cl}_2$  clearly demonstrate that the active form of the destructive sorbent is formed only after induction period. Apparently, during the induction period certain active sites not existing before reaction are accumulated on the  $\text{MgO}$  surface. Bulk transformation of magnesium oxide to magnesium fluoride begins only when such sites are formed in sufficient concentration.

Electron-acceptor sites are very reactive species present on the surface of some heterogeneous catalysts, which are capable of abstracting a single electron from an aromatic probe molecule [6]. The concentration of electron-acceptor sites during the solid-state reaction was studied using a recently developed original procedure [7]. A sample was loaded into a tube suitable for EPR measurements and subjected to the reaction with the  $\text{CF}_2\text{Cl}_2$  for desired time followed by fast cooling to ambient temperature and the perylene adsorption from solution in toluene. The concentration of electron-acceptor sites was measured by double integration of the EPR signal obtained after perylene ionization on them.

The data on the concentration of electron-acceptor sites on the surface of AP- $\text{MgO}$  and 5%  $\text{V}_2\text{O}_5$ /AP- $\text{MgO}$  samples as a function of the reaction time are presented in Figure 1. Electron-acceptor sites were not found on the surface of the initial sample. Such sites appear during the reaction with the halocarbon due to the  $\text{MgO}$  chlorination and fluorination. Their concentration gradually increased during the induction period, reaching a clearly defined maximum in the active state when the rapid topochemical destructive sorption reaction occurred [7].

The induction period before the increase of the concentration of electron-acceptor sites is much shorter on the sample with 5% of vanadium than that on

pure AP-MgO. This result is in a good agreement with the kinetic data. Moreover, the concentration of electron-acceptor sites on this sample is higher. Overall, the results obtained in this study prove that there is a good correlation between the formation of weak electron-acceptor sites and the activity of nanocrystalline AP-MgO and V<sub>2</sub>O<sub>5</sub>/AP-MgO aerogels in the reaction with CF<sub>2</sub>Cl<sub>2</sub>.

## CONCLUSION

Destructive sorption of CF<sub>2</sub>Cl<sub>2</sub> on MgO aerogels is characterized by a long induction period after which fast solid-state reaction takes place. Apparently active sites are accumulated on the surface during the induction period. Vanadia addition to nanocrystalline MgO was found to shorten the induction period in the reaction with CF<sub>2</sub>Cl<sub>2</sub>. A method for characterization of electron-acceptor sites during solid-state and catalytic reactions was developed in our lab. Using this method we found a good correlation between the rate of the halocarbon destructive sorption on AP-MgO and V<sub>2</sub>O<sub>5</sub>/AP-MgO and the concentration of weak electron-acceptor sites tested using perylene as spin probe.

## Acknowledgement

This study was partially supported by Russian Foundation for Basic Research (Grant 15-03-08070-a).

## REFERENCES

- [1] R. Richards, W. F. Li, S. Decker, C. Davidson, O. Koper, V. Zaikovskii, A. Volodin, T. Rieker, and K. J. Klabunde, *J. Am. Chem. Soc.*, 2000, **122**, 4921.
- [2] I. V. Mishakov, A. F. Bedilo, R. M. Richards, V. V. Chesnokov, A. M. Volodin, V. I. Zaikovskii, R. A. Buyanov, and K. J. Klabunde, *J. Catal.*, 2002, **206**, 40.
- [3] E. V. Ilyina, I. V. Mishakov, A. A. Vedyagin, S. V. Cherepanova, A. N. Nadeev, A. F. Bedilo and K. J. Klabunde, *Microporous Mesoporous Mater.*, 2012, **160**, 32.
- [4] I. V. Mishakov, V. I. Zaikovskii, D. S. Heroux, A. F. Bedilo, V. V. Chesnokov, A. M. Volodin, I. N. Martyanov, S. V. Filimonova, V. N. Parmon and K. J. Klabunde, *J. Phys. Chem. B*, 2005, **109**, 6982.
- [5] E. V. Ilyina, I. V. Mishakov, A. A. Vedyagin, A. F. Bedilo and K. J. Klabunde, *Microporous Mesoporous Mater.*, 2013, **175**, 76.
- [6] A. F. Bedilo, E. I. Shuvarakova, A. A. Rybinskaya and D. A. Medvedev, *J. Phys. Chem. C*, 2014, **118**, 15779.
- [7] A. F. Bedilo, E. I. Shuvarakova, A. M. Volodin, E. V. Ilyina, I. V. Mishakov, A. A. Vedyagin, V. V. Chesnokov, D. S. Heroux and K. J. Klabunde, *J. Phys. Chem. C*, 2014, **118**, 13715.

## APPLICATION OF QUASI-CHEMICAL REACTION APPROACH TO KINETICS OF DIFFUSION IN POROUS MATERIAL

N. Ostrovskii<sup>1</sup> and K. Mészáros-Szécsényi<sup>2</sup>

<sup>1</sup>*Hipol a.d., Gračački put b.b., 25250 Odžaci, Serbia  
(nikolaj.ostrovski@hipol.rs)*

<sup>2</sup>*University of Novi Sad, Cara Lazara 1, 21000 Novi Sad, Serbia*

### ABSTRACT

The model of moisture diffusion in polydisperse porous particles is proposed, based on quasi-chemical reaction approach. The diffusion flux is expressed in Onsager form  $J_i = \sum L_i X_{ji}$ , according to the concept of linear non-equilibrium thermodynamics, but with non-linear thermodynamic force  $X_{ji}$ . The driving force is considered as a product  $X_{ji} = x_j (1-x_i)$  of fullness degree by moisture of one type of pores  $x_j$  and emptiness of another type  $(1-x_i)$ .

The model is applied to drying of polypropylene porous particles filled with heptane. Three types of moisture were assumed inside porous particles, which are corresponded to three sizes of pores. Results of experiments and model formulation are presented in this report.

### INTRODUCTION

In many processes such as adsorption, drying, solid fuel combustion, and catalytic reactions, the mass transfer of fluid in porous media is often the rate limiting step. Despite of heterogeneous porous structure, and different mechanisms of transport, the mass transfer is often characterized by an effective diffusivity, which is a lumped parameter.

In some models (especially in drying and adsorption) the effective diffusivity is represented as a function of moisture content and temperature [1, 2]. Other authors consider the combination of parallel/series models with different diffusivities and porosities [3, 4].

The so-called reaction engineering approach (REA) to modelling the convective drying of food materials [5, 6], is also reduced to diffusivity as a semi-empirical function of temperature and moisture.

Another approach is based on assumption of heterogeneous porous structure and on models of multi-phase mass transfer. Such models are applied successfully for drying of fruits because are based on their cellular structure [7, 8]. Authors postulate two phases of moisture: (i) free liquid water inside intercellular space; (ii) bound water within the cell structure.

An interaction of these types of water within the macroscopic multiphase model is taken as a Mass Action Law (MAL) in chemical kinetics.

Gorban et al. [9] have developed a generalized approach to nonlinear multicomponent diffusion based on the idea of the reaction mechanism borrowed from chemical kinetics. They have proposed also the suitable equations for Fick's diffusion and for Cell-jump formalism, as well as complex balance conditions for MAL application in diffusion.

Based on these approaches, we have proposed the model of moisture diffusion in a poly-disperse porous particles. The polypropylene powder was used, where the porous structure was filled with heptane.

The model of drying has been derived assuming three types of moisture inside porous particles, which correspond to three sizes of pores. Based on the experimental results, a model for the solvent diffusion is presented.

## EXPERIMENTAL

For the study of moisture diffusion the polypropylene porous particles were used, obtained in slurry polymerization process where heptane is used as a solvent. So, heptane plays the role of "moisture". The range of particles diameter was 50–500  $\mu\text{m}$ , and the range of moisture 10–20 % wt.

Kinetic experiments (Fig. 1) were carried out by TG–DSC thermal analysis using Q600 SDT equipment of TA Instruments. Measurements were conducted in  $\text{N}_2$  atmosphere (flow rates: 20 and 100  $\text{cm}^3/\text{min}$ ), with sample masses of 2–4 mg and heating rates of 5, 10 and 20  $^\circ\text{C}/\text{min}$  using alumina sample pan and the corresponding empty pan as reference for DSC measurements. One experiment was carried out under stepwise isothermal (SWI) conditions with a heating rate of 10  $^\circ\text{C}/\text{min}$ .

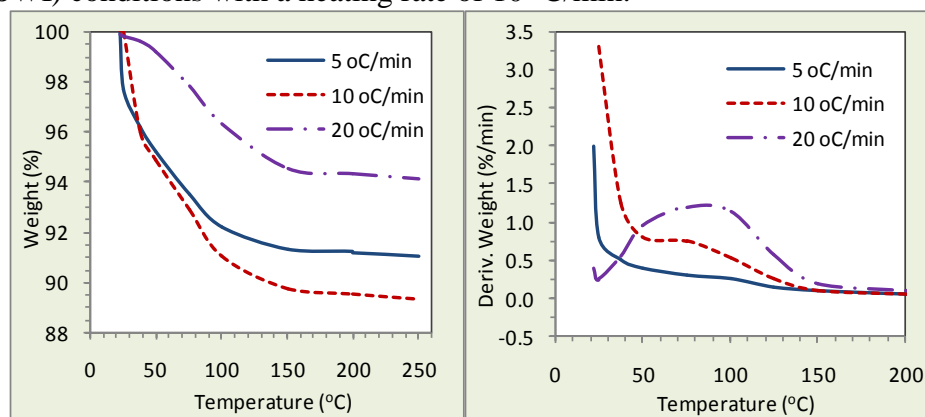
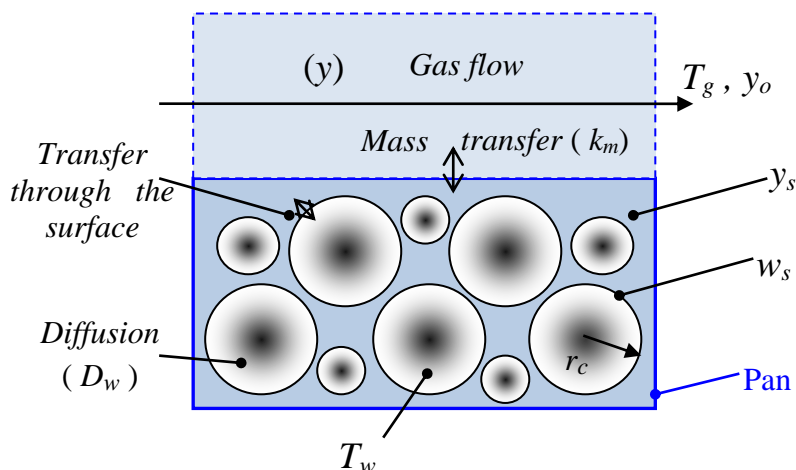


**Figure 1.** TG and DTG curves measured at different heating rates.

### FORMULATION OF THE MODEL

The model of drying process in thermogravimetric experiments is based on the following scheme:



Differential mass balance of moisture in sample:

$$G_{pol} \frac{dw}{dt} = -F_g (y - y_o) \quad (1)$$

and in gas phase:

$$V_g \frac{dy}{dt} + F_g (y - y_o) = k_m S_s (y_s - y) \quad (2)$$

$G_{pol}$  – mass of polymer, mg;  $w$  – relative moisture;  $V_g$  – gas volume,  $\text{cm}^3$ ;  
 $F_g$  – gas flow rate,  $\text{cm}^3/\text{min}$ ;  $y_o, y$  – inlet and outlet gas humidity,  $\mu\text{g}/\text{cm}^3$ ;  
 $y_s$  – moisture of gas near particles,  $\mu\text{g}/\text{cm}^3$ ;  $k_m$  – mass transfer coefficient  
 (from sample to gas),  $\text{cm}^3/\text{cm}^2 \text{ min}$ ;  $V_s$  – volume of sample in pan,  $\text{cm}^3$ ;  
 $S_s$  – cross section of pan,  $\text{cm}^2$ .

Balance equation for the gas phase near particles surface:

$$V_s \varepsilon_s \frac{dy_s}{dt} + k_m S_s (y_s - y) = D_w V_s (1 - \varepsilon_s) a_p G_{pol} \left. \frac{dw}{dr} \right|_{r=r_p} \quad (3)$$

$$D_w = D_L \varepsilon_p / h_p, \quad a_p = 3(1 - \varepsilon_s) / r_p$$

$r_p$  – radius of particle, cm;  $\varepsilon_s$  – voidage of sample;

$D_w, D_L$  – moisture diffusivity in particle and in liquid,  $\text{cm}^2/\text{s}$ ;

$a_p$  – specific surface area of particles,  $\text{cm}^2/\text{cm}^3$ ;

$\varepsilon_p$  – particle porosity;  $h_p$  – tortuosity of the particle.

Process in gas phase is much faster than in particles, so we can consider that the drying proceeds in a quasi-steady regime:  $dy/dt \approx dy_s/dt \approx 0$ . It means that the change of moisture in gas slaves to the dynamics of moisture inside particles. Therefore, for the modelling only one equation is enough:

$$-\frac{dw}{dt} = D_w V_s (1 - \varepsilon_s) a_p \left. \frac{dw}{dr} \right|_{r=r_p} \quad (4)$$

Because of small particles diameter (50 to 500  $\mu\text{m}$ ), the diffusion flux in (4) one can approximate by the expression of linear driving force:

$$\left. \frac{dw}{dr} \right|_{r=r_p} \approx (w - w_r) / r_p \quad (5)$$

$w_r$  – moisture of particles in equilibrium with gas, mg/mg.

Then, an equation for drying rate takes the form:

$$-\frac{dw}{dt} \approx D_w(T) \frac{a_p}{r_p} (w - w_r) \quad (6)$$

Since the diffusivity  $D_L$  depends on temperature, we can write:

$$D_w(T) = D_L^0 \exp\left(\frac{E_D}{R} \left[\frac{1}{T_0} - \frac{1}{T}\right]\right) \frac{\varepsilon_p}{h_p} \quad (7)$$

The analysis of experimental data (Fig. 1) shows that using only one equation (6) is not enough for describing the real drying kinetics (Fig. 2). It means that the state of liquid inside particles is not homogeneous, and it should be consider as depending on porous structure of particles.

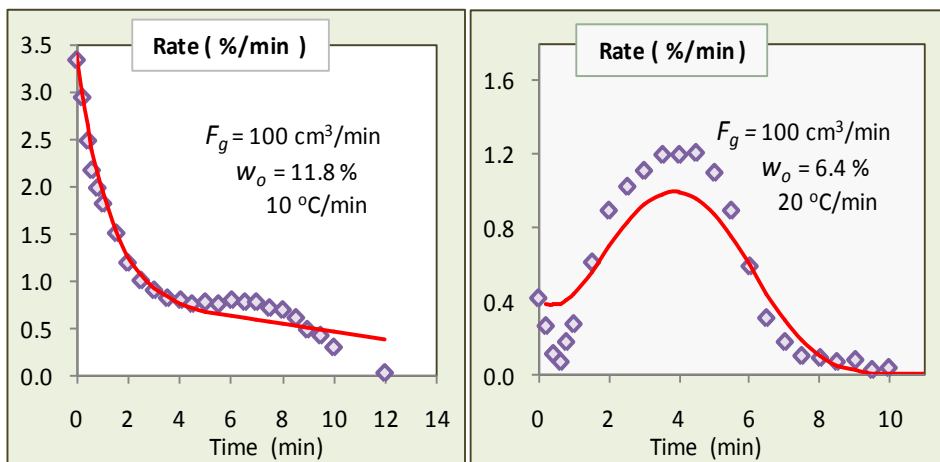


**Figure 2.** Rate of drying. Points – experiment; lines – equations (6-7).

## RESULTS AND DISCUSSION

Polymer particles have various structure, depending on polymerization conditions, such as a catalyst type, electron donor, concentration of  $H_2$ , etc. In our case the porous structure looks like in Fig. 3.

Most authors consider the growing polymer particle (macroparticle) as aggregate of smaller particles (microparticles), with a crystallite of catalyst inside [10-13]. Such a model formally corresponds with bidisperse structure of porous materials. Thus, we can assume that „three types of liquid“ take places in particles distinguished by their localization, and thus, by the rate of diffusion (Fig. 4).

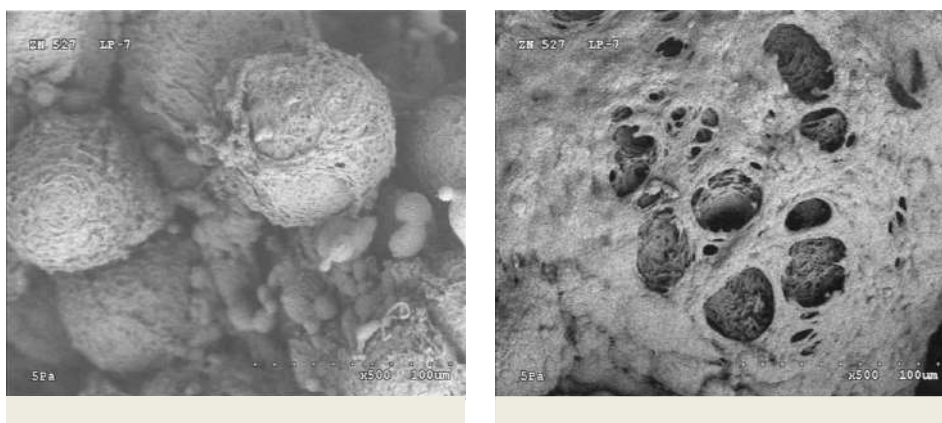


**Figure 3.** SEM micrographs of the polypropylene particles.

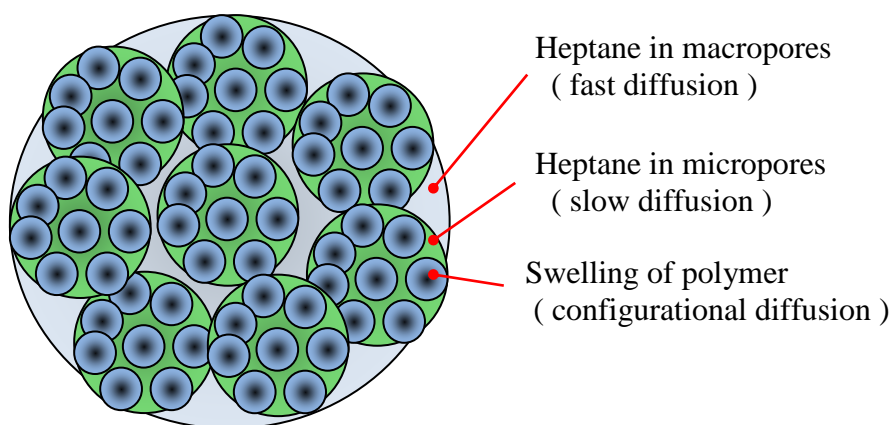


**Figure 4.** Schematic model of wetted porous particles.

The moisture of particle ( $w$ ) one can express via the volume of liquid ( $V_w$ ), of pores ( $V_v$ ), of particle ( $V_p$ ), and of polymer in it ( $V_{pol}$ ). Because of  $V_v / V_p = \varepsilon_p$ , and  $V_{pol} = V_p (1 - \varepsilon_p)$ , we can write:

$$w = \frac{G_w}{G_{pol}} = \frac{V_w}{V_{pol}} \frac{\rho_w}{\rho_{pol}} = \frac{V_w}{V_p (1 - \varepsilon_p)} \frac{\rho_w}{\rho_{pol}} \quad (8)$$

The volume of liquid ( $V_w$ ) is then a sum of volumes of „three types of liquid“ in the corresponding pores ( $V_w = V_i x_i$ ), where ( $x_i$ ) is a degree of filling the corresponding structures with liquid.

$$\begin{aligned} \frac{V_w}{V_p} &= \frac{1}{V_p} (V_{mac} x_{mac} + V_{mic} x_{mic} + V_{pol} x_{pol}) = \\ &= \varepsilon_{mac} x_{mac} + \varepsilon_{mic} x_{mic} + (1 - \varepsilon_p) x_{pol} \end{aligned} \quad (9)$$

$\varepsilon_{mac}$ ,  $\varepsilon_{mic}$  – portion of macro-, and micro-pores;

$x_{mac}$ ,  $x_{mic}$ ,  $x_{pol}$  – degree of filling the pores and the polymer with liquid.

It is important that  $\varepsilon_{mac} + \varepsilon_{mic} = \varepsilon_p$ , and  $\varepsilon_i$  values remain unchanged with drying, because they characterise the particle structure. As for partial moisture ( $x_i$ ), they changes in the interval from 0 to 1.

With (9), the equation (8) for total moisture becomes as follows:

$$w = \frac{\rho_w}{\rho_{pol}} \frac{1}{1 - \varepsilon_p} (\varepsilon_{mac} x_{mac} + \varepsilon_{mic} x_{mic} + (1 - \varepsilon_p) x_{pol}) \quad (10)$$

Diffusion fluxes for partial moisture  $x_i$  we write using quasi-chemical reaction approach in Onsager form:  $J_i = \Sigma L_i X_{ji}$ . The driving force  $X_{ji}$  has a non-linear expression  $X_{ji} = x_j (1 - x_i)$ , like in cell-jump diffusion [9] or in Langmuir adsorption kinetics.

In our case,  $x_j$  is a degree of saturation by moisture of one type of pores, and  $(1 - x_i)$  is an emptiness of the nearby pores.

$$dx_{mac} / dt = -\beta_{mac} (x_{mac} - x_r) + \beta_{mic} x_{mic} (1 - x_{mac}) \quad (11)$$

$$dx_{mic} / dt = -\beta_{mic} x_{mic} (1 - x_{mac}) + \beta_{pol} x_{pol} (1 - x_{mic}) \quad (12)$$

$$dx_{pol} / dt = -\beta_{pol} x_{pol} (1 - x_{mic}) \quad (13)$$

Mass-transfer coefficients  $\beta_i$  ( $\text{min}^{-1}$ ) are defined similar to (6) and (7):

$$\beta_i(T) = D_i^o \exp\left(\frac{E_i}{R} \left[\frac{1}{T_o} - \frac{1}{T}\right]\right) \frac{\varepsilon_p}{h_p} \frac{a_p}{r_p} \quad (14)$$

According to the model, the moisture diffusion starts from macro-pores. Because  $x_r$  in (11) is proportional to  $w_r$ , the diffusion continues until saturation of the gas phase or emptying of macropores. The diffusion from micropores is possible only toward macropores if they are not filled.

The „liquid“ in a polymer ( $x_{pol}$ ) is a consequence of polymer swelling in the presence of monomer, some oligomers and solvent. It is a very small value but can influence the drying of polymer at high temperature [14].

The model gave a good prediction of the experimental drying rates at different operating conditions and moisture contents (Figs. 5, 6).

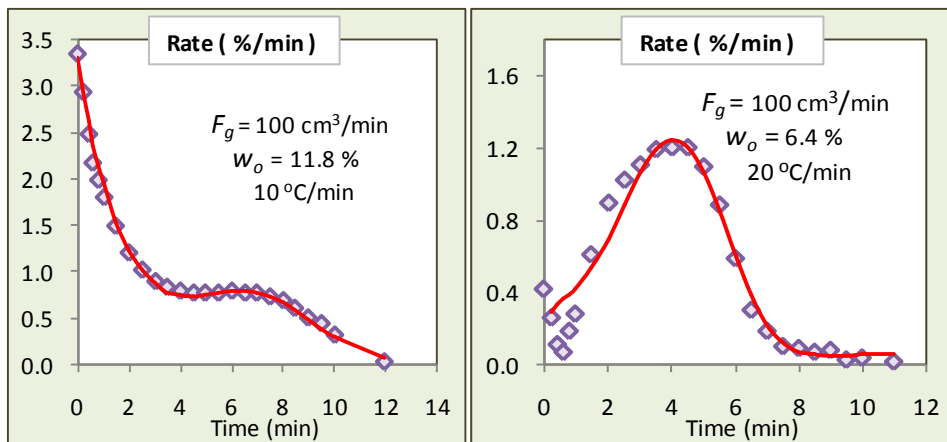


**Figure 5.** Drying dynamics. Points – experiment; lines – model (10-14).

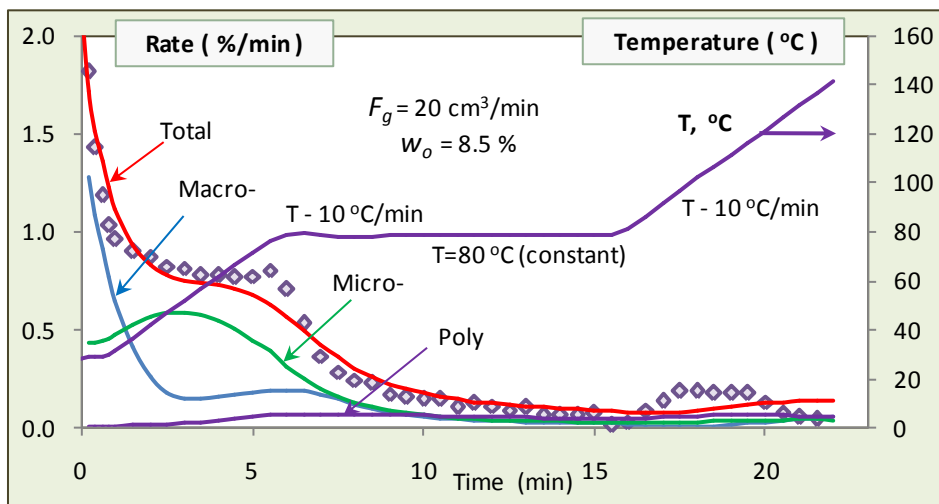


**Figure 6.** Drying at SWI. Points – experiment; lines – model (10-14).

## CONCLUSION

We have studied the mass transfer (diffusion) of moisture (heptane) in polymer porous particles (polypropylene). Kinetic experiments were carried out by TG–DTA thermal analysis. Drying of the same polymer powder was studied earlier in industrial dryer with fluidized bed [14].

Based on these investigations, we have claimed that the process inside particles is characterised by non-uniform diffusivity, related to polydisperse structure of porous particles.

The new model of moisture diffusion in porous particles is proposed, based on quasi-chemical reaction approach. The driving force of moisture transfer is non-linear and expresses a product  $x_j (1-x_i)$ . Here,  $x_j$  is a degree of saturation by moisture of one type of pores, and  $(1-x_i)$  is an emptiness of the nearby pores. The model demonstrates a good description of experiments, and is used for optimization of industrial dryer with multizone fluidized bed.

## REFERENCES

- [1] C.T. Kiranoudis, Z.B. Maroulis, D. Marinou-Kouris, *Int. Journ. Heat & Mass Transfer*, 1995, **38**, 463–480.
- [2] T. Loulou, B. Adhikari, D. Lecomte, *Chem. Eng. Sci.*, 2006, **61**, 7185-7198.
- [3] M.A. Silva, P.J.A.M. Kerkhof, W.J. Coumans, *Ind. Eng. Chem. Res.*, 2000, **39**, 1443-1452.
- [4] M.M. Mezedur, M. Kaviani, W. Moore, *AIChE Journal*, 2002, **48**, 15-24.
- [5] X.D. Chen, *Drying Technology*, 2008, **25**, 1203–1213.
- [6] A. Putranto, X.D. Chen, *AIChE Journal*, 2013, **59**, 55-67.
- [7] N. Shahari, Ph.D. Thesis, University of Nottingham, 2012.
- [8] N. Shahari, S. Hibberd, *WSEAS Transactions on Mathematics*, 2014, **13**, 840-851.
- [9] A.N. Gorban, H.P. Sargsyan, H.A. Wahab, *Math. Modelling Natural Phenomena*, 2011, **6**, 184-262.
- [10] G.D. Bukatov, V.I. Zajkovsky, V.A. Zakharov, et al., *Vysokomol. Soedin.*, 1982, **24**, 542-548.
- [11] J.A. Debling, W.H. Ray, *Ind. Eng. Chem. Res.*, 1995, **34**, 3466-3480.
- [12] C. Martin, T.F. McKenna, *Chem. Eng. Journal*, 2002, **87**, 89-99.
- [13] N.M. Ostrovskii, D. Stoiljković, *Theoretical Foundation Chem. Eng.*, 2011, **45**, 40-52.
- [14] N.M. Ostrovskii, *Chemical Industry*, 2014, **68**, 661-671.

## FALLACIES IN REACTION KINETICS

G. Lente

<sup>1</sup> *University of Debrecen, Department of Inorganic and Analytical Chemistry, Egyetem tér 1, 4032 Debrecen, Hungary.  
(lente@science.unideb.hu)*

### ABSTRACT

This contribution lists a number of common misconceptions encountered in chemical kinetics, which are termed fallacies throughout this text. These fallacies often appear even in otherwise high-quality publications and can typically be avoided only through maintaining constant awareness about their possible occurrence.

### INTRODUCTION

Logical traps, i.e. frequently used and seemingly correct lines of thought often make scientific reasoning a challenging task. Reaction kinetics seems to be an especially sensitive field in this respect. Following the basic ideas published in a recent book [1], this text will present those logical traps, termed ‘fallacies’ in this contribution, which have been recognized by the author as (at least potential) major sources of erroneous conclusions.

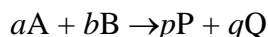
In many cases, numerous articles could be cited from the high-quality scientific literature where the authors fell into these traps. However, negative citations are avoided here as the objective of this text is not to single out certain authors for some mistakes, but to provide the reader with a collection of short warnings on typical cases. Yet it should be remarked that a major general fallacy in science is that printing an argument in a peer reviewed publication automatically makes the reasoning correct. Scientific logic obliges all the readers to re-think arguments and not simply accept what was written by others.

This text provides very similar information to the last chapter of the textbook already cited [1] but in a more concise form. Some novel observations have also been added, these are based on the recent experience and discussions of the author. Catalysis science and mechanistic kinetic research have developed to be remarkably distinct disciplines with very little communication between the experts in the two fields. This is why the present author welcomes the recent attempts to develop some sort of general standards in catalysis science in a process called benchmarking [2], which includes kinetically relevant lines of thought as well.

## DISCUSSION

In the main part of this contribution, each logical trap will be stated in a single sentence in a negative way, which is followed by a longer explanation about the possible origin of the fallacy.

**The first fallacy of the reaction rate** is that it exists for any reaction. In a typical textbook on kinetics, a general reaction is formulated as follows:



Then the rate of this general reaction is defined by including the stoichiometric coefficients:

$$v = -\frac{1}{a} \frac{d[A]}{dt} = -\frac{1}{b} \frac{d[B]}{dt} = \frac{1}{p} \frac{d[P]}{dt} = \frac{1}{q} \frac{d[Q]}{dt}$$

However, as pointed out even in the relevant IUPAC recommendations [3-4], this definition is only useful for if no intermediates exist in the process. Otherwise, the equations in the above formula are not true and the general rate of reaction is meaningless. In fact, it would be better to restrict the concept of reaction rates to elementary reactions.

**The second fallacy of the reaction rate** is that it is characteristic of a chemical reaction, or even one of its reagents.

The rate of a chemical process is typically dependent on the concentrations of the reactants, sometimes also on the concentrations of the products or other materials that do not even appear in the stoichiometric equation. Although it is not incorrect to speak about the typical time scale of a reaction in a casual manner, developing this into a quantitative concept is by no means advisable. Nowhere this contradiction is stronger than for the "turnover frequency" (TOF) often used in catalysis science to characterize a catalyst [5-7]. In fact, TOF is the ratio of the reaction rate and the catalyst concentration and depends on all the concentrations. Therefore, it is unsuitable for the very purpose it was designed for. There are known examples when TOF values depend on the concentration of the catalyst [8].

**The fallacy of rate constants** is that they are suitable for comparing reaction rates.

Although when one wishes to compare reaction rates (especially within one reaction system), the values of rate constants are certainly important, it should not be forgotten that the typical concentrations this constant must be multiplied with to obtain the reaction rate may be very different, even by several orders of magnitude. A less nuanced mistake when a comparison of rate constants of different order is attempted: they obviously have different physical dimension and, therefore, are not comparable.

**The fallacy of the rate coefficient** is that this is the correct term to be used instead of the term rate constant.

This is only a question of semantics. Some experts often argue that rate constants are not in fact constants because they depend on a number of external parameters such as temperature. While this is not incorrect, this argument misunderstands the mathematical idea behind calling a quantity a constant. The rate constant is a constant in this sense because it is independent of the explicitly stated variables in a rate equation, which are the concentrations and time. The recommendations of IUPAC [3,4] fully endorse this usage.

**The fallacy of consecutive processes** is that the first process always has a higher rate constant than the second one in the series.

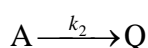
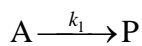
It is unlikely that any kineticist would fall into this trap directly. However, a more disguised and very common case is when the time dependence of an instrumental signal ( $A_t$ ) measured in a two-step process is evaluated with a biexponential function of the following form:

$$A_t = A_1 e^{-k_1 t} + A_2 e^{-k_2 t} + A_\infty$$

In this case, it is very tempting to assume that the faster pseudo-first order rate constant belongs to the first process in the consecutive series. In fact, the sequence must be established by separate considerations.

**The fallacy of parallel processes** is that the rate constant of one of the parallel steps can be obtained by selectively monitoring its product.

When parallel reactions are encountered, it must be remembered that the rate of the parallel pathways are typically not influenced by the concentrations of the products and following one product selectively does not give the rate constant of the pathway leading to it. For example, consider the following simple two parallel processes:



The concentration of the products as a function of times is given as:

$$[P] = [P]_0 + \frac{k_1}{k_1 + k_2} [A]_0 e^{-(k_1 + k_2)t} \quad [Q] = [Q]_0 + \frac{k_2}{k_1 + k_2} [A]_0 e^{-(k_1 + k_2)t}$$

Therefore, the first order rate constant determined from the measurement will be the same, no matter if P or Q is followed selectively.

**The first fallacy of the rate determining step** is that it is slower than other steps following it.

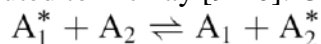
In fact, a rate determining step determines the rates (but obviously not the rate constants) of all later steps, which cannot be higher than the rate of the rate determining step. This misconception is closely connected to the fallacy of rate constants because it is true that processes after the rate determining step typically feature much higher rate constants.

**The second fallacy of the rate determining step** is that no information can be gained about reactions occurring after it.

This sentence would be less of a fallacy if the word ‘kinetic’ were included in it. If one considers a system where parallel reactions occur after the rate determining process, the ratio of their rate constants can still be determined from the final product ratio. However, parameters obtained in this way will seldom include time in their dimensions.

**The fallacy of exchange reactions** is that first order dependence with respect to the limiting reagent can be deduced from detecting an exponential curve similarly to true chemical reactions.

In fact, exchange reactions represent a whole different world within chemical kinetics. This recognition and the detailed derivations are typically attributed to McKay [9-10]. Consider a simple exchange reaction:



The molar fraction of the label in  $A_1$  changes in time as follows:

$$x_{1,t} = (x_{1,0} - x_{1,\infty}) \exp\left(\frac{[A_1]_T + [A_2]_T}{[A_1]_T [A_2]_T} R_{\text{ex}} t\right) + x_{1,\infty}$$

This formula describes an exponential function without pre-conditions of any sort. Most importantly, the independence from the rate equation of the process and the initial concentrations should be noted. The quantity  $R_{\text{ex}}$  means the exchange rate, which does not change during a single experiment involving the re-distribution of labels (most often these are isotopes of the same element) between the different forms present. So the rate equation can be explored only by learning how  $R_{\text{ex}}$  depends on the initial concentrations.

**The fallacy of the induction period** is that it is always caused by autocatalysis.

Although autocatalytic rate equations certainly often lead to detectable induction periods, there are a number of further possibilities. These have been explained in detail in the interpretation of clock reactions [11-12].

**The fallacy of the activation energy** is that it indicates the rate of a process.

The experimental activation energy is typically obtained from the Arrhenius equation, which has a visually very attractive and widely reproduced interpretation, the reaction energy profile. In this, the activation energy is shown as an energy barrier. However, this line of thought totally forgets the other variable parameter in the Arrhenius equation, which is the pre-exponential factor. The activation energy and the pre-exponential factor determine the rate constant together.

**The fallacy of the activation free energy** is that it carries information not already present in the rate constant.

The Eyring equation connects the rate constant of a first order process to the activation free energy:

$$k = \frac{k_B T}{h} e^{-\frac{\Delta^\ddagger G}{RT}} = \frac{k_B T}{h} e^{-\frac{\Delta^\ddagger H}{RT} + \frac{\Delta^\ddagger S}{R}}$$

The activation free energy of a process is fully equivalent to the rate constant at a given temperature. There is a recent trend in the literature to give both of these parameters. This is probably driven by the ever-increasing number of theoretical studies, which yield energies rather than rate constants as the direct results.

**The fallacy of activation entropy** is that its value is unreliable because of an extrapolation to infinite temperature.

In the Eyring equation, there is no reason to single out the activation entropy. This fallacy stems from the usual linearization of the Eyring equation, in which  $\ln(k/T)$  is plotted as a function of  $1/T$ . In this plot, the activation entropy is determined from the intercept, and the procedure is often declared to be “an extrapolation”, which is a significant source of numerical error. However, thorough statistical analysis does not support this view [13]. In fact, the errors of activation entropy and activation enthalpy are strictly correlated, their ratio gives the average temperature of the measurements [13]:

$$\frac{\sigma_{\Delta^\ddagger H}}{\sigma_{\Delta^\ddagger S}} = T_{\text{av}} \left( = \frac{1}{N} \sum_{i=1}^N T_i \right)$$

**The fallacy of the activation volume** is that it has an extremum in the transition state.

In fact, the transition state is a saddle point on the energy hypersurface: in one direction it is a maximum, in all other directions, a minimum in energy. This property of the transition state has no consequences for activation volume at all.

**The fallacy of the isokinetic temperature** is that it has any scientific meaning.

The isokinetic temperature is typically calculated for a series of reactions as the slope of the straight line in a plot of the activation enthalpy against the activation entropy. However, this correlation is totally statistical in nature without any scientific implications. In a classic paper that should be read by every practicing kineticist, McBane created a perfect isokinetic plot from the phone numbers of his friends [14].

**The first fallacy of the diffusion limited rate constant** is that reaction rates are limited by diffusion and not rate constants.

There is a well known sequence of thought that estimates the upper limit of the rate constant of a bimolecular process by determining the number of bimolecular collisions. The most useful form of the derived equation is [1]:

$$k_d = \frac{8RT}{3\eta}$$

It is to be remembered the rate of a diffusion limited process can increase when the concentrations are increased. Although the values of the concentrations also have obvious physical constraints, these have nothing to do with diffusion.

**The second fallacy of the diffusion limited rate constant** is that diffusion can limit unimolecular processes.

Unimolecular reactions do not involve any collision of reactants. Therefore, diffusion cannot be a limiting factor for them. The ultimate upper limit of the unimolecular rate constant is probably set by the speed of intramolecular movement. In the absence of better ideas, substituting zero as the activation free energy in the Eyring equation ( $= k_B T/h$ ,  $6 \times 10^{12} \text{ s}^{-1}$  at room temperature) gives a reasonable estimate.

**The fallacy of unimolecular reactions** is that they are paradoxical.

A common interpretation for bimolecular reactions is that the collision of particles with extra energy is needed to overcome the limitation posed by the activation energy in an elementary reaction. No similar line of thought can be valid for unimolecular processes because of the lack of collisions. As a consequence, unimolecular reactions are often declared to be in conflict with the concept of activation.

In fact, molecules necessarily have several internal degrees of freedom between which energy transfer is possible. For a reaction to occur, energy must be accumulated along one (or a few) of these internal degrees of freedom. The formal description of a process could even be the same as the description of the intermolecular energy transfer between different particles. At this point, it should be recalled that the theoretically reasonably well supported Eyring equation interprets unimolecular processes. In the transition state theory, it is bimolecular reactions that need extra considerations.

**The fallacy of the termolecular elementary reaction** is that its rarity can be used as an argument against proposing it.

It is true that three-molecule collisions are much less frequent than two-molecule collisions, but this fact has no consequence for reactions. An upper limit for the termolecular rate constant was derived recently [15]:

$$k_{\text{ter}} = r^3 \frac{64\pi N_A RT}{9\eta}$$

Whenever an experimental third order rate constant is smaller than this upper limit, a termolecular pathway cannot be excluded automatically.

**The fallacy of radical scavengers** is that an assumption of a radical type mechanism can be confirmed by the fact that a radical scavenger has an effect (any sort of effect!) on the rates of concentration change.

Originally, the idea of using radical scavengers was that they react with certain, previously encountered radicals quite rapidly, and the product formed in this process (typically some sort of adduct) is easily detectable. Over time, this concept underwent a complete overhaul: if the addition of any supposed “radical scavenger” has any sort of effect on the time dependence of the concentrations, the reaction is concluded to involve radicals. Needless to say, this approach is completely wrong.

**The fallacy of linearization** is that it should be used whenever possible.

From the history of science, it is well known that linearization techniques were developed not because they were thought to be theoretically advantageous, but out of sheer necessity as there was no way to carry out the detailed numerical calculations that were already understood to be theoretically desirable even centuries ago. Recent advances in computation power made linearized plots thoroughly obsolete. It is clear that statistical considerations call for using untransformed data when they are compared with theoretical equations.

**The fallacy of the R value** (coefficient of determination) is that it characterizes the goodness of a fit.

In fact, the regression coefficient is just one of the statistical descriptors that can be used to characterize the results of a fitting procedure and it is easy to find cases when it is misleading [1]. There are a number of further descriptors as well, but none of them have universal value in science.

**The first fallacy of curve fitting** is that the purpose of curve fitting is to learn the values of certain parameters in a theoretical function.

The primary purpose of curve fitting is model validation: it must be demonstrated that the chosen theoretical function provides an acceptable interpretation of the measured data. The model is validated if the fitted curve and the experimental points show reasonable agreement. During the evaluation of curve fitting results, the user must first decide whether the fit is acceptable. If it is not, then the parameters obtained as a result of the fit are absolutely meaningless.

**The second fallacy of curve fitting** is that it is needed to find a function that describes measured data within some pre-determined precision.

Simply predicting the numerical results of experiments is sometimes a worthwhile scientific or technological objective. If this is the case, then finding a good function for this prediction is a respectable goal. However,

scientific research is typically about interpreting experimental findings, so the function fitted to the data must be physically reasonable and supported by some sort of theory. Predicting is by no means the same as understanding.

### CONCLUSION

The list of the misconceptions about kinetics given above is long but by no means exhaustive. The basic error in most of these fallacies is obvious when viewed without scientific context, but details and specific information very often cloud these issues and make the errors difficult to recognize. A prepared scientific mind must take precautions to avoid these traps.

### REFERENCES

- [1] G. Lente, *Deterministic Kinetics in Chemistry and Systems Biology*, Springer, New York, 2015.
- [2] T. Bligaard, R. M. Bullock, C. T. Campbell, J. G. Chen, B. C. Gates, R. J. Gorte, C. W. Jones, W. D. Jones, J. R. Kitchin, S. L. Scott, *ACS Catal.*, 2016, **6**, 2590–2602.
- [3] P. Muller, *Pure Appl. Chem.* 1994, **66**, 1077–1184.
- [4] K. J. Laidler, *Pure Appl. Chem.*, 1996, **68**, 149–192.
- [5] S. Kozuch, J. M. L. Martin, *ACS Catal.*, 2012, **2**, 2787–2794.
- [6] S. Kozuch, *ACS Catal.* 2013, **3**, 380–380.
- [7] G. Lente, *ACS Catal.*, 2013, **3**, 381–382.
- [8] A. B. Crooks, K. H. Yih, L. Li, J. C. Yang, S. Ozkar, R. G. Finke, *ACS Catal.*, 2015, **5**, 3342–3353.
- [9] H. A. C. McKay, *Nature*, 1938, **142**, 997–998.
- [10] H. A. C. McKay, *J. Am. Chem. Soc.*, 1943, **65**, 702–706.
- [11] G. Lente, I. Fábián, G. Bazsa, *New J. Chem.*, 2007, **31**, 1707–1707.
- [12] A. K. Horváth AK, I. Nagypál, *ChemPhysChem*, 2015, **16**, 588–594.6.
- [13] G. Lente, I. Fábián, A. Poë, *New J. Chem.*, 2005, **29**, 759–760.
- [14] G. C. McBane, *J. Chem. Ed.*, 1998, **75**, 919–922.
- [15] M. Gabricevic, G. Lente, I. Fábián, *J. Phys. Chem. A*, 2015, **119**, 12627–12634.

## MECHANISM OF BRØNSTED ACID CATALYZED DECOMPOSITION OF 4-DIAZOFURAN-3-ONES

D.V. Semenok and J. J. Medvedev

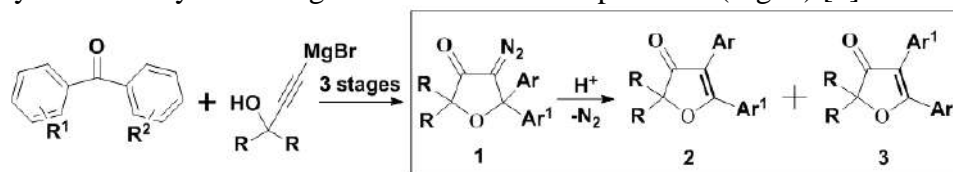
*Saint-Petersburg State University, University Prosp. 26, St.-Petersburg, 198504, Russia. E-mail: altmark6871@gmail.com*

### ABSTRACT

In this paper the mechanism of acid-catalyzed decomposition of 4-diazo furan-3-ones was investigated. It was found that the ratio of reaction products can be described by the Hammett equation with Brown constants  $\sigma^+$  with a good accuracy and does not depend on  $pK_a$  of Brønsted acids. This fact argues for passing of the reaction through a rearrangement of a positively-charged intermediate (diazonium cation). Dependence of the reaction regioselectivity on solvent polarity is explained by stabilization of the charged transition states ( $A_3'$ ,  $A_2'$ ) via the solvation.

### INTRODUCTION

Instability of diazo compounds in the presence of acids has always been noted as their characteristic property [1]. Decomposition of diazo compounds accompanied by 1,2-nucleophilic rearrangement was studied, for instance, in [2], but the detailed mechanism of catalytic action of Brønsted acids was not investigated. Herein we carried out a systematic study of acid-catalyzed decomposition of  $\alpha$ -diazo carbonyl compounds **1**, which were previously synthesized by a three-stage method from benzophenones (Fig. 1) [3].



R = CH<sub>3</sub>, Ar = C<sub>6</sub>H<sub>5</sub>-, Ar<sup>1</sup> = *p*-MeS-C<sub>6</sub>H<sub>5</sub> (a), *p*-MeSO-C<sub>6</sub>H<sub>5</sub> (b), *p*-MeSO<sub>2</sub>-C<sub>6</sub>H<sub>5</sub> (c), etc.

**Figure 1.** Scheme of synthesis and decomposition of diazo compounds **1**.

Objectives of the research included clarification of the influence of acid nature and its strength on the ratio of regioisomers **2** and **3**; the effect of solvent polarity on the regioselectivity of the reaction; and identification of the reaction mechanism.

**EXPERIMENTAL**

All reactions of the acid-catalyzed decomposition of diazo compounds were carried out by the same procedure: 5-fold molar excess of a Brønsted acid was added drop wise to solution 30-50 mg of diazo compound in 3-5 ml of selected solvent. Refluxing during 2-15 hours led to the mixture of 4,5-diaryl-3(2*H*)furanones **2** and **3**, whose ratio was determined by <sup>1</sup>HNMR spectroscopy after removing of solvent and acid. All yields are preparative.

**RESULTS AND DISCUSSION**

The first task of this reaction investigation was determination of dependence of its result on the nature and strength of used acid. For that purpose we have investigated six acids: CF<sub>3</sub>SO<sub>2</sub>OH (pK<sub>a</sub> = -12), HClO<sub>4</sub> (70 %, pK<sub>a</sub> = -8-10), HCl (pK<sub>a</sub> = -7), H<sub>2</sub>SO<sub>4</sub> (pK<sub>a</sub> = -3), TsOH (pK<sub>a</sub> = -2.8), CF<sub>3</sub>COOH (pK<sub>a</sub> = 0.5). The results for different Ar<sup>1</sup> groups in **1** are shown in Table 1. Weaker acids like Dowex-H<sup>+</sup> (pK<sub>a</sub> = + 0.16), HCOOH (pK<sub>a</sub> = + 3.75) and AcOH (pK<sub>a</sub> = + 4.75) do not cause significant decomposition of diazo compounds in this conditions. All pK<sub>a</sub> values above correspond to dissociation in water.

**Table 1.** Dependence of reaction results on the acid nature.

Entry	Ar <sup>1</sup> , ( <i>Ar</i> = <i>Ph</i> )	Acid	Solvent	Ratio 2/3	Yield
1	<i>p</i> -MeS-C <sub>6</sub> H <sub>4</sub>	TfOH	CHCl <sub>3</sub>	<b>3 : 1</b>	65 %
2	CH <sub>3</sub>	TfOH	CHCl <sub>3</sub>	<b>1 : 1.9</b>	85 %
3	9,9'-Fluorenyl	TfOH	CHCl <sub>3</sub>	<b>1 : 0</b>	85 %
4	<i>p</i> -MeS-C <sub>6</sub> H <sub>4</sub>	H <sub>2</sub> SO <sub>4</sub>	HCOOH	-	74 %
5	<i>p</i> -MeS-C <sub>6</sub> H <sub>4</sub>	HCl <sub>g</sub>	CHCl <sub>3</sub>	<b>3 : 1</b>	98 %
6	<i>p</i> -MeS-C <sub>6</sub> H <sub>4</sub>	TsOH	CHCl <sub>3</sub>	<b>2.7 : 1</b>	98 %
7	<i>p</i> -MeS-C <sub>6</sub> H <sub>4</sub>	TFA	CHCl <sub>3</sub>	<b>3.2 : 1</b>	99 %
8	<i>p</i> -MeS-C <sub>6</sub> H <sub>4</sub>	HClO <sub>4</sub>	HClO <sub>4</sub>	<b>1.3 : 1</b>	99 %

The Table 1 data show using TfOH and H<sub>2</sub>SO<sub>4</sub> leads to lower yields of products (**2+3**, 65-85 %) while using weaker acids (TFA, TsOH) and such strong acids as HCl, HClO<sub>4</sub> (entry 5, 8) gives almost quantitative yield (98-99 %). The ratios of migration products **2a/3a** in chloroform (entry 1, 5-7) are almost similar for all four acids: CF<sub>3</sub>SO<sub>2</sub>OH, HCl, TsOH and TFA, **2a/3a** ≈ 3:1 and do not depend on acid dissociation constant.

The second task of research was to establish relationships between the ratio of rearrangement products **2** and **3** and solvent polarity (i.e. dielectric permittivity and dipole moment). Results are shown in Table 2.

**Table 2.** Dependence of regioselectivity on solvent polarity ( $\epsilon$ , D).

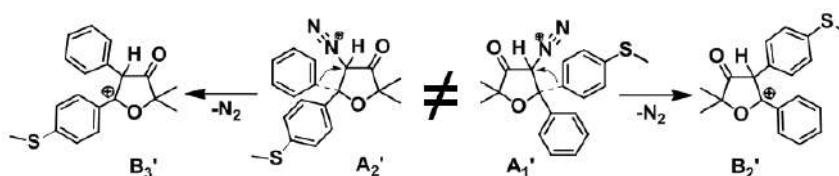
Entry	Solvent	$\epsilon(t_{b.p.})$	D	Ratio		
				2a/3a	2b/3b	2c/3c
1	Benzene	2.2	0	3.8 : 1	1 : 2.6	1 : 5.9
2	CHCl <sub>3</sub>	4.1	1.1	3.2 : 1	1 : 4.6	1 : 6.1
3	Hexane	1.8	0.1	3 : 1	1 : 4	1 : 4.5
4	TFA	7.5	2.3	2.6 : 1	1 : 2.7	1 : 2.7
5	(CH <sub>3</sub> ) <sub>2</sub> CO	17.4	2.8	2.3 : 1	1 : 2.3	1 : 2.4
6	HCOOH	24.2	1.4	2.2 : 1	1 : 2.1	1 : 3.4

Table 2 shows the ratio of rearrangement products (**2/3**) generally levels with increasing of solvent polarity, but regioselectivity- decreases.

The experimental data, related to the ratio of products of 1,2-nucleophilic rearrangement (Table 2) can be interpolated by Hammett-like logarithmic equation (1) with a good accuracy,

$$\lg \frac{k_{Ar}}{k_{Ph}} = \sigma_X \cdot \rho_{1,2-mig} \quad (1)$$

Where  $k_{Ar}$ ,  $k_{Ph}$  – are migration rate constants for **Ar** and **Ph** groups,  $\rho_{1,2-mig}$  – is a constant which is equivalent to the parameter of reaction sensitivity in the basic Hammett equation, and  $\sigma_X$  – constant of substituents.



**Figure 2.** Two possible and nonequivalent ways of 1,2-migration, which combination leads to the mixture of regioisomers.

In the kinetic control conditions, the ratio **2/3** in this reaction will be numerically equal to the ratio of the migration rate constants of aryl ( $k_{Ar}$ ) and phenyl ( $k_{Ph}$ ) groups. Calculation shows (Table 3, TS on Fig. 2), the best correlation with experimental data – is equation (1) with Brown constants  $\sigma^+$  with  $\rho = -0.96$  ( $R^2 = 0.94$ ). Moreover, indicated value of  $\rho$ , obtained in the experiment, is near to the same parameter of pinacol rearrangement [4], which indirectly confirms passing the reaction through

positively-charged intermediate, where the degree of charge stabilization is defined mainly by possibility of resonance interaction with *para*-substituent of migrating group.

**Table 3.** Calculations of ratio **2/3** according to the Hammett equation.

Ar <sup>1</sup>	k <sub>Ar</sub> /k <sub>Ph</sub>	lg (k <sub>Ar</sub> /k <sub>Ph</sub> )	σ <sup>+</sup> <sub>X</sub>	Calculations <i>k<sub>Ar</sub>/k<sub>Ph</sub> = 10<sup>-0.96 σ+</sup></i>
<i>p</i> -MeS-C <sub>6</sub> H <sub>4</sub>	3.17	0.50	-0.6	3.76
<i>p</i> -Me-C <sub>6</sub> H <sub>4</sub>	1.75	0.24	-0.3	1.94
<i>p</i> -CF <sub>3</sub> -C <sub>6</sub> H <sub>4</sub>	0.38	-0.42	+0.61	0.26
<i>p</i> -MeSO-C <sub>6</sub> H <sub>4</sub>	0.22	-0.65	+0.49	0.34
<i>p</i> -MeSO <sub>2</sub> -C <sub>6</sub> H <sub>4</sub>	0.16	-0.80	+0.72	0.2

## CONCLUSION

Summing up the discussed experiments we can make three main conclusions. Firstly, the regioselectivity of acid-catalyzed decomposition of diazo compounds decreases with increasing of solvent polarity. Secondly, the regioselectivity directly depends on difference of σ<sup>+</sup> (for Ar and Ar<sup>1</sup>) constants of substituents in aryls. Finally, the total yield of products (**2+3**) depends on the acid nature, but the regioselectivity is invariant with type of used acid. Quantum chemical calculations and kinetic data that we can not present here, confirm proposed mechanism and allow us to calculate the ratio of products with even more accuracy than equation (1).

## Acknowledgement

The authors express their gratitude to the SPbSU resource center “Center for Magnetic Resonance”, J.J.M. thanks to “UMNIK-2015” and RFBR (mol\_a\_16-33-00059\16) foundation for financial support of this work.

## REFERENCES

- [1] M. Regitz, G. Maas, Diazo Compounds. Properties and Synthesis, Academic Press, New York, 1986.
- [2] Nan Jiang, Zhaohui Qu, Jianbo Wang, Org. Lett., 2001, **3**, 2989.
- [3] L. Rodina et al., Eur. J. Org. Chem., 2014, 2993-3000.
- [4] B. P. Nikol'sky, Handbook of chemist, Russian edition, book3, p.958, Moscow, 1965.

**EFFECT OF PLASMA-CHEMICAL  
TREATMENT OF  
NASICON-TYPE PHOSPHATES  $\text{Me}_{0.5}\text{Zr}_2(\text{PO}_4)_3$   
WITH  $\text{Me}=\text{Ni}, \text{Co}$  IN ISOBUTANOL DEHYDRATION**

A. Pylinina, M. Danilova and V. Yagodovskii

*Peoples' Friendship University of Russia, Department of Science,  
6, Miklucho-Maklaya str., 117198, Moscow, Russia*

**ABSTRACT**

Treating  $\text{Me}_{0.5}\text{Zr}_2(\text{PO}_4)_3$  ( $\text{Me}=\text{Ni}, \text{Co}$ ) with high-frequency (HF) hydrogen plasma is found to affect the catalytic activity of these NASICON-type phosphates in the dehydration reaction of isobutanol leading to an increase in the conversion of alcohol and the yield of isobutene. The increased activity of phosphates results from the formation of new, more active sites with low experimental activation energy, rather than a change in the surface acidity.

**INTRODUCTION**

Solid-state ion conducting materials, also known as superionic or fast ion conductors, have been intensively developed. These materials can be used in solid-state electrochemical devices such as membranes [1] and catalysts [2]. The last years new catalysts family was developed on the base of complex phosphates of NASICON type, possessing the significant acidity and high thermal and phase stability. The basic structure of NASICON-phosphates is a framework that consists of  $\text{PO}_4$ -tetrahedra and  $\text{ZrO}_6$ -octahedra, along with cavities of various sizes and geometries (conducting channels) that can be filled by various polyvalent cations.

It was shown NASICON compounds are active and stable catalysts of alcohol's dehydration [3], dehydrogenation [4], paraffin isomerization and oxidation [5].

Plasma treatment of catalysts produces a significant effect on their activity [6-7]. This type of treatment changes the structure and chemical composition of the surface through the action of reactive species forming in the plasma and through plasma radiation.

The purpose of this study was to elucidate the effect of hydrogen radio-frequency (RF) plasma treatments of the NASICON-type nickel- and cobalt zirconium phosphate  $\text{Me}_{0.5}\text{Zr}_2(\text{PO}_4)_3$  with  $\text{Me}=\text{Ni}, \text{Co}$  on its catalytic activity in vapor-phase reactions of isobutanol.

## EXPERIMENTAL

The  $\text{Me}_{0.5}\text{Zr}_2(\text{PO}_4)_3$  catalysts with  $\text{Me}=\text{Ni}, \text{Co}$  were prepared by sol-gel processing using the following: zirconium dioxide  $\text{ZrO}_2$ , phosphoric acid  $\text{H}_3\text{PO}_4$ , and metal chloride  $\text{NiCl}_2 \cdot 6\text{H}_2\text{O}$  or  $\text{CoCl}_2 \cdot 4\text{H}_2\text{O}$ . X-ray diffraction data for the synthesized phosphate allowed us to assign it to the NASICON structure.

The phosphates were treated with hydrogen RF plasma in a vacuum unit. The sample, placed in a quartz cell, was treated with RF discharge at a gas pressure of 0.1 Torr. The copper wire coil inside which the reactor was placed was energized with 40.68 MHz voltage pulses from a generator. The discharge duration was 20 min.

Catalytic tests were carried out in a flow reactor. The reaction products were analyzed on a Kristall 2000M gas chromatograph (Khromatek, Russia; helium carrier gas, flame-ionization detector, column packed with Porapak Q, analytical temperature of 125°C). Alcohol vapor, entrained by flowing helium from a temperature controlled bubbler, was fed into the reactor at a rate of 1.2 L h<sup>-1</sup>. The reactor contained a thin layer of the catalyst powder (30 mg) placed on the surface of a wide-pore glass frit. Chromatographic data were used to determine the alcohol conversion (X, %), selectivity (S, %), and the mean product formation rate (N, mol g<sup>-1</sup> h<sup>-1</sup>).

## RESULTS AND DISCUSSION

The catalytic activity of the samples was estimated for reactions of isobutanol in the temperature range from 473 to 673 K. Isobutanol dehydration into isobutene and isobutanol dehydrogenation yielding isobutanal occur simultaneously on the initial  $\text{Me}_{0.5}\text{Zr}_2(\text{PO}_4)_3$  surface. The main alcohol conversion pathway is dehydration, characterized by an olefin formation selectivity of 85–95% at 550–670 K. The total isobutanol conversion at T=663K does not exceed 55% for  $\text{Ni}_{0.5}\text{Zr}_2(\text{PO}_4)_3$  and 35% for  $\text{Co}_{0.5}\text{Zr}_2(\text{PO}_4)_3$ .

The treatments of the catalyst with the RF hydrogen plasmas increase the total alcohol conversion by a factor of ~1.5 – 6 (table 1).

The catalyst surface activation enhancing the acidity function of the double phosphate is due to the change in the morphology of the outer layers and, possibly, to the significant increase in the number of acidic groups, whose interaction with the phosphate framework weakens. The plasma generated more defects on the surface. This assumption is confirmed by the  $\text{CO}_2$  adsorption data [8].

**Table 1.**

Catalytic activity of  $\text{Me}_{0.5}\text{Zr}_2(\text{PO}_4)_3$ : total conversion of isobutanol ( $W$ , %), selectivity, activation energies ( $E_a$ ) and logarithm of prefactors ( $\ln N_0$ ) in isobutanol dehydration

Me	Treatment	$W_{643}$ , %	$S_{643}$ , %	$E_a$ , kJ/mol	$\ln N_0$
Ni	initial	27	95	76	-5
	FR ( $\text{H}_2$ ) plasma	53	87	93	-2
Co	initial	10	96	86	-3,7
	FR ( $\text{H}_2$ ) plasma	75	86	86	-1,7

## CONCLUSION

It was investigated the hydrogen RF-plasma treatment effects on the catalytic activity of the nickel- and cobalt zirconium phosphate  $\text{Me}_{0.5}\text{Zr}_2(\text{PO}_4)_3$  in isobutanol dehydration and dehydrogenation. It was established that the dominant reaction occurring on the untreated sample is alcohol dehydration. The catalyst treated with the  $\text{H}_2$ -RF plasma shows a ~2-6 time higher activity in dehydration. These plasma treatment effects are due to the activation of the phosphate surface through an increase in the number of adsorption and catalysis sites and in their accessibility to the alcohol molecules under going adsorption and chemical reaction.

## Acknowledgement

This work was partially supported by the PFUR grants (Project no. 011615-0-000).

## REFERENCES

- [1] L. Puech, C. Cantau, P. Vinatier, G. Toussaint, P. Stevens, *Journal of Power Sources*, 2012, **214**, 330-336
- [2] V.A. Sadykov, S.N. Pavlova, G.V. Zabolotnaya, et al., *Kinetika and Catalysis*, 2001, **42**, 432-441.
- [3] A.I. Pylinina, I.I. Mikhaleenko, M.M. Ermilova, N.V. Orekhova, V.I. Pet'kov, *J. Rus. Phys. Chem.A*, 2010, **84**, 400-404.
- [4] A. I. Pylinina and I. I. Mikhaleenko, *Russ. J. of Phys. Chem. A*, 2011, **85** (12), 2109-2114.
- [5] M.V. Sukhanov, M.M. Ermilova, N.V. Orekhova, V.I. Pet'kov, G.F. Tereshchenko, *Russ. J.Appl.Chem.*, 2006, **79**, 622-626.
- [6] A. I. Pylinina, E. I. Povarova, I. I. Mikhaleenko, T. V. Yagodovskaya, *Russ. J. Phys. Chem. A*, 2013, **87** (6), 929-934.

- [7] V.D. Yagodovskii, *Russ. J. Phys. Chem. A*, 2015, **89**, 2022–2031.
- [8] M.N. Danilova, A.I. Pylina, E.M. Kasatkin, I.G. Bratchikova, I.I. Mikhalenko, and V.D. Yagodovskii, *Kinetika and Catalysis*, 2015, **56** (4), 476–479

## **SODIUM-DOPED GRAPHITIC CARBON NITRIDE: PHOTOCATALYTIC AND ADSORPTION PROPERTIES**

M. Fronczak, M. Krajewska and M. Bystrzejewski

*University of Warsaw, Faculty of Chemistry,  
Pasteura 1, 02-093 Warsaw, Poland(macfro@gmail.com)*

### **ABSTRACT**

In the presented work, materials based on the graphitic carbon nitride were studied. The materials were obtained via thermal polycondensation of cyanamide at 550°C with the addition of sodium chloride. The obtained products were investigated as a photocatalyst in the degradation of methyl orange. The band gap of the products was determined by the Kubelka-Munk method. Moreover, the adsorption properties in reference to methyl blue were also studied. The surface area of the materials was determined by the low-temperature nitrogen adsorption method. The addition of sodium chloride to the cyanamide causes poorer photocatalytic properties of the products and reduces the band gap in comparison with the unmodified carbon nitride. On the other hand, the adsorption capacity for the products obtained with sodium chloride is extremely high, in contrast to the low uptake observed for the unmodified carbon nitride.

### **INTRODUCTION**

Graphitic carbon nitride (g-C<sub>3</sub>N<sub>4</sub>) is an example of a non-metallic semiconducting material. The band gap of the material is 2.7 eV. This value is related to the wavelength of 460 nm, thus to the range of the visible light (380-780 nm). The material is yellow-orange powder, which is thermally stable up to 500°C. Moreover, graphitic carbon nitride is resistant to the weak acids and bases [1].

The synthesis of graphitic carbon nitride is carried out using a wide variety of the precursors, which comprise of carbon and nitrogen, e.g. cyanamide and melamine. The energy needed to convert these compounds to graphitic carbon nitride can be delivered by heating under non-oxidizing atmosphere [2], combustion synthesis [3] or solvothermal treatment [4]. The synthesis of material involves the polycondensation of simple compounds, which finally transforms to the polymeric structure of graphitic carbon nitride.

The graphitic carbon nitride exists in two different polymorphic types: the poly-s-triazine-based graphitic carbon nitride (gt-C<sub>3</sub>N<sub>4</sub>) (Figure 1) and poly-s-heptazine-based graphitic carbon nitride (gh-C<sub>3</sub>N<sub>4</sub>) (Figure 2).

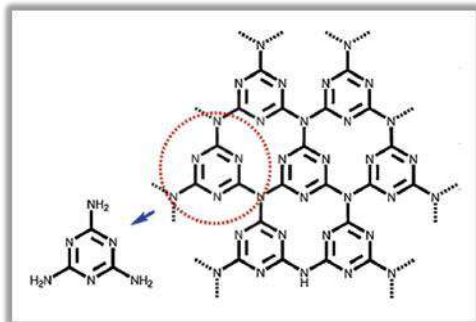


**Figure 1.** The structure of poly-s-triazine-based graphitic carbon nitride [1]

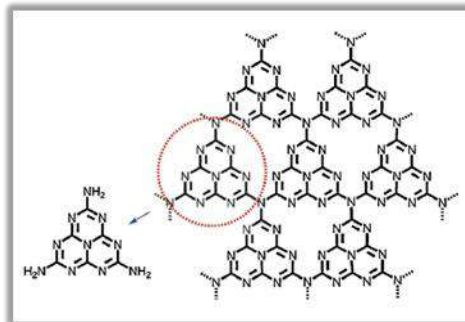


**Figure 2.** The structure of poly-s-heptazine-based graphitic carbon nitride [1]

The most prospective application of graphitic carbon nitride and its derivatives is photocatalysis, e.g. water splitting, which lead to obtain radicals from molecules of water. The radicals due to their instant reactivity are able to decompose other molecules. This phenomenon is commonly used to observe and compare efficiency of photocatalysts by decomposition of dyes [5]. The adsorption onto graphitic carbon nitride in a novel approach to the research on this material. The wide variety of compounds can be studied as a possible adsorbates, e.g. phthalates [6] and inorganic cations, e.g. copper (II) [7].

## EXPERIMENTAL

The materials were obtained by the thermal treatment of the solid mixture of sodium chloride and cyanamide under argon atmosphere at temperature of 550°C. The amount of sodium chloride was between 0 and 75 wt. %. After the synthesis the products were washed with distilled water. The products were characterized by the low-temperature adsorption of nitrogen to determine the surface area. Kubelka-Munk method of determination of band gap from diffuse reflectance spectra was also applied. The materials were studied in photodegradation of methyl orange experiments. 300ml of methyl orange solution (10mg dm<sup>-3</sup>) and 1g of studied material was put into a water-cooled glass reactor. The system was irradiated by a 400W halogen lamp (irradiation similar to visible solar spectrum). The reaction mixture was stirred by air flow. The reaction was carried out during 9 hours and petite samples (ca. 3 cm<sup>3</sup>) were taken every each 30 min. The decay of the concentration of methyl orange was observed using UV-Vis spectroscopy.

Moreover, the adsorption properties related to methyl blue were investigated. The adsorption isotherms and the kinetics curves were determined for each material. The isotherm was studied in the equilibrium concentration up to  $250 \text{ mg dm}^{-3}$  and kinetics was analyzed during 300 min.

## RESULTS AND DISCUSSION

The conversion of cyanamide to the product in each case was higher than 30% and lower than 50%. The best conversion yield was obtained for the case of synthesis without the addition of inorganic compound and was ca. 46%. So, it can be seen that the addition of sodium chloride has slightly disadvantageous influence on the conversion yield.

The specific surface area of the products is in the range of  $1 - 20 \text{ m}^2\text{g}^{-1}$  (Table 1). However, the materials, obtained with the addition of sodium chloride, demonstrate extremely high adsorption capacities related in reference to methyl blue within the range of  $200 - 650 \text{ mg g}^{-1}$ . In the case of synthesis without the addition of inorganic compound, the adsorption capacity is as low as  $10 \text{ mg g}^{-1}$ . It can be seen, that the adsorption of methyl blue onto materials is not connected with porosity. The most possible source of this high affinity between the adsorbate and the adsorbent is the electrostatic interaction between sodium ions, incorporated in the structure of the material, and the molecule of dye, which has a negative net charge in the solution.

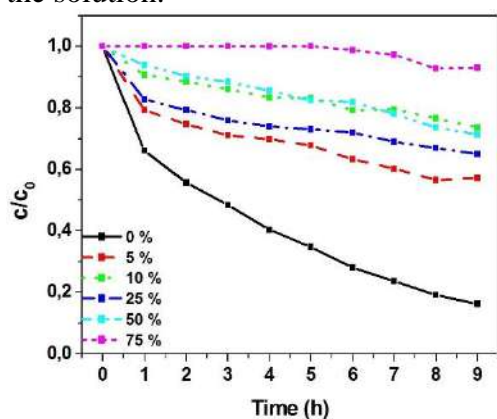


**Figure 3.** Kinetics curves of photodegradation of methyl orange

The band gap of the materials obtained with addition of sodium chloride are smaller than 2.9 eV, which is value of the band gap of the product synthesized without additions. The lowest value of 2.4 eV was determined in the product obtained with the addition of sodium chloride with 25% 50% and 75 wt. %. Thus, the content of sodium chloride has the influence on the photocatalytic properties of graphitic carbon nitride. Fig. 3 shows the photodegradation curves of methyl orange.

It can be seen that addition of sodium chloride to cyanamide causes weaker photocatalytic properties of the synthesized materials.

All mentioned properties of the obtained materials are summarized in Table 1.

**Table 1.** Results of experiments.

Amount of sodium chloride in the mixture (%)	Conversion of cyanamide to product(%)	Surface area ( $\text{m}^2 \text{g}^{-1}$ )	Adsorption capacity ( $\text{mg g}^{-1}$ )	Band gap (eV)
0	$46 \pm 2$	19	10	2.9
5	$37 \pm 5$	20	200	2.6
10	$39 \pm 6$	8	400	2.6
25	$35 \pm 5$	8	250	2.4
50	$43 \pm 7$	1	650	2.4
75	$40 \pm 8$	6	200	2.4

## CONCLUSION

The addition of sodium chloride to the synthesis of materials based on graphitic carbon nitride is an elegant method of obtaining the adsorbent dedicated to removal of methyl blue from aqueous solutions. On the other hand, the inclusion of sodium chloride weakens their photocatalytic properties.

The material and the method of synthesis are the subjects of the patent application (Poland) no. P.417123.

## Acknowledgement

This work was supported by the National Centre for Research and Development (Poland) through the project LIDER 527/L-4/2012

## REFERENCES

- [1] Y. Wang, X. Wang, M. Antonietti, *Angewandte Rev.*, 2012, **51**, 68-89
- [2] E. Kroke, *Angewandte Chem. Int. Ed.*, 2014, **53**, 11134-11136
- [3] S. Dyjak, W. Kiciński, A. Huczko, *J. Mater. Chem. A*, 2015, **3**, 9621–9631
- [4] Z. Zhang et al., *J. Am. Chem. Soc.*, 2001, **123**, 7788
- [5] G. Dong, Y. Zhang, Q. Pan, J. Qiu, *J. Photochem. Photobiol C: Photochem. Rev.*, 2014, **20**, 33-50
- [6] M. Wang, X. Yang, W. Bi, *J. Sep. Sci.*, 2014, **38**, 445-452
- [7] E. Z. Lee et al., *Chem. Comm.*, 2012, **48**, 3942-3944

## OPTICAL AND PHOTOCATALYTIC PROPERTIES OF ZnO:SnO<sub>2</sub> COMPOSITE

S. Marković<sup>1</sup>, A. Stanković<sup>1</sup>, Lj. Veselinović<sup>1</sup>, S. Stojadinović<sup>2</sup>,  
J. Dostanić<sup>3</sup>, S. Škapin<sup>4</sup> and D. Uskoković<sup>1</sup>

<sup>1</sup>*Institute of Technical Sciences of SASA, Knez Mihailova 35/IV, 11000 Belgrade, Serbia. (smilja.markovic@itn.sanu.ac.rs)*

<sup>2</sup>*University of Belgrade, Faculty of Physics, Belgrade, Serbia.*

<sup>3</sup>*University of Belgrade, IChTM Center for catalysis, Belgrade, Serbia.*

<sup>4</sup>*Jožef Stefan Institute, Ljubljana, Slovenia.*

### ABSTRACT

ZnO:SnO<sub>2</sub> composite powder, in 0.9:0.1 molar ratio, was prepared by high-energy ball milling. The phase composition and crystal structure of the prepared powder were determined by X-ray diffraction (XRD), the particles morphology was characterized using field emission scanning electron microscopy (FE-SEM), while the optical properties were studied by UV-Vis diffuse reflectance (DRS) and photoluminescence (PL) spectroscopy. The photocatalytic activity of 0.9ZnO:0.1SnO<sub>2</sub> powder was examined through decomposition of methylene blue (MB) water solution under: (1) direct sunlight irradiation, (2) UV lamp and (3) lamp which simulates sunlight. 0.9ZnO:0.1SnO<sub>2</sub> composite shows good photocatalytic activity, for all the irradiation sources, being higher than 90 % after 1 h of irradiation.

### INTRODUCTION

Water pollution caused by discharging of untreated industrial waste is one of the increasing problems that the world is facing today. The main classes of water pollutants are heavy metals, inorganic, and organic compounds. Heterogeneous photocatalysis can be used as an effective process for the decomposition of many kinds of organic pollutants without any trace of secondary pollution [1]. ZnO, TiO<sub>2</sub> and SnO<sub>2</sub> are recognized as useful materials for photocatalytic degradation process due to their high photoactivity, low cost and chemical inertness. However, their practical application for the degradation of organic pollutants is restricted by the high degree of electrons and holes recombination. Such disadvantage can be overcome to some level by coupling of semiconductors with different band gap energies. For example, ZnO:SnO<sub>2</sub> composite material show improved photocatalytic efficiency by lowering the electron-hole recombination [2].

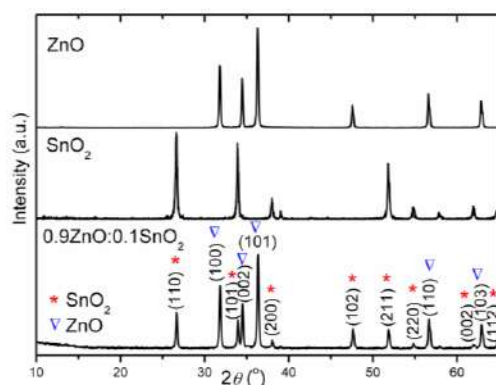
## EXPERIMENTAL

ZnO:SnO<sub>2</sub> composite was prepared by high-energy ball milling of ZnO (99%, Sigma-Aldrich) and SnO<sub>2</sub> (> 99%, Kemika, Zagreb) powders in a 0.9:0.1 molar ratio. The oxides were milled during 2 h in planetary ball mill (Across International PQ-NO4) with stainless steel vessels (100 ml) and balls (∅ 5 mm). The balls to powder weight ratio was 10:1. The angular velocity of the vessels was 400 rpm.

The phase composition and crystal structure were analyzed by XRD data, collected on a Philips PW-1050 over 10–70° 2θ (step size 0.05° 2θ and counting time 5 s). The particles morphology was observed by FE-SEM (SUPRA 35 VP Carl Zeiss). The UV-Vis DRS were recorded in the range 300–800 nm (Evolution 600 UV-Vis spectrophotometer, Thermo Scientific). PL spectra were recorded on Horiba Jobin Yvon Fluorolog FL3–22 **spectrofluorometer** using Xe lamp excitation (wave length 325 nm).

The photocatalytic activity was studied by the decomposition of methylene blue (MB) dye under: direct sunlight, UV lamp (medium-pressure mercury vapor UV lamps, UVA region, Philips, 4x15 W) and lamp which simulates sunlight (Osram Ultra Vitalux lamp, 300 W). In each of the experiments 100 mg of a powder was mixed with 100 ml of MB (10 ppm). Prior to irradiation, the suspension was magnetically stirred for 1 h in a dark to establish an adsorption-desorption equilibrium. During the irradiation stirring was maintained to keep the mixture in suspension. At specific time intervals 3 ml of aliquots was withdrawn and centrifuged (8000 rpm, 10 min) to remove particles from solution before the absorbance measurement. The concentration of MB after decomposition was calculated according to the absorbance value at 665 nm determined on a GBC Cintra UV–Vis spectrophotometer in the wavelength range of 300–800 nm.

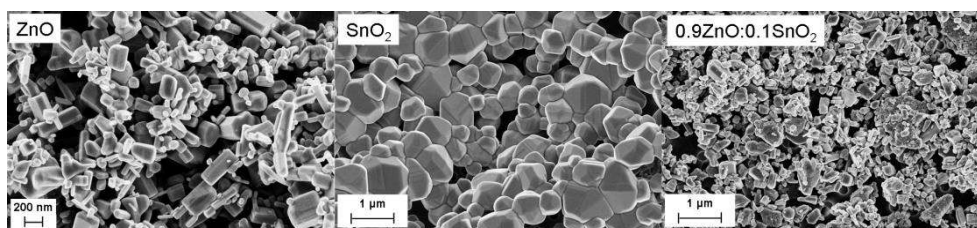
## RESULTS AND DISCUSSION



**Figure 1.** XRD patterns.

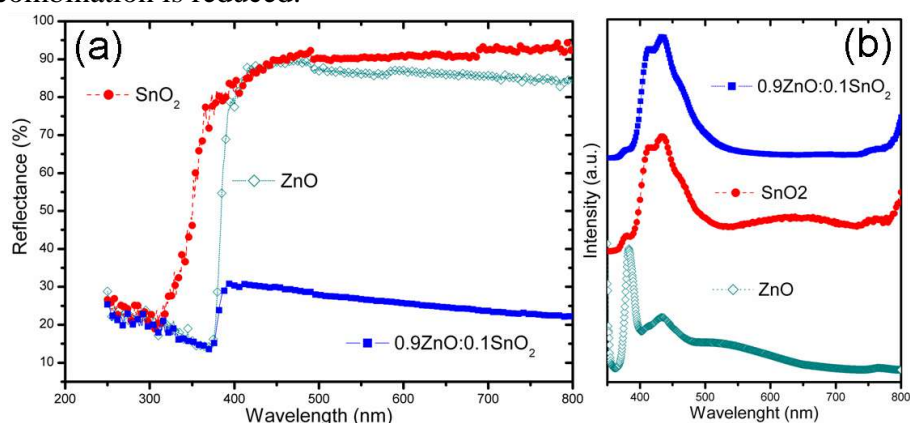
Figure 1. represents the XRD patterns of ZnO, SnO<sub>2</sub> and 0.9ZnO:0.1SnO<sub>2</sub> powders. The patterns indicate that after 2 h of mechanical treatment of the reactants mixture, resulting powder is consisted of hexagonal wurtzite (ZnO) phase and tetragonal cassiterite (SnO<sub>2</sub>) phase. There are no extra peaks of any other crystal phases or impurities.

Figure 2. shows the FE-SEM images of ZnO, SnO<sub>2</sub> and 0.9ZnO:0.1SnO<sub>2</sub> powders. The ZnO particles were mainly of irregular hexagonal rod-shapes with the average diameter of about 95 nm and the average length of about 180 nm. The SnO<sub>2</sub> powder is consisted of coarsen polygonal grains with average size of about 600 nm; besides, the grains were organized in agglomerates of about 2 μm sizes. It can be seen that after 2 h of milling SnO<sub>2</sub> agglomerates were broken and the powders have been homogenized. The average particle size in 0.9ZnO:0.1SnO<sub>2</sub> powder is about 160 nm.



**Figure 2.** FE-SEM images of the examined powders.

The optical properties of the powders, examined by UV-Vis DRS, are presented in Figure 3 (a). The direct band gap energies, calculated by the Kubelka–Munk method, are 3.25, 3.56 and 3.24 eV for ZnO, SnO<sub>2</sub> and 0.9ZnO:0.1SnO<sub>2</sub> powders, respectively. In the visible light region, 400 to 800 nm, composite particles revealed the highest absorbance capacity. PL spectra of ZnO, SnO<sub>2</sub> and composite powder are shown in Figure 3 (b). For all the samples two emission bands appeared at 382 and 433 nm, attributed to exciton recombination and oxygen vacancies, respectively. According to the PL spectra it can be concluded that concentration of oxygen vacancies is larger in the composite than in the ZnO powder, while number of exciton recombination is reduced.



**Figure 3.** (a) UV-Vis DRS and (b) PL spectra of the examined powders.

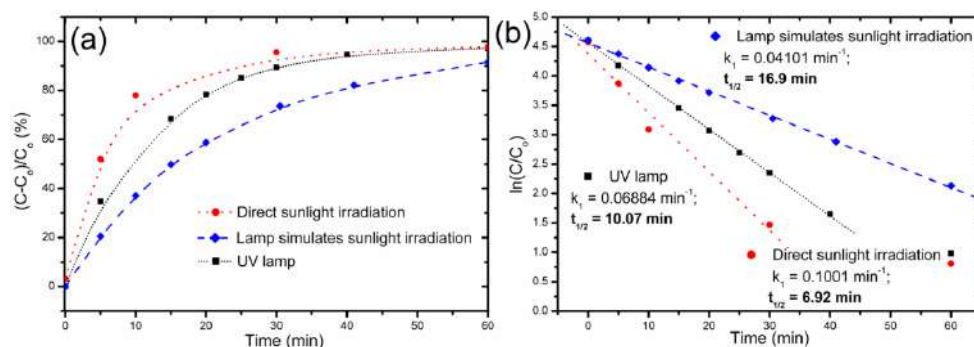


**Figure 4.** (a) Photocatalytic efficiency and (b) kinetic plot for the degradation of MB in the presence of 0.9ZnO:0.1SnO<sub>2</sub> composite powder.

Figure 4 (a) shows the efficiency of the photocatalytic degradation of MB dye in the presence of the composite under different irradiation sources. The composite shows photocatalytic activity higher than 90% after 1h of irradiation, for all the irradiation sources. Figure 4 (b) shows a linear plot of  $\ln(C/C_0)$  versus irradiation time, suggesting pseudo-first-order kinetics. The rate constant,  $k_1$  [ $\text{min}^{-1}$ ], and the time necessary for the degradation of 50% of the dye,  $t_{1/2}$  [min], are calculated and denoted in Figure 4 (b).

## CONCLUSION

0.9ZnO:0.1SnO<sub>2</sub> composite prepared by a mechanical milling is consisted of particles with significant amount of oxygen vacancies. The band gap energy of 0.9ZnO:0.1SnO<sub>2</sub> composite is 3.24 eV; in the Vis range it absorbs about 70% of the incident light intensity. The oxygen vacancies enhanced visible-light absorption and promoted photocatalytic activity under direct sunlight irradiation. Due to the difference in the band gap energy of ZnO and SnO<sub>2</sub>, photo-generated electrons and holes were effectively separated in 0.9ZnO:0.1SnO<sub>2</sub> composite, which also improved photocatalytic efficiency.

## Acknowledgement

This study was supported by the Ministry of Education, Science and Technological Development of the Republic of Serbia under Grant no III45004.

## REFERENCES

- [1] Hamrouni, H. Lachheb, A. Houas, *Materials Science and Engineering B*, 2013, **178**, 1371-1379.
- [2] R. Lamba, A. Umar, S. K. Mehta, S. K. Kansal, *Talanta*, 2015, **131**, 490-498.

## EFFECT OF NICKEL SALTS ON THE DISPERSION OF NICKEL AND REDUCIBILITY OF SUPPORTED Ni-Mg CATALYST PRECURSORS PREPARED BY PRECIPITATION-DEPOSITION

M. Stanković<sup>1</sup>, J. Krstić<sup>1</sup>, V. Radonjić<sup>1</sup>, D. Lončarević<sup>1</sup>, M. Gabrovska<sup>2</sup>,  
D. Nikolova<sup>2</sup> and S. Pavlović<sup>3</sup>

<sup>1</sup>*University of Belgrade, Institute of Chemistry, Technology and Metallurgy, Njegoševa 12, 11000 Belgrade, Serbia, (mikastan@nanosys.ihtm.bg.ac.rs).*

<sup>2</sup>*Institute of Catalysis, Bulgarian Academy of Sciences, Acad. G. Bonchev, str., bl. 11, Sofia 1113, Bulgaria.*

<sup>3</sup>*University of East Sarajevo, Faculty of Technology, Karakaj 34a, 75400 Zvornik, Republic of Srpska, Bosnia and Herzegovina.*

### ABSTRACT

Diatomite supported Ni-Mg catalyst precursors (Ni-Mg/D) with a constant Ni/Mg ratio, prepared by the precipitation-deposition method using different nickel salts, sulfamate, nitrate, chloride, acetate or formate, were studied by hydrogen chemisorptions and temperature programmed reduction (H<sub>2</sub>-TPR). The results showed that the dispersion of nickel and the reducibility of the prepared catalyst precursors were different depending upon the counter ion of nickel salt. Among the studied nickel salts, the best results for the dispersion of metallic Ni and reducibility of Ni-Mg/D catalyst precursors were achieved using nickel sulfamate salt.

### INTRODUCTION

The common procedure for the preparation of supported nickel catalysts requires different successive operations: (i) introduction of suitable nickel salt on the support by the appropriate preparative method, (ii) drying, and (iii) reduction. Precipitation-deposition (PD) is the simplest method of preparation for supported catalysts with high nickel loading. Although this method allows a homogeneous distribution of nickel salt on the support, the best dispersion of nickel does not achieve due to its high loading in the catalyst.

In the hydrogenation processes, a catalyst with high activity and selectivity is required. To meet these requirements, the catalyst support should provide sufficient surface area for the metal to disperse, and there must be an adequate metal-support interaction. The nickel phase on different support surfaces exhibits different extents of metal-support effects. The

metal-support interaction is generally affected by the identity of the nickel salt and the thermal treatment reduction procedure used in preparation. This implies that the surface properties of a catalyst could be changed by the nature of the supported Ni phase, thus acquiring different characteristics and exhibiting different performances toward activity and selectivity.

In this paper, Ni dispersion and reducibility in Ni-Mg/D hydrogenation catalyst precursors, prepared according to the same preparation procedure using different Ni salts, were studied by H<sub>2</sub>-chemisorption and H<sub>2</sub>-TPR to elucidate the effect of nickel salt on the studied characteristics.

## EXPERIMENTAL

Diatomite supported Ni-Mg catalyst precursors were prepared by the PD method, using five different nickel salts: nickel(II) sulfate, nickel(II) nitrate, nickel(II) chloride, nickel(II) acetate or nickel(II) formate. The catalyst precursors derived from these Ni salts were designated as follows: NiS-Mg/D, NiN-Mg/D, NiC-Mg/D, NiA-Mg/D and NiF-Mg/D. A detailed description of the preparation procedure of studied catalyst precursors was given in our previous paper [1].

*Hydrogen chemisorption - Pretreatment procedure:* The first step was cleaning the gas line with argon. The second step is pretreatment with 4.9% H<sub>2</sub>/Ar (flow: 20 cm<sup>3</sup> min<sup>-1</sup>; heating rate: 2 °C min<sup>-1</sup>) at 430 °C. Finally, temperature programmed desorption at 425 °C is carried out with argon.

*Analysis:* After pretreatment, the catalyst precursor sample was subjected to a known number of calibrated pulses of pure H<sub>2</sub> at 45 °C.

*Temperature programmed reduction - H<sub>2</sub>-TPR runs* were performed with 4.9 vol% hydrogen in argon (flow: 20 cm<sup>3</sup> min<sup>-1</sup>; heating rate: 2 °C min<sup>-1</sup>), the hydrogen consumption was measured by thermal conductivity detector (TCD) in temperature range 50-900 °C. TPR profiles were normalized to the same catalyst precursor mass.

Hydrogen chemisorption and temperature programmed reduction (H<sub>2</sub>-TPR) measurements were performed in an automatic apparatus Thermo Scientific TPDRO 1100.

## RESULTS AND DISCUSSION

### *H<sub>2</sub> chemisorption results*

Nickel loading, BET surface area, and nickel phase characteristics obtained from H<sub>2</sub>-chemisorption data are given in Table 1. The chemisorption results show that the nickel phase characteristics are affected by the counter ion of the Ni salt. From the data presented in Table 1, all prepared catalyst precursors can be divided in two groups: group A containing the catalyst precursors having acceptable dispersion characteristics (NiS-Mg/D, NiN-

Mg/D and NiC-Mg/D), and group B with the catalyst precursors having poor dispersion features (NiA-Mg/D and NiF-Mg/D).

Generally, under the selected experimental conditions for all prepared

**Table 1.** Nickel loading, BET surface area and H<sub>2</sub>-chemisorption data

Catalyst precursors			Nickel phase characteristics (Ni <sup>0</sup> )				
Designation	Ni <sup>a</sup> wt%	S <sub>BET</sub> <sup>b</sup> m <sup>2</sup> g <sup>-1</sup>	H <sub>2</sub> uptake <sup>c</sup> μmol g <sub>cat p</sub> <sup>-1</sup>	S <sub>Ni</sub> <sup>d</sup> mNi <sup>2</sup> gNi <sup>-1</sup>	Ni <sub>mpd</sub> <sup>e</sup> nm	Ni <sub>s</sub> × 10 <sup>-23</sup> g At <sub>Ni acc</sub> g <sub>cat p</sub> <sup>-1</sup>	D <sup>h</sup> %
NiS-Mg/D	34.99	255	161.7	36.2	18.6	1.95	5.4
NiN-Mg/D	36.32	224	132.7	28.6	23.6	1.60	4.3
NiC-Mg/D	36.20	208	158.3	34.2	19.7	1.91	5.1
NiA-Mg/D	36.64	223	94.8	20.3	33.3	1.14	3.0
NiF-Mg/D	36.57	177	89.1	19.1	35.3	1.07	2.9

<sup>a</sup> Determined gravimetrically; <sup>b</sup> N<sub>2</sub>-physisorption; <sup>c</sup> Hydrogen chemisorbed; <sup>d</sup> Nickel surface area; <sup>e</sup> Mean particle diameter of nickel (spheres) assuming stoichiometry H/Ni<sub>s</sub>=1; <sup>h</sup>Number of accessible nickel atoms; <sup>h</sup>Dispersion degree.

catalyst precursors, a low Ni dispersion was achieved. It is more likely that the main reason is the high nickel loading of prepared catalyst precursors[2]. A good agreement between the BET surface areas of catalyst precursors and active metal surface areas of metallic nickel phase suggests that larger total surface areas allow better distribution of metallic nickel phase.

### H<sub>2</sub>-TRP results

The TPR profiles of catalyst precursors, including the deconvolution curves, are shown in Fig. 1. It is very complicated to attribute the reduction peaks to the transformation of corresponding nickel(II) phases by analyzing the reduction profiles. It is more likely that different extents of metal-support are responsible for the complicated profiles. A peak due to the reduction of the Ni<sup>2+</sup> phase, which corresponds to the basic nickel carbonate (BNC) decomposition, was seen only in the catalyst precursors of group A (Fig. 1a). Among the prepared catalyst precursors, the relative content of Ni<sup>2+</sup> phase from BNC decreased in the following order:



The stronger interaction of Ni<sup>2+</sup> phase with support hinders the reduction of catalyst precursors. This leads to a shift in the T<sub>max</sub> value of peaks corresponding to the reduction of Ni<sup>2+</sup> phases interacting with the support from 320 °C over NiS-Mg/D catalyst precursor to 462 °C over NiA-Mg/D catalyst precursor (Fig. 1a and b). From TPR study, it can be concluded that

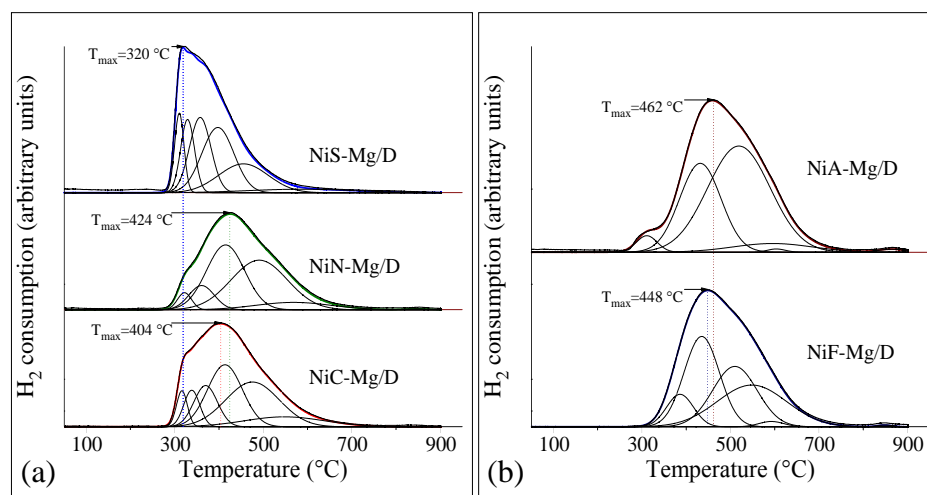


**Figure 1.** TPR profiles of prepared Ni-Mg/D catalyst precursors

two kinds of  $\text{Ni}^{2+}$  phase were observed on the diatomite support, one in which  $\text{Ni}^{2+}$  interacts with support and the other as  $\text{Ni}^{2+}$  (BNC) with no or very weak metal-support interaction.

## CONCLUSION

$\text{H}_2$ -chemisorption and  $\text{H}_2$ -TPR characterization methods were utilized for determining metallic nickel phase characteristics and reducibility of prepared diatomite supported Ni-Mg hydrogenation catalyst precursors by precipitation-deposition using different nickel salts. The chemisorption results showed that the metallic Ni phase properties in the catalyst precursors are affected by the counter ion of nickel salt. The TPR study revealed that the reduction features depend on the nature of nickel salt and its interaction with the support. An order of the nickel salts effect on the reducibility of catalyst precursors was established.

## Acknowledgement

This work was supported by the Ministry of Education, Science and Technological Development of the Republic of Serbia (Project III 45001).

## REFERENCES

- [1] M. Stanković, V. Radonjić, J. Krstić, D. Marinković, Proc. Phys. Chem., 2014, **I**, 284-287.
- [2] M.P. González-Marcos, J. I. Gutiérrez-Ortiz, C. González-Ortiz de Elguea, J. A. Delgado, J. R. González-Velasco, Applied Catalysis A: General, 1997, **162**, 269-280.

## EFFECT OF BASICITY ON THE CATALYTIC PERFORMANCE OF HETEROGENEOUS CATALYSTS FOR BIODIESEL PRODUCTION

D. Marinković, M. Stanković and D. Jovanović

*University of Belgrade, Institute of Chemistry, Technology and Metallurgy, Njegoševa 12, 11000 Belgrade, Serbia. (dalibor@ihtm.bg.ac.rs)*

### ABSTRACT

In a heterogeneous base methanolysis of vegetable oils, among of the most important characteristics of the catalysts are the basicity and the availability of basic centers. The impact of these factors on the catalytic activity was investigated in the reaction of sunflower oil methanolysis by CaO/ $\gamma$ -Al<sub>2</sub>O<sub>3</sub> catalyst. The particle morphology of CaO-dispersed onto  $\gamma$ -Al<sub>2</sub>O<sub>3</sub> surface was analyzed by field emission scanning electron microscopy (FESEM), while basicity and basic strength of prepared catalysts were determined using Hammett indicators method. The results showed a strong dependance of catalytic activity on its basicity. The catalyst with the highest basicity was the most active, and decreasing basicity reduces activity of the catalyst. In addition, it was shown that the catalyst activity depends on the favorable spatial distribution of basic sites, i.e. of their availability.

### INTRODUCTION

Fatty acid methyl esters (FAMES) - biodiesel, produced from renewable resources such as vegetable oils or animal fats is expected to be one of the biomass-based alternative for fossil diesel fuel, due to its numerous advantages.

The usual method of biodiesel production is based on triacylglycerols methanolysis to FAMES using homogeneous base catalysts. Heterogeneous solid base catalyzed processes are nowadays very promising alternatives for biodiesel production from vegetable oils [1]. Using the Ca-based catalysts for the biodiesel production is well known [2], particularly good results were obtained by loading of CaO on alumina carrier [3]. As this is a heterogeneous solid base catalyzed reaction, one of the most important factors affecting the reaction yield is catalyst basicity and the availability of basic sites on its surface.

The aim of this study was to examine the effect of basicity and basic sites distribution on the catalyst activity in the methanolysis of sunflower oil over the CaO/ $\gamma$ -Al<sub>2</sub>O<sub>3</sub> catalyst.

## EXPERIMENTAL

### Catalyst preparation

CaO/ $\gamma$ -Al<sub>2</sub>O<sub>3</sub> catalysts were prepared according to the modified wet impregnation (MWI) method [4], using Ca(CH<sub>3</sub>COO)<sub>2</sub> as precursor salt,  $\gamma$ -Al<sub>2</sub>O<sub>3</sub> (spherical shape) as support, and deionized water as medium. The sample designation, CaO content and preparation procedure are shown in Table 1.

**Table 1.** CaO content and preparation procedure for CaO/ $\gamma$ -Al<sub>2</sub>O<sub>3</sub> samples

Sample		Preparation procedure			
Designation	CaO* (wt%)	MWI		Calcination conditions	
		C <sub>CaAc</sub> <sup>a</sup> (wt%)	t <sub>WI</sub> <sup>b</sup> (h)	t <sub>c</sub> <sup>c</sup> (h)	T <sub>c</sub> <sup>d</sup> (°C)
Ca-500/ $\gamma$ -Al <sub>2</sub> O <sub>3</sub>	4.2	25	2	4	500
Ca-550/ $\gamma$ -Al <sub>2</sub> O <sub>3</sub>	4.4	25	2	4	550
Ca-600/ $\gamma$ -Al <sub>2</sub> O <sub>3</sub>	4.1	25	2	4	600
Ca-650/ $\gamma$ -Al <sub>2</sub> O <sub>3</sub>	4.2	25	2	4	650
Ca-700/ $\gamma$ -Al <sub>2</sub> O <sub>3</sub>	5.5	25	2	4	700
Ca-750/ $\gamma$ -Al <sub>2</sub> O <sub>3</sub>	5.3	25	2	4	750

\*Determined gravimetrically as CaC<sub>2</sub>O<sub>4</sub>·H<sub>2</sub>O; <sup>a</sup>CaAc - Ca(CH<sub>3</sub>COO)<sub>2</sub>; <sup>b</sup>Impregnation time; <sup>c</sup> Calcination time; <sup>d</sup>Calcination temperature.

*Catalyst characterization* - FESEM was carried out on a Tescan MIRA3 XMU with accelerating voltage of 10 kV. Samples were placed over an aluminum drum and covered with an Au and Pt film. Basic strength and basicity ( $H_-$ ) were determined using volumetric titration with the Hammett indicators. The following Hammett indicators were used: neutral red ( $H_-$ =6.8), phenolphthalein ( $H_-$ =9.3), **thymolphthalein** ( $H_-$ =9.9) and thymol violet ( $H_-$ =11.0).

*Methanolysis procedure* - The activity of the prepared catalysts was examined in the methanolysis of sunflower oil. All methanolysis reactions were performed in a 250 ml three-neck glass flask equipped with a reflux condenser and a magnetic stirrer. Experiments were conducted under the following conditions: catalyst loading of 0.5 wt. % CaO (relative to the amount of oil), methanol/oil molar ratio of 12/1, at temperature of 60 °C and reaction time of 5 h.

## RESULTS AND DISCUSSION

Loading CaO to  $\gamma$ -Al<sub>2</sub>O<sub>3</sub> carrier and subsequent calcination leads to the formation of cluster structure on the catalyst surface (Fig. 1). Scattered large rod-shaped crystals are present mainly on the surface of the catalyst calcined at the lowest temperature. By increasing the calcination temperature, the granular particles on the surface of catalyst become bigger. Also, it leads to the occurrence of agglomeration and clustering of particles. Evidently, on the Ca-500/ $\gamma$ -Al<sub>2</sub>O<sub>3</sub> only some cluster of irregular shape can be seen, on the

Ca-650/ $\gamma$ -Al<sub>2</sub>O<sub>3</sub> catalyst the entire surface is covered with clusters of spherical shapes, while on the catalyst calcined at the highest temperature (Ca-750/ $\gamma$ -Al<sub>2</sub>O<sub>3</sub>) spherical clusters are not visible due to massive agglomeration and sintering.

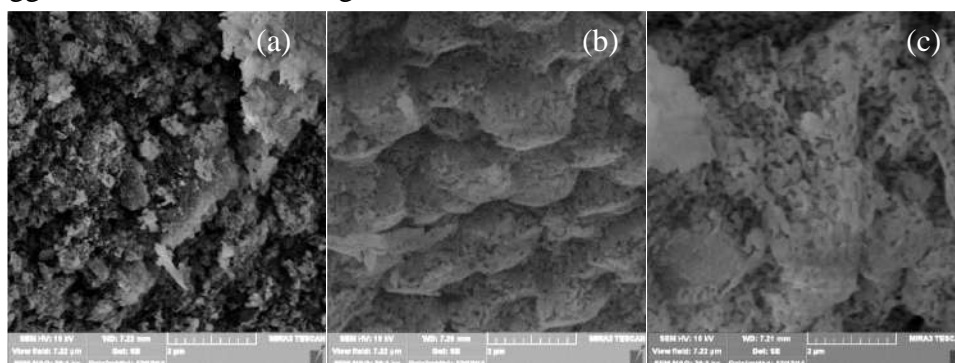


**Figure 1.** FESEM micrograph of the catalysts surface: (a) Ca-500/ $\gamma$ -Al<sub>2</sub>O<sub>3</sub>, (b) Ca-650/ $\gamma$ -Al<sub>2</sub>O<sub>3</sub> and (c) Ca-750/ $\gamma$ -Al<sub>2</sub>O<sub>3</sub>

The base strength of CaO loaded onto  $\gamma$ -Al<sub>2</sub>O<sub>3</sub> and thermally activated at different temperatures was measured by using Hammett indicators. As evident in Table 2, all catalysts are within the same range of the base strength,  $9.3 < H_- < 9.9$ . Therefore, these catalysts can be classified as materials with a medium base strength. Although belonging to the same base strength group, their basicity is not equal. Basicity of the samples increases with calcination temperature up to 700 °C at which reaches the maximum value (Table 2, Ca-700/ $\gamma$ -Al<sub>2</sub>O<sub>3</sub>). The basicity of the catalyst obtained by calcination at the highest temperature (Ca-750/ $\gamma$ -Al<sub>2</sub>O<sub>3</sub>) is lower, which is in accordance with the results of FESEM (Fig. 1). On the surface of Ca-750/ $\gamma$ -Al<sub>2</sub>O<sub>3</sub> catalyst it was observed the

**Table 2.** Basicity and basic strength ( $H_-$ ) of the CaO/ $\gamma$ -Al<sub>2</sub>O<sub>3</sub> catalysts

Sample designation	Basic strength ( $H_-$ )	Basicity (mmol g <sup>-1</sup> )
Ca-500/ $\gamma$ -Al <sub>2</sub> O <sub>3</sub>	$9.3 < H_- < 9.9$	0.036
Ca-550/ $\gamma$ -Al <sub>2</sub> O <sub>3</sub>	$9.3 < H_- < 9.9$	0.102
Ca-600/ $\gamma$ -Al <sub>2</sub> O <sub>3</sub>	$9.3 < H_- < 9.9$	0.120
Ca-650/ $\gamma$ -Al <sub>2</sub> O <sub>3</sub>	$9.3 < H_- < 9.9$	0.157
Ca-700/ $\gamma$ -Al <sub>2</sub> O <sub>3</sub>	$9.3 < H_- < 9.9$	0.298
Ca-750/ $\gamma$ -Al <sub>2</sub> O <sub>3</sub>	$9.3 < H_- < 9.9$	0.228

massive sintering of particles. With the appearance of larger particles on the catalyst surface, the number and the availability of base catalytically active sites are reduced, despite the same concentration level of catalytically active compound - CaO (Table 1).

Activity of the catalyst samples was evaluated by analysing the FAMEs yield after 5 h. As can be seen, the Fig. 2 reveals a clear correlation between FAMEs content after 5 h of the reaction and the basicity of the catalysts. The catalyst sample with the highest

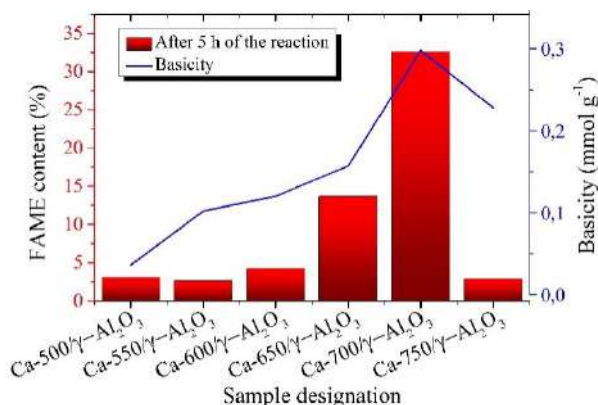


**Figure 2** Comparison of the catalytic activity and the basicity of the CaO/γ-Al<sub>2</sub>O<sub>3</sub> catalyst

basicity(Ca-700/γ-Al<sub>2</sub>O<sub>3</sub>) showed the highest activity, and the samples with the lowest basicity (Ca-500/γ-Al<sub>2</sub>O<sub>3</sub> and Ca-550/γ-Al<sub>2</sub>O<sub>3</sub>) showed the lowest activity. Despite the relatively high basicity Ca-750/γ-Al<sub>2</sub>O<sub>3</sub> catalyst did not show adequate activity, probably due to reduction of base sites space availability.

## CONCLUSION

Heterogeneous CaO/γ-Al<sub>2</sub>O<sub>3</sub> catalyst samples were synthesized by modified wet impregnation method and thermally activated under inert atmosphere. The analysis of the catalyst activity in the reaction of sunflower oil methanolysis and basicity of synthesized catalysts a correlation between basicity and catalyst activity was observed. The catalyst with higher basicity had higher activity. The exception was the catalyst thermally activated at the highest temperature in which, probably due to sintering effect that leads to agglomeration of active sites on surface causes a reduction in its activity.

## Acknowledgement

This work was supported by the Ministry of Education, Science and Technological Development of the R. of Serbia (Project III 45001).

## REFERENCES

- [1] D.M. Marinković, M.V. Stanković, A.V. Veličković, J.M. Avramović, M.R. Miladinović, O.O. Stamenković, V.B. Veljković, D.M. Jovanović, *Renewable and Sustainable Energy Reviews.*, 2016, **56**, 1387-1408.
- [2] M. Kouzu, T. Kasuno, M. Tajika, Y. Sugimoto, S. Yamanaka, J. Hidaka, *Fuel*, 2008, **87**, 2798-2806.
- [3] N. Pasupulety, K. Gunda, Y. Liu, G.L. Rempel, F.T.T. Ng, *Applied Catalysis A: General*, 2013, **452**, 189-202.
- [4] D.M. Marinković, M.V. Stanković, A.V. Veličković, J.M. Avramović, M.D. Cakić, V.B. Veljković, *Advanced Technologies*, 2015, **4**(1), 26-32.

## IDENTIFICATION OF METHOMYL PHOTOCATALYTIC DEGRADATION PRODUCTS

M. Radišić<sup>1</sup>, A. Tomašević<sup>2</sup>, D. Mijin<sup>3</sup>, A. Marinković<sup>3</sup>, Lj. Tolić<sup>1</sup> and  
M. Laušević<sup>3</sup>

<sup>1</sup>*Innovation Center, Faculty of Technology and Metallurgy, University of Belgrade, Karnegijeva 4, 11120 Belgrade, Serbia(marinar@tmf.bg.ac.rs)*

<sup>2</sup>*Institute of Pesticides and Environmental Protection, Banatska 31b,  
P.O. Box 163, 11080 Belgrade-Zemun, Serbia*

<sup>3</sup>*Faculty of Technology and Metallurgy, University of Belgrade,  
Karnegijeva 4, P.O. Box 3503, 11120 Belgrade, Serbia.*

### ABSTRACT

Photocatalytic degradation of the methomyl pesticide in aqueous suspension of TiO<sub>2</sub> using an Osram ultra-vitalux<sup>®</sup> lamp (315-400 nm) was investigated. The effect of parameters such as initial concentration of catalyst, initial methomyl concentration, and pH were studied. Complete removal of methomyl was achieved but mineralization of organic carbon was incomplete indicating the formation of methomyl degradation products. Liquid chromatography tandem mass spectrometry technique was used in order to identify the methomyl degradation products and three major degradation products have been identified.

### INTRODUCTION

Pesticides are very important class of water pollutants, especially because of their extensive application. Agricultural and urban runoffs, industrial-scale pest control operations, direct application of pesticides to control aquatic insects and vegetation, as well as their domestic usage are possible causes of water contamination by pesticides. Whereas wastewaters often contain very high level (milligram per liter or more) of pesticides, surface water and groundwater usually contain only trace amounts of pesticides (microgram per liter or less).

Methomyl,thioacetimidate is an insecticide/acaricide widely used in agriculture. It is a very toxic and hazardous compound and a pollutant of environmental concern. Because of its high solubility in water (57.9 g/L at 25°C),low Koc value and long hydrolysis DT<sub>50</sub> value [1], methomyl could be potentially carried by field runoff into surface water. Methomyl has been detected in surface and ground waters across Europe and USA not only during actual application, but also after a long period of use.

Various processes have been investigated to reduce pesticide concentrations in water, and to minimize the potential health risks. Advanced oxidation processes include catalytic and photochemical methods which use  $\text{H}_2\text{O}_2$ ,  $\text{O}_3$  or  $\text{O}_2$  as the oxidant. The principal active species in these systems is the hydroxyl radical  $\cdot\text{OH}$ , which is an extremely reactive and non-selective oxidant for organic contaminants [2]. Among different methods, the process of heterogeneous photocatalytic degradation has been suggested as an attractive way for the treatment of water polluting pesticides, due to the cost effective and non-toxic nature [3, 4].

The objective was to identify potential degradation products of methomyl photocatalytic degradation in aqueous suspension of  $\text{TiO}_2$ . A identification of pesticide degradation products is of interest because these products will often possess activities and lifetimes different from the parent compound. Photocalysis conditions were optimized and degradation products were identified using liquid chromatography tandem mass spectrometry (HPLC-MS/MS) analytical technique.

## EXPERIMENTAL

All chemicals used in the investigation were of reagent grade and were used without further purification. Analytical standard of methomyl (99.8%) was received from Du Pont de Nemours, USA. The photodegradation of methomyl was studied using solutions at the concentration of  $16.22 \text{ mg L}^{-1}$ .

The experiments were performed with  $0.5 \text{ g L}^{-1}$ ,  $1 \text{ g L}^{-1}$ ,  $2 \text{ g L}^{-1}$ , and  $3 \text{ g L}^{-1}$  of  $\text{TiO}_2$ . The effect of parameters such as initial concentration of catalyst, initial methomyl concentration, and pH were studied. The reactions were performed in a glass thermostated reactor (cylindrical shape, volume  $100.0 \text{ cm}^3$ ,  $20 \text{ }^\circ\text{C}$ ) with an 300 W Osram Ultra-Vitalux<sup>®</sup> lamp (UV-A:UV-B=13.6:3) placed 300 mm from the surface of the reaction mixture. The irradiation time was 60 min. At the specific time interval an appropriate samples of the suspension was withdrawn, centrifuged, and filtered through a  $0.20 \text{ }\mu\text{m}$  filter.

Photodegradation products were analysed using HPLC-MS technique. Prior to the analysis samples were filtered through  $0.2 \text{ }\mu\text{m}$  syringe filter. HPLC-MS system consisted of a Thermo Fisher Scientific (Waltham, MA, USA) apparatus including quaternary pump (Surveyor), LTQ XL mass spectrometer with liner ion trap (Thermo Scientific, USA) with electrospray interface, and Xcalibur v. 2.1 software package. Chromatographic separation was performed on the reversed-phase Zorbax Eclipse<sup>®</sup> XDB-C18 column,  $75 \times 4.6 \text{ mm (i.d.)} \times 3.5 \text{ }\mu\text{m}$  (Agilent Technologies, Santa Clara, CA, USA). Chromatographic analysis was carried out using gradient

elution and mobile phase consisted of water (A), methanol (B), and 10% acetic acid (C). Mobile phase gradient was: 0 min, B 19%, C 1%; 15 min B 50%, C 1%; 20 min B 100%; 25 min B 100%; 26 min B 19%, C 1%; 35 min B 19%, C 1%. The flow rate of the mobile phase was  $0.3 \text{ mL min}^{-1}$ . In the first step of the HPLC-MS analysis full MS spectra were recorded in the range of 50–400  $m/z$ . MS<sup>n</sup> analysis was conducted for the most abundant ions by repeated injection of the sample.

## RESULTS AND DISCUSSION

For methomyl degradation the optimal concentration of the catalysts was found to be  $2 \text{ g L}^{-1}$ . The results imply that the photodegradation rate was highest in acidic solution and lowest in alkaline solution. Under these conditions degradation of methomyl was complete after 60 min of irradiation. Ion chromatography results showed that mineralization led to the formation of sulfate, nitrate and ammonium ions during the process. Mineralization of organic carbon was incomplete and about 80% of initial total organic carbon (TOC) was removed after one hour. Because the TOC elimination rates were not proportional to the rates of methomyl removal, obtained results suggested the formation of methomyl degradation products.

Three major by-products of photocatalytical degradation have been identified: (E)-methyl-N-hydroxyethanimidothioate (methomyl oxime), By-product I ((E)-methyl-N-hydroxymethylcarbamoyloxyethanimidothioate) and By-product II ((E)-methyl-N-carbamoyloxyethanimidothioate). Mass chromatograms of methomyl and its degradation products are presented in Figure 1.

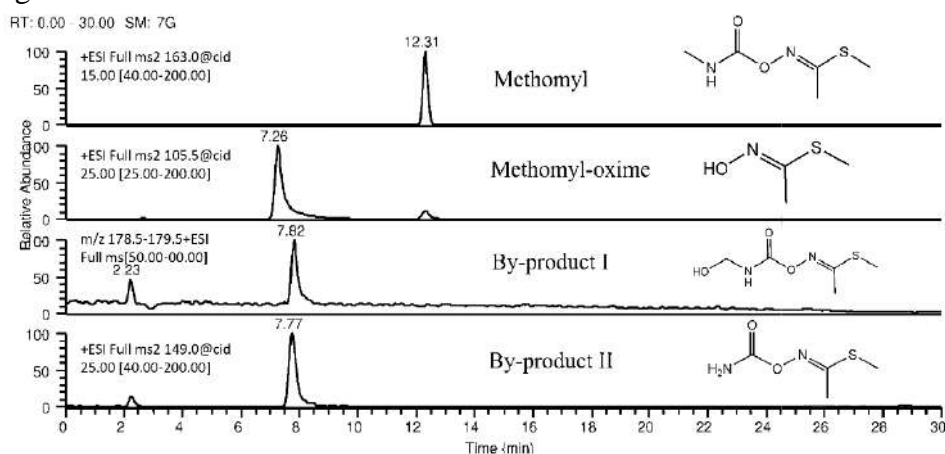


**Figure 1.** Mass chromatograms of methomyl and its degradation products.

During methomyl degradation the increase in concentration of three products: methomyl oxime (ion at  $m/z$  106), By-product I (ion at  $m/z$  179)

and By-product II (ion at  $m/z$  149), were recorded. The highest intensities of the peaks corresponding to these products are found in the period from 10 to 40 min of the reaction process.

The main degradation product found was methomyl-oxime which is always present as degradation product during methomyl photocatalytic degradation process. Hydroxylation of methyl group attached to the nitrogen atom produces By-product I, which consecutively produces By-product II through decarboxylation of hydroxylated methyl group [5]. Methomyl-oxime can be generated either from methomyl itself or from the By-product I and II through rupture of ester bond. Detected degradation products were subjected to the subsequent MS<sup>2</sup> analysis in order to confirm their identity. By-product I showed no detectable fragments in MS<sup>2</sup> spectra. On the other hand, methomyl, methomyl-oxime and By-product II showed similar fragmentation pathways which enabled their structural confirmation.

## CONCLUSIONS

The paper proves the effectiveness of the heterogeneous photocatalysis for the removal of the methomyl from water. It was found that photocatalytic reactions proceed faster in acidic than in alkaline media. During the process sulfate and nitrate ions were detected, but the mineralization of nitrogen and organic carbon was incomplete. Three major by-products have been identified and confirmed by means of liquid chromatography tandem mass spectrometry technique.

## Acknowledgement

The authors are grateful to the Ministry of Education, Science and Technological Development of the Republic of Serbia for financial support (Projects No. 172007, III 46008 and 172013).

## REFERENCES

- [1] C. D. S. Tomlin, *The Pesticide Manual*, fifteenth ed., BCPC, Hampshire, 2009. p. 757.
- [2] O.O.E. Legrini, A. M. Braun, *Chem. Rev.*, 1993, **93**(2), 671–698.
- [3] A. Tomašević, A. Kiss, E. Petrović, S. D. Mijin, *Desalination*, 2010, **262**, 228–234.
- [4] A. Tomašević, D. Mijin, S. Gašić, E. Kiss, *Desalin. Water Treat.*, 2014, **52**, 4342–4349.
- [5] S. Raut-Jadhav, D. Saini, S. Sonawane, A. Panidt, *Ultrason. Sonochem.*, 2016, **28**, 283–293.

## ONE-STEP HYDROTHERMAL SYNTHESIS OF PHOTOCATALYTICALLY ACTIVE TiO<sub>2</sub>/CARBON COMPOSITE

M. Maletić<sup>1</sup>, M. Vukčević<sup>1</sup>, A. Kalijadis<sup>2</sup>, I. Janković-Častvan<sup>1</sup>, A. Dapčević<sup>1</sup>, Z. Laušević<sup>2</sup> and M. Laušević<sup>1</sup>

<sup>1</sup>*Faculty of Technology and Metallurgy, University of Belgrade, Karnegijeva 4, 11001 Belgrade, Serbia. (mvukasinovic@tmf.bg.ac.rs)*  
<sup>2</sup>*Laboratory of Physics, Vinča Institute of Nuclear Sciences, University of Belgrade, P.O.Box 522, 11001 Belgrade, Serbia.*

### ABSTRACT

TiO<sub>2</sub>/carbon composite (TiO<sub>2</sub>/HTC), synthesized by hydrothermal carbonization, was characterized by thermogravimetric analysis, nitrogen adsorption–desorption isotherms and X-ray diffraction. The possibility of using TiO<sub>2</sub>/HTC as photocatalysts for UV and visible light assisted degradation of methylene blue in aqueous solution was examined. It was found that carbon presence in TiO<sub>2</sub>/HTC leads to the higher porosity and increase in the share of photocatalytically active anatase phase. Compared to the hydrothermally synthesized TiO<sub>2</sub>, TiO<sub>2</sub>/HTC showed the superior photocatalytic activity under UV irradiation. In addition, TiO<sub>2</sub>/HTC show high recycling ability with degradation ratio of methylene blue higher than 81 % after five cycles. Also, TiO<sub>2</sub>/HTC is expected to be a promising candidate for photocatalytic processes using visible light.

### INTRODUCTION

Photocatalytic processes, in the presence of different photocatalysts, have proven to be efficient methods for removal of organic pollutants (drugs, pesticides and organic dyes). Titanium dioxide (TiO<sub>2</sub>) is one of the most effective and the most commonly used photocatalysts. Also, highly reactive photocatalysts can be obtained by combining titanium dioxide with different carbon materials, as a catalysts carrier [1]. In this work photocatalytic activity of hydrothermally synthesized TiO<sub>2</sub>/carbon composite was examined in the process of photocatalytic degradation of methylene blue (MB) under UV and visible irradiation, and compared to photocatalytic activity of hydrothermally synthesized TiO<sub>2</sub>. The possibility of reusing TiO<sub>2</sub>/carbon composite was examined through the determination of photocatalytic activity after each of five cycles.

## EXPERIMENTAL

Hydrothermal synthesis of TiO<sub>2</sub>/carbon composite (TiO<sub>2</sub>/HTC) was carried out using titanium isopropoxide and glucose solution to achieve Ti/C molar ratio of 0.30. TiO<sub>2</sub> – hydrothermal (TiO<sub>2</sub> – hyd) was obtained by similar procedure, using water instead of glucose solution.

The thermogravimetric (TG) analysis was performed from room temperature to 800 °C in O<sub>2</sub> atmosphere using SDT Q600 instrument (TA Instruments). Nitrogen adsorption–desorption isotherms were determined using a Micromeritics ASAP 2020 instrument. From obtained data, specific surface area ( $S_{\text{BET}}$ ), pore size distribution and volume of the mesopores ( $V_{\text{meso}}$ ) was calculated. XRD spectra were recorded in the range of  $2\theta$  of 20° – 60° with a scan speed 1° C/min<sup>1</sup> using a Philips PW1710 diffractometer with CuK $\alpha$  radiation. Anatase and rutile phase content were determined [2], and grain sizes were calculated by Debye–Scherrer equation.

Photocatalytic experiments were performed at room temperature with 1 g/dm<sup>3</sup> of TiO<sub>2</sub>/HTC and the initial concentration of MB was 10 mg/dm<sup>3</sup>. The suspension was magnetically stirred in the dark for 60 min to establish the adsorption/desorption equilibrium, and then exposed to the either UV or visible irradiation. The TiO<sub>2</sub>/HTC reuse was examined through the five cycles. Concentration of MB was measured using visible spectrophotometer (Specol, Carl-Zeiss, Jena), by measuring absorbance at 675 nm.

## RESULTS AND DISCUSSION

Thermogravimetric analysis showed that TiO<sub>2</sub>/HTC contained 11.02 wt.% of carbon. Textural properties TiO<sub>2</sub> – hydrothermal and TiO<sub>2</sub>/HTC, summarized in Table 1, show that carbon present in TiO<sub>2</sub>/HTC leads to the decrease of average pore diameter and  $V_{\text{meso}}$  and to the increase in  $S_{\text{BET}}$  and  $V_{\text{micro}}$ . XRD patterns (Fig. 1) of TiO<sub>2</sub> – hydrothermal and TiO<sub>2</sub>/HTC show characteristic peaks for the anatase (101) ( $2\theta = 25.6^\circ$ ) and rutile (110) ( $2\theta = 27.7^\circ$ ) phase.

**Table 1.** Textural properties of examined samples

Sample	$S_{\text{BET}}$ , m <sup>2</sup> /g	$V_{\text{meso}}$ , cm <sup>3</sup> /g	$D_{\text{av}}^*$ , nm
TiO <sub>2</sub> -hyd	49.63	0.2375	17.22
TiO <sub>2</sub> /HTC	174.08	0.1995	3.78

$D_{\text{av}}^*$  - Average pore diameter

It can be observed that presence of carbon in TiO<sub>2</sub>/HTC induces increase of peak intensity of the anatase phase, while peak intensity of the rutile phase decreases. The observed increase of anatase phase is confirmed by the results presented in

Fig. 1. The average grain size decrease with carbon presence can be the consequence of inhibitory effect of amorphous carbon on grain growth of TiO<sub>2</sub>. Grain size decrease, accompanied with increase in BET surface area,

is in very good agreement with the values of average pore diameters, indicating that pores measured are most likely interparticle spaces.

The process of removing MB in the presence of  $\text{TiO}_2/\text{HTC}$  (shown in Fig. 2) takes place in two phases. The first phase involves the removal of MB by adsorption in the dark, while the second phase represents photocatalytic degradation of MB under UV or visible irradiation. As it can be observed (Fig. 2),  $\text{TiO}_2/\text{HTC}$  showed superior photocatalytic activity in the overall process of MB removal.

Carbon species present in  $\text{TiO}_2/\text{HTC}$  can provide more active sites and adsorb more reactive species due to large surface area and pore volume, which causes the enhanced photocatalytic activity. Additionally, high photocatalytic activity of  $\text{TiO}_2/\text{HTC}$  can be explained by the presence of photocatalytically active anatase phase and the ratio of anatase and rutile phase (Fig. 1) which is nearly identical with the one in photocatalytically active Degussa P25.

Obtained results (Fig. 2) showed that UV irradiation induces a higher decrease of MB concentration than the visible light. Nevertheless, concentration of MB was decreased for about 70 % in the presence of  $\text{TiO}_2/\text{HTC}$  and visible irradiation. The regeneration and recycling of  $\text{TiO}_2$  photocatalysts is one of key steps in practical applications of this heterogeneous photocatalysis in water purification. Therefore, an examination of the photocatalytic activity of the recycled  $\text{TiO}_2/\text{HTC}$  was carried out under UV light irradiation. The results are presented in Fig. 3.

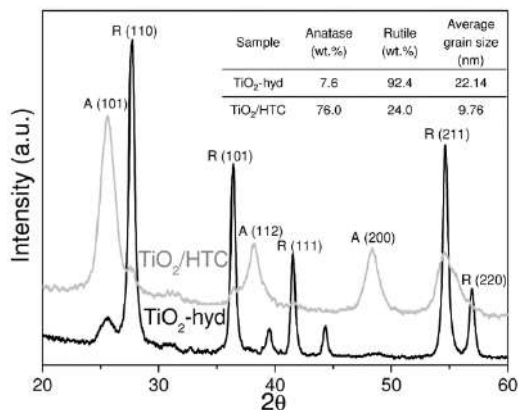


**Figure 1.** XRD patterns of obtained samples

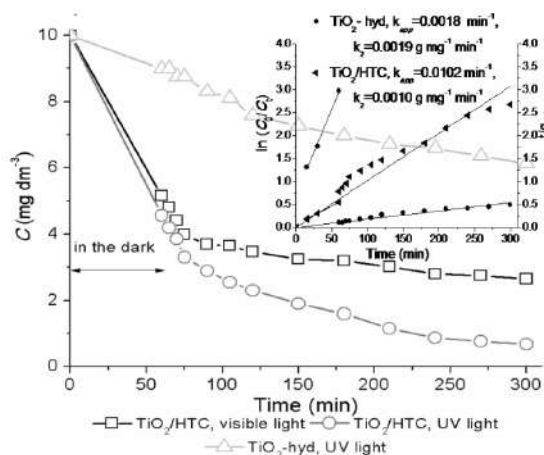


**Figure 2.** MB removal in the presence of  $\text{TiO}_2/\text{HTC}$  under the UV and visible light with embedded kinetics graph

The degradation rate in first cycle was 91.9 %, while after five cycles degradation rate was decreased to 81.2 %.

### CONCLUSION

Photocatalytically active  $\text{TiO}_2$ /carbon composite was obtained by hydrothermal carbonization, using titanium isopropoxide and glucose as a titanium and carbon precursors, respectively. It was found that photocatalytic activity increases with addition of glucose precursor solution, due to the increase in the share of photocatalytically active anatase phase in obtained  $\text{TiO}_2$ /carbon composite. Also,

carbon presence in  $\text{TiO}_2$ /HTC leads to the higher surface area, which synergistically improved the photocatalytic activity by enhancing the adsorption of the organic pollutants. Consequently,  $\text{TiO}_2$ /HTC showed the superior photocatalytic activity toward methylene blue, under UV irradiation and satisfactory photocatalytic activity under the visible light. In addition,  $\text{TiO}_2$ /HTC could be used for multiple degradation cycles with slight decrease in photocatalytic activity, as well as a promising candidate for photocatalytic processes using visible light.

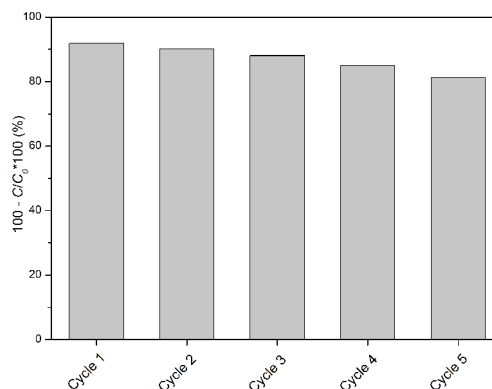


**Figure 3.** Recycle of the  $\text{TiO}_2$ /HTC<sub>4</sub> composite for the degradation of MB (initial concentration of MB  $10 \text{ mg dm}^{-3}$ , 50 ml)

### Acknowledgement

This work was supported by Ministry of Education, Science and Technological Development Republic of Serbia through the project No 172007 and No 45006.

### REFERENCES

- [1] M. Maletić, M. Vukčević, A. Kalijadis, Z. Laušević, M. Laušević, *Advances in Materials Science and Engineering*, 2015, **2015**, Article ID 803492, <http://dx.doi.org/10.1155/2015/803492>.
- [2] W. Zhao, Z. Bai, A. Ren, B. Guo, C. Wu, *Applied Surface Science*, 2010, **256**, 3493–3498.

## EXTRACTION OF CAFFEINE FROM COFFEE USING HYDRODYNAMIC CAVITATION

B. Koturević<sup>1</sup>, J. Jovanović<sup>2</sup> and B. Adnađević<sup>2</sup>

<sup>1</sup>*The Academy of Criminalistic and Police Studies, Cara Dušana 196, 11080 Belgrade, Zemun, Serbia*

<sup>2</sup>*Faculty of Physical Chemistry, Studentski trg 12-16, 11001 Belgrade, Serbia (bora@ffh.bg.ac.rs)*

### ABSTRACT

A novel rotary-pulsatory hydrodynamic cavitator was constructed. The effects of process parameters of cavitation extraction (liquid-solid ratio, solvent type, time, temperature and flow) on the degree of caffeine extraction from roasted ground coffee beans of Robusta coffee (*Coffea canephora*) were investigated. Maximal degree of caffeine extraction was achieved after one minute with water as solvent at ambient temperature. It was found that the degree of caffeine extraction increases with increasing liquid-solid ratio, flow, and temperature. Results show that hydrodynamic cavitation (HC) is inexpensive and energy efficient extraction method for the extraction of caffeine from coffee beans.

### INTRODUCTION

Coffee beans are an important source of caffeine, which is the most common consumed alkaloid in the world. Depending on the coffee variety, caffeine content averages from 12 mg/g (seeds) to over 20 mg/g [1]. For the extraction of caffeine from coffee, different techniques are applied: conventional extraction methods (heating reflux extraction and Soxhlet extraction) [2]; supercritical fluid extraction [3]; microwave-assisted extraction (MAE) [4]; ultrasonic-assisted extraction (UAE) [5]; solid phase extraction (SPE) [6]; pulsed electric energy assisted extraction, and accelerated solvent extraction (PEE). Recently, it was found that the extraction of active substances from plants materials under the conditions of negative pressure cavitation extraction (NPC) is an extremely fast, efficient and low-energy consuming method [7]. The aim of this study was to investigate the effects of different process parameters (liquid-solid ratio (LS), solvent type, time (t), temperature (T) and flow (Q)) on the degree of caffeine extraction from roasted ground coffee beans of Robusta coffee (*Coffea canephora*).

## EXPERIMENTAL

**Materials and methods:** Roasted coffee beans of *Coffea robusta* (var. India Kaapi Royale) were obtained from Cafe & Factory, Serbia. Ethanol, p.a. was purchased from Zorka Pharma, Serbia, Methanol, p.a. purchased from Poch S.a., Poland. The extraction was carried out in newly constructed hydrodynamic rotary-pulsatory cavitator.

**Extraction procedure:** Predetermined mass of coffee was added at a predefined volume of solvent to maintain desired liquid-solid ratio. A suspension was continually stirred and introduced into the cavitator under the predefined flow. At predetermined time intervals, aliquots were taken from the reaction mixtures and filtered through filter paper (Munktell, Grycksbo, Sweden). The caffeine concentration in the extract was determined by following the method proposed by Yao et al. [8]. The efficiency of extraction of caffeine was expressed as the degree of caffeine extraction:  $\alpha = C/C_{\max} * 100\%$ , where  $C$  (mg/L) is the caffeine concentration in water extract in the time interval  $t$ , and  $C_{\max}$  is the maximal theoretical concentration of caffeine in coffee.

## RESULTS AND DISCUSSION

Fig. 1 shows the effects of time on the degree of hydrodynamic extraction of caffeine from coffee under the following process conditions:  $T=298$  K,  $LS=54:1$ ,  $Q=0.1$  L/sec, with water as a solvent. The results indicate that under mentioned conditions a complete extraction of caffeine from coffee beans was finished after one minute.

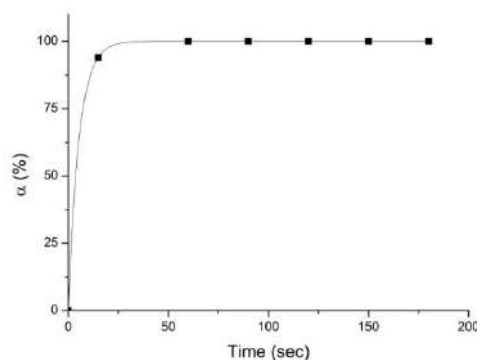


**Figure 1.** The dependence of degree of caffeine extraction on time in conditions of HC

The effect of  $LS$  (v/w) on the degree of caffeine extraction from roasted coffee beans in the conditions of HC was investigated under following process conditions:  $T=298$  K,  $Q=0.1$  L/sec,  $t = 1$  min, water as a solvent.

As can be seen from Fig. 2, the increase in the LS ratio leads to the increase in the degree of caffeine extraction. The optimal LS ratio for the efficient extraction of caffeine in conditions of HC is 10:1.

Fig.3 shows the effect of flow on the degree of caffeine extraction under following process conditions:  $T=298\text{ K}$ ,  $LS=75:1$ ,  $t=1\text{ min}$ , water as a solvent. It can be seen that maximal degree of caffeine extraction was achieved under the flow of  $0.1\text{ L/sec}$ .

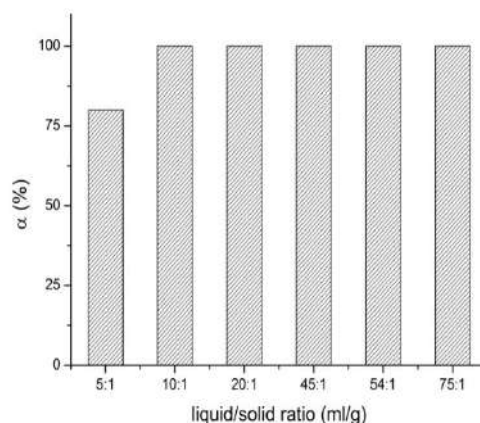


**Figure 2.** Effects of liquid-solid ratio on the degree of caffeine extraction in conditions of HC

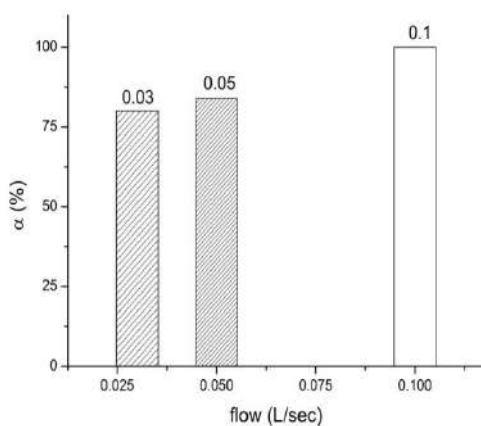


**Figure 3.** Effects of flow on the degree of caffeine extraction in conditions of HC

The effect of solvent on the degree of caffeine extraction from roasted coffee beans in the conditions of HC was performed using water, absolute ethanol, water solution of ethanol, and water/ethanol/methanol mixture, maintaining a constant following process conditions:  $T=298\text{ K}$ ,  $LS=75:1$ ,  $Q=0.1\text{ L/sec}$ ,  $t=1\text{ min}$ .

The results presented in Fig. 4 show that the maximal degree of caffeine extraction was accomplished using water as the extraction solvent.

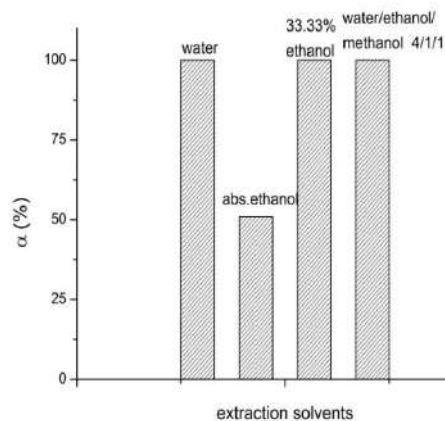


**Figure 4.** Effects of solvents on the degree of caffeine extraction in conditions of HC

## CONCLUSION

Hydrodynamic cavitation is inexpensive and energy efficient method for the extraction of caffeine from coffee beans. It is found that the optimal conditions for caffeine extraction are: water as a solvent, LS=10:1, Q=0.1 L/sec, t=1 min, 298 K. The results show that hydrodynamic cavitation could be an appropriate alternative process to conventional extraction techniques.

## Acknowledgement

The authors gratefully acknowledge the financial support from the Ministry of Science and Technical Development of the Republic of Serbia, through Project No.142025G.

## REFERENCES

- [1] P. Mazzafera, M.B. Paulo Silvarolla, *Seed Science Research*, 2010, **20** (3), 163-167.
- [2] D.J. Adam, J. Mainwaring, M.N. Quigley, *Journal of chemical education*, 1996, **73** (12), 1171.
- [3] J. Tello, M. Viguera, L. Calvo, *J. of Supercritical Fluids*, 2011, **59**, 53–60.
- [4] R. Upadhyay, K. Ramalakshmi, L. J. Mohan Rao, *Food Chemistry*, 2012, **130**, 184–188.
- [5] C.-C. Wang, S-R. Sheu, Y-Y. Chou, M-J. Jang, L-C. Yang, *Thermal Science*, 2011, **15**(1), S53-S59.
- [6] M. E. Salinas-Vargas, M. P. Cañizares-Macías, *Food Chemistry*, 2014, **147**, 182–188.
- [7] S. Roohinejad, M. Koubaa, F. J. Barba, R. Greiner, V. Orlien, N. I. Lebovka, *Trends in Food Science & technology*, 2016, **52**, 98-108.
- [8] L.H. Yao, X. Liu, Y. Jiang, N. Caffin, B. D’Arcy, R. Singanusong, et al., *Food Chemistry*, 2006, **94**, 115–122.

## INFLUENCE OF NEWLY SYNTHESIZED HEXAVANADATES ON Na<sup>+</sup>/K<sup>+</sup>-ATPase ACTIVITY

D. Krstić<sup>1</sup>, N. Bošnjaković-Pavlović<sup>2</sup>, X. Xu<sup>3</sup>, A. Spasojević-de Biré<sup>3</sup>,  
V. Vasić<sup>4</sup> and M. Čolović<sup>4</sup>

<sup>1</sup>*Institute of Medical Chemistry, Faculty of Medicine, University of  
Belgrade, Serbia, e-mail: danijela.krstic@med.bg.ac.rs*

<sup>2</sup>*Faculty of Physical Chemistry, University of Belgrade, Serbia*

<sup>3</sup>*Université Paris Saclay, CentraleSupélec, Grande Voie des Vignes,  
92295 Châtenay-Malabry, France*

<sup>4</sup>*Department of Physical Chemistry, Vinča Institute of Nuclear  
Sciences, University of Belgrade, Serbia*

### ABSTRACT

The influence of four newly synthesized hexavandates: [V<sub>6</sub>-CH<sub>3</sub>][Na]<sub>2</sub>, [V<sub>6</sub>-NO<sub>2</sub>][TBA]<sub>2</sub>, [V<sub>6</sub>-C3][H]<sub>2</sub>, and [V<sub>6</sub>-C5d][TBA]<sub>2</sub> on Na<sup>+</sup>/K<sup>+</sup>-ATPase activity, was investigated *in vitro*. All tested compounds inhibited the activity of Na<sup>+</sup>/K<sup>+</sup>-ATPase in a dose-dependent manner but with different inhibitory potency. [V<sub>6</sub>-NO<sub>2</sub>][TBA]<sub>2</sub> was found to be most potent, showing 50 % inhibition IC<sub>50</sub> = 1.87 × 10<sup>-5</sup> mol/L, while [V<sub>6</sub>-C5d][TBA]<sub>2</sub> showed the lowest inhibitory power, IC<sub>50</sub> = 1.31 × 10<sup>-4</sup> mol/L.

### INTRODUCTION

Polyoxovanadates (POVs) are very interesting vanadium-containing compounds due to their fascinating electronic and magnetic properties, their capacity to form various thermodynamically stable redox isomers, and their catalytic capabilities [1,2]. Due to these properties, there is also a great interest in using POVs clinically, primarily as antibacterial, antiviral and antitumor agents. Recently, we have found that POVs exhibit inhibitory influence on Na<sup>+</sup>/K<sup>+</sup>-ATPase activity [3,4]. Na<sup>+</sup>/K<sup>+</sup>-ATPase (sodium pump) belongs to the P-type ATPase family, the members of which are able to utilize the energy of ATP to transport ions against their electrochemical gradient. Considering the key role of Na<sup>+</sup>/K<sup>+</sup>-ATPase in normal functioning of most animal cells, as well as its pivotal role in cancer cell migration, the aim of this work was to examine the influence of four newly synthesized hexavandates: [V<sub>6</sub>-CH<sub>3</sub>][Na]<sub>2</sub>, [V<sub>6</sub>-NO<sub>2</sub>][TBA]<sub>2</sub>, [V<sub>6</sub>-C3][H]<sub>2</sub>, and [V<sub>6</sub>-C5d][TBA]<sub>2</sub> on Na<sup>+</sup>/K<sup>+</sup>-ATPase activity, using commercially available Na<sup>+</sup>/K<sup>+</sup>-ATPase from porcine cerebral cortex as a model system.

## MATERIAL AND METHODS

Na<sup>+</sup>/K<sup>+</sup>-ATPase from porcine cerebral cortex was purchased from Sigma Chemicals Co. (Germany). All investigated hexavanadates were synthesized according to the route described by Chen et al [5,6]. Stock solutions (0.1 mol/L) of the hexavanadates were prepared by solving the solid compounds in DMSO. Working solutions were prepared daily by diluting the stock solutions with water to the desired concentrations, shortly before use. Final DMSO volume fraction in the incubation medium did not exceed 1%. The activity of Na<sup>+</sup>/K<sup>+</sup>-ATPase was followed in the absence (control) and presence (during 20 min) of increasing concentration of hexavanadates by monitoring spectrophotometrically (Perkin Elmer Lambda 35 UV-VIS spectrophotometer) the released P<sub>i</sub> liberated from the enzymatic hydrolysis of ATP [3].

## RESULTS AND DISCUSSION

The influence of the newly synthesized hexavanadates on Na<sup>+</sup>/K<sup>+</sup>-ATPase activity was investigated in the concentration range from 1×10<sup>-8</sup> to 1×10<sup>-3</sup> mol/L. Enzyme activity, expressed as a percentage of the control value (obtained without inhibitor) decreased for increasing hexavanadates concentration, showing in all cases a monophasic sigmoidal curve (OriginPro 8) (Fig.1).

The inhibition parameters, the concentrations of the investigated compounds with capability to inhibit 50% of the enzyme activity after given exposure time (IC<sub>50</sub> values) and Hill coefficient, n<sub>H</sub>, were determined using the Hill method and are summarized in Table 1. Obtained results indicate that all investigated compounds inhibit the Na<sup>+</sup>/K<sup>+</sup> ATPase activity, but with different inhibiting power. [V<sub>6</sub>-NO<sub>2</sub>][TBA]<sub>2</sub> (IC<sub>50</sub> = 1.87 × 10<sup>-5</sup> mol/L) was the most potent inhibitor of Na<sup>+</sup>/K<sup>+</sup> ATPase activity, while [V<sub>6</sub>-C5d][TBA]<sub>2</sub> showed the lowest inhibitory potency (IC<sub>50</sub> = 1.31 × 10<sup>-4</sup> mol/L). The calculated n<sub>H</sub> values (n<sub>H</sub> ≤ 1) suggest (Table 1) that there is no positive cooperativity in hexavanadates binding to the enzyme.

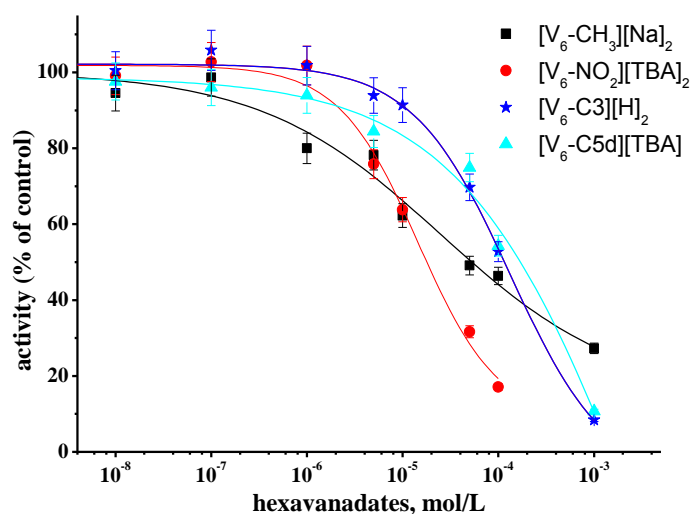


**Figure 1.** The concentration-dependent inhibition of  $\text{Na}^+/\text{K}^+$ -ATPase induced by four new synthesized hexavanadates

**Table 1.** The inhibition parameters of hexavanadates for  $\text{Na}^+/\text{K}^+$  - ATPase obtained by Hill analysis

Compound	$\text{IC}_{50}$ , mol/L	$n_H$
$[\text{V}_6\text{-CH}_3][\text{Na}]_2$	$(5.50 \pm 0.28) \times 10^{-5}$	0.44
$[\text{V}_6\text{-NO}_2][\text{TBA}]_2$	$(1.87 \pm 0.09) \times 10^{-5}$	0.89
$[\text{V}_6\text{-C3}][\text{H}]_2$	$(1.05 \pm 0.05) \times 10^{-4}$	0.98
$[\text{V}_6\text{-C5d}][\text{TBA}]$	$(1.31 \pm 0.06) \times 10^{-4}$	0.99

The obtained results are in agreement with previously reported concentration-dependent inhibitory effect of POVs on synaptic plasma membrane and purified porcine cerebral cortex  $\text{Na}^+/\text{K}^+$ -ATPase [3,4].

Although a few different isoforms of brain  $\text{Na}^+/\text{K}^+$ -ATPase have been known [7] the obtained monophasic inhibition curves do not suggest that the heterogeneity of the hexavanadate binding sites, which is in agreement with previously published findings related to polyoxometalate-induced inhibition of different types of ATPases [3,4,8].

## CONCLUSION

Based on the results, we can conclude that the examined compounds exhibit concentration-dependent inhibitory effect on  $\text{Na}^+/\text{K}^+$ -ATPase activity.

Inhibiting power of tested hexavanadates are weaker (about two orders of magnitude) than inhibiting power of decavanadate (tested earlier) on  $\text{Na}^+/\text{K}^+$ -ATPase activity, which is probably due to differences in charge, size and shape of these polyoxometalates. In order to interpret the obtained differences in inhibitory potencies of investigated POVs a combined crystallographic analysis and *ab initio* calculations will be carried out.

### **Acknowledgement**

This work was supported by the Ministry of Education, Science and Technological Development of the Republic of Serbia (Projects No. 172043 and 172023).

### **REFERENCES**

- [1] M.T. Pope, A. Muller, Polyoxometalates: From Platonic Solids to Anti-Retroviral Activity, Kluwer, Dordrecht, 1994.
- [2] Polyoxometalates, C. Hill (Ed.) in Chem. Rev. 1998, **98**, 1-390.
- [3] D. Krstić, M. Čolović, N.Bošnjaković-Pavlović, A.Spasojević-De Bire, V.Vasić, Gen. Physiol. Biophys. 2009, **28**, 302-308.
- [4] X. Xu, N. Bošnjaković-Pavlović, M. Čolović, D.Krstić, V.Vasić, J.M. Gillet, P.Wu, Y. Wei, A. Spasojević-de Biré, J. Inorg. Biochem. 2016, DOI: 10.1016/j.jinorgbio.2016.04.029.
- [5] Q. Chen, J.A. Zubieta, Inorg. Chim. Act. 1992, **95**, 198-200.
- [6] P. Wu, J. Chen, P. Yin, Z. Xiao, J. Zhang, A. Bayaguud, Y. Wei, Polyhedron 2013, **52**, 1344–1348.
- [7] D. Krstić, N. Tomić, K. Krinulović, V. Vasić, J. Enzym. Inhib. Med. Ch. 2006, **21**, 471-475.
- [8] M. Čolović, D. Bajuk-Bogdanović, N. Avramović, I. Holclajtner-Antunović, N. Bošnjaković-Pavlović, V.Vasić, D.Krstić, Bioorgan. Med. Chem. 2011, **19**, 7063–7069.

## ADSORPTION OF STRONTIUM ON DIFFERENT BENTONITES

S. Marinović<sup>1</sup>, M. Ajduković<sup>1</sup>, N. Jović-Jovičić<sup>1</sup>, P. Banković<sup>1</sup>, T. Mudrinić<sup>1</sup>, B. Nedić Vasiljević<sup>2</sup> and A. Milutinović-Nikolić<sup>1</sup>

<sup>1</sup> *University of Belgrade, Institute of Chemistry, Technology and Metallurgy, Njegoševa 12, 11000 Belgrade, Serbia. (sanja@nanosys.ihtm.bg.ac.rs)*

<sup>2</sup> *University of Belgrade, Faculty of physical chemistry, Studentski trg 12-16, 11000 Belgrade, Serbia.*

### ABSTRACT

Three different bentonites with similar cation exchange capacities were investigated as adsorbents for Sr<sup>2+</sup> ions in aqueous solutions. Textural properties of the bentonite samples were determined using low-temperature N<sub>2</sub> physisorption method. Adsorption was carried out with respect to contact time. It was found that adsorption capacity of all adsorbents towards Sr<sup>2+</sup> ions was similar. It was shown that ion exchange mechanism is the dominant mechanism of Sr<sup>2+</sup> ions adsorption on the Na-enriched bentonites. Adsorption dynamics obeyed pseudo-second-order kinetics model for all bentonites.

### INTRODUCTION

Strontium (Sr) is abundantly present in Earth's crust in the form of minerals: SrCO<sub>3</sub>, SrSO<sub>4</sub> and Al<sub>2</sub>O<sub>3</sub>·SrO·(SiO<sub>2</sub>)<sub>6</sub>·4H<sub>2</sub>O. In surface waters strontium originates from weathering of the rocks, or from the discharge of waste water from industries that use strontium compounds. Ionic strontium is not toxic in small concentrations, and since its concentration in water is generally low. Beyond four stable Sr isotopes naturally present in soil, there are also artificial, radioactive isotopes <sup>89</sup>Sr and <sup>90</sup>Sr [1, 2]. These radioactive isotopes occur as waste products in nuclear power plants and in the reprocessing of nuclear fuels [3]. The disposal of radioactive wastewater from commercial nuclear plants is one of the major problems in nuclear waste management [4]. Similar adsorptive behavior of the radioactive Sr isotopes with the non-radioactive ones enables the investigation of the adsorptive removal of radioactive Sr from aqueous solutions on model systems containing non-radioactive isotopes.

The present work was focused on the removal of strontium ions (Sr<sup>2+</sup> ions) from aqueous solutions using three different sodium enriched bentonites with similar cation exchange capacities (CEC) but with different specific

surface areas. The adsorption was studied as a function of adsorption time, and the results were interpreted using kinetic models of pseudo-first and pseudo-second order.

## EXPERIMENTAL

Three bentonite samples (Texas, Wyoming and Bogovina) were used as adsorbents. Two bentonites were supplied by the Clay Minerals Society originated from Texas (CEC=71.2) and Wyoming (CEC=71.4). The third one was from domestic Bogovina Coal and Bentonite Mine in Serbia (CEC=67.2). The samples were sieved through 74  $\mu\text{m}$  sieves. Sodium enrichment of the bentonite samples was performed using previously reported procedure [5] and the obtained materials based on Wyoming, Texas and Bogovina bentonites were denoted as NaW, NaT and NaB, respectively.

$\text{SrCl}_2 \cdot 6\text{H}_2\text{O}$  was obtained from Carlo Erba and used as received.

Nitrogen physisorption isotherms were determined on a Sorptomatic 1990 Thermo Finnigan instrument at  $-196^\circ\text{C}$  and textural parameter values were calculated according to common models [6–8].

Batch-type adsorption experiments were conducted in aqueous solutions in a temperature-controlled water bath shaker (Memmert WNE 14 and SV 1422). The adsorption of  $\text{Sr}^{2+}$  ions was investigated with respect to contact time. The aliquots were withdrawn from the shaker at regular time intervals and the solution was centrifuged at 17000 rpm for 10 min (Hettich EBA-21). The  $\text{Sr}^{2+}$  content in the supernatant solutions was determined by inductively coupled plasma optical emission spectrometry (ICP–OES). The ICP–OES measurements were performed using a Thermo Scientific iCAP 6500 Duo ICP instrument (Thermo Fisher Scientific, Cambridge, UK).

All experiments were carried out at  $T=298,15\text{ K}$ , using the same mass of adsorbent ( $m_{ads}=20.0\text{ mg}$ ) and volume of solution ( $v=50.0\text{ cm}^3$ ). The initial concentration of  $\text{Sr}^{2+}$  ions was  $50\text{ mg dm}^{-3}$ .

The amount of  $\text{Sr}^{2+}$  adsorbed after time  $t$  -  $q_t$  ( $\text{mg g}^{-1}$ ), was calculated from the following mass balance relationship:

$$q_t = \frac{(C_0 - C_t)v}{m_{ads}} \quad (1)$$

where:  $C_0$  and  $C_t$  are the initial  $\text{Sr}^{2+}$  solution concentration ( $\text{mg dm}^{-3}$ ) and the  $\text{Sr}^{2+}$  concentration after the adsorption time  $t$ , respectively. The obtained data were investigated using the pseudo-first and pseudo-second kinetics models.

## RESULTS AND DISCUSSION

Low temperature  $\text{N}_2$  physisorption measurements resulted in isotherms characteristic for mesoporous materials that contain aggregated planar

particles forming slit shape pores, with the presence of micropores. Selected textural properties parameters are presented in Table 1.

**Table 1.** Selected textural properties

Sample	$S_{\text{BET}}$ [ $\text{m}^2\text{g}^{-1}$ ]	$V_{0,98}$ [ $\text{cm}^3\text{g}^{-1}$ ]	$V_{\text{mes}}^{\text{BJH}}$ [ $\text{cm}^3\text{g}^{-1}$ ]	$S_t$ [ $\text{m}^2\text{g}^{-1}$ ]	$S_{\text{mic}}=S_{\text{BET}}-S_t$ [ $\text{m}^2\text{g}^{-1}$ ]
NaW	50	0,0759	0,0871	31	19
NaT	106	0,2000	0,2101	83	23
NaB	87	0,0853	0,0788	43	44

Where:  $S_{\text{BET}}$  – specific surface area (Brunauer, Emmett, Teller – two parameter plot);  $V_{0,98}$  – total pore volume (Gurvitch);  $V_{\text{mes}}^{\text{BJH}}$  mesopore volume (Barett, Joyner, Hallenda), and  $S_t$  – specific surface area (t-plot),  $S_{\text{mic}}$  – micropore specific surface area

All Na-enriched materials exhibited microporosity developed to different extents. While mesoporous surface area increased in the NaW>NaB>NaT sequence, the increase of the surface area of micropores followed the NaW>NaT>NaB sequence. Microporous surface area should be considered as more relevant in the investigated cation exchange process, since it takes place in the interlamellar smectite region.

The effect of contact time on the amount of  $\text{Sr}^{2+}$  ions adsorbed on bentonites is presented in Fig. 1.

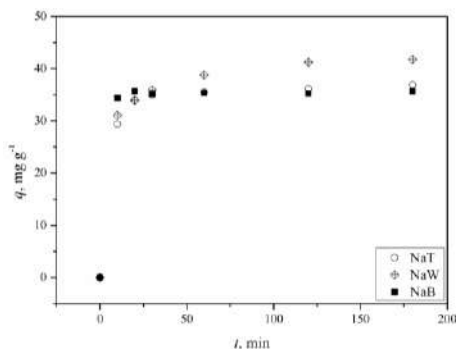


**Figure 1.** The effect of contact time on the adsorption of  $\text{Sr}^{2+}$  ions on three different bentonites

For all adsorbents, adsorption rate was initially high and then, it gradually reached plateau. The adsorption capacity of the domestic adsorbent from Bogovina was similar to the capacity of commercial bentonites, independently on the difference in their textural properties. This indicates that the ion exchange mechanism was the dominant mechanism. The pseudo-first order and pseudo-second order kinetics models were tested in the case of  $\text{Sr}^{2+}$  adsorption on the bentonites. Coefficients of determination ( $R^2$ ) for

the pseudo-first order model were relatively low, indicating poor correlation of data with the model. On the other hand,  $R^2$  values for the pseudo-second order model were  $>0.999$  for all bentonites. Besides, equilibrium adsorption capacities ( $q_e$ ), calculated from the equation for the pseudo-second order kinetics model showed good agreement with the experimental values, confirming that the adsorption of  $\text{Sr}^{2+}$  ions on different bentonites obeyed the pseudo-second order kinetics.

## CONCLUSION

In this work, it was shown that the adsorption of  $\text{Sr}^{2+}$  ions from aqueous solutions on three different Na-enriched bentonites is mainly governed by ion exchange mechanism, since bentonites with similar CEC values and different specific surface areas had similar adsorption capacities. The adsorption dynamics was described well by the pseudo-second-order kinetics model. All investigated adsorbents could be used for the removal of radioactive strontium, considering the fact that it has similar adsorption behavior as the non-radioactive counterpart.

## Acknowledgement

This work was supported by the Ministry of Education, Science and Technological Development of the Republic of Serbia (Project III 45001).

## REFERENCES

- [1] J. R. Dojlido, G. A. Best, Chemistry of water and water pollution, Ellis Horwood Limited, Chichester, West Sussex, 1993.
- [2] S. Chegrouche, A. Mellah, M. Barkat, Desalination, 2009, **235**, 306–318.
- [3] S. Yusasn, S. Erenturk, World journal of nuclear science and technology, 2011, **1**, 6-12.
- [4] A. Ahmadpour, M. Zabihi, M. Tahmasbi, T. Rohani Bastami, Journal of Hazardous Materials, 2010, **182**, 552–556.
- [5] N. Jović-Jovičić, A. Milutinović-Nikolić, I. Gržetić, D. Jovanović, Chemical engineering & technology, 2008, **31**, 567-574.
- [6] S.H. Gregg, K.S. Sing, Adsorption, Surface Area and Porosity, Academic Press, New York, 1967.
- [7] F. Rouquerol, J. Rouquerol, K. Sing, Adsorption by powders and porous solids, Academic Press, London, 1999.
- [8] P.A. Webb, C. Orr, Analytical methods in fine particle technology, Micromeritics Instrument Corporation, Norcross, GA, USA, 1997.

## KINETICS OF ADSORPTION OF NICOTINE BY NATURAL AND ACID-ACTIVATED MONTMORILLONITE

N. Jović-Jovičić, I. Ilić, S. Marinović, P. Banković, D. Jovanović,  
B. Dojčinović and A. Milutinović-Nikolić

*University of Belgrade, Institute of Chemistry, Technology and Metallurgy,  
Njegoševa 12, 11000 Belgrade, Serbia. (natasha@nanosys.ihm.bg.ac.rs)*

### ABSTRACT

The adsorption of nicotine from aqueous solutions was performed on natural and acid-activated Wyoming montmorillonite. The adsorption experiments showed that acid-activation increases adsorption capacity of montmorillonites toward nicotine molecules. The pseudo-first and pseudo-second order kinetics models were tested. The nicotine adsorption was well represented by the pseudo-second-order kinetics model for both montmorillonite samples.

### INTRODUCTION

The presence of nicotine – highly toxic alkaloid – is often detected in wastewaters of tobacco industry. Different methods have been used for nicotine containing wastewater treatment, but adsorption shows many advantages [1,2]. Numerous investigations have been focused on the adsorption of nicotine using different materials as adsorbents [3,4] but there is a lack of studies where montmorillonite clays are used as nicotine adsorbents. In this paper, natural and acid-activated Wyoming montmorillonite were tested for nicotine removal from water, and the kinetics of the investigated adsorption processes was determined.

### EXPERIMENTAL

Montmorillonite clay mineral (MW) was obtained from The Source Clays Repository - The Clay Minerals Society, Wyoming, USA. According to the supplier the Cation Exchange Capacity of the material is 76.4 meq/100g.

Nicotine ((S)-3-(1-Metil-2-pirolidinil) pyridine), with purity of 99% was purchased from Alfa – Aesear.

The acid-activated montmorillonite was obtained using a common procedure [5]. Dried MW sample (5 g) was treated with 22.50 cm<sup>3</sup> of 4.5 M HCl by stirring at 90 °C for 2 h; after acid activation, the sample was

collected and dialyzed against demineralized water until the filtrate was free of  $\text{Cl}^-$  ions (test with 0.1 M  $\text{AgNO}_3$ ).

All adsorption experiments were carried out at room temperature with solution volume of  $v = 0.050 \text{ dm}^3$ . The adsorptions were run for 10, 20, 30, 60, 120, 180 and 1440 min; the initial concentration of nicotine was  $0.75 \text{ mmol dm}^{-3}$  and the mass of adsorbent was  $m_{\text{adsorb}} = 0.05 \text{ g}$ . A period of 24 h was taken as the equilibrium time, although in some experiments the equilibrium was reached much earlier.

Nicotine concentration was monitored using spectrophotometer Nicolet Evolution 500 UV-VIS, Thermo Electron using  $\lambda_{\text{max}} = 261 \text{ nm}$ .

The amount of adsorbed nicotine molecule for time  $t - q_t$  ( $\text{mmol g}^{-1}$ ) was calculated according the following relationship:

$$q_t = \frac{(C_0 - C_t) \cdot V}{m_{\text{ads}}}$$

where:  $C_0$  – initial concentration of nicotine ( $\text{mmol dm}^{-3}$ ),  $C_t$  – concentration of nicotine after adsorption time  $t$  ( $\text{mmol dm}^{-3}$ ),  $V$  – volume of nicotine solution ( $\text{cm}^3$ ),  $m_{\text{ads}}$  – adsorbent mass (mg).

## RESULTS AND DISCUSSION

The effect of contact time on the adsorption of nicotine from aqua solution onto natural and acid – activated montmorillonite is presented in Figure 1.

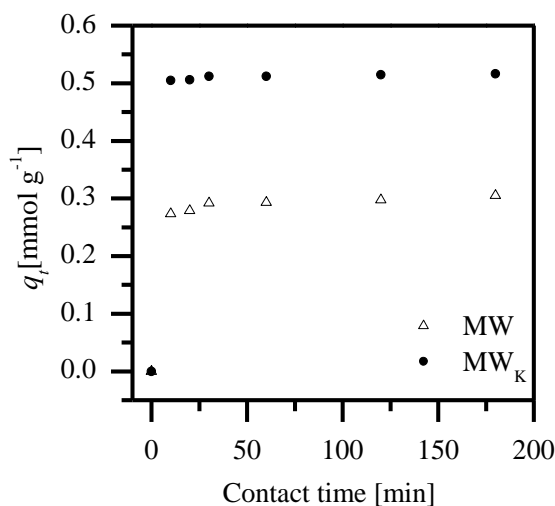


**Figure 1.** Adsorption of nicotine on natural (MW) and acid-activate (MWA) montmorillonites

Acid-activation of montmorillonite increased its adsorption toward nicotine molecules.

Based on the results presented in Fig. 1. the kinetic study was performed for each of the investigated adsorbents.

Kinetic data were tested with both pseudo-first-order and pseudo-second-order kinetics models [6].

The linear form of the integrated rate law for the pseudo-first-order and pseudo-second-order reactions are presented in Eq. (1) and Eq. (2) respectively.

$$\log(q_e - q_t) = \log q_e - \frac{k_1 t}{\ln 10} \quad (1)$$

$$\frac{t}{q_t} = \frac{1}{k_2 q_e^2} + \frac{1}{q_e} t \quad (2)$$

Here,  $q_t$  is the amount of adsorbed nicotine ( $\text{mmol g}^{-1}$ ) at any time  $t$ ,  $q_e$  is the amount of adsorbed nicotine at the equilibrium ( $\text{mmol g}^{-1}$ ),  $k_1$  is the pseudo-first order rate constant ( $\text{min}^{-1}$ ), and  $k_2$  is the pseudo-second-order rate constant ( $\text{g mg}^{-1} \text{min}^{-1}$ ). The values of the pseudo-first-order constant were calculated from the plots of  $\log(q_e - q_t)$  versus  $t$  for each initial dye concentration, while for the pseudo-second-order these parameters were calculated from the  $t/q_t$  versus  $t$  plot. The plots for pseudo-first and pseudo-second-order reaction of nicotine adsorption on both adsorbents are given in Figure 2.a and 2.b, respectively.

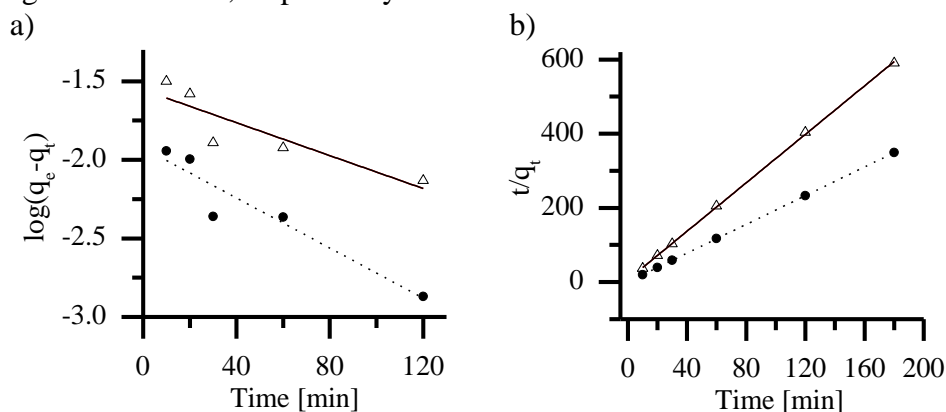


**Figure 2.** a) pseudo-first order b) pseudo-second order reaction

Since the correlation coefficients for the pseudo-second-order kinetics model are closer to unity than the corresponding correlation coefficients for the first-order kinetics model, the second-order kinetics model was proven to be more adequate. The kinetic parameters for nicotine adsorption on both investigated adsorbents are presented in Table 1.

The  $q_e^{exp}$  and  $q_e$  values obtained for the pseudo-second reaction order for nicotine exhibited excellent agreement. Therefore, the experimental data undoubtedly confirmed that the adsorption of nicotine from aqueous solution onto natural montmorillonite and acid-activated montmorillonite obeyed the pseudo-second-order kinetics model.

**Table 1.** Kinetic parameters for adsorption

Adsorbents	MW	MWA
$q_e^{exp}$ [mmol g <sup>-1</sup> ]	0.305	0.516
Pseudo first order reacton		
$q_e$ [mmol g <sup>-1</sup> ]	0.0281	0.0119
$k_1$ [min <sup>-1</sup> ]	0.0023	0.0035
$r_1$	0.7941	0.9068
Pseudo second order reacton		
$q_e$ [mmol g <sup>-1</sup> ]	0.3062	0.5168
$k_2$ [g mmol <sup>-1</sup> min <sup>-1</sup> ]	5.5895	4.9912
$r_2$	0.9997	1

## CONCLUSION

Acid-activation of Wyoming montmorillonite was performed. The adsorption of nicotine from aqueous solutions was studied on both natural and acid-activated montmorillonite. The acid-activation increased adsorption capacity of montmorillonite toward nicotine molecules. The pseudo-first and pseudo-second order reaction models were tested. The pseudo-second order reaction showed to be characteristic for nicotine adsorption on the investigated adsorbents.

## Acknowledgement

This work was supported by the Ministry of Education and Science of the Republic of Serbia (Project III 45001).

## REFERENCES

- [1] C. Gerard-Gomez, M. Dufaux, J. Morel, C. Naccache, Y. Ben Taarit, *Appl. Catal. A*, 1997, **165**, 371–377.
- [2] S.N. Wang, P. Xu, H. Z. Tang, J. Meng, L. X. Liu, J. Huang, H. Chen, Y. Du, *Biotechnol. Lett.* 2004, **26**, 1493–1496.
- [3] A. Mihranyan, S. B. Andersson, R. Eka, *Eur. J. Pharm. Sci.* 2004, **22**, 279–286.
- [4] E. C. Girao, S.B. Fagan, I. Zanella, A. G. Souza Filho, *J. Hazard. Mater.*, 2010, **184**, 678–683.
- [5] P. Komadel and J. Madejova in: *Handbook of Clay Science, Part A, Fundamentals*, Bergaya, F., Lagaly, G. (Eds.), Elsevier, 2nd Edition, Amsterdam, 2013.
- [6] S. Azizian, *J. Coll. Inter. Sci.*, 2004, **274**, 47-52.

## **DISTRIBUTED ACTIVATION ENERGY MODEL AS A NEW METHOD FOR INVESTIGATION OF POLY(ACRYLIC ACID)-G-GELATIN HYDROGEL NON-ISOTHERMAL DEHYDRATION KINETICS**

B. Stanković, J. Jovanović and B. Adnađević

*University of Belgrade, Faculty of Physical Chemistry, Studentski trg 12-16,  
11000 Belgrade, Serbia. (branislav@ffh.bg.ac.rs)*

### **ABSTRACT**

Kinetics of poly(acrylic acid)-g-gelatin hydrogel non-isothermal dehydration is investigated by thermogravimetric analysis at four heating rates: 5, 10, 15 and 20 K/min. It has been found that this process has complex kinetics. The shape of activation energy distribution function has been determined. Kinetic curves of poly(acrylic acid)-g-gelatin hydrogel dehydration have been entirely described by distributed activation energy model.

### **INTRODUCTION**

Hydrogels are often described as three-dimensional cross-linked polymeric structures that are able to swell in the aqueous environment. Kinetics of non-isothermal hydrogel dehydration is investigated by various kinetic methods such as: Kissinger, Coats–Redfern, van-Krevelen, and Horowitz–Metzger, as well as by the use of normalized Weibull distribution function and logistic function [1 - 3]. Since hydrogel structure undergoes changes during the dehydration, distributed activation energy model (DAEM) is used to describe non-isothermal dehydration kinetics of the poly(acrylic acid)-g-gelatin (PAG) hydrogel.

### **EXPERIMENTAL**

Non-isothermal thermogravimetric curves of the PAG dehydration have been recorded using a TG Analyser, TA Instruments. The samples (20±1 mg) were heated in the temperature range from 290K to 460 K at different heating rates  $v_h$ , from 5 to 25 K/min under nitrogen atmosphere, flow 20 ml/min.

Procedure proposed by Miura [4] and Miura and Maki [5] is used for determination of values of activation energy,  $E_a$ , and pre-exponential factor,  $A$ , at certain degree of dehydration,  $\alpha$ , i.e. values of  $E_{a,\alpha}$  and  $A_\alpha$ , respectively.

Also, shape of activation energy distribution function,  $g(E_a)$ , is established by the same procedures the  $E_a$  derivative with respect to the  $\alpha$ .

## RESULTS AND DISCUSSION

The thermogravimetric (TG) curves of PAG hydrogel non-isothermal dehydration at four different heating rates are presented in Fig. 1a. It can be seen that TG curves, at all  $v_h$ , have complex concave shape. Also, as  $v_h$  increases TG curves move toward higher temperatures and become more concave.

Activation energy dependence on  $\alpha$  was established (Fig. 1b.) in order to find does PAG hydrogel has complex non-isothermal dehydration kinetics. As it can be seen from Fig. 1b., when  $\alpha \leq 0.2$ ,  $E_a$  changes almost linearly from 62.5 kJ/mol to 40.5 kJ/mol. On the other hand, when  $\alpha \geq 0.2$ , the  $E_a$  slowly decreases and reaches the value of 23.1 kJ/mol at the end of the process. Complex shape of activation energy dependence on  $\alpha$  confirms that non-isothermal dehydration process of PAG hydrogel has complex kinetics and approve utilization of DAEM on investigated process.

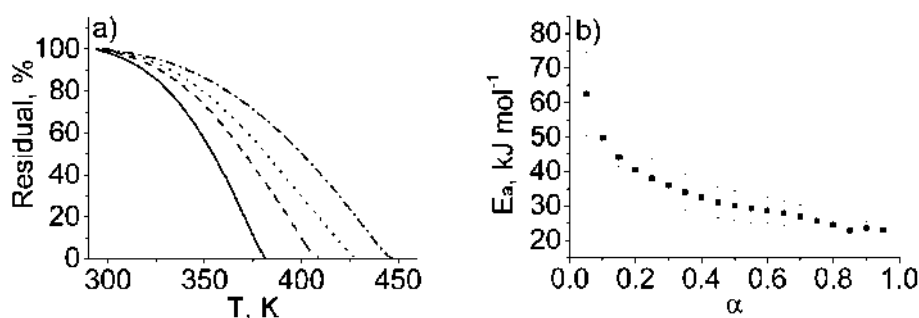


**Figure 1.** a) TG curves of PAG hydrogel non-isothermal dehydration (5 K/mol (solid line), 10 K/mol (dashed line), 15 K/mol (dotted line) and 20 K/mol (dashed and dotted line)) and b) dependence of  $E_a$  on  $\alpha$

It has been shown that dependence of  $\ln A$  on  $\alpha$  is similar, by its shape, to the dependence of  $E_a$  on  $\alpha$ , which indicates that  $E_a$  and  $\ln A$  are correlated by so-called compensation equation:

$$\ln A_{\alpha} = -6.43 + 0.469 E_{a,\alpha} \quad (1)$$

Further, based on dependence of  $E_a$  on  $\alpha$ ,  $g(E_a)$  function has been determined by Miura-Maki method (Fig. 2a.). From here, it can be seen that  $g(E_a)$  function has characteristic right (positive) skewed asymmetric peak with conspicuous maximum at  $E_a = 29$  kJ/mol.

Based on knowledge of  $g(E_a)$  and  $A_a$  as a function of  $\alpha$ , in accordance with the basic equation of DEAM, conversion curves of PAG hydrogel non-isothermal dehydration process are calculated:

$$\alpha = 1 - \int_0^{\infty} \exp\left[-\frac{\exp(-6.43 + 0.469E_a)}{v_h} * \int_{290}^T \exp\left(-\frac{E_a}{RT}\right) dT\right] g(E_a) dE_a \quad (2)$$

The comparison of experimental and data predicted by eq. 2 is shown in Fig.2b.

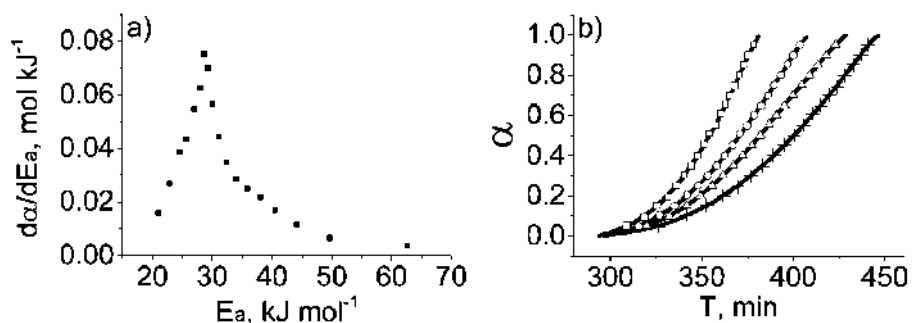


**Figure 2.** a)  $g(E)$  function and b) the comparison of experimental (solid lines) and data predicted by eq. 2 (5 K/mol (Y), 10 K/mol (○), 15 K/mol (▲) and 20 K/mol (+)).

As it can be seen from Fig. 2b. calculated dependence of  $\alpha$  on temperature, at all  $v_h$ , are in complete agreement with experimental data. This confirms that non-isothermal dehydration kinetics of PAG hydrogel can be entirely described by DAEM.

## CONCLUSION

Non-isothermal dehydration of poly(acrylic acid)-g-gelatin hydrogel is kinetic ally complex process. Shape of activation energy distribution function has been determined by Muira-Maki method. Distributed activation energy model can be used in describing non-isothermal kinetics of poly(acrylic acid)-g-gelatin hydrogel dehydration.

## Acknowledgement

This work was partially supported by the Ministry for Science of the Republic of Serbia (Grants no. 172015).

**REFERENCES**

- [1] B. Janković, B. Adnađević, J Jovanović, J. Therm Anal Calorim., 2005, **82**, 7-13.
- [2] B. Adnađević, B. Janković, Lj. Kolar-Anić, D.Minić, ChemEng J., 2007, **130**, 11-7.
- [3] B. Adnađević, G. Tasić, J. Jovanović, Thermochim. Acta. 2011, **512**, 157-62.
- [4] K. Miura, K, Energy Fuels, 1995, **9**, 302-307.
- [5] K. Miura, T. Maki, Energy Fuels, 1998, **12**, 864-869.

## STOPPED-FLOW DETERMINATION OF IODATE PRODUCED IN IODINE OXIDATION WITH HYDROGEN PEROXIDE

K. Stevanović, D. Stanisavljev and I. N. Bubanja

*University of Belgrade, Faculty of Physical Chemistry, Studentski trg 12-16, 11000 Belgrade, Serbia. (kristina.stevanovic91@gmail.com)*

### ABSTRACT

Iodine oxidation reaction was monitored potentiometrically. Iodate amount produced in this reaction was determined by stopped-flow technique for the first time. Five experiments are repeated and for each experiment, six measurements of produced iodate are performed. Under the given conditions, high degree of iodine conversion to iodate ( $95.4 \pm 0.6\%$ ) is obtained with good repeatability.

### INTRODUCTION

The oxidation of iodine to iodate with hydrogen peroxide (eq 2) is an intriguing step of the Bray-Liebhafsky (BL) oscillatory reaction [1,2]. Unlike the first step, the reduction of iodate to iodine (eq 1), which has been shown to have kinetics closely related to Dushman reaction, oxidation of iodine (eq 2) is not investigated enough [3,4]. The study of the iodine oxidation can contribute to a better understanding of the BL reaction mechanism which, despite the continuous research during almost 100 years, is still unknown in many details.



Determination of iodate amount originating from iodine oxidation is one of the ways for studying mechanism of this reaction. It has been done for the first time by Furrow [5]. He measured ratio between formed iodate and iodide by precipitation silver iodate and silver iodide with silver ions in excess. Either they didn't measure amount of produced iodate, Olexová et al. analyzed influence of the interphase area, initial concentrations of reactants, light and stirring on iodine oxidation reaction [6].

In our recently published paper it was shown that stopped-flow technique may be successfully utilized for iodate determination in the presence of hydrogen peroxide by titration with excess of iodide [7]. The main characteristic of this technique is possibility to distinguish titration products

of the fast Dushman reaction (eq 3) from the same products which originate from the slower peroxide-iodide reaction (eq 4).



Therefore, our aim here is to use stopped-flow technique to measure iodate, as a product of iodine oxidation with hydrogen peroxide.

### EXPERIMENTAL

Experiments were carried out at 27°C in a 60 mL glass vessel wrapped in a water recirculation jacket, connected to a thermostat (Fig. 1.). For homogenization of the reaction mixture, a magnetic stirrer ( $\sigma = 100$  rpm) was used for 20s. For determination of the concentrations of  $\text{I}_2$  and  $\text{I}_3^-$  species, at the beginning and at the end of iodine-peroxide reaction, Agilent UV/VIS Diode Array Spectrophotometer with Applied Photophysics Pro.-K.2000 Stopped-Flow Accessory was used. The working Pt electrode was connected to a double-junction Ag/AgCl reference electrode. Data acquisition voltmeter (PC-Multilab EH4 16-bit ADC) coupled with a personal computer was used to record the potential-time evolution during the reaction. The start-up procedure was performed in the following way. Thermostated and protected from light, the reaction vessel was filled with the reactants. First 10 ml of 5 M  $\text{H}_2\text{SO}_4$  (Zorka Šabac, Serbia) was added. After 10 minutes 50 ml of  $9.6 \cdot 10^{-4}$  M  $\text{I}_2$  (Zorka Šabac, Serbia) solution was added. Finally when temperature achieved constant value 125  $\mu\text{l}$  9.54M  $\text{H}_2\text{O}_2$  (Merck, Germany) was added and stirrer was turned on for 20 s. That was the moment when potentiometric recording started. For stopped-flow measurements, at the end of reaction, 2ml sample was taken and diluted to 25ml.

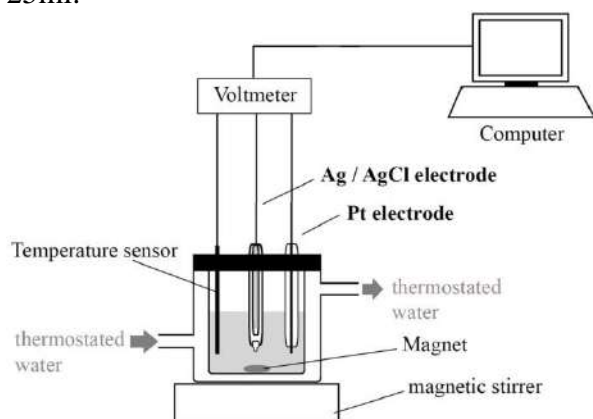


**Figure 1.**  
Schematic view of experimental setup.

## RESULTS AND DISCUSSION

Experiments were taken at five different days. Reaction of iodine oxidation was monitored potentiometrically. After a relatively short induction period, changes of the redox properties of the solution are recorded. When signal reaches the value, which does not change during time, it can be assumed that reaction is finished (equilibrium is achieved). After that, the sample for further analysis was taken. For each sample six stopped-flow titrations of the reaction mixture were done. Under the given conditions, iodate titration is finished after 11 seconds allowing kinetic separation from peroxide-iodide reaction (eq. 4) within 0.3 %. The mean values obtained from these titrations are given in Table 1 for five individual experiments. The stated errors represent 95 % confidence limit of the mean value.

From Table 1. it can be seen that large fraction of  $I_2$  is being oxidized with peroxide to iodate with good repeatability. Obtained conversion is a little less than 100%, which is probably due to a small loss of iodine in the gas phase. Also, it can be observed that high repeatability is obtained for induction periods and for the times in which reaction is completed. The reaction times,  $\tau_{end}$  are longer than 2h and it is still under investigations how to relate obtained results with its fast evolving in the BL oscillations. Further investigations are needed.

**Table 1.** Induction period ( $\tau_{ind}$ ), time in which reaction is completed ( $\tau_{end}$ ) and percent of  $I_2$  converted in oxidation reaction.

$\tau_{ind}$ (min)	$\tau_{end}$ (min)	Percent of converted $I_2$
12.06	167.23	95.8±0.5
10.14	169.17	97.9±0.9
11.68	168.36	91.7±0.3
12.17	166.89	96.2±0.5
11.85	167.97	95.5±0.4

## CONCLUSION

Iodate amount produced in reaction of iodine oxidation by hydrogen-peroxide was measured with stopped-flow technique. Values obtained at different experiments are in good agreement. Results show that, at considered conditions, almost all iodine ends up as iodate. We hope that obtained results will contribute to better understanding mechanism of this reaction and related iodine oscillators.

***Acknowledgement***

This work was partially supported by the Ministry for Science of the Republic of Serbia (Grants no. 172015).

**REFERENCES**

- [1] W. C. Bray, *J. Am. Chem. Soc.*, 1921, **43**, 1262 – 1267.
- [2] W. C. Bray, H. A. Liebhafsky, *J. Am. Chem. Soc.*, 1931, **53**, 38–44.
- [3] S. Dushman, *J. Phys. Chem.*, 1903, **8**, 453–482.
- [4] G. Schmitz, *Phys. Chem. Chem. Phys.*, 1999, **1**, 1909-1914.
- [5] S. D. Furrow, *J. Phys. Chem.*, 1987, **91**, 2129 - 2135.
- [6] A. Olexová, M. Mrákavová, M. Melicherčík, L'. Treindl, *Collect. Czech. Chem. Commun.*, 2006, **71**, 91-106.
- [7] D. Stanisavljev, I. N. Bubanja, K. Stevanović, *React. Kinet. Mech. Catal.*, 2016, **118**, 143 – 151.

## FRactal Kinetics as a Tool for Modelling of Isothermal Kinetics of Exchange of Water Absorbed in Silica Hydrogel with Ethanol

S. Maćešić<sup>1</sup>, B. Adnađević<sup>1</sup> and N. Cvetković<sup>2</sup>

<sup>1</sup> *University of Belgrade, Faculty of Physical Chemistry, Studentski trg 12-16, 11000 Belgrade, Serbia, e-mail: stevan.macesic@ffh.bg.ac.rs*

<sup>2</sup> *College of Agriculture and food technology, Prokuplje, Ćirila i Metodija 1, Serbia*

### ABSTRACT

The applicability of fractal kinetics to describe isothermal kinetics of exchange of water absorbed in silica hydrogel with ethanol was investigated. It was found that fractal kinetic equation can give complete mathematical description of conversion curves of exchange. The values of the fractal kinetic equation parameters were calculated. It was determined that kinetics of exchange of molecules of absorbed water with ethanol is limited by exchange rate at reaction space whose fractal spectral dimensions varying in range between 3.42-3.76.

### INTRODUCTION

Nanoporous silica aerogels are unique materials characterized by their specific physicochemical properties such as: high specific surface area (1000 m<sup>2</sup>/g), high porosity (80-99%), low density (30-50 kg/m<sup>3</sup>), high thermal insulation value (0.005 W/mK), ultra low dielectric constant (1.0 - 2.0), low index of refraction (1.05) which made them subject of numerous studies and allowed them wide range of applications.

Drying of the silica hydrogel is final and most critical step in the production process of silica aerogel. Ambient pressure drying is attractive alternative method for the commercial production of silica aerogel. However, if the aerogels are dried under the ambient conditions, the solvent exerts a capillary pressure on the gel network resulting into the collapse of the silicagel network structure[1]. In order to preserve the network structure intact drying of the gels is done by exchanging the water absorbed in silica hydrogel with the solvent whose surface tension is lower than the surface tension of the water (methanol, ethanol).

Considering the fact that there are no previous studies, in this work investigation of isothermal kinetics of exchange of water absorbed in silica hydrogel with ethanol was done. Since the exchange process affects the

structure of the hydrogel and as result rate coefficients are time dependent, for predicting the rate at which water is released from silica hydrogel fractal kinetic equation[2] was used.

## EXPERIMENTAL

### *Hydrogel synthesis*

Silica hydrogel was synthesized according to the procedure described in Shewale et al [1].

### *Kinetic of exchange of water absorbed in silica hydrogel with ethanol*

Kinetic curves of exchange were measured according to the following procedure. In 250 mL of absolute ethanol, preheated at predetermined temperature a  $1.0 \pm 0.1$  g of equilibrium swollen, grounded silica xerogel was added. The reaction mixture was stirred with a mechanic stirrer with 400 rpm. Water concentration was determined by measuring the refractive index of reaction mixture. Quantity of water exchange was determined as:

$$q = \frac{c_{\text{H}_2\text{O}} \cdot m_{\text{RS}}}{M_{\text{HG}}} \quad (1)$$

where:  $c_{\text{H}_2\text{O}}$  is mass concentration of water in reaction system at reaction time ( $t$ ),  $m_{\text{RS}}$  is mass of reaction system,  $M_{\text{HG}}$  is mass of water in hydrogel. The degree of water exchange with ethanol  $\alpha$  was calculated as:

$$\alpha = \frac{q}{q_{\text{max}}} \quad (2)$$

### *Modeling of the kinetics of exchange*

Conversion kinetic curves were fitted with fractal kinetic equation[3]

$$\alpha(t) = \alpha_{\text{max}} \left[ 1 - (n-1) \left( \frac{t}{\tau_c} \right)^\beta \right]^{\frac{1}{n-1}} \quad (3)$$

where  $\alpha_{\text{max}}$  represents the maximum exchanged quantity (in our case  $\alpha_{\text{max}} = 1$ ),  $n$  is the overall reaction order,  $\beta$  represents fractional time index while  $\tau_c$  is characteristic time. Value of fractal spectral dimension ( $d_s$ ) is calculated as  $d_s = 2/(n-1)$ . The effective time-dependent rate coefficient  $K_{n,\beta}$  can be calculated from

$$K_{n,\beta} = \beta \frac{t^{\beta-1}}{\tau_c^\beta} \left( 1 + (n-1) \left( \frac{t}{\tau_c} \right)^\beta \right)^{-1} \quad (4)$$

In order to find the values of the parameters  $n$ ,  $\beta$  and  $\tau_c$  that produce most accurate fit of equation (3) to the experimental data, Levenberg–Marquardt algorithm was used. For this purpose a program in MATLAB programming package was developed.

## RESULTS AND DISCUSSION

Isothermal conversion curves of exchange of water absorbed in silica hydrogel with ethanol measured at 297 K, 306 K and 316 K are presented on Figure 1.

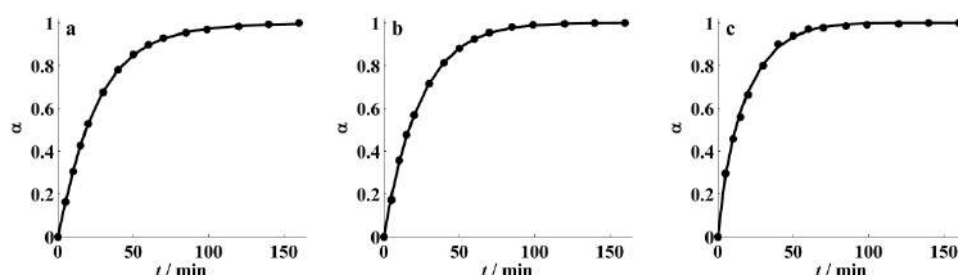


**Figure 1.** Kinetic curves of exchange of water absorbed in silica hydrogel with ethanol measured at: a) 297 K b) 306 K c) 316 K. Dots (•) represent experimental data while line (—) represents simulated values.

In all conversion curves are observed three distinct shapes of  $\alpha$  changes with  $t$ : linear, convex and plateau region. In the beginning of the exchange,  $\alpha$  increases almost linearly with  $t$ . Then, increase of  $\alpha$  with  $t$  decelerates (convex region) end then process ends (plateau region). With increasing temperature the slope of the linear region of the conversion curves increase which indicates that exchange rate also increases. The fit of the conversion curves to equation (3) are represented with line (—) in Figure 1. As can be seen equation (3) fit very accurately isothermal conversion curves. Calculated values of the fractal kinetic equation parameters are presented in Table 1.

**Table 1.** Temperature effect on the fractal kinetic equation parameters

T / K	$n$	$\beta$	$\tau_c$	$d_s$	$rss$
297	1.5847	0.90637	0.85501	3.42	$4.5613 \times 10^{-5}$
306	1.5411	0.88031	0.73873	3.69	$3.3061 \times 10^{-4}$
316	1.5308	0.88843	0.58510	3.76	$7.7737 \times 10^{-4}$

The value of the fractal kinetic equation parameters  $n$  and  $\tau_c$  decreases with temperature increase, while  $\beta$  has maximum on 306 K. Calculated

values of  $d_s$  indicate that exchange process occurs at reaction space whose fractal dimension varying in range between 3.42-3.76. Due to the fractal nature of the investigated process effective time-dependent rate coefficients  $K_{n,\beta}$  were calculated (Figure 2).

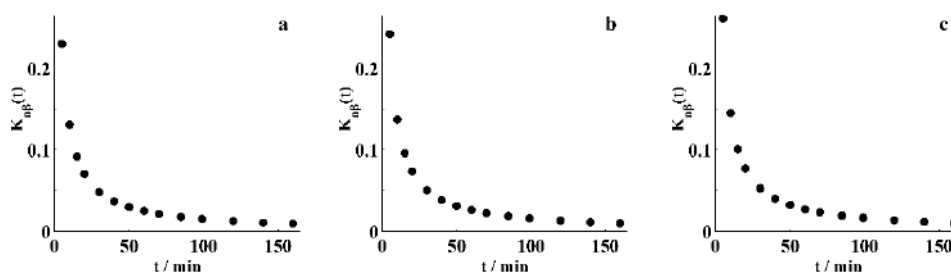


**Figure 2.** Time dependence of the rate coefficient  $K_{n,\beta}$  at a) 297 K b) 306 K c) 316 K

From Figure 2. it can be seen that the rate coefficient is time-dependant and decrease with time.

## CONCLUSION

Isothermal kinetic curves of exchange of water absorbed in silica hydrogel with ethanol can be completely described with the fractal kinetic equation. It was determined that value of  $d_s$  increase with increasing temperature. On the other hand the value of  $n$  and  $\tau_c$  decrease with increasing temperature while  $\beta$  has maximum value on 306 K. Rate coefficients  $K_{n,\beta}$  were calculated and it was shown they are time dependant. Exchange occurs at reaction space whose fractal dimensions varying in range between 3.42-3.76.

## Acknowledgement

The presented investigations were supported by The Ministry of Education, Science and Technological Development of the Republic of Serbia, under Project 172015.

## REFERENCES

- [1] P. M. Shewale, A. V. Rao, A. P. Rao, S. D. Bhagat, J. Sol-Gel Sci. Technol., 2009, **49**, 285-292.
- [2] F. Brouers, O. Sotolongo-Costa, Phys. Stat. Mech. Its Appl., 2006, **368**, 165-175.
- [3] R. Kopelman, Science, 1988, **241**, 1620-1626.

*D - Nonlinear Dynamics,  
Oscillatory Reactions,  
Chaos*



## OXYGEN PRODUCTION IN BRAY-LIEBHAFSKY REACTION: GENETIC ALGORITHM SEARCH FOR IMPROVED AGREEMENT OF A MODEL WITH EXPERIMENT

E. Szabo

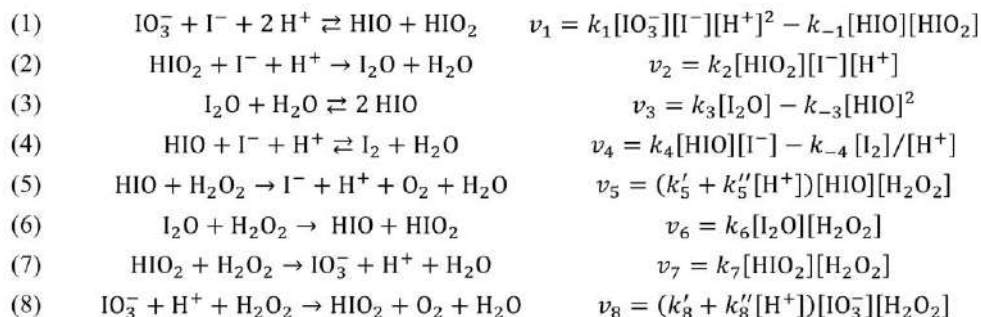
*Department of Physical and Theoretical chemistry, Faculty of Natural  
Sciences, Comenius University in Bratislava,  
Mlynská dolina, 84215 Bratislava, Slovakia. (erik.szabo@fns.uniba.sk)*

### ABSTRACT

Majority of gas produced in the Bray-Liebhafsky (BL) oscillating reaction is a single species, O<sub>2</sub>. The production thus reflects rates of specific reaction steps more directly than many other analytical signals conveniently used. Unfortunately, its measurements are rare, and they are not a typical point of reference for checking our understanding of the BL reaction. Simulations do exhibit periodic surges in O<sub>2</sub> production rates, but the integral volumes do not evolve in the typical bursts that are observed in experiments. To see how the simulations could be modified for better agreement, we navigated the parameter space with the use of a genetic algorithm. This was implemented successfully, including a working fitness function, efficient population sizes, mutation rates, etc. However, desired improvement in the simulations could be achieved only after adding a new channel for gas production.

### INTRODUCTION

Currently the most serviceable model of the BL reaction is the one based on the approach of Furrow [1], developed mainly around the cornerstone works of Kolar-Anić and Schmitz [2-5]:



Not too long ago, we presented a careful experimental reexamination of the rate of gas production from the BL reaction. [3] Our experiments confirmed that majority of  $O_2$  is produced in distinctive bursts, and the recorded shapes were fitted very well with a simple three-component model.

Firstly, there is a baseline rate of  $O_2$  production, which diminishes stepwise as the concentration of  $H_2O_2$  is decreased with each burst. Superimposed on this baseline, the bursts were fitted as a two-step process. In the first step, an intermediate is produced at a rate represented by a very sharp peak. We used narrow Gaussian peaks, but the shape played little role; the intermediate appears practically at once. In the second step, the build-up is released as gaseous  $O_2$  through a process with first-order kinetics. This model was sufficient to fit all recorded gas bursts.

In our experiments, the maximum baseline production of gas, at the end of the induction period, was proceeding towards the total amount of gas at a rate of 1.5-1.7 % per minute. The first burst, however, yielded a peak rate more than 20-times higher, and the half-width of the peak was 8-11 s. Overall, the areas under the peaks were significant. Analysis of the burst shapes assigned 40-55 % (depending on stirring) of total gas to the abrupt component. In the oscillatory phase, the amount of gas produced by the steady baseline component was around 50 % at low stirring, and only 30 % at high stirring. This is in a dramatic contrast with simulations.

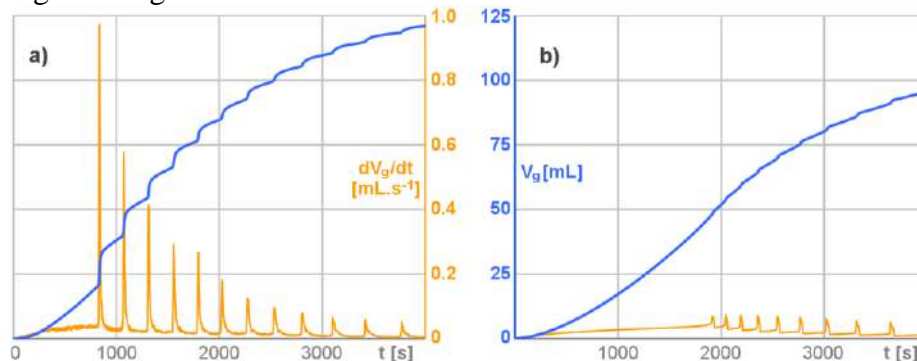


**Figure 1.** Gas production in BL found a) experimentally and b) in simulation based on mechanism (1)-(8): integral volume (blue) and rate of production (yellow).  $[KIO_3]_0 = 0.360$  M,  $[H_2O_2]_0 = 0.345$  M,  $[HClO_4]_0 = 0.055$  M,  $V_{tot} = 30$  mL. Experiment:  $60.0 \pm 0.1$  °C, dark, 1000 rpm stirring. Simulation:  $[I^-]_0 = 10^{-9}$  M, rate constants from [5]:  $k_1 = 3000$  M<sup>-3</sup>/s,  $k_{-1} = 1.32 \times 10^6$  M<sup>-1</sup>/s,  $k_2 = 8.33 \times 10^9$  M<sup>-2</sup>/s,  $k_3 = 83.3$  1/s,  $k_{-3} = 5.25 \times 10^6$  M<sup>-1</sup>/s,  $k_4 = 5 \times 10^9$  M<sup>-1</sup>/s,  $k_{-4} = 0.075$  M/s,  $k_5' = 200$  M<sup>-1</sup>/s,  $k_5'' = 500$  M<sup>-2</sup>/s; constants adapted as in [6] for better induction period and oscillations:  $k_6 = 3330$  M<sup>-1</sup>/s,  $k_7 = 10$  M<sup>-1</sup>/s,  $k_8' = 4.5 \times 10^{-6}$  M<sup>-1</sup>/s,  $k_8'' = 1.87 \times 10^{-4}$  M<sup>-2</sup>/s.

Regardless the induction period, which was somehow excessive even with rate constants  $k_6$ - $k_8$  slightly modified as in [6], the baseline rates of  $O_2$  production were reproduced by the model quite well. However, the following peaks did not even double that value, and they were quite short. The integral trace of  $O_2$  volume in simulation makes the periodic changes hardly noticeable.

### GENETIC ALGORITHM SEARCH

The question of how a mechanism of an oscillating reaction might be optimized is easy to pose, but only sometimes can be solved analytically. Guided trial and error is often the only method readily available, and chemical kinetics is one of the fields where genetic algorithms (GAs) may be extremely helpful [7-9].

**Genes.** In order to delineate the task within reasonable size and controllability, we decided that stoichiometry and rate equations should be fixed, and if needed, modified manually. The genetic material to be optimized were only the rate constants.

**Genetic code and mutation operator.** An obvious option of encoding a numeric values in a linear string is to use binary representation, as in [7]. Mutations are very simple in this case. However, if they are equally likely at any position of the string, the resulting numeric values might vary too wildly for searching the parameter space efficiently. In our approach, the binary representation was omitted, and our code was continuous-valued.

The objective was to optimize 13 rate constants, and so the genotypes consisted of 13 decimal numbers,  $\log k_1 - \log k_8$ . This way of coding also offered much more flexibility in formulation of the mutation operator. Ours was a multiplication of a rate constant by a random number,  $10^m$ . When  $m$  was normally distributed around 0, the search for new values could be directed to concentrate around those values that were already working. Still, completely random mutations could also be achieved, just by selecting  $m$  with a very large standard deviation.

**Phenotype and fitness function.** Expression of the genes into traits was simply a numeric integration of the model with the given rate constants. Since the system of differential equations derived from (1)-(8) is generally a

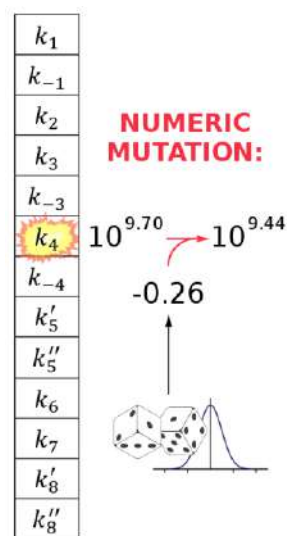


**Figure 2.** Numeric genetic code and mutation operator.

stiff ODE system, we implemented the 4<sup>th</sup> order semi-implicit integration by Rosenbrock's method with Kaps-Rentrop stepping [10].

Finally, the key aspect of any GA is the function that evaluates fitness. In our case, this had to quantify how well the rates of O<sub>2</sub> production in a model match the shape that was set as a benchmark, based on experimental data. However, their agreement or disagreement had to be evaluated cautiously. Sum-of-squares measures, for instance, would not be sufficient, as these could lead to solutions that match average rates of gas production, but have, in fact, no periodic component.

In order to avoid this, our fitness function was a product of two factors. One was for agreement in how numbers of oscillations increase with time. The other evaluated agreement in the values of the rates of O<sub>2</sub> production within individual periods. To compensate for the shortness of peaks, higher rates contributed with higher weights. In the end, both factors were between 0 and 1, where 1 represented perfect agreement. The trace in Figure 1b, for instance, has oscillation distribution fitness 0.201, and shape fitness 0.021.

#### GA parameters.

Optimization was run many times while we were optimizing all settings for the GA. Efficient evolution was observed with populations of 60 trial solutions, each generation replacing the weakest 15 with 9 new trial solutions formed by

mutation (the optimal standard deviation in  $m$  was 0.50) and 6 formed by cross-over. The crossover recombination was much more progressive if the parental genotypes were picked with probability proportional to their fitness.

Added to mutation and cross-over, we found that the rate of evolution could be greatly enhanced by including a rescaling operator. New solutions were adjusted for increased match with the benchmark by properly rescaling their time axes, changing all rate constants at once by the same factor.

Finally, although each optimization was individual, it was found that evolution of the populations to 10000 generations gave in just 3 repetitions average fitness which in 90 % of cases was no more than 10 % away from the average fitness obtained in 20 repetitions.

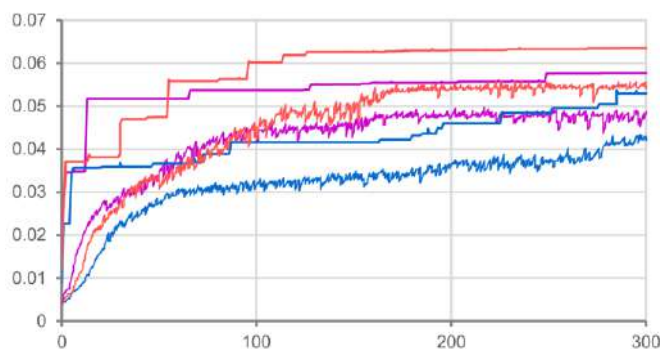


**Figure 3.** Illustration of evolution of maximum fitness and average population fitness in 3 runs of optimization during first 300 generations.

### OPTIMIZATION WITH NO ADDED REACTIONS

In optimizations of rate constants with the original model (1)-(8), the average fitness of initial populations rarely exceeded 0.002, but usually, the fittest genotype was already around 0.01. By 300 generations vast majority of optimizations converged to solutions with fitness around 0.06.

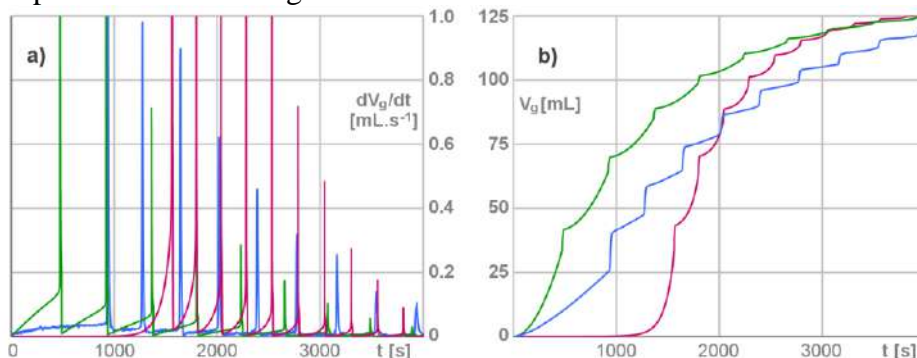


**Figure 4.** Results of GA-optimization (green, red) of rate constants in model (1)-(8) for better agreement with experimental record (blue) of gas bursts: a) rates of production b) integral volumes produced. Optimized rate constants, in the same units as in Fig. 1: green  $k_1 5670$ ,  $k_{-1} 4.42 \times 10^4$ ,  $k_2 3.60 \times 10^{10}$ ,  $k_3 18.7$ ,  $k_{-3} 3.58 \times 10^6$ ,  $k_4 1.98 \times 10^8$ ,  $k_{-4} 0.040$ ,  $k_5' 102$ ,  $k_5'' 1970$ ,  $k_6 178$ ,  $k_7 0.045$ ,  $k_8' 2.03 \times 10^{-8}$ ,  $k_8'' 2.10 \times 10^{-6}$ ; red  $k_1 10.3$ ,  $k_{-1} 1.54 \times 10^5$ ,  $k_2 1.85 \times 10^8$ ,  $k_3 2.88$ ,  $k_{-3} 1.58 \times 10^6$ ,  $k_4 4.67 \times 10^5$ ,  $k_{-4} 0.477$ ,  $k_5' 1900$ ,  $k_5'' = 4.07$ ,  $k_6 1670$ ,  $k_7 0.362$ ,  $k_8' 6.78 \times 10^{-8}$ ,  $k_8'' = 3.28 \times 10^{-7}$ .

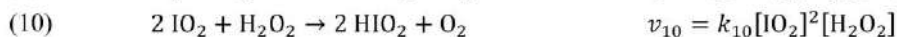
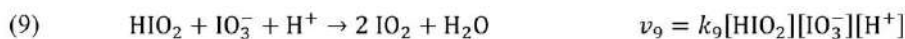
If we look at optimized rate constants of  $\text{O}_2$  production,  $k_5 = k_5' + k_5''[\text{H}^+]$  changed only little, and  $k_8 = k_8' + k_8''[\text{H}^+]$  always decreased, in some cases by almost 2 orders. More pronounced bursts of  $\text{O}_2$  were a result of higher levels of HIO. Only  $k_1$  and  $k_2$  increased (2-6 $\times$ ), all other rate constants went down. Ratios  $k_3/k_{-3}$  and  $k_4/k_{-4}$  dropped (2-3 $\times$  and 5-12 $\times$ , respectively), but ratio  $k_1/k_{-1}$  rose significantly (50-70 $\times$ ). Unfortunately, larger bursts were also accompanied with higher baseline production rates. Moreover, these were markedly increasing long before each burst.

Besides this kind of solutions, around a third of populations also yielded a modification that achieved even higher fitness, 0.1-0.2. The peaks in  $\text{O}_2$  production were even more pronounced, however, at the cost of drastic changes in most intermediates. In this case,  $k_5$  increased (4-8 $\times$ ), and all other rate constants, except  $k_{-4}$ , went down. A few decreased dramatically, mainly  $k_1$  (200-400 $\times$ ) and  $k_4$  ( $10^4$ - $10^5$  $\times$ ). This modification added a great increase in the induction period, while the baseline production of gas was undesirably deformed, as before.

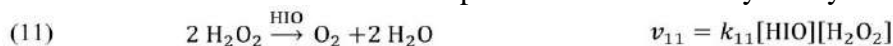
Overall, it seems that the model (1)-(8) was simply unable to produce more pronounced gas bursts without simultaneously increasing the baseline production rates and the leading edge before the bursts. The major channel in O<sub>2</sub> production in (1)-(8) is reaction (5) involving HIO, and it seems that this cannot be appropriately enforced without negative effects on other components of the model.

### OPTIMIZATION WITH NEW CHANNELS OF O<sub>2</sub> PRODUCTION

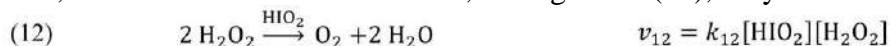
We considered several possibilities for expanding (1)-(8) with an added channel of O<sub>2</sub> production, which would be activated mainly in the oxidized stages of the BL reaction. First of all, we considered reduction of H<sub>2</sub>O<sub>2</sub> with an additional intermediate, IO<sub>2</sub> radical, inspired by the autocatalytic loop in bromate oscillators:



Of course, we cannot completely disregard the possibility that our results were somehow specific to our choices of the initial values of  $k_9$  and  $k_{10}$ . However, in our optimizations, this modification did not perform better than the original model. The results were very similar, and even more deformed on the leading edges of the gas bursts as before. The same was observed for modification of the model with decomposition of H<sub>2</sub>O<sub>2</sub> catalyzed by HIO:



Even after optimization, the model yielded gas production rates similar to those observed after optimization of the original model. Interestingly, the rate equation of (11) is, in essence, the same as of (5). So we tried to see if its insufficiency might be due to the fact that concentrations of HIO simply cannot change significantly enough between the baseline and the peaks. To do that, we tried an alternative channel, analogous to (11), only with HIO<sub>2</sub>:



These optimizations exhibited O<sub>2</sub> productions that were much closer to experimentally observed bursts. The values of  $k_{12}$  stabilized around 20-80 M<sup>-1</sup>.s<sup>-1</sup>, and  $k_5$  and  $k_8$  decreased (3-15× and 100-300×, respectively). So did  $k_{-1}$ ,  $k_{-3}$  and  $k_7$  (100-200×, 10-30×, and 10-50×, respectively). All other rate constants increased slightly (2-10×). The baseline rates of O<sub>2</sub> production were more or less flat and the bursts were strong, as desired. Even the oscillations periods were in better agreement compared to the original model, only the induction period was too small.

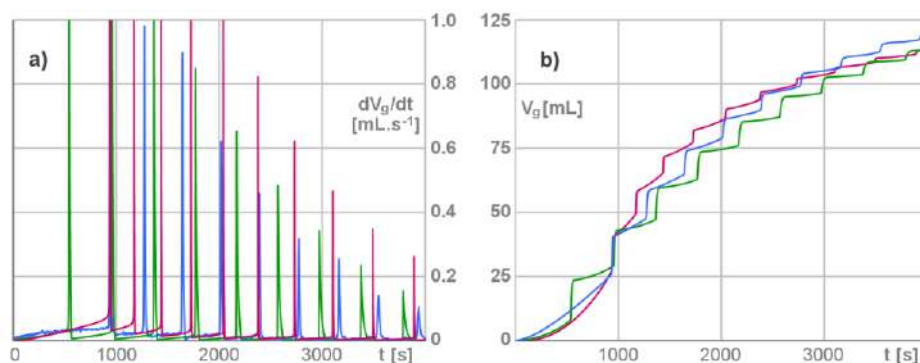
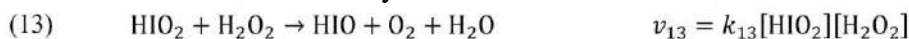


**Figure 5.** Results of GA-optimization (green, red) of rate constants in model (1)-(8) extended with reactions (12) or (13) for better agreement with experimental records (blue) of gas bursts: a) rates of production b) integral volumes produced. Optimized rate constants, in the same units as in Fig. 1: green  $k_{12} = 43.3 \text{ M}^{-1}/\text{s}$  and  $k_1 1.38 \times 10^4$ ,  $k_{-1} 7450$ ,  $k_2 1.90 \times 10^{10}$ ,  $k_3 165$ ,  $k_{-3} 4.37 \times 10^5$ ,  $k_4 3.6 \times 10^9$ ,  $k_{-4} 0.158$ ,  $k_5 55.8$ ,  $k_{-5} 0.285$ ,  $k_6 7070$ ,  $k_7 0.460$ ,  $k_8 6.65 \times 10^{-8}$ ,  $k_{-8} 1.12 \times 10^{-9}$ ; red  $k_{13} = 992 \text{ M}^{-1}/\text{s}$  and  $k_1 28.0$ ,  $k_{-1} 1.41 \times 10^6$ ,  $k_2 1.43 \times 10^9$ ,  $k_3 3.67$ ,  $k_{-3} 4.17 \times 10^6$ ,  $k_4 2.97 \times 10^8$ ,  $k_{-4} 2.20$ ,  $k_5 253$ ,  $k_{-5} 7.37$ ,  $k_6 183$ ,  $k_7 2.37$ ,  $k_8 2.75 \times 10^{-7}$ ,  $k_{-8} = 1.92 \times 10^{-8}$ .

Encouraged by this improvement, we also tried another reaction with the same rate equations as in (12), only this time not a catalytic decomposition, but a direct reduction of  $\text{H}_2\text{O}_2$  by  $\text{HIO}_2$ :



Optimizations of the model (1)-(8) with added reaction (13) were even more successful. Most rate constants dropped, mainly  $k_1$  (80-180 $\times$ ). Only  $k_{-4}$  increased significantly (20-100 $\times$ ). The value of  $k_{13}$  was around  $0.5\text{-}1.5 \times 10^3 \text{ M}^{-1}\cdot\text{s}^{-1}$ , and  $k_5$  decreased only very little. Reaction (5) maintained the role of the main channel of  $\text{O}_2$  production in the baseline rates. However, the peaks were dominated by the new channel, reaction (13). Overall, it seems that it was addition of the new channel, independent of  $\text{HIO}$ , which was the key to a successful model of gas bursts.

## CONCLUSION

We managed to implement a GA optimization of rate constants in a model of the BL reaction (1)-(8) for improved agreement of  $\text{O}_2$  production with experimental results. However, even after optimization, typical bursts of gas could not be observed in the original model without unrealistic deformation of the baseline rates of  $\text{O}_2$  production. The results suggest that this is because there is a single dominant channel of  $\text{O}_2$  production, the reduction of  $\text{H}_2\text{O}_2$

with HIO. That cannot be enforced without negative effects on other processes. To improve this, we tried adding alternative channels of O<sub>2</sub> production. Optimized model with added reduction of H<sub>2</sub>O<sub>2</sub> by HIO<sub>2</sub> was very successful in reproducing the experimental data of gas production. This suggests that a new channel of gas production should be considered for better agreement of (1)-(8) with reality.

## REFERENCES

- [1] S. Furrow, *J. Phys. Chem.*, 1987, **91**, 2129-2135.
- [2] L. Kolar-Anić, G. Schmitz, *J. Chem. Soc., Faraday Trans.*, 1992, **88**, 2343-2349.
- [3] L. Kolar-Anić, D. Misljenović, S. Anić, G. Nicolis, *React. Kinet. Catal. Lett.*, 1995, **54**, 35-41.
- [4] G. Schmitz, *Phys. Chem. Chem. Phys.*, 2001, **3**, 4741-4746.
- [5] L. Kolar-Anić, Z. Cupić, S. Anić, G. Schmitz, *J. Chem. Soc., Faraday Trans.*, 1997, **93**, 2147-2152.
- [6] I. Valent, L. Adamčíková, P. Ševčík, *J. Phys. Chem. A*, 1998, **102**, 7576-7579.
- [7] J. Ross, I. Schreiber, M. O. Vlad, *Determination of Complex Reaction Mechanisms*, Oxford University Press, Oxford, 2006.
- [8] M. Tsuchiya, J. Ross, *J. Phys. Chem. A*, 2001, **105**, 4052-4058.
- [9] E. J. Crampin, S. Schnell, P. E. McSharry, *Prog. Biophys. Mol. Biol.*, 2004, **86**, 77-112.
- [10] W. H. Press, S. A. Teukolsky, W. T. Vetterling, B. P. Flannery, *Numerical Recipes in FORTRAN 77*, 2<sup>nd</sup> ed., Cambridge University Press, Cambridge, 1992.

## ADVANCES IN THE MODELLING OF THE OSCILLATING CHEMICAL REACTIONS

S. Maćešić

*University of Belgrade, Faculty of Physical Chemistry, Studentski trg 12-16, 11000 Belgrade, Serbia, e-mail: stevan.macesic@ffh.bg.ac.rs*

### ABSTRACT

Model of Bray-Leibhafsky (BL) reaction was analyzed with aim to present a powerful method for detection of the reactions and intermediate species essential for the existence of the Andronov-Hopf bifurcation. By applying stoichiometric network analysis (SNA) it was shown that interaction between intermediate species HIO, HIO<sub>2</sub> and I<sub>2</sub>O represents a core of instability in the considered model. By applying combinatorial approach we derived three minimal sub-models essential for existence of Andronov-Hopf bifurcation in the considered model.

### INTRODUCTION

Nonlinear reaction systems are most common system in nature which due to the presence of the nonlinearities can exhibit very complex and exotic behavior. Special class of nonlinear reaction systems are those with feedback, an mechanism which allow them to have unstable non-equilibrium steady-sates and therefore exhibit diverse dynamics.

Oscillating chemical reactions are example of the nonlinear reaction systems with feedback, in which concentrations of the reactants and products, due to oscillatory changes in the concentration of intermediates, show cascading change.

Modeling of the oscillating chemical reactions is very complicated task which consist from several steps. Stability analysis and bifurcation analysis are most important steps in the modeling process since they allow efficient model optimization. Detection of the reactions and intermediate species responsible for existence of the certain types of dynamics is crucial for model optimization. But, in the case of the complex models without direct autocatalytic step this can be very difficult task to perform.

Thus, in this paper we present an powerful method based on *stoichiometric network analysis* (SNA)[1] that allows detection of the reactions and intermediate species responsible for emergence of the Andronov-Hopf bifurcation in the complex models of oscillating chemical reactions.

**MODEL**

The model of Bray-Leibhafsky (BL) reaction used for the purpose of this paper is presented in Table 1.

**Table 1.** Model of Bray-Leibhafsky reaction M(1-8) [2-5]

$\text{IO}_3^- + \text{I}^- + 2\text{H}^+ \xrightleftharpoons[k_{-1}]{k_1} \text{HIO} + \text{HIO}_2$	$v_1 = k_1[\text{I}^-]$	(R1)
	$v_{-1} = k_{-1}[\text{HIO}][\text{HIO}_2]$	(R-1)
$\text{HIO}_2 + \text{I}^- + \text{H}^+ \xrightarrow{k_2} \text{I}_2\text{O} + \text{H}_2\text{O}$	$v_2 = k_2[\text{I}^-][\text{HIO}_2]$	(R2)
$\text{I}_2\text{O} + \text{H}_2\text{O} \xrightleftharpoons[k_{-3}]{k_3} 2\text{HIO}$	$v_3 = k_3[\text{I}_2\text{O}]$	(R3)
	$v_{-3} = k_{-3}[\text{HIO}]^2$	(R-3)
$\text{HIO} + \text{I}^- + \text{H}^+ \xrightleftharpoons[k_{-4}]{k_4} \text{I}_2 + \text{H}_2\text{O}$	$v_4 = k_4[\text{I}^-][\text{HIO}]$	(R4)
	$v_{-4} = k_{-4}[\text{I}_2]$	(R-4)
$\text{HIO} + \text{H}_2\text{O}_2 \xrightarrow{k_5} \text{I}^- + \text{H}^+ + \text{O}_2 + \text{H}_2\text{O}$	$v_5 = k_5[\text{HIO}][\text{H}_2\text{O}_2]_0$	(R5)
$\text{I}_2\text{O} + \text{H}_2\text{O}_2 \xrightarrow{k_6} \text{HIO} + \text{HIO}_2$	$v_6 = k_6[\text{I}_2\text{O}][\text{H}_2\text{O}_2]_0$	(R6)
$\text{IO}_3^- + \text{H}^+ + \text{H}_2\text{O}_2 \xrightarrow{k_8} \text{HIO}_2 + \text{O}_2 + \text{H}_2\text{O}$	$v_8 = k_8[\text{H}_2\text{O}_2]_0$	(R8)

Model M(1-8) consists of eight reactions among which three are reverse. There are ten chemical species in the model:  $\text{H}_2\text{O}_2$ ,  $\text{O}_2$ ,  $\text{H}^+$ ,  $\text{IO}_3^-$ ,  $\text{I}^-$ ,  $\text{HIO}$ ,  $\text{HIO}_2$ ,  $\text{I}_2$ ,  $\text{I}_2\text{O}$  and  $\text{H}_2\text{O}$ . Dynamics of the model is determined by interaction between five intermediates species ( $\text{I}^-$ ,  $\text{HIO}$ ,  $\text{HIO}_2$ ,  $\text{I}_2$ ,  $\text{I}_2\text{O}$ ) while external species ( $\text{H}_2\text{O}_2$ ,  $\text{O}_2$  and  $\text{H}_2\text{O}$ ) which represent reactants and products in reaction (D) have much slower evolution and they are not of great importance for dynamics of the system and thereby for stability and bifurcation analysis. As regards for  $\text{H}^+$  and  $\text{IO}_3^-$  their concentrations are much higher than concentrations of other intermediate species and therefore they are considered to be constant and their concentrations are incorporated into the values of the appropriate rate constants.

**STOICHIOMETRIC NETWORK ANALYSIS**

Stability analysis in SNA is based on determination of the steady state stability and steady state reaction rates for considered model. The rates at a steady state  $r_{ss}$  are solutions of the relation

$$\mathbf{S} r_{ss} = 0 \quad (1)$$

where  $\mathbf{S}$  is stoichiometric matrix consisting of only independent intermediate species. For model M(1-8) matrix  $\mathbf{S}$  has form

$$\mathbf{S} = \begin{array}{cccccccccc} R_1 & R_{-1} & R_2 & R_3 & R_{-3} & R_4 & R_{-4} & R_5 & R_6 & R_8 \\ \left[ \begin{array}{cccccccccc} -1 & 1 & -1 & 0 & 0 & -1 & 1 & 1 & 0 & 0 \\ 1 & -1 & 0 & 2 & -2 & -1 & 1 & -1 & 1 & 0 \\ 1 & -1 & -1 & 0 & 0 & 0 & 0 & 0 & 1 & 1 \\ 0 & 0 & 1 & -1 & 1 & 0 & 0 & 0 & -1 & 0 \\ 0 & 0 & 0 & 0 & 0 & 1 & -1 & 0 & 0 & 0 \end{array} \right] \begin{array}{l} \Gamma^- \\ \text{HIO} \\ \text{HIO}_2 \\ \text{I}_2\text{O} \\ \text{I}_2 \end{array} \end{array} \quad (2)$$

The overall process can be presented as a linear combination of several elementary reaction pathways with non-negative coefficients. These elementary reaction pathways are known as extreme currents  $E_i$  and they all contribute to the steady state values of reaction rates. The contributions of the extreme currents  $E_i$ , denoted as the current rates  $j_i$ , are the components of the corresponding current rate vector  $\mathbf{j}$ , whereas the extreme currents  $E_i$  are the columns of the extreme current matrix  $\mathbf{E}$ . [4,6,7] For considered model matrix  $\mathbf{E}$  is

$$\mathbf{E} = \begin{array}{ccccc} E_1 & E_2 & E_3 & E_4 & E_5 \\ \left[ \begin{array}{ccccc} 1 & 0 & 0 & 0 & 0 \\ 1 & 0 & 0 & 0 & 1 \\ 0 & 0 & 0 & 1 & 1 \\ 0 & 1 & 0 & 0 & 0 \\ 0 & 1 & 0 & 0 & 0 \\ 0 & 0 & 1 & 0 & 0 \\ 0 & 0 & 1 & 0 & 0 \\ 0 & 0 & 0 & 1 & 0 \\ 0 & 0 & 0 & 1 & 1 \\ 0 & 0 & 0 & 0 & 1 \end{array} \right] \begin{array}{l} R_1 \\ R_{-1} \\ R_2 \\ R_3 \\ R_{-3} \\ R_4 \\ R_{-4} \\ R_5 \\ R_6 \\ R_8 \end{array} \end{array} \quad (3)$$

The basic equation of the SNA which gives relation between steady state reaction rates and current rates is

$$r_{ss} = \mathbf{E} \mathbf{j} \quad (4)$$

The stability of the steady state is defined by the sign and character of the eigenvalues of the Jacobian matrix  $\mathbf{M}$  which in SNA notation can be written as

$$\mathbf{M} = -\mathbf{V}(\mathbf{j}) \text{diag} \mathbf{h}, \text{ where } \mathbf{V}(\mathbf{j}) = -\mathbf{S} \text{diag}(\mathbf{E} \mathbf{j}) \mathbf{K}^T \quad (5)$$

where  $\mathbf{V}(\mathbf{j})$  is *current rate matrix*,  $\mathbf{K}$  is a matrix of the order of reactions,  $\text{diag} \mathbf{h}$  is a diagonal matrix whose elements are the reciprocals of steady state concentrations while  $\text{diag}(\mathbf{E} \mathbf{j})$  is a diagonal matrix whose elements are the reaction rates at the steady state. For model M(1-8) matrix  $\mathbf{K}$  is

$$\mathbf{K} = \begin{array}{cccccccc} R_1 & R_{-1} & R_2 & R_3 & R_{-3} & R_4 & R_{-4} & R_5 & R_6 & R_8 \\ \left[ \begin{array}{cccccccc} 1 & 0 & 1 & 0 & 0 & 1 & 0 & 0 & 0 & 0 \\ 0 & 1 & 0 & 0 & 2 & 1 & 0 & 1 & 0 & 0 \\ 0 & 1 & 1 & 0 & 0 & 0 & 0 & 0 & 0 & 0 \\ 0 & 0 & 0 & 1 & 0 & 0 & 0 & 0 & 1 & 0 \\ 0 & 0 & 0 & 0 & 0 & 0 & 1 & 0 & 0 & 0 \end{array} \right] & \begin{array}{l} \Gamma^- \\ \text{HIO} \\ \text{HIO}_2 \\ \text{I}_2\text{O} \\ \text{I}_2 \end{array} \end{array} \quad (6)$$

whereas matrix  $\mathbf{V}(\mathbf{j})$  has the form

$$\mathbf{V}(\mathbf{j}) = \begin{array}{ccccc} & \Gamma^- & \text{HIO} & \text{HIO}_2 & \text{I}_2\text{O} & \text{I}_2 \\ \left[ \begin{array}{ccccc} j_1+j_2+j_4+j_5 & -j_1+j_2-j_4-j_5 & -j_1+j_4 & 0 & -j_2 \\ -j_1+j_2 & j_1+j_2+4j_3+j_4+j_5 & j_1+j_5 & -(2j_3+j_4+j_5) & -j_2 \\ -j_1+j_4+j_5 & j_1+j_5 & j_1+j_4+2j_5 & -(j_4+j_5) & 0 \\ -(j_4+j_5) & -2j_3 & -(j_4+j_5) & j_3+j_4+j_5 & 0 \\ -j_2 & -j_2 & 0 & 0 & j_2 \end{array} \right] & \begin{array}{l} \Gamma^- \\ \text{HIO} \\ \text{HIO}_2 \\ \text{I}_2\text{O} \\ \text{I}_2 \end{array} \end{array} \quad (7)$$

The eigenvalues of jacobian matrix  $\mathbf{M}$  are the roots  $\lambda$  of the characteristic polynomial

$$\text{Det}[\lambda \mathbf{I} - \mathbf{M}] = \sum_{i=0}^{i=n} \alpha_i \lambda^{n-i} = 0 \quad (8)$$

where  $\alpha_i$  is coefficient of the characteristic polynomial while  $n$  represent the number of intermediate species ( $n = 1, 2, \dots, 5$ ). When more than three

intermediate species are present in the model, which is almost always the case, analytical calculation of the eigenvalues and therefore obtaining condition for appearance of Andronov-Hopf bifurcation cannot be done. However, the analytical solution that describes condition for appearance of Andronov-Hopf bifurcation can be obtained by means of current rate matrix  $\mathbf{V}(\mathbf{j})$ . Since any  $\alpha_i$  is the sum of minors of  $\mathbf{V}(\mathbf{j})$  with dimension  $i \times i$  multiplied by the product of the corresponding  $h_i$  values ( see equation (5)) we look for a negative diagonal minors of  $\mathbf{V}(\mathbf{j})$ . Considering this new criterion, for Andronov-Hopf bifurcation to be possible it is necessary that at least one diagonal minor of order  $(n-1) \times (n-1)$  has negative terms while for possible occurrence of saddle-node bifurcation it is necessary that determinant of  $\mathbf{V}(\mathbf{j})$  has at least one negative term.[6] Although it is an approximation, this criterion often gives very accurate results.[4,7,8]

Analysis of the matrix  $\mathbf{V}(\mathbf{j})$  of model M(1-8) given in equation (7) showed that there are three negative diagonal minors. They are given in Table 2.

From Table 2 we can see that Andronov-Hopf bifurcation can occur with proper choice of parameter values, since there are two diagonal minors of dimension  $4 \times 4$  with negative terms while determinant  $\mathbf{V}(\mathbf{j})$  doesn't have negative terms and therefore saddle-node bifurcation cannot occur.

**Table 2.** Negative diagonal minors of matrix  $\mathbf{V}(\mathbf{j})$  presented in (7). Minor dimensions are given in the first column and corresponding combination of rows-columns of matrix  $\mathbf{V}(\mathbf{j})$  is indicated by plus sign in other columns. In the first row, columns and rows of matrix  $\mathbf{V}(\mathbf{j})$  are identified by ordinal numbers and corresponding intermediary species.

Minor dimensions	1 (I <sup>-</sup> )	2 (HIO)	3 (HIO <sub>2</sub> )	4 (I <sub>2</sub> O)	5 (I <sub>2</sub> )
3×3		+	+	+	
4×4	+	+	+	+	
4×4		+	+	+	+

Now, if we continue with analysis of diagonal minors we can see that the smallest negative minor  $M_{234}$  is of dimension  $3 \times 3$  and it is a part of all other negative diagonal minors. From this we can see that instabilities in the considered model are results of interactions between intermediate species HIO, HIO<sub>2</sub> and I<sub>2</sub>O. The corresponding determinant is given by the expression

$$M_{234}(\mathbf{j}) = j_5^3 + (j_1 + 5j_2 + j_3 + 3j_4)j_5^2 + (2j_1 - j_2 + 2j_5)j_4^2 + (8j_1j_2 + j_1j_3 + 3j_1j_5 + j_2j_3 + 5j_2j_5 + j_3j_5)j_4 + (7j_1j_2 + j_1j_3 + 2j_2j_3)j_5 + j_1j_2j_3 \quad (9)$$

### DETERMINATION OF THE REACTIONS RESPONSIBLE FOR ANDRONOV-HOPF BIFURCATION

Next step is to detect reactions, and therefore appropriate sub-models of M(1-8), responsible for existence of Andronov-Hopf bifurcation. In order to achieve this we applied combinatorial approach, that is, we performed analysis using only certain reaction pathways, which are represented by corresponding extreme currents of (3).

Analysis showed that minimal combinations of extreme currents which produce Andronov-Hopf bifurcation are:  $E_1E_2E_4$ ,  $E_2E_3E_4$  and  $E_2E_4E_5$ . As can be seen, extreme currents  $E_2$  and  $E_4$  (reactions (R3), (R-3), (R5) and (R6)) represent the core of instability but they alone cannot produce Andronov-Hopf bifurcation. The sub-models deriving from the found combinations of extreme current are presented in Tables 3, 4 and 5.

Sub-model obtained from the combination of the extreme currents  $E_1E_2E_4$  has two reaction less ((R4) and (R-4)) than the model M(1-8). Also, intermediate specie  $I_2$  is not involved in the mechanism of this sub-model. Sub-model obtained from the combination of the extreme currents  $E_2E_3E_4$  (Table 4) has two reaction less ((R1) and (R-1)) than the model M(1-8) and same number of intermediate species. Sub-model obtained from the combination of the extreme currents  $E_2E_3E_4$  (Table 5) has three reaction less ((R1), (R4) and (R-4)) than the model M(1-8) and same number of intermediate species.

All derived sub-models are capable to simulate Andronov-Hopf bifurcation for the certain values of the parameters. Existence of these three different sub-models can be possible explanation for complex dynamics like mixed-mode oscillations and chaos that have been found in this model.[10]

**Table 3.** Sub-model obtained from the combination of the extreme currents  $E_1E_2E_4$

Reactions	$E_1$	$E_2$	$E_4$
$IO_3^- + I^- + 2H^+ \xrightarrow{k_1} HIO + HIO_2$	(R1)		
$HIO + HIO_2 \xrightarrow{k_{-1}} IO_3^- + I^- + 2H^+$	(R-1)		
$HIO_2 + I^- + H^+ \xrightarrow{k_2} I_2O + H_2O$			(R2)
$I_2O + H_2O \xrightarrow{k_3} 2HIO$		(R3)	
$2HIO \xrightarrow{k_{-3}} I_2O + H_2O$		(R-3)	
$HIO + H_2O_2 \xrightarrow{k_5} I^- + H^+ + O_2 + H_2O$			(R5)
$I_2O + H_2O_2 \xrightarrow{k_6} HIO + HIO_2$			(R6)

**Table 4.** Sub-model obtained from the combination of the extreme currents

$E_2E_3E_4$			
Reactions	$E_2$	$E_3$	$E_4$
$\text{HIO}_2 + \text{I}^- + \text{H}^+ \xrightarrow{k_2} \text{I}_2\text{O} + \text{H}_2\text{O}$			(R2)
$\text{I}_2\text{O} + \text{H}_2\text{O} \xrightarrow{k_3} 2\text{HIO}$	(R3)		
$2\text{HIO} \xrightarrow{k_3} \text{I}_2\text{O} + \text{H}_2\text{O}$	(R-3)		
$\text{HIO} + \text{I}^- + \text{H}^+ \xrightarrow{k_4} \text{I}_2 + \text{H}_2\text{O}$			(R4)
$\text{I}_2 + \text{H}_2\text{O} \xrightarrow{k_4} \text{HIO} + \text{I}^- + \text{H}^+$			(R-4)
$\text{HIO} + \text{H}_2\text{O}_2 \xrightarrow{k_5} \text{I}^- + \text{H}^+ + \text{O}_2 + \text{H}_2\text{O}$			(R5)
$\text{I}_2\text{O} + \text{H}_2\text{O}_2 \xrightarrow{k_6} \text{HIO} + \text{HIO}_2$			(R6)

**Table 5.** Sub-model obtained from the combination of the extreme currents

$E_2E_3E_4$			
Reactions	$E_2$	$E_4$	$E_5$
$\text{HIO} + \text{HIO}_2 \xrightarrow{k_1} \text{IO}_3^- + \text{I}^- + 2\text{H}^+$			(R-1)
$\text{HIO}_2 + \text{I}^- + \text{H}^+ \xrightarrow{k_2} \text{I}_2\text{O} + \text{H}_2\text{O}$		(R2)	(R2)
$\text{I}_2\text{O} + \text{H}_2\text{O} \xrightarrow{k_3} 2\text{HIO}$	(R3)		
$2\text{HIO} \xrightarrow{k_3} \text{I}_2\text{O} + \text{H}_2\text{O}$	(R-3)		
$\text{HIO} + \text{H}_2\text{O}_2 \xrightarrow{k_5} \text{I}^- + \text{H}^+ + \text{O}_2 + \text{H}_2\text{O}$			(R5)
$\text{I}_2\text{O} + \text{H}_2\text{O}_2 \xrightarrow{k_6} \text{HIO} + \text{HIO}_2$		(R6)	(R6)
$\text{IO}_3^- + \text{H}^+ + \text{H}_2\text{O}_2 \xrightarrow{k_8} \text{HIO}_2 + \text{O}_2 + \text{H}_2\text{O}$			(R8)

## CONCLUSION

In this paper we carried out analysis of the model of BL reaction M(1-8) (Table 1) with aim to present a powerful method for detection of the reactions and intermediate species essential for existence of the Andronov-Hopf bifurcation. By analyzing diagonal minors of matrix  $\mathbf{V}(j)$  we showed that model M(1-8) can simulate Andronov-Hopf bifurcation which emerge as result of interaction between intermediate species HIO, HIO<sub>2</sub> and I<sub>2</sub>O. By applying combinatorial approach on the model M(1-8) we derived three minimal sub-models capable to simulate Andronov-Hopf bifurcation and for each of them reactions (R3), (R-3), (R5) and (R6) represent core of

instability. Existence of these three different sub-models can be possible explanation for complex dynamics like mixed-mode oscillations and chaos that have been found in this model.

### *Acknowledgement*

This work was partially supported by the Ministry for Science of the Republic of Serbia (Grants no. 172015).

### **REFERENCES**

- [1] B.L. Clarke, *Cell Biophys.*, 1988, **12**, 237–253.
- [2] Lj. Kolar-Anić, G. Schmitz, *J. Chem. Soc. Faraday Trans.*, 1992, **88**, 2343–2349.
- [3] Lj. Kolar-Anić, D. Misljenović, S. Anić, G. Nicolis, *React. Kinet. Catal. Lett.*, 1995, **54**, 35–41.
- [4] G. Schmitz, Lj.Z. Kolar-Anić, S.R. Anić, Ž.D. Čupić, *J. Phys. Chem. A*, 2008, **112**, 13452–13457.
- [5] Lj. Kolar-Anić, Ž. Čupić, G. Schmitz, S. Anić, *Chem. Eng. Sci.*, 2010, **65**, 3718–3728.
- [6] B.L. Clarke in: *Advances in Chemical Physics*, I. Prigogine, S.A. Rice (Eds.), John Wiley & Sons Inc., 1980: pp. 1–215.
- [7] Ž. Čupić, V.M. Marković, A. Ivanović, Lj. Kolar-Anić in: *Mathematical Modelling*, C.R. Brennan (Eds.), Nova Science Publishers Inc., 2011: pp. 111–178.
- [8] S. Maćešić, Ž. Čupić, Lj. Kolar-Anić, *Hem. Ind.*, 2012, **66**, 637–646.
- [9] S. Maćešić, Ž. Čupić, Lj. Kolar-Anić, *React. Kinet. Mech. Catal.*, 2016, **118**, 39–55.
- [10] A. Z. Ivanović, Ž.D. Čupić, M.M. Janković, Lj.Z. Kolar-Anić, S.R. Anić, *Phys. Chem. Chem. Phys.*, 2008, **10**, 5848–5858.

## I<sub>2</sub>O PREPARATION AND REACTIONS IN AQUEOUS SOLUTIONS

G. Schmitz

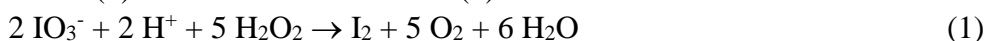
*Université Libre de Bruxelles, F. Roosevelt Av. 50, 1050 Brussels.  
(gschmitz@ulb.ac.be)*

### ABSTRACT

I<sub>2</sub>O is an essential intermediate in the oscillating Bray-Liebhafsky reaction mechanism and explains simply the feedback leading to oscillations. We show also that the reaction  $2 \text{HOI} \rightleftharpoons \text{I}_2\text{O} + \text{H}_2\text{O}$  is the first step of the HOI disproportionation mechanism. A comparison with the known compounds Cl<sub>2</sub>O and Br<sub>2</sub>O properties is presented. The discovery in 2012 of a new method for I<sub>2</sub>O preparation in sulfuric acid will allow knowing better the properties of this compound.

### I<sub>2</sub>O AND THE BL REACTION

I<sub>2</sub>O is an unstable compound which has never been observed directly. Its existence is accepted only because it allows explaining experimental facts for which there is no other explanation. We have proposed it [1] to explain the feedback leading to oscillations during the Bray-Liebhafsky (BL) reaction, the decomposition of hydrogen peroxide catalyzed by iodate and iodine. This decomposition is the result of two reactions, the reduction of iodate (1) and the iodine oxidation (2).



Any mechanism of the BL reaction must include at least one reaction where H<sub>2</sub>O<sub>2</sub> acts as a reducer and one where it acts as an oxidant. Under the experimental conditions where the BL oscillations are generally studied, the direct reduction of iodate by H<sub>2</sub>O<sub>2</sub> is much too slow to explain the rate of reaction (1) and the rate of the direct oxidation of iodine (2) is almost zero. When the concentration of hydrogen peroxide is very large, another reaction involving free radicals may participate [2] but we do not discuss complications which are not part of the core of the BL mechanism. Reactions (1) and (2) are complex and H<sub>2</sub>O<sub>2</sub> must reduce and oxidize intermediate compounds. Two of them are formed by the hydrolysis of iodine, a very fast reaction.



An explanation of the reduction (1) was quickly accepted. Iodate is reduced by iodide in the Dushman reaction producing HOI which is reduced to iodide by  $\text{H}_2\text{O}_2$  according to (4). The kinetics of this reaction was studied by Liebhafsky [3] and we have recalculated his rate constant [4]. The kinetics of reaction (2) was more difficult to explain. We have shown [1] that the main features of the oscillations can be explained if the compound oxidized by  $\text{H}_2\text{O}_2$  is  $\text{I}_2\text{O}$  formed by the reversible reaction (5). The resulting feedback leading to oscillations is not the result of a direct autocatalysis as in many models giving oscillations but is a consequence of the competition between reaction (4) of order 1 with respect to [HOI] and reactions (5) and (6) of order 2 with respect to [HOI].



The ratio  $r_6/r_4$  between the rates of oxidation and reduction by  $\text{H}_2\text{O}_2$  is proportional to [HOI]. When [HOI] is small,  $r_6/r_4$  is small and [I<sup>-</sup>] is large because of the quasi-equilibrium (3). We observe mainly the iodate reduction (1) and reaction (4) tends to decrease further [IOH]. When [IOH] is large,  $r_6/r_4$  is large and [I<sup>-</sup>] is small. We observe mainly the iodine oxidation (2) which tends to increase further [IOH]. This feedback destabilizes the quasi-steady state where the rates of reactions (1) and (2) are equal. The destabilizing effect of reactions (3) to (6) has been confirmed by Stoichiometric Network Analysis [5, 6]. When the quasi-steady state is unstable, it is surrounded by a limit cycle with four parts, two stable branches where there is mainly either reaction (1) or reaction (2) and two transitions from one to the other. These transitions are controlled by the iodine concentration and the quasi-equilibrium (3). Reactions (4) to (6) also explain that the rate of iodine oxidation by  $\text{H}_2\text{O}_2$  decreases when the concentration of the reagent  $\text{H}_2\text{O}_2$  increases. Under the conditions of the BL reaction, reaction (6) quickly consumes the  $\text{I}_2\text{O}$  produced by (5) so that this reaction is not at equilibrium and the rate of oxidation of HOI increases less than proportionally to  $[\text{H}_2\text{O}_2]$ . On the other hand, the reduction rate  $r_4$  is proportional to  $[\text{H}_2\text{O}_2]$ . Therefore, the net result, oxidation rate less reduction rate, decreases when  $[\text{H}_2\text{O}_2]$  increases. Numerical simulations explain quantitatively the experimental results [4, 7].

### **I<sub>2</sub>O AND HOI DISPROPORTIONATION**

The kinetics of HOI disproportionation (7) was the subject of dozens of studies for more than a century with seemingly contradictory results. The rate law changes with the experimental conditions, mainly the pH but also

the iodide concentration and the various buffers. The kinetic constants differ sometimes by several orders of magnitude. HOI was usually formed by the pre-equilibrium (3) giving the overall reaction (8) and conversion at equilibrium greater than 90% only if  $\text{pH} > 6.4$ . HOI can also be prepared according to  $\text{HOCl} + \text{I}^- \rightarrow \text{HOI} + \text{Cl}^-$  or  $\text{ICl}(\text{g}) + \text{H}_2\text{O} \rightarrow \text{HOI} + \text{Cl}^- + \text{H}^+$  to isolate reaction (7). Then, the conversion at equilibrium of a  $10^{-4}$  M HOI solution is greater than 90% if  $\text{pH} > 4.1$ . Studies in more acidic solutions need to eliminate iodide with  $\text{Ag}^+$  or  $\text{Hg}(\text{II})$ .



In alkaline solutions, HOI can form  $\text{I}_2\text{OH}^-$  [8-10] and, perhaps, also as  $\text{I}_3\text{OH}$  [11]. Depending on the experimental conditions, there are several rate-determining steps preceded by quasi-equilibria explaining that the problem is still not completely solved. Discrepancies between reported rate constants are also the result of the catalysis by the buffers discovered by Buxton and Sellers [12]. Borate, acetate, carbonate and phosphate buffers do not have the same effect [10]. In less alkaline and in acidic solutions, the kinetics seems simpler and the authors agree [12-16] that the disproportionation is order 2 with respect to  $[\text{I}(+1)] = [\text{IOH}] + [\text{IO}^-]$ .

$$-\frac{1}{3} \frac{d[\text{I}(+1)]}{dt} = k'_7[\text{HOI}]^2 + k''_7[\text{HOI}][\text{OI}^-] + k_B[\text{HOI}]^2[\text{B}^-]$$

The factor 1/3 (sometimes forgotten) is a stoichiometric coefficient and  $\text{B}^-$  represents the buffer anion. This kinetic law suggests the mechanism  $2 \text{HOI} \rightarrow \text{IO}_2\text{H} + \text{I}^- + \text{H}^+$  followed by  $\text{HOI} + \text{IO}_2\text{H} \rightarrow \text{IO}_3^- + \text{I}^- + 2 \text{H}^+$  and equivalent reactions of  $\text{IO}^-$  and  $\text{IO}_2^-$ . The buffer effect could be explained by the formation of a complex  $\text{HOIB}^-$ .

Furrow [17] studied the HOI disproportionation in non-buffered acid solutions by three methods, elimination of  $\text{I}^-$  by the fast reactions  $\text{Hg}(\text{II}) + \text{I}^- \rightarrow \text{HgI}^+$  or  $\text{Ag}^+ + \text{I}^- \rightarrow \text{AgI}$  and preparation of  $\text{I}(+1)$  by reaction of iodine with iodate in concentrated sulphuric acid. The three methods give nearly the same value  $k'_7 = 25 \text{ M}^{-1} \text{ s}^{-1}$ . We confirmed this value [18] in perchloric acid 0.02 to 0.5 M. We showed also that  $\text{H}_2\text{OI}^+$  is much less stable than previously believed:  $K(\text{HOI} + \text{H}^+ \rightleftharpoons \text{H}_2\text{OI}^+) \sim 0.5$ . On the other hand, Buxton and Sellers [12] got  $k'_7 = 2.1 \text{ M}^{-1} \text{ s}^{-1}$  in borate buffer by extrapolation to  $\text{pH} = 7$  and zero buffer concentration (Their published values are those of  $3 k'_7$ .) and Bichsel and von Gunten [16] got  $k'_7 = (0.3 \pm 0.2)$  in borate and carbonate buffer at  $\text{pH} = 8-9$  by subtracting the buffer effect to the measured values. Urbansky et al. [15] got  $k'_7 < 2$  in acetic acid buffer at  $\text{pH} 4-5$ . It is therefore clear that the value of  $k'_7$  decreases as the  $\text{pH}$  increases. Moreover, the value of  $k'_7$  in acidic solutions

decreases when the temperature increases [18] what is usually explained by the shift of equilibrium before the rate-determining step.  $2 \text{HOI} \rightarrow \text{IO}_2\text{H} + \text{I}^- + \text{H}^+$  is clearly not an elementary reaction and we propose that it is the sum of reactions (5) and (9).

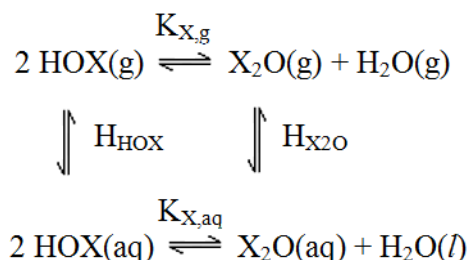


To explain the decrease of  $k_7$  with the pH, we had suggested that reaction (5) is catalysed by  $\text{H}^+$  [4]. This could explain qualitatively  $k_{\text{obs}}(\text{neutral}) < k_{\text{obs}}(\text{acidic})$  but a problem appears when we try to quantify this explanation.  $k_{\text{obs}}(\text{acidic}) = 25 \text{ M}^{-1} \text{ s}^{-1}$  [17, 18] and  $k_{\text{obs}} < 2 \text{ M}^{-1} \text{ s}^{-1}$  already at pH = 4 [15]. Such a fast decrease cannot be explained with orders of magnitude of kinetic constants consistent with the kinetics of iodine oxidation by  $\text{H}_2\text{O}_2$  and we suggest a new explanation.

Urbansky et al. [15] studied the effect of acetic buffers in a large range of concentrations on the rate of HOI disproportionation between pH 3.5 and 5 and observed that the acetate ion  $\text{OAc}^-$  has a catalytic effect, as expected, but can also have an inhibitory effect. They also observed that even the stoichiometry is not simple because a significant amount of  $\text{IO}_2\text{H}$  can be formed transiently. They propose a mechanism involving the formation of a reactive complex  $\text{IOAc}$  and inactive complex  $\text{I}(\text{OAc})_2^-$ . Their mechanism includes  $\text{I}_2\text{O}$  but they do not discuss the non-catalyzed path whose rate is negligible under their conditions. Our new assumption is that  $\text{I}_2\text{O}$  can also form a complex with the buffers,  $\text{I}_2\text{O} + \text{OAc}^- \rightleftharpoons \text{IOIOAc}^-$ . The buffers could decrease the concentration of free  $\text{I}_2\text{O}$  and thus inhibit the non-catalysed pathway. After suggesting that  $\text{I}_2\text{O}$  is a key intermediate in the BL mechanism, we believe that it is a key intermediate in the mechanism of HOI disproportionation.

### OTHER RELATED SYSTEMS

$\text{I}_2\text{O}$  having not been observed directly, its properties are unknown. Trying to have a more exact idea, we consider similar compounds and a thermodynamic cycle.  $K_{\text{X,g}}$  et  $K_{\text{X,aq}}$  are the equilibrium constants in the gas phase and in solution of HOX dehydration to  $\text{X}_2\text{O}$  ( $\text{X} = \text{Cl}, \text{Br}, \text{I}$ ) and  $H_{\text{HOX}}$  et  $H_{\text{X}_2\text{O}}$  are the Henry's constants of HOX and  $\text{X}_2\text{O}$  (M/atm). The values of  $K_{\text{X,g}}$  et  $H_{\text{HOX}}$  are more or less well known and, if we can estimate the values of  $H_{\text{X}_2\text{O}}$ , we can calculate  $K_{\text{X,aq}} = 31.56 \times K_{\text{X,g}} H_{\text{X}_2\text{O}} / H_{\text{HOX}}^2$  where  $31.56 = a_{\text{H}_2\text{O}}/p_{\text{H}_2\text{O}}$ .  $\text{Cl}_2\text{O}$  is a well-known gas which can be prepared by reaction of  $\text{Cl}_2$  with



HgO or NaHCO<sub>3</sub> [19]. He is involved in several important reactions in the atmosphere and stratospheric clouds and participated in the destruction of the ozone [20, 21]. Its thermodynamic properties are quite well known in the gas phase, but much less in solution. We must distinguish the concentration [Cl<sub>2</sub>O] from the total concentration [Cl<sub>2</sub>O]<sub>tot</sub> = [Cl<sub>2</sub>O] + ½ [HOCl] and a confusion exists in the literature between the hydrolysis of Cl<sub>2</sub>O(aq) and Cl<sub>2</sub>O(g). The most reliable value of the Henry's constant is that of Roth [22], H<sub>Cl<sub>2</sub>O</sub> = 7.1 M.atm<sup>-1</sup> at 3.46°C. Corrected to 25°C, it gives H<sub>Cl<sub>2</sub>O</sub> ~ 2.4 M.atm<sup>-1</sup> and K<sub>Cl, aq</sub> ~ 2×10<sup>-3</sup> M<sup>-1</sup>. The thermodynamic values of Reinhard [23] are incompatible with all previous results. Although the concentration of Cl<sub>2</sub>O in solution is always very small, it is often considered an important intermediate of HOCl reactions because its high reactivity offsets its low concentration. The term of order two with respect to the total concentration [Cl(+1)] in the kinetics of organic pollutants degradation is interpreted as the action of Cl<sub>2</sub>O [24, 25]. It is also considered as an intermediary of several inorganic reactions [26, 27].

Br<sub>2</sub>O is much less stable than Cl<sub>2</sub>O. It can be prepared by reaction of HgO with Br<sub>2</sub> in CCl<sub>4</sub> giving a brown solid stable below - 40°C. Its importance in atmospheric chemistry has motivated several studies [20, 28, 29]. As for Cl<sub>2</sub>O, the order two with respect to the total concentration [Br(+1)] in the rate law of bromination reactions in solution suggest that it is an intermediate compound [30, 31]. It is much more reactive than HOBr and could also act as intermediate in inorganic reactions, among others the BZ reaction [32].

I<sub>2</sub>O is a compound yet less stable. Its thermodynamic properties in the gas phase were obtained only by theoretical calculations [33, 34] and are unknown in aqueous solution. Like other X<sub>2</sub>O compounds, it is considered an important intermediate in the chemistry of the atmosphere [35, 36] and some iodinations [37].

After a critical study of the data from the literature, we offer the equilibrium constants in table I. These values are obtained using the NBS Gibbs energies of formation [38], Δ<sub>f</sub>G°(g) and Δ<sub>f</sub>G°(aq) for H<sub>2</sub>O, X<sub>2</sub> and X<sup>-</sup>. Other Δ<sub>f</sub>G°(g) values are taken from theoretical calculations [33, 39, 40]. Experimental values were obtained for K<sub>Cl,g</sub> [41] and K<sub>Br,g</sub> [42, 43]. Some Henry's constants are more or less known [22, 44, 45] and others are calculated from Δ<sub>f</sub>G° values. Δ<sub>f</sub>G°(HOX, aq) values are obtained from corresponding hydrolysis constants [18, 44, 46]. For Br<sub>2</sub>O(aq), we have found only a theoretical estimation of the hydration energy [30]. There is no published value about I<sub>2</sub>O(aq). The only information comes from our simulations of the BL reaction [4] suggesting K<sub>I,aq</sub> > 1 giving H<sub>I<sub>2</sub>O</sub> > H<sup>2</sup><sub>HOI</sub> /

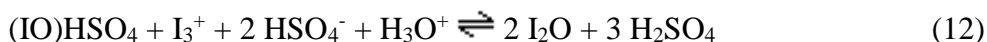
( $31.56 \times K_{I,g}$ ). The calculations use  $\Delta_f H^\circ(I_2O,g) = 92.4$  kJ/mol [40]. The higher value 111.2 kJ/mol [33] would give  $K_{I,g} = 2.5 \times 10^{-4}$  atm<sup>-1</sup> and  $H_{I_2O} > 10^8$ . The value of  $H_{I_2O}$  is clearly very large and  $I_2O(aq)$  should probably be represented as  $H_2O$ -IOI. As for  $Cl_2O$  and  $Br_2O$ , its high reactivity should offset its very low concentration.

**Table 1.** Selected equilibrium constants at 25°

X =	Cl	Br	I
$K_{X,g}$ (atm <sup>-1</sup> )	10.9	35.5	0.68
$H_{HOX}$ (M.atm <sup>-1</sup> )	660	570	970
$H_{X_2O}$ (M.atm <sup>-1</sup> )	2.4	1840	> 4E+04
$K_{X,aq}$ (M <sup>-1</sup> )	2E-03	6.3	> 1

### I<sub>2</sub>O PREPARATION

$I_2O$  can be prepared by reacting  $HgO$  and  $I_2$  [37] but the reaction  $HIO_3 + I_2$  in 96% sulfuric acid shows more potential [47]. If the ratio  $[I_2]/[HIO_3]$  is less than 5, this reaction gives mainly I(+3) according to reaction (10) [48]. If it is higher, it gives a mixture of I(+3) and I(+1). In pure acid, I(+1) is mainly in the form of  $I_3^+$  according to reaction (11) [49]. One can also form  $I_5^+$ . On the other hand, in 96% sulfuric acid, one gets also reaction (12). A recent study by Stanley Furrow and the author confirms this discovery and specifies the conditions favoring reaction (12).  $I_2O$  formation was not observed in pure acid because the concentration  $[HSO_4^-]$  is very low and the equilibrium (12) is shifted to the left.



Stanley Furrow (private communication) also discovered that when a solution of  $I_2O$  in 96 % sulphuric acid is placed in a closed container next to pure 96% acid, the  $I_2O$  can be transferred from one to the other via the gas phase, which makes possible the direct study of the properties of  $I_2O(g)$ .  $I_2O$  can also be extracted in  $CH_2Cl_2$ , where its properties could be studied, and the dilution of this  $I_2O$  solution in water is a new method of preparation of HOI [47].

### CONCLUSION

Little known a few years ago,  $I_2O$  appears as intermediate in several important reactions. The reaction  $2 HIO \rightleftharpoons I_2O + H_2O$  should be taken into account in atmospheric chemistry models. It should also be taken into

account in solution in the reaction of BL, the HOI disproportionation, different iodination reactions [30] and probably other reactions of I(+1). A new method for preparation of I<sub>2</sub>O should allow new studies of its properties.

## REFERENCES

- [1] G. Schmitz, J. chim. phys. 1987, **84**, 957.
- [2] G. Schmitz, S. D. Furrow, Phys. Chem. Chem. Phys. 2012, **14**, 5711.
- [3] H.A. Liebhafsky, J. Am. Chem. Soc. 1932, **54**, 3504.
- [4] G. Schmitz, Phys. Chem. Chem. Phys. 2010, **12**, 6605.
- [5] G. Schmitz, Lj. Kolar-Anić, S. Anić and Ž. D. Čupić, J. Phys. Chem. A, 2008, **112**, 13452.
- [6] Lj. Kolar-Anić, Ž. D. Čupić, G. Schmitz and S. Anić, Chem. Eng. Sci. 2010, **65**, 3718.
- [7] G. Schmitz, Phys. Chem. Chem. Phys. 2011, **13**, 7102.
- [8] V. W. Truesdale, J. Chem. Soc. Faraday Trans. 1995, **91**, 863.
- [9] V. W. Truesdale, J. Chem. Soc. Faraday Trans. 1997, **93**, 1909.
- [10] V. W. Truesdale, G. W. Luther, J.E. Greenwood, Phys. Chem. Chem. Phys. 2003, **5**(16), 3428.
- [11] A. Skrabal, Z. Elektrochem. Ange. Physik. Chem. 1912, **17**, 665-8.
- [12] G. V. Buxton, R. M. Sellers, J. Chem. Soc., Faraday Trans. 1, 1985, **81**(2), 449.
- [13] J. Paquette, B. L. Ford, Can. J. Chem. 1985, **63**, 2444.
- [14] V. W. Truesdale, C. Canosa-Mas, J. Chem. Soc. Faraday Trans. 1995, **91**, 2269.
- [15] E. T. Urbansky, B.T. Cooper, D.W. Margerum, Inorg. Chem., 1997, **36**(7), 1338.
- [16] Y. Bichsel, U. von Gunten, Water Research 2000, **34**(12), 3197.
- [17] S. Furrow, J. Phys. Chem. 1987, **91**, 2129.
- [18] G. Schmitz, Int. J. Chem. Kinet. 2004, **36**, 480.
- [19] J. J. Renard, H. I. Bolker, Chemical Reviews 1976, **76**( 4), 487.
- [20] A. Aguzzi, M.J. Rossi, J. Phys. Chem. A 2002, **106**(24), 5891.
- [21] J. C. Hansen, R. Friedl, S.P. Sander, J. Phys. Chem. A 2008, **112**(39), 9229.
- [22] W. A. Roth, Z. physik. Chem. A, 1942, **191**, 248
- [23] M. Reinhard, G. D. Redden, E.A. Voudrias, in "Water Chlorination: Environmental Impact and Health Effects", R. L. Jolley et al. Eds., Ann Arbor Science 1990, pp 859-870.
- [24] J. D. Sivey, C.E. McCullough, A.L. Roberts, Environ. Sci. Tech. 2010, **44**(9), 3357.
- [25] J. D. Sivey, A.L. Roberts, Environ. Sci. Tech. 2010, **46**(4), 2141.

- [26] J. S. Nicoson, T. F. Perrone, K.E. Hartz, L. Wang, *Inorg. Chem.* 2003, **42**(19), 5818.
- [27] B. Kormanyos, I. Nagypal, G. Peintler, A. K. Horvath, *Inorg. Chem.* 2008, **47**(17), 7914.
- [28] H. Mueller, C. F. Miller, E.A. Cohen, *Angewandte Chem. (English)* 1996, **35**(18), 2129.
- [29] B. Deters, J. P. Burrows, S. Himmelmann, C. Blindauer, *Annales Geophys.* 1996, **14**(4), 468.
- [30] J. D. Sivey, J.S. Arey, P.R. Tentscher, A.L. Roberts, *Environ. Sci. Tech.* 2013, **47**(3), 1330.
- [31] J. D. Sivey, M.A. Bickley, D.A. Victor, *Environ. Sci. Tech.* 2015, **49**(8), 4937.
- [32] S. M. Blagojevic, S.R. Anic, Z. D. Cupic, *Russ. J. Phys. Chem. A* 2011, **85**(13), 2274.
- [33] N. Begović, Z. Marković, S. Anić, Lj. Kolar-Anić, *J. Phys. Chem. A* 2004, **108**, 651.
- [34] D.J. Grant, E.B. Garner, M.Y. Matus, Minh Tho Nguyen, K.A. Peterson, J. S. Francisco, D.A. Dixon, *J. Phys. Chem. A* 2010, **114**, 4254.
- [35] S. Solomon, R.R. Garcia, A.R. Ravishankara, *J. Geophys. Res.* 1994, **99**, 491.
- [36] J.C. Gomez Martin, O. Galvez, M.T. Baeza-Romero, T. Ingham, J. M. C. Plane, M.A. Blitz, *Phys. Chem. Chem. Phys.* 2013, **15**(37), 15612.
- [37] C. P. Forbes, A. Goosen, H. A. Laue, *J. South Afr. Chem. Inst.* 1972, **25**, 328.
- [38] D.D. Wagman et al., The NBS tables of chemical thermodynamic properties, *J. Phys. Chem. Ref. Data, Supp. 2*, **11**, 1982.
- [39] P.A. Denis, *J. Phys. Chem. A* 2006, **110**, 5887.
- [40] A. Misra, P. Marshall, *J. Phys. Chem. A* 1998, **102**(45), 9056.
- [41] C. A. Ennis, J. W. Birks, *J. Phys. Chem.* 1985, **89**, 186.
- [42] J. J. Orlando, J. B. Burkholder, *J. Phys. Chem.* 1995, **99**, 1143.
- [43] O. V. Rattigan, D.J. Lary, R. L. Jones, R. A. Cox, *J. Geophys. Research [Atmospheres]* (1996), **101**(D17), 23021.
- [44] R. Sander, *Atmos. Chem. Phys.* 2015, **15**, 4399.
- [45] J. R. Harrell, J. B. Lutz, J. L. Kelly, *J. Radioanal. Nucl. Chem.* 1988, **127**, 13.
- [46] R.C. Beckwith, Tian Xiang Wang, D.W. Margerum, *Inorg. Chem.* 1996, **35**(4), 995.
- [47] N. Muntean, Lawson Bich Thuy, K. Kaly-Kullai, M. Wittmann, Z. Noszticzius, L. Onel, S. D. Furrow, *J. Phys. Chem. A* 2012, **116**(25), 6630.
- [48] Z. Noszticzius, E. Noszticzius, Z.A. Schelly, *J. Am. Chem. Soc.* 1982, **104**(23), 6194.
- [49] R. A. Garrett, R. J. Gillespie, J. B. Senior, *Inorg. Chem.* 1965, **4**, 563.

## POSSIBILITIES AND LIMITATIONS OF SELECTED ANALYTICAL TOOLS TO TRACE NON-LINEAR CHEMICAL PROCESSES

T. Kowalska and M. Sajewicz

*Institute of Chemistry, University of Silesia, 9 Szkolna Str., Katowice, Poland, e-mail: [teresa.kowalska@us.edu.pl](mailto:teresa.kowalska@us.edu.pl); e-mail: [mieczyslaw.sajewicz@us.edu.pl](mailto:mieczyslaw.sajewicz@us.edu.pl)*

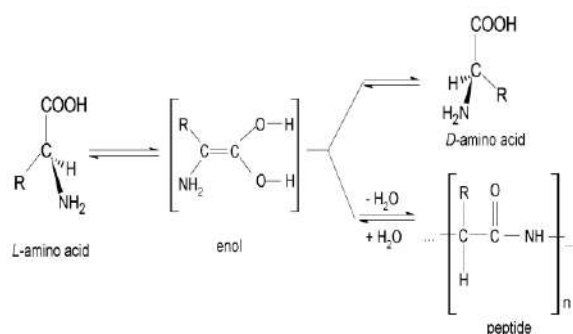
### INTRODUCTION

Intuitively, many researchers – and especially those involved in life sciences – are well aware of the fact that the non-linear chemical processes are omnipresent (if not predominant) in biochemistry and very likely, in an entire field of chemistry also. This intuition comes from two rather independent sources, i.e., from visual observation of striking non-linear patterns in the kingdoms of animals and plants, and from the laboratory benchtop experience, when measured data – although repeatedly obstinate – sometimes seem to contradict the so-called common sense and resemble artifacts generated by a damaged equipment. On the other hand, physical chemistry of non-linear processes is absent from the most university undergraduate curricula worldwide, similar as it is absent from the predominant majority of the chemical and life sciences research laboratories. This absence cannot be explained by a persistent addiction of one generation after another of scientists to equilibrium thermodynamics alone, and this addiction characterizes even quantum chemists, commonly regarded as those in a research forefront. A real problem with a reliable detection of the non-linear chemical processes and further acquisition of the respective kinetic data hampers the development of the research in this field and results in a limited interest in non-linear phenomena. Needless to add that psychological factor plays an important role as most researchers are keen on instantaneous and spectacular success rather, than on toiling an unpromising land. Thus a justified statement can be made that limitations of the available analytical techniques are the main reason of a relatively slow progress with discovering and detailed physicochemical description of new non-linear chemical processes. These processes which attract our sight with a spectacular change of colors are among the first discovered (e.g., the Belousov-Zhabotinsky reaction). Then the electrochemical measuring techniques come, with their well established position as handy tools in the exploration of the oxidation/reduction processes and a relatively low

demand on expensive equipment. In a case of the non-linear processes running in colorless solutions and without any spectacular visual effects, to which colorimetric or electrochemical analytical techniques do not apply, a problem arises with finding adequate measuring tools, capable of capturing characteristic kinetic and mechanistic features of an investigated non-linear process. Three main features of an adequate analytical technique are demanded, namely that (i) it is sensitive enough, (ii) enables quick registration, and (iii) makes continuous data acquisition possible. Although applicable measuring techniques are to a large extent problem-dependent, in this paper we will discuss a selection of analytical tools with a broad enough applicability range upon a selected case study.

### CASE STUDY

The practical case which is used in this study to demonstrate applicability (or otherwise) of different analytical tools to tracing a non-linear process was first presented in papers [1,2], and then extensively discussed in a vast number of other publications (e.g., [3-7]). The quintessence of the investigated phenomenon is an ability of the low-molecular-weight chiral carboxylic acids to spontaneously undergo two parallel processes, i.e., the non-linear chiral conversion and the non-linear condensation. Among the investigated chiral compounds, there were the non-steroidal anti-inflammatory drugs (NSAID) from the group of profens, hydroxyl acids, and  $\alpha$ -amino acids, all of them of an indisputable biological importance. The below scheme illustrates these two non-linear processes spontaneously running in parallel upon an example of an  $\alpha$ -amino acid:



**Scheme 1.** Two spontaneous non-linear processes of chiral conversion and condensation of a low molecular carboxylic acid running in parallel. Processes following the presented scheme do not produce any spectacular visual effects, because the compounds of interest are colorless and dissolved in a colorless aqueous or aqueous-organic solvent. For this reason,

colorimetric analytical techniques cannot be considered as adequate tools to monitor the reaction course. The electrochemical techniques have also not been considered, because no evident oxidation/reduction process can be ascribed to the chiral conversion and condensation (although contribution from such processes at unknown elementary steps cannot be excluded). Therefore our main interest has focused on two liquid chromatographic techniques (thin-layer chromatography, TLC, and high-performance liquid chromatography, HPLC) known for their sensitivity, and on turbidimetry operating in continuous mode (to trace advanced stages of the condensation process resulting in precipitation of higher molecular weight insoluble products after long enough periods of time). As auxiliary techniques to confirm the progress of condensation, mass spectrometry (MS), infrared absorption spectroscopy (IR), hydrogen and carbon nuclear magnetic resonance spectroscopy ( $^1\text{H}$  and  $^{13}\text{C}$  NMR), and scanning electron microscopy (SEM) are going to be mentioned. Eventually, we will briefly mention two techniques of a limited or even illusive applicability only, i.e., gas chromatography (GC) and polarimetry. At the end, some general conclusions will be drawn.

## **ANALYTICAL TECHNIQUES OF FIRST CHOICE**

### **Thin-layer chromatography (TLC)**

TLC is an analytical technique with a sufficient enough sensitivity (enabling detection of nanograms of a given analyte), yet the TLC measurements are relatively slow. Hence, registration of the results in continuous mode and investigation of the non-linear dynamics of chiral conversion or condensation with its use is impossible. However, the chiral TLC enables a relatively easy confirmation of the process of chiral conversion, owing to its ability to directly (i.e., without a need of a preliminary derivatization) enantioseparate the two counterparts. Surprisingly, quite spectacular performance of this particular analytical technique was not given any attention in the monograph on the dynamic stereochemistry of chiral compounds [8], in spite of an abundant data on this particular subject matter available in the literature and summarized in another monograph published roughly about the same time [9]. An appreciable performance of TLC in tracing spontaneous chiral conversion of several  $\alpha$ -amino acids (Pro, Hyp, Cys, and Met) was presented in papers [10-13] and acknowledged in the book chapter [14].

TLC can also be used to document spontaneous condensation of the chiral low molecular weight carboxylic acids, and a favorable option is coupling the thin-layer chromatogram through the TLC-MS interface with the mass spectrometric detector [10-14].

**High-performance liquid chromatography (HPLC)**

HPLC also is an analytical technique with a sufficient enough sensitivity. Moreover, it enables faster registration of the separation results than TLC and it can operate in a continuous mode, providing data acquisition of a semi-kinetic relevance. In its chiral mode (i.e., with use of the chiral mobile or stationary phase), HPLC can be used for the enantioseparation and provide evidence on the mechanism of spontaneous non-linear chiral conversion. In spite of its apparent advantage, to our best knowledge the chiral HPLC was used only once for the aforementioned purpose and the report on the oscillatory chiral conversion of two amino acids, *L*-Phg and *D*-Phg, is given in paper [15]. In that study, the authors managed to capture a ca. 12 h lasting period of the coalescence of the two chromatographic peaks originating from *L*-Phg and *D*-Phg, in that way supporting an anticipated mechanism of chiral conversion *via* a non-chiral enol/enolate ion structure.

An achiral HPLC mode is a convenient option for acquisition of the kinetic data characteristic of the non-linear condensation of the chiral low molecular weight carboxylic acids [2,5-7]. To make it a universal tool able to recognize all types of analytes, the chromatograph should be equipped with a universal evaporative light scattering detector (HPLC-ELSD). With use of such setup, the non-linear concentration changes of the reaction substrates and the condensation products can be registered (e.g., see papers [15,16]).

**Turbidimetry**

Spontaneous non-linear condensation of the low molecular weight chiral carboxylic acids which is carried out for longer periods of time often results in precipitation of insoluble higher molecular weight condensation products. The non-linear nature of this process manifests itself by sequential precipitation and the dissociation of the precipitates, which is visually perceived as pulsation, as schematically shown in paper [17].

Pulsating instability of the precipitated microstructures can be registered with use of turbidimetry operating in continuous mode. Turbidimetric measurements do not result in unequivocally definable physicochemical magnitudes and this measuring technique is applied mostly in the laboratories of the water supply networks and the breweries (as an element of the analytical control systems of the water quality and the beer brewing process, respectively). Moreover, turbidimetric measurements are sensitive even to minute temperature changes, which generate chaotic floating of the precipitated microstructures, induced by thermal convection. An evident advantage of these measurements is that turbidimetry captures turbidity changes of an investigated solution much earlier than the human eye does.

In order to obtain reliable turbidimetric results, these measurements should be carried out under strictly thermostatic conditions.

Turbidimetric measurements in continuous mode and under thermostatic conditions were performed in our laboratory to compare pulsating instability patterns of the peptide precipitation observed for a series of *L*- and *D*-amino acid enantiomers [17,18]. In all cases, strikingly different pulsating instability patterns characterized counterparts of the investigated amino acid pairs, with a tendency of certain *L*-amino acids to follow a circadian pulsation rhythm (as shown in paper [18]).

### **AUXILIARY MEASURING TECHNIQUES**

The discussed case study is an uncontrolled chemical process which includes spontaneous non-linear chiral conversion and spontaneous non-linear condensation running in parallel. The latter reaction results in a wide spectrum of the condensation products of different molecular weight and structure. Confirmation of the condensation process can be performed with use of a number of advanced instrumental techniques and the most recommended one certainly is MS (e.g., [2,4-7,15,16]). With use of MS, one can gain a deeper insight in chemical structure of the obtained condensed entities. The IR spectroscopy can prove helpful in confirming the presence of the peptide bonds [17], and with use of  $^1\text{H}$  NMR and  $^{13}\text{C}$  NMR spectroscopy an arrangement of the monomer units in a molecule of an average condensate can be assessed (e.g., [5,10]). There are also other helpful analytical techniques enabling deeper insight in molecular structure of the condensates and one of them is visualization of the solid condensation products by means of SEM (e.g., [12,13,17]).

### **ANALYTICAL TECHNIQUES OF LIMITED OR EVEN ILLUSIVE APPLICABILITY**

#### **Gas chromatography (GC)**

Historically, GC is the first chromatographic technique which enabled separation of the enantiomer pairs [19-21]. Right from the beginning, the enantioseparation by means of GC has focused on amino acids. However, its potential for the investigation of spontaneous non-linear chiral conversion of the low molecular weight carboxylic acids has not been explored. The reasons of this evident restraint are the necessity to derivatize carboxylic acids prior to the analyses (to enhance the volatility thereof) and elevated temperatures of running them. These two factors can affect (and even falsify) a quantitative and kinetic insight in the long-term spontaneous non-linear processes of chiral conversion and peptidization, otherwise carried out at ambient temperatures. Nevertheless, GC is still considered as an

analytical tool well suited for the analysis and the enantioseparation of amino acids. The best proof is that the miniaturized GC-MS device with the three different fused silica GC columns developed within the framework of the Cometary Sampling and Composition (COSAC) project at the Max-Planck-Institute for the Solar System Research (Göttingen, Germany) was included in the Rosetta mission launched in 2004, with an aim to explore the comet 67P/Churyumov-Gerasimenko, nicknamed as Chury [22]. The aim of that device was to analyze possible presence of chiral  $\alpha$ -amino acids, chiral hydrocarbons, and unspecified chiral compounds in an interstellar space, and assess the enantiomer configuration thereof. The performance of the column dedicated to the enantioseparation of  $\alpha$ -amino acids enables enantioseparation of the four  $\alpha$ -amino acid pairs only (i.e., Val, Ile, Asp, and Phe) and the results obtained (if any) still remain unknown.

### **Polarimetry**

Polarimetry might seem an analytical technique of choice to investigate the phenomenon of chiral conversion and there are available quite sophisticated laser-based polarimetric detectors operating in continuous mode. However, the experimental case discussed in this study includes the non-linear chiral conversion and the non-linear condensation running in parallel. In such systems, the self-assembled supramolecular structures formed by small organic molecules as well as the condensation products are usually fibroid aggregates with occasional linking nodes that are able to embrace the entity of a solution with a 3D network [23]. Dynamic assembly and disassembly of these chiral structures under ambient temperature conditions is reflected in continuous changes of the sample's specific rotation, which to a large extent eclipses (and can erroneously be taken for) the phenomenon of chiral conversion, as experimentally shown in paper [24]. Therefore contrary to a popular thinking, polarimetry is not a measuring technique which might purposefully be engaged in the discussed case study.

### **GENERAL CONCLUSIONS**

For the investigation of the non-linear chemical processes which involve organic compounds, currently the liquid chromatographic techniques (TLC and HPLC) seem the analytical tools of the first choice, due to a broad applicability scope thereof. Sensitivity of chromatographic techniques enabling identification and quantification of the compounds of interest is excellent. However, neither TLC nor HPLC enables fast enough registration in continuous mode to provide the results of a truly kinetic importance (as the so-called short analytical runs usually last up to several minutes). Hence, selected chromatographic techniques can provide semi-kinetic information on a given process only, which makes the detection of non-linear

phenomena rather difficult and the results obtained not very precise. This lack of sufficient registration speed is the main bottleneck hampering free discovery and detailed kinetic characterization of the non-linear chemical processes. Only a significant breakthrough in the development of a new generation analytical tools can open the path to free detection and precise characterization of the otherwise omnipresent non-linear phenomena.

## REFERENCES

- [1] M. Sajewicz, R. Piętka, A. Pieniak, T. Kowalska, *Acta Chromatogr.*, 2005, **15**, 131-149.
- [2] M. Sajewicz, M. Gontarska, D. Kronenbach, M. Leda, T. Kowalska, I.R. Epstein, *J. Syst. Chem.*, 2010, **1**:7; DOI:10.1186/1759-2208-1-7.
- [3] M. Sajewicz, M. Gontarska, Ł. Wojtal, D. Kronenbach, M. Leda, I.R. Epstein, T. Kowalska, *J. Liq. Chromatogr. Relat. Technol.*, 2008, **31**, 1986-2005.
- [4] M. Sajewicz, R. Wrzalik, M. Gontarska, D. Kronenbach, M. Leda, I.R. Epstein, T. Kowalska, *J. Liq. Chromatogr. Relat. Technol.*, 2009, **32**, 1359-1372.
- [5] M. Sajewicz, M. Matlengiewicz, M. Leda, M. Gontarska, D. Kronenbach, T. Kowalska, I.R. Epstein, *J. Phys. Org. Chem.*, 2010, **23**, 1066-1073.
- [6] M. Sajewicz, M. Dolnik, D. Kronenbach, M. Gontarska, T. Kowalska, I.R. Epstein, *J. Phys. Chem. A*, 2011, **115**, 14331-14339.
- [7] M. Sajewicz, M. Dolnik, T. Kowalska, I.R. Epstein, *RSC Advances*, 2014, **4**, 7330-7339.
- [8] C. Wolf, "Dynamic Stereochemistry of Chiral Compounds", RSC Publishing, Cambridge, UK, 2008.
- [9] R. Bhushan, J. Martens, "Amino Acids. Chromatographic Separation and Enantioresolution", HBN Publishing, New York, U.S.A., 2010
- [10] M. Sajewicz, M. Matlengiewicz, M. Juziuk, M. Penkala, M. Weloe, M. Schulz, T. Kowalska, *J. Liq. Chromatogr. Relat. Technol.*, 2013, **36**, 2497-2511.
- [11] A. Maciejowska, A. Godziek, M. Sajewicz, T. Kowalska, *Acta Chromatogr.*, 2014, **26**, 355-369.
- [12] A. Godziek, A. Maciejowska, E. Talik, M. Sajewicz, T. Kowalska, *J. Planar Chromatogr. – Modern TLC*, 2015, **28**, 144-151.
- [13] A. Maciejowska, A. Godziek, E. Talik, M. Sajewicz, T. Kowalska, *J. Liq. Chromatogr. Relat. Technol.*, 2015, **38**, 1164-1171.
- [14] A. Godziek, A. Maciejowska, M. Sajewicz, T. Kowalska, „Spontaneous Chiral Conversion and Peptidization of Amino Acids Traced by TLC-MS”, Chapter 19 in: "Planar Chromatography – Mass Spectrometry",

- Eds T. Kowalska, M. Sajewicz, and J. Sherma, *Chromatographic Science Series*, CRC Press, Francis and Taylor, Boca Raton, USA, 2015, **110**, 345–366.
- [15] M. Sajewicz, M. Gontarska, T. Kowalska, *J. Chromatogr. Sci.*, 2014, **52**, 329-333.
- [16] A. Godziek, A. Maciejowska, M. Sajewicz, T. Kowalska, *J. Chromatogr. Sci.*, 2015, **53**, 401–410.
- [17] A. Godziek, A. Maciejowska, E. Talik, R. Wrzalik, M. Sajewicz, T. Kowalska, *Curr. Protein Pept. Sci.*, in press.
- [18] A. Maciejowska, A. Godziek, M. Sajewicz, T. Kowalska, *Acta Chromatogr.*, 2017, **29**, DOI: 10.1556/1326.2017.29.1.00.
- [19] E Gil-Av, B Feibush, R Charles-Sigler, *Tetrahedr. Lett.*, 1966, **7**, 1009-1015.
- [20] E. Gil-Av, B. Feibush, R. Charles-Sigler, in: A.B. Littlewood (Ed.), *Gas Chromatography 1966*, Institute of Petroleum, London, 1967, p. 227 and 254 (discussion part).
- [21] E. Gil-Av, D. Nurok, in: G.C. Giddings, R.A. Heller (Eds.), *Advances in Chromatography*, vol. 10, Marcel Decker, New York, 1974, p. 99.
- [22] V. Schurig, “Exploring Chirality in Outer Space”, *The Analytical Scientist*, December 2015, Issue # 1215-402.
- [23] F. Schoonbeek, “Making it all stick together – The gelation of organic liquids by small organic molecules”, PhD Thesis, University of Groningen, Groningen, 2001.
- [24] J. Polański, M. Sajewicz, M. Knaś, T. Kowalska, *J. Chromatogr. Sci.*, 2013, **51**, 349–354.

## NETWORK MOTIFS AND MECHANISMS FOR OSCILLATORY DYNAMICS OF BIOCHEMICAL REACTIONS

F. Muzika, D. Denisov, V. Radojković, L. Schreiberová, M. Příbyl and  
I. Schreiber

*Department of Chemical Engineering, University of Chemistry and  
Technology, Prague, Technická 5, 166 28 Prague 6, Czech Republic*

### ABSTRACT

Based on our experimental observations, we formulate detailed mechanisms for several enzyme oscillatory reactions and analyze the underlying subnetworks that take part in generating the oscillatory dynamics. In particular, we explore the glucose–glucose oxidase– catalase–hydrogen peroxide reaction, the urea–urease reaction and glucose–glucose oxidase–ferricyanide reactions. Topology of the core oscillatory subnetworks are compared against one another as well as against other enzyme reactions known to oscillate, such as oxidase–peroxidase reaction and some enzyme systems of biological importance including the mitogen-activated protease kinase (MAPK). The main tool for such a comparison is provided by the stoichiometric network analysis – a theory of stability of reaction networks.

## FROM SMALL TO LARGE MOLECULE SUBSTRATES IN OSCILLATORY CARBONYLATION

K. Novaković<sup>1</sup>, J. C. Nwosu<sup>1</sup> and J. Parker<sup>1</sup>

<sup>1</sup>Newcastle University, School of Chemical Engineering and Advanced  
Materials, Merz Court, Newcastle upon Tyne, NE1 7RU, UK.  
(katarina.novakovic@ncl.ac.uk)

### ABSTRACT

Over the past two decades the oscillatory nature of the PdI<sub>2</sub>-catalysed oxidative carbonylation of phenylacetylene has been experimentally studied and reproducible oscillations in pH were reported. Oscillatory behaviour has been reported over the temperature range 0-40 °C under batch or semi-batch conditions. Recently, oscillatory palladium-catalysed carbonylation has been achieved using mono alkyne-terminated poly(ethylene glycol) methyl ether at 20 °C demonstrating that alkyne-terminated macromolecules are also suitable substrates. In this work, studies of both oscillatory systems (phenylacetylene and mono alkyne-terminated poly(ethylene glycol) methyl ether) conducted in a 1 litre automated reactor system are reported.

### INTRODUCTION

Oxidative carbonylation reactions are important C-C bond forming reactions that generate a number of products depending on the substrates, catalyst and reaction conditions [1-7]. Using a PdI<sub>2</sub>-KI catalyst with alkynes under mild conditions good catalytic efficiencies have been achieved leading to a mixture of dicarbonylation products[8]. Importantly, when phenylacetylene (PhAc) was used as the substrate in methanol, oscillations in pH, redox potential, gas uptake (CO and O<sub>2</sub>), reaction heat (Q<sub>r</sub>) and turbidity were discovered[9-17]. The observed duration of oscillations varied from several hours[9-13] to several days[15, 16], with reaction temperatures ranging from 0 to 40°C [15, 16]. The magnitude of heat released is significant and based on the initial charge of PhAc alone up to 10.37 kJmol<sup>-1</sup> per oscillation was recorded. Oscillations in Q<sub>r</sub> were exothermic and no corresponding endotherm was observed. Heat release was in phase with the pH fall and decreased as the pH increased indicating the formation of reaction products in a stepwise manner[12]. While the PhAc oscillatory system was initially of interest as a novel organic pH oscillator operating in a stirred batch reactor system, the recent discovery of oscillatory alkyne-terminated polymeric systems has opened new avenues and unambiguously indicated

opportunities for the discovery of otheralkyne-based oscillatory reaction systems. Oscillatory palladium-catalysed carbonylation has been reported using mono alkyne-terminated poly(ethylene glycol) methyl ether at 20 °C [18]. Reproducible, synchronised oscillations in pH and solution turbidity have been recorded over several days [18]. In this study both PhAc and mono alkyne-terminated poly(ethylene glycol) methyl ether were experimentally studied on the same scale using a 1 litre automated reactor. The initial conditions used to achieve oscillatory behavior as well as trends in the recorded pH oscillations are discussed.

### EXPERIMENTAL

The study was conducted in a HEL Similar reaction calorimeter. The setup consists of a 1 L double-jacketed glass reactor. Reactor temperature is monitored by a Pt100 temperature probe while internal heating is provided by a 150W internal heater. The oil jacket temperature is controlled by a Julabo FP50-HD circulator. The reactor is fitted with a combined pH electrode. Stirring is provided by an overhead pitched blade impeller. The reactor has two mass flow controllers which dose air and CO. The installed WinISO software allows the HEL Similar to run unaided once it is set up. All data are automatically saved via the HEL IQ data logging software. The PhAc experiment was conducted in methanol (450 mL) heated to 20°C while stirring at 250 rpm. The palladium(II) iodide ( $2.64 \times 10^{-3} \text{ mol dm}^{-3}$ ) and KI ( $0.494 \text{ mol dm}^{-3}$ ) were added and, after approximately 50 min, purging with CO and air at  $50 \text{ mL min}^{-1}$  commenced. PhAc ( $0.124 \text{ mol dm}^{-3}$ ) was added to the reactor 20 min after purging began. The mono alkyne-terminated poly(ethylene glycol) 2000 Da (PEGA2000) derivative was synthesised according to literature procedures [19-21]. When PEGA2000 was used, instead of PhAc, the initial substrate concentration was  $1.52 \times 10^{-3} \text{ mol dm}^{-3}$  in 450 mL of methanol. The concentrations of PdI<sub>2</sub> and KI were  $2.9 \times 10^{-5}$  and  $5.7 \times 10^{-3} \text{ mol dm}^{-3}$  respectively. Both experiments were conducted using the power compensation mode of the reaction calorimeter. Temperature was maintained at 20 °C and pH was recorded throughout with additional methanol added as necessary to compensate for evaporative loss of the solvent.

### RESULTS AND DISCUSSION

The pH recorded employing PhAc is shown in Figure 1. while the pH recorded in the oscillatory PEGA2000 run is given in Figure 2. A summary of trends observed in these two experiments is given in Table 1.

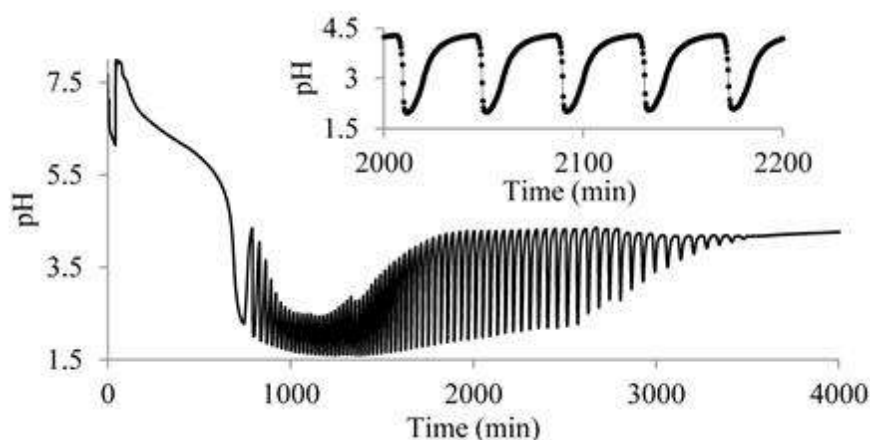


**Figure 1.** The pH in PhAc carbonylation at 20°C.  $[\text{PhAc}] = 0.124 \text{ mol dm}^{-3}$ ;  $[\text{PdI}_2] = 2.64 \times 10^{-3} \text{ mol dm}^{-3}$ ;  $[\text{KI}] = 0.494 \text{ mol dm}^{-3}$ ;  $\text{CO} = 50 \text{ mL min}^{-1}$ ;  $\text{Air} = 50 \text{ mL min}^{-1}$ .

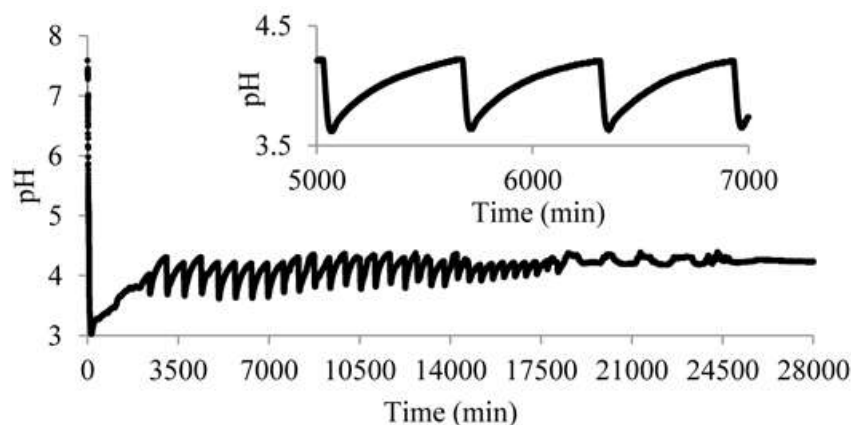


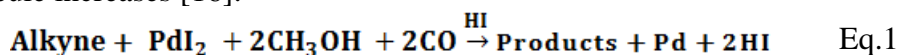
**Figure 2.** The pH in PEGA2000 carbonylation at 20°C.  $[\text{PEGA2000}] = 1.52 \times 10^{-3} \text{ mol dm}^{-3}$ ;  $[\text{PdI}_2] = 2.9 \times 10^{-5} \text{ mol dm}^{-3}$ ;  $[\text{KI}] = 5.7 \times 10^{-3} \text{ mol dm}^{-3}$ ;  $\text{CO} = 50 \text{ mL min}^{-1}$ ;  $\text{Air} = 50 \text{ mL min}^{-1}$ .

While long lasting oscillations were achieved under semi-batch conditions in both experiments (Figures 1. and 2.), pH oscillations recorded when PEGA2000 was employed as substrate lasted approximately 16 days which is more than eight times longer than when PhAc was used (Table 1). Importantly, this was achieved with an approximately 82 times lower initial concentration of substrate and 91 times lower concentration of catalyst.

**Table 1.** A summary of trends in the pH oscillations in the PhAc and PEGA2000 reactions at 20 °C.

Run	PhAc	PEGA2000
pH at onset of oscillations	2.27	3.74
Onset time of oscillations (min)	744	2390
Duration of oscillations (min)	2737	22610
Max amplitude (pH units)	2.35	0.6
Max period (min)	71	677

The transition to polymeric substrate in this oscillatory reaction system likely led to a reduction in the carbonylation reaction rate. This postulation is supported by the observed increase in period of oscillations which is in agreement with the previously proposed key step responsible for product formation (Eq.1) the rate of which is anticipated to decrease as the size of molecule increases [16].



The reduction in the reaction rate in the PEGA2000 system is also likely to be responsible for the significantly longer induction period prior to the onset of oscillations (Table 1). At the same time, the lower PdI<sub>2</sub> concentration used in the PEGA2000 experiment will lead to smaller reaction cycles resulting in a reduced amplitude of oscillations.

## CONCLUSION

This work shows two oscillatory carbonylation systems, PhAc and PEGA2000, studied at the same scale. The transition from small molecule (PhAc) to polymeric substrate (PEGA2000) enabled a significant reduction in initial concentration of both substrate and catalyst needed for the oscillations to occur. Furthermore, the polymeric substrate significantly affected the rates involved in this oscillatory process prolonging the period as well as the duration of oscillations (approximately 16 days). At the same time, the reduced catalyst concentration reduced the amplitude of the oscillations. Oscillatory alkyne-functionalised polymeric substrate carbonylation reactions and the additional degrees of freedom macromolecules bring (e.g. chain length and multifunctionality) open new avenues in the area of nonlinear dynamics and has the potential to enable the transition from liquid based oscillators to solid state oscillatory systems.

**Acknowledgement**

The authors wish to acknowledge the UK Engineering and Physical Sciences Research Council (EPSRC) Grant no. EP/H003908/1 for funding this research. Miss Nwosu would like to acknowledge Newcastle University's Faculty of Science, Agriculture and Engineering Doctoral Training Award scheme for funding her Ph.D. studies. Mrs Parker would like to acknowledge Professor Allen Wright for funding her Ph.D. studies.

**REFERENCES**

- [1] H. M. Colquhoun, D. J. Thompson, and M. V. Twigg, *Carbonylation: direct synthesis of carbonyl compounds*. 1991, New York, Plenum Press.
- [2] S. A. Vizer, K. B. Yerzhanov, A. A. A. Al Quntar, and V. M. Dembitsky, *Tetrahedron*, 2004, **60**(26), 5499-5538.
- [3] B. Gabriele, G. Salerno, and M. Costa, in *Catalytic Carbonylation Reactions*, M. Beller, (Ed), 2006, Springer Berlin Heidelberg.
- [4] R. Grigg and S. P. Mutton, *Tetrahedron*, 2010, **66**(30), 5515-5548.
- [5] N. D. Ca', P. Bottarelli, A. Dibenedetto, M. Aresta, B. Gabriele, G. Salerno, and M. Costa, *Journal of Catalysis*, 2011, **282**(1), 120-127.
- [6] B. Gabriele, R. Mancuso, and G. Salerno, *European Journal of Organic Chemistry*, 2012(35), 6825-6839.
- [7] M. Queirolo, A. Vezzani, R. Mancuso, B. Gabriele, M. Costa, and N. Della Ca', *Journal of Molecular Catalysis A: Chemical*, 2015, **398**, 115-126.
- [8] B. Gabriele, M. Costa, G. Salerno, and G. P. Chiusoli, *Journal of the Chemical Society, Perkin Transactions 1* 1994, 83-87.
- [9] A. V. Malashkevich, L. G. Bruk, and O. N. Temkin, *The Journal of Physical Chemistry A*, 1997, **101**(51), 9825-9827.
- [10] S. N. Gorodskii, A. N. Zakharov, A. V. Kulik, L. G. Bruk, and O. N. Temkin, *Kinetics and Catalysis*, 2001, **42**(2), 251-263.
- [11] S. N. Gorodskii, E. S. Kalenova, L. G. Bruk, and O. N. Temkin, *Russian Chemical Bulletin*, 2003, **52**(7), 1534-1543.
- [12] K. Novakovic, C. Grosjean, S. K. Scott, A. Whiting, M. J. Willis, and A. R. Wright, *Chemical Physics Letters*, 2007, **435**(1-3), 142-147.
- [13] K. Novakovic, C. Grosjean, S. K. Scott, A. Whiting, M. J. Willis, and A. R. Wright, *Physical Chemistry Chemical Physics*, 2008, 749-753.
- [14] C. Grosjean, K. Novakovic, S. K. Scott, A. Whiting, M. J. Willis, and A. R. Wright, *Journal of Molecular Catalysis A: Chemical*, 2008, **284**(1-2), 33-39.
- [15] K. Novakovic, A. Mukherjee, M. J. Willis, A. R. Wright, and S. K. Scott, *Physical Chemistry Chemical Physics*, 2009, 9044-9049.

- 
- [16] J. Parker and K. Novakovic, *Reaction Kinetics, Mechanisms and Catalysis*, 2016, 1-13.
- [17] L. Donlon, J. Parker, and K. Novakovic, *Reaction Kinetics, Mechanisms and Catalysis*, 2014, **112**(1), 1-13.
- [18] L. Donlon and K. Novakovic, *Chemical Communications*, 2014, **50**(98), 15506-15508.
- [19] J. A. Opsteen and J. C. M. van Hest, *Chemical Communications*, 2005 (1), 57-59.
- [20] A. J. Inglis, P. Pierrat, T. Muller, S. Brase, and C. Barner-Kowollik, *Soft Matter*, 2010, **6**(1), 82-84.
- [21] H. Shimotahira, S. Fusazaki, I. Ikeda, and Y. Ozoe, *Bioorganic & Medicinal Chemistry Letters*, 2011, **21**(6), 1598-1600.

## LATERAL FRONT INSTABILITIES INDUCED BY ELECTRIC FIELD

Á. Tóth<sup>1</sup> and D. Horváth<sup>2</sup>

<sup>1</sup>*Department of Physical Chemistry and Materials Science, University of Szeged, Aradivértanúktér 1, H-6720 Szeged, Hungary(atoth@chem.u-szeged.hu)*

<sup>2</sup>*Department of Applied and Environmental Chemistry, University of Szeged, Rerrich Béla tér 1, H-6720 Szeged, Hungary(horvathd@chem.u-szeged.hu)*

### ABSTRACT

Spatiotemporal coupling of an autocatalytic chemical reaction between ions with diffusion may yield reaction-diffusion fronts. Using electric field separating the reactant anions and the autocatalyst cation, lateral instability can be induced while planar fronts can be stabilized with the externally imposed constant electric field in the opposite orientation. When an appropriate inhomogeneous electric field to maintain a constant current density parallel to the direction of propagation is created, the enhanced migrational flux of the reactant can also destabilize the planar front giving rise to a cellular structure. In ionic systems, in the presence of the diffusional flux of the key species, a local electric field at the concentration gradients can build up even in the absence of external electric fields. The arising additional migrational flux not only decreases but also enhances the instability of planar reaction fronts, depending on the charge distribution among the components.

### INTRODUCTION

When autocatalytic reactions are carried out in an unstirred reaction vessel, the coupling of the transport processes with the chemical reaction may lead to spatiotemporal patterns. The simplest scenario is when convection is eliminated and only diffusion occurs yielding so-called reaction-diffusion fronts, i.e., narrow reaction zones separating the reactants from the products. Typically a front sustains its original shape unless the flux of the autocatalyst is lowered below that of the reactant for superautocatalytic reactions. In that case, the initial fluctuations are amplified and a cellular structure with leading segments and trailing cusps develops. The lowering of the flux can be achieved by using immobile reversible complex formation or irreversibly removing the autocatalyst via a simple first-order reaction.

Autocatalytic reactions typically involve ions, therefore in the presence of electric field, migration may alter the existing patterns. In the talk, we review the theoretical analysis and numerical modeling of the governing equations describing autocatalytic reactions coupled to diffusion and migration. Finally the experimental achievements will be discussed.

### MODELING

The simplest autocatalytic reaction exhibiting cellular pattern formation is chosen between two reactants (A and B) where the reaction order is 2 with respect to the autocatalyst B (cubic autocatalysis):

$$\frac{\partial c_i}{\partial t} = D_i \nabla^2 c_i + \frac{z_i F D_i}{R T} \nabla(c_i \nabla \Psi) + \nu_i r$$

where  $c_1$  and  $c_2$  are the concentration of charged reactants A and B, respectively,  $D_i$  the appropriate diffusion coefficients, and  $z_i$  the charges of the ions, while  $\Psi$  corresponds to the electric potential. In the source term,  $\nu_A = -1$  and  $\nu_B = 1$  and the reaction rate is  $r = k c_1 c_2^2$ .

The charge balance should also be considered as

$$\frac{\partial Q}{\partial t} = \sum_i (z_i F D_i \nabla^2 c_i + (z_i F^2 D_i) / (R T) \nabla(c_i \nabla \Psi)) = 0$$

where  $Q$  is the net charge

Two cases are considered: in the first scenario the electric field strength,  $\varepsilon = \nabla \Psi$ , is constant, while in the second the current density  $j$  is constant. The boundary conditions are set to mimic the experiments. Far ahead and behind the front the concentration gradients are zero, the potential gradients for the case of inhomogeneous electric field are

$$\frac{\partial \Psi}{\partial x} \Big|_{\pm \infty} = \frac{-j}{\sum_{i=1}^2 z_i^2 D_i c_{i, \pm \infty}}$$

### RESULTS AND DISCUSSION

We have found that in the presence of constant electric field a cellular structure may develop when the electric field separates the reactant anions and the autocatalyst cation, while planar fronts can be stabilized with that in opposite orientation[1-3]. When an appropriate inhomogeneous electric field to maintain a constant current density parallel to the direction of propagation is created, the enhanced migrational flux of the reactant can also destabilize the planar front giving rise to a cellular structure[4]. Our experiments and modeling calculations show for the selected reaction that lateral instability is

avored for field orientation where the mixing of the reactants and the autocatalyst is enhanced[5,6]. The onset of instability depends not only on the charge difference between the reactant and the autocatalyst but also on the variation of specific conductance in the course of the reaction.

In ionic systems, in the presence of the diffusional flux of the key species, a local electric field at the concentration gradients can build up even in the absence of external electric fields[7,8]. The arising additional migrational flux not only decreases but also enhances the instability of planar reaction fronts, depending on the charge distribution among the components.

#### REFERENCES:

- [1] Á. Tóth, D. Horváth, W. Van Saarloos, J. Chem. Phys., 1999, **111**, 10964-10968.
- [2] D. Horváth, Á. Tóth, K. Yoshikawa, J. Chem. Phys., 1999, **111**, 10-13.
- [3] Zs. Virányi, A. Szommer, Á. Tóth, D. Horváth, Phys. Chem. Chem. Phys., 2004, **6**, 3396-3401.
- [4] Zs. Virányi, Á. Tóth, D. Horváth, J. Eng. Math., 2007, **59**, 229-238.
- [5] Zs. Virányi, Á. Tóth, D. Horváth, Chem. Phys. Lett., 2005, **401**, 575-578.
- [6] Zs. Virányi, D. Horváth, Á. Tóth, J. Phys. Chem. A, 2006, **110**, 3614-3618.
- [7] Zs. Virányi, Á. Tóth, D. Horváth, Phys. Rev. Lett., 2008, **100**, 088301.
- [8] Á. Tóth, D. Horváth, Chaos, 2015, **25**, 064304.

## CONTROLLED TRANSITIONS BETWEEN OSCILLATIONS AND INHOMOGENEOUS STATIONARY STATES

F. Muzika, L. Schreiberová and I. Schreiber

*Department of Chemical Engineering, University of Chemistry and Technology, Technická 5, 16628 Praha 6, Czech Republic.  
(Frantisek.Muzika@vscht.cz)*

### ABSTRACT

This work is focused on experimental observation of transitions between oscillations and inhomogeneous stationary states (discrete Turing patterns) induced by carefully targeted perturbations in a cyclic array of coupled cells with glycolytic oscillatory reaction. The cyclic array is formed by two cells and two capillaries. The coupling is realized via a peristaltic pump using reciprocal pumping delivering reaction mixture in both directions. Glycolytic reaction of yeast extract Y1625 with D-glucose, enhanced by  $\text{HCO}_3^-$  ions occurs in the cuvettes as well as in the coupling capillaries. Dynamic and stationary behavior is observed by using a UV-Vis spectrophotometer, at 340nm (NADH). We report controlled transitions between oscillations and inhomogeneous stationary states.

### INTRODUCTION

Silicon based digital processors have limited performance due to relatively high power consumption, waste heat and architecture. On the other hand, natural systems are not digital based [1, 2] and they do not have mentioned issues. By employing Turing's idea of pattern formation in reaction-diffusion systems, specifically in a ring of discrete coupled cells [3], we proposed a digital chemical computing technique [4, 5] based on targeted perturbations of discrete Turing patterns. The technique also works using addition and/or subtraction of signals/perturbations, which lead to transitions between oscillations and inhomogeneous stationary states (i.e. discrete Turing patterns).

Glycolysis is one of the oldest and the most common biochemical oscillatory reaction occurring in living cells. It can be simplified to the reaction steps responsible for oscillations involving positive feedback occurring on the enzyme phosphofructokinase (PFK) and reaction steps imposing negative feedback mediated by pyruvate kinase and phosphoglycerate kinase. Addition or presence of glycolytic metabolites,

including ATP, can directly or indirectly influence reaction rate of steps representing positive or negative feedback [6]. The most important are in our case addition of  $\text{HCO}_3^-$ , which increases the reaction rate 3 times [7], it also helps maintain the pH of solution at  $\text{pH} \approx 8$ , which doubles the activity of PFK [6], and also temperature of the solutions, which increases reaction rate, using rule of thumb, 4-6 times. Therefore, parameters given by Moran and Goldbeter in their core model of glycolysis [8], can be increased 10-12 times, which allows for occurrence of Turing patterns with equal transport rate coefficients for both the activator ADP and the inhibitor ATP [9], taken as a product and a substrate, respectively, in the core model of glycolysis [8]. In addition, effect of AMP can be included through connection to the pair  $\text{NAD}^+$  and  $\text{NADH}$  via reaction of phosphates. Therefore information about inhomogeneous stationary states of ATP, reported in our previous work [4, 5], can be ascertained from the concentration of  $\text{NADH}$  having absorbance maximum at 340nm.

## EXPERIMENTAL

### Chemicals

Yeast extract powder Y1625 was supplied by Sigma Aldrich (France), D-Glucose monohydrate was supplied by Lachner (Czech Republic) and  $\text{NaHCO}_3$  was supplied by Penta (Czech Republic). All solutions were made using demineralized water with conductivity  $< 1 \mu\text{Scm}^{-1}$ . pH of D-glucose solution was 8.3, pH of yeast extract solution was 7.2, pH inside cells was around 7.7. Temperature of both solutions was maintained between 42-43°C, ambient temperature was maintained at 24°C.

### Experimental Setup

Schematic diagram of the experimental setup is shown in Fig. 1.

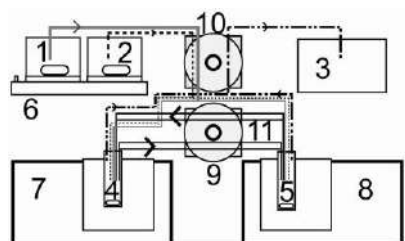


**Figure 1.** Schematic diagram of the experimental setup: (1) yeast extract solution, (2) D-glucose solution, (3) waste tank, (4) measured, stirred and heated cuvette No. 1, (5) measured, stirred and heated cuvette No. 2, (6) stirrer and heater, (7) UV-Vis spectrophotometer No. 1, (8) UV-Vis spectrophotometer No. 2, (9) peristaltic pump used for cuvette coupling, (10) peristaltic pump drawing feed and output stream for both cuvettes, (11) coupling tubes.

For measurement of absorbance levels within wavelength range 180nm to 1100nm, UV-Vis spectrophotometers were used. Spectrophotometer No. 1 was Agilent model 8453, spectrophotometer No. 2 was Agilent model 8454. Both spectrophotometers were set to measure at 1s steps.

The cyclic array is made by two 3.0 ml cuvettes and two 1.05 ml capillaries in the order: cuvette, capillary, cuvette, capillary. The capillaries are not stirred, but they can be thought of as a linear cascade of a number of CSTR swith axial dispersion [9].

## RESULTS AND DISCUSSION

Examples of our results representing transitions between inhomogeneous concentration profiles, various oscillatory regimes and homogenous oscillations are shown in Figs. 2,3. Fig.2a shows, 2EXd1 perturbation can switch an inhomogeneous stationary state into regime with one oscillating cell, while G perturbation can quench it and make the second cell oscillating, while still keeping the concentration inhomogeneous in two types of patterns(1<sup>st</sup> and 3<sup>rd</sup> perturbation by G). Fig. 2b shows, 2EXd1 is able to make inhomogeneous patters, while 2Gd1 can induce homogeneous oscillations. Fig. 3a shows an inhomogeneous stationary state mechanically perturbed and returning to its original state. Fig. 3b show new type of oscillatory regime with period around 67 seconds, coincidentally equal to residence time in the cell.

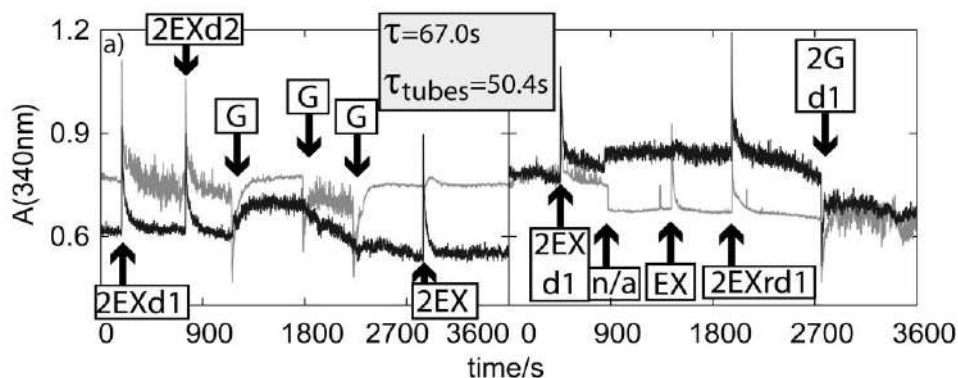


**Figure 2.** Continuous experimental recording of absorbance at 340 nm a) first experiment, b) second experiment. Gray line – cell (4) in Fig. 1. Black line cell (5) in Fig. 1. EX-yeast extract; G-glucose; (r)d(number)-(reverse)delay(seconds), where delay means perturbation of cell (4) and after (number) seconds, perturbation of cell (5), reverse means opposite sequence; 2EX/2G perturbation of both cells by a mentioned species; n/a – spontaneous transition.

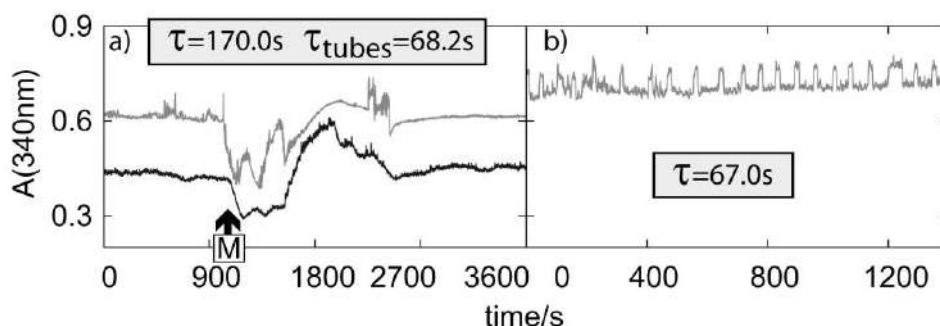


**Figure 3.** Continuous experimental recording of absorbance at 340 nm a) coupled cells experiment, b) one cell experiment. Gray line – cell (4) in Fig. 1. Black line - cell (5) in Fig. 1. M – mechanical perturbation.

### CONCLUSIONS

Glycolytic oscillatory reaction in an array of four coupled cells was studied. Different oscillatory regimes were observed in uncoupled cells. Inhomogeneous concentration profiles, various dynamic regimes and reproducible transitions between inhomogeneous concentration profiles and oscillations were observed in coupled cells using perturbation by yeast extract and D-glucose solution.

### Acknowledgement

This work was supported by the grant 15-17367S from the Czech Science Foundation.

### REFERENCES

- [1] D. J. Felleman and D. C. Van Essen, *Cerebral Cortex*, 1991, **91**, 1-47.
- [2] N. J. Majaj, H. Hong, E. A. Solomon and J. J. DiCarlo, *J. Neurosci.*, 2015, **35**, 13402-13418.
- [3] A. Turing, *Phil. Trans. R. Soc. Lond. B*, 1952, 237, 37-72.
- [4] F. Muzika and I. Schreiber, *Journal of Chemical Physics*, 2013, **139**, 164108:1-10.
- [5] F. Muzika, L. Schreiberová and I. Schreiber, *RSC Advances*, 2014, **4**, 56165-56173.
- [6] D. Mediavilla, I. Metón and I. V. Baanate, *Biochimica et Biophysica Acta*, 2007, **1770**, 706-715.
- [7] T. H. Hereng, K. B. P. Elgstøen, L. Eide, K. R. Rosendal, B. S. Skålhegg, *Human Reproduction*, 2014, **29**, 918-930.
- [8] A. Goldbeter, F. Moran, *Biophys. Chem.*, 1984, **20**, 149-156.
- [9] F. Muzika, L. Schreiberová and I. Schreiber, *Reac. Kinet. Mech. Cat.*, 2016, **118**, 99-114.

## DYNAMIC BEHAVIOUR OF UREA–UREASE–ACETIC ACID SYSTEM: AN EXPERIMENTAL STUDY

V. Radojković and I. Schreiber

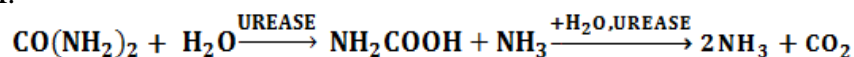
*Department of Chemical Engineering, University of Chemistry and Technology, Technická 5, 16628 Praha 6, Czech Republic  
(radojkov@vscht.cz)*

### ABSTRACT

Our previous experimental studies of the buffered decomposition of urea by urease in a CSTR indicated system's diverse dynamic behaviour and the possibility of pH oscillations. We aimed to (1) identify conditions under which pH oscillates with a constant period and amplitude, (2) construct an experimental phase diagram that describes other types of dynamic behaviour and (3) investigate how premixing of acetic acid and urea influences the phase diagram. Flow rate and acid concentration were systematically varied. As opposed to the expected distinct regions of bistability, only a few randomly occurring bistabilities were observed when the solutions were premixed. On the other hand, regular and irregular pH oscillations of various amplitudes and periods were observed when solutions were not premixed. The occurrence and properties of these oscillations follow certain patterns. Thus, it appears that the stable chemical oscillations are possible in the urea–urease–acetic acid system.

### INTRODUCTION

A reaction which is believed to be capable of exhibiting oscillatory behaviour and which has been studied and modelled by several authors in recent years, is a reaction of urea and urease in the presence of an acid, which is used to create a buffer solution and decrease the rate of change of pH.



Wrobel [1] reports that when the system was buffered by acetic acid in a flow-through (CSTR) reactor, large amplitude oscillations were observed for a range of parameters (substrate concentration, acetic acid concentration, temperatures). Unfortunately, none of the observed oscillations were regular, with a constant period and amplitude. Furthermore, a mathematical model predicted existence of a bistability region, which was not experimentally confirmed. Hu et al. [2] reported the presence of aperiodic

oscillations with large amplitude transitions as response to acid/base perturbations in the same system, yet they attribute these to noise-induced bistable switching or mixing effects. Their mathematical model successfully simulated experimentally observed behaviour.

## **EXPERIMENTAL**

### **Chemicals**

Enzyme solution was prepared using Jack Beans urease (*Sigma Aldrich*), activity 31340 U/g of solid, urea solutions were prepared from *Penta* pellets of 99% purity. Acetic acid was prepared by diluting the 99% acetic acid (*Penta*) to concentration 0.256mol/l and then it was diluted further to a concentration of interest.

### **Experimental Setup**

All experiments were performed in a CSTR open to the atmosphere in order to allow for an undisturbed transfer of gases evolved during the reaction from the reaction mixture to the ambient air. Mixture was stirred using a stirring bar on a magnetic stirring plate at 900 rpm. Temperature was maintained nearly constant, in the range of  $23.0 \pm 0.5$  °C, by submerging all stock solutions into a pool of thermostated water. Air temperature was maintained constant as well, using an air conditioner set to 23.0 °C. *Ismatec* peristaltic pumps were used to pump the solutions into and from of the reactor. The inflow pump was calibrated daily. The outflow pump was set to its maximum pumping rate for all inflow rates, in order to quickly eliminate all fluctuations of reaction volume and maintain its constant value. pH was measured using a pH electrode connected to a Hanna HI4221 measuring device, further connected to a PC equipped with a suitable software. The pH electrode was calibrated daily, before conducting experiments or preparing stock solutions. pH values of stock solutions were measured before and after experiments. Six experiments, corresponding to a set of six  $k_0$  values were usually done per day. For a set of experiments, concentrations of all stock solutions, as well as stirring rate, were kept constant and only  $k_0$  values were manipulated by increasing the flow rate from the lowest to the highest value. One experimental run was approximately one hour long. In the first set of experiments we used three pure, independently prepared solutions, whereas in the second one we premixed acetic acid and urea. Experimental setup is presented in Figure 1.



**Figure 1.** - Experimental setup

## RESULTS AND DISCUSSION

Examples of observed oscillations and steady states / bistability switches are presented in the following Figures 2 and 3.

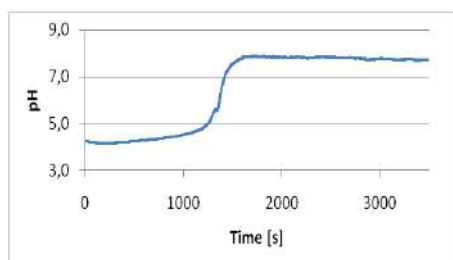


**Figure 2.** - Bistability switch

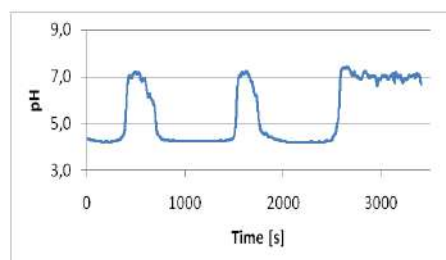


**Figure 3.** - Regular, large amplitude oscillations

The results are summarized in the phase diagrams in Figures 3 and 4.

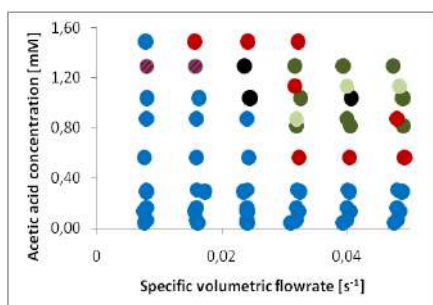


**Figure 4.** - Experimentally obtained bifurcation diagram for 3 unmixed stock solutions; Blue points - high pH steady-state, red - low pH steady-state, striped - bistability switch, black - transient behaviour, light green - irregular oscillations, dark green - regular oscillations.

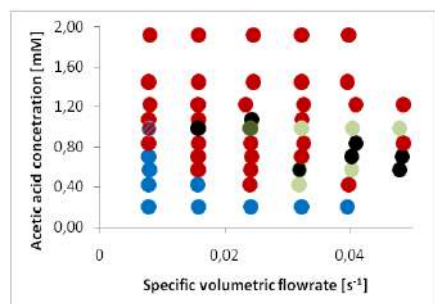


**Figure 5** - Experimentally obtained bifurcation diagram for unmixed stock solutions.

## CONCLUSIONS

The results indicate that the studied system can exhibit oscillatory behaviour, in addition to bistability switches and high and low steady states. Observed oscillations were both regular (with constant period and amplitude) and irregular (one of the two or both were not constant; "period" here has the meaning of peak-to-peak time interval and "amplitude" is pH-difference between consecutive minimum and maximum of pH), with regular oscillations having both small and high amplitudes and periods. Observed bistability switches were from low to high pH steady states. Obtained results were reproducible. Experiments also indicate that stability of stock solutions influences behaviour of the system.

## Acknowledgement

This work was supported by the International Višegrad Fund, Bratislava and the grant 15-17367S from the Czech Science Foundation.

## REFERENCES

- [1] H. Gang, J. A. Pojman, S. K. Scott, M. A. Wrobel, A. F. Taylor, *Base-Catalyzed Feedback in the Urea—Urease Reaction*. *J. Phys. Chem. B*, 2010, **114**, 14059-14063.
- [2] M. A. Wrobel, *pH-driven instabilities in chemical systems*. PhD Thesis, University of Leeds, Leeds, 2012.

## COALESCENCE AND ELECTROCOALESCENCE BASED ON ELECTROHYDRODYNAMICS PRINCIPLES

A.M. Spasić<sup>1</sup>, J. M. Jovanović<sup>2</sup>, V. Manojlović<sup>1</sup>, M. Jovanović<sup>3</sup>,  
S. Alexandrova<sup>4</sup> and A. Saboni<sup>5</sup>

<sup>1</sup>*Institute for Technology of Nuclear and Other Mineral Raw Materials,  
Dept. of Chem. Engng., 86 F. d'Esperey St., 11000 Belgrade, Serbia,*

<sup>2</sup>*Innovationi Center, Dept. of Met. & Tech., University of Belgrade, 4  
Karnegijeva St., 11000 Belgrade, Serbia*

<sup>3</sup>*Dept. of Met. & Tech., University of Belgrade, 4 Karnegijeva St., 11000  
Belgrade, Serbia*

<sup>4</sup>*Laboratoire de Thermique et Procédés, ENSGTI, rue Jules Ferry, BP 7511,  
64 075 Pau, France;*

<sup>5</sup>*Laboratoire SIAME-IUT, UPPA, Avenue de l'Université, 64 000 Pau,  
France*

### ABSTRACT

Developed liquid-liquid interfaces play an important role in some physical, chemical, and biochemical processes, for example strongly related are the processes of formation, existence and destruction of emulsions and double emulsions, life of biological cells, and various membrane separation processes. Since the particular events and phenomena that occur in these processes are not sufficiently well or deeply understood the introduction of theoretical models known in classical and quantum electrodynamics is needed. Hence, the objective of this research is a try to provide an approach to elaborate the complex phenomena that occur at developed liquid-liquid interfaces or at small separations. The representative events that are to be discussed in this presentation are coalescence and electrocoalescence using electrohydrodynamics (EHD) principles.

### INTRODUCTION

This story begins in the pilot plant for uranium extraction from wet phosphoric acid by D2EHPA-TOPO process. The light phase loop for solution of the entrainment problems was developed and constructed. Equipment, of particular interest for this research, used for a breaking of double emulsions, was the lamellar coalescer. Double emulsion passing through the lamellar coalescer involves the sequences: approach, rest, disturbance, rupture on an inclined plate, coalescence/electrocoalescence, and flow up. Physical chemical system, which has been used to corroborate

the validity of theoretical predictions, was a heavy-phase droplet/light-phase film structure immersed in a heavy-phase continuum, double emulsion. This system was the heavy-phase output from a “pump-mix” mixer-settler battery together with its entrained light phase. The heavy liquid was 5.6 M phosphoric acid, and the light liquid was the synergistic mixture of 0.5 M di(2-ethylhexyl) phosphoric acid and 0.125 M tri-n-octylphosphine oxide in dearomatized kerosene (DTK). It was necessary to develop two concepts for easier understanding of the physical events at developed liquid-liquid interfaces [1-5].

### THEORETICAL CONCEPTS AND CONSTITUTIVE MODEL

The first is a concept of an entity, and the corresponding classification of finely dispersed systems; this concept permit consideration of the electron transfer phenomenon beside the heat, mass, and momentum transfer phenomena commonly used in chemical engineering. The second concept is an introduction of almost forgotten basic electrodynamics element the memdiode or memristor as a current controlled device, and the corresponding memristive systems. This concept is needed because the fundamental electrodynamics elements, the resistor, the inductor, and the capacitor are not sufficient for a satisfactory explanation of complex phenomena at developed liquid-liquid interfaces. A corresponding constitutive model of liquids was developed and applied to the selected emulsions and double emulsions.. Now, considering these concepts, ectromechanical analogies, and developed constitutive model of liquids the representative model of double emulsion and/or biological cell is presented in figure 1.

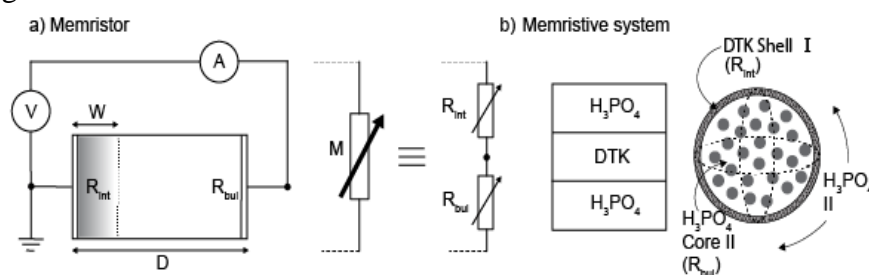


**Figure 1.** a) The memristor-M, b) Droplet-film structure or biological cell; film as a shell/region I DTK- $R_{int}$ , and droplet as a core/region II  $H_3PO_4$ - $R_{bul}$ .

From this picture a hysteretic behavior controlled by the intrinsic nonlinearity of  $M$  and the boundary conditions on the state variable  $w$  follows. Now, the current-potential anomalies, switching and hysteretic

conductance, multiple conductance states, and apparent negative differential resistance, for example in thin-film structures may be discussed. Some propositions, related to the microscopic nature of resistance switching and charge transport at small separations, consider atomic rearrangements and its influence on the electronic current.

### COALESCENCE AND ELECTROCOALESCENCE

Although the film thinning, the drainage, and the rupture processes are depending on many factors the coalescence and/or electrocoalescence process itself may take into account the following:

- Droplet-film structure size;
- Distance of fall of droplet to the interface;
- Curvature of the droplet-side interface;
- Density difference between two phases;
- Viscosity ratio of the phases;
- Interfacial tension effects;
- Temperature effects;
- Vibration and electrical effects;
- Electromagnetic effects;
- Presence of the electrical double layers;
- Solute transfer effects.

It is not necessary that all factors are in the game for a particular case. Probably one qualitative and quantitative physical picture, including electrocoalescence, can be withdrawn considering Marangoni instabilities of the first and second order and possible electrical analogues as well as using developed theory of electroviscoelasticity, figures 2 and 3. Now, imagine the case of double emulsion, and/or biological cell, then the situation in figure 2 may be expected, but replacing the mechanical force and surface tension with electrical force and electrical interfacial potential. This is the case when the droplets are small or the separation is in a nanometer scale. Although, there may be several possible cases, such as droplet rotation, droplet go-back rotation, film rotation, quasi equilibrium-no rotation at all.

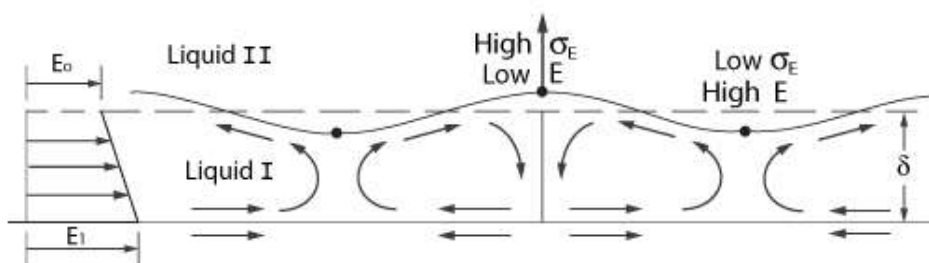


**Figure 2.** Marangoni instability mechanism-the electrical analog.

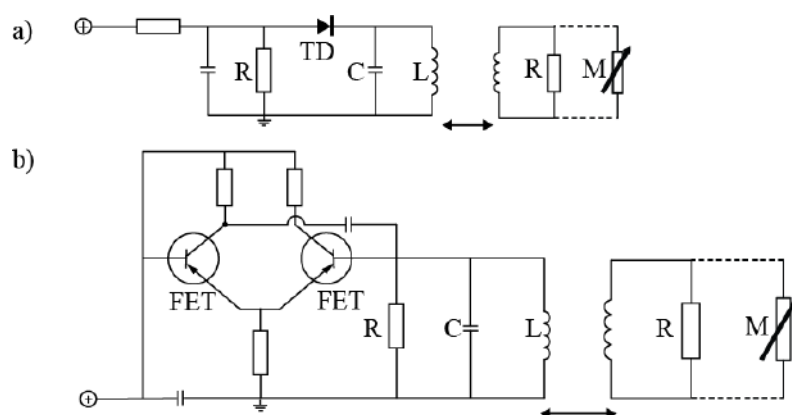


**Figure 3.** Model of double emulsion or biological cell as a memristive system—a resultant antenna output circuit: a) tunnel diode oscillator; TD—tunnel diode, R—resistor and L—inductor as electroviscous elements, C—capacitor and M—memristor as electroelastic elements; b) emitter coupled oscillator; FET—field effect transistor.

### IMPLICATIONS

This theory and models discussed, using EHD principles, may facilitate the understanding of, for example, entrainment problems in solvent extraction, very developed interfaces in colloid and interface science, chemical and biological sensors, electro-analytical methods, biology or biomedicine, in particular hematology (non-Newtonian fluid flow), genetics (DNA models, electron transfer) and electroneurophysiology (quantum spin transport).

### Acknowledgment

Financial support by Ministry of Education and Science – Republic of Serbia, grants: former 142034 and present 34009 and 46010.

### REFERENCES

- [1] A.M. Spasic et al., CHISA All Congresses (1987-2016), Prague.
- [2] A.M. Spasic et al., PHYSICAL CHEMISTRY All Conferences (1992-2014), Belgrade.
- [3] J-P. Hsu, A.M. Spasic, Interfacial Electroviscoelasticity and Electrophoresis, CRC Press-Taylor & Francis, Boca Raton London New York, 2010.
- [4] A.M. Spasic, J.M. Jovanovic, M. Jovanovic, Adv. Colloid Interface Sci., 2012; **174**, 31-49.
- [5] A.M. Spasic, M.P. Lazarevic, M.V. Mitrovic, D.N. Krstic in: Finely Dispersed Particles: Micro-, Nano-, and Atto-Engineering, A.M. Spasic, J.P. Hsu (Eds.), CRC Press-Taylor and Francis, Boca Raton London N.Y., 2006.

## MATHEMATICAL MODELING OF INTERLEUKIN 6 EFFECTS ON THE HYPOTHALAMIC-PITUITARY-ADRENAL AXIS

A. Stanojević<sup>1</sup>, V. M. Marković<sup>1</sup>, Ž. Čupić<sup>2</sup> and V. Vukojević<sup>3</sup>

<sup>1</sup>University of Belgrade, Faculty of Physical Chemistry, Studentski trg 12-16, 11158 Belgrade, Serbia (ana.stanojevic@ffh.bg.ac.rs)

<sup>2</sup>University of Belgrade, ICTM, Department of Catalysis and Chemical Engineering, Njegoševa 12, 11000 Belgrade, Serbia

<sup>3</sup>Karolinska Institute, Department of Clinical Neuroscience, Center for Molecular Medicine CMM L8:01, 17176 Stockholm, Sweden

### ABSTRACT

A stoichiometric network model is developed to succinctly describe the complex effects of interleukin 6 (IL-6) on the activity of the hypothalamic-pituitary-adrenal (HPA) axis. Dynamic properties of the model were investigated for varying IL-6 levels and conditions under which qualitative transitions between dynamic states occur are determined. Numerical simulations were then used to investigate *in silico* how chronically increased IL-6 levels affect the HPA axis capacity to respond to stress. Our study shows that significantly elevated IL-6 levels considerably alter the ultradian HPA axis rhythmicity and diminish its capacity to respond to acute stress.

### INTRODUCTION

The neuroendocrine and immune systems are tightly coupled in vertebrates and mutually affect each other's activity – the neuroendocrine system orchestrates the activity of the immune system through the action of glucocorticoids and, reciprocally, the immune system exerts its own influence on the neuroendocrine system through the action of soluble immune factors [1]. Interactions between the neuroendocrine and immune systems are altered in many acute and chronic disorders [2], but these interactions are intricate and notoriously difficult to dissect experimentally.

In order to further our understanding of complex interactions between the neuroendocrine and immune systems, we have used literature findings to develop a stoichiometric network model that concisely describes interleukin 6 (IL-6) effects on neurochemical transformations underlying the Hypothalamic-Pituitary-Adrenal (HPA) axis, and use numerical simulations and approaches from dynamical systems theory to investigate *in silico* the effects of IL-6 on the HPA axis capacity to respond to acute stress.

## RESULTS AND DISCUSSION

**Stoichiometric network model development** To describe the bidirectional interactions between IL-6 and the HPA axis we have, based on literature findings [1,2], extended the stoichiometric network model of HPA axis described in detail in reference [3] to include relations that describe IL-6 biogenesis/release in the peripheral circulation; its stimulating action on corticotrophin releasing hormone (CRH) and the negative feedback of cortisol (CORT) on the immune system to suppress IL-6 synthesis/release, as schematically depicted in Fig. 1 (green lines).

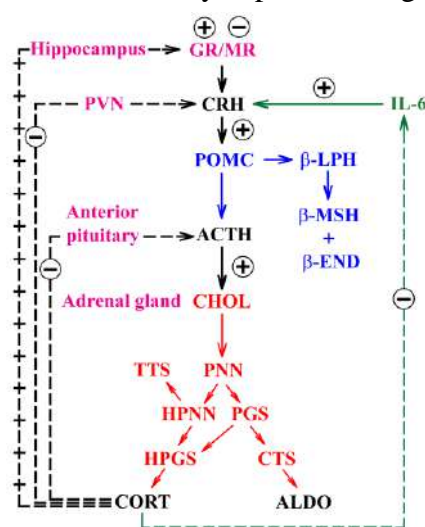


**Figure 1.** Schematic presentation of bidirectional interactions between IL-6 and the HPA axis.

Interactions between the paraventricular nucleus (PVN) of the hypothalamus, anterior lobe of the pituitary gland and the cortex of the adrenal gland *via* the actions of corticotrophin-releasing hormone (CRH), adrenocorticotrophic hormone (ACTH), cortisol (CORT) and aldosterone (ALDO) on their corresponding receptors, comprise the backbone of the HPA axis (magenta/black). This core model is augmented to include neuropeptides derived by proopiomelanocortin (POMC) processing ( $\beta$ -lipotropin ( $\beta$ -LPH),  $\beta$ -melanocyte-stimulating hormone ( $\beta$ -MSH) and  $\beta$ -endorphin ( $\beta$ -END); blue), cholesterol (CHOL) and products of adrenal steroidogenesis (pregnenolone (PNN), hydroxyprogesterone (HPNN), progesterone (PGS), hydroxyprogesterone (HPGS), corticosterone (CTS) and testosterone (TTS); red). Positive (+) and negative (-) feedback actions of CORT are represented by full and dashed black lines, respectively. Dual, positive and negative feedback actions of CORT on the hippocampus, *via* its distinct action on glucocorticoid (GR) and mineralocorticoid (MR) receptors, are represented by the +/- black line. Bidirectional interactions between the HPA axis and IL-6 are presented by the green lines.

progestosterone (PGS), hydroxyprogesterone (HPGS), corticosterone (CTS) and testosterone (TTS); red). Positive (+) and negative (-) feedback actions of CORT are represented by full and dashed black lines, respectively. Dual, positive and negative feedback actions of CORT on the hippocampus, *via* its distinct action on glucocorticoid (GR) and mineralocorticoid (MR) receptors, are represented by the +/- black line. Bidirectional interactions between the HPA axis and IL-6 are presented by the green lines.

**Numerical simulations** Numerical simulations were performed using the MATLAB ode15s solver that is based on the Gear algorithm for integration of stiff differential equations. Absolute and relative error tolerance values were  $1 \times 10^{-20}$  and  $1 \times 10^{-14}$ , respectively. Initial conditions for the integration of ODEs in all numerical simulations were:  $[\text{CHOL}]_0 = 3.40 \times 10^{-4} \text{ M}$ ,  $[\text{CRH}]_0 = 1.00 \times 10^{-12} \text{ M}$ ,  $[\text{ACTH}]_0 =$

$8.00 \times 10^{-13}$  M,  $[\text{CORT}]_0 = 4.00 \times 10^{-8}$  M,  $[\text{ALDO}]_0 = 1.50 \times 10^{-9}$  M,  $[\text{POMC}]_0 = 1.50 \times 10^{-10}$  M,  $[\beta\text{-END}]_0 = 1.50 \times 10^{-11}$  M,  $[\beta\text{-LPH}]_0 = 1.50 \times 10^{-10}$  M,  $[\beta\text{-MSH}]_0 = 1.50 \times 10^{-11}$  M,  $[\text{PNN}]_0 = 1.00 \times 10^{-10}$  M,  $[\text{MC}_2]_0 = 1.50 \times 10^{-15}$  M,  $[\text{MC}_2^{\text{active}}]_0 = 1.50 \times 10^{-15}$  M,  $[\text{HPNN}]_0 = 4.00 \times 10^{-8}$  M,  $[\text{PGS}]_0 = 4.00 \times 10^{-8}$  M,  $[\text{HPGS}]_0 = 4.00 \times 10^{-8}$  M,  $[\text{TTS}]_0 = 4.00 \times 10^{-8}$  M,  $[\text{CTS}]_0 = 4.00 \times 10^{-8}$  M,  $[\text{IL-6}]_0 = 4.00 \times 10^{-13}$  M.

To simulate the effects of chronic IL-6 action, the rate constant of IL-6 biosynthesis/secretion was varied and the observed dynamic states and dynamical transitions between them were examined. To simulate the effect of acute perturbations with CRH, numerical integration of the system of ordinary differential equations was stopped at a specified time point and new initial conditions for subsequent integration were defined. For the new initial conditions, CRH concentration was specified ( $5 \times 10^{-8}$  M), while the concentrations of all other species retained their previously attained values.

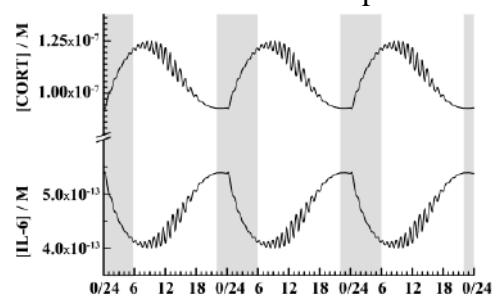


**Figure 2.** Daily fluctuations in cortisol (top) and IL-6 (bottom) levels in the peripheral blood circulation. Shaded areas indicate the dark phase, lasting from 22 o'clock in the evening until 6 o'clock in the morning.

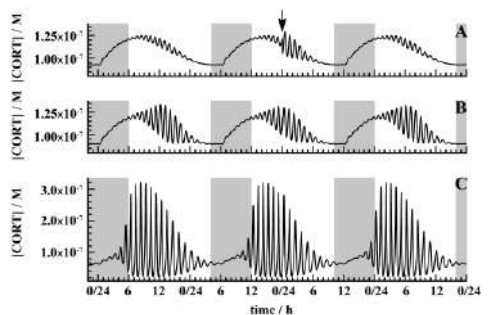


**Figure 3.** Increased IL-6 levels may markedly alter the HPA axis activity. *Top left:* CORT levels under normal physiology. *Top right:* CORT dynamics under highly elevated IL-6 levels (as in septic shock). *Bottom:* Orbit diagram showing changes in the amplitude of a selected ultradian CORT oscillation (circles), and a transition to a stable stationary state (dots) at high IL-6 levels.

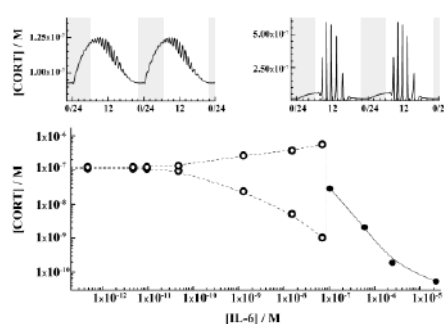


**Figure 4.** The HPA axis responds to acute CRH challenge of the same intensity ( $5 \times 10^{-8}$  M) elicited always at the same time, 12:00 AM, is different under normal physiology and when mean daily IL-6 levels are chronically increased. **A)**  $[\text{IL-6}] = 4.7 \times 10^{-13}$  M, **B)**  $[\text{IL-6}] = 4.7 \times 10^{-12}$  M, **C)**  $[\text{IL-6}] = 4.7 \times 10^{-11}$  M.

**Numerical simulations of IL-6 daily dynamics** In agreement with experimental findings [4], numerical simulations show that under normal physiology, IL-6 levels are several orders of magnitude lower than CORT levels and show a trough in the morning (Fig. 2).

**Effect of chronically increased IL-6 levels on HPA axis dynamics** Numerical simulations show that chronically elevated IL-6 levels alter HPA axis activity, increasing the amplitude of ultradian cortisol oscillations and decreasing their frequency (Fig. 3).

**Chronically increased IL-6 levels diminish the HPA axis capacity to respond to stress** Numerical simulations show that HPA axis response to an acute stressful challenge of the same intensity,  $[CRH] = 5 \times 10^{-8}$  M, elicited at the same time, at noon, is different under normal physiology (Fig. 4 A) and under conditions when IL-6 levels are chronically elevated (Fig. 4B and C).

## CONCLUSION

Numerical simulations and approaches from dynamical systems theory show that highly chronically elevated IL-6 levels, which are common in individuals with persistent activation of the immune system, can markedly increase the amplitudes of ultradian oscillations of the HPA system hormones. This eventually leads to a reduction of HPA axis capacity to respond to acute stress.

## Acknowledgement

Support from the Foundation for Strategic Research (SBE13-0115), the Knut and Alice Wallenberg Foundation (KAW 2011.0218), the Rajko and Maj Đermanović Fund, CMST COST Action CM 1304 “Emergence and Evolution of Complex Chemical Systems”, and the Ministry of Education, Science and Technological Development of the Republic of Serbia, grants 172015 and 45001, is gratefully acknowledged.

## REFERENCES

- [1] V. Turnbull, C. L. Rivier, *Physiol. Rev.* 1999, **79**, 1-71.
- [2] D. A. Papanicolaou, R. L. Wilder, S. C. Manolagas, G. P. Chrousos, *Ann. Intern. Med.* 1998, **128**, 127-137.
- [3] Ž. Čupić, A. Stanojević, V. M. Marković, Lj. Kolar-Anić, L. Terenius, V. Vukojević, *Addict. Biol.* 2016, doi:10.1111/adb.12409.
- [4] G. Nilsson, M. Lekander, T. Åkerstedt, J. Axelsson, M. Ingre, Diurnal variation of circulating interleukin-6 in humans: a meta-analysis. *bioRxiv preprint* first posted online Apr 4, 2016; doi: <http://dx.doi.org/10.1101/042507> (<http://biorxiv.org/content/biorxiv/early/2016/04/14/042507.full.pdf>)

## SCANNING ELECTRON MICROSCOPIC AND CHROMATOGRAPHIC EVIDENCE OF SPONTANEOUS HETEROPEPTIDE FORMATION IN THE BINARY $\alpha$ -AMINO ACID SOLUTIONS

A. Maciejowska<sup>1</sup>, A. Godziek<sup>1</sup>, E. Talik<sup>2</sup>, M. Sajewicz<sup>1</sup> and T. Kowalska<sup>1</sup>

1) *Institute of Chemistry, University of Silesia, 9 Szkolna Street, 40-006 Katowice, Poland*

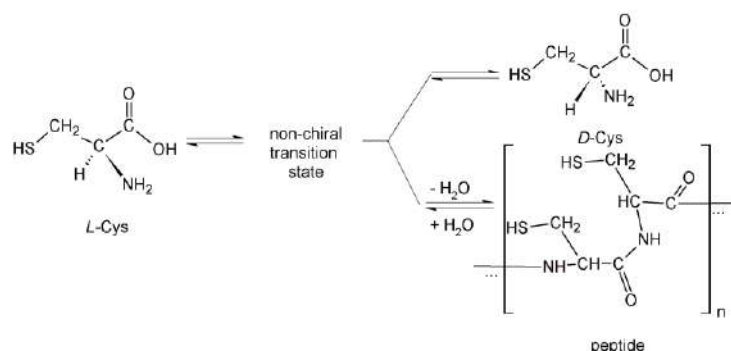
2) *Department of Physics of Crystals, Institute of Physics, University of Silesia, 4 Uniwersytecka Street, 40-007 Katowice, Poland*

### ABSTRACT

Peptide amino acids dissolved in 70% aqueous methanol undergo spontaneous non-linear peptidization followed by spontaneous self-assembly to give supramolecular nano- and microstructures. In this study, we present the results of spontaneous peptidization and self-assembly running in two binary amino acid mixtures (*L*-Phe-*L*-Pro and *L*-Phe-*L*-Cys), traced with use of scanning electron microscopy (SEM), high-performance liquid chromatography (HPLC), and liquid chromatography with mass spectrometric detection (LC-MS). By means of SEM, it was demonstrated that the shape of nano- and microstructures derived from *L*-Phe-*L*-Pro is determined by *L*-Phe, and that of nano- and microstructures derived from *L*-Phe-*L*-Cys is determined by *L*-Cys. By means of HPLC, an oscillatory nature of peptidization was proven and with use of LC-MS, chemical structures of some selected homo- and heteropeptides were established.

### INTRODUCTION

In our earlier studies, it has been shown that single low molecular weight chiral carboxylic acids and the mixtures thereof (amino acids [1], hydroxyl acids [2], and profen drugs [3]) undergo spontaneous processes of chiral inversion and peptidization in the parallel (see Scheme 1). In this study, we focus on the two amino acid pairs (*L*-Phe-*L*-Pro and *L*-Phe-*L*-Cys) sharing one compound (i.e., *L*-Phe) in common. It is our intent to compare an effect of *L*-Phe on spontaneous peptidization with each compared amino acid pair.



**Scheme 1.** Molecular mechanisms of chiral conversion and peptidization running in the parallel upon an example of Cys (conversion: *L*-Cys to *D*-Cys; peptidization: *L*-Cys to (Cys-Cys)<sub>n</sub>).

## RESULTS AND DISCUSSION

In Figs 1(a)-(c)), we show the SEM micrographies of the peptides spontaneously formed in the monocomponent solutions of *L*-Phe (the fibrous structures), *L*-Phg (the flat irregular structures), and *L*-Cys (the spherical structures). The shapes of these structures are apparently governed by the two functionalities (-COOH and -NH<sub>2</sub>) and phenyl ring as a steric hindrance with *L*-Phe, the two functionalities (-COOH and =NH in the pyrrolidine ring) with *L*-Pro, and three functionalities (-COOH, -NH<sub>2</sub>, and -SH) with *L*-Cys, respectively.

In the case of the binary *L*-Phe-*L*-Pro system, peptide nano and microfibrils are formed, showing an evidently predominant role of *L*-Phe in the peptide formation (Figs 1(d)-(f)). In the case of the binary *L*-Phe-*L*-Cys system, peptide nano- and microspheres are formed, pointing out to the predominant role of *L*-Cys in the peptide formation (Figs 1(g)-(i)). However, nano- and microspheres derived from the binary system are smoother than those originating from *L*-Cys alone.

In order to prove that the investigated peptidization processes are oscillatory in nature, the semi-continuous HPLC-ELSD control was performed of changing concentrations with individual amino acids in the *L*-Phe-*L*-Pro system (sample ageing lasted 250 h) and in the *L*-Phe-*L*-Cys system (sample ageing lasted 48 h). In Figs 2(a),(b), time dependence of the chromatographic peak heights for the investigated amino acids and the peptidization products is presented. Respective plots confirm the oscillatory nature of the investigated peptidization processes. The non-monotonous concentration changes are equally observed with the monomeric amino acids and the reaction product for *L*-Phe-*L*-Pro (Fig. 2(a)), and with cysteic acid for *L*-Phe-*L*-Cys (Fig. 2(b)).

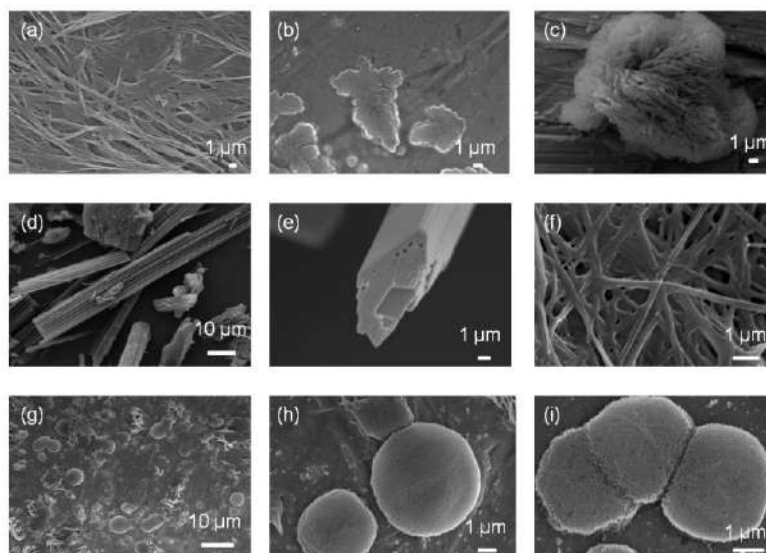


**Figure 1.** Scanning electron micrographs recorded for (a) *L*-Phe, (b) *L*-Pro, (c) *L*-Cys, (d)-(f) *L*-Phe-*L*-Pro, and (g)-(i) *L*-Phe-*L*-Cys, dissolved in 70% aqueous methanol, aged (a)-(c) and (g)-(i) for two weeks and (d)-(f) for one year and then evaporated to dryness. Magnification of (a) X3300, (b) X5000, (c) X4000, (d) X1300, (e) X6000, (f) X13000, (g) X1600, (h) X8000, (i) X14000. Size bars make insets in each individual picture.

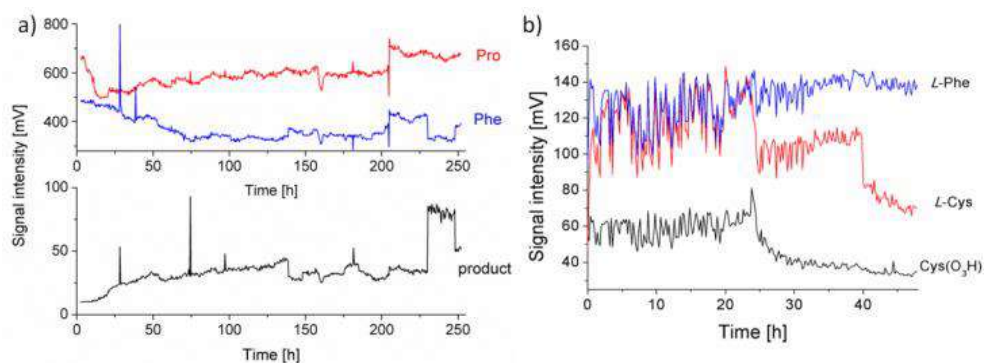


**Figure 2.** Time series of the chromatographic peak heights recorded with the ELSD detector for (a) Phe, Pro and the peptidization product (250 h ageing period), and (b) Phe, Cys, and Cys(O<sub>3</sub>H) (48 h ageing period).

In order to confirm the presence of homo- and heteropeptides among the amino acid ageing products, the LC-MS analyses were performed. For the sake of example, in Fig. 3(a) the mass spectrum recorded for the freshly prepared *L*-Phe-*L*-Pro system is given, and in Fig. 3(b), the mass spectrum

for the same sample after six weeks sample ageing. A striking difference between these two mass spectra can be observed, in the latter case with an abundance of peptidization products with the mass weights up to 3500 Da.

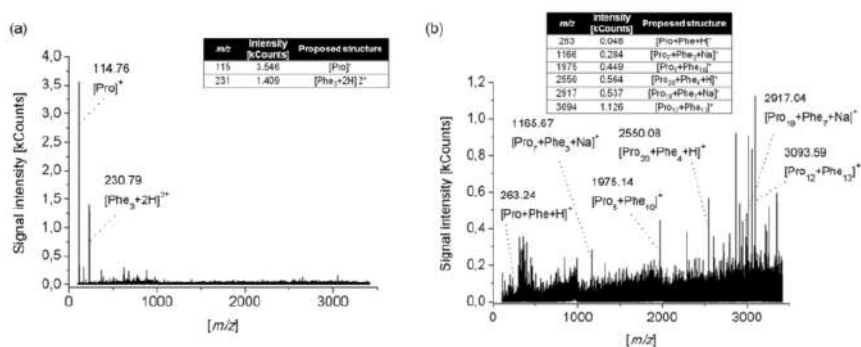


**Figure 3.** Mass spectra recorded in the positive electrospray ionization mode for a) the freshly prepared *L*-Phe-*L*-Pro sample and b) the same sample after 6 weeks ageing, and the tables with ion intensities and the suggested chemical structures of certain cations.

## CONCLUSION

The SEM investigations showed that the shape of the peptide nano- and microstructures spontaneously formed in the binary amino acid samples is governed by one amino acid from a given pair. The HPLC investigations confirmed an oscillatory nature of peptidization, and the LC-MS examination of peptide structures confirmed the presence of the homo- and heteropeptides in the aged solutions.

## REFERENCES

- [1] M. Sajewicz, D. Kronenbach, M. Gontarska, M. Wróbel, R. Piętka, T. Kowalska, *J. Planar Chromatogr. – Modern TLC*, 2009, **22**, 241-248
- [2] M. Sajewicz, D. Kronenbach, M. Gontarska, T. Kowalska, *J. Liq. Chromatogr. Relat. Technol.*, 2010, **33**, 1047-1057
- [3] M. Sajewicz, R. Piętka, A. Pieniak, T. Kowalska, *Acta Chromatogr.*, 2005, **15**, 131-149

## OSCILLATIONS AND TRISTABILITY IN ENZYMIC GLUCOSE OXIDATION USING POTASSIUM FERRICYANIDE AS A SUBSTRATE IN CONTINUOUS STIRRED TANK REACTOR

K. Ponomareva, I. Schreiber, L. Schreiberova and F. Muzika

*Department of Chemical Engineering,  
University of Chemistry and Technology, Technická 5  
166 28, Prague, Czech Republic. (Frantisek.Muzika@vscht.cz)*

### ABSTRACT

Oscillations and tristability were observed in experiments in CSTR with the enzymatic oxidation of glucose with glucose oxidase, potassium ferricyanide as a substrate and sodium hydroxide providing negative feedback, depending on variable input concentrations of reactants.

### INTRODUCTION

Non-linear dynamics is typical for biological systems and it is mostly related to the enzymatically catalyzed reactions. Oscillation is a periodic behavior of a dynamical system, when one or more characteristics of the system periodically vary [1]. Periodic solutions of dynamical system arise at a Hopf bifurcation point, i.e. in the point, where stationary solutions switch their stability via complex conjugate eigenvalues. Together with change of stability of stationary solution, periodic solution arises at that point.

The enzyme glucose oxidase (GOx) is a protein with two active units of flavin adenine dinucleotide (FAD). In nature GOx catalyzes oxidation of glucose by oxygen where gluconic acid and hydrogen peroxide are the products. The mechanism of the reaction is based on electron transfer from glucose to oxidized enzyme in the first step, i.e. reduction of GOx. Then in the second step the electron transfers from the reduced enzyme to oxygen, after that the oxidized GOx returns to the first step of reaction cycle. This reaction has a great importance in developing enzyme glucose sensors as it allows to detect blood glucose level by measuring the electrical signal produced by the enzymatic glucose oxidation [2], [3]. However, *in vivo* implantable glucose sensor using this reaction seemed to be unstable in continuous measurements as there were output fluctuations caused by fluctuation of blood oxygen and blood glucose concentrations and local variations of blood flow as well [4]. An enzymatic bio fuel cell based on this

reaction has been fabricated, which seems to be attractive in terms of developing a promising alternate energy source [5], [6].

The mechanism of enzymatic glucose oxidation permits to use other substrates as electron acceptors, which can substitute oxygen, for example, potassium ferricyanide  $K_3[Fe(CN)_6]$  [7]. The complete equations which express the mechanism of enzymatic glucose oxidation by potassium ferricyanide are as follows:



Where  $GO_{\text{ox}}$  is an oxidized enzyme,  $GO_{\text{xr}}$  is a reduced enzyme,  $GO_{\text{xs}}$  is a semi-quinoneenzyme. Enzymatic glucose oxidation with ferricyanide has a bistability in CSTR over a wide range of such parameters as input concentrations of reactants and reciprocal time. Oscillations were achieved by implementing into the reactor sodium hydroxide feed managed by a computer as a negative feedback over a wide range of its concentration. Generated oscillations mostly had amplitude between pH 3.5 and pH 5 with a period of 2-20 min [8].

## EXPERIMENTAL

GOx from *Aspergillus niger* was purchased from Sigma-Aldrich.  $\beta$ -D-glucose, NaOH,  $K_3[Fe(CN)_6]$  were purchased from Lach-Ner.

Four solutions of reactants, i.e. glucose (25, 50 and 100 mM), GOx (17 U/mL,  $[Fe(CN)_6]^{3-}$  (173, 203 and 234 mM) and NaOH used to introduce negative feedback (1, 3, 5, 7, 8.5 and 10 mM) were fed separately by the peristaltic pump into CSTR, where they were mixed by the magnetic stirrer. pH of the reaction mixture was measured continuously by the Ag/AgCl/pH-electrode inserted into the reactor, the electrode was connected with the pH-meter, which was continuously recording pH each second. Temperature of the products was measured continuously on the output. Solutions of reactants were always prepared fresh before each experiment. Each measurement had a duration of 50000 s and was carried out under normal

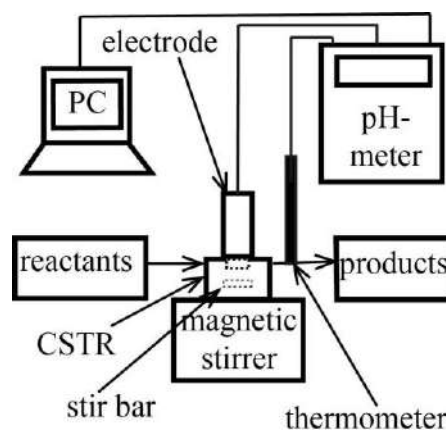


**Figure 1.** Experimental setup

laboratory conditions. The reactor had a volume 0.1927 ml. Reciprocal time was 14 min in each experiment.

## RESULTS AND DISCUSSION

In experiments with inlet concentration of glucose 50 mM and 100 mM we observed oscillatory behavior of the reaction system (Fig. 2). In case of glucose inlet concentration 50 mM one large peak ( $\Delta\text{pH} = 2.0$ , period = 1660 s) and four smaller peaks (first three:  $\Delta\text{pH} = 0.5$ , period = 550 s, fourth one:  $\Delta\text{pH} = 0.25$ , period = 400 s) appeared in first 12600 s of experiment, but then pH of reaction reached a steady state at pH = 3.2. While in case of  $c_{\text{glucose},0} = 100 \text{ mM}$  oscillations were systematic during 45000 s of experiment ( $\Delta\text{pH} = 0.06$ , period about 7000 s).

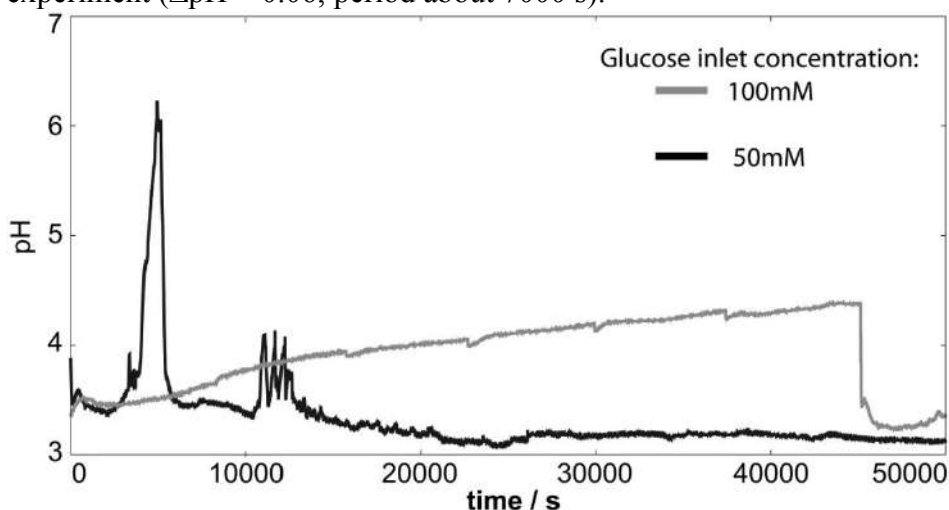


**Figure 2.** Continuous experimental recording of pH:  $c_{\text{NaOH},0} = 3 \text{ mM}$ ,  $c_{\text{K}_3[\text{Fe}(\text{CN})_6],0} = 234 \text{ mM}$ ,  $c_{\text{GOx},0} = 17 \text{ U/ml}$

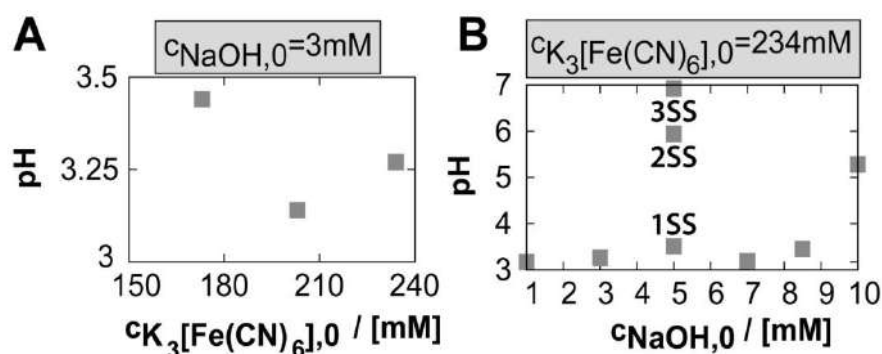


**Figure 3.** Bifurcation diagrams for (A)  $c_{\text{K}_3[\text{Fe}(\text{CN})_6],0}$ , (B)  $c_{\text{NaOH},0}$ ;  $c_{\text{GOx},0} = 17 \text{ U/ml}$ ,  $c_{\text{glucose},0} = 25 \text{ mM}$ , SS – steady state

Experiments with inlet glucose concentration 25 mM show mostly one steady state (Fig.3) and for  $c_{\text{NaOH},0} = 5$  mM three steady states (tristability). We plan to make further experiments close to this parameter region to elucidate transition from one steady state to three steady states and vice versa.

## CONCLUSIONS

Data obtained in experiments with the reaction of enzymatic oxidation of glucose by ferricyanide let us conclude that this reaction displays oscillations and tristability in CSTR depending on inlet values of concentration of glucose, NaOH and  $\text{K}_3[\text{Fe}(\text{CN})_6]$ . Oscillations were currently found only with higher concentration of glucose, which is not regular in case of detecting blood glucose level in a human body. In our future experiments we are going to examine other values of parameters such as input reactants concentration, enzyme activity and reciprocal time to find bifurcation regions of parameter space. Mathematical model of the reaction mechanism has been already developed and is being tested.

## Acknowledgement

This work was supported by the grant 15-17367S from the Czech Science Foundation.

## REFERENCES

- [1] F. Sagués, I.R. Epstein, Dalton Trans., 2003, 1201–1217.
- [2] Y.-S. Chen, J.-H. Huang, C.-C. Chuang, Carbon, 2009, **47**, 3106 – 3112.
- [3] B. Jugović, B. Grgur, M. Antov, Z. Knežević-Jugović, J. Stevanović, M. Gvozdenović, Int. J. Electrochem. Sci., 2016, **11**, 1152 – 1161.
- [4] W.K. Ward, M.D. Wood, J.E. Troupe, ASAIJ Journal, 2000, 540– 546.
- [5] B. Mecheri, A. Geracitano, A. D'Epifanio, S. Licoccia, ECS Transactions, 2011, **35** (26), 1 – 8.
- [6] B. Mecheri, D. De Porcellinis, P.T. Campana, A. Rainer, M. Trombetta, A. Marletta, O.N. Oliveira, S. Licoccia, ACS Appl. Mater. Interfaces, 2015, **7**, 28311 – 28318.
- [7] V. Leskovac, S. Trivic, G. Wohlfahrt, J. Kandrač, D. Peričin, The International Journal of Biochemistry & Cell Biology, 2005, **37**, 731–750.
- [8] V.K. Vanag, D.G. Míguez, I.R. Epstein, Chem. Phys., 2006, **125**, 194515–1-194515-12

## BRAY-LIEBHAFSKY REACTION IN CSTR: INTERMITTENT OSCILLATIONS AND SPECIFIC FLOW RATE

I. N. Bubanja,<sup>1</sup> A. Ivanović-Šašić,<sup>2</sup> Ž. Čupić,<sup>2</sup> S. Anić<sup>1,2</sup> and Lj. Kolar-  
Anić<sup>1,2</sup>

<sup>1</sup> *University of Belgrade, Faculty of Physical Chemistry, Studentski trg 12-16, 11000 Belgrade, Serbia (itana.bubanja@ffh.bg.ac.rs)*

<sup>2</sup> *University of Belgrade, Institute of Chemistry, Technology and Metallurgy, Njegoševa 12, 11000 Belgrade, Serbia*

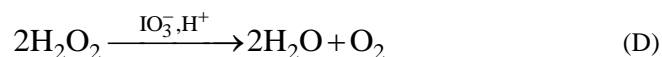
### ABSTRACT

Intermittent oscillations were generated in a Bray-Liebhafsky (BL) oscillator in an isothermal (62.3 °C) continuously-fed well-stirred (stirring speed  $\sigma = 900$  rpm) tank reactor only under variations of specific flow rate, while the tank concentrations of the reactants in the tank were  $3.46 \times 10^{-2}$  KIO<sub>3</sub>,  $7.72 \times 10^{-2}$  H<sub>2</sub>SO<sub>4</sub> and  $2.40 \times 10^{-1}$  H<sub>2</sub>O<sub>2</sub> mol dm<sup>-3</sup>. Specific flow rate was varied in range from 0.024 min<sup>-1</sup> to 0.1257 min<sup>-1</sup>, and in that range the same type of intermittent oscillations but with different regularity (in terms of parts of time that system spent in bursts and gaps) were obtained from 0.024 min<sup>-1</sup> to 0.1005 min<sup>-1</sup>.

### INTRODUCTION

Intermittent oscillations are a specific form of the chaotic state. Usually, intermittency is considered a complex dynamic state where transition between two qualitatively different dynamic states occurs randomly [1]. Although this type of oscillations is often prescribed to the influence of external perturbations, this self-organized phenomenon is an inherent property of the system that is governed by the values of the applied control parameters [2, 3].

The present investigations are devoted to the examination of intermittent dynamic states, obtained by specific flow rate changes, in the oxi-halide Bray-Liebhafsky (BL) oscillator [4, 5]. This oscillator is a famous homogeneous inorganic oscillatory reaction which represents complex decomposition of hydrogen peroxide into water and oxygen in the presence of iodate and hydrogen ions, [4, 5]



Although simple at first glance, it is a very complex reaction in which a number of reactions occur between many oxi-iodine, peroxide and other species [6 - 8]. Changing the balance of the reaction rate, which is determined by the values of the control parameters (composition, temperatures, flow through the reaction cell...) produces a series of different regular and irregular (chaotic) dynamical states of the observed BL systems [4, 9 - 13].

### EXPERIMENTAL

Experiments were carried out in a continuously-fed well-stirred tank reactor (CSTR), at constant temperature of  $62.3 \pm 0.1$  °C (the temperature of the system was monitored by thermometer), under specific flow rate  $j_0$  with changes in range from  $0.024 \text{ min}^{-1}$  to  $0.1257 \text{ min}^{-1}$ . The experimental setup was the same as in our previous published paper [3].

The experimental procedure was performed in the following way. First, thermostatted and protected from light, the reaction vessel was filled with the reactants (concentrations of stock solutions were calculated so that their concentration in reactor was  $3.46 \times 10^{-2} \text{ mol dm}^{-3} \text{ KIO}_3$ ,  $7.72 \times 10^{-2} \text{ mol dm}^{-3} \text{ H}_2\text{SO}_4$  and  $2.40 \times 10^{-1} \text{ mol dm}^{-3} \text{ H}_2\text{O}_2$ ), at the flow rate of 5 ml/min. After 1 min the stirrer was turned to 900 rpm. After 3.2 min the flow rate was set to 0.304 ml/min and the other pump for removing the surplus volume of the reaction mixture was turned on. The specific flow rate ( $j_0$ ) was calculated so that sum of flow rates of all three channels used for delivering reactants was divided by the total volume of reaction mixture (22.2 ml). Every following experiment was performed as an extension of the previous one with a decreased or increased specific flow rate. Between every next experiment, the experimental recording was paused for a period of one retention time ( $1/j_0$ ) in order to allow system to stabilize in a new dynamic state with changed specific flow rate.

### RESULTS AND DISCUSSION

Under CSTR conditions, specific flow rate change has an important influence on the dynamical state of the Bray-Liebhafsky reaction. Figure 1. shows only a few time series, one of a continuous train of regular oscillations and two of intermittent chaos, obtained for different values of specific flow rate  $j_0$ .

In our current research, the specific flow rate ( $j_0$ ) was varied from  $0.024 \text{ min}^{-1}$  to  $0.1257 \text{ min}^{-1}$ . At  $j_0 = 0.1257 \text{ min}^{-1}$  and  $j_0 = 0.1131 \text{ min}^{-1}$ , regular sustained large-amplitude oscillations are obtained, while intermittent oscillations occur in the range of specific flow rates from  $0.024 \text{ min}^{-1}$  to  $0.1005 \text{ min}^{-1}$ .

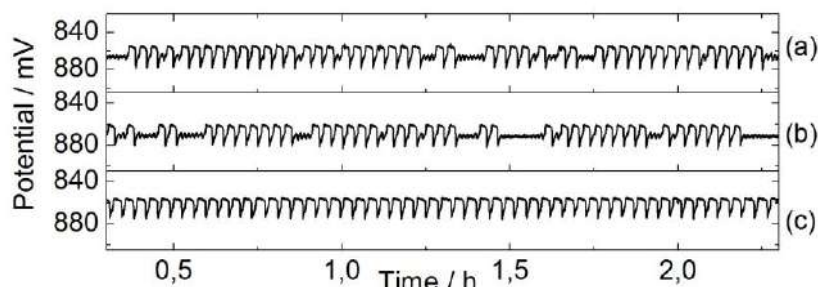


**Figure 1.** Time-series of BL reaction obtained in CSTR for different flow rate values: (a)  $j_0 = 0.0382 \text{ min}^{-1}$ , (b)  $j_0 = 0.0628 \text{ min}^{-1}$  and (c)  $j_0 = 0.1257 \text{ min}^{-1}$ .

In the present experimental investigation, for peristaltic pumps and tubes that were used, the lowest specific flow rate that could be achieved was  $0.024 \text{ min}^{-1}$ . In our recently published paper [3], it was demonstrated that the number of burst packages per unit of time can be used as a measure of chaos of intermittent dynamic states because of its excellent correlation with the largest Lyapunov exponent. Therefore, the most chaotic intermittent oscillations in terms of the number of bursts (Fig. 2a) per unit of time ( $N_B/\tau$ ) are somewhere between  $0.03$  and  $0.04 \text{ min}^{-1}$  (Fig. 2b). It is obvious that specific flow rate dependence of ( $N_B/\tau$ ) has an asymmetrical distribution function form.

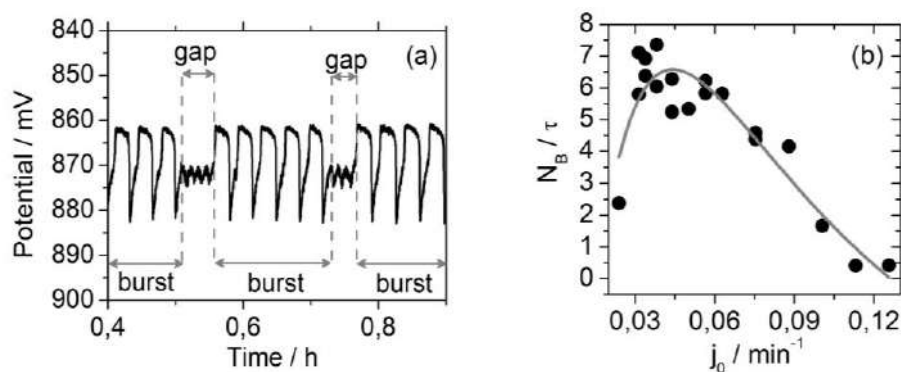


**Figure 2.** (a) Part of time series obtained for specific flow rate  $j_0 = 0.05026 \text{ min}^{-1}$  with marked individual burst packages and gaps (with small oscillations) between them. (b) Specific flow rate ( $j_0$ ) dependence of the number of bursts per unit of time ( $N_B/\tau$ ).

## CONCLUSION

Intermittent chaotic oscillations in the BL reaction were generated in a CSTR reactor under variations of specific flow rate  $j_0$  in a range from  $0.024$

$\text{min}^{-1}$  to  $0.1005 \text{ min}^{-1}$ . The nature of the asymmetrical distribution function of the specific flow rate dependence of  $(N_B/\tau)$  should be identified. We hope that future research will show that some other quantities (used to describe chaos) will give a similar correlation such as  $(N_B/\tau) = f(j_0)$ .

### ***Acknowledgement***

This work was partially supported by the Ministry for Science of the Republic of Serbia (Grants no. 172015 and 45001).

### **REFERENCES**

- [1] R. C. Hilborn, *Chaos and Nonlinear Dynamics: An Introduction for Scientists and Engineers*, Oxford University Press, 2000.
- [2] Ž. D. Čupić, L. Z. Kolar-Anić, S. R. Anić, S. R. Maćešić, J. P. Maksimović, M. S. Pavlović, M. C. Milenković, I. N. M. Bujanja, E. Greco, S. D. Furrow and R. Cervellati, *Helv. Chim. Acta*, 2014, **97**, 321–333.
- [3] I. N. Bujanja, S. Maćešić, A. Ivanović-Šašić, Ž. Čupić, S. Anić and L. Kolar-Anić, *Phys. Chem. Chem. Phys. PCCP*, 2016, **18**, 9770–9778.
- [4] W. C. Bray, *J. Am. Chem. Soc.*, 1921, **43**, 1262–1267.
- [5] W. C. Bray and H. A. Liebhafsky, *J. Am. Chem. Soc.*, 1931, **53**, 38–44.
- [6] H. A. Liebhafsky, R. Furruichi, G. M. Roe, *J. Am. Chem. Soc.* 1981, **103**, 51-56.
- [7] S. D. Furrow, *J. Phys. Chem.*, 1987, **912**, 129-2135.
- [8] G. Schmitz, *J. Chim. Phys.*, 1987, **84**, 957-965.
- [9] M. G. Peard, C. F. Cullis, *Trans. Faraday Soc.* 1951, **47**, 616-630.
- [10] J. Chopin-Dumas, *Compt. Rend. Hebd., Sceances Acad. Sci., Ser. C*, 1978, **287**, 553-556.
- [11] J. A. Odutola, C. A. Bohlander, R. M. Noyes, *J. Phys. Chem.*, 1982, **86**, 818-824.
- [12] V. Vukojević, S. Anić, Lj. Kolar-Anić, *J. Phys. Chem. A*, 2000, **104**, 10731-10739.
- [13] Lj. Kolar-Anić, V. Vukojević, N. Pejić, T. Grozdić, S. Anić, *Experimental Chaos: 8<sup>th</sup> Experimental Chaos Conference*, S. Boccaletti at al. (eds.), *AIP Conference Proceedins*, 2004, **742**, 3-8.

## ON THE USE OF VOLTAMMETRIC DATA IN BIFURCATION ANALYSIS OF ELECTROCHEMICAL OSCILLATORY SYSTEM: Cu | 1.0 M TFA

N. I. Potkonjak<sup>1</sup>, T. N. Potkonjak<sup>2</sup> and Z. Nikolić<sup>3</sup>

<sup>1</sup> *Chemical Dynamics Laboratory, Vinča Institute of Nuclear Sciences,  
University of Belgrade, P.O. Box 522, 11001 Belgrade, Serbia.  
(npotkonjak@vinca.rs)*

<sup>2</sup> *Urban Planning Institute of Belgrade, 30 Palmotićevo, 11000 Belgrade,  
Serbia*

<sup>3</sup> *Faculty of Physics, 12 Studentski trg, 11000 Belgrade, Serbia*

### ABSTRACT

Bifurcation analysis of the Cu | 1 M TFA electrochemical oscillatory system was done by using voltammetric data, obtained under quasi-potentiostatic polarization conditions. A super-critical Hopf bifurcation and a saddle-loop bifurcation were identified at following bifurcation potentials  $E_{BIF1} = 0.5446$  V and  $E_{BIF2} = 0.7536$  V, respectively.

### INTRODUCTION

Being far-from-equilibrium, the electrochemical systems can spontaneously form a wide spectrum of spatio-temporal patterns [1, 2]. Spontaneous emergence of such patterns implies that the dynamical systems, such as electrochemical, undergo self-organization [2]. Appearance of oscillations implies that the electrochemical system can no longer achieve stable steady states, and that its existence is only possible through oscillatory states [1]. Transition from a stable steady state to an oscillatory state goes via bifurcation point. In order to be identified, evolution of the system has to be monitored through phase space diagram; constructed from a series of coordinates characterized by a parameter (controlled quantity) and a variable (quantity which is an appropriate representative of the system's state) [3,4]. Looking from this perspective, linear sweep voltammetry can be observed as an instrumental technique which dynamically drives the system throughout a series of variable-to-parameter points [5]. Therefore, voltammogram is in fact a phase space diagram. In this study, a copper electrode in a trifluoroacetic acid (TFA) will be anodically polarized by means of linear sweep voltammetry, under quasi-potentiostatic polarization conditions. Bifurcation analysis will be conducted by using voltammetric data.

## EXPERIMENTAL

Experiments were carried out in a three-electrode electrolytic cell, at 293 K, with a copper rod (Goodfellow, 99.99%) as the working electrode, Pt foil as the counter electrode, and a saturated calomel electrode (SCE) as the reference one. The working electrode was embedded in a plastic capillary, leaving only the rod cross-section ( $0.0314 \text{ cm}^2$ ) exposed to the electrolyte solution. Prior to each experiment the working electrode was abraded by a series of wet sanding paper with different grit size (320, 600, 800, 1000, 1200 and 2000). Thereupon, the working electrode was rinsed with deionized water in an ultrasonic bath for 2 min. A Luggin capillary was used. Electrolyte solution was 1 M TFA. Experiments were carried under natural convection of electrolyte in the electrolytic cell, without any external resistance applied in the circuit. Linear sweep voltammetry was performed using anodic scan, starting from 0.5 V<sub>SCE</sub>, at a rate of  $1 \text{ mV s}^{-1}$ . All applied circuit potentials ( $E$ ) are given with the respect to the SCE.

## RESULTS AND DISCUSSION

By carefully selection of initial conditions, we were able to locate an oscillatory state (OsS) region of investigated system at the current-potential ( $I$ - $E$ ) polarization curve, Fig.1. The first bifurcation point occurs at  $E_{\text{BIF1}} = 0.5446 \text{ V}$  (looking from the direction of polarization). This bifurcation point can be observed as an entering one, marking a discontinuity in evolution of the system from the steady stable state (SSS1) to OsS; it is a characteristic of the SSS1  $\rightarrow$  OsS transient.

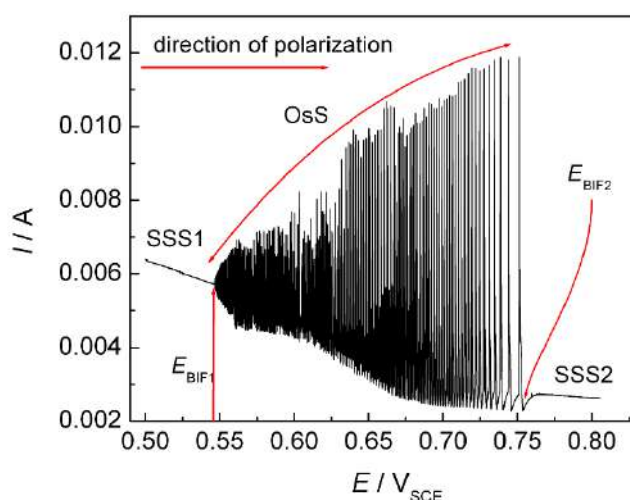


**Figure 1.**  $I$ - $E$  polarization curve of Cu electrode in 1M TFA.

With respect to above mention perspective, the second bifurcation point, located at  $E_{\text{BIF2}} = 0.7536 \text{ V}_{\text{SCE}}$ , can be taken as the exit point; it is a feature of the  $\text{OsS} \rightarrow \text{SSS2}$  transient, Fig.1.

Smooth increase of current oscillation amplitudes observed near on the  $\text{SSS1} \rightarrow \text{OsS}$  transient is shown in Fig.2 (a). Linear dependence between the square amplitude of current oscillations ( $A^2$ ) and increase of the distance of controllable parameter from  $E_{\text{BIF1}}$  ( $|E_{\text{OSC}} - E_{\text{BIF1}}|$ ) was found, Fig.2 (b). Along with the lack of hysteresis at the  $\text{SSS1} \rightarrow \text{OsS}$  transient[5] (not shown in abstract), suggests on super-critical Hopf (SUPH) bifurcation[5, 6].

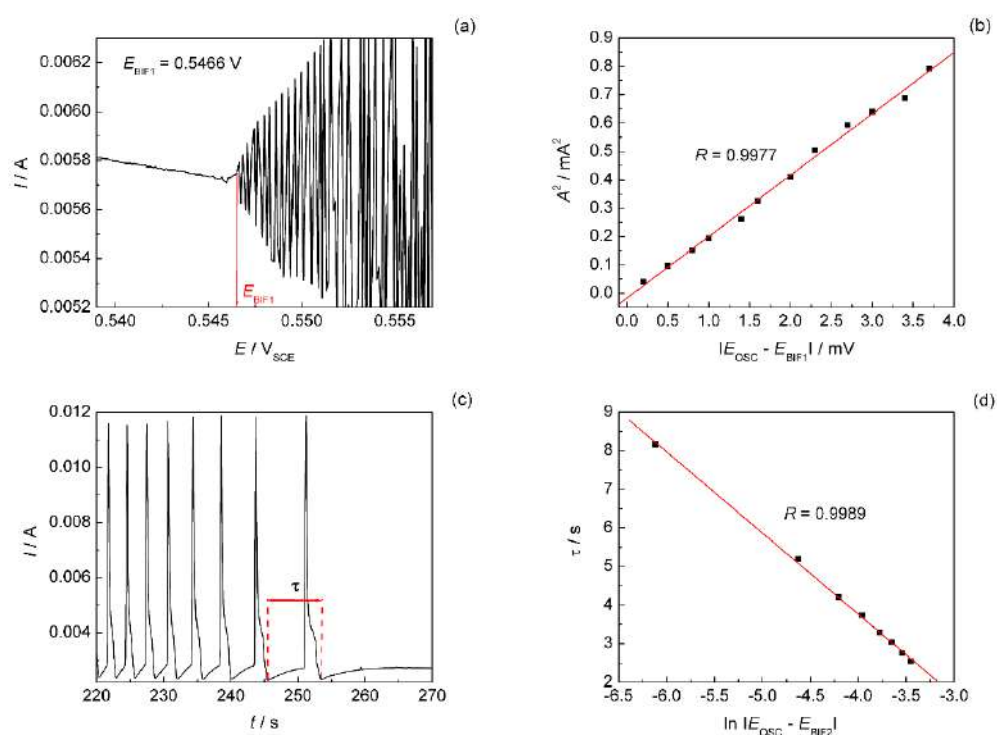


**Figure 2.** (a) Detail from  $I$ - $E$  polarization curve, Fig.1, in the vicinity of the  $\text{SSS1} \rightarrow \text{OsS}$  transient. (b) Dependence of the square amplitude of current oscillations ( $A^2$ ) vs. distance of controllable parameter from  $E_{\text{BIF1}}$  ( $|E_{\text{OSC}} - E_{\text{BIF1}}|$ ). (c) Detail from  $I$ - $E$  polarization curve, Fig.1, in the vicinity of the  $\text{OsS} \rightarrow \text{SSS2}$  transient (units of x-axis are converted from potential to time). (d) Semilogarithmic plot of the period current oscillations ( $\tau$ ) vs. the distance of controllable parameter from  $E_{\text{BIF2}}$  ( $\ln |E_{\text{OSC}} - E_{\text{BIF2}}|$ ).

On the other hand, the period of current oscillations ( $\tau$ ) increases as the system approaches the  $\text{OsS} \rightarrow \text{SSS2}$  transient, ending with sudden termination of oscillatory behaviour, Fig.2 (c). Linear dependence between  $\tau$

and logarithmic value of the distance from  $E_{BIF2}$  ( $\ln |E_{OSC} - E_{BIF2}|$ ) is shown in Fig. 2 (d). Combined with an existence of hysteresis [5] (not shown in abstract), it implies that the OsS $\rightarrow$ SSS2 transient goes via the saddle-loop bifurcation [3, 5, 6]. Correlation coefficients ( $R$ ), shown in Fig. 2(b) and 2(d), were found to be considerably high. Hence, we can say that the procedure for bifurcation analysis was verified.

## CONCLUSION

In this study, a voltammetric data, obtained from quasi-potentiostatic polarization curve of the Cu | 1M TFA electrochemical oscillatory system, were used for bifurcation analysis. This was based on the presumption that voltammogram can be considered as a phase space diagram. Results presented have showed that bifurcation scenario can be built from voltammetric data with a high accuracy.

## Acknowledgement

This work was supported by the Ministry of Education, Science and Technological Development of Republic of Serbia (Grants no. 172015).

## REFERENCES

- [1] M. Orlik, Self-Organization in electrochemical systems I: General principles of self-organization. Temporal Instabilities, Springer-Verlag, Berlin, Heidelberg, 2012
- [2] K. Krischer, N. Mazouz, P. Grauel, *Angewandte Chemie*, 2001, **40**, 850-869.
- [3] M.T.M. Koper, *Journal of Chemical Society, Faraday Transactions*, 1998, **94**, 1369-1378.
- [4] D. Kondepudi, I. Prigogine, *Modern Thermodynamics: from heat engines to dissipative structures*, John Wiley & Sons Ltd, Baffins Lane, Chichester, West Sussex Po19 1UD, England, 1998.
- [5] N. Potkonjak, Ph.D. Thesis, Faculty of Physical Chemistry, University of Belgrade, Belgrade, 2015 (in Serbian).
- [6] D. Sazou, M. Pagitsas, *Journal of Electroanalytical Chemistry* 1998, **451**, 77-87.

## METHOD FOR PREDICTION OF PERIODIC WINDOWS INSIDE CHAOTIC STATES IN A MODEL OF THE BRAY-LIEBHAFSKY REACTION

Ž. Čupić<sup>1</sup>, A. Ivanović-Šašić<sup>1</sup>, S. N. Blagojević<sup>2</sup>, S. M. Blagojević<sup>3</sup>, S. Anić<sup>4</sup> and Lj. Kolar-Anić<sup>4</sup>

<sup>1</sup>*University of Belgrade, ICTM– Department of Catalysis and Chemical Engineering, Njegoševa 12,*

<sup>2</sup>*Institute of General and Physical Chemistry, Studentski trg 12–16,*<sup>3</sup>*Faculty of Pharmacy, University of Belgrade, Vojvode Stepe 450,*

<sup>4</sup>*Faculty of Physical Chemistry, University of Belgrade, Studentski trg 12–16*

### ABSTRACT

Various dynamic states were investigated by the return maps of the phase trajectories obtained from numerical simulations based on the well-known model of the Bray-Liebhaftsky reaction mechanism in a continuously fed well stirred tank reactor. The specific flow rate was used as the control parameter. ( In considered region, periodic and aperiodic period-doubling sequences were found. The advantages of slow manifold mapping techniques were used here to predict position of periodic windows in the interval of control parameter values.

### INTRODUCTION

The model [1] of the Bray–Liebhafsky BL reaction [2] under isothermal continuously fed well stirred tank reactor (CSTR) conditions was used to analyze variety of dynamic states [3]. Numerical simulations have shown that various simple and complex periodic as well as various types of chaotic oscillatory states were obtained for different values of the flow rate  $j_0$  as control parameter. Return maps were used to make a distinction between periodic and aperiodic (chaotic) motion in phase space [4]. However, return maps based on Poincare section of trajectory over the attractor which lies on critical manifold give us good information about chaotic dynamic states, [5] but insufficient information about periodic states where there are only several points in this Poincare section. Therefore, Poincare section of trajectory over the slow manifold is used here to obtain representative return maps in both cases. Hence, slow manifold mapping method, which gives return maps with waste of details, even in the case of periodic dynamic states [6], is used here to analyze behavior of the BL reaction model, with a

special aim to develop technique for prediction of the position of periodic windows within a region of the specific flow rates where chaotic dynamic states are common.

## METHODS

All calculations were performed using MATLAB program package. The differential equations derived from the model were integrated using the ode15s solver. Relative and absolute error tolerance values of  $3 \times 10^{-14}$  and  $1 \times 10^{-20}$  were used in all simulations. Initial values of the concentrations were:  $[\text{IO}_3^-]_0 = 0.0474 \text{ moldm}^{-3}$ ,  $[\text{H}^+]_0 = 0.0958 \text{ moldm}^{-3}$ , and  $[\text{H}_2\text{O}_2]_0 = 0.155 \text{ moldm}^{-3}$ . We analyzed time series of iodide ion concentrations, obtained for different values of the flow rate  $j_0$  as control parameter in the interval of the dynamical states between  $1^2$  and  $1^3$ . For typical return map, time series with  $2 \times 10^6$  data points at time interval of about 2000 min were appropriate in most cases [4].

The slow manifold maps [6] are obtained from sequences of short simulations with initial conditions (concentrations) systematically varied in very small steps. In present study, small changes of hydrogen peroxide initial concentrations were used. The initial concentrations of all other species were generated by one, long enough, preliminary simulation, ensuring that attractor is reached by the end, in the same way as in classical attractor 1D maps. Thus, in generated sequences of short numerical simulations, movement over the slow manifold is recorded. The slow manifold maps are then generated in the same way as previously described elsewhere [4] for regular maps obtained from the trajectories over the attractor.

## RESULTS AND DISCUSSION

For the construction of the return map the Poincaré section at  $[\text{I}^-] = 3.5 \times 10^{-8} \text{ M}$  of slow manifold that correspond to the large-amplitude oscillations, was used. In considered narrow interval of flow rates the periodic and aperiodic mixed mode oscillations were found [3]. All of them have the period-doubling form. In Figure 1, several slow manifold maps are given for specific flow rate values corresponding to different periodic and period-doubling chaotic sequences. Smooth bending of the map with increasing specific flow rate value is obvious, and followed by increasing distance between the curve minimum and main diagonal, while preserving the position of the minimum on the X axis at the value of  $[\text{I}_2]_n = 1.3803112 \times 10^{-4} \text{ M}$ . The Y coordinate of the slow manifold map at the minimum is plotted against the specific flow rate and present in Figure 2. From the

observed trend, it is easy to interpolate the specific flow rate value where curve minimum touches the main diagonal – at this point, the Y coordinate of the minimum is equal to its X coordinate ( $[I_2]_{n+1}=[I_2]_n$ ). This point is important since it corresponds to the center of the periodic window for the  $1^2$  dynamic state.

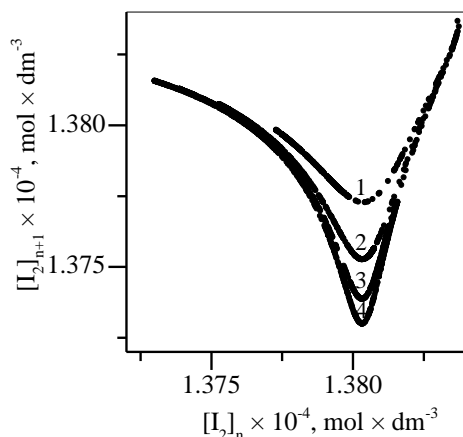


**Figure 1.** Slow manifold maps for specific flow rate values corresponding to different period doubling sequences. (1)  $j_0=4.9196 \times 10^{-3} \text{ min}^{-1}$  ( $1^2$ )<sub>2</sub> periodic, (2)  $j_0=4.920 \times 10^{-3} \text{ min}^{-1}$  ( $1^2$ )<sub>2</sub> periodic, (3)  $j_0=4.92013 \times 10^{-3} \text{ min}^{-1}$  ( $1^2$ )<sub>8</sub> period doubling chaos, (4)  $j_0=4.92018 \times 10^{-3} \text{ min}^{-1}$  ( $1^2$ ) unstructured chaos.

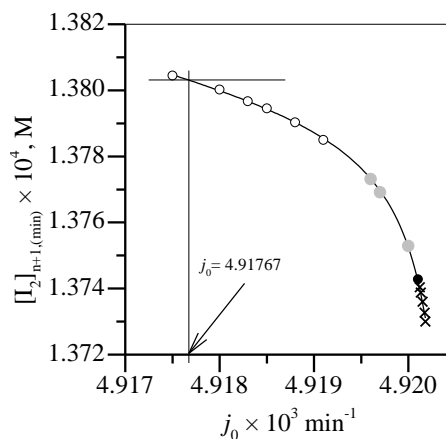


**Figure 2.** The Y coordinates of the slow manifold map at the minimum as a function of the  $j_0$ . Horizontal thin line indicates the position of the map minima at the X axis of the Fig. 1. Vertical thin line points to the center of the periodic window. Symbols correspond to  $1^2$  periodic ( $\circ$ ), ( $1^2$ )<sub>2</sub> periodic ( $\bullet$ ), ( $1^2$ )<sub>4</sub> periodic ( $\bullet$ ) and to various chaotic ( $\times$ ) dynamics.

Hence, the principle is identified for prediction of the position of periodic windows within a region of the specific flow rates corresponding to chaotic dynamic states. The same principle is also applicable to higher order maps for prediction of other periodic windows in period doubling sequences.

## CONCLUSION

By means of slow manifold maps, we developed a technique for prediction of the position of periodic windows within an interval of control parameter values, corresponding to chaotic dynamic states. Moreover, applying this technique to the model of BL reaction, we analyzed the period-doubling sequences as the function of the specific flow rates.

**Acknowledgment**

The support of this research by the Ministry of Education, Science and Technological Development of Republic of Serbia through projects No.172015 and 45001 is gratefully acknowledges.

**REFERENCES**

- [1] Lj. Kolar-Anić, Ž. Čupić, G. Schmitz and S. Anić, *Chem. Eng. Sci.*, 2010, **65**, 3718–3728 and references therein.
- [2] W. C. Bray, H. A. Liebafsky, *J. Am. Chem. Soc.*, 1931, **53**, 38–44
- [3] A. Ivanovic-Šašić, V. Marković, S. Anić, Lj. Kolar-Anić, Ž. Čupić, *Phys. Chem. Chem. Phys.*, 2011, **13**, 20162–20171.
- [4] S. N. Blagojević, Ž. Čupić, A. Ivanović-Šašić and Lj. Kolar-Anić, *Russ. J. Phys. Chem. A*, 201, **5**, 132349-2358.
- [5] F. Aicardi, A. L. Kawczynski, *Complex Systems*, 1992, **6**,95-104.
- [6] Ž. Čupić, A. Ivanović-Šašić, S. Blagojević, S. Blagojević, Lj. Kolar-Anić, S. Anić, *Reaction Kinetics, Mechanisms and Catalysis*, 2016, **118**, 27-38.

## PRELIMINARY INVESTIGATION OF CAFFEIC ACID INFLUENCE ON THE ENDING MODE IN BRIGGS-RAUSCHER REACTION

J. P. Maksimović<sup>1</sup>, I. N. Bubanja<sup>1</sup>, S. Anić<sup>1</sup>, N. I. Potkonjak<sup>2</sup> and M. C. Pagnacco<sup>1</sup>

<sup>1</sup>*Faculty of Physical Chemistry, University of Belgrade, Studentski trg 12, Belgrade, Serbia (maja.milenkovic@gmail.com)*

<sup>2</sup>*Chemical Dynamics Laboratory, Vinča Institute of Nuclear Sciences, University of Belgrade, P.O. Box 522, 11001 Belgrade, Serbia*

### ABSTRACT

The influence of caffeic acid on the ending mode in the Briggs-Rauscher oscillatory reaction including malonic acid substrate, characterized with sudden transition from low to high iodide concentration (I → II transition), was investigated. Caffeic acid, as a radical scavenger quenches  $\text{HOO}\cdot$ , and therefore delays decomposition of iodomalonic and diiodomalonic acids, which are responsible for sudden iodine return to the solution, generating state II of high iodide concentration.

### INTRODUCTION

Briggs-Rauscher [1] (BR) reaction is a hybrid oscillating reaction formed from two chemical oscillators, Bray-Liebhafsky [2] and Belousov-Zhabotinskii [3]. BR reaction typically consists of  $\text{H}_2\text{O}_2$ ,  $\text{H}_2\text{SO}_4$ ,  $\text{KIO}_3$ ,  $\text{Mn}^{\text{II}}$  as metal catalyst, and malonic acid, ( $\text{H}_2\text{MA}$ ) as an organic substrate and overall reaction can be described by the equation:



The BR reaction is recognized as a source of  $\text{HOO}\cdot$  radicals and it has been used as a test for antioxidant activity [4] by monitoring the inhibitory effects of antioxidant species on the oscillations. In this work, the influence of caffeic acid (CA), as an antioxidant and a free radical scavenger on the ending mode of BR reaction is investigated. CA is classified as hydroxycinnamic acid, and it is recognized as an active plant-originating antioxidant present in human dietary. [5] The ending mode of the BR reaction system depends on the initial conditions, particularly on the ratio  $R: [\text{H}_2\text{MA}]_0 / [\text{IO}_3^-]_0$ . It can occur throughout three different scenarios. [6] If  $R$  is low, there is an immediate transition from oscillation to state II, described with high  $[\text{I}_2]$  and  $[\text{I}^-]$ . Such transition is preceded by oscillations of decreasing frequency and constant amplitude. If  $R$  is high (higher than 2)

oscillations could end (with damping amplitudes and increasing frequency) initially to state I, which is typified by low  $[I_2]$  and low  $[I^-]$ . [6] The third possibility of ending mode is sharp transition from state I to state II, that is from low to high  $[I_2]$  and  $[I^-]$ . It occurs after a time delay spent in the state I and it is characteristic only for BR systems which contains malonic acid (or iodomalonic acid, IHMA) as substrate. The sharp ending mode is a focus of intensive experimental and theoretical research. [7] Due to assumption, that free radical reactions have an important role in the sudden state transition  $I \rightarrow II$  [7], the aim of this work is to explore influence of caffeic acid, as a free radical scavenger, on  $I \rightarrow II$  transition when CA is present from the beginning of oscillatory reaction.

### EXPERIMENTAL

The experiments were carried out in a closed well-stirred (magnetic stirrer of 900 rpm) system and thermostated at 36.0°C. The reaction volume was 35 ml. Initial concentrations (in M) were for  $[H_2MA]_0=0.05$ ,  $[MnSO_4]_0=0.00667$ ,  $[HClO_4]_0 = 0.0266$ ,  $[KIO_3]_0 = 0.0667$  and  $[H_2O_2]_0 = 1.2$ . Caffeic acid (volume 50  $\mu$ l) was added in three different initial concentrations ( $9.0 \cdot 10^{-6}$ ,  $1.5 \cdot 10^{-5}$ ,  $3.0 \cdot 10^{-5}$ ). Experiment without CA was done with same volume (50  $\mu$ l) of deionized water addition. The substances were P.A. grade, prepared in deionized water and added by the following order:  $H_2MA$ ,  $MnSO_4$ ,  $HClO_4$ ,  $KIO_3$  and finally CA was added when the temperature and the potential were stabilized.  $H_2O_2$  was added to the reaction vessel 3 min after the addition of CA and this moment was taken as beginning of the reaction. The time evolution of the BR reaction was followed potentiometrically, by means of a Pt electrode connected to the Ag/AgCl reference electrode. The temperature of the BR system was controlled by temperature sensor with accuracy of  $\pm 0.1$  °C.

### RESULTS AND DISCUSSION

Time series for BR reaction (lower graph) and appropriate temperature measurement (upper graph) without CA presence is shown at Fig.1. The target reaction, answerable for the sharp transition, elevated the temperature of reaction mixture for more than three degrees. This suggest on exothermic processes. The asymmetric oscillation with a sharp tip on one side followed by a wide tail indicating  $I \rightarrow II$  state transition is a feature of the system with Pt indicator electrode. (See Figure 1 in ref. [6]) It is supposed that the iodination products, such as IHMA and diiodomalonic acid ( $I_2MA$ ), are responsible for the transition [7]. Decomposition reactions of IHMA and  $I_2MA$  return much of the iodine to the solution, generating state II. Due to the presence of free radicals ( $HOO^\bullet$ ,  $HO^\bullet$ ,  $IO_2^\bullet$ ) in the BR reaction has been

verified [8a] one of the possible explanation is radical breakdown of iodinated products (I<sub>2</sub>MA and IHMA).

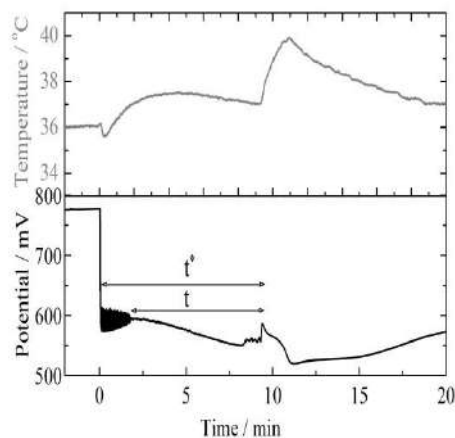


**Figure 1.** Pt potential vs time (lower graph) and temperature changes(upper graph) obtained for BR reaction when 50 µl of deionized water was added at the beginning instead of caffeic acid, at 36 °C, with following initial conditions:  $[H_2MA]_0 = 0.05$  M,  $[MnSO_4]_0 = 0.00667$  M,  $[HClO_4]_0 = 0.0266$  M,  $[KIO_3]_0 = 0.0667$  M and  $[H_2O_2]_0 = 1.2$  M.

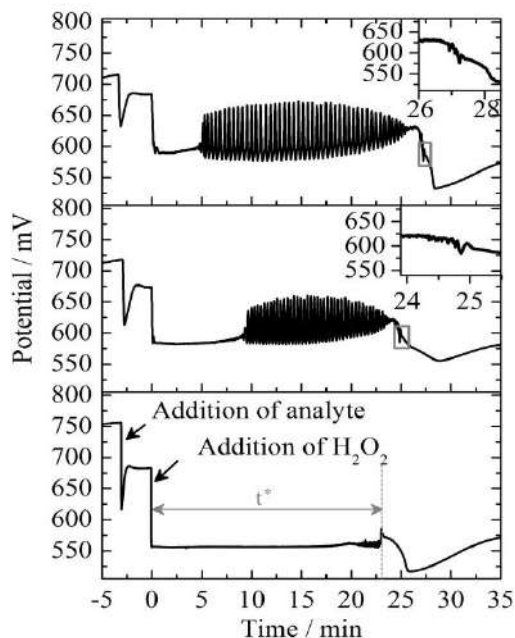


**Figure 2.** Time series, (Pt potential vs time) at 36 °C obtained with  $[CA]_0 = 0.9 \cdot 10^{-5}$  M (upper),  $1.5 \cdot 10^{-5}$  M (middle) and  $3.0 \cdot 10^{-5}$  M (lower graph). Other conditions as in Fig. 1.

**Table 1.** BR oscillogram parameters

Caff.acid conc. / [M] $10^{-5}$	$t_{ind}$ [min]	$t_{osc}$ [min]	$t_{I \rightarrow II}^*$ [min]	$t$ [min]
0 / water	0	2.3	9.3	7.0
0.9	4.9	20.6	27.4	1.9
1.5	9.1	14.6	25.1	1.4
3.0	quench.osc.	quench.osc.	23.3	/

CA as radical scavenger affects both, induction period and ending mode of BR reaction (Fig. 2 and Table 1.).

When CA is added before starting BR reaction (experimental procedures applied in this work) the time ( $t^*$ , defined in Fig.1.) when asymmetric oscillation occurs is prolonged compare with BR reaction with same volume of deionized water added (Fig. 1 and Table 1.). On the other hand, the time measured from the last oscillation, in the package, to the asymmetric oscillation appearance ( $t$ , defined in Fig.1.) slightly decreases with increasing CA concentration. Also, it is very interesting that asymmetric oscillation occurs even if the oscillations have been quenched (Fig. 2, lower

graph). It should be stressed that in our experiments, CA was added before H<sub>2</sub>O<sub>2</sub> addition and obtained results are consequence of complex and relatively unknown mechanism of interaction between CA and BR in all dynamic states (during induction, oscillatory and post-oscillatory period). Since the caffeic acid is recognized as antioxidant which is presumed to lower the concentration of HOO• radicals, the prolongation of t\* (~25 min with CA and 9.3 min without CA, Table 1.) can be understood if the following reaction takes place:



CA, having two OH groups, is efficient free-radical scavengers. Using Bond Dissociation Enthalpies (BDE) theory, we calculated  $\Delta\text{BDE} = (-9.2-4.7)$  kcal/mol = -13.9 kcal/mol [8b]. As the reaction between radicals and generic radical scavenger, such as CA, is more exothermic, the energy barrier should be lower than for the reaction with substrate. Thus, CA will react faster with radical species, preventing reaction with substrate, and finally resulting in delayed decomposition of iodinated products (IHMA and I<sub>2</sub>MA).

## CONCLUSION

Caffeic acid affects ending mode in BR oscillatory reaction by lengthening the time of I→II transition appearance, in comparison to BR reaction with same volume of deionized water addition.

## Acknowledgement

This work was supported by the Ministry for Science of the Republic of Serbia (Grants no. 172015).

## REFERENCES

- [1] T. S. Briggs and W. C. Rauscher, *J. Chem. Educ.*, 1973, **50**, 496.
- [2] W. C. Bray, *J. Am. Chem. Soc.*, 1921, **43**, 1262–1267.
- [3] B. P. Belousov, *Med. Publ., Moscow*, 1958, 145.
- [4] R. Cervellati, K. Höner, S. D. Furrow, C. Neddens and S. Costa, *Helv. Chim. Acta*, 2001, **84**, 3533–3547.
- [5] İ. Gülçin, *Toxicology*, 2006, **217**, 213–220.
- [6] S. D. Furrow, R. Cervellati and E. Greco, *Z. Für Naturforschung B*, 2012, **67**, 89–97.
- [7] S. D. Furrow, R. Cervellati and E. Greco, *ReacKinetMech Cat*, 2016, **118**, 59–71.
- [8] a) D. Stanisavljev, M. C. Milenkovic, M. Mojović, A. Popovic-Bijelić, *J. Phys. Chem. A* 2011, **115**, 7955–7958 b) M. C. Milenković, Potkonjak N., *B. Chem. Soc. Jpn.* 2014, **87**, 1255-1259.

## MATHEMATICAL MODELING OF INTERACTIONS BETWEEN THE CENTRAL CIRCADIAN CLOCK, THE HYPOTHALAMIC-PITUITARY-ADRENAL (HPA) AXIS AND ALCOHOL

A. Stanojević<sup>1</sup>, V. M. Marković<sup>1</sup>, Lj. Kolar-Anić<sup>1,2</sup> and V. Vukojević<sup>3</sup>

<sup>1</sup>University of Belgrade, Faculty of Physical Chemistry, Studentski trg 12-16, 11158 Belgrade, Serbia (ana.stanojevic@ffh.bg.ac.rs;)

<sup>2</sup>University of Belgrade, ICTM, Department of Catalysis and Chemical Engineering, Njegoševa 12, 11000 Belgrade, Serbia (zcupic@ihtm.bg.ac.rs)

<sup>3</sup>Karolinska Institute, Department of Clinical Neuroscience, Center for Molecular Medicine CMM L8:01, 17176 Stockholm, Sweden

### ABSTRACT

Mathematical modeling and numerical simulations are used to investigate *in silico* the effects of the central circadian pacemaker on the Hypothalamic–Pituitary–Adrenal (HPA) axis function, and study the implication of these interactions on human response to alcohol intake. Our study shows that the intensity of coupling between the central circadian clock and the HPA axis critically defines the stress axis activity and its response to ethanol.

### INTRODUCTION

Adaptation to the environment is fundamental to the survival of all living organisms. To cope with environmental impact, vertebrates have developed several dynamical regulatory systems, including the circadian clock and the stress response systems. These systems are tightly coupled and mutually affect each other's activity – the circadian system orchestrates the activity of the stress axis and, reciprocally, the stress axis exerts its own influence on the circadian rhythm. The intensity of interactions between the circadian and the stress system is altered in numerous diseases [1], including alcohol abuse [2-5].

Intricate interactions between the circadian system, the stress system, *i.e.* the Hypothalamic-Pituitary-Adrenal (HPA) axis, and alcohol are not understood in detail. However, they need to be elucidated as alcohol abuse causes various disorders that are associated with qualitative changes in the neuroendocrine system function and dynamical disorders, such as sleep disorders, psychosis and neurocognitive disorders.

### MATHEMATICAL MODELLING

A recently developed stoichiometric network model that succinctly describes biochemical transformations underlying the HPA axis and the effect of ethanol on its dynamics was used [6]. In the model, circadian regulation of corticotrophin releasing hormone (CRH) production, which is centrally governed by the circadian clock system in the suprachiasmatic nucleus (SCN) in the anterior hypothalamus, is described by a periodic forcing function ( $D$ ) that appropriately mimics the asymmetry of the 24-hour rhythm in humans, with the nocturnal phase lasting 8 hours:  $D = d_1 - 0.079145093 \times d_2 + \{(0.064 \times \sin(2\pi t/1440) + 0.12 \times \text{abs}[\sin(\pi t/1440)]\} \times d_2$

Here  $t$  is time in minutes, and 1440 in the denominator of the trigonometric function argument represents the number of minutes in one day, that is, the period of the circadian oscillation. Parameters  $d_1$  and  $d_2$  define the mean daily CRH level in the hypothalamic-pituitary portal vessels and the amplitude of the circadian CRH oscillation, respectively [7].

Numerical simulations were performed using the MATLAB ode15s solver that is based on the Gear algorithm for integration of stiff differential equations. Absolute and relative error tolerance values were  $1 \times 10^{-20}$  and  $1 \times 10^{-14}$ , respectively. The model was integrated with stricter tolerances in order to minimize numerical artefacts, but the same dynamical behavior was observed using values of  $1 \times 10^{-9}$  and  $3 \times 10^{-6}$ .

Concentrations of all reaction species are expressed in moles *per* cubic decimeter ( $\text{mol dm}^{-3} = \text{M}$ ). Initial conditions for the integration of ODEs in all numerical simulations were:  $[\text{CHOL}]_0 = 3.40 \times 10^{-4} \text{ M}$ ,  $[\text{CRH}]_0 = 1.00 \times 10^{-12} \text{ M}$ ,  $[\text{ACTH}]_0 = 8.00 \times 10^{-13} \text{ M}$ ,  $[\text{CORT}]_0 = 4.00 \times 10^{-8} \text{ M}$ ,  $[\text{ALDO}]_0 = 1.50 \times 10^{-9} \text{ M}$ ,  $[\text{POMC}]_0 = 1.50 \times 10^{-10} \text{ M}$ ,  $[\beta\text{-END}]_0 = 1.50 \times 10^{-11} \text{ M}$ ,  $[\beta\text{-LPH}]_0 = 1.50 \times 10^{-10} \text{ M}$ ,  $[\beta\text{-MSH}]_0 = 1.50 \times 10^{-11} \text{ M}$ ,  $[\text{PNN}]_0 = 1.00 \times 10^{-10} \text{ M}$ ,  $[\text{MC}_2]_0 = 1.50 \times 10^{-15} \text{ M}$ ,  $[\text{MC}_2^{\text{active}}]_0 = 1.50 \times 10^{-15} \text{ M}$ ,  $[\text{HPNN}]_0 = 4.00 \times 10^{-8} \text{ M}$ ,  $[\text{PGS}]_0 = 4.00 \times 10^{-8} \text{ M}$ ,  $[\text{HPGS}]_0 = 4.00 \times 10^{-8} \text{ M}$ ,  $[\text{TTS}]_0 = 4.00 \times 10^{-8} \text{ M}$ ,  $[\text{CTS}]_0 = 4.00 \times 10^{-8} \text{ M}$ ,  $[\text{EtOH}]_0 = 0$ ,  $[\text{AcALD}]_0 = 0$ .

When HPA axis dynamics was modelled under normal physiological conditions, the concentrations of ethanol and acetaldehyde were set to zero. To simulate the effect of acute perturbations with ethanol, numerical integration of the system of ordinary differential equations was stopped at a specified time point and new initial conditions for subsequent integration were defined. For the new initial conditions, ethanol concentration was specified while concentrations of all other species retained their previously attained values.

## RESULTS AND DISCUSSION

Mathematical modelling shows that coupling between the external forcing function that mimics the dynamics of the central circadian clock and the ultradian HPA oscillations *via* CRH level in the hypothalamic-pituitary portal vessels, introduces a delay in the onset/termination of ultradian hormone oscillations, which arise as the stationary state changes its stability by passing through a supercritical Andronov–Hopf bifurcation [7]. Due to this coupling, oscillations in hormone levels with two characteristic periods – circadian and ultradian, are observed (Fig. 1). The control parameter  $d_1$ , which determines the intensity of coupling between the central circadian clock and the stress response axis, acts as a bifurcation parameter and its magnitude defines the distance from the supercritical Andronov–Hopf bifurcation. Thus, the larger  $d_1$ , the farther is the system from the bifurcation point and the amplitude of ultradian cortisol oscillations increases (Fig. 1).

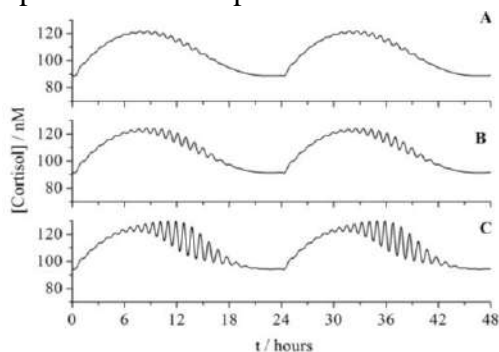


**Figure 1.** Temporal evolution of cortisol concentration for different  $d_1$  values: A)  $d_1 = 0.28$ , B)  $d_1 = 0.29$  and C)  $d_1 = 0.3025$ .

Acute ethanol challenge of the same intensity (6.3 mM) applied at the same time, 11:30 AM, shows that ethanol effects on the increase in cortisol levels are different when parameter  $d_1$  has different values (Fig. 2).

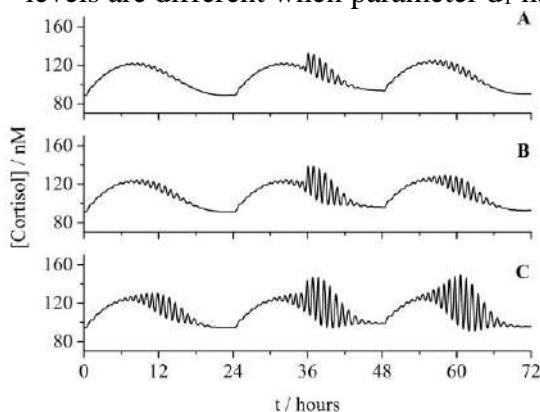


**Figure 2.** The HPA axis responses to the acute ethanol challenge of the same intensity (6.3 mM) used always at the same time, 11:30 AM, but for different values of parameter  $d_1$ : A)  $d_1 = 0.28$ , B)  $d_1 = 0.29$  and C)  $d_1 = 0.3025$ .

## CONCLUSION

Our study shows that intensity of coupling between the central circadian clock and the stress response axis is an important parameter that defines both, the HPA axis activity (Fig. 1) and its response to ethanol (Fig. 2). This finding suggests that disease states

where the intensity of coupling between the circadian system and the stress axis altered, such as schizophrenia, depression and Alzheimer's disease [1], are likely to be associated with changes in the individual's sensitivity to alcohol intake. This is in line with empirical observations, but the underlying mechanisms were unclear. Our work shows that intricate interactions between vital rhythmic regulatory systems, which are difficult to characterize experimentally, can be efficiently dissected using mathematical modelling and approaches from dynamical systems theory. Using theoretical approaches, we could obtain relevant mechanistic insights on so far inconclusive empirical observations in psychoneuroendocrinology.

### *Acknowledgement*

Support from the Karolinska Institute Research Funds, the Swedish Research Council, the Knut and Alice Wallenberg Foundation, the Rajko and Maja Đermanović Fund, CMST COST Action CM 1304 "Emergence and Evolution of Complex Chemical Systems", and the Ministry of Education, Science and Technological Development of the Republic of Serbia, grants 172015 and 45001, is gratefully acknowledged.

### **REFERENCES**

- [1] E. N. Kassir, G. P. Chrousos, The central CLOCK system and the stress axis in health and disease. *Hormones* 2013, **12**, 172-191
- [2] R. Spanagel, A. M. Rosenwasser, G. Schumann, D. K. Sarkar, Alcohol consumption and the body's biological clock. *Alcoholism: Clinical and Experimental Research*, 2005, **29**, 1550-1557.
- [3] M. A. Stephens, G. Wand, Stress and the HPA axis: role of glucocorticoids in alcohol dependence. *Alcohol Res*, 2012, **34**, 468-483.
- [4] Sarkar, D.K., Circadian genes, the stress axis, and alcoholism. *Alcohol Res*. 2012, **34**, 362-366.
- [5] C. C. P. Wong, G. Schumann, Integration of the circadian and stress systems: influence of neuropeptides and implications for alcohol consumption. *J. Neural. Transm.* 2012, **119**, 1111-1120.
- [6] Ž. Čupić, A. Stanojević, V. M. Marković, Lj. Kolar-Anić, L. Terenius, V. Vukojević, The HPA axis and ethanol: a synthesis of mathematical modelling and experimental observations, *Addict. Biol.* 2016, doi:10.1111/adb.12409.
- [7] V. M. Marković, Ž. Čupić, S. Maćešić, A. Stanojević, V. Vukojević, Lj. Kolar-Anić, Modelling cholesterol effects on the dynamics of the hypothalamic-pituitary-adrenal (HPA) axis. *Math. Med. Biol.* 2016, **33**, 1-28.

*E - Electrochemistry*



## PROTONS IN AN AQUEOUS ELECTROHYDRODYNAMIC LIQUID BRIDGE

E. C. Fuchs

*WETSUS, European Centre of Excellence for Sustainable Water  
Technology, Oostergoweg 9, 8911 MA Leeuwarden, The Netherlands*

### ABSTRACT

The floating water bridge is a special case of an electrohydrodynamic liquid bridge and constitutes an intriguing phenomenon that occurs when a high potential difference ( $\sim \text{kV cm}^{-1}$ ) is applied between two beakers of water. High voltage electrolysis is responsible for proton production, transport through the bridge and recombination with hydroxyl ions in the catholyte. We have measured the quasi-elastic neutron scattering (QENS) of such a liquid bridge. Two proton populations were distinguished: one consisting of protons strongly bound to oxygen atoms (immobile population, elastic component) and a second one of quasi-free protons (mobile population, inelastic component). The diffusion coefficient of the quasi-free protons was found to be  $D = (26 \pm 10) \times 10^{-5} \text{ cm}^2 \text{ s}^{-1}$  with a jump length  $\lambda_{\text{av}} \sim 3 \text{ \AA}$  and an average residence time of  $\tau_0 = 0.55 \pm 0.08 \text{ ps}$ . The associated proton mobility in the proton channel of the bridge is  $\sim 9.34 \times 10^{-7} \text{ m}^2 \text{ V}^{-1} \text{ s}^{-1}$ , twice as fast as diffusion-based proton mobility in bulk water. It also matches the so-called electrohydrodynamic or “apparent” charge mobility, an experimental quantity which so far has lacked molecular interpretation. Impedance spectroscopy was used to measure excess positive and negative Bjerrum-defect like charge (protonic and ‘aterprotonic’) in anolyte and catholyte during and after the experiment. These results corroborate the proton channel model for liquid water under high voltage and give new insights into the molecular mechanisms behind electrohydrodynamic charge transport phenomena in liquid water.

## NATURAL AND BIOMIMETIC RECEPTORS FOR BIOSENSOR DESIGN

R. Săndulescu, A. Florea, M. Tertiș, L. Fritea, O. Hosu, B. Ciui  
and C. Cristea

*“IuliuHațieganu” University of Medicine and Pharmacy Cluj-Napoca,  
Analytical Chemistry, Pasteur 4, 400439 Cluj-Napoca, Romania  
(rsandulescu@umfcluj.ro)*

### ABSTRACT

Most of the biological processes, either normal or pathological, are based on molecular recognition, which, may be exploited in the analytical sciences. In living organisms the molecular recognition system is represented by natural receptors, characterized by the highest affinity and specificity and by consequence, a large variety of bioelements, such enzymes, antibodies, nucleic acids, and cells were integrated in various sensing devices, successfully applied in biomedical and environmental analyses or monitoring. However, their isolation, purification, stability and cost are critical issues. Therefore, the development of artificial biomimetic receptors focused the attention of many research groups. The most recent achievements in the electrochemical sensing techniques based on molecular recognition are revised.

### INTRODUCTION

Molecular recognition is the ability of one host molecule to “recognize” another complementary, guest molecule, through bonding interactions and molecular geometry. The effects of the molecular recognition, consisting in the specific interaction between host and guest molecules (such as, DNA hybridization, specific interactions between biotin and avidin or between protein A/G and antibody), through covalent (disulfide bridges between cysteine side chains) and non-covalent binding of various strength such as: hydrogen bonding, metal coordination, hydrophobic forces, van der Waals forces,  $\pi$ - $\pi$  interactions, halogen bonding, electrostatic and electromagnetic effects, may be exploited in the analytical sciences, as long as the specific interaction produces a detectable change that can be measured by an instrument.

The electrochemical methods are the most sensitive analytical techniques (in the range of  $10^{-9}$ - $10^{-12}$  M), but they are not selective, meaning that all the electroactive species from a given sample or matrix are non-specifically

detected. Therefore, the design of specific or at least very selective interfaces between the analyte and the measuring systems still is of a great interest for many research teams around the world. The development and functioning of biological systems are based on a multitude of “signal molecules” and the corresponding “natural receptors”, offering several examples of such sensing entities. Thus, many efforts are made in order to modify the electrode surface with an immobilized ligand in such a manner, to be able to distinguish a specific analyte in a multicomponent matrix. Due to the fact that “natural receptors” present the greatest selectivity or even specificity, a great number of papers about various sensors and biosensors were published in the last decades.

### **BIOLOGICAL RECOGNITION SYSTEMS**

The ideal molecular recognition part of a sensor is represented by natural receptors, characterized by the highest affinity and specificity, being the natural targets for toxins and mediators of physiological processes.

**Natural receptors** (membrane molecular receptors) are cellular, typically membrane, proteins that bind specific chemical species changing their conformation, followed by a cellular response, like the opening of an ion channel or secreting an enzyme [1]. Unfortunately, there is very little information on natural receptor-based sensors, due to their low stability, high cost, and the difficulty to transform the interaction between the natural receptor and the target molecule into a measurable signal.

The first **bioelements** included in the biosensors were the **enzymes**, generally immobilized in a layer deposited onto the electrode surface [2]. Enzymes have the ability to increase reactions rate by specific binding with substrates, which suffer structure or conformation changes that enable the reaction to occur [3]. The molecular recognition process between the enzyme and the analyte, based on this specific catalytic reaction of the enzyme, induces a signal that defines the biosensor electroanalytical features [4], allowing the detection of much lower limits than with normal binding techniques [5]. A crucial step, in using enzymes as sensing element in the biosensors elaboration, is the enzyme immobilization at the transducer's surface. If the properties and the activity of the enzyme are preserved after deposition, it will react and recognize the analyte.

**Antibodies** (immunoglobulins) are glycoproteins produced by specialized B lymphocyte cells of the host, as response of the immune system to the presence of foreign species called antigen. Among the five classes of immunoglobulins, IgG being the most widely spread in nature and commonly used in the immunosensors fabrication [6]. Due to their high

affinity and selectivity for binding various antigens, antibodies have been widely employed in developing immunoassays and immunosensors.

A great variety of immunosensors configurations applied in biomedical field were reported in the last years. Thus, a sensitive sandwich immunoassay for the detection of cancer biomarker MUC1 has been developed based on the immobilization on protein G modified magnetic particles of specific anti-MUC1 antibodies. After blocking of remaining free binding sites with albumin and the reaction with the MUC1 antigen, a second and a third labeled antibody were successively added to form a sandwich assay. The addition of the substrate of the enzyme label alkaline phosphatase and its conversion into an electroactive compound allowed the quantification of the captured MUC1 antigen by differential pulse voltammetry (DPV) measurements with a limit of detection (LOD) of 3.5 ng/mL and high reproducibility [7].

In a similar approach, magnetic beads served as immobilization platforms for anti-acetaminophen antibodies for the development of a label-free sensor. Anti-acetaminophen antibodies were firstly immobilized on protein G magnetic beads followed by blocking of free sites with albumin and the reaction with the antigen. The antibody-antigen binding reaction was monitored by electrochemical impedance spectroscopy (EIS) and DPV. A linear decrease in the current peak obtained by DPV was observed with the increase of the concentration due to the hindering of electron transfer and a LOD of 1.76  $\mu\text{M}$  was obtained for the detection of acetaminophen in drug formulations [8].

Another label free immunosensor for the detection of acetaminophen based on a graphene oxide immobilization platform in a layer by layer technique was described. Graphene oxide was chemically functionalized with N-hydroxysuccinimide in the presence of 1-ethyl-3-(3-dimethyl aminopropyl) carbodiimide hydrochloride in order to provide a high number of carboxylic groups which bind to the amino groups of anti-acetaminophen antibodies. After incubation with various concentrations of acetaminophen electrochemical quartz crystal microbalance (EQCM) measurements were performed. The developed immunosensor showed high recoveries in pharmaceuticals and in diluted serum samples with a LOD of 0.17  $\mu\text{M}$  [9].

**Nucleic acids** were also immobilized onto electrode surface in various configurations. *Deoxyribonucleic acid (DNA)* consists of a linear array of nucleotides, each of which comprising a base (cytosine, thymine, adenine, and guanine) linked by a pentose sugar and phosphate, arranged in two strands that resemble a ladder coiled into a spiral shaped the double helix. The genetic information content of the DNA is embodied in the sequential arrangement of those nucleotides. The biosensing working principle is based

on recognition of the complementary strand of ssDNA to form a stable hydrogen bond between two nucleic acids in order to become dsDNA. Usually, an ssDNA, immobilized with a linker such as thiol or biotin [10], is used as a probe in a bioreceptor in which the base sequence is complementary to the target of interest. Exposure of the target to the probe will result in hybridization of complementary ssDNA to form dsDNA and the biochemical reaction will be detected by the transducer and converted into a measurable signal. Unlike DNA, **ribonucleic acid (RNA)** is single stranded containing ribose instead of deoxyribose as its sugar phosphate backbone and uracil instead of thymine in its pyrimidine bases. It can be assembled from nucleotides using DNA sequence as a template and RNA polymerase. RNAs are classified into messenger RNAs (mRNAs), which is the short-lived intermediary in the transfer of genetic information from DNA to protein, and nonprotein-coding RNAs (ncRNAs) [11], being able to store and transmit information and controlling the gene expression. **MicroRNAs (miRNAs)** are antisense transcripts, and transcriptional units containing a high density of stop codons and lacking any extensive open reading frame. The miRNAs are 18-24 nucleotide-long non coding RNA molecules that regulate the expression of target genes at the post-transcriptional level by either translational repression or degradation of miRNAs[12].

The use of the living **cells** (bacteria and fungi) as the biosensing element is based on their ability to detect the intracellular and extracellular microenvironment conditions, the physiological parameters, and to produce a response through the interaction between stimulus and cell [13].

### BIOMIMETIC RECEPTORS

Biological receptors are able of specific *host-guest* interaction, but their fabrication is very difficult and very expensive. Therefore, the development of artificial biomimetic receptors focused the attention of many research groups. A large variety of cyclodextrins and derivatives, calixarenes, various ligands (valinomycin, crown-ethers, etc), aptamers and molecularly imprinted polymers were studied and a great number of related papers were published in the last decade.

Various **ligands**, such as crown ethers (cyclic oligomers of ethylene oxide), cryptands, and ionophores (Valinomycin), exhibit excellent selectivity for alkali and alkaline earth metals,  $\text{NH}_4^+$ , and lanthanides, being widely used in ion-selective electrodes fabrication [14, 15].

**Cyclodextrins**(CDs)are cyclic oligosaccharides consisting of six, seven, eight or more glucopyranose units linked by 1,4-bonds. The cavity is lined by the hydrogen atoms and the glycoside oxygen bridges, resulting in a

relatively hydrophobic/nonpolar inside compared to water and with a hydrophilic outside described as a „micro heterogeneous environment” [16, 17]. The most notable characteristic of CDs is the inclusion complexes formation with various organic and inorganic molecules in aqueous or nonaqueous media, consisting in a dimensional fit between host cavity and guest molecule. The main driving forces for the inclusion complexes include Van der Waals interactions, hydrophobic interactions between the guest hydrophobic moiety and the CD cavity, hydrogen bonding between the polar groups of the guest molecules and the CDs hydroxyl groups and electrostatic interactions for ionic guests [18]. CDs found a lot of applications in electrochemistry, being used either as anchoring system for glucose oxidase [19], tyrosinase [20] and carbon based nanomaterials [21], or as biomimetic receptors for the simultaneous detection of uric and ascorbic acids [22].

**Calixarenes** (three-dimensional macrocycles with a truncated cone shape, consisting of 4 to 16 phenol molecules connected by methylene bridges) attracted much interest in recent years due to their hollow structure that allows them to form inclusion complexes with numerous neutral and charged chemical species, such as cations (alkaline ions [23], silver, lead, calcium, copper, zinc and mercury), being used to detect air pollution or water in toxicology or in pharmaceutical and clinical analysis [24-26].

**Aptamers** are short single stranded DNA or RNA oligonucleotides that specifically bind a wide range of target molecules with high affinity and specificity [27]. They can selectively bind to small molecules, such as organic dyes, drugs, nucleotides, amino acids or to small parts of macromolecules, such as protein, polypeptides, and polysaccharides [28-30]. Aptamers have dissociation constants in the pico to micromolar range [30,31] with affinity and specificity equal or superior to monoclonal antibodies [32]. Therefore they successfully substitute antibodies as recognition elements in immunoassays and immunosensors, being more stable and able to discriminate between closely related targets.

In order to increase the selectivity of the immunoassay for MUC1 detection, antibodies were replaced with aptamers, a much better discrimination between different tumor marker glycoproteins (MUC1, MUC4 and MUC16) being observed. The protocol of fabrication involved the binding of a biotinylated aptamers on streptavidin-coated magnetic beads, which specifically bind MUC1 protein. The aptamer-MUC1 complex is then incubated with a second aptamer labeled with streptavidin and with biotin alkaline phosphatase. Beside its higher selectivity the sensor also proved to be more sensitive allowing the detection of lower concentrations of MUC1 by DPV (1.4 ng/mL) [8].

Another electrochemical aptasensor for the detection of tumor marker MUC1 was developed using immobilized aptamers. The nanostructured layer by layer graphene oxide platform provides a high number of carboxyl groups which bind to the amino terminated aptamer specific for MUC1. The detection was achieved by DPV, measuring the reduction signal of redox probe methylene blue intercalated in the immobilized aptamer. Upon binding of unfolded aptamer the methylene blue molecules are situated further away from the electrode surface and the reduction signal decreases. Upon binding of MUC1 protein the aptamer folds to bind the protein, thus the redox probe is situated in the proximity of the electrode surface, leading to a higher reduction signal, allowing the detection of MUC1 with a LOD of 0.6 ng/ $\mu$ L [33].

**Molecularly Imprinted Polymers (MIPs)** are synthetic receptors produced in polymers which exhibit recognition abilities similar to their biological counterparts. MIPs are obtained by polymerization of functional and cross-linking polymers in the presence of target molecules (templates). Polymerization can be performed by UV exposure or thermally, and in the case of electrochemical applications involving biosensing, polymerization is performed electrochemically, which may be performed under galvanostatic, potentiometric or most frequently potentiodynamic conditions. In the next step, upon the removal of the template, three dimensional cavities will result in the polymeric matrix, complementary in shape and chemical functionality arrangement with the template.

A generic protocol was developed by our team for the fabrication of sensitive MIP-based sensors, which can be applied for a wide range of analytes, electroactive as well as non-electroactive. The general protocol of preparation involves several steps. Firstly, a monolayer of monomer, *p*-aminothiophenol, is self-assembled at the surface of gold electrodes via Au-S bonds. In the next step, the molecularly imprinted film is deposited on the electrode via electropolymerization in a solution containing *p*-aminothiophenol functionalized gold nanoparticles (AuNPs) and the template molecule. The non-covalent interactions promote the embedding of the host molecules in a three-dimensional polymer-AuNP network. Finally, the template is removed from the complex matrix, forming surface imprinted sites. The presence of AuNPs in the matrix enhances the conductivity (increasing the electron transfer) and the number of imprinted sites, leading to more homogenous distribution of the recognition sites. Several compounds of biomedical interest, such as gemcitabine [34], tetracycline [35], estradiol [36], were used as template molecules and were successfully detected using MIP-sensors with low detection limits in the fM range.

## CONCLUSION

The process of molecular recognition has been extensively employed in the field of analytical sciences, either for analytical separation or purification, or for sensors/ biosensors development, as a chemo- or bioreceptor intimately connected to a given transducer. Relying on very small energetic differences between the forming transient complexes, chiral molecular recognition is also exploited for numerous applications in the biomedical and environmental fields. The high selectivity of biosensors is achieved and adapted to the target analyte by a careful selection from the large variety of natural or biomimetic recognition systems. Among the various signal transduction methodologies reported in sensor development, electrochemical techniques are widely investigated because of their potential advantages such as low-cost, miniaturization, and portable instrumentation. Label-free and impedance biosensors have other attractive advantages with respect to speed and simplicity of inexpensive alternative technique for the detection of biomarkers. The continuously increasing number of papers published in the recent years, once again demonstrate the great potential and interest towards this topic.

## Acknowledgement

*The authors are grateful for the financial support to the Romanian National Authority for Scientific Research UEFISCDI for project PN-II-ID-PCE-2011-3-0355 and to Iuliu Hațieganu University of Medicine and Pharmacy for doctoral research grants 7690/24/15.04.2016 and 7690/56/15.04.2016.*

## REFERENCES

- [1] S. Subrahmanyam, S. A. Piletsky, A.P.F. Turner, *Anal. Chem.*, 2002, **74**, 3942-3951.
- [2] B. Leca-Bouvier, L. Blum in: *Recognition Receptors in Biosensors*, M. Zourob (Ed.), Springer, New York, 2010.
- [3] N. A. Ackaah-Gyasi, P. Patel, Y. Zhang, B.K. Simpson in: *Improving and Tailoring Enzymes for Food Quality and Functionality*, R.Y. Yada (Ed.), Elsevier B.V, Amsterdam, 2015.
- [4] M. Ammam, *Biosens. Bioelectron.*, 2014, **58**, 121-131.
- [5] V. Perumal, U. Hashim, *J. Appl. Biomed.*, 2014, **12**, 1-15.
- [6] J.M. Fowler, D.K.Y Wong, H.B. Halsall, W.R. Heineman in: *Electrochemical sensors, biosensors and their biomedical applications*; X. Zhang, H. Ju, J. Wang (Eds), Academic Press, Amsterdam, 2008.
- [7] A. Florea, A. Ravalli, C. Cristea, R. Săndulescu, G. Marrazza, *Electroanalysis*, 2015, **27**, 1594-1601.

- [8] O. Hosu, M. Tertiş, R. Săndulescu, C. Cristea, *Farmacia*, 2015, **63**(1), 140-145.
- [9] M. Tertiş, O. Hosu, L. Fritea, C. Farcău, C. Cristea, R. Săndulescu, *Electroanalysis*, 2015, **27**(3), 638-647.
- [10] S. Cagnin, M. Caraballo, C. Guiducci, P. Martini, M. Ross, M. SantaAna, D. Danley, T. West, G. Lanfranchi, *Sensors*, 2009, **9**, 3122–3148.
- [11] C.K. Kwok, S. Balasubramanian, *Angew. Chem. Int. Edit.*, 2015, **54**, 23, 6751–6754.
- [12] V. Ambros, *Nature*, 2004, **431**, 7006, 350-355.
- [13] T. Wang, G.Hui, S. Deng, *Biosens. Bioelectron.* 2010, **26**, 929–934.
- [14] K. Suzuki, K. Watanabe, Y. Matsumoto, M. Kobayashi, S. Sato, D. Siswanta, H. Hisamoto, *Anal. Chem.*, 1995, **67**, 2, 324–334.
- [15] D. Safiulina, V. Veksler, A. Zharkovsky, A. Kaasik, *J. Cell. Physiol.* 2006, **206**, 2, 347–353.
- [16] R. Abd-Elgawad, E. Shima, *The Open Chemical and Biomedical Methods Journal*, 2010, **3**, 74-85.
- [17] H. Dodziuk, *Cyclodextrins and their complexes*; Wiley-VCH Verlag GmbH & Co. KGaA: Weinheim, 2006.
- [18] L. Fritea, M. Tertiş, R. Săndulescu in: *Cyclodextrins: Synthesis, Chemical applications and Role in drug delivery*, F.G. Ramirez (Ed), Nova Science Publishers, Inc. Hauppauge, NY, 2015.
- [19] L. Fritea, P. Audebert, L. Galmiche, K. Gorgy, A. Le Goff, R. Villalonga, R. Săndulescu, S. Cosnier, *Chem.Phys.Chem*, 2015, **16**(17), 3695-3699.
- [20] L. Fritea, A. Le Goff, J.L. Putaux, M. Tertiş, C. Cristea, R. Săndulescu, S. Cosnier, *Electrochimica Acta*, 2015, **178**, 108-112.
- [21] L. Fritea, M. Tertiş, S. Cosnier, C. Cristea, R. Săndulescu, *Int. J. Electrochem. Sci.*, 2015, **10**, 7292-7302.
- [22] L. Fritea, M. Tertiş, C. Cristea, S. Cosnier, R. Săndulescu, *Analytical Letters*, 2015, **48**, 89-99.
- [23] K. Yagi, S. Khoo, M. Sugawara, T. Sakaki, S. Shinkai, K. Odashima, Y. Umezawa, *J. Electroanal. Chem.*, 1996, **401**, 65-79.
- [24] V. K. Gupta, A. K. Jain, U. Khurana, L. P. Singh, *Sens. Actuat. B-Chem.*, 1999, **55**, 201-211.
- [25] G. Duţu, C. Cristea, E. Bodoki, V. Hârceagă, A. Saponar, E.-J. Popovici, R. Săndulescu, *Farmacia*, 2010, **58**, 4, 430-446.
- [26] G. Duţu, C. Cristea, E. Bodoki, V. Hârceagă, A. Saponar, E.-J. Popovici, R. Săndulescu, *Farmacia*, 2011, **59**, 2, 147 – 160.
- [27] B. Hock, *Anal. Chim. Acta*, 1997, **347**, 177-186.

- [28] N. J. Ronkainen, H. B. Halsall, W. R. Heineman, *Chem. Soc. Rev.*, 2010, **39**, 1747-1763.
- [29] S. Tombelli, M. Minunni, M. Mascini, *Biosens. Bioelectron.*, 2005, **20**, 2424-2434.
- [30] R. Nezlin, *Immunol. Lett.* 2014, **162**, 252-255.
- [31] T. Smuc, I.Y. Ahn, H. Ulrich, *J. Pharm. Biomed. Anal.*, 2013, **81-82**, 210-217.
- [32] Z. Ling, M. Wang, J. Wang, Z. Ye, *Chinese J. Anal. Chem.*, 2011, **39**, 3, 432-438.
- [33] B. Ciui, M. Tertiş, D. Peia, C. Cristea, R. Săndulescu, *Farmacia*, 2016, **64**, 43-47.
- [34] A. Florea, Z. Guo, C. Cristea, F. Besueille, F. Vocanson, F. Goutaland, S. Dzyadevich, R. Săndulescu, N. Jaffrezic-Renault, *Talanta*, 2015, **138**, 71-76.
- [35] M. Bougrini, A. Florea, C. Cristea, R. Săndulescu, F. Vocanson, A. Errachid, B. Bouchikhi, N. El Bari, N. Jaffrezic-Renault, *Food Control*, 2016, **59**, 424-429.
- [36] A. Florea, C. Cristea, F. Vocanson, R. Săndulescu, N. Jaffrezic-Renault, *Electrochem. Comm.*, 2015, **59**, 36-39.

## **ELECTROCHEMICAL RECOVERY OF METALLIC COPPER FROM GALVANIC EFFLUENTS**

K. I. Dermentzis, D. I. Marmanis, A. K. Christoforidis  
and D. K. Stergiopoulos

*Department of Petroleum and Mechanical Engineering, Eastern Macedonia  
and Thrace Institute of Technology, 65404 Agios Loukas, Kavala, Greece  
(demerz@otenet.gr).*

### **ABSTRACT**

The present work proposes an integrated process to recover pure metallic copper from industrial galvanic waste comprising electrocoagulation treatment of copper bearing galvanic effluents and production of electrocoagulation sludge, acid digestion of the produced sludge and final recovery of pure metallic copper by electrowinning.

The proposed technology offers relevant metal companies the opportunity for significant cost benefit through metal recovery from industrial waste which would otherwise result in landfill.

### **IN INTRODUCTION**

Many industries produce significant quantities of solid or liquid industrial waste containing heavy metals without recovery of valuable materials from the waste streams. The present work proposes an integrated process to recover pure metallic copper from industrial galvanic copper containing waste. The process involves three subsequent steps: A) treatment of copper bearing electroplating effluents by electrocoagulation with aluminum electrodes and production of a sludge containing mainly  $\text{Cu}(\text{OH})_2$  and  $\text{Al}(\text{OH})_3$ . B) acid digestion of the sludge at  $50\text{ }^\circ\text{C}$  followed by controlled pH increase to preferentially precipitate the  $\text{Al}(\text{OH})_3$ . The  $\text{Al}(\text{OH})_3$  solid can then be filtered out producing a concentrated copper solution with low aluminum content, suitable for electrowinning. C) recovery of pure metallic copper by electrowinning.

### **EXPERIMENTAL**

The actual wastewater was obtained from an electroplating unit located near Thessaloniki, Greece with following main characteristics: 5.6 pH, 1365  $\mu\text{S}/\text{cm}$  conductivity, 296 mg/L COD, 86 mg/L  $\text{Cu}^{2+}$ , 137 mg/L  $\text{SO}_4^{2-}$  and 26 mg/L  $\text{Cl}^-$ .

A laboratory model DC power supply apparatus (Agilent) was used to maintain constant DC current. Conductivity was measured by means of a conductometer (WTW). The pH and the temperature were measured using a Hanna pH-meter. A 500 mL cylindrical glass vessel served as the electrocoagulation and electrowinning reactor. The electrodes for electrocoagulation were three symmetrical cylindrical aluminum plates (the two outer plates used as cathodes and the middle one as anode), while for electrowinning two outer copper plates served as cathodes and the middle platinized titanium plate (Ti/Pt) as anode. All electrodes had the same dimensions of 10 x 5x 0.2 cm with a total effective area of 60 cm<sup>2</sup> each.

The residual copper concentration was determined by Atomic Absorption Spectroscopy AAS (Perkin Elmer 5100). The chemical oxygen demand (COD) was analyzed using a COD reactor (Thermoreaktor TR 420, MERCK) and spectrophotometer (Spectroquant Pharo100, MERCK).

## RESULTS AND DISCUSSION

### *Treatment of copper bearing electroplating effluents by electrocoagulation*

The main reactions occurring during electrocoagulation with aluminum electrodes produce aluminum ions at the sacrificial anode and hydroxide ions as well hydrogen gas at the cathode. The generated aluminum hydroxide flocks act as absorbents for heavy metal ions [1].

Experiments were conducted using the Cu<sup>2+</sup> ion bearing wastewater of 86 mg/L in the initial pH range 2-10. As can be obtained from Table 1, the removal efficiency of Cu<sup>2+</sup> ions after 30 minutes of electrolysis time at the constant current density of 20 mA/cm<sup>2</sup> reached very high values (95-99 %) in the pH range 4-10.

**Table 1.** Removal percentage of copper at various initial solution pHs

Initial pH :	Removal %:
2	26.6
4	95.7
6	98.8
8	99.4
10	99.2

Organic compounds contained in the treated wastewater sample also compete for absorption on the Al(OH)<sub>3</sub> flocks. Thus, at the same time, the COD of the wastewater also decreased from the initial value of 330 to 108 mg/L after 30 min of electrocoagulation time at the applied current density of 20 mA/cm<sup>2</sup> corresponding to a removal efficiency of about 67.3 %.

***Sludge leaching***

The precipitated sludge was collected, dried at 80 °C for 24 h, cooled and weighed. It consists mainly of  $\text{Cu}(\text{OH})_2$  and  $\text{Al}(\text{OH})_3$  and additionally of some absorbed organics originated from the organic additives contained in the treated actual electroplating wastewater.

A fixed amount of 10 g dried sludge was leached with 1000 ml  $\text{H}_2\text{SO}_4$  of different concentrations in stirring conditions of 200 rpm and constant temperature of 50 °C. The copper and aluminum extraction occurred in only a few minutes of leaching time and amounted to 97 and 92 % respectively. According to Table 2, the obvious difference between the initial and final pH is indicative of the  $\text{H}_2\text{SO}_4$  consumption needed for digestion of the treated sludge. The acid consumption was found to range between 0.6 and 0.9 g of  $\text{H}_2\text{SO}_4$  per g of sludge.

**Table 2.** Leaching results of electrocoagulation sludge at various  $\text{H}_2\text{SO}_4$  concentrations

Temperature (°C)	[ $\text{H}_2\text{SO}_4$ ] (M)	pH initial	pH final
50	0.05	1.15	2.22
	0.1	0.93	1.55
	0.2	0.59	1.02

***Separation of  $\text{Cu}^{2+}$  from  $\text{Al}^{3+}$  ions***

The separation of  $\text{Cu}^{2+}$  from  $\text{Al}^{3+}$  ions can occur under controlled pH, due to the different solubility of their hydroxides. Therefore, after the acid digestion and solubilization of the produced  $\text{Al}(\text{OH})_3/\text{Ni}(\text{OH})_2$  electrocoagulation sludge, the solution pH is increased by addition of appropriate amount of 0.1 M NaOH solution until it reaches pH=4.8. At this pH value aluminum is almost quantitatively precipitated in form of  $\text{Al}(\text{OH})_3$ , while  $\text{Cu}^{2+}$  ions remain in solution. The  $\text{Al}(\text{OH})_3$  solids are filtered out. Concentrated  $\text{Cu}^{2+}$  solutions of 1 to 10 g/L can be obtained, appropriate for electrowinning.

***Recovery of metallic copper by electrowinning***

The electrodeposition of metallic copper can occur from acidic solutions with optimum pH 2-2.2 [2]. Electrowinning experiments were conducted at 40 °C in galvanostatic operations and stirring conditions of 200 rpm. By applying constant current densities of 5, 10 and 20  $\text{mA}/\text{cm}^2$ , almost quantitative electrodeposition of pure metallic copper was achieved on the cathodes in 80, 40 and 30 minutes of electrolysis time respectively, leaving

a residual solution with  $\text{Cu}^{2+}$  ion concentration of less than 5 mg/L, as illustrated in Table 3. It was estimated that about 1.5 g of high value metallic nickel could be obtained from 10 g of electrocoagulation sludge.

**Table 3.** Mass of electrodeposited metallic copper versus electrolysis time at various applied current densities

Time (min)	5 mA/cm <sup>2</sup>	10 mA/cm <sup>2</sup>	20 mA/cm <sup>2</sup>
0	1000	1000	1000
20	524	305	152
40	226	4	3
60	48		
80	3		

The electrical energy consumption at the applied current density of 20 mA/cm<sup>2</sup> for the electrocoagulation treatment amounts to 12.24 kWh per kg of Cu removed from treated wastewater and for electrowinning to 2.85 kWh per kg of Cu produced at the cathode.

## CONCLUSIONS

Highest removal percentage of copper by electrocoagulation treatment of galvanic effluents was achieved in the pH range 4-10. At the same time, dissolved organic compounds present in effluent were also removed.

After the acid digestion of the electrocoagulation sludge, controlled pH increase to 4.8 and filtration of the precipitated aluminum hydroxide, pure metallic copper could be obtained from the concentrated copper solution by electrowinning.

The proposed technology yields 1.5 g of high value metallic copper from 10 g of electrocoagulation sludge, leaving almost copper free solid waste and water. The technology utilizes pure metallic copper recovery from industrial waste which would otherwise result in landfill.

## REFERENCES

- [1] Dermentzis K., Davidis A., Papadopoulou D., Christoforidis A., Ouzounis K., *Journal of Engineering Science and Technology Review*, 2009, **4**, 33-42.
- [2] Veglio F., Quaresima R., Fornari P., Ubaldini S., *Waste Management*, 2003, **23**, 245-252.

## **ELECTROCHEMICAL DETECTION OF PHENOL AND NITROPHENOLS ON SMECTITE-CHITOSAN-BASED ELECTRODES**

Z. Mojović, N. Jović-Jovičić, T. Mudrinić, M. Ajduković, S. Marinović, P. Banković and A. Milutinović-Nikolić

*University of Belgrade, Institute of Chemistry, Technology and Metallurgy, Department of Catalysis and Chemical Engineering, Njegoševa 12, 11000 Belgrade, Republic of Serbia (zoricam@nanosys.ihm.bg.ac.rs)*

### **ABSTRACT**

Smectite-chitosan bionanocomposite (SM-C) was used for the modification of a glassy carbon electrode (GCE). The modified electrode (GCE/SM-C) was tested in the electrooxidation of phenol and different nitrophenols in acidic solution. The cathodic limit set to allow encompassing of nitro group reduction led to the appearance of additional peaks of nitrophenol and decrease of the electrode passivation rate. The first-order derivative linear sweep voltammetry improved the sensitivity of the detection of different phenolic compounds from their mixed solution. Although, the quantitative determination of phenol and nitrophenols in a mixture had some disadvantages, the concept of electrooxidation as a method for the detection and distinction of phenol and its nitro derivatives from water solution was proven.

### **INTRODUCTION**

The environmental impact of phenol and its derivatives is severe because of their high toxicity and degradation effect on human tissues [1]. Separate quantification of phenolic compounds has been addressed by the application of different methods with low detection limits and good selectivity. Much simpler electrochemical methods do not require previous sample treatment and can be performed in opaque media, which makes them more advantageous in comparison to spectrophotometric methods. However, there is a limited number of reports concerning simultaneous detection of phenol and nitrophenols [2]. Clay modified electrodes, for phenol oxidation have been extensively investigated [3]. GCE modified with smectite bioorganoclays were tested neither in phenol nor in phenol derivatives reactions. Chitosan is a natural-based biopolymer derived from chitin. Chitosan provides the system with functional groups that allow the application of the resulting electrodes in the potentiometric detection of

anions and can have beneficial effects on the electrocatalytic activity [4]. In this work chitosan modified clay was used as electrode material for the simultaneous detection of phenol and nitrophenols. The distinguishing of different phenolic compounds was based on the oxidation of phenolic group.

### EXPERIMENTAL

Chitosan solution was prepared by the addition of 640 mg of chitosan into 25.00 ml of 1% (v/v) acetic acid and stirred until complete dissolution. After the pH was adjusted to 4.6–5, the chitosan solution was added to a 1% sodium-exchanged clay dispersion and stirred at room temperature for 48 h. The obtained sample was centrifuged, air-dried at 50 °C, ground to powder and denoted as SM-C. Clay samples (10 mg) were homogeneously dispersed in 100  $\mu$ l of original Nafion® solution. Droplets (10  $\mu$ l) of these dispersions were placed on the surface of a glassy carbon electrode (area = 0.0314 cm<sup>2</sup>). Modified GCE was denoted as GCE/SM-C. The GCE/SM-C was used as the working electrode, while the reference electrode was Ag/AgCl in 3 M KCl and a platinum foil served as the counter electrode. Cyclic voltammetry was performed in 10.0 ml of 0.1 M H<sub>2</sub>SO<sub>4</sub> containing adequate concentrations of single or mixed phenolic compounds (phenol (Ph), 2-nitrophenol (2-NP) and 4-nitrophenol (4-NP)). The device used for the electrochemical measurements was a 797 VA Computrace Metrohm.

### RESULTS AND DISCUSSION

The cyclic voltammogram of phenol obtained using the GCE/SM-C electrode showed only one peak at 0.95 V, while that of 4-NP showed peaks at 0.43 V and 1.14 V, and that of 2-NP at 0.47 V and 1.07 V (Fig.1a). Higher potential peaks resulted from the oxidation of –OH group, while those at lower potentials probably originated from the oxidation of products that were formed after the reduction of the nitro group. The reduction peak for the nitro group GCE/SM-C electrode appeared at the potential values of –0.62 V for 2-NP and –0.65 V for 4-NP, being the onset of the reaction at –0.46 V (Fig.1b). Compared with the bare GCE (not shown), the reduction peak potentials of the nitrophenols investigated were shifted positively, indicating that electrode process was facilitated in the case of GCE/SM-C electrode. Peak currents of –NO<sub>2</sub> reduction were significantly lower than those recorded for the bare GCE, probably repulsion due to repulsion of negative charge of Nafion. The rate of electrode passivation was decreased when cathodic limit was set to –1.1 V.

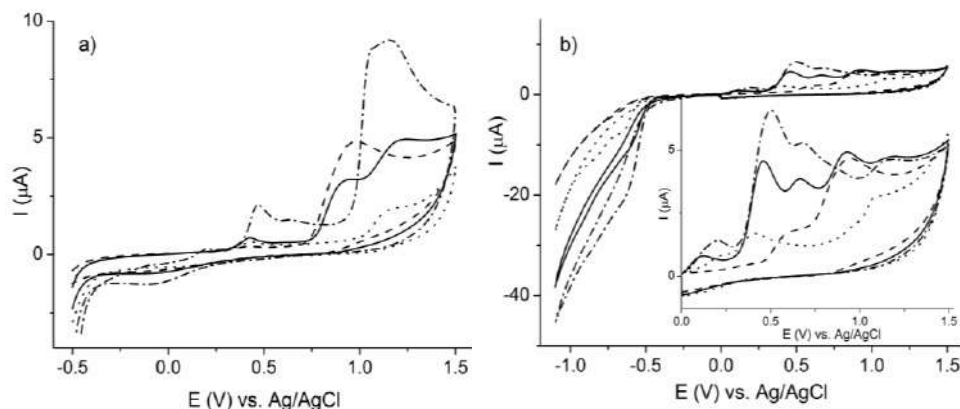


**Figure 1.** Cyclic voltammograms of GCE/SM-C electrode for 10 mM Ph (dash), 10 mM 4-NP (dot), 10 mM 2-NP (dash-dot) and 2 mM Ph+ 2 mM 4-NP+2 mM 2-NP (solid) at scan rate of  $50\text{ mV s}^{-1}$  and potential ranges: from  $-0.5\text{ V}$  to  $+1.5\text{ V}$  and b) from  $-1.1\text{ V}$  to  $1.5\text{ V}$ .

In order to improve the sensitivity of detection, first-order derivative linear sweep voltammetry was used in the analytical procedure (Fig. 2). The

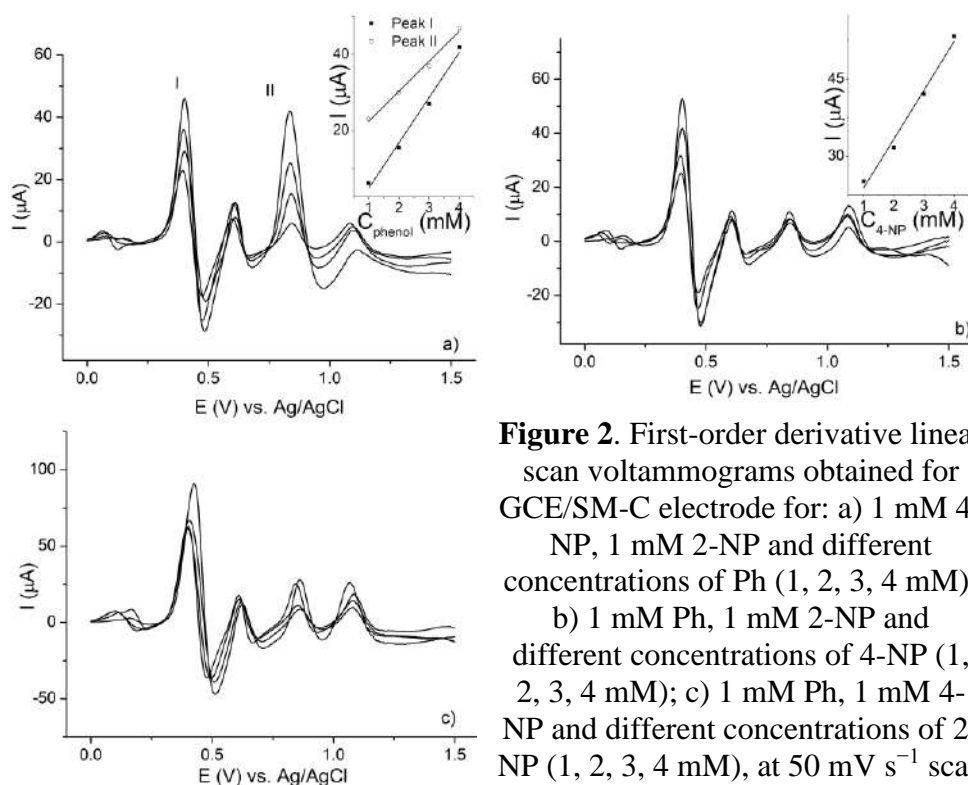


**Figure 2.** First-order derivative linear scan voltammograms obtained for GCE/SM-C electrode for: a) 1 mM 4-NP, 1 mM 2-NP and different concentrations of Ph (1, 2, 3, 4 mM); b) 1 mM Ph, 1 mM 2-NP and different concentrations of 4-NP (1, 2, 3, 4 mM); c) 1 mM Ph, 1 mM 4-NP and different concentrations of 2-NP (1, 2, 3, 4 mM), at  $50\text{ mV s}^{-1}$  scan rate.

investigated analyte concentration was varied in the 1–4 mM range, while the other two concentrations were held constant (1 mM). The results show that the anodic peak current for phenol (0.93 V) was proportional to the concentration of phenol (Fig. 2a). Unfortunately, the current of the peak at lower potential (0.47 V) also showed linear correlation to the concentration of phenol, although the concentrations of both NPs were constant. The peak current of 4-NP was proportional to the concentration of 4-NP, while other peak currents were almost constant (Fig. 2b). The peak currents obtained for 2-NP were the highest among all investigated compounds but the electrode's current response was not sensitive toward changes in the concentration of 2-NP (Fig. 2c). The application of the GCE/SM-C electrode in acid environment displayed several disadvantages. The electrode was easily passivated and a new electrode had to be made for each concentration change. The peaks were not clearly separated and cannot be attributed to a specific analyte, although first-order derivative linear sweep voltammetry significantly increased the sensitivity of the measurement.

## CONCLUSIONS

The obtained smectite-chitosan bionanocomposite was used for the modification of a glassy carbon electrode that was tested in the detection of phenol and its nitro derivatives in acidic solution. The applied potential range had significant impact on the shape of the cyclic voltammograms. Broadening of the potential range resulted in increased sensitivity the appearance of new peaks related to nitrophenol. The rate of electrode passivation decreased when cathodic limit was shifted from  $-0.5$  V to  $-1.1$  V. The first order derivative linear sweep voltammetry improved the sensitivity of the detection of different compounds from their mixed solutions.

## Acknowledgment

This work was supported by the Ministry of Education, Science and Technological Development of Republic Serbia (contract No III 45001).

## REFERENCES

- [1] US Environmental Protection Agency, 2000. Phenol. <http://www3.epa.gov/airtoxics/hlthef/phenol.html>.
- [2] G.H. Zhao, Y.T. Tang, M.C Liu, Y.Z. Lei, X.E. Xiao, *Chin. J. Chem.*, 2007, **25**, 1445–1450.
- [3] G. Avci, B. Yazci, M. Erbil, *Russ. J. Electrochem.*, 2009, **45**, 263–270.
- [4] L. Hea, H. Wang, G. Xiac, J. Sund, R. Song, *Appl. Surf. Sci.*, 2014, **314**, 510–515.

## FORMATION OF HYDROQUINONE AND CATECHOL DURING ELECTROOXIDATION OF PHENOL ON CLAY-MODIFIED ELECTRODES

T. Mudrinić, A. Ivanović-Šašić, M. Ajduković, Z. Mojović and D. Jovanović

*University of Belgrade, Institute of Chemistry, Technology and Metallurgy, Njegoševa 12, 11000 Belgrade, Serbia. (tihana@nanosys.ihm.bg.ac.rs)*

### ABSTRACT

Clay was modified by pillaring, which was performed by combinations of pillaring cations:  $\text{Al}^{3+}$  and  $\text{Fe}^{3+}$  or  $\text{Al}^{3+}$ ,  $\text{Fe}^{3+}$  and  $\text{Ni}^{2+}$ . The synthesized materials were used to obtain glassy carbon electrode (GCE) coatings. Electrochemical oxidation of phenol from acidic solution was investigated on clay-modified electrodes by method of cyclic voltammetry. As a consequence of electrode fouling the peak current registered in the tenth cycle dropped in the comparison to the current obtained in the first cycle. The first-order derivative linear sweep voltammetry was used in the analytical procedure. Hydroquinone/catechol current ratio increased in the opposite manner to the phenol oxidation current drop.

### INTRODUCTION

Electrooxidation of phenol has been studied as a model reaction as well as due to phenols classification as a priority contaminant [1]. Oxidation mechanism of phenol is well-known [2]. Electrooxidation mechanism starts with the formation of phenoxy radical. Phenoxy radicals can be further oxidized to oxidation products like hydroquinone, quinone etc, or can be involve in polymerization reaction. Polymerization reaction leads to formation of insulating film on the electrode surface and passivates electrode. Literature results showed that electrodes, such as graphite,  $\text{IrO}_2$ ,  $\text{RuO}_2$  and Pt rapidly passivate. Complete phenol oxidation to  $\text{CO}_2$  is favored on antimony-doped tin oxide, lead or boron-doped diamond electrodes. Unfortunately, these electrodes encounter several problems such as short service life, the release of toxic ions and high cost, respectively [3]. Modification of the electrode surface can improve electrode performances. Clay minerals have been extensively studied as electrode surface modifiers due to their availability, well-defined layered structure, thermal and chemical stability and low cost [4]. Therefore, either clay modifications or designed clay synthesis are used for the preparation of clay-modified

electrodes. Pillaring is one of the common techniques of clay modification. It was shown that the electrocatalytic activity and stability depend on the type of incorporated metals. Electrode modified with clay pillared with Al, Fe, Ni polyhydroxy cations showed the best stability, regarding electrode fouling due to polymer formation [5], in comparison to electrode modified with clay pillared with other transition metals (Al,Fe; Al,Co and Al,Cu) [6]. The goal of this work was to investigate the influence of hydroquinone and catechol formation on clay-modified electrode with the degree of its passivation during electrooxidation of phenol. In order to investigate the effect, a series of modified bentonite based materials was synthesized. Clay from seldom investigated deposit Mečji Do in Serbia was modified by pillaring, which was performed using the following combinations of pillaring cations:  $\text{Al}^{3+}$  and  $\text{Fe}^{3+}$  or  $\text{Al}^{3+}$ ,  $\text{Fe}^{3+}$  and  $\text{Ni}^{2+}$ . The synthesized materials were used to obtain glassy carbon electrode (GCE) coatings.

## EXPERIMENTAL

Bentonite clay from seldom investigated deposit Mečji Do, Serbia was used as a raw material. The raw clay was subjected to the common Na-exchange procedure and denoted as Na-MD. The process of pillaring was carried out according to previously established procedure [6]. Pillaring solutions were adjusted to have the molar ratio of  $\text{OH}^-/\text{Me}^{n+} = 2.0$  (where  $\text{Me}^{n+} = \text{Al}^{3+}$ ,  $\text{Fe}^{3+}$ ,  $\text{Ni}^{2+}$ ) and metal cation/clay ratio of 10 mmol  $\text{Me}^{n+}/\text{g}$ . The pillaring solutions contained the following molar ratios of each species: a) 90% Al and 10% Fe and b) 90% Al, 5% Fe and 5% Ni. Accordingly, the obtained pillared samples were denoted: AlFe10-MD and AlFe5Ni5-MD, respectively. The drop of dispersion of investigated sample with 10 wt. % of carbon black in 5 wt. % Nafion was applied on the surface of glassy carbon electrode. The electrochemical response of samples was tested by method of cyclic voltammetry at polarization rate  $10 \text{ mVs}^{-1}$  in the range of potential from hydrogen evolution at  $-0.3 \text{ V}$  to oxygen evolution at  $1.1 \text{ V}$ . First, prepared electrodes were tested in  $0.1 \text{ M H}_2\text{SO}_4$ . Then, the freshly prepared electrodes were tested in  $0.01 \text{ M phenol} + 0.10 \text{ M H}_2\text{SO}_4$ . All potentials are reported versus Ag/AgCl (3 M KCl) reference electrode, and platinum rod served as counter electrode.

## RESULTS AND DISCUSSION

Cyclic voltammograms (CVs) obtained in acid solution and phenol containing solution were similar for Na-MD and AlFe10-MD. For clarity sake CVs for AlFe10-MD and AlFe5Ni5-MD are presented in Figs. 1 and 2. The CV obtained in acid solution (dashed line in Figs. 1a and 2a) is presented together with the first cycle obtained in phenol containing solution

(solid line in Fig. 1a and 2a). CVs obtained in acid solution showed a pair of peaks around 0.45 V attributed to oxidation/reduction of the  $\text{Fe}^{2+}/\text{Fe}^{3+}$  redox couple [5]. In the first cycle of the electrooxidation of phenol, phenol oxidation wave and two cathodic peaks were obtained on all investigated electrodes (Fig. 1a and 2a). From the second to tenth cycle two additional anodic peaks appeared (Fig. 1b and 2b).

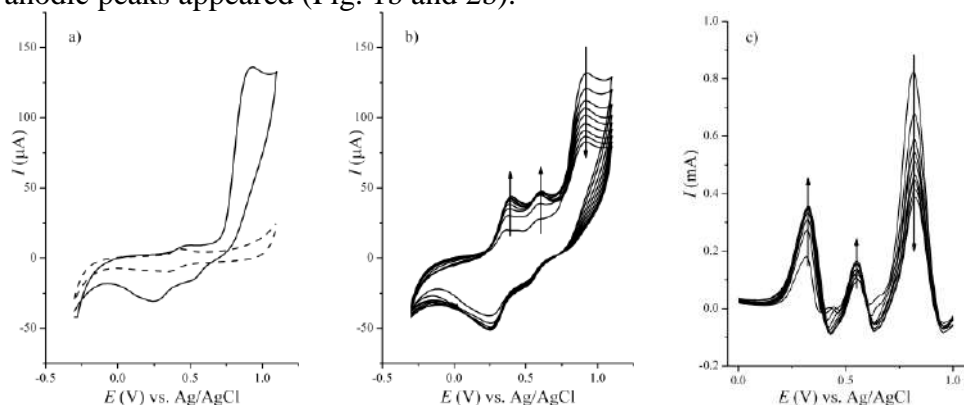


**Figure 1.** Cyclic voltammograms of AlFe10-MD electrode: (a) in 0.1 M  $\text{H}_2\text{SO}_4$  (dashed line) and the first scan in 0.01 M phenol+0.1 M  $\text{H}_2\text{SO}_4$  (solid line) (b) successive cycles in 0.01 M phenol+0.1 M  $\text{H}_2\text{SO}_4$  and (c) The first-order derivative linear sweep voltammograms.

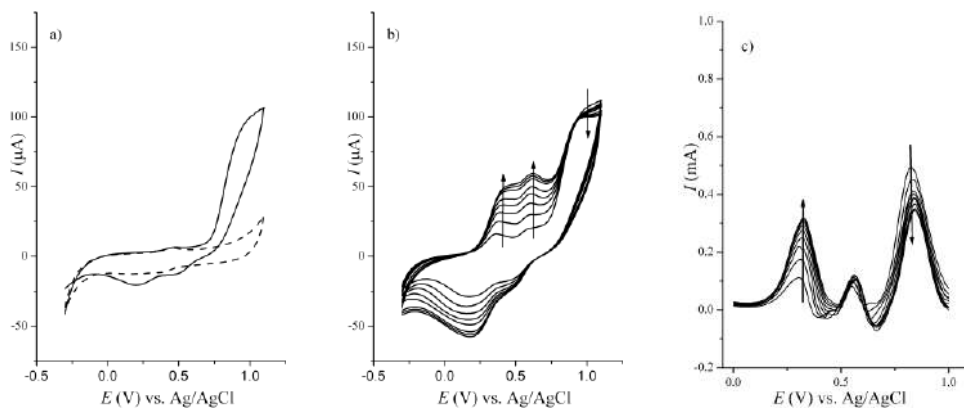


**Figure 2.** Cyclic voltammograms of AlFe5Ni5-MD electrode: (a) in 0.1 M  $\text{H}_2\text{SO}_4$  (dashed line) and the first scan in 0.01 M phenol+0.1 M  $\text{H}_2\text{SO}_4$  (solid line) (b) successive cycles in 0.01 M phenol+0.1 M  $\text{H}_2\text{SO}_4$  and (c) The first-order derivative linear sweep voltammograms.

The obtained cathodic and anodic pairs of peaks corresponded to the oxidation/reduction of hydroquinone and catechol. After 10 cycles, the current of the phenol oxidation peak on the Na-MD and AlFe10-MD electrodes decreased substantially (52.1 % and 41.2 %, respectively) as a

consequence of electrode fouling. In the case of Ni containing electrode the stability was significantly improved. The AlFe5Ni5-MD based electrode showed phenol oxidation current decrease of 5.4 % during ten CV cycles. In order of sensitivity of detection to be improved, the first-order derivative linear sweep voltammetry was used in the analytical procedure (Fig. 1c and 2c). The hydroquinone/catechol current ratio was 1.3, 2.2 and 3.1 for Na-MD, AlFe10-MD and AlFe5Ni5-MD, respectively. According to Li et al. [2] polymerization can also proceed via phenoxy radicals attack either on hydroquinone or catechol. According to the findings presented in this work it can be concluded that catechol is more likely candidate for polymerization reaction than hydroquinone. Addition of nickel ion in the structure of modified clay probably promoted hydroquinone formation path over catechol formation path.

## CONCLUSIONS

Pillared clays were used as modified electrodes for the electrooxidation of phenol. Clays were pillared by combination of cations:  $\text{Al}^{3+}$  and  $\text{Fe}^{3+}$  or  $\text{Al}^{3+}$ ,  $\text{Fe}^{3+}$  and  $\text{Ni}^{2+}$ . Cyclic voltammograms recorded from 0.01 M phenol + 0.10 M  $\text{H}_2\text{SO}_4$  showed phenol oxidation current decrease of 52.1%, 42.1% and 5.4% for Na-MD, AlFe10-MD and AlFe5Ni5-MD based electrode, respectively. The first-order derivative linear sweep voltammetry was used in the analytical procedure. Hydroquinone/catechol current ratios were 1.3, 2.2 and 3.1 for Na-MD, AlFe10-MD and AlFe5Ni5-MD, respectively.

## Acknowledgment

This work was supported by the Ministry of Education, Science and Technological Development of R. Serbia (Project III 45001 and 172015).

## REFERENCES

- [1] Environmental Protection Agency, Appendix A to Part 423—126 Priority Pollutants, (2014)
- [2] X. Li, Y. Cui, Y. Feng, Z. Xie, J. Gu, *Water Research*, 2005, **39**, 1972-1981.
- [3] M. Panizza in: *Electrochemistry for the Environment*, C. Comninellis, G. Chan (Eds.), Springer, New York, 2010.
- [4] L. Fernández, C. Borrás, H. Carrero, *Electrochimica Acta*, 2006, **52**, 872-884.
- [5] T. Mudrinić, Z. Mojović, A. Milutinović-Nikolić, P. Banković, B. Dojčinović, N. Vukelić, D. Jovanović, *Electrochimica Acta*, 2014, **144**, 92-99.
- [6] P. Banković, Z. Mojović, A. Milutinović-Nikolić, N. Jović-Jovičić, S. Marinović, D. Jovanović, *Applied Clay Science*, 2010, **49**, 84 -89.

## ELECTROANALYTICAL DETERMINATION OF CHLOROPROMAZINE ON BORON-DOPED DIAMOND ELECTRODE

B. B. Petković<sup>1</sup>, D. Stanković<sup>2</sup>, D. Kuzmanović<sup>3</sup>, T. Dimitrijević<sup>3</sup>  
and M. P. Krstić<sup>4</sup>

<sup>1</sup>*Department of Chemistry, Faculty of Natural Sciences and Mathematics,  
University of Priština, Lole Ribara 29, 38220 Kosovska Mitrovica, Serbia  
(bedpet@orion.rs, branka.petkovic@pr.ac.rs)*

<sup>2</sup>*Innovation center of the Faculty of Chemistry, University of Belgrade, P.O.  
Box 118, 11158 Belgrade, Serbia*

<sup>3</sup>*Faculty of Chemistry, University of Belgrade, Studentski trg 12-16, 11000  
Belgrade, Serbia*

<sup>4</sup>*Faculty of Veterinary Medicine, University of Belgrade, Bulevar  
oslobođenja 18, 11000 Belgrade, Serbia*

### ABSTRACT

The electrochemical behavior and determination of chlorpromazine (CPZ) by differential-pulse voltammetry (DPV) at unmodified boron-doped diamond electrode (BDDE) is proposed. Effect of pH on electrochemical oxidation of chlorpromazine in Britton–Robinson (BR) buffer solution was investigated. Cyclic voltammetry results showed four oxidation peaks for CPZ and peaks at 0.6 V and 1.3 V were chosen for CPZ quantification. The electrode reaction is controlled by diffusion as a rate-determining step. Under optimized DPV conditions at pH 4.0, a linear analytical curve was obtained for wide the chlorpromazine concentration range from  $1.0 \times 10^{-7}$  to  $4.0 \times 10^{-5}$  M with a detection limit of  $0.3 \times 10^{-7}$  M.

### INTRODUCTION

Chlorpromazine (CPZ) (2-chloro-10-(3-dimethylaminopropyl)phenothiazine) is a member of phenothiazine class of psychotropic drugs with an aliphatic side chain [1]. The most important field of its applications is treatment of schizophrenia and behavioral disorders while CPZ is also active in treatment of cancer, viral and bacterial infections and neurodegenerative illnesses [2]. Bearing in mind the problems that can cause overdose of this drug, it is important to find simple, fast and low cost method which no requires using of several steps, highly evolved instruments and special training.

The aim of this work was to find a new, simple, sensitive and fast analytical procedure for detection of chlorpromazine by differential pulse voltammetry bearing in mind the advantages of BDDE, foremost the sensitivity and wide potential window. This procedure should be primary based on so far not applied determination of chlorpromazine due to quantization of the peak originating from oxidation of nitrogen in phenothiazine side chain.

## EXPERIMENTAL

*Electrode preparation:* BDDE was anodically pretreated as it is previously reported [3].

*Electrochemical measurements:* Cyclic voltammetric (CV) measurements and differential pulse voltammetry (DPV) measurements were performed using an electrochemical system CH Instruments (USA). The cell (10 mL) consisted of three-electrode system, boron-doped diamond electrode (inner diameter of 3 mm; Windsor Scientific Ltd., Slough, Berkshire, United Kingdom), an Ag/AgCl (saturated KCl) reference electrode and Pt counter electrode. The cyclic and the differential pulse voltammograms of standard chlorpromazine solutions were recorded in the potential range from 0.0 to 1.5 V, using a scan rate from 10 to 300 mV/s (for CV) and 20 mV/s (for DPV), a modulation time of 40 ms, a pulse amplitude of 40 mV and pulse time of 0.2 s. All pH values were measured with pH meter model Jenco Instruments Model No. 6071 (Taiwan). All experiments were obtained at an ambient temperature.

## RESULTS AND DISCUSSION

Influence of pH on electrochemical oxidation of chlorpromazine is presented on Figure 1. (a). Cyclic voltammograms of 0.1 mM CPZ in BR buffer solution as supporting electrolyte (pH values from 2 to 10) at BDDE revealed that four oxidation peaks, originated from phenothiazine core and aliphatic chain [4], are highly sensitive to changing of pH. Cyclic voltammograms of 0.1 mM CPZ in BR buffer solution at pH 4 (selected pH for further investigations) on BDDE were recorded at different potential sweep rates and the graph of peak current for all peaks as function of the square root of potential scan rate was shown on Fig. 1 (b). Hence, the mass transport in diffusion layer during oxidation reaction is controlled by diffusion and the adsorption and/or other specific interactions on self-assembled BDDE electrode surface are negligible.

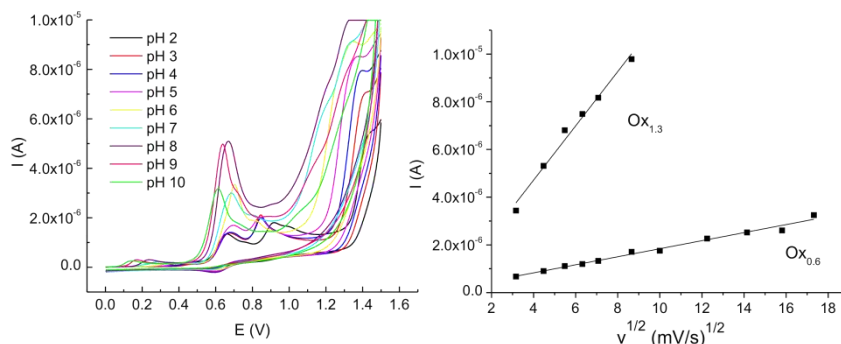


**Figure 1.** Cyclic voltammetric profiles of 0.1 mM CPZ in different pH BR buffer solutions at BDDE, scan rate of 20 mV/s; b) The peak current as function of  $v^{1/2}$  derived from cyclic voltammograms of 0.1 mM CPZ for various scan rates ( $v$ ) ( $10\text{--}300\text{ mV s}^{-1}$ ) in BR buffer solution at pH 4 on BDDE.

Differential pulse voltammetry (DPV) was selected as a suitable electroanalytical technique for detection of trace amounts of CPZ. By varying one parameter while others were kept fixed, the optimal modulation time of 40 ms and pulse amplitude of 50 ms were chosen taking into account the width and height of the peaks of quantification (0.6 V and 1.3 V). Peak on 0.6 V is usually used for quantization of phenothiazines [5, 6], while peak at 1.3 V is originated from specific CPZ side chain group [4] and it is more selective due to high potential value.

Differential pulse voltammograms of various concentrations of CPZ from  $3.0 \times 10^{-7}$  to  $4.5 \times 10^{-5}$  M recorded on BDDE were showed in Fig.2 (a).

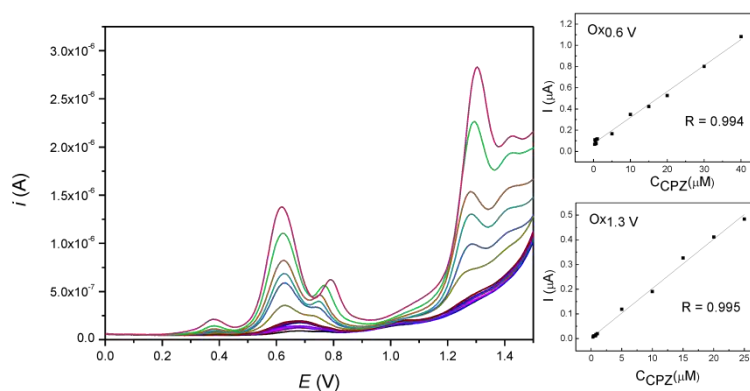


**Figure 2.** DPV of CPZ added in concentration of  $1.0 \times 10^{-7}$  –  $4.5 \times 10^{-5}$  M, pH = 4 (a); calibration curves for Ox<sub>0.6</sub> v (b) and Ox<sub>1.3</sub> v (c)

The calibration curve was constructed by plotting the current density of anodic peaks at 0.6 and 1.3 V vs. the concentration of CPZ. The resulting calibration plots for both oxidation peaks (Fig. 4, b) and c)) are followed by equations:

$$\text{Ox}_{0.6 \text{ V}}: I_p (\text{A}) = 2.45 \times 10^{-8} \times C_{\text{TFP}} + 7.53 \times 10^{-8}$$

$$\text{Ox}_{1.3 \text{ V}}: I_p (\text{A}) = 1.99 \times 10^{-8} \times C_{\text{TFP}} + 0.31 \times 10^{-8}$$

Detection limit (LOD) of CPZ determination for oxidation peaks on 0.6 and 1.3 V are  $0.6 \times 10^{-7} \text{M}$  and  $0.3 \times 10^{-7} \text{M}$ , respectively. The repeatability of method was evaluated by five replicate DPV measurements at the  $15 \times 10^{-6} \text{M}$  CPZ concentration under the same operating conditions. The relative standard deviation for peak current for  $\text{Ox}_{0.6 \text{ V}}$  and  $\text{Ox}_{1.3 \text{ V}}$  were 2.72 % and 1.64 %, respectively.

## CONCLUSION

The present study is related to the application of unmodified BDDE for determination of prominent phenothiazine derivate, chlorpromazine. The proposed sensor exhibited the advantage of simple preparation, good reproducibility and electrochemical surface stability. As BDDE is, up to date, one of the best solid electrode materials, this investigation provides valuable information about the possibility of a selective determination of CPZ over many interfering compounds from biological samples. The developed procedure has potential for use in analyzing of biological fluids and pharmaceutical formulations.

## Acknowledgement

Financial support for this study was granted by the Ministry of Science and Technological Development of the Republic of Serbia, Project Number 45022.

## REFERENCES

- [1] A. Jaszczyszyn, et al., *Pharmacol Rep.*, 2012, **64**, 16.
- [2] T. A. Ban, *Neuropsychiatric disease and treatment*, 2007, **3**, 495
- [3] L. Švorc, K. Cinková, J. Sochr, M. Vojs, P. Michniak, M. Marton, J. *Electroanal. Chem.*, 2014, **728**, 86.
- [4] D. Stanković, T. Dimitrijević, D. Kuzmanović, M. P. Krstić and B. B. Petković, *RSC Adv.* 2015, **5**, 107058.
- [5] M. H. Parvin, *Electrochemistry Communications*. 2011, **13**, 366.
- [6] M. Amiri, S. Sohrabnezhad, A. Rahimi, *Materials Science and Engineering C*, 2014, **37**, 342.

## ELECTROCHEMICAL OXIDATION AND INTERACTION OF 9-CHLOROACRIDINE WITH DNA AT GLASSY CARBON ELECTRODE

J. Pantić<sup>1</sup>, M. M. Aleksić<sup>1</sup>, V. Dobričić<sup>2</sup>, O. Čudina<sup>2</sup>, J. Brborić<sup>2</sup> and S. Vladimirov<sup>2</sup>

*University of Belgrade- Faculty of Pharmacy, <sup>1</sup>Department of Physical Chemistry and Instrumental Methods (mara@pharmacy.bg.ac.rs)*

*<sup>2</sup>Department of Pharmaceutical Chemistry, Vojvode Stepe 450, 11000 Belgrade, Serbia*

### ABSTRACT

Interaction of 9-chloroacridine (9Cl-A) with calf thymus double stranded DNA was investigated by square wave voltammetry using DNA-modified glassy carbon electrode. Voltammetric measurements performed in wide pH range showed the electroactivity of the acridine moiety. The oxidation of 9-chloroacridine is pH dependent and occurs as irreversible, diffusion controlled process. Binding interaction was investigated by incubating DNA-modified glassy carbon electrode for different incubation times in the 9Cl-A solution. Decrease of the DNA oxidation peak confirmed the interaction and suggested the aggregation of DNA strands and formation of more rigid structures due to the intercalation of 9Cl-A into DNA strands.

### INTRODUCTION

Historical facts show that the drug family of acridines was discovered in 1870 when Graebe and Caro isolated a substance from the high boiling fraction of coal tar and designated it "acridine" or acrid substance, due to the irritating effects of its vapor on the mucus membranes [1]. Since then acridines attract much attention and, due to their numerous actions, are used as bactericidal, antiseptic, inhibitory and genetically active agents. The most important property of acridines is their chemotherapeutic action [2], thus the interaction of acridine derivatives with DNA has been the subject of considerable research [3].

DNA-based electrochemical biosensors have been successfully used for investigation and evaluation of DNA-drug interaction mechanisms [4]. To be able to use the biosensor, the electrochemical behavior of the investigated drug has to be known. There are no literature

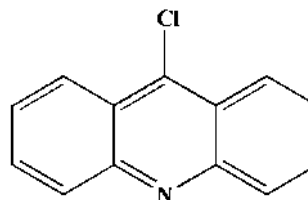


**Figure 1.** 9Cl-A structure

data concerning 9Cl-A, but some other acridine derivatives were investigated by different voltammetric methods at different electrodes [5,6], proving the electroactivity of the acridine moiety. The objective of this work is to investigate 9Cl-A (Fig.1.) oxidation at glassy carbon electrode (GCE) and its interaction with DNA immobilized on an electrode surface.

### EXPERIMENTAL

The voltammetric measurements were performed with  $\mu$ Autolab analyzer (Eco Chemie, Utrecht, The Netherlands). Three-electrode system was employed with GCE working electrode, Ag/AgCl reference and Pt-auxiliary electrode. Before each experiment the GCE was manually polished using the aqueous slurry of  $\text{Al}_2\text{O}_3$  powder (particle size  $0.05\mu\text{m}$ ) on a smooth polishing pad, sonicated in bidistilled water and then in absolute ethanol. Chloride, acetate, phosphate and ammonia buffers were used as supporting electrolytes. An appropriate volume of supporting electrolyte of different pH values was placed in electrochemical cell, de-aerated for 10 minutes with high purity nitrogen and 9Cl-A stock solution ( $c_0=1\times 10^{-3}\text{ molL}^{-1}$ ) was added to make its final concentration of  $2.5\times 10^{-4}\text{ molL}^{-1}$ . The cyclic voltammograms were recorded at scan rate ranged  $10 - 100\text{ mVs}^{-1}$ .

The development of DNA biosensor involved the immobilization of double-stranded calf thymus DNA in multilayer at the GCE surface. The DNA-modified electrode was prepared by three times consecutively drying of small volumes of DNA ( $5\mu\text{L}$ , concentration  $73.95\mu\text{gmL}^{-1}$ ) solution at the GCE surface. After placing each drop on the top of the electrode surface, the electrode was dried under nitrogen atmosphere, and rinsed in water to remove unadsorbed DNA.

Square-wave voltammetry (SWV) was used to detect signals of adsorbed DNA on the GCE surface using acetate buffer (pH 4.5) as supporting electrolyte. Interaction between 9Cl-A ( $c=1\times 10^{-4}\text{ molL}^{-1}$ ) and adsorbed DNA was also examined by SWV in acetate buffer (pH 4.5). The experimental parameters for SWV were: frequency 25 Hz and potential increment 1 mV, corresponding to an effective scan rate of  $26\text{ mVs}^{-1}$ , and the pulse amplitude of 50 mV.

### RESULTS AND DISCUSSION

The redox behavior of  $2.5\times 10^{-4}\text{ molL}^{-1}$  9Cl-A was studied by cyclic voltammetry (CV) at different pH values. The cyclic voltammograms were recorded in three successive scans starting from 0.0V, to the positive potential limit of +1.3 V, at a scan rate  $10 - 100\text{ mVs}^{-1}$ . The oxidation peak existed at all investigated pH values, from 2.0 to 10.0, and the peak potential

was shifted to negative values with increasing pH. Anodic peak appeared at  $E_p \sim 0.8V - 1.15V$  as seen in Fig.2. The absence of cathodic peak in the reverse scan confirmed the irreversibility of process. The linear dependence of  $E_p$  vs. pH (at pH < 8) was obtained following the equation:  $E_p = 1.259 V - 0.061V \times pH$  ( $r=0.998$ ) at GCE. Slope of 61mV suggested the same number of electrons and protons involved in the oxidation process.

Cyclic voltammograms were recorded at different scan rates, the linear dependences of  $I_p$  vs.  $v^{1/2}$  obtained at all investigated pH indicate the diffusion controlled process. Also, the corresponding slopes of  $\log I_p$  vs.  $\log v$  dependences, which were always less than 0.5, proved diffusion nature of the 9Cl-A oxidation.

The interaction between 9Cl-A and DNA was investigated by square wave voltammetry (SWV) using DNA-modified glassy carbon electrode as biosensor in acetate buffer pH 4.5. A SW voltammogram of DNA layer at DNA-electrochemical biosensor showed two anodic peaks corresponding to the oxidation of deoxyguanosine, dG, ( $E_p = +1.1V$ ), and deoxyadenosine, dA, ( $E_p = +1.32V$ ) (Fig.3, curve 1). A SW voltammogram of 9Cl-A adsorbed at GCE shows oxidation peak at  $E_p = +0.98V$  (Fig.3, curve 2). Binding interaction was investigated by incubating DNA-electrochemical biosensor for different incubation

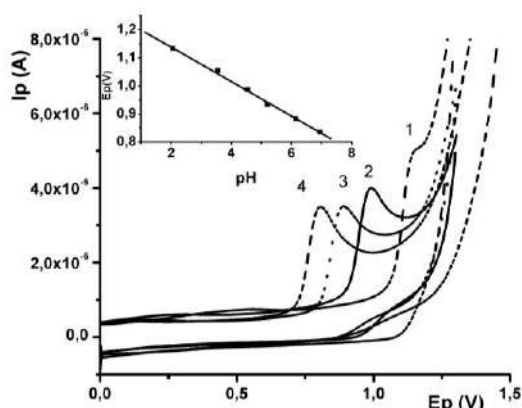


**Figure 2.** Cyclic voltammograms of  $2.5 \times 10^{-4} \text{ mol L}^{-1}$  9Cl-A at different pH values: 1-pH 2.0, 2-pH 4.5, 3-pH 6.1, 4-pH 7.0,  $v=50 \text{ mV s}^{-1}$

*Attached:* The influence of the pH on the CV peak potential response.

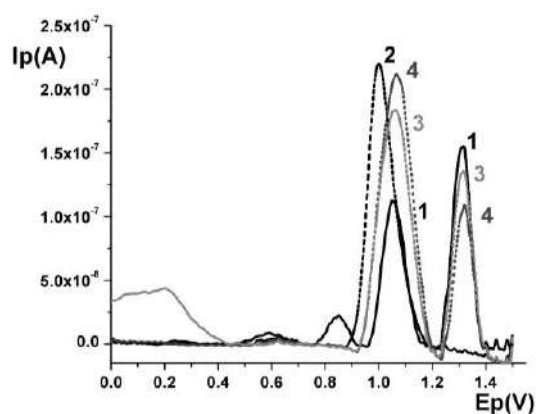


**Figure 3.** SW voltammograms of: 1 - DNA layer, 2 - 9Cl-A after 5 min adsorption at bare GCE, 3 - DNA-9Cl-A interaction after 10 min incubation, 4 - DNA-9Cl-A interaction after 30 min incubation.

times (10 – 30 min) in the 9Cl-A solution. Recorded SW voltammograms showed decrease of the oxidation dA peak current with incubation time, as shown in Fig.3, curves 3 and 4. The peak corresponding to dG and 9Cl-A oxidation became wider and with higher current due to their superposition and overlapping after the incubation, and therefore was not informative. Very emphasized decrease in dA peak intensity after 30 min of incubation ( $\Delta I_p = 120\text{nA} \sim 30\%$ ) is probably a consequence of the preferential interaction between 9Cl-A and DNA at adenine residues leading to the formation of DNA aggregates, as described for other intercalative drugs [7].

### CONCLUSION

According to the results obtained, the oxidation of 9Cl-A at GCE occurred in the wide pH range as irreversible, diffusion controlled process. The interaction between 9Cl-A and DNA was investigated using multilayer DNA modified glassy carbon electrode as electrochemical biosensor. Decrease of DNA oxidation peaks may be attributed to the aggregation of DNA strands and formation of more rigid structures due to the intercalation of 9Cl-A into DNA strands, what leads to the conformational changes in the DNA structure. This study used simple electroanalytical methodology and showed the potential use of biosensors for investigation of DNA-drug interaction.

### Acknowledgement

This work was supported by the Ministry of Education, Science, and Technological Development of the Republic of Serbia, Grants no. 172033 and 172041.

### REFERENCES

- [1] N. T. Brychcy, *Mutation Res.*, 1979, **65**, 261-288.
- [2] R. O. Pons, M. D. Gregorio, G. J. V. Mateo, M. J. Calatayud, *Anal. Chim. Acta*, 2001, **438**, 149-156.
- [3] M. Choudhury, R. Basu, *J. Photochem. Photobiol. A*, 1995, **85**, 89-92.
- [4] V. C. Diculescu, A. M. Chiorcea-Paquim, A. M. Oliveira-Brett, *Trends in Analytical Chemistry*, 2016, **79**, 23-36.
- [5] S. T. Girousi, D. K. Alexiadou, A. K. Ioannou, *Microchim. Acta*, 2008, **160**, 435-439.
- [6] A. D. R. Pontinha, S. Sparapani, S. Neidle, A. M. Oliveira-Brett, *Bioelectrochemistry*, 2013, **89**, 50-56.
- [7] P. V. F. Santos, I. C. Lopes, V. C. Diculescu, A. M. Oliveira-Brett, *Electroanalysis*, 2012, **24**, 547-553.

## DOES THE SODIATION OF $\text{Fe}_{0.95}\text{V}_{0.05}\text{PO}_4$ INDEED PRESENT AN ONE-STAGE PROCESS?

M. J. Vujković<sup>1</sup>, M. C. Pagnacco<sup>1</sup> and S. V. Mentus<sup>1,2</sup>

<sup>1</sup>*Faculty of Physical Chemistry, University of Belgrade, Studentski trg 12-16, P.O. Box 137, Belgrade, Serbia, (milica.vujkovic@ffh.bg.ac.rs)*

<sup>2</sup>*The Serbian Academy of Science and Arts, Knez Mihailova 35, 11158 Belgrade, Serbia*

### ABSTRACT

High storage capacity of  $\text{NaFe}_{0.95}\text{V}_{0.05}\text{PO}_4/\text{C}$  composite in an aqueous sodium nitrate solution amounting to  $104 \text{ mAh g}^{-1}$  at high charging/discharging rate of  $500 \text{ mA g}^{-1}$  ( $\sim 3.2 \text{ C}$ ), we evidenced by chronopotentiometry, makes it applicable in aqueous sodium-ion batteries. Cyclovoltammogram of this material in an aqueous nitrate solution contains two anodic peaks, and apparently unique cathodic peak, indicating two-stage desodiation and only one-stage sodiation process. Since that looks like a strange property, we performed a detailed analysis of sodiation process. By a careful deconvolution of cathodic peak, we evidenced that sodiation proceeds also through the two stages.

### INTRODUCTION

The sodium ion batteries have started to attract great attention due to the higher abundance and lower price of sodium compared to those of lithium. The main challenge in this field is to reach or overcome both the energy and the power of Li-ion batteries. Therefore, the understanding of complex sodiation/desodiation redox processes at the electrode/electrolyte interface and in electrode material depth is necessary [1]. The aim of this study was to obtain  $\text{NaFe}_{0.95}\text{V}_{0.05}\text{PO}_4/\text{C}$  material for sodium aqueous rechargeable batteries and investigate the relationship (i.e. symmetry) between its desodiation and sodiation processes.

### EXPERIMENTAL

The nanodispersed  $\text{LiFe}_{0.95}\text{V}_{0.05}\text{PO}_4/\text{C}$  composite (carbon content 11% by weight), synthesized by the malonic-assisted gel-combustion procedure [2], was used as a precursor to obtain the  $\text{NaFe}_{0.95}\text{V}_{0.05}\text{PO}_4/\text{C}$  composite. For this purpose,  $\text{LiFe}_{0.95}\text{V}_{0.05}\text{PO}_4/\text{C}$  composite, carbon black (10%) and poly(vinylidene fluoride) (PVDF) binder (5% PVDF solution) were mixed in N-methyl 2-pyrrolidone. Prepared slurry was homogenized for about 40 min

in an ultrasonic bath, deposited on a conductive support, and dried under vacuum at 120 °C for 4h. Such obtained electrode was subjected to a potentiodynamic cycling in aqueous NaNO<sub>3</sub> solution to replace Li<sup>+</sup> ions by Na<sup>+</sup> ions. Both potentiodynamic (cyclic voltammetry, CV) and chronopotentiometric measurements were performed in a typical three-electrode electrochemical cell, with the Pt-foil counter electrode, and saturated calomel (SCE) reference electrode, connected to Gamry PCI4/300 Potentiostat/Galvanostat. The electrolyte was saturated aqueous NaNO<sub>3</sub> solution. The CV curve was deconvoluted using PeakFit program, designed especially for fitting hidden peaks with noisy data. Deconvolution parameters are following: for oxidation peaks are used Pearson IV a3=2 function, while best fit for reduction peaks are obtained with Pearson VII Amp function. In both, the linear baseline is generated.

## RESULTS AND DISCUSSION

The charge/discharge profile of electrochemically obtained NaFe<sub>0.95</sub>V<sub>0.05</sub>PO<sub>4</sub>/C, measured at a current density of 500 mA g<sup>-1</sup> in an aqueous solution of NaNO<sub>3</sub>, is presented in Fig. 1. The charge (desodiation – rising potential) and discharge (sodiation – decreasing potential) capacity amounted to 104 mAh g<sup>-1</sup> and 107 mAh g<sup>-1</sup>, respectively. These large values, measured at a relatively high charging/discharging rate of ~3.2 C, make this material a very promising cathode material for aqueous sodium rechargeable batteries.

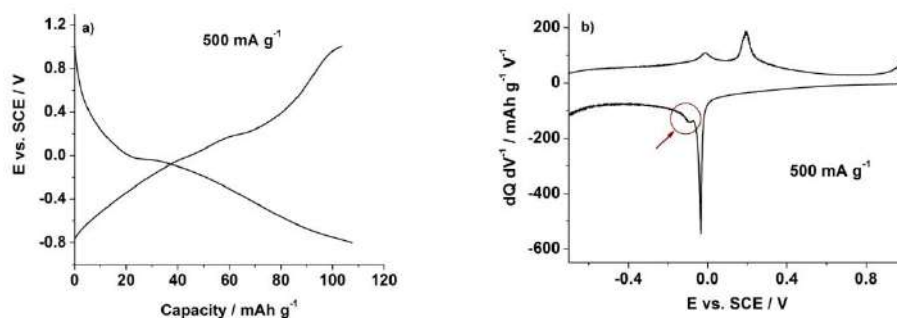


**Figure 1.** The chronopotentiometric curve of NaFe<sub>0.95</sub>V<sub>0.05</sub>PO<sub>4</sub> electrode in NaNO<sub>3</sub> solution recorded at 500 mA g<sup>-1</sup> and its first derivative (dQ/dV).

Two distinct potential plateaus registered in charging (NaFe<sub>0.95</sub>V<sub>0.05</sub>PO<sub>4</sub>/C → Fe<sub>0.95</sub>V<sub>0.05</sub>PO<sub>4</sub>/C) procedure, and one potential plateau in discharging (Fe<sub>0.95</sub>V<sub>0.05</sub>PO<sub>4</sub>/C → NaFe<sub>0.95</sub>V<sub>0.05</sub>PO<sub>4</sub>/C) procedure, are well visible when microcrystalline samples were investigated. The

appearance of two plateaus during desodiation process, indicating the two-phase equilibria, was ascribed to the formation of an intermediate phase  $\text{Na}_{\sim 0.7}\text{Fe}_{0.95}\text{V}_{0.05}\text{PO}_4$  [3]. In Figure 1. the plateaus can be barely observed. The disappearance of two-phase equilibria plateaus, indicates more pronounced role of surface against bulk reaction [4] caused by the nanoparticulate nature of the electrode material. In order to outline charge/disharge plateaus more clearly, the first derivation of chronopotentiometric curve ( $dQ/dV$ ) was plotted in Fig. 1 (right). The double-peak shape in both desodiation and sodiation directions confirm that sodiation proceeds through two stages, analogously to the desodiation.

In order to verify the sodiation/desodiation behavior of  $\text{NaFe}_{0.95}\text{V}_{0.05}\text{PO}_4/\text{C}$ , its cyclic voltammogram in  $\text{NaNO}_3$ , was also measured (Fig. 2). Two anodic peaks (at  $\sim 0.034$  V and  $\sim 0.24$  V vs. SCE) which correspond to desodiation process, and one cathodic peak ( $\sim -0.13$  V vs. SCE) corresponding to sodiation process are clearly visible. These redox peaks are well-documented in the literature for  $\text{NaFePO}_4$ , in both organic and aqueous electrolytes [3]. Two adjacent anodic peaks corresponds to the phase transition from  $\text{NaFe}_{0.95}\text{V}_{0.05}\text{PO}_4$  to  $\text{Na}_{\sim 0.7}\text{Fe}_{0.95}\text{V}_{0.05}\text{PO}_4$  and a phase transition from  $\text{Na}_{\sim 0.7}\text{Fe}_{0.95}\text{V}_{0.05}\text{PO}_4$  to  $\text{Fe}_{0.95}\text{V}_{0.05}\text{PO}_4$ , respectively, while reduction peak allegedly corresponds to the direct  $\text{Fe}_{0.95}\text{V}_{0.05}\text{PO}_4 \rightarrow \text{NaFe}_{0.95}\text{V}_{0.05}\text{PO}_4$  phase transition [4].

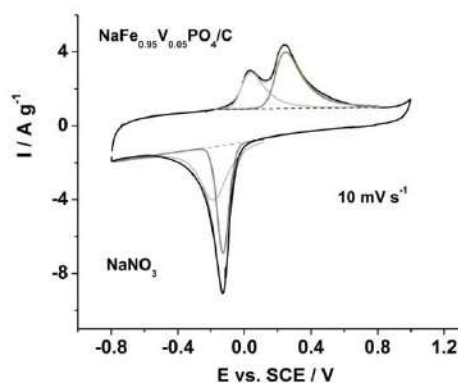


**Figure 2.** The CV redox peaks of  $\text{NaFe}_{0.95}\text{V}_{0.05}\text{PO}_4$  in  $\text{NaNO}_3$  and their deconvoluted peaks.

The one-stage sodiation is explained in a way that the overvoltage required for the first phase transition  $\text{Fe}_{0.95}\text{V}_{0.05}\text{PO}_4 \rightarrow \text{Na}_{\sim 0.7}\text{Fe}_{0.95}\text{V}_{0.05}\text{PO}_4$  (13% difference in unit cell volume) is as high as necessary to overcome the second phase transition  $\text{Na}_{\sim 0.7}\text{Fe}_{0.95}\text{V}_{0.05}\text{PO}_4 \rightarrow \text{NaFe}_{0.95}\text{V}_{0.05}\text{PO}_4$  (3%

difference in the unit cell volume). However, having in mind the conclusion derived from Fig.1 (right), we performed careful deconvolution of the cathodic peak of the cyclic voltammogram, which revealed that the sodiation proceeds also through the two phase transformations. Figure 2 illustrates the deconvoluted CV peaks. This means, the sodiation  $\text{Fe}_{0.95}\text{V}_{0.05}\text{PO}_4 \rightarrow \text{NaFe}_{0.95}\text{V}_{0.05}\text{PO}_4$  goes also through the intermediate stage  $\text{Na}_{\sim 0.7}\text{Fe}_{0.95}\text{V}_{0.05}\text{PO}_4$ . Also, the nature of each of two individual phase transitions can be predicted by the shape of deconvoluted CV peaks. Sharp and high peak is indicative of diffusion-controlled process (belonging to intercalation) while the broad peaks indicate the dominance of surface redox process (pseudocapacitance) [4].

This is the first approach to deconvolute CV curve of an intercalation process. The deconvolution method was found to be an effective way of kinetic analysis of the redox processes taking place at close potentials.

## CONCLUSION

Olivine  $\text{NaFe}_{0.95}\text{V}_{0.05}\text{PO}_4/\text{C}$  was successfully obtained by the aqueous electrochemical displacement method from  $\text{LiFe}_{0.95}\text{V}_{0.05}\text{PO}_4/\text{C}$ . High sodium storage capacity of  $\text{NaFe}_{0.95}\text{V}_{0.05}\text{PO}_4/\text{C}$ , measured in  $\text{NaNO}_3$ , shows that this material is a promising candidate for sodium aqueous rechargeable batteries. We checked in this study its strange behavior following from cyclic voltammetry, that desodiation proceeds as two-stage process while sodiation proceeds as only one-stage process. By deconvolution of cathodic (sodiation) peak, we evidenced that sodiation nevertheless presents also two-stage process. Both stages take place at close potentials, thus offering the impression of an unique stage.

### *Acknowledgement:*

This work was supported by the Ministry of Education, Sciences and Technological Development of the Republic of Serbia (Project III 45014 and 172015)

## REFERENCES

- [1] V. Palomeras, P. Serras, I. Villaluenga, K. Hueso, J. Carretero-González, T. Rojo, *Energy Environ. Sci.* 2012, **5**, 5884–5901.
- [2] M. Vujković, D. Jugović, M. Mitrić, I. Stojković, N. Cvjetičanin, S. Mentus, *Electrochimica Acta*, 2013, **109**, 835-842.
- [3] Y. Fang, Qi. Li, L. Xiao, X. Ai, H. Yang, Y. Cao, *ACS Appl. Mater. Interfaces*, 2015, **7**, 17977-17984.
- [4] M. Sussman, A. Yasin, G. Demopoulos, *J. Power Sources* 2014, **272**, 58-67.

## ELECTROCATALYTIC APPLICATION OF GOLD-POLYANILINE NANOCOMPOSITE

U. Bogdanović,<sup>1</sup> V. Vodnik,<sup>1</sup> I. Pašti,<sup>2</sup> G. Ćirić-Marjanović,<sup>2</sup> M. Mitrić,<sup>1</sup>  
and S. P. Ahrenkiel<sup>3</sup>

<sup>1</sup>*Vinča Institute of Nuclear Sciences, University of Belgrade, P. O. Box 522,  
11001 Belgrade, Serbia (una.bogdanovic@gmail.com)*

<sup>2</sup>*Faculty of Physical Chemistry, University of Belgrade, Studentski trg  
12-16, 11158 Belgrade, Serbia*

<sup>3</sup>*South Dakota School of Mines and Technology, 501 E. Saint Joseph St.,  
Rapid City, SD 57701, USA*

### ABSTRACT

Gold-polyaniline (Au-PANI) nanocomposite, with granular morphology of PANI and rod-like Au nanoparticles (NPs) as dominant structure distributed in it, was prepared by interfacial polymerization method in an immiscible water/toluene biphasic system. Simultaneously with the aniline polymerization to polyaniline (PANI) by  $\text{HAuCl}_4$ , as an oxidant, AuNPs are formed. Au-PANI composite as green precipitate is collected from aqueous phase. Polyaniline in the composite is in the conductive emeraldine salt form (PANI-ES), with high amount of Au (28.85 wt %). Nanocomposite showed great electrocatalytic activity towards the electrochemical  $\text{O}_2$  reduction reaction (ORR), with high ORR onset potential and high selectivity for  $\text{O}_2$  reduction to water. This makes it a good candidate for a new class of Pt-free ORR catalyst.

### INTRODUCTION

In order to obtain new functional materials, nanocomposites, conductive polymer PANI with excellent optical, electrical and morphological properties, has been combined with metal nanoparticles, such as AuNPs [1-3]. By combining these two components, nanocomposite materials were created, which possess the merits of their organic and inorganic components, and may also exhibit new properties that one component does not have. The interaction between them is important from an applications point of view in various electronic devices with regard to the charge transfer at their regions of contact. In this paper we present Au-PANI nanocomposite prepared by simple method based on the oxidizing properties of  $\text{HAuCl}_4$ , which initiates the polymerization process of aniline, but at the interface of water/toluene biphasic system [1]. This approach is

based on the fact that  $\text{Au}^{3+}$  ions in water phase can oxidize aniline due to their standard reduction potential (+1.498 V), and simultaneously aniline in toluene phase is used as reductant to prepare AuNPs. The aim of this work was to synthesize Au–PANI nanocomposite with PANI chains in its doped, ES form, with high amount of AuNPs in it, in order to improve its electrical conductivity and develop highly active Pt-free ORR catalyst with appreciable catalytic performance.

### EXPERIMENTAL

10 ml of 100 mM aniline in toluene was placed into a round bottom flask containing 10 ml of 50 mM  $\text{HAuCl}_4$  in water. The system was stirred for 20 h. As the reaction proceeds, the color of the lower water phase changes to deep green, indicating the formation of conductive PANI–ES, while due to formation of aniline oligomers as byproducts, the color of the upper toluene phase turns to orange. In order to collect the green powder of composite, the water phase was first filtered, and then the collected precipitate was rinsed with 5 mM aqueous solution of sulphuric acid and dried under vacuum at 60 °C for 3 h. The content of gold in Au–PANI nanocomposite determined by inductively coupled plasma atomic emission spectrometer was 28.85 wt %. Electrochemical activity of the nanocomposite toward the electrochemical ORR was examined by rotating disk electrode (RDE) voltammetry in  $\text{O}_2$  saturated 0.1 M KOH, in a one-compartment three-electrode electrochemical cell with wide Pt foil as a counter electrode and a saturated calomel electrode (SCE) as a reference electrode [see details in ref 1].

### RESULTS AND DISCUSSION

Molar ratio of  $\text{Au}^{3+}$  to aniline plays a significant role in controlling the reaction products. It was found that optimal molar concentration ratio of reactants  $\text{Au}^{3+}$  and aniline for the formation of conductive nanocomposite with dispersed AuNPs is 1:2, which is indicated by the absorption spectrum of Au-PANI nanocomposite water dispersion, obtained after isolation process (Fig. 1a Inset). Wide band consisting of two superimposed peaks at 350 nm ( $\pi$ – $\pi^*$  electron transition within benzenoid rings) and 440 nm (polaron– $\pi^*$  transition of PANI) and second band at 750 nm ( $\pi$ –polaron transition of PANI) confirm the formation of PANI□ES form [1,3]. It can also be seen that absorption band of AuNPs is not observed (Fig. 1a Inset), similar to our previous report [2], due to AuNPs interaction with PANI chains, through the charge transfer. In the polymerization process,  $\text{H}^+$  ions from chloroauric acid first protonates the aniline monomers to radical cations, while  $\text{AuCl}_4^-$  act as oxidizing agent that oxidize these cations. Each

polymerization step is accompanied by the release of electrons that can reduce the  $\text{Au}^{3+}$  ions to Au atoms. As the reaction proceeds, PANI forms in its doped, hydrophilic emeraldine salt form, and rapidly move away from the interface diffusing into the water layer. PANI chains in nanocomposite are organized in granular structures (Fig 1a), due to polymerization conditions. Namely, initial reactants concentrations are high, and  $\text{HAuCl}_4$  is a strong oxidizing agent (high electrode potential) which provides short induction period of reaction and fast polymerization process, causing agglomeration of aniline phenazine segments nuclei to granules. These quasi-spherical formations are found in the range of 64-400 nm. TEM measurements indicated that Au nanorods with 10 nm in diameter are dominated nanostructures in composite (Fig 1b).

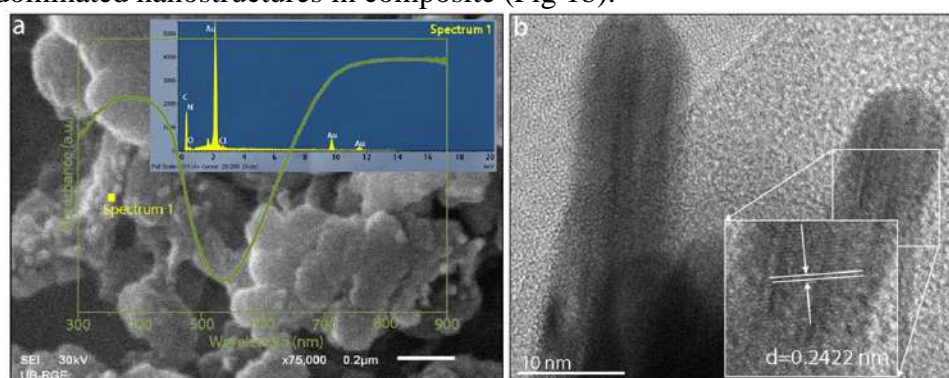


**Figure 1.** a) SEM image of Au–PANI nanocomposite with EDX and absorption spectrum; b) TEM image of nanocomposite

It was found that electrical conductivity of the nanocomposite (1.19 S/cm) is four-fold higher than that of the PANI itself (0.29 S/cm) [3]. More conductive Au nanorods – conductive nodes, dispersed in less conductive PANI matrix – conductive cables, enables formation of infinitely long conductive pathways and consequently drastically increase the conductivity.

The results of electrocatalytic activity of the Au–PANI, showed that nanocomposite, as electrocatalyst, had much higher ORR onset potential (Fig. 2a) due to fast charge transfer kinetics compared to similar nanocomposite reported so far [2], which contained exceedingly high Au content of 97 wt %. Furthermore, based on K–L analysis (Fig. 2b), evaluated number of electrons consumed per  $\text{O}_2$  molecule was found to be 2.25–3.2, which indicated that Au–PANI nanocomposite provided high selectivity for  $\text{O}_2$  reduction to water ( $\text{OH}^-$ ). This led us to conclude that the presence of PANI in this composite enhances Au surface oxophilicity, facilitating charge transfer kinetics and ORR selectivity to  $\text{OH}^-$ .

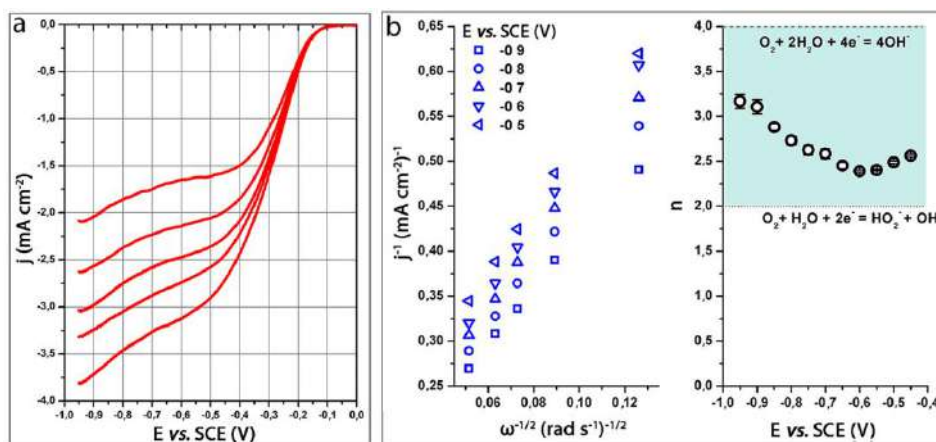


**Figure 2.** a) ORR RDE polarization curves recorded at different electrode rotation rates (600, 1200, 1800, 2400 and 3600 rpm); b) Koutecky–Levich (K–L) plots (left) and evaluated number of electrons consumed *per* O<sub>2</sub> molecule in the potential range  $-0.95$  to  $-0.45$  V vs. SCE (right).

## CONCLUSION

A novel nanomaterial presented in this paper, Au–PANI nanocomposite, with granular morphology and incorporated Au nanorods, shows relatively high electrical conductivity due to formation of long “infinite” conductive pathways of PANI chains. Moreover, compared to other Au–based ORR catalysts reported so far, Au–PANI composite provided excellent electrocatalytic activity towards electrochemical O<sub>2</sub> reduction to water (OH<sup>-</sup>), which makes it a promising candidate for a new class of Pt–free ORR catalyst.

## Acknowledgement

Financial support was granted by the Ministry of Education, Science and Technological Development of the Republic of Serbia (Projects 45020 and 172043). Contributions from South Dakota School of Mines and Technology were supported by the U.S. Department of Energy, contract no. DE–FG02–08ER64624.

## REFERENCES

- [1] U. Bogdanović, I. A. Pašti, G. Ćirić-Marjanović, M. Mitrić, S. P. Ahrenkiel, V. V. Vodnik, *ACS Applied Materials & Interfaces*, 2015, **7**, 28393–28403.
- [2] J. Song, J. Yuan, F. Li, D. Han, J. Song, L. Niu, *Journal of Solid State Electrochemistry*, 2010, **14**, 1915–1922.
- [3] U. Bogdanović, V. Vodnik, S. P. Ahrenkiel, M. Stoiljković, G. Ćirić-Marjanović, J. M. Nedeljković, *Synthetic Metals*, 2014, **195**, 122–131.

## POLAROGRAPHIC INVESTIGATION OF VANADIUM MONOMER UPTAKE/ REDUCTION IN PHYCOMYCES BLAKESLEEANUS MYCELIUM

M. Hadžibrahimović<sup>1</sup>, D. Sužnjević<sup>2</sup>, F. Pastor<sup>3</sup>, J. Zakrzewska<sup>2</sup>, M. Zičić<sup>4</sup>  
and M. Živić<sup>5</sup>

<sup>1</sup>*State University of Novi Pazar, Department of Biomedical Sciences, Vuka Karadžića bb, 36300 Novi Pazar, Serbia*

<sup>2</sup>*Institute of General and Physical Chemistry, Studentski trg 12-16, 11000 Belgrade, Serbia.*

<sup>3</sup>*University of Belgrade, Faculty of Chemistry, Studentski trg 12-16, 11000 Belgrade, Serbia.*

<sup>4</sup>*Institute for Multidisciplinary Research, University of Belgrade, Kneza Višeslava 1, 11030 Belgrade, Serbia.*

<sup>5</sup>*University of Belgrade Faculty of Biology, Studentski trg 16, 11000 Belgrade, Serbia. (mzivic@bio.bg.ac.rs)*

### ABSTRACT

The behavior of vanadate ( $V^{5+}$ ) and vanadyl ( $V^{4+}$ ) was investigated in 24h old mycelium of fungus *P. blakesleeanus* using polarography. The results showed that *P. blakesleeanus* is able to uptake both vanadium forms, and indicated negligible reduction of  $V^{5+}$  monomer.

### INTRODUCTION

We have already proposed that in *P. blakesleeanus* mycelium, tetramer is  $V^{5+}$  species preferentially reduced by membrane enzyme with ferricyanide reductase activity (FRA) [1]. We have also determined that both,  $V^{5+}$  and  $V^{4+}$  are present in *P. blakesleeanus* cells after  $V^{5+}$  treatment [2]. However, in all previous experiments  $V^{5+}$  was added at concentration, when various  $V^{5+}$  oligomeric species are present in solution [3], and monomer reduction could not be determine. Vanadate monomer is targeting as the one entering the cell, therefore here we presented polarographic measurements of  $V^{5+}$  reduction/uptake by *P. blakesleeanus* as this method enables measurements at low  $V^{5+}$  concentration (below 1mM) when the monomer is the only  $V^{5+}$  species in solution. The polarographic measurements of  $V^{5+}/V^{4+}$  are scare, while that with living organism as reducing factor are almost completely missing.

## EXPERIMENTAL PROCEDURES

The wild-type strain of the fungus *P. blakesleeanus* (Burgeff) (NRRL 1555(-)) was used, and cultivated as described previously [4].

The direct current polarography (DCP) curves were recorded by Princeton Applied Research (PAR) 174A Polarographic Analyzer equipped with Houston instrument, Omnigraphic 2000 X-Y recorder. DCP experiments were performed in a mixture: of 18 ml of HEPES (10 mM, pH 7.2) and 2 ml of mycelium suspension (containing about 20 mg mycelium dry weight), with addition of different concentration of  $V^{5+}$  or  $V^{4+}$  (0.1 – 1 mM).

## RESULTS

DCP curves of  $V^{5+}$  have different characteristic dependently on electrolyte used for measurements and pH [5]. Therefore, DCP curves of different  $V^{5+}$  concentration (0.1 – 1 mM) in HEPES, pH 7.2, were recorded at first (Fig. 1A). To elucidate the contribution of various reduction processes, derived from complex vanadium chemistry, we have also recorded DCP curves for different concentration of  $V^{4+}$  under similar condition, and results are shown in Fig. 1B. The resemblance of  $E_{1/2}$  values (around -1.1 V for  $V^{4+}$  and  $V^{5+}$ ) and differences of current amplitude ( $iD$ ) are clearly visible Fig. 1C.

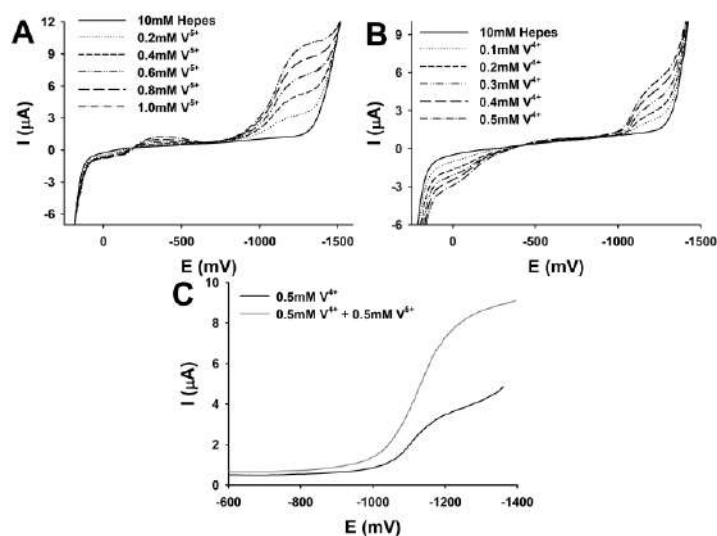


**Figure 1.** DCP curves of different concentration of vanadate (A), vanadyl (B); recorded in 10mM Hepes, pH 7.2; (C) after simultaneous addition of 0.5 mM of both  $V^{5+}$  and  $V^{4+}$ .

The recorded DCP curves of  $V^{5+}$  (1 mM) or  $V^{4+}$  (0.5 mM) added into the suspension of *P. blakesleeanus* mycelium differs from that obtained in HEPES buffer, as can be seen from Figure 2.

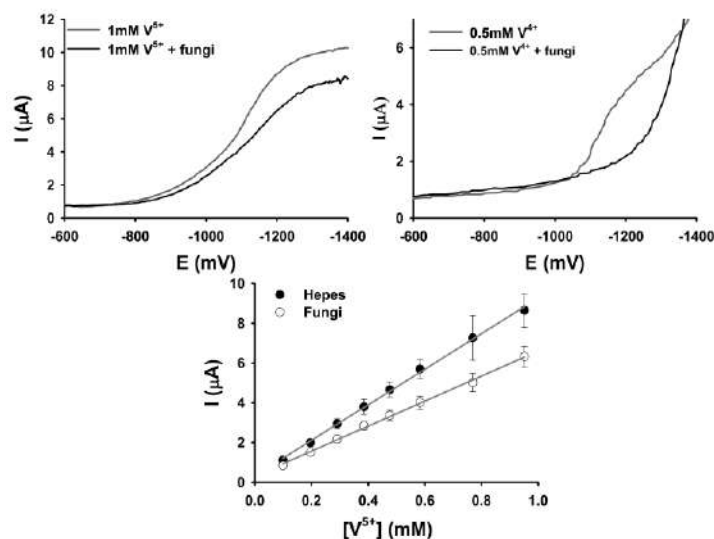


**Figure 2.** The cathodic part of DCP curves obtained after vanadate (A); and vanadyl (B), addition to the mycelial suspension. (C) Dependency of  $iD$  on concentration of added  $V^{5+}$  obtained in HEPES buffer (black circles) and mycelial suspension (open circles).

The main effect observed after addition of various concentration of  $V^{5+}$  into *P. blakesleeanus* mycelium suspension was the considerable lowering of  $iD$ , about 23% comparing to that in buffer (Fig. 2A, C). The comparison of concentration dependency of  $iD$  of this polarographic wave in buffer and fungal suspension is given in Fig. 2C. The linear dependency was obtained in the presence of mycelium, in whole investigated concentration range. This indicated that even at the highest applied  $V^{5+}$  concentration (1 mM), the reduction/uptake capacity of the fungal cell was not saturated.

Addition of different  $V^{4+}$  concentrations (0.1-0.5 mM) into mycelium suspension has as result complete disappearance of the polarographic wave (Fig. 2B). Such result indicates that *P. blakesleeanus* is capable to uptake all added  $V^{4+}$  i.e., removed it from external solution.

Consequently, the results obtained for  $V^{5+}$  in *P. blakesleeanus* mycelium suspension (Fig. 2A, C) indicate that uptake of  $V^{5+}$  monomer prevails its reduction to  $V^{4+}$ , when taking into account similar position of  $V^{4+}/V^{5+}$  waves (Fig.1C) and capability of mycelium for  $V^{4+}$  uptake (Fig.2.B).

***Acknowledgement***

Supported by Serbian Ministry of Education, Science and Technological Development grant No. 173040.

**REFERENCE**

- [1] M. Žižić, Z. Miladinović, M. Stanić, M. Hadžibrahimović, M. Živić, J. Zakrzewska, *Res. Microbiol.*, 2016, doi:10.1016/j.resmic.2016.04.012
- [2] M. Žižić, T. Dučić, D. Grolimund, D.V. Bajuk-Bogdanović, M. Nikolić, M. Stanić, S. Križak, J. Zakrzewska, *Anal. Bioanal. Chem.*, 2015, **407**, 7487-7496.
- [3] D. Rehder, *Bioinorganic vanadium chemistry*. J. Wiley and Sons, Chichester, New York, 2008.
- [4] M. Žižić, M. Živić, V. Maksimović, M. Stanić, S. Križak, T. Cvetić Antić, J. Zakrzewska, *Plos One*, 2014, **9**, 102849.
- [5] M. S. Qureshi, A. R. M. Yusoff, A. Shah, A. Nafady, Sirajuddin, *Talanta* 2015, **132**, 541–547.

## ELECTROCHEMICAL PROPERTIES OF $\text{Na}_{1.2}\text{V}_3\text{O}_8/\text{C}$ COMPOSITE IN $\text{LiNO}_3$ , $\text{NaNO}_3$ AND $\text{Mg}(\text{NO}_3)_2$ AQUEOUS SOLUTION

L. Radisavljević<sup>1</sup>, M. Vujković<sup>1</sup>, I. Stojković Simatović<sup>1</sup> and S. Mentus<sup>1,2</sup>

<sup>1</sup>*Faculty of Physical Chemistry, University of Belgrade, Studentski trg 12-16, P.O. Box 137, Belgrade, Serbia. (ivana@ffh.bg.ac.rs)*

<sup>2</sup>*The Serbian Academy of Science and Arts, Knez Mihailova 35, 11158 Belgrade, Serbia*

### ABSTRACT

In this paper, the  $\text{Na}_{1.2}\text{V}_3\text{O}_8$ , in the form of nanodispersed  $\text{Na}_{1.2}\text{V}_3\text{O}_8/\text{C}$  composite, was synthesized by a sol-gel method. Carbon was added, during the synthesis procedure, in order to provide a better electrical contact between oxide particles. The synthesized powder was characterized by X-ray powder diffraction (XRD) and thermogravimetric analysis (TGA) while its electrochemical performances were investigated by cycling voltammetry (CV) at various scan rates. The initial discharge capacities were found to be 132.8, 100.4 and 111.8  $\text{mA h g}^{-1}$  in the aqueous solutions of  $\text{LiNO}_3$ ,  $\text{NaNO}_3$  and  $\text{Mg}(\text{NO}_3)_2$ , respectively. The synthesized composite has the best cycling stability in the solution of  $\text{Mg}(\text{NO}_3)_2$ .

### INTRODUCTION

Although Li-ion batteries have excellent charging/discharging performances that are necessary for the high technology applications, the high cost and small abundance of lithium are the main disadvantages of these batteries. For this reason, more attention has been given to the sodium and magnesium batteries. These batteries work on the same principle as lithium batteries. The materials used in sodium and magnesium batteries are the same or similar to those used in lithium batteries:  $\text{NaMnO}_2$ ,  $\text{Na}_x\text{VO}_2$ ,  $\text{Na}_{1.2}\text{V}_3\text{O}_8$ ,  $\text{LiFePO}_4$ . To improve the initial capacity of these materials and their stability during the cycling, the carbon is often added during the synthesis to increase the conductivity of the material [1-3]. In order to reduce the price and from ecological reasons, there is plenty of research done on this type of batteries in aqueous electrolytes.

In this work, the  $\text{Na}_{1.2}\text{V}_3\text{O}_8/\text{C}$  composite was successfully synthesized as a potential anode material for aqueous lithium, sodium and magnesium batteries. The source of carbon was a highly conductive and stable LITX200 carbon ( $S_{\text{BET}}=200 \text{ m}^2 \text{ g}^{-1}$ ), which is used as a conductive additive for Li-ion

batteries [3]. The purpose was to see the influence of LITX on the  $\text{Na}_{1.2}\text{V}_3\text{O}_8$  electrochemical behavior in an aqueous medium, by adding it during the synthesis route.

### EXPERIMENTAL

$\text{Na}_{1.2}\text{V}_3\text{O}_8/\text{C}$  composite was prepared by precipitation in aqueous solution. Crystalline  $\text{V}_2\text{O}_5$  (Merck, p.a.) was dissolved in 10 % aqueous solution of hydrogen peroxide. Under continuous stirring, the solution of NaOH (Merck, p.a.) was added in an amount that provides the stoichiometry of  $\text{Na}_{1.2}\text{V}_3\text{O}_8$ . The carbon (LITX200) was added and the  $\text{Na}_{1.2}\text{V}_3\text{O}_8$ :LITX200 mass ratio was 10:1. The obtained solution was stored in air at ambient temperature until the solvent was evaporated. The resulting solid powder precursor was heated at 400 °C in argon atmosphere for 6 h.

The X-ray diffractograms (XRPD) were recorded using  $\text{CuK}_{\alpha 1,2}$  radiation in  $2\theta$  range 10-70° with the 0.05° step and 2 seconds exposition time. Thermogravimetric analysis was carried out in the air atmosphere using the TA SDT device, model 2960, with the rate of 10 °C  $\text{min}^{-1}$ .

Electrochemical performances were tested by cyclic voltammetry using a Gamry PCI4/300 potentiostat/galvanostat/ZRA) at various scan rates in saturated aqueous solutions of  $\text{LiNO}_3$ ,  $\text{NaNO}_3$  and  $\text{Mg}(\text{NO}_3)_2$ . In order to prepare an electrode, the synthesized material, LITX200 and PVDF binder were mixed in mass ratio of 85:10:5, respectively. After homogenization in *N*-methyl-2-pyrrolidone in an ultrasonic bath, the

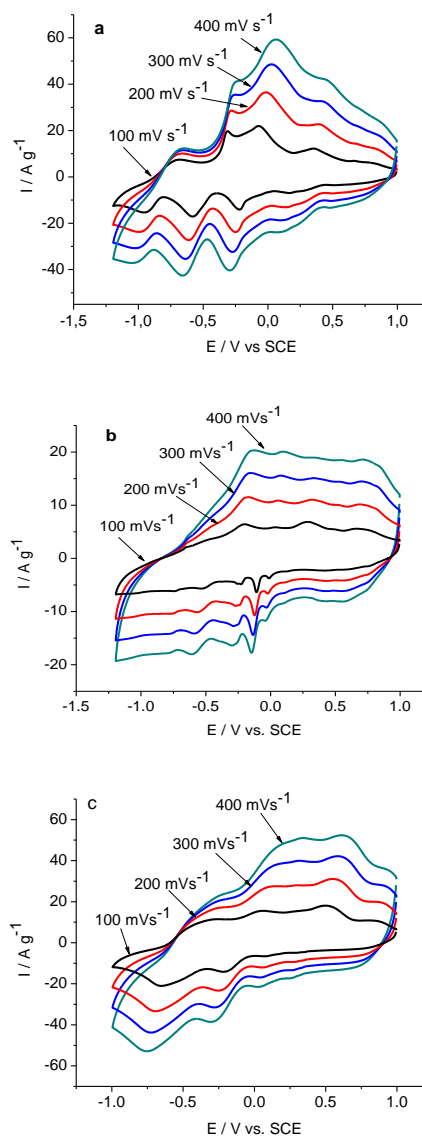


**Figure 1.** CVs of  $\text{Na}_{1.2}\text{V}_3\text{O}_8/\text{C}$  in aqueous solution of a)  $\text{LiNO}_3$ , b)  $\text{NaNO}_3$  and c)  $\text{Mg}(\text{NO}_3)_2$  at the scan rates of 100, 200, 300 and 400 mV

mixture was applied on glassy carbon rod and dried under vacuum  $10^{-2}$  mbar at  $140^{\circ}\text{C}$  for 12 hours. A platinum foil was used as a counter electrode. The potentials, ranged from -1.2 to 1 V were measured against the saturated calomel reference electrode (SCE). Faradaic discharge capacity was calculated by coulometric analysis of cyclovoltammetric curves.

## RESULTS AND DISCUSSION

According to the TGA analysis, the combustion of carbon started at  $400^{\circ}\text{C}$ . For this reason, the precursor powder was annealed at  $400^{\circ}\text{C}$  in argon atmosphere. The sample after thermal treatment contained 7 mass% of carbon. XRPD analysis of the product evidenced that all reflections can be indexed to a monoclinic  $\text{Na}_{1.2}\text{V}_3\text{O}_8$  phase, JCPDS 245225 [1]. Also, the mixtures of different vanadium oxides were present.

Cyclic voltammograms (CVs) of  $\text{Na}_{1.2}\text{V}_3\text{O}_8/\text{C}$  recorded in saturated aqueous solution of  $\text{LiNO}_3$ ,  $\text{NaNO}_3$  and  $\text{Mg}(\text{NO}_3)_2$  at high scan rates ranged from 100 to  $400\text{ mVs}^{-1}$ , are shown on Figure 1a-c, respectively. In all three solutions, the shape of CVs and position of peaks are similar at all scan rates. That means that process of intercalation/deintercalation of  $\text{Li}^+$ ,  $\text{Na}^+$  and  $\text{Mg}^{2+}$  are reversible. This indicates that synthesized material can be used in lithium, sodium and magnesium batteries at high rates of charging/discharging. The impact of the LITX200 addition, during the synthesis, is the most significant in the case of intercalation/deintercalation  $\text{Mg}^{2+}$  since the currents of the response increase about three times [1].

The specific discharge capacity of  $\text{Na}_{1.2}\text{V}_3\text{O}_8/\text{C}$ , obtained from the first ten cycles in aqueous solutions of  $\text{LiNO}_3$ ,  $\text{NaNO}_3$  and  $\text{Mg}(\text{NO}_3)_2$  are shown in

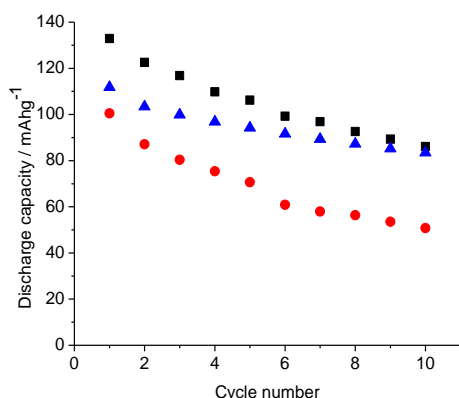


**Figure 2.** Discharge capacity of  $\text{Na}_{1.2}\text{V}_3\text{O}_8/\text{C}$  during the ten cycles in  $\text{LiNO}_3$  (■),  $\text{NaNO}_3$  (●) and  $\text{Mg}(\text{NO}_3)_2$  (▲)

Figure 2. The specific capacity ( $\text{mA h g}^{-1}$ ) was calculated from the area under the redox peaks of CVs, recorded by  $20\text{ mV s}^{-1}$  scan rate, which is equivalent to 33 C. It is calculated according to the equation  $C = (\int I \cdot V \cdot dV) / (m \cdot v)$ , where  $I$  is the measured current,  $V$  is the potential,  $m$  is the mass of electroactive material,  $v$  is the scan rate. It is known that the redox peak area, which is normalized with

the respect to the scan rate, decreases with the increase of scan rate. The initial discharge capacities of  $\text{Na}_{1.2}\text{V}_3\text{O}_8/\text{C}$  in  $\text{LiNO}_3$ ,  $\text{NaNO}_3$  and  $\text{Mg}(\text{NO}_3)_2$  solution are 132.8, 100.4 and 111.8  $\text{mA h g}^{-1}$  while in the case of  $\text{Na}_{1.2}\text{V}_3\text{O}_8$  the initial capacities were about 50, 30 and 30  $\text{mA h g}^{-1}$ , respectively [1]. This shows that the addition of carbon during the synthesis led to the improvement of the initial capacity. The initial capacity of composite is the highest in the solution of  $\text{LiNO}_3$ , but the capacity fade after 10 cycles was found to be 35.3% of the initial value. The least initial capacity and the largest drop capacity is in solution of  $\text{NaNO}_3$ . The least capacity fade (about 25%) after ten cycles is in solution of  $\text{Mg}(\text{NO}_3)_2$ . The decrease in capacity is due to the dissolution of a part of vanadium from the material, but could also be the result of structural changes during intercalation/deintercalation ions. Changes in the structure and the presence of other phases in the material result in dissolution of vanadium from materials which are manifested during the cycling as color change of the electrolyte (appearance of a green color). During the cycling, material demonstrated high efficiency (the ratio of the charging and discharging capacity) amounting to ~95% in all solutions.

## CONCLUSION

The  $\text{Na}_{1.2}\text{V}_3\text{O}_8/\text{C}$  composite was synthesized by the sol-gel method. Intercalation/deintercalation of lithium, sodium and magnesium ions, in the synthesized composite are reversible at high scan rates indicating that the material can be used as the anode material in aqueous batteries. Addition of carbon during the synthesis has led to an increase in initial capacity. Material showed the most stable behavior during the cycling in a solution of  $\text{Mg}(\text{NO}_3)_2$ .

## Acknowledgement

This work was supported by the Ministry of Education, Sciences and Technological Development of the Republic of Serbia (Project III 45014) and SANU (Electrocatalysis in the contemporary process of energy conversion).

## REFERENCES

- [1] M. Vujković, B. S. Paunković, I. S. Simatović, M. Mitrić, C.A.C.Sequeira, S. Mentus, *Electrochimica Acta*, 2014, **147**, 167–175.
- [2] H. Pan, Y.-S. Hu, L. Chen, *Energy Environ. Sci.*, 2013, **6**, 2338-2360.
- [3] X. Qi, B. Blizanac, A. DuPasquier, M. Oljaca, J. Li, M. Winter, *Carbon*, 2013, **64**, 334-340.

## ELECTROANALYTICAL SENSING OF BROMIDES USING SILVER NANOPARTICLE ELECTOCATALYST

J. Milikić<sup>1</sup>, I. Stoševski<sup>1</sup>, J. Krstić<sup>2</sup>, Z. Kačarević–Popović<sup>2</sup>, Š. Miljanić<sup>1</sup>  
and B. Šljukić<sup>1</sup>

<sup>1</sup>*University of Belgrade, Faculty of Physical Chemistry, Studencki trg 12–16, 11158 Belgrade, Serbia. (biljka@ffh.bg.ac.rs)*

<sup>2</sup>*University of Belgrade, Vinča Institute of Nuclear Sciences, POB 522, 11001 Belgrade, Serbia.*

### ABSTRACT

Silver nanoparticles supported on carbon (AgNP/C) were prepared by the  $\gamma$ -radiation reduction method and characterised using transmission electron microscopy and X-ray diffraction. Subsequently, glassy carbon electrode was modified with the prepared AgNP/C and further characterized using electrochemical methods for possible application for sensing of bromide. AgNP/C proved to be highly active for bromide electrochemical detection.

### INTRODUCTION

Monitoring the level of bromide in water is now a days of great importance for the protection of both human health and environment. For instance, in the oxidative disinfection of drinking water with ozone or chlorine, bromide is oxidised to bromate, which can cause carcinoma [1,2]. Methods so far used or suggested for the detection of bromide (and other halogens) in water include neutron activation analysis, inductively coupled plasma–mass spectrometry and ion chromatography. Herein, electrochemical sensing of bromides is proposed, offering benefits of low cost, simplicity and rapidity.

### EXPERIMENTAL

**Electrocatalyst preparation.** Carbon-supported silver nanoparticles (AgNP/C) were synthesized by the  $\gamma$ -radiation reduction method using poly(vinyl alcohol) (PVA, mean molecular weight of 72 kDa, degree of hydrolysis of 99 %) as a stabilizer. Two aqueous solutions, one 4 wt.% PVA solution and the second with 0.4 M silver nitrate (AgNO<sub>3</sub>) and 0.2 M 2-propanol, were prepared in separated glasses and then mixed so that the weight ratio of Ag to PVA was 1:1. Vulcan XC 72R was added to the solution to obtain the weight ratio of Ag to C of 1:1. The obtained dispersion was homogenized ultrasonically, and then deaerated with argon for 20 min in an air-tight glass vessel, after which it was exposed to  $\gamma$ -rays

( $^{60}\text{Co}$  source) at the temperature of  $22^\circ\text{C}$ . The absorbed dose and the dose rate were  $710\text{ kGy}$  and  $12\text{ kGy h}^{-1}$ , respectively.

**Characterization.** Transmission electron microscopy (TEM) analysis was done using the JEOL JEM-1400Plus device, while the X-ray diffraction (XRD) analysis was done using Bruker D8 Advance Diffractometer (Cu  $K_{\alpha 1}$  radiation,  $\lambda = 0.1541\text{ nm}$ ).

**Electrochemical Characterization.** The working electrode was prepared as follows: 0.5 wt.% solution of gallic acid (GA) was added to the Ag dispersion, to obtain the molar ratio of GA to PVA of 8.2:1, after which the dispersion was diluted and the appropriate volume of 1 M HCl was added, in order to obtain HCl concentration of 0.1 M in the final dispersion.  $10\ \mu\text{L}$  of this dispersion was dropped on the glassy carbon electrode (GCE, 5 mm diameter, Pine Instruments, Co) so that the loading of Ag on the electrode was  $20\ \mu\text{g cm}^{-2}$ . Crosslinking of PVA with GA was achieved by HCl during the drying (under the nitrogen atmosphere), and gel that was formed acted as a binder.

The electrochemical characterisation of AgNP/C electrocatalyst was done by cyclic voltammetry (CV) in a conventional one-compartment glass cell of 100 mL volume connected to Gamry PCI4/750 potentiostat/galvanostat. Pt foil was employed as the counter electrode and a saturated calomel electrode (SCE, Radiometer Analytical) as a reference. All potentials within the paper are reported relative to the SCE. Electrochemical characterisation was performed in 0.1 M phosphate buffer, while bromide sensing was performed in 0.1 M  $\text{K}_2\text{SO}_4$  as supporting electrolyte.

## RESULTS AND DISCUSSION

A major advantage of radiation methods for the synthesis of metal nanoparticles is a homogenous reduction of metal ions throughout the solution. The radiation induced reduction of  $\text{Ag}^+$  starts with the radiolysis of water and formation of hydrated electrons, hydrogen and hydroxyl radicals ( $\text{H}^\bullet$  and  $\text{OH}^\bullet$ ). Hydrated electrons and  $\text{H}^\bullet$  radicals reduce  $\text{Ag}^+$  to  $\text{Ag}^0$ , which further dimerize when they encounter or associate with  $\text{Ag}^+$  and progressively grow yielding the formation of metal clusters and particles. The detailed mechanism of Ag NP formation by radiation methods has been explained by Belloni[3]. Since the  $\text{OH}^\bullet$  radicals can oxidize the metal atoms into a higher oxidation state and thus counterbalance the reduction, 2-propanol is used as a scavenger to convert them to 2-propanol radicals, which further act as strong reducing species.

The detailed XRD and TEM analysis of the carbon-supported Ag NPs obtained by the  $\gamma$ -radiation method was reported in our previous publication

[4], in which different Ag/C samples were investigated as electrocatalysts for the oxygen reduction and borohydride oxidation reaction. TEM analysis of Ag/C sample corresponding to the one prepared in this work in terms of the synthesis parameters and components content, revealed a crystallite size of 13.9 nm. XRD analysis revealed the formation of face centred cubic crystal structure of bulk metallic Ag (JCPDS File No. 89–3722). Furthermore, crystallite size determined by XRD was found to be 15 nm, which is in good agreement with the crystallite size obtained by TEM.

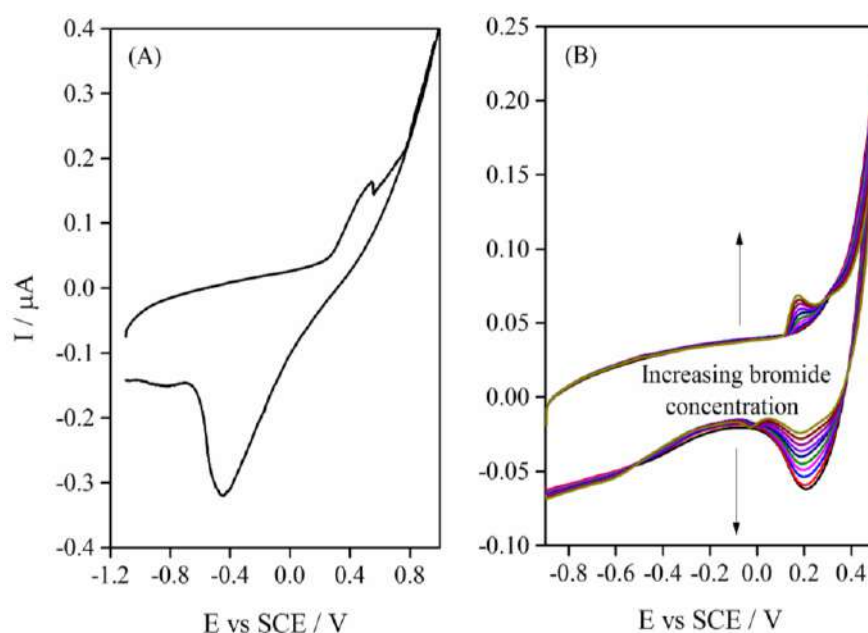


**Figure 1.** (A) CV of AgNP/C in pH 7 phosphate buffer at scan rate of  $200 \text{ mV s}^{-1}$ . (B) CVs of AgNP/C in  $0.1 \text{ M K}_2\text{SO}_4$  solution at scan rate of  $100 \text{ mV s}^{-1}$  with increasing bromide concentration.

The AgNP/C electrocatalyst was characterised by recording CV in  $0.1 \text{ M}$  phosphate buffer in the potential range from  $-1.1 \text{ V}$  to  $1.0 \text{ V}$  at scan rate of  $200 \text{ mV s}^{-1}$ . A peak of Ag surface oxide formation at ca.  $0.50 \text{ V}$  (Fig. 1A) could be observed on the anodic scan. Subsequently, a well-defined peak corresponding to the reduction of this oxide was observed at  $-0.44 \text{ V}$  on the cathodic scan [5].

The detection of bromide was initially studied in  $0.025 \text{ M KBr} + 0.1 \text{ M K}_2\text{SO}_4$  scanning the potential from  $-1.0 \text{ V}$  to  $0.9 \text{ V}$  at a rate of  $100 \text{ mV s}^{-1}$ . A peak originating from the formation of AgBr could be seen at ca.  $0.20 \text{ V}$  on the anodic scan (Fig. 1B) [5]. Accordingly, a well-defined cathodic peak

was observed at ca. 0.16 V corresponding to the reduction of formed AgBr. Subsequently, the possibility of quantitative determination of bromides with AgNP/C was addressed. Thereafter, 10 subsequent 50  $\mu\text{M}$  additions of KBr to 0.1 M  $\text{K}_2\text{SO}_4$  were done, with the solution being stirred after each addition by the electrode rotation. Increase of peak current ( $I_p$ ) could be observed with increase of KBr concentration ( $c$ ), with  $I_p$  vs  $c$  dependence resulting in a straight line. The limit of detection (LOD) of bromide with AgNP/C electrocatalyst was evaluated using the 3 sigma method

$$\text{LOD} = 3\sigma/b \quad (1)$$

where  $\sigma$  is the standard deviation of the  $y$ -coordinates from the line of best fit and  $b$  the slope of the same line. Thus the LOD was found to be 1.8  $\mu\text{M}$ . The obtained LOD is comparable or lower than LODs obtained using different electrode substrates (1.2 – 20  $\mu\text{M}$  range) [5], thus indicating high activity of AgNP/C electrocatalyst studied herein for bromide sensing.

## CONCLUSION

In this work synthesis of AgNP/C electrocatalyst was presented, followed by characterisation using transmission electron microscopy, X-ray diffraction and electrochemical techniques. AgNP/C demonstrated high activity for bromide electrooxidation, enabling its determination with low limit of detection of 1.8  $\mu\text{M}$ .

## Acknowledgement

The authors would like to thank the Ministry of Education, Science and Technological Development of the Republic of Serbia for financial support within projects III-45014 and III-45005.

## REFERENCES

- [1] K. Tagami, S. Uchida, *Chemosphere*, 2006, **65**, 2358–2365.
- [2] K. Tagami, S. Uchida, I. Hirai, H. Tsukada, H. Takeda, *Ana. Chimi. Acta*, 2006, **570**, 88–92.
- [3] J. Belloni, *Catal. Today*, 2006, **113**, 141–156.
- [4] I. Stoševski, J. Krstić, J. Milikić, B. Šljukić, Z. Kačarević–Popović, S. Mentus, Š. Miljanić, *Energy*, 2016, **101**, 79–90.
- [5] B. Šljukić, R. Baron, C. Salter, A. Crossley, R. G. Compton, *Anal. Chim. Acta*, 2007, **590**, 67–73.

*F - Biophysical Chemistry,  
EPR Investigations of bio-systems,  
Photochemistry, Radiation Chemistry*

*The Session F is dedicated  
to the professor Goran Bačić*



## ABOUT OUR PROFESSOR GORAN BAČIĆ



**Dr Goran Bačić, professor**

He received his PhD in 1985 from the Faculty of Physical Chemistry in Belgrade in the field of the use of nuclear magnetic resonance to determine the status of water and ions in biological systems. During 1985, he received a scholarship from the British Council, for the studies in the same area at Oxford University, United Kingdom. In the period from 1986 to 1988, he was a visiting researcher at the Medical Faculty of the University of Illinois, Urbana, USA. During this period, he worked with Dr. P. C. Lauterbur, winner of the Nobel Prize for Physiology and Medicine in 2003.

Goran Bačić is one of the pioneers of several techniques: electron paramagnetic resonance (EPR) oximetry, in vivo EPR measurements, EPR high-resolution microscopy of biological samples, as well as 2D / 3D EPR imaging. One of the founders of the World Association for EPR spectroscopy. From 1989 to 1992, he was head of the Center for Magnetic Resonance in Clinical Center of Serbia, where he worked on the education of Serbian radiologists and on development

of MR techniques, but also on clinical and fundamental research in the field of MRI. As a visiting professor he was at Dartmouth Medical School, Hanover, USA in the period 1992-1994, where he continued to develop EPR techniques and merging of EPR and MRI techniques in the study of various pathologies in experimental animals. From 1995 to 2003. worked as head of research at MRI at the Institute for Oncology and Radiology, primarily on the development of MRI technology for the detection and differentiation of various tumors. In addition, he worked on the EPR / NMR in vitro biological systems, dosimetry of ionizing radiation in radiotherapy, as well as the development of neural networks application for examination of radioactivity of environmental samples.

The last decade of his life dedicated to the research related to new MRI-based biomarkers for the diagnosis of neurodegenerative and malignant diseases, early identification of therapeutic response of tumors (especially breast cancer) to different types of chemotherapeutics, testing of new radioprotective agents and improving the application of EPR methods for monitoring free radicals in biological systems.

He has published over 130 papers in Scientific Journals on the SCI list and has over 1200 citations according to Scopus. He was one of the founders of the Society of Physical Chemists of Serbia, and a member of the Biophysical Society of Serbia and the International EPR Society. At the Faculty of Physical Chemistry he was responsible for the teaching of Biophysical Chemistry at the undergraduate level, as well as, Physicochemical methods in Biomedicine and Radiation Biology at doctoral studies. He was coordinator of the compulsory subjects in Biophysical Chemistry and Dynamics of non-equilibrium processes at the master degree.

Miloš Mojović, Marko Daković

*University of Belgrade,*

*Faculty of Physical Chemistry*

## MATHEMATICAL MODELING OF PLAQUE FORMATION AND PROGRESSION

N. Filipović<sup>1,2</sup>, D. Nikolić<sup>1,2</sup>, I. Saveljić<sup>1,2</sup>, Z. Milošević<sup>1,2</sup>, T Exarchos<sup>3</sup>, W. Pelosi<sup>4</sup> and O. Parodi<sup>4</sup>

<sup>1</sup>*Faculty of Engineering, University of Kragujevac, Sestre Janjića 6, 34000 Kragujevac, Serbia ([fica@kg.ac.rs](mailto:fica@kg.ac.rs))*

<sup>2</sup>*BioIRC, Bioengineering Research and Development Center, Prvoslava Stojanovića 6, 34000 Kragujevac, Serbia*

<sup>3</sup>*University of Ioannina, Ioannina, Greece*

<sup>4</sup>*National Research Council Pisa, Pisa, Italy*

### ABSTRACT

Atherosclerosis is a local process in the context of a systemic disease. Multiple factors contribute to plaque formation/progression/complication, by a complex interaction between biological and mechanical elements. Integrating coronary imaging techniques with finite element modelling (FEM) techniques allows for detailed examination of local morphological and biomechanical characteristics of atherosclerotic lesions that can assist a clinical therapy.

Mathematical model for plaque formation and progression is developed. The blood flow is modeled by the Navier-Stokes equations, together with the continuity equation. Mass transfer within the blood lumen and through the arterial wall is coupled with the blood flow and is modeled by the convection-diffusion equation. LDL transport in lumen of the vessel is described by Kedem-Katchalsky equations. The inflammatory process is solved using three additional reaction-diffusion partial differential equations.

Several patients' study predicts new plaque formation after at follow up which corresponds to size and plaque composition. Matching of plaque location, size and composition progression in time between experimental and computer model shows a potential benefit for future prediction of this vascular decease.

### INTRODUCTION

Atherosclerosis is an inflammatory disease that starts with intima alterations. Over the past decade, scientists come to appreciate a prominent role for inflammation in atherosclerosis. Formerly focused on luminal narrowing due to the bulk of atheroma, the current concepts recognize the

biological attributes of the atheroma as key determinants of its clinical significance [1].

Inflammatory process starts with penetration of low density lipoproteins (LDL) in the intima. This penetration, if too high, is followed by leucocyte recruitment in the intima (Figure 1). This process may participate in formation of the fatty streak, the initial lesion of atherosclerosis and then in formation of a plaque [2].

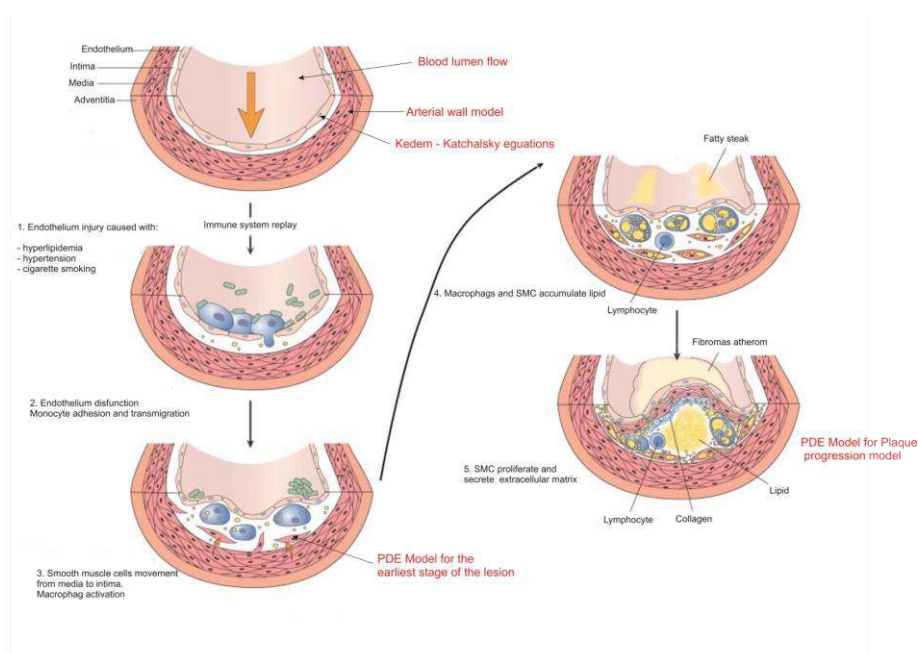


**Figure 1.** Atherosclerotic plaque development

Several mathematical models have recently been set up for the transport of macromolecules, such as low-density lipoproteins, from the arterial lumen to the arterial wall and inside the wall [3-5].

In this study we used mass transport of LDL through the wall and the simplified inflammatory process which is coupled with the Navier-Stokes equations, the Darcy equation for model blood filtration and Kedem-Katchalsky equations [6-7] for the solute and flux exchanges between the lumen and the intima. We developed system of three additional reaction-diffusion equations for the inflammatory process and lesion growth model in the intima. Some examples on real patient case are given as validation of the proposed mathematical model of plaque formation and progression.

## METHODS

In this section we present a continuum based approach for plaque formation and development in three-dimension. The governing equations and numerical procedures are given. The blood flow is simulated by the three-dimensional Navier-Stokes equations, together with the continuity equation

$$-\mu\nabla^2 u_l + \rho(u_l \cdot \nabla)u_l + \nabla p_l = 0 \quad (1)$$

$$\nabla u_l = 0 \quad (2)$$

where  $u_l$  is blood velocity in the lumen,  $p_l$  is the pressure,  $\mu$  is the dynamic viscosity of the blood, and  $\rho$  is the density of the blood.

Mass transfer in the blood lumen is coupled with the blood flow and modelled by the convection-diffusion equation as follows

$$\nabla \cdot (-D_l \nabla c_l + c_l u_l) = 0 \quad (3)$$

in the fluid domain, where  $c_l$  is the solute concentration in the blood lumen, and  $D_l$  is the solute diffusivity in the lumen.

Mass transfer in the arterial wall is coupled with the transmural flow and modelled by the convection-diffusion-reaction equation as follows

$$\nabla \cdot (-D_w \nabla c_w + k c_w u_w) = r_w c_w \quad (4)$$

in the wall domain, where  $c_w$  is the solute concentration in the arterial wall,  $D_w$  is the solute diffusivity in the arterial wall,  $K$  is the solute lag coefficient, and  $r_w$  is the consumption rate constant.

LDL transport in lumen of the vessel is coupled with Kedem-Katchalsky equations:

$$J_v = L_p (\Delta p - \sigma_d \Delta \pi) \quad (5)$$

$$J_s = P \Delta c + (1 - \sigma_f) J_v \bar{c} \quad (6)$$

where  $L_p$  is the hydraulic conductivity of the endothelium,  $\Delta c$  is the solute concentration difference across the endothelium,  $\Delta p$  is the pressure drop across the endothelium,  $\Delta \pi$  is the oncotic pressure difference across the endothelium,  $\sigma_d$  is the osmotic reflection coefficient,  $\sigma_f$  is the solvent reflection coefficient,  $P$  is the solute endothelial permeability, and  $\bar{c}$  is the mean endothelial concentration.

### Plaque formation and progression modelling – continuum approach

Continuum based methods is an efficient way for modelling the evolution of plaque. In our model, LDL concentration is first introduced into the system of partial differential equations as a boundary condition. The model simulates the inflammatory response formed at the initial stages of plaque formation.

Regarding the particle dynamics, the model is based on the involvement of LDL/oxidized LDL, monocytes and macrophages, and foam cells and extra cellular matrix. Reaction-diffusion differential equations are used to model these particle dynamics. The adhesion rate of the molecules depends on the local hemodynamics which is described by solving the Navier-Stokes equations. Intima LDL concentration is a function of the wall shear stress, while the adhesion of monocytes is a function of shear stress and VCAM. Finally, the alterations of the arterial wall are simulated. A finite element solver is used to solve the system of the equations.

The LDL penetration is defined by the convection-diffusion equation, while the endothelial permeability is shear stress dependent. This model produces results about the initial stages of the atherosclerotic plaque formation. More specifically, concentration of LDL is calculated on the artery wall and in the next step the oxidized LDL. Furthermore, monocytes and their modified form (macrophages) are also counted. Solution to the system provides to the user the concentration of foam cells created when a threshold on LDL concentration is reached.

The inflammatory process is modeled using three additional reaction-diffusion partial differential equations [8]:

$$\begin{aligned}\partial_t O &= d_1 \Delta O - k_1 O \cdot M \\ \partial_t M + \text{div}(v_w M) &= d_2 \Delta M - k_1 O \cdot M + S / (1 + S) \\ \partial_t S &= d_3 \Delta S - \lambda S + k_1 O \cdot M + \gamma(O - O^{thr})\end{aligned}\quad (7)$$

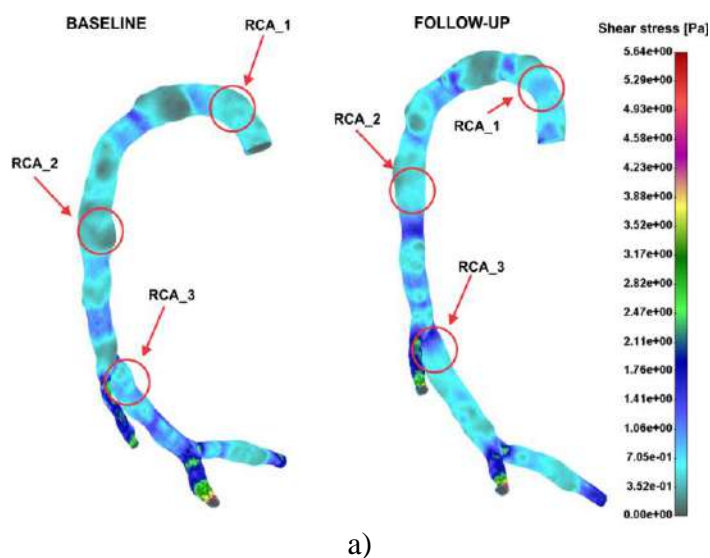
where  $O$  is the oxidized LDL in the wall,  $M$  and  $S$  are concentrations in the intima of macrophages and cytokines, respectively;  $d_1, d_2, d_3$  are the corresponding diffusion coefficients;  $\lambda$  and  $\gamma$  are degradation and LDL oxidized detection coefficients; and  $v_w$  is the inflammatory velocity of plaque growth [9], [10].

## RESULTS AND DISCUSSION

One case study for patient is presented for validation of the computer model. The clinical study was designed to expand, test and strengthen the indications already acquired in the previous coronary study. Patients with a previous CTA analysis were enrolled to repeat this examination (average follow-up time of >2 years). New onset coronary plaques were assessed by this approach, a novel finding respect to previous studies on this research line. The second study was focused on the anatomical non-invasive assessment of the coronary tree, using coronary CTA, with the same data collection of clinical and biochemical features performed in the former clinical study. To discriminate the best predictors of stenosis progression a

multivariate logistic analysis we put in the model the following baseline variables and the relative delta values of follow-up and baseline measurements (percentage and absolute value): Framingham Risk Score, left ventricular ejection fraction (LVEF), total cholesterol, HDL, LDL, creatinine, glucose, E-Selectin, ICAM-1, VCAM-1; diabetes was not included because its incidence was strongly unbalanced between the two groups and, if put in the model, masked the effects of the remaining variables.

In Figure 2a shear stress distribution at baseline and follow up was presented. Three different locations were selected from the clinicians and same location was tested with computer simulation for plaque concentration (Figure 2b). Plaque volume was determined from CT measurement and location are presented in angiographic image (Figure 2c). Comparison between measurement and numerical simulation for area of plaque and wall has been shown in Figure 2d. It can be seen that at least matching of plaque location was achieved as well as functional same order of the wall/plaque areas.



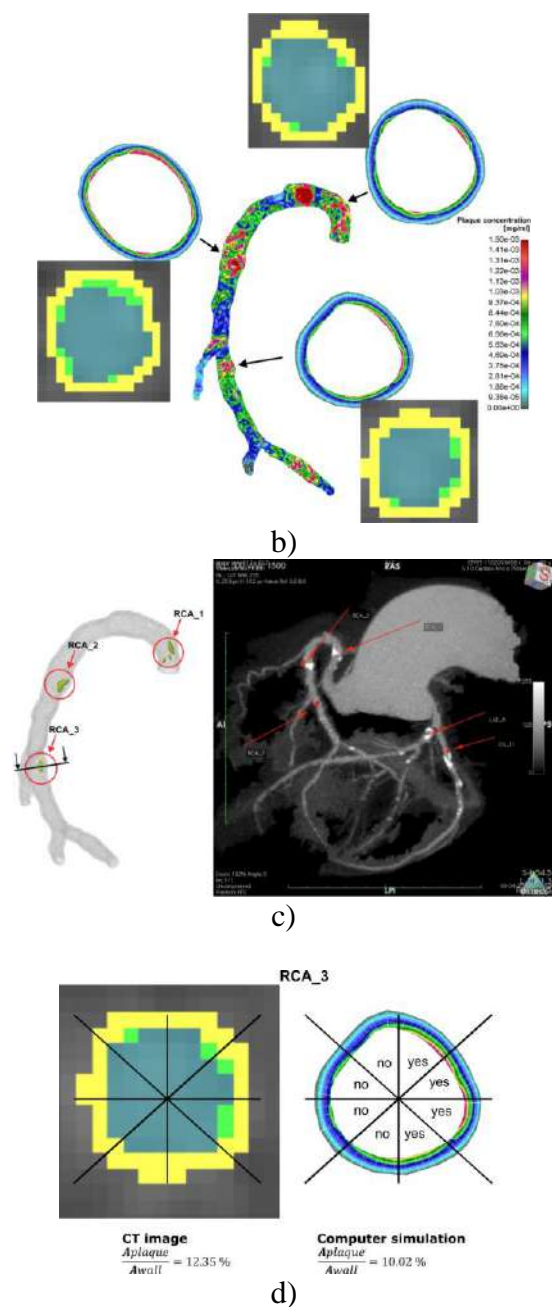


**Figure 2.** Case study for patient from Clinical Center in Pisa. a) Shear stress distribution; b) Plaque concentration distribution; c) Plaque volume location and angiography; d) Comparison CT image and computer simulation for plaque/wall areas

## CONCLUSION

Patient specific study has shown three different position of plaque location where low shear stress appear. Even more, after 28 months of follow up, the plaque size simulated and measured were matching. Computer analysis gave more insight for possible structure of the plaque.

This study is a novel way of modeling plaque formation and development. Matching of plaque location and progression in time between clinical and computer model shows a potential benefit for future prediction of this vascular disease using computer simulation. Further development should investigate influence of the pulsatility flow condition on our model, a proliferation of the smooth muscle cells and direct values of the threshold parameters which could be obtained from appropriate experiments which are not available currently.

## *Acknowledgement*

This study was funded by a grant from FP7-ICT-2007 project (grant agreement 224297, ARTreat) and grants from Serbian Ministry of Education, Science and Technological Development III41007 and ON174028.

## REFERENCES

- [1] P. Libby Inflammation in atherosclerosis. *Nature* 2002, 868–874.
- [2] J. Loscalzo, AI Schafer, *Thrombosis and Hemorrhage*. Third edition. Lippincott Williams & Wilkins 2003, Philadelphia.
- [3] J.M. Tarbell, Mass transport in arteries and the localization of atherosclerosis. *Annual Review of Biomedical Engineering* 2003, **5**, 79–118.
- [4] P. Zunino, Mathematical and numerical modeling of mass transfer in the vascular system. PhD thesis, Lausanne 2002, Switzerland: EPFL
- [5] Quarteroni, A. Veneziani, P. Zunino, Mathematical and numerical modeling of the solute dynamics in blood flow and arterial walls. *SIAM Journal of Numerical Analysis* 2002, **39**, 1488–1511.
- [6] O. Kedem, A. Katchalsky, A physical interpretation of the phenomenological coefficients of membrane permeability. *The Journal of General Physiology* 1961, **45**, 143–179.
- [7] Kedem O, Katchalsky A. Thermodynamic analysis of the permeability of biological membranes to non-electrolytes. *Biochim. Biophys* 1958, **27**, 229–246.
- [8] N. Filipovic, M. Rosic, I. Tanaskovic, Z. Milosevic, D. Nikolic, N. Zdravkovic, A. Peulic, D. Fotiadis, O. Parodi, ARTreat project: Three-dimensional Numerical Simulation of Plaque Formation and

- Development in the Arteries, *IEEE Trans Inf Technol Biomed* 2012, **16**(2), 272-278.
- [9] N. Filipovic, Z. Teng, M. Radovic, I. Saveljic, D. Fotiadis and O. Parodi, Computer simulation of three dimensional plaque formation and progression in the carotid artery, *Medical & Biological Engineering & Computing* 2013, DOI: 10.1007/s11517-012-1031-4.
- [10] O. Parodi, T. Exarchos, P. Marraccini, F. Vozzi, Z. Milosevic, D. Nikolic, A. Sakellarios, P. Siogkas, D. Fotiadis, N. Filipovic, Patient-specific prediction of coronary plaque growth from CTA angiography: a multiscale model for plaque formation and progression. *IEEE Transaction on Information Technology in Biomedicine* 2012, **16**(5), 952-965.

## CONTRAST AGENTS BASED ON INSULIN HEXAMER

M. Stojanović

*Departments of Medicine, Biomedical Engineering, and Systems Biology  
Columbia University*

Insulin molecules self-assemble into exceptionally stable hexamers in the presence of *in situ* formed  $\text{Co}^{3+}$  ions ( $\text{Ins}_6 \cdot \text{Co}^{3+}_2$ ), with two cations capping a water-filled channel formed within two interdigitated tris-alpha-helical bundles. We captured one  $\text{Gd}^{3+}$  ion per cavity during *in situ* oxidation of  $\text{Co}^{2+}$  and demonstrated that resulting  $\text{Ins}_6 \cdot \text{Co}^{3+}_2 \text{Gd}^{3+}$  has an exceptional potential as a contrast agent. Structure, relaxivity, and possible origins of exceptional properties of this reagent will be discussed, together with potential barriers for practical applications.

## MICROTUBULES: DYNAMICS, SOLITON WAVES, SOME ROLES IN THE CELL

S. Zdravković

*Institut za nuklearne nauke Vinča, Univerzitet u Beogradu, Laboratorija za atomsku fiziku (040), 11001 Beograd, Serbia. (szdjidji@vinca.rs)*

### ABSTRACT

In the present paper we deal with nonlinear dynamics of microtubules (MTs). The structure and role of MTs in cells are explained. One model explaining MT dynamics is explained. Solutions of the crucial nonlinear differential equation depend on used mathematical procedures. Two of them, continuum and semi-discrete approximations, are explained. Finally, these solutions are shown and discussed. They are solitonic waves. Three different kinds of them are known in the moment. They are kink solitons, breathers and bell-type solitons.

### INTRODUCTION

A cell is defined as eukaryotic if it has a membrane-bound nucleus. Such cells are generally larger and much more sophisticated than prokaryotic cells due to the many different types of specialized organelles present in most eukaryotic cells. Plant and animal cells are eukaryotic while bacteria cells are prokaryotic.

All eukaryotic cells produce two kinds of tubulin proteins. Alpha and beta tubulins spontaneously bind one another to form a functional subunit that we call a heterodimer, or a dimer for short. When intracellular conditions favour assembly, the dimers assemble into long structures called protofilaments (PFs). Microtubules (MTs) are usually formed of 13 PFs, as shown in Fig. 1. Hence, MTs are long cylindrical polymers whose lengths vary from a few hundred nanometers up to meters in long nerve axons [1]. Each dimer is an electric dipole whose mass is  $m = 1.8 \times 10^{-22}$  kg. Its length is  $l = 8$  nm, while the remaining two dimensions are 6.5 nm and 4.6 nm [2]. The component of its electric dipole moment in the direction of PF and charge displacement are:  $p = 337$  Debye  $= 1.13 \times 10^{-27}$  Cm and  $d \approx 4$  nm, respectively [3].

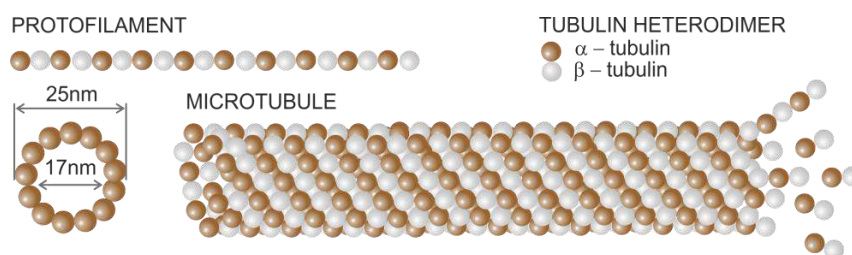


**Figure 1.** A tubulin dimers, a protofilament and a microtubule [4].

MTs are the major part of cytoskeleton (Fig. 2). They are long structures that spread between a nucleus and a cell membrane. MTs are involved in nucleic and cell division and organization of intracellular structure. They also serve as a network for motor proteins. This is shown in Fig. 3. There are two families of them called dyneins and kinesins. One can see, in Fig. 3, that the motor proteins carry different cargos, dynein towards the nucleus and kinesin towards the cell membrane. Motor proteins move with a velocity of  $0.1-2\mu\text{m/s}$  [5]. For this activity they use the energy derived from repeated cycles of adenosine triphosphate (ATP) hydrolysis. One ATP molecule is hydrolyzed for each step of motor protein. The step of motor protein is 8nm distance, as this is nothing but one dimer. Energy released during ATP hydrolysis is about 14kcal/mol, which corresponds to activation energy of the motor proteins [5].

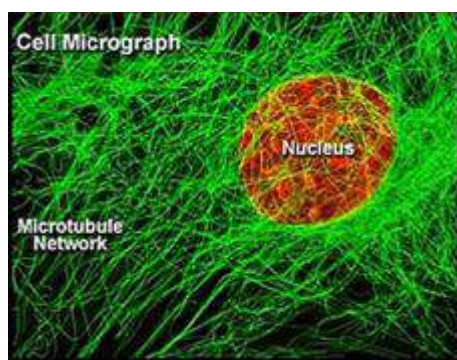


**Figure 2.** A nucleus and MT network in a eukaryotic cell [4]

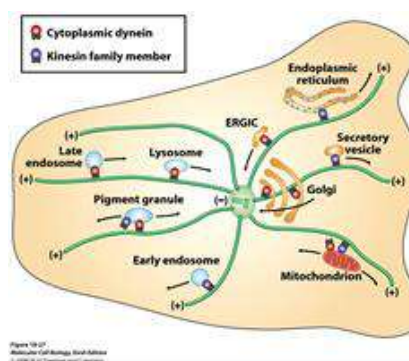


**Figure 3.** Microtubule as a network for motor proteins in a eukaryotic cell [4].

MTs in non-neuronal cells are unstable structures. They undergo repeated cycles of cell division for which MTs disassemble and reassemble [1]. Populations of such MTs usually consist of some that are shrinking and some that are growing. Hence, they exhibit dynamic instability behaviour existing in phases of elongation or rapid shortening. MTs grow steadily and then shrink rapidly by loss of tubulin dimers at the plus end. The rapid disassembly is referred to as catastrophe. MTs elongate and shorten at velocities of  $7.2\mu\text{m}/\text{min}$  and  $17.3\mu\text{m}/\text{min}$ , respectively [6]. In the interphase the half lifetime of individual unstable MT is 5–10min [5].

MTs existing in neuronal cells are uniquely stable and, consequently, neurons, once formed, don't divide [1]. This stability is crucial as there are evidences that neuronal MTs are responsible for processing, storage and transduction of biological information in a brain [1,7].

It was pointed out that MT was a hollow cylinder. This should not yield to a possible wrong conclusion that motor proteins move through it. Quite opposite, they “walk” along PFs carrying their cargos, as shown in Fig. 4.

Finally, meanings of the plus and the minus ends should be explained. MT polymerizes more quickly from the plus end, which is terminated by the  $\beta$ -subunit, i.e.  $\beta$ -monomer. The other end, growing more slowly, is known as the minus end, and is terminated by the  $\alpha$ -subunit. These dynamics ends do not correspond to electric ones. Namely, the dimers are electric dipoles and, consequently, the whole MT can be seen as a giant dipole, with its electric plus and minus ends. The electric plus end corresponds to the minus dynamics one and vice versa.

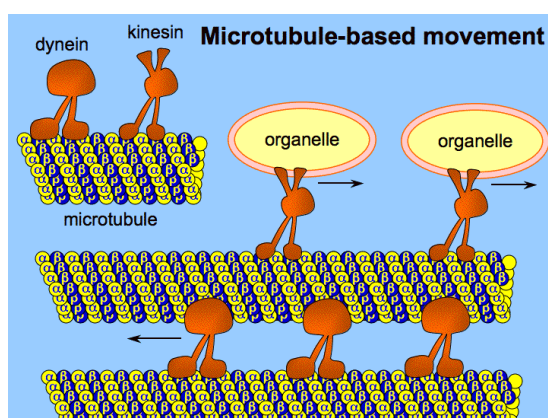


**Figure 4.** Motor proteins move along MTs carrying cargo [4].

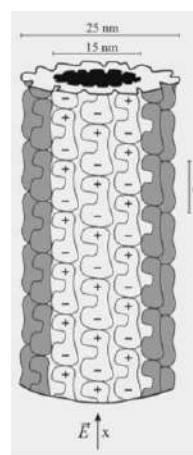


**Figure 5.** Microtubule.

### NONLINEAR DYNAMICS OF MTs

To study dynamics of MTs we need an appropriate model. The dimers are electric dipoles and the whole MT can be regarded as ferroelectric. That was assumed for the first nonlinear model of MT [8].

The tubulin polymerization process involves two types of contacts between the dimers. These are head-to-tail binding of dimers, resulting in protofilaments, and interactions between parallel protofilaments, which complete the MT wall. Since the longitudinal contacts along PFs appear to be much stronger than those between adjacent PFs, we construct a simplified Hamiltonian of MT, which is, practically, Hamiltonian for a single PF only. However, the influence of the neighbouring PFs is taken into consideration through the electric field. Namely, each dimer exists in the electric field coming from the dimers belonging to all PFs. Also, the nearest neighbour approximation, very common in physics, is assumed.

There is one additional approximation. The dimers oscillate performing both radial oscillations around more than one axis and longitudinal ones along more than one direction. Hence, there are a few degrees of freedom but all existing models assume only one degree of freedom per dimer, though some attempts to use two degrees of freedom are in progress. Thus, according to the chosen coordinates describing dimers' oscillations we can talk about either radial or longitudinal model. The latter one we call as  $u$ -model [9]. Notice that the  $u$ -model assumes radial oscillations of the dimers but the coordinate  $u$  is the projection of the top of the dimer on the direction of PF. There is a real longitudinal model assuming longitudinal displacements of the dimers that we call as  $z$ -model [10]. Both  $u$ - and  $z$ -models bring about equal differential equations but meanings of the coordinates  $u$  and  $z$  are different.

The second kind of the model is a radial one [11] and we call it as  $\varphi$ -model for short. Of course, the angle  $\varphi$  determines the radial displacement of the dimer representing the angle between the dimer and the direction of PF.

The equation describing the  $u$ - and  $z$ -models comprises a term which does not exist in the one coming from the  $\varphi$ -model. Hence, it is more complicated and interesting and, in what follows, we concentrate on the  $u$ -model only.

Each model requires a simplified picture according to which we write Hamiltonian describing the physical system. Also, an elementary mass, i.e. the smallest particle whose internal structure is neglected, should be indicated. The  $u$ -model, as well as all the models mentioned above, assumes that the dimer is the elementary particle

. The simplified picture, allowing us to write the Hamiltonian, could be the one in Fig. 5. The figure shows a segment of MT with three PFs clearly indicated.

The Hamiltonian for the  $u$ -model is

$$H = \sum_n \left[ \frac{m}{2} \dot{u}_n^2 + \frac{k}{2} (u_{n+1} - u_n)^2 - \frac{1}{2} A u_n^2 + \frac{1}{4} B u_n^4 - C u_n \right], \quad C = QE, \quad (1)$$

where dot means the first derivative with respect to time,  $m$  is a mass of the dimer,  $k$  is an intra-dimer stiffness parameter,  $Q > 0$  represents the excess charge within the dipole,  $E > 0$  is internal electric field and the integer  $n$  determines the position of the considered dimer in PF [8,9]. The first term represents the kinetic energy of the dimer. The second one is the potential energy of the chemical interaction between the neighbouring dimers belonging to the same PF, where, obviously, the nearest neighbour approximation is used, as explained above. The next two terms are called W-potential and they were introduced due to the fact that MT is ferroelectric and  $A$  and  $B$  are parameters that should be determined or, at least, estimated [8,9]. The very last term is coming from the fact that the dimer is the electric dipole existing in the field of all other dimers. The last three terms together can be called as the combined potential which looks like unsymmetrical W-potential.

Introducing generalized coordinates  $q_n$  and  $p_n$ , defined as  $q_n = u_n$  and  $p_n = m\dot{u}_n$ , and using well-known Hamilton's equations of motion we obtain the following discrete differential equation that should be solved

$$m\ddot{u}_n - k(u_{n+1} + u_{n-1} - 2u_n) - Au_n + Bu_n^3 - C = 0. \quad (2)$$

Therefore, nonlinear dynamics of MTs has been described by Eq. (2), which will be solved in the next section. Obviously, nonlinearity is coming from the 4<sup>th</sup> degree term in W-potential.

### SOLUTIONS OF EQ. (2)

We are not going through all the tedious derivations. Instead, two known approaches will be explained briefly. It is interesting that the final results depend on applied mathematical procedures.

Some approximations used in derivation of Eq. (2) were introduced above. We now explain the two mathematical methods for solving this equation. Practically, these two approaches are two approximations. In other

words, the approximations mentioned above were important for derivation of Eq. (2), while the mathematical ones are important for its solutions.

The first mathematical approximation that we explain is a continuum approximation  $u_n(t) \rightarrow u(x,t)$ , which allows a series expansion of the terms  $u_{n\pm 1}$ . This brings about the following continuum dynamical equation of motion

$$m \frac{\partial^2 u}{\partial t^2} - kl^2 \frac{\partial^2 u}{\partial x^2} - qE - Au + Bu^3 + \gamma \frac{\partial u}{\partial t} = 0. \quad (3)$$

The last term is coming from the introduced viscosity force  $F_v = -\gamma \dot{u}$ , where  $\gamma$  is a viscosity coefficient [8].

The remaining mathematical approximation is a semi-discrete one [9,12,13]. We assume small oscillations  $u_n(t) = \varepsilon \Phi_n(t)$ , where  $\varepsilon \ll 1$ , and look for wave solution which is a modulated wave. Its envelope is continual, while its carrier component is discrete. Such solution can be written as

$$\Phi_n(t) = F(\xi)e^{i\theta_n} + \varepsilon F_0(\xi) + \varepsilon F_2(\xi)e^{i2\theta_n} + \text{cc} + \text{O}(\varepsilon^2), \quad (4)$$

where  $\xi = (\varepsilon nl, \varepsilon t)$ ,  $\theta_n = nql - \omega t$ ,  $\omega$  is the optical frequency of the linear approximation,  $q = 2\pi/\lambda > 0$  is the wave number, cc represents complex conjugate terms and the function  $F_0$  is real. The dimers length  $l$ , mentioned above, is nothing but a period of one dimensional crystal lattice. Obviously, the continuous function  $F$  represents an envelope, while  $e^{i\theta_n}$ , including discreteness, is the carrier component. The first term in the expansion (4) is a leading one, while the remaining ones, multiplied by  $\varepsilon$ , are higher harmonics, representing a certain correction. Notice that the parameter  $\varepsilon$  exists in the function  $F$  but does not in  $e^{i\theta_n}$ . This is so because the frequency of the carrier wave is much higher than the frequency of the envelope and we need two time scales,  $t$  and  $\varepsilon t$ , for those two functions. Of course, the same holds for the coordinate scales.

This method is very tedious and we do not go through all the derivations. The complete procedure and important explanations can be found in Ref. [14]. The point is that the functions  $F_0(\xi)$  and  $F_2(\xi)$ , existing in Eq. (4), can be expressed through  $F(\xi)$ . In this particular case they turned out to be

constants [9]. Hence, we only need the equation for the function  $F(\xi)$  and this is a well-known solvable nonlinear Schrödinger equation (NLSE)

$$iF_{\tau} + PF_{SS} + Q|F|^2F = 0, \quad (5)$$

where the dispersion coefficient  $P$  and the coefficient of nonlinearity  $Q$  are explained in the aforementioned references, as well as the coordinates  $\tau$  and  $S$ .

Therefore, the crucial Eq. (2), describing nonlinear dynamics of MTs, has been transformed into Eqs. (3) and (5). The final step is the solutions of these two equations. This is a topic of the next section.

### SOLITONIC WAVES IN MICROTUBULES

The very first observation of a soliton was made in 1834 by the hydrodynamic engineer John Scott Russel [13]. He was riding his horse, while a pair of horses drew a boat along a narrow channel. When the boat was suddenly stopped he noticed an interesting wave moving along the channel. That was a smooth and well defined heap of water, which moved along the channel without change of form or diminution of speed [13]. The wave was so stable that the engineer followed it about one or two miles. He called this phenomenon the wave of translation.

Understanding of this interesting observation is nothing but a derivation of an equation whose solution is the observed wave. This equation is now called as KdV equation according to the initials of its authors Korteweg and de Vries, who derived it in 1895. More than 20 years earlier this equation existed in an implicit form in research of Boussinesq.

Nonlinear equations and solitonic waves are nowadays very common in many branches of sciences. Being a non-linear, it became fashionable. Now we return to nonlinear biophysics, i.e. to Eqs. (3) and (5). The former one is a partial differential equation (PDE). Generally, PDEs cannot be easily solved. Hopefully, Eq. (3) can be transformed into an ordinary differential equation (ODE) introducing a unified variable  $\xi$  defined as  $\xi \equiv \kappa x - \omega t$ , where  $\kappa$  and  $\omega$  are constants. Substitution of  $x$  and  $t$  by  $\xi$  transforms Eq. (3) into the following ODE

$$\alpha\psi'' - \rho\psi' - \psi + \psi^3 - \sigma = 0, \quad (6)$$

where a dimensionless function  $\psi$  has been introduced through the relation  $u = \sqrt{A/B}\psi$ . The values of the parameters  $\alpha$ ,  $\rho$  and  $\sigma$  can be found in

aforementioned references. It is important to keep in mind that  $\rho$  and  $\sigma$  are proportional to the viscosity coefficients and electric field, respectively, while  $\alpha$  can be determined.

Eq. (6) has been solved using a couple of mathematical procedures such as standard procedure [8], modified extended tanh-function method, procedure based on Jacobian elliptic functions, method of factorization and the simplest equation method (SEM). Beside a couple of diverging functions all these procedures bring about the same solutions having physical sense. These are three kink solitons, shown in Fig. 6. Of course, the function  $\psi(\xi)$  is the solution of Eq. (6). These solitons are kink-solitons or kinks ( $\psi_3$ ) and antikink-solitons ( $\psi_1$  and  $\psi_2$ ). It is common to call both of them as kinks for short. If we look at any of them we see that the kinks represent transition between two asymptotic states ( $\xi \rightarrow \pm\infty$ ). In other words, orientation of the dimers is changed. Regarding the present figure the transition occurs in the approximate interval of  $\xi \in (-6,+6)$ . This interval is moving along MT.

The most general method SEM brings about infinitely many parallel lines corresponding to all the three functions in Fig. 6. Of course, this is of mathematical interest but all those functions have the same physical meaning.

The advantage of SEM method over the remaining ones was demonstrated in Ref. [15]. A completely new solution was obtained. This is a bell-type soliton, shown in Fig. 7. This solution of Eq. (6) can be obtained only for  $\rho = 0$ , i.e. when viscosity is neglected.

Therefore, two completely different solutions of Eq. (6) have been derived. A final step is derivation of Eq. (5). Even though this is PDE its solution exists [13,14]. Hence, we know  $F$ , the functions  $F_0$  and  $F_2$ , existing in Eq. (4), can be expressed through  $F$  and all this brings about the final expression for  $u$ . This interesting solution is

$$u_n(t) = A_0 \operatorname{sech}\left(\frac{nl - V_e t}{L}\right) \cos(\Theta nl - \Omega t) - \frac{C}{A}, \quad (7)$$

where the expressions for all the parameters can be found in Ref. [9]. The hyperbolic function represents the envelope, while the remaining one is the carrier wave. This is shown in Fig. 8. Obviously, this is a localized modulated wave usually called as breather. We see that its width is about 200nm, which means that it covers about 25 dimers.

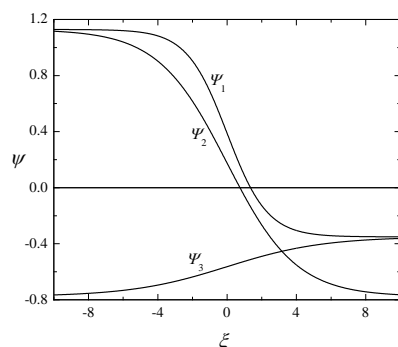


**Figure 6.** The functions  $\psi(\xi)$  for  $\rho = 2$  and

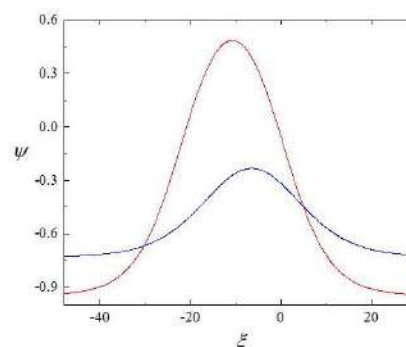


**Figure 7.** A bell-type soliton for  $\sigma = 0.34$  (blue) and  $\sigma = 0.1$  (red).

As a conclusion we can say that all the three known kinds of solitonic waves have been found in MTs. All these analytical results have been numerically supported.

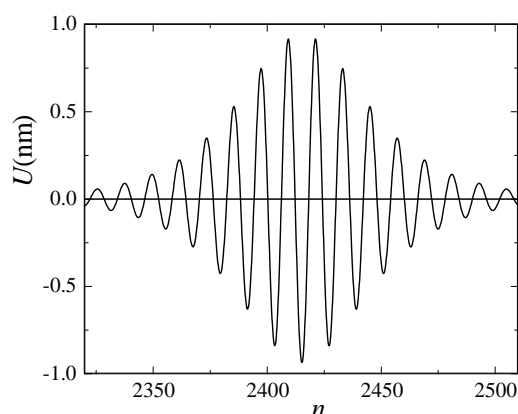


**Figure 8.**  
A localized modulated soliton  
(breather)

## CONCLUSION AND FUTURE RESEARCH

The three different solitons have been predicted as possible candidates for information carriers along MTs. They are shown in Figs. 6-8. A crucial question is their stability, which is very important task that should be performed.

A weak point in the  $u$ -model is the last term in Eq. (1). The  $\varphi$ -model was an attempt to overcome the problem. A better potential energy  $U(\varphi) = -\vec{p} \cdot \vec{E} = -qdE \cos \varphi$  was introduced instead but the W-potential has been lost. Hence, research in progress has been carried out with a goal to create a general model which will include both  $U(\varphi)$  and W-potential.

Let us return to Eq. (1) and Fig. 5. According to the latter, one would conclude that all the dimers are positioned in the direction of PFs. Of course, this is a simplified picture. The last three terms in Hamiltonian given by Eq. (1) represent the nonsymmetrical *W*-potential. The graph of this function has two minima. This means that there are two possible orientations of the dimers, i.e. two possible angles between them and PFs. According to the dimensions of the dimers we can expect that it should be possible to measure these angles. Such experiments would prove or disapprove the theoretical expectation regarding *W*-potential. In case that the used potential has been a good choice the measured angles would improve theory a lot.

Therefore, stability analysis, the general model and the experimental verifications are new tasks that should be performed in near future.

### *Acknowledgement*

This work was supported by funds from Serbian Ministry of Education, Sciences and Technological Development (grant No. III45010).

### REFERENCES

- [1] S. Hameroff, R. Penrose, *Physics of Life Reviews*, 2014, **11**, 39–78.
- [2] S. Sahu, S. Ghosh, K. Hirata, D. Fujita, A. Bandyopadhyay, *Applied Physics Letters*, 2013, **102**, 123701.
- [3] D. Havelka, M. Cifra, O. Kučera, J. Pokorný, J. Vrba, *Journal of Theoretical Biology*, 2011, **286**, 31–40.
- [4] Taken from Internet on the 13<sup>th</sup> of May, 2016. ([https://www.google.rs/search?q=microtubule&biw=1680&bih=913&tbm=isch&tbo=u&source=univ&sa=X&sqi=2&ved=0ahUKEwi\\_4duGgdfMAhXIDsAKHWVACEAQsAQIJw](https://www.google.rs/search?q=microtubule&biw=1680&bih=913&tbm=isch&tbo=u&source=univ&sa=X&sqi=2&ved=0ahUKEwi_4duGgdfMAhXIDsAKHWVACEAQsAQIJw))
- [5] M. Cifra, J. Pokorny, D. Havelka, O. Kučera, *BioSystems*, 2010, **100**, (2010) 122–131.
- [6] L. Cassimeris, N. K. Pryer, E. D. Salmon, *Journal of Cell Biology*, 1988, **107**, 2223-2231.
- [7] S. R. Hameroff, R. C. Watt, *Journal of Theoretical Biology*, 1982, **98**, 549-561.
- [8] M. V. Satarić, J. A. Tuszyński, R. B. Žakula, *Physical Review E*, 1993, **48**, 589-597.
- [9] S. Zdravković, S. Zeković, A. N. Bugay, M. V. Satarić, *Applied Mathematics and Computation*, 2016, **285**, 248–259.
- [10] S. Zdravković, M. V. Satarić, S. Zeković, *Europhysics Letters*, 2013, **102**, 38002.

- 
- [11] S. Zdravković, M. V. Satarić, A. Maluckov, A. Balaž, *Applied Mathematics and Computation*, 2014, **237**, 227-237.
- [12] M. Remoissenet, *Physical Review B*, 1986, **33**, 2386-2392.
- [13] T. Dauxois, M. Peyrard, *Physics of Solitons*, Chapter 3, Cambridge University Press, Cambridge, UK, 2006.
- [14] S. Zdravković, *Journal of Nonlinear Mathematical Physics*, 2011, **18** (Suppl. 2), 463–484.
- [15] S. Zdravković, G. Gligorić, *Chaos*, 2016, **26**, 063101.

## THEORETICAL STUDY OF THE ANTIOXIDANT ACTIVITY OF DOPAMINE AND ITS METABOLITES IN WATER

D. Dimić<sup>1</sup>, D. Milenković<sup>2</sup>, Z. Marković<sup>3</sup> and J. Dimitrić Marković<sup>1</sup>

<sup>1</sup>*Faculty of Physical Chemistry, University of Belgrade, Studentski trg 12-16, 11000 Belgrade, Republic of Serbia (ddimic@ffh.bg.ac.rs).*

<sup>2</sup>*Bioengineering Research and Development Center, Prvoslava Stojanovića 6, 34000 Kragujevac, Republic of Serbia.*

<sup>3</sup>*Department of Chemical-Technological Sciences, State University of Novi Pazar, Vuka Karadžića bb, 36300 Novi Pazar, Republic of Serbia.*

### ABSTRACT

Dopamine (DA) and three of its metabolites, homovanillic acid (HA), 3-methoxytyramine (3-MT) and 3,4-dihydroxyphenilacetic acid (DO) were subjected to structure-antioxidant activity investigation. Neutral molecules, radical cations, radical and anions were optimized at M062x/6-311++G(d,p) and thermodynamic parameters describing possible radical scavenging mechanisms were calculated. Based on these values, these mechanisms are competitive in aqueous solution. Catechol hydroxyl groups are the most reactive groups, when compared to carboxyl and amino, present in molecule. The highest antioxidant activity is expected for DO and DA.

### INTRODUCTION

Dopamine is one of the most important neurotransmitters in organism, proven to have an important role against oxidative stress [1]. Through complex reaction pathways it decomposes into various metabolites. In the present study three of them were selected for the antioxidant activity investigation – homovanillic acid, 3-methoxytyramine and 3,4-dihydroxyphenilacetic acid. The selected molecules share similar characteristic groups – aromatic ring (or catechol moiety in case of DA and DO) and aliphatic chain with different functional groups (Figure 1). Antioxidant activity is discussed based on the structure-activity relationships, because better

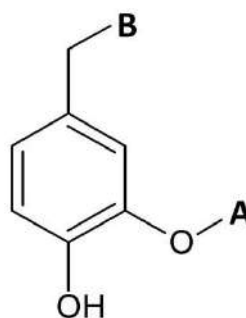


**Figure 1.** Structure of investigated molecules: DA (A=H, B=CH<sub>2</sub>NH<sub>2</sub>), 3-MT (A=CH<sub>3</sub>, B=CH<sub>2</sub>NH<sub>2</sub>), DO (A=H, B=COOH), HO (A=CH<sub>3</sub>, B=COOH).

understanding of the mechanism of their activity might help decomposing the complex formation of diseases like Parkinson's, Alzheimer's and other.

In the radical scavenging mechanisms reactive radical species are inactivated by accepting a hydrogen atom from the hydroxyl group (or other groups containing hydrogen atom connected to electronegative atoms) of the antioxidant. All of the selected molecules have either one hydroxyl group (3-MT and HA) or two (DA and DO). The transfer of hydrogen atom can be described through three mechanisms: hydrogen atom transfer (HAT, Eq. 1), sequential proton loss electron transfer (SPLET, Eqn. 2) and single electron transfer followed by proton transfer (SET-PT, Eqn. 3).



## THEORETICAL METHODS

The structures of dopamine and its metabolites were optimized at M062x/6-311++G(d,p) level, with Gaussian Program Package [2]. The absence of imaginary frequencies proved that the structures were at the minimum of potential energy surface. Several conformers of each species were selected based on previous through-out search in order to ensure that, at chosen level of theory, these were the most stable conformers. The M062x functional [3] was selected because it is suggested by its developers to give good results for the thermochemical parameters, which the present study is based on. For each of the species radical cations, radicals (formed by one of X-H homolytic bond breakage, where X=N, O) and anions (formed by X-H heterolytic bond breakage) were optimized.

## RESULTS AND DISCUSSION

Reactions related to antioxidant mechanisms, all of which have the same net result, are governed by different molecular properties: bond dissociation enthalpy (BDE) of ArOH in HAT mechanism, proton affinity (PA) of ArOH coupled with electron energy transfer (ETE) of ArO<sup>·</sup> in SPLET mechanism, and ionization potential (IP) of ArOH in SET-PT mechanism. These values for all of the possible deprotonation pathways of selected molecules are given in Table 1.

**Table 1.** Parameters for radical scavenging activity of dopamine and its metabolites in water, in kJ/mol.

	Water										
	HA T	SET-PT		SPLET			HA T	SET-PL		SPLET	
	BD E	IP	PDE	PA	ETE		BD E	IP	PDE	PA	ETE
<b>DA</b>		479				<b>DO</b>		487			
<b>1</b>	347		31	141	369	<b>1</b>	346		22	140	369
<b>2</b>	342		26	143	363	<b>2</b>	347		23	139	371
<b>3</b>	412		96	320	255	<b>3</b>	418		94	110	471
<b>3-M T</b>		474				<b>HA</b>		482			
<b>1</b>	349		38	157	355	<b>1</b>	354		35	154	363
<b>2</b>	412		100	320	255	<b>2</b>	412		94	109	466

The values for 1 and 2 for DA and DO are for the catechol moiety hydroxyl groups, and 3 is for NH<sub>2</sub> group for DA and COOH for DO. For 3-MT 1 is for OH group directly connected to aromatic ring, and 2 for NH<sub>2</sub>, and for HA 1 is the same as for previous, but 2 is for COOH. Based on the data presented above, it can be concluded that the lowest BDE value is for DA and DO, within 1 kJ/mol. The BDE values for HA and 3-MT are higher for about 2-5 kJ/mol. This proves that the most reactive groups are hydroxyl groups connected to aromatic ring, while other electronegative groups have much lower BDE values, for about 80 kJ/mol. IP is much higher than BDE, more than 140 kJ/mol for each of the species. The values for the second step of SET-PT are much lower, but in total these reactions are less energetically favorable than HAT.

The lowest energy requirements in all of the investigated mechanisms are for SPLET, especially for PA which is 140 kJ/mol. The order of investigated molecules is DO<DA<HA<3-MT(the PA values for all of them are within 28 kJ/mol). The values of proton affinity are similar for all of the hydroxyl groups, especially if catechol moiety is present. PA values for carboxyl groups are lower than hydroxyl groups PA because of higher acidity of these hydrogen atoms, present in both DO and HA. Based on these values it could be concluded that dominant radical scavenging activity mechanism is SPLET which proceeds through carboxyl group. The second step of SPLET, has much higher energy requirement, for about 200 kJ/mol. The second step that goes through carboxyl group is 100 kJ/mol higher than for hydroxyl groups. When two of the steps are added, the energy requirement for SPLET is thermodynamically more favorable if mechanism includes catechol

hydroxyl group. The highest energy requirement is for the reaction that would include NH<sub>2</sub> group.

If the values of BDE are compared to the sums PA+ETE (SPLET) and IP+PDE (SET-PT), it can be concluded that these values are for 140 kJ/mol lower than the respective sums. On the basis of this, it can be concluded that all of these mechanisms are competitive in the aqueous solutions. The values of BDE, PA and PDE show that the hydroxyl groups are the most probable places for the hydrogen loss. When these values are compared, DO has lowest thermodynamic values and thus expected to have the highest antioxidant activity towards different radicals.

### CONCLUSION

Dopamine and its metabolites, homovanillic acid, 3-methoxytyramine and 3,4-dihydroxyphenyl acetic acid are naturally occurring molecules that have prominent antioxidant activity. Based on the calculated thermodynamic parameters it can be concluded that molecules with hydroxyl groups connected to aromatic ring have the lowest values for BDE, PA and PDE i.e. they have the highest probability to be the first groups entering the reactions with free radicals. Carboxyl groups present in HA and DO, because of higher acidity of hydrogen atoms, are also possible groups for interactions with radicals. The least probable mechanism includes amino groups. Because of this structure-activity relationships, the following order for antioxidant activity is: DO > DA > HA > 3-MT.

### *Acknowledgement*

Authors would like to thank to the Ministry of Education, Science and Technological Development of the Republic of Serbia (Grants No. 172015, 174028 and 172040).

### REFERENCES

- [1] G-C. Yen and C-L. Hsieh, *Biosci., Biotechnol., Biochem.* 1997, **61**, 1646-1649.
- [2] M. J. Frisch, G. W. Trucks, H. B. Schlegel, et al. *Gaussian 09*, Revision C. 01, Gaussian Inc. Wallingford, CT, USA, 2010.
- [3] Y. Zhao and D. G. Truhlar, *Theor. Chem. Acc.*, 2008, **120**, 215-41.

## THE EFFECTS OF FLUOXETINE ON HIPPOCAMPAL ANTIOXIDATIVE DEFENSE IN DEPRESSIVE-LIKE RATS

I. Perić, N. Todorović, A. Stanisavljević, N. Đorđević and D. Filipović

*Laboratory of Molecular Biology and Endocrinology, Vinča Institute of Nuclear Sciences, University of Belgrade, Mike Petrovića Alasa 12-14, 11001 Belgrade, Serbia (dragana@vinca.rs)*

### ABSTRACT

Exposure of an organism to chronic social isolation (CSIS) causes modulation of antioxidant defense system in the brain which has been shown to have important role in depression. Fluoxetine (Flx) is the first-line treatment for depression; however, precise mechanism of its action still remains elusive. The aim of this study was to investigate the effect of 3 weeks of Flx treatment on malondialdehyde (MDA) level, an oxidative stress parameter as well as on the activities of GSH-dependent antioxidative enzymes in the hippocampus of rats exposed to 6 weeks of CSIS. Increased MDA content following CSIS and Flx treatment (controls or CSIS) of rats, suggests on hippocampal oxidative damage. CSIS induced reduction of hippocampal glutathione-S-transferase that was reversed by Flx treatment, as well as an increase in glutathione peroxidase/reductase activities. The present study contributes to our understanding of the mechanisms that underlie the antidepressant activity of Flx in rats exposed to CSIS, an animal model of depression.

### INTRODUCTION

Psychosocial stress is one of the major factors that could contribute to depression. Chronic social isolation (CSIS), an animal model of depression, causes changes in redox state in the hippocampus which may be responsible for depressive-like behavior in rats [1]. Fluoxetine (Flx, Prozac) belongs to the class of the new antidepressive drugs and it has been used as a first line treatment for depression and anxiety [2]. It acts as a selective serotonin reuptake inhibitor but its precise mechanism of action still remains unknown. The aim of this study was to examine the effect of 3 weeks of Flx treatment (15 mg/kg/day) on malondialdehyde (MDA) level, an oxidative stress parameter, and glutathione (GSH)-related antioxidative defense, as indirect marker of oxidative stress, in the hippocampus of rats exposed to six weeks of CSIS. Hence, we measured the

glutathione (GSH) content, as the main redox buffer in the cell, and activities of GSH-dependent antioxidative enzymes including glutathione peroxidase (GPx), glutathione reductase (GLR) and glutathione-S-transferase (GST).

### EXPERIMENTAL

Twenty four adult male Wistar rats, 2.5 months old, at the onset of the experiment served as subjects. Rats were housed under standard conditions (temperature-controlled environment (21-23°C), 12/12h light/dark cycle with food and water available *ad libitum*). Prior to stress exposure, the animals were housed in groups of four per cage and randomly divided into two groups. Control group consisted of four animals per cage while rats subjected to CSIS stress were housed individually for 6 weeks during which animals had normal auditory and olfactory experiences, but without any visual and tactile contact with other animals. Flx-HCl solution was administered daily by intraperitoneal (i.p.) injections of 15 mg/kg, during the last 3 weeks in both control (Con+Flx) and socially isolated (CSIS+Flx) rats. We reported in previous study that the chosen dose of Flx is the one corresponding to serum levels within the therapeutically effective dose range for the treatment in depressive patients [3]. Vehicle-treated animals received i.p. physiological saline injections (0.9 % NaCl) (Con+Veh and CSIS+Veh). Hippocampal cytosolic fractions were used for biochemical parameters determination. Protein concentrations were measured by the method of Lowry [4], using bovine serum albumin as a standard. GSH content was measured according to the method of Ellman [5]. We used spectrophotometric assays for measuring the activity of GPx, GLR and GST enzymes [6, 7, 8]. All data are displayed as mean  $\pm$  S.E.M. and analyzed by two-way ANOVA followed by Duncan's post-hoc test.

### RESULTS AND DISCUSSION

Significant increase in MDA content in CSIS+Veh group shows the signs of oxidative stress (\*\* $p < 0.01$ ) (Figure 1). Interestingly, Flx treatment caused the increase in MDA content in both control and isolated (\*\* $p < 0.01$ ) animals indicating its detrimental effect of lipid oxidation.

According to data presented in Table 1., CSIS led to slight decrease of GSH content that was not statistically significant ( $p > 0.05$ ). However, treatment with Flx induced increase of GSH level in Flx-treated CSIS animals ( $p < 0.05$ ) as compared to vehicle-treated CSIS.

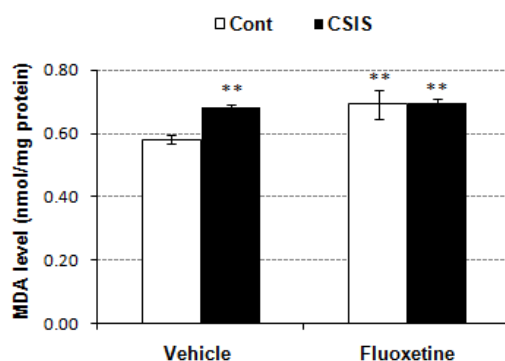


**Figure 1.** Changes of MDA content (nmol/mg protein) in hippocampus of control and chronic social isolation (CSIS) rats treated either with vehicle (0.9% NaCl), or fluoxetine. Asterisk indicates significant differences between all treated experimental groups and Con+Veh (\*\* $p < 0.01$ ).

CSIS stress brought to distinguishable changes in GSH-dependent antioxidant enzyme activities. GPx activity was significantly increased in all three groups compared to Con+Veh, with the most significant changes observed in Con+Flx and CSIS+Flx ( $***p < 0.001$ ), demonstrating the role of Flx in enhancing antioxidative defense. GLR activity didn't undergo any significant change in CSIS rats ( $p > 0.05$ ) but Flx treatment increased its activity in control ( $*p < 0.05$ ) and CSIS ( $**p < 0.01$ ) groups. Therefore, based on aforementioned results, Flx intensifies GSH-dependent antioxidative defense by stimulating the catalytic activity of both GPx and GLR.

**Table1.** Hippocampal GSH content and activity of GPx, GLR and GST enzymes of control and chronic social isolation (CSIS) rats treated either with vehicle (0.9% NaCl) or fluoxetine. Symbols indicate significant differences between: all treated experimental groups and Con+Veh,  $*p < 0.05$ ,  $**p < 0.01$ ,  $***p < 0.001$ ; CSIS+Flx and CSIS+Veh  $^{\wedge}p < 0.05$ ,  $^{\wedge\wedge}p < 0.001$ ; CSIS+Flx and Con+Flx  $^{\#}p < 0.05$ .

Groups	GSH content (nmol/mg protein)	GPx activity (mU/mg protein)	GLR activity (mU/mg protein)	GST activity (mU/mg protein)
Con + Vehicle	43.35 ± 2.32	25.10 ± 0.66	30.44 ± 0.68	122.55 ± 4.09
Con + Flx	47.70 ± 2.71	31.22 ± 0.77 <sup>***</sup>	33.31 ± 0.93 <sup>*</sup>	122.45 ± 5.17
CSIS + Vehicle	39.79 ± 1.23	27.58 ± 0.11 <sup>**</sup>	31.26 ± 1.03	99.72 ± 2.76 <sup>***</sup>
CSIS + Flx	47.57 ± 1.91 <sup>^</sup>	29.35 ± 0.61 <sup>***^#</sup>	33.91 ± 0.35 <sup>***^</sup>	123.16 ± 2.08 <sup>^^^</sup>

The compromised GST activity in CSIS group (\*\* $p < 0.001$ ) could be one of the contributing factors that led to the reduced consumption of GSH, a cosubstrate essential for its activity. Treatment of Flx restored GST activity in CSIS rats as compared to CSIS alone ( $p < 0.001$ ) indicating that it interferes with CSIS-induced pathways of oxidative defense as well as its role in improvement of the cell capabilities in detoxification of drug. Moreover, increased GPx activity in vehicle-treated CSIS group and consequently consumption of GSH did not affect its level although increased GPx activity was not accompanied with increased activity of GLR enzyme responsible for GSH restoration, suggesting on de novo synthesis of GSH.

### CONCLUSION

The data revealed that Flx may cause state of oxidative stress, judging by the overall MDA content increment in control rats. In addition, it unambiguously triggered the cellular defense against ROS by enhancing the activities of GPx, GLR as well as reversing GST activity to the normal level, thereby improving the cell capacity in toxic electrophile molecules removal, but relying on the fact that some GSTs may act as peroxidases.

### Acknowledgement

This work was supported by the Ministry of Education, Science and Technological Development of the Republic of Serbia (Grants no. 173044).

### REFERENCES

- [1] J. Zlatković, N. Todorović, M. Bošković, S. B. Pajović, M. Demajo, D. Filipović, *Mol. Cell Biochem.*, 2014, **1**, 43-57.
- [2] L. R. Magni, M. Purgato, C. Gastaldon, D. Papola, T. A. Furukawa, A. Cipriani, C. Barbui, *Cochrane Database Syst. Rev.*, 2013, **7**, CD004185.
- [3] J. Zlatković, N. Todorović, N. Tomanović, M. Bošković, S. Djordjević, T. Lazarević-Pašti, R. E. Bernardi, A. Djurdjevic, D. Filipović, *EJPS*, 2014, **59**, 20-30.
- [4] O. H. Lowry, N. J. Rosebrough, A. L. Farr, and R. J. Randall, *J. Biol. Chem.*, 1951, **193**, 265-275.
- [5] G. L. Ellman, *Arch. Biochem. Biophys.*, 1959, **82**, 70-77.
- [6] D.E. Paglia, W. N. Valentine, *J. Lab. Clin. Med.*, 1967, **70**, 158-169.
- [7] I. Cariberg, and B. Mannervik, *J. Biol. Chem.*, 1975, **250**, 5475-5480.
- [8] W. H. Habig, M. J. Pabst, W. B. Jakoby, *J. Biol. Chem.*, 1974, **249**, 7130-7139.

## OLANZAPINE INTENSIFIES LIPID PEROXIDATION AND MODULATES CATALASE ACTIVITY IN LIVER OF SOCIAL ISOLATED RATS

A. Stanisavljević, I. Perić, N. Todorović, N. Đorđević and D. Filipović

*Laboratory of Molecular Biology and Endocrinology, Vinča Institute of Nuclear Sciences, University of Belgrade, Mike Petrovića Alasa 12-14, 11001 Belgrade, Serbia (dragana@vinca.rs)*

### ABSTRACT

Olanzapine is an antipsychotic proved to be effective in stress associated psychiatric diseases, but its effect on the liver, main site of drug metabolism, still remain unclear. We investigated the effects of chronic treatment of olanzapine (three-week) on the malondialdehyde (MDA) content and protein expression and activity of antioxidant enzyme catalase (CAT) in the liver of rats exposed to chronic social isolation (CSIS) (six-week), an animal model of depression. The increased cytosolic MDA content in both vehicle- and olanzapine-treated CSIS animals suggests oxidative stress. Increased CAT activity in vehicle-treated CSIS animals, which was not consistent with its protein expression, suggests induction of antioxidant defense mechanisms, while olanzapine significantly reduced CAT activity in CSIS group. Data revealed that although olanzapine treatment reversed the alterations in CAT activity, it has the ability to cause hepatotoxicity, as indicated by increased MDA content.

### INTRODUCTION

Olanzapine, an atypical antipsychotic, is used to treat depressive disorder and schizophrenia [1]. Compared to older antipsychotics demonstrated to cause oxidative stress within the liver [2], the newer atypical antipsychotics, including olanzapine, may have protective properties against oxidative stress. Given that olanzapine is *extensively metabolized in the liver*, its effect on the liver is important. Recently, we have shown that chronic social isolation (CSIS), an animal model of depression, causes oxidative stress in the rat liver [2]. Oxidative stress may induce peroxidation of membrane lipids leading to the formation of malondialdehyde (MDA), where its increased production is associated with different pathological states. Moreover, oxidative stress may also affect protein expression and the activity of antioxidant enzymes, such as catalase (CAT). CAT is in the first line of cellular defense against oxidative damage and degrades hydrogen

peroxide ( $\text{H}_2\text{O}_2$ ) into water and oxygen. Thus, we examined the effect of 3 weeks of olanzapine administration (7.5 mg/kg/day) on rat hepatic cytosolic MDA content and protein expression and activity of CAT following 6 weeks of CSIS, which causes depressive- and anxiety-like behavior in adult male Wistar rats.

### EXPERIMENTAL

Adult male Wistar rats, 2.5 months old, were used at the onset of the experiment. Prior to CSIS exposure, the animals were housed in groups of four per cage and randomly divided into two groups. Control group consisted of four animals per cage, while rats that underwent CSIS, were individually housed for 6 weeks, during which they had normal auditory and olfactory experience, but were deprived of any visual and tactile contact. Following 3 weeks, both groups were subdivided into vehicle-treated rats receiving daily intraperitoneally (i.p.) injections of normal saline (0.9% NaCl) (Cont+Veh and CSIS+Veh) and olanzapine-treated receiving a 7.5 mg/kg/day of olanzapine-hydrochloride (Cont+Olan and CSIS+Olan). This selected dose of olanzapine in rats is within the therapeutic plasma concentration range in humans [3]. Lipid peroxidation was determined by estimating MDA content by the method which involves its reaction with thiobarbituric acid and spectrophotometric detection at 535 nm [4]. Cytosolic CAT activity was determined by spectrophotometric assays, monitoring the decrease in absorbance at 240 nm, and expressed as  $\mu\text{mol}$  of degraded  $\text{H}_2\text{O}_2$  per minute per milligram of protein, using the extinction coefficient of  $43.6 \text{ M}^{-1}\text{cm}^{-1}$  [5]. The results were analyzed using two-way ANOVA followed by Duncan's post hoc test and expressed as mean  $\pm$  SEM of 6 rats per group.

### RESULTS AND DISCUSSION

MDA content is presented in the Fig.1. Significant increase in hepatic MDA content in both vehicle- and olanzapine-treated CSIS rats as compared to vehicle-treated controls ( $^{***}p < 0.001$ ) suggests increased oxidative stress caused by CSIS alone and/or olanzapine treatment. Interestingly, increased MDA in olanzapine-treated CSIS group compared to vehicle-treated CSIS group ( $^{^^}p < 0.001$ ) or olanzapine-treated controls ( $^{###}p < 0.001$ ) suggests a synergistic action of olanzapine and CSIS on induction of lipid peroxidation. This synergism could be, at least in part, explained by the olanzapine oxidation to a pro-oxidant radical nitrenium ion [6], which may be produced in the CSIS-induced pro-oxidant environment and may further contribute oxidative damage in hepatic cells.

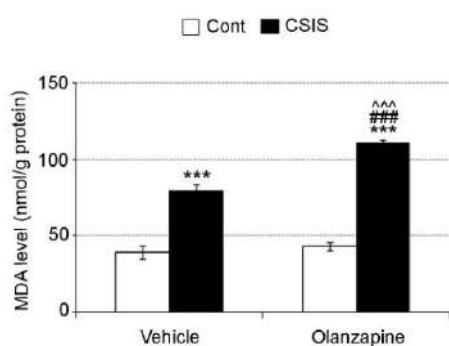


**Figure 1.** MDA content in liver cytosol of controls (Cont) and rats exposed to chronic social isolation (CSIS) treated with vehicle (0.9% NaCl) or olanzapine-hydrochloride (7.5 mg/kg/day). Symbols indicate differences as follow: \*\*\*  $p < 0.001$  CSIS+Veh or CSIS+Olan vs. Cont+Veh, ###  $p < 0.001$  CSIS+Olan vs. Cont+Olan; ^^  $p < 0.001$  CSIS+Olan vs. CSIS+Veh.

Protein expression and activity of hepatic cytosolic CAT are shown in Fig. 2 A and 2 B, respectively. Regard to CAT protein expression, two-way ANOVA followed by Duncan's post-hoc test revealed no significant differences between all tested groups of rats.

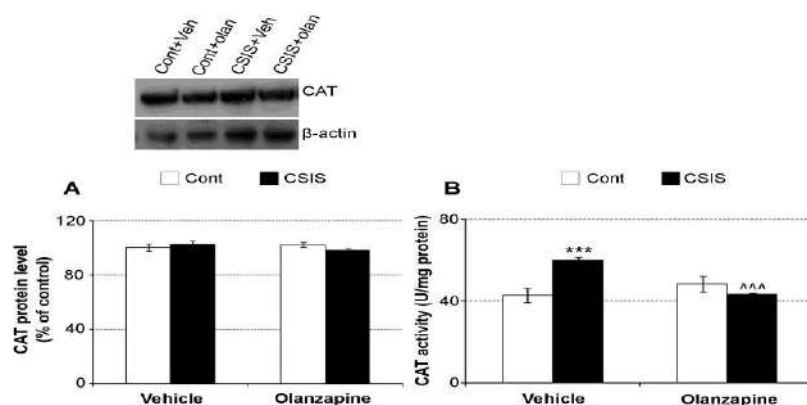


**Figure 2.** Hepatic cytosolic CAT protein levels (A) and activity (B) (U/mg protein) of controls (Cont) and rats exposed to chronic social isolation (CSIS) treated with vehicle (0.9% NaCl) or olanzapine-hydrochloride (7.5 mg/kg/day). Symbols indicate differences as follow: \*\*\*  $p < 0.001$  CSIS+Veh vs. Cont+Veh; ^^  $p < 0.001$  CSIS+Olan vs. CSIS+Veh.

Significant increases of CAT activity could be compensatory increase for meeting the demand to convert overloads  $H_2O_2$  in the liver of CSIS rats. After olanzapine treatment in CSIS rats, CAT activity went back to the

normal level, which may indicate that olanzapine significantly reduces H<sub>2</sub>O<sub>2</sub> and oxidative stress in the liver. Lack of correspondence between CAT protein expression and its activity in vehicle-treated CSIS group may be consequence of the presence of large amounts of its substrate, stress-induced H<sub>2</sub>O<sub>2</sub>.

### CONCLUSION

Our results suggest increased oxidative stress in the liver of CSIS rats, judged by increased cytosolic MDA content and CAT activity. Olanzapine treatment had no any detrimental effect on the liver of control animals but it failed to alleviate CSIS-induced hepatic lipid peroxidation and this mechanism has yet to be worked out. We found that olanzapine down regulates the activity of CAT which reflects that olanzapine significantly reduced H<sub>2</sub>O<sub>2</sub> and hepatic oxidative stress.

### *Aknowledgment*

This work was supported by the Ministry of Education, Science and Technological Development of the Republic of Serbia (Grant no. 173044).

### REFERENCES

- [1] M. Narassimhan, T. O. Brus, P. Masand, *Neuropsychiatr. Dis. Treat.*, 2007, **3** (5), 579-587.
- [2] J. Zlatković, N. Todorović, N. Tomanović, M. Bošković, S. Djordjević, T. Lazarević-Pašti, R.E. Bernardi, A. Djurdjević, D. Filipović, *Eur J Pharm Sci.*, 2014, **59**, 20-30.
- [3] M. Aravagiri, Y. Teper, S.R. Marder, *Biopharm. Drug Dispos.*, 1999, **20**, 369-377
- [4] P. W. Albro, J. T. Corbett, J. L. Schroeder, *J. Biochem. Biophys. Methods* 1986, **13**, 185-194.
- [5] A. Clairborne, *Handbook of Methods for Oxygen Radical Research*, 1985, CRC Press, 283-284.
- [6] W. Ng, R. Kennar, J. Uetrecht, *Chem. Res. Toxicol.*, 2014. **27**, 1104-1108.

## DULOXETINE ENHANCES HEPATIC GSH-DEPENDENT DEFENSE IN RATS

N. Đorđević, I. Perić, A. Stanisavljević, N. Todorović and D. Filipović

*Laboratory of Molecular Biology and Endocrinology, Vinča Institute of Nuclear Sciences, University of Belgrade, Mike Petrovića Alasa 12-14, 11001 Belgrade, Serbia (dragana@vinca.rs)*

### ABSTRACT

Duloxetine (DLX) is antidepressant for the treatment of depression, but its effect on the liver, a primary site for drug metabolism, has yet to be determined. The effect of 3 weeks of DLX treatment on protein carbonyl groups and activities of GSH-dependent defense including reduced glutathione (GSH), glutathione peroxidase (GPx) and glutathione S-transferase (GST) in liver of rats exposed to 6 weeks of chronic social isolation (CSIS), an animal model of depression, were investigated. CSIS induced increase in protein carbonyl content, which was decreased by DLX treatment. We noticed increase in GPx and GST activity in DLX-treated (controls and CSIS) rats and CSIS group, whereby GPx activity was significantly higher in DLX- compared to vehicle-treated CSIS rats. Results indicate protective effect of DLX against CSIS-induced oxidative damage of hepatic proteins, which may be due to intensified protective mechanisms mediated by GSH-dependent defense.

### INTRODUCTION

It has been shown that chronic social isolation (CSIS) induced the oxidative stress in the rat liver, judged by increased concentrations of protein carbonyl groups [1]. CSIS is mild psychosocial stress used for studying pathophysiology of mood disorders [2]. A duloxetine (DLX), a selective serotonin/norepinephrine reuptake inhibitor, is used for the treatment of some mood and nerve disorders including depression and some anxiety disorders [3].

In order to defend against oxidative stress, liver uses glutathione (GSH)-dependent defense system. Glutathione peroxidase (GPx) reduces lipid hydroperoxides to their corresponding alcohols and free hydrogen peroxide to water, using GSH as cosubstrate. Glutathione S-transferase (GST) catalyses the conjugation of the reduced form of GSH to xenobiotic substrates for the purpose of detoxification.

Since the liver possesses one of the highest antioxidant enzyme capacities in the body, and is primary organ for drug activation and detoxification, we examined the chronic effect of DLX on protein carbonyls as well as GSH-dependent defense system in liver of rats exposed to CSIS.

### EXPERIMENTAL

Adult (2.5 month old) male Wistar rats were used for the experiments. Rats were housed under standard conditions (temperature-controlled environment (21-23°C), 12-h light/dark cycle with food and water available *ad libitum*). Rats were divided into control groups (four animals per cage) and rats that underwent CSIS for a period of 6 weeks, which were housed individually. After 3 weeks of experiments, rats were subdivided on groups treated either with intraperitoneal (i.p.) injections of DLX (10 mg/kg/day) (Con+DLX, CSIS+DLX) or 0.9% NaCl (Con+Veh and CSIS+Veh) for next 3 weeks. Hepatic cytosolic fractions were used for biochemical parameters determination. GPx and GST activity were determined by spectrophotometric assays [4, 5], while GSH content was measured according to Hissin and Hilf [6]. Protein carbonyl content was determined using Levine et al. method [7]. Data were analyzed by two-way ANOVA followed by Duncan's post-hoc test. The results are presented as mean  $\pm$  S.E.M. of 6 animals per group.

### RESULTS AND DISCUSSION

Significant increase in protein carbonyl content in CSIS+Veh group compared to Con+Veh group (\*\* $p < 0.001$ ) (Figure 1) indicates the presence of oxidative stress. Also, it can be noticed that DLX alone probably had no effect on the liver, according unchanged protein carbonyl content in Con+DLX group compared to Con+Veh group ( $p > 0.05$ ). Chronic administration of DLX in CSIS group induced significant decrease in protein carbonyl content compared to CSIS+Veh group ( $p < 0.001$ ). This indicates a protective effect of DLX in relation to the changes in the proteins created by oxidative stress.

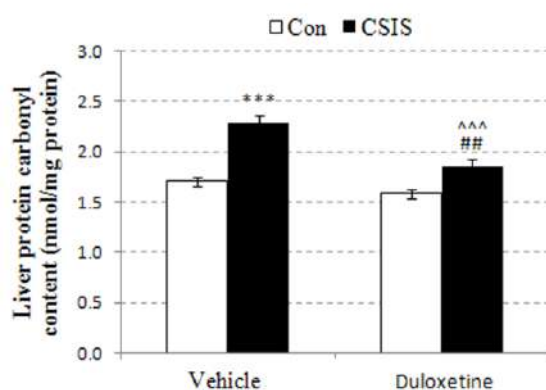


**Figure 1.** Cytosolic protein carbonyl contents (nmol/mg protein) in rat liver of controls and chronic social isolation (CSIS) rats treated with saline (0.9% NaCl) or duloxetine (DLX) (10 mg/kg/day). Significant differences between tested groups are indicated as follows: CSIS+Veh vs Con+Veh \*\*\* $p < 0.001$ ; CSIS+DLX vs CSIS+Veh  $\hat{\hat{p}} < 0.001$ ; CSIS+DLX vs Con+DLX  $\#\#p < 0.01$ .

Results of hepatic GSH content and activity of GPx and GST are shown in Table 1. GSH content in CSIS+DLX group was increased compared to Con+Veh ( $*p < 0.05$ ) and CSIS+Veh ( $\hat{p} < 0.05$ ) groups. Unchanged GSH content in CSIS compared to control group was observed ( $p > 0.05$ ). GPx and GST activity in all treated experimental groups compared to Con+Veh group was significantly increased ( $**p < 0.01$ ,  $***p < 0.001$ ). Post-hoc test also showed significant increase of GPx activity in DLX-CSIS group in comparison with CSIS+Veh ( $\hat{\hat{p}} < 0.01$ ) and Con+DLX ( $\#p < 0.05$ ).

**Table 1.** GSH content, GPx and GST activity in liver of controls and chronic social isolation (CSIS) rats treated with vehicle (0.9% NaCl) or duloxetine (DLX) (10 mg/kg/day). Symbols show significant differences between: treated experimental groups and Con+Veh  $*p < 0.05$ ,  $**p < 0.01$ ,  $***p < 0.001$ ; CSIS+DLX and CSIS+Veh  $\hat{p} < 0.05$ ,  $\hat{\hat{p}} < 0.01$ ; CSIS+DLX and Con+DLX  $\#p < 0.05$ .

Groups	GSH content (nmol/mg protein)	GPx activity (U/mg protein)	GST activity (U/mg protein)
Con+Veh	46.87 ± 0.72	1.37 ± 0.05	0.48 ± 0.03
Con+DLX	47.49 ± 0.84	1.82 ± 0.03 ***	0.62 ± 0.02 **
CSIS+Veh	46.89 ± 1.06	1.72 ± 0.04 ***	0.64 ± 0.03 ***
CSIS+DLX	50.16 ± 0.98 * $\hat{}$	1.98 ± 0.08 *** $\hat{\hat{}}$ $\#$	0.64 ± 0.03 ***

We found that chronic DLX treatment increased antioxidant status of control and CSIS groups relative to vehicle controls. This may reveal that DLX possesses antioxidant effects in the absence of oxidative stress as well

as it directly interfere with CSIS-induced pathways of oxidative defense. Increased activity of GPx in CSIS+DLX rats may be the consequence of increased levels of GSH in these animals, since it represents a cosubstrate necessary for its activity. Moreover, increase in GPx activity, at least in part, may be responsible for reduction of protein carbonyl content in CSIS rats, suggesting protective role of DLX. Increased GST activity in DLX-treated (control or CSIS) rats, was probably due to engagement of this enzyme in the detoxification of xenobiotics, including drug..

### CONCLUSION

Our data reveal that CSIS causes oxidative damage of proteins and affects the GSH-dependent defense system in the rat liver. CSIS resulted in enhanced hepatic GPx and GST activity which indicate protective effect against oxidative stress. DLX treatment increases reduced GSH and GPx activity that suggest its protective effect against CSIS-induced oxidative protein damage.

### *Acknowledgement*

This work was supported by the Ministry of Education, Science and Technological Development of the Republic of Serbia (Grant no. 173044).

### REFERENCES

- [1] J. Zlatković, N. Todorović, N. Tomanović, M. Bošković, S. Đorđević, T. Lazarević-Pašti, R. E. Bernardi, A. Đurđević, D. Filipović, EJPS, 2014, **59**, 20-30.
- [2] L. M. Heinrich, E. Gullone, Clin Psychol Rev., 2006, **26**, 695-718.
- [3] D. J. Goldstein, Y. Lu, M. J. Detke, C. Wiltse, C. Mallinckrodt, M. Demitrack, J. Clin Psychopharmacol., 2004, **24** (4), 389-399.
- [4] D. E. Paglia, W. N. Valentine, J. Lab. Clin. Med., 1967, **70**, 158-169.
- [5] W. H. Habig, M. J. Pabst, W. B. Jakoby, J. Biol. Chem., 1974, **249**, 7130-7139.
- [6] P. J. Hissin, R. Hilf, Anal. Biochem., 1976, **74**, 214-226.
- [7] R. L. Levine, J. A. Williams, E. R. Stadtman, E. Shacter, Methods Enzymol, 1994, **233**, 346-357.

## **RADIO-PROTECTIVE EFFECT OF DMSO AND GLYCEROL IN HUMAN NON-SMALL CELL LUNG CANCER IRRADIATED WITH GAMMA RAYS**

V. Petković<sup>1</sup>, O. Keta<sup>1</sup>, N. Vojinović<sup>2</sup>, S. Incerti<sup>3</sup>, I. Petrović<sup>1</sup>  
and A. Ristić-Fira<sup>1</sup>

<sup>1</sup>*University of Belgrade, Vinča Institute of Nuclear Sciences,  
Mike Petrovića Alasa 12-14, 11001 Belgrade, Serbia. (aristic@vin.bg.ac.rs)*

<sup>2</sup>*University of Banja Luka, Faculty of Sciences, Mladena Stojanovića  
2,78000Banja Luka, Bosnia and Herzegovina.*

<sup>3</sup>*Université Bordeaux 1, CNRS/IN2P3, CENBG, 33175 Gradignan, France.*

### **ABSTRACT**

Direct effects of radiation affect the DNA molecule, causing DNA damage and finally cell death. We examined the role of DMSO and glycerol as free-radical scavengers in HTB177 cells irradiated with gamma rays. Direct effects of radiation were estimated through DNA double strand break (DSB) quantification and cell survival. Results of this work revealed that chosen concentration of DMSO exhibit higher protective effect comparing to glycerol.

### **INTRODUCTION**

It is known that ionizing radiation causes cell damage through direct and indirect effects [1]. Direct effects refer to straight interaction of gamma rays or charged particles with DNA molecule causing damages (single and double strand breaks, modification of bases and DNA backbone). If not repaired properly, DNA lesions provoke genomic instability and consequently lead to cell death. Indirect effects of radiation refer to formation of free radical species during water hydrolysis. These highly reactive ions interact with DNA, but also with other biomolecules and cellular compartments, triggering oxidative stress [1]. In the field of radioprotection, many chemical compounds are tested for their capacity to prevent DNA and cell damage. It is known that DMSO and glycerol act as free radical scavenger thus lowering oxidative stress caused by indirect effects of radiation. In this study we used non-toxic concentrations of DMSO and glycerol that represent low and high scavenging conditions (1 and 100mM DMSO and 2 and 200 mM glycerol)[2, 3].

Clonogenic assay is used in radiobiology as standard test to determine cell survival after irradiation alone or in combination with chemical

treatment [4]. The impact of DMSO and glycerol on radio-sensitivity of HTB177 non-small lung cancer was tested.

Phosphorylated histone H2AX ( $\gamma$ H2AX) acts as a sensor of DSB. Due to its role in DNA repair, it is used as a DSB biomarker. Immunocytochemical analysis of  $\gamma$ H2AX is considered to be sensitive method for DSB detection and quantification [5].

## EXPERIMENTAL

The HTB177 cells were purchased from the ATCC (Rockville, MD, USA) and grown as a monolayer culture in RPMI-1640 medium supplemented with 10% fetal bovine serum (FBS) and penicillin/streptomycin (Sigma-Aldrich Chemie GmbH, Steinheim, Germany) in humidified atmosphere at 5% CO<sub>2</sub> and 37°C (Heraeus, Hanau, Germany).

Cells were grown in 3 ml of serum-free medium for 18 h and seeded in six well culture dishes for clonogenic assay and on cover slips for immunocytochemical analyses. One hour prior to irradiation, scavengers were added in final concentrations of 1 and 100mM (DMSO) and 2 and 200 mM (glycerol). The medium was discarded and cells were irradiated with gamma rays from <sup>60</sup>Co source at the dose rate of ~ 1 Gy/min. Irradiation was performed in air at room temperature at the Vinča Institute of Nuclear Sciences, Belgrade, Serbia. After irradiation, cells were incubated in medium without DMSO and glycerol.

Irradiation doses for clonogenic assay were 0.5, 1, 2, 3, 4, 5 Gy. After seven days, cells were fixed and stained with 10% Giemsa solution [4]. More than 50 cells per colony were scored as a surviving cell. Survival was calculated by comparing the number of colonies in irradiated dishes with untreated control. Dose dependent cell survival data were fitted using the linear-quadratic equation:  $S = \exp(-\alpha D - \beta D^2)$ , where S is the surviving fraction for the dose D, while  $\alpha$  and  $\beta$  are the fitting parameters. Surviving fractions were evaluated from the best fit survival curves using the computer software TableCurve 2Dv 5.00.

Immunocytochemical analyses were performed as previously described [4]. Cells were fixed 30 minutes after irradiation with the dose of 1 Gy. Fluorescently labeled phosphorylated H2AX antibody (Alexa Fluor 488, BioLegend Inc. San Diego, California, United States) was used. Micrographs were made on laser confocal microscope Leica TCS SP5 II in LAS AF Lite software program (Leica Microsystem CMS GmbH).  $\gamma$ H2AX foci were quantified using Image J software.

Statistical analyses of experimental results were done using Student's *t* test and the level of significance was set at  $p < 0.05$ .

## RESULTS AND DISCUSSION

Comparing to irradiated control, SF2 value was significantly higher in cells pre-treated with 100 mM DMSO ( $p < 0.05$ ), while 1 mM DMSO had no significant effect on SF2 (Figure 1a). Therefore, 100 mM DMSO expressed higher radio-protective effect after seven days of incubation. Lower concentration of glycerol slightly stimulated cell survival while higher decreased SF2 but with no statistical significance (Figure 1.b). These results indicate that 2 mM glycerol may have radio-protective and 200 mM glycerol cytotoxic effect seven days after the treatment.

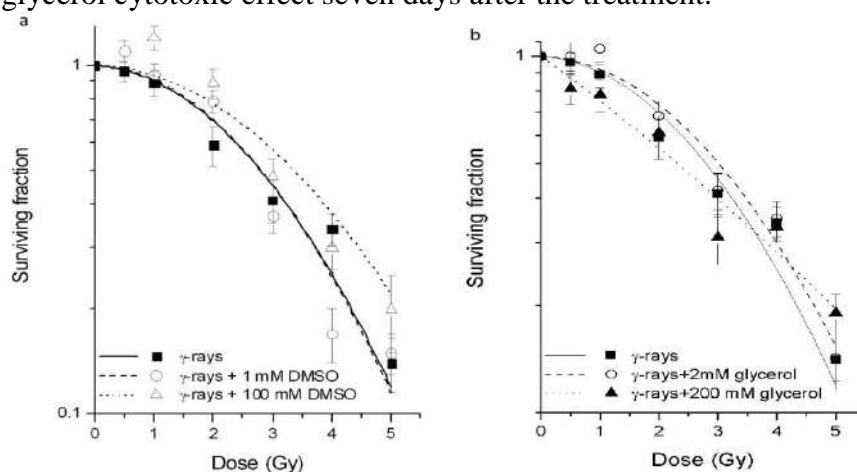


**Figure 1.** Clonogenic survival of HTB 177 cells 7 days after irradiation with 0.5, 1, 2, 3, 4, 5 Gy of gamma rays. Cells were treated with 1 and 100 mM DMSO (a) or 2 and 200 mM glycerol (b). Results are shown as mean  $\pm$  SEM.

DNA DSBs were analysed through the formation of  $\gamma$ H2AX foci 30 minutes after irradiation, when the level of  $\gamma$ H2AX expression was the highest [5]. Dose of 1 Gy was selected for fine detection of foci, as higher doses could cause signal overlapping [6]. The number of foci per cell were significantly lower in both experimental groups treated with DMSO comparing to irradiated control ( $p < 0.001$ ) (Figure 2.a) implicating its radio-protective role. 200 mM glycerol decreased number of foci per cell, ( $p < 0.001$ ) (Figure 2.b) thus showing radio-protective effect.

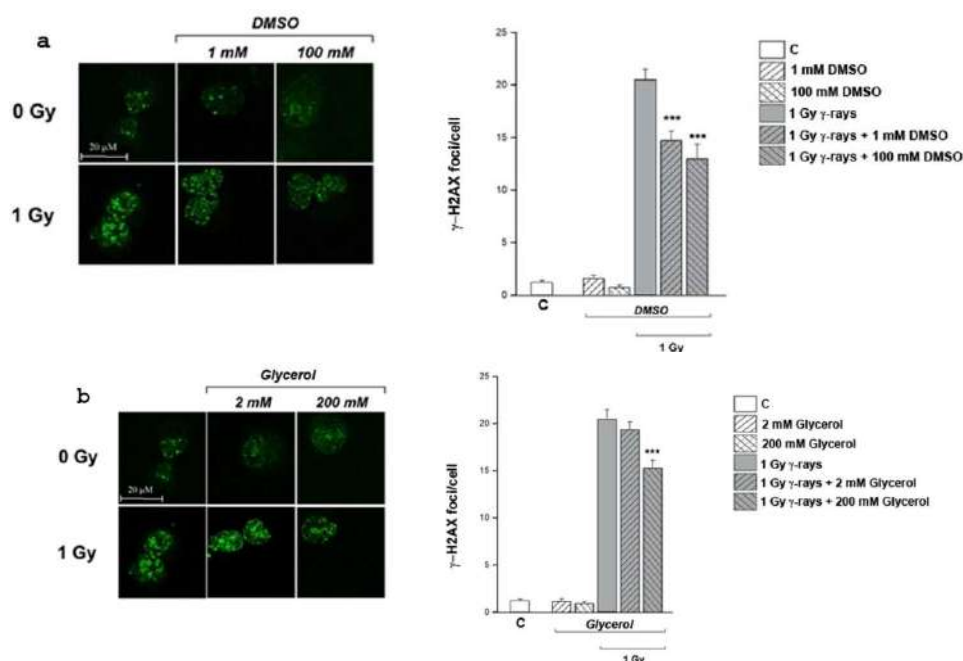


**Figure 2.** Immunocytochemical analyses of  $\gamma$ H2AX in DMSO (a) and glycerol (b) treated cells irradiated with 1 Gy of gamma rays. Results are shown as mean value of  $\gamma$ H2AX foci per cell  $\pm$ SEM.

## CONCLUSION

The results showed that DMSO and glycerol pre-treatment can stimulate cell survival seven days after irradiation with gamma rays. The possible mechanism is inhibition of DNA lesions by reducing the level of DNA DSBs. These data will be further analysed.

## Acknowledgement

This work was supported by the Ministry for Education, Science and Technological Development of the Republic of Serbia (Grants no. 173046 and 171019).

## REFERENCES

- [1] M.E. Lomax, L.K.Folkes, P. O'Neill, Clin. Oncol., 2013, **25**, 578 - 585.
- [2] G. Kashino et al., J. Radiat. Res, 2007, **48**, 327 - 333.
- [3] C. Leloup et al., Int. J. Radiat. Biol., 2005, **81**, 41 - 54.
- [4] O. Keta et al., Nucl. Technol. Radiat., 2014, **29**, 233 - 241.
- [5] W.M. Bonner et al., Nat. Rev. Cancer, 2008, **8**, 957 - 967.
- [6] O. Keta et al., Cell Biol. Toxicol., 2016, **32**, 83 - 101.

## MODULATION OF ACETYLCHOLINESTERASE ACTIVITY INDUCED BY POLYOXOTUNGSTATES

M. Čolović<sup>1</sup>, A. Bondžić<sup>1</sup>, U. Kortz<sup>2</sup>, V. Vasić<sup>1</sup> and D. Krstić<sup>3</sup>

<sup>1</sup> *Department of Physical Chemistry, Vinča Institute of Nuclear Sciences, University of Belgrade, Serbia (colovicm@vin.bg.ac.rs)*

<sup>2</sup> *Department of Life Sciences and Chemistry, Jacobs University, Bremen, Germany*

<sup>3</sup> *Institute of Medical Chemistry, Faculty of Medicine, University of Belgrade, Serbia*

### ABSTRACT

The *in vitro* influence of five polyoxotungstates containing various central atoms on acetylcholinesterase (AChE) activity was investigated.  $K_6[PV_3W_9O_{40}] \times 3H_2O$ ,  $K_6H_2[TiW_{11}CoO_{40}] \times 13H_2O$ ,  $(NH_4)_{14}[NaP_5W_{30}O_{110}] \times 31H_2O$ ,  $K_7[SiV_3W_9O_{40}] \times 10H_2O$ , and  $K_7[Ti_2PW_{10}O_{40}]$  induced the enzyme inhibition in a concentration-dependent manner. Inhibitory power of the investigated compounds was evaluated using  $IC_{50}$  values.  $K_7[SiV_3W_9O_{40}] \times 10H_2O$  affected AChE activity with lowest potency ( $IC_{50} = 4.80 \times 10^{-4}$  mol/L).  $K_6H_2[TiW_{11}CoO_{40}] \times 13H_2O$  and  $K_7[Ti_2PW_{10}O_{40}]$  exhibited high affinity toward the enzyme, inducing half-maximum inhibition at micromolar concentrations ( $1.14 \times 10^{-6}$  and  $1.04 \times 10^{-6}$  mol/L, respectively), while the same effect was achieved in the presence of about fifty times higher concentration of  $K_6[PV_3W_9O_{40}] \times 3H_2O$ . Finally,  $(NH_4)_{14}[NaP_5W_{30}O_{110}] \times 31H_2O$  was found as the most potent inhibitor of AChE activity ( $IC_{50} = 6.36 \times 10^{-7}$  mol/L), and consequently the most promising candidate for the treatment of neurological diseases associated with acetylcholine leakage.

### INTRODUCTION

Polyoxometalates (POMs) are negatively charged inorganic complexes containing transition metal ions surrounded by oxygen atoms [1]. These anionic clusters are relatively stable, some of them are even highly stable in aqueous solutions at physiological pH values [2]. POMs have been shown to exhibit biological activities *in vitro* as well as *in vivo*, including anticancer [3], antibacterial [4], antiviral [5], and antidiabetic [6] activities. Their biological mechanisms of action at the molecular level are not well understood. It has been speculated that POMs are likely to act extracellularly, inhibiting several different enzyme families such as

phosphatases, kinases, sulfotransferases, sialyltransferases, and ecto-nucleotidases, which are mostly located on the plasma membrane and display extracellular binding sites [7]. In a recent study, Iqbal et al. [8] demonstrated the inhibition of acetylcholinesterase (AChE) and butyrylcholinesterase activities induced by micromolar concentrations of a group of polyoxotungstates. AChE (EC.3.1.1.7) belongs to a group of membrane bound serine hydrolases, and is involved in the termination of impulse transmission by rapid hydrolysis of the neurotransmitter acetylcholine in numerous cholinergic pathways in the central and peripheral nervous systems [9]. Reversible inhibitors mostly have therapeutic applications, while toxic effects are associated with irreversible AChE activity modulators. The reversible inhibition of brain AChE is the major therapeutic target in the treatment of Alzheimer's disease associated with loss of cholinergic neurons in the brain and the decreased level of acetylcholine [10].

Considering the fact that AChE inhibition presents one of the strategies in the therapy of neurological diseases, and the literature data about high inhibitory potential of POMs, the aim of this study is to investigate the *in vitro* influence of five newly synthesized heteropolyoxotungstates on AChE activity, as potential anti-Alzheimer drugs.

## EXPERIMENTAL

Polyoxotungstates were synthesized and characterized by prof. Ulrich Kortz at Jacobs University, Bremen. Commercially available AChE purified from electric eel (Sigma, Germany) was exposed to the various concentrations of the investigated compounds during 20 minutes at 37°C. Afterwards, AChE activity was determined by slightly modified Ellman's method [11].

## RESULTS AND DISCUSSION

The effect of five newly synthesized polyoxotungstates:  $K_6[PV_3W_9O_{40}] \times 3H_2O$ ,  $K_6H_2[TiW_{11}CoO_{40}] \times 13H_2O$ ,  $(NH_4)_{14}[NaP_5W_{30}O_{110}] \times 31H_2O$ ,  $K_7[SiV_3W_9O_{40}] \times 10H_2O$  and  $K_7[Ti_2PW_{10}O_{40}] \times 10H_2O$  on AChE activity was investigated by *in vitro* exposure of the enzyme to the polyoxotungstates in concentration range  $1 \times 10^{-10}$  -  $2 \times 10^{-3}$  mol/L. The dependence of the enzyme activity, expressed as a percentage of control value (the enzyme activity obtained without inhibitor), on the polyoxotungstate concentration fitted a sigmoidal function for all investigated compounds (Fig. 1a).  $IC_{50}$  values, the parameters of the inhibitory potential defined as the concentration which induces 50% inhibition of the enzyme activity, were determined by sigmoidal fitting the

experimental results as well as by Hill analysis (Fig. 1b) and are summarized in Table 1. The obtained results show that all five investigated polyoxotungstates inhibit AChE activity in concentration dependent manner, but with various potencies.  $(\text{NH}_4)_{14}[\text{NaP}_5\text{W}_{30}\text{O}_{110}] \times 31\text{H}_2\text{O}$  is the most potent AChE inhibitor ( $\text{IC}_{50} = 4.79 \times 10^{-7}$  mol/L), about a thousand times stronger than the inhibitory power of  $\text{K}_7[\text{SiV}_3\text{W}_9\text{O}_{40}] \times 10\text{H}_2\text{O}$  ( $\text{IC}_{50} = 4.80 \times 10^{-4}$  mol/L). The sensitivity of AChE toward  $\text{K}_6\text{H}_2[\text{TiW}_{11}\text{CoO}_{40}] \times 13\text{H}_2\text{O}$  and  $\text{K}_7[\text{Ti}_2\text{PW}_{10}\text{O}_{40}] \times 10\text{H}_2\text{O}$  was similar with  $\text{IC}_{50}$  values of  $1.14 \times 10^{-6}$  and  $1.04 \times 10^{-6}$  mol/L, respectively, but their inhibitory potentials were about two times weaker compared to  $(\text{NH}_4)_{14}[\text{NaP}_5\text{W}_{30}\text{O}_{110}] \times 31\text{H}_2\text{O}$ . The obtained diversity in the inhibitory power of the investigated compounds could result from their differences in size, shape and charge.

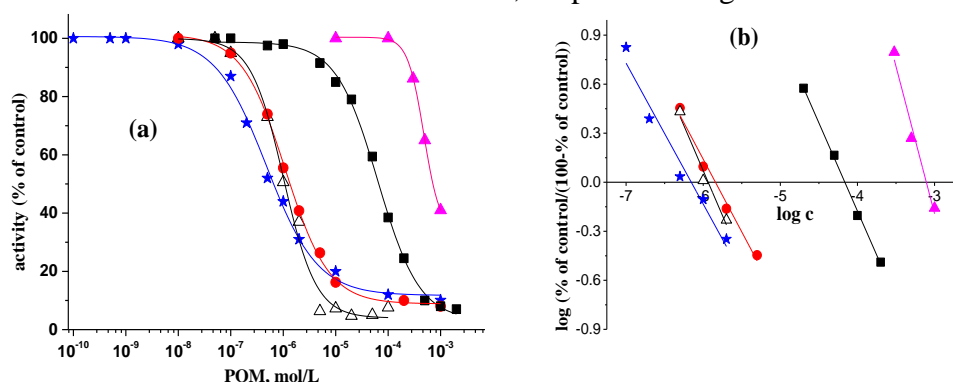


**Figure 1.** The concentration dependent (a) and Hill analysis (b) inhibition of AChE from electric eel induced by  $\text{K}_6[\text{PV}_3\text{W}_9\text{O}_{40}] \times 3\text{H}_2\text{O}$  (square),  $\text{K}_6\text{H}_2[\text{TiW}_{11}\text{CoO}_{40}] \times 13\text{H}_2\text{O}$  (circle),  $(\text{NH}_4)_{14}[\text{NaP}_5\text{W}_{30}\text{O}_{110}] \times 31\text{H}_2\text{O}$  (asterisk),  $\text{K}_7[\text{SiV}_3\text{W}_9\text{O}_{40}] \times 10\text{H}_2\text{O}$  (solid triangle), and  $\text{K}_7[\text{Ti}_2\text{PW}_{10}\text{O}_{40}] \times 10\text{H}_2\text{O}$  (open triangle).

**Table 1.**  $\text{IC}_{50}$  values of AChE inhibition by five newly synthesized polyoxotungstates obtained by fitting the experimental points by sigmoidal function and Hill analysis.

POM	Hill analysis	Sigmoidal function
	$\text{IC}_{50}$ , mol/L	$\text{IC}_{50}$ , mol/L
$\text{K}_6[\text{PV}_3\text{W}_9\text{O}_{40}] \times 3\text{H}_2\text{O}$	$6.56 \times 10^{-5}$	$6.36 \times 10^{-5}$
$\text{K}_6\text{H}_2[\text{TiW}_{11}\text{CoO}_{40}] \times 13\text{H}_2\text{O}$	$1.23 \times 10^{-6}$	$1.14 \times 10^{-6}$
$(\text{NH}_4)_{14}[\text{NaP}_5\text{W}_{30}\text{O}_{110}] \times 31\text{H}_2\text{O}$	$6.00 \times 10^{-7}$	$4.79 \times 10^{-7}$
$\text{K}_7[\text{SiV}_3\text{W}_9\text{O}_{40}] \times 10\text{H}_2\text{O}$	$5.82 \times 10^{-4}$	$4.80 \times 10^{-4}$
$\text{K}_7[\text{Ti}_2\text{PW}_{10}\text{O}_{40}] \times 10\text{H}_2\text{O}$	$1.15 \times 10^{-6}$	$1.04 \times 10^{-6}$

## CONCLUSION

In the present study, the potencies of five newly synthesized polyoxotungstates to decrease AChE activity were investigated for the purpose of their potential application in the therapy of neurological diseases associated with acetylcholine deficiency. The obtained results showed that three of five investigated compounds -  $(\text{NH}_4)_{14}[\text{NaP}_5\text{W}_{30}\text{O}_{110}] \times 31\text{H}_2\text{O}$ ,  $\text{K}_6\text{H}_2[\text{TiW}_{11}\text{CoO}_{40}] \times 13\text{H}_2\text{O}$ , and  $\text{K}_7[\text{Ti}_2\text{PW}_{10}\text{O}_{40}] \times 10\text{H}_2\text{O}$  remarkably affected the enzyme activity at micromolar concentrations. Consequently, these polyoxotungstates could be considered promising therapeutics in the treatment of Alzheimer's disease, and require further preclinical studies.

## Acknowledgement

This study was supported by the Ministry of Education, Science and Technological Development of the Republic of Serbia (Project No. 172023).

## REFERENCES

- [1] B. Hasenknopf, *Front. Biosci.*, 2005, **10**, 275–287.
- [2] G. Geisberger, S. Paulus, M. Carraro, M. Bonchio, G.R. Patzke, *Chem. Eur. J.*, 2011, **17**, 4619–4625.
- [3] X. Wang, J. Liu, J. Li, Y. Yang, J. Liu, B. Li, et al. *J. Inorg. Biochem.*, 2003, **94**, 279–284.
- [4] A. Seko, T. Yamase, K. Yamashita, *J. Inorg. Biochem.*, 2009, **103**, 1061–1066.
- [5] Y. Qi, Y. Xiang, J. Wang, Y. Qi, J. Li, J. Niu, et al. *Antiviral Res.*, 2013, **100**, 392–398.
- [6] K. Nomiya, H. Torii, T. Hasegawa, Y. Nemoto, K. Nomura, K. Hashino, et al. *J. Inorg. Biochem.*, 2001, **86**, 657–667.
- [7] S-Y. Lee, A. Fiene, W. Li, T. Hanck, K. Brylev, V. Fedorov, et al. *Biochem. Pharmacol.*, 2015, **93**, 171–181.
- [8] J. Iqbal, M. Barsukova-Stuckart, M. Ibrahim, S. Ali, A. Khan, U. Kortz, *Medicinal Chem. Res.*, 2013, **22**, 1224–1228.
- [9] J. Bajgar, *Adv. Clin. Chem.*, 2004, **38**, 151–216.
- [10] M. Čolović, D. Krstić, T. Lazarević-Pašti, A. Bondžić, V. Vasić, *Curr. Neuropharmacolog.*, 2013, **11**, 315–335.
- [11] G.L. Ellman, K.D. Courtney, V. Andreas, R.M. Featherstone, *Biochem. Pharmacol.*, 1961, **7**, 88–90.

## PROGESTERONE UPREGULATES ACTIVITY AND PROTEIN EXPRESSION OF ECTO-5'-NUCLEOTIDASE IN ISCHEMIC BRAIN OF MALE WISTAR RATS

I. Guševac Stojanović<sup>1</sup>, D. Drakulić<sup>1</sup>, M. Stanojlović<sup>1</sup>, I. Grković<sup>1</sup>, J. Martinović<sup>1</sup>, N. Mitrović<sup>1</sup>, M. Zarić<sup>1</sup>, F. Veljković<sup>2</sup> and A. Horvat<sup>1</sup>

<sup>1</sup>*University of Belgrade, VINCA Institute of nuclear sciences, Department of molecular biology and endocrinology, P.O. Box 522, 11001, Belgrade, Serbia.*

<sup>2</sup>*University of Belgrade, VINCA Institute of nuclear sciences, Department of physical chemistry, P.O. Box 522, 11001, Belgrade, Serbia.  
([filipveljkovic@vinca.rs](mailto:filipveljkovic@vinca.rs))*

### ABSTRACT

Reduction of oxygen and glucose supply to the brain due to diminished cerebral blood flow leads to damage of tissue which in experimental conditions can be mimicked by permanent ligation of common carotid arteries (2VO). Besides numerous genomic and non-genomic processes, cerebral ischemia enhances expression of ecto-5'-nucleotidase (eN), a main enzyme in the central nervous system that produces potent neuromodulator and neuroprotector, adenosine. Since progesterone (P), a potent sex steroid, is recognized as neuroprotective, aim of this study was to examine whether repeated low-dose P treatment is capable to induce changes in activity and protein expression of eN, at rat cortical membrane fraction following 2VO. Obtained results indicate that P modulates investigated parameters and through stimulation of adenosine generation might promote cytoprotection in ischemic brain.

### INTRODUCTION

The energy disturbance due to mild, permanent reduction of cerebral blood flow leads to the activation of microglia and astrocytes, subsequent production of inflammatory mediators, blood-brain barrier disruption and consequently, neuronal death [1]. This type of brain injury might induce massive release of ATP in the extracellular space, where it influences numerous aspects of neuronal, astrocytic, and microglial responses by activating purinergic receptors [2]. The extracellular ATP actions are controlled by members of ectonucleotidase family. Specifically, the rate-limiting enzyme in the ectonucleotidase pathway is ecto-5'-nucleotidase

(eN), which catalyzes the final step of AMP dephosphorylation and enables generation of adenosine, a potent neuromodulator and neuroprotector [3].

In the past few decades many therapeutic agents have been suggested for the treatment of ischemic brain injury. For instance, progesterone (P), a sex steroid, is involved in functions that extend beyond reproduction like synaptic plasticity, cognition, neurogenesis, etc. Although, its exogenous administration has been shown to improve the outcome in ischemic brain [4, 5], the mechanism by which P modulates adenosine generation, as one of the key neuroprotective agents, is not yet elucidated.

### EXPERIMENTAL

Three months old male Wistar rats, kept according to the standards of Ethical Committee for the use of laboratory animals of University of Belgrade, VINCA Institute of Nuclear Sciences, Serbia, were subjected either to sham or 2VO surgery as previously described [4, 6]. Following 2VO surgeries animals were subcutaneously injected with P (4-Pregnene-3,20-dione, dissolved in commercial flax oil, 1.7 mg/ml, 2VO + P) or equal volume of vehicle (commercial flax oil, 2VO + V), while sham operated animals were subjected to vehicle (Sham + V). The treatments were administered for seven consecutive days starting immediately after both types of surgeries [4].

To examine the activity and protein expression of eN, after decapitation and priory presented isolation of cortical synaptic plasma membranes (SPMs) [7], the samples were subjected to *in vitro* colorimetric assay for estimation of AMP hydrolysis and immunoblot analysis using anti CD73 antibody (Santa Cruz) for determination of changes in investigated enzyme's expression [7].

Presented results were obtained from three independent SPMs preparations and all measurements were done in triplicate. Statistical significance was determined by one-way ANOVA followed by Tuckey's posthoc test. Data are presented as mean  $\pm$  SEM.

### RESULTS AND DISCUSSION

Since our previous studies [4, 6] indicated that 2VO induces neurodegeneration due to provoked apoptotic processes observed in, both, cell body and terminals while P is capable to alter those processes by modifying BCl2 family expression and modulating caspase3 activity [4, 8], of interest was to examine whether repeated low-dose P treatment is able to modulate activity and protein expression of eN in the cerebral cortex.

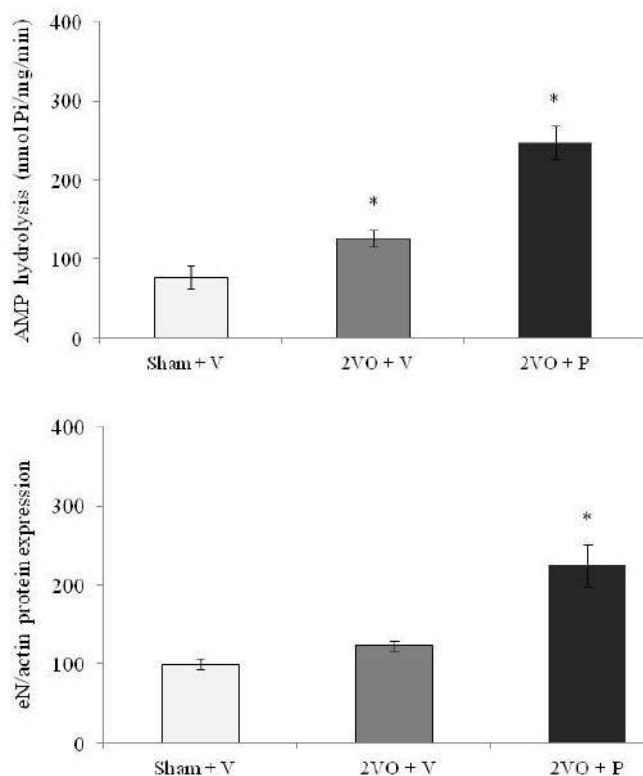


**Figure 1. AMP hydrolysis at cortical SPMs of sham operated animals treated with vehicle (Sham + V) and 2VO rats subjected either to vehicle (2VO + V) or progesterone treatment (2VO + P) as a marker of eN activity presented as a mean  $\pm$  SEM (\*  $p < 0.05$ ).**

**Figure 2. Protein expression of eN at cortical SPMs of sham operated animals treated with vehicle (Sham + V) and 2VO rats subjected either to vehicle (2VO + V) or progesterone treatment (2VO + P). Results are presented as a percentage of Sham + V, mean  $\pm$  SEM (\* $p < 0.05$ ).**

As shown in Figures 1. and 2, the rate of AMP hydrolysis in 2VO animals treated with vehicle increased significantly comparing to Sham + V group, but without altering eN protein abundance, while level of AMP hydrolysis and protein expression of eN were increased in 2VO animals treated with P.

The literature emphasizes that adenosine, a potent endogenous neuromodulator and homeostatic regulator, through balanced activation of its inhibitory and facilitatory receptors, mostly controls excitatory glutamatergic synapses thus mediating various neuroprotective events. In the brain that underwent ischemic conditions, observed augmentation in eN activity probably increased its concentration in extracellular milieu conferring its cytoprotection feature [9]. Thus, according to obtained results, it could be expected that in imposed experimental condition, P treatment might also lead to up-regulation of adenosine production in extracellular milieu attempting to ameliorate deleterious effects of 2VO.

## CONCLUSION

According to presented results, repeated low-dose P treatment is able to modulate activity and protein expression of eN following 2VO surgery and thus, through increased adenosine production, moderates the effect of ischemic insult. Our findings should be considered significant for establishing an adequate therapy for ischemic brain injury, given much controversy remains in this area and the connection between ischemia, adenosine and sex steroids is still poorly understood.

## *Acknowledgement*

This work is supported by Ministry of Education, Science and Technological development, Project No. 173044.

## REFERENCES

- [1] E. Farkas, P. G. M. Luiten, F. Bari, *Brain Res. Rev.*, 2007, **54**, 162-180.
- [2] G. Burnstock G, *Physiol. Rev.*, 2007, **87**, 659-797.
- [3] Zimmermann H, Zebisch M, Strater N, *Purinergic Signal*, 2012, **8**, 437-502.
- [4] M. Stanojlović, I. Guševac, I. Grković, J. Zlatković, N. Mitrović, M. Zarić, A. Horvat, D. Drakulić, *Neuroscience*, 2015, **311**, 308-321.
- [5] T. Ishrat, I. Sayeed, F. Atif, F. Hua, and D. G. Stein, *Neuroscience*, 2012, **210**, 442-450.
- [6] M. Stanojlović, J. Zlatković, I. Guševac, I. Grković, N. Mitrović, M. Zarić, A. Horvat, D. Drakulić, *Neurochem. Int.*, 2015, **83-84**, 1-8.
- [7] N. Mitrović, M. Zarić, D. Drakulić, J. Martinović, M. Stanojlović, J. Sévigny, A. Horvat, N. Nedeljković, I. Grković, *Neuroscience*, 2016, **324**, 286-296.
- [8] C. Espinosa-García, R. M. Viguera-Villaseñor, J. C. Rojas-Castañeda, A. Aguilar-Hernández, T. Monfil, M. Cervantes, G. Moralí, *Neurosci. Lett.*, 2013, **550**, 98-103.
- [9] S. S. Frassetto, M. R. C. Schetinger, R. Schierholt, A. Webber, C. D. Bonan, A. T. Wyse, R. D. Dias, C. A. Netto, J. J. F. Sarkis, *Braz. J. Med. Biol. Res.*, 2000, **33**, 1369-1377.

## **RADIOSENSITIZING PROPERTIES OF LABELLED DNA-PEPTIDE CONJUGATES**

P. Wityk and J. Rak

*University of Gdansk, Chemistry Department, Biological Sensitizer  
Laboratory, Wita Stwosza 63, 80-308 Gdansk, Poland  
(pawel.wityk@phdstud.ug.edu.pl)*

### **ABSTRACT**

In order to increase the efficacy of radiotherapy, radiosensitizers which sensitize tumour cells to radiation are introduced into this anticancer treatment. In hypoxic tumor cells the efficiency of radiation-induced DNA breakage is lower than in normal ones. Therefore, new high-affinity compounds which make DNA more sensitized to solvated electrons or compounds which enhance radical DNA damage should be introduced. Sensitizers making solvated electrons more reactive against DNA are brominated nucleobases which trigger strand breaks in DNA.

It is worth noticing, that in the cellular environment DNA permanently interacts with proteins via hydrogen bonding between nucleobases and amino acids and these interactions may influence both the primary electron attachment process and the secondary reactions leading to DNA damage. In order to study these important effects an access to the well-defined molecular models that could mimic such complexes, simultaneously being sufficiently simple for LC-MS, DHPLC or qPCR analysis, is necessary.

### **INTRODUCTION**

Radiotherapy, the most common modality for solid cancer treatment, is geared on DNA damage induced by the product of water radiolysis. Under hypoxia, typical for solid cancer cells, the efficacy of hydroxyl radicals ( $\bullet\text{OH}$ ) to trigger DNA damage is significantly lowered as compared to the oxygenated cells, while the yield of production of hydrated electrons is equal to that of  $\bullet\text{OH}$ . However, hydrated electrons ( $e_{\text{hyd}}$ ) are not able to induce a serious damage as strand breaks (SBs) to native DNA [1]. In order to make  $e_{\text{hyd}}$  harmful one can modify DNA with specifically altered nucleosides (radiosensitizers) so that an irreversible electron attachment to them may lead to SBs and ultimately to lethal effects [1,2]. In order to investigate such processes an appropriate model is necessary. Here we will present how a complex of BrdG-labeled double stranded DNA (dsDNA) with a covalently

linked peptide can mimic native cellular DNA environment and serve as a tool for the development of radio- or photosensitizers.

## EXPERIMENTAL

In order to verify the designed complex stability and its similarity to natural DNA/GCN4 complex a variety of techniques such as mass spectrometry, dHPLC analysis, nano-DSC (to obtain  $\Delta G$  value of binding and verify theoretical approach) or CD measurements to check conformation of DNA/peptide complex (BDNA and  $\alpha$ -helix form respectively), as well as molecular biology tools like digestion with restriction enzymes to inspect specific binding pattern [3] were employed. The sensitizing properties of BrdG labeled dsDNA alone or interacting with a peptide was investigated using high resolution mass spectrometry. Synthesis of dsDNA/peptide complex was performed using the CLICK chemistry catalyzed by Cu [4], N3-labeled 25 aa peptide, C8-alkyne-DC as well as BrdG labeled ssDNA and ssDNA complementary to the labelled strand. Analysis of radiolysis products was performed using LC-MS (Shimadzu-NEXERA, Triple-TOF 5600+, negative ionization mode, Waters BEH 1x50, 1.7  $\mu$ m). The electronic structure of the labelled dsDNA/peptide complexes was obtained using the Gaussian package (ONIOM scheme, 631+G(d,p)/ $\omega$ B97XD/Amber).

## RESULTS AND DISCUSSION

The thermodynamic properties such as  $\Delta G$  and  $\Delta H$  of the binding of peptide to dsDNA (Fig 1.) as well as the melting temperature (fluorescence labeling) of the system were measured and juxtaposed with the theoretical estimates

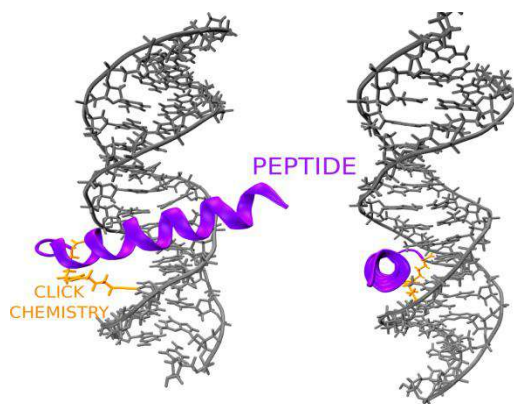


**Figure 1.** Schematic representation of  $\alpha$ -helical peptide interacting with dsDNA, obtained by CLICK chemistry reaction.

of binding free energy obtained by metadynamics ( $\Delta G \sim 11$  kcal/mol). Melting temperature (measured by CD) and DSC measurement confirmed that peptide in vicinity of DNA takes  $\alpha$ -helix conformation which melts cooperatively with DNA at 69 °C (Fig 2.).

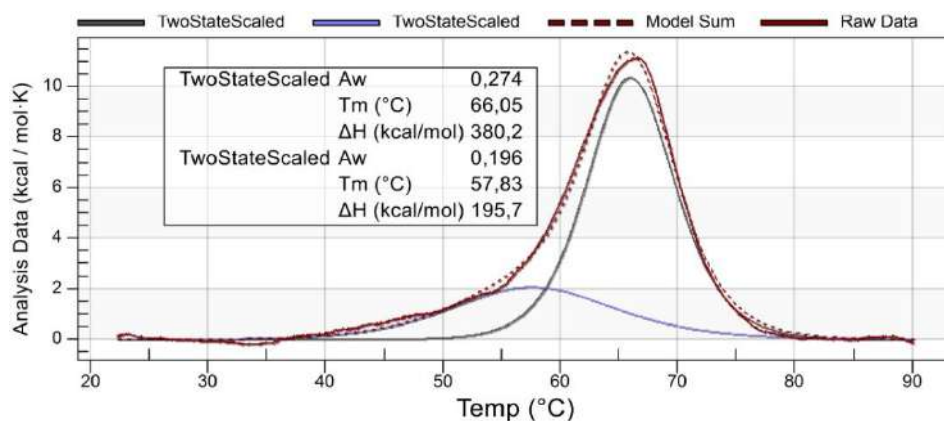


**Figure 2.** Thermogram of dsDNA-peptide complex and deconvolution of peptide and DNA melting processes.

Additionally, enzymatic digestion (DNase I footprinting) of the DNA-peptide conjugate confirmed that peptide strongly interacts with DNA recovering the native interactions [5,6,7] (e.g. ARG-GUA hydrogen bonding pattern). ATG-GUA interaction improves the adiabatic electron affinity (AEA) of BrdG incorporated into dsDNA/peptide conjugate. Studies concerning DNA damage carried out with the help of the above mentioned techniques revealed that solvated electrons produced by X-rays lead to DNA damage. The yield of DNA damage is different for labeled ssDNA, dsDNA and dsDNA/peptide conjugates (3%, 0.1% and 0.1% respectively). Undeniably, the most susceptible to solvated electrons is the labeled ssDNA.

## CONCLUSION

BrdG labeled DNA reveal different patterns of radiation damage. The most susceptible to solvated electrons is single stranded DNA, due to conformational freedom. The molecule in contrast to dsDNA alone or with peptide is not shielded by hydration sphere or peptide, respectively. This kind of interaction prevent DNA from being damage, due to not allowing reactive species appear in vicinity of phosphodiester bond.

DNA, the main target of anticancer therapy, is not sensitive to the near UV photons and hydrated electrons, one of the major products of water radiolysis under hypoxic conditions. A possible way to overcome these obstacles to

the efficient radio- and photodynamic therapy of cancer is to sensitize the cellular DNA to electrons by labeling it with suitable sensitizers (e.g. BrdG, SCN-dU, OCN-dU etc.).

Synthesis of dsDNA/Peptide complexes is quite challenging and requires usage of a variety of experimental techniques (dHPLC, HPLC, CD, nano-DSC, gel electrophoresis, mass spectrometry etc.). The sensitizing properties of 8-bromo,2'-deoxyguanosine differ in dsDNA/peptide complex and in the isolated dsDNA.

### ***Acknowledgement***

This work was supported by the project within the research of the development of young scientists in 2016 with a no.538-8227-B101-15/16(P.W.) and Polish National Science Centre under Grant No. 2014/14/A/ST4/00405 (J.R.)

### **REFERENCES**

- [1] J. Rak et al, J. Phys. Chem. B, 2015, **119**, 26,8227-8238.
- [2] L. Sanche. Radiat. Prot. Dosimetry, 2002, **99**, 57–62,.
- [3] D. Stanojevic , G. L. Verdine. Nat. Struct. Biol, 2:450–457, 1995.
- [4] M. Meldal, C. W. Tornøe, Chem. Rev., 2008, **108**, 2952-3015.
- [5] A.C.Cheng et al, Journal of Molecular Biol., 2003, 781-796.
- [6] M.M. Hoffman, et al, Nucleic Acid Res., D174-D181 2004.
- [7] G. J. Peters. Deoxynucleoside analogs in cancer therapy. Springer, 2006.
- [8] Y. Mandel-Gutfreund, O. Schueler, and H. Margalit, J Mol.Biol., 1995, **253**, 370–382.

## ARCHAEAN UNSTRUCTURED PROTEIN REGIONS DEPENDENCE ON GENOME AND PROTEOME CHARACTERISTICS

M. V. Beljanski<sup>1</sup>, S. N. Malkov<sup>2</sup>, N. S. Mitić<sup>2</sup>, G. M. Pavlović-Lažetić<sup>2</sup>  
and M. D. Pavlović<sup>1</sup>

<sup>1</sup>*Institute of General and Physical Chemistry, Bio-lab, P.O.B. 45, Studentski trg 14/V, 11001 Belgrade, Serbia(mbel@matf.bg.ac.rs)*

<sup>2</sup>*Faculty of Mathematics, University of Belgrade, P.O.B. 550, Studentski trg 16/IV, 11001 Belgrade, Serbia*

### ABSTRACT

Dependence of content of Archean Unstructured protein Regions on genome/proteome characteristics has been studied. There is in general nonlinear approximate dependence of Unstructured Protein Regions content for each of the genome/proteome characteristics considered: genome size, %GC, proteome size and APL.

### INTRODUCTION

Archaea are non-eukaryotic organisms constituting a domain and superkingdom of single-cellular microorganisms characterized by a unique and mosaic combination of Bacteria and Eukarya properties. Although initially viewed as extremophiles (living under extreme temperature, salt concentration, pH, pressure etc), they have been found in broad range of habitats including human microbiome. Until now, pathogenic Archaea are not known, but they are often found as mutualists or commensals. Because of their peculiar characteristics, organization of their genomes and proteome are currently under investigation in many laboratories [1].

In last 15 to 20 years it was well established that many of proteins in all of the three superkingdoms possess unstructured/disordered regions; i.e., regions in which protein amino acid (AA) chains have no fixed spatial structure. Such Unstructured Protein Regions (UPRs) are characterized by specific AA compositions, being enriched in polar and charged residues. They function via two basic mechanisms: (a) as entropic chains that fluctuate between many alternative conformations and have biological functions such as: linkers, spacers, bristles or springs and (b) by molecular recognition via short recognition elements that interact with other molecules such as: molecular recognition features, short linear motifs etc. They are mostly represented in protein belonging, as classifies according to Cluster of

Orthologous Groups, to Information storage and processing and Cellular processing and Structure groups, while proteins belonging to Metabolic group have less UPRs. Since they are difficult and expensive to study experimentally, a number (over 50) of computational prediction tools were developed. Predictors are grouped based on principle of their operation into those: (a) based on physico-chemical properties of AA, (b) based on homologous protein sequences alignment and (c) those based on consensus and cross validation of more individual predictors. Taxonomically, UPR are represented in the proteomes of all of the three superkingdoms. Depending on predictor and measure used, UPR content vary in ranges of 12% to 32% for Archaea, 18% to 35% for Bacteria and 35% to 50% for Eukarya [2], [3], [4].

Previous analysis of UPR content of Archaeal proteomes, by us and others, revealed correlation of UPR content on various genome/proteome characteristics [2], [4], [5]. Here, we present more detailed analyze of UPRs content coded by Archaeal genomes for dependence on genome size, %GC, proteome size and average protein length (APL).

## EXPERIMENTAL

Dataset has been collected from NCBI database and includes 139 fully sequenced Archeal organisms, with 296534 different protein of APL in the range between 215.10 and 344.00 AA [6].

UPR content of each residue of each protein has been calculated using IUPred L predictor and measure the fraction of AA in long disordered regions (>30 AA) [7]. Relationship of UPR with genome size (in Mbp), %GC, proteome size (number of proteins), and APL in Archea is presented as dot plot matrix with nonlinear approximation.

## RESULTS AND DISCUSSION

Previous analysis of UPRs content of Archaeal proteomes, on smaller sample, for dependence on genome size, %GC, proteome size and average protein length (APL), revealed linear correlation of UPR content [4]. Here, we present more detailed analyze of UPRs content of Archaeal proteomes. We show, as revealed in Fig. 1. (A) – (D), that there is, in general, nonlinear increasing approximation of UPR content with increase of values of every of the tree of genome/proteome characteristics considered: genome size, %GC, proteome size and APL. (1) There is an increase in UPR content at high genome (after ~2Mbp) and proteome size, (after  $\sim 10^5$ ) (Fig. 1. A, C).

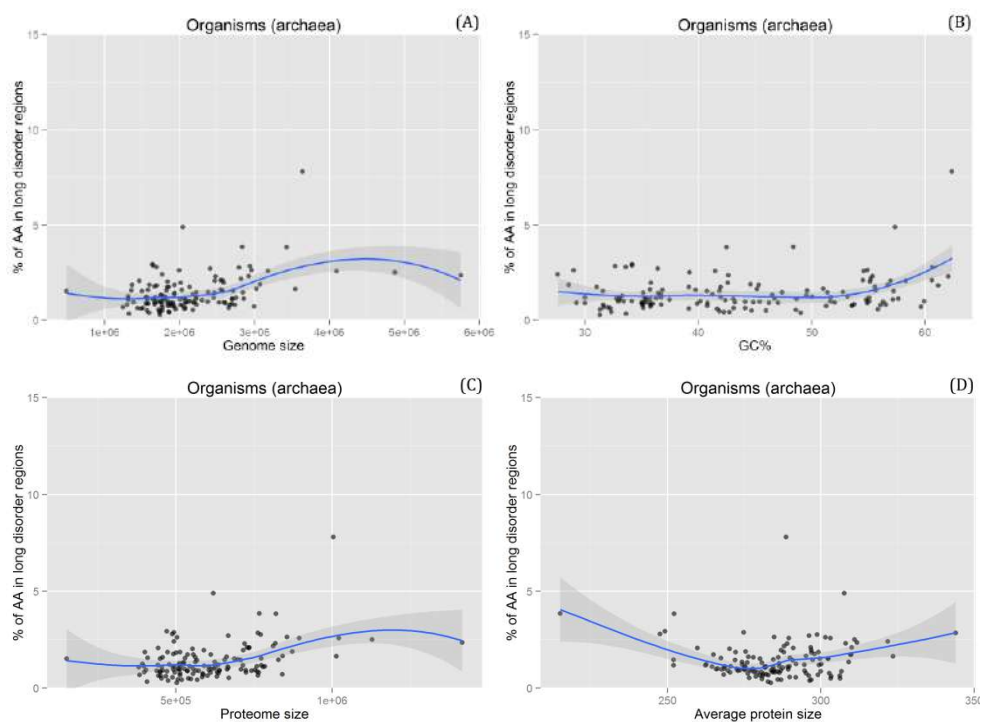


**Figure 1.** Nonlinear approximation of UPRs content (%AA in long unstructured/disordered regions (>30 AA)), as a function of Archaeal (A) genome size, (B) %GC, (C) proteome size and (D) AVL.

More proteins imply bigger interactome and, since one of the main functions of UPRs is in molecular interaction and recognition, more UPRs [2], [3]. (2) As it concerns to APL, smaller proteins are generally more unstructured, while bigger ones may poses more interacting sites, which in both cases results in higher UPR content (Fig. 1, D). This finding is in agreement with previous observations made for small and large proteins in UniProt [7], [8]. (3) UPR content in Archeal proteomes increases with increase of %GC for values of 55% GC and more (Fig. 1B). Increase may be explained by the fact that high GC value in codons results in an increased propensity of Gly, Ala, Arg and Pro AA found in UPRs [4]. However, relatively constant level of UPRs up to 55% GC may result from selective pressure to codon usage, via appearance of higher %GC on third and/or first position in AA codons. The same analysis performed for UPRs dependence on geno/proteo characteristics for Bacteria (2554 organisms) showed similar results (work in preparation). Finally, it should be noted that, also, there is apparent

correlation between mentioned geno/proteo characteristics: bigger genome → bigger proteome size → bigger APL → bigger %GC [9],[10].

### CONCLUSION

All mentioned geno/proteo characteristics are highly inter-connected and inter-dependent not only to each others, but to other organism characteristics such as morpho/physiological and ecological characteristics [5], [11], [12]. Such analysis may help to understand complex geno/proteo, morpho/physiological and ecological inter-dependencies in Arcaea organisms in the course of evolution.

### Acknowledgement

This work was partially supported by the Ministry for Science of the Republic of Serbia (Grant no.174021).

### REFERENCES

- [1] R. Cavicchioli, *Archaea: Molecular and Cellular Biology*. American Society for Microbiology 2007.
- [2] V. N. Uversky, *Chemical reviews*, 2014, **114**, 6557-6560.
- [3] P. Tompa, *Structure and Function of Intrinsically Disordered Proteins*. Chapman and Hall/CRC, 2009.
- [4] G. M. Pavlović-Lažetić, N. S. Mitić, J. J. Kovačević, Z. Obradović, S. N. Malkov, M. V. Beljanski, *BMC Bioinformatics*, 2011, **12**, 66.
- [5] B. Xue, R. W. Williams, C. J. Oldfield, A. K. Dunker, V. N. Uversky, *BMC Systems Biology*, 2010, **4**, S1.
- [6] [www.ncbi.nlm.nih.gov](http://www.ncbi.nlm.nih.gov)
- [7] [http://iupred.enzim.hu/IUP\\_links.php](http://iupred.enzim.hu/IUP_links.php)
- [8] M. Howell, R. Green, A. Killeen, L. Wedderburn, V. Picascio, A. Rabionet, Z. Peng, M. J. Mizianty, M. Larina, B. Xue, L. Kurgan, V. N. Uversky, *Journal of Biological Systems*, 2012, **20**, 471-511.
- [9] E. V. Koonin, Y. I. Wolf, *Nucleic Acids Research*, 2008, **66**, 6688-6719.
- [10] E. Schad, P. Tompa, H. Hegyi, *Genome Biology*, 2011, **12**, R120.
- [11] N. Sabath, E. Ferrada, A. Wagner, *Genome Biology and Evolution*, 2013, **5**, 966-977.
- [12] Z. Peng, J. Yan, X. Fan, M. J. Mizianty, B. Xue, V. N. Uversky, L. Kurgan, *Cellular and Molecular Life Sciences*, 2015, **72**, 137-151.

## AROMATIC-AROMATIC INTERACTIONS IN AMYLOIDSTRUCTURES

I. M. Stanković<sup>1</sup>, D. M. Božinovski<sup>2</sup>, Edward N. Brothers<sup>3</sup>, M. R. Belić<sup>3</sup>, M. B. Hall<sup>4</sup> and S. D. Zarić<sup>2,3</sup>

<sup>1</sup> *University of Belgrade, Institute of Chemistry, Technology and Metallurgy, Njegoševa 12, 11000 Belgrade, Serbia.*

<sup>2</sup> *Department of Chemistry, University of Belgrade, Studentski trg 12-16, 11000 Belgrade, Serbia. (szaric@chem.bg.ac.rs)*

<sup>3</sup> *Science Program, Texas A&M University at Qatar, Texas A&M Engineering Building, Education City, Doha, Qatar*

<sup>4</sup> *Department of Chemistry, Texas A&M University, College Station, TX 77843-3255, USA*

### ABSTRACT

Aromatic-aromatic interactions exist in various molecular systems, including amyloids. These interactions have been considered important in amyloid self-assembly process. In this study, the occurrence and geometry of aromatic-aromatic interactions were analyzed in the amyloid structures found in the Protein Data Bank. The present data confirms that aromatic-aromatic interactions are not necessary for amyloid formation. The analysis of the interaction geometries shows difference between intersheet and intrasheet aromatic-aromatic interactions.

### INTRODUCTION

Amyloids are protein aggregates found as fibrillar deposits and associated with many human diseases [1]. Because of their role in human diseases, as well as because of unusual structure and physical properties, amyloids are very interesting and they have been extensively studied. Amyloids are formed by short polypeptides that self-assemble into  $\beta$ -sheets with backbone hydrogen bonds. The polypeptide side chains of  $\beta$ -sheets interact keeping  $\beta$ -sheets together and forming long linear protofilaments with an axis nearly perpendicular to a polypeptide strand. Independent of peptide sequence, all amyloids form very similar cross- $\beta$  structure, made of  $\beta$ -strand parallel arrays. Depending on the side chains, these structures can have different morphology of a fibril and can have different intersheet distance [2]. Presence of aromatic amino acids, as well as aromatic-aromatic interactions have been considered important for amyloid formation.

In this work we present the results on frequency, and geometric properties of aromatic-aromatic interactions in amyloid structures from the Protein Data Bank. We studied separately aromatic-aromatic interactions within sheet (intrasheet interactions) and between two sheets (intersheet interactions).

### EXPERIMENTAL

Amyloid Database was created by filtering Protein Data Bank by keyword and geometric criteria as described in paper by Stankovic and Zaric (2016) [3]. We used geometrical criteria to find aromatic-aromatic interactions in amyloid structures in Amyloid Database. As amyloid fibril growth can be conducted through intrasheet interactions within the same  $\beta$ -sheet, or by side chain interactions between different  $\beta$ -sheets (intersheet interactions), these two types of interactions were treated separately [2]. The program written by our group was used to find geometrical parameters in amyloid structures. The contact between two rings was considered aromatic-aromatic interaction if the distance between centers of the rings was equal or shorter than 6.0 Å. The geometry parameters such as distance between centers of the rings, angles between aromatic rings, and parallel displacement (offset) values between centers of the rings, were determined, as well as correlations of these geometrical parameters.

### RESULTS AND DISCUSSION

In the study we considered three aromatic amino acids, phenylalanine, tyrosine, and tryptophan and all the combinations of interactions between aromatic rings of these amino acids were taken into account. The five-membered ring of tryptophan was not accounted for the aromatic-aromatic interactions. Also, only the interacting cross- $\beta$  fragments were analyzed in the study.

The criteria for aromatic-aromatic interactions was that the distance between the aromatic ring centers should be equal or less than 6.0 Å. Although the analysis of the number of structures and interactions indicate significant number of aromatic-aromatic interactions (Table 1), neither aromatic amino acids nor their  $\pi$ - $\pi$  interactions are crucial for the amyloid existence. It is in agreement with previous studies on amyloids, as well as with our recent quantum chemical calculations indicating stronger interactions of aromatic-aliphatic than aromatic-aromatic interactions [4].

**Table 1.** Number of structures and aromatic-aromatic interactions in amyloid structures

	№ structures	№ interactions
Containing aromatic amino acids	251	---
Intrasheet aromatic-aromatic interactions	150	2309
Intersheet aromatic-aromatic interactions	49	273

The aromatic-aromatic interactions found in amyloid structures have the characteristic that the normal distance between rings ( $R$ ) decreases along the offset values ( $r$ ). This is similar to the previously observed aromatic-aromatic interactions in crystal structures of small molecules from Cambridge Structural Database [6,7], and in protein structures from Protein Data Bank [5]. Different geometric properties of the intersheet and intrasheet aromatic-aromatic interactions in amyloid structures were observed. The intersheet aromatic-aromatic interactions are mostly parallel displaced with offset values in the range 2.5-3.0 Å and exhibit high values and angles between rings, 30-40°, while the intrasheet interactions have larger range of offset values 2.5-5.0 Å, they are mostly parallel with angles 0-5°, and always involve aromatic rings stacked in array. Interactions of angles up to  $P_1/P_2=40^\circ$  could be considered stacking  $\pi$ - $\pi$  interactions as they exhibit very similar energy-offset dependence as the parallel interactions [5]. Also, in our previous work we found significantly strong aromatic-aromatic interactions at larger offsets up to 5.0 Å [6, 7]. The intrasheet interactions are far more frequent than the intersheet interactions. It is known that intrasheet hydrogen bonds between backbone atoms are responsible for the  $\beta$ -sheet formation and that they are stronger than  $\pi$ - $\pi$  interactions. Aromatic rings are not always positioned one along another in a  $\beta$ -sheet formation in amyloids: in our survey, there are 150 structures containing intrasheet aromatic-aromatic interaction out of total 251 structures containing aromatic rings, Table 1. In the structures where intrasheet interactions are present, they are always arranged in an array of several rings. This could be the consequence of maximized intrasheet backbone hydrogen bonds between parallel  $\beta$ -strands because the strands are always aligned along the entire length. Thus, the intrasheet aromatic-aromatic interactions are probably the consequence of the steric condition inside a protein  $\beta$ -sheet. Our data show that in amyloids the most frequent are interactions between two phenylalanine rings, number of interactions

between two tyrosine rings is significantly smaller, while number of interactions between two tryptophan rings is even smaller. It is interesting to notice that the number of the interactions between two different aromatic rings is the smallest. Considering type of amino acids involved in the interactions, large difference between intersheet and intrasheet interactions was observed. Among intersheet interactions the most frequent are tyrosine-tyrosine interactions, while among intrasheet interactions the most frequent are phenylalanine-phenylalanine interactions.

## CONCLUSION

By analyzing the aromatic-aromatic interactions in amyloids from Protein Data Bank it was established that aromatic amino acids are not present in every amyloid structure and they are not essential for the amyloid self-assembly. The aromatic-aromatic interactions between adjacent  $\beta$ -strands within the same  $\beta$ -sheet of an amyloid structure are far more frequent than the intersheet interactions. For the intrasheet aromatic-aromatic interactions, a parallel geometry is the most frequent, with the  $P_1/P_2$  interplanar angles of  $0-5^\circ$  and offset values in the range of  $2.5-5.0 \text{ \AA}$ . In the case of the intersheet interactions, there are no parallel ring arrangements. The most frequent are displaced rings with  $P_1/P_2$  interplanar angle between  $30-40^\circ$ .

## Acknowledgement

This work was supported by the Serbian Ministry of Education, Science and Technological Development [grant number 172065] and made possible by an NPRP grant from the Qatar National Research Fund (a member of the Qatar Foundation) [grant number NPRP8-425-1-087].

## REFERENCES

- [1] W. Pulawski, U. Ghoshdastider, V. Andrisano and S. Filipek, *Appl. Biochem. Biotechnol.*, 2012, **166**, 1626–1643.
- [2] R. S. Harrison, P. C. Sharpe, Y. Singh, D. P. Fairlie, *PhysiolBiochemPharmacol*, 2007, **159**, 1–77.
- [3] I. M. Stanković and S. D. Zarić (accepted for publication in *Transactions on Internet Research*).
- [4] D. B. Ninković, D. P. Malenov, P. V. Petrović, E. N. Brothers, S. Niu, M. B. Hall, M. Belić, S. D. Zarić (in preparation)
- [5] D. B. Ninković, J. M. Andrić, S. N. Malkov, S. D. Zarić, *Physical chemistry chemical physics : PCCP*, 2014, **16**(23), 11173–7.
- [6] D. B. Ninković, G. V. Janjić, D. Z. Veljković, D. N. Sredojević, S. D. Zarić, *ChemPhysChem*, 2011, **12**(18), 3511–3514.
- [7] D. B. Ninković, J. M. Andrić, S. D. Zarić, *ChemPhysChem*, 2013, **14**, 237–243.

## VANADATE UPTAKE AND INFLUENCE ON PHOSPHATE METABOLISM OF *COPRINELLUS MICACEUS* MYCELIUM

M. Žižić<sup>1</sup>, K. Tešanović<sup>2</sup>, M. Karaman<sup>2</sup> and J. Zakrzewska<sup>3</sup>

<sup>1</sup>*Institute for Multidisciplinary Research, University of Belgrade, Kneza Višeslava 1, 11030 Belgrade, Serbia*

<sup>2</sup>*Department of Biology and Ecology, Faculty of Sciences, University of Novi Sad, 21000 Novi Sad, Serbia*

<sup>3</sup>*Institute of General and Physical Chemistry, Studentski trg 12-16, 11000 Belgrade, Serbia*

### ABSTRACT

The possibility of uptake and influence of vanadate ( $V^{5+}$ ) on phosphate metabolism of the mycelium of *Coprinellus micaceus* was examined in this study. For these purposes,  $^{31}P$  and  $^{51}V$  NMR were used. It was determined that 10 mM vanadate induced rise in intensities of sugar phosphate signals in  $^{31}P$  NMR spectrum was observed immediately after treatment. The produced changes suggested significant influence of vanadate to the phosphate metabolism without considerable side consequences to the cell reflected through unchanged signals of the energy important signals. Such effect can be attributed to the action of intracellular vanadate monomer which represented the only vanadate species accumulated intracellularly

### INTRODUCTION

Vanadium in the oxidation state 5+, vanadate, evinces significant role in inhibition of various enzymes in phosphate metabolism in many organisms [1]. One of the main advantages of such vanadate action was its application in the treatments of insulin deficiency and insulin tolerance [2]. However, its usage as a therapeutic agent was limited due to its toxic effects [3]. The fungi are known as the organisms which have a capacity for uptake of the majority of metals, including vanadium [4]. The cellular response to the uptake of vanadium depends on the fungal species and oxidation state of this element [5, 6]. *C. micaceus* is an edible mushroom from genus of *Coprinella*, able to absorb the metals such as Pb, Cd, Cu, Zn, Mn, Fe and Ni [7]. but the knowledge about entrance and effects of vanadium, [6, 8], remain unsolved. Having in mind inhibitory and stimulatory effects of vanadate to the enzymes of phosphate metabolism [8, 9], the various possibility of  $V^{5+}$  absorption by fungal species [5, 6] and resistance of some

of them to high vanadate concentration [5, 6, 8, 9], its uptake and physiological effects were examined in this study.

### EXPERIMENTAL PROCEDURES

Isolated mycelia of fungi were cultivated on the Malt agar at 26°C during 10 days. Submerged cultivation was carried out in an Erlenmeyer flask (300 ml). After initial cultivation, 5 plugs of mycelia were transferred into 100 ml of fermentation medium, pH 6.5. Incubation was at temperature 26°C, 21 days on a rotary shaker at 100 rpm. The NMR experiments were performed using Apollo upgrade, Bruker MSL 400 spectrometer operating at 161.978 MHz for  $^{31}\text{P}$  and 105.169 MHz for  $^{51}\text{V}$ .  $^{31}\text{P}$  NMR spectra were accumulated with 14  $\mu\text{s}$  pulse duration (about 45°) and 300 ms recycle time. The assignment of NMR spectra and spectral line intensities evaluation were performed as described previously [8]. Sodium orthovanadate was added in concentration of 10 mM in 10 day old mycelium and spectra were acquired immediately upon addition. For  $^{51}\text{V}$  spectra, pulse duration was 20  $\mu\text{s}$  (45°), duration of spectrum recording of 3.6 min to 36 min for the spectra collected from vanadium treated unwashed and washed mycelium, respectively. Mycelia were washed with deionised water by vacuum filtration. Chemical shifts are given relatively to the external 1M sodium metavanadate at pH =12 ( $\text{VO}_4^{3-}$  at -535.7 ppm) [10]. For  $^{31}\text{P}$  NMR analysis of mycelial extracts mycelium was treated with  $\text{V}^{5+}$  at final concentration of 10 mM for 10 minutes and then washed with deionised water. Control and treated mycelia were suspended in 0.5 M perchloric acid (1:5 w/v), and homogenized in mortar on ice for 15 min. Obtained homogenate was stirred for 15 min on ice and centrifuged at 10000 x g for 12 min. The precipitate was discarded and supernatant was treated with 2M KOH until pH was 7. The aliquots were kept on -20 °C and unfrozen just before experiments.

### RESULTS

The major peaks in the  $^{31}\text{P}$  NMR spectrum of the mycelium of *C. micaceus* with chemical shifts of -22.1 ppm, -12 ppm, -10.2 ppm, 2.4 ppm and 0.9 ppm was assigned to core-polyphosphates ( $\text{PP}_c$ ), UDPG, NADP(H)+UDPG, and cytoplasmic inorganic phosphates ( $\text{P}_{ic}$ ) and vacuolar inorganic phosphate ( $\text{P}_{iv}$ ), respectively. Vanadate addition caused the appearance of a new signal positioned at about 3.3 ppm and increase in intensity of signal of hexose 6 phosphate (HP) (Fig 1A). At the first glance, the new signal could be attributed to  $\text{P}_{ic}$  shifted due to the pH increase after vanadate addition. To prove the pH value upon vanadate addition  $^{51}\text{V}$  NMR spectrum of vanadate treated mycelium was recorded. (Fig 1B). In

addition to monomer (V1) and dimer (V2), signal from vanadate tetramer (V4) was detected. Having in mind that tetramer does not enter cells [9], monomer and/or dimer is proposed to be accumulated intracellularly. Monomer at -559 ppm and dimer at -572 ppm indicated the pH  $\sim$  7.4 which correspond to the  $P_i$  signal at  $\sim$ 2.4 ppm in  $^{31}\text{P}$  NMR spectra; this excluded the possibility of  $P_{ic}$  at 3.3 ppm. The existence of only one signal at -559 ppm in the  $^{51}\text{V}$  NMR spectrum of washed mycelium (Fig 1B) substantiated the intracellular accumulation of vanadate monomer.

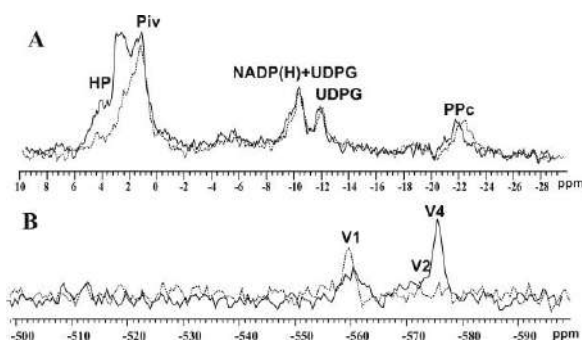


**Figure 1.**  
(A)  $^{31}\text{P}$  NMR spectrum of fresh mycelium (dotted line) and mycelium treated with 10 mM vanadate (solid line) (B)  $^{51}\text{V}$ -NMR spectrum of vanadate treated mycelium before (solid line) and after washing (dotted line)

As the appearance of the peak at 3.3 ppm in  $^{31}\text{P}$  NMR spectrum could not be a result of pH changes in the cell, the possibility of accumulation of glucose 1 phosphate (G1P) was considered, due to the fact that this G1P in the approximately neutral pH it resonances in this spectral region [11] and knowing the ability of species from orders of *Agricales* to synthesize glycogen [12] For this purposes, we recorded spectrum of mycelium perchloric extract (pH 7). Obtained results are shown in Fig 2.

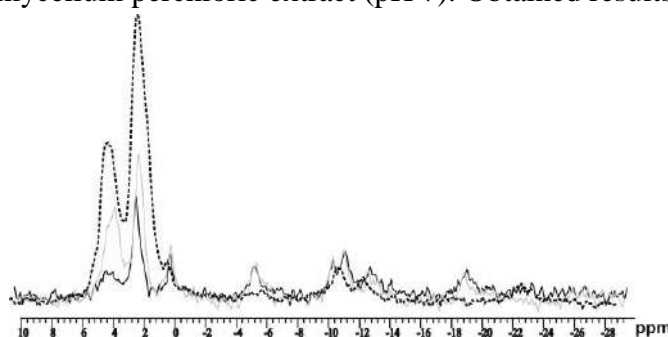


**Figure 2.**  
 $^{31}\text{P}$  NMR spectrum of the extract of mycelium (black), the extract of mycelium treated with 10 mM vanadate (gray) and fresh mycelium treated with G1P and G6P (dashed).

The position of Pi in the spectrum of the extract of untreated mycelium substantiated data obtained *in vivo* that the cytoplasm has the pH about 7. All signals in the spectra of extracts had almost the same intensities after treatment, except of the signal of HP that undergone impressive increase i.e., intensity increase by 96% (Fig 2) and the signal of Pi which seems to be broader and slightly shifted. If we compare the spectrum of mycelium extract treated with vanadate, with the spectrum of fresh mycelium treated with G1P and glucose 6 phosphate (G6P) (Fig. 2, gray and dashed spectra) similarity between sugar phosphates signals is clearly visible, because of similar pH conditions in the cell and in the cell environments. In summary, treatment of mycelium of *C. micaceus* with 10 mM vanadate caused the increase in concentration of sugar phosphates. The importance of such effects is greater due to almost negligible influence of added vanadate to other phosphorus compounds in the cell. Observed effects are attributed to the action of monomer which represents the only intracellular vanadate species.

**Acknowledgement:**

Supported by Ministry of Education, Science and Technological Development of Republic of Serbia, grant No. 173040.

**REFERENCES**

- [1] D. Rehder (2015). *Metallomics* 2015, **7**: 730-742.
- [2] D. Rehder (2003). *Inorg Chem Commun.* **6**: 604-617.
- [3] E. Tsiani and I. G. Fantus, (1997). *TEM*, **8**: 52-58.
- [4] P. Kalac, L. Svoboda (2000). *Food Chem.* **69**, 273-281
- [5] M. A. Zoroddu (1999). *Annals of the New York Academy of Sciences*, **879**, 288–291.
- [6] I. Mannazzu, (2001). *Ann. Microbiol.* **51**, 1-9
- [7] N. Das (2007). *Indian Forester* **133** (2), 171-178.
- [8] M. Žižić, M. Živić, V. Maksimović, M. Stanić, S. Križak, T. Cvetić Antić, J. Zakrzewska (2014). *Plos One* **9**, 102849
- [9] C. Han, B. Cui, and J. Qu (2009). *Biol Trace Elem Res.* **127**, 278-283.
- [10] D. Rehder (2008). *Bioinorganic vanadium chemistry*. J. Wiley and Sons, Chichester, New York
- [11] M. Barany, T. Glonek (1984). *Phosphorus <sup>31</sup>P NMR. Principles and Applications*. Academic Press, Orlando, Florida.
- [12] J. Ji, D. Moore (1993). *Mycol. Res.* **97**(3), 283-299.

**STRUCTURE-ACTIVITY RELATIONSHIPS OF  
PROPAFENONE ANALOGUES ON *PSEUDOMONAS  
AERUGINOSA*: EXPERIMENTAL AND DOCKING  
STUDIES**

M. Senćanski<sup>1</sup>, B. Ivković<sup>2</sup>, D. Božić<sup>3</sup>, S. Grubišić<sup>4</sup>,  
M. Milenković<sup>3</sup> and Z. Vujić<sup>2</sup>

<sup>1</sup>*Center for Multidisciplinary Research, Institute of Nuclear Sciences Vinca,  
University of Belgrade, Mihaila Petrovica Alasa 14, Belgrade, Serbia*

<sup>2</sup>*Department of Pharmaceutical Chemistry,*

<sup>3</sup>*Department of Microbiology and Immunology, Faculty of Pharmacy,  
University of Belgrade,*

*Vojvode Stepe 450, Belgrade-Serbia. (blucic@pharmacy.bg.ac.rs)*

<sup>4</sup>*Center for Chemistry, IHTM, University of Belgrade, Njegoševa 12,  
Belgrade, Serbia*

**ABSTRACT**

Series of six propafenone analogues has been evaluated for antimicrobial activities against *Pseudomonas aeruginosa*. Antimicrobial activity were confirmed for all tested compounds. The Docking studies of propafenone analogues into a X-ray crystal structures of porin *Pseudomonas aeruginosa* suggest that propafenone analogues show an interactions which may affect the functionality of porin i.e. bacterial cell.

**INTRODUCTION**

Earlier pharmacological studies discovered that propafenone analogues impair proliferation of cancer as well as microbial cells. Previous SAR studies of propafenone derivatives have selected the ethers, carbonyl, benzyl and amino groups as determinants for pharmacological activity of the propafenone and its derivatives [1-2]. Six of the synthesized derivatives are distinguished by the substitution of the benzyl moiety -F, -Cl atoms or -CH<sub>3</sub>, -CF<sub>3</sub> groups (Table 1). These new substituents cause significant changes of lipophilicity and stereoelectronic properties of the benzyl moiety. These structural modifications could result in formation of intermolecular bonds of the benzyl moiety of the propafenone derivatives with hydrophobic amino acid residues in the inner pore of the porin and enhanced antimicrobial activities.

## EXPERIMENTAL

The X-ray crystal structures of porin *Pseudomonas aeruginosa* opdl PDB ID: 2Y0H [Crystal Structure of *Pseudomonas Aeruginosa* Opdl, Touw, D.S., Vijayaraghavan, J., Vandenberg, B., To Be Published] was obtained from the Protein Data Bank (<http://www.rcsb.org/pdb>). Compounds 1-7, Table 1, were constructed in Accelrys Draw 4.2 [3], protonated at pH 7.4 and geometrically optimized at MM level of theory using MMFF94 force field. Obtained structures were, along with protein structure, prepared for docking in Autodock Tools 1.5. Docking was carried in Autodock Vina 1.1.2. [4]. All calculations were carried on PARADOX computer cluster (Scientific Computing Laboratory of the Institute of Physics, Belgrade, Serbia).

## RESULTS AND DISCUSSION

The binding site in porin, from docking results, consists of pocket between three inner loops, including following aminoacids: Val 123, Arg 124, Asp 121, Met 167, Leu 288, Thr 293, Thr 295 and Arg 296 (Fig. 1).

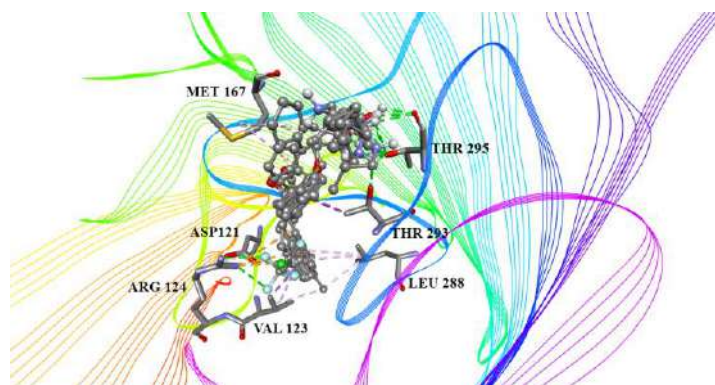


**Figure 1.** Binding site of porin with marked aminoacids, docked compounds and marked interactions. Green: hydrogen bonds, orange: electrostatic interactions, purple: alkyl-Pi interactions, pink: hydrophobic alkyl-alkyl

Having this series of compounds, Table 1, analogues of **PRO 12**, which differ only in substituent group and its position on aromatic ring, from docking poses analysis we can divide protein-ligand interactions into those that are common and subdivision of those determining the activity of compounds.

**Table 1.** Structures with measured and calculated activities

compound	Structure	IC50 mM	lnIC50	*E
	R			
1. 5OF	2-F	1.27	-13.6	-7.3
2. 5CF3	2-CF <sub>3</sub>	2.24	-13.0	-7.1
3. 5PF	4-F	1.27	-13.6	-7.3
4. 5PCH3	4-CH <sub>3</sub>	1.28	-13.6	-7.9
5. 5OCH3	2-CH <sub>3</sub>	2.56	-12.9	-7.7
6. PRO	H	2.66	-12.8	-7.2
7. 5OCL	2-Cl	1.22	-13.6	-7.3

E-vina binding energy, kcal/mol

Thus, all compounds from series form following stabilizing hydrogen bonds with residues Thr 295 and Thr 293, via protonated nitrogen atom or hydroxyl group. Moreover, there are stabilizing hydrophobic interactions, originating from Sulfur-Pi with Met 167, alkyl-Pi with Val 123 and Leu 288, and cation-Pi with Arg 124. Pi-alkyl interaction is also possible with methyl group of Thr 293. There is also found anion – Pi interaction with Asp 121. Mentioned subdivision consists of Arg124, Leu 288 and Val 123. As one can see from Table 1, compound with lowest activity is **PRO**, which has no substituent groups. The very close activity, somewhat higher has **5OCH3**, which includes methyl group in *ortho*- position. The explanation for this small difference could be presence of methyl group, which can contribute to stabilization in hydrophobic pocket, close to Val 123 and Leu 288. On the other hand, **5PCH3** has higher activity, for the methyl group is closer to hydrophobic binding pocket, forming more stabilizing interactions. In compounds pair **5OF**- **5PF**, there is no significant difference, for the stabilizing electrostatic interaction – hydrogen bond is formed between fluorine group and Arg 124. The position of Arg 124 is such that difference in substituent position on aromatic ring does not affect the magnitude of interaction. The binding mode of **5OCl** is the same as **5OF** and the such small difference in activity can be neglected. Finally, **5CF3** has somewhat lower activity than **5OF** and **5OCl**, more similar to **5OCH3**. Although -CF<sub>3</sub> group form stabilizing electrostatic interactions with Arg 124, its volume gives contribution to repulsive dispersive interactions with hydrophobic pocket, mostly with Val 123 and therefore lower activity is measured.

Binding energies as result from Autodock Vina are correlated with experimental values in manner of difference between *ortho- para-* pairs, ie **5PCH3 7** is calculated to be more active than **5OCH3**, which does not stand for different substituents with same position on aromatic rings (**5OF-5OCH3 - 5OCl**). However, the **5CF3** is calculated to have lowest activity and **5PCH3** to have the highest. This does not stand for **5OCl** and **5PF**, which are calculated to have same binding energy values, but much lower than **5PCH3**. This differences originate from docking program forcefield and under/overestimation of hydrophilic and hydrophobic interactions.

### CONCLUSION

The performed docking studies studies of the propafenone derivatives indicates that their antimicrobial activity against *Pseudomonas aeruginosa* are realizing by modulating activity of porins.

### Acknowledgement

This work was partially supported by the Ministry for Science of the Republic of Serbia (Grants no.172041 and No. ON171017).

### REFERENCES

- [1] Lowes D, Pradhan A, Lalitha V. et al. Lead Optimization of Antimalarial Propafenone Analogues, *J. Med. Chem.* **2012**, **55**, (13):6087–6093.
- [2] Klepsch F, Chiba P, Ecker GFExhaustive sampling of docking poses reveals binding hypotheses for propafenone type inhibitors of P-glycoprotein., *PLoS Comput Biol.* 2011, **5**, e1002036.
- [3] Avogadro: an advanced semantic chemical editor, visualization, and analysis platform, Marcus D Hanwell, Donald E Curtis, David C Lonie, Tim Vandermeersch, Eva Zurek and Geoffrey R Hutchison, *Journal of Cheminformatics* 2012, 4:17 doi:10.1186/1758-2946-4-17].
- [4] O. Trott, A. J. Olson, AutoDock Vina: improving the speed and accuracy of docking with a new scoring function, efficient optimization and multithreading, *Journal of Computational Chemistry*, 2010, **31**, 455-461.

## PHOTODAMAGE TO THE LABELLED DNA WITH 5-BROMO-2'-DEOXYURIDINE AND ITS DEPENDENCY ON LOCAL DNA SEQUENCE

K. Westphal and J. Rak

*Faculty of Chemistry, University of Gdańsk, Wita Stwosza 63, 80-308  
Gdańsk, Poland (kinga.westphal@phdstud.ug.edu.pl)*

### ABSTRACT

Halogenoderivatives of nucleobases, when incorporated into DNA, sensitize it to UV radiation. So far, experiments had focused on choosing the best electron donor and linker between unmodified and modified nucleotide, which resulted in definition of 5'-GAA<sup>Br</sup>U-3' sequence as a "hot spot". The presence of that sequence in double-stranded DNA guarantees high biopolymer's photosensitivity. Unquestionably, the unclear issue is the effect of modification of the adjacent nucleotide (X or Y) on the ionization energy of the guanine and electron affinity of the modified nucleotide within 5'-XG/CAA<sup>Br</sup>UY-3' motif. In the current study we elucidate the mechanism linking the sensitizing properties of BrdU with local DNA sequence. The outcome of this project will allow to select a sequence that provides the highest efficiency of photodamage in double stranded DNA.

### INTRODUCTION

DNA is the main target of anticancer therapy and is not sensitive to UV photons and hydrated electrons. The latter are the major product of water radiolysis under hypoxic conditions, typical for tumor cells. A possible way to overcome these obstacles is to sensitize the cellular DNA to electrons or UV photons. Incorporation of modified nucleosides such as 5-bromodeoxyuridine sensitizes cell to both UV-radiation and gamma rays. It is believed that in both cases, the reactive nucleobase radical is formed as a primary product. This radical may abstract a hydrogen atom from adjacent sugar residue which ultimately produces strand breaks. [1]

However, radio- and photosensitizations of DNA seem to be ruled by different mechanisms. The most important factors deciding on radiodamage to the labelled DNA are: (i) the electron affinity of modified nucleoside; (ii) the strength of chemical bond holding together the substituent and a nucleobase. On the other hand, the formation of UV-induced damages is governed by long-range photoinduced electron transfer and its dependency on local DNA sequence.[2]

It means that sensitivity of DNA not only does depend on the presence of the selected sensitizer but also on its local sequence. In the past many experiments regarding the selection of this combination of nucleobases arrangement that guarantees the highest sensitivity of modified DNA were conducted. Finally, the 5'-G/CAABrU-3' sequence was proposed as a "hot spot"[3], which means that its presence in double stranded DNA leads to the formation of the greatest amount of damage. Moreover, the results of several UV experiments with duplexes of different sequences demonstrated that long-range electron transfer from guanine to BrU (or 5-iodouridine) was responsible for the observed photoreactivity.[4,5] Undoubtedly still unexplained issue is the impact of nucleotides, which are located outside the bridge, and directly adjacent to the guanine, on the yield of the photodamage. There are four combination of arrangement of nucleotides within selected motif: 5'-XG/CAABrU-3' wherein X (G, C, A, T) nucleotide residues determines the ionization potential of guanine/cytosine. So far we determined the amount of photodamage in sequence containing 5'-GCAABrUA-3' core.

## EXPERIMENTAL

**DNA fragment.** The sequence was synthesized and purified with HPLC by Generi Biotech (Czech Republic)

**Table 1.** Sequence of 30 bp oligonucleotide

Name	Sequence
dsGCAABrUA	5'-TATCTAGACAGCAA <sup>Br</sup> UAACTCATATCAGTCA-3'

**Annealing.** Hybridization was carried out by mixing an equal amount of complementary oligonucleotides in K/PO<sub>4</sub> and NaCl buffer (10mM, pH = 7.5), heating the solution to 90 °C and incubating it for 1 min, and then cooling slowly (for 10 min) to 50 °C. The sample containing the hybridized oligonucleotides was kept at 4 °C.

**Irradiation Conditions.** The DNA solution was freshly prepared prior to irradiation. Photolysis was carried out in quartz capillaries (3 x 3 mm) filled with the DNA solution in concentration of 10 μM and a total volume of 50 μl with a 500 W high-pressure mercury lamp for 15 min at 320 nm.

**Identification of DNA breaks by the LC-MS method.** Chromatographic separations of DNA were carried out using an Ultra High Performance Liquid Chromatography (UHPLC) system Nexera X2 with a binary solvent manager (Shimadzu, Japan). The analytes were separated at a flow rate of 0.1 mL/min on a 1.7  $\mu\text{m}$  Acquity UPLC BEH C18 1.0 x 50 mm column (Waters, USA). The mobile phase A consisted of 400 mM HFIP and 50 mM TEA in deionized water, and mobile phase B consisted of the same concentration of HFIP and TEA in water:methanol (50:50, v/v). A 2  $\mu\text{l}$  injection of sample was loaded onto the column and separated using the following gradient conditions [time (min), % mobile phase B]: (0,0) (10, 15) (40, 40). The column temperature was maintained at 85  $^{\circ}\text{C}$ . The effluent was diverted to waste for 2 min after injection. The UHPLC was coupled directly to a Triple TOF 5600+ mass spectrometer (AB SCIEX, USA) equipped with a duo-electrospray ion source operated in the negative ionization mode. MS operation parameters were as follows: the spray voltage was 4.5 kV, the nebulizer gas (N<sub>2</sub>) pressure was 25 psi, the flow rate was 11 L min<sup>-1</sup> and the source temperature was 300  $^{\circ}\text{C}$ . Spectrum was obtained by averaging 3 scans, and the time of each scan was 0.25 s.

## RESULTS AND DISCUSSION

The employment of liquid chromatography coupled with high resolution mass spectrometry (LC-MS) is a classical, easy and fast way to measure the amount of SSBs (single strand breaks). The Total Ion Current Chromatograms obtained for the non-irradiated samples and the irradiated one are shown in Fig. 1.

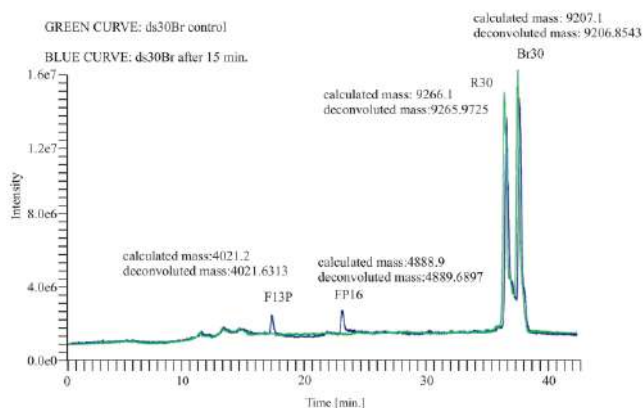


**Figure 1 .** Total Ion Chromatogram (TIC) of ds30 before (green) and after irradiation at 320 nm for 10 min (blue).

Using this technique we were able to assess the yield of photodamage based on the decay of brominated strand (25%) and also confirm the identity of the products formed after irradiation. For the undamaged sample two main signals related to the brominated, (Br30), and native complementary strand, (R30), are observed (Fig. 1). For irradiated sample we observed the formation of two additional signals – F13 and F16. Analysis of raw ESI mass spectra (not shown) of the four fragments depicted in Fig. 1 confirms that UV irradiation leads to the conversion of BrdU into dU and a concomitant release of two oligonucleotide fragments, 13 and 16 bases in length, carrying the phosphate group at their 3' and 5' end, respectively.

### CONCLUSION

The accomplishment of a part of this project determined the yield of the photodamage within the double-stranded DNA sequence of 30 base pairs in length containing a characteristic motif 5'-GCAA<sup>Br</sup>U-3'. By the LC-MS analysis we estimated that as a result of irradiation of ds30Br about 25% of brominated strand is damaged. Moreover, we confirmed the identity of two shorter fragments formed after irradiation (F13P and FP16). Studies on the impact of other nitrogenous bases on the yield of the formation of photodamage within the double-stranded DNA containing a characteristic motif 5'-XCAA<sup>Br</sup>U-3' are under way.

### Acknowledgement

This work was supported by the Polish National Science Centre (NCN), Grant No. UMO-2014/14/A/ST4/00405 (J.R) and via the Young Scientists Grants, Grant No. 538-8227-B099-15 (K.W)

### REFERENCES

- [1] H. Sugiyama, K. Fujimoto, I. Saito, E. Kawashima, T. Sekine, Y. Ishido, *Tetrahedron Lett.* 1996, **37**, 1805-1808.
- [2] H. Sugiyama, Y. Tsutsumi, I. Saito, *J. Am. Chem. Soc.* 1990, **112**, 6720-6721.
- [3] T. Watanabe, R. Tashiro, H. Sugiyama, *J. Am. Chem. Soc.*, 2007, **129**, 8163-8168.
- [4] T. Watanabe, K. Nakamura, H., Sugiyama, *Tetrahedron Lett.*, 2008, **49**, 428-431
- [5] T. Watanabe, B. Toshikazu, Y. Xu, R. Tashiro, H. Sugiyama, *J. Am. Chem. Soc.* 2005, **127**, 44-45

## MOLECULAR DYNAMICS OF PRO-THR LINKER OF A BACTERIAL CELLULASE

I. Stanković<sup>1</sup> and M. Skaf<sup>2</sup>

<sup>1</sup> *University of Belgrade, Institute of Chemistry, Technology and Metallurgy, Njegoševa 12, 11000 Belgrade, Serbia. (ivana\_stankovic@chem.bg.ac.rs)*

<sup>2</sup> *State University of Campinas, Institute of Chemistry, 6154, Campinas, São Paulo, 13084-862, Brazil.*

### ABSTRACT

The linker of the Endoglucanase from *Xanthomonas campestris* pv. *campestris* composed of a specific sequence, an array of a repeating Pro-Thr motif. In order to understand the role of it, free energy profile along the end-to-end linker distance from an enhanced sampling replica exchange simulation have been calculated. The linker exhibits pronounced elasticity in comparison to ordinary linkers due to rigidity of proline itself and a rigidity induced by threonine side chain hydrogen bonds with neighbouring residues. The elastic profile is bimodal with the length difference corresponding to 3 glucose units allowing processivity in cleaving cellulose every 3 units. Also, the elasticity unexpectedly increases with the temperature due to breaking of the hydrogen bonds between sequentially distant residues that have suspending effect on elasticity. This enables thermophilic activity of the enzyme as the linker elasticity introduces constant distance between enzyme domains important for its function.

### INTRODUCTION

Linkers are unstructured peptides which connect two enzyme domains. In cellulases, they connect the catalytic domain and the cellulose binding domain. Function of these two domains are known. Now, the function of linker needs to be understood in order to understand the entire physico-chemical aspect of the mechanism of the cellulose hydrolysis. The linker function is very little known, but there are some suggestions like the function of molecular rulers fixing the distance between the domains [1]. In this sense, rigidity would be a favourable mechanical property. Rigidity provides a necessary force for elasticity, thus more elastic linkers are better molecular rulers.

Another problem is their mobility which implies a large conformational space so the structural modelling needs employment of an enhanced sampling simulation technique. The linker of the Endoglucanase from

*Xanthomonas campestris* sp. *Campestris*((PT)<sub>12</sub>) is composed of a specific sequence containing 12 blocks of Thr-Pro [2]. Here, we explain the role of this strange sequence by comparing it to an ordinary sequence linker of the Cellobiohydrolase 2 from *Trichoderma reesei* (CBH<sub>2</sub>) [3]. In order to explore thermodynamic and mechanical properties, we have used the enhanced sampling simulation technique Replica Exchange Molecular Dynamics.

### SIMULATIONS

The initial structure modelling of the two linkers, (PT)<sub>12</sub> and CBH<sub>2</sub>, has been done by the I-TASSER [4]. All the simulations were performed with NAMD [5] applying CHARMM parameters. Each system has been simulated in replicas of the temperature 298K-550K, distributed exponentially. The number of replicas for (PT)<sub>12</sub> has been set to 16 and 24 for CBH<sub>2</sub>. From the total simulation time of the replicas, it has been extracted 32ns for (PT)<sub>12</sub> and 33ns for CBH<sub>2</sub> from the trajectory at 298K which has been used in all the analysis. The free energy profile along the end-to-end distance  $R$  has been estimated as  $F = -kT \ln W(R)$  where  $W(R)$  is the distribution of the distance  $R$  during the simulation, which has been calculated as histogram of the values  $R$  considering 1 Å bins. In order to compare elastic behaviour of the two linkers, the obtained curves have been fitted to the Hook's law:  $F = (1/2)k(R-R_0)^2 + F_0$ . A hydrogen bonding was considered existent if the distance between the hydrogen donor and acceptor is less than 3 Å and the angle donor-hydrogen-acceptor is more than 160°.

### RESULTS AND DISCUSSION

The free energy profile along the linker end-to-end length, fitted to the Hook's law is shown in Figure 1. The (PT)<sub>12</sub> linker is more elastic and stable than the CBH<sub>2</sub> linker because it exhibits higher force constant  $k$  and more negative energy minimum  $F_0$ . Its free energy profile is slightly bimodal with the modes  $R_1$  and  $R_2$  and their length difference of approximately 3 glucoses in a crystal cellulosic chain. This can be relevant for processive hydrolysis when the catalytic domain of the enzyme is shifted after one hydrolytic event in order to proceed with the hydrolysis at the next spot on the cellulose chain [6].

As seen in the simulations, this elasticity is caused by change in main chain angles change, not by bonds change. The atom position fluctuations show higher structural rigidity of (PT)<sub>12</sub>, which is consistent with higher elasticity because this rigidity provides a restitutive force necessary for the elastic behaviour. This higher rigidity could be explained by the (PT)<sub>12</sub> sequence. Proline is the most rigid amino acid due to the ring in the main chain.

Threonine forms similar ring through hydrogen linking to a neighbour residue due to the proximity of the hydroxile group, which was not observed in CBH<sub>2</sub>. Thus, the elasticity exhibited by (PT)<sub>12</sub> has its origin in intraresidue (Pro) and interresidue (Thr) rigidity.

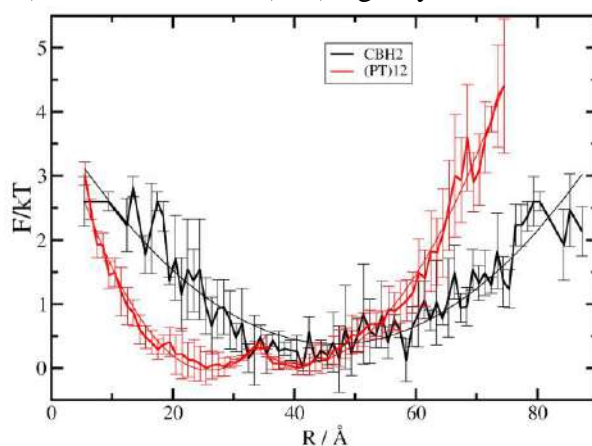


**Figure 1.** The free energy profile along the end-to-end linker length and the fitting to the Hook's law. Red for (PT)<sub>12</sub>, black for CBH<sub>2</sub>.

Finally, we raise the question of the alternated Pro-Thr distribution. As Pro apolar and Thr polar, when interspersed, these two residues are prevented to group through hydrophobic or hydrophilic contacts and thus to compress the linker length. Pro provides more rigidity than Thr, being its ring composed of covalent bonds in contrast to the threonine ring formed by one hydrogen bond. So interspersed proline and threonine induce more evenly distributed rigidity.

The (PT)<sub>12</sub> exhibits higher elasticity with temperature (the force constant  $k$ ) and almost does not change the length (the end-to-end distance). The analysis of all the hydrogen bonds in (PT)<sub>12</sub> has been done as a function of a sequence position of residues, Figure 2. At elevated temperatures, the hydrogen bonds between sequentially distant residues are broken and those between neighbours are preserved with the unchanged frequency.

## CONCLUSION

Thorough replica exchange molecular dynamics simulations have been performed to probe mechanical properties and explain the specific Pro-Thr sequence of the linker of the Endoglucanase from *Xanthomonas campestris* sp. *Campestris*. The linker exhibits pronounced elasticity in comparison to ordinary linkers due to rigidity of proline itself and a rigidity induced by threonine side chain hydrogen bonds with neighbouring residues. The elastic profile is bimodal with the length

difference corresponding to 3 glucose units allowing processivity in cleaving cellulose every 3 units. Also, the elasticity unexpectedly increases with the temperature due to breaking of the hydrogen bonds between sequentially distant residues that have suspending effect on elasticity. This enables thermophilic activity of the enzyme as the linker elasticity introduces constant distance between enzyme domains important for its function.

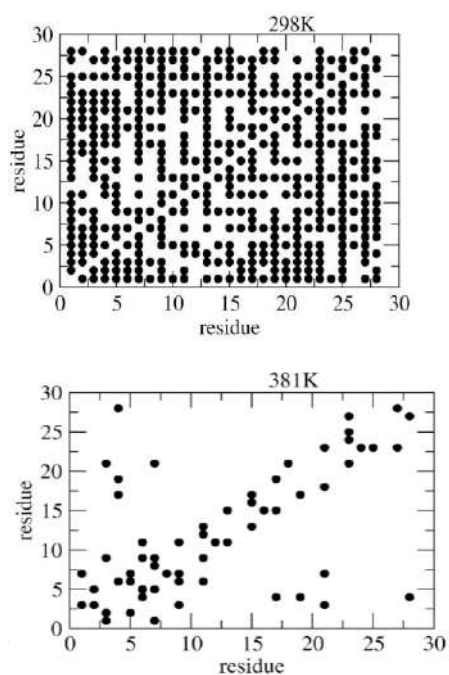


**Figure 2.** The hydrogen bond spatial distribution in  $(PT)_{12}$ . Dots represent the existence of hydrogen bonds in simulations. At higher temperature (381K) the bonds between neighbours prevail (the bonds closer to the graphic's diagonal).

## REFERENCES

- [1] W. Wriggers *et al.*, Protein Functional Dynamics, 2005, **80**, 736-746.
- [2] <http://www.ncbi.nlm.nih.gov/protein/21232950?report=fasta>
- [3] D. W. Sammond *et al.*, Plos One, 2012, **7**, e48615.
- [4] Y. Zhang, BMC Bioinformatics, 2008, **9**, 40.
- [5] J. C. Philips *et al.*, Journal of Computational Chemistry, 2005, **26**, 1781-1802.
- [6] B. J. Watson *et al.*, J Bacteriol, 2009, **191**, 5697-5705.

## CARBOHYDRATE – AROMATIC RING STACKING: A PDB SURVEY

I. Stanković<sup>1</sup> and S. Zarić<sup>2</sup>

<sup>1</sup> *University of Belgrade, Institute of Chemistry, Technology and Metallurgy, Njegoševa 12, 11000 Belgrade, Serbia. (ivana\_stankovic@chem.bg.ac.rs)*

<sup>2</sup> *Department of Chemistry, University of Belgrade, Studentski trg 12-16, 11000 Belgrade, Serbia.*

### ABSTRACT

In many different families of carbohydrate active proteins, the sliding, parallel stacking of a hydrophobic character between a monosaccharide unit and a protein aromatic ring has been detected crystallographically. They play a big role in carbohydrate recognition and bonding in many biological processes. We showed that C-H/ $\pi$  interactions cause the parallel arrangement and that their unspecific character leads to sliding in the plane parallel to aromatic ring. As suggested before, only one sugar face stacks with aromatic ring.

### INTRODUCTION

The recognition of saccharides by proteins has far reaching implications in biology, technology, and drug design. Carbohydrate – receptor interactions play an important role in many cellular processes, such as cell-cell adhesion, cell differentiation and in-cell signaling [1].

Unexpectedly, researchers observed that despite the highly hydrophilic character of most sugars, aromatic rings of the receptor are the most frequent to interact with carbohydrate rings [2]. Aromatic protein rings, phenylalanine, tyrosine and tryptophan, stack with the hydrophobic face of a carbohydrate six-membered rings giving rise to hydrophobic contacts that are loose enough to release substrate after the enzymatic reaction in order to proceed with hydrolysis on the next spot in sugar chain, as observed in molecular dynamics simulations [3, 4, 5].

Along with the hydrophobic effect, interactions between carbohydrates and aromatic amino acid side chains are supplemented by nonconventional hydrogen bonds: the C-H/ $\pi$  interactions [6, 7, 8]. Neither of these interactions is highly directional, therefore enabling sliding.

Here, we systematically describe the geometry of monosaccharide unit-aromatic amino acid geometry found in structures resolved at molecular level by X-ray crystallography or nuclear magnetic resonance spectrometry.

## EXPERIMENTAL

The carbohydrate-protein database has been constructed within Protein Data Bank (PDB) by searching for enzymes resolved together with carbohydrates in the form of pyranose. Glycoproteins were not taken into account. We searched for any aromatic ring with centre-centre distance up to 7 Å around a monosaccharide unit, than we excluded all the interactions with any foreign atoms within the sphere encompassing the two rings, and finally, we observed the most frequent arrangements. The criteria for the C-H/ $\pi$  interaction are the same as in [9]. The CH groups hydrogen atoms coordinates were added computationally by determining vector perpendicular to the plane of other three atoms covalently bound to the C-atom and taking the C-H bond length from the CHARMM [10] parameters, 1.111 Å. Homemade scripts for the search were written in Python [11] and for PDB file parsing MDAnalysis [12] python library was used.

## RESULTS AND DISCUSSION

The PDB survey gave no significant difference in geometry of interaction with different aromatic amino acids, phenylalanine, tyrosine and tryptophan. The 3D graph representing the monosaccharides centres positions in relation to an aromatic ring, Figure 1, confirms the sliding character of these interactions. The interactions are not specific in the plane parallel to the aromatic ring, they only show tendency for the normal distance between rings of around 4 Å.

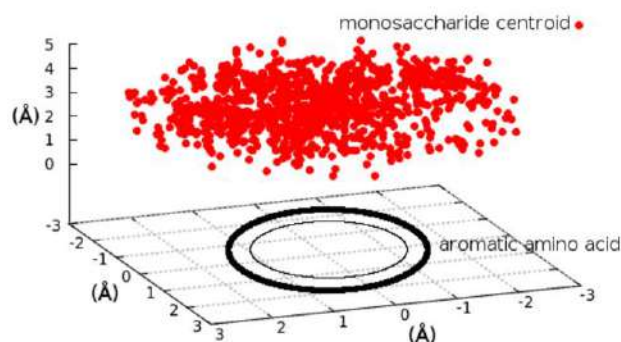


**Figure 1.** Monosaccharides centroids positions in 3D space in relation to an aromatic ring represented by circles.

The sugar-aromatic interactions tend to be parallel, Figure 2, as a consequence of the sugar CH group nearly perpendicular to the sugar plane, see Figure 3. The angles between rings higher than 30° are the consequence of C-H/ $\pi$  on distorted high-energy sugar rings, or C-H/ $\pi$  interactions in vicinity of more flexible glycosidic bond.

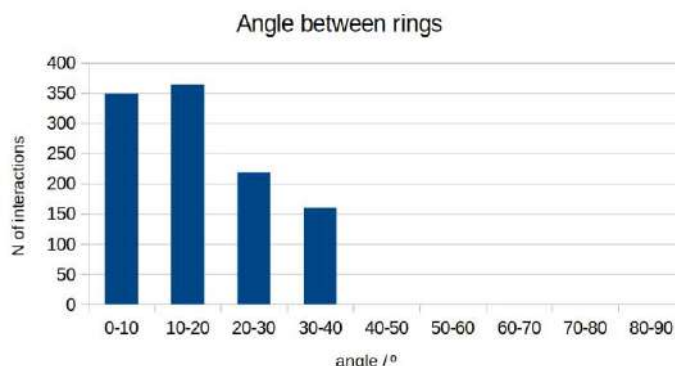


**Figure 2.** Distribution of the angle between sugar and aromatic ring found in the constructed protein-carbohydrate structural database.

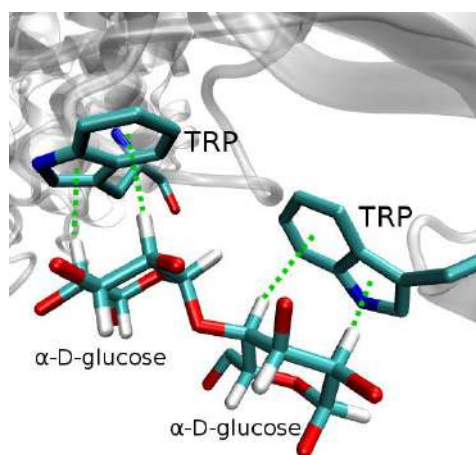


**Figure 3.** A typical pyranose-aromatic interaction. Green dotted lines represent C-H/ $\pi$  interactions. PDB ID: 1VEM, hydrogens (white) added computationally.

The survey pointed to very rare sandwich arrangements: the sugars usually interact only with their hydrophobic face exposing their polar groups to polar amino acids or solvent.

### CONCLUSION

It was shown that the preference for the pyranose-aromatic ring interactions within proteins is parallel with only one face of pyranose interacting. The influence of aromatic substituent was not observed. The sliding character was confirmed by analyzing the frequency of geometric parameters.

### Acknowledgement

This work was supported by the Serbian Ministry of Education, Science and Technological Development (Grant no. 172065).

**REFERENCES**

- [1] M. Wimmerová, S. Kozmon, I. Nečasová, S. K. Mishra, J. Komárek, J. Koča, PLoS ONE, 2012, **7**(10): e46032.
- [2] K. L. Hudson, G. J. Bartlett, R. C. Diehl, J. Agirre, T. Gallagher, L. L. Kiessling, and D. N. Woolfson, J. Am. Chem. Soc. 2015, **137**, 15152–15160.
- [3] ě. T. Prates, I. Stankovic, R. L. Silveira, M. V. Liberato, F. Henrique-Silva, N. Pereira, Jr., I. Polikarpov, M. S. Skaf, PLoS ONE, 2013, **8**(3): e59069.
- [4] L. Bu, M. R. Nimlos, M. R. Shirts, J. Stohlberg, M. E. Himmel, M. F. Crowley, and G. T. Beckham, The Journal of Biological Chemistry, 2012, **287**(29), 24807–24813.
- [5] H. Zhang, J. Zhang, L. Sun, X. Niu, S. Wang and Y. Shan, J. Mol. Recognit., 2014, **27**, 438–447.
- [6] E. Jiménez-Moreno, G. Jiménez-Osés, A. M. Gómez, A. G. Santana, F. Corzana, A. Bastida, J. Jiménez-Barbero and J. L. Asensio, Chem. Sci., 2015, **6**, 6076.
- [7] J. L. Asensio, A. Ardđ, F. J. Cađada, and J. Jiménez-Barbero, Accounts of Chemical Research, 2013, **46**(4), 946–954.
- [8] S. Kozmon, R. Matuška, V. Spiwok, J. Koča, Chem.; Eur. J. 2011, **17**, 5680–5690.
- [9] M. K. Milčić, V. B. Medaković, D. N. Sredojević, N. O. Juranić, and S. D. Zarić, Inorg. Chem. 2006, **45**, 4755–4763.
- [10][http://mackerell.umaryland.edu/charmm\\_ff.shtml](http://mackerell.umaryland.edu/charmm_ff.shtml)
- [11]<http://www.python.org/>
- [12] N. Michaud-Agrawal, E. J. Denning, T. B. Woolf, O. J. Beckstein, *Comput. Chem.* 2011, **32**, 2319–2327.

## THE POTENTIAL OF *IN VIVO*EPR IN EVALUATING FREE RADICAL REACTIONS IN IRRADIATED RATS AND MECHANISMS OF RADIOPROTECTION

M. Jovanović<sup>1</sup>, B. Šećerov<sup>2</sup> and G. Bačić<sup>3</sup>

<sup>1</sup>University of Belgrade – Faculty of Biology, Studentski trg 3, 11158 Belgrade, Serbia

<sup>2</sup>Vinča Institute of Nuclear Sciences, Belgrade, Serbia

<sup>3</sup>University of Belgrade – Faculty of Physical Chemistry, EPR Laboratory, Studentski trg 12-16, 11158 Belgrade, Serbia. (ggbacic@ffh.bg.ac.rs)

### ABSTRACT

We investigated the potential of *in vivo* electron paramagnetic resonance (EPR) in assessing chemical reactions that occur during ionizing irradiation and capabilities of two radioprotectors (an antibiotic, anisomycin and a naturally occurring thiol, GL2011) to enhance survival during irradiation. Radioprotectors selected are supposed to have different modes of action and *in vivo* EPR was used to assess whether free radical scavenging has a role in their action as radioprotectors. Both compounds exhibited similar and highly efficient radioprotective capabilities according to the 30-days survival test (96% and 87%, respectively after the dose of 6.7 Gy). *In vivo* EPR showed that free radical scavenging has an important role in the action of GL2011, but not in the case of anisomycin. In conclusion, EPR have unique capabilities in studying free radicals *in vivo* and can be useful addition to battery of methods needed to study radioprotectors *in vivo*.

### INTRODUCTION

Investigation of mechanisms of radioprotection *in vivo* is a challenging task due to the complexity of biochemical and physiological events that occur during and after irradiation of the body. Radiation-induced cell damage is mostly done via free radicals produced by radiation, hence, molecules with scavenging properties for radicals, such as thiols, attracted attention as potential radioprotectors and a number of synthetic or naturally occurring thiols have been investigated as potential radioprotectors. These and other protectors have been investigated through survival studies or experiments using *in vitro* samples (cell cultures or isolated cells and organs). However, it is difficult to translate results of later studies to the *in vivo* conditions; hence there is a need to develop methods suitable for direct *in vivo* investigations of free radicals involved into radiation damage and radiation

protection. The EPR can, in principle, detect free radicals but their direct observation *in vivo* is almost impossible. One of the potential solutions is to use *in vivo* EPR technique to study interactions between the endogenous free radicals, produced by the irradiation, with the exogenous radicals (nitroxides, stable free radicals), which were added after irradiation [1]. Here, we used this technique to study action of natural thiol (GL2011), a substance we previously investigated as a potential radioprotector [2]. We also included in the study the anisomycin, an antibiotic, well-known as the inhibitor of protein synthesis. It has been suggested that it can have radioprotecting capabilities so it is included here for comparison with GL2011, as an agent acting through different mechanisms than GL2011.

### EXPERIMENTAL

Healthy 2 month's old male albino Wistar rats grown under standard conditions were used. Total body irradiation was performed on non-anaesthetized rats using 60-cobalt gamma ray source (dose = 6.7 Gy). For EPR measurements, anesthetized rats were placed in supine position into the rat-bed, loaded into the Bruker Eleksys II EPR spectrometer and L-band surface coil was placed above the rat liver area. Body temperature was maintained at around 33°C. Administration of radio protectors: GL2011, intraperitoneally 30 min prior to radiation, dose = 100 mg/kg body weight; anisomycin, subcutaneously 1 hour prior to irradiation, dose = 150 mg/kg b.w. One milliliter of the 3CP spin probe (3-carbamoyl proxyl, Sigma), dose = 2 μmol/g b.w., was injected via the tail vein and spectra were recorded for the period of 30 min using 20s scan time. For survival studies, animals were kept in cages (two per cage), regularly inspected twice a day and moribund animals were killed according to the IACUC Guidelines, Policy#5.

### RESULTS AND DISCUSSION

Figure 1. demonstrates radio protecting capabilities of both compounds used, GL2011 leading to a survival of 87%, while protection with anisomycin was 96%. This is a rather high radio protective efficiency achieved without apparent toxic effects, except for occasional local skin irritation at the injection site of anisomycin.

The EPR signal decay in control, unirradiated rats (Fig. 2) shows pronounced non-exponential curve reflecting participation of several processes beside reduction of injected 3CP to EPR silent hydroxylamine in the overall decay. These can include the rate of distribution of the spin probe from the blood to the tissue and within different tissue compartments, urinary excretion through kidneys, fecal excretion through liver and bile, etc and such curves should, in principle, be analyzed using multicompartment pharmaceutical models [3].

Here, we will only use half-elimination times ( $t_{1/2}$ ) to analyze the effect of irradiation and radioprotectors on *in vivo* reduction of nitroxide.

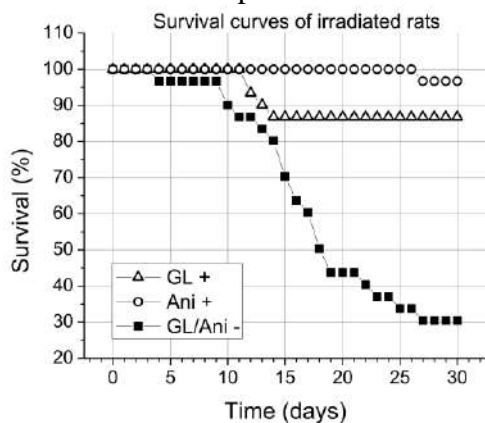


**Figure 1.** Survival of rats after radiation (6.7 Gy) and different treatments. *Squares* – no treatment (protection); *Triangles* – protection with GL2011; *Circles* – protection with ansomycin. The survival curves were significantly different as predicted by log rank test. (+++ $p$  value <0.001). Thirty rats pergroup.

Data in Fig.2 illustrate the basic concept of the experimental approach. The curve for irradiated rats with no protection showed faster signal decay, most certainly due to the reduction of injected 3CP to hydroxylamine with additional amount of reactive free radicals produced during and after irradiation. Measured  $t_{1/2}$ 's are 14.5 min and 11 min, respectively. In rats, protected by the GL2011, measured  $t_{1/2}$  is the same as in control, indicating that GL2011 scavenged extra free radicals produced by irradiation thus restoring the original redox capacity of tissues. No apparent changes in the redox status were observed in rats receiving anisomycine since  $t_{1/2}$  in these rats had the same value as in non-protected rats.

In biological systems, ionizing radiation induces formation of reactive oxygen radicals ( $\text{OH}^\bullet$  and  $\text{O}_2^{\bullet-}$ ) through radiolysis of water.

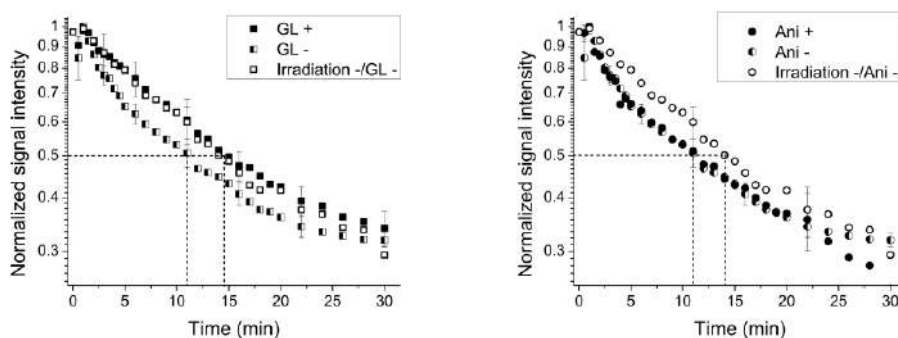


**Figure 2.** Semilogarithmic plots (pharmacokinetic curves) of *in vivo* reduction kinetic of 3CP nitroxide from the liver region of rats. *Open symbols* – control rats, no irradiation and no protection; *closed symbols* – irradiated rats protected with either GL2011 (left) or anisomycin (right); *semifilled symbols* – irradiated animals without protection. Dotted lines denote decay half-times. Error bars are standard deviations,  $n = 3$  animals per group.

Nitroxides can readily react with these species, but it is virtually impossible that nitroxides, injected 1 h after irradiation to study pharmacokinetic, interact with these primarily formed species, because of their extremely short life time. It is more likely that injected nitroxides react with secondary radicals formed in radicals chain reactions initiated by the primary ROS induced by irradiation. In any case, these data show that at least part of action of the GL2011 can be attributable to the free radical scavenging.

This research demonstrates usefulness of EPR in investigating of radioprotection mechanisms *in vivo*. It also can be useful in connecting mechanisms of protection and efficiency of certain radioprotector, but one has to be cautious while doing this. There are substances that suppress various oxidative stresses *in vivo* but exhibit no radioprotective action and others, such as anisomycin, studied here, exhibiting good protection actions but through different mechanisms. *In vivo* EPR can't replace the 30-day survival test in studying the efficiency of certain substance as a potential radioprotector since the survival presents is a systemic effect while reduction of nitroxides *in vivo* EPR is observing short term effect immediately following irradiation. Nevertheless, besides being useful in revealing underlying mechanisms of radioprotection *in vivo*, EPR can be used, to a certain extent, as a screening technique for assessing potential radioprotectors instead of the animal consuming 30-day survival which requires the large number of animals (typically 30 per group).

### ***Acknowledgement***

Supported by the Ministry of Education and Science of the Republic of Serbia, project III#41005.

### **REFERENCES**

- [1] Y. Miura, K. Anzai, S. Urano, T. Ozawa, *Free Rad. Biol. Med.*, 1997, **23**, 533-540.
- [2] M.K. Ganeshan, *et al.*, *Amino Acids*, 2014, **46**, 4681-1696.
- [3] G. Bačić, A. Pavičević, F. Peyrot, *Redox Biol.*, 2016, **8**, 226-242.

## ACRIDAN ESTERS – SYNTHESIS, X-RAY STRUCTURE AND CHEMILUMINESCENCE PROPERTIES

A. Kawecka<sup>1</sup>, K. Kowalska<sup>2</sup>, A. Sikorski<sup>2</sup> and K. Krzyminski<sup>1</sup>

<sup>1</sup>*University of Gdańsk, Faculty Chemistry, Laboratory of Luminescence Research, Wita Stwosza Str. 63, 80–308 Gdansk, Poland  
(alicja.kawecka@phdstud.ug.edu.pl)*

<sup>2</sup>*University of Gdańsk, Faculty Chemistry, Laboratory of Rentgenography and Spectroscopy, Wita Stwosza Str. 63, 80–308 Gdansk, Poland*

### ABSTRACT

A series of aryl 9,10-dihydro-10-methylacridine-9-carboxylates (acridan esters), bearing substituents of various properties (2-halogen, 2,6-dihalogen, 2,4,6-trihalogen) in the lateral phenyl ring were synthesized with high yields, identified and subjected to comprehensive physicochemical investigation.

### INTRODUCTION

Chemiluminogenic acridinium esters were first described by F. McCapra in the 1960's, but they found applications in medical diagnostics about two decades later [1]. They do not require the use of a catalyst to trigger the chemiluminescence (CL) and they are characterized by high temporary intensity of emission – up to 100-fold higher than luminol [2,3].

Acridinium derivatives have been used as labels and indicators in many assays e.g. thyroid stimulating hormone (TSH), viruses, markers of cancer cells, nucleic acids, oxidative enzymes (e.g. horseradish peroxidase) and other important bioanalytes [2,3,5].

To take a deeper look at the physicochemical and luminogenic properties we have synthesized a series of chemiluminogenic acridan esters, differing in terms of the location and the electronic and steric properties of the substituents introduced into the structure.

### EXPERIMENTAL

Substituted aryl 9,10-dihydro-10-methylacridine-9-carboxylates (acridan esters) were synthesized in five steps: synthesis of respective acridine-9-carboxylic acid (step I) and 9-(chlorocarbonyl)acridinium chloride (step II), estrification of the last intermediate compound (step III), synthesis of 10-methylacridinium salts (step IV) and the reduction of the resulting acridinium salts (step V).

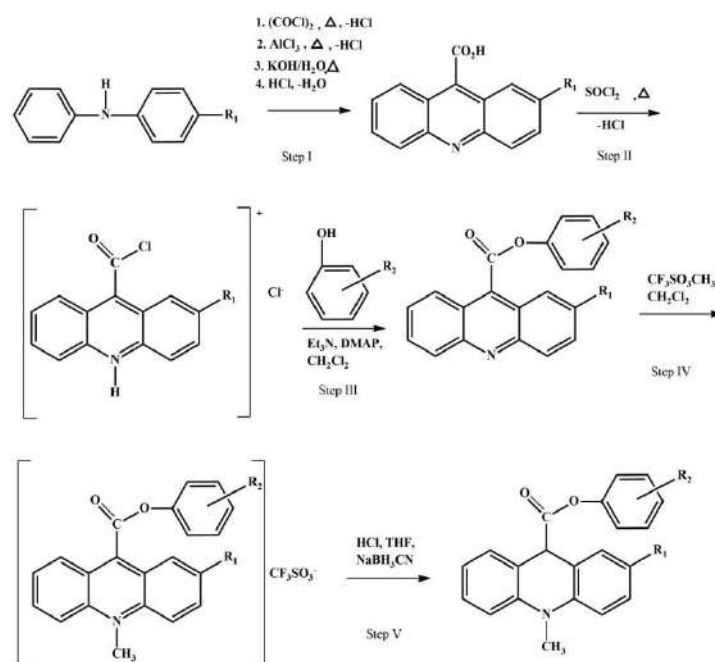


**Figure 1.** Synthesis steps for substituted aryl 9,10-dihydro-10-methylacridine-9-carboxylates (acridan esters) subjected to physicochemical investigations.

The methods for the preparation of 10-substituted 9-(phenoxy-carbonyl)acridinium salts (Steps I – IV) have been described in the literature [2,4]. As for the Step V the procedure is as follows: to a solution of 1 mmol of an acridinium salt in 3 ml dry THF and 1 ml 1M HCl, 5% molar excess of sodium cyanoborohydride (NaBH<sub>3</sub>CN) was added. The solution was stirred at room temperature under inert atmosphere (Ar, 1–2 h). The mixture was concentrated under reduced pressure and the residue was washed with water and CH<sub>2</sub>Cl<sub>2</sub>. The organic layer was then washed with aqueous sodium bicarbonate (5% NaHCO<sub>3</sub>), dried over magnesium sulfate, filtered and concentrated. Average yield of the reaction fall in the range of 85–95%. The white solid crude products were purified by use of the RP-HPLC technique (stationary phase: column 5μ C18 300A, 150×10,0 mm, mobile phase: isocratic, 1 ml/min, acetonitrile/0.1% TFA in water (1/1 v/v), later methanol; absorbance detection at 254 nm. The <sup>1</sup>H NMR and mass spectrometry indicated chemically pure products (>98% in all cases).

For selected compounds single-crystal X-ray diffraction measurements were performed (T = 295K) [5]. Diffraction data were collected using an Oxford Diffraction Gemini R ULTRA Ruby CCD diffractometer with MoKα (α = 0.71073 Å) radiation.

Preliminary investigations of chemiluminescent properties of the new acridan esters were conducted using Fluoroskan Ascent FL plate luminometer (Labsystems-Thermo). To compare the efficiency of the emission, the equipment was operated at high sensitivity, by setting up the voltage of photomultiplier tube (PMT) at 1000 mV and at a resolution of 20 ms per point. To record kinetic profiles the obtained compounds were dissolved in anhydrous DMF (Aldrich) to assess the concentration of 5.0 mM. Portions of such prepared stocks solutions were diluted with Tris HCl buffer (pH= 6.5) to obtain concentration of  $2 \times 10^{-7}$  M and  $5 \times 10^{-9}$  M. The solutions were dispensed over a 96-well white polystyrene plate and 10  $\mu$ l of horseradish peroxidase (350 pM HRP, pH =6.5) was added to half of the wells. Next, portions of H<sub>2</sub>O<sub>2</sub> solution (0.06%) in 0.01 M HNO<sub>3</sub> were added to each well, plate was shaken for 30 seconds and incubated for at least 5 minutes. The emission of light (CL) was triggered by adding NaOH (0.2M) to each well and the light output was collection over 1 minute periods at 298 K. The integral light outputs were assessed by calculating the areas under each kinetic profile, applying the Ascent FL-implemented software.

## RESULTS AND DISCUSSION

Although the methods for steps I–IV have been described in the literature [2,4], a few notes concerning the synthesis of the compounds should be made, especially concerning step V. The compounds with high amount of halogen atoms (especially F) expressed limited photochemical stability, so the reaction mixture was shielded from light. The salts were obtained in high yields and purity thanks to the efficient purification of their immediate precursors, that are substituted 9-[(phenoxy)carbonyl]acridines (the bases). The identity of obtained compounds (acridan esters) was confirmed by mass spectrometry (TripleTOF™ 5600<sup>+</sup>, AB SCIEX, Canada) and <sup>1</sup>H NMR spectroscopy (Bruker ADVANCE III 500 MHz Bruker, USA). Example analysis for 2,6-difluorophenyl 2-fluoro-10-methyl-9,10-dihydroacridine-9-carboxylate: <sup>1</sup>H NMR 7,46 ppm(d, 2H); 7,31 (d, 1H); 7,19 (t, 1H); 6,99 (m, 2H); 6,92 (t, 2H); 6,81 (q., 2H); 5,25 (s, 1H); 3,62 (s, 3H); 3,21 (s, 3H); MALDI-QTOF: m/z 502,1998 [M+H]<sup>+</sup>; 2,6-difluorophenyl 2-bromo-10-methyl-9,10-dihydroacridine-9-carboxylate: <sup>1</sup>H NMR 7,46 ppm(s, 1H); 7,35 (m, 2H); 7,21 (t, 1H); 7,19 (m, 1H); 7,02 (d, 2H); 6,95 (q, 3H); 5,25 (s, 1H); 3,2 (s, 3H); m/z = 428,2276 [M+H]<sup>+</sup>.

The emission efficiency of the acridan esters (AE) was, in general, higher than their precursors, that are respective acridinium salts. Addition of the HRP substantially increased the efficiency of emission of corresponding AE upon triggering the chemiluminescence. Preliminary results demonstrated,

that the investigated new CL systems based on AE are stable in the acidic environment.

## CONCLUSIONS

The new acridan esters, containing substituents of various electronic and steric properties (F, Br, OCH<sub>3</sub>) were obtained in several steps of synthesis and subjected to physicochemical investigations, including MS and NMR spectroscopy, crystal structure determination and measurements of chemiluminescence in various environments. The main task of this work was to assess the chemiluminescence properties and stability of the substances in the environment suitable for their performance. The obtained knowledge will let us tailor optimal experimental conditions in order to utilize obtained acridan esters as chemiluminogenic indicators of proteins, that are labelled with oxidizing enzymes (such as horseradish peroxidase) in the presence of specific additives (enhancers). Therefore, the new chemiluminogenic systems might find application in ultrasensitive biomedical assays.

## Acknowledgement

This work was supported by the funds gained within the project entitled "The Research of Young Scientists", No. 538-8226-B044-16, granted for M.Sc. Alicja Kawecka in 2015.

## REFERENCES

- [1] G. Zomer and J. F. C. Stavenuiter, *Anal. Chim. Acta*, 1989, **227**, 11–19.
- [2] B. Zadykowicz, J. Czechowska, A. Ożóg, A. Renkevich, K. Krzyimiński, *Org. Biomol. Chem.*, 2016, **14**, 652–668.
- [3] A. A. Waldrop III, J. Fellers and C. P. H. Vary, *Luminescence*, 2000, **15**, 169–182.
- [4] K. Krzyimiński, A.D. Roshal, B. Zadykowicz, A. Białk-Bielińska A. Sieradzan, *J. Phys. Chem. A* 2010, **114**, 10550–10562.
- [5] CrysAlis CCD and CrysAlis RED, Version 1.171.36.24, Oxford Diffraction Ltd, Yarnton, England, 2012.

## UV-A RADIATION INFLUENCE ON DEHP LEVEL IN PVC MEDICAL DEVICES

I. Kostić<sup>1</sup>, T. Anđelković<sup>1</sup>, D. Anđelković<sup>1</sup>, T. Cvetković<sup>2</sup>  
and D. Pavlović<sup>2</sup>

<sup>1</sup> *University of Niš, Faculty of Science and Mathematics,  
Višegradska 33, 18000 Niš, Serbia (ivana.kostic83@gmail.com)*

<sup>2</sup> *University of Niš, Faculty of Medicine, Boulevard Zorana Đinđića 81,  
18000 Niš*

### ABSTRACT

The presence of di-(2-ethylhexyl) phthalate (DEHP) in 6 different parts of transfusion set (Quadruple blood bag, SAG-M transfer bag, Transfer bag and their coupled tubings) was determined and influence of UV radiation on DEHP level was investigated. Results obtained for investigated samples showed that Quadruple blood bag and Transfer bag contain almost the same amount of DEHP (256.31 mg g<sup>-1</sup> and 269.25 mg g<sup>-1</sup> by weight, respectively) while SAG-M transfer bag contains lower amount of DEHP (160.73 mg g<sup>-1</sup>). All samples of tubing material showed higher concentration level of DEHP than coupled bags. Results obtained after UV treatment showed that UV radiation has a certain influence on DEHP level in samples. All investigated samples contained smaller amount of DEHP after UV-A treatment. UV-A radiation showed the biggest influence on DEHP level in SAG-M transfer bag (> 74%), but the lowest on tubing coupled to the same bag.

### INTRODUCTION

Phthalates may be found in many industrial products because they are widely used as plasticizers. They are added to polyvinyl chloride (PVC) to increase flexibility and softness [1]. Due to their widespread use, relatively large amounts of these compounds are released into the environment [2].

In general, PVC medical devices contain up to 40% of plasticizers by weight and di-(2-ethylhexyl) phthalate (DEHP) is the most abundant plasticizer [3,4]. Various types of medical devices are made from PVC, such as parenteral nutritional tubing, infusion and transfusion tubings, blood bags and tube systems for blood cell separation and patients undergoing different medical procedures are exposed to DEHP. In humans, phthalates are rapidly hydrolyzed to the monoesters and then further metabolized and they can be detected in urine, breast milk, faeces, etc. [5]. DEHP is introduced in the list of potentially endocrine disruptors and some of health outcomes may be the

result of phthalate-induced increases in oxidative stress or inflammation, which have been demonstrated in animal studies [6].

Phthalates are not bound to plastic material therefore phthalates can migrate to the medium that is in contact. Various conditions may enhance the migration of phthalates from PVC medical devices into the surrounding media. It is possible that the content and transfer properties of phthalates may be influenced by optical radiation and temperature change during storage [3,7].

### EXPERIMENTAL

Transfusion set was taken from the local Clinical Center Niš, Serbia. Set consisted of three bags filled with appropriate solutions and coupled tubing (TIANHE Pharmaceutical, China).

All used chemicals (DEHP, DBA, hexane and tetrahydrofuran (THF)) were purchased from Sigma Aldrich, USA. Solvents were HPLC grade and screened to determine the DEHP background. Amount of DEHP standard was accurately weighted out by analytical balance with precision at  $\pm 0.0001$  g (Kern, Germany) and diluted with n-hexane to 5 mL. Working standard solutions were obtained by diluting of stock solution, obtaining the series of the concentration range from 0.25 to 10  $\mu\text{g mL}^{-1}$ . All sample manipulation was done avoiding any contact with plastic equipment and special care was taken to avoid the contamination of solvents with plastic laboratory materials during standards and sample preparation.

Analysis was carried out by gas chromatography coupled to mass spectrometer (Hewlett Packard 6890 series GC System with autosampler connected with Agilent 5973 Mass Selective Detector (Electron Ionization MSD-EI, single quadrupole). The separation was achieved with 30 m  $\times$  0.25 mm  $\times$  0.25  $\mu\text{m}$  a non-polar AGILENT DB-5MS column coated with 5% phenyl, 95% dimethylpolysiloxane. The oven temperature was programmed from 65  $^{\circ}\text{C}$  (holding time 1 min) to 220  $^{\circ}\text{C}$  (1 min) at rate of 20  $^{\circ}\text{C min}^{-1}$ , then to 280  $^{\circ}\text{C}$  at rate of 5  $^{\circ}\text{C min}^{-1}$  (4 min). Volume of 1  $\mu\text{L}$  was injected in the splitless mode. Helium was the carrier gas (1.0 ml  $\text{min}^{-1}$ ) and the inlet temperature was 250  $^{\circ}\text{C}$ . The operating temperature of the MSD was 280 $^{\circ}\text{C}$  with the emission energy of 70 eV. The MSD was used in the single ion-monitoring (SIM) mode. The identification of target compound was based on the relative retention time, the presence of target ion and its relative abundance. The most abundant ion  $m/z$  149 was chosen for quantification of DEHP, with no qualifier ions, due to the simplicity of the matrix. The dwell time was 100 ms. Ion  $m/z$  185 was chosen as representative ion of DBA internal standard.

PVC medical devices were kept in the shade and at room temperature. Some PVC samples were irradiated with UV-A light, using UV-A lamps at 365 nm (PHILIPS, 18w/10 BL, 25 W, G 13), at the distance of 10 cm for 12 hours. After radiation treatment, the samples were stored in shade.

DEHP content in all investigated samples was determined in the same way. About 0.01 g of sample was dissolved in 10 mL of THF by soaking overnight at room temperature. Next day, totally dissolved plastic polymer was precipitated by addition of 10 ml of hexane. After filtering, sample solution was put into 2 mL vials and DBA was added as internal standard. Samples were analyzed by GC-MS.

## RESULTS AND DISCUSSION

The analytical curve obtained for DEHP within concentration range 0.25 – 10  $\mu\text{g mL}^{-1}$  was linear with determination coefficient  $R^2 = 0.99853$  and linear equation  $y = (2.94352 \pm 0.03017)x - 0.18073 \pm 0.15241$ . Limit of quantitation (LOQ) was determined using signal to noise ratio of 10 to 1, for repeated measurements with RSD less than 20%. The obtained LOQ value was 0.05  $\mu\text{g mL}^{-1}$ .

The determined DEHP concentration levels showed that Quadruple blood bag and transfer bag contain almost the same amount of DEHP by weight (256.31  $\text{mg g}^{-1}$  and 269.25  $\text{mg g}^{-1}$  by weight, respectively). Samples of SAG-M transfer bag contained lower amount of DEHP, 160.73  $\text{mg g}^{-1}$  (Table 1.).

**Table 1.** DEHP level ( $\text{mg g}^{-1}$ ) in parts of transfusion set before and after UV treatment

Part of transfusion set	DEHP ( $\text{mg g}^{-1}$ ) before UV treatment	DEHP ( $\text{mg g}^{-1}$ ) after UV treatment
Quadruple blood bag	256.31 $\pm$ 13.41	189.15 $\pm$ 7.73
Tubing of Quadruple blood bag	312.72 $\pm$ 15.92	171.28 $\pm$ 5.57
SAG-M transfer bag	160.73 $\pm$ 9.85	40.24 $\pm$ 1.58
Tubing of SAG-M transfer bag	316.48 $\pm$ 13.33	222.91 $\pm$ 8.26
Transfer bag	269.25 $\pm$ 8.50	187.27 $\pm$ 2.49
Tubing of Transfer bag	356.61 $\pm$ 18.72	132.73 $\pm$ 1.48

The determined DEHP concentration levels in tubing material showed that all samples contain more than 300  $\text{mg g}^{-1}$  DEHP by weight and all obtained values were higher than values obtained for coupled bags. The most significance difference was found between SAG-M transfer bag and coupled tubing.

Results obtained after UV treatment showed that UV radiation has a certain influence on decrease of DEHP level in samples of PVC medical

devices. All investigated samples contained smaller amount of DEHP after UV-A treatment than samples which were not treated by UV radiation. Results showed that UV-A radiation had greater influence on DEHP leaching from samples of SAG-M transfer bag (> 74%) than from samples of Quadruple blood bag and transfer bag (< 27% and 31%, respectively). Also, UV-A radiation had greater influence on DEHP leaching from samples of tubing coupled to Transfer bag (62%), than tubing coupled to Quadruple blood bag (45%) and the lowest influence on DEHP leaching from samples of tubing coupled to SAG-M transfer bag (30%).

### CONCLUSION

The content of DEHP in 6 different parts of transfusion set (bags and tubing) were determined and UV-A effect on DEHP leaching was investigated. Obtained results showed that majority of investigated samples of medical devices contains DEHP > 30% by weight and all investigated tubing material contain DEHP in higher amount than coupled bags. Results obtained after UV-A treatment showed that UV-A radiation has a certain influence on DEHP level in PVC materials. UV-A radiation showed the biggest influence on DEHP level in samples of SAG-M transfer bag. The lowest influence was obtained for samples of Quadruple blood bag.

### *Acknowledgement*

This work was partially supported by the Ministry for Education, Science and Technological Development of the Republic of Serbia (Grant no. III 41018).

### REFERENCES

- [1] T. Fierens, M. Van Holderbeke, H. Willems, S. De Henauw, I. Sioen, *Environ. Int.* 2013, **51**, 1-7.
- [2] H.-Y. Shen, *Talanta*, 2005, **66**, 734-739.
- [3] K. Inoue, M. Kawaguchi, R. Yamanaka, T. Higuchi, R. Ito, K. Saito, H. Nakazawa, *Clin. Chim. Acta*, 2005, **358**, 159-166.
- [4] G. Latini, M. Ferri, F. Chiellini, *Curr. Med. Chem.*, 2010, **17**, 2979-2989.
- [5] M. J. Silva, E. Samandar, J. L. Preau Jr., L. L. Needham, A. M. Calafat, *Toxicology*, 2006, **219**, 22-32.
- [6] E. Fasano, F. Bono-Blay, T. Cirillo, P. Monzuori, S. Lacorte, *Food Control*, 2012, **27**, 132-138.
- [7] P. D. Zygoura, E. K. Paleologos, M. G. Kontominas, *Food Chem.*, 2011, **128**, 106-113.

CIP - Каталогизација у публикацији - Народна библиотека Србије, Београд

544(082)  
621.35(082)  
577.3(082)  
543.42(082)

INTERNATIONAL Conference on Fundamental and Applied Aspects of Physical Chemistry (13 ; 2016 ; Beograd)

Physical Chemistry 2016 : proceedings. Vol. 1 / 13th International Conference on Fundamental and Applied Aspects of Physical Chemistry, Belgrade, 26-30 September 2016 ; [editors Željko Čupić and Slobodan Anić]. - Belgrade : Society of Physical Chemists of Serbia, 2016 (Belgrade : Jovan). - VI, 502 str. : ilustr. ; 24 cm

Tiraž 200. - Bibliografija uz svaki rad.

ISBN 978-86-82475-34-7

1. Society of Physical Chemists of Serbia (Beograd)

a) Физичка хемија - Зборници b) Електрохемијско инжењерство - Зборници  
c) Биофизичка хемија - Зборници d) Спектроскопија - Зборници  
COBISS.SR-ID 225801996

08. 09. 2016





# **PHYSICAL CHEMISTRY 2016**

*13<sup>th</sup> International Conference on  
Fundamental and Applied Aspects of  
Physical Chemistry*

*Proceedings  
Volume II*

**BELGRADE**  
**September 26-30, 2016**





# **PHYSICAL CHEMISTRY 2016**

*13<sup>th</sup> International Conference on  
Fundamental and Applied Aspects of  
Physical Chemistry*

*Proceedings  
Volume II*

**BELGRADE**  
**September 26-30, 2016**

**ISBN 978-86-82475-33-0**

**Title:** Physical Chemistry 2016 (Proceedings)

**Editors:** Željko Čupić and Slobodan Anić

**Published by:** Society of Physical Chemists of Serbia, Studentski trg 12-16,  
11158, Belgrade, Serbia.

**Publisher:** Society of Physical Chemists of Serbia

**For Publisher:** Slobodan Anić, President of Society of Physical Chemists of  
Serbia

**Printed by:** "Jovan", Printing and Publishing Company; 200 Copies

**Number of pages:** 3+434; Format B5; printing finished in September 2016

Text and Layout: "Jovan"

Neither this book nor any part may be reproduced or transmitted in any form or by any means, including photocopying, or by any information storage and retrieval system, without permission in writing from the publisher.

200 - *Copy printing*

## CONTENT

<i>Volume II</i>	
<i>Material Science</i>	505
<i>Macromolecular Physical Chemistry</i>	621
<i>Environmental Protection, Forensic Sciences, Geophysical Chemistry</i>	691
<i>Phase Boundaries, Colloids, Liquid Crystals, Surface-Active Substances</i>	747
<i>Complex Compounds</i>	761
<i>General Physical Chemistry</i>	777
<i>Pharmaceutical Physical Chemistry</i>	795
<i>Education, History</i>	853
<i>Food Physical Chemistry</i>	883
<i>Physico-Chemical Analysis</i>	913
<i>Index</i>	919



*H - Material Science*



## QUANTUM DOTS IN DISPLAY TECHNOLOGY – PRESENT AND FUTURE

Z. Popović

*ZP Technology Solutions Inc.  
Research Fellow, Xerox Corporation (retired)*

### **ABSTRACT**

Quantum dots (QDs) have unique tunable luminescence properties with narrow spectral distributions. That makes them suitable for lighting and display applications. In this presentation the physics of quantum dot luminescence will be discussed and compared to luminescence properties of organic molecules used in OLEDs and PhOLEDs (phosphorescent OLEDs). Applications of QDs will be described covering high color rendering index light sources, liquid crystal displays with special backlights which utilize QDs to provide wider color gamut, and QD based LEDs (QLEDs). Mechanisms of QLED operation and strategies for improvement of QLED performance will also be discussed.

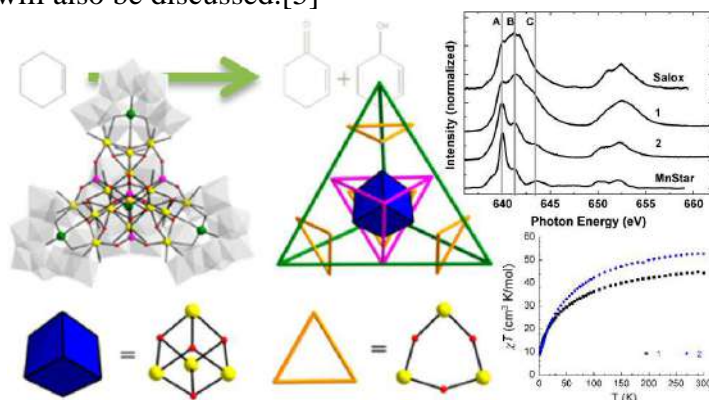
## POLYOXOMETALATE CHEMISTRY: FROM SYNTHESIS AND STRUCTURE TO CATALYSIS AND BIOMEDICINE

U. Kortz

*Jacobs University, Department of Life Sciences and Chemistry, P.O. Box  
750561, 28725 Bremen, Germany, u.kortz@jacobs-university.de*

POMs are discrete metal-oxo anions of early-transition metals in high oxidation states (e.g.  $W^{VI}$ ,  $V^V$ ), usually composed of edge- and corner-shared  $\{MO_6\}$  octahedra and frequently also one or more central, tetrahedral hetero elements (e.g. P, Si).[1] This class of inorganic compounds has gained increasing attention during the last 40 years, largely owing to a unique combination of their properties. In addition to the enormous structural and compositional variety, which is unmatched in inorganic chemistry, POMs can be tuned with respect to solubility, redox activity, color, thermal stability, and charge density. As a result, POMs exhibit potential applications in many different and diverse areas such as catalysis, energy, magnetism, and health/environment.[2]

In this presentation the synthesis and structure of several POMs will be presented as well as their associated physicochemical properties. This includes  $3d$  metal substituted heteropolytungstates as well as the novel class of polyoxo-noble-metalates, in particular polyoxopalladates(II).[3] The latter exhibit unprecedented electronic, spectroscopic and magnetic properties. Examples of POMs as homogeneous and heterogeneous oxidation catalysts will be shown, including water splitting.[4] The role of POMs in the biomedical area, for example as antiviral agents or inhibitors of enzymes, will also be discussed.[5]



- 
- [1] Pope, M. T. *Heteropoly and IsopolyOxometalates*; Springer: Berlin, 1983.
- [2] Pope, M. T.; Kortz, U. *Polyoxometalates*. In *Encyclopedia of Inorganic and Bioinorganic Chemistry*; John Wiley & Sons, Ltd.: Hoboken, NJ, 2012.
- [3] Yang, P.; Xiang, Y.; Lin, Z.; Bassil, B. S.; Cao, J.; Fan, L.; Fan, Y.; Li, M.; Jiménez-Lozano, P.; Carbó, J. J.; Poblet, J. M.; Kortz, U. *Angew. Chem. Int. Ed.* 2014, **53**, 11974-11978.
- [4] Al-Oweini, R.; Sartorel, A.; Bassil, B. S.; Natali, M.; Berardi, S.; Scandola, F.; Kortz, U.; Bonchio, M. *Angew. Chem. Int. Ed.* 2014, **53**, 11182-11185.
- [5] Lee, S.-Y.; Fiene, A.; Li, W.; Hank, T.; Brylev, K.; Fedovrov, V.; Lecka, J.; Haider, A.; Pietzsch, H.-J.; Zimmermann, H.; Sévigny, J.; Kortz, U.; Stephan, H.; Müller, C. E. *Biochem. Pharmacol.*, 2015, **93**, 171-181.

## METHOD OF SELECTIVE RECOVERY OF YTTRIUM OXIDE FROM TITANIUM-ALUMINIUM BASED WASTES

S. Stopic and B. Friedrich

*RWTH Aachen University,  
Institute for Process Metallurgy and Metal Recycling  
Intzestrass3, 52056 Aachen, Germany(sstopic@ime-aachen.de)*

### ABSTRACT

Yttrium and yttrium oxide are mostly used in fluorescent lamps, production of electrodes, in electronic filters, lasers, superconductors and as additives in various Al-Ti materials to improve their properties. Recovery of yttrium oxide from secondary sources such as red mud, coatings from ceramic industry and phosphors is extremely important. The main aim of this study is to examine the selective recovery of yttrium oxide from Al-Ti based secondary materials using one combined method based mostly on hydrometallurgical treatment. Method of *selective* recovery of yttrium from Al-Ti based *wastes* contains: crashing and grinding of materials, sieving, leaching of chosen fine fraction with hydrochloric acid, neutralization with calcium carbonate, filtration, precipitation with oxalic acid in order to produce a pure yttrium oxalate and finally thermal decomposition in order to produce yttrium oxide. The present study summarized the influence of different reaction parameters such as leaching temperature, time and concentration of hydrochloric acid on yttrium dissolution from Al-Ti based secondary materials. Scale up of the laboratory investigations was studied, too. The produced yttrium oxide was analyzed using SEM and EDS-analysis.

### INTRODUCTION

Yttrium is a silvery transition metal and has similar chemical properties to lanthanoids. Because of this similarity, yttrium belongs to rare earth elements. Rare earth metals are increasingly establishing themselves as crucial industrial materials, with unique applications in numerous fields [1]. Because of thermal stability in the presence of most reactive engineering metals including titanium, and titanium alloys, yttrium oxide ( $Y_2O_3$ ) is an important and useful metal casting refractory. As such, crucibles and other casting materials used by the aviation industry for the manufacture of metal alloys contain yttrium, a valuable rare-earth element. The feasibility of using

yttrium oxide as a crucial material or a coating for induction melting of titanium is widely used in metallurgy. The native source of yttrium can be found in hard rocks and placer sands. Hard rock deposits are mined by open pit and underground methods. The aim of physical beneficiation is increasing the necessary mineral content by exploiting some physical processes. During physical beneficiation, accompanying minerals such as ilmenite, rutile, zircon, magnetite, and quartz are separated, which results in the formation of a concentrate with an increased content of rare earth elements. During a chemical treatment of a concentrate, rare earths are separated from impurities, especially thorium and uranium from minerals. This is accomplished by attacking minerals with some leaching agents. The process parameters such as temperature, pressure, chemical type and concentration of the leaching agent differ in accordance with the mineral type. In monazite applications, sodium hydroxide and sulfuric acid are mostly used as leaching agents. In the dissolution process, rare earth elements and thorium are precipitated in the hydroxide and sulfate forms. In the alkali application, the formed rare hydroxides are dissolved in the next step with either hydrochloric or nitric acid where thorium is not soluble [2]. Cold water is used to dissolve rare earth sulfates in an acid treatment. The dissolution of xenotime is similar to monazite digestion. It requires more concentrated leaching agents and higher process conditions. During the subsequent separation, individual rare earth elements are separated from their mixtures. As reported by Amaral and Morais [3] fractional crystallization and solvent extraction are mostly used for this separation. Because of the presence of uranium and thorium in ores, environmental protection and small available amount of deposits of rare earth elements in the European countries, recycling of rare earth from different secondary materials has a high importance. Due to the absence of economical primary deposits on their territories, many European countries have to be included into the recycling of REEs from pre-consumer scrap, industrial residues and REE-containing End-of-Life products.

Stopic and Friedrich [4] summarized the influence of different reaction parameters such as leaching temperature, time and concentration of hydrochloric acid on yttrium dissolution from waste ceramic dust with 1.34 % of yttrium and impurities in weight %: 0.56 Fe<sub>2</sub>O<sub>3</sub>, 0.5 TiO<sub>2</sub>; 0.48 SiO<sub>2</sub>; and residue of Al<sub>2</sub>O<sub>3</sub>. This fine dust fraction was approx. below 250 μm. An increase of dissolution time and temperature increases yttrium dissolution. The maximal yttrium dissolution efficiency was obtained using 2M HCl at atmospheric pressure at 70°C (about 80%). An increase of pressure from atmospheric pressure to 0.5 MPA at 150°C leads to the maximum dissolution of yttrium (about 98.6 %). A kinetic analysis revealed that the

dissolution of yttrium with hydrochloric acid can be described using a kinetic model based on the reaction at the solid-liquid phase as a limiting step. The calculated activation energy  $E_A$  between 20°C and 70°C amounts to 31.2 kJ/mol.

One of the major challenges in the processing of used phosphors for the extraction of rare earths lies in a large number of different compounds by Poscher et al. [5]. The summary of this work showed that the hydrochloric leaching of a screened luminophore powder followed by the precipitation of a contaminated RE oxalate, converting the mixture into their oxides and subsequent raffination in order to dissolve most of the alkali metal oxides leads to a RE concentrate which could be applied as a new raw material for the subsequent process steps of refining.

In this study a new combined hydrometallurgical and pyrometallurgical method for the dissolution of yttrium from Ti-Al based secondary materials was studied in order to obtain powder of yttrium oxide. After crushing, grinding, and a sieving, the fine fraction below 250  $\mu\text{m}$  was leached with hydrochloric acid under an atmospheric pressure in order to reach a selective leaching. The main aim of this work is to establish the optimal parameters for maximal recovery of yttrium from secondary materials in laboratory conditions and transfer these optimal results to a technical scale.

## EXPERIMENTAL

Different sample Ti-Al based secondary were used in this work, The initial material, which consists of more than 90% of  $\text{Al}_2\text{O}_3$ , also contains the yttrium oxide layer used on the casting component side, which should be separated by the following very selective hydrometallurgical extraction processes from the rest of the ceramics. The still adhesive slurry layer of  $\text{Y}_2\text{O}_3$  in the ceramic left overs of different molds is recognizable by its brownish coloring in Figure 1.

By an ICP analysis, the concentration in yttrium and by an RFA-WROXI analysis, the fraction of remaining elements was ascertained. In Table 1 is to be seen that the provided initial material consists mainly of  $\text{Al}_2\text{O}_3$ , which serves as a back-up layer in the process of



**Figure 1. Ti-Al based waste material**

the investment casting at Access e.V. Aluminum oxide is consequently the matrix of the initial material.

**Table 1.** Chemical composition of the molds in wt.-% (Y measured by ICP, remaining elements by RFA)

Element	Y	SiO <sub>2</sub>	TiO <sub>2</sub>	Al <sub>2</sub> O <sub>3</sub>	Fe <sub>2</sub> O <sub>3</sub>	Mn <sub>3</sub> O <sub>4</sub>
concentration in wt.-%	6.83	0.26 0.15	0.17 0.13	Matrix	2.09	0.37

To recover of the yttrium from the ground molds of the investment casting, the powder obtained from the sieving with a grain size smaller than 250  $\mu\text{m}$  was firstly leached in the liquid agent. Here, special interest is in selectively dissolving the valuable rare earth metal to distinguish thus from impurities and by-elements such as Al<sub>2</sub>O<sub>3</sub>, Fe<sub>2</sub>O<sub>3</sub>, and TiO<sub>2</sub>. For leaching tests under atmospheric pressure, the aggregate shown in Figure 2. was used at the IME.



**Figure 2:** Aggregate for leaching with heater and pH electrode

This, for such leaching processes specifically manufactured construction, consists of a double-walled glass vessel with a capacity of 2 liters. Thanks to this construction, the temperature of the leach is adjustable by circulating partially very hot water between those walls without coming in direct contact with the reaction chamber. The mobile heating device allows temperatures from up to 120 °C. The glass vessel is placed on a height adjustable stage that guarantees an optimal alignment and tight connection

to minimize possible leakage and resulting evaporation losses. The leaching tests with hydrochloric acid were carried out within the scope of this work to be able to ascertain the effects of different test parameters on the leaching efficiency of yttrium and the impurities. On this occasion, the focus was on the following parameters:

- leaching temperature (70-150°C)
- leaching time (2-5 h)
- solid / liquid ratio (0.1-0.5)
- concentration of the hydrochloric acid (1-3 mol/L)

## RESULTS AND DISCUSSION

The most important results for the leaching were shown at the Fig. 3.

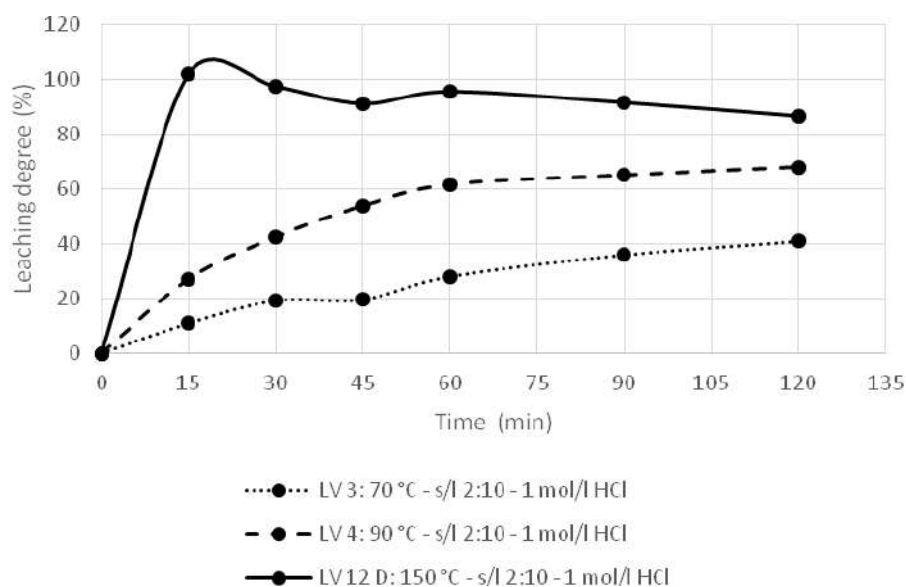
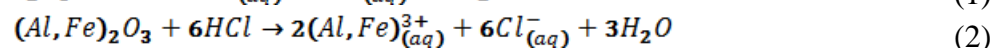
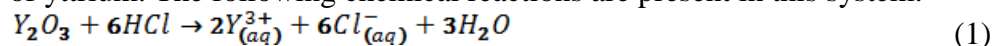


**Figure 3.** The leaching degree of yttrium with HCl at different temperatures

As shown at Fig.3 an increase of temperature increases the leaching degree of yttrium. The following chemical reactions are present in this system.



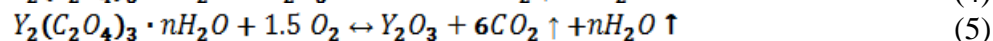
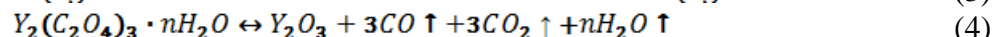
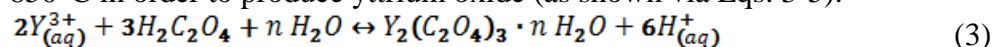
Some dissolution of Al and Fe is present during leaching of Y, what is not desired. In order to remove the impurities such as Fe, Al, Mn, the precipitation with  $CaCO_3$  was performed. The final step is filtration.

Scale up of or developed method was performed using the equipment, as shown at Fig. 4: leaching unit (2 x 100 L), neutralization unit (3 x 10 L and 1 x 8.5 L), stirred collecting tank (250l) and separation unit (filter press).



**Figure 4.** Scale up of the developed method

The last step is production of yttrium oxalate and thermal decomposition at 850°C in order to produce yttrium oxide (as shown via Eqs. 3-5).



The mass of 20 kg previously prepared secondary materials was leached using 1M HCl in a two leaching units at 70°C in two hours. Using our previously mentioned strategy, finally the powder of  $Y_2O_3$  was obtained after of thermal decomposition of yttrium oxalate (as shown at Fig. 5)

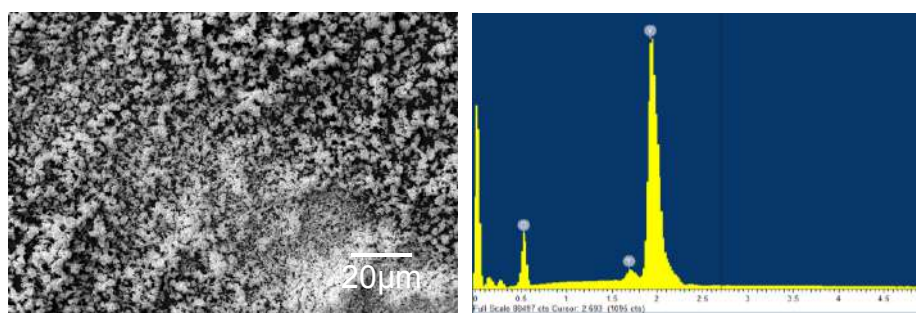


**Figure 5.** SEM- and EDS- analysis of obtained yttrium oxide

## CONCLUSION

Y<sub>2</sub>O<sub>3</sub>-owder was obtained from secondary Ti-Al wastes using a combined hydrometallurgical and pyrometallurgical method. The scale up of developed method was successfully performed. Regarding to the purity of final yttrium oxide some improvements of this method are addressed an use of solvent extraction in order to separate of the remained impurities and increase the concentration of yttrium in the final solution.

## *Acknowledgement*

Within the scope of the aviation research program (LuFo) of the BMWi, the results of the co-operative project TiAl-2020: Increase of the raw material efficiency with the production processes of TiAl components are presented. We thank the BMWi for the financing of the project between 7/1/2015 and 12/31/2016.

## REFERENCES

- [1] E. Kim, K. Osseo-Asare, Hydrometallurgy, 2012, **113-114**, 67-68.
- [2] K. Sung-Don, L., Jin-Young, K. Chul-Joo, Y. Ho-Sung, K. Joon-Soo, Journal of the Korean Institute of Resources Recycling, 2010, **19**, 70-76.
- [3] J. Amaral, J., C. Morais. Minerals Engineering, 2010, **23**, 498-503.
- [4] S. Stopic, B. Friedrich, Military Technical Courier, 2016, **64**, 383-395.
- [5] A. Poscher, S. Luidold, M. Kaindl, H. Antrekowitsch, Proc. of EMC, 2013, 1217-1222

## MAGNETIC NANOPARTICLES

B. Kalska-Szostko<sup>1</sup>, U. Klekotka<sup>1</sup> and D. Satuła<sup>2</sup>

<sup>1</sup>*University of Białystok, Institute of Chemistry, Ciolkowskiego 1K 15245  
Białystok, Poland. (kalska@uwb.edu.pl)*

<sup>2</sup>*University of Białystok, Faculty of Physics, Ciolkowskiego 1L 15245  
Białystok, Poland.*

### ABSTRACT

Modification of the composition, morphology and shape are an important issue in respect of magnetic properties characteristic of the nanostructures. This can be realized by alloy like or layer-by-layer growth of the nanoparticles and nanowires. Controlled fabrication methods allow to follow changes of an adequate particles properties in relatively gentle way. To resolve some unanswered question concerning relation between structure, properties and application is required. In this paper fabrication methods of nanostructures (particles, tubes and wires) will be presented. Some properties needed for particular application such as protection from spontaneous oxidation process and specific functionalization will be shown. Besides that their incorporation into nano- or bionanocomposites and its relation with magnetic state of the particles will be discussed. Structural characteristic of presented materials will be done with use of Transmission Electron Microscopy, Scanning Electron Microscopy, Energy dispersive X-ray, X-ray diffraction, Infrared spectroscopy, Mössbauer spectroscopy, and other methods.

### INTRODUCTION

Despite of all studies which were done up to now in field of nanotechnology and nanomaterials science there are still numerous challenges open for scientists. Most of them are related to representation of: well defined structures, physical and chemical properties of separately the core and surface of nanomaterials. Continuously growing interest in nanotechnology and its application causes the development of large variety of materials with different shape and size in nano scale. Magnetic dots, nanoparticles, cylinders and wires are subjected to study due to possibility of interesting fundamental research and parallel technological development. Unfortunately (or fortunately) properties of nanostructures strongly dependent on the type, composition, shape, and mutual interaction between objects. Especially great interest in magnetic nanomaterials is due to their wide potential

application, among others the most technological important one are: memories storage media, sensors and logical devices [1]. Another important application target is medicine where nanomaterials can play various roles starting from: drug delivery media, via structural material in biological composites ending on biosensors [2]. Much effort have been made to achieve multifunctional materials with simple synthetic procedure and easy post processing required for subsequent application. Chemical and/or electrochemical fabrication methods are one of the easiest options for obtaining an interesting new class of the nanomaterials.

### EXPERIMENTAL

For detailed structural and morphological characterization of nanowires and nanoparticles, transmission electron microscopy (TEM) was performed. X-ray diffractometry based on Mo ( $K\alpha=0.7136 \text{ \AA}$ ) microfocused source (XRD) was used for crystallinity characterization. Infrared spectroscopy allowed to analyze surface of the studied nanomaterials. Mössbauer spectra (MS) were registered at room temperature with  $^{57}\text{CoCr}$

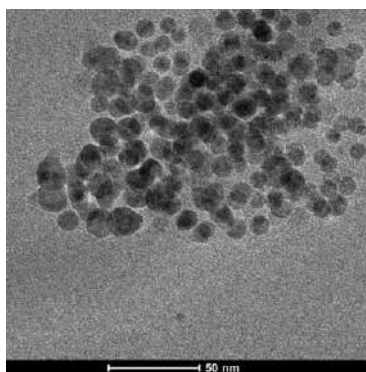


**Figure 1.** TEM image of Ag@Fe<sub>3</sub>O<sub>4</sub> core-shell nanoparticles

radioactive source. The used MS spectrometer was calibrated by  $\alpha$ -Fe foil at room temperature.

Magnetite nanoparticles were synthesized by thermal decomposition of iron acetylacetonate ( $\text{Fe}(\text{acac})_3$ ) [3], or by co-precipitation of iron (II) and (III) chlorides in ammonia environment [4]. Iron nanowires were deposited electrochemically in AAO matrix from the solution containing of:  $\text{FeSO}_4$ ,  $\text{FeCl}_3$ ,  $\text{H}_3\text{BO}_3$  and ascorbic acid [5].

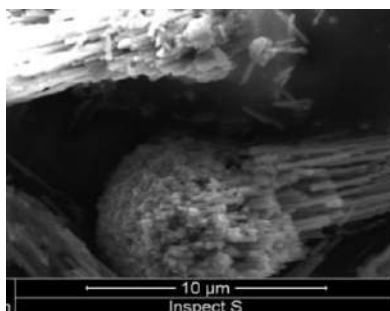


**Figure. 2** SEM image of Fe nanowires.

## RESULTS AND DISCUSSION

In Fig 1 Ag@Fe<sub>3</sub>O<sub>4</sub> nanoparticles were obtained by two steps method. Firstly magnetite core was obtained by thermal decomposition of Fe(acac)<sub>3</sub>, and secondly silver shell was grown on core. This time as a precursor AgNO<sub>3</sub> was used. Such way obtained nanoparticles are regular and round in shape, with estimated average size of 12±2 nm. Fig. 2 shows Fe nanowires obtained by electrodeposition in anodic aluminum oxide (AAO) matrix. Current value of 10 mA and a counter Pt electrode was used. Obtained by this method nanowires has diameter of about 170 nm, and more than 1 μm length.

## CONCLUSIONS

Nanomaterials can be obtained by many various experimental methods. It may represent different shapes (elongated like: nanowires, nanotubes, or round particles, etc.). Modification of fabrication procedures and therefore composition of nanomaterials, allows to obtain different and in most cases tunable properties. This causes that it further can be used in various applications.

### *Acknowledgement*

Mössbauer spectroscopy was done in close collaboration with Faculty of Physics at University of Białystok. Work was partially financed by EU funds via the project with a contract number POPW.01.03.00-20-034/09-00, by NCN funds, project number UMO-2014/13/N/ST5/00568 and COST Action Nanospectroscopy MP1302.

**REFERENCES**

- [1] R. Cowburn, M. Welland, *Science*, 2000, **287**, 1466
- [2] S. Khizroev, M. Kryder, D. Litvinov, & D. Thomson, *Appl. Phys. Lett.*, 2002, **81**, 2256
- [3] B. Kalska-Szostko, U. Wykowska, & D. Satuła, *Applied Surface Science*, 2014, **360**, 7-15
- [4] B. Kalska-Szostko, M. Rogowska, A. Dubis, & K. Szymański, *Applied Surface Science*, 2012, **258**, 2783–2787
- [5] B. Kalska-Szostko, & E. Orzechowska, *Current Applied Physics*, 2011, **11** (5), S103–S108.

## FERROMAGNETIC BEHAVIOR OF Mn<sup>2+</sup> DOPED TITANIA NANOTUBES

M. Vranješ<sup>1</sup>, J. K. Jakovljević<sup>1</sup>, Z. Konstantinović<sup>2</sup>, T. Radetić<sup>3</sup>, M. Stoiljković<sup>1</sup>, M. Mitrić<sup>1</sup> and Z. Šaponjić<sup>1</sup>

<sup>1</sup>*Vinča Institute of Nuclear Sciences, University of Belgrade,  
P. O. Box 522, 11001 Belgrade, Serbia*

<sup>2</sup>*Institut de Ciència de Materials de Barcelona, CSIC,  
Campus UAB, 08193 Bellaterra, Spain*

<sup>3</sup>*Faculty of Technology and Metallurgy, University of Belgrade,  
Karnegijeva 4, 11120 Belgrade, Serbia*

### ABSTRACT

Hydrothermal synthesis of Mn doped titaniananotubes, which showed room temperature ferromagnetism (RTFM) is reported. Morphology of Mn doped nanotubes was characterized by transmission electron microscopy (TEM). The size of nanotubes was relatively uniform with outer diameter of about 10 nm and lengths of up to few hundred nanometers. The x-ray powder diffraction (XRPD) analysis of resultant powder confirmed the appearance of mixed crystalline phases in Mn doped nanotubes: hydrogentitanate (H<sub>2</sub>Ti<sub>2</sub>O<sub>5</sub> x H<sub>2</sub>O) and tetragonal anatase titania. RTFM ordering with saturation magnetic moment ( $M_s$ ) of the order of 1.27  $\mu_B$  per Mn atom was observed.

### INTRODUCTION

The ability to control the spin of electrons in addition to their charge in diluted magnetic semiconductors would expand their applications in conventional electronic devices. The term diluted magnetic semiconductor (DMS) refers to a non-magnetic semiconductor material where the host cations are replaced with magnetic impurities up to a few atomic percent. DMSs were mostly based on II-VI or III-V compounds, but those materials were unattractive for practical electronic applications, since ferromagnetism has been achievable far below room temperature [1]. Recently it was theoretically predicted that transition metal ions doped metal oxides (TiO<sub>2</sub>, SnO<sub>2</sub>, In<sub>2</sub>O<sub>3</sub>, ZnO) are suitable material for DMSs with ferromagnetic behavior at room temperature [2-4]. In this paper we reported a novel method for the synthesis of Mn doped titania nanotubes as well as their structural and magnetic properties.

## EXPERIMENTAL

All chemicals were reagent-grade from Aldrich and used as received. Mn doped titania nanotubes were synthesized according to Kasuga et al. using powder of 1 at.%  $\text{Mn}^{2+}$  doped anatase  $\text{TiO}_2$  nanoparticles as a precursor [5]. The 1 at.%  $\text{Mn}^{2+}$  doped  $\text{TiO}_2$  nanoparticles were synthesized using the slightly modified synthetic procedure already reported [6, 7]. For the synthesis of nanotubes, 250 mg of 1 at.%  $\text{Mn}^{2+}$  doped  $\text{TiO}_2$  nanoparticles was dispersed in 10 ml 10 M NaOH and hydrothermally treated 20 h under saturated vapor pressure of water at 150 °C. After autoclaving, the ensuing powder of nanotubes was washed with distilled water until pH 7. The powder was then air dried at 70 °C. Film for magnetic characterization was prepared by drop casting of dispersions of Mn doped nanotubes onto pre-cleaned glass substrate. The films were annealed in air for 2 min at 150 °C after each drop. The shape and size of Mn doped nanotubes were characterized using JEM 1400 transmission electron microscope operating at 120 kV. The XRPD pattern was obtained on a Philips PW-1050 automated diffractometer. The percent of Mn ions in nanotubes was determined using *inductively coupled plasma* (ICP) emission spectrometry. The concentration of Mn ions in the sample of titaniananotubes was 0.016 at.% of the amount of  $\text{Ti}^{4+}$  ions. The field dependence of the magnetic moment was measured using a superconducting quantum interference device magnetometer (SQUID). Hysteresis loop measurement has been performed up to 60 kOe.

## RESULTS AND DISCUSSION

Mn doped titania nanotubes were synthesized by hydrothermal processing of  $\text{Mn}^{2+}$  doped anatase  $\text{TiO}_2$  nanoparticles in proton deficient aqueous solution [5]. Conventional TEM image of the 0.016 at.% Mn doped titaniananotubes is shown in Fig. 1. Uniform size distribution of nanotube diameters ( $d \sim 10$  nm) was observed. The length of the nanotubes was in a wide range from one hundred to a few hundred nanometers. The nanotubes had an open-ended multiwall structure. Structural analysis of

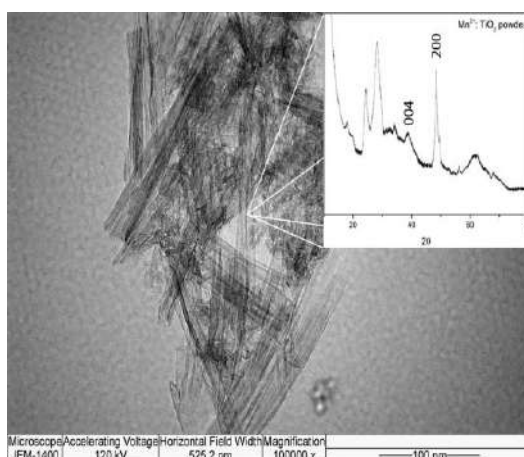


**Figure 1.** TEM image of Mn doped titania nanotubes; Inset: XRPD pattern of Mn doped titania nanotubes.

0.016 at.% Mn doped nanotubes, inset Fig. 1, revealed the presence of mixed crystalline phases in the sample. Diffraction peaks at  $2\theta = 24.5^\circ$ ,  $28.1^\circ$  and  $34.1^\circ$  confirmed the presence of hydrogentitanate ( $\text{H}_2\text{Ti}_2\text{O}_5 \times \text{H}_2\text{O}$ ), which usually appear in the samples of hydrothermally synthesized titania nanotubes, while the intense peak at  $2\theta = 48.5^\circ$  and peak appearing at  $38.7^\circ$  could be indexed as diffractions from the anatase  $\text{TiO}_2$  crystal planes (200) and (004)[8, 9].

The magnetic response for film made of 0.016 at.% Mn doped titania nanotubes as a function of magnetic field strength ( $H$ ) was followed at room temperature. The field dependent magnetization after diamagnetic correction is shown in Fig. 2. As can be seen from Fig. 2, the ferromagnetic ordering with coercive field of  $H_c \sim 180\text{Oe}$  and  $M_s$  of the order of  $1.27 \mu_B/\text{Mn}$ , appeared in 0.016

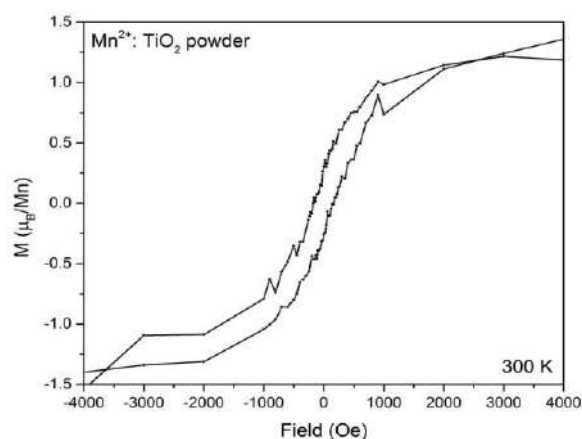


**Figure 2.** Magnetization curve for Mn doped titania nanotubes

at.% Mn doped titania nanotubes. Based on the experimental results and theoretical models it was proposed that oxygen vacancies ( $\text{F}^+$  centers) play an important role in mediating the magnetic ordering in oxide based DMS materials[10, 11]. It is known that RTFM of Mn doped  $\text{TiO}_2$  nanocrystals significantly depends on structural defects and only the  $\text{F}^+$  centers in bulk mediate the FM ordering[10]. Titania nanotubes contain a large fraction of structural defects and majority of them is located on the interior walls of the nanotubes [9]. Also, Ahmed et al. showed that lower content of  $\text{Mn}^{2+}$  dopant ions ( $< 1$  at. %) favors the ferromagnetic interaction while the higher concentrations of  $\text{Mn}^{2+}$  lead to the formation of antiferromagnetic ordering of  $\text{Mn}^{2+}$  clusters[10]. Relatively high value of  $M_s$  in our sample is not only due to the low concentration of Mn ions but also the presence of F centers should be taken into account. Our results indicate a high content of bulk  $\text{F}^+$  centers in titania nanotubes and that the high fraction of Mn ions involved in FM ordering.

## CONCLUSION

The Mn doped titania nanotubes were synthesized applying hydrothermal treatment on proton deficient aqueous dispersion of 1 at.%  $\text{Mn}^{2+}$  doped

anatase TiO<sub>2</sub> nanoparticles. XRPD study confirmed that the nanotubes possessed a mixed phase crystalline structure. The H<sub>2</sub>Ti<sub>2</sub>O<sub>5</sub> x H<sub>2</sub>O and anatase crystalline phases were detected in the sample. The ferromagnetic ordering at room temperature with closed loop ( $H_c \sim 180$  Oe) and  $M_s$  of the order of 1.27  $\mu_B$ /Mn atom were observed in the film made of Mn doped titania nanotubes. The reason for observed ferromagnetism and relatively high value of  $M_s$  could be found in the high content of bulk oxygen vacancies (F<sup>+</sup> centers) and their interaction with the substitutional Mn impurity.

### **Acknowledgement**

This work was supported by the Ministry of Education, Science and Technological Development of the Republic of Serbia (project: 172056).

### **REFERENCES**

- [1] R. Janisch, P. Gopal and N. A. Spaldin, *J. Phys.: Condens. Matter*, 2005, **17**, 657.
- [2] J. Y. Kim, J. H. Park, B. G. Park, H. J. Noh, S. J. Oh, J. S. Yang, D. H. Kim, S. D. Bu, T. W. Noh, H. J. Lin, H. H. Hsieh and C. T. Chen, *Phys. Rev. Lett.*, 2004, **90**, 017401.
- [3] M. Venkatesan, C. B. Fitzgerald, J. G. Lunney and J. M. D. Coey, *Phys. Rev. Lett.*, 2004, **93**, 177206.
- [4] A. Gupta, H. Cao, K. Parekh, K. V. Rao, A. R. Raju and U. V. Waghmare, *J. Appl. Phys.*, 2007, **101**, 09N513.
- [5] T. Kasuga, M. Hiramatsu, A. Hoson, T. Sekino, K. Niihara, *Adv. Mater.*, 1999, **11**, 1307-1311.
- [6] C. Wang, D. W. Bahnemann, J. Dorhmann, *Chem. Commun.* (2000) 1539.
- [7] M. Carević, N. D. Abazović, T. Savić, T. B. Novaković, M. D. Mojović, and M. I. Čomor, *Cer. Int.* 2016, **42**, 1521–1529.
- [8] T. Brunatova, D. Popelkova, W. Wan, P. Oleynikov, S. Danis, X. Zou and R. Kuzel, *Mat. Char.*, 2014, **87**, 166.
- [9] Z. V. Šaponjić, N. M. Dimitrijević, D. M. Tiede, A. J. Goshe, X. Zuo, L. X. Chen, A. S. Barnard, P. Zapol, L. Curtiss and T. Rajh, *Adv. Mater.*, 2005, **17**, 965.
- [10] S. A. Ahmed *J. Magnet. Magnet. Mat.*, 2016, **402**, 78.
- [11] S. V. Chong, J. Xia, N. Suresh, K. Yamaki and K. Kadowaki *Solid State Comm.*, 2008, **148**, 345.

## ADSORPTION PROPERTIES OF MAGNETIC POROUS CARBON MATERIALS OBTAINED FROM VARIOUS PRECURSORS

P. Strachowski and M. Bystrzejewski

*University of Warsaw, Faculty of Chemistry,  
Pasteur 1, 02-093 Warsaw, Poland, (p.strachow@gmail.com).*

### ABSTRACT

The synthesis method of new magnetic carbon adsorbent is presented. The main idea of this material is to combine the magnetic properties of carbon encapsulated iron nanoparticles and porous carbon matrix. In consequence such fusion results in magnetic composite material with adsorption properties comparable to commercial activated carbons.

### INTRODUCTION

Activated carbon, due its porous structure, is commonly used material dedicated to the removal of organic pollutants from aqueous solutions. The application of this material in waste water treatment causes severe problems related to its separation. Sedimentation and filtration are commonly used to remove the spent activated carbon from the solution. A new composite material based on carbon encapsulated iron nanoparticles (CEINs) as magnetic phase solves the problem of separation. The use of a permanent magnet facilitates the separation of the adsorbent from the solution. Carbon encapsulated magnetic nanoparticles are core-shell nanoparticles which comprise of nanocrystals of ferromagnetic metals and protective carbon coating. The diameter of carbon encapsulates is between 5 and 100 nm, whilst the thickness of the carbon shell is ca.5-10nm [1]. This way of protection of the magnetic phase in CEINs allows to use this material in a wide range of chemical and thermal conditions. The synthesis of magnetic adsorbent includes the preparation of a mixture containing CEINs, carbon precursor and activating agent, and then such impregnate is carbonized in the temperature range between 600 and 800°C under inert atmosphere. The thermal decomposition of carbon precursor results in formation of an additional carbon matrix which surrounds the magnetic particles, and in the same way the porosity is developing due to the presence of the activating agent. Magnetic composites of activated carbon and other carbon materials are described in a number of papers [2,3]. The immobilization of metal nano- and microcrystals such as Fe, Co, Ni or their alloys and oxides

(including ferrites, mixed oxides) in the porous structure of carbon material leads to the magnetic adsorbent. There are several ways to obtain carbon magnetic adsorbents, however, in general the process involves the use of previously synthesized magnetic particles (e.g.  $\text{Fe}_2\text{O}_3$ ,  $\text{Fe}_3\text{O}_4$ ,  $\text{CoFe}_2\text{O}_4$ ) and their subsequent immobilization into the network of pores. Such idea of the synthesis of magnetic adsorbent based on activated carbon results in the adsorbent with magnetic properties, however, in this case the magnetic phase is protected not enough against external corrosive factors. Magnetic composites of activated carbon at low pH undergo irreversible leaching of magnetic particles. Moreover, a network of pores in such material is significantly less developed because the magnetic phase occupies the pores. The use of carbon encapsulated iron nanoparticles solves the above problems. Firstly, carbon coating around the magnetic core guarantees the corrosion resistance, secondly in the case of this composite the magnetic phase is not fixed in the porous structure

### EXPERIMENTAL

Carbon encapsulated iron nanoparticles were synthesized via carbon arc discharge method which is described in details elsewhere [4]. The main idea of the synthesis protocol includes the carbonization of a mixture containing carbon precursor, CEINs and activating agent. Various carbon precursors including sucrose, glucose, poly(ethylene terephthalate) waste were used as carbon precursors. KOH and  $\text{ZnCl}_2$  were used as activating agents and their amounts are described in next section. The initial mixture consisted of 1g of CEINs and 10g of carbon precursor, whilst the content of the activating agent was changed. The carbonization of the initial mixture was carried out in a tubular furnace with the heating rate of  $10^\circ\text{C}/\text{min}$  up to  $800^\circ\text{C}$ , and then the furnace was cooled to room temperature under inert atmosphere. The obtained material was purified in boiling 3M HCl to remove the non-encapsulated iron particles. Several combinations of carbon precursor/activating agent were studied. The adsorption of phenol and its derivatives (2-chlorophenol, 4-chlorophenol) from water solution onto the synthesized materials was studied. The adsorption methodology is described in details in our recent paper [5]. Briefly, the adsorption studies were carried out using the batch solutions with the initial concentration between 10-600 mg/L. A vial containing 25 mg of the adsorbent and 50 mL of the solution were shaken using a rotary shaker for 24 h. Next, the adsorbents were separated using a permanent magnet and the equilibrium concentration of the solutes was evaluated using UV spectroscopy.

## RESULTS AND DISCUSSION

Firstly, some tests were prepared to determine the best ratio between the activating agent and the carbon precursor. In the case of KOH the ratio 4:1 gives the best results, whereas 3:1 is the best ratio to use  $\text{ZnCl}_2$ . Fig.2a presents the adsorption isotherm of phenol onto magnetic adsorbent obtained from sucrose and various activating agents. The maximum adsorption capacity for materials activated with KOH and  $\text{ZnCl}_2$  is found to be 91 and 142 mg/g, respectively. This finding shows that  $\text{ZnCl}_2$  is better activator than KOH. The use of  $\text{ZnCl}_2$  in the activation process is connected with the preliminary dehydration of carbon precursor what develops the porosity in the adsorbent. Fig.2b in turn shows the adsorption isotherms of phenol and its derivatives onto the material made from sucrose activated with  $\text{ZnCl}_2$ . The adsorption capacity for 2-chlorophenol and 4-chlorophenol markedly exceeds the uptake values for phenol (ca. 2 times). This is presumably related to lower water solubility of these halogen derivatives of phenol. Next, the adsorption performance of materials obtained from glucose and PET waste was evaluated. The use of glucose and KOH as the activating agents results in a materials which has weaker adsorption properties the composites obtained from sucrose (Fig.3a). The material obtained from PET waste has comparable adsorption performance to the adsorbent made from glucose (Fig. 3b). Interestingly, in this case the adsorption capacity is not influenced by the kind of the activating agent.

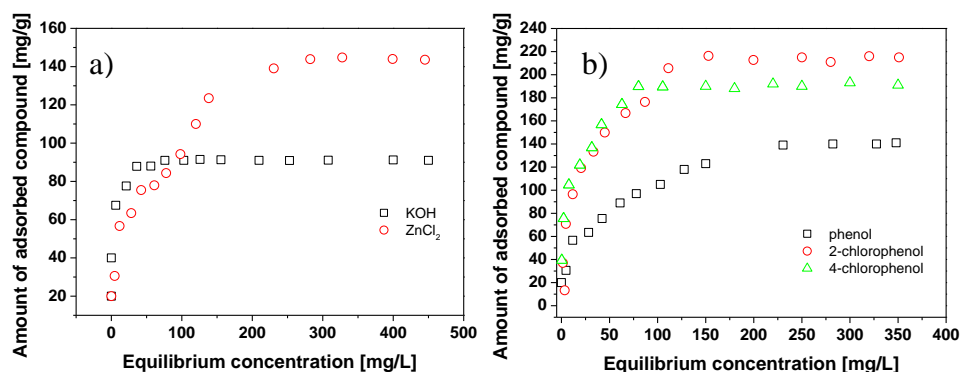


**Figure 2.** Adsorption isotherms of phenol onto material activated with different activating agents (a), and adsorption isotherms of phenolic compounds onto material made from sucrose activated with  $\text{ZnCl}_2$  (b)

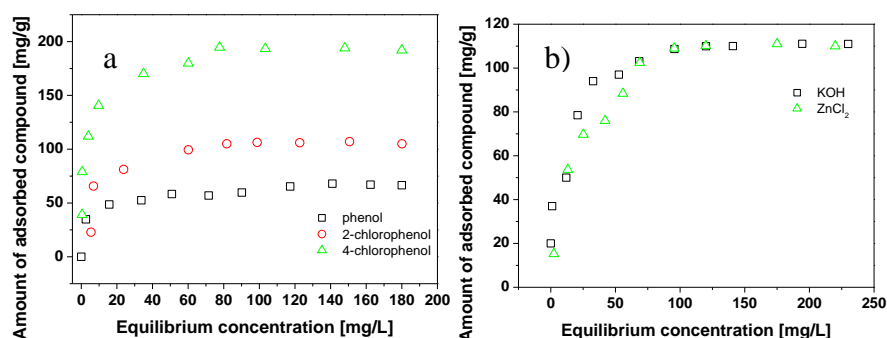


**Figure 3.** Adsorption isotherms of phenolic compounds onto material obtain from glucose activated with KOH (a), adsorption isotherms of phenol onto material made from PET with different activating agents.

## CONCLUSION

This paper presents the method of synthesis of new magnetic carbon adsorbents. A simple one step method yields an adsorbent dedicated to the removal of organic compounds from water solution. It has been shown that the most dangerous pollutants – chlorinated phenols derivatives are efficiently removed from aqueous solutions.

## Acknowledgement

This work was supported by the National Centre for Research and Development (Poland) through the project LIDER 527/L-4/2012

## REFERENCES

- [1] M. Bystrzejewski et. al., *Biomolecular Engineering* 24 (2007) 555–558.
- [2] A. M. Abdalla, S. Ghosh, I. K. Puri, *Diamond & Related Materials* 66 (2016) 90–97.
- [3] M. Fayazi, M. Ghanei-Motlagh, M. A. Taher, *Materials Science in Semiconductor Processing* 40(2015)35–43.
- [4] M. Bystrzejewski, O. Łabędź, W. Kaszuwara, A. Huczko, H. Lange, *Powder Technology* 246 (2013) 7–15.
- [5] P. Strachowski, M. Bystrzejewski, *Colloids and Surfaces A: Physicochem. Eng. Aspects* 467 (2015) 113–123

## SIMULATION OF LIQUID MIGRATION DURING LIQUID PHASE SINTERING

Z. S. Nikolić

*University of Niš, Faculty of Electronic Engineering, Department of Microelectronics, 18000 Niš, Serbia (zoran.nikolic@elfak.ni.ac.rs).*

### ABSTRACT

This paper outlines a computer-based method that can be used for direct two-dimensional simulation of liquid migration by tracking liquid interfaces during liquid phase sintering. This phenomenon will be simulated by pure grain rearrangement combined with coalescence of three or more liquid bridges. In order to avoid shrinkage by other processes than rearrangement, in this approach the system W-Cu will be chosen since tungsten is practically insoluble in liquid copper.

### INTRODUCTION

During the initial stage of liquid phase sintering (LPS) surface tension forces act to bring about physical movement of the constituents of sintering body [1] causing rapid densification. There is also considerable evidence that the liquid phase may also migrate under the action of surface tension forces which act during LPS [2]. For LPS with a relatively large amount of liquid, such a liquid migration could be observed using scanning electron microscopy [3]. When the liquid content is very small, this technique becomes inappropriate because the liquid usually presents as a thin intergrain film.

Liquid migration was investigated introducing a liquid into a two-dimensional (2D) array of uniform circular particles [2]. It was found that the liquid tend to fill smaller low-coordination-number pores first, whereas the larger pores will be filled only when there is sufficient liquid phase. Due to such behavior the liquid usually tend to migrate to the more densely packed regions.

Grof *et al.* [4] presented a particularly interesting approach for the simulation of spatially evolving liquid–vapor interfaces in arbitrary 2D granular media. The main advantage of the method is the possibility to account for topological transitions such as interface coalescence or rupture.

In this paper liquid migration will be simulated taking into account both grain rearrangement and coalescence of liquid bridges. The grain rearrangement will be accepted as driven by the capillary forces between

solid grains embedded in liquid matrix. The coalescence of liquid bridges will be modeled as process in which more bridges join to form a larger one.

### MODEL SYSTEM TOPOLOGY

Let there be a mixture of two components: a major component that forms the particulate solid, and an additive phase as a liquid-producing component. The liquid phase will be formed when the mixed powders are heated to a certain temperature. When a liquid phase is dispersed from between solid grains, the liquid bridges with a curved meniscus shape will form (Fig. 1a) [5]. Thus, an interface as a common boundary among two different phases of matter is ubiquitous in LPS. In 2D the  $k$ -th interface will be defined by the set of  $n_q^k$  points, i.e.

$$I_q^k = \{(x_s^k, y_s^k), s = 1, 2, \dots, n_q^k\}, \quad (1)$$

where the subscript  $q = \text{SV, SL or LV}$  represents solid-vapor, solid-liquid and liquid-vapor interfaces, respectively. According to (1), the pendular liquid bridge can be defined by  $m$  node polygon filled by liquid phase, i.e.

$$\text{LB}_P^{ij} = I_{\text{SL}}^i \cup I_{\text{LV}}^{ij} \cup I_{\text{SL}}^j \cup I_{\text{LV}}^{ji} = \{(x_s, y_s), s = \overline{1, m}\}, \quad (2)$$

where  $I_{\text{LV}}^{ij}$  is liquid meniscus between  $i$ -th and  $j$ -th grains.

The rearrangement process during LPS has been generally accepted that driven by the capillary forces between solid grains embedded in liquid matrix. A detailed description of the numerical model to simulate the grain rearrangement has already been given in the previous work [6].

Due to grain rearrangement three or more  $\text{LB}_P$  can form new capillary liquid bridge, which can be defined by recursive formula

$$\text{LB}_C = I_{\text{SL}}^1 \cup \left\{ \bigcup_{k=1}^{N-1} [I_{\text{LV}}^{k, k+1} \cup I_{\text{SL}}^{k+1}] \right\} \cup I_{\text{LV}}^{N, 1} = \{(x_s, y_s), s = \overline{1, m}\}, \quad (3)$$

where  $N$  is the number of solid grains connected by capillary bridge.

### RESULTS AND DISCUSSION

Liquid migration is characterized by three topological transformations: (i) two  $\text{LB}_P$  undergoing coalescence transform into  $\text{LB}_C$ , (ii)  $\text{LB}_P$  and  $\text{LB}_C$  transform into new  $\text{LB}_C$ , and (iii) two  $\text{LB}_C$  transform into larger  $\text{LB}_C$ . Due to increased liquid bridge volume new menisci for new  $\text{LB}_C$  and given the wetting angle must be updated followed by increasing the length of SL interfaces. At the same time, all LV interfaces lying inside new  $\text{LB}_C$  will be removed followed by decreasing of the number of  $\text{LB}_P$ .

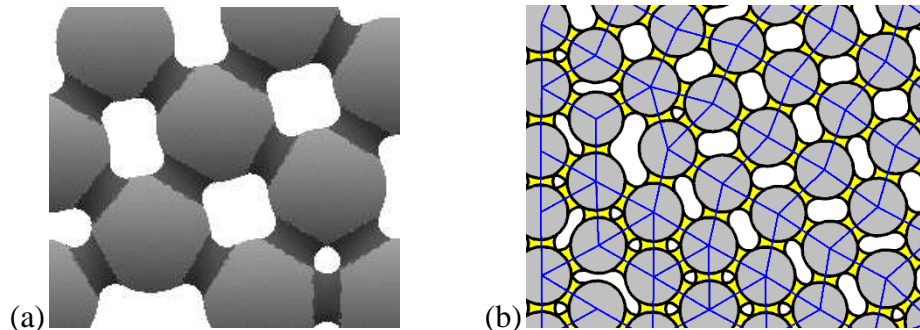


**Figure 1.** Inserts of multi grain models with liquid bridges interconnecting solid grains. (a) Three-dimensional model. (b) 2D model (an insert only) and bridge network (blue colored lines).

In order to avoid shrinkage by other processes than rearrangement, in this approach the system W-Cu will be chosen since tungsten is practically insoluble in liquid copper. The geometry being analyzed in this simulation will be randomly generated planar multi-grain model shown in Fig. 1b, with average grain radius of  $\sim 57 \mu\text{m}$  and average inter-grain distance of  $\sim 14 \mu\text{m}$ . Taking into account applied grain size distribution the next value will be used:  $\chi = 10 \text{ N}^{-1}$  and the wetting angle  $\theta = 10^\circ$ . Specific volume of liquid (usually defined as a fraction of the volume of the liquid  $V_L$ , compared to the volume of the solid grains  $V_S$ ,  $\phi = V_L/V_S$ )  $\phi = 0.065$  will be assigned to all grain-grain gaps where the liquid bridges are able to form.

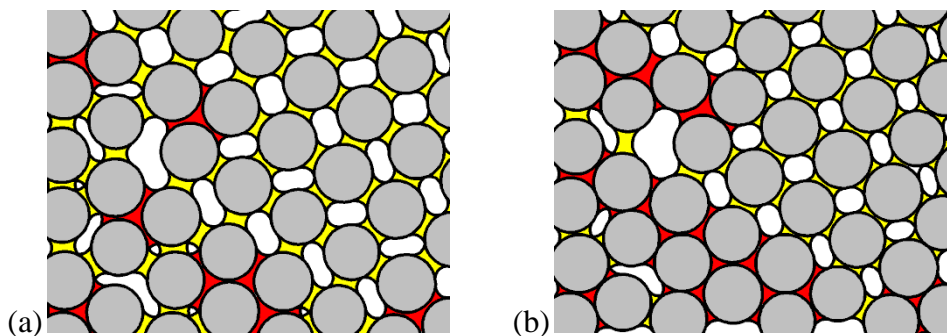


**Figure 2.** Snapshots of microstructure after a sequence of sintering. (a) 700 RS. (b) 2800 RS. Capillary liquid bridges colored in red.

Initial model system is characterized by evenly distributed liquid (within  $LB_p$  only). The result of rearrangement after 700 RS (rearrangement steps [6]) is shown in Fig. 2a, where the average inter-grain distance was  $\sim 12 \mu\text{m}$ . It can be seen remarkable approaching of some grains

combined with filling pores process and liquid migration. At the same time it can be also seen small enlargement of some inter-grain distances followed by growing of some inter-grain pores. Due to rearrangement after 2800 RS (Fig. 2b), the average inter-grain distance decreased to the value of  $\sim 5.6 \mu\text{m}$ . These topological transformations are followed by the formation of clusters of the capillary liquid bridges (appropriate 2D multi-grain arrangement joined by capillary liquid bridge). Computed microstructure shows both evenly distributed  $\text{LB}_P$  (mainly on the left side) and  $\text{LB}_C$  (on the right-bottom side).

## CONCLUSION

In this paper the coalescence of liquid bridges was modeled so that when two domains come in contact with each other they immediately coalesce to form a single domain defined by the equations (2) or (3). The real condition for domains coalescence is that they intersect (overlapping domains if they contain at least one element in common). It should be noted that the coalescence of types (ii) and (iii) prevails against type (i).

The overall model system rearrangement followed usually by decreasing of inter-grain distances was a result of local relative motion of each grain toward its neighbors. Although some grains can be constrained by the neighboring ones during their relative motion, it can be expected that some pores will be filled due to the coalescence of the liquid bridges which processes can give rise to a capillary liquid bridge between them. Such liquid migration is exactly that observed in the early stages of sintering experiments of Kwon and Yoon [7].

## Acknowledgments

The present study was performed under the project No. OI172057 supported by the Ministry of Education, Science and Technological Development of the Republic of Serbia.

## REFERENCES

- [1] W. D. Kingery, J. Appl. Phys., 1959, **30**, 301–306.
- [2] T. M. Shaw, J. Am. Ceram. Soc., 1986, **69**, 27–34.
- [3] Y. S. Kim, J. K. Park and D. N. Yoon, Int. J. Powder Metall., 1985, **21**, 30–37.
- [4] Z. Grof, C. J. Lawrence, F. Štěpánek, Granular Matter, 2008, **10**, 93–103
- [5] V. N. Eremenko, Yu. V. Naidich and I. A. Lavrinenko, Liquid Phase Sintering (New York: Consultants Bureau), 1970.
- [6] Z. S. Nikolic, F. Wakai, Math. Comput. Model., 2012, **55**, 1251–1262.
- [7] O. J. Kwon and D.N. Yoon, Int. J. Powder Metall., 1981 **17**, 127–33.

## SIMULATION OF GRAIN COARSENING WITHIN PENDULAR AND CAPILLARY LIQUID BRIDGES

Z. S. Nikolic<sup>1</sup> and K. Shinagawa<sup>2</sup>

<sup>1</sup>*University of Niš, Faculty of Electronic Engineering, Department of Microelectronics, 18000 Niš, Serbia (zoran.nikolic@elfak.ni.ac.rs).*

<sup>2</sup>*Kyushu University, Faculty of Engineering, Department of Mechanical Engineering, 744 Motoooka, Nishi-ku, Fukuoka, 819-0395, Japan.*

### ABSTRACT

In this paper computer simulation of grain coarsening within pendular and capillary liquid bridges during sintering of W-Ni alloy will be demonstrated. It will be assumed that morphological development is governed by diffusion through the liquid between grains and by the reduction of the total interfacial energy. Under interfacial equilibrium condition, grain coarsening will occur by the exchange of solute between grains.

### INTRODUCTION

Typical phenomenon of liquid phase sintering (LPS) is that solid grains of different size dispersed in a liquid matrix show a tendency of grow of larger grains at the expense of smaller ones which dissolve. The explanations of this phenomenon are largely based on the empirically established laws [1].

In recent years, many computer simulation models have been developed with the aim of simulating the detailed microstructural evolution during grain coarsening. Voorhees *et al.* [2] employed a boundary integral technique to determine the morphological evolution of a small number of particles during Ostwald ripening in two dimensions (2D).

Recent advances in modeling grain coarsening using finite element (FE) method was reported in [3]. To the best of our knowledge, it was the first computer study of grain coarsening from within liquid bridge only.

The objective of this paper is to perform FE method for simulation of grain coarsening within pendular and capillary liquid bridges during LPS. The method will be based on calculation the diffusion field and intergrain diffusional interactions. Multi grain model represented by interfaces will be defined by discrete sets of points, where each point can evolve according to its local environment. Computer simulation of the grain coarsening within the capillary bridge for W-Ni alloy (which usually serves as a model system) will be demonstrated as a first step.

### MODEL DESCRIPTION

When a liquid phase is dispersed from between solid grains, liquid bridges with a curved meniscus shape will form. The unit cell is usually represented by two grains of different size joined by a liquid bridge (Fig. 1a).

The generation of a digital microstructure needs to use a discretized 2D model based on individual grains, liquid phase which forms at additive grain sites, and interfaces between them. The latter ones as common boundaries among two different phases are responsible for a number of phenomena occurring during LPS, e.g. dissolution and reprecipitation, coarsening, etc.

An interface in 2D can be represented with curved (boundary) line. Thus, the  $k$ -th interface can be defined by the set of  $n_q^k$  points

$$I_q^k = \{(x_s^k, y_s^k), s = 1, 2, \dots, n_q^k\}, \quad (1)$$

where the subscript  $q = \text{SV, SL or LV}$  represents solid-vapor, solid-liquid and liquid-vapor interfaces, respectively.

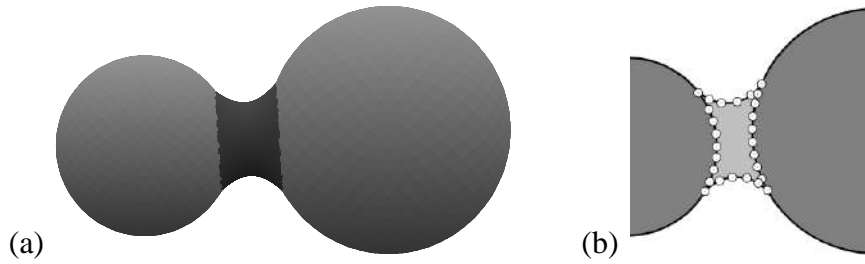


**Figure 1.** Two-grain model. (a) Three dimensional representation. (b) 2D representation of liquid phase interface defined by a set of discrete points.

Taking into account mentioned liquid phase between two grains and the interface definition (1), the pendular liquid bridge in 2D (shown in Fig. 1b) can be defined by

$$\text{LB}_P^{ij} = I_{\text{SL}}^i \cup I_{\text{LV}}^{ij} \cup I_{\text{SL}}^j \cup I_{\text{LV}}^{ji},$$

where  $I_{\text{LV}}^{ij}$  and  $I_{\text{LV}}^{ji}$  are liquid menisci between two grains  $i$ -th and  $j$ -th. Due to grain rearrangement and redistribution of liquid phase, two or more pendular bridges can form capillary liquid bridge. Such bridge that connects  $N$  solid grains can be defined by recursive formula

$$\text{LB}_C = I_{\text{SL}}^1 \cup \left\{ \bigcup_{k=1}^{N-1} [I_{\text{LV}}^{k,k+1} \cup I_{\text{SL}}^{k+1}] \right\} \cup I_{\text{LV}}^{N,1}.$$

Suppose that the system consists of dispersion of spherical grains in liquid in which the solid phase has some solubility. Thus, the concentration

of the dissolved solid around grain of radius  $r$  can be mathematically expressed by Thomson-Freundlich's equation [1]

$$\ln \frac{c_r}{c_\infty} = \alpha \cdot \frac{2\gamma_{SL}}{r},$$

where  $c_\infty$  and  $c_r$  are the solubility of a solid grain with an infinite radius and a radius  $r$ , respectively,  $\alpha$  is a function of the molecular weight and the density of solid grains, the gas constant and the temperature, and  $\gamma_{SL}$  is the solid-liquid interfacial energy. The concentration at an interface  $I_{SL}$  with high curvature will be above that at an interface with low curvature, thus a higher concentration around a smaller grain gives rise to a net flux of matter from the smaller to the larger grain defined by  $\mathbf{J} = -D_L \nabla c$ , where  $D_L$  is the concentration independent diffusivity of the solid in the liquid.

Applying FE methodology, the time-dependent concentration at nodes within liquid bridge can be updated using the numerical method described in details elsewhere [3]. The initial concentration at LV interfaces will be represented by the model for slow diffusion or small grain spacing [1].

## SIMULATION RESULTS

The sintered performance of W-Ni system depends on several factors, including the tungsten (solid) content and matrix composition (initially liquid nickel as a bridge). In this simulation same data as in [3] will be used.

Computed microstructure with grain coarsening of multi-grain model ( $N=15$ ) shown in Fig. 2. Although dissolved matter is redistributed between grains, two different morphologies can be recognized due to the local diffusional interactions. As it can be seen, after 4 min. pure dissolution occurred onto smaller grains and pure precipitation onto larger grains forming solid solution W(Ni). Some medium size solid grains are characterized by partial dissolution and precipitation at the same time, which processes depend on location of grains and their intergrain distances.

## CONCLUSION

This paper presents FE computer simulation of grain coarsening during LPS. It can be seen that the morphological evolution very much depends on grain location and grain size, but also on their intergrain distances. The result is in very good agreement with the experimental results [4,5]. There is also very good agreement with liquid-phase sintered tungsten heavy alloy [6] where the tungsten grains within capillary liquid matrix were coarsened and rounded as a result of the continued solution-precipitation process that depends on tungsten solubility and contributes to tungsten grain shape

accommodation releasing additional liquid to fill any remaining inter-grain pores [7]. There is a fairly good agreement with the boundary integrals approach too [2], but our approach treats LPS case with liquid located inside pendular and capillary liquid bridges only. The numerical coarsening model incorporates much of the essential physics of the coarsening process in this context, including two phases (solid and liquid), important interfaces and a mechanism for mass transport. As much as we do know, simulation method for investigation of grain coarsening inside the capillary liquid bridge was presented for the first time.

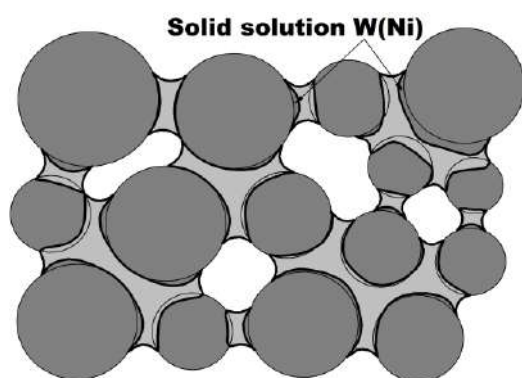


**Figure 2.** The morphology of SL interfaces after 4 min. Light gray colored areas are pendular or capillary liquid bridges.

### **Acknowledgments**

First author was performed present study under the project No. OI172057 supported by the Ministry of Education, Science and Technological Development of the Republic of Serbia.

### **REFERENCES**

- [1] H. Fischmeister, G. Grimvall, in *Sintering and Related Phenomena*, Materials Science Research, 1973, **6**, 119-149.
- [2] P. W. Voorhees, G. B. McFadden, R. F. Boisvert, D. I. Meiron, *Acta Metall.*, 1988, **36**, 207-222.
- [3] B. Randelović, K. Shinagawa, Z. S. Nikolić, *Science of Sintering*, 2013, **45**, 261-271.
- [4] D. N. Yoon, W. J. Huppmann, *Practical Metall.*, 1978, **15**, 399-401.
- [5] D. N. Yoon, W. J. Huppmann, *Acta Met.*, 1979, **27**, 973-977.
- [6] Y. Wu, R.M. German, B. Marx, R. Bollina, M. Bell, *Mater. Sci. Eng. A*, 2003, **344**, 158-167.
- [7] R. M. German, S. Farooq, C. M. Kipphut, *Mater. Sci. Eng.*, 1988, **A105/106**, 215-224.

## NICKEL-DOPED ALUMINA

T. Novaković<sup>1</sup>, Z. Mojović<sup>1</sup> and M. Mitrić<sup>2</sup>

<sup>1</sup>*University of Belgrade, Institute of Chemistry, Technology and Metallurgy, Department of Catalysis and Chemical Engineering, Njegoševa 12, 11000 Belgrade, Republic of Serbia (tbnovakovic@gmail.com)*

<sup>2</sup>*Vinča Institute of Nuclear Sciences, University of Belgrade, Mike Petrovića Alasa 12-14, Belgrade, Republic of Serbia*

### ABSTRACT

Alumina powders, pure and doped with nickel, were synthesized by sol gel method and calcined at 500°C in order to obtain mesoporous structures with a high specific surface area, well adaptable to catalytic application. XRD analysis showed that the addition of Ni<sup>2+</sup> affect the structural properties of the synthesized oxides. In order to test electrochemical activity of introduced nickel GCE modified with synthesized material was tested in 0.1 M NaOH solution without and with methanol.

### INTRODUCTION

Transition aluminas are important in the of various catalysis fields because of their high specific surface areas, surface property and crystalline structure [1–4]. The role of alumina in the catalyst system is often assumed to be purely physical acting as an inert solid onto which a catalyst can be dispersed. However, the surface of alumina is chemically reactive and acts as a catalyst for many acid/base reactions [1,5]. The surface reactivity of an alumina phase depends on the preparation conditions and sample history. There are various crystal structures for alumina and the obtained phases depend on the precursor, additives and the calcinations conditions. The sol–gel process is the most studied chemical method to prepare nanostructured materials [6]. This process allows the easy preparation of very diverse mesoporous structures.

The aim of this paper was to investigate the chemical state of Ni in alumina doped samples and its effect on structure and texture of alumina-based electrodes on electrochemical response.

### EXPERIMENTAL

Alumina powders, pure and doped with nickel, were synthesized by sol gel method [7] and calcined at 500°C in order to obtain materials with different structural and textural properties. Samples were denoted as A-500, A10-

500, A20-500, A40-500, to indicate temperature of calcinations and the amount of nickel added to sample. The X-ray powder diffraction measurements were performed on a PHILIPS 1050 X-ray diffractometer using Ni-filtered Cu K $\alpha$  radiation and Bragg-Brentano focusing geometry. The patterns were taken in the 5–90  $^{\circ}2\theta$  range with the step length of 0.058  $^{\circ}2\theta$  and exposure time of 5 s per step. The drop of dispersion of investigated sample in 5 wt. % Nafion was applied on the surface of glassy carbon electrode. The electrochemical response of samples was tested by cyclic voltammetry in 0.1 M NaOH with and without methanol. All potentials are reported versus Ag/AgCl (3 M KCl) reference electrode, and platinum rod served as counter electrode.

## RESULTS AND DISCUSSION

Introduction of nickel species in alumina matrix resulted in materials with different properties from starting alumina. In order to test electrochemical activity of introduced nickel GCE modified with synthesized material was tested in alkaline solution (Fig. 1a and b). Cyclic voltammograms recorded in 0.1 M NaOH for A10-500 only showed current rise at high anodi potential due to oxygen evolution reaction. With increase of Ni content in

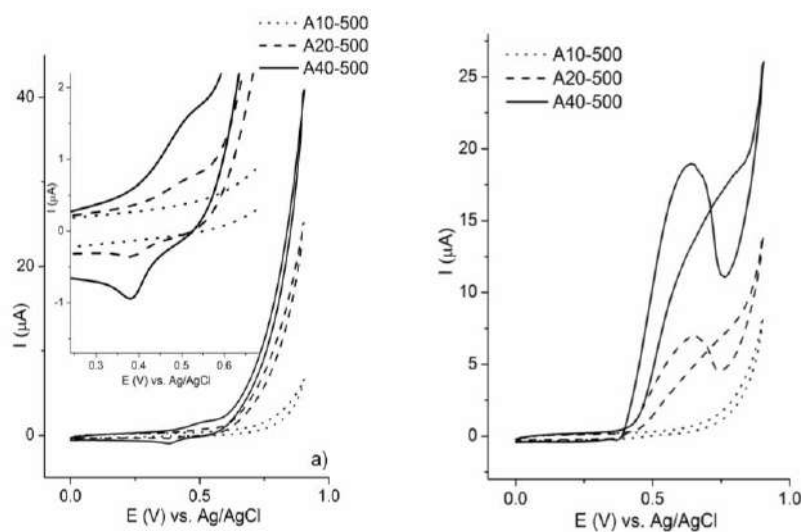


**Figure 1.** Cyclic voltammograms of alumina samples recorded at 50  $\text{mVs}^{-1}$  in 0.5 M NaOH without methanol (left) (Inset: enlarged part of CV in potential range 0.25 V – 0.6 V) and with methanol (right).

sample characteristic Ni(II)  $\rightarrow$  Ni(III) pair of peaks appeared at potential range 0.3 - 0.6 V vs. Ag/AgCl electrode and was well pronounced for A40-

500 sample. The redox  $\text{Ni(II)} \rightarrow \text{Ni(III)}$  originates from electroactive layer of  $\text{Ni(OH)}_2$  that is formed over  $\text{NiO}$  upon immersion in alkaline solution. The current of oxygen evolution also increased with increase of Ni content, as expected since Ni-based electrodes are good catalyst for the OER [7]. Further testing was performed in the reaction of methanol oxidation from alkaline solution. The current rise due to methanol oxidation was observed at same potential as the formation of  $\text{NiOOH}$ . There was no current of  $\text{NiOOH}$  reduction during reverse scan. The same dependence of current of methanol oxidation on Ni content and calcinations temperature as for the current of  $\text{NiOOH}$  formation was observed. The characteristic feature of recorded voltammograms is hysteresis between the anodic and the cathodic sweeps, in which a higher methanol oxidation charge is observed in the cathodic sweep. The possible explanations for this behavior are: a) different nature of processed occurring in forward and reverse scan; b) the ratio of methanol and supporting electrolyte concentration and c) the difference of the electrode surface in forward and reverse scan.

The electrochemical activity of nickel-doped alumina samples was dictated by the amount of present  $\text{NiO}$ . XRD patterns of the pure and  $\text{Ni}^{2+}$ -doped alumina samples, thermally treated at  $500^\circ\text{C}$ , show amorphous character (Fig. 2). Only broad peaks with very low intensity, attributed to the  $\gamma\text{-Al}_2\text{O}_3$  are observed at

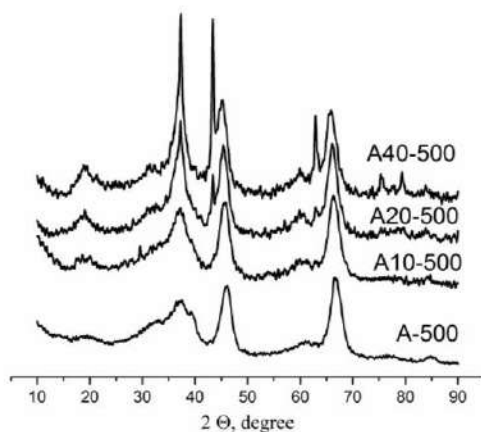


**Figure 2.** X-ray diffraction patterns of pure and  $\text{Ni}^{2+}$ -doped alumina samples

at  $2\theta$  angle of about  $38^\circ$ ,  $46^\circ$  and  $67.2^\circ$ , for pure alumina sample. The intensity of these peaks in the doped samples is reduced proportional to the amount of added nickel. XRD data confirmed the formation of the  $\text{NiAl}_2\text{O}_4$  and the oxides of Ni in all the samples. The presence of  $\text{NiO}_2$  is observed in the sample A10-500, whereas, in the samples with higher contents of Ni, the formation of  $\text{NiO}$  is confirmed and its

content increases with increasing amount of added  $\text{Ni}^{2+}$ -ions. The XRD analysis showed that ratio of  $\text{NiO}/\text{NiAl}_2\text{O}_4$  changed in same manner indicating that only  $\text{NiO}$  was electrochemically active. It is unclear how much Ni inside alumina structure affects the electrochemical response of nickel-doped alumina. According to Ojani et al. [8], who investigated Ni

modified zeolite Y, the presence of Ni ions inside zeolite cages beside Ni ions present on the surface of the zeolite was essential for good electrochemical activity of NiY. It was proposed that the methanol oxidation takes place on the oxy-hydroxide species formed on the surface of the electrode, while nickel species incorporated in zeolite act as an electron relay to the Ni(OH)<sub>2</sub>/NiOOH redox system.

## CONCLUSIONS

Samples of alumina with different amount of nickel were synthesized by sol gel method and calcined at 500°C. XRD analysis confirmed that all samples have a low ordered structure (almost amorphous), whereby, disorder and crystallites size of the structure of the doped samples are higher in comparison to the structure of the non-doped sample and increase with the Ni<sup>2+</sup>-content. The electrochemical activity of nickel-doped alumina samples was dictated by the amount of present NiO.

## Acknowledgment

This work was supported by the Ministry of Education, Science and Technological Development of Republic Serbia (Project Nos. III 45001 and ON 172015).

## REFERENCES

- [1] X. Chen, Y. Liu, G. Niu, Z. Yang, M. Bian, A. He, Applied Catalysis A: General, 2001, **205**, 159-172.
- [2] A. I.Y. Tok, F.Y.C. Boey, X.L. Zhao, J Mater Process Tech, 2006, **178**, 270-273.
- [3] H. Sun, X. Quan, S. Chen, H. Zhao, Y. Zhao, App Surf Sci, 2007, **253**, 3303-3310.
- [4] J. Okal, W. Tylus, L. Kępiński, J. Catal, 2004, **225**, 498-509.
- [5] G. S. Walker, D. R. Pyke, C. R. Werrett, E. Williams, A. K. Bhattacharya, App Surf Sci, 1999, **147**, 228-234.
- [6] H. Guleryuz, I. Kaus, C. Filiatre, T. Grande, M. A. Einarsrud, J of Sol-Gel Sci Technol 2010, **54**, 249-257.
- [7] B. E. Yoldas, Am Ceram Soc Bull, 1975, **54** 289-290
- [8] N. Spinner, W. E. Mustain, Electrochim. Acta, 2011, **56**, 5656-5666.
- [9] R. Ojani, J.-B. Raouf, S. Fathi, S. Alami-Valikchali, J. Solid. State Electrochem., 2011, **15**, 1935-1941.

## **SYNTHESIS OF MOBILE MAGNETIC ADSORBENTS FOR EFFICIENT REMOVAL OF HEAVY METAL IONS FROM AQUEOUS SOLUTION**

W. Kiciński<sup>1</sup>, S. Dyjak<sup>1</sup>, E. Olechno<sup>2</sup>, M. Kowalik<sup>2</sup>, P. Strachowski<sup>2</sup>  
and M. Bystrzejewski<sup>2</sup>

<sup>1</sup>*Military University of Technology, Faculty of Advanced Technologies and Chemistry, 00-908 Warsaw, Poland*

<sup>2</sup>*University of Warsaw, Faculty of Chemistry, Pasteur 1, 02-093 Warsaw, Poland (mibys@chem.uw.edu.pl)*

### **ABSTRACT**

This paper reports the synthesis of mobile composite adsorbents dedicated to the removal of heavy metal ions from aqueous solutions. The basic concept of our innovative solution involves the combination of carbon-encapsulated iron nanoparticles and polymer matrix decorated with sulfonic groups. The adsorption performance was evaluated via adsorption experiments of Fe(III) and compared with commercially available ion exchange resin.

### **INTRODUCTION**

Magnetic separable composite adsorbents are unique materials because they combine properties of magnetic phase and the desired matrix which has efficient capability for the uptake of different solutes. The inclusion of magnetic phase in the composite causes its inherent mobility in the presence of external magnetic field and facilitates its separation from the solution. Usually, ferrite nanoparticles are used. However, the composites obtained with ferrites have poor corrosion resistance. Herein we present a novel strategy to obtain a composite based on organic polymer and carbon-encapsulated iron nanoparticles (CEINs). CEINs are core-shell nanoparticles comprising magnetic (iron) core and protective thin carbon coating. This nanomaterial exhibits superior corrosion resistance and has controllable magnetic properties [1].

### **EXPERIMENTAL**

Carbon-encapsulated iron nanoparticles were synthesized according to our procedure described elsewhere [1]. The as-obtained raw CEINs were purified in 3M boiling HCl in order to remove the non-encapsulated metal particles.

The resorcinol/2-thiophenecarboxaldehyde cross-linked polymers (RT) were obtained utilizing the advantages of sol-gel polycondensation reaction [2]. In a typical synthesis resorcinol and 2-thiophenecarboxaldehyde were dissolved in methanol. Then carbon-encapsulated iron nanoparticles were dispersed in the solution. The amount of carbon-encapsulated iron nanoparticles in the organic polymer matrices varied between 0 and 30 wt.%. Once the dispersion became homogeneous, a few drops of concentrated HCl was added (polycondensation catalyst). The scheme of the synthesis and the proposed structure of the resorcinol/2-thiophenecarboxaldehyde polymer (RT resin) is presented in Fig. 1. The obtained RT gels (containing carbon-encapsulated iron nanoparticles) were cured for 24 h at 60 °C in a sealed container. Next, the composites were dried for 24 h at 75 °C.

Finally, the composites were subjected to sulfonation in order to introduce the surface sulfonic groups. The sulfonation agent was obtained by a direct reaction between acetic anhydride and fumed sulfuric acid in dichloroethane. This mixture was then added to dichloroethane containing the composite. Next, the suspension was heated at 60 °C for 2h with subsequent washing with acetone, ethanol and water. Finally, the sulfonated composite was dried in air at 80 °C for 24 h.

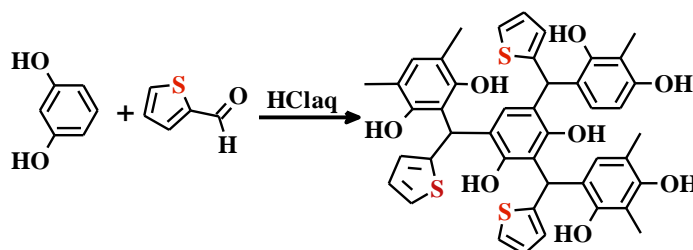


**Figure. 1.** Scheme of the acid-catalyzed synthesis of resorcinol/2-thiophenecarboxaldehyde resin (RT gel) and proposal of its chemical structure.

The morphological details of the studied composites were studied by scanning electron microscopy. The surface chemistry features were evaluated by IR spectroscopy. The adsorption of Fe(III) was studied (pH=1.5) onto pristine and sulfonated composites. The equilibrium concentration of the solute was evaluated spectrophotometrically using the thiocyanate method.

## RESULTS AND DISCUSSION

The chemical composition of obtained composite adsorbents is listed in Table 1. It is evident that the content of Fe is linearly correlated with the CEINs content in the initial mixture of the precursors. This finding shows that the polycondensation process of resorcinol and aldehyde is not affected by CEINs. The SEM images (Fig. 2) revealed the general morphological features of the composites. Both, “pure” polymer (RT-1) and composites have nearly the same morphological details. They are comprised of semi-spherical particles aggregated in bigger fractal-like objects.

The chemical composition (namely Fe-content) of the composite adsorbents linearly depends on the CEINs content in the initial mixture (Table 1). The samples with Fe content larger than 6.9 wt. % had enough mobility in the presence of external magnetic field to be effectively and easily separated from the solution.

**Table 1.** Chemical composition and adsorption performance of magnetic composites.

Sample	CEINs content [wt. %]	Fe content [wt. %]	Adsorption capacity [mg/g]	Adsorption capacity [mg/g]*
RT-1	0	0	110	195
RT-2	5	4.0	102	190
RT-3	10	6.9	95	150
RT-4	20	12.1	85	121
RT-5	30	21.7	29	80

\* adsorption capacity for sulfonated composites

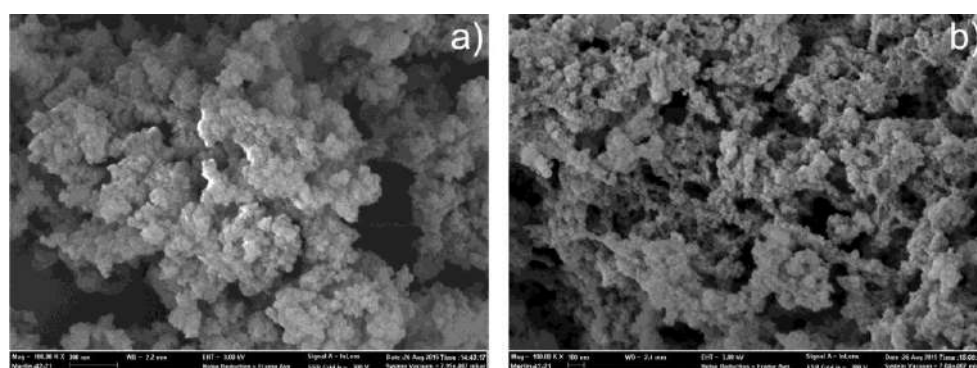


**Figure 2.** SEM images of RT-1 and RT-4 samples.

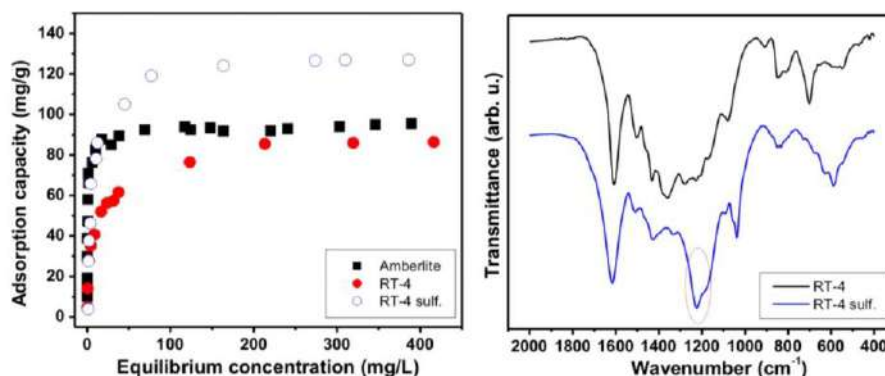


**Figure 3.** Adsorption isotherms and FT-IR spectrum of pristine and sulfonated composite. Red oval shows band typical for S=O groups.

Fig. 3 shows the representative adsorption isotherms of Fe(III) at pH=1.5. It is clear that RT-4 sample has nearly identical adsorption capacity in comparison to the commercial and very popular Amberlite ion exchange resin. The adsorption capacity values for other samples are listed in Table 1. Noteworthy, the adsorption capacity of the pure polymer (RT-1) is ca. 20-25% higher in comparison to Amberlite. Further enhancement of the adsorption performance has been achieved for sulfonated samples. In this case the adsorption capacity for all samples was higher in comparison to Amberlite. The presence of sulfonic groups was confirmed by IR spectroscopy (Fig. 3).

### CONCLUSION

The acidic polycondensation of resorcinol and 2-thiophenecarboxaldehyde in the presence of carbon-encapsulated iron nanoparticles leads to mobile composite adsorbents with high adsorption capacity of Fe(III). The sulfonation process introduces surface sulfonic groups and results in further enhancement of the adsorption performance.

### Acknowledgement

This work was supported by the National Centre for Research and Development (Poland) through the project LIDER 527/L-4/2012.

### REFERENCES

- [1] M. Bystrzejewski, O. Łabędź, W. Kaszuwara, A. Huczko, H. Lange, *Powder Technol.* 2013, **246**, 7-15.
- [2] W. Kiciński, M. Norek, M. Bystrzejewski, *J. Phys. Chem. Sol.* 2013, **74**, 101-109.

## SYNTHESIS OF CdIn<sub>2</sub>S<sub>4</sub> MESOCRYSTALS

M. V. Carević<sup>1</sup>, M. I. Čomor<sup>1</sup>, T. D. Savić<sup>1</sup>, S. P. Ahrenkiel<sup>2</sup> and N. D. Abazović<sup>1</sup>

<sup>1</sup>*Vinča Institute of Nuclear Sciences, University of Belgrade, P.O. Box 522, Belgrade, Serbia, (kiki@vin.bg.ac.rs)*

<sup>2</sup>*South Dakota School of Mines and Technology, 501 E. Saint Joseph Street, Rapid City, SD 57701, USA*

### ABSTRACT

Ternary nanosized sulfide CdIn<sub>2</sub>S<sub>4</sub> was synthesized using hot-injection method in oleic acid/oleylamine mixture as reaction media at 270°C. TEM images have shown that obtained material grows through multistep process, forming marigold structures built out from mesocrystals. Influence of oleic acid and oleic acid/oleylamine mixture as reaction media on mesocrystal formation is tracked and discussed.

### INTRODUCTION

Classical crystallization theory explains material growth through three separated steps: nucleation, normal growth and competitive growth (Ostwald ripening). In nucleation step, elementary building units (atoms, ions or molecules) form clusters. Primary formed clusters then grow during normal growth step.[1] In a third step, all clusters that reach critical size (nanocrystals) will continue to grow through Ostwald ripening at the expense of smaller once, that will dissolve, giving on that way additional material.[1] Briefly, this process can be represented as: ions/atoms/molecules → clusters → nanocrystals → single crystal.

In the past decade, new, non-classical theory of crystal growth emerged, mainly to explain formation of mesocrystals (*mesoscopically structured crystals*), new class of nanostructured solid materials[2]. This theory starts from nanocrystals as primary building blocks. In the basis of the theory lays oriented attachment, i.e. alignment of nanocrystals in such a manner that they share common crystal plane forming larger units-*mesocrystals*. If surface of primary nanocrystals is covered with organic molecules as surfactants, in the process of nanocrystals merging these organic molecules will be included in final mesocrystal, forming defects.[2]

What is needed to be underlined here is that mesocrystals mainly have characteristics inherited from primary building units, but also can have new,

improved ones. In order to meet needs for different applications, it is necessary to understand mesocrystals formation mechanism, to design proper synthetic methods and to fully characterize obtained structures.

Here, attempts to synthesize mesocrystals of ternary sulfide  $\text{CdIn}_2\text{S}_4$  (CIS) are presented. CIS is direct band-gap semiconductor, with the bulk band-gap energy of about 2.1 eV, which places its absorption threshold deep in visible part of solar spectrum (~560 nm). This characteristic makes it interesting for applications where light-semiconductor interaction can be utilized, like photocatalysis or photovoltaics.

In synthesis of nanosized chalcogenide materials (sulfides, selenides, tellurides) method that in last 30 years gave the most impressive results is hot-injection method, which is, basically, injection of precursor solution in hot ( $T > 200^\circ\text{C}$ ) pre-heated coordination solvent. Wide choice of precursors, surfactants, coordination solvents and reaction media gives freedom to manipulate with shape, size, crystal phase and overall characteristics of outcome materials. All previous facts supports decision to use hot-injection method as method of choice in synthesis of CIS mesocrystals. In order to minimize number of factors that can have influence on characteristics of obtained material, oleic acid and oleylamine were simultaneously used as coordinating agents, surfactants and reaction media.

## EXPERIMENTAL

Chemicals: cadmium acetate dihydrate ( $\text{Cd}(\text{Ac})_2$ ), indium-acetate ( $\text{In}(\text{Ac})_3$ ), oleic acid ( $\text{OA}-\text{C}_{17}\text{H}_{33}\text{COOH}$ ), oleylamine ( $\text{OLAM}-\text{C}_{18}\text{H}_{35}\text{NH}_2$ ) and 2-mercaptoethanol ( $2\text{ME} - \text{HS}-\text{C}_2\text{H}_4-\text{OH}$ ) were purchased from Sigma - Aldrich. Sulfur powder was obtained from Alfa Aeser. Toluene and acetone were purchased from JT Baker.

Cadmium precursor solution was prepared as follows: 0.0177g of  $\text{Cd}(\text{Ac})_2$  and 2 ml of OA were loaded in three-neck flask and heated at  $200^\circ\text{C}$  under constant Ar flow. After about 30 min, brown solution is formed, and was left at room temperature to cool down.

Indium precursor solution was prepared as follows: 0.0584 g of  $\text{In}(\text{Ac})_3$  and 2ml OA were loaded in three-neck flask and heated at  $270^\circ\text{C}$  under constant Ar flow. After about 30 min, pale yellow solution is formed.

Sulfur precursor solution was prepared as follows: 0.0128g of sulfur powder and 2ml of OA or 1ml of OLAM were loaded in three-neck flask and heated at  $90^\circ\text{C}$  under constant Ar flow. After about 30 min solution was left at room temperature to cool down. After preparation of the precursor solutions, Cd and S solutions were swiftly injected in. In solution at  $270^\circ\text{C}$ , and reaction mixture was kept at that temperature for 4h (S1 in pure

OA) or 1h (S2 with addition of 1ml OLAM). TEM and STEM images are obtained using JEOL JEM-2100 LaB6 microscope (200kV acceleration voltage).

## RESULTS AND DISCUSSION

In order to confirm formation of ternary semiconductor CIS, XRD measurements (not presented) were performed. It was revealed that sample S1 is a mixture of hexagonal binary sulphide CdS and ternary cubic CIS (which was a dominant phase). TEM images (Fig.1) have confirmed existence of two materials characterized with different particle sizes and morphology.

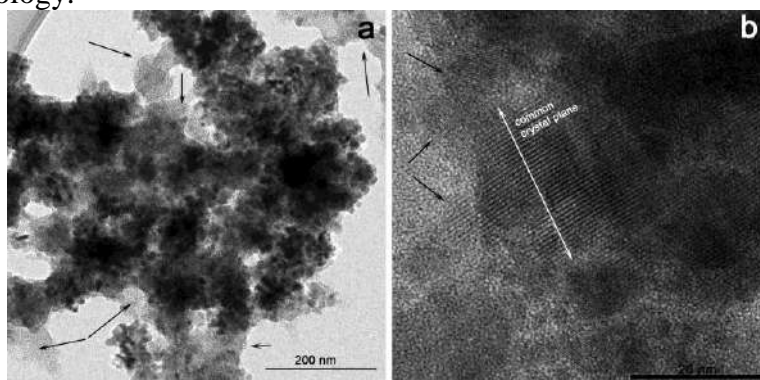


**Figure 1.** TEM images of sample S1 at different magnifications

In Fig 1a, by arrows are indicated areas where small spherical particles (average size  $\sim 4$  nm) are clearly visible. Their particle size distribution is very uniform, and it was confirmed that these particles are hexagonal CdS. Larger, irregularly shaped particles belong to cubic CIS. At higher magnifications (Fig. 1b), it became clear that particles of CIS start to orient along common crystal planes, forming larger structures (white arrow). However, the fact that in the sample S1 there are still present separated particles that are not oriented in a common manner (black arrows) along with the presence of binary sulphide in the sample, indicated that even after 4h of reaction mesocrystal formation is not finished. In order to speed up reaction we have added OLAM to reaction mixture (see Experimental). OLAM as an organic base, provides conditions for faster decomposition of cation-oleic acid complex[3], accelerating in that way subsequent formation of desired sulphide. After only 1h of reaction, as XRD measurements (not presented) confirmed, pure CIS was formed. STEM image (Fig. 2a) revealed that complex marigold-like structures were formed, with sizes ranging from around 50 to 200 nm.

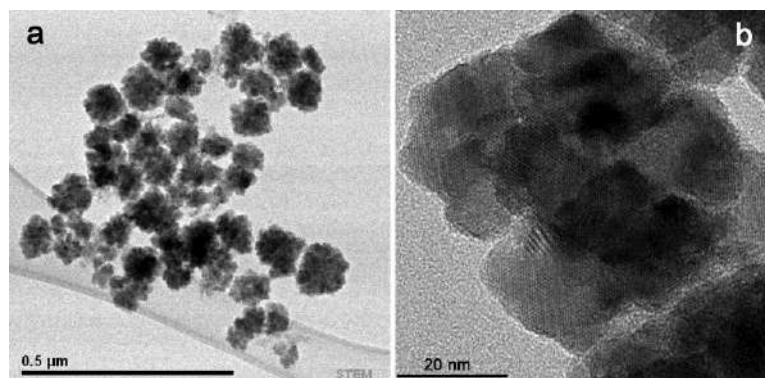


**Figure 2.** a) STEM and b) TEM image of sample S2

From image at higher magnification (Fig 2b) it is clear that marigolds are made of flake-like structures, which are formed from even smaller sub-unites, with sizes in range from 8 to 14 nm. Such multi-levelled architecture is, as explained by non-classical nucleation theory, characteristic for mesocrystals. In presented experimental conditions, their formation was easier, since after initial acceleration of reaction by addition of OLAM, system have enough time to arrange in complex manner. Presence of organic molecules (as capping agents) at nanocrystal surface provided their easier rotation in process of oriented attachment.

## CONCLUSION

Hot-injection method of  $\text{CdIn}_2\text{S}_4$  mesocrystals is proposed. It was shown that addition of OLAM was crucial for formation of pure cubic CIS in given experimental conditions. TEM images revealed that material is characterized with multi-levelled structure: primary nanocrystals through oriented attachment process form mesocrystals that than are arranged in marigold-like structures.

## Acknowledgement

Financial support for this study was granted by the Ministry of Education and Science of the Republic of Serbia (Projects: III45020 and OI172056).

## REFERENCES

- [1] S. V. Gaponenko in: Optical properties of semiconductor nanocrystals. Cambridge University Press, Cambridge, 1998
- [2] Y. Liu, Y. Zhang and J. Wang, Cryst. Eng. Comm, 2014, **16**, 5948-5967.
- [3] N. Bao, X. Qiu, Y.-H. A. Wang, Z. Zhou, X. Lu, C. A. Grimes, A. Gupta, Chem. Commun., 2011, **47**, 9441-9443.

## THERMAL STABILITY OF CT- COMPLEXES FORMED AT THE SURFACE OF ANATASE NANOPARTICLES

T. D. Savić<sup>1</sup>, M. I. Čomor<sup>1</sup>, I. A. Janković<sup>1</sup>, V. M. Rakić<sup>2</sup>, N. D. Abazović<sup>1</sup>  
and M. V. Carević<sup>1</sup>

<sup>1</sup>*Vinča Institute of Nuclear Sciences, University of Belgrade, P.O. Box 522, 11001 Belgrade, Serbia. (tanja030@vinca.rs)*

<sup>2</sup>*Department of Chemistry, Faculty of Agriculture, University of Belgrade, Nemanjina 6, 11080 Zemun, Serbia.*

### ABSTRACT

The surface modification of nanocrystalline TiO<sub>2</sub> particles (45 Å) with salicylate-type ligands consisting of an extended aromatic ring system, specifically 1-hydroxy-2-naphthoic acid (1H2NA) and 1,4-dihydroxy-2-naphthoic acid (1,4DH2NA), was found to alter the optical properties of nanoparticles in a similar way to salicylic acid (2HBA). The formation of the inner-sphere charge-transfer (CT) complexes results in a red shift of the semiconductor absorption onset compared to unmodified nanocrystallites and a reduction in the band gap upon the increase in the electron delocalization when including an additional ring. From absorption measurements of CT complexes in methanol/water=90/10 solutions, stability constants in the order of 10<sup>3</sup> M<sup>-1</sup> have been determined at pH 2. Thermal stability of CT-complexes was investigated by using TPD analysis (TG/DTA/MS).

### INTRODUCTION

Nanocrystalline TiO<sub>2</sub> has attracted widespread attention as a photocatalyst with various practical applications as well as a part of photoelectrochemical systems, such as Grätzel cells. Due to its large band gap ( $E_g=3.2$  eV), TiO<sub>2</sub> absorbs less than 5% of the available solar light photons. Sensitization of TiO<sub>2</sub> nanoparticles (NPs) with appropriately chosen molecules can indeed lead to a significant red shift of their absorption threshold from the UV to the visible, thus improving the absorption of the solar spectrum as well as the efficiency of photocatalytic and photovoltaic devices. Owing to the large curvature of TiO<sub>2</sub> particles on the nanosize scale, the surface reconstructs itself in such a manner that distorts the crystalline environment of surface Ti atoms forming coordinatively unsaturated Ti atoms which are very reactive. Absorption of light by the CT complexes, formed upon adsorption of surface-active ligands onto TiO<sub>2</sub>, yields to the excitation of electrons from the chelating ligand directly into the conduction band of TiO<sub>2</sub> NPs

(DSSC Type II) [1]. The subject of this work is obtaining optical properties, UV/Vis absorption, stability constants, using Benesi-Hildebrand analysis, and thermal stability of CT-complexes formed between surface defects at TiO<sub>2</sub> NPs and 2HBA as a model system for all studied ligands.

## EXPERIMENTAL

The colloidal TiO<sub>2</sub> dispersions were prepared by the dropwise addition of TiCl<sub>4</sub> to cooled water [2]. Surface modification of TiO<sub>2</sub>, in methanol/water=90/10 solutions at pH 2, resulting in the formation of CT complexes was achieved by the addition of surface-active ligands up to concentrations required to cover all surface sites. For the determination of CT complex binding constants the absorption spectra were recorded at room temperature using a Thermo Scientific Evolution 600 UV/Vis spectrophotometer. The thermal stability of the samples was investigated by simultaneous non-isothermal thermo-gravimetric analysis (TG) and differential thermal analysis (DTA) using a SETARAM SETSYS Evolution 1750 instrument. On-line thermogravimetric–mass spectrometry analyses (TG–MS) were used to study the gases evolved during thermal decomposition and the experiments were performed using the TG/DSC 111 from Setaram.

## RESULTS AND DISCUSSION

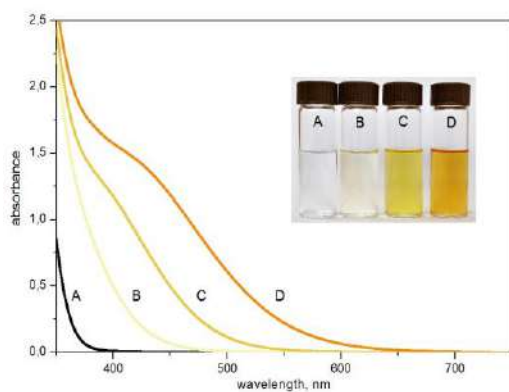


**Figure 1** Absorption spectra of surface modified TiO<sub>2</sub>: A) bare TiO<sub>2</sub>; B) 2HBA; C) 1H2NA; D) 1,4DH2NA

eV, respectively. From the absorption measurements (Benesi-Hildebrand plot), the stability constants were determined to be 3800 M<sup>-1</sup> for 2HBA, 4300 M<sup>-1</sup> for 1H2NA and 4500 M<sup>-1</sup> for 1,4DH2NA.

The formation of the inner-sphere CT-complexes leads to a shift in the effective band gap of semiconductor to a lower energy i.e. the onset of the absorption of these CT nanocrystallites is red shifted when compared to unmodified TiO<sub>2</sub>. By extracting the corresponding onset energies from the absorption spectra of surface modified TiO<sub>2</sub> nanoparticles (Fig. 1), the effective band gap energies ( $E=hc/\lambda$ ) of 2HBA, 1H2NA and 1,4DH2NA modified TiO<sub>2</sub> nanoparticles were calculated to be 2.6, 2.3 and 1.9

Thermal analysis of bare TiO<sub>2</sub> nanoparticles and TiO<sub>2</sub> nanoparticles modified with 2HBA (TiO<sub>2</sub>-2HBA) were performed in helium (Fig 2) and air flow (Fig 3) in the 30-600°C range at the heating rate of 10°C min<sup>-1</sup>. As expected, the overall weight loss amounts (TG curves) were higher for TiO<sub>2</sub>-2HBA than for bare TiO<sub>2</sub>. Heat flow (DSC) curves for TiO<sub>2</sub>-2HBA

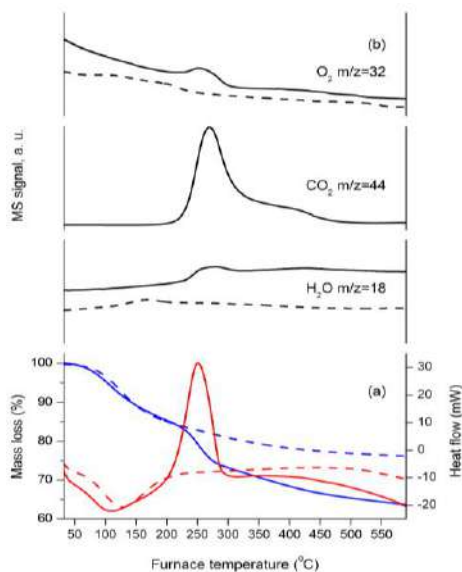


**Figure 2.** TG (blue lines) and DSC (red lines) curves of bare TiO<sub>2</sub> (dashed lines) and TiO<sub>2</sub>-2HBA (solid lines) recorded in He (a). MS profiles (b).

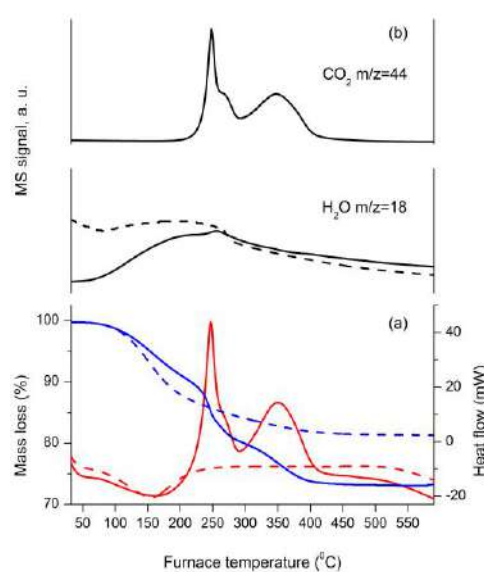


**Figure 3.** TG (blue lines) and DSC (red lines) curves of bare TiO<sub>2</sub> (dashed lines) and TiO<sub>2</sub>-2HBA (solid lines) recorded in air (a). MS profiles (b).

show one endothermic process with a maximum around 150°C and one (maximum at 250°C) or two (maximum at 250 with shoulder at 270 and 350°C) exothermic processes in helium and air, respectively. DSC curves for bare TiO<sub>2</sub> show just the endothermic process (maximum around 150°C), the same as in the case of TiO<sub>2</sub>-2HBA. The profiles of MS signals revealed that H<sub>2</sub>O (m/z=18) and CO<sub>2</sub> (m/z=44) were evolved as a result of heating of TiO<sub>2</sub>-2HBA in air, while the oxygen molecules O<sub>2</sub> (m/z=32) were detected together with H<sub>2</sub>O and CO<sub>2</sub> in helium. It is quite evident that the mass profiles of CO<sub>2</sub> follow the profile of DSC curves, while MS curves of H<sub>2</sub>O show that water is liberated nearly in the whole temperature range. From literature data it is known that upon heating of anatase, between room temperature and 200°C, a mass loss occurs mainly through the desorption of water followed by the condensation/elimination of surface OH groups [3]. Hence, the endothermic process as well as the total weight loss in the case

of bare TiO<sub>2</sub> can be explained in such a way. The exothermic process, according to MS signals, correspond to the decomposition of bound 2HBA and its incomplete (He) or complete (air) mineralization to H<sub>2</sub>O and CO<sub>2</sub>. Although in inert atmosphere, the incomplete oxidation of the organic part takes place as the consequence of the oxygen liberation proved by MS measurements both in TiO<sub>2</sub>-2HBA and bare TiO<sub>2</sub>. This can be explained by the fact that thermal treatment of pure TiO<sub>2</sub> under oxygen depleted conditions (He, N<sub>2</sub>, Ar) leads to the formation of oxygen vacancies and evaluation of molecular O<sub>2</sub> [4]. Complex exothermic DSC profile obtained for the thermal decomposition of TiO<sub>2</sub>-2HBA (Fig 3) by heating in air indicates the existence of different binding states of 2HBA at the oxide surface.

### CONCLUSION

All investigated ligands (2HBA, 1H2NA and 1,4DH2NA) form inner-sphere charge-transfer complexes with TiO<sub>2</sub> NPs. The binding of the modifier molecules to undercoordinated surface Ti atoms results in a significant shift in the onset of absorption to the visible spectral range. From the absorption measurements of CT complexes, stability constants were calculated and values of about 10<sup>3</sup> M<sup>-1</sup> have been determined at pH 2. The complexity of the DSC profiles obtained from thermal analysis measurements can be comprehended as an indication of salicylate-type ligands interacting with different active sites on the TiO<sub>2</sub> surface that express energetic heterogeneity.

### Acknowledgement

Financial support for this study was granted by the Ministry of Education, Science and Technological Development of the Republic of Serbia (Project 172056 and 45020).

### REFERENCES

- [1] W. Macyk, K. Szaciłowski, G. Stochel, M. Buchalska, J. Kunczewicz, P. Łabuz, *Coord. Chem. Rev.*, 2010, **254**, 2687-2701.
- [2] T. D. Savić, I. A. Janković, Z. V. Šaponjić, M. I. Čomor, D. Ž. Veljković, S. D. Zarić, J. M. Nedeljković, *Nanoscale*, 2012, **4**, 1612–1619.
- [3] M. Becuwe, P. Rouge, C. Gervais, M. Courty, A. Dassonville-Klimpt, P. Sonnet, E. Baudrin, *J. Colloid Interface Sci.*, 2012, **388**, 130–136.
- [4] X. Pan, M.-Q. Yang, X. Fu, N. Zhang, Y.-J. Xu, *Nanoscale*, 2013, **5**, 3601–3614.

## CHARACTERIZATION OF HYDROTHERMALY SYNTHESIZED ZIRCONIA NANOPOWDERS

M. V. Carević<sup>1</sup>, N. D. Abazović<sup>1</sup>, T. D. Savić<sup>1</sup>, T. B. Novaković<sup>2</sup>  
and M. I. Čomor<sup>1</sup>

<sup>1</sup>University of Belgrade, Vinča Institute of Nuclear Sciences, P.O. Box 522,  
11001 Belgrade, Serbia, -belos.milica@gmail.com

<sup>2</sup>University of Belgrade, IchTM - Department of Catalysis and Chemical  
Engineering, Njegoševa 12, 11000 Belgrade, Serbia

### ABSTRACT

In this paper, a hydrothermal method for synthesis of zirconia nanopowders: pure and with incorporated Si<sup>4+</sup> ions is presented. Zirconyl chloride and tetraethyl orthosilicate were used as precursors. As prepared powders were annealed at 600 °C and their structural (XRD), morphological (TEM) and textural (BET method) properties were obtained. It has been shown that by using hydrothermal synthesis method pure monoclinic ZrO<sub>2</sub> highly crystalline powder can be obtained with crystallites of about 25 nm. Incorporation of Si<sup>4+</sup> ions induced stabilization of tetragonal crystalline phase at room temperature, decreasing particle sizes to about 3-6 nm and increasing specific surface area of nanopowders.

### INTRODUCTION

Zirconia (ZrO<sub>2</sub>) is an important and widely used ceramic material. In recent years, much attention has been paid to the preparation of high surface area nano-zirconia due to its wide application as a catalyst and catalyst support, sorbent, oxygen sensor, etc.[1]. The objective of this publication was to synthesize zirconia nanopowders with high specific surface area without surfactants/additives. High surface area, small particle sizes, is correlated with crystalline phase of zirconia: monoclinic phase demands large volumes for development ( $D \geq 25$  nm), metastable tetragonal phase is common for small particles ( $D \leq 20$  nm). We choose hydrothermal method for synthesis because it can be easily controlled and reproduced, it can be carried out at moderate temperatures and it already has been used to prepare nanosized powders. In order to influence specific surface area and crystallinity of zirconia we introduced Si<sup>4+</sup> ions in zirconia matrix during synthesis.

## EXPERIMENTAL

The following commercial reagents were used: Zirconyl chloride octahydrate (reagent grade, SigmaAldrich, 98%), TEOS (Tetraethyl orthosilicate, Aldrich, 98%), Sodium hydroxide (Aldrich,  $\geq 97\%$ ). All chemicals were used as received. In all experiments deionized water from Mili Q system was used. Pure and  $\text{Si}^{4+}$  incorporated zirconia nanopowders were synthesized by hydrothermal treatment. In a Teflon vessel (125 ml volume) 50 ml of 2 M NaOH, 2 g of zirconyl chloride powder for pure  $\text{ZrO}_2$ , and appropriate amount of TEOS for powders with  $\text{Si}^{4+}$  ions (2.3 mM or 23 mM, samples  $\text{ZrO}_2$ -1 and  $\text{ZrO}_2$ -2, respectively) were added. Dispersion was vigorously stirred for 1 h and then autoclaved for 24 h at 150 °C. After that, the powder was separated from the washing solution by centrifugation. The XRD powder patterns were obtained using a Philips PW 1050 powder diffractometer with Ni filtered  $\text{Cu K}\alpha$  radiation ( $\lambda = 1.5418 \text{ \AA}$ ). The morphology and sizes of photocatalysts were obtained using transmission electron microscopy, TEM, JEOL JEM 1400, accelerating voltage 120 kV. Textural properties of our samples were determined using nitrogen adsorption/desorption parameters. The nitrogen adsorption was performed at -196 °C and relative pressure interval between 0.05 and 0.98 in automatic adsorption apparatus (Sorptomatic 1990 Thermo Finningen).

## RESULTS AND DISCUSSION

Typical XRD patterns of pure  $\text{ZrO}_2$  powder and  $\text{ZrO}_2$  powders with incorporated Si ions are shown in Fig. 1.(a and b). The pure  $\text{ZrO}_2$  powder has peaks that can be indexed as monoclinic- $\text{ZrO}_2$  (Baddeleyite JCPDS 65-1025) (Fig. 1.(a)). Monoclinic  $\text{ZrO}_2$  is the stable phase formed at temperatures less than 1170 °C in the absence of additives (where it transforms to tetragonal and then to cubic phase at temperatures above 2370 °C up to the melting point at 2680 °C) [2,3].  $\text{ZrO}_2$  nanopowders with incorporated Si ions are much less crystalline with broad peaks, Fig. 1.(b), which can be assigned to tetragonal crystalline structure (JCPDS 81-1544).  $\text{ZrO}_2$ -1 crystallized partially in monoclinic phase moving the most intensive peak of tetragonal crystalline phase to lower  $2\theta$  value (from 30.2° to ~ 29.5°). Powder with higher concentration of Si ions showed a mixture of t- $\text{ZrO}_2$  and amorphous  $\text{SiO}_2$ ; the low intensity broad peak at approximately  $2\theta = 22^\circ$  corresponds to amorphous  $\text{SiO}_2$ . Particle sizes were calculated using Debye-Scherrer equation. Pure  $\text{ZrO}_2$  had diameters of about 25 nm and both samples with incorporated Si ions had diameters of about 3 nm. As reported previously, the monoclinic phase is the stable phase at low temperatures, but the tetragonal phase is the first formed in nucleation

process and heat treatment [4]. The presence of the metastable tetragonal phase at low temperatures can be attributed to several factors such as chemical effects (the presence of anionic impurities), structural similarities between the tetragonal phase and the amorphous zirconia phase that is precursor of crystallization, as well as particle size effects (based on the lower surface energy in the tetragonal phase compared to the monoclinic phase).

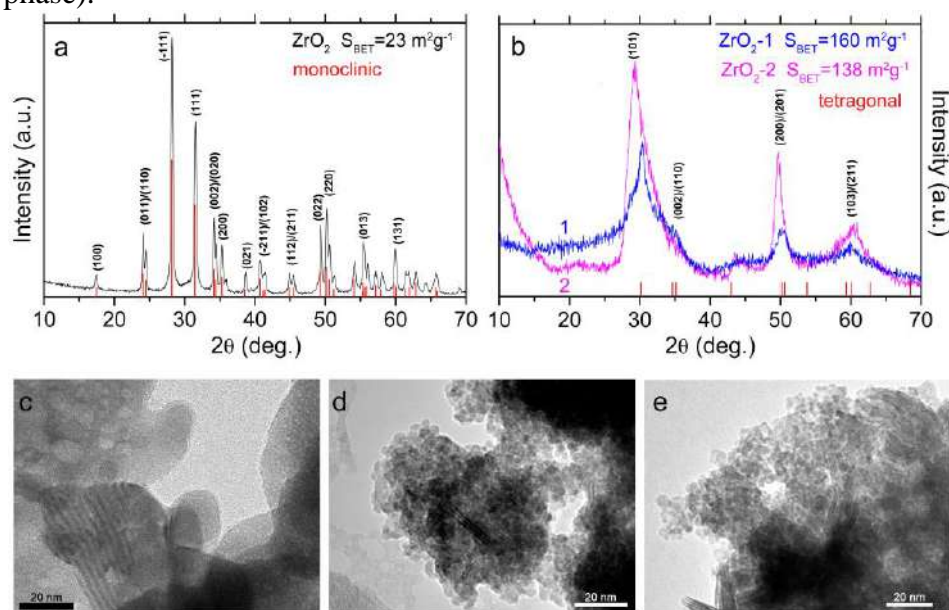


**Figure 1.** XRD patterns and specific surfaces of (a) pure  $\text{ZrO}_2$  and (b)  $\text{ZrO}_2$  with incorporated  $\text{Si}^{4+}$  ions. Typical TEM images of  $\text{ZrO}_2$  based photocatalysts: (c) pure and (d, e) with incorporated  $\text{Si}^{4+}$  ions.

In Fig. 1.(c,d,e) a typical TEM images of pure zirconia (c) and zirconia powders with incorporated Si ions (d and e) are presented. Pure  $\text{ZrO}_2$  is constituted of large particles,  $D \geq 20$  nm and even larger agglomerates of about 100 nm, although this size should be taken cautiously as it was difficult to distinguish boundaries between entities. These findings are in agreement with diameter/sizes of crystallites calculated from XRD. Crystalline domains gained using Debye-Scherrer equation can be smaller than real sizes of the particles due to presence of amorphous phase present as well. In addition to well defined crystalline nanoparticles, with visible crystal planes, some defects can also be observed like spots with diameters of 5–10 nm. These spots are small amorphous zones embedded in the crystalline zirconia matrix [4]. In Fig. 1. (d and e) small particles of 3–6 nm can be seen in both samples with Si ions,  $\text{ZrO}_2$ -1 and  $\text{ZrO}_2$ -2, with sizes in

agreement to those calculated using Bebye-Scherrer equation. Also some larger elongated particles/agglomerates ( $D \approx 20$  nm) with defect/twinned structure can be observed. In these larger particles with twinned domains, most probably started the  $t \rightarrow m$  transformation [5], but the volume fraction of monoclinic crystalline phase still being too low in order to be registered by XRD. It can be seen that Si incorporation process through hydrothermal synthesis process and subsequent annealing, suppresses effectively the growth of nanoparticles. Textural properties of  $ZrO_2$  nanopowders were investigated using BET method. Obtained specific surface areas of the samples are indicated in Fig. 1. (a and b). As can be seen, incorporation of  $Si^{4+}$  ions in zirconia induced a significant increase of specific surface area -  $S_{BET}$  of powders with Si ions was 7 times larger than pure zirconia. The specific surface area is slightly larger when smaller concentration of Si ions (15 mol%) was incorporated in zirconia matrix, as a consequence of saturation of particle surface with Si ions or presence of amorphous silica layer on the surface of the particles for sample  $ZrO_2$ -2.

## CONCLUSION

The hydrothermal method was successfully used for synthesis of pure zirconia and zirconia with incorporated  $Si^{4+}$  ions. Pure  $ZrO_2$  had monoclinic crystalline phase and particles of about 25 nm, powders with incorporated Si ions remained in metastable tetragonal crystalline phase with diameters of about 3–6 nm. Significant increase of specific surface area was achieved by incorporation of Si ions in zirconia matrix, which was one of the main goals that we wanted to achieve with this study.

## Acknowledgement

Financial support for this study was granted by the Ministry of Education, Science and Technological Development of the Republic of Serbia (Project OI172056).

## REFERENCES

- [1] S. F. Yin, B.-Q. Xu, *Chemphyschem*, 2003, **3**, 277-281.
- [2] J. Chevalier, L. Gremillard, A. V. Virkar, D. R. Clarke, *J. Am. Ceram. Soc.*, 2009, **92**, 1901–1920.
- [3] S. Vasanthavel, P. N. Kumar, S. Kannan, *J. Am. Ceram. Soc.*, 2014, **97**, 635-642.
- [4] C. Tiseanu, B. Cojocaru, V. I. Paravulescu, M. Sanchez-Dominguez, P. A. Primus, M. Boutonnet, *Phys. Chem. Chem. Phys.*, 2012, **14**, 12970-12981.
- [5] N. L. Wu, T.F. Wu, I. A. Rusakova, *J. Mater. Res.*, 2001, **16**, 666–669.

## THE EFFECT OF $\gamma$ -IRRADIATION ON MECHANICAL PROPERTIES OF NR/BR/SBR TERNARY RUBBER BLEND REINFORCED WITH CARBON BLACK

S. Jovanović<sup>1</sup>, V. Jovanović<sup>2</sup>, S. Samaržija-Jovanović<sup>2</sup>,  
G. Marković<sup>3</sup>, B. Petković<sup>2</sup> and M. Marinović-Cincović<sup>4</sup>

<sup>1</sup>*Mitas, d.o.o. Ruma, Serbia*

<sup>2</sup>*Faculty of Natural Science and Mathematics, University of Priština, Kosovska Mitrovica, Serbia, (vojani@sbb.rs; suzana.samarzija@pr.ac.rs )*

<sup>3</sup>*Tigar, Pirot, Serbia,*

<sup>4</sup>*University of Belgrade, Institute of Nuclear Science Vinča, Serbia*

### ABSTRACT

In this study the effect of radiation dose on the mechanical properties of ternary NR/BR/SBR (25/25/50) rubber blend reinforced with carbon black (CB) (0–100 phr) has been investigated. The cure characteristics of compounds were assessed using the rheometer with an oscillating disk. The mechanical properties hardness, modulus at 100% elongation, tensile strength and elongation at break were assessed before and after  $\gamma$ -irradiation (100–600 kGy). The vulcanizates were prepared in a hydraulic press. It was estimated that the values for tensile strength increased when the CB content increased up to 80 phr. Tensile strength and elongation at break are decreasing, but hardness and cross linking density are increasing with the increase of the irradiation dose.

### INTRODUCTION

Polymer blend are preparing to meet performance requirement that cannot be satisfied by the current available commodity polymer or properties lacking in the component polymers [1]. Blending of rubbers also enhance the physical properties of the final vulcanized product [2]. The properties of polymer blends can be controlled by regulating blend morphology, compositions and processing condition [3]. A standard tire formulation for trucks as well as cars is a physical blend of natural rubber/styrene-butadiene rubber (NR/SBR) or natural rubber/butadiene rubber (NR/BR) blends. Natural rubber and styrene/butadiene rubber have been blended for a long time for many purposes such as lowering the compound cost [4]. Reinforcement of elastomers is of great importance for the structuring of materials in new technologies, and it is a particularly complicated process if cross linked material contains more than one type of precursor cross linking. By creating a multi-phase system, characteristics of individual phases can be

partly preserved or significantly changed due to the influence of intermolecular interactions. Therefore, the modern research and industrial practice of tire industry leaders are directed towards the use of existing starting polymers and the obtainment of elastomeric materials based on new modified macromolecules. The mechanism of characteristic changes in  $\gamma$ -ray irradiated polymers, including degradation and cross linking has been studied in lot of publication. Gamma irradiation is also a powerful method for rubber cross linking; however, exposure to higher dosage of final elastomeric products degrades the materials. The cross linking and chain degradation are dependent on chains structural characteristics and the presence of some curing system. The research subject of this study is the multiscale structuring of elastomeric nanocomposites based on different precursors: polyisoprene (NR), polybutadiene (BR) and styrene-butadiene rubber (SBR) and its ternary blend (NR/BR/SBR) and the assessment of the carbon black content on the material mechanical properties before and after  $\gamma$ -irradiation.

### EXPERIMENTAL

Polyisoprene rubber, NR SMR-20 was supplied by Malaysia; polybutadiene rubber, BR SKD N with 94% of 1,4 *cis* content – was supplied by Njižnjekamsk (Russia); Styrene butadiene rubber, SBR Europa Intol 1783, is an emulsion styrene-butadiene rubber with 23.5% bound styrene was supplied by Versalis (Italy). The carbon black type N-330 (primary particle size 28-36 nm) - Volgograd (Russia). Content of filler was 0 - 100 phr. The curing system was: N-cyclohexyl-2-benzothiazolsulfonamide-CBS (1,4 phr); diphenyl guanidine, DPG, (1 phr); N-(cyclohexylthio) phthalimide, CTP 100 (0.2 phr) and sulfur (2 phr). In all rubber blend compounds the network precursor ratio was 25/25/50 (w/w/w). Content of zinc oxide was 3 phr. The stearic acid content was 2 phr. Plastificator as naphthenic oil content was 10 phr. Irradiations have been performed in air in the Co 60 radiation sterilization unit at the Vinca Institute of Nuclear Sciences with the dose rate of 10 kGy h<sup>-1</sup> and total absorbed dose of 100-600 kGy. The Radiation Unit of the Vinca Institute has been described in more detail elsewhere [5], the facility core is Co-60 gamma irradiator with wet storage working in batch mode (CEA, France).

### RESULTS AND DISCUSSION

The essence of cross linking is a chemical reaction between the rubber macromolecules, which in the presence of selected fillers, softeners, activators, curing agents, accelerators and retarders form a crosslink.

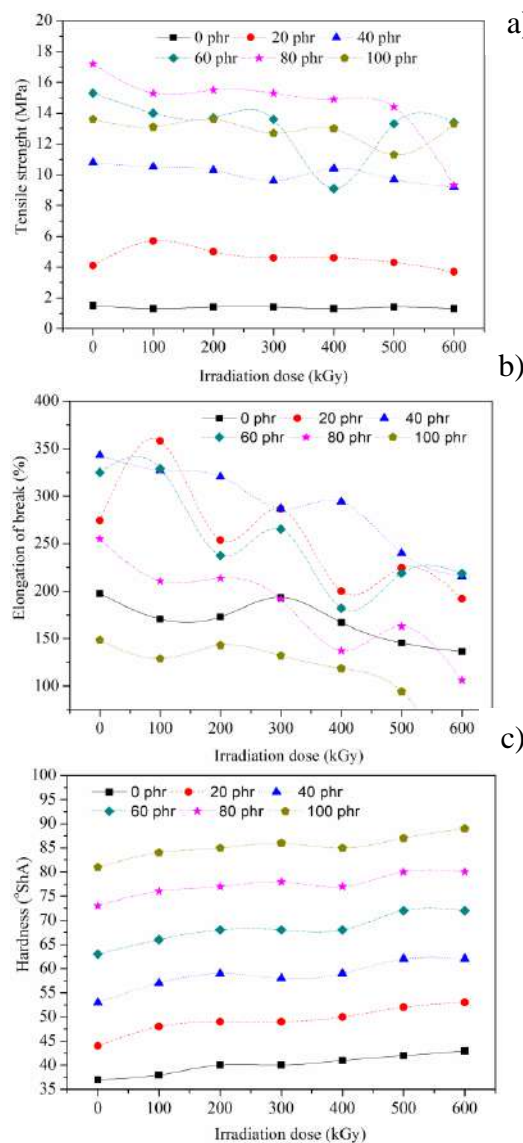


**Figure 1.** The mechanical properties after irradiation aging of ternary NR/BR/SBR rubber blend reinforced with CB: a) Tensile strength, b) Elongation of break and c) Hardness.

The tensile strength values attained for unloaded as well as loaded blends increase with irradiation dose reaching its maximum value at 200 kGy for CB filler and then they decrease over any further increase in dose (Figure 1 (a)).

a) Cross linking of rubber macromolecules represent topologically critical phenomenon, when the ensemble of linear chains forms a three-dimensional crosslink's of macromolecules. The aging experiments conducted under high energy radiation exposure offer useful information for the selection of technological parameters [6]. High-energy radiation is a well-known tool for the modification of polymers. In polymer irradiation, two phenomena occur at the same time: cross-linking and chain scission. The balance of cross linking and scission reactions in polyolefin chains, exposed to high-energy radiation processes that produce free radicals, may result in good properties and new applications. Figure 1. illustrates the variation of the mechanical properties as a function of irradiation dose for unloaded as well as loaded blends. In cross linked materials based on ternary rubber blend, the values of tensile strength increase with CB content increase up to 80 phr. This is also optimum charging for NR/BR/SBR rubber blend. The values of elongation at break increase up to 40 phr (343.3 %), and then decrease.

The variation of elongation at break values, as a function of irradiation dose is depicted on Figure 1 (b). As it was expected, the values of elongation at break for filled and unfilled ternary NR/BR/SBR rubber blends decrease with irradiation dose increase. The hardness values of ternary NR/BR/SBR rubber blends composites are increase effectively with the filler content increase (Figure 1 (c)). On the other hand, comparatively a limited increase has been attained for the hardness value for one and the same composition, whether filled or unfilled, with the irradiation dose increase from 100 to 600 kGy.

### CONCLUSION

The mechanical properties and service life of rubber blends could be improved using reinforcing fillers and irradiation process to increase crosslinking process. The effect of irradiation dose on mechanical properties (tensile strength, hardness and elongation at break) of the sulphur cured NR/BR/SBR ternary rubber blends have been investigated. NR/ BR/SBR ternary rubber blends with 80 phr CB content have better mechanical properties as compared to compounds with other CB content. For the NR/BR/SBR/80CB blends with increase in irradiation dose up to 200kGy, the tensile strength and elongation at the break decrease, while the hardness increase. Irradiation increase in crosslink density of NR/BR/SBR/80CB ternary rubber blend. At higher filler content and higher irradiation doses a chain degradation process becomes more predominant than cross linking.

### *Acknowledgment*

This work was partially supported by the Ministry for Science and Technological Development of the Republic of Serbia (Projects Num. 45022 and 45020).

### REFERENCES

- [1] Mushtaq, H. B. Mukhtar, A. M. Shariff, *Int. J. Chem. Eng. Appl.*, 2014, **5**, 127-132.
- [2] C. Ngudsuntear, S. Limtrakul, T. Vatanatham, A. N. Wichien, G. L. Rempel, W. Arayapranee, *Int. Trans. J. Eng. Manag. Sci. Tech.*, 2014, **5**, 11-24.
- [3] M. A. Nawawi, S. L. Har, C. C. Han, *Int. J. Chem. Eng. Appl.*, 2012, **3**, 410-412.
- [4] R. Manshaie, S. Nouri Khorasani, S. Jahanbani Veshare, M. Rezaei Abadchi, *Radiation Physics and Chemistry* 2011, **80**, 100–106.
- [5] V. M. Marković, R. Eymery, H.C. Yuan, *Radiat. Phys. Chem.*, 1977, **9**, 625–631.
- [6] T. Zaharescu, T.M.E. Lungulescu, A.R. Caramitu, V. Marinescu, *Iran Polym J* 2015, **24**, 883–889.

## PULSED TEA CO<sub>2</sub> LASER IRRADIATION OF TITANIUM- CONTROLLABLE GAS AMBIENCE

J. Ciganović<sup>1,2</sup>, P. Matavulj<sup>2</sup>, M. Trtica<sup>1</sup>, J. Stasić<sup>1</sup>, J. Savović<sup>1</sup>, S. Živković<sup>1</sup> and M. Momčilović<sup>1</sup>

<sup>1</sup> *University of Belgrade, Institute of Nuclear Sciences Vinca, Mike Alasa 12-14, 11001 Belgrade, Serbia. (jovanc@vinca.rs)*

<sup>2</sup> *School of Electrical Engineering, University of Belgrade, Bulevar kralja Aleksandra 73, Belgrade 11120, Serbia*

### ABSTRACT

Interaction of a TEA CO<sub>2</sub> laser, operating at 10.6 μm wavelength and pulse length of 100 ns, with titanium target (implant), in nitrogen and carbon-dioxide gas ambience was studied. The Ti-surface modifications were studied at moderate fluence (~17 J/cm<sup>2</sup>) and intensity (~60 MW/cm<sup>2</sup>) regime. The energy absorbed from the laser beam was partially converted to thermal energy, which generated a series of effects, such as melting, vaporization of the molten material, shock waves, etc. The following Ti-surface changes and phenomena were observed: (i) superficial damages in both atmospheres; (ii) creation of cone- and hill- like structures in atmosphere of N<sub>2</sub> and CO<sub>2</sub>, respectively; (iii) possible formation of TiN, Ti-oxide(s) and, Ti-carbide layers, in N<sub>2</sub> and CO<sub>2</sub> gas, respectively and, (iv) occurrence of plasma in both gas ambiances. It can be concluded that the applied laser fluence was high enough to produce effective modification of the Ti- implant target in nitrogen as well as in carbon-dioxide gas. Creation of plasma may provide sterilization effect.

### INTRODUCTION

One of possible methods for processing and surface modification of refractory metals is by lasers [1]. Generally, study of laser-refractory metal interaction is scarce in the literature. Titanium is metal which possesses extraordinary properties such as high melting point, high strength-to-weight ratio, excellent corrosion and erosion resistance, etc. Because of that, titanium has been used in a variety of fields like medicine (as implant), industry, aerospace engineering, etc. Recently, titanium and its alloys have been considered for fusion area applications.

Bio-integration of Ti-implant depends on the state of the surface [2-4]. One of possible approaches for surface morphology alternations is a laser

treatment [3-5]. In addition, formation of compounds at the surface, e.g. oxides, can have positive effect on bio-compatibility [5].

The present paper studies the effects of a pulsed TEA CO<sub>2</sub> laser emitting in the infrared (10.6 μm), at moderate fluences ~17 J/cm<sup>2</sup> and intensity of ~60 MW/cm<sup>2</sup>, on a titanium surface in controlled nitrogen and carbon-dioxide gas atmosphere. As the TEA CO<sub>2</sub> laser–titanium interaction was accompanied by the appearance of plasma, optical emission spectroscopy was applied to analyse the plasma emission.

### EXPERIMENTAL

The experimental set-up used in this study was described in details in reference [5]. It consists of the laser source, target placed in a vacuum chamber which could be filled with various gases, and plasma emission detection system (spectrometer coupled with a CCD detector). A CO<sub>2</sub> laser was a commercial version of the system developed at the VINCA Institute of Nuclear Sciences [6]. The pulse repetition rate was 1 Hz, and the laser was running under moderate fluence (~17 J/cm<sup>2</sup>) and intensity (~60 MW/cm<sup>2</sup>) regime. The optical pulse had a gain switched spike followed by a slowly decaying tail. FWHM of the spike was about 100 ns while the tail duration was ~2 μs. The laser beam was focused on the Ti-target with a ZnSe lens (focal length 13.0 cm). The angle of incidence of the laser beam with respect to the target surface was ~90°. A disk-shaped Ti samples (30 mm diameter and 5 mm thickness) were prepared by a standard metallographic procedure.

Various techniques were used for the analysis of Ti-target surface before and after the laser irradiation, e.g. optical microscopy, scanning electron microscopy and interferometric profilometric analysis. A time-integrated spatially-resolved plasma emission spectroscopy was applied for the analysis of plasma emission.

### RESULTS AND DISCUSSIONS

Surface modification of titanium generally depends on the laser output parameters (energy density, intensity, pulse duration, number of accumulated pulses, etc.), physicochemical characteristics of the material, as well as on irradiation conditions (working atmosphere and pressure). Laser induced morphological features depend, among other, from the temperature attained at the irradiated surface area and the heat affected zone. Under the applied experimental conditions, the heat affected zone was of the order of micrometers. A nanosecond TEA CO<sub>2</sub> laser interaction with titanium was accompanied by a series of processes, such as heating, melting, vaporization of the molten materials, dissociation, ionization of the vaporized material,

plasma creation, shock waves in the vapour and in the solid, etc. Surface features, generated during the interaction, can be described as follows:

**N<sub>2</sub> ambience:**

Irradiation of Ti-target in N<sub>2</sub> ambience was conducted at the pressure of one atmosphere. The obtained surface variations (Fig. 1.), can be summarized as follows: (i) superficial target damages with sporadic cracking (damage depth at 300 pulses was several micrometers); (ii) generation of conical forms; (iii) creation of the golden color layer and, (iv) creation of plasma which had yellow-white color. The appearance of the golden colored layer may imply a possible creation of TiN [5]. In the region close to the target, plasma emission mainly consisted of neutral and singly ionized spectral lines of titanium and nitrogen atomic lines.

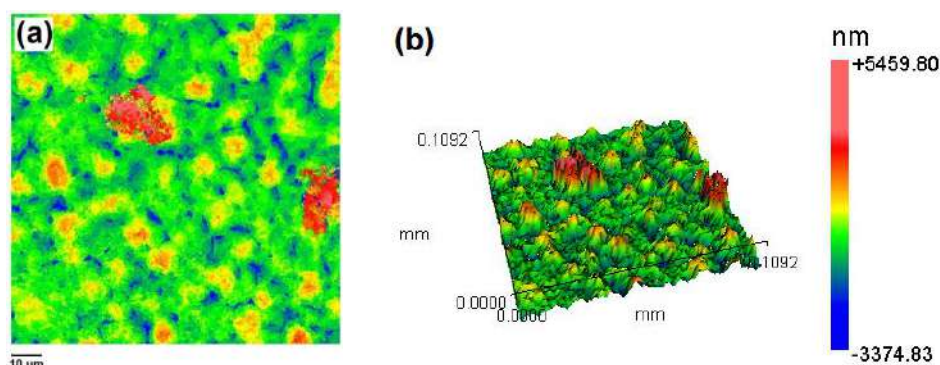


**Figure 1.** Interferometric profilometry (IP) analysis. (a) 2D- and (b) 3D-view of Ti-surface after irradiation with 300 pulses in N<sub>2</sub> ambience.

**CO<sub>2</sub> ambience:**

Irradiation of Ti-target in CO<sub>2</sub> ambience was conducted at the pressure of one atmosphere. Obtained morphology changes were different from those obtained in N<sub>2</sub> ambience (Fig. 2.). Changes can be summarized as follows: (i) superficial damage with intensive cracking (central zone); (ii) appearance of hill-like structures; (iii) creation of black and white colored regions; (iv) creation of intensive plasma which had blue-white color. Appearance of the characteristic colored locations may imply formation of Ti-oxides and Ti-carbide layer at the surface. In CO<sub>2</sub> gas, analysis of plasma emission showed the presence of Ti-atomic and ionic spectral lines, oxygen lines as well as CO bands.

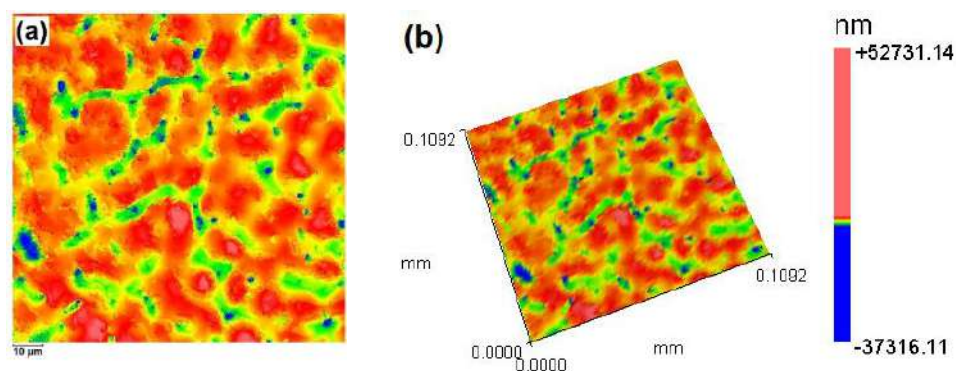


**Figure 2.** IP analysis. (a) 2D- and (b) 3D-view of Ti-surface after irradiation with 300 pulses in CO<sub>2</sub> ambience.

### CONCLUSION

Irradiation of titanium implant target by pulsed TEA CO<sub>2</sub> laser, in controllable gas ambience of N<sub>2</sub> and CO<sub>2</sub>, resulted in intensive morphological changes. Generally, the surface roughness was increased with simultaneously possible formation of layers such as, TiN, Ti-oxides, Ti-carbide. Irradiation process was accompanied by plasma creation in front of the target which can provide additional effects at the surface, i.e. sterilization effect.

### Acknowledgements

This work was partially supported by the: (i) Ministry of Education, Science and Technological Development of Republic of Serbia. Project No. 172019 and No. 171011 and, (ii) International Atomic Energy Agency (IAEA), Contract No. 20636.

### REFERENCES

- [1] Patschger, A. Hopf, M. Gupner, J. Bliedtner, *Laser Tech. Jour.*, 2016, **13**, 24-27.
- [2] M. Long, H. J. Rack, *Biomaterials*, 1998, **19**, 1621–1639.
- [3] M. Bereznai, I. Pelsoczi, Z. Toth, K. Turzo, M. Radnai, Z. Bor, A. Fazekas, *Biomaterials*, 2003, **24**, 4197–4203.
- [4] F. Guillemot, F. Prima, V. N. Tokarev, C. Belin, M.C. Porte-Durrieu, T. Gloriant, C. Baquey, S. Lazare, *Appl. Phys. A*, 2004, **79**, 811–813.
- [5] J. Ciganovic, J. Stasic, B. Gakovic, M. Momcilovic, D. Milovanovic, M. Bokorov, M. Trtica, *Appl. Surf. Sci.*, 2012, **258**, 2741–2748.
- [6] M. Kuzmanovic, M. Momcilovic, J. Ciganovic, D. Rankovic, J. Savovic, D. Milovanovic, M. Stoiljkovic, M. S. Pavlovic, M. Trtica, *Physica Scripta*, 2014, **T162**, 014011 (4pp).

## THE RECYCLING OF $\text{LiCo}_{0.415}\text{Mn}_{0.435}\text{Ni}_{0.15}\text{O}_2$ CATHODE MATERIAL FROM SPENT LI-ION BATTERIES

J. Senćanski<sup>1</sup>, M. Vujković<sup>2</sup>, I. Stojković-Simatović<sup>2</sup>, D. Majstorović<sup>1</sup> and S. Mentus<sup>2,3</sup>

<sup>1</sup>*Institute of General and Physical Chemistry, Studentski trg 12/V, P.O. Box 551 Belgrade, Serbia.*

<sup>2</sup>*Faculty of Physical Chemistry, University of Belgrade, Studentski trg 12-16, P.O. Box 137, Belgrade, Serbia (milica.vujkovic@ffh.bg.ac.rs)*

<sup>3</sup>*The Serbian Academy of Science and Arts, Knez Mihailova 35, 11158 Belgrade, Serbia*

### ABSTRACT

The spent Li-ion batteries contain oxides of Co, Ni and Mn and metals Al and Cu as main components, with potential impact on the environment. Recycling of spent Li-ion batteries was the subject of this study. As a first attempt, only the cathode material of spent batteries was collected, in order to obtain the solution from which it might be recycled. The recycling method based on the co-precipitation of dissolved metal salts is presented. Upon the re-synthesis, the obtained cathode material was characterized by structural, morphological and electrochemical methods.

### INTRODUCTION

The number of spent Li-ion batteries exponentially increases. In the time period 2000-2010 only, the world production of Li-ion batteries increased by 800 % [1] which means a potentially high ecological problem. Lithium-ion batteries contain hazardous metals like Al, Co, Ni, Mn which may have a negative impact on the environment [2] if dispersed around without any control. Because of that, their recycling is an actual research area. There are many studies about the obtaining metals from Li-ion batteries, but, the studies about the re-synthesized cathode materials are rarely published. In this paper, the re-synthesis of the cathode material by co-precipitation method will be presented.

### EXPERIMENTAL

The spent Li-ion batteries were manually dismantled and their components (anode, cathode and separators) were uncurled and separated. The cathode of spent Li-ion batteries was dissolved in  $5 \text{ mol dm}^{-3}$  NaOH to obtain the cathodic material separated from the Al-foil support. After that, the cathode

material was annealed at 700 °C in air in order to remove carbon additive and PVDF binder by combustion. The composition of separated cathode material was analyzed by Atomic absorption spectrometer after dissolving in 2 mol dm<sup>-3</sup> HNO<sub>3</sub>. The re-synthesis of the cathode material was done by the co-precipitation method. Briefly, the salts solution obtained by dissolving initial cathode materials in nitric acid were co-precipitated in form of a mixture of hydroxides by addition of 10 mol dm<sup>-3</sup> NaOH dropwise. The residue was rinsed with ethanol. After drying, the Li<sub>2</sub>CO<sub>3</sub> was added to the residue to satisfy the molar ratio Li:ΣM = 1:1 (M = Co, Mn, Ni). The obtained mixture was annealed at 700 °C and at 850 °C. Such obtained powders were labeled as re-LCMNO@700 and re-LCMNO@850.

The structure of the obtained powders was identified by X-Ray diffractometer Rigaku Ultima IV (CuKα, λ=1.54178Å), and the morphology was observed by scanning electron microscope Model JSM-6610LV. The functionality of recycled material was checked in LiNO<sub>3</sub> by Cyclic Voltammetry (CV) using Gamry PCI4/300 Potentiostat/Galvanostat. The CV was performed in electrochemical cell of the three electrode type, with the Pt electrode as the counter electrode and the saturated calomel electrode as the reference electrode. The Li(Co-Mn-Ni)O<sub>2</sub> working electrode was prepared by using the typical procedure shown in ref [3].

## RESULTS AND DISCUSSION

The composition of commercial cathode material was found to be LiCo<sub>0.415</sub>Mn<sub>0.435</sub>Ni<sub>0.15</sub>O<sub>2</sub>.

XRD pattern of re-LCMNO@700 and re-LCMNO@850 was presented in Fig. 1. The position of the well-defined reflections, corresponding to (003), (101), (006), (104), (105) and (110), shows that recovered materials belong to the layered structure type α-NaFeO<sub>2</sub> with the space group of R $\bar{3}m$  (ICSD153447). The split of the (006)/(102) and (108)/(110) pairs, which is characteristic of the highly ordered hexagonal structure,

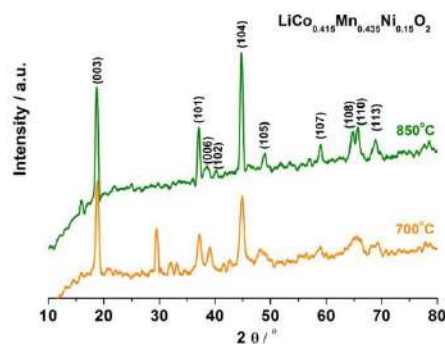


**Figure 1.** XRD patterns of re-LCMNO@700 and re-LCMNO@850

is not pronounced in the LNMN@700 due to the low temperature of calcination. The low  $I(003)/I(104)$  intensity for both samples, amounting to 1.12 for LCMNO@700 and 0.85 for LCMNO@850, was found. Both are lower than 1.2 [4] which reveals the position exchange between lithium and transition metal ions known as "cation mixing".

Figure 2. illustrates representative SEM micrographs of recycled cathode material. It can be seen that morphology changes with the increase of the temperature. At the lower temperature (Fig.2, left), the particles have rice shape. Interestingly, with the temperature rise, they changed in shape from rice to rod one (Fig.2,right).

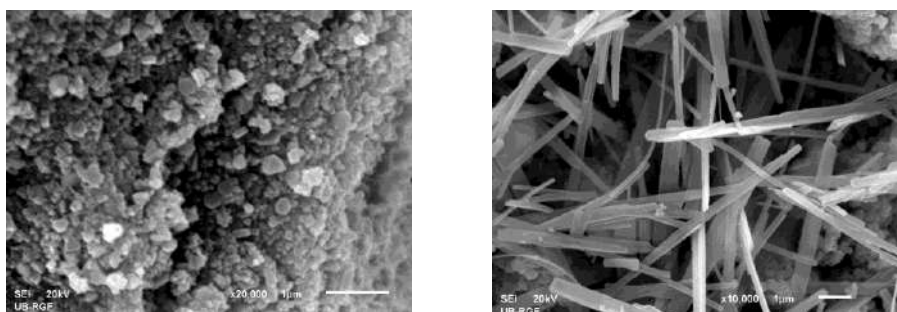


**Figure 2.** SEM micrographs of re-LCMNO@700 (left) and re-LCMNO@850 (right)

The Cyclic Voltammetry was used as a quick method to check the functionality of recycled material in aqueous electrolyte solution of  $\text{LiNO}_3$ .

A typical pair of CV redox peaks (Fig.3), measured in  $\text{LiNO}_3$  at scanning rate  $10 \text{ mV s}^{-1}$ , confirmed clearly the functionality of the recycled material. Namely, the well-defined CV peaks, which correspond to  $\text{Ni}^{2+}/\text{Ni}^{4+}$  redox process [5], indicate a fast lithiation/delithiation reactions of recycled  $\text{LiCo}_{0.415}\text{Mn}_{0.435}\text{Ni}_{0.15}\text{O}_2$ . Both high current response and small peak potential separation are observed. The current response turns out to be practically independent of temperature. The peak-to-peak potential separation, which is the main parameter of electrochemical reversibility, is lower in the case of re-LCMNO@700. It indicated a faster charge transfer

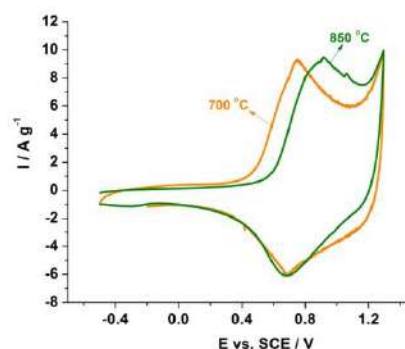


**Figure 3.** CVs of re-LCMNO@700 and LCMNO@850

of the material which was annealed at 700 °C. It may be due to slightly lower degree of cation mixing in re-LCMNO@700 than in re-LCMNO@850. Additionally, spherical particles have shorter path for Li<sup>+</sup> ions and electrons than the rod shape particles, which enables the better lithiation/delithiation kinetics of re-LCMNO@700. The lithiation and delithiation capacity, obtained by integration of CV curve at high scan rate of 10 mV s<sup>-1</sup>, amounted to ~79 mAh g<sup>-1</sup> and ~55 mAh g<sup>-1</sup> for re-LCMNO@700 and 74.5 mAh g<sup>-1</sup> and 52.8 mAh g<sup>-1</sup> for re-LCMNO@850, respectively. The capacity of recycled material is quite encouraging from the aspect of the use of this material as cathode material for lithium aqueous batteries.

### CONCLUSION

The LiCo<sub>0.415</sub>Mn<sub>0.435</sub>Ni<sub>0.15</sub>O<sub>2</sub> has been re-synthesized by simple and effective co-precipitation method using the cathode material of spent Li-ion batteries. It was shown that the structure of material obtained from coprecipitated oxide mixture upon Li<sub>2</sub>CO<sub>3</sub> addition, heated at 700 °C and 850 °C, belongs to the layered structure type α-NaFeO<sub>2</sub>, with a certain degree of cation mixing. The temperature increase resulted in the change of morphology from spherical to rod shape. A fast lithiation/delithiation reactions of both examined oxides was observed in an aqueous LiNO<sub>3</sub> solution. Faster charge transfer was found for the sample annealed at 700 °C.

### Acknowledgement

This work was supported through the Project III 45014.

### REFERENCES

- [1] X. Zhang, H. Cao, Y. Xie, P. Ning, H. An, H. You, F. Nawaz, Sep. Purif. Technol. 2015, **150**, 186–195.
- [2] C. M. Julien, A. Mauger, K. Zaghib, Henri Groult, Inorganics, 2014, **2**, 132-154.
- [3] M. Vujković, M. Mitrić, S. Mentus, J. Power Sources, 2015, **288**, 176-186.
- [4] X. Luo, X. Wang, Li Liao, X. Wang, S. Gamboa, P. J. Sebastian, J. Power Sources, 2006, **161**, 601-605.
- [5] K. M. Shaju, G. V. S. Rao, B. V. R. Chowdari, Electrochim. Acta, 2002, **48**, 145-151.

## MAGNETIC PROPERTIES OF LITHIUM-PHOSPHATE SYSTEMS

C. Andronache<sup>1</sup> and D. Racolta<sup>1</sup>

<sup>1</sup> *Technical University of Cluj Napoca, North University Center of Baia Mare, Str. Victoriei 76 430122, Baia Mare, Romania.*

### ABSTRACT

Glasses from the systems,  $xFe_2O_3 (100-x)[P_2O_5 Li_2O]$  with  $0 < x < 50$  mol% were prepared and characterized by magnetic susceptibility. The iron ions generally modify in a different way the local structure of these glasses, depending on the presence of the  $Li_2O$  in the glass matrix. The results have shown the presence of antiferromagnetic or ferromagnetic interactions between the iron ions in the studied glass and temperature range. These data revealed that the valence states and the distribution of iron ions in the glass matrix depend on the  $Fe_2O_3$  content, and can determine the decreasing of magnetic momentum ( $\mu_{eff}$ ).

### INTRODUCTION

Magnetic susceptibility measurements revealed as very useful to determine the valence states of transition metal ions and the type of interactions involving them over various composition ranges. Their magnetic properties depend on the concentration of the  $3d$  element and the valence states ratio as well as on the structure of the vitreous matrix and implicitly on the conditions of sample preparation. The superexchange interaction of the iron ions in the oxide glasses was most frequently attributed to an antiferromagnetic coupling within the pairs  $Fe^{3+}-Fe^{3+}$ ,  $Fe^{3+}-Fe^{2+}$  and  $Fe^{2+}-Fe^{2+}$  [1-3]. An antiferromagnetic coupling between iron ions was reported in borate [4-7], phosphate [3,8], tellurite [8,9] and oxide glasses [8-12]. This work aims to present our results obtained by means of magnetic susceptibility measurements performed on  $P_2O_5 \cdot Li_2O$  glass matrix gradually doped with the iron ions.

### EXPERIMENTAL

The starting materials used in the present investigation were  $(NH_4)_2HPO_4$ ,  $Li_2CO_3$  and  $Fe_2O_3$  of reagent grade purity. The samples were prepared by weighing suitable proportions of components, powder mixing and mixture melting in sintered corundum crucibles at 977K for 5 minutes. The mixtures were put into the furnace direct at this temperature. The melts were poured

into stainless steel plates. The structure of samples was analyzed by means of X-ray diffraction using a Bruker D8 ADVANCE X-ray Diffractometer. The pattern obtained did not reveal any crystalline phase in the samples up to 50 mol %  $\text{Fe}_2\text{O}_3$ . The magnetic susceptibility ( $\chi$ ) measurements were performed with a Faraday-type balance which give some information about magnetic field strength in the temperature range 80-300K. Correction due to the diamagnetism of the  $\text{P}_2\text{O}_5$ ,  $\text{Li}_2\text{O}$  and  $\text{Fe}_2\text{O}_3$  were taken into account in order to obtain the real magnetic susceptibility of iron ions in the studied glasses.

## RESULTS AND DISCUSSION

The  $x\text{Fe}_2\text{O}_3 \cdot (100-x)[\text{P}_2\text{O}_5 \cdot \text{Li}_2\text{O}]$  glass samples were investigated by magnetic susceptibility for  $x$  varying in the range  $3 < x < 50 \text{ mol}\%$  and the temperature dependence of the reciprocal magnetic susceptibility is presented in Fig. 1. The concentration dependence of the paramagnetic Curie temperature ( $\theta_P$ ) is given in Fig. 2.

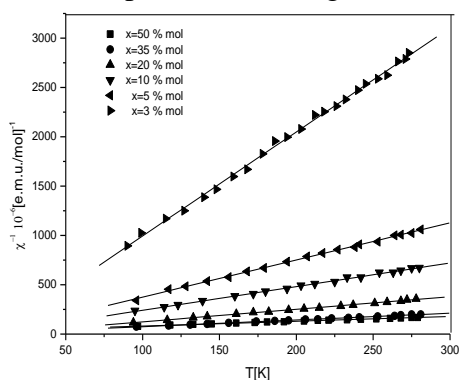


**Figure 1.** Temperature dependence of the reciprocal magnetic susceptibility for  $x\text{Fe}_2\text{O}_3 \cdot (100-x)[\text{P}_2\text{O}_5 \cdot \text{Li}_2\text{O}]$  glasses with  $3 \leq x \leq 50 \text{ mol}\%$

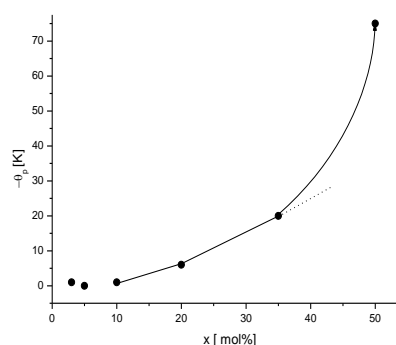


**Figure 2.** Composition dependence of the paramagnetic Curie temperature for  $x\text{Fe}_2\text{O}_3 \cdot (100-x)[\text{P}_2\text{O}_5 \cdot \text{Li}_2\text{O}]$  glasses

The temperature dependence of the reciprocal magnetic susceptibility show a Curie-Weiss-type behaviour, with negative paramagnetic Curie temperature for all studied glasses (Fig. 2). This fact suggests a superexchange interaction between the iron ions which are antiferromagnetically coupled. Therefore, in the  $\text{P}_2\text{O}_5 \cdot \text{Li}_2\text{O}$  glass matrix, in the studied concentration range, the iron ions behave magnetically similarly as in other oxide glasses, but concentration of  $\text{Fe}_2\text{O}_3$  over which magnetic super exchange interactions occur is lower. This is in agreement with experimental remarks according with the concentration range of transition

metal ions over which these interactions occur depends of the nature of the glass matrix. The absolute magnitude of  $\theta_p$  values increases when content of  $Fe_2O_3$  are increased (Fig. 2). The exchange integral increase as the content of the magnetic ions is increased in the glass and as a result the magnitude of the  $\theta_p$  increases.

The values of the magnetic moment of iron ions in the studied samples were estimated as  $\mu_{eff} = 2.827 \cdot [C_M/2X]^{1/2}$ . These results and the molar Curie constant values,  $C_M$ , are given in Table 1.

**Table 1.** Molar Curie constant, experimental values of  $\mu_{eff}$  and molar fraction of  $Fe^{3+}$  ( $x_1$ ) and  $Fe^{2+}$  ( $x_2$ ) ions for  $xFe_2O_3 \cdot (100-x)[P_2O_5 \cdot Li_2O]$ .

$x$ [mol % $Fe_2O_3$ ]	$C_M$ [emu/mol]	$\mu_{ef}$ [ $\mu_B$ ]	$x_1$ [mol% $Fe^{3+}O_3$ ]	$x_2$ [mol% $Fe^{2+}O_3$ ]
3	0.26	5.90	2.98	0.02
5	0.42	5.78	4.25	0.75
10	0.79	5.60	8.62	1.38
20	1.47	5.42	6.63	13.37
35	2.19	5.01	3.18	31.82
50	3.07	4.96	2.73	47.27

The composition dependence of the molar Curie constant is presented in Table 1. For the glass with  $x=3mol\%$  the experimental value obtained for effective magnetic moment ( $\mu_{eff}$ ) is  $5.90\mu_B$  (Table 1) and is very close to the atomic magnetic moment of free  $Fe^{3+}$  ion:  $\mu_{Fe^{3+}} = 5.90\mu_B$ . Therefore, we consider that in the glasses with  $x < 3mol\%$  only the  $Fe^{3+}$  ions present. For the glasses with  $3 < x < 35mol\%$ , the  $C_M$  and consequently the  $\mu_{eff}$  values (Table 1) are smaller than those corresponding to a  $Fe_2O_3$  content having all iron ions as  $Fe^{3+}$  species but higher than those of  $Fe^{2+}$  ions. For this reason, both  $Fe^{3+}$  and  $Fe^{2+}$  ions may be assumed to be present in these glasses. The presence of  $Fe^{3+}$  and  $Fe^{2+}$  ions has been evidenced in other oxide glasses[8,12]. Therefore, the molar fractions of these ions were estimated to a first approximation by using the relations:

$$x \cdot \mu_{eff}^2 = x_1 \cdot \mu_{Fe^{3+}}^2 + x_2 \cdot \mu_{Fe^{2+}}^2 \quad (2)$$

and

$$x = x_1 + x_2 \quad (3)$$

where  $\mu_{eff} = 2.827(C_M/2X)^{1/2}$  representing the experimental effective magnetic moment value (Table 1) determined from the temperature variation of the magnetic susceptibility (Fig. 1). A molar fraction  $x_1$  and

$x_2$  correspond to  $Fe^{3+}$  and  $Fe^{2+}$  ions, while  $\mu_{Fe^{2+}} = 4.90\mu_B$  is the value of the magnetic moment of the free  $Fe^{2+}$  ion. The results obtained are listed in Table 1. For the glass with  $x = 50 \text{ mol } \%$ , the experimental value obtained for  $\mu_{eff}$  is  $4.96\mu_B$  (Table 1).

## CONCLUSION

Glasses of the  $xFe_2O_3 \cdot (100-x)[P_2O_5 \cdot Li_2O]$  system were obtained within a large concentration range, i.e.  $0 < x < 50 \text{ mol } \%$ .

For the glasses with  $x < 3 \text{ mol } \%$  only  $Fe^{3+}$  ions are evidenced. In  $3 < x < 35 \text{ mol } \%$  composition range, iron enters the  $P_2O_5 \cdot Li_2O$  glass matrix in both  $Fe^{3+}$  and  $Fe^{2+}$  valence states, the  $Fe^{2+}$  ions concentration exceeding the  $Fe^{3+}$  one for glasses with  $x > 20 \text{ mol } \%$ . For the glasses with  $x > 35 \text{ mol } \%$ , the estimated values of the  $\mu_{eff}$  reflects the coordination influence on the magnetic moment of iron ions presents in species simultaneously like  $Fe^{2+}$  and  $Fe^{3+}$  ions, but is not excluded the presence in small quantities, in studied temperature range, of the antiferromagnetic or ferrimagnetic interactions which can determine the decrease of  $\mu_{eff}$ .

## Acknowledgement

This study was supported by JINR-Romania, Scientific Projects, Topic no.04-4-1121-2015/2017, Protocol No. 4407-4-15/17.

## REFERENCES

- [1] R. Yang, et al, Journal of Alloys and Compounds, 2012, **513** 97.
- [2] S. P. Chaudhuri and S.K.Patra, *Mat. Sci.*, 2000, **35**, 4735.
- [3] L. K. Wilson, E. J. Friebele and D. L. Kinser, *Proc. Int. Symp. On Amorphous Magnetism*, (Plenum Press, New York), (1975) p. 65.
- [4] A. Mogus-Milankovic, et al, *Phys. Chem. Glasses*, 1995, **36**, 31.
- [5] R. Iordanova, et al, *J. Non-Cryst. Solids* **221** (1998)227.
- [6] G. Srinivasarao and N. Veeraiyah, *J. Phys. Chem. Solids.*, 2002, **63**, 705.
- [7] R. Todoran, D. Todoran, Zs. Szakacs, *Phys. Scripta*, 2013, **T157**, **25**.
- [8] B. Kumar and C. H. Chen, *J. Appl. Phys.*, 1994, **75**, 6760.
- [9] L. D. Bogomolova. N. A. Krasilnikova. V. L. Bogdanov. V. D. Khalilev and V. Mitrofanov, *J. Non-Cryst. Solids*, 1995, **188**, 130.
- [10] A. M. Vorotinov, K. A. Sablina, *Solid State Communications*, 1993, **87**, 209
- [11] R. K. Singha, G.P. Kothiyalb, A. Srinivasan, *J. Non-Cryst. Solids*, 2008, **354**, 3166.

## **SYNTHESIS OF POLYPYRROLE/CARBON NANOTUBES COMPOSITE FOR SUPER CAPACITORS APPLICATIONS**

G. Ljubek<sup>1</sup>, J. Perić Ivanagić<sup>2</sup>, S. Kožuh<sup>3</sup> and M. Kraljić Roković<sup>2</sup>

<sup>1</sup>*University of Zagreb, Faculty of Mining, Geology and Petroleum  
Engineering, Pierottijeva 6, 10000 Zagreb, Croatia.  
(gabrijela.ljubek@oblak.rgn.hr)*

<sup>2</sup>*University of Zagreb, Faculty of Chemical Engineering and Technology,  
Marulićev trg 19, 10000 Zagreb, Croatia.*

<sup>3</sup>*University of Zagreb, Faculty of Metallurgy, Aleja narodnih heroja 3,  
44103 Sisak, Croatia.*

### **ABSTRACT**

Synthesis and characterization of polypyrrole (PPy) layers were conducted in order to obtain a porous material whose electrochemical properties will be suitable for applications in supercapacitors. In order to improve PPy properties, it was combined with carbon nanotubes (CNTs). The electrochemical and pseudocapacitive properties of the prepared materials were investigated by cyclic voltammetry, electrochemical impedance spectroscopy and electrochemical quartz crystal nanobalance. The results show that PPy/CNTs composite had better pseudocapacitive properties compared to pure polypyrrole.

### **INTRODUCTION**

Supercapacitors are electronic devices that store electrical energy. Compared to batteries and fuel cells, supercapacitors have a higher specific power, much longer cycle life, but their specific energy is somewhat lower. In order to enhance electrical properties of supercapacitors a wide variety of active materials have been investigated [1]. Carbon materials are usually used in electrochemical double-layer supercapacitors (EDLC). They have large surface, which results in larger capacitance. Another class of materials that are suitable for supercapacitors applications are the electrically conducting polymers and metal oxides. These materials are used in redox supercapacitors where energy storage takes place through the reversible redox reactions, so they are often called pseudocapacitors. In comparison with EDLC, redox supercapacitors exhibit a much higher specific capacitance [1-2].

Polypyrrole (PPy) is electrically conducting polymer and promising electrode material for supercapacitor application due to its low cost, high pseudocapacitance and ease of synthesis by chemical and electrochemical methods[3]. In order to improve PPy properties, composites of PPy and other materials have been used [4]. In particular, carbon nanotubes (CNTs) because they improve mechanical properties of conducting polymers during long cycling and they increase material porosity and conductivity that enables a high charge/discharge rate[5].

In this work various layers of polypyrrole and PPy/CNTs composites were prepared by electrochemical method in a  $0.5 \text{ mol dm}^{-3} \text{Na}_2\text{SO}_4$  solution as a supporting electrolyte, in order to obtain a porous material whose electrochemical properties will be suitable for applications in supercapacitors. The properties of the obtained materials were characterized by cyclic voltammetry (CV), electrochemical quartz crystal nanobalance (EQCN) and electrochemical impedance spectroscopy (EIS) measurements.

## EXPERIMENTAL

The polypyrrole layers were prepared using  $0.1 \text{ mol dm}^{-3}$  pyrrole (FlukaChemika) aqueous solutions and  $0.5 \text{ mol dm}^{-3} \text{Na}_2\text{SO}_4$  (Kemika) supporting electrolyte. Electropolymerization was carried out on  $0.07 \text{ cm}^2$  Pt-disc electrode under potentiodynamic conditions from  $-500$  to  $+800 \text{ mV}$  (PPy1) or  $+900 \text{ mV}$  (PPy2) vs. saturated calomel electrode (SCE) at a scan rate of  $50 \text{ mV/s}$ . Carbon nanotubes modified with carboxyl group (Chendu Organic Chem Co.) were applied on the  $0.07 \text{ cm}^2$  Pt-disc electrode using poly(vinylidene fluoride) (Sigma-Aldrich) as a binder in order to prepare PPy/CNTs composite layer. PPy was electrodeposited onto the carbon nanotubes modified Pt electrode by CV method from the  $0.1 \text{ mol dm}^{-3}$  pyrrole in  $0.5 \text{ mol dm}^{-3} \text{Na}_2\text{SO}_4$  in the potential range from  $-500 \text{ mV}$  to  $+600 \text{ mV}$  (PPy/CNTs1) or  $+800 \text{ mV}$  (PPY/CNTs2) vs. SCE at a scan rate of  $50 \text{ mV/s}$ . All cyclic voltammetry experiments were carried out in one-compartment three-electrode electrochemical cell and all solutions were prepared from bi-distilled water.

PPy and PPy/CNTs layers were tested using CV, EIS and EQCN. CV and EQCN measurements were carried out in  $0.5 \text{ mol dm}^{-3} \text{Na}_2\text{SO}_4$  in the potential range from  $-600$  to  $+600 \text{ mV}$  vs. SCE at a scan rate of  $50 \text{ mV/s}$ . EIS measurements were carried out at dc potential of  $-400, -200, 0, +200, +400 \text{ mV}$  vs. SCE with the amplitude of  $5 \text{ mV}$  in the frequency range from  $100 \text{ kHz}$  to  $10 \text{ mHz}$ .

## RESULTS AND DISCUSSION

In this work PPy and PPy/CNTs layers of various thickness were obtained by applying different final potential during the synthesis. Figure 1 illustrates cyclic voltammograms of the layers tested in  $\text{Na}_2\text{SO}_4$  solution. It is evident that PPy layers show characteristic current peak in the potential range from -500 mV to 0mV, as well as that thinner layer shows higher reversibility of redox reaction. Additionally, it is also obvious that significant current decrease is obtained for both PPy layers above 200mV indicating low PPy activity in that potential range. The cyclic voltammograms of PPy/CNTs layers show almost constant current over the whole potential range of investigation. It can be concluded that the reversibility is more pronounced when PPy is modified by carbon nanotubes due to the more porous structure and facile counter-ion exchange process [4]. Obtained results also indicate that CNTs significantly increase activity of the material at potential above 200mV.

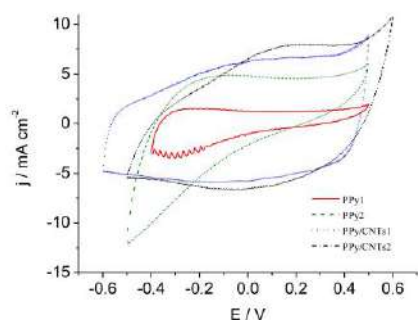


**Figure 1.** CV response of PPy and PPy/CNTs layers.

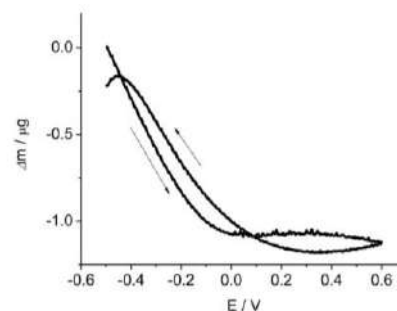


**Figure 2.** EQCN mass change for PPy layer.

During polarization of PPy layers in  $\text{Na}_2\text{SO}_4$  mass change was monitored using the EQCN method. The generation of positive charge at polymer backbone during the anodic process is compensated by electrostatic forces between anions from the solution and the polymer positive charge. This process is followed by anion uptake or cation expulsion at polymer/solution interface which depends on the porosity of layer [4]. During oxidation of PPy layer prepared in this work (Figure 2) cations are released from the layer and the mass decrease was registered. When the polymer is reduced the mass increases due to the insertion of cations into the polymer structure. Considering that  $\text{Na}^+$  is intercalated/deintercalated during PPy redox reaction rather than  $\text{SO}_4^{2-}$  it can be concluded that obtained PPy is not porous [4]. Additionally, in a potential range higher than 200 mV there is no significant mass change which indicates poor polymer activity.

The observed electrochemical behavior of PPy and PPy/CNTs composite layers were also confirmed by EIS and illustrated in Figure 3. The decreased values for charge transfer resistance,  $R_{ct}$ , with the incorporation of carbon nanotubes in the layer could be notice. For the pure PPy film at 400 mV the calculated value of resistance was  $R_{ct}= 124.74 \Omega\text{cm}^2$  and for the composite  $R_{ct}= 18.08 \Omega\text{cm}^2$ . Thus, carbon nanotubes significantly decrease  $R_{ct}$  of PPy film and improve its properties for supercapacitor application.

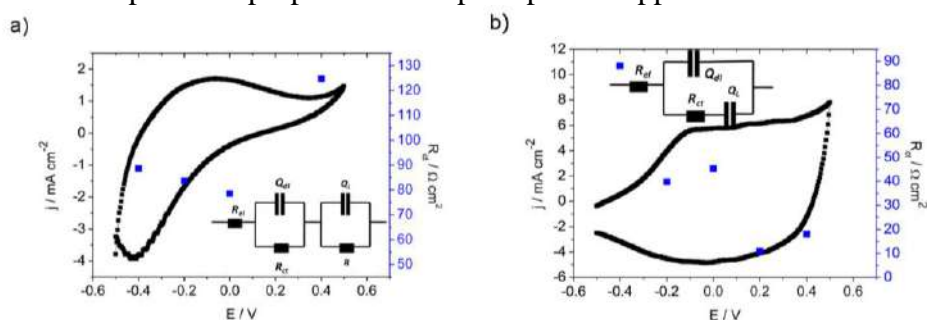


**Figure 3.** CV response, electrical equivalent circuit and  $R_{ct}$  values for a) PPy and b) PPy/CNTs layer.

## CONCLUSION

Cyclic voltammetry response of PPy layer shows two current peaks at negative potentials and low current activity above 200 mV. Reversibility of the response significantly depends on the layer thickness. It is concluded that obtained behavior is result of low PPy porosity. Incorporation of carbon nanotubes within the polypyrrole layer results in improved polymer activity in wide potential range, higher degree of redox reaction reversibility, decrease of charge transfer resistance and thus improved pseudocapacitive properties.

## Acknowledgement

The authors are grateful to the “Croatian Science Foundation” for the financial support of the project ESUP-CAP (IP-11-2103.8825).

## REFERENCES

- [1] G. Pandolfo, A. F. Hollenkamp, *Journal of Power Sources*, 2006, **157**, 11-27.
- [2] C. Peng, S. Zhang, D. Jewell, G. Z. Chen, *Progress in Natural Science*, 2008, **18**, 777-788.
- [3] K. Qi, Y. Qiu, X. Guo, *ElectrochimicaActa*, 2014, **137**, 685-692.
- [4] D. Sačer, D. Čapeta, I. Šrut Rakić, R. Peter, M. Petravić, M. Kraljić Roković, *ElectrochimicaActa*, 2016, **193**, 311-320.
- [5] E. Frackowiak, V. Khomenko, K. Jurewicz, K. Lota, F. Béguin, *Journal of Power Sources*, 2006, **153**, 413-418.

## SYNTHESIS AND CHARACTERISATION OF HETEROPOLY ACID/BEA ZEOLITE COMPOSITES

A.Jović<sup>1</sup>, D. Bajuk-Bogdanović<sup>1</sup>, B. Nedić Vasiljević<sup>1</sup>, M. Milojević-Rakić<sup>1</sup>,  
V. Dondur<sup>1</sup>, A. Popa<sup>2</sup> and I. Holclajtner-Antunović<sup>1</sup>

<sup>1</sup>*Faculty of Physical Chemistry, University of Belgrade,  
Studentski trg 12-16, 11000 Belgrade, Serbia.  
(aleksandar.jovic@ffh.bg.ac.rs)*

<sup>2</sup>*National Institute for Laser, Plasma and Radiation Physics, Bucharest,  
Romania*

### ABSTRACT

Optimized synthetic route for obtaining heteropoly acid species supported on beta zeolite surfaces was applied and different composites, comprising 20 to 50 wt.% H<sub>3</sub>PW<sub>12</sub>O<sub>40</sub> were prepared. Characterization of composites was performed by means of infrared spectroscopy and X-ray powder diffraction analysis and results suggest interaction of heteropoly acid with zeolitic part of the composites. Catalytic activity of synthesized materials was investigated in ethanol dehydration reaction. The lower heteropoly acid loadings induced higher conversion. Acid sites distribution and accessibility for ethanol molecules were found to be more pronounced for catalytic activity than amount of active sites present in these composite materials.

### INTRODUCTION

The Keggin-type polyoxometalates are widely investigated because of their stability, commercial availability, low price and remarkable chemical properties. Accordingly, 12-phosphotungstic acid (HPW) has been used in various industrially important catalytic processes [1]. However, low surface area and high solubility of HPW in polar solvents are restricting properties of this material and improved catalytic performance is studied by their impregnation on inorganic supports. The use of different zeolites and zeolitic structures is attractive in this area [2], because of their ordered pore structures, high thermal stability and large surface area. As the applications of zeolites are very limited due to their low stability in acidic medium, in this work we investigated zeolite BEA because of its known strength toward acid degradation. The aim of this study was to investigate the influence of Keggin-type HPW/BEA ratio and different preparation routes on catalytic activities of synthesized composites. Different samples, comprising 20 to 50

wt.% HPW supported on zeolite BEA, were characterized by XRD, FTIR and their catalytic activities in ethanol dehydration reaction were studied.

### EXPERIMENTAL

Beta zeolite was obtained from Zeolyst Int. (CP814E,  $\text{SiO}_2/\text{Al}_2\text{O}_3 = 25$ , ammonium form). It was thermally treated at 550 °C for 5 hours and converted to hydrogen form (HBEA). 12-tungstophosphoric acid hexahydrate ( $\text{HPW} \cdot 6\text{H}_2\text{O}$ ) was synthesized according to the literature method [3] and recrystallized prior to use. Four suspensions were made by mixing 10 g of HBEA zeolite and 150 mL of distilled water. Certain amount of HPW was added to each suspension so desired HPW : BEA mass ratio (20, 30, 40 and 50 wt%) was achieved. Suspensions were stirred using magnetic stirrer for 4 hours and then left to age for 24 hours. One part of each composite was dried at 80 °C and these samples are marked as BPW 20-50. The other part was dried at 80 °C and then thermally treated at 300 °C for 4 hours (samples BPW20c-50c). Powder X-ray diffraction patterns were collected using a Philips PW-1710 automated diffractometer. The instrument was equipped with a Cu anode, curved monochromator and Xe-filled proportional counter. Diffraction data were collected in the 5–40  $2\theta$  range with a step size of 0.02 and a counting time of 1 s per step for all samples. FTIR spectra of the powdered samples, dispersed in potassium bromide and compressed into pellets, were recorded in the range of 1600–400  $\text{cm}^{-1}$  at 64 scans per spectrum at 2  $\text{cm}^{-1}$  resolution using a Nicolet 6700 FTIR Spectrometer (Thermo Scientific). The catalytic activities of synthesized composites were tested in a vapor phase ethanol dehydration reaction at 300 °C under atmospheric pressure. Liquid ethanol was pumped at a flow rate of 1.2 mL/h into the evaporator (150 °C) where it was mixed with nitrogen and air. The products were detected by means of Hewlett Packard 5890 GC gas chromatograph equipped with a flame ionization detector (FID) and Porapak QS column.

### RESULTS AND DISCUSSION

Crystallinity of synthesized composites and the influence of HPW on the structure of BEA zeolite were investigated using XRPD technique. Diffractograms of selected samples are shown in Fig.1. and no reflections belonging to HPW were observed, so it could be assumed that HPW molecules are impregnated mostly on the surface of BEA zeolite. Small but observable widening of two strongest reflections ( $2\theta = 7.68^\circ$  and  $22.54^\circ$ ) of BEA zeolite could be noticed in patterns belonging to composites. This indicates that HPW molecules bring some disorder in the crystal structure of

BEA zeolite.

FTIR spectra of the synthesized samples are shown in the Fig. 2. Fingerprint region of HPW shows strong vibrational bands at  $983\text{ cm}^{-1}$ ,  $890\text{ cm}^{-1}$  and one very broad and strong band at around  $800\text{ cm}^{-1}$ . These three bands are assigned as W-O<sub>d</sub>, W-O<sub>b</sub>-W and W-O<sub>c</sub>-W stretching vibrations

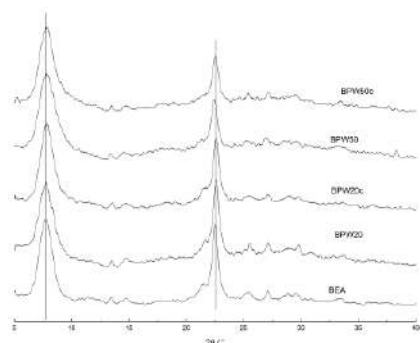


**Figure 1.** XRPD patterns of selected composites.

where W is heteroatom, O<sub>b</sub> is corner-sharing oxygen from WO<sub>6</sub>, O<sub>c</sub> is edge sharing oxygen from WO<sub>6</sub> and O<sub>d</sub> is terminal oxygen [4]. All three vibrations are present in spectra of composite samples, so Keggin structure is not disturbed during the synthesis process. In the selected region, BEA zeolite has one absorption band at around  $800\text{ cm}^{-1}$  which could be assigned to Si-O stretching vibration and one weak and very broad band at  $940\text{ cm}^{-1}$ . Absorption band at around  $800\text{ cm}^{-1}$  is present in all

spectra and its width increases with increasing amount of HPW due to superposition of zeolite band and HPW band. Band at  $940\text{ cm}^{-1}$  is not present in composite samples, but there is band at  $960\text{ cm}^{-1}$  and weak shoulder at  $750\text{ cm}^{-1}$ . This shoulder is more pronounced in spectra of dried composites at  $80\text{ °C}$  (figure not shown) comparing to the calcinated samples. The appearance of new band at  $960\text{ cm}^{-1}$  and weak shoulder at  $750\text{ cm}^{-1}$  indicates the interaction of the active phase and the support.

Catalytic activity of the calcinated samples was investigated for ethanol conversion reaction, see Fig. 3. Dehydration of ethanol to ethylene and diethyl ether occurs on acid sites of catalyst, thus, the high catalytic activity is presumed for HPW [4]. It would be expected that presence of both, HPW and BEA zeolite with acid active sites could enhance the composite catalytic activity. It is obvious that lower PW loadings induce higher conversion, when compared to the samples with 50 % loading.

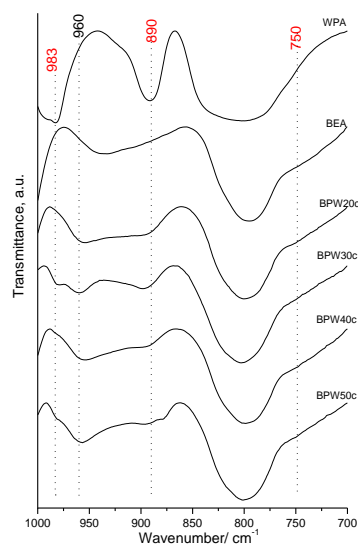


**Figure 2.** FTIR spectra of selected composites.

This result could point to the better dispersion of HPW active phase and larger surface area of samples with lower HPW content. Large HPW molecules could block zeolitic channels and active sites when high loadings were accomplished. Acid sites dispersion and availability for ethanol molecules were found to be essential for catalytic activity rather than amount of active sites in composite samples.

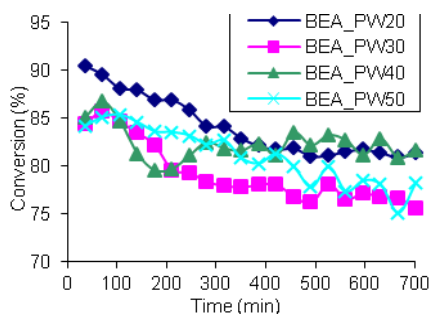


**Figure 3.** Ethanol conversion a obtained for BPW 20-50 composites

interactions of heteropoly acid and zeolitic part of composite samples were found by means of XRPD and FTIR measurements. Catalytic activity of calcinated samples was investigated for ethanol conversion reaction. It was found that lower HPW loadings induce higher conversion, which could point to the better dispersion of HPW active phase and larger surface area of samples with lower HPW content. Acid sites dispersion and availability for ethanol molecules were found to be essential for catalytic activity rather than amount of active sites in composite samples.

## CONCLUSION

In this study the Keggin-type HPW species were supported on BEA zeolite via different composite preparation routes. Strong

## Acknowledgement

This work was partially supported by the Ministry for Science of the Republic of Serbia (Grants no. OI172018 and OI172043).

## REFERENCES

- [1] G. S. Armatas, Heterogeneous Polyoxometalate-Containing Mesoporous Catalysts. 2013, 311–342.
- [2] J. B. Moffat, Metal-oxygen clusters: the surface and catalytic properties of heteropolyoxometalates. Kluwer Academic, New York, 2001.
- [3] G. Brauer, Handbuch der Preparativen Anorganischen Chemie, Ferdinand Enke Verlag, Stuttgart, 1981.
- [4] I. D. Holclajtner-Antunović, A. Popa, D. V. Bajuk-Bogdanović, S. Mentus, B. M. Nedić Vasiljević, S. M. Uskoković-Marković, Synthesis and characterization of acid silver salts of 12-tungstophosphoric acid. *Inorganica Chimica Acta*, 2013, **407**, 197–203.

## FTIR SPECTROSCOPIC CHARACTERIZATION OF COMPOSITE BIOMATERIAL NANO HYDROXYAPATITE COATED WITH CHITOSAN- POLY(LACTIC-CO-GLYCOLIC ACID)

Ž. Mitić<sup>1</sup>, S. Najman<sup>1</sup>, S. Stojanović<sup>1</sup>, A. Stolić<sup>1</sup>, M. Trajanović<sup>2</sup>, N. Ignjatović<sup>3</sup>, J. Veselinović<sup>1</sup>, A. Veselinović<sup>1</sup> and M. Cakić<sup>4</sup>

<sup>1</sup>*Faculty of Medicine, University of Niš, RS-18000 Niš, Serbia  
(zak\_chem2001@yahoo.com)*

<sup>2</sup>*Faculty of Mechanical Engineering, University of Niš, RS-18000 Niš, Serbia*

<sup>3</sup>*Institute of Technical Sciences of the Serbian Academy of Sciences and  
Arts, RS-11000 Belgrade, Serbia*

<sup>4</sup>*Faculty of Technology, University of Niš, RS-16000 Leskovac, Serbia*

### ABSTRACT

Chitosan is considered to be one of the most valuable polymers which are used in the pharmaceutical and biomedical purposes. The analysis of hydroxyapatite/chitosan (HAp/Chi) and hydroxyapatite/chitosan-poly(lactic-co-glycolic acid) (HAp/Chi-PLGA) particles by Fourier transform infrared (FTIR) spectroscopy were examined in this work. As a result of strong interactions between single components, there is a formation of homogeneous Chi blends with HAp and PLGA. FTIR results confirmed well-modified surface of polymer blends after coating of nano HAp and formation of particles.

### INTRODUCTION

FTIR spectroscopy can provide molecular structure information about mineralized and non-mineralized connective tissues and different composite biomaterials were used as bone substitutes [1]. Chitosan is the one of the most abundant naturally biopolymer and the supporting material of insects, crustaceans etc. Structurally chitosan is a copolymer composed of randomly distributed  $\beta$ -(1 $\rightarrow$ 4)-linked D-glucosamine and N-acetyl-D-glucosamine, being obtained by the deacetylation of chitin, although this deacetylation is almost never complete [2]. Chitosan is considered one of the most valuable polymers for biomedical and pharmaceutical applications due to its biodegradability, biocompatibility, antimicrobial, non-toxicity, and anti-tumor properties [3, 4]. Chitosan and its derivatives are useful as carriers in drug delivery systems or cell culture owing to their specificity, as antibacterial agents, and in other medical applications. [3–5].

## EXPERIMENTAL

PLGA (50:50, Sigma, USA) and chitosan (Aldrich, deacetylation >75%) dissolved in acetone and acetic acid were mixed with the HAp gel in a mass ratio of 2:2:6. Water solution of poloxamer 188 (polyethylenepolypropylene glycol, 0.1 vol.%) was added drop-wise to the mixture of chitosan, PLGA and HAp gel, while stirring at 21,000 rpm [6]. The FTIR spectra as an average of 200 scans were recorded at room temperature on a BOMEM MB-100 spectrometer equipped with a standard DTGS/KBr detector in the range of 4000–400  $\text{cm}^{-1}$  with a resolution of 2  $\text{cm}^{-1}$ . The spectrometer was purged with dry nitrogen gas. In the region all spectra were baseline-corrected and area-normalized. A Fourier self-deconvolution method was applied to enhance the resolution in a spectral region of 4000–400  $\text{cm}^{-1}$ .

## RESULTS AND DISCUSSION

The results of IR analysis are shown in Fig. 1 (FTIR spectra), and the assignments of characteristic IR bands of single components were explained in details previously [6].

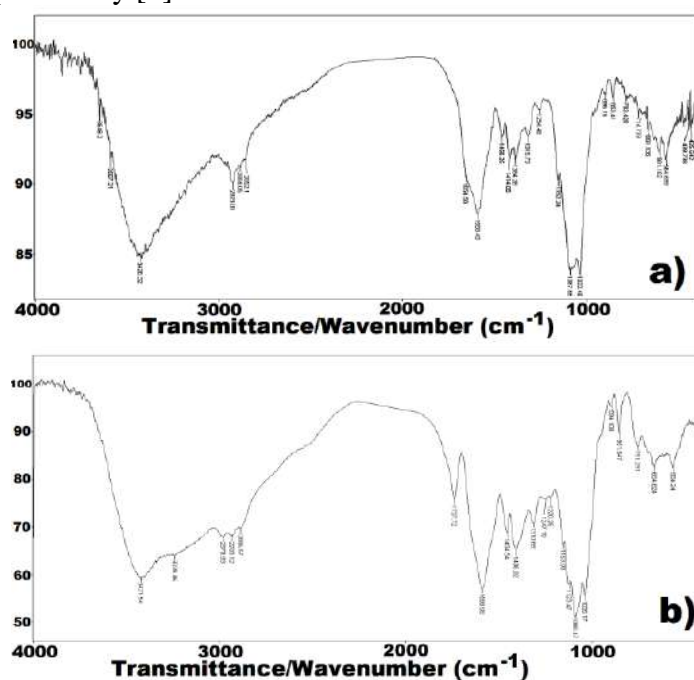


**Figure 1.** FTIR spectra of (a) HAp/Chi and (b) HAp/Chi-PLGA particles samples

**HAp/Chi.** The IR spectrum of HAp/Chi particles sample is shown in Fig. 1a. The IR spectrum is characterized by absorption bands arising from HAp and

Chi, determined by analogy with the IR spectra of pure HAp and the same Chi standard samples. Analysis of the FTIR spectrum on Fig. 1a was revealed significant differences from the spectra of the single component materials. The sharp bands at 2923 and 2862  $\text{cm}^{-1}$  are assigned to  $\nu(\text{CH})$  of the polysaccharide chitosan [7] and IR bands with maxima at 1087, 1033, 601 and 564  $\text{cm}^{-1}$  arise from the phosphate groups of HAp [8]. A part of FTIR spectra, in the range on 1000–700  $\text{cm}^{-1}$  indicates no influence of blending process on the conformation change of C<sub>1</sub> glucopyranose units [6]. Formation of homogeneous Chi blends with HAp and PLGA is a result of strong interactions by hydrogen bonds between the functional groups of the blend components in which amino and amide groups present in Chi take part [9]. The analysis of FTIR spectra of the blends enables these interactions to be identified. Broadening of the strong IR band approx. 1087  $\text{cm}^{-1}$ , corresponding to the  $\text{PO}_4^{3-}$  ions of HAp (Fig. 1a), shows the presence of polysaccharide chitosan and its interaction with phosphate groups. It implies that the hydrogen bonding may be formed between the  $\text{PO}_4^{3-}$  ions and  $-\text{N}-\text{H}$  of the Chi [10].

The peaks at 1655  $\text{cm}^{-1}$ , 1588  $\text{cm}^{-1}$  and 1315  $\text{cm}^{-1}$  are due to the amide I, amide II and amide III bands of polysaccharide chitosan. The band at 1655  $\text{cm}^{-1}$  decreased and the band at 1588  $\text{cm}^{-1}$  increased in the Chi after coating with HAp, indicating the interaction of the amide on the chitosan and OH groups on the HAp (Fig. 1a). Much greater changes are observed in the spectrum of HAp/Chi-PLGA particles sample (Fig. 1b).

**HAp/Chi-PLGA.** The IR spectrum of HAp/Chi-PLGA particles sample is shown in Fig. 1b. The IR spectrum contains already mentioned absorption bands arising from HAp, PLGA and Chi. Specific IR bands of polysaccharide chitosan were observed at around 3500–3200  $\text{cm}^{-1}$  for N–H stretching, at 2980–2880  $\text{cm}^{-1}$  for C–H stretching, at 1737  $\text{cm}^{-1}$  for C=O stretching, at 1588  $\text{cm}^{-1}$  for N–H bending, at 1500–1350  $\text{cm}^{-1}$  for C–H bending and approx. 1310  $\text{cm}^{-1}$  for C–N stretching.

The most significant differences in the FTIR spectra of **HAp/Chi-PLGA** (Fig. 1b) in comparison with **HAp/Chi** (Fig. 1a) are increasing the band at 1588  $\text{cm}^{-1}$  (amide II) and overlapping the band at 1655  $\text{cm}^{-1}$  (amide I) in the polymer blends of Chi-PLGA after coating of HAp, indicating the interaction of the amide on the chitosan and OH groups on the HAp (Fig. 1a). The appearance of new band, pronounced as a shoulder, at lower frequency approx. 3239  $\text{cm}^{-1}$  which is from hydrogen bonded OH (Fig. 1b) is due to the HAp and Chi-PLGA interactions, which confirms well-modified surface of polymer blends Chi-PLGA after coating of HAp. The addition of chitosan also affected the localized bonding structure of the

phosphate groups in HAp seen from the broadening of  $\text{PO}_4^{3-}$  group bands [11].

### CONCLUSION

FTIR results of HAp/Chi and HAp/Chi-PLGA particles show the interaction between single components, which confirms well-modified surface of polymer blends Chi and Chi-PLGA after coating of HAp. A part of FTIR spectra, in the range on  $1000\text{--}700\text{ cm}^{-1}$  indicates no influence of blending process on the conformation change of  $\text{C}_1$  glucopyranose units.

### Acknowledgement

This work was supported by the Ministry for Science of the Republic of Serbia (Grant **III 41017**; <http://vihos.masfak.ni.ac.rs/site/>).

### REFERENCES

- [1] N. Ignjatović, V. Savić, S. Najman, M. Plavšić, D. Uskoković, *Biomaterials*, 2001, **22**, 571–575.
- [2] N.V. Majeti, R. Kumar, 2000, **46**, 1–27.
- [3] M. N. V. R. Kumar, R. A. A. Muzzarelli, C. Muzzarelli, H. Sashiwa, A.J. Domb, *Chemical Reviews*, 2004, **104**, 6017–6084.
- [4] S. Hitoshi, A. Sei-ichi, *Prog. Polym. Sci.* 2004, **29**, 887–908.
- [5] I. Manjubala, S. Scheler, J. Bössert, K.D. Jandt, *Acta Biomaterialia*, 2006, **2**, 75–84.
- [6] N. Ignjatović, S. Vranješ Djurić, Ž. Mitić, D. Janković, D. Uskoković, *Materials Science and Engineering C*, 2014, **43**, 439–446.
- [7] J. Brugnerotto, J. Lizardi, F.M. Goycoolea, W. Argüelles-Monal, J. Desbrières, M. Rinaudo, *Polymer*, 2001, **42**(8), 3569–3580.
- [8] S. Marković, L. Veselinović, M.J. Lukić, L. Karanović, I. Bračko, N. Ignjatović, D. Uskoković, *Biomedical Materials*, 2011, **6**. art. no. 045005.
- [9] A. Pawlak, M. Mucha, *Thermochimica Acta*, 2003, **396**, 153–166.
- [10] G. Zu, Y. Li, Z. Li, H. Li, M. Wang, L. Cheng, Y. Wang, H. Wang, P. Shi, *J Mater Sci* 2007, **42**, 2591–2597.
- [11] R. Kumar, K.H. Prakash, P. Cheang, L. Gower, K.A. Khor, *J. R. Soc. Interface*, 2008, **5**, 427–439.

## SILVER-COATED SELF-ASSEMBLED POLYSTYRENE SPHERES FOR SURFACE-ENHANCED RAMAN SPECTROSCOPY

L. Mikac<sup>1</sup>, M. Ivanda<sup>1</sup>, M. Gotić<sup>1</sup>, V. Janicki<sup>2</sup>, H. Zorc<sup>2</sup>, T. Janči<sup>3</sup>  
and S. Vidaček<sup>3</sup>

<sup>1</sup>*RuđerBošković Institute, Center of Excellence for Advanced Materials and Sensing Devices, Bijenička c. 54, Zagreb, Croatia (ivanda@irb.hr)*

<sup>2</sup>*RuđerBošković Institute, Laboratory for optics and thin films, Bijenička c. 54, Zagreb, Croatia*

<sup>3</sup>*University of Zagreb, Faculty of Food Technology and Biotechnology, Department of Food Engineering, Laboratory for Meat and Fish Technology, Pierottijeva 6, Zagreb, Croatia*

### ABSTRACT

In this work, monodispersed polystyrene (PS) spheres were drop coated on hydrophilic glass substrates to form a self-assembled 2D monolayer. Silver films over nanospheres (AgFONs) were prepared by depositing 120, 180 and 240 nm of Ag over 1  $\mu\text{m}$  spheres and 80, 120, 160 and 200 nm of Ag over 370 nm spheres as well as on their mixture. Ag was deposited from an electron beam evaporation source. These substrates were used to record the Surface-enhanced Raman scattering (SERS) spectra of rhodamine 6G and pyridine ( $\lambda_{\text{ex}}=514.5$  nm). For 1  $\mu\text{m}$  spheres optimal thickness of Ag film was 180 nm, while for 370 nm spheres and the mixture of spheres the best results were achieved for 80 nm Ag film. The detection limit for R6G was  $10^{-9}$  M. The SERS spectrum of pyridine was measured from a drop of solution before it had dried. The pyridine detection limit was  $1.2 \times 10^{-4}$  M.

### INTRODUCTION

Nowadays, a number of spectroscopic techniques are available for the analysis of various materials and substances. Among them, Raman spectroscopy is a powerful analytical technique that allows the identification and quantification of a large number of molecules even in complex matrices. The discovery of Surface-enhanced Raman spectroscopy (SERS) in 1974 has attracted great attention because of the high increase of otherwise weak Raman signal [1]. For a successful detection of an analyte by SERS most important are a good selection of metal and nanostructure of the substrate that determine the increase of Raman signal. There are a number of methods to produce SERS substrates [2]. Recently, interest has focused on affordable

substrates and simpler production processes. In addition, the motive for the design of simple SERS substrate is the development of portable Raman spectrometers and the use of SERS in the field of medicine, forensics, security, food industry, environmental protection etc.

In this paper, we present the SERS substrates produced by drop coating of monodispersed polystyrene (PS) nanospheres and the deposition of Ag films with electron beam evaporator. It was possible to detect low concentration of SERS probe molecules on thus prepared substrates.

### EXPERIMENTAL

The microscopic slides were cut into  $\sim 1.5 \times 2.5$  cm pieces and sonicated in acetone. The slides were treated in ultrasonic bath using SC1 solution ( $\text{NH}_4\text{OH}:\text{H}_2\text{O}_2:\text{H}_2\text{O}=1:1:5$ (v/v)) at  $80^\circ\text{C}$  for 20 minutes.

Polystyrene microspheres, PS, (370 and 1000 nm and the mixture) were diluted with methanol and Triton X-100 (1: 400) and drop coated on the slide. Thus prepared slides were put in a vacuum to dry.

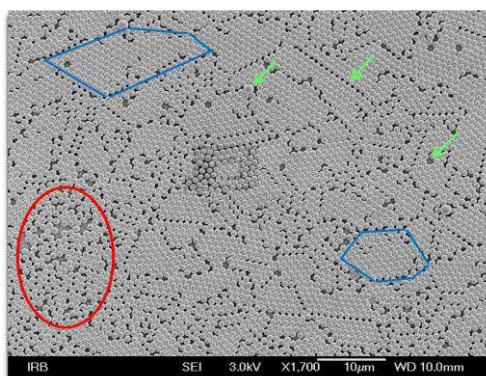
Silver was deposited from an electron beam evaporation source in various thicknesses: on 1  $\mu\text{m}$  PS - 120, 180 and 240 nm, while on 350 nm and (350+1000) nm PS - 80, 120, 160 and 200 nm films were evaporated.

The morphology was examined with Jeol JSM 7000F field emission scanning electron microscope coupled with Energy-dispersive spectroscopy.

SERS spectra were recorded by Horiba Jobin Yvon T64000 micro Raman system (514.5 nm). To reduce the photo degradation, filters were used. SERS spectra were acquired using  $100\times$  objective. Prior to recording the spectra, 2  $\mu\text{L}$  of the testing molecules was applied to the substrate.

### RESULTS AND DISCUSSION

The number of PS in the monolayer that can cover a specific area can be determined mathematically. Excessive amounts of spheres leads to the formation of multiple layers while too little results in spheres islands. To spread PS evenly across the surface they must be diluted. Various dilutions with methanol have been tried (1:1, 1:2, 1:3), but the best results gave 1:1 ratio. We used Triton X-100 because it was shown to increase the monolayer area due to reduction of hydrophobic interactions between spheres [3]. The optimum size of monolayer area (Fig. 1) was achieved after drying the substrate in a vacuum in an ethanol atmosphere on a flat surface.



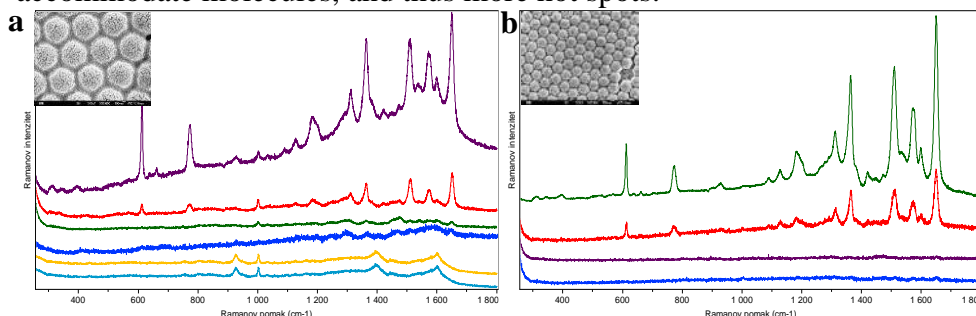
**Figure 1.** SEM image of 1  $\mu\text{m}$  PS: red - spheres not organized in hexagonal close packing, blue - monolayer subdomains, green arrows - defects.

Fig. 2. a shows the resulting R6G SERS spectra on 180 nm Ag/1000 nm PS substrate. In the case of substrates with 1  $\mu\text{m}$  spheres by far the best enhancement for R6G was obtained for 180 nm silver layer. The lowest concentration of R6G that could be detected in this sample was  $10^{-9}$  M. The spectrum of PS (yellow spectrum) and the spectrum of 180 nm Ag evaporated on PS (light blue) are similar and corresponds to the spectra of polystyrene spheres in literature (band at  $\sim 1002\text{ cm}^{-1}$ ) [4]. However, there are other bands ( $1390, 1590\text{ cm}^{-1}$ ) that could result from amorphous carbon or degradation of spheres although low laser power was used (0.5 mW).

When using 350 nmPS, the best results were obtained for 80 nm silver layer. The resulting spectra are shown in Fig. 2b. The limit of detection for R6G on this sample is between  $10^{-8}$  and  $10^{-9}$  M. R6G SERS spectra were also obtained from surfaces that were prepared by mixing spheres (350+1000 nm). In this case the best enhancement was obtained for 80 nm Ag film and the lowest detected R6G concentration was  $10^{-8}$  M. The enhancement of the Raman signal was tested with R6G on substrates where Ag was evaporated on clean glass slide (without PS). In the case of 180 nm Ag film LOD was  $10^{-6}$  M while in the case of 80 nm film LOD was  $10^{-5}$  M.

The spectrum of pyridine (as a second test molecule) was recorded before the applied drop had dried. The best enhancement was obtained for the same film thickness as in the case of R6G. The LOD for pyridine was  $1.02 \times 10^{-3}$  M. We noticed that for the good SERS enhancement small changes in the structure and size of evaporated silver particles are essential. A significant enhancement (of the order of 2-3) on samples where silver is evaporated on PSas compared to samples where silver is evaporated on glass surface can be attributed to a much greater area which is available for adsorption of the

test molecules, i.e. there is a greater number of channels and gaps that can accommodate molecules, and thus more hot spots.



**Figure 2.** R6GSERS spectra: a) 180 nm Ag over 1000 nm PS and b) 80 nm Ag over 350 nm PS. From top to bottom  $10^{-6}$  M,  $10^{-8}$  M,  $10^{-9}$  M and  $10^{-5}$  M R6G on Ag without PS (514.5 nm, 0.5 mW, accumulation 30 s).

## CONCLUSION

SERS substrates were prepared using monodisperse polystyrene spheres (350 and 1000 nm) which were deposited in a monolayer on a hydrophilic glass surface. For the deposition of spheres drop coating method was used due to its simplicity and speed. On the prepared spheres silver films of varying thickness were evaporated. Using the test molecules, rhodamine 6G and pyridine, SERS activity of our substrate was tested and optimal thickness of the deposited Ag film was determined. Best increase of Raman signal for both test molecules was obtained on the 180 nm Ag film deposited on 1  $\mu$ m spheres and on the 80 nm film deposited on 350 nm spheres. The lowest detectable concentration of R6G was  $10^{-9}$  mol L $^{-1}$  and pyridine  $1.2 \times 10^{-3}$  mol L $^{-1}$ . By using monodisperse polystyrene spheres suitable SERS substrates were obtained in a quick and easy way.

## Acknowledgement

This work has been fully supported by Croatian Science Foundation under the project (IP-2014-09-7046).

## REFERENCES

- [1] M. Fleischmann, P. J. Hendra, A. J. McQuillan, *Chem. Phys. Lett.*, 1974, **26**, 163-166.
- [2] L. Mikac, M. Ivanda, V. Đerek, M. Gotić, *J. Raman Spectrosc.* (2016) doi: 10.1002/jrs.4911.
- [3] J. C. Hulteen, R. P. Van Duyne, *J. Vac. Sci. Technol., A*, 1995, **13**, 1553-1558.
- [4] B. Jasse, R.S. Chao, J. L. Koenig, *J. Polym. Sci. Pol. Phys.*, 1978, **16**, 2157-2169.

## RADIOLYTIC INCORPORATION OF GOLD NANOPARTICLES INTO PVA HYDROGEL

A. Radosavljević, J. Krstić, J. Spasojević and Z. Kačarević-Popović

*Vinča Institute of Nuclear Sciences, University of Belgrade, P.O. Box 522,  
11001 Belgrade, Serbia (krkljes@vinca.rs)*

### ABSTRACT

This work describes the Au-PVA hydrogel nanocomposites synthesized by radiolytic *in situ* incorporation of gold nanoparticles (Au NPs) into poly(vinyl alcohol) (PVA) hydrogel. Synthesis of nanocomposites was conducted as two-step gamma irradiation induced process. In the first step, the crosslinking of polymer chains occurs and PVA hydrogel with a large number of pores was obtained. In the second step, these pores serve as nanoreactors for the formation of Au NPs. The presence of Au NPs was confirmed by absorption spectra, while morphological and structural analysis reveals the spherical shape of Au NPs, with the diameter around 15 nm and *fcc* crystal structure. The structural parameters of xerogels indicate that incorporation of Au NPs induce the expansion of polymer network. Long-time stability of Au-PVA hydrogel nanocomposites is caused by interactions between the surface of Au NPs and OH groups of PVA chains.

### INTRODUCTION

Hydrogel nanocomposites are a new class of hybrid materials which can be defined as swollen crosslinked polymer networks with incorporated nanoparticles or some other nanostructures [1]. This crosslinked structures are capable to absorb significant amounts of water or biological liquids without dissolving or losing their structural integrity [2]. In recent years, numerous studies have been focused on the hydrogel nanocomposites, because the crosslinked polymer networks (hydrogels) represent a promising solution for stabilization, size control and uniform distribution of NPs. The presence of NPs can improve the existing properties of hydrogels and/or add them new unique physical properties, which make the hydrogel nanocomposites as ideal candidates for application in the electronics, optics, sensors, catalysis, drug delivery and other biotechnological areas [2,3].

In this study, PVA hydrogel (previously obtained by gamma irradiation) was used as template for stabilization of Au NPs, during their *in situ* gamma irradiation induced synthesis. PVA is water-soluble transparent polymer, biocompatible and biodegradable, while Au NPs have received great interests

due to attractive thermal, catalytic, optical, electronic and antimicrobial properties. The radiolytic synthesis was chosen because it is suitable for both formation of polymer network and metal NPs. It has many advantages over conventional methods: the process is easily controlled, do not leave any toxic residues, and promote simultaneous synthesis and sterilization of materials [4].

### EXPERIMENTAL

The 5 wt% PVA solution was exposed to gamma irradiation ( $^{60}\text{Co}$  source, absorbed dose 25 kGy, dose rate 0.5 kGy/h) to induce crosslinking and formation of polymer network. PVA hydrogel was extracted in water for 7 days and dried to the constant mass. The obtained PVA xerogel was swelled by Ar-saturated solutions containing  $3.5 \times 10^{-3}$  M and  $7.0 \times 10^{-3}$  M of  $\text{HAuCl}_4$ , with addition of 0.2 M 2-propanol, and exposed to gamma irradiation (dose rate 10 kGy/h) up to 17 kGy and 34 kGy, respectively, to perform *in situ* reduction of gold ions and formation of Au NPs. Optical properties of Au-PVA hydrogel nanocomposites were investigated by Thermo Fisher Scientific Evolution 600 UV-Vis spectrophotometer. Morphology of lyophilized PVA hydrogel as a matrix was analyzed by SEM (JEOL JSM-6610LV, operated at 20 kV). The size and shape of Au NPs were investigated by TEM (Philips EM 400, operated at 120 kV). Au-PVA xerogel nanocomposite was grinded in ball mill, dispersed in distilled water and deposited on C-coated copper grid. Microstructural properties of nanocomposites were examined by XRD (Bruker D8 Advance Diffractometer,  $\text{Cu K}\alpha_1$  radiation,  $\lambda = 0.1541$  nm), while the interaction between incorporated Au NPs and PVA hydrogel was investigated by FTIR spectroscopy (Thermo Electron Corporation Nicolet 380 spectrophotometer, ATR mode). Macroscopic properties of xerogels (xerogel density ( $\rho_{\text{xg}}$ ) and equilibrium swelling degree ( $\text{SD}_{\text{eq}}$ )) and their primary structural properties (average molar mass between crosslinks ( $M_c$ ), crosslinking density ( $\rho_c$ ) and pore size ( $\xi$ )) were determined as described in the literature [5].

### RESULTS AND DISCUSSION

PVA hydrogel was obtained by gamma irradiation induced crosslinking of polymer chains.  $\text{PVA}^\bullet$  radicals, generated in the process of hydrogen abstraction from polymer chain by  $\text{OH}^\bullet$  and  $\text{H}^\bullet$  radicals (products of water radiolysis), interact with each other and finally form crosslinked polymer network [6]. The SEM micrograph (Fig. 1) clearly illustrates the porous

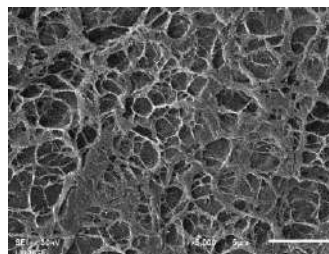


**Figure 1.** SEM micrograph of PVA hydrogel.

structure of obtained PVA hydrogel, with a large number of pores. Under the gamma irradiation,  $\text{Au}^{3+}$  ions are reduced by solvated electrons and 2-propanol radicals (primary and secondary reduction species) through the complex multi-step process. Formation of  $\text{Au}^0$  atoms is followed by their aggregation into the clusters of higher nuclearity, and finally resulting in formation of Au NPs [7]. The obtained Au-PVA hydrogel nanocomposites have wine-red color which indicates the formation of Au NPs, while the UV-Vis absorption spectra (Fig. 2(a)) clearly show the characteristic surface plasmon resonance (SPR) band of Au NPs around 540 nm. The position, intensity and width of the SPR band depends on size, shape and surface structure of NPs as well as on dielectric constant and refractive index of medium in which NPs are embedded. Therefore, absorption spectra can be used to determine the size of metal NPs [8]. The mean diameter of Au NPs incorporated in PVA hydrogel is around 15 nm.

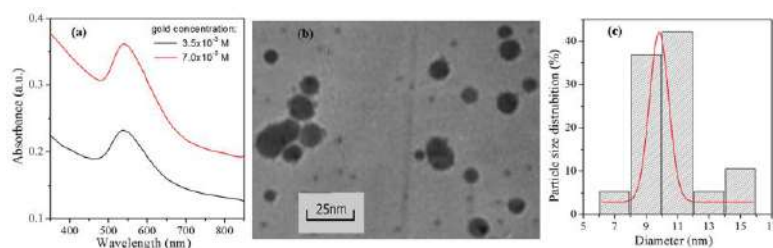


**Figure 2.** (a) UV-Vis absorption spectra of Au-PVA hydrogel nanocomposites, (b) TEM micrograph and (c) size distribution of Au NPs.

The shape and size distribution of the Au NPs were examined by TEM. Typical micrograph (Fig. 2(b)) reveals presence of spherical non-aggregated Au NPs in the size range from 6 nm to 16 nm, with the average diameter around 10 nm (Fig. 2(c)).

The XRD pattern of Au-PVA xerogel nanocomposite is shown in Fig. 3(a). The XRD peaks correspond to Bragg's reflections from the crystalline planes (111), (200) and (220) of Au NPs with the face centered cubic (*fcc*) crystal structure (JCPDS Card No. 04-0784). According to the Scherrer's equation [9], the crystalline domain size was found to be around 20 nm, which is slightly higher compared to size of Au NPs determined by UV-Vis spectroscopy and TEM analysis.

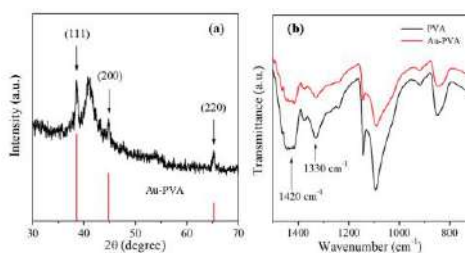


**Figure 3.** (a) XRD pattern and (b) FTIR spectra of investigated samples.

The primary structural properties of xerogels were calculated using equations given in the literature [5]. The increased values of  $SD_{eq}$ ,  $M_c$  and  $\xi$  for nanocomposites indicate that incorporation of Au NPs induce the expansion of polymer network.

**Table 1.** The structural parameters for xerogels in distilled water at 25 °C.

Sample	$\rho_{xg}$ (g/cm <sup>3</sup> )	$SD_{eq}$ (g/g)	$M_c$ (g/mol)	$\rho_c \times 10^4$ (mol/cm <sup>3</sup> )	$\xi$ (nm)
PVA	1.27	16.4	3834	3.3	16.4
Au(3.5)-PVA	1.36	17.1	4879	2.8	19.1
Au(7.0)-PVA	1.43	17.9	5938	2.4	21.7

The interaction of Au NPs and PVA matrix was investigated by FTIR spectroscopy (Fig. 3(b)). The decrease in the intensity ratio between bands at 1420 cm<sup>-1</sup> (O–H in plane vibration) and 1330 cm<sup>-1</sup> (C–H wagging vibrations) with incorporation of Au NPs implies that decoupling between these vibrations takes place. These results indicate that main interaction between surface of Au NPs and PVA chains occurs over OH groups [9].

## CONCLUSION

The gamma irradiation induced *in situ* incorporation of Au NPs into PVA hydrogel was successfully performed. The synthesized Au NPs are spherical in shape, with the mean diameter around 15 nm and *fcc* crystal structure. The structural parameters of xerogels indicate that incorporation of Au NPs induce the expansion of polymer network. Long-time stability of Au NPs and Au-PVA hydrogel nanocomposites occurs as a result of interactions between the surface of Au NPs and OH groups of PVA chains.

## Acknowledgement

This work is financed by the Ministry of Education, Science and Technological Development of the Republic of Serbia, project III 45005.

## REFERENCES

- [1] P. Schexnailder et al., Coll. Polym. Sci., 2009, **287**, 1-11.
- [2] N.A. Peppas, A.G. Mikos in: Hydrogels in Medicine and Pharmacy, N.A. Peppas (Ed.), CRC Press, Boca Raton, 1986.
- [3] P. Thoniyot et al., Adv. Sci., 2015, **2**, Article No. 1400010.
- [4] J.M. Rosiak et al., Radiat. Phys. Chem., 1999, **55**, 139-151.
- [5] J. Jovanović et al., J. Appl. Polym. Sci., 2013, **127**, 3550-3559.
- [6] A. Chapiro, Radiation Chemistry of Polymeric Systems, Interscience, New York, 1962.
- [7] E. Gachard, et al., New J. Chem., 1998, **22**, 1257-1265.
- [8] W. Haiss et al., Anal. Chem., 2007, **79**, 4215-4221.
- [9] Radosavljević et al., J. Appl. Polym. Sci., 2012, **125**, 1244-1251.

## TUNABLE (STRAIN RESPONSIVE) MICROLENSSES

B. Murić, D. Pantelić, D. Vasiljević, S. Savić-Šević, and B. Jelenković

*Institute of Physics, University of Belgrade  
Pregrevica 118, Zemun 11 080, Belgrade, Serbia (muric@ipb.ac.rs)*

### ABSTRACT

Microlenses prepared on elastic tot'hema eosin sensitized gelatin (TESG) layer can be tuned in a focal length by controlled strain application. By varying the strain, the lenses were deformed uniaxially such that focal lengths from 0.05 mm to 0.2 mm were obtained.

### INTRODUCTION

The microlenses are the small lenses ranging in diameter from several micrometers to nearly 1mm. Tunable microlenses offer attractive applications such as: tunable photonic waveguides, miniature optical sensing, displays, cell phone cameras, and artificial compound eyes [1-5]. Different methods are used for microlenses fabrication: direct laser writing, hot embossing, thermal reflow, droplet process and gray scale photolithography [6-9]. In this paper, TESG microlenses focal length tynability, obtained by applying controlled strain, was presented. The microlenses with different diameter and depth, were produced on a TESG layer using Nd:YAG laser light (532 nm). The elastic, biocompatible, thermally stable, nontoxic, cost-effective layer was prepared easily [10, 11]. The produced adaptive concave TESG microlenses (individual or microlens array) are suitable for various applications. They can be copied onto polydimethylsiloxane (PDMS) and used as convex lenses.

### EXPERIMENTAL

The TESG layer was prepared on a very clean thermoplastic foil that can be easily removed. The TESG preparing procedure described in our previous papers [10, 11]. The layers were dumbbell-shaped specimens (see Fig. 1a) cut from the mold brass (ASTM D412) as shown in Fig.1b.

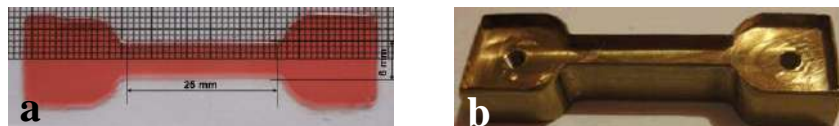


**Figure 1.** The photograph of: a) TEGS layer; b) brass mould- (with ASTM standards dimensions -gauge length 25 mm, width 6 mm)

The microlenses were produced by direct laser writing, using 2<sup>nd</sup> harmonic Nd:YAG laser. The laser power was 60mW with an exposure time of 20 s. The mechanical properties of the TEGS layers were determined in a tensile stress testing machine, as described in [12]. The morphology of TEGS microlenses were investigated using a high resolution scanning electron microscope equipped with a high brightness Schottky field emission gun (FEGSEM) [13].

## RESULTS AND DISCUSSION

According to the TEGS layer elasticity it can be removed from the substrate easily, without damage, even when microlenses are already fabricated. It can be successfully transferred to other, even curved, substrates. During laser irradiation, eosin bleaches, making TEGS microlens colorless. The dumbbell-shaped TEGS layer (before and after stretching) with a formed microlens is shown in Figure 2.

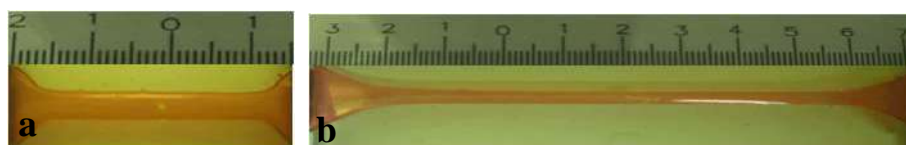


**Figure 2.** The microlens produced on the dumbbell-shaped TEGS layer: a) unstretched; and b) stretched

Microlens fabrication was followed by formation of a diffraction picture on a diffuse screen, with a millimeter scale, placed behind the TEGS layer. A camera was used to record these diffraction patterns shown in Figure 3.

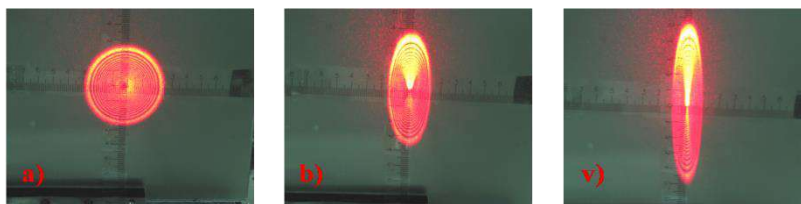


**Figure 3.** Diffraction picture recorded after the TEGS microlens was: a) formed; b and v) stretched in one direction. Millimeter scale is visible.

As a result of material elasticity, it is shown that microlenses formed on the TEGS layer change their properties in response to strain. The stretching of TEGS microlenses in one direction is investigated and extension of the diffraction picture is recorded, as shown in Figure 3. The toric microlenses were obtained, because of uniaxial strain. They are astigmatic, with two

focal lengths along orthogonal directions. For uniform extension (along x and y direction) sphericity of microlenses can be retained.

The relation between the focal length, strain, and diffraction pattern width is shown in Figure 4. As can be seen the microlens focal length exponentially increases with increasing strain of TEGS layer. It was noticed that there is a linear dependence between the microlens focal length and diffraction pattern width. The microlenses focal length was reversibly changed as long as the applied strain is inside the elastic limit.

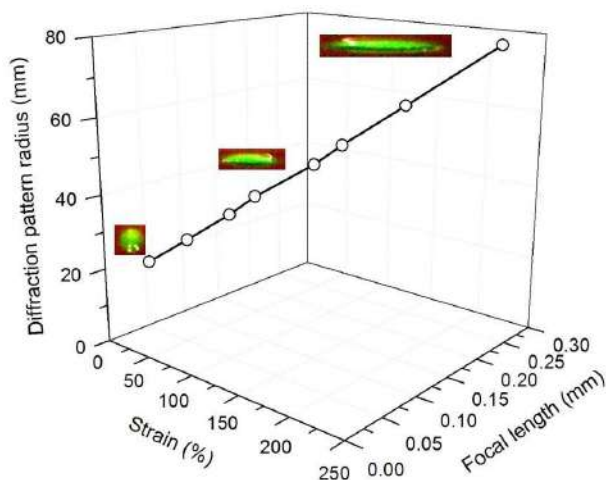


**Figure 4.** TEGS microlens focal length variation with strain and diffraction pattern width

Strain responsive, transparent TEGS microlenses offer interesting possibilities in tunable optical devices and sensors [4-9]. Also, closely packed microlenses arrays can be used to imitate biological compound eyes structure. Hexagonal and 3x3 TEGS microlenses arrays are shown in Figure. 5. The microlenses are capable of producing high-quality image of the any text at its centre (see Figure 5(b)).

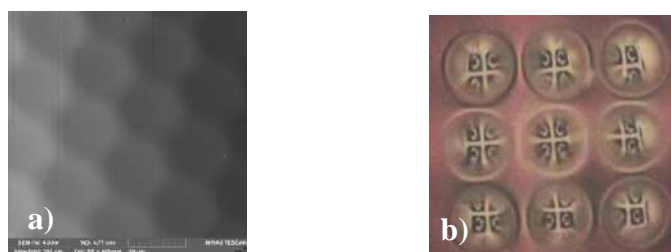


**Figure 5.** Image of hexagonal TEGS microlenses array is recorded using a field-emission gun scanning electron microscope (a) and image of 3x3 microlenses array is recorded using an optical microscope (b)

## CONCLUSION

Tunable (strain responsive) microlenses were prepared on a flexible TEGS layer. By varying the strain to about 250%, the lenses were deformed uniaxially such that focal lengths were changed. The microlenses focal lengths from 0.05 mm to 0.2 mm were obtained.

The TEGS microlenses show good optical and imaging properties. The individual concave microlenses can be used. Also, the large-area square or hexagonal close-packed microlens array can be used for various applications such as: medical laser, optical sensors, light-field cameras, biological structure. Convex microlenses can be produced by coping TEGS lenses onto polydimethylsiloxane (PDMS).

## Acknowledgement

This paper was written as a part of research on the projects ON 171038 and III 45016 supported by the Ministry of education, science and technological development of the Republic of Serbia.

## REFERENCES

- [1] W. L. Liang, G. D. J. Su, *Appl. Opt.* 2014, **53**, H121-H128.
- [2] Z. Deng, F. Chen, Q. Yang, H. Bian, G. Du, J. Yong, C. Shan, X. Hou, *Adv. Funct. Materials* 2016, **26**, 1995-2001
- [3] H. Zhang, L. Li, D. L. McCray, S. Scheiding, N. J. Naples, A. Gebhardt, S. Risse, R. Eberhardt, A. Y. Yi, *Opt. Expr.* 2013, **21**, 22232-22245.
- [4] W. Zhang, H. Zappe, A. Seifert, *Light: Science & Applications* 2014 **3**, e145.
- [5] A. Varshney, S. Gohil, S. K. Tadavani, A. Yethiraj, S. Bhattacharya, S. Ghosh, *Lab Chip* 2014, **14**, 1330-1335.
- [6] D. X. Lu, Y.L. Zhang, D. D. Han, H. Wang, H. Xia, Q. D. Chen, H. Ding, H. B. Sun, *J. Mater. Chem. C* 2015, **3**, 1751-1756.
- [7] J. M. Pavia, M. Wolf, E. Charbon *Opt. Express* 2014, **22**, 4202-4213.
- [8] T. Nisisako, H. Suzuki, T. Hatsuzawa, *Micromac.* 2015, **6**, 1435-1444.
- [9] K. K. Sadasivuni, D. Ponnamma, H. U. Ko, L. Zhai, H. C. Kim, J. Kim, *J. Phys. Chem. B* 2016, **120**, 4699-4705.
- [10] B. Murić, D. Pantelić, D. Vasiljević, B. Panić, *Opt. Mater.* 2008, **30**, 1217-1220.
- [11] A. J. Krmpot, G. J. Tserevelakis, B. D. Murić, G. Filippidis, D. V. Pantelić, *J. Phys. D: Appl. Phys.* 2013, **46**, 195101.
- [12] B. Murić, D. Pantelić, D. Vasiljević, B. Zarkov, B. Jelenković, S. Pantović, M. Rosić, *Phys. Scr.* 2013, **T157**, 014018 (4pp).
- [13] B. Murić, D. Pantelić, D. Vasiljević, S. Savić-Sević, B. Jelenković, *Current Appl. Phys.* 2016, **16**, 57-62.

**THERMALLY INDUCED STRUCTURAL  
TRANSFORMATIONS OF MULTICOMPONENT  
Fe<sub>72</sub>Cu<sub>1</sub>V<sub>4</sub>Si<sub>15</sub>B<sub>8</sub> ALLOY**

M. M. Vasić<sup>1</sup>, R. Surla<sup>2</sup>, J. Papan<sup>3</sup>, N. Begović<sup>4</sup>, N. Mitrović<sup>5</sup> and  
D. M. Minić<sup>1</sup>

<sup>1</sup>*Faculty of Physical Chemistry, University of Belgrade, Serbia*

<sup>2</sup>*Military Technical Institute, Belgrade, Serbia*

<sup>3</sup>*Vinča Institute of Nuclear Sciences, University of Belgrade, Serbia*

<sup>4</sup>*Institute of General and Physical Chemistry, Belgrade, Serbia*

<sup>5</sup>*Faculty of Technical Sciences in Čačak, University of Kragujevac, Serbia*

**ABSTRACT**

Thermally induced structural transformations of Fe<sub>72</sub>Cu<sub>1</sub>V<sub>4</sub>Si<sub>15</sub>B<sub>8</sub> alloy were examined. Thermal analysis revealed multistep structural stabilization process starting at around 470 °C, manifested by two complex exothermic DTA peaks, which were deconvoluted. Microstructure of the as-prepared and thermally treated alloy was studied using XRD. Kinetic triplets of individual steps were determined and further checked by comparing simulated and experimental DTA curves.

**INTRODUCTION**

Nanocrystalline alloys, obtained from the amorphous precursors, have been widely studied in recent time due to many applications based on their favorable functional properties [1,2]. Thermodynamic and kinetic metastability of these materials allow the controlled heat treatment to be used to obtain materials with targeted microstructure and morphology, convenient for many technologically interesting applications. In that way it is possible to obtain nanocrystalline alloys with better functional properties than the purely amorphous and purely crystalline ones. This can be achieved starting with amorphous precursors by controlling the rates of nucleation and crystal growth and by proper choice of chemical composition of the alloy and thermal treatment procedure.

**EXPERIMENTAL**

The nanocrystalline samples of the Fe<sub>72</sub>Cu<sub>1</sub>V<sub>4</sub>Si<sub>15</sub>B<sub>8</sub> alloy were prepared by melt-spinning method. The obtained alloy samples were ribbon-shaped, 2 mm wide and 40 μm thick.

DTA measurements at constant heating rates (5, 10, 20 °Cmin<sup>-1</sup>) were conducted to study thermally induced structural transformations of the alloy. TA SDT 2960 instrument was used to this purpose. Measurements were done under helium atmosphere to prevent the oxidation of material. Complex DTA peaks were deconvoluted into several peaks using Origin Pro 8.5 software applying Gaussian Lorentzian cross-product function.

XRD data were collected at room temperature using Philips PW-1710 automated diffractometer with Cu K<sub>α</sub> line, operated at 40 kV and 30 mA. Thermal treatment of the samples subjected to XRD analysis included isothermal annealing under argon atmosphere, at different temperatures.

## RESULTS AND DISCUSSION

The influence of thermal treatment on the structure of the multicomponent nanostructured Fe<sub>72</sub>Cu<sub>1</sub>V<sub>4</sub>Si<sub>15</sub>B<sub>8</sub> alloy was investigated in the temperature range 25-800 °C. It was shown that the alloy was stable up to around 470 °C when structural transformations started, manifested as two well separated exo maxima, reflecting the processes of crystallization and growth of the formed crystallites, Fig. 1a.

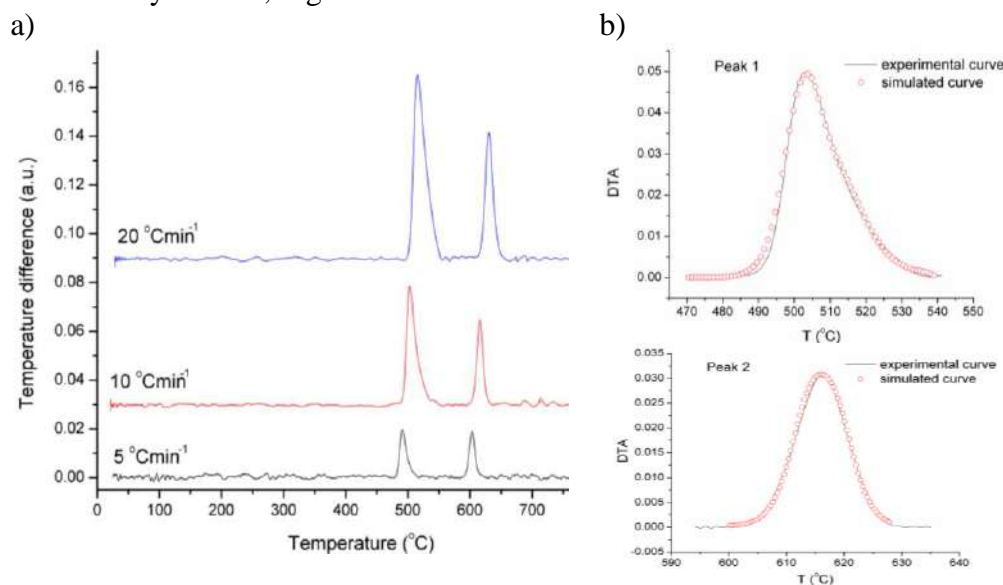


**Figure 1.** a) Baseline-corrected DTA curves for different heating rates; b) DTA curves, experimental and simulated, based on kinetic triplets for 10 °Cmin<sup>-1</sup>.

The X-ray diffractogram of initial alloy, Fig.2a, revealed the presence of both the amorphous and crystalline phases. It was shown that the  $\alpha$ -Fe(Si) phase is the dominant one (crystallite size 40nm) while the metastable Fe<sub>3</sub>B

crystalline phase is the minor one. On the other hand, the alloy isothermally treated at 700 °C for 210 min was completely crystalline, containing two solid solutions with different percentages of Si and one with relatively high V content, and Fe<sub>2</sub>B phase, Fig. 2b. This result is in good accordance with EDAX (results aren't presented here).

With a view to determining kinetic triplets of individual crystallization steps, complex DTA peaks were deconvoluted. In this way we obtained four well formed peaks corresponding to single step processes of crystallization of different phases. Kinetic parameters, obtained by using Kissinger's and Ozawa's methods, Table 1, correspond to simultaneous correlated movements of large number of atoms during transformations. The presence of considerable number of quenched-in nuclei in the initial alloy provokes considerably lower value of apparent activation energy of crystallization of  $\alpha$ -Fe phase, in comparison with the similar systems [3].

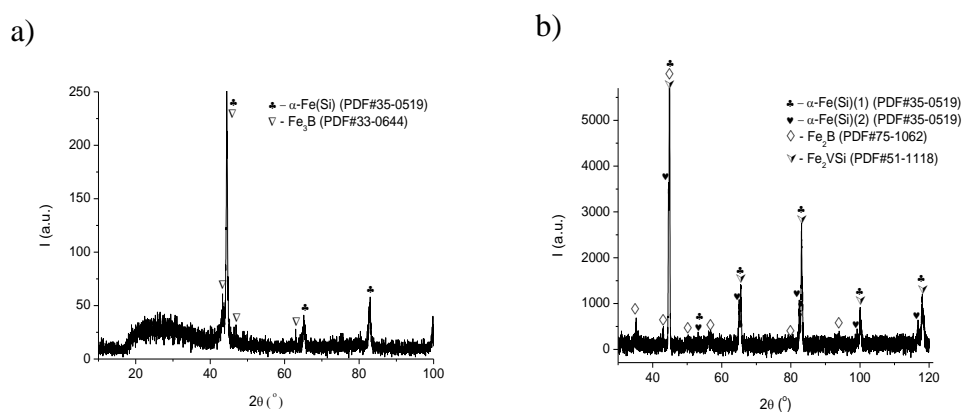


**Figure 2.** a) XRD of the as-prepared Fe<sub>72</sub>Cu<sub>1</sub>V<sub>4</sub>Si<sub>15</sub>B<sub>8</sub> alloy; b) XRD of the alloy sample thermally treated at 700 °C for 210 min.

Conversion function,  $f(\alpha)$ , was found by application of Málek's method [4]. This method suggested that empirical Šesták-Berggren model [5] can be used for description of the individual steps, as presented in Table 1. The determined kinetic triplets were applied to simulate experimental DTA curves. Comparison of simulated DTA curves, calculated using the determined kinetic triplets, and experimental DTA curves Fig. 1b showed very good accordance with correlation factor of 0,99. In this way obtained kinetic triplets can be used to predict the lifetime and the rate of processes for initial material as well as for partially or fully crystallized materials, which is very important for their application in electronics.

**Table 1.** Kinetic triplets of individual crystallization steps

Method	Experimental peak 1		Experimental peak 2	
	Step 1	Step 2	Step 1	Step 2
Kissinger, $E_a$ (kJ/mol)	$281 \pm 1$	$248 \pm 4$	$346 \pm 4$	$322 \pm 1$
$\ln(A/\text{min}^{-1})$	$43.0 \pm 0.1$	$37.3 \pm 0.8$	$46.3 \pm 0.8$	$42.7 \pm 0.1$
Ozawa, $E_a$ (kJ/mol)	$280 \pm 1$	$248 \pm 4$	$343 \pm 4$	$320 \pm 1$
$\ln(A/\text{min}^{-1})$	$42.8 \pm 0.1$	$37.3 \pm 0.5$	$46.0 \pm 0.6$	$42.4 \pm 0.1$
$f(\alpha)$	$\alpha^{0.48}(1-\alpha)^{0.83}$	$\alpha^{0.89}(1-\alpha)^{1.34}$	$\alpha^{0.79}(1-\alpha)^{1.0}$	$\alpha^{0.79}(1-\alpha)^{1.0}$

## CONCLUSION

Thermal treatment of nanocrystalline  $\text{Fe}_{72}\text{Cu}_1\text{V}_4\text{Si}_{15}\text{B}_8$  alloy induces multi-step thermal stabilization process at temperatures higher than 470 °C. This process includes, beside the nucleation, the growth of the present nuclei and recrystallization, yielding  $\alpha$ -Fe solid solutions with different contents of Si and V and  $\text{Fe}_2\text{B}$  phase as the final products. Lower values of apparent activation energy of crystallization in comparison with the similar systems originate from the presence of significant number of quenched-in nuclei in the as-prepared alloy. The determined values of kinetic parameters and conversion functions of individual steps fit very well experimental DTA curves, and can be used to predict lifetime of the material in different stages of crystallization and the rate of the process in different temperature regions.

## Acknowledgement

This work was supported by the Ministry of Education, Science and Technological Development of the Republic of Serbia.

## REFERENCES

- [1] C. Suryanarayana, A. Inoue, International Materials Reviews, 2013, **58**, 131-166.
- [2] T. Kulik, Journal of Non-Crystalline Solids, 2001, **287**, 145-161.
- [3] M. Vasić, D.M. Minić, V.A. Blagojević, D.M. Minić, Thermochemica Acta, 2013, **562**, 35-41.
- [4] J. Málek, Thermochemica Acta, 2000, **355**, 239-253.
- [5] J. Šesták, G. Berggren, Thermochemica Acta, 1971, **3**, 1-12.

**THERMALLY INDUCED DEGRADATION OF *cis*-  
DICHLORIDO[(E)-ETHYL-2-(2-((8-HYDROXY-  
QUINOLIN-2-YL)METHYLENE)HYDRAZINYL)  
ACETATE-κ-2N]-PALLADIUM(II) COMPLEX**

N. Begović<sup>1</sup>, M. M. Vasić<sup>2</sup>, N. Filipović<sup>3</sup>, A. S. Malešević<sup>3</sup> and D. M. Minić<sup>2</sup>

<sup>1</sup>*Institute of General and Physical Chemistry, Belgrade, Serbia*

<sup>2</sup>*Faculty of Physical Chemistry, University of Belgrade, Serbia*

<sup>3</sup>*Faculty of Chemistry, University of Belgrade, Serbia*

**ABSTRACT**

*Cis*-dichlorido[(E)-ethyl-2-(2-((8-hydroxyquinolin-2-yl)methylene)hydrazinyl) acetate-κ2N]-palladium(II) complex was synthesized and characterized by a combination of XRD, IR, DSC and TG measurements. It was determined that the initial degradation step involves the release of Cl free radical, which reacts with both the initial compound and degradation products. Some of these reactions are exothermic, resulting in overlapping endothermic and exothermic peaks in DSC curves. Deconvolution of DTG curves was used to identify primary fragments of the initial degradation process and to propose the most likely reaction mechanism.

**INTRODUCTION**

Palladium(II) complexes have been recognized as effective catalysts and pre-catalysts for a number of reactions [1], and potential metal based anti-cancer drugs [2], because they possess the same geometry and electronic configuration as platinum. However, the ligand-exchange kinetics of platinum(II) and palladium(II) derivatives is quite different: hydrolysis of palladium(II) compounds is nearly 10<sup>5</sup> times faster, resulting in very reactive species, which are unable to reach pharmacological targets [3]. Considering their potential application, thermal stability of palladium(II) complexes has been considered an important issue [4], although there have been very few investigations of the impact of ligand peripheral substitution on thermal stability.

As a part of our multidisciplinary investigation of a series of palladium(II) complexes with NN bidentate chelate hydrazone ligands derived from ethyl hydrazino acetate and various N-heteroaromatic carbonyl compounds, here we present the investigation of thermal stability and decomposition of *cis*-dichlorido[(E)-ethyl-2-(2-((8-hydroxyquinolin-2-

yl)methylene)hydrazinyl)- acetate- $\kappa$ 2N]-palladium(II) complex. The ligands in this series contain the same donor atoms, but different ligand periphery backbones, affecting their lipophilicity and having a crucial impact on their cytotoxic activity [5].

### EXPERIMENTAL

DSC experiments were carried out using DSC Q1000 (TA Instruments). Measurements were performed in nitrogen (flow: 50 mL min<sup>-1</sup>), at heating rates ranging from 2 to 40 K min<sup>-1</sup>, with sample masses of about 2.0  $\pm$  0.2 mg. TG analyses were conducted by Q500 TGA (TA Instruments). Runs were carried out in nitrogen (flow: 50 mL min<sup>-1</sup>) at heating rates of 5, 10 and 20 K min<sup>-1</sup> with sample masses of about 10.0  $\pm$  0.5 mg.

### RESULTS AND DISCUSSION

Non-isothermal measurements of the complex show that it is thermally stable up to 460 K, after that it undergoes complex thermal decomposition, which manifests as a complex asymmetric exothermic peak in non-isothermal DSC curves. This is preceded by another structural transformation around 330 K, which appears to be a second order phase transition overlapping with a subsequent exothermic process (Fig. 1). This transition originates from structural reorganization of the ligand in the crystal structure. The shape of the DSC curves changes from two clearly visible overlapping peaks at lower heating rates (ranging from 2 to 10 K min<sup>-1</sup>), to a single asymmetric complex peak at higher heating rates ( $\geq$  20 K min<sup>-1</sup>). This indicates that different steps of the process of thermal degradation exhibit different thermal activation. Considering that overlapping endothermic and exothermic processes in DSC curve could not be separated, to gain a better understanding of the mechanism of decomposition, deconvoluted TG and DTG curves were used.

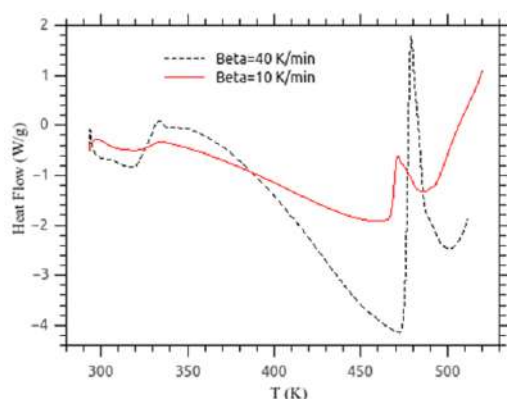


**Figure 1.** DSC curves at two heating rates.

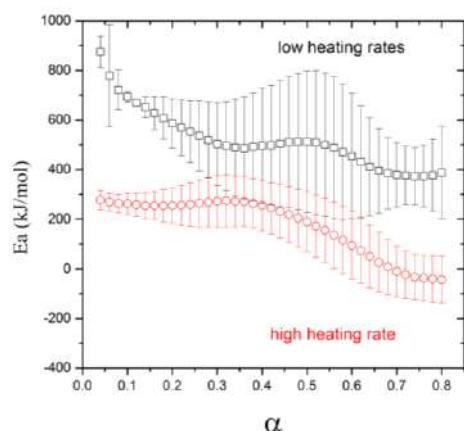


**Figure 2.** Isoconversion curves (Kissinger-Akahira-Sunose method) at high (20-40 K min<sup>-1</sup>) and low (2-10 K min<sup>-1</sup>) heating rates.

Complex shape of dependences of the effective values of the apparent activation energy on the reaction conversion degree (Fig. 2) indicates that the process of thermal degradation occurs with a change in the limiting step during the thermal degradation. In order to identify the individual fragments corresponding to each step of the complex decomposition process, DTG curves were deconvoluted using Fraser-Suzuki function. This showed that the loss of mass during decomposition can be separated into three distinct contributions at lower heating rates and four at higher heating rates (Fig. 3).

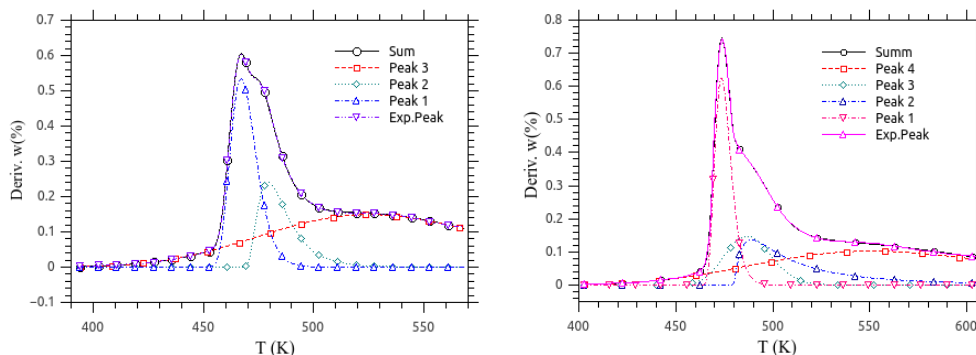


**Figure 3.** Deconvoluted DTG curves of thermal decomposition at 5 K min<sup>-1</sup> (left) and 20 K min<sup>-1</sup> (right).

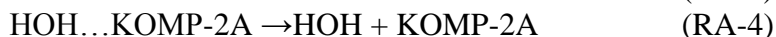
A broad deconvoluted peak, observed at both low and high heating rates, corresponds to a fragment of relatively large mass, which diffuses slower than the other, lighter, fragments. The remaining two deconvoluted peaks at lower heating rates were assigned to the release of HCl and water molecules, while the remaining three deconvoluted peaks at higher heating rates were assigned to the release of HCl, C<sub>2</sub>H<sub>5</sub> and water, respectively. This

suggests that higher heating rates lead to faster fragmentation of the aliphatic part of the complex.

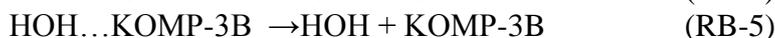
### CONCLUSION

Through correlation of the experimental results with structure of complex, two sets of equations (RA1-RA4 and RB1-RB5) describing potential reaction paths of thermal degradation of the complex, at different heating rates, were proposed:

#### Intermolecular pathway



#### Intramolecular pathway



### *Acknowledgement*

This work was supported by the Ministry of Education, Science and Technological Development of the Republic of Serbia.

### REFERENCES

- [1] E. Peris, J. A. Loach, J. Mata, R. H. Crabtree, *Chem Commun*, 2001, 201–202.
- [2] M. L. Teyssot, A. S. Jarrouse, M. Manin, A. Chevry, S. Roche, F. Norre, C. Beaudoin, L. Morel, D. Boyer, R. Mahiou, A. Gautier, *Dalton Trans*, 2009, 6894–6902.
- [3] E. Gao, C. Liu, M. Zhu, H. Lin, Q. Wu, L. Liu, *Anti-Cancer Agents Med Chem*, 2009, **9**, 356–368.
- [4] R. B. Singh, S. Mitra, P. Kundu, *Thermochim. Acta*, 1996, **285**, 191–197.
- [5] N. Filipović, S. Grubišić, M. Jovanović, M. Dulović, I. Marković, O. Klisurić, A. Marinković, D. Mitić, K. Anđelković, T. Todorović, *Chem. Biol. Drug Des.* (2014) in print, DOI: 10.1111/cbdd.12322

## TOWARDS TO NEW BIOMATERIALS BASED ON HYDROXYAPATITE/CHITOSAN COMPOSITES

E. N. Bulanov<sup>1</sup>, N. E. Silina<sup>1</sup>, A. G. Blokhina<sup>1</sup>, V. Zh. Korokin<sup>1</sup>, K. S. Korshak<sup>1</sup>, M. I. Lelet<sup>1</sup>, I. V. Ladenkov<sup>2</sup>, A.V. Knyazev<sup>1</sup>  
and L. A. Smirnova<sup>1</sup>

<sup>1</sup>*Chemistry Department, Lobachevsky State University of Nizhni Novgorod, 23, Gagarin av., 603950 Nizhni Novgorod, Russia (bulanoven@yandex.ru)*

<sup>2</sup>*JSC "RPC "Salut", 7, Larin St., 603950, Nizhni Novgorod, Russia*

### ABSTRACT

Hydroxyapatite is one of the best-known and investigated compound for bone tissue engineering. In presented work, we give a brand new information about its thermophysical properties with following interpretation. Moreover, here we describe a first step of obtaining a new kind of biocompatible materials which are organic-inorganic composites based on hydroxyapatite and chitosan – another nature biomaterial.

### INTRODUCTION

Injuries and diseases of bone tissue, such as osteosarcoma, requiring surgery, usually accompanied by the formation of large bone defects. There are two approaches to solving the problem of restoring the physiological functions of the bone [1]:

- 1) mechanical replacement of bone,
- 2) the regeneration of damaged bone.

In according with aforementioned facts two types of materials differ in behavior *in vivo* in humans are designed. The general requirement for both is biocompatibility - the absence of a negative reaction to an implantable material.

Hydroxyapatite is compound with chemical formula  $\text{Ca}_5(\text{PO}_4)_3\text{OH}$ . It is known as natural mineral and inorganic basis of hard tissues of mammal's organisms.

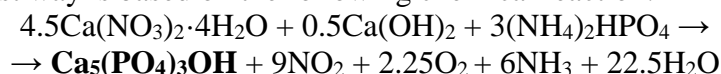
It can be used as a second type of biomaterials, because it is similar to chemical composition of the bone. In spite of a huge amount of information about hydroxyapatite physical-chemical properties, there is still no systematic approach of them and there is no information about hydroxyapatite behavior in changing conditions. Moreover, there are few lacks of its physical properties such as hardness and plasticity. To improve

such properties we provide to use composites based on hydroxyapatite and chitosan, which is a natural biocompatible polymer.

## EXPERIMENTAL

Samples of hydroxyapatite were obtained using two approaches: solid state reaction and sol-gel technique.

The first way is based on the following chemical reaction:



While sol-gel approach can be described using scheme:



which is described in details in application for Russian Federation patent (№2015154409 from December 17<sup>th</sup>, 2015). We can only say that we use conditions similar to internal human body conditions.

Hydroxyapatite/chitosan composites was created by adding of 5-40 mas% of hydroxyapatite to chitosan solutions (3 mas % and 1.2 % in CH<sub>3</sub>COOH) with thoroughly mixing. Composite films were prepared by casting method from homogenized aqueous dispersions of hydroxyapatite/chitosan on a glass substrate, and then they were dried to constant weight at 343 K.

The phase individuality of synthesized compounds was monitored by X-ray diffraction. X-ray diffraction patterns were recorded on a XRD-6000 Shimadzu diffractometer (CuK<sub>α</sub> radiation, geometry θ-2θ) in the 2θ range from 10° to 120° with scan increment of 0.02°.

Microphotos of obtained phases was done using workstation AURIGA CrossBeam Workstation (Carl Zeiss).

High-temperature X-ray diffraction experiments in the range from 298 to 1173 K were carried out on the same diffractometer with increments of 0.02° ranging from 10° to 60° using an HA-1001 Shimadzu attachment.

The behavior of individual compounds and composites in the wide range of temperature was investigated with thermoanalyser Shimadzu DTG-60H (heating rate 10 K/min).

## RESULTS AND DISCUSSION

As it was shown, sol-gel approach allows to get hydroxyapatite in form of nanoparticles (Figure 1a and 2), whereas the result of sol-gel method is microparticles (Figure 1b).

Nanosized hydroxyapatite is more useful for making biomaterials because it makes easier the processes of obtaining ceramics with controlled properties (form, porosity, etc.). It also was showed that hydroxyapatite obtained using our approach, has higher biocompatibility in comparison with

other artificial obtained hydroxyapatite. As follows from Table high-temperature behavior of these two modifications of compound vary from each other in spite of comparability of unit-cell linear dimensions [2].

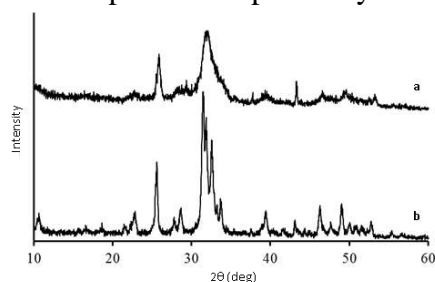


**Figure 1.** XRD patterns of hydroxyapatites obtained using different techniques.

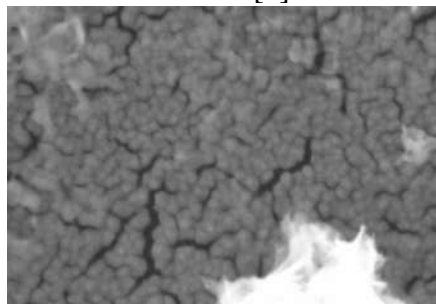


**Figure 2.** Nanoparticles (80 nm) of hydroxyapatite synthesized using sol-gel approach.

**Table.** Temperature dependencies of thermal expansion coefficients for the hexagonal (sp. gr.  $P6_3/m$ ) and pseudo-hexagonal (monoclinic, sp. gr.  $P2_1/b$ ,  $a = b$ ,  $\gamma = 120.0(0)^\circ$ ) forms of hydroxyapatite.

	Parameter	$\alpha_l = \alpha_{l0} + \alpha_{l1}T$ ( $\cdot 10^6 \text{ K}^{-1}$ )		Temperature interval (K)
		$\alpha_{l0}$	$\alpha_{l1}$	
$\text{Ca}_5(\text{PO}_4)_3\text{OH}$ (sol-gel)	$\alpha_a$	31.7	-0.001	298-992
	$\alpha_c$	7.0	-0.00005	
	$\alpha_V$	-340.74	0.4869	
	$\alpha_a$	63.9	-	992-1173
	$\alpha_c$	58.8	-	
	$\alpha_V$	187.0	-	
$\text{Ca}_5(\text{PO}_4)_3\text{OH}$ (solid-state)	$\alpha_a$	10.5	0.0048	298-1173
	$\alpha_c$	3.1	0.0133	
	$\alpha_V$	24.0	0.0229	

According to previous investigations of hydroxyapatite [3] this compound synthesized at room temperature has monoclinic symmetry with disordered orientation of OH-groups. At 473 K ordering of hydroxyl ions in columns is observed. This fact makes for rising unit-cell symmetry to hexagonal. In our case presence of polymorphic transition in hydroxyapatite obtained by sol-gel method is confirmed firstly by endothermic effect at 992 K on DTA curve, secondly by high-temperature X-ray diffraction data: there are a discontinuity on the unit-cell parameter and volume temperature dependences and strongly thermal expansion anisotropy of low-temperature modification in

comparison with high-temperature one. Great difference between polymorphic transition temperatures can be explained on the basis of size effect in nanosized hydroxyapatite.

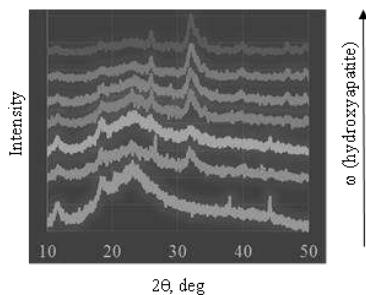


**Figure 3.** XRD patterns of composites under study\*

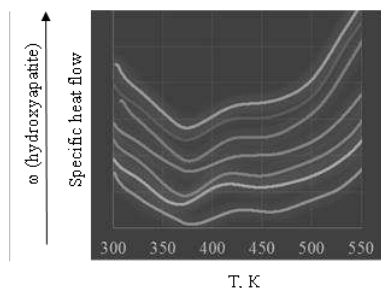


**Figure 4.** DSC-data of composites under study\*

\*Hydroxyapatite content: 0%, 5%, 10%, 15%, 20%, 30%, 40%

As for hydroxyapatite/chitosan composites, it was shown that adding of hydroxyapatite to chitosan leads to decreasing of chitosan crystallinity (Figure 3). From DSC-analysis of the composites under study (Figure 4) we observe that adding of hydroxyapatite results in lowering of chitosan softening temperature.

### CONCLUSION

Using nanosized hydroxyapatite for creating composites with hydroxyapatite is preferable because in such case polymorphic transition of hydroxyapatite even at it high content can't influence on the properties of composites in relatively wide range of temperatures. High-temperature modification of apatites usually has bigger volume thermal expansion coefficients what could lead to destruction of bioimplant with temperature variation.

### Acknowledgement

The work was done with using of equipment of Centre for Collective Use of Equipment "New materials and resource saving technologies" (Research Institute of Chemistry, Lobachevsky State University of Nizhni Novgorod). The work was performed with the financial support of the Russian Foundation of Basic Research (Project Number 16-33-601721).

### REFERENCES

- [1] M. M. Stevens, *Materials Today*, 2008, **11**, 18-25.
- [2] E. N. Bulanov, A. V. Knyazev, N. G. Chernorukov, in "Apatite: Synthesis, Structural Characterization and Biomedical Applications", Nova Science Publishers, Inc. NY, 2014, 173-200.
- [3] O. Hocherin, R. Kniep, D. Zahn, *Chem. Mater.*, 2005, **17**, 1978–1981.

## JOINT USE OF CALORIMETRIC, DIFFRACTION AND SPECTROSCOPIC METHODS FOR THE STUDY OF COMPLEX OXIDES

A. V. Knyazev, O. V. Krashennikova, S. S. Knyazeva, M. E. Komshina,  
A. A. Murav'eva, E. V. Syrov, I. A. Savushkin, E. N. Bulanov  
and K. V. Baidakov

*Chemistry Department, Lobachevsky State University of Nizhni Novgorod  
Gagarin Av. 23/2, 603950, Nizhni Novgorod, Russia  
(knyazevav@gmail.com)*

### ABSTRACT

The present work presents the results of investigating complex oxides obtained in thermodynamic field over the past few years. There is realized crystal chemistry systematization of studied compounds. The temperature dependences of heat capacities at constant pressure for more than 50 compounds in a temperature interval from 7 to 350 K were studied in an adiabatic vacuum calorimeter. The description of transitions in compounds was made by means of McCallaf–Vestrum classification of physical transitions. The study of phase transitions was carried out with the use of complex physical and chemical methods such as X-ray spectroscopy and calorimetry.

### INTRODUCTION

Since the inception of chemical thermodynamics one of the most important tasks of this science is to determine the standard thermodynamic functions of individual substances. Such data are required primarily for calculating equilibrium chemical reactions at various temperatures and pressures. In this case the limiting factor in such calculations is usually relatively low accuracy in determining the enthalpy of a chemical reaction, which is calculated as the algebraic sum of the enthalpies of formation of the reactants. In the measurements of entropy admissible large errors, particularly when it comes to reactions involving condensed substances. Therefore, determination of standard enthalpies of formation and absolute entropies of individual substances is necessary and important task of chemical science and technology. The thermodynamic functions of compounds allow to predict the behavior of phases in different geological and technological conditions.

## EXPERIMENTAL

The synthesis of the complex was carried out by three various methods:

(1) solid state reactions and reactions in melt in a temperature range from 773K to 1573K; (2) reactions under hydrothermal conditions; and (3) precipitation reactions from solutions. The techniques, developed by us, allowed obtaining in total of more than 400 compounds and more than half of them were prepared and identified for the first time.

For structural investigations and confirming phase individuality, X-ray diffraction patterns of all samples were recorded on a Shimadzu X-ray diffractometer XRD-6000 (CuK $\alpha$  radiation, geometry  $\theta$ - $2\theta$ ) in the  $2\theta$  range from 10° to 120° with scan increment of 0.02°. The low-temperature and high-temperature X-ray diffraction were carried out on a Shimadzu X-ray diffractometer XRD-6000 using Attachment TTK-450 (Anton Paar) and Sample Heating Attachment HA-1001 (Shimadzu) respectively.

To measure the heat capacity of the tested substances in the range from 7 to 350 K a BKT-3.0 automatic precision adiabatic vacuum calorimeter with discrete heating was used. To measure the heat capacity of the sample between 330 and 650 K an automatic thermoanalytical complex (ADKTTM) – a dynamic calorimeter operating by the principle of triple thermal bridge – was used. The data on the heat capacity of the objects under study were obtained in the range from 330 to 650 K at the average rate of heating of the calorimeter and the substances of 0.0333 K/s.

The experimental thermochemical data set was obtained using a modified Skuratov calorimeter.

Thermal behavior was carried out with DSC Labsys from Setaram in a platinum crucible ranging from 293 to 1173 K (heating rate 0.167 K/s).

## RESULTS AND DISCUSSION

Realized crystal chemistry systematization of studied compounds allows concluding that the element with the highest oxidation number determines the forming structure, as usual for majority others complex compounds. We could sort all the compounds into three types according to structural features, that is, compounds with frame, layer and isle structures.

A sufficiently important task of the work was the estimating thermodynamic functions of the compounds with the purpose of describing processes with their participation and detecting criteria of their stability. For this purpose we choose the thermochemical schemes. The enthalpies of formation of about 250 inorganic compounds containing uranium were experimentally determined for the first time using a reaction adiabatic calorimeter.

The temperature dependences of heat capacities at constant pressure for more than 50 compounds in a temperature interval from 7 to 350 K were studied in an adiabatic vacuum calorimeter. The obtained data allowed describing possible phase transitions and calculating absolute entropies of formation of the compounds. It is significant to note that heat capacities at constant pressure of the majority complex oxides monotonously grow with rising temperature without any visible anomalies. On the contrary, the physical transitions are observed in uranylcarbonates, uranysulfates, several tungstates and spinels (Table 1). The description of transitions was made by means of McCallaf–Vestrum classification of physical transitions. According to this classification phenomenological all phase transitions in solids can be categorized into seven types (I, 2I, 3I, 2N, 3N, G, H).

**Table 1.** Thermodynamic characteristics of physical transitions in compounds.

Compound	Phase transition	T <sub>tr</sub> , K	Δ <sub>tr</sub> H° (kJ/mol)	Δ <sub>tr</sub> S° (J/(mol·K))
KTh <sub>2</sub> (PO <sub>4</sub> ) <sub>3</sub>	H	6.7		
Li <sub>4/3</sub> Ti <sub>5/3</sub> O <sub>4</sub>	H	7.5		
Co <sub>7/3</sub> Sb <sub>2/3</sub> O <sub>4</sub>	H	60.3	15.8 ± 0.5	0.258±0.007
K <sub>2</sub> Fe <sub>2</sub> Ti <sub>6</sub> O <sub>16</sub>	G	72		
Na <sub>4</sub> (UO <sub>2</sub> (CO <sub>3</sub> ) <sub>3</sub> )	G	60.5	1500±3	33.0±1.0
	I	386	50200±200	130. ±3.0
K <sub>3</sub> Na(UO <sub>2</sub> (CO <sub>3</sub> ) <sub>3</sub> )	I	395	800±100	2.00±0.02
K <sub>4</sub> (UO <sub>2</sub> (CO <sub>3</sub> ) <sub>3</sub> )	I	403	6900±100	17.1±0.5
Mn(UO <sub>2</sub> (SO <sub>4</sub> ) <sub>2</sub> )·5H <sub>2</sub> O	H	176	510±3	2.90±0.02
	I	238	190±3	0.80±0.02
Fe(UO <sub>2</sub> (SO <sub>4</sub> ) <sub>2</sub> )·5H <sub>2</sub> O	H	182	200±3	1.10±0.02
Co(UO <sub>2</sub> (SO <sub>4</sub> ) <sub>2</sub> )·5H <sub>2</sub> O	I	237	1920±3	8.10±0.02

The most widespread type of transitions in the layered compounds is isothermal (I) transitions connected with polymorphic transitions in the crystal. The polymorphism is caused by possible shifts or rotations of layers relatively to each other in the crystalline structure. Isothermal transitions are seen as “peaks” on the curve of heat capacity; the area of “peaks” is numerically equal to the enthalpy of phase transition. The physical transitions, which are more rarely met with, are H-transitions and they are observed as “humps” on the curve of heat capacity. According to physical point of view the given anomaly may be connected with “defreezing” of rotations around M–OH<sub>2</sub> bond in structures of the appropriate crystallohydrates. Furthermore, these transitions are detected for the

compounds which are contain in their composition the d- and f-transition elements.

The compounds  $\text{Na}_4\text{UO}_2(\text{CO}_3)_3$  and  $\text{K}_2\text{Fe}_2\text{Ti}_6\text{O}_{16}$  show the G-type (glass-like) of physical transitions (Table 1). The nature of this anomaly is, probably, related to the presence of cation–cation interactions in the structure of this compound that is confirmed by us using Voronoi–Dirihle calculations of polyhedra with program complex TOPOS.

It should be noted that great attention is paid to the joint use of calorimetric, diffraction and spectroscopic methods for the study of phase transitions. Significant structural changes were studied by using low-temperature and high- temperature X-ray diffraction. Slight structural changes were studied by using low-temperature infrared and Raman spectroscopy.

Thus, the calorimetric methods allowed estimating all necessary thermodynamic functions of some inorganic compounds.

## CONCLUSION

The techniques for the synthesis of individual compounds and solid solutions were developed, more than half of which were obtained and identified for the first time. The standard enthalpies of formation at  $T=298.15$  K of 250 inorganic compounds were determined first by the method of reaction calorimetry. The heat capacity at constant pressure of more than 50 compounds was studied also first by adiabatic vacuum calorimetry. The standard entropies and Gibbs functions of formation at  $T=298.15$  K were calculated as well. All the results were discussed and tabulated and those made up the foundation of thermodynamics of the given class of inorganic compounds.

## *Acknowledgement*

The work was performed with the financial support of the Russian Foundation of Basic Research (Project Number 16-03-00288).

## REFERENCES

- [1] A. V. Knyazev, M.E. Manyakina, in “Thorium: Chemical Properties, Uses and Environmental Effects”, Nova Science Publishers, Inc. NY, 2014, 179-210.
- [2] A. V. Knyazev, M. E. Manyakina, in “Uranium: Sources, Exposure and Environmental Effects”, Nova Science Publishers, Inc. NY, 2015, 171-229.

## THE EFFECT OF SINTERING TEMPERATURE ON MESOPOROUS STRUCTURE OF WO<sub>3</sub> DOPED TiO<sub>2</sub> POWDERS

Lj. Rožić<sup>1</sup>, Z. Vuković<sup>1</sup>, B. Grbić<sup>1</sup>, S. Petrović<sup>1</sup>, N. Radić<sup>1</sup>, S. Stojadinović<sup>2</sup>  
and R. Vasilčić<sup>2</sup>

<sup>1</sup>*University of Belgrade, IChTM-Department of Catalysis and Chemical Engineering, Njegoševa 12, Belgrade, Republic of Serbia  
srlepp@nanosys.ihtm.bg.ac.rs*

<sup>2</sup>*University of Belgrade, Faculty of Physics, Studentski trg 12-16, 11000 Belgrade, Serbia*

### ABSTRACT

In this study, WO<sub>3</sub> doped TiO<sub>2</sub> powders were synthesized via sol-gel method combined with hydrothermal process. The physical analysis via X-ray diffraction indicated that the prepared sample had a mixed anatase-rutile TiO<sub>2</sub> phase. It was also observed that when calcination temperature goes above 600 °C, the Keggin molecule breaks up to form a WO<sub>3</sub> species which is stable at higher temperature. The results of N<sub>2</sub> adsorption-desorption analysis showed that the mesoporous WO<sub>x</sub>-TiO<sub>2</sub> samples prepared in this work exhibited a bimodal pore size distribution. Sintering temperature induces a change of topography and it was observed that the increase in temperature causes a systematic shift towards larger mesopores.

### INTRODUCTION

TiO<sub>2</sub> is an excellent material for environmental applications, including photodegradation of various pollutants and the purification of water and air [1]. When TiO<sub>2</sub> is illuminated by UV light, electrons and holes are generated within, thus oxidizing the organic compounds dissolved in water. To increase the overall efficiency of this process it is very important to develop methods for broadening the spectrum of absorbed light in the visible range and increase the photocatalytic properties of TiO<sub>2</sub> in the UV range.

To improve the photocatalytic efficiency of such materials many efforts have been made, including various synthesis pathways and change of the TiO<sub>2</sub> powder properties. Coupling TiO<sub>2</sub> with other semiconducting materials is considered beneficial because coupling two semiconductors with different redox energy levels can increase the separation of their corresponding conduction and valence bands [2].

The structural, morphological and photocatalytic properties of TiO<sub>2</sub> nanocrystals are strongly dependent of the synthesis process [3]. Sol-gel processing has become one of the most successful techniques for preparing powders or gels of TiO<sub>2</sub> with photocatalytic properties [4]. Nevertheless, TiO<sub>2</sub> materials obtained by sol-gel processing are either amorphous or not well crystallized and consequently, they must undergo a suitable treatment to become active photocatalysts. An enhancement of crystallinity can be obtained by thermal treatment but the temperature must be carefully selected.

In this study, WO<sub>x</sub>-TiO<sub>2</sub> samples were prepared by sol-gel method combined with a hydrothermal treatment. WO<sub>x</sub>-TiO<sub>2</sub> powders with varying amount of anatase and rutile phases were obtained by carefully controlling the sintering temperature. By combining two analytical techniques (XRD and N<sub>2</sub> adsorption-desorption), we determined the correlation between the change of phase composition, nanoparticle growth, and textural properties with sintering temperature.

## EXPERIMENTAL

Titanium (IV) isopropoxide and tungstophosphoric acid were used for synthesis of WO<sub>x</sub>-TiO<sub>2</sub> powders in this study. All chemicals were of analytical grade.

Amorphous powders were prepared by a sol gel method. For the synthesis of samples, titanium isopropoxide was slowly dissolved in isopropyl alcohol. After that, an appropriate amount of H<sub>3</sub>PW<sub>12</sub>O<sub>40</sub> (20 %) was dissolved in water and then added into solution drop by drop. The resulting mixture was heated to 45 °C until homogeneous hydrogel was formed. This hydrogel was subsequently heated to 200 °C at a heating rate of 2 °C/min and after that washed with hot water three times. The wet gel was calcined at 500, 600, 650, 700, 750 and 800 °C for 3 hours, which resulted in the formation of WO<sub>x</sub>-TiO<sub>2</sub> powder.

The phase structure of samples was analyzed by X-ray diffraction method, using a Rigaku Ultima IV diffractometer in Bragg-Brentano geometry, with Ni-filtered CuK<sub>α</sub> radiation (40 kV, 30 mA,  $\lambda=1.54178$  Å). The crystallite size was calculated using full width at half maximum of intense diffraction peaks of anatase (101) and rutile (110) according to Scherrer equation. N<sub>2</sub> adsorption-desorption isotherms of all samples were measured with an automatic adsorption apparatus (Sorptomatic 1990 Thermo Finnigan) at 77 K. The specific surface areas ( $S_{BET}$ ) were calculated by fitting the adsorption data to Brunauer–Emmett–Teller (BET) equation and the pore size distributions were calculated by the Barrett-Joyner-Halenda method.

## RESULTS AND DISCUSSION

The physical properties of  $\text{WO}_x\text{-TiO}_2$  powder often vary with its preparation history and post-treatment. Therefore, it is necessary first to characterize the samples synthesized in present study. In the  $\text{WO}_x\text{-TiO}_2$  powder, the XRD

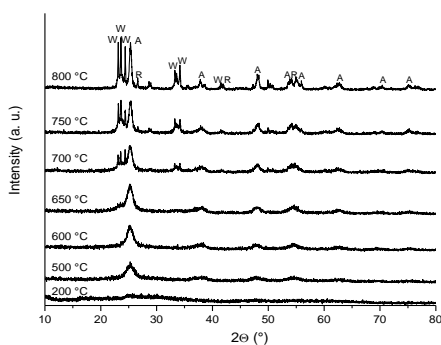


**Figure 1.** XRD spectra of  $\text{WO}_x\text{-TiO}_2$  powder with different temperature sintering (A: anatase, R: rutile, W: tungsten oxide)

patterns (Fig. 1) showed that without annealing the sample possessed weak broad peaks in the positions corresponding to characteristic peaks of the anatase phase.

This is an indication of poorly crystallized and/or mostly amorphous solids. After annealing from 500 to 800 °C all diffraction peaks become more intensive, which is related to crystallization and particle growth. However, when annealing temperature was elevated to 700 °C, small rutile

peaks are observed, indicating the onset of anatase-to-rutile transformation. It was also observed that when annealing temperature goes above 600 °C, the Keggin molecule breaks up to form a  $\text{WO}_3$  species. The orthorhombic  $\text{WO}_3$  and a non-stoichiometric form of tungsten oxide ( $\text{WO}_{2.92}$ ) were observed in the samples annealed at 700 °C and 800 °C.

At the temperature between 700 °C and 800 °C,  $\text{WO}_x\text{-TiO}_2$  powder is a mixture of anatase and rutile phases, and content of anatase in the samples decreases with sintering temperature. Moreover, all samples show a progressive increase in the primary particle size with temperature sintering. All samples display isotherms of type IV with steep hysteresis loops at high relative pressure, which is typical for mesoporous materials. However, as sintering temperature increases, the hysteresis loop gradually shifts toward the high pressure side, indicating an increase of pore size. Upon thermal treatment, small micropores (3.7 nm) did not change while the larger ones continuously increased from 8.8 to 21 nm with increasing annealing temperature (Fig. 2). Besides, with raising the sintering temperature, the relative amount of the smaller sized mesopores decreased gradually and disappeared at 800 °C, while the larger ones constantly increased.

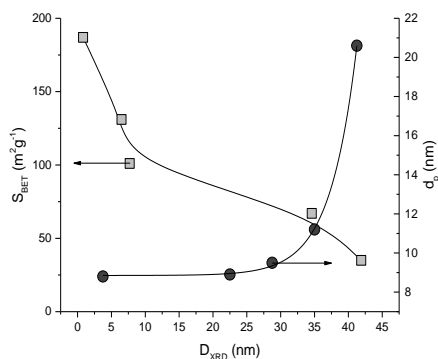


**Figure 2.** Crystal size ( $D_{XRD}$ ), pore size ( $d_p$ ) and specific surface area ( $S_{BET}$ ) for  $WO_x$ - $TiO_2$  powders sintered at different temperatures (from 500 to 800 °C)

## CONCLUSIONS

Nanocrystalline  $WO_x$ - $TiO_2$  powder was prepared by sol-gel method combined with a hydrothermal treatment. The XRD analysis revealed that  $WO_x$ - $TiO_2$  powders mostly consist of anatase phase with minor portion of rutile and tungsten oxides. The raise of sintering temperature caused an increase of crystallinity, crystallite and pore size, while specific surface area decreases continuously. All the samples exhibited bimodal pore size distribution and the smaller pores (3.7 nm) retained within the

whole temperature range while larger mesopores were shifted towards large values, from 8.8 to 21 nm.

## Acknowledgments

This work was supported by the Ministry of Education, Science and Technological Development of the Republic of Serbia (Projects number 172022, 172026, 172015, 172018, 172001 and III 45001).

## REFERENCES

- [1] Turolla, A. Piazzoli, J. Farner Budarz, M. Wiesner, M. Antonelli, *Chem. Eng. J.*, 2015, **271**, 260-268.
- [2] R. A. Carcel, L. Andronic, A. Duta, *Mater. Charact.*, 2012, **70**, 68-73.
- [3] S.A.K. Leghari, Sh. Sajjad, F. Chen, J. Zhang, *Chem. Eng. J.*, 2011, **166**, 906-915.
- [4] M.A. Behnajady, H. Eskandarloo, N. Modirshahla, M. Shokri, *Desalination*, 2011, **278**, 10-17.

**THE INFLUENCE OF TYPE OF DATA  
NORMALIZATION ON KINETIC PARAMETERS  
OBTAINED FROM IN SITU <sup>27</sup>Al NMR ANALYSIS OF  
ZEOLITE A CRYSTALLIZATION**

Z. Miladinović<sup>1</sup>, J. Zakrzewska<sup>1</sup> and J. Miladinović<sup>2</sup>

<sup>1</sup>*Institute of General and Physical Chemistry, Studentski trg 12-16, 11000  
Belgrade, Serbia. (zmiladinovic@iofh.bg.ac.rs)*

<sup>2</sup>*Faculty of Technology and Metallurgy, University of Belgrade,  
Karnegijeva 4, 11000 Belgrade, Serbia.*

**ABSTRACT**

In this study *in situ* <sup>27</sup>Al NMR spectroscopy is used to obtain kinetic parameters of zeolite A synthesis. Changes of relative intensity of NMR lines at 59 ppm ascribed to Al(OSi)<sub>4</sub> solid structures units and at 79 ppm to Al(OH)<sub>4</sub> ions in liquid phase during crystallization, are observed. Comparative analysis of curves obtained by normalization to the sum of peak areas provides kinetic parameter of  $k$  ranged between  $4.15 \cdot 10^{-4}$  to  $9.63 \cdot 10^{-4} \text{ s}^{-1}$  and  $n$  from 2.5 to 3.4 indicating Avrami–Erofe’ev nucleation and crystal growth model.

**INTRODUCTION**

NMR has been frequently used in kinetic investigation of zeolite formation since it gives possibility of gaining detailed information about speciation in all phases of interest [1–3]. For that purpose different kinds of data normalization was adopted including normalization to the highest peak intensity (peak heights) [3] or to the sum of the peak intensities (more precisely peak areas) [2]. Normalization to sum of peak areas was applied in NMR spectroscopy basically to overcome the effect of dilution [4], but also for the comparison of *in situ* <sup>27</sup>Al NMR spectra during the zeolite synthesis [2].

In our previous study, Sharp-Hancock kinetic model [5] was adopted for investigation of zeolite A crystallization by *in situ* <sup>27</sup>Al NMR spectroscopy in liquid and solid phase [3]. The primary goal of this study is to determine the relation between batch chemical composition and obtained kinetic parameters by comparing the results of different type of data normalization of obtained <sup>27</sup>Al NMR lines during zeolite A syntheses.

## EXPERIMENTAL

All zeolite A syntheses were performed under hydrothermal conditions, at 80 °C and atmospheric pressure. The batch composition was  $\text{Al}_2\text{O}_3$ :  $1.7\text{SiO}_2$ :  $y\text{Na}_2\text{O}$ :  $z\text{H}_2\text{O}$ , where  $y$  ranged between 2.6 and 4.2 and  $z$  from 63 to 133. The  $^{27}\text{Al}$  NMR spectra of *in situ* crystallization were recorded on a Bruker MSL 400 NMR spectrometer at 104.262 MHz, using experimental procedure described earlier [3].

## RESULTS AND DISCUSSION

The result of normalization to sum of peak areas in the case of synthesis with  $\text{SiO}_2/\text{Al}_2\text{O}_3 = 1.7$  is shown in Fig. 1. Comparison between normalized area of lines at 79 ppm and 59 ppm, enables following of the aluminum amount interchanged between the solution and solid phase, during crystallization [3].

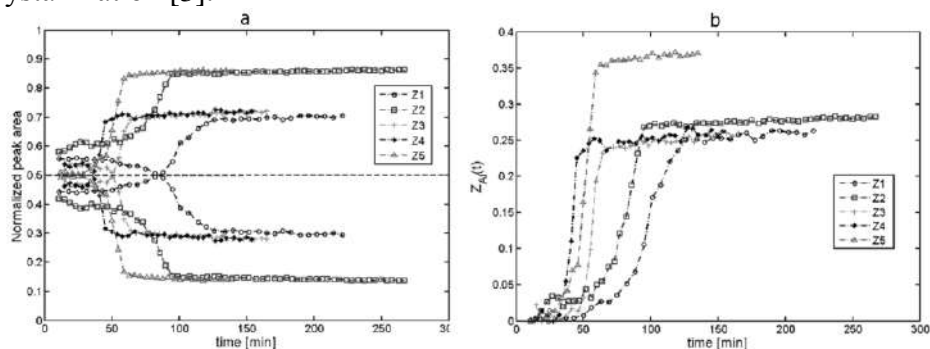


**Figure 3.** a) Normalized values of peak areas of NMR lines at 59 (top) and 79 ppm (bottom) for synthesis with  $\text{SiO}_2/\text{Al}_2\text{O}_3 = 1.7$ ; b) Distribution function of aluminum quantity  $Z_{\text{Al}}(t)$  during the course of the same zeolite A syntheses.

Based on theoretical consideration of relating changes of  $C_{\text{Al}}$  in a gel and liquid phase during the zeolite crystallization [6], both experimental NMR curves can be fitted by empirical expressions given as:

$$J_{79}(t) = J_{A0} - Z_{\text{Al}}(t) \quad (1)$$

$$J_{59}(t) = J_{B0} + Z_{\text{Al}}(t) \quad (2)$$

where  $J_{79}(t)$  and  $J_{59}(t)$  represent normalized areas of NMR lines at 79 ppm and 59 ppm respectively;  $J_{A0}$  and  $J_{B0}$  constants connected to initial amount of aluminum in solution and solid gel phase, respectively, and  $Z_{\text{Al}}(t)$  the function of aluminum content interchanged during the time of synthesis. Observed exponential dependency of  $Z_{\text{Al}}(t)$  with reaction time for all the

syntheses (Fig. 1b), is in concordance to the first ordered kinetics for the rate of crystalline product formation [7]. Since curves of interchanged aluminum represent contribution of overall processes involved in crystal growth (diffusion of constitutive species into liquid phase, gel dissolution, crystal growth, etc), only averaged values for the kinetic parameters can be determined from these curves. However, precaution should be taken when the NMR lines of quadrupolar nuclei originating from solution and solid phase are compared, since the linewidth of the peak at 59 ppm (representing solid structures) can be significantly influenced by the second-order quadrupolar interaction [3]. For that reason, obtained values of  $n$  and  $k$  should be used only for comparison between zeolite syntheses recorded under the same NMR conditions.

**Table 1.** Results of Sharp – Hancock kinetic analysis applied on the curves obtained from data normalized to the sum of peak areas.

Sample no.	$t_0$ [s]	$A_0$ [79 ppm]	$B_0$ [59 ppm]	$n$	$k$ [ $s^{-1}$ ] $10^{-4}$	Na <sub>2</sub> O [mol/dm <sup>3</sup> ] total
Z 1	3780	0.5582	0.4418	2.51	4.15	1.685
Z 2	3120	0.4197	0.5803	2.87	5.31	1.706
Z 3	2220	0.5392	0.4608	3.35	5.76	2.671
Z 4	1680	0.5416	0.4584	3.16	9.63	2.707
Z 5	2040	0.5097	0.4903	2.77	6.42	2.858

For the purpose of kinetic analysis of data obtained from *in situ* <sup>27</sup>Al NMR spectra, Sharp-Hancock method was applied [5]. Results of kinetic analysis of curves normalized to the sum of peak areas are presented in Table 1. Increasing trend of obtained values for the rate constant  $k$  with increasing Na<sub>2</sub>O content can be observed; with the only exception in the case of synthesis Z 4 where the rate constant is inconsistent with this trend regardless of applied type of data normalization [3]. There is no significant difference between  $k$  values obtained from data normalized to highest peak intensity [3], and normalized to the sum of peak areas (Table 1). In addition, values of initial amount of aluminum present in liquid phase ( $J_{A0}$  in Table 1), is significantly higher in comparison to values in solid phase ( $J_{B0}$ ). This indicates that initial distribution of aluminum between liquid and solid/gel phase strongly depends on SiO<sub>2</sub>/Al<sub>2</sub>O<sub>3</sub> ratio. Such aluminum distributions also emphasize mechanism governed by solution mediated processes that prevails over the mechanism by direct gel to solid transformation. On the other hand, values of  $n$  ranging between 2.5 and 3.4, are approximately

doubled comparing to the values obtained for normalized intensity curves of peak at 79 ppm [3]. No correlation between  $n$  and  $\text{SiO}_2/\text{Al}_2\text{O}_3$  molar ratio or NaOH batch concentration, is observed. However, these values of  $n$  are consistent with predictions of the Avrami nucleation and crystal growth model for zeolitic systems [8].

## CONCLUSION

In the present study normalization to the sum of peak areas of  $^{27}\text{Al}$  NMR data was used to obtain kinetic parameters of zeolite A syntheses. Such kinetic parameters represent averaged contribution of overall processes involved in crystal growth and its values indicate Avrami–Erofe'ev nucleation and crystal growth model. Increasing trend of obtained values for the rate constant  $k$  with increasing  $\text{Na}_2\text{O}$  contents was also observed. Determined parameters connected to initial aluminum content in each of the involved phases, were primarily the consequence of the used  $\text{SiO}_2/\text{Al}_2\text{O}_3$  molar ratio, but also indicate significant contribution of solution mediated mechanism of crystal growth, which is in agreement with previously obtained results by different normalization methods.

## Acknowledgements

This work was supported by projects TR 34026 and III 45019 of Ministry of Education, Science and Technological Development, Republic of Serbia

## REFERENCES

- [1] Aerts, C. E. A. Kirschhock, J.A. Martens, Chem. Soc. Rev., 2010, **39**, 4626.
- [2] J. Shi, M. W. Anderson, S.W. Carr, Chem. Mater., 1996, **8**, 369–375.
- [3] Z. P. Miladinović, J. Zakrzewska, B. T. Kovačević, J. M. Miladinović, Microporous Mesoporous Mater., 2014, **195**, 131–142.
- [4] A. Craig, O. Cloarec, E. Holmes, J. K. Nicholson, J. C. Lindon, Anal Chem, 2006, **78**, 2262–2267.
- [5] J. D. Hancock, J. H. Sharp, J. Am. Ceram. Soc., 1972, **55**, 74–77.
- [6] Thompson, A. Dyer, Zeolites, 1985, **5**, 202–210.
- [7] G. T. Kerr, J. Phys. Chem., 1966, **70**, 1047–1050.
- [8] R. I. Walton, F. Millange, D. O'Hare, A. T. Davies, G. Sankar, C.R.A. Catlow, J. Phys. Chem. B, 2001, **105**, 83–90.

*J - Macromolecular Physical Chemistry*



## NANOSTRUCTURED POLYANILINES AND THEIR CARBONIZED FORMS: PREPARATION, CHARACTERIZATION AND APPLICATION

G. Ćirić-Marjanović

*Faculty of Physical Chemistry, University of Belgrade, Studentski trg 12-16,  
11158, Belgrade, Serbia*

### ABSTRACT

Polyaniline (PANI) is one of the most extensively studied conductive polymers due to its unique electronic, redox, acid-base and other properties which enable its applicability in many fields. The interest in the study of PANI nanostructures has dramatically increased during the last decade due to the significantly enhanced dispersibility and processibility as well as improved performance of nanostructured PANIs in many applications (sensors, catalysts, field-effect transistors, corrosion protection, data storage, membranes, actuators, solar cells, rechargeable batteries, fuel cells, Schottky diodes, super capacitors, electromagnetic interference shielding, microwave absorption, antistatic coatings etc.) in comparison with ordinary granular PANIs. This lecture is focused on overview of the methods of preparation, characterization of structure and physico-chemical properties, and applications of zero-dimensional, one-dimensional, two-dimensional and complex hierarchical PANI nanostructures. Carbonization of PANI has proven to be an efficient method to prepare new N-containing carbon materials with desirable properties for different applications. The properties of carbonized PANI (c-PANI) can be tuned by the choice of PANI precursor (by adjusting its structure, morphology, conductivity), and carbonization method. Since the PANI morphology is mainly preserved upon the carbonization, PANI nanostructures served frequently as precursors for producing c-PANI nanostructures with the desirable morphologies. They exhibited excellent performance for applications such as super capacitors, electrocatalysts for fuel cells, Li batteries, sensors. Here, an overview of the carbonization methods, physico-chemical properties and applications of nanostructured carbonized forms of PANIs is given. For both type of materials, PANI and c-PANI, special attention is devoted to the advances in the field during the last five years.

## WATER-BORNE POLYMER AND COMPOSITE NANOSTRUCTURED PARTICLES

R. Tomovska<sup>1,2</sup>

<sup>1</sup>*Polymat and Departamento de Química Aplicada, Facultad de Ciencias Químicas, University of the Basque Country UPV/EHU, Jose Mari Korta Zentroa, Tolosa Hiribidea 72, Donostia/San Sebastian, Spain*

<sup>2</sup>*IKERBASQUE, Basque Foundation for Science, 48011, Bilbao, Spain*

### ABSTRACT

Water borne polymer and composite nanostructured particles are products by process; therefore their final characteristics are influenced by the formulation and the process parameters. In the present work, controlled synthesis of hybrid nanostructured particles based on (meth)acrylic monomers and polyurethanes (PU) prepolymers, obtained in different type of reactors (continuous, semi-continuous and batch) and different type of initiation system (thermally or UV light) and their application are presented.

### INTRODUCTION

A nanoparticle is a fundamental component in the fabrication of nanostructures and their synthesis is important issue within various field of investigations.[1] On the other hand, polymers are most widely applied materials in almost all spheres of modern life. The synthesis of polymeric nanoparticles extends even further the application possibilities of polymers. Usual way of synthesis of polymer nanoparticles are the techniques of polymerization in aqueous dispersed media, such as emulsion, miniemulsion, microemulsion, suspension and dispersion polymerization.<sup>2</sup> Their common features are that the polymerization mostly proceeds through free radicals and the dispersed phase is stabilized by means of surface-active compounds (surfactants, suspension agents). Major advantages of these techniques are: environmental friendly nature of the solvent, cheap and versatile process (wide range of experimental conditions, various monomers), efficient heat transfer- easy control of reaction temperature no organic volatile compounds, high polymer content – low viscosity, controlled polymer particle morphology, radical compartmentalization effect in droplets/particles.

Water-borne polymeric nanoparticles dispersions are widely used in a huge number of applications: coatings, adhesives, paints, paper coatings, additives for concrete, tires, textile and leather industry, cosmetics,

flocculants and biomedicine.[2] Water borne nanostructured particles are products by process, therefore their final characteristics depend on the formulation (type and amount of monomers, surfactant, initiator) and the process parameters (temperature, agitation, type of reactor and reaction, feed strategy). In our work the variation of these parameters is used to achieve control of the product properties. In the present work, selected results of few independent studies, based on hybrid (meth)acrylic monomers/polyurethanes (PU) formulations are presented. For composite nanostructured particles synthesis, graphene nanoplatelets were added to (meth)acrylic/PU. The thin films are formed from the aqueous dispersions by water evaporation usually under atmospheric conditions, which gives environmental friendly dimension of the presented techniques, as no volatile organic substances are released during film formation.

## RESULTS AND DISCUSSION

### Water-borne polymer nanoparticles

This study has been performed in continuous narrow tube quartz reactor, where the free radical miniemulsion polymerization of (meth)acrylic/PU hybrid formulation was initiated by UV light and suitable photoinitiator. To prepare polymer with a carefully selected glass transition temperature ( $T_g$ ) for adhesive application (much below room temperature), a monomer system composed of more than 90% 2-ethylhexyl acrylate (2-EHA), and minor amounts of methyl methacrylate (MMA) and methacrylic acid (MAA) was selected. This hybrid miniemulsion has been previously polymerized by thermally induced reaction, however higher temperature limited the possibility of control of the final polymer microstructure. As UV light initiation is effective at room temperature it was an interesting option in attempts of better control of the polymer microstructure.

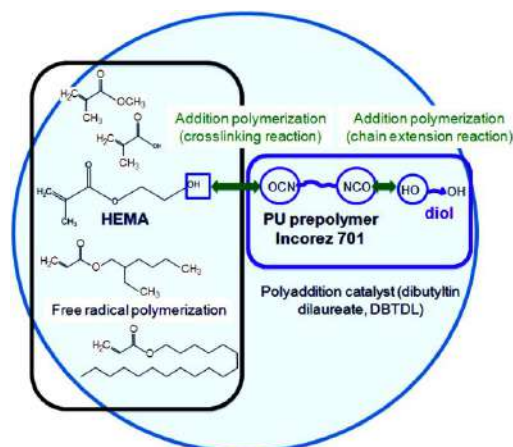


**Figure 1.** Reaction occurring in a miniemulsion droplet of (meth)acrylic/PU hybrid formulation

In Fig. 1 the reactions occurring within a miniemulsion droplet are presented. The free radical polymerization of the acrylic monomers is started after formation of radicals from oil soluble initiator upon light

absorption. Due to the very fast addition of the first monomer unit ( $10^5$ - $10^7$   $\text{Lmol}^{-1}\text{s}^{-1}$ ), the polymer chains grow fast.[3] In parallel, PU prepolymer due to the presence of diol in the formulation suffer addition polymerization and chain extension. The functional monomer hydroxyethyl methacrylate creates crosslinking between them. In Fig. 2 the influence of incident light irradiance (ILI) and photoinitiator (PI) content on the reaction kinetics and polymer microstructure is shown.[4]

Fig. 2a shows that by increasing the content of PI at constant ILI reaction rate increased due to the higher number of radicals, which leads to decreased gel fraction and sol molecular weight (molecular weight of the soluble part after extraction of the crosslinked-gel part) likely due to the important termination. Similar effect was noticed when ILI was increased at constant PI content (Fig. 2b). The presented process has shown to be quite flexible, resulting in wide variety of hybrids with different microstructures using the same formulation and only by changing the reaction parameters.

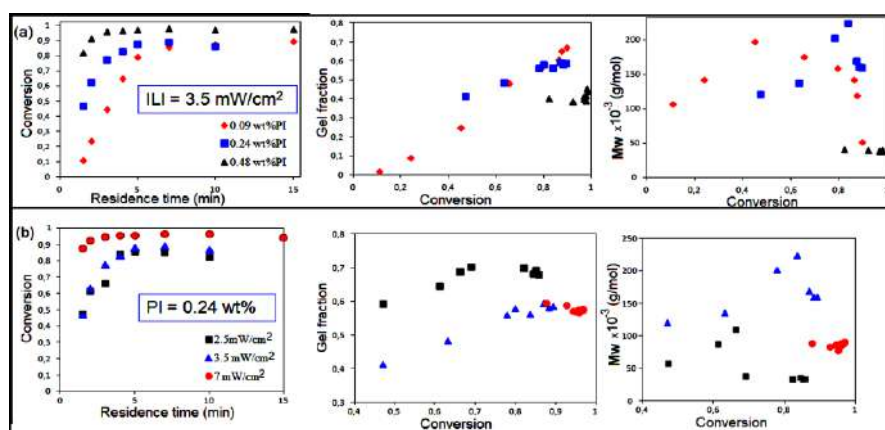


**Figure 2.** Kinetics data and polymer microstructure dependence on (a) PI content and (b) Incident light irradiance (ILI) in miniemulsion photopolymerization of PU/acrylic hybrid

From the nanoparticles dispersions adhesive films were prepared by water evaporation and probe-tack, property characteristic for PSAs that tests the short-time, low-pressure adhesion, was measured. This test has the advantage of applying a fairly uniform displacement (uniform stress field and strain rate) to the adhesive film over the whole surface of the probe, and for those soft systems where failure involves the formation of cavities and fibrils, it facilitates the analysis of the process.[5] For the determination of the polymer molecular weight and distribution we usually use Gel permeation chromatography (GPC), which requires well soluble samples

within the solvent carrier. Thus, the characterization was limited on analysis of the soluble part, and was not enough to explain the difference in performance.

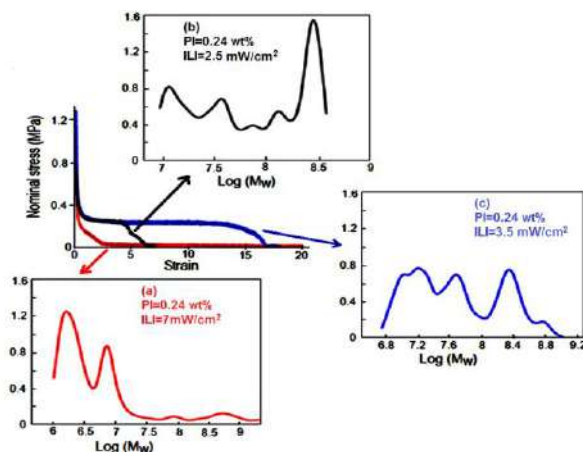


**Figure 3.** Microstructure/performance relationship of PU/acrylic hybrids obtained under different process conditions

By relatively new technique Asymmetric flow field flow fractionation it was possible to analyze the whole polymer,[6] without

extracting the insoluble gel fraction, resulting in the molecular weight distribution of whole polymer (Fig. 3).[8] Up to  $10^6$  g/mol, soluble part of the polymer is presented, after which value the crosslinked part appeared.[6] These measurements allowed development of relationship between the microstructure of the polymers and their performance as PSAs. Fig. 3 shows a set of probe-tack curves obtained for different PSA's. At high ILI due to the instantaneous formation of high number of radicals and subsequently important termination, relatively high molecular weight soluble chains with very small gel fraction were formed, resulting in liquid like behavior of this hybrid PSA (Fig. 3a). In case of very low ILI (Fig. 2b) the chains grow larger and important amount of gel is formed, resulting in too-cohesive PSA. And finally, at intermediate ILI (Fig. 3c), balanced PSA were obtained coming from both high molecular weight soluble chains and high fraction of gel part.

#### Water-borne composite nanoparticle synthesis

The same chemistry of PU/acrylics presented previously has been used to prepare highly crosslinked composite nanoparticles with graphene nanoplatelets. We are all aware about the emergency of graphene based materials and their wide possibilities of application. One of the important areas of graphene application is in polymer composite materials, where addition of small graphene amount within the polymer matrix provides the new materials with electrical or thermal conductivity, mechanical strength and thermal resistivity. Water-borne dispersions are advantageous due to the fact that large-aspect-ratio GNPs are placed in the limited space between the

polymer nanoparticles (excluded volume), as it prevents graphene aggregation and improve the dispersion within the matrix.[7,8]

For the synthesis reduced graphene oxide (rGO) was used, containing minor amount of oxygen functional groups, stabilized in aqueous dispersion by polyvinyl pyrrolidone (PVP). In the present study the monomer formulation composed of methyl methacrylate (MMA) and butyl acrylate (BA) in 50/50 weight ratio was used (coating formulation).

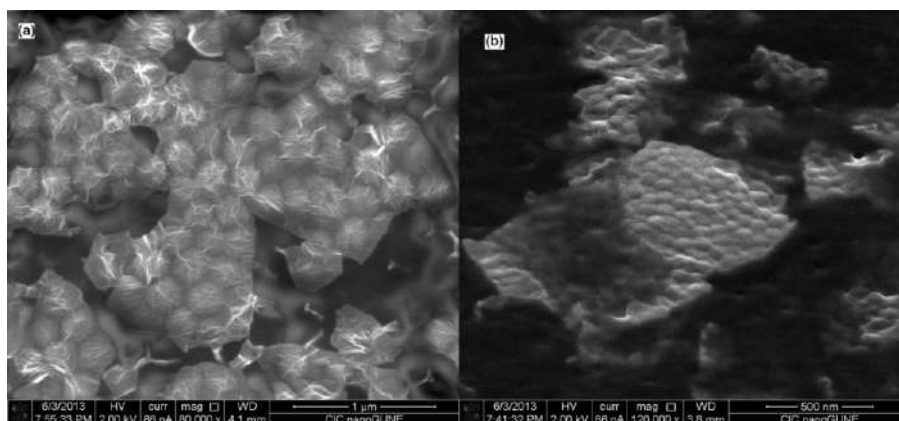
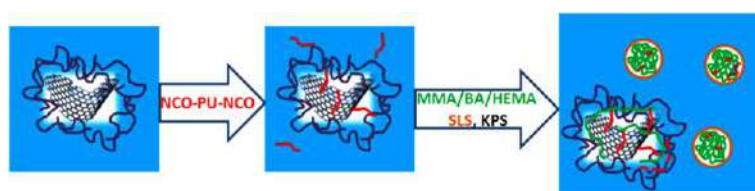


**Figure 4.** SEM images of the monolayers of polymer nanoparticles/rGO dispersions: a) hybrid composite blends, and b) hybrid dispersions obtained by in situ reaction.

In the first step (meth)acrylic monomers were polymerized by in situ batch emulsion polymerization in presence of rGO (0.25-1 wt%) and the it was compared with simple blend of water-borne polymer nanoparticles and rGO platelets. In order to evaluate the size and interactions of the nanoparticles in the hybrid dispersions, the monolayer of the hybrid dispersions were cast onto the silicone substrate, to avoid the interactions during water evaporation and film formation. The SEM images of the monolayers are presented in Fig. 4.[9] Fig. 4a shows that after mixing of rGO platelets and MMA/BA polymer particles of average diameter of around 300 nm, the nanoparticles are adsorbed strongly onto rGO platelets, likely due to the presence of PVP.[10] In the Fig. 4b, the monolayer composite film from in situ hybrid dispersion presents a kind of composite platelets with average dimensions of around 500 nm, composed of rGO with polymer particles densely packed on the surface. This indicates that the polymer particles were nucleated from the rGO platelets that results in covalent bonding between them. This behavior in similar systems has been already reported.[11]

In order to covalently bond rGO and polymer in more controlled way, reactions sites were created by introduction of suitable functionalities onto both components (rGO and polymer), by introduction of OH functionalities onto polymer nanoparticle and PU prepolymer with isocyanate groups on both chain ends. PU was dispersed in rGO aqueous dispersions, and covalent bond with OH of rGO was established resulting in *in situ* modification of the platelets. After that the monomers MMA/BA were slowly introduced in the system. As the modified rGO platelets contain NCO reactive groups on their surface, we expect that the polymer nanoparticles will start to grow from these reaction sites (Scheme 1).[12]



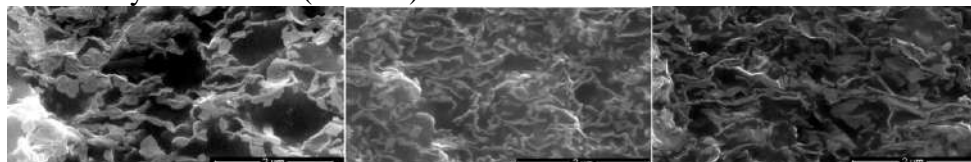
**Scheme 1.** rGO/PU/polymer reactions.

As a result nanostructured particles containing highly crosslinked polymer/rGO were obtained, from which composite films were prepared by water evaporation. Tab.1 shows the compositions and some characteristics of these films.

**Table 1.** Composition and characteristics of rGO/PU/MMA/BA composites

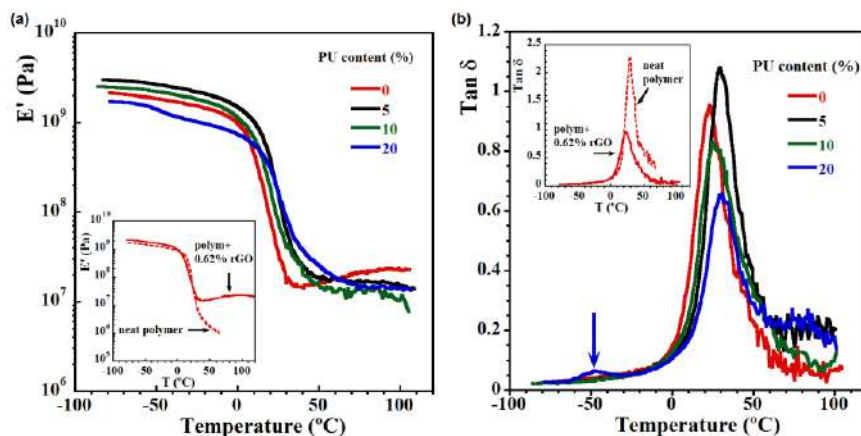
PU content (%wt.)	rGO content (%wt.)	Gel content (%wt.)	Swelling at 25°C	Electrical conductivity (S m <sup>-1</sup> )
0	0.62	14	8.7	$(2.68 \pm 0.220) \cdot 10^{-4}$
5	0.62	63	4.9	$(2.20 \pm 0.004) \cdot 10^{-3}$
10	0.62	48	6.8	$(0.66 \pm 0.110) \cdot 10^{-3}$
20	0.62	47	7.0	$(1.04 \pm 0.001) \cdot 10^{-3}$
10	0.75	53	6.5	$(3.00 \pm 0.006) \cdot 10^{-2}$
10	1.00	65	5.0	$(2.96 \pm 0.011) \cdot 10^{-2}$

Table 1 shows that in presence of both rGO and PU the gel content (the crosslinked part of the composite) increased significantly and its amount depends on the added amounts of PU, as it acts as a crosslinker. The composite films placed in THF solvent swelled in the solvent, showing that the composites have a crosslinked structure. The composite films are electrically conductive (Table 1).



**Figure 5.** SEM cross-sectional images of composite films containing (a) 5 wt% PU and 0.62 wt% rGO; (b) 10 wt% PU and 0.75 wt% rGO; and (c) 10 wt % PU and 1 wt% rGO.

In Fig. 5 the SEM images of the cross-sectional area of the films broken under liquid nitrogen are shown. The composites presented in Fig. 5a and 5b shows random distribution of rGO in the matrix, likely due to the crosslinked structure (Table 1) that decreases the mobility of the rGO platelets during film formation. For the composite with 10%PU and 0.75% rGO with lower crosslinked fraction (53%), Fig. 5b shows that rGO platelets are ordered in direction perpendicular to the view, with defined polymeric areas of 300 nm, which is prosperous for the electrical conductivity.[9]



**Figure 6.** Viscoelastic properties of the composites containing 0.62 wt% rGO with respect to monomers and different amounts of PU: (a) dependence of storage modulus on temperature; and (b) dependence of  $\tan \delta$  on temperature

Viscoelastic properties of the composites, presented in Fig. 6, were obtained by DMTA measurements and show the influence of PU content on storage modulus (Fig. 6a) and on  $\tan \delta$  (Fig. 6b). The significant drop of the modulus and abrupt increase in  $\tan \delta$  is obvious for the neat polymer (insets). The addition of rGO allowed retaining a higher modulus even beyond the glass transition temperature ( $T_g$ ). It is observed a combination of the reinforcement effects from the filler and highly crosslinked structure. The presence of PU apparently improves the interactions between the matrix and the filler resulting in the expected increase of  $T_g$  (Fig.6b).

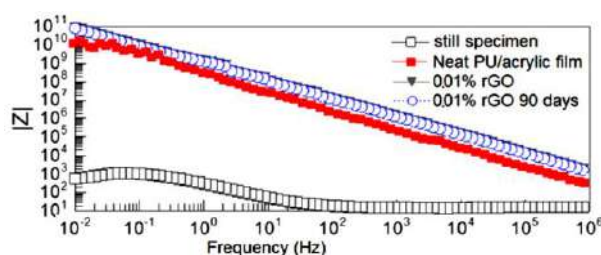


**Figure 7.** Impedance versus frequency after 90 days immersion in 3.5% NaCl

To determine the anticorrosion properties of these composite films containing different amounts of PU and rGO, the thin film of a thickness of 30  $\mu\text{m}$  were prepared on the still specimens that were exposed to NaCl (3%) aqueous solution for 90 days.

Fig. 7 shows the impedance dependence on the frequency for composites containing 0.01 wt% of rGO and 1 w% of PU, compared to the blank samples without rGO. Addition of very small amount of rGO improve the anticorrosion action of the PU/acrylic coating, which remain constant even after 90 days of immersion within NaCl solution.

## CONCLUSIONS

In this work the synthesis of PU/acrylics polymer and composite nanostructured particles were presented by polymerization in aqueous dispersed media (emulsion and miniemulsion). On one hand it was shown that by changing the process parameters the control of the final properties may be achieved and the performance as PSAs were explained by the difference in the polymer microstructure. In the composite nanoparticles, by changing in the (meth)acrylic formulation the application may be switch toward coating application. The polymer was reinforced by rGO platelets and PU, actuating as crosslinker between both phases (polymer and graphene). The improvement of mechanical properties and anticorrosion activities were determined.

**Acknowledgements**

The authors acknowledge the financial support of the Basque Government (GV IT373-10 and IE14-393) and NATO (SfP 984399) and to all PhD and postdoc students involved in the presented studies.

**REFERENCES**

- [1] J. Estelrich, M. Quesada-Perez, J. Forcada, J. Callejas-Fernandez, Chapter1 in RSC Nanoscience & Nanotechnology No. 34, Edited by J. Callejas-Fernandez, J. Estelrich, M. Quesada-Perez and J. Forcada, Publisher: The Royal Society of Chemistry, 2014.
- [2] R. Tomovska, J.C. de la Cal, J. M. Asua, Chapter4, In: Monitoring Polymerization Reactions: From Fundamentals to Applications, Edited by Wayne F. Reed and Alina M. Alb, Publisher: Wiley, Hoboken, 2014.
- [3] V. Daniloska, R. Tomovska, J. M. Asua, Chemical Engineering Journal 2012, **184**, 308–314
- [4] V. Daniloska, R. Tomovska, J. M. Asua, Polymer 2014, **55**, 5050 – 5056
- [5] Daniels et al.; Polymer Colloids, ACS Symposium Series; American Chemical Society: Washington, DC, 2001.
- [6] Daniloska, P. Carretero, R. Tomovska, M. Paulis, J.M. Asua, ACS Appl. Mater. Interfaces 2014, **6**, 3559–3567
- [7] Y. V. Syurik, M. G. Ghislandi, E. E. Tkalya, G. Paterson, D. McGrouther, O. A. Ageev, J. Loos, Macromol. Chem. Phys. 2012, **213**, 1251.
- [8] N. Yousefi, M. M. Gudarzi, Q. Zheng, S. H. Aboutalebi, F. Sharif, J. K. Kim, J. Mater. Chem. 2012, **22**, 12709
- [9] A. Arzac, G. P. Leal, R. Fajgar, R. Tomovska, Part.Part.Syst. Charact. 2014, **31**, 143–151
- [10] M. M. Gudarzi, F. Sharif, J. Coll. Interface Sci. 2012, **366**, 44
- [11] H. Hu, X. Wang, J. Wang, L. Wan, F. Liu, H. Zheng, R. Chen, C. Xu, Chem. Phys. Lett. 2010, **484**, 247
- [12] D. Spasevska, G. P. Leal, M. Fernandez, J. Blazevska Gilev, M. Paulis, R. Tomovska, RSC Adv., 2015, **5**, 16414–16421

**THE INFLUENCE OF MICROSTRUCTURE OF  
POLYMER CHAIN ON ADHESIVE PROPERTIES OF  
POLY(STYRENE/n-BUTYL ACRYLATE) BINARY  
COPOLYMER FILMS  
FORMED FROM VARIOUS SOLVENTS**

Yu. Bogdanova<sup>1</sup>, V. Dolzhikova<sup>1</sup>, A. Shapagin<sup>2</sup>, J. Kostina<sup>3</sup>, A. Plutalova<sup>1</sup>,  
A. Scherbina<sup>2</sup> and E. Chernikova<sup>1</sup>

<sup>1</sup>*Moscow Lomonosov State University, Leninskie Gory, 1/3, 119991,  
Moscow, Russia (yulibogd@yandex.ru),*

<sup>2</sup>*Frumkin Institute of Physical Chemistry and Electrochemistry RAS,  
Leninsky prospect, 31/4, 119071, Moscow, Russia,*

<sup>3</sup>*Topchiev Institute of Petrochemical Synthesis RAS,  
Leninsky prospect, 29, 119071, Moscow, Russia.*

#### **ABSTRACT**

The surface properties of the films of poly(styrene/n-butyl acrylate) binary copolymers (PS/PNBA) with 30% styrene (ST) mole fraction and various monomer unit distribution (random and gradient), formed from various solvents (toluene, acetone) were studied. The original approach for investigation of the influence of the chain microstructure and solvent thermodynamic quality on the energy characteristics of the surface of the copolymer films and their adhesive properties with respect to solid substrates of various polarity (glass, steel, polyethylene and polyethylene terephthalate) was developed [1]. This approach is based on the combination of contact angle measurements, ATR-FTIR (Attenuated Total Reflection Fourier Transform Infrared), quantum chemical calculations of polymer–solvent interactions and strength tests. The sensitivity of adhesive characteristics to solvent nature of the films of the gradient copolymers differed from the same characteristics of random copolymers. The results obtained demonstrated the principle possibility of regulation of the copolymer adhesion by varying chain architecture and nature of the solvent from which the copolymer films were formed.

#### **INTRODUCTION**

The gentle regulation of polymer adhesion is one of the actual problems of modern material science. The insertion of second monomer in polymer chain is one of the common synthetic approaches for the realization of this goal. But it should be noted that the development of principles of polymer

design is currently outpacing the understanding of regularities of influence on the polymer adhesive properties such parameters as polymer chain microstructure and thermodynamic quality of solvent, from which polymer films were formed.

The aim of our study was the development of experimental methodology with respect to study of adhesion of binary copolymers to various solid substrates using the combination of contact angle measurements and other techniques, namely – with ATR-FTIR, quantum chemical simulation and strength tests.

### EXPERIMENTAL

The objects of our study were films of PS/PNBA with gradient (GC-30) and random (RC-30) monomer distribution (Fig.1). These copolymers were synthesized via controlled radical polymerization via the reversible addition-fragmentation chain-transfer mechanism (RAFT polymerization) using dibenzyl trithiocarbonate as chain transfer agent [1]. The characteristics of copolymers were:  $M_n = 51$  kDa,  $M_w/M_n = 1.11$  for GC-30 and  $M_n = 58.7$  kDa,  $M_w/M_n = 1.56$  for RC-30.

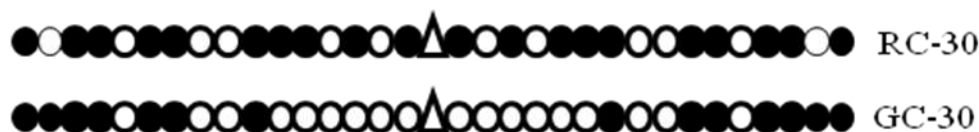


**Figure 1.** Scheme of order of sequence of monomer units in PS/PNBA chains with random (RC) and gradient (GC) microstructure:  
 ○ butyl acrylate, ● styrene, Δ trithiocarbonate group.

The polymer films were formed from toluene (thermodynamically «good» solvent for ST and «bad» for NBA) and acetone («good» for n-butyl acrylate (NBA) and «bad» for ST). The alumina plates were used as a solid carriers. In our previous study the interrelation between PS/PNBA chain microstructure, solvent nature and surface energy characteristics of polymer films was illustrated; the styrene mole fractions were 10 and 60% [1]. In this study the ST mole fraction was 30% in order to allow the formation of adhesion compounds and, on the other hand, to provide the relatively high glass temperatures to avoid the impropriety of strength tests caused by the high fluidity of polymer adhesive.

The sessile drop technique was applied for contact angle measurements. The surface energy of polymer films ( $\gamma_{sv}$ ), its polar ( $\gamma_{sv}^p$ ) and dispersive ( $\gamma_{sv}^d$ ) components were calculated using experimental contact angles of the drops of probe liquids (water and diiodomethane) in accordance with Owens-

Wendt-Kaelble approach [2]. The methods of calculation of the work of adhesion of PS/PNBA to water, simulating the polar solid substrate ( $W_{pp}$ ) and octane, simulating the nonpolar one ( $W_{dd}$ ) as well as technique of ATR-FTIR study are presented in details in [1].

The quantum chemical simulation of interaction of the NBA and ST with acetone or toluene was performed by semi-empirical method AM-1 with MOPAC software package.

The strength tests were performed at the breaking machine Zwick/Roell Z010. The destruction of the adhesive compounds of PS/PNBA with solid substrates was performed by exfoliation technique (peel angle  $180^\circ$ ) with subsequent identification of exfoliation mechanism using scanning electronic microscope Philips SEM-500. The solid substrates were glass, steel, polyethylene and polyethylene terephthalate (PET). The PS/PNBA layer thickness was  $50\mu\text{m}$ . All measurements were carried out at  $20^\circ\text{C}$ .

## RESULTS AND DISCUSSION

The  $\gamma_{sv}^d$  of PS/PNBA brings a dominant contribution in the surface energy value for all copolymer films, independently of the solvent nature from which polymer film was formed (Table 1). Thus, the close values of  $W_{dd}$

**Table 1.** PS/PNBA films surface energy ( $\gamma_{sv}$ ), its polar ( $\gamma_{sv}^p$ ) and dispersive ( $\gamma_{sv}^d$ ) modes and the work of adhesion of PS/PNBA to polar ( $W_{pp}$ ) and nonpolar ( $W_{dd}$ ) liquid, simulating solid substrates.

polymer	solvent	$\gamma_{sv}$ , $\text{mJ}\cdot\text{m}^{-2}$	$\gamma_{sv}^d$ , $\text{mJ}\cdot\text{m}^{-2}$	$\gamma_{sv}^p$ , $\text{mJ}\cdot\text{m}^{-2}$	$W_{dd}$ , $\text{mJ}\cdot\text{m}^{-2}$	$W_{pp}$ , $\text{mJ}\cdot\text{m}^{-2}$
	toluene	44	44	-	61	77
GC-30	acetone	45	43	2	61	106
	toluene	42	41	1	60	96
RC-30	acetone	41	40	1	59	101

for all copolymer films are rather expectable.

In comparison to  $\gamma_{sv}^d$ , the  $\gamma_{sv}^p$  values are negligibly low. Nevertheless, a difference between the  $W_{pp}$  for PS/PNBA of different microstructure with respect to solvent nature was found. The noticeable difference between  $W_{pp}$  is observed in case of GC-30. The strength of adhesive compounds ( $A$ ) of GC-30 with different substrates also differs considerably for polyethylene and other polar substrates, for example, PET (Fig. 2).

In case of RC-30 the relationship between  $A$  and  $W_{pp}$  could not be established due to the cohesion destruction of adhesive compounds.

The adhesion of PS/PNBA to polar phases is realized due to NBA comonomer, containing the polar groups. Thus, the result obtained may be

caused by the higher mobility of NBA monomer units in polymer chain with gradient microstructure in comparison to random one.

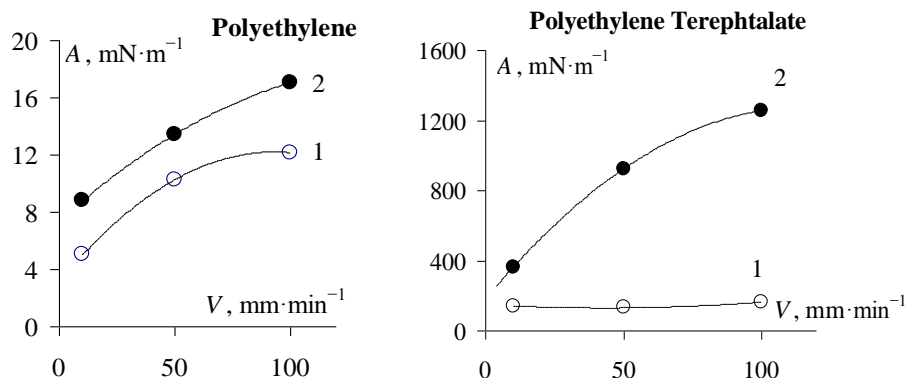


**Figure 2.** Plot peel strength ( $A$ ) versus delaminating speed ( $V$ ) for adhesive compounds of RC-30 films, formed from toluene (1) and acetone (2) on solid substrates.

Indeed, quantum chemical calculations proved the energetic benefit of reorientation of NBA units contacting with polar phase (water). For example, in the case of triad of NBA units (highly probable in case of GC-30) the energy of intermolecular interaction  $\Delta E = -10 \text{ kJ}\cdot\text{mol}^{-1}$  is lower in comparison to NBA-water interaction  $\Delta E = -20,8 \text{ kJ}\cdot\text{mol}^{-1}$ .

## CONCLUSIONS

The new methodological approach to study of influence of chain microstructure and solvent nature on adhesion of polymer films [3] was developed for the new objects. The distinction between the adhesive properties of copolymer films with gradient distribution of monomer units with respect to polar and nonpolar solid substrates formed from different solvents was confirmed by using contact angle measurements, quantum chemical calculations and the strength tests.

## Acknowledgement

This work was supported by Russian Foundation of Basic Research, project 14-03-00142.

## REFERENCES

- [1] Y. G. Bogdanova, J. V. Kostina, V. D. Dolzhikova et al, Russian Journal of Physical Chemistry A, 2015, **89** (13), 2466–2472.
- [2] J. Kloubek, Adv. in Colloid and Interface Sci, 1992, **38**, 99–142.

## INTRAPARTICLE DIFFUSION AND ADSORPTION OF HEAVY METALS ONTO POROUS POLYMER

B. M. Ekmešćić<sup>1</sup>, Z. P. Sandić<sup>2</sup>, Lj. T. Suručić<sup>1</sup>, J. P. Marković<sup>3</sup>,  
I. S. Stefanović<sup>1</sup> and A. B. Nastasović<sup>1</sup>

<sup>1</sup>*University of Belgrade, Institute of Chemistry, Technology and Metallurgy, Njegoševa 12, 11000 Belgrade, Serbia. (bojanae@chem.bg.ac.rs)*

<sup>2</sup>*University of Banja Luka, Faculty of Science, 78000 Banja Luka, Mladena Stojanovića 2, B&H (Republic of Srpska).*

<sup>3</sup>*University of Belgrade, Vinča Institute of Nuclear Sciences, P.O. Box 522, 11001 Belgrade, Serbia.*

### ABSTRACT

Intraparticle diffusion kinetic model (IPD) was used to elucidate the influence of macroporous glycidyl methacrylate (GMA) and ethylene glycol dimethacrylate (EGDMA) copolymer (PGME) with attached diethylene triamine (PGME-deta) on the competitive Cu(II), Cd(II), Co(II) and Ni(II) ions sorption from aqueous solutions. Surface sorption was examined by SEM-EDS analysis.

### INTRODUCTION

Copper, cadmium, cobalt and nickel (Co, Cd, Co and Ni) are among the most common pollutants in industrial effluents [1]. Chronic exposure to high Cd levels causes renal dysfunction, bone degeneration, liver and blood damage. Co and Ni cause skin rashes, asthma, allergies, pneumonia, etc. Cu can also be toxic, even at very low concentrations. The EPA requires Cu and Cd levels in drinking water not to exceed 1.3 and 0.005 mg L<sup>-1</sup>, respectively [2]. Maximum permitted levels in drinking water for Cu, Ni and Cd in Republic of Serbia are 2.0, 0.02 and 0.003 mg L<sup>-1</sup> [3]. Polymeric adsorbents have been frequently used for heavy metals removal from aqueous solutions. Amino-functionalized macroporous PGME has high capacity and good selectivity for the precious and heavy metal ions over alkali and alkaline earth metals [4]. Depending on pH, it can coordinate heavy and precious metals or bind them as chloro complexes [5].

### EXPERIMENTAL

Macroporous PGME was prepared by free-radical suspension polymerization of GMA and EGDMA thermally initiated by decomposition of 2,2'-azobis (isobutyronitrile) (AIBN) as the source of radicals in the

presence of inert component (cyclohexanol and hexadecanol) [6]. The copolymerization was carried out at 70 °C for 2 h and at 80 °C for 6 h with a stirring rate of 200 rpm. PGME sample was purified with ethanol, additionally functionalized with diethylene triamine and labeled as PGME-10/16-deta. Specific pore volume (0.66 cm<sup>3</sup>), pore diameter (60 nm) which corresponds to half of pore volume and specific surface area (50 m<sup>2</sup> g<sup>-1</sup>), of PGME-10/16-deta were determined by mercury porosimetry (Carlo Erba 2000, software Milestone 200). SEM-EDS (energy-dispersive X-ray spectroscopy) analysis was performed on Jeol JSM 5800 instrument operating at 20 kV. The amino group concentration calculated from elemental analysis was  $C_{AG}=4.9$  mmol g<sup>-1</sup>. Sorption of metal ions was investigated under batch competitive conditions. PGME (0.5 g) was contacted with 50 cm<sup>3</sup> of mixed metal salt solution ( $C_i=0.05$  M, pH=5.0,  $t=180$  min,  $T=298$  K). The concentration of Cu(II), Cd(II), Co(II) and Ni(II) ions in the aqueous phases was determined by atomic absorption spectrometry (AAS, SpektrAA Varian Instruments). The sorption capacity ( $Q_t$ , mmol g<sup>-1</sup>) at any time  $t$ , was calculated from:

$$Q_t = \frac{(C_i - C_t)V}{m} \quad (1)$$

Where:  $C_i$  and  $C_t$  are concentrations of metal ions in the initial solution and in aqueous solution at time  $t$  (min),  $V$  is the volume of the aqueous phase (dm<sup>3</sup>) and  $m$  is the mass of the sorbent particles (g).

## RESULTS AND DISCUSSION

Previous study showed that the maximum sorption capacities of PGME-10/16-deta under competitive conditions were 1.18 mmol g<sup>-1</sup> for Cu(II), 0.67 mmol g<sup>-1</sup> for Cd(II), 0.24 mmol g<sup>-1</sup> for Co(II) and 0.23 mmol g<sup>-1</sup> for Ni(II) ions [4].

For the sake of additional understanding of Cu(II), Cd(II), Co(II) and Ni(II) ions sorption, the surface of

PGME-10/16-deta particles with sorbed metal ions was examined by SEM-EDS analysis. The results are presented in Figure 1 and Table 1.

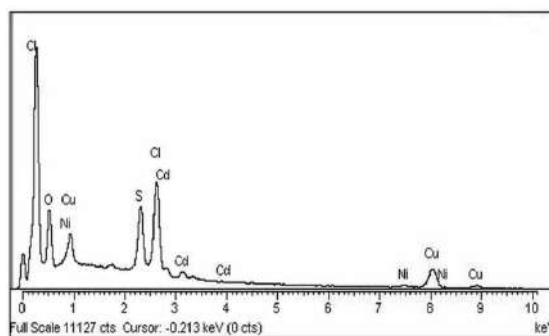


**Figure 1.** EDS spectra of PGME-10/16-deta with sorbed heavy metal ions.

As expected, EDS analysis confirmed that amount of metal ions bounded to the amino groups on the particle surface decreased in the order: Cu(II) >> Cd(II) > Ni(II) ions. Previously, it was established that Cu(II), Cd(II), Co(II) and Ni(II) ions sorption under competitive conditions obeys pseudo-second order (PSO) kinetics [4]. Namely, the coefficients of determination ( $R^2$ ) for the PSO kinetics model were closer to unity in comparison to the corresponding  $R^2$  values for PFO kinetics. Also, the experimental equilibrium capacity ( $Q_e^{\text{exp}}$ ) values were almost identical to the values calculated ( $Q_e^{\text{calc}}$ ) using PSO kinetics model, indicating that the sorption rate is controlled by both the sorbent capacity and the sorbate concentration.

In this study, intraparticle (IPD) model was applied to determine whether the process rate in the studied sorption system is directed by film and/or pore diffusion [7, 8]:

**Table 1.** SEM-EDS analysis of PGME-10/16-deta with sorbed heavy metal ions

Element	Mass. %	Atomic %
O K	54.68	76.40
S K	9.71	6.77
Cl K	17.45	11.00
Ni K	0.98	0.37
Cu K	13.34	4.69
Cd L	3.84	0.76

$$Q_t = k_{id}t^{1/2} + C_{id} \quad (2)$$

where  $k_{id}$  is the intraparticle diffusion coefficient and  $C_{id}$  is a constant related to the thickness of the boundary layer.

IPD ( $Q_t - t^{1/2}$ ) plots for the Cu(II), Cd(II), Co(II) and Ni(II) ions sorption are given in Figure 2. The maximal sorption capacities and kinetic parameters calculated from

IPD kinetic model are presented in Table 2.

According to the literature, multilinear IPD plots observed in Fig. 2 might represent the stages of sorbate sorption into the macro-, meso-, and microporous structure of sorbent [8,9]. The first and the fastest stage of heavy metal ions sorption can be ascribed to the sorption over the external surface and in the macropores of PGME-deta, the second to the IPD through mesopores, while the third could be regarded as the diffusion through micropores, and achieving the equilibrium.

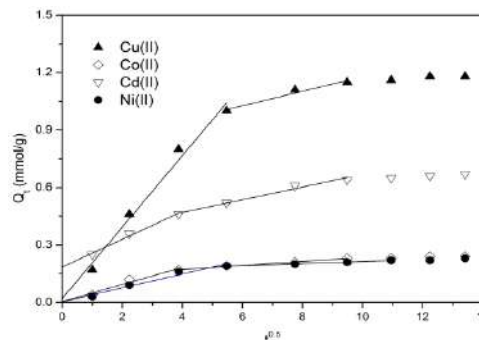


**Figure 2.** Plots of IPD model for competitive Cu(II), Cd(II), Co(II) and Ni(II) ions sorption on PGME-10/16-deta.

**Table 2.** Kinetic parameters for Cu(II), Cd(II), Co(II) and Ni(II) ions sorption using PGME-10/16-deta calculated from IPD kinetic model.

Intraparticle diffusion	Metal ions			
	Co(II)	Cd(II)	Cu(II)	Ni(II)
$k_{1id}$ , mmol/(g min <sup>0.5</sup> )	0.045	0.073	0.187	0.036
$C_{1id}$ , mmol/g	0.005	0.186	0.020	0.004
$R^2$	0.955	0.988	0.983	0.966
$K_{2id}$ , mmol/(g min <sup>0.5</sup> )	0.010	0.033	0.038	0.005
$C_{2id}$ , mmol/g	0.131	0.338	0.799	0.159
$R^2$	0.996	0.979	0.965	0.990

## CONCLUSION

Kinetics of competitive Cu(II), Cd(II), Co(II) and Ni(II) ions sorption from aqueous solutions by macroporous PGME-deta was analyzed using intraparticle diffusion (IPD) kinetic model. The analysis revealed that pore diffusion was the only rate-controlling step in the process of heavy metal sorption by the porous copolymer.

## Acknowledgement

This work was supported by the Ministry of Education, Science and Technological Development of the Republic of Serbia (Grants no. TR37021, ON172062 and III43009).

## REFERENCES

- [1] Agency for Toxic Substances and Disease Registry (ATSDR), Toxicological Profiles, Public Health Service, Atlanta, 1999.
- [2] <http://www.epa.gov/your-drinking-water/table-regulated-drinking-water-contaminants#Inorganic>
- [3] Regulation about sanitary correctness of drinking water ("Sl. list SRJ", br. 42/98 i 44/99).
- [4] A. Nastasović, D. Jakovljević, Z. Sandić, D. Đorđević, Lj. Malović, S. Kljajević, J. Marković, A. Onjia in: Reactive and Functional Polymers Research Advances, Chapter 2, M. I. Barroso (Ed.) Nova Science Publishers, Inc., 2007.
- [5] E. Kalalova, P. Thuy, Angew. Makromol. Chem. 1990, **180**, 159-167.
- [6] Lj. Malović, A. Nastasović, Z. Sandić, J. Marković, D. Đorđević, Z. Vuković, J. Mater. Sci., 2007, **42**, 3326-3337.
- [7] W.J. Weber, J.C. Morris, J. Sanitary Eng. Div., 1963, **89**, 31-60.
- [8] C. Valderrama, J. L. Cortina, A. Farran, X. Gamisans, F. X. de las Heras, React. Funct. Polym., 2008, **68** (3), 718-731.
- [9] F.C. Wu, R.L. Tseng, R.S. Juang, Chem. Eng. J., 2009, **153**, 1-8.

## A NOVEL Tc <sup>99m</sup> SORBENT BASED ON MACROPOROUS MAGNETIC POLYMER

B. M. Ekmešćić<sup>1</sup>, D. Lj. Janković<sup>2</sup>, A. A. Vukadinović<sup>2</sup>,  
D. V. Ranđelović<sup>1</sup>, I. S. Stefanović<sup>1</sup> and A. B. Nastasović<sup>2</sup>

<sup>1</sup> University of Belgrade, Institute of Chemistry, Technology and Metallurgy,  
Njegoševa 12, 11000 Belgrade, Serbia. (bojanae@chem.bg.ac.rs)

<sup>2</sup> University of Belgrade, Vinča Institute of Nuclear Sciences, P.O. Box 522,  
Belgrade, Serbia.

### ABSTRACT

A novel magnetic macroporous poly(glycidyl-*co*-ethylene glycol dimethacrylate) (mPGME) synthesized by suspension copolymerization and functionalized with diethylene triamine (mPGME-deta) was evaluated as sorbent for pertechnetate ion (TcO<sub>4</sub><sup>-</sup>) removal from aqueous solutions. Atomic force microscopy (AFM) was used for characterization. The kinetics of TcO<sub>4</sub><sup>-</sup> adsorption onto mPGME-deta is relatively fast and depends on pH.

### INTRODUCTION

Magnetic polymers have been used in biomedical applications like cell separation [1], affinity chromatography [2], targeted drug delivery [3], etc. In this study, magnetic macroporous mPGME microspheres were prepared by suspension polymerization, functionalized with diethylene triamine (mPGME-deta) and tested as technetium-99 sorbent from aqueous solutions.

### EXPERIMENTAL

#### *mPGME synthesis and amino-functionalization*

Macroporous mPGME was prepared by suspension copolymerization of glycidyl methacrylate (GMA) and ethylene glycol dimethacrylate (EGDMA, crosslinker), in the presence of inert component and suspended magnetite nanoparticles prepared via improved chemical coprecipitation method [4]. The aqueous phase consisting of 225.0 g of water and 2.25 g poly(*N*-vinyl pyrrolidone) was placed in polymerization reactor and heated to 70 °C. The monomer phase containing monomer mixture (19.5 g GMA and 29.1 g EGDMA), AIBN as initiator (0.5 g), 63.8 g of inert component (51.0 g of cyclohexanol and 12.8 g of tetradecanol) and 1.15 g of magnetite (Fe<sub>3</sub>O<sub>4</sub>) nanoparticles was sonicated for 30 min at 300/600 W within an ultrasonic water bath (Sonic 12GT). The resulting mixture was dropped into polymerization reactor. The reaction mixture was stirred at 350 rpm during

the monomer addition and heating was started. The copolymerization was carried out under nitrogen atmosphere at 75 °C for 2 h and at 80 °C for 2 h with a stirring rate of 250 rpm. After the reaction, the magnetic copolymer beads (mPGME) were washed with water and ethanol, kept in ethanol for 12 h, and dried in vacuum at 50 °C. The mPGME was additionally functionalized with diethylene triamine as described elsewhere [5] and labeled as mPGME-deta.

The pore size distribution of mPGME was determined by mercury porosimetry (Carlo Erba 2000, software Milestone 200). The surface morphology of mPGME was studied by atomic force microscopy (AFM). Measurements were performed in air with AutoProbe CP-Research SPM (TM Microscopes-Bruker). Bruker Phosphorus (n) doped silicon Tap300 metrology probes, model MPP-11123-10 with Al reflective coating and symmetric tip Nominal spring constant of these cantilevers is 40N/m, while their resonance frequency is around 300 kHz. Due to the nature of the samples non-contact mode was applied. Both topography and “error signal” AFM images were taken and later analysed using the software Image Processing and Data Analysis Version 2.1.15 and SPMLab Analysis software from VEECO DI SPMLab NT Ver. 6.0.2.

#### **Sorption of Tc <sup>99m</sup>**

The pH-dependent sorption of TcO<sub>4</sub><sup>-</sup> by mPGME-deta was studied in aqueous buffer solutions at pH range 2-8. Aqueous buffer solutions were prepared from reagent grade chemicals and deionized water (Milli-Q Millipore 18 MΩcm<sup>-1</sup> conductivity). Batch experiments were performed at room temperature by mixing 50 mg of mPGME-deta, 4.9 ml of buffer solution and 0.1 ml of pertechnetate solution with activity of *ca* 10 MBq in a vial. The blanks were prepared in the same way but without mPGME-deta. The calculated amount of pertechnetate ions (<sup>99</sup>Tc + <sup>99m</sup>Tc) in every vial was *ca* 8.987·10<sup>11</sup>. Aliquots of 100 μl were drawn at predefined time points from the vials containing mPGME-deta as well as from the blanks. The aliquot activity was measured in well-type NaI (TI) gamma counter (2470 WIZARD2, *PerkinElmer, USA*). Relative measurements of adsorbed radioactivity were obtained using the following equation:

$$R = \frac{R_b - R_s}{R_b} \cdot 100\% \quad (1)$$

where R is the adsorbed <sup>99m</sup>Tc activity (%), R<sub>b</sub> is the measured activity of the blank aliquot (counts per min) and R<sub>s</sub> is the activity of the supernatant aliquot from the vials containing mPGME-deta (counts per min).

## RESULTS AND DISCUSSION

The specific surface area of the magnetic mPGME particles ( $92 \text{ m}^2 \text{ g}^{-1}$ ) was calculated as the sum of incremental specific surface areas from the pore size distribution curves as described in the literature [6]. The surface morphology of mPGME-deta was studied by atomic force microscopy (AFM). The measurements were performed at  $(5 \times 5) \mu\text{m}^2$  scan size with the resolution of  $(256 \times 256)$  data points per image. The Figure 1 shows 2D “error signal” AFM image of the top view of mPGME-deta. As can be seen, the sample surface is covered with a layer of absorbed magnetite.

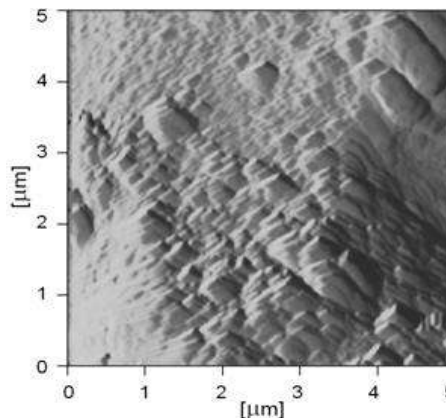


**Figure 1.** The 2D AFM image of the mPGME-deta

The average roughness ( $R_a$ ) and root mean square roughness ( $R_q$ ) were used for studying the sample morphology. The average roughness,  $R_a$ , and root mean square roughness,  $R_q$ , values were calculated to be  $0.181 \mu\text{m}$  and  $0.231 \mu\text{m}$ , respectively.

### The effect of pH on $\text{TcO}_4^-$ sorption

The solution pH is crucial parameter that affects the surface charge of the sorbent, the protonation-deprotonation of surface functional groups, metal speciation in the aqueous solution and consequently, the sorbate/sorbent interactions [7]. Thus, the effect of solution pH on  $\text{TcO}_4^-$  removal by mPGME-deta was investigated (Figure 2). Since previous experiments

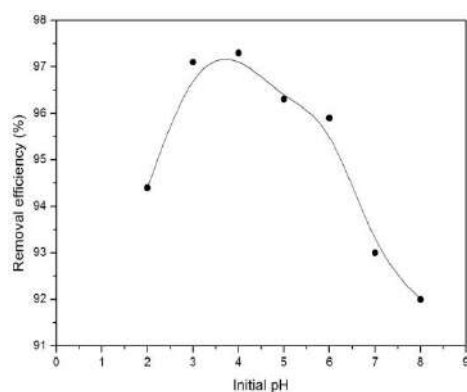


**Figure 2.** The effect of pH on the  $\text{TcO}_4^-$  removal efficiency,  $t=180 \text{ min}$

showed rapid sorption, with 90% of  $\text{TcO}_4^-$  sorbed within the first 5 min, the equilibrium time of 180 min was chosen for experiments in this study. The  $\text{TcO}_4^-$  sorption by mPGME-deta was pH-dependent, with optimal sorption pH between 3.0 and 6.0 and maximum at  $\text{pH} \sim 4.0$ . In acidic medium, the interactions between the protonated amino groups of mPGME-deta and negatively charged  $\text{TcO}_4^-$  anions promote high pertechnetate

removal. However, at  $\text{pH} \geq 6$ , the  $\text{TcO}_4^-$  sorption sharply decreased due to the decrease of the number of protonated amino groups in mPGME-deta.

### CONCLUSION

A novel magnetic macroporous mPGME was tested as sorbent for pertechnetate ion ( $\text{TcO}_4^-$ ) removal from aqueous solutions. AFM measurement showed mPGME surface covered with a layer of absorbed magnetite. The  $\text{TcO}_4^-$  sorption onto mPGME-deta was fast and pH-dependent, with high removal efficiency of 96% for 180 min in the pH range 3.0-6.0.

### Acknowledgement

This work was supported by the Ministry of Education, Science and Technological Development of the Republic of Serbia (Grants no. III43009, III45015, ON172062, TR32008 and III43001).

### REFERENCES

- [1] S. Çakmak, M. Gümüşderelioglu, A. Denizli, *React. Funct. Polym.* 2009, **69**, 586–593.
- [2] D. Turkmen, H. Yavuz, A. Denizli, *Int. J. Biol. Macromol.* 2006, **38**, 126–133.
- [3] A. S. Lubbe, C. Alexiou, C. Bergemann, *J. Surg. Res.* 2001, **95**, 200–206.
- [4] K. Can, M. Ozmen, M. Ersoz, *Colloids Surf. B.* 2009, **71**, 154–159.
- [5] Lj. Malović, A. Nastasović, Z. Sandić, J. Marković, D. Đorđević, Z. Vuković, *J. Mater. Sci.* 2007, **42**, 3326–3337.
- [6] P.A. Webb, C. Orr, *Analytical Methods in Fine Particle Technology*, Micromeritics Instrument Corporation, Norcross, Georgia, 1997.
- [7] G. M. Rashad, M. R. Mahmoud, A. M. Elewa, E. Metwally, E. A. Saad, *J. Radioanal. Nucl. Chem.* 2016, DOI 10.1007/s10967-016-4726-4.

## IMPACT OF THE TiO<sub>2</sub> NANOPARTICLES ON THE PROPERTIES OF URETHANE-SILOXANE COPOLYMERS

I. S. Stefanović<sup>1</sup>, B. M. Ekmešić<sup>1</sup>, J. Dostanić<sup>1</sup>, D. Lončarević<sup>1</sup>,  
D. Vasiljević-Radović<sup>1</sup>, S. Marković<sup>2</sup> and M. V. Pergal<sup>1</sup>

<sup>1</sup>University of Belgrade, Institute of Chemistry, Technology and Metallurgy,  
Njegoševa 12, Belgrade, Serbia. (istefanovic@chem.bg.ac.rs)

<sup>2</sup>University of Belgrade, Institute of Technical Sciences of the Serbian  
Academy of Sciences and Arts, Knez Mihailova 35/IV, Belgrade, Serbia.

### ABSTRACT

Rutile/anatase TiO<sub>2</sub> was incorporated in different amounts (1, 2, 3 and 5 wt.%) in relative to the polyurethane-siloxane (PUS) matrix in order to investigate the influence of nano-fillers on the hydrophobicity, thermal properties and morphology of the PUS. A series of PUS nanocomposites (PUSN) based on  $\alpha,\omega$ -dihydroxy-ethoxypropyl-poly(dimethylsiloxane) (EO-PDMS) as the soft segment (SS) and 4,4'-diphenylmethane diisocyanate (MDI) and 1,4-butanediol (BD) as the hard segment (HS), was prepared via two-step polyaddition reaction in solvent mixture. Prepared PUSNs were characterized using FTIR spectroscopy, thermogravimetric analysis, water absorption, water contact angle and AFM analysis. In summary, the synthesized PUSNs and especially PUSN with 2 wt.% of TiO<sub>2</sub> had better water resistivity and nonwettability, higher thermal stability, and more pronounced surface morphology that can be potentially used as protective coatings.

### INTRODUCTION

The recent decades have seen an increase in developing novel organic/inorganic materials for different applications (protecting coatings, elastomers, adhesives, etc). These materials often incorporate colloidal inorganic nanoparticles into an organic matrix yielding physical features superior than conventional polymer [1]. Generally, PUS copolymers have good thermal and oxidative stability, elasticity, hydrophobicity, chemical and UV resistance, etc. Interaction of TiO<sub>2</sub> nanoparticles with components in the PUS matrix enables improvement of the mentioned properties. To date, plenty research have been focused on the usage of TiO<sub>2</sub> with proper dispersion and enhanced compatibility with the polymer matrix [2]. The goal of this research was to synthesize TiO<sub>2</sub>-PUS nanocomposites and to

investigate the influence of different loadings of TiO<sub>2</sub> nanoparticles on thermal, barrier and surface properties of PUS matrix.

## EXPERIMENTAL

$\alpha,\omega$ -Dihydroxy-ethoxypropyl-poly(dimethylsiloxane) (EO-PDMS) ( $M_n = 1000 \text{ g mol}^{-1}$ ) was dried over molecular sieves before use. 4,4'-Diphenylmethane diisocyanate (MDI) was used as received. 1,4-Butanediol (BD) was purified with distillation before use. Tetrahydrofuran (THF) and *N,N*-dimethylacetamide (DMAc) were purified with distillation before use. Stannous octoate (Sn(Oct)<sub>2</sub>) was used as a diluted catalyst solution in THF/DMAc. AEROXIDE<sup>®</sup> TiO<sub>2</sub> P 25 (anatase/rutile=80/20) was supplied from Evonic Industry. The PUSNs with 20 wt.% of HS, were synthesized with addition of TiO<sub>2</sub> nanoparticles by *in situ* two-step polyaddition process in solvent mixture (THF/DMAc; 1/1 v/v). The last number in the name of the PUSN represents the weight percent of the TiO<sub>2</sub> nanoparticles. The initial reaction mixture and final polymer solution were sonicated on ultrasonic bath for a period of 1 hour. Synthesis was carried out as follows: firstly, the isocyanate terminated prepolymer was synthesized by the reaction between the EO-PDMS and MDI in solvent mixture at 40 °C for 30 min under N<sub>2</sub> atmosphere, and with presence of Sn(Oct)<sub>2</sub> solution used as a catalyst. Then, in the second phase of reaction, dilute solution of BD was drop-wise added and the reaction was continued at 50 °C for 10 hours. From the final polymer solutions were prepared PUSN films that had been used for characterization. The synthesized PUSNs were characterized by means of infrared spectroscopy (ATR-FTIR), atomic force microscopy (AFM) and thermal gravimetric analysis (TGA). Water absorption (WA) was performed at room temperature by immersion of PUSNs in phosphate buffers (pH = 7.4). Water contact angles (WCA) were measured on Krüss DSA 100 instrument using the sessile drop method. Measurements were performed at room temperature, 30 s after placing the single drops on the surface of the films.

## RESULTS AND DISCUSSION

The chemical structures of the prepared PUSNs, initial PUS copolymer and TiO<sub>2</sub> nanoparticles were confirmed by FTIR spectroscopy (Figure 1). Characteristic bands of PUS and PUSN samples appeared at 3330 cm<sup>-1</sup> ( $\nu_{\text{N-H}}$ ), 2960 and 2900 cm<sup>-1</sup> ( $\nu_{\text{asym}}$  and  $\nu_{\text{sym}}$  of -CH<sub>2</sub>-), 1705 cm<sup>-1</sup> ( $\nu_{\text{C=O}}$ ), 1535 cm<sup>-1</sup> and 1260 cm<sup>-1</sup> (amide II and amide III bands), 1020 cm<sup>-1</sup> and 1080 cm<sup>-1</sup> ( $\nu_{\text{Si-O}}$  and  $\nu_{\text{C-O}}$ ), 1600 and 1410 cm<sup>-1</sup> ( $\nu_{\text{C=C}}$ <sub>arom</sub>), 800 cm<sup>-1</sup> ( $\rho_{\text{SiCH}_3}$ ). In the FTIR spectra of TiO<sub>2</sub> nanoparticles two wide absorption bands appeared from 3630 to 2300 cm<sup>-1</sup> (hydroxyl groups on the surface of TiO<sub>2</sub>) and one absorption band at about 600 cm<sup>-1</sup> ( $\nu_{\text{Ti-O}}$ ).

Thermal degradation of the PUSN samples, i.e.  $T_{5\%}$  values, started between 294 and 305 °C in comparison to initial PUS that started to degrade at 281 °C (Table 1). It can be observed that thermal stability of PUSNs was improved for ~ 15 to 25 °C, while the temperature of 50% weight loss,  $T_{50\%}$  values, are improved for ~ 110 °C compared to the initial PUS. Moreover, TGA curves (Figure 2) also show that thermal stability of PUSN copolymers was significantly improved with increasing the content of TiO<sub>2</sub> nanoparticles.

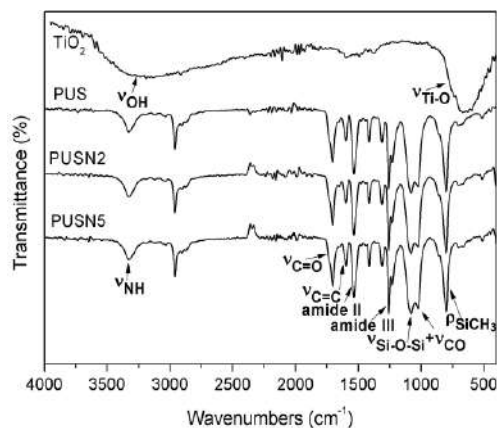


**Figure 1.** FTIR spectra of the initial PUS and PUSN copolymers with 2 and 5 wt.% of TiO<sub>2</sub>

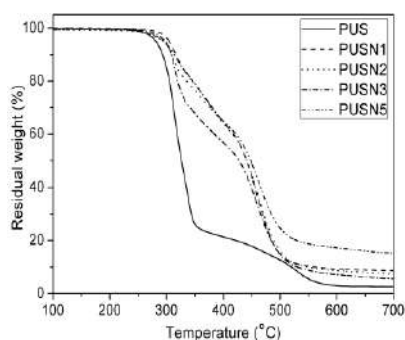


**Figure 2.** TGA curves of the prepared PUSNs and initial PUS

**Table 1.** Thermal properties, water absorption (WA) and water contact angle (WCA) values of the prepared PUSNs and initial PUS

Sample	$T_{5\%}$ (°C)	$T_{50\%}$ (°C)	$T_{85\%}$ (°C)	WA <sup>a)</sup> (%)	WCA (°)
PUS	281	327	478	1.2	94.4
PUSN1	305	441	499	0.8	101.6
PUSN2	296	442	503	0.5	108.7
PUSN3	298	427	499	0.6	104.9
PUSN5	294	448	>700	0.8	104.0

a) measured after 48 hours

Water absorption and water contact angle values (Table 1) show that addition of TiO<sub>2</sub> nanoparticles leads to decrease of amount of absorbed water and increase of water contact angles. These obtained values indicate improvement of hydrophobicity of the PUSN samples.

AFM images presented in Figure 3 showed that the surface morphology of PUS copolymer is significantly changed and becomes rougher after incorporation of TiO<sub>2</sub> nanoparticles. With incorporation of 2 wt.% of TiO<sub>2</sub>, the resulting PUSN exhibited a high uniformity of nanoparticles dispersion with minimal agglomeration giving more pronounced surface morphology.

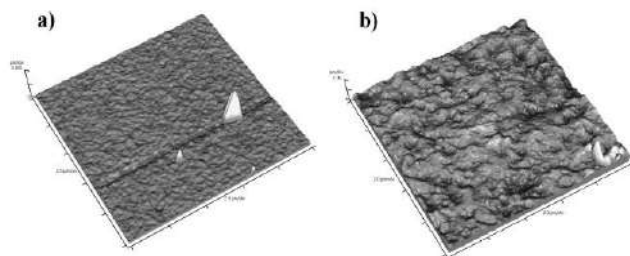


**Figure 3.** 3D AFM images of the surface of films of a) initial PUS and b) PUSN with 2 wt.% of TiO<sub>2</sub> (scan area 10 × 10 μm<sup>2</sup>)

## CONCLUSION

In this work, series of PUSN were prepared from PUS copolymers, synthesized via two-step polyaddition reaction in solvent mixture, and with incorporation of different percentages of TiO<sub>2</sub> nanoparticles. The structure of PUSNs and presence of the TiO<sub>2</sub> nanoparticles were confirmed by FTIR spectroscopy. TGA analysis showed that incorporation of the TiO<sub>2</sub> led to significant increase of thermal stability of PUSNs. The introduction of TiO<sub>2</sub> led to a noticeable increase in hydrophobicity and nonwettability of the PUSNs. Moreover, homogenous TiO<sub>2</sub> dispersion on the surface results in pronounced surface morphology of the PUSNs. Therefore, the prepared PUSN copolymers with TiO<sub>2</sub> nanoparticles led to significant improvement of investigated features and potentially can be applied as protective coatings.

## Acknowledgement

This work was supported by the Ministry of Education, Science and Technological Development of the Republic of Serbia (Project No. 172062, III 45001 and III43009).

## REFERENCES

- [1] V. D. Da Silva, L. M. Dos Santos, S. M. Subda, R. Ligabue, M. Seferin, C. L. P. Carone, S. Einloft, *Polym. Bull.* 2013, **70**, 1819-1833.
- [2] S. M. Mirabedini, M. Sabzi, J. Zohuriaan-Mehr, M. Atai, M. Behzadnasab, *Appl. Surf. Sci.* 2011, **257**, 4196-4203.

## PREPARATION OF ALL-SOLID-SUPERCAPACITOR BASED ON POLYANILINE AND NAFION®

B. Burmas , M. Gergorić , M. Šarić, M. Kraljić Roković and S. Sopčić

*University of Zagreb, Faculty of Chemical Engineering and Technology,  
Marulićevtrg 19, 10000 Zagreb, Croatia, (sopcic@fkit.hr)*

### ABSTRACT

Two different symmetric supercapacitors with polyaniline as active electrode material were prepared. One supercapacitor was consisted of polyaniline applied onto Pt foil and immersed in hydrochloride acid electrolyte, and the other was consisted of the polyaniline casted to a carbon cloth current collector with a solid Nafion® as the electrolyte. The assembled supercapacitors were tested using cyclic voltammetry and chronopotentiometry. Results showed that the supercapacitor with liquid electrolyte has slightly higher value of specific capacitance compared to supercapacitor with the Nafion® membrane, but the latest showed that Nafion® can be used as solid electrolyte as well as that the Nafion® provides protons and counter ions essential for polyaniline conductivity. With the Nafion® membrane the flexible supercapacitor was constructed and good cycling stability was achieved.

### INTRODUCTION

Supercapacitors are devices that are used for storage and conversion of energy. The prefix super- refers to the excellent properties which reflect throughout the higher values of specific capacity, specific power and specific energy, compared to conventional capacitors. There are two types of supercapacitors, double layer capacitors and pseudocapacitors which can be distinguished by the mechanism of the charge storage. In the first one, the charge is stored electrostatically in the double layer at solid/liquid interphase, while in the case of pseudocapacitors the charge is stored by the redox reaction of the electrode material.

Polyaniline (PANI) electrodes are used in pseudocapacitors where during the charging/discharging process the leucoemeraldine/emeraldine transformation occurs. The usage of PANI electrodes in supercapacitors has many positive properties such as high electroactivity, easy processability, high specific capacitance, low cost and easy synthesis, but also there are few disadvantages. Its redox reaction involves the intercalation/deintercalation of counterions which are causing the physical changes in the structure and

affect the cycle life of supercapacitor. In this work the impact of current collector to a stability of PANI electrode was examined. Furthermore, in order to be electrically conductive, PANI has to be protonated thus the acidic electrolyte in the supercapacitor is essential. The aim of this work was to replace aggressive acid electrolyte with Nafion<sup>®</sup>assolid electrolyte, and to find out whether the hydrated sulfonic groups of Nafion<sup>®</sup> are able to protonate the PANI layer and provide good electric conductivity of polymer.

### EXPERIMENTAL

Chemical synthesis of PANI was carried out using ammonium peroxydisulfate as oxidant. The oxidant was added to the aniline/HCl solution with constant stirring. The synthesis was discontinued when the constant open circuit potential was reached. The green precipitate was then filtrated, washed with water, ethanol and 1 mol dm<sup>-3</sup>HCl, respectively. The precipitate was deprotonated by stirring in 0.1 mol dm<sup>-3</sup> NH<sub>4</sub>OH for 48 hours, filtrated and then dried in vacuum overnight. The obtained PANI (emeraldine base) was dissolved in N-Methyl-2-pyrrolidone (NMP).

For assembly of supercapacitors, two types of current collectors were used, Pt foil (supercapacitor **SC1**) and carbon cloth (supercapacitor **SC2**), both with surface area of 1 cm<sup>2</sup>. The solution of PANI/NMP was drop-casted onto Pt foil and carbon cloth where up on they were dried overnight at the 60°C in the vacuum oven. The two-electrode setup for **SC1** was immersed in 1 mol dm<sup>-3</sup>HCl, while the electrodes for **SC2** supercapacitor were protonated by dropping excess of Nafion<sup>®</sup> solution (5 wt % in lower aliphatic alcohols and water) over carbon cloth/emeraldine base electrode. The degree of PANI protonation was examined with UV-vis spectroscopy from 330 - 800 nm wavelengths in 1 cm path length cuvette. Nafion<sup>®</sup> membrane 117 was placed between two pieces of carbon cloth/PANI electrodes and hot pressed together for short period of time at 180°C. The unit obtain by this method is all-solid-supercapacitor. Before testing, **SC2** was immersed in water in order to achieve good hydration of Nafion<sup>®</sup> membrane.

Assembled supercapacitors were tested using different electrochemical methods. Cyclic voltammetry was performed in potential range from -400 mV to 400 mV at the 50 mV/s. By thechronopotenciometry method the charging/discharging curves was recorded at the constant current of 0.2 mA.

### RESULTS AND DISCUSSION

In the Fig. 1 the cyclic voltammograms of carbon cloth/PANI (red curve) and Pt/PANI electrode (black curve) in 1 mol dm<sup>-3</sup>HCl are shown. For both electrodes, well developed current peaks can be noticed; peak A corresponds

to leucoemeraldine/emeraldine transformation and peak Bemeraldine/pernigranilinetransformation. The carbon cloth/PANI response indicates that carbon cloth is suitable current collector for PANI layer. The main advantage of carbon cloth as support is the flexibility of the obtained PANI electrode and therefore it can be used for assembly of flexible supercapacitor. Another advantage is the low weight of cloth and the fact that the carbon materials improve the stability of conductive polymer electrodes and facilitates the cycle life of supercapacitor [1].

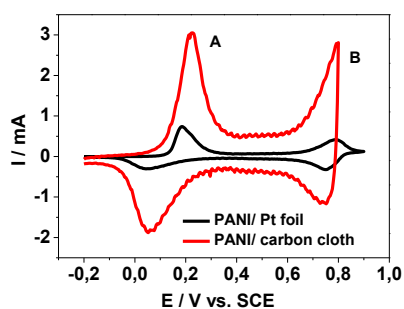


**Figure 1.** Cyclic voltammograms for Pt/PANI and carbon cloth/PANI electrodes in  $1 \text{ mol dm}^{-3} \text{HCl}$ , at  $50 \text{ mVs}^{-1}$ .

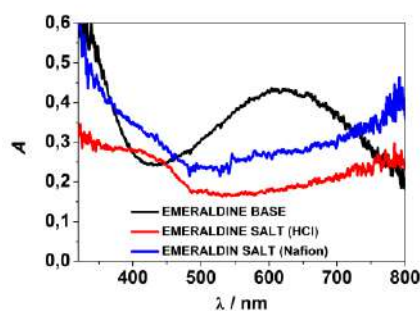


**Figure 2.** UV-vis spectra of deprotonated PANI, PANI/HCl and PANI/Nafion<sup>®</sup> at  $E_{oc}$  potential.

In order to find out whether PANI is protonated in the presence of Nafion<sup>®</sup>, UV-vis spectra were taken. The absorption maximum at 620 nm is registered for unprotonated demeraldine base (black curve). The band obtained at 420–440 nm (red and blue curves) can be assigned to the polaronic state (Fig. 2) and it proves existence of protonated emeraldine salt for PANI/HCl and for PANI/Nafion<sup>®</sup> layers.

Assembled supercapacitors were tested by cyclic voltammetry which revealed almost rectangular response within entire potential range of testing, for both SC1 and SC2 (Fig 3). The SC2 has slightly slower current drop at switching potential which is indication of lower reversibility of redox reaction. This effect could be caused by slow compensation of PANI charge by the sulfonic groups attached to Nafion<sup>®</sup>. Figure 4 illustrates charging/discharging curves of both SC1 and SC2 supercapacitors. The curves are characterized with almost linear response which is characteristic of capacitor with good properties. From the discharge time and current value the specific capacitance for SC1 and SC2 supercapacitor was calculated and the obtained values are  $71.8 \text{ F g}^{-1}$  and  $51.8 \text{ F g}^{-1}$ , respectively. Specific energy obtained for SC1 was found to be  $5.72 \text{ W s g}^{-1}$ , while for SC2 the

value was  $4.69 \text{ W s g}^{-1}$ . During charging/discharging process performance of SC2 was improved after first 500 cycles, however, deterioration of properties is registered during further cycling up to 1000 cycles. Improvement of the properties could be explained with better hydration of electrodes and Nafion<sup>®</sup> membrane over time and additionally by enhanced the stability of PANI in the presence of Nafion<sup>®</sup> and carbon [2, 3].

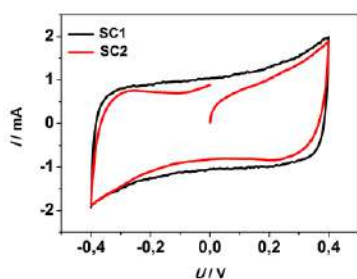


**Figure 3.** Comparison of cyclic voltammograms for SC1 and SC2 supercapacitors

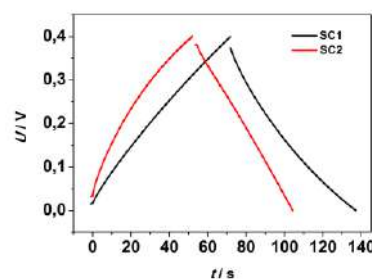


**Figure 4.** Charging/discharging curves of SC1 and SC2 with the constant current of 0.2 mA

## CONCLUSION

The obtained results indicate that the PANI can be protonated by Nafion<sup>®</sup> and the usage of aggressive acid electrolyte can be avoided. Obtained values of specific capacitance for supercapacitor with Pt current collector and acidic electrolyte was higher, but results showed that carbon cloth and Nafion<sup>®</sup> facilitate the stability of PANI electrodes which improved the cycle life of supercapacitor. Furthermore, it is shown that by using carbon cloth/PANI electrode and solid Nafion<sup>®</sup> electrolyte, the flexible all-solid-supercapacitor is possible to prepare.

## Acknowledgement

This work was partially supported by the **Croatian Science Foundation** under the project ESUP-CAP (IP-11-2013-8825).

## REFERENCES

- [1] G. A. Snook, P. Kao, A. S. Best *J. Power Sources*, 2011, **196**, 1-12
- [2] M. A. Bavio, G. G. Acosta, T. Kessler, *J. Pow. Sources*, 2014, **245**, 475-481
- [3] D. Belanger, T. Brousse, J. W. Long, *The electrochemical society Interface*, Spring 2008, 49-52.

## ANTIMICROBIAL ACTIVITY OF COPPER-POLYANILINE NANOCOMPOSITE

U. Bogdanović<sup>1</sup>, V. Vodnik<sup>1</sup>, M. Mitrić<sup>1</sup>, S. Dimitrijević<sup>2</sup>, S. D. Škapin<sup>3</sup>, V. Žunič<sup>3</sup>, M. Budimir<sup>1</sup> and M. Stoiljković<sup>1</sup>

<sup>1</sup>*Vinča Institute of Nuclear Sciences, University of Belgrade, P. O. Box 522, 11001 Belgrade, Serbia (una.bogdanovic@gmail.com)*

<sup>2</sup>*Department of Bioengineering and Biotechnology, Faculty of Technology and Metallurgy, University of Belgrade, Karnegijeva 4, 11000 Belgrade, Serbia*

<sup>3</sup>*Jožef Stefan Institute, Department of Advanced Materials, Jamova 39, 1000 Ljubljana, Slovenia*

### ABSTRACT

By combining copper nanoparticles (CuNPs) as a good antimicrobial agent with polyaniline (PANI), which also shows some degree of antimicrobial activity, we were able to synthesize a novel promising antimicrobial material – copper-polyaniline (Cu-PANI) nanocomposite. It was prepared by simple *in situ* polymerization method, when the polymer and metal nanoparticles ( $d_{av} = 6$  nm) are produced simultaneously. Quantitative (antimicrobial assay) and qualitative (atomic force microscopy – AFM) analyses showed that synergistic effect of CuNPs and PANI against bacteria *E. coli* and *S. aureus*, and fungus *C. albicans*, provides its faster and higher antimicrobial activity than any component acting alone. This makes it a great candidate for fast waste water treatment.

### INTRODUCTION

Microbial contamination of water presents a major threat to public health. With the emergence of strains resistant to multiple antimicrobial agents, there is increased demand for novel antimicrobial materials with superior performance for disinfection applications. Nanocomposites based on metal nanoparticles such as CuNPs and conductive PANI, that expose some antimicrobial effect, represent one of these materials [1,2]. Antimicrobial activity of metal NPs is inversely proportional to their average size as a result of large number of the low-coordinate atoms on their surface available to interact with microbial membranes or to release metal ions, while PANI chains generate electrostatic interaction with microbial functional groups, altering their function [1,2]. Combining these two components, these effects become intense making Cu-PANI nanocomposite very effective antimicrobial agent [2]. Here, we present a cheap Cu-PANI nanocomposite

material with improved antimicrobial action, comparing to CuNPs and PANI components alone.

## EXPERIMENTAL

Cu-PANI nanocomposite was synthesized by a simple process of oxidative polymerization of aniline, in methanol as a medium [2]. Copper salt ( $\text{CuCl}_2 \cdot 2\text{H}_2\text{O}$ , 0.12 M) dissolved in methanol with adjusted pH < 4 by 1 M HCl, was first added in a round bottom flask equipped with a magnetic stirrer. Then, aniline (0.04 M) in molar relation to Cu salt  $[\text{aniline}]/[\text{CuCl}_2] = 1/3$ , was added. The mixture was stirred for 20 h at room temperature. The initial fluorescent green color of copper salt almost immediately turns dark red-brown and then to brownish-green as Cu-PANI nanostructures form. The final solution was evaporated by rotary evaporator to remove methanol and soluble oligomers. The precipitate was then washed with 5 mM HCl and dried at 30 °C. After collecting the powder, the amount of the Cu in the nanocomposite determined by ICP-AES was found to be 14.25 wt%. For comparison of antimicrobial activity, pure PANI sample without CuNPs was synthesized using the procedure described in our previous report [3]. Antimicrobial activity of synthesized samples was determined according to our previous work [2], for Cu-PANI and pure PANI, concentrations of 1, 2, 5, 10 and 20 ppm, and incubation time of 1h.

## RESULTS AND DISCUSSION

Since the only reactants in this synthetic route are  $\text{Cu}^{2+}$  ions as an oxidizing agent and aniline as a reductant, the nucleation and growth of CuNPs, and polymerization of aniline takes place simultaneously. The formation of Cu-PANI nanocomposite was first confirmed by the UV-Vis spectrum (Fig 1a, Inset), with CuNPs absorption band at 550 nm due to collective oscillations

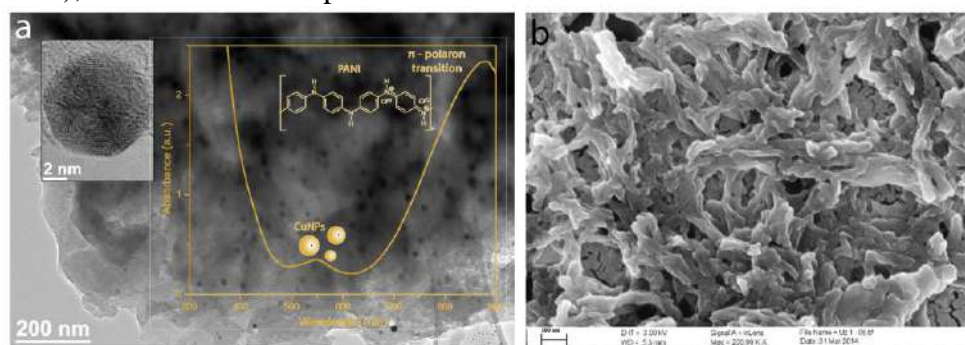


**Figure 1.** a) TEM image with UV-Vis spectrum and b) FESEM image of Cu-PANI nanocomposite.

of a surface Cu electrons and characteristic peak of PANI protonated by HCl visible at 880 nm ( $\pi$ -polaron transition) [3]. During the polymerization of aniline, spherical CuNPs with mean diameter of about  $6.0 \pm 3.3$  nm were formed. They are well separated and homogeneously dispersed throughout the polymer matrix (Fig. 1a). FESEM image of Cu-PANI (Fig. 1b) indicated that PANI chains form coral-like dendritic nanofibers in a large quantity and good uniformity with pores between the branches nanofibers. Such nanostructure offer great effective surface area of Cu-PANI composite. The results of quantitative antimicrobial efficiency of the Cu-PANI nanocomposite of different concentrations over 1 h incubation time with the microbes are schematically represented in Fig. 2. The stronger antimicrobial effect is achieved for the higher Cu-PANI or pure PANI concentrations.

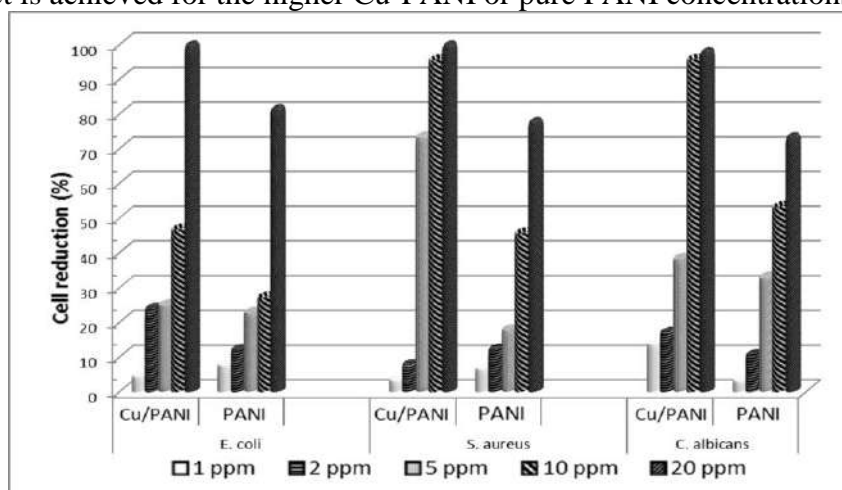


**Figure 2.** Concentration-dependent reduction ability of the Cu-PANI and PANI on *E. coli*, *S. aureus* and *C. albicans*, over 1 h incubation time

After 1 h, the number of strains is significantly reduced with increasing the Cu-PANI concentration, and almost complete growth inhibition was achieved (99.9 % microbial reduction) against *E. coli* and *S. aureus*, but slightly smaller fungal reduction (97.9 %) at highest composite concentration of 20 ppm. These results are much better than for pure PANI, which reduced  $\leq 81.5$  % of all tested strains for the same incubation time and concentrations, as well as CuNPs for higher concentrations and longer incubation time (2h), presented in the previous work [1].

Antimicrobial activity of Cu-PANI nanocomposite was also visually confirmed by AFM analysis (Fig. 3). It can clearly be seen that morphology of all tested strains is drastically changed. Smooth and compact surface of all tested strains, after 1 h contact with Cu-PANI, becomes rough, with a lot

of indentations on the cell wall, indicated by arrows. As can be seen, the effect of Cu-PANI to cells' morphology, is more intense in the case of *E. coli* (Fig. 3a) than for two other cells (Fig. 3b,c), because of the intrinsic difference in the cell wall structure. These results are in agreement with the results of antimicrobial assays. Beside synergistic effect of CuNPs and PANI in the composite, important role in the antimicrobial activity of the Cu-PANI has PANI dendrite morphology, which provides great surface area in contact with microbes, preventing the nutrient-uptake process of the microbes from the surroundings. This allows increasing of the interaction between CuNPs, cycling redox  $\text{Cu}^{2+}/\text{Cu}^{+}$  reactions at the surface of the cells and their electrostatic interactions with microbes' peptidoglycans and lipids. These interactions lead to conformational changes of biomolecules, altering their biological function and finally causing cells death.

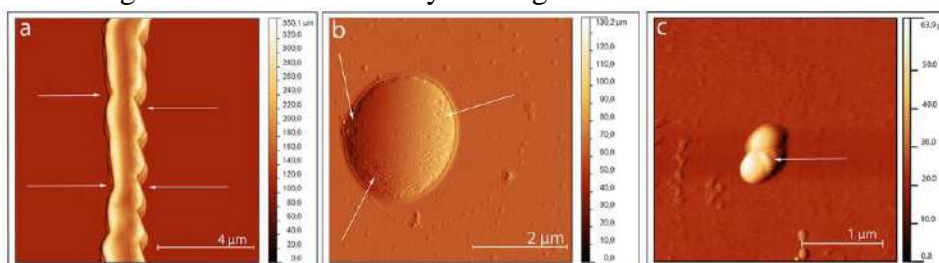


**Figure 3.** AFM images of treated cells *E. coli* (a), *S. aureus* (b) and *C. albicans* (c) after 1 h incubation with Cu-PANI nanocomposite

## CONCLUSION

The presented Cu-PANI nanocomposite has shown excellent antimicrobial activity as a result of CuNPs and PANI synergy, after only 1 h of the strains exposure. This composite can serve as a template for the development of novel antimicrobial agent for fast control microbial infections and waste water treatment.

## Acknowledgement

This work was supported by the Ministry of Education, Science and Technological Development of the Republic of Serbia (grants 172056 and TR 31035).

## REFERENCES

- [1] U. Bogdanović, V. Lazić, V. Vodnik, M. Budimir, Z. Marković, S. Dimitrijević, *Materials Letters*, 2014, **128**, 75–78.
- [2] U. Bogdanović, V. Vodnik, M. Mitrić, S. Dimitrijević, S. Škapin, V. Žunič, M. Budimir, M. Stoiljković, *ACS Applied Materials & Interfaces*, 2015, **7**, 1955–1966.
- [3] U. Bogdanović, V. Vodnik, S. Ahrenkiel, M. Stoiljković, G. Ćirić-Marjanović, J. Nedeljković, *Synthetic Metals*, 2014, **195**, 122–131.

## EFFECT OF THE CHEMICAL STRUCTURE OF SEGMENTED POLYURETHANES ON THEIR SURFACE PROPERTIES

M. V. Pergal<sup>1</sup>, D. Vasiljević-Radović<sup>1</sup>, P. Jovančić<sup>2</sup>, V. Živković-Radovanović<sup>3</sup> and M. Antonijević-Nikolić<sup>4</sup>

<sup>1</sup>*University of Belgrade, Institute of Chemistry, Technology and Metallurgy, Njegoševa 12, Belgrade, Serbia (marijav@chem.bg.ac.rs)*

<sup>2</sup>*University of Belgrade, Faculty of Technology and Metallurgy, Karnegijeva 4, Belgrade, Serbia*

<sup>3</sup>*University of Belgrade, Faculty of Chemistry, P.O. Box 158, Belgrade, Serbia*

<sup>4</sup>*Higher Technological School of Professional Studies, Šabac, Serbia*

### ABSTRACT

The surface properties of a series of segmented polyurethanes (PS-TPUs) containing pol(dimethylsiloxane) soft segment and diphenylmethane diisocyanate/1,4-butanediol hard segment, were evaluated. PS-TPUs were characterized by atomic force microscopy (AFM), wide-angle X-ray scattering (WAXS), contact angle measurements and surface free energy determination. The aim of this work is to examine the effect of the content of soft segment on the surface properties of the prepared PS-TPUs. AFM results revealed globules in the prepared materials ascribed to hard segment-rich superstructures. The synthesized polyurethanes showed lower degree of crystallinity, lower surface free energy and higher hydrophobicity with increasing content of soft segment.

### INTRODUCTION

Segmented polyurethanes (TPUs) containing poly(dimethylsiloxane)s have been widespread use as biomaterials due to their good biocompatibility and elastomeric properties. [1] These properties are attributed to their two-phase morphology which consists of hard, glassy or crystalline phase and soft, rubbery phase. Poly(dimethylsiloxane)s (PDMS) were used as soft segments in TPUs and possess one of the lowest glass transition temperature values (-123°C) among synthetic polymers, and show low-temperature flexibility, low surface energy, good biocompatibility, excellent thermal and thermo-oxidative stability, ultraviolet resistance and high permeability to many gases.[2] The surface properties of PS-TPUs are affected by the surface topography and degree of microphase separation. It was established that the

chemical structure and content of PDMS macrodiols predominantly influences the surface and physical properties of PS-TPUs.[1]

### EXPERIMENTAL

$\alpha,\omega$ -Dihydroxy-(ethylene oxide-poly(dimethylsiloxane)-ethylene oxide) (PDMS;  $\overline{M}_n = 1000$  g/mol, ABCR) was dried over molecular sieves before use. Diphenylmethane diisocyanate (MDI, Aldrich) with an isocyanate content of 33.6 wt. %, was used as received. 1,4-Butanediol (BD, Aldrich) was purified by vacuum distillation. *N,N*-Dimethylacetamide (DMAc, Acros) was dried over calcium hydride and then distilled under vacuum. Tetrahydrofuran (THF, J. T. Baker) was dried over lithium aluminum hydride and distilled before use. Stannous octoate was supplied by Aldrich. The PS-TPUs were synthesized by two-step polyaddition in solution using PDMS, MDI and BD. A prepolymer was prepared by adding MDI to a reaction vessel containing solution of PDMS macrodiol in DMAc/THF. For chain extension, solution of BD in DMAc/THF was added to the prepolymer. The catalyst was stannous-octoate and mixture DMAc/THF (1/1 v/v) was employed as reaction medium. Synthesized series consisted of three samples (PS-TPU35, PS-TPU50 and PS-TPU60) prepared with different contents of hard segments. The last two numbers in the name of the samples represent the weight percent of the hard segment. The PS-TPUs were synthesized under the optimal polymerization conditions [3]: concentration of reactants was 15 wt. %, the time of the first step of reaction was 30 minutes, while the time of the second step was 24 h. The reaction temperature of the second step was 40 °C and the optimal molar ratio of NCO/OH groups was 1.05. In our previous paper, [3] we have found that molar ratio of NCO/OH groups smaller (i.e. stoichiometric) or higher than 1.05, led to a decreased intrinsic viscosity and molecular weight of the final copolymer. A slight excess of isocyanate (1.05) is necessary to obtain the higher possible molecular weight. This is attributed to compensation of isocyanates that are consumed during the synthesis of copolymers, probably due to hydrolysis of isocyanate groups. The second reason are the impurities in commercially supplied MDI.

The surface topography was observed by atomic force microscopy (AFM). The AFM characterizations were performed with an AutoProbe CP-Research SPM (TM Microscopes-Veeco) instrument. Wide angle X-ray scattering (WAXS) was done using a Diffractometric System APD 2000 diffractometer with  $\text{CuK}\alpha$  radiation using a copper anode. Surface free energy data (SFE) were calculated from the contact angle values obtained using distilled water, formamide and diiodomethane and the acid-base

theory for solids according to the van Oss-Chaudhury-Good approach.[4] Contact angle measurements were performed in a Krüss DSA100 at room temperature using the sessile drop method.

## RESULTS AND DISCUSSION

The influence of the PDMS soft segment was examined in order to understand its effect on the formation of the microtopology of surface of PS-TPUs. Contact mode AFM images of the surface topology of PS-TPUs are presented in Fig. 1. AFM images show spheroidal or globular superstructures in copolymers which correspond to the crystallinity of the hard (MDI-BD) segment. The RMS roughness coefficient ( $R_q$ ) increases with decreasing content of soft segments (18.1, 34.8 and 55.8 nm for the samples PS-TPU35, PS-TPU50 and PS-TPU60, respectively).

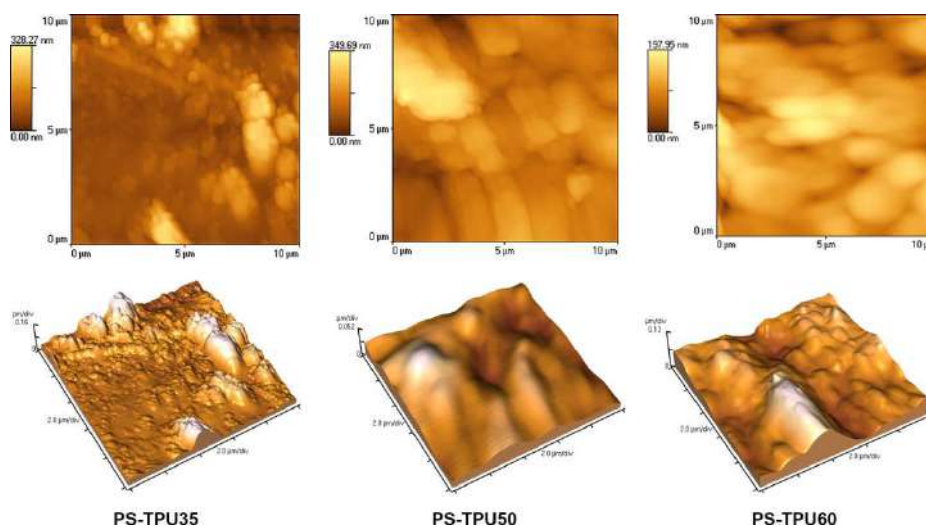


**Figure 1.** 2D height and 3D AFM images of the surface of the synthesized PS-TPUs with different soft segment content

The degree of crystallinity of PS-TPUs, determined by deconvolution of the signals belonging to the crystalline and amorphous parts of samples in WAXS diffractograms, was from 15.1 to 33.2% (Table 1). The degrees of crystallinity decreased with the increasing weight fraction of soft segments. The results of SFE measurements were presented in Table 1. These results suggest that it is long-range interaction  $\gamma_S^{LW}$  (dispersive component) to be decisive for the value of SFE, while acid-base interaction  $\gamma_S^{AB}$  (polar component) as well as parameters  $\gamma_S^+$  (Lewis acid parameter) and  $\gamma_S^-$  (Lewis

base parameter) are negligible. It was clearly observed that  $\gamma$  (surface free energy) decreased with increasing PDMS content due to the surface activity of hydrophobic siloxane incorporated in the soft segment. [5]

**Table 1.** Results of surface free energy, its components and parameters and degree of crystallinity of PS-TPU<sub>s</sub>

Sample	$\gamma_s^{LW}$ (mJ/m <sup>2</sup> )	$\gamma_s^+$ (mJ/m <sup>2</sup> )	$\gamma_s^-$ (mJ/m <sup>2</sup> )	$\gamma_s^{AB}$ (mJ/m <sup>2</sup> )	$\gamma$ (mJ/m <sup>2</sup> )	$X_{cWAXS}$ (%)
PS-TPU35	28.1	1.8	2.1	3.8	31.9	15.1
PS-TPU50	35.8	1.9	2.2	4.4	40.2	24.8
PS-TPU60	39.4	2.6	2.8	5.1	44.5	33.2

## CONCLUSION

The surface properties of segmented thermoplastic polyurethane elastomers with 35 wt. %, 50 wt. % and 60 wt. % soft segment content based on PDMS, were analyzed by AFM and surface free energy determination. AFM analysis revealed the existence of globules in PS-TPU<sub>s</sub> that is believed to arise from the crystallization of the hard segments, which was also assessed by the WAXS results. The surface of the PS-TPU<sub>s</sub> with higher PDMS contents was more hydrophobic, because of the low surface tension of the PDMS segments and their ability to migrate to the surface.

## Acknowledgement

This work was supported by the Ministry of Education, Science and Technological Development of the Republic of Serbia (Project No. 172062).

## REFERENCES

- [1] R. Hernandez, J. Weksler, A. Padsalgikar, J. Runt, J. Biomed. Mater. Res. A 2008, **87A**, 546-556.
- [2] İ. Yilgör, J. McGrath, Adv. Polym. Sci. 1988, **86**, 1-86.
- [3] M. V. Pergal, V. V. Antić, M. N. Govedarica, D. Gođevac, S. Ostojić, J. Djonlagić, J. Appl. Polym. Sci. 2011, **122**, 2715-2730.
- [4] C. J. Van Oss, R. J. Good, M. Chaudhury, Langmuir 1988, **4**, 884-891.
- [5] H. D. Hwang, H. J. Kim, React. Funct. Polym. 2011, **71**, 655-665.

## STRUCTURAL CHARACTERIZATION OF MICROBIAL LEVAN BY SMITH DEGRADATION

B. Kekez<sup>1</sup>, G. Gojgić-Cvijović<sup>2</sup>, D. Jakovljević<sup>2</sup>  
V. Beškoski<sup>1</sup> and M. M. Vrvčić<sup>1</sup>

<sup>1</sup>Faculty of Chemistry, University of Belgrade, 11158 Belgrade, Studentski trg 16, POB 51, Serbia. (brankakekez@chem.bg.ac.rs)

<sup>2</sup>Institute of Chemistry, Technology and Metallurgy, University of Belgrade, 11158, Belgrade, Njegoševa 12, POB 473, Serbia.

### ABSTRACT

In this work, microbial polysaccharide levan from *Bacillus licheniformis* strain was firstly oxidized to polyaldehyde, then reduced to polyalcohol, completely hydrolyzed, and finally acetylated. Resulting peracetylated alcohols were characterized by GC-MS and compared to the results from corresponded acetylated standards.

### INTRODUCTION

Microbial polysaccharides have a great potential as functional biopolymers for food, industrial, cosmetic or medical applications. Depending on type of monosaccharide units, they could be homopolymers or heteropolymers. Fructans are fructose based homopolymers, with dominant glycosidic linkages: (2,1)- inulin, (2,6)- levan, or mixed type [1].

Levan is composed of  $\beta$ -(2 $\rightarrow$ 6) linked  $\beta$ -D-fructofuranose units with occasional  $\beta$ -(2 $\rightarrow$ 1) branching and carry D-glucosyl residue at the end of a chain. Microbial levan could be competitive replacement to commercial synthetic polymers due to its biocompatibility, biodegradability and renewability. It also shows a significant antioxidant, antitumor and anti-inflammatory effects [2].

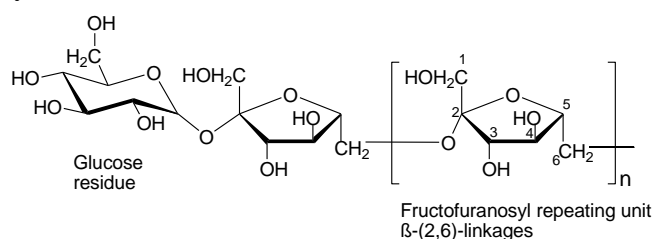


**Figure 1.** Structure of levan

The aim of this work was structural characterization of levan from *Bacillus licheniformis* strain by periodate oxidation and Smith degradation.

### EXPERIMENTAL

Levan used in this work was produced by the *B. licheniformis* strain [3]. Other reagents and solvents were purchased from commercial sources and used as supplied. The dried polysaccharide (100 mg), which was dissolved in 50 mL distilled water, was oxidized with 0.1 M NaIO<sub>4</sub> (50 mL) at 20 °C in the dark. Aliquots were removed at suitable intervals for estimation of periodate and formic acid by the arsenite method and iodometric titration, respectively [4]. The oxidation was completed after 18 h, and the periodate consumption and releasing of formic acid were calculated from analytical data by extrapolation to zero time. The oxidized fructan was then degraded by the Smith procedure [4]. The solution of polyaldehyde was reduced with NaBH<sub>4</sub>, neutralized and dialyzed. The obtained polyalcohol was hydrolyzed by oxalic acid [5]. The hydrolysate and standards (reduced fructose and glycerol) were acetylated [6] and then analyzed by GS-MS. GS-MS experiments were performed on Agilent 7890A GC system equipped with a HP-5MS column (30 m x 250 μm x 0,25 μm). The oven was programmed to 40 °C for 1 min, and then heated by 10 °C/min to 315 °C (held for 16.5 min). The run time was 45 min. Mass spectra were acquired in the electron ionization mode (EI) with ion energy of 70 eV.

### RESULTS AND DISCUSSION

Levan isolated from *B. licheniformis* strain was characterized by elemental analysis, NMR and FTIR spectroscopy [3]. The structure of this polysaccharide was additionally investigated by the periodate oxidation followed by Smith degradation. The extent of periodate oxidation of fructan was monitored at intervals of 6 h [4]. The oxidation became constant after 18 h and corresponded to 0.89 mol of periodate and 0.020 mol of formic acid, respectively, per hexose residue. Oxidized fructan was subjected to Smith degradation (reduction of oxidized polysaccharide with NaBH<sub>4</sub> and subsequent complete hydrolysis with acid). After esterification of obtained products, resulting mixture of alditol acetates was subjected to GC-MS analysis (Figure 2). The components were identified by their retention times and typical breakdown patterns obtained on EI-MS. The total ion chromatogram (Fig. 2.) showed dominant peak at 12.98 min retention time, which corresponded to referent standard glycerol triacetate. In the mass spectrum (Fig. 2.) the obtained fragments m/z 43, 103, 116 and 145 are characteristic for fragmentation pattern of glycerol triacetate.

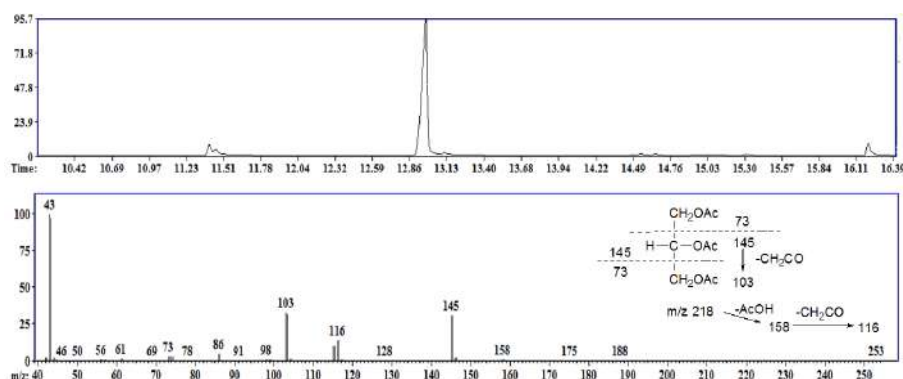


**Figure 2.** GC-MS of levan after periodate oxidation and Smith degradation

It was found that the periodate oxidation and Smith degradation of investigated fructan were resulted one component, glycerol, i.e. loss of fructose. After acetylation it is detected as glycerol peracetate. Scheme of these reactions is shown in Fig. 3.

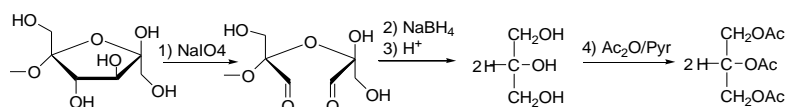


**Figure 3.** Reaction scheme of the periodate oxidation, Smith degradation and acetylation of 2,6-O-substituted fructofuranose, of which consisting the main chain of levan

These results indicated the presence of (2,6)-linkages in the main chain of the investigated fructan. Branching through the position of O-2 and terminal nonreducing glucose unit also give only glycerol, i.e. loss of fructose, as a result of these oxidative transformations. Products of Smith degradation indicated that the investigated glycan does not contain (2,3)- or (2,4)- linkages, considering that these types of bonds do not give glycerol as the resulting product. Obtained results are in accordance with the data for levans from other microbial sources [7].

## CONCLUSION

Structure of levan isolated from *B. licheniformis* strain was investigated by periodate oxidation followed by Smith degradation. On the basis of the GC-MS analysis of degraded products, it has been found only one component, glycerol. The obtained results are in consistency with those related to the structures of levan from other microbial sources. The differences can exist

in the mode and frequency of branching, as well as in the length of the side chains, which will be the subject of further investigations.

### ***Acknowledgement***

This work was supported by the Ministry of Education, Science and Technological Development of the Republic of Serbia through scholarships for PhD students and funding for Project III 43004.

### **REFERENCES**

- [1] M. Matulová, S. Husárová, P. Cepek, M. Sancelme, A-M. Delort, *Carbohydr. Res.*, 2011, **346**, 501-507.
- [2] R. Srikanth, S. S. H. C. Sundhar Reddy, G. Siddartha, J. M. Ramaiah, B. K. Uppuluri, *Carbohydr. Polym.*, 2015, **120**, 102-114.
- [3] B. D. Kekez, D. D. Gojic-Cvijovic, D. M. Jakovljevic, J. R. Stefanovic Kojic, M. D. Markovic, V. P. Beskoski, M. M. Vrvic, *Appl. Biochem. Biotechnol.*, 2015, **175**, 3068-3083.
- [4] G. W. Hay, B. A. Lewis, F. Smith, in *Methods in Carbohydrate Chemistry*, R. L. Whistler, Ed., Vol. 5, Academic Press, New York 1965, p. 357-361.
- [5] I. Dahech, S. K. Belghith, H. Belghith, H. Mejdoub H, *Int. J. Biol. Macromol.*, 2012, **51**, 329-335.
- [6] T. Tanaka, S. Oi, T. Yamamoto, *J. Biochem.*, 1980, **87**, 297-303.
- [7] E. T. Öner, L. H., J. Combie, *Biotechnol. Adv.*, 2016, doi:10.1016/j.biotechadv.2016.05.002

## THERMAL STABILITY AND MORPHOLOGY OF COPPER POWDER FILLED COMPOSITES

M. Pavlović, M. Pantović, M. Zarić and V. Pavelkić

*University in Belgrade, NU ICTM-CEH, Njegoševa 12, Belgrade. Serbia  
mpavlovic@tmf.bg.ac.rs*

### ABSTRACT

In this manuscript the results of experimental studies of the properties of composite materials based on lignocellulosic (LC) and poly(methylmetacrylate) matrices filled with electrolytic copper powder are presented. Composites were prepared with metal fillers volume fractions at percolation threshold, i.e. for LC matrix composite it was 7.2% (v/v) and for PMMA based one was 2.8% (v/v), and the samples were prepared by compression and molding. Characterization included examination of thermal stability and morphology of prepared samples at percolation threshold using a variety of testing techniques: SEM, TGA, AFM. Thermal analysis of the prepared composites showed the improvement of the thermal characteristics of the composites. This was due to the presence of the metallic fillers, which are very good thermal conductors, hence accumulating the heat emitted during TGA measurements primary to matrix, whether it was lignocellulosic or PMMA. Presence of three dimensional conductive pathways was confirmed.

### INTRODUCTION

In recent years, scientists and engineers have focused on reducing carbon dioxide emissions of all existing products, either by mixing bio-plastics and synthetic plastics and/or reinforcing it with synthetic fibers and fillers [1]. All biocomposites obtained from natural fibers and biodegradable plastics derived from natural origin (biopolymers and bioplastics) are highly environmentally friendly [2]. These environmentally friendly green composites have the potential to become new materials XXI century and can be a partial solution to many global problems. Consequently, renewable polymer materials have positive impact on sustainable development, and they represent economically and environmentally attractive and acceptable technologies[2]. Lignocellulose is a term used to describe the three-dimensional polymer composite formed by plants as their structural material. It consists of a variable amount of cellulose, hemicellulose and lignin [1,2]. Lignocellulosic raw materials are mainly composed of

carbohydrate polymers (cellulose and hemicellulose) and phenolic polymers (lignin). Minor concentrations of various other compounds, such as proteins, acids, salts and various minerals are also present. Research in the field of electro-conducting polymer composites filled with metal powders have experienced great development in the last two decades. Adding metal filler to polymer matrix allows the preservation of the mechanical properties of polymers while, at the same time, exploiting the electric conductive properties of metal [3]. The conductivity of composites with conductive fillers depends on the nature of contacts between the conductive filler particles and filler volume fraction, which is well explained by the percolation theory [3-5]. Composites with metal fillers have found application as self-regulating heaters, photothermal optical recorders, chemical sensors and electronic noses, chemical and electrochemical catalysts and adsorbents [3-5].

## EXPERIMENTAL

In the experimental part of the work, lignocellulose and poly(methylmethacrylate) (PMMA) were used as matrices. Lignocellulose was produced in *Maize Research Institute "Zemun Polje"* was used for synthesis of tested composites [5]. Celgran<sup>®</sup> C fraction was used, which was milled in a ball mill, and then dry sieved through mesh with openings of 45  $\mu\text{m}$ . PMMA used was commercial PMMA in form of beads, supplied by Sigma-Aldrich, having average molecular weight of  $M_w \sim 350000$ , with a density of  $1.20 \text{ g / cm}^3$  and the electrical conductivity of about  $10^{-12} \text{ S / cm}$ . Before use, the polymer was dried in a tunnel furnace at  $60 \text{ }^\circ\text{C}$  in a controlled nitrogen atmosphere. The electrolytic copper powder used in this study was galvanostatically produced as described in [5]. Polymer composites were prepared with the Cu powder volume fraction of 7.2% (v/v) for LC composites and 2.8% (v/v) for PMMA composites. All the samples were produced from thoroughly homogenized mixtures of powders. SEM and EDS analysis of lignocellulose and PMMA composites were examined in more detail using VEGA TS 5130MM microscope (Tescan), TGA measurements were performed on TA Instruments Q600 thermal analyzer with heating rate of  $10^\circ\text{C/min}$  in dynamic nitrogen atmosphere. "Nanoscope E" AFM "MultiModeScanning probe Microscope" from "Digital Instruments" was used for AFM analysis.

## RESULTS AND DISCUSSION

The conductivity of the conductive polymer composites is highly dependent on the nature of contacts between the conductive filler elements. In order to achieve better electrical fillers with highly developed free surfaces were

used[5,6]. However, thermal stability of LC and PMMA composites filled with galvanostatically obtained copper powder was not previously investigated. TGA curves shown in Figure 1. illustrate the thermal behavior (stability) of lignocellulose and PMMA composites filled with electrochemically deposited copper powder at percolation threshold. Characteristic temperatures of the observed thermal events in Figure 1 confirm presence of the main constituents (cellulose, hemicellulose, PMMA and lignin) [7]. All presented results showed improvement in the thermal characteristics of the composites due to the presence of copper powder, which is extremely good thermal conductor, so that the amount of heat emitted during the TGA measurements was originally accumulated in the copper powder particles, and only after this accumulation there is a change in matrices themselves[5].

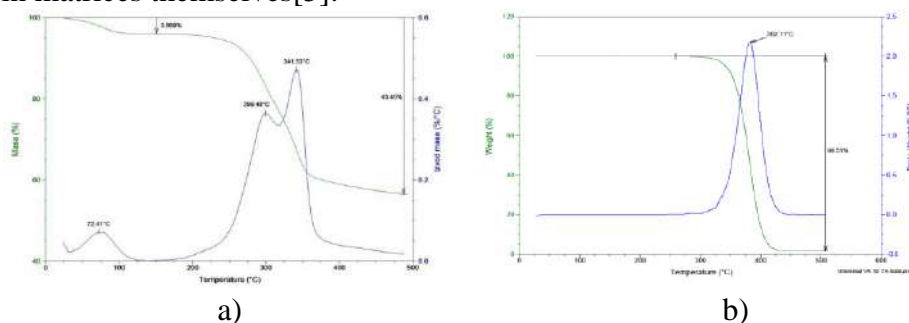


**Figure 1.** The results of thermogravimetric analysis of composites a) lignocellulose matrix filled with copper powder; b) PMMA matrix filled with copper powder.

EDS measurements (Figure 2.) show the existence of copper conductive pathways throughout the composites volumes. Due to the packaging effect and more pronounced interparticle contact with smaller, highly porous, highly dendritic particles with high values of specific area lead to “movement” of percolation threshold towards lower filler content [5]. This feature can be observed on both on Figure 2 and Figure 3. Figure 3 presents AFM image of the lignocellulose and PMMA composite surfaces after breaking. Conductive pathways were confirmed by EDS measurements, and the conductivity of the composite is obtained through conductive pathways of the filler that form in the composites. These pathways are formed in 3D in a pure random order. Morphology of polymer composites after brakeage was examined by AFM and is presented on Figure 3. Roughness that can be seen on Figure 3 is assigned to copper powder, since it has greater hardness and greater free surface area than the matrix.

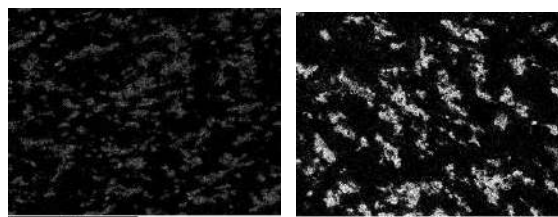


**Figure 2.** EDS images of the LC (left) and PMMA composites (right) prepared at percolation threshold. White dots represent Cu.

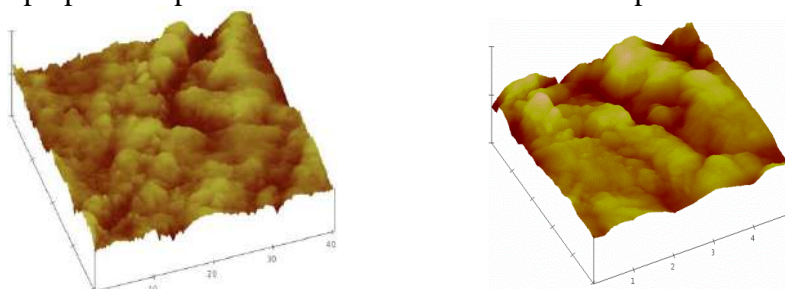


**Figure 3.** 3D AFM images of the PMMA (left) and LC (right) composite filled with copper powder at percolation threshold

## CONCLUSION

The results showed that thermal stability of LC and PMMA composites is improved comparing to pure polymers [5] due to presence of conductive copper powder filler. Morphology of the samples show presence of conductive pathways throughout the sample.

## Acknowledgements

This work was supported by the Ministry of Education and Science of Republic of Serbia (Projects ON 172015 and ON 172046)

## REFERENCES

- [1] L. Averous, F. L. Digabel, *Carbohydrate Polymers*, **66(4)**, 480, (2006).
- [2] S. Pilla (Ed.), *Handbook of Bioplastics and Biocomposites Engineering Applications*, John Wiley and Sons, New Jersey, (2011).
- [3] V. H. Pobleto, M. P. Alvarez, V. M. Fuenzalida, *Polymer Composites*, **30**, 328, (2009).
- [4] M. M. Pavlović, V. Čosović, M. G. Pavlović, N. Talijan, V. Bojanić, *International Journal of Electrochemical Science*, **6**, 3812, (2011).
- [5] M. M. Pavlović, Doktorska disertacija, Univerzitet u Beogradu, Tehnološko - metalurški fakultet, Beograd, (2015).
- [6] S. M. Zhang, L. Lin, H. Deng, X. Gao, E. Bilotti, T. Peijs, Q. Zhang, Q. Fu, *Express Polymer Letters*, **6 (2)**, 159, (2011).

## ELECTRICAL CONDUCTIVITY OF PMMA FILLED WITH COPPER POWDER

M. Pantović, M. Pavlović, M. Zarić and V. Pavelkić,

*University in Belgrade, NU ICTM-CEH, Njegoševa 12, Belgrade. Serbia  
m.pantovic@ihm.bg.ac.rs*

### ABSTRACT

This article is concerned with synthesis and characterization of electroconductive composite materials prepared by hot molding of mixtures of PMMA and electrochemically deposited copper powder and investigation of conductivity and percolation threshold of obtained composites. Electrodeposited copper powder content was varied from 0.5-8.8 vol%. Analysis of the most significant properties of individual components and prepared composites was performed using DC U/I measurements and AFM technique. The significant increase of the electrical conductivity was observed as the copper powder content reaches the percolation threshold at 2.98 vol%. In the investigated range of electrodeposited copper powder concentrations the increase of the electrical conductivity of composites is as much as sixteen orders of magnitude.

### INTRODUCTION

Properties of the composites are heavily influenced by properties of the starting constituent materials, their distribution, processing method and the interaction between them. The properties of the composite do not depend only on the concentration of filler, but also on size, shape (geometric ratio), interstitial interaction between filler and matrix and filler orientation [1,2]. Attempts to improve material properties by adding fillers, either inorganic or organic, are not new. For a long time synthetic polymer composites are used in various industrial fields, equipment, automotive industry, and even in the aviation industry. Conductive or semiconductive polymer composites are widely studied because of their numerous high-tech, electrical and electronic applications in various fields, such as self-regulating heaters, electric and temperature regulators for device protection and materials for removal of electromagnetic/radio frequency interferences (EMI / RFI) in electronic devices [3,4]. Conductive polymer composites can be prepared by different techniques and with different materials [5-7]. It is well known that the electrical resistance of polymer composites do not increase linearly with the increase of electrically conducting filler, but there is a critical volume

fraction of filler (percolation concentration) at which the resistance of material sharply decreases from insulating range to the values of semiconductors or metallic conductors [7].

## EXPERIMENTAL

In the experimental part of the work poly(methylmethacrylate) (PMMA) was used as matrix. The used PMMA was commercial PMMA in form of beads, supplied by Sigma-Aldrich, having average molecular weight of  $M_w \sim 350000$ , with a density of  $1.20 \text{ g / cm}^3$ , and the electrical conductivity of about  $10^{-12} \text{ S / cm}$ . Before use, the polymer was dried in a tunnel furnace at  $60 \text{ }^\circ\text{C}$  in a controlled nitrogen atmosphere. Composites were prepared by molding, from homogenized mixtures of PMMA and Cu powder heated at  $160 \text{ }^\circ\text{C}$ . The electrolytic copper powder used in this study was galvanostatically produced as described in [7]. Polymer composites of PMMA filled with copper powder were prepared with the filler volume fraction from 0.5% (v/v) - 8.8% (v/v). All the samples were produced from thoroughly homogenized mixtures of powders. SEM analysis of PMMA composites was performed using VEGA TS 5130MM microscope (Tescan), DC U/I measurements were performed using Digital Multimeter, Model 464, Simpson Electric Company. "Nanoscope E" AFM "MultiMode Scanning probe Microscope" from "Digital Instruments" was used for AFM analysis.

## RESULTS AND DISCUSSION

Conductivity of the conductive polymer composites strongly depends on nature of contacts between the conductive filler elements. In order to achieve better electrical conductivity fillers highly developed free surfaces, are used. For this reason the copper powder was galvanostatically produced with distinct dendritic morphology, having high specific surface area, as shown in Figure 1.

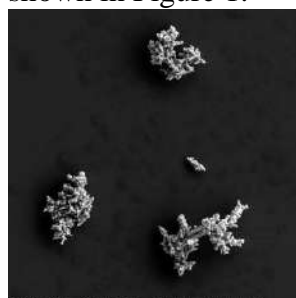


**Figure 1.** SEM photograph of copper powder particles obtained by constant current deposition and sieved through mesh  $<45 \mu\text{m}$ .

Presented results of copper powder morphological analysis showed that the powder has very large free surface. The powder shows specific characteristics typical of highly dendritic particles with distinctly developed primary and secondary dendritic arms with angles between them typical for centered cubic lattice. Therefore, this powder is a good prerequisite for the formation of great number of

interparticle contacts between the conductive copper powder particles, hence decreasing percolation threshold. Electrical conductivity of the composites, as a function of filler volume fraction, for all samples, was measured as mentioned in the Experimental part. DC I/O characteristics conductivity measurements for samples with a particle size  $\leq 45 \mu\text{m}$  is shown in Figure 2. Typical S shaped dependence, with three different regions (insulating, transitional and conductive) can be observed. Percolation threshold value was obtained from the maximum of conductivity derivative as a function of volume fraction of filler.

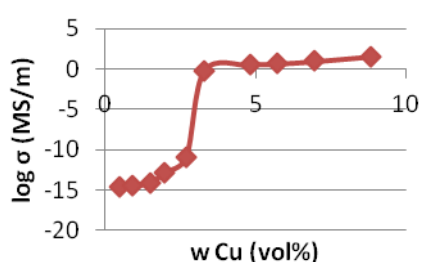


**Figure 2.** Change in electrical conductivity as a function of filler volume fraction for PMMA composites filled with copper powder

Experiments have shown that the morphology of the particles plays a significant role for the percolation threshold appearance. Due expressed interparticle contact with small particles having a high specific surface area, and the impact of packaging phenomenon, the percolation threshold occurs at lower value of filler volume fraction for particles  $\leq 45 \mu\text{m}$  than stated in the literature [6]. As it can be seen in Figure 2, the percolation threshold was 2.98% (v/v), which is an improvement of over 10 times than stated in literature [6].

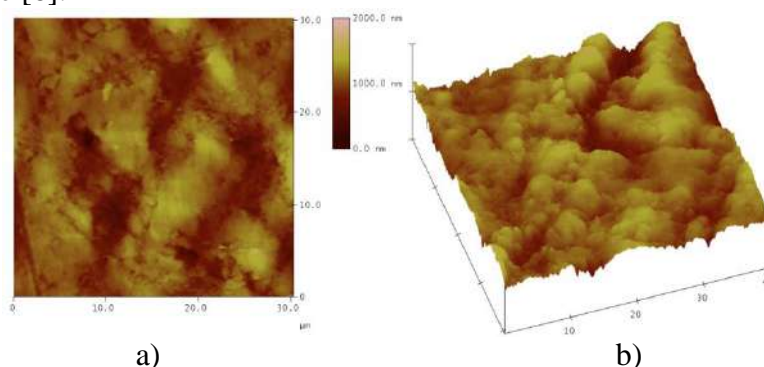


**Figure 3.** AFM images of the PMMA composite filled with copper powder at percolation threshold. a) surface plot and b) top 3D view of the surface from a)

Figure 3 presents AFM image of the PMMA composite surface after breaking. Conductive pathways can be observed, i.e. electrical conductivity

of the composite is obtained through conductive pathways that copper powder filler forms in the composites. These pathways are formed in 3D in a pure random order.

### CONCLUSION

This article has shown the experimental study of deposited copper powder particles morphology effects on the electrical conductivity of the PMMA matrix composites filled with powder of this metal. The results showed that the morphology of the powder with a large specific surface area and a distinct dendritic features play an important role in the electrical conductivity of the prepared samples. Conductivity measurements have shown typical S shape dependence, with the percolation transition from non-conductive to conductive region. The effect of packaging and pronounced interpartical contact with smaller, highly porous, highly dendritic particles with a large specific surface area values has led to a "shift" of percolation threshold towards lower filler volume fraction values. For given range of filler volume fractions the increase in composites electrical conductivity was as much as 16 orders of magnitude. AFM measurements confirm the presence of conductive pathways in composite volume that are formed in 3D in a pure random order.

### *Acknowledgements*

This work was supported by the Ministry of Education and Science of Republic of Serbia (Projects ON 172015 and ON 172046)

### REFERENCES

- [1] K. Mohanty, M. Misra, L. T. Drzal (Eds.), Natural Fibers, Biopolymers, and Biocomposites, Taylor and Francis Group, Florida, (2005).
- [2] L. Averous, F. L. Digabel, Carbohydrate Polymers, 2006, **66(4)**, 480.
- [3] V. H. Poblete, M. P. Alvarez, V. M. Fuenzalida, Polymer Composites, 2009, **30**, 328.
- [4] D. S. McLachlan., M. Blaszkiewicz, R. E. Newnham, Journal of the American Ceramic Society, 1990, **73(8)**, 2187.
- [5] L. J. Huijbregts, Charge transport and morphology in nanofillers and polymer nanocomposites, Doctoral Disertation, Technische Universiteit Eindhoven, Eindhoven, (2008).
- [6] G. Pinto, A. K. Maaroufi, Journal of Applied Polymer Science, 2005, **96**, 2011.
- [7] M. M. Pavlović, Doktorska disertacija, Univerzitet u Beogradu, Tehnološko - metalurski fakultet, Beograd, (2015).

## THE EFFECT OF FREQUENCY AND WATER CONTENT ON DIELECTRIC PROPERTIES OF PAA HYDROGEL

F. Marinković<sup>1</sup>, B. Stanković<sup>2</sup> and J. Jovanović<sup>2</sup>

<sup>1</sup>*University of Belgrade, Faculty of Physics, Studentski trg 12-16,  
11000 Belgrade, Serbia. (filip@ff.bg.ac.rs)*

<sup>2</sup>*University of Belgrade, Faculty of Physical Chemistry, Studentski trg 12-  
16, 11000 Belgrade, Serbia.*

### ABSTRACT

The effects of electric field frequency (from 24 Hz to 75 kHz) and content of absorbed water (from 0% wt to 50% wt) on dielectric properties of poly (acrylic acid) (PAA) hydrogel has been studied at 310 K. It was found that dielectric properties of hydrogel originate from the absorbed water. The values of the dielectric constant ( $\epsilon'$ ) and dielectric loss ( $\epsilon''$ ) decrease with increasing frequency at all investigated water contents. The values of  $\epsilon'$  and  $\epsilon''$  increase with the increase of the content of absorbed water within the hydrogel at all frequencies. It has been found that the value of  $\epsilon'$  for all hydrogels samples is significantly lower than the one for the water. Dielectric relaxation times of water absorbed within hydrogel have been calculated.

### INTRODUCTION

Hydrogels are hydrophilic macromolecular networks which are able to absorb large amounts of water but swell rather than dissolve in water. Absorbed water exists in different states (freezable, and non-freezable water; mobile, immobile and cluster water; free and bound water, etc.). Various techniques are used for water state investigation, such as: calorimetry, thermogravimetric analysis, NMR, dielectric relaxation spectroscopy, etc [1].

In order to get deeper insight into the state of water absorbed in hydrogel, the effects of frequency and water content on the dielectric constant ( $\epsilon'$ ) and the dielectric loss ( $\epsilon''$ ) values has been analyzed.

### EXPERIMENTAL

Poly (acrylic acid) hydrogel, which has been applied for this investigation was synthesized using the procedure given in one of our previous work [2]. Structural properties of synthesized xerogel were present in Table 1.

**Table 1.** Structural properties of the synthesized PAAG xerogel: equilibrium swelling degree ( $SD_{eq}$ ), network meshsize ( $\xi$ ), average molecular weight between cross-links ( $M_c$ ), crosslinking density ( $\rho_c$ ) and Flory's polymer-solvent interaction parameter ( $\chi$ )

Property	$SD_{eq}/\%$	$\xi/\text{nm}$	$M_c/\text{g mol}^{-1}$	$\rho_c/\text{mol dm}^{-3}$	$\chi$
Value	8500	7.76	$6.14 \cdot 10^4$	$2.10 \cdot 10^{-5}$	-0.504

The obtained hydrogel was grounded and dried in an air oven at 380 K to constant mass. The powdered xerogels samples were pressed at 125 bar and put in exiccator filled with water in order to absorb water vapor. The samples were kept in exiccator for different time intervals: half hour, hour and two hours, resulting in different degrees of water in hydrogel, 14% wt, 33% and 50%, respectively.

Dielectric spectroscopy measurements were performed in a vacuumed cell using the Hameg 8118 instrument in the frequency range from 24 Hz to 75 kHz. Applied voltage were 1 V. Measurements of AC conductivity were performed at constant temperature 310 K using the Lake Shore 340 temperature controller. The conductance ( $G$ ) and susceptance ( $B$ ) were measured in parallel mode ( $C_p$ ). The details of equipment and calculation of dielectric parameters,  $\epsilon'$  and  $\epsilon''$  were given elsewhere [3].

Dielectric relaxation times of water absorb on hydrogel have been calculated according to the procedure given by Higasi [4].

## RESULTS AND DISCUSSION

The obtained results of frequency influence on  $\epsilon'$  and  $\epsilon''$  values of hydrogel with different water content were represented in Fig. 1 and Fig. 2, respectively. From these figures, it can be seen that values of  $\epsilon'$  and  $\epsilon''$  decrease with increasing frequency for all water content, as well as that xerogel has small  $\epsilon'$  values like all other insulators. Values of  $\epsilon'$  for hydrogel are significantly lower than one for water. The fact that  $\epsilon'$  and  $\epsilon''$  decrease with increasing frequency can be explained by the dielectric dispersion resulting from the lag of the molecules behind the alternations of the applied electric field [5]. With increasing water content, values of  $\epsilon'$  increase for certain frequency, which can be explained by charge carrier mobility increasing with increase in the amount of water.

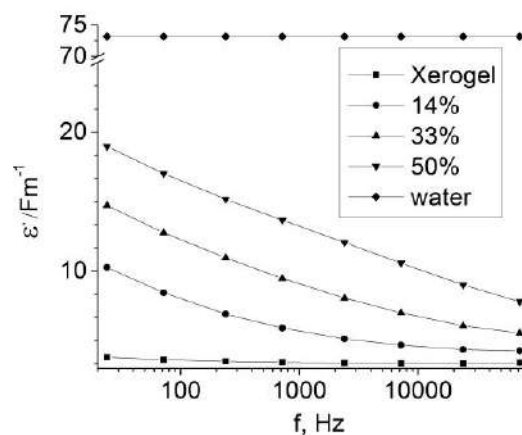


**Figure 1.** The dependence of  $\epsilon'$  versus frequency at 310K for xerogel, hydrogel with different water content and ordinary water.

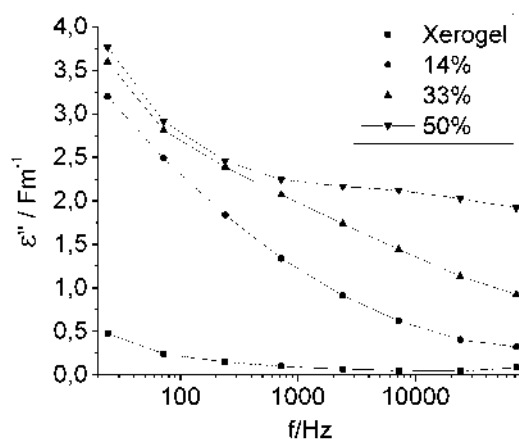


**Figure 2.** The dependence of  $\epsilon''$  versus frequency at 310K for xerogel and hydrogel with different water content.

Fig. 3 shows influence of frequency on dielectric relaxation time values. Relaxation times of absorbed water are drastically different than relaxation times of ordinary water and close to the one of ice. Relaxation times of absorbed water slightly decrease with the increase in the frequency.

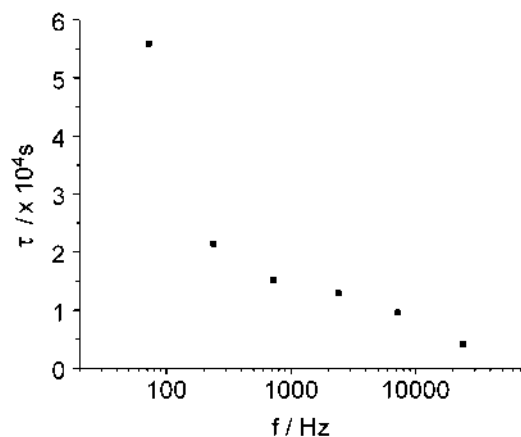


**Figure 3.** Dependence of dielectric relaxation time versus frequency at 310K for water adsorbed in hydrogel.

### CONCLUSION

Based on dependence of the dielectric constant  $\epsilon'$  on frequency and water content it was concluded that phase state of water adsorbed in hydrogel is different than the phase state in ordinary water. It was also founded, that the values of the dielectric constant  $\epsilon'$  and dielectric loss  $\epsilon''$  decrease with frequency increase for all investigated water content, as well as, that values of  $\epsilon'$  and  $\epsilon''$  increase with water content for the all investigated frequencies. Adsorbed water has dominant influence on dielectric properties of poly (acrylic acid) hydrogel. Dielectric relaxation times of water adsorbed on hydrogel is significantly lower than those which correspond to ordinary water.

### Acknowledgement

This work was partially supported by the Ministry for Science of the Republic of Serbia (Grants no. 172015 and 171029).

### REFERENCES

- [1] P. Pissis, A. Kyritsis, *Polymer Physics*, 2012, **51**, 159-175.
- [2] B. Jankovic, B. Adnadjevic, J. Jovanovic, *Chemical Engineering Research and Design*, 2011, **89**, 373-383
- [3] S. Maletic, D. Cerovic, F. Marinkovic, J. Dojcilovic, *Journal of applied polymer science*, 2015, **132**, DOI: 10.1002/app.42834.
- [4] K. Higasi, *Bulletin of the Chemical Society of Japan*, 1966, **39**, 2157-2160.
- [5] I.M. El-Anwar, O.M. El-Nabawy, S.A. El-Hennwii, A.H.Salama, *Chaos, Solitons & Fractals*, 2000, **11**, 1303-1311.

## A PSEUDO-HOMOGENEOUS MODEL DESCRIBING SOYBEAN OIL EPOXIDATION WITH PERACETIC ACID BASED ON THE FATTY ACID COMPOSITION

M. Janković, O. Govedarica, S. Sinadinović-Fišer, V. Teofilović,  
J. Pavličević and J. Budinski-Simendić

*University of Novi Sad, Faculty of Technology,  
Bul. Cara Lazara 1, 21000 Novi Sad, Serbia*

### ABSTRACT

A pseudo-homogeneous kinetic model describing soybean oil epoxidation with peracetic acid formed *in situ* in the presence of an acidic ion exchange resin was proposed. The difference in double bond reactivity of linolenic acid compared to other fatty acids in soybean oil triglycerides during the epoxidation was considered. The temperature dependency of the apparent reaction rate coefficients is described by a reparameterized Arrhenius equation. The constants in the model were estimated by fitting the experimental data obtained for the epoxidations of soybean oil run under defined reaction conditions. The established model correctly interprets data of double bond and epoxy ring contents. The model fits the experimental data about 1.3 times better than the model in which was disregarded the influence of the soybean oil fatty acid composition on the process kinetics.

### INTRODUCTION

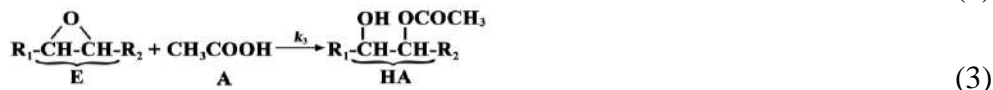
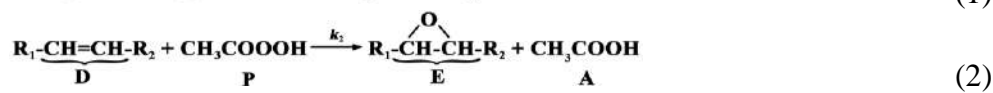
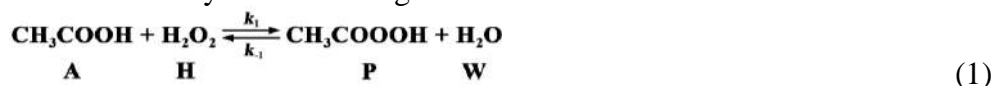
Epoxidation of C=C bonds in the fatty acid (FA) chains of triglycerides, the main constituents of vegetable oils, yields chemicals used as intermediates or final products. The dominant unsaturated FA chains in vegetable oils are oleic (C18:1), linoleic (C18:2) and linolenic (C18:3). It is reported that the reactivity of double bonds in oleic and linolenic chains is equal, but lower than in linolenic chain when vegetable oils are epoxidized with pre-formed performic acid [1]. Till now, the effect of unsaturation level on epoxidation rate was not taken into account in modeling the epoxidation with *in situ* formed perorganic acid catalyzed by an acidic solid catalyst. Therefore, a pseudo-homogenous model describing soybean oil (SO) epoxidation with peracetic acid formed *in situ* over an ion exchange resin is established considering the difference in double bonds reactivity of trienes (C18:3) and other double bonds.

## EXPERIMENTAL

The epoxidation of SO with peracetic acid formed *in situ* in the presence of Amberlite IR120 as the catalyst was carried out according to the method reported elsewhere [2]. The influence of the temperature of incremental 30% aq. hydrogen peroxide addition ( $T_H$ ), reaction temperature ( $T$ ), catalyst loading and stirring speed were studied in the following ranges: 323-338 K, 323-353 K, 1.98-7.86 wt% of oil weight, and 900-1100 rpm [2]. The molar ratio of oil unsaturation:acetic acid:hydrogen peroxide was 1:0.5:1.35 for all nine runs. The progress of the epoxidation was quantified by measuring the iodine value (IN) and epoxy oxygen content (EO) for samples withdrawn during the run. The IN and EO, as well as the FA composition of soybean oil, were determined according to the appropriate standard methods.

## RESULTS AND DISCUSSION

The *in situ* epoxidation of soybean oil occurs in the three-phase oil-water-solid reaction system involving few reactions:



namely, an acid-catalyzed formation of peracetic acid (P) and water (W) from acetic acid (A) and hydrogen peroxide (H) (1), followed by an uncatalyzed conversion of double bond (D) into the epoxy ring (E) (2), and formation of hydroxy acetate (HA) as dominant product of epoxy ring opening (3) [3]. Since the effective mixing was ensured in the reaction mixture, the external mass transfer resistance between the system phases was reduced. By varying the stirring speed, it was found that the mass transfer is faster than the intrinsic kinetics. Therefore, the mass transfer resistance was neglected in the model. Also, the internal mass transfer inside the resin pores was not considered when describing the kinetics of the peracetic acid formation due to reports about its negligible effect [4]. In the proposed pseudo-homogeneous model, the effect of FA composition was considered by assuming that the epoxidation reaction rate is different for trienes (T) *i.e.* firstly epoxidized double bond in linolenic chain compared to all other double bonds. Also, the corresponding mono-epoxy derivative of trienes (ET) has different degradation rate than other epoxy rings. Based on aforementioned assumptions, the following system of the first order differential equations may be written as:

$$\frac{d[H]}{dt} = -m \cdot C_s \cdot k_1 \left( [A][H] - \frac{[P][W]}{K_1} \right) + F_H \quad (4)$$

$$\frac{d[A]}{dt} = -m \cdot C_s \cdot k_1 \left( [A][H] - \frac{[P][W]}{K_1} \right) + k_2 [P][D] - k_3 [E][A]^2 + k_{2T} [P][T] - k_{3T} [ET][A]^2 \quad (5)$$

$$\frac{d[P]}{dt} = m \cdot C_s \cdot k_1 \left( [A][H] - \frac{[P][W]}{K_1} \right) - k_2 [P][D] - k_{2T} [P][T] \quad (6)$$

$$\frac{d[W]}{dt} = m \cdot C_s \cdot k_1 \left( [A][H] - \frac{[P][W]}{K_1} \right) + F_W \quad (7)$$

$$\frac{d[D]}{dt} = -k_2 [P][D] \quad (8)$$

$$\frac{d[T]}{dt} = -k_{2T} [P][T] \quad (9)$$

$$\frac{d[E]}{dt} = k_2 [P][D] - k_3 [E][A]^2 \quad (10)$$

$$\frac{d[ET]}{dt} = k_{2T} [P][T] - k_{3T} [ET][A]^2 \quad (11)$$

$$\frac{d[HA]}{dt} = k_3 [E][A]^2 + k_{3T} [ET][A]^2 \quad (12)$$

where  $t$  (min) is the reaction time.  $[j]$  is the number of moles of component or functional group  $j$  per 100 g of oil.  $m$ (g) is the mass of the catalyst and  $C_s$  (mol/g) is the concentration of catalyst active sites.  $k_1$  (mol<sup>-2</sup>min<sup>-1</sup>),  $k_2$  and  $k_{2T}$  (mol<sup>-1</sup>min<sup>-1</sup>), and  $k_3$  and  $k_{3T}$  (mol<sup>-2</sup>min<sup>-1</sup>) are the rate coefficients for the reactions 1, 2 and 3, respectively;  $k_{2T}$  and  $k_2$  correspond to trienes and other double bonds, respectively, while  $k_{3T}$  and  $k_3$  correspond to mono-epoxy intermediate of trienes epoxidation and other epoxy rings, respectively.  $K_1$  is the equilibrium constant for the reaction 1 [2]. A drop-wise addition of the hydrogen peroxide solution to the reaction mixture is approximated with continuous flows of H,  $F_H$ , and W,  $F_W$ , both in (mol/(min·100 g oil)) [2]. The temperature dependency of the rate coefficient  $k_i$  for the reaction  $i$  is expressed with reparameterized form of the Arrhenius equation (Table 1), where  $T_a$  is the average temperature of experiments accepted as 338 K. The molar fraction of double bonds reacting as trienes is 0.041 in used SO. The equation constants  $k_{i,0}$  and  $k_{i,Ea}$  were determined by fitting [D] and [E] changes with reaction time for SO epoxidations. [D] and [E] were calculated on the basis of experimental data for IN and EO, respectively. The Marquardt method was used to fit the data by minimizing the objective function, F. At  $T_a$ , the epoxidation rate for trienes is >1.4 times higher than

for all other double bonds. However, the corresponding epoxy ring is opened about 3.6 times slower than the other epoxy rings. To confirm the influence of the unsaturation level in FA chains on the process kinetics (model I), the experimental data were also fitted considering that all double bonds are equally reactive. The description of this reaction system excluded eqs 9 and 11 and particular terms in other eqs (mode III in Table 1). The lower value of F for model I indicates that FA composition has to be taken into account when modeling this reaction system.

### CONCLUSION

To develop a kinetic model for the soybean oil epoxidation with peracetic acid in the presence of the ion exchange resin, it was assumed that the fatty acid composition of the oil influences the kinetics. The viability of the established pseudo-homogeneous model is confirmed with positive values of all calculated reactant and product amounts. It was obtained that proposed model fits the experimental data better than the model in which was neglected the difference in reactivity of double bonds in soybean oil trienes.

### Acknowledgement

This work was partially supported by the Ministry of Education, Science and Technological Development of R. Serbia (Project no. III45022).

### REFERENCES

- [1] J. La Scala, R. Wool, J. Am. Oil Chem. Soc., 2002, **79**, 59-63.
- [2] M. Janković, S. Sinadinović-Fišer, O. Govedarica, J. Pavličević, J. Budinski-Simendić, Chem. Ind.Chem. Eng. Q., 2016, DOI: 10.2298/CICEQ150702014J
- [3] A. Campanella, M. A. Baltanas, Chem. Eng. J., 2006, **118**, 141-152.
- [4] V. Goud, A. Patwardhan, S. Dinda, N. Pradhan, Chem. Eng. Sci., 2007, **62**, 4065-4076.

**Table 1.** Model parameters determination.

	Model	
	I	II
F	0.09062	0.11800
$k_i = \exp \left[ k_{i,0} - \frac{k_{i,Ea}}{R} \left( \frac{1}{T} - \frac{1}{T_a} \right) \right]$		
$(k_1 C_s)_0$	-5.166687	-5.172997
$(k_1 C_s)_{Ea}$	85374.96	79039.30
$k_{2,0}$	-1.363825	-1.282917
$k_{2,Ea}$	-8614.313	-13083.98
$k_{2T,0}$	-1.004619	-
$k_{2T,Ea}$	131703.0	-
$k_{3,0}$	-4.363073	-4.010654
$k_{3,Ea}$	3842.45	-3174.165
$k_{3T,0}$	-5.641566	-
$k_{3T,Ea}$	183549.3	-

## DENSITIES OF SOYBEAN OIL, EPOXIDIZED SOYBEAN OIL AND ACETIC ACID BINARY MIXTURES: EXPERIMENTAL DATA AND CORRELATION

O. Govedarica, M. Janković, S. Sinadinović-Fišer, R. Radičević, T. Erceg, N. Vukić and J. Budinski-Simendić

*University of Novi Sad, Faculty of Technology,  
Bul. Cara Lazara 1, 21000 Novi Sad, Serbia*

### ABSTRACT

For the predication of partition coefficient of acetic acid between an oil and water phases in the soybean oil epoxidation reaction system, densities of system's phases have to be correlated with the reaction mixture composition and temperature that change during the process. Among reported models for the calculation of mixtures density, eleven were selected for the regression of experimental data. Measurements of densities of acetic acid, soybean oil, epoxidized soybean oil, and their binary mixtures were performed in the temperature range from 20 to 80°C and for nine mixture compositions that correspond to the component ratios in an industrial epoxidation process. The model that best fits experimental data, with an average relative error of 0.31%, was found to be Campbell-Thodos.

### INTRODUCTION

On an industrial scale, the epoxidation of vegetable oils is currently carried out with a percarboxylic acid, such as peracetic acid, usually formed *in situ* through the acid catalysed peroxidation of acetic acid with hydrogen peroxide aqueous solution. The process optimization requires a reliable mathematical model which comprises kinetic, mass transfer and thermodynamic parameters, one of which is the partition coefficient of acetic acid between an oil and water phases,  $K_A$ . The coefficient is dependent on a liquid-liquid equilibrium constant for acetic acid, and molar masses and densities of the system phases. Since the composition of the phases is changing during the epoxidation, a correlation that describes the variation of phase's densities with composition, as well as with the process temperature, is necessary. Because of that, the aim of this work was to select a model that reasonable well correlate the density of oil phase i.e. the mixture of soybean oil, epoxidized soybean oil and acetic acid, with its composition and temperature.

## EXPERIMENTAL

Oscillating U-tube densitometer Anton Paar DMA 4500 M was used to determine densities of soybean oil, epoxidized soybean oil, acetic acid and their binary mixtures in the temperature range 20-80°C with precision of 0,00005 g/cm<sup>3</sup>. The molar ratios of soybean oil and epoxidized soybean oil in their binary mixtures with acetic acid were approximately 1:0.4, 1:0.7 and 1:1 based on the initial unsaturation of soybean oil. In the binary mixtures of soybean oil and epoxidized soybean oil the molar ratios were adjusted to simulate the soybean oil double bond conversion of approximately 25, 50 and 75% to epoxide.

## RESULTS AND DISCUSSION

To correlate the experimental values of densities, eleven models given in Table 1 were applied for the calculation of the saturated liquid density,  $\rho_s$ , while Tait equation [2] was used to calculate the compressed liquid density,  $\rho$ . The objective function S was minimized with Marquardt algorithm, where N is the total number of experimental points  $i$  (N=77). Statistical

**Table 1.** Statistical values of the model parameters determination.

Model	<sup>a</sup> S · 10 <sup>3</sup>	<sup>b</sup> ARE (%)
Costald [3]	4.139	0.622
Spencer-Danner-Rackett [4]	3.892	0.594
Yen-Woods [5]	3.887	0.601
Nasrifar [6]	14.96	1.188
Modified Nasrifar [6]	132.0	3.664
Inglesias-Silva-Hall [7]	103.0	3.280
Reid [8]	3.343	0.513
Joffe-Zudkevitch [9]	2.633	0.464
Campbell-Thodos [10]	1.535	0.315
Peng-Robinson EoS	0.171	4.531
Amagat's law	6.078	0.586

$$^a \text{ Square deviation: } S = \sum_{i=1}^N (\rho_i^{\text{calc}} - \rho_i^{\text{exp}})^2$$

<sup>b</sup> Average relative error:

$$\text{ARE} = \frac{100}{N} \cdot \sum_{i=1}^N \left| \frac{\rho_i^{\text{calc}} - \rho_i^{\text{exp}}}{\rho_i^{\text{exp}}} \right|$$

parameters of the modeling of the oil phase density are presented in Table

1for all models. Due to the lowest value of objective function, S, the best fit model for saturated liquid density was Campbell-Thodos model:

$$\rho_s = \frac{M}{v_c} [I + \alpha(1-T_r)^m + \beta(1-T_r)^n]$$

where  $M$ (g/mol),  $v_c$ (dm<sup>3</sup>/mol) and  $T_r$  are the component molecular mass, critical molar volume and reduced temperature, respectively, and  $\alpha$ ,  $\beta$ ,  $m$  and  $n$  are the parameters.

For employing the Campbell-Thodos model, the values of critical pressure of 5970 kPa and acentric factor of 0.431 for acetic acid, which are necessary for the Tait equation, were taken from the literature [11]. The critical parameters and Campbell-Thodos model parameters for acetic acid were also adopted from the literature (Table 2). The critical pressures for soybean oil and epoxidized soybean oil were obtained on the basis of Ambrose method as 500 and 400 kPa, respectively [11], while the values of

**Table 2.** Critical parameters and Campbell-Thodos model parameters for acetic acid (A) [10]

	$T_c$ (K)	$v_c$ (m <sup>3</sup> /kmol)	$\alpha$	$\beta$	$n$
A	592.7	0.171	2.4438	0.4319	2.1843

acentric factors as 0.586 and 0.61, respectively, resulted from the experimental data fitting with Spencer-Danner-Rackett model. Soybean oil and epoxidized soybean oil were each considered as one pseudo-component. Their molecular masses of 878 and 963 kg/kmol, respectively, were determined on the basis of the soybean oil fatty acid composition and yield of epoxide. For the accepted value of 0.375 for  $m$ , the values of the parameters in the Campbell-Thodos model and critical parameters for soybean oil and epoxidized soybean oil were obtained by fitting the experimental data. The values are presented in Table 3.

**Table 3.** Parameters for soybean (SO) and epoxidized soybean oil (ESO) determined by fitting the experimental data with Campbell-Thodos model

	$T_c$ (K)	$v_c$ (m <sup>3</sup> /kmol)	$\alpha$	$\beta$	$n$
SO	871.17	2.8678	1.8593	0.64127	1.1576
ESO	2800.262	3.04915	-0.64731	3.4713	2.07549

## CONCLUSION

The density of the oil phase i.e. of the mixture of soybean oil, epoxidized soybean oil and acetic acid, for temperature and composition ranges relevant for the industrial process of soybean oil epoxidation with peracetic acid formed *in situ* can be successfully correlated using Campbell-Thodos model.

## Acknowledgement

This work was partially supported by the Ministry of Education, Science and Technological Development of R. Serbia (Project no. III45022).

## REFERENCES

- [1] S. Sinadinović-Fišer, M. Janković, J. Am. Oil Soc., 2007, **84**, 591 – 600.
- [2] R.W. Hankinson, G.H. Thomson, Hydrocarbon Process., 1979, **9**, 277 – 283.
- [3] R. W. Hankinson, G. H. Thomson, AIChE J., 1979, **25**, 653 – 663.
- [4] C. F. Spencer, R. P. Danner, Chem. Eng. Data, 1972, **17**, 236 – 241.
- [5] L. C. Yen, S. S. Woods, AIChE J., 1966, **12**, 95 – 99.
- [6] A. Mchaweh, A. Alsaygh, Kh. Nasrifar, M. Moshfeghian, Fluid Phase Equilib., 2004, **224**, 157 – 167.
- [7] G. A. Iglesias-Silva, K. R. Hall, Fluid Phase Equilib, 1997, **11**, 97 – 105.
- [8] R. C. Ried, J. M. Prausnitz, T. K. Sherwood, The properties of gases and liquids, McGraw-Hill, New York, 1977.
- [9] J. Joffe, D. Zudkevitch, in Thermodynamics Data and Correlations, D. Zudkevitch, I. Zaremebr (Eds.), AIChE, New York, 1974.
- [10] S. W. Campbell, G. Thodos, Ind. Eng. Chem. Fundam., 1984, **23**, 500 – 510.
- [11] R. C. Ried, J. M. Prausnitz, B. E. Poling, The properties of gases and liquids, McGraw Hill, New York, 1987.

## THE SYNTHESIS OF POLYACRYLIC ACID WITH CONTROLLED MOLECULAR WEIGHTS

I. Ristić<sup>1</sup>, A. Miletić<sup>1</sup>, S. Cakić<sup>2</sup>, O. Govedarica<sup>1</sup>, M. Janković<sup>1</sup>,  
S. Sinadinović-Fišer<sup>1</sup> and J. Budinski-Simendić<sup>1</sup>

<sup>1</sup> *University of Novi Sad, Faculty of Technology, Blvd. Cara Lazara 1, Novi Sad, Serbia. (ivan.ristic@uns.ac.rs)*

<sup>2</sup> *University of Niš, Faculty of Technology Leskovac, Blvd. oslobođenja 124*

### ABSTRACT

Poly(acrylic acid) is synthesized in water-borne system via radical polymerization reaction using potassium persulfate and sodium pyrosulfate as initiator and iron(II) sulfate pentahydrate as chain length regulator. Characterization of obtained polymers was done regarding average molecular weights and structural properties. It is shown that molecular weights can be successfully controlled using proposed initiator system and iron(II) sulfate for synthesis of polymers.

### INTRODUCTION

In recent years industry is changing regarding chemicals and processes implemented, looking for solutions for eco-friendly materials production, which is in accordance with postulates of “green chemistry” [1]. Usage of harmful chemicals should be avoided and for this reason water-borne systems are becoming more and more popular [2]. Production of polymers is fields where is very hard to implement new process and improve it to become eco-friendly. This is because polymers are usually not soluble in water and in most of the synthesis procedures the water is byproduct and cannot be used as reaction medium. One of rare polymers which can be synthesized in water is poly(acrylic acid) which has application as the absorber, thickening, dispersing, suspending and emulsifying agent in pharmaceutical, cosmetic and paint industry [3]. The neutralized gels can be used in medicine as the basis for skin care or skin disease treatment products. Reaction mechanism for obtaining poly(acrylic acid) is radical polymerization with the use of different oxo- and amino-based initiators [4]. This kind of reaction is exothermic so good control of reaction temperature is needed. As monomer for synthesis of poly(acrylic acid) can be used acrylic acid or some butyl or methyl derivate of acrylic acid [5]. Also, building copolymers with maleic and other unsaturated acids are convenient.

The aim of this work is examination of molecular weight control for poly(acrylic acid) using iron(II) sulfate as regulator of chain length.

### EXPERIMENTAL

Acrylic acid (98%), potassium persulfate, sodium pyrosulfate and iron(II) sulfate pentahydrate were purchased from Fisher Scientific. As reaction medium was used distilled water. Poly(acrylic acid) polymers were synthesized in water-borne system by radical polymerization using potassium persulfate and sodium pyrosulfate as initiator and iron(II) sulfate pentahydrate. Concentration of the acrylic acid in the system was 30 wt%. Samples were synthesized at 65 °C for 6 hours with reflux. The sample for desired molecular weight of 50000 g mol<sup>-1</sup> has notation PA5, for 80000 g mol<sup>-1</sup> the notation is PA8 and for 100000 g mol<sup>-1</sup> the notation is PA10. For the characterization of structure the pastille of poly(acrylic acid) with KBr were prepared. Measurements were performed in the range from 4000 to 400 cm<sup>-1</sup> using FTIR spectrophotometer Bomem Hartmann MB-series. Average molecular weights ( $\bar{M}_n$ ,  $\bar{M}_w$  and  $\bar{M}_z$ ) and polydispersity (Q) were determined by gel permeation chromatography GPC Agilent 1100 Series with RID detector 1200. The column was Zorbax-Bimodal-S, for range of molecular weights 10<sup>2</sup>-10<sup>6</sup> g/mol. Water with feed rate of 1 cm<sup>3</sup>/min was used as the eluent. The sodium salts of poly(styrenesulphonate) with narrow molecular weight distribution (Mn=12523 g/mol, Q=1,12; Mn=63158 g/mol, Q=1,25; Mn=640870 g/mol, Q=1,3) were used for calibration. The ordered structures of polymers was studied using Diffractometer PW 1729 CuK $\alpha$ , XRD Philips.

### RESULTS AND DISCUSSION

FTIR spectra of acrylic acid monomer and poly(acrylic acid) are shown at Figure 1a and 1b, respectively. Valent vibrations of O-H group [ $\nu(\text{OH})$ ] of acrylic acid are present in the wide range of 3500-2500 cm<sup>-1</sup>, together with two other peaks: one at 3061 cm<sup>-1</sup> and the other at 2989 cm<sup>-1</sup> which originate from absorption of valent C-H vibrations [ $\nu_{\text{as}}(\text{CH})$ ], while the peak of [ $\nu(\text{OH})$ ] of poly(acrylic acid) is at 3430 cm<sup>-1</sup> and [ $\nu_{\text{as}}(\text{CH})$ ] is at 2959 cm<sup>-1</sup>. Middle intensity peak in IR spectra of acrylic acid at 1298 cm<sup>-1</sup> originates from deformational C-H vibrations in plane [ $\delta(\text{CH})$ ], and [ $\delta(\text{CH})$ ] of poly(acrylic acid) is present at 1256 cm<sup>-1</sup>.

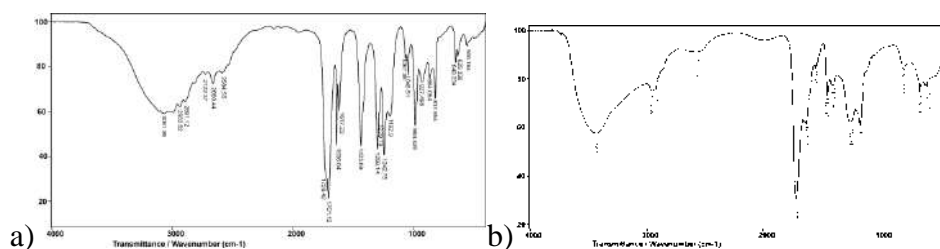


**Figure 1.** FTIR spectra of acrylic acid (a) and poly(acrylic acid) (b)

Valent vibrations of C=O [ $\nu(\text{C}=\text{O})$ ] are present as very sharp strips at  $1701\text{ cm}^{-1}$  at the IR spectra of acrylic acid and at  $1718\text{ cm}^{-1}$  at the IR spectra of poly(acrylic acid). Sharp stripe of C-O vibrations at  $1433\text{ cm}^{-1}$  at IR spectra of acrylic acid is the evidence of COOH group presence, while two sharp stripes at  $1636\text{ cm}^{-1}$  and at  $1617\text{ cm}^{-1}$  originated from absorption of C=C valent vibrations of acid. Another sharp stripe at  $984\text{ cm}^{-1}$  is from presence of deformational vibrations of O-H group out of plane [ $\gamma(\text{OH})$ ]. At the IR spectra of poly(acrylic acid) the peak from valent vibrations of C-O group at  $1453\text{ cm}^{-1}$  have low intensity. By comparing the spectra it was assessed that the absorption occurs at higher wave lengths and that the intensity of peaks is lower for poly(acrylic acid). The results obtained by GPC measurements are given in the Table 1. While the values of  $M_n$  are similar for all samples, the higher difference is obvious for  $M_w$  and  $M_z$  values and it is influenced by the concentration of chain length regulator. Good control of molecular weights was achieved using iron sulfate as chain length regulator. According to the XRD analysis of obtained polymers can be concluded that they have ordered structure, probably due to strong ion and hydrogen bonds. Wide peaks were registered at  $10,8$  and  $17,2^\circ$  (figure 2.)

**Table 1.** The results obtained by GPC measurements.

Sample	$M_n$ , g/mol	$M_w$ , g/mol	$M_z$ , g/mol	Q
PA 5-1	$5,34 \cdot 10^4$	$1,65 \cdot 10^5$	$5,21 \cdot 10^5$	3,1
PA 5-2	$5,12 \cdot 10^4$	$1,43 \cdot 10^5$	$5,31 \cdot 10^5$	2,8
PA 8-1	$8,27 \cdot 10^4$	$2,31 \cdot 10^5$	$5,78 \cdot 10^5$	2,8
PA 8-2	$8,51 \cdot 10^4$	$1,78 \cdot 10^5$	$5,99 \cdot 10^5$	2,1
PA 10	$10,51 \cdot 10^4$	$4,09 \cdot 10^5$	$7,01 \cdot 10^5$	3,9

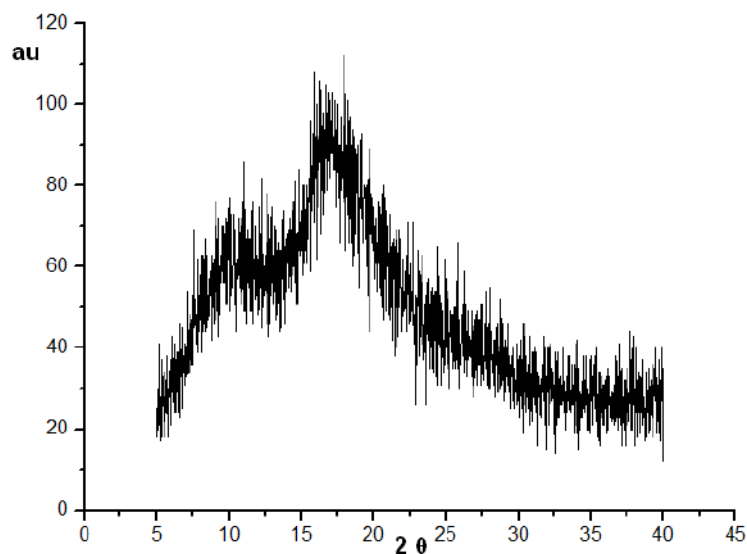


**Figure 2.** XRD graph of sample PA 8-1

## CONCLUSION

Water-borne system for synthesis of eco-friendly poly(acrylic acid) was developed using the regulator of chain length. It has been assessed that polymer molecular weights can be successfully controlled by proposed initiator system and iron(II) sulfate for synthesis of poly(acrylic acid). Poly(acrylic acid) synthesized via this procedure has possible application in pharmaceutical and paint industry.

## Acknowledgement

This work is funded by Ministry of Education, Science and Technological Development Republic of Serbia through project III45022.

## REFERENCES

- [1] J. Loiseau , N. Doërr , J. Suau, J. Egraz , M. Lauro, C. Ladavière, J. Claviere, *Macromolecules*, 2003, **36** (9), 3066–3077.
- [2] V. Vetriselvi, R. Santhi, *Research Journal of Chemical Sciences*, 2014, **4**, 1-9.
- [3] A. Li, A. Wang, J. Chen, *Journal of Applied Polymer Science*, 2004, **92**, 1596-1603.
- [4] D. Benoit, S. Grimaldi, S. Robin, J. Finet, P. Tordo, Y. Gnanou, *Journal of American Chemical Society*, 2000, **122** (25), 5929-5939.
- [5] J. Elliot, M. Macdonald, J. Nie, C. Bowman, *Polymer*, 2004, **45**, 15031510.

*K - Environmental Protection,  
Forensic Sciences,  
Geophysical Chemistry*



## DESORPTION OF $^{137}\text{Cs}$ FROM *HYPNUM* *CUPRESSIFORME* AND *ISOTHECIUM MYURUM* MOSS USING WEAKLY ACID SOLUTIONS

A. A. Čučulović<sup>1</sup> and D. S. Veselinović<sup>2</sup>

<sup>1</sup>University of Belgrade, INEP- Institute for the Application of Nuclear Energy, 11080 Zemun, Serbia, [anas@inep.co.rs](mailto:anas@inep.co.rs)

<sup>2</sup>University of Belgrade, Faculty of Physical Chemistry, P. Fax 137, 11001 Belgrade, Serbia

### ABSTRACT

Desorption of  $^{137}\text{Cs}$  from: *Hypnumcupressiforme* (**A**) and *Isotheciummyurum* (**B**) moss was investigated. The following solutions were used for desorption:  $\text{H}_2\text{SO}_4$  (**I**),  $\text{HNO}_3$  (**II**) and a mixture of  $\text{H}_2\text{SO}_4$ - $\text{HNO}_3$  (**III**), for three pH values (4.61; 5.15 and 5.75) and also distilled water (**D**) pH=6.50. After five successive desorptions lasting 24 hours the following amounts of  $^{137}\text{Cs}$  (%) were desorbed from mosses: (**A**) 19.1-34.7; (**B**) 18.4-30.5 and distilled water (**A**) 29.1 and (**B**) 26.9. The mosses did not undergo any noticeable structural changes after desorption. Sorption of  $^{137}\text{Cs}$  is performed in at least two sorption points in moss tissue.

### INTRODUCTION

Mosses are an old, primitive, non-vascular plant species, with a specific build, specific ecology and physiology in regard to other species[1]. Acid rain is formed of  $\text{SO}_2$  and also of  $\text{NO}_2$ , building  $\text{H}_2\text{SO}_4$  and  $\text{HNO}_3$  after oxidation during atmospheric fallout. Acid rain represents any acid precipitation, regardless whether it is wet or dry precipitation[2]. If moss sorbs a certain substance (for example  $^{137}\text{Cs}$ ) it becomes polluted with it[3,4]. When moss is put into water or is periodically soaked with solutions not containing the sorbed substance, this substance undergoes desorption. The amount of desorbed substance depends on the type of desorption solutions influencing pollution spreading of this substance into the environment. In our previous work desorption of  $^{137}\text{Cs}$  and metals was followed in *Cetraria islandica* lichen using acid solution with pH values from 2.00 to 5.75, and also desorption of  $^{137}\text{Cs}$  from *Homalotheciumsericeum* (Hedw.) Schimp. moss[5,6]. A system for following desorption of  $^{137}\text{Cs}$  with acid solutions similar to acid rain was setup. With the aim of confirming the determined possibility of using moss as pollution bioindicators and also sources of  $^{137}\text{Cs}$  pollution, desorption of this isotope in two more moss species was investigated.

## MATERIALS AND METHODS

Samples of *Hypnumcupressiforme* (**A**) and *Isotheciummyurum* (**B**) moss were collected in the National park Djerdap (Serbia) in 2006, (10 g dry mass) and covered with 200 mL of distilled water (**D**) and acid solutions: (**I**)H<sub>2</sub>SO<sub>4</sub>, (**II**)HNO<sub>3</sub>and (**III**) H<sub>2</sub>SO<sub>4</sub>-HNO<sub>3</sub>. Solutions (**I**) and(**II**) were made by adding concentrated H<sub>2</sub>SO<sub>4</sub>, HNO<sub>3</sub>, respectively to 200 mL of distilled water (pH 6.50) to the required pH value: 4.60; 5.15 and 5.75. Solution (**III**) was made by mixing 100.0 mL of solution (**I**) and 100.0 mL of solution (**II**), with identical pH values. Samples were consecutively desorbed with a solution five times and desorption series were repeated twice. Desorption were performed at room temperatureand lasted 24 hours. After each desorption, after filtration, moss samples were dried at room temperature to a constant mass. Activity levels of <sup>137</sup>Cs were measured in samples before and after each desorption on an ORTEC-AMETEK gammaspectrometerwith 8192 channels, resolution of 1.65 keVand efficiency 34% at 1.33 MeV <sup>60</sup>Co with a measurement error below 5%. Specific activity were calculated based on measurements(Bq/kg).

## RESULTS AND DISCUSSION

Table I shows the activity of <sup>137</sup>Cs in mosses *H. cupressiforme* (**A**) and *I. myurum* (**B**) before desorption (Bq/kg) and the percentage of remaining <sup>137</sup>Cs in mosses after each of the five successive desorptions using solutions (**I**), (**II**), (**III**) and distilled water (**D**), and also the total amount (%)of desorbed<sup>137</sup>Cs. Starting activities of <sup>137</sup>Cs in moss were: 2682-2757 (**A**) and 2002-2040 (**B**) Bq/kg. Solutions (**I**), (**II**) and (**III**) after five desorptions desorbedfrom 19.1% (**III**, pH 5.75) to 34.7% (**I**, pH 4.61) <sup>137</sup>Cs from moss (**A**), and from 18.4% (**III**, pH 5.75) to 30.5% (**I**, pH 4.61) from moss (**B**). Distilled water (**D**) desorbed29.1% <sup>137</sup>Cs from moss (**A**) and 26.9% from moss (**B**). Using equation (1) from our previous paper [5-7]

$$\ln C_x = \ln C_0 - a n_x \quad (1)$$

i.e. the change of the sorbed amount of substance,  $C_x$ , in the sorbent with the desorption number,  $n_x$ , for successive desorptions with the same volume of desorption solution the value  $C_0$  has been determined by extrapolation on  $n_x=0$ ,  $C_0$  is the content of the sorbed substance (<sup>137</sup>Cs) before desorption and  $a$  is a constant.

The dependence of the logarithm of the amount of sorbed substance in the solid sorbent phase on the number of successive desorptions,  $n_x$  (equation 1) is in all cases linear, showing that only one sorption type is active, or one or more sorption types prevail (the rest are negligible).

**Table 1.** Activity of  $^{137}\text{Cs}$  in moss before desorption (Bq/kg), percentage of remaining  $^{137}\text{Cs}$  in moss after each desorption, total desorbed  $^{137}\text{Cs}$  from mosses (A) and (B) (%) and values of the starting activity of  $^{137}\text{Cs}$  ( $C_{0e}$ ) (%), determined by extrapolation of the curves, given as a percentage in relation to the values of  $C_0$  (100%) in starting solution\*

pH	4.60			5.15			5.75			6.50
Solu- tion	I	II	III	I	II	III	I	II	III	D** *
No of desorp- tion	Activity levels of $^{137}\text{Cs}$ in moss A before desorption (Bq/kg)									
	2757	2749	2737	2697	2703	2682	2737	2741	2720	2650
	Percentage of remaining $^{137}\text{Cs}$ in moss A after each desorption (%)									
I	84.4	85.5	85.4	83.1	89.9	84.1	86.9	87.9	87.6	83.2
II	73.8	80.1	81.0	77.8	83.7	79.9	81.9	84.9	82.3	76.7
III	68.2	77.4	78.3	75.7	81.5	77.7	79.8	83.8	79.7	73.3
IV	65.9	76.3	76.1	73.5	79.2	76.9	78.1	82.1	78.5	72.0
V	65.3	76.0	75.0	73.1	78.7	76.8	77.5	80.9	78.0	70.9
	Total desorbed $^{137}\text{Cs}$ from moss A (%)									
	34.7	24.0	25.0	26.9	21.3	23.2	22.5	19.1	22.0	29.1
$C_{0e}$	85.6	94.6	87.4	84.4	90.9	84.8	87.8	89.1	86.5	83.9
$\Delta C_0^{**}$	14.4	5.6	12.6	15.6	9.1	15.2	12.2	10.9	13.5	16.1
No of desorp- tion	Activity levels of $^{137}\text{Cs}$ in moss B before desorption (Bq/kg)									
	2028	2016	2021	2002	2011	2017	2040	2034	2025	2061
	Percentage of remaining $^{137}\text{Cs}$ in moss B after each desorption (%)									
I	86.9	86.4	87.3	84.0	88.0	85.3	87.2	88.1	87.4	87.3
II	77.3	80.8	78.5	78.3	83.3	78.0	82.4	84.4	83.2	79.3
III	74.0	78.2	74.8	76.7	82.2	76.5	79.8	82.8	80.1	75.9
IV	71.2	77.0	73.1	75.2	81.1	75.1	79.2	81.9	79.2	73.9
V	69.5	77.3	72.3	74.8	80.8	74.4	79.0	81.6	78.7	73.1
	Total desorbed $^{137}\text{Cs}$ from moss B (%)									
	30.5	22.7	27.7	25.2	19.2	25.6	21.0	18.4	22.3	26.9
$C_{0e}$	82.2	85.6	87.8	77.5	88.7	85.6	87.8	89.1	88.2	88.2
$\Delta C_0$	17.8	14.4	12.2	22.5	11.3	14.6	12.2	10.9	11.8	11.8

\*solution compositions are given in the Material and Methods,

(A) *Hypnumcupressiforme*, (B) *Isotheciummyurum*, \*\*  $\Delta C_0 = 100 - C_{0e}$  (%)

\*\*\*distilled water

## CONCLUSION

The results obtained for total desorption of  $^{137}\text{Cs}$  for all pH values show that the highest desorption occurred when solution (I) was used, followed by solution (III), and desorption was the lowest when solution (II) was used. This means that the anion type influences desorption, regardless from the fact that these are strong acids. In this case the sulphate anion has a stronger influence. As cesium is an alkali metal, the influence of the acid anion type on desorption is the consequence of the influence of acid anions on corresponding components of the organic molecule in moss tissue to which the sorbed cesium was bonded. The obtained results indicate that in all cases with increased pH values of the desorption solution the amount of desorbed  $^{137}\text{Cs}$  is reduced. This indicates that hydrogen ions have an influence on

$^{137}\text{Cs}$  desorption from moss. Desorption of  $^{137}\text{Cs}$  with distilled water shows that water is also a desorption medium with a significant efficiency, as the percentage of totally desorbed  $^{137}\text{Cs}$  in all cases is higher than when using acid solutions, except in one case when the  $\text{H}_2\text{SO}_4$  solution with  $\text{pH}=4.61$  was used. From this follows that  $^{137}\text{Cs}$  desorption is a complex process, influenced besides water as a solvent, by a series of other components present in the desorption solution, i.e. acid rain performing desorption in natural conditions.

### **Acknowledgement**

This work was financed by the Ministry of Education, Science and Technological Development of the Republic of Serbia (Project number: III43009)

### **REFERENCES**

- [1] D. H. S. Richardson, *The Biology of Mosses*. Blackwell Scientific Publications. Oxford, 1981.
- [2] D. Veselinović, I. A. Gržetić, Š. A. Đarmati, D. Marković, Stanja i procesi u životnoj sredini, Fizičko hemijski osnovi zaštite životne sredine, knjiga I, Udžbenici Fizičke hemije, Fakultet za fizičku hemiju, Univerzitet u Beogradu, Beograd, 1995.
- [3] A. Čučulović, D. Popović, R. Čučulović, J. Ajtić, *Nucl. Technol. Radiat.*, 2012, **27**(1), 44-51.
- [4] A. Čučulović, R. Čučulović, M. Sabovljević, D. Veselinović, *Arch. Biol. Sci.*, 2012, **64**(3), 917-925.
- [5] A. Čučulović, Desorpcija  $^{137}\text{Cs}$  i drugih metala iz lišaja *Cetraria islandica* kiselim rastvorima, doktorska disertacija, Fakultet za fizičku hemiju, Univerzitet u Beogradu, Beograd, 2007.
- [6] A. Čučulović, D. Veselinović, *Hem. Ind.*, 2013, **67**(6), 975-980.
- [7] A. Čučulović, D. Veselinović, *Russ. J. Phys. Chem. A*, 2015, **89**(13), 2473-2477.

## SODIUM CONCENTRATION IN WATER SAMPLES FROM COAL-FIRED POWER PLANTS

N. Sarap<sup>1</sup>, M. Pagnacco<sup>2</sup>, J. Senćanski<sup>3</sup> and M. Janković<sup>1</sup>

<sup>1</sup>*University of Belgrade, Vinča Institute of Nuclear Sciences, Radiation and Environmental Protection Department, Belgrade, Serbia  
(natasas@vinca.rs)*

<sup>2</sup>*University of Belgrade, Faculty of Physical Chemistry, Belgrade, Serbia*

<sup>3</sup>*Institute of General and Physical Chemistry, Belgrade, Serbia*

### ABSTRACT

This paper provides findings from the study of total content of sodium (Na) macro-element in environmental water samples around five of the largest coal-fired power plants in the region. Also, pH value of these waters was examined. The concentration of Na was determined by Atomic absorption spectrometry (AAS). The obtained results for the concentration of Na were found to be in range between 8.9 and 61.6 mg/L. In general, the obtained values for Na content were below the recommended maximum permissible limit for drinking water given in the Serbian regulation on the quality of water for human use, as well as European Union (EU) directive and directive of World Health Organization (WHO).

### INTRODUCTION

Coal-fired power generation comes with a significant cost to the environment and human health. The water runoff from coal washeries carries pollution loads of metals that contaminate ground water, rivers and lakes, as well as soil during irrigation process and thus affecting flora and fauna [1].

Sodium is an essential element for all animals and some plants, but it also has a vital function in human body for the regulation of blood volume, blood pressure, osmotic equilibrium and pH. Sodium salts are used in water treatment systems to improve pH (sodium hydroxide), for the coagulation of calcium and magnesium to reduce hardness (sodium carbonate), for the addition of fluoride (sodium fluorosilicate) and the ion exchange removal of heavy metals (sodium alumino-silicate or zeolite) [2]. Because of high solubility of most sodium salts in cold water, sodium is an ideal carrier of anions for precipitation of disruptive colloids. Due to of the mentioned above, sodium has recently appeared as a potentially hazardous element and its concentration reaches levels that would be considered unsuitable for many applications.

The coal-fired power plants could be recognized as an additional source of sodium pollution and in this paper an examination of the presence of Na macro-element in the waste water samples around the coal-fired power plants in the Republic of Serbia, as well as the control of its impact on the environment is presented.

### **EXPERIMENTAL**

The sampling of landfill overflow waters, drain and river waters, groundwater as well as drinking water was performed during September and October of 2013 in five coal-fired power plants and their surrounding areas in the Republic of Serbia: "Nikola Tesla A and B" (TENT A, TENT B) - Obrenovac, "Morava" (TE MORAVA) - Svilajnac, "Kolubara" (TE KOLUBARA) - Veliki Crljeni and "Kostolac" (TE KOSTOLAC) - Kostolac. About a liter of each sample was taken to determine the Na content.

Water samples were first analyzed on pH. For pH measurement pH meter (Hanna Instruments, pH<sup>0</sup>C Tester pHep4) was used. Calibration of the instrument was carried out by 4, 7 and 10 pH standard solutions.

Before of Na content analysis, the samples are filtered through membrane filter and then acidified with 0.5 % HNO<sub>3</sub> to pH 1. Also, the preparation of the samples for determination of Na involved the addition of the certain concentration of Cs modifier. The stock solution was purchased from Fluka Analytical Sigma Aldrich (Sodium Standard). Multistandard for curve control was purchased from Merck.

The concentration of Na in collected water samples was performed using Atomic absorption spectrometer SensAA (GBC scientific equipment) in which the air-acetylene gas was used. Na content was determined by flame technique. HOLLOW CATHODE lamp (S & J Juniper & Co) was used for the determination of Na at 330.2 nm wavelength.

### **RESULTS AND DISCUSSION**

The results of Na content, as well as the pH values in the analyzed water samples are given in the Table 1.

**Table 1.** Concentration of macro-element Na and pH value of analyzed water samples

Power plant	Location	Na (mg/L)	pH
TENT A	Landfill overflow water	15.1	8.3
	Drain water at well	17.0	8.4
	Drain water between wells	19.0	8.4
	Sava river upstream	12.8	8.5
	Sava river downstream	16.7	8.5
TENT B	Landfill overflow water	17.6	8.3
	Drain water	21.3	8.0
	Sava river upstream	13.3	8.9
	Sava river downstream	14.0	8.3
TE MORAVA	Landfill overflow water	34.3	12.4
	Drain water	32.8	12.5
	Morava river upstream	20.1	8.7
	Morava river downstream	19.6	9.0
TE KOLUBARA	Landfill overflow water	57.5	7.9
	Drain water	23.0	8.4
	Turija river upstream	26.7	8.3
	Kolubara river downstream	25.9	8.3
	Drinking water	61.6	7.7
TE KOSTOLAC	Landfill overflow water	14.5	8.0
	Landfill drain water	14.8	7.9
	Drain water (Drmno)	13.7	8.1
	Drain groundwater (Ćirikovac)	8.9	5.4

As can be seen from Table 1, all water samples are alkaline (pH values are from 7.7 to 12.5), except for a single sample of drain groundwater from Ćirikovac surface mine which has pH of 5.4. According to regulation on quality and other requirements for natural mineral water, spring water and bottled drinking water, the recommended value for pH is between 6.5 and 9.5 [3]. In addition, the same range is prescribed by EU Directive [4]. The obtained results point out that three pH values were found to be outside of the recommended range, but these investigated water samples are not from water suitable for drinking. For one analyzed drinking water from TE KOLUBARA (pH is 7.7), this criterion is met and it is important.

The concentrations of Na in analyzed samples were in the range from 8.9 to 61.6 mg/L, while the median for analyzed macro-element was 18.3 mg/L. In the Serbian [3] and EU regulations [4,5], as well as directive of WHO [6], the

maximum allowed concentrations of individual elements are prescribed only for drinking waters. The recommended value of Na content by these regulations is 200 mg/L. It can be seen that regulation in Serbia is in accordance with directive of EU and WHO for maximum allowed concentration of Na. Also, the concentrations of Na in water samples analyzed in this paper are less than the above mentioned value, even though all the analyzed water samples were not suitable for drinking. Due to no considerable changes in river upstream and downstream sodium concentration, we can also conclude that coal-fired power plants do not discharge extra sodium concentration into the environment.

### CONCLUSION

Sodium has been recently recognized as a potentially hazardous element, because its concentration in rivers and soil reaches levels that would be considered unsuitable, especially for vegetation. The concentration of Na macro-element, as well as pH value in 22 water samples taken around the five coal-fired power plants in the Republic of Serbia are presented in this paper. The only one of analyzed water samples is acidic (pH 5.4), while the rest of the water samples are alkaline (pH values higher than 7.7). Landfill overflow water and drain water from TE MORAVA are extremely alkaline with pH values of 12.4 and 12.5, respectively. Accordingly, the obtained pH values for 19 from 22 analyzed waters meet the limited values according to drinking water regulations. Due to no considerable changes in river upstream and downstream sodium concentration, it can be concluded that coal-fired washeries are not water polluters. Also, the concentrations of Na in analyzed water samples are within the recommendation values by Serbian regulation (below 200 mg/L), as well as EU and WHO directives for drinking water.

### *Acknowledgement*

The authors would like to thank to the Ministry of Education, Science and Technological Development of the Republic of Serbia for material support (Grants no. III 43009, 172015, III 45014).

### REFERENCES

- [1] S.K. Guttikunda and P. Jawahar, *Atmospheric Environment*, 2014, **92**, 449-460.
- [2] M.E.R. Huguet and E. Darre, *Atomic Spectroscopy*, 2006, **27**, 80-85.
- [3] *Official Gazette of Serbia and Montenegro*, No. 53/05, 2005.
- [4] *Official Journal of the European Communities*, L 330/32, 1998.
- [5] *Official Journal of the European Union*, L 164/45, 2009.
- [6] *World Health Organization (WHO)*, 3rd ed., Vol. 1, 2008.

## USING OF THE NATURAL AND Fe(III)-MODIFIED ZEOLITE-ALGINATE BEADS FOR ADSORPTION OF LEAD IONS FROM WATER SOLUTIONS

M. Kragović, A. Daković, M. Marković, A. Petković, J. Petrović,  
J. Stojanović and J. Milojković

*Institute for technology of nuclear and other mineral raw materials,  
Franšed'Eparea 86, Belgrade, Serbia. (m.kragovic@itnms.ac.rs)*

### ABSTRACT

In this paper, adsorption of lead ions from water solutions by the natural (NZA) and Fe(III)-modified zeolite-alginate (FeA) beads was investigated. Experiments were performed for different initial concentrations and results showed improving adsorption properties of the starting materials (natural (NZ) and Fe(III)-modified zeolite (FeZ)) after modification with alginate. Also, for both adsorbents, direct relation between initial concentration and adsorbed amount of lead was observed. Much higher adsorption of lead was obtained by FeA than NZA. Results also showed that presence of alginate, beside improving adsorption properties have a positive influence on physical properties of starting samples. After immobilization of the starting samples with alginate no falling apart of the beads was noticed and there was no water turbidity.

### INTRODUCTION

Clinoptilolite is the most common natural zeolite in the nature. Due to its high crystallinity, non-toxicity, highly selective ion-exchange capacity, etc. It has found wide application and very often is used as heavy metals adsorbents. In our previous studies [1, 2] in order to improve adsorption properties of natural zeolite-clinoptilolite (NZ) for lead ions from water solutions, its surface with particle size  $\sim 43\mu\text{m}$  (NZ) was modified with Fe(III) ions under strongly basic conditions. Results showed that although NZ has high adsorption capacity for lead ( $0.32\text{mmol/dm}^3$ ) after its modification (FeZ) adsorption capacity increased to  $0.64\text{mmol/dm}^3$ . However, even NZ and especially FeZ showed good adsorption properties, their powder form and micrometric particle size may cause water turbidity and problems with separation liquid from solid and that could limit their practical use. Using materials with higher particle size for solving these problems is not the best solution due to inverse proportionality of the adsorption capacity and particle size [2]. Thus,

immobilization and using polymer molecule such as alginate for solving these problems could be better choice.

Alginate, is a polysaccharide composed of anionic blocks of 1,4-linked  $\alpha$ -L-gluronic acid (G) and  $\beta$ -D-mannuronic acid (M). It is biodegradable and non-toxic biopolymer. Also, alginate can decrease the pressure drop in the columnar operations, and the most important has high affinity for heavy metals, especially for  $Pb^{2+}$  ions [3, 4]. Thus, alginate has recently been used to improve properties of different materials and increase their chemical, mechanical stability and applicability.

In this study, adsorption of lead from water solutions by the natural and Fe(III)-modified zeolite-alginate beads was followed. The influence of initial lead concentration on adsorption properties of materials in batch mode was investigated.

## EXPERIMENTAL

The natural zeolite clinoptilolite from Zlatokop, Serbia with a particle size - 43  $\mu$ m (NZ) was used as a starting material. The mineralogical composition of the natural zeolitic tuff was primarily clinoptilolite with small amounts of quartz and feldspar determined by X-ray powder diffraction analysis (XRPD) (Figure 1a). The Fe(III)-modified zeolite (FeZ) was obtained according to procedure given elsewhere [1].

Natural zeolite-alginate (NZA) and Fe(III)-modified zeolite-alginate (FeA) composites were obtained by using a method described by Viraraghavan and Yuan [5]. Briefly, 2g of Na-alginate was dissolved in 100  $cm^3$  of distilled water and agitated for 24h at 300rpm. Then, 10g of the NZ or FeZ was blended with 100  $cm^3$  of 2% Na-alginate solution for 2h. Spherical beads were prepared by dropping the mixed solution into 0.1  $mol/dm^3$   $CaCl_2$  solution. The beads were hardened by placing them in 2% solution of  $CaCl_2$  for 24h. The remaining beads were washed by mixing with 250  $cm^3$  of distilled water and agitated at 100rpm for 30min, discarding the solution and then repeating the process 5 times. Finally, the beads were dried at room temperature to the constant weight.

Adsorption of lead by NZA and FeA was investigated by mixing 0.5g of the adsorbents with 50  $cm^3$  of aqueous solutions, containing various initial concentrations of  $Pb^{2+}$  (1.6-15  $mmol/dm^3$ ) at 25°C and initial pH 4.2. After 24h, suspensions were centrifuged and amounts of  $Pb^{2+}$  were determined on atomic absorption spectrophotometer "Analytic Jena Spekol 300".

## RESULTS AND DISCUSSION

Encapsulation of the NZ and FeZ with alginate, improved their mechanical properties. Thus, after modification, NZ and FeZ were transformed from

powder with particle size  $-43\mu\text{m}$  into 2-3 mm spherical beads form. The shape of beads remains constant in water solutions and consequently there was no water turbidity what is very important for experiments in column and application under real conditions.

The natural and Fe(III)-modified zeolite before and after encapsulation were characterized by XRPD analysis and patterns are shown in Figure 1.

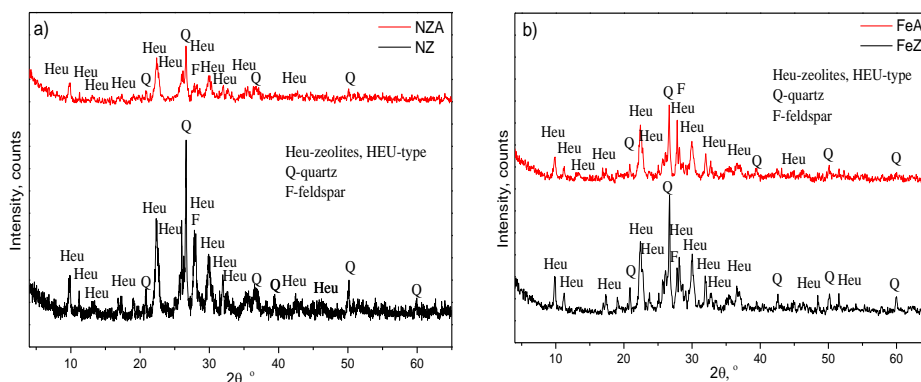


**Figure 1.** XRPD patterns of: a) NZ and NZA; b) FeZ and FeA.

As can be seen from Figure 1, Fe(III)-modified zeolite is characterized by lower crystallinity than the NZ. It seems that the FeZ maintain the main characteristic peaks of starting zeolite, but with the significantly lower intensity. However, additional Fe-oxidic or oxo-hydroxidic crystalline phases were not observed at X-ray diffractograms. In spectra of the NZA and FeA decreasing of intensities of all peaks were also obtained indicating lowering of the crystallinity of the parent samples. Also, after modification with alginate additional peaks were not observed, meaning that there are no new crystalline phases in NZA and FeA.

For practical application it is also important that applied modification has no negative effect on adsorption properties of the starting samples. From that reason removal of lead from water solutions by NZA and FeA was investigated for different initial lead concentrations and results are shown at Figure 2. As can be seen from Figure 2 for NZA as well as for FeA, adsorbed amount of lead increased with increasing its initial concentration. However, even both adsorbents were modified under same conditions, for all initial concentrations higher amount of removed lead ions was obtained for FeA. Thus, for initial concentration  $1.6\text{ mmol/dm}^3$  adsorbed amounts of lead ions were  $0.15\text{ mmol/dm}^3$  for NZA and  $0.17\text{ mmol/dm}^3$  for FeA, while for initial concentration of  $15.1\text{ mmol/dm}^3$  adsorbed amounts were  $0.50$  and  $0.66\text{ mmol/dm}^3$  for NZA and FeA, respectively. Since both adsorbents were treated with the same amount of alginate, obtained differences in adsorption

properties indicated that beside alginate, adsorption of lead also occurred on active centers on NZ in NZA and FeZ in FeA. Comparing the results obtained in this study for NZA and FeA with those for NZ and FeZ (0.32 and 0.64 mmol/dm<sup>3</sup>, respectively) [1] showed that encapsulation with Na-alginate has positive influence on removal of lead ions from water solutions by both, NZ and FeZ.

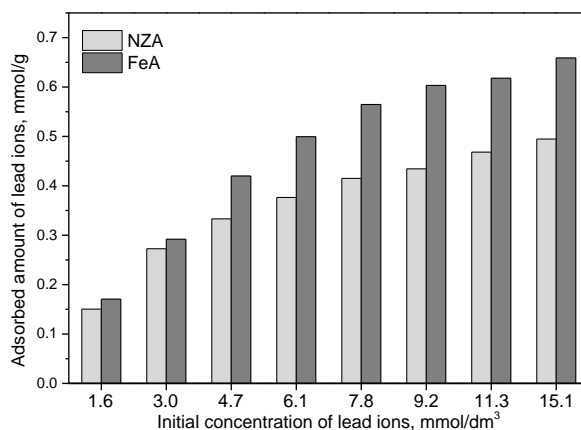


**Figure 2.** Adsorption of lead by NZA and FeA for different initial concentrations

## CONCLUSION

From presented results it can be concluded that modification of the NZ or FeZ with Na-alginate improved adsorption properties of the starting materials. For both samples, adsorbed amount of lead increased with increasing its initial concentration in solution. For all initial concentration adsorbed amount of lead by FeA was higher than by NZA.

## Acknowledgement

We are thankful to the Ministry of Education, Science and Technological Development of the Republic of Serbia, which has been financing projects TR34013 and ON172018 a part of which is presented in this paper.

## REFERENCES

- [1] M. Kragović, A. Daković, Ž. Sekulić, M. Trgo, M. Ugrina, J. Perić, G. Diego Gatta, *Appl. Surf. Sci.* 2012, **258**, 3667–3673.
- [2] M. Kragović, A. Daković, M. Marković, J. Krstić, G.D. Gatta, N. Rotiroti, *Appl. Surf. Sci.* 2013, **283**, 764–774.
- [3] R. Cheraghali, H. Tavakoli, H. Sepehrian, *Sci. Iran.* 2013, **20**, 1028-1034.
- [4] F. Wang, X. Lu, X. Li, *J. Hazard. Mater.* 2016, **306**, 75-83.
- [5] G. Yan, T. Viraraghavan, *Bioresour. Technol.* 2001, **78**, 243–249.

## VARIATIONS IN LARCH TREE-RINGS METAL CONCENTRATIONS OF FOUR FORESTRY LOCATIONS

I. R. Milošević<sup>1</sup>, D.M. Marković<sup>2</sup>, D. Manojlović<sup>3</sup> and G. Roglić<sup>3</sup>

<sup>1</sup> *University of Belgrade, Institute of Physics, Pregrevica 118, 11070 Belgrade, Serbia. (novovic@ipb.ac.rs)*

<sup>2</sup> *Singidunum University, The Faculty of Applied Ecology, Požeška 83a, 11030 Belgrade, Serbia.*

<sup>3</sup> *University of Belgrade, Faculty of Chemistry, Studentski trg 12-16, 11000 Belgrade, Serbia.*

### ABSTRACT

Cd, Fe, Mn, Pb, Sr and Zn were measured in larch (*Larix europaea* Lam.) tree-rings and corresponding soil samples collected at four forestry sites to investigate the variations in their concentrations from 1980. Concentrations were generally lowest at background sites. Elemental concentrations in soil samples were substantially higher than those measured in tree-rings. Among investigated elements the highest tree-ring concentration were measured for Mn while the Cd had the lowest concentration. The highest average tree-ring concentrations for Cd, Fe, Mn, Pb and Zn can be seen at the Avala location.

### INTRODUCTION

The occurrence of trace elements in the environment is of particular concern due their environmental persistence, biogeochemical recycling and adverse effects. Several trace elements currently found in the environment are originated from anthropogenic impacts [1]. It has long been recognized that the tree-ring archive can capture changes in the chemical environment related to atmospheric chemistry, biogeochemical cycling and climate influences. Choosing tree-rings as potential bioindicators was due to trees large geographic distribution, long living and the fact that each year tree forms a new tree-ring that can be easily dated. Dendrochemistry relies on the basic assumption that the pollutant content of tree-rings reflects to some degree the chemical signal from the environment during the year of ring formation [2].

### EXPERIMENTAL

The field studies were conducted in the three woodland locations in Serbia and one in Montenegro. Tree-rings of larch (*Larix europaea* Lam.) were collected together with corresponding soil (0-20 cm in depth). The first location is Avala (AA), a mountain located 16 km south-east of Belgrade. The Belgrade-Niš

highway, Kruni put and regional road to Mladenovac runs east, north and west from the mountain. The second location is REIK Kolubara (AK). Larch at the Kolubara location has been applied for the rehabilitation by afforestation of the mechanically damaged land. Background locations were management unit Donji Pek in Kučevo (AKC) and village Trepča in Andrijevica municipality in the north-east part of Montenegro (ACG).

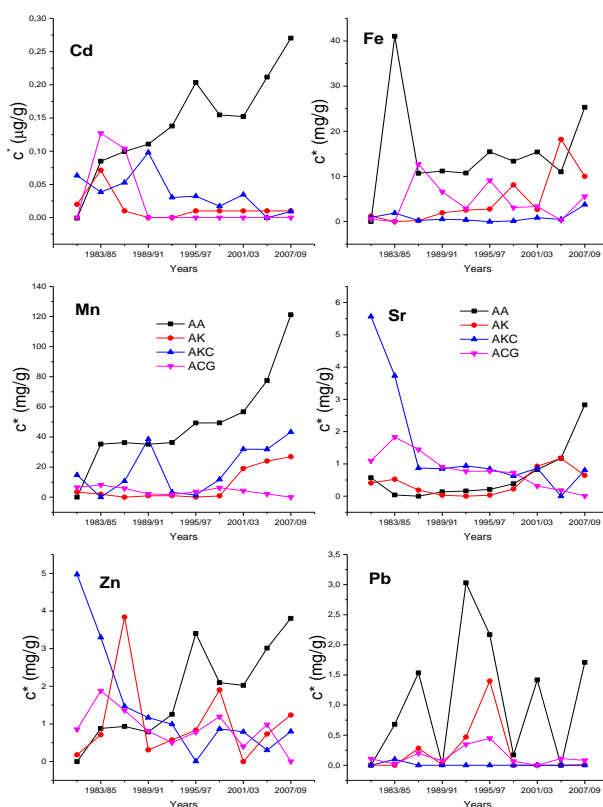


**Figure 1.** Mean Cd, Fe, Mn, Sr, Zn and Pb concentrations,  $c^*$  ( $\mu\text{g/g}$ ), in larch tree-rings at four forestry locations

At each site three larch trees of similar size were selected and their stem disks were taken at breast height (1.3 m). For further analysis the disks were cut into 3 year segments starting from 1980 with a stainless steel knife. Inductively coupled plasma atomic emission spectrometry (ICP-OES) was used to determine element content in solution samples. ICP-OES measurement was performed using Thermo Scientific iCAP 6500 Duo ICP spectrometer equipped with CID86 detector, standard glass concentric type nebulizer, quartz torch, and alumina injector and purged with argon. The digestion of tree-rings was performed on an Advanced Microwave Digestion System ETHOS 1, using HPR-1000/10S high pressure segmented rotor. In the digestion, about 0.5 g of powdered tree-ring sample precisely weighed was mixed in each clean vessel with a mixture of 3 ml  $\text{H}_2\text{SO}_4$  and 5 ml  $\text{HNO}_3$  for tree-ring sample and then heated with microwave energy for 30 min. After cooling and without filtration, the solution was diluted to a fixed volume of 25 ml. The sequential extraction using the Tessier procedure [3] was used for the

examination of soil samples. The method involves five fractions (exchangeable, carbonate, Fe/Mn oxides, organic and residual), in which the mobility and bioavailability of elements decrease with increasing extraction phase. The extraction was carried out progressively based on an initial amount of about 1.0 g of soil, accurately weighed. The first three fractions form “mobile content”, i.e. the part of the total concentration which under certain conditions can be mobilized and thus enter biogeochemical cycles. Soil pH was measured as follows: 5.0 g of soil was precisely weighed and 5ml of 1M KCl added. The suspension was then subjected to continuous agitation for 10 min and left to stand before pH was determined.

## RESULTS AND DISCUSSION

Element concentrations measured in tree-rings and soil are summarized in Figure 1 and Table 1. The variation in tree-ring concentrations due to different local conditions (the variation of the background levels) was minimize by subtracting the minimum value from the actual concentration. Element tree-ring concentrations,  $c^*$ , shown in Figure 1 do not refer to actual concentration in wood, but to the level of this content relative to the lowest level recorded for that tree. Subtracting the minimum value from the actual concentration reduces

**Table 1.** Average concentrations in larch tree-rings, mobile and total content in soil as well as pH values at four forestry locations.

Locations		AA	AK	AKC	ACG
Cd	Tree-ring	0.14	0.02	0.04	0.02
	Mobile content	0.36	<0.10	<0.10	<0.10
	Total content	0.46	0.23	0.94	0.90
Fe	Tree-ring	15.42	4.77	0.92	4.42
	Mobile content	1243	496	12409	10117
	Total content	8176	6723	66835	54436
Mn	Tree-ring	49.73	7.83	18.74	4.06
	Mobile content	603	141	1246	1607
	Total content	662	191	1949	1897
Pb	Tree-ring	1.07	0.22	0.01	0.15
	Mobile content	7.21	5.55	33.76	38.06
	Total content	16.50	13.04	51.14	55.53
Sr	Tree-ring	0.63	0.41	1.51	0.80
	Mobile content	15.59	7.33	16.38	30.00
	Total content	18.90	10.04	52.93	46.75
Zn	Tree-ring	1.82	1.03	1.47	0.88
	Mobile content	11.30	3.97	45.54	30.71
	Total content	33.35	23.08	147.58	151.11
pH		5.80	6.00	4.50	5.30

differences between trees that are due to different local conditions, and concentrate on the trends over time. From Figure 1 it can be seen that concentrations were generally lowest at background sites. The highest average tree-ring concentrations for Cd, Fe, Mn, Pb and Zn (Table 1) can be seen at the Avala location. Among investigated elements the highest tree-ring concentration were measured for Mn while the Cd had the lowest concentration. Highest Pb concentration fluctuations in tree-rings can be seen at the Avala location. Similar Pb fluctuations were observed in our investigation in linden tree-rings [4]. Expected trends in tree-ring concentrations for the majority of trace elements is that on locations where anthropogenic influence is low there is no trend [5-6]. At the Avala location growing trend of Cd, Mn, Zn and Sr was observed while at other locations, depending of the element, the weaker trend or a decline in the concentration can be seen. Elemental concentrations in soil samples (Table 1) were substantially higher than those measured in tree-rings. This could be attributed to the relatively longer exposure of the soil to the atmospheric pollutants. Soil act as final sink for the elements deposited from air and also transferred by falling needles. Mobile content, relative to the total content, is for the majority of investigated elements highest at the Avala location.

## CONCLUSION

At the Avala location during the last 12 years (1998-2009) the increase of Cd, Fe, Mn, Sr and Zn in larch tree-rings, relative to the entire period of study, expressed in percentage is 30%, 4%, 43%, 85% i 40%. At this location the highest fluctuations in Pb concentration can be seen, the highest average Pb tree-ring concentrations, as well as decrease in Pb concentration for 18%. Traffic activity at this site appears to be the main reason. Other investigated location has lower tree-ring trace element concentrations.

## *Acknowledgement*

This work was partially supported by the Ministry of Education and Science of the Republic of Serbia (Grants no. III 43007 and OI 171005).

## REFERENCES

- [1] G. Blackmore, *Science of the Total Environment*, 1998, **214**, 21-48.
- [2] H.C. MacDonald, C.P. Laroque, D. E. B. Fleming, M. R. Gherase, *Dendrochronologia*, 2011, **29**, 9-15.
- [3] A. Tessier, P.G.C. Campbell, M. Bisson, *Analytical Chemistry*, 1979, **51**, 844-851.
- [4] D.M. Marković, I.R. Milošević, D. Vilotić, 2013, *Environmental Science and Pollution Research*, **20**, 136-145.
- [5] S.A. Watmough, 1999, *Environmental Pollution*, **106**, 391-403.
- [6] C. Liang, H. Huang, 1992, *Trees*, **6**, 103-108.

## ASSESSMENT OF HEAVY METAL CONTENT IN SOILS OF SOME URBAN AND RURAL ENVIRONMENTS IN SERBIA

M. Ćujić, J. Petrović, Lj. Janković Mandić and S. Dragović

*University of Belgrade, Vinča Institute of Nuclear Sciences,  
Belgrade, Serbia (cujicm@vinca.rs)*

### ABSTRACT

This study deals with the assessment of heavy metals contents in soil of Serbia in urban and rural environment. Analysed heavy metals (Cd, Co, Cr, Cu, Mn, Ni, Pb, Zn) were determined using an atomic absorption spectrometry. Concentrations of Co, Cu, Ni and Zn at some sampling sites of urban environment exceeded the limit values, which are still far from the remediation values established by Legislation of the Republic of Serbia.

### INTRODUCTION

The soil is the main repository of heavy metals in terrestrial ecosystems. These metals reach the soil environment through both pedogenic and anthropogenic processes. The major sources of heavy metals enrichment in soils are anthropogenic activities, associated with industrial processes. The spatial distribution and source identification of heavy metals in soil is important in order to reveal the areas of pollution and assess the potential sources. Health authorities in many parts of the world are becoming increasingly concerned about the effects of heavy metals on environmental and human health. Different statistical tools, such as correlation analysis (principal component analysis, cluster analysis) and geostatistical analysis (GIS-based spatial mapping) are applied in environmental studies to highlight pollutant sources and to study spatial distribution patterns [1-4]. In this study heavy metals contents in soils of Serbia were assessed in the three urban areas: surroundings of the coal fired power plant (CFPP) in Obrenovac, Belgrade; surroundings of the steel production facility (CPF) in Smederevo; the city zone of Subotica; and a rural area of Pčinja and South Morava River Basin, southeastern Serbia.

### EXPERIMENTAL

Soil samples were collected up to 10 cm depth. Applying the 'systematic random sampling' procedure, a total of 60 samples were collected, 15 from each investigated area [5]. Soil samples for metal content determination were

digested according to USEPA procedure [6]. Total metal content (Cd, Co, Cr, Cu, Mn, Ni, Pb, Zn) was determined by using atomic absorption spectrometer Shimadzu AA7000. Standards used in the analysis were AccuStandard solutions obtained from Carlo Erba Reagenti. The quality assurance checks were performed using the certified reference material SRM 2711 (National Institute of Standards and Technology). The overall uncertainty of the analytical procedure was below 10%.

## RESULTS AND DISCUSSION

The concentrations of analysed heavy metals were summarized in Table 1. Concentrations of Cd, Co, Cr, Cu, Mn, Ni, Pb and Zn at some sampling sites were higher than the concentrations for uncontaminated European soils, i.e.  $0.145 \text{ mg kg}^{-1}$ ,  $7.78 \text{ mg kg}^{-1}$ ,  $60 \text{ mg kg}^{-1}$ ,  $13 \text{ mg kg}^{-1}$ ,  $650 \text{ mg kg}^{-1}$ ,  $18 \text{ mg kg}^{-1}$ ,  $22.6 \text{ mg kg}^{-1}$  and  $52 \text{ mg kg}^{-1}$  for these elements, respectively [7]. Concentrations of Co, Cu, Ni and Zn at some sampling sites exceeded the limits values ( $9 \text{ mg kg}^{-1}$  for Co,  $36 \text{ mg kg}^{-1}$  for Cu,  $35 \text{ mg kg}^{-1}$  for Ni and  $140 \text{ mg kg}^{-1}$  for Zn) established by Serbian regulations for land use [8]. Detailed explanation about elevated concentrations around CFPP and CFP could be found elsewhere [1, 3]. In the investigated areas of this study, only the average values of Co slightly exceeded the limit values of  $9 \text{ mg kg}^{-1}$ , which is far from the remediation value of  $240 \text{ mg kg}^{-1}$  [8]. At four and at two sites in Smederevo and Subotica, respectively, elevated concentrations for Cu, higher than limit value of  $36 \text{ mg kg}^{-1}$  were determined. At one location in Subotica extremely high value for Cu of  $3660 \text{ mg kg}^{-1}$ , greater from the remediation value of  $190 \text{ mg kg}^{-1}$  was determined and this value was excluded from statistical analysis presented in Table 1. Further analysis is required in order to distinguish pollution source of Cu in this site. Increased concentrations of investigated heavy metals in urban areas of this study are associated with pollution sources. The highest average value for Mn was revealed in rural area in southeastern Serbia. It could be associated with its natural origin, but detailed geochemical analysis is needed to confirm this finding. In area surrounding CFPP elevated concentrations of Mn at some sampling locations were attributed to its leaching during and after transport of the coal ash. Elevated concentrations for Ni in Belgrade and Smederevo are both natural and anthropogenic local sources of contamination. There is still no need for remediation actions on these sites, as values are lower than  $210 \text{ mg kg}^{-1}$  for Ni [8]. At two locations in each urban areas of Serbia investigated here, the values higher than limit value of  $140 \text{ mg kg}^{-1}$  for Zn were determined, but these values are still far from the remediation value of  $720 \text{ mg kg}^{-1}$  [8].

**Table 1.** Average (min-max) values of heavy metal concentrations in analyzed soils( $\text{mg kg}^{-1}$ ).

Element	Study areas of Serbia			
	Belgrade	Smederevo	Subotica	Southeastern Serbia
Cd	0.26 (0.04-1.05)	3.33 (2.31-4.61)	1.10 (0.38-5.95)	0.17 (0.10-0.25)
Co	10.5 (6.2-13.4)	28.2 (13.9-41.3)	13.9 (5.5-19.1)	9.5 (3.8-13.8)
Cr	29.7 (11.7-45.4)	55.7 (34.1-97.9)	21.5 (12.5-40.4)	25.6 (10.7-41.2)
Cu	19.3 (12.4-26.9)	39.1 (13.3-148.4)	29.6 (1.4-61.4)	19.3 (12.4-26.9)
Mn	620 (195-1270)	730 (400-860)	400 (340-530)	830 (360-1050)
Ni	62.6 (24.3-106)	78.2 (47.4-148)	23.5 (7.7-64.8)	15.9 (6.7-26.1)
Pb	26.4 (17.4-70.2)	33.0 (20.2-64.6)	52.8 (17.4-81.1)	14.1 (7.1-20.8)
Zn	89.2 (48.5-207)	98.9 (71.2-152)	30.5 (3.9-170)	48.6 (28.8-70.1)

Applying geostatistical analysis based on ordinary kriging method Ćujić et al. (2016) and Dragović et al. (2014) found the highest concentrations of heavy metals at sites in predominant wind directions in areas surrounding CFPP in Obrenovac and SPF in Smederevo. The distribution of heavy metals in soils around the point source (e.g. CFPP, CFP) is highly needed for the assessment of perturbations of geochemical cycles of heavy metals in the environment and their effects on environmental and human health as well as for development of appropriate remediation strategies.

## CONCLUSION

This study was performed in order to assess environmental consequence of anthropogenic activities in urban and rural areas in Serbia, with regard of heavy metals in soil. The assessment study revealed some hot spots for: Cd, Co, Mn and Ni in the study area of Belgrade, as a consequence of CFPP

operation; Cd, Co, Cu Ni, Pb and Zn in the study area of Smederevo, as a consequence of SPF operation; Cu and Pb in Subotica, as a consequence of traffic. In general, operations of CFPP and SPF have no significant negative impact on the surrounding environment with regard to the content of investigated heavy metals. In the rural area of southeastern Serbia anthropogenic activities were not significant in the terms of heavy metals in soil; the higher Mn concentrations could be attributed to natural sources.

### ***Acknowledgement***

This work was supported by the Ministry of Education, Science and Technological Development of the Republic of Serbia (Project no. III43009).

### **REFERENCES**

- [1] M. Čujić, S. Dragović, M. Đorđević, R. Dragović, B. Gajić, *Catena* 2016, **139**, 44-52.
- [2] S. Dragović, B. Gajić, R. Dragović, L. Janković-Mandić, L. Slavković-Beškoski, N. Mihailović, M. Momčilović, M. Čujić, *J. Environ. Monit.*, 2012, **14**, 127-137.
- [3] R. Dragović, B. Gajić, S. Dragović, M. Đorđević, M. Đorđević, N. Mihailović, A. Onjia, *J.Clean Prod.*, 2014, **84**, 550-562.
- [4] A. Chandrasekaran, R. Ravisankar, N. Harikrishnan, K.K. Satapathy, M.V.R. Prasad, K.V. Kanagasabapathy, *Spectrochim. ActaA Mol. Biomol. Spectrosc.*, 2015, **137**, 589-600.
- [5] IAEA (International Atomic Energy Agency) *Soil Sampling for Environmental Contaminants*, IAEA-TECDOC-1415, Vienna, 2004.
- [6] USEPA (United States Environmental Protection Agency) *Method 3050B: Acid Digestion of Sediments, Sludges, and Soils. (Revision 2)*1996.
- [7] R. Salminen, M.J. Batista, M. Bidovec, A. Demetriades, B. De Vivo, W. De Vos, et.al., *Geochemical Atlas of Europe. Part 1. Background information, Methodology and Maps*, Geological Survey of Finland, Espoo, 2005.
- [8] Official Gazette of the Republic of Serbia, 88/2010.

## RELATIONSHIP BETWEEN ISOPRENE, RELATED GASEOUS POLLUTANTS AND METEOROLOGICAL FACTORS IN AN URBAN AREA

S. Stanišić Stojić<sup>1</sup>, A. Stojić<sup>2</sup> and M. Perišić<sup>2</sup>

<sup>1</sup>*Singidunum University, 32 Danijelova St., 11010 Belgrade, Serbia.  
(sstanisic@singidunum.ac.rs)*

<sup>2</sup>*Institute of Physics Belgrade, University of Belgrade, 118 Pregrevica St.,  
11080 Belgrade, Serbia.*

### ABSTRACT

In this paper we used multivariate regression methods to examine the relationships between isoprene, related volatile organic compounds (VOC), inorganic gaseous pollutants (NO<sub>x</sub>, NO, NO<sub>2</sub>, SO<sub>2</sub> and CO), PM<sub>10</sub> and meteorological data. The concentrations of 36 VOC-related masses were measured in Belgrade urban area during a two-month campaign by the use of a proton transfer reaction mass spectrometer. The results have shown that isoprene exhibited significant associations with several volatile species, including propyne, 1,3-butadiene, isoprene oxidation products, hexenal and monoterpene fragments, styrene, ethylbenzene and xylenes. Conversely, the associations between meteorological factors and inorganic gaseous pollutants with isoprene variations were estimated as less significant.

### INTRODUCTION

Isoprene, as a globally dominant biogenic VOC, is mostly emitted by deciduous vegetation, while in urban areas it can also originate from anthropogenic sources. Known for its high reactivity, isoprene can undergo either photolysis or oxidation by ozone, OH and NO<sub>3</sub> radicals, with a number of resulting degradation products, oxidant species and intermediates, e.g. organic peroxy radicals and secondary organic aerosols, which can affect atmospheric radical chemistry and the oxidizing capacity of the atmosphere. Previous findings have shown that the first-generation photochemical products are more toxic than isoprene itself [1].

### EXPERIMENTAL

The concentrations of 36 VOC-related protonated masses (m) were measured in real time using a proton transfer reaction mass spectrometer (Standard PTR-quad-MS, Ionicon Analytik, GmbH, Austria). Additionally, the concentrations of inorganic gases (IG) including NO<sub>x</sub>, NO, NO<sub>2</sub>, SO<sub>2</sub> and CO,

PM<sub>10</sub>, and meteorological data were obtained from the standard automatic monitoring station of the Institute of Public Health Belgrade. The measurements were conducted in Belgrade urban area in the period from January 23<sup>rd</sup> to March 24<sup>th</sup> 2014 as described in Stojić et al., 2015 [2]. In order to investigate the relationships between isoprene, related gaseous pollutant species and meteorological data, three regression MVA methods including Linear Regression method (LR), Multilayer Perceptron (MLP) and Support vector machine (SMO SVM), implemented in Weka [3], were applied.

## RESULTS AND DISCUSSION

According to the results, high correlation coefficients ( $r > 0.8$ ) were calculated between isoprene and several volatile species, including propyne, 1,3-butadiene, isoprene oxidation products, hexenal and monoterpene fragments, styrene, ethylbenzene and xylenes, registered at m 41, 55, 71, 81, 105 and 107, respectively (Figure 1). Conversely, correlation coefficients between meteorological data and isoprene were in the range from 0.19 to 0.30, thus suggesting that meteorology plays a relatively small role in spatio-temporal distribution of isoprene in the urban environment, which could be explained by its high reactivity.

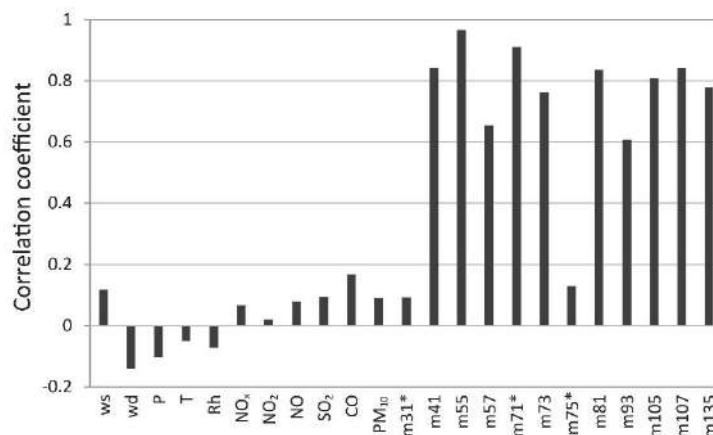


**Figure 1.** Correlation coefficients ( $r$ ) between isoprene and meteorological parameters, inorganic gaseous pollutants, PM<sub>10</sub>, potential isoprene oxidation products (\*) and highly correlated VOC ( $r > 0.6$ ).

Regression analysis performed on isoprene and highly correlated VOC concentrations resulted in the relative errors ranging from 9.9 to 12.8%, whereas the correlation coefficients between the modelled and observed isoprene levels were in the range from 0.97 to 0.99 for all three applied methods (Table 1). Furthermore, three species alone, including 1,3-butadiene,

isoprene oxidation product at m71 and styrene, explained the concentrations of isoprene with the relative error ranging between 11.5 and 13.8%.

Vehicular exhaust is often the single most dominant source of anthropogenic isoprene and 1,3-butadiene. Previous studies have shown that the regression analysis with 1,3-butadiene gives the greatest estimation of the anthropogenic fraction of isoprene [4]. In addition to their known traffic-related origin, styrene, 1,3-butadiene and isoprene are used in rubber and polymer industry, and thus, another potential source is one of the leading producers of petrochemical feedstock, plastic and rubber polymers in the region, located in the industrial zone about 13 km from the measurement site.

**Table 1.** MVA method performance for highly correlated VOC, meteorological parameters (Meteo) and inorganic gaseous pollutants (IG) used as inputs.

Method	VOC		VOC+Meteo		VOC+Meteo+IG	
	Rel. error	Corr.	Rel. error	Corr.	Rel. error	Corr.
LR	12.84	0.98	9.54	0.99	9.51	0.99
SMO	11.52	0.97	8.80	0.98	8.79	0.99
MLP	9.91	0.99	7.16	0.99	6.94	0.99

As regards isoprene oxidation products at m71, the OH-initiated oxidation is complicated by the fact that OH radical may attach to isoprene at four different positions, resulting in peroxy radical isomers that further undergo atmospheric reactions and produce methyl vinyl ketone (MVK), methacrolein (MACR), both registered at m71, and 3-methylfuran [5]. Conversely, the reactions with ozone are of secondary importance for isoprene oxidation, with major products including MVK, MACR and formaldehyde, whereas the reactions between isoprene and NO<sub>3</sub> radicals are least understood and their occurrence is mostly expected at night.

Inclusion of meteorological data in the analysis resulted in a decrease in the relative error of only 3%, whereas accounting for IG and second-generation photooxidation isoprene product, hydroxyacetone registered at m 75, led to an increase in the relative error. Based on the results of LR and SMO, only CO was associated with isoprene. In compliance with this, previous studies aimed at investigating the importance of hydrocarbons for CO tropospheric distribution, have shown that oxidation of isoprene only contributes with 10% to the global tropospheric CO burden [6].

The best performing method used highly correlated VOC, IG and meteorological data and provided relative error of 6.94% (MLP), with the correlation coefficient of 0.99% (Figure 2).

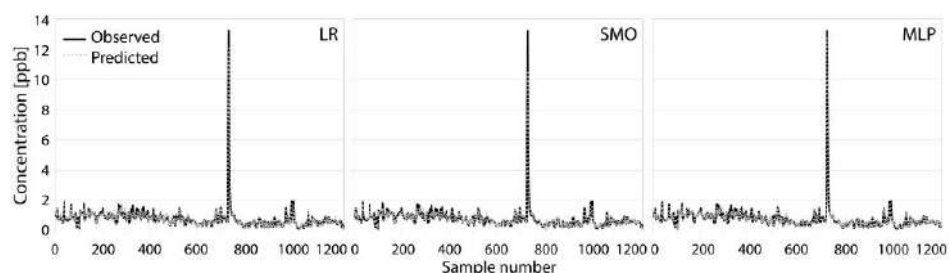


**Figure 2.** Best performing MVA regression based on highly correlated VOC, inorganic gaseous pollutants and meteorological parameters as inputs.

## CONCLUSION

Volatile organic compounds are known for their detrimental effects on human health and the environment, although the factors and complex atmospheric reactions that affect their spatio-temporal distribution are still the matter of scientific research. According to the results, isoprene exhibited strong associations with several volatile species, while its associations with meteorological factors and inorganic gaseous pollutants were estimated as less significant.

## Acknowledgement

This paper was realized as part of projects No III43007 and III41011, which were financed by the Ministry of Education, Science and Technological Development of the Republic of Serbia for the period 2011-2016.

## REFERENCES

- [1] M. Doyle, K. G. Sexton, H. Jeffries, K. Bridge, I. Jaspers, *Environ health persp.*, 2004, 1488-1495.
- [2] A. Stojić, S. Stanišić Stojić, A. Šošarić, L. Ilić, Z. Mijić, S. Rajšić, *Environ Sci Poll Res.*, 2015, **22**(17), 13137-13152.
- [3] M. Hall, E. Frank, G. Holmes, B. Pfahringer, P. Reutemann, I. H. Witten, (2009). *SIGKDD Explor.*, 2009, **11**(1), 10-18.
- [4] J. L. Wang, C. Chew, C. Y. Chang, W. C. Liao, S. C. C. Lung, W. N. Chen, P. J. Lee, P. H. Lin, C. C. Chang, *Atmos Environ.*, 2013, **79**, 369-379.
- [5] P. Warneck, *Chemistry of the natural atmosphere*, 1999, Academic press. K. M. Spencer, M. R. Beaver, J. M. St Clair, J. D. Crouse, F. Paulot, P. O. Wennberg, *Atmos Chem Phys Discuss.*, 2011, **11**, 23619-23653.
- [6] C. Granier, G. Pétron, J. F. Müller, G. Brasseur, *Atmos. Environ.*, 2000, **34**(29), 5255-5270.

## ADSORPTION OF COPPER INTO SULFONATED LAGENARIA VULGARIS SHELL – PRELIMINARY STUDY

M. N. Stanković<sup>1</sup>, N. S. Krstić<sup>1</sup>, V. D. Dimitrijević<sup>1</sup>, R. S. Nikolić<sup>1</sup>  
and A. Lj. Bojić<sup>1</sup>

<sup>1</sup>*University of Niš, Faculty of Sciences and Mathematics, Department of  
Chemistry, Višegradska 33, 18000 Niš, Serbia.  
(vladimir15041987@gmail.com)*

### ABSTRACT

Lagenaria vulgaris shell represents a lignocellulosic material with ability for binding metal cations due to hydroxyl, carboxylic, lactonic and phenolic groups present in its structure. Oxidation and successive sulfonation was used to introduce greater amount of sulphonic groups, characterized by significant ion-exchanging capacity. The efficiency of biosorbent based on chemically modified Lagenaria vulgaris shell for Cu(II) ion removal from aqueous solution was studied in batch conditions on various initial pHs. Results showed that removal efficiency (95%) did not change in pH range from 2.0 to 5.0.

### INTRODUCTION

The cellulose is the most abundant polysaccharide on the earth. It is the main structural component of plants and seaweed cell walls and, therefore, is mainly obtained from forest, agricultural, industrial, and animal waste. The biomass which is obtained from all these sources has three main components: cellulose, hemicellulose, and lignin, which content highly depending on the obtained source [1]. Despite, the cellulose has lot of hydroxyl groups which can complex with metal ions, it has no good adsorption properties. Chemical modifications on cellulosic material surfaces introducing reactive agents improve its ability to adsorb contaminants from aqueous medium.

The oxidation of cellulose by sodium periodate followed by the sulfonation reaction is well known procedure for improving the dry and wet tensile strength and water absorbency and solubility properties of cellulose [2-4]. Nowadays, this procedure was, also, used for improving the adsorption of heavy metals from water solutions [5]. Our attempts with paper pulp showed that this material is not practical because it is difficult to remove swelled cellulose from water. On the other hand, oxidized and successive sulfonated cotton fibers could not reach significant adsorption capacity for

copper ions. Therefore, we used ligno-cellulosic material as shell of *Lagenaria vulgaris* as starting material.

### EXPERIMENTAL

The *Lagenaria vulgaris* fruit used in this study was harvested in vicinity of Leskovac, Serbia, where it grows in controlled conditions without using of fertilizers. The fruit sample was washed with deionized water, air-dried on sunlight cut into 5 cm pieces and ground using a crusher mill (Waring 8010 ES, Germany). Then it was dried at 55 °C for 24 h and then sieved to fractionize particles sizes ranging from 0.8-1.25 mm using successive sieving. The native biomass (ligno-cellulosic substrate) was oxidized by soaking 3.00 g biomass in 200 mL solution of NaIO<sub>4</sub> (16.4 mmol) in the absence of light. Periodate ions react with the cellulose without destroying its fibrous nature and result primarily in the conversion of cellulose C2 and C3 secondary hydroxyl groups to dialdehyde groups [6,7]. The suspension was heated at 55°C, because at temperatures below 20°C the reaction proceeds too slowly, and at temperatures greater than 55 °C periodate decomposes and reaction is too fast causing non-uniformity of the product [8]. In order to enhance dialdehyde content different reaction time (3h, 5h, and 24h) was used. Sulfonation was carried out by adding the dialdehyde intermediate to 0.1M sodium bisulfite solution and stirred during 72h at room temperature. After filtration, this material was washed with deionized water until the pH reached a constant value close to neutrality and dried at 30°C.

The adsorption experiments were conducted in 250 mL Erlenmeyer flasks, containing 125 mL of 50.0 mg L<sup>-1</sup> Cu(II) model solution during 120 min. All experiments were conducted at ambient temperature (20±0.5°C), at varying pH. Aliquots of solutions (4.0 mL) were withdrawn at preset time intervals, filtrated and the filtrates were analyzed for Cu(II) by AAS. All the experiments were carried out in duplicates and the average values were used for further calculations.

The removal efficiency at time  $t$ , RE (%), was obtained as follows:

$$RE = (C_0 - C_t) / C_0 * 100\%$$

where  $C_0$  and  $C_t$  (mg dm<sup>-3</sup>) are the liquid-phase concentrations of Cu(II) ions at initial and any time  $t$ , respectively.

### RESULTS AND DISCUSSION

The first aim of this study was to find out the optimal time of the oxidation reaction. Three systems were performed under the same conditions but varying reaction time (3h, 5h, and 24h). After filtration, the material was washed with deionized water to remove the spent oxidant and freeze-dried providing a yield of 96-98%. The dialdehyde content was determined using

alkaline dissolving technique which is consistent with the redox reaction named after Cannizzaro [9,10]. It was observed that oxidation during 5h yield material with the highest dialdehyde content (80%, 36%, and 32% for treatment during 5h, 24h and 3h, respectively), which means that material was more active for further modification, in this case, sulfonation.

Within the adsorption experiments, focus was on studying the influence of solution pH on removal of copper(II) ions from aqueous medium. In that order, we investigated removal efficiency of sulfonated *Lagenaria vulgaris* shell in pH range of 1.0-5.0 (Fig. 1). It could be assumed that at lower pH, sulfonic groups would be protonated, and competition of  $H^+$  ions are significant which would result in bad Cu(II) ions adsorption. But, in this case, removal efficiency was up to 95% at pH 5.0 and did not change even at pH 2.0. Considerably fall in removal efficiency was observed at pH 1.5 (75%), while at pH 1.0 it reached 23%.

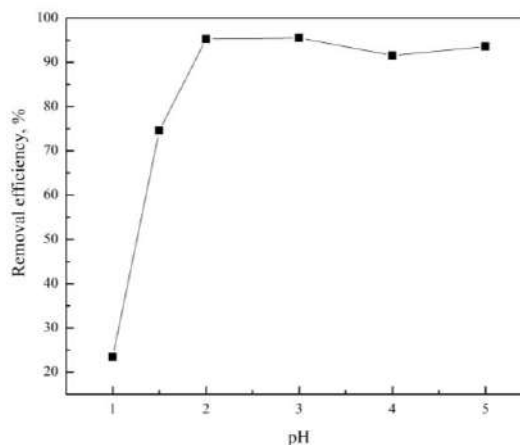


**Figure 1.** Effect of pH on removal efficiency of sulfonated *Lagenaria vulgaris* shell (Cu(II) conc.  $50.0 \text{ mg L}^{-1}$ , biosorbent dose  $4.0 \text{ g L}^{-1}$ , temp.  $20 \pm 0.5^\circ\text{C}$ ,

## CONCLUSION

The chemical modification (oxidation and successive sulfonation) of *Lagenaria vulgaris* shell is very important for the application in the removal of copper ions and other contaminants from aqueous solutions, because materials prove new chemical properties that are more favorable than the starting materials. These new properties improve the interactions between the modified material and copper ions during adsorption processes in aqueous solutions. Results showed that solution pH does not strongly influence on these interactions. Therefore, the sulfonated *Lagenaria vulgaris* shell is promising for application in removing copper ions from natural waters and industrial waste waters.

**Acknowledgement**

This work was supported by the Ministry for Education, Science and Technology Development of the Republic of Serbia (Grant no. TR34008).

**REFERENCES**

- [1] R. D. S. Bezerra, P. R. S. Teixeira, A. S. N. M. Teixeira, C. Eiras, J. A. Osajima and E. C. Silva Filho in: Cellulose - Fundamental Aspects and Current Trends, M. Poletto, H. L. Ornaghi Jr. (Eds.), InTech, Rijeka, 2015.
- [2] R. T. Shet, P. R. R. Wallajapet, Manufacture of sulfonated cellulose with improved absorbent properties, US 5703225, 1997.
- [3] J. Zhang, N. Jiang, Z. Dang, T. J. Elder, A. J. Ragauskas, Cellulose, 2008, **15**, 489–496.
- [4] D. Rajalaxmi, N. Jiang, G. Leslie, A. J. Ragauskas, Carbohydrate Research, 2010, **345**(2), 284-290.
- [5] T. Suopajarvi, Liimatainen, M. Karjalainen, H. Upola, J. Niinimaki, Journal of Water Process and Engineering, 2015, **5**, 136–142.
- [6] U.-J. Kim, S. Kuga, M. Wada, T. Okano, T. Kondo, Biomacromolecules, 2000, **1**(3), 488–492.
- [7] U.-J. Kim, M. Wada, S. Kuga, Carbohydrate Polymers, 2004, **9**(2), 56 (1), 7-10.
- [8] R. T. Shet, Sulfonated cellulose and method of preparation, US5522967 A, 1996.
- [9] B. T. Hofreiter, B. H. Alexander, I. A. Wolff, Analytical Chemistry, 1955, **27**(12), 1930–1931.
- [10] X. Wang, G. Fang, C. Hu, T. Du, Journal of Applied Polymer Science, 2008, **109**, 2762-2767.

## THE PRELIMINARY BIOSORPTION INVESTIGATION OF COPPER ION BY URTICA DIOICA L. BIOMASS MATERIAL

V. D. Dimitrijević<sup>1</sup>, N. S. Krstić<sup>1</sup>, M. N. Stanković<sup>1</sup>, R. S. Nikolić<sup>1</sup>, D. M. Djordjević<sup>1</sup> and A. Lj. Bojić<sup>1</sup>

<sup>1</sup>*University of Niš, Faculty of Sciences and Mathematics, Department of Chemistry, Višegradska 33, 18000 Niš, Serbia  
(vladimir15041987@gmail.com)*

### ABSTRACT

The adsorption of Cu<sup>2+</sup> from aqueous solutions by nettle biomass material has been studied. Correlation between raw material biosorption and biomass material after incomplete incineration (IIN) and also the effects of initial Cu(II) concentration on adsorption have been studied in batch mode. The experimental isotherm results have been fitted using Langmuir, Freundlich, Temkin and Dubinin-Radushkevich equations.

### INTRODUCTION

Heavy metal pollution has become one of the biggest problems in the context of environmental pollution due to their solubility, mobility and ability to accumulate in the soil. All rigorous standards of allowable concentrations of contaminants and environmental protection have caused the quest for better and cheaper methods of purification of polluted water. For this purpose, various kinds of materials capable to adsorb pollutants have been developed [1, 2].

Copper is an essential element for living organisms at trace levels, but acute or chronic exposure to higher concentrations can cause severe kidney and liver disease, even death. The maximum allowed concentration for drinking water which is regulated by the United States Environmental Protection Agency in 2010 is 1.3 mg dm<sup>-3</sup> [3].

Nettle is traditionally used as a medicinal plant. Medicinal raw materials are leaves and above-ground part. In the literature there are data about use of nettle as a low cost adsorbent for the removal heavy M(II) metals from aqueous solution [4, 5].

The aim of this study was to show that the product of incomplete incineration obtained from a disused plant material nettle can be used as a potentially inexpensive and readily available biosorbent for the removal of heavy metals from aqueous solutions.

## EXPERIMENTAL

Biosorbent was obtained by incomplete incineration of dried nettle in covered porcelain pot. Nettle of the same levels of vegetation were collected from localities environmental niche and air dried prior to testing. Standard stock solutions of  $\text{Cu}^{2+}$  ion of  $1000 \text{ mg dm}^{-3}$  were used to prepare appropriate concentrations for the adsorption studies. The adsorption equilibrium experiments were conducted in  $250 \text{ cm}^3$  Erlenmeyer flasks, containing different concentrations (from  $10.0$  to  $400.0 \text{ mg dm}^{-3}$ ) of the copper model solution during  $120 \text{ min}$ . Aliquots of solutions ( $4.0 \text{ cm}^3$ ) were withdrawn at preset time intervals. All experiments were conducted at ambient temperature ( $20.0 \pm 0.5^\circ\text{C}$ ), at initial pH  $5.0 \pm 0.1$ , using magnetic stirrer on  $200 \text{ rpm}$ .

The concentrations of residual  $\text{Cu}^{2+}$  ion in the solution before and after adsorption were determined by using an atomic absorption spectrophotometer (AASAnalyst 300, Perkin–Elmer, USA) at a wavelength of  $324.8 \text{ nm}$ .

The amount of adsorbed metal ions,  $q_e$  ( $\text{mg g}^{-1}$ ), at equilibrium was calculated as:

$$q_e = \frac{(C_0 - C_e)V}{m}$$

where  $q_e$  is the amount of  $\text{M(II)}$  ion adsorbed per unit weight of the adsorbent at equilibrium time,  $V$  is the volume of solution,  $C_0$  is the initial concentration of metal ion ( $\text{mg dm}^{-3}$ ),  $C_e$  is the equilibrium metal ion concentration ( $\text{mg dm}^{-3}$ ), and  $m$  is the mass of the adsorbent ( $\text{g}$ ).

The metal removal efficiency,  $RE$  (%), of the adsorbent was estimated according to the following equation:

$$RE = \frac{C_0 - C_e}{C_0} \times 100\%$$

Where  $C_0$  and  $C_e$  are the initial and equilibrium concentrations ( $\text{mg dm}^{-3}$ ) of  $\text{M(II)}$  ions in solution, respectively.

## RESULTS AND DISCUSSION

The effect of contact time on the residual concentration of  $\text{Cu(II)}$  ions in aqueous solution with raw nettle and nettle after incomplete incineration is shown at Fig. 1. These results indicate that raw nettle is not efficient biosorbent, but after incomplete incineration it became a very efficient biosorbent for removal  $\text{Cu(II)}$  ions from wastewater. The initial fast phase occurs due to a high availability of the number of active binding sites (functional groups) on the biosorbent surface. A further increase in contact time did not show a significant decrease of  $\text{Cu(II)}$  concentration [6].

Batch experiments were performed at different initial Cu(II) concentrations ranging from 10.0 to 200.0 mg dm<sup>-3</sup> in contact with 4.0 g dm<sup>-3</sup> of nettle biosorbent at 20±0.5 °C and pH 5.0±0.1. Previous study [7] showed that pH 5.0 is an optimal value because above pH 6.0 copper precipitates as a hydroxide and at low pH the sorption capacity is negligible. The influence of initial Cu(II) concentration on removal efficiency is shown in Fig. 2.

The initial copper concentration is a driving force to overcome mass transfer resistance for metal ion transport between the solution and the surface of the adsorbent. At low concentrations of copper(II) ions, greater availability of the exchangeable sites on the surface area interact with all adsorbate ions, and, on the other hand saturation of the available active sites on the surface functional groups prevent further copper ion uptake with increase of Cu(II) concentration [4].

The adsorption isotherm data have been determined by changing the initial metal concentration while the other parameters are kept constant. The fitting of the data to the Langmuir, Freundlich, Temkin and Dubinin-Radushkevich isotherms was based on the coefficients of determination ( $R^2$ ) and it was found to be 0.8193, 0.9698, 0.8041 and 0.8741, respectively. These results show that the biosorption of Cu(II) ions by IIN follows Freundlich model.

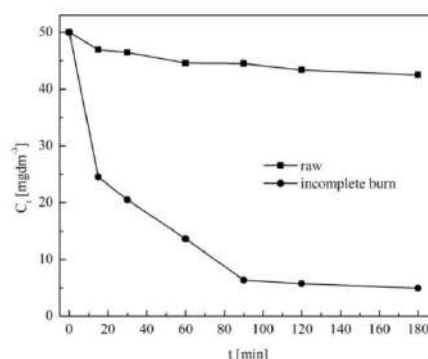


**Figure 1.** Effect of contact time on removal Cu(II) by raw nettle and nettle after incomplete incineration (initial Cu(II) concentration 50 mg dm<sup>-3</sup>, temp. 20±0.5 °C, pH 5.0±0.1, biosorbent dose 4.0 g dm<sup>-3</sup>)

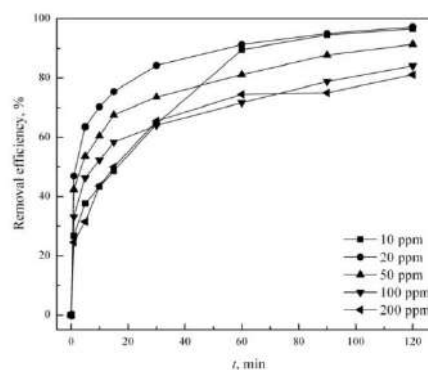


**Figure 2.** Effects of initial Cu(II) concentration on removal Cu(II) by IIN (initial Cu(II) conc. 10.0-200.0 mg dm<sup>-3</sup>, temp. 20±0.5 °C, pH 5.0±0.1, biosorbent dose 4.0 g dm<sup>-3</sup>)

## CONCLUSION

The effect of contact time on the residual concentration of Cu(II) ions in aqueous solution with raw nettle and nettle after IIN indicated that raw nettle is not efficient biosorbent, but IIN became very efficient. Batch experiments with different initial Cu(II) concentrations showed that copper uptake was increased by increasing the initial Cu(II) concentration, but, in the same time, adsorption percentages decreases. The batch adsorption data was successfully correlated with Freundlich model ( $R^2 = 0.9698$ ) which suggests that multilayer sorption takes place on the surface of biomass.

The present study indicated that the nettle after incomplete incineration is very cheap and effective biosorbent for the removal of Cu(II) from wastewaters.

## Acknowledgement

This work was partially supported by the Ministry for Science of the Republic of Serbia (Grant No TR34008).

## REFERENCES

- [1] B. Volesky, Biosorbent materials, Biotechnology and Bioengineering Symposium 16, Wiley, New York, USA1986, **16**, 121-126.
- [2] P. Nowicki, M. Skrzypczak, R. Pietrzak, Chemical Engineering Journal, 2010, **162**, 723-729.
- [3] R. S. Nikolić, J. M. Jovanović, G. M. Kocić, N. S. Krstić, Malondialdehyde (MDA): Structure, Biochemistry and Role in Disease, Biochemistry Research Trends, J. Campbell (Ed.), Nova Science Publisher, New York, 2015.
- [4] Z. H. Mousavi, S. R. Seyedi, Journal of Chilean Chemistry Society, 2010, **55**(3), 307-311.
- [5] Z. H. Mousavi, S. R. Seyedi, International Journal of Environmental Science and Technology, 2011, **8**(1), 195-202.
- [6] N. M. Salem, A. M. Farhan, A. M. Awwad, American Journal of Environmental Engineering, 2012, **2**(5), 123-127.
- [7] M. N. Stanković, N. S. Krstić, I. J. Slipper, J. Z. Mitrović, M. D. Radović, D. V. Bojić, A. Lj. Bojić, Australian Journal of Chemistry, 2013, **66**, 227-236.

## ANNUAL VARIATIONS OF FINE RESPIRABLE AEROSOL FRACTION IN URBAN RESIDENTIAL AREAS

M. Radenković<sup>1</sup> and R. Radić<sup>2</sup>

<sup>1</sup>*University of Belgrade, Vinča Institute of Nuclear Sciences, P.O.Box 522,  
11001 Belgrade, Serbia. (mirar@vin.bg.ac.rs)*

<sup>2</sup>*Republic Hydrometeorological Service of Republic of Srpska, Put  
Banjalučkog odreda b.b. 78000 Banja Luka, Bosnia and Herzegovina.*

### ABSTRACT

Fine particulate matter fraction (PM 2.5) of urban aerosol collected daily for one year with 3/7 frequency at urban background locations in Banja Luka (BL) and Belgrade (BG) had been analyzed and discussed. Mass concentrations of aerosol deposit were determined by standard gravimetric procedure and concentrations of elements with antropogenic and crustal origin have been obtained by application of nuclear analytical techniques (PIXE, XRF). Resulted descriptive statistic parameters have shown that PM 2.5 annual limit value  $25 \mu\text{g m}^{-3}$  was exceeded during the heating period in both investigated regions but with significantly higher values in Banja Luka due to different heating type and structure and local traffic characteristics. Observed concentrations of S and K are high and based on other metals concentration some industrial influences have been indicated.

### INTRODUCTION

Numerous studies over the past decade have shown that a large proportion of diseases and deaths can be attributed to air pollution. Atmospheric particulate matter (PM) level turns as a key parameter in the cause/effect relationship between exposure to pollution and health impacts especially with high risk respirable fine particles, PM 2.5 [1]. The international and national legislative has stipulated annual mean limit value of  $25 \mu\text{g m}^{-3}$  for PM2.5 mass concentration. [2]. Apart the size, chemical composition of the particles and their capacity to carry potentially toxic substances such as organic substances or metallic compounds adsorbed on their surfaces have a crucial role to the effects. Trace elements may be released into the atmosphere by human activities, such as combustion of fossil fuels and wood, high temperature industrial activities and waste incinerations, gasoline exhaust emissions, etc. Urban antropogenic particles are mainly in the PM 2.5 range and its sampling diminishes the interference of natural sources. They could remain

in the air with relatively long residence time and could efficiently penetrate human lungs. Although PM 2.5 fraction of particulate matter is of a great concern for public health, no systematic studies have been performed in Balkans countries. The first measurements have been initiated in Belgrade, in 2002, Republic of Serbia, and in Banjaluka Bosnia and Herzegovina within this study. Here will be presented data on mass concentrations and chemical composition of PM 2.5 fraction of urban aerosol collected during 2014/15 as a starting point for the creation of short-term and long-term policy of air quality management

### EXPERIMENTAL

The air sampling of PM 2.5 aerosol fraction was performed from Aug 2014 till Aug 2015 at both locations using a MVS6 Sven Leckel reference samplers, with air flow rate 2.3m<sup>3</sup>/h. Suspended particles were collected on preconditioned (48 h at 20°C and constant relative humidity around 50%.) and pre-weighed PTFE filters exposed 24 hours with 3/7 frequency. Sampling locations were in Banja Luka (BL) urban background site (H<sub>s</sub>= 175m φ=44.75N, λ=17.24E) in residential area and in Belgrade (BG), sampling of PM 2.5 was performed at suburban site (H<sub>s</sub>= 243 m φ=44.78N, λ=20.52E) in residential area using the same standard procedures as in Banja Luka. The PM 2.5 mass concentration were determined by weighting of the unloaded and loaded preconditioned filters using semi-micro balance Mettler Toledo XS205DU (BL) and Sartorius, R 160P (BG) with a minimum resolution of 0.01 mg in accordance with EN12341 SOP.

Elemental analysis of PM 2.5 was done by nuclear analytical techniques XRF (BL) in Laboratory of Ion Beam Applications, NCSRE, Demokritos, Greece, and PIXE (BG) in Laboratory of Ion Beam Applications, institute of Nuclear Research, Hungarian Academy of Sciences. The elements observed within the study are: Al, Si, S, Cl, P, K, Ca, Na, Mg, Cr, Fe, Cu, Zn, Ni, Cd, As, Ti and V.

### RESULTS AND DISCUSSION

Gravimetric analysis of PTFE filters exposed in urban background areas of Belgrade and Banja Luka from Aug 2014 till Aug 2015 have shown daily mean values of PM 2.5 mass concentrations presented at Figure 1. Maximum concentrations may be noticed in heating period that was from 15 October to 15 April with the episode in Banja Luka in January 2015.

Statistical parameters of daily PM 2.5 mass concentrations (μg m<sup>-3</sup>) over the year have been determined for heating (H), non-heating (NH) and whole sampling time (All) as presented in Table 1.

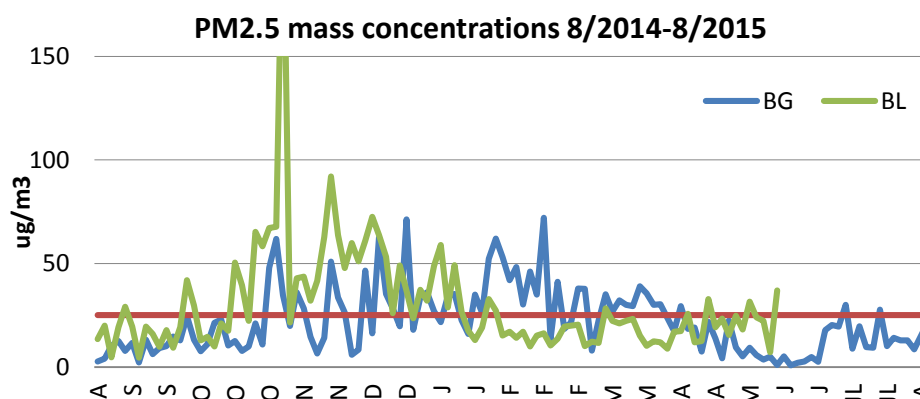


**Figure 1.** Daily mean mass concentrations of PM 2.5 ( $\mu\text{g}/\text{m}^3$ ) in Belgrade (BG) and Banja Luka (BL) residential areas in 8/2014 -8/2015

The PM 2.5 mean 24-hours mass concentrations over the whole sampling time in Belgrade was  $20.63 \mu\text{g m}^{-3}$ , which is below annual limit given by national and European legislations ( $25 \mu\text{g m}^{-3}$ ) but it exceeded  $30.27 \mu\text{g m}^{-3}$  in Banja Luka.

**Table 1.** Statistical parameters of daily PM 2.5 mass concentrations ( $\mu\text{g m}^{-3}$ ) in Belgrade and Banja Luka in Aug 2014 to Aug 2015

Location	Time	N	Mean	SD	Max	Min	Median	98 <sup>th</sup>
Belgrade	NH	60	9.83	7.45	29.92	0.10	9.17	27.14
	H	71	29.76	15.63	72.10	5.84	29.40	67.81
	All	131	20.63	16.00	72.10	0.10	17.85	62.24
Banja Luka	NH	55	18.04	7.76	41.88	4.49	17.27	36.57
	H	45	45.22	34.73	233.61	9.84	41.54	108.97
	All	100	30.27	27.45	233.61	4.49	21.85	72.92

In general, seasonal variations are obvious with much higher concentrations in heating season, when maximum value  $29.76 \mu\text{g m}^{-3}$  was observed in Belgrade and  $45.22 \mu\text{g m}^{-3}$  in Banja Luka, both higher than prescribed annual limit value. Although Banja Luka have almost 10 times less inhabitants and vehicles than Belgrade the pollution by fine particulate matter is higher, probably due to different prevailing heating structure and type: combustion of fossil fuels or biomass burning, industry influences as well as

to the location characteristics and certain meteorological conditions e.g. inversed layers, low temperature and stagnation of air masses.

Besides the mass concentrations, elemental analysis of fine particulate matter aerosol fraction revealed seasonal variations of anthropogenic trace elements. The concentrations  $110.75 \text{ ng m}^{-3}$  Fe and  $9.40 \text{ ng m}^{-3}$  V are higher in Banja Luka than corresponding values in Belgrade:  $88.18 \text{ ng m}^{-3}$  and  $2.67 \text{ ng m}^{-3}$  respectively. Crustal elements Ca, Na, Mn, Al and Si have higher values in Banja Luka than in Belgrade that refer to soil dust as the main source. Concentration of Zn in Belgrade:  $22.50 \text{ ng m}^{-3}$  has higher value than in Banja Luka ( $6.68 \text{ ng m}^{-3}$ ) that is in accordance with earlier research [2]. Concentrations of Pb and Cu in Banja Luka has values  $5.56 \text{ ng m}^{-3}$  and  $3.96 \text{ ng m}^{-3}$  respectively, in compare with  $18.66 \text{ ng m}^{-3}$  and  $1.83 \text{ ng m}^{-3}$  in Belgrade. Concentration of K is significantly higher in Banja Luka ( $571.22 \text{ ng m}^{-3}$ ) than in Belgrade ( $319.53 \text{ ng m}^{-3}$ ) indicating biomass burning as a dominant heating fuel. Sulphure concentration is very high on both location with value  $1522.93 \text{ ng m}^{-3}$  in Banja Luka and  $1012.77 \text{ ng m}^{-3}$  in Belgrade indicated bad quality of coal and high contents of S in traffic emissions.

## CONCLUSION

Mean annual  $\text{PM}_{2.5}$  mass concentrations exceeded the EU air quality standard in Banja Luka in investigated time interval. Seasonal variations of elemental concentrations indicated a great influence of fuel combustion in the heating season. In general anthropogenic trace element are higher in Belgrade than in Banja Luka while the crustal elements have higher concentrations in Banja Luka.

## Acknowledgement

This study was partially supported by the Serbian MESTD through the Project III43009 and by IAEA through the Project RER/1013.

## REFERENCES

- [1] World Health Organization (WHO): 2003 *Health aspects of air pollution with particulate matter, ozone and nitrogen dioxide*. Report, RO Europe; Bonn, Germany 2003. EUR/03/5042688.
- [2] Tasić M, Rajšić S, Tomašević M, Mijić Z, Aničić M, Novaković V, Marković D. M, Marković D. A, Lazić L, Radenković M, Joksić J in: *Environmental Technologies, New Developments*, Ed.E. Burcu Ozkaraova Gungor, I-Tech Education and Publishing, Vienna, Austria, 2008:209-244

## PHOSPHATE REMOVAL BY ELECTROCOAGULATION PROCESS USING STEEL ELECTRODE

B. N. Malinović and T. Đuričić

*University of Banja Luka, Faculty of Technology, 73 Stepe Stepanovica  
Street, 78000 Banja Luka, B&H, (borislav.malinovic@unibl.rs)*

### ABSTRACT

This study focused on testing the efficacy of steel (min. 98,75% Fe) electrodes in an electrocoagulation treatment of wastewater containing phosphates (P-PO<sub>4</sub>). Research has followed the effect of the electrolysis duration, current density, different concentration of supporting electrolyte and phosphate in wastewater. For 40 minutes of treatment is achieved removal efficiency of 93,5%, at the initial pH value 3,  $j=1$  mA/cm<sup>2</sup> and  $\gamma_0=50$  mg/L P-PO<sub>4</sub>. Addition of NaCl as a supporting electrolyte ( $\gamma=0.25$  g/L), is achieved 64,1% removal efficiency for 20 minutes of treatment (pH=3,  $j=1$  mA/cm<sup>2</sup>).

### INTRODUCTION

This study considers the electrocoagulation (EC) as the treatment for the phosphate removal from the synthetic wastewater. There are numerous studies on phosphate removal from wastewater with some of them dealing with the EC with the application of the aluminium electrode itself [1-8]. In the process of EC wastewater the initial pH-value is an important parameter, and previous research has shown that for the case of steel electrodes optimum pH=3 [1-3]. To achieve the removal efficiency of 97.7% using steel electrode, the optimum values of the parameters are as follows: pH= 3,  $j=6$  mA/cm<sup>2</sup>,  $t=15$  min [3]. The increase of the current density increases and the phosphate removal efficiency, as well as specific consumption of electric energy [4]. Applying the steel electrode, removal efficiency decreases with the increase in the initial concentration of wastewater, 100% ( $\gamma_{0(P-PO_4)}=25$  mg/L,  $W_{sp}=0,81$  kWh/m<sup>3</sup>), 98% ( $\gamma_{0(P-PO_4)}=50$  mg/L,  $W_{sp}=0,50$  kWh/m<sup>3</sup>), 61% ( $\gamma_{0(P-PO_4)}=100$  mg/L,  $W_{sp}=0,444$  kWh/m<sup>3</sup>) respectively [4]. It is well known that the pollutant removal from the wastewater increases with increase of the solution conductivity [5,9]. As a supporting electrolyte commonly has used NaCl in various concentration ranges [6-9]. Results of the research by Attor *et al.*, indicate that with addition of the NaCl as the supporting electrolyte in concentrations of 25,5 mM, a complete phosphate removal is achieved (pH= 3,  $\gamma_{0(P-PO_4)}=100$  mg/L,  $j=10$  mA/cm<sup>2</sup>) [7].

## EXPERIMENTAL

In present experimental research, a batch electrochemical reactor of 250 cm<sup>3</sup> capacity made from polypropylene with constant mixing was used, combined with two electrodes of the same area surface  $P=37,3$  cm<sup>2</sup>, separated at  $d=20$  mm distance. The electrode material (anode and cathode) is steel (EN10130-91). All the experiments were performed at 20°C and pH=3 in accordance to the literature recommendations [1-3]. Synthetic wastewater was analysed for the phosphate concentration by spectrophotometry ( $\lambda_{max}=410$  nm) at Perkin Elmer, Lambda 25 in accordance with the standard method [10].

## RESULTS AND DISCUSSION

Results for the phosphate removal by EC are expressed by removal efficiency,  $E_u$ , in percent calculated by the formula (1). There the  $\gamma_i$  and  $\gamma_f$  are the initial and the final concentration of the phosphate in mg/L. Energy consumption is expressed through the formula (2), where  $U$  is the tension,  $I$  - electric current,  $t$  - time,  $m$  - mass of the phosphates removed.

$$E_u = \frac{\gamma_i - \gamma_f}{\gamma_i} \cdot 100 [\%] \quad (1); \quad W_{sp} = \frac{\int_0^t I E_r dt}{3600 \cdot 1000m} \left[ \frac{\text{kWh}}{\text{kg}_{\text{polutant}}} \right] \quad (2)$$

Figure 1. and 2. show the influence of the electrolysis duration on wastewater phosphate concentration decrease ( $\gamma_0=50$  mg/L), or, it can also be said, on the  $E_u$  without supporting electrolyte. A current density used was  $j=1$  mA/cm<sup>2</sup> which, in accordance to the literature, was cited as the optimal current density [4]. It can be clearly seen that with electrolysis duration prolongation, the phosphate concentration in wastewater decreases, reaching the values of  $E_u=93,5\%$ , in 40 min of treatment. Influence of the NaCl as the supporting electrolyte on  $E_u$  is shown at Figure 3. Efficiency is highest at  $\gamma_{NaCl}=2,0$  g/L concentration, being  $E_u=52,2\%$ . Since there are no greater differences in removal efficiencies at concentrations of  $\gamma_{NaCl}=0,25$  g/L ( $E_u=50,2\%$ ) and  $\gamma_{NaCl}=2,0$  g/L, the rest of the research was performed under  $\gamma_{NaCl}=0,25$  g/L. Under the optimal experimental conditions ( $j=0,25$  mA/cm<sup>2</sup>,  $t=10$  min,  $\gamma_{NaCl}=0,25$  g/L) the efficiency is increasing with the decrease of the initial phosphate concentration in the wastewater, which is in accordance with previous findings [4]. Efficiency is highest at the phosphate concentration of  $\gamma=25$  mg/L and goes up to  $E_u=63,4\%$  (Fig. 4). Figure 5. shows dependence of the phosphate removal efficiency on the current density with  $\gamma_0=50$  mg/L,  $\gamma_{NaCl}=0,25$  g/L and  $t=10$  min.

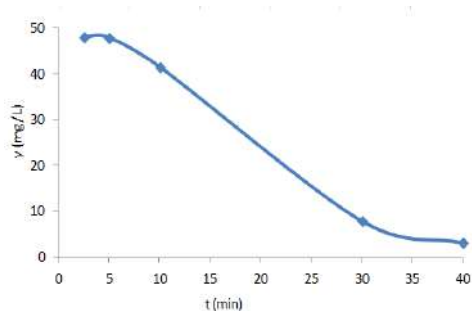


**Figure 1.** Phosphate concentration decrease in relation to the electrolysis duration ( $j=1 \text{ mA/cm}^2$ ,  $t=40 \text{ min.}$ )

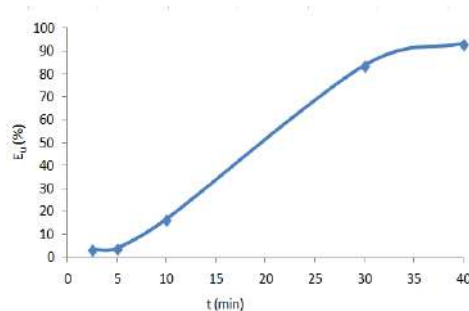


**Figure 2.**  $E_u$  in relation to the electrolysis duration ( $j=1 \text{ mA/cm}^2$ ,  $t=40 \text{ min.}$ )

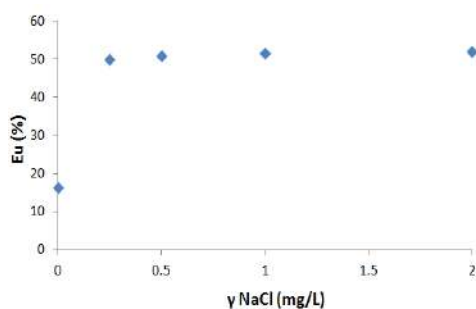


**Figure 3.** Relationship between  $E_u$  and the  $\gamma_{NaCl}$  ( $j=1 \text{ mA/cm}^2$ ,  $t=10 \text{ min.}$ )

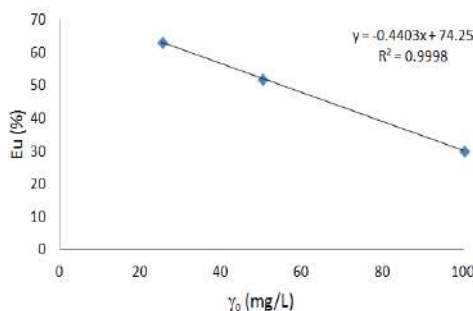


**Figure 4.** Relationship between efficiency and the phosphate initial concentration in wastewater

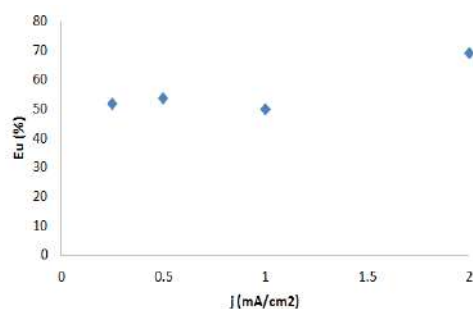


**Figure 5.** Efficiency at varying  $j$  ( $\gamma_0=50 \text{ mg/L}$ ,  $\gamma_{NaCl}=0,25 \text{ g/L}$ )

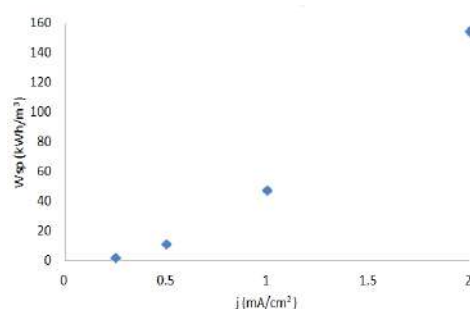


**Figure 6.** Relation between the  $W_{sp}$  and the current density

Highest efficiency is reached under the current density of  $j=2 \text{ mA/cm}^2$  and it has shown the value of  $E_u=69,5\%$ , while for the lower current densities, the removal efficiency did not differ significantly. Due to the small difference in

efficiency achieved, but significantly higher energy consumption (Fig. 6.) under higher current densities (for  $j=0,25$  mA/cm<sup>2</sup>, energy consumption was  $W_{sp}=2,15$  kWh/m<sup>3</sup>, and for  $j=2$  mA/cm<sup>2</sup> energy consumption was  $W_{sp}=155,1$  kWh/m<sup>3</sup>). Therefore in farther experiments the current density was set to  $j=0,25$  mA/cm<sup>2</sup>.

## CONCLUSION

The study has shown that the EC is an efficient method for phosphate removal from wastewater. Efficiency of 93,5% in phosphate removal was achieved in 40 minutes under pH=3,  $j=1$  mA/cm<sup>2</sup> and  $\gamma_0=50$  mg/L P-PO<sub>4</sub>. By applying lower current densities, somewhat lower efficiency was achieved, however, process was significantly more economical as far as the energy consumption is concerned ( $j=0,25$  mA/cm<sup>2</sup>,  $E_u=52\%$ ,  $W_{sp}=0,043$  kWh/kg<sub>P-PO<sub>4</sub></sub>).

## Acknowledgement

This work was supported in part by the Ministry of Science and Technology of the Republic of Srpska under Project 19/6-020/961-171/14.

## REFERENCES

- [1] M. Behbahani, M. R. Alavi Moghaddam, M. Arami, *Int. J. Environ. Res.*, 2011, **5**(2) 403-412.
- [2] S. Irdemez, N. Demircioglu, Y. S. Yildiz, *J. Hazard Mater.*, 2006, **B137**, 1231–1235.
- [3] M. Kobya, E. Demirbas, A. Dedeli, M.T. Sensoy, *J. Hazard Mater.*, 2010, **173**, 326–334.
- [4] S. Irdemez, N. Demircioglu, Y. S. Yildiz, Z. Bingul, *Separ. Purif. Method*, 2006, **52**, 218–223.
- [5] A. Shalaby, E. Nassef, A. Mubark, M. Hussein, *American Journal of Environmental Engineering and Science*, 2014, **1**(5) 90-98.
- [6] E. Nassef, *Engineering Science and Technology*, 2012, **2**(3) 2250-3498.
- [7] A. Attour, M. Touati, M. Tlili, M. Ben Amor, F. Lapique, J.-P. Leclerc, *Sep. Purif. Technol.*, 2014, **123**, 124-129.
- [8] V. Kuokkanen, T. Kuokkanen, J. Ramo, J. Lassi, J. Roininen, *Journal of Water Process Engineering*, 2015, **8**, e50-e57.
- [9] B. Malinović, M. Pavlović, N. Gorgi, *Zaštita materijala*, 2014, **55**(4), 171-179.
- [10] *Standard Methods for the Examination of Water and Wastewater*. APHA, EPA, American public health association, New York, 1999.

## DETERMINATION OF HEAVY METALS CONTENT IN SELECTED HERBS AND THEIR WATER EXTRACTS

S. M. Blagojević<sup>1</sup>, N. Erić<sup>1</sup>, I. Borić<sup>1</sup>, D. Majstorović<sup>2</sup>  
and J. Senčanski<sup>2</sup>

<sup>1</sup>*University of Belgrade – Faculty of Pharmacy, Department of Physical Chemistry and Instrumental Methods, Vojvode Stepe 450, Belgrade, Serbia*

<sup>2</sup>*Institute of General and Physical Chemistry, Studentski trg 12, Belgrade, Serbia*

### ABSTRACT

The content of essential (Fe, Mn) and toxic (Pb, Cd) heavy metals were determined in dried herbal drugs and their water extracts consumed for medical purposes, such as mint and nettle leaves, marigold inflorescence, hibiscus flower and marshmallow root, applying flame and graphite furnace atomic absorption spectrometry techniques. The heavy metal contents in herbs and their water extracts varied widely in the range 0.24 (Cd) – 855.70 (Fe) mg kg<sup>-1</sup> and 0.02 (Cd) – 23.08 (Mn) mg kg<sup>-1</sup>, respectively. Analyzed water extracts as herbal beverages, due to low or moderate transfer of toxic heavy metals during the extraction process, are safe for consumption.

### INTRODUCTION

The herbal drugs contain both organic pharmacologically active compounds and trace heavy metals, which can be available to the human body from any kind of consumption of herbs and their water extracts. Some metals are essential nutrients (Cu, Zn Cr, Fe and Mn), yet become toxic at high concentrations, while others (Pb, Cd, As, and Hg) and are toxic at very low concentrations due to their nonbiodegradable nature, solubility in water and potential to accumulate in different body parts [1]. The herbs and their water extracts contain essential and toxic heavy metals in a wide range of concentrations [1–4]. The amount of metals in herbal extracts depend on whether the metal is strongly bound to the matrix or more soluble in the solution employed, on the extraction efficiency of the metals, applied extraction methods, as well as the total concentrations of the metal in herbs. The extraction efficiency of metal (E%) was estimated as the ratio of its concentration in herbal extract to total concentration in herb. The metals extracted from various herbs into water extracts could be classified as highly (> 55%), moderately (22 – 50%) and poorly (< 20%) extractable elements [3]. Although herbs beverages plays an important role of the consumers

health, herbal drugs can present a health risk if toxic elements are present at high concentrations and above the maximum permissible level. The aim of this study was to investigate the content of Fe, Mn, Pb and Cd in dried mint, nettle marigold, hibiscus and marshmallow samples and efficiency of heavy metals extraction in water from herbs, as well as to examine the safety of selected water extracts as herbal beverages.

### EXPERIMENTAL

Selected samples of dried mint (*Menthae X piperitae folium*) and nettle (*Urticae dioicae folium*) leaves, marigold inflorescence (*Calendulae officinalis flos.*), hibiscus flower (*Hibisci sabdariffae flore*) and marshmallow root (*Althaeae officinalis radix*) were purchased directly from a health food store in Belgrade where they are sold in bulk. The reference standard stock solutions of Fe, Mn, Pb and Cd at a concentration of 1000 ppm (J.T. Baker, USA) as well as 69.7% HNO<sub>3</sub> and 30% H<sub>2</sub>O<sub>2</sub> (Merck, USA) were of spectroscopic grades. The samples of 0.6 g ground dried herb were digested using the microwave digestion system (Milestone Start E), with high pressure supports. To complete the digestion process, the solid residue was dissolved in 7 mL 69.7% HNO<sub>3</sub> and 1 mL 30% H<sub>2</sub>O<sub>2</sub>, and filtered. To prepare water extracts, accurately weighed mass of dried herbs poured with 200 mL of boiling deionized water, left to cool during the 10 or 30 minutes, filtered and the solution was evaporated to near dryness. To the solid residue, 6 mL 69.7% HNO<sub>3</sub> and 2 mL 30% H<sub>2</sub>O<sub>2</sub> were added, and samples were evaporated to near dryness. All filtered samples were transferred in a 25 mL volumetric flask and completed to the mark with deionized water (18 MΩ cm<sup>-1</sup>, Milli Q, Millipore). Digested samples were analyzed applying flame (Fe, Mn) and graphite furnace atomic (Pb, Cd) absorption techniques, using atomic absorption double beam spectrophotometer (GBC Scientific Equipment, Australia) with a deuterium lamp for background correction and hollow cathode lamp for Fe, Mn, Pb and Cd at wavelengths of 248.3, 279.5, 217.0 and 228.8 nm, respectively. Relative standard deviation (RSD) was below 8%, for all elements. Quantification of metals was achieved by using a calibration curve that was fitted by the least squares method.

### RESULTS AND DISCUSSION

The results of the total content of heavy metals in selected herbal drugs and the content in their water extracts are summarized in Table 1. The content of heavy metals, presented as a mean value ± standard deviation (SD) for five determinations. The highest mean total content of Fe (855.70 mg kg<sup>-1</sup>), Pb (4.92 mg kg<sup>-1</sup>) and Cd (0.46 mg kg<sup>-1</sup>) determined in marigold sample, while

the hibiscus sample is very rich of Mn (301.30 mg kg<sup>-1</sup>). The content of Cd were comparable in marshmallow, nettle and hibiscus samples and nearby the maximum permissible level (0.3 mg kg<sup>-1</sup>) declared by FAO/WHO [5], but in the mint and marigold samples to be above the FAO/WHO limit. The content of Pb in all selected herbs were below maximum permissible level (10 mg kg<sup>-1</sup>) established by the national legislation [6] and FAO/WHO.

**Table 1.** Heavy metal content in selected herbal drugs and water extracts

Sample	Heavy metal content expressed on dry basis (mg kg <sup>-1</sup> )			
	Fe	Mn	Pb	Cd
Mint leaves				
Herb	170.61 ± 5.85	73.84 ± 0.57	3.84 ± 0.13	0.390 ± 0.018
Extract	2.58 ± 0.16	11.04 ± 0.17	0.82 ± 0.04	0.051 ± 0.003
Marigold inflorescence				
Herb	855.70 ± 18.22	29.64 ± 0.82	4.92 ± 0.08	0.46 ± 0.03
Extract	1.91 ± 0.13	3.45 ± 0.12	0.48 ± 0.04	0.021 ± 0.001
Hibiscus flower				
Herb	90.00 ± 4.26	301.30 ± 7.83	4.83 ± 0.35	0.280 ± 0.005
Extract	1.13 ± 0.06	23.08 ± 0.23	0.43 ± 0.02	0.041 ± 0.003
Marshmallow root				
Herb	67.21 ± 4.34	10.56 ± 0.34	3.60 ± 0.29	0.241 ± 0.014
Extract	0.57 ± 0.02	0.40 ± 0.02	0.41 ± 0.03	0.022 ± 0.001
Nettle leaves				
Herb	285.20 ± 17.02	36.25 ± 0.40	3.56 ± 0.21	0.261 ± 0.016
Extract	1.53 ± 0.09	2.80 ± 0.11	1.09 ± 0.08	0.080 ± 0.004

The analyzed metals were transferred into the water extract at different ratios, which significantly depended on the type of metal and herb. Highest mean concentration of essential metals Fe and Mn determined in mint and hibiscus extracts, respectively, while in nettle sample is determined highest mean concentration of toxic Pb and Cd. According to the extraction efficiency presented in Figure 1, toxic heavy metals Cd (4.3 – 30.8%) and Pb (9.7 – 30.6%) could be classified as moderately or poorly extractable elements, while the essential metals Mn (3.8 – 15.0%) and Fe (0.2 – 1.5%), due to the low metal transfer during the process of extraction, poorly extractable elements. On the basis of the mean value of extraction efficiency, the analyzed metals can be classified as poorly extractable and presented by the following decreasing order: Pb > Cd > Mn > Fe.

Fraction of the quantity of analyzed metals, assuming one cup (a volume of 200 mL) of daily consumption of mint, hibiscus and nettle water extracts

with highest content of Fe, Mn and both Pb and Cd, respectively, represents only 0.05% (Fe) and 1.75% (Mn) of the recommended daily intake, as well as 1.45% (Pb) and 0.38% (Cd) of provisional tolerable daily intake (calculated from provisional tolerable weekly intake for a 60 kg bw)) [5].

However, results of determination of heavy metals content are in accordance with the values obtained for herbs cultivated in different geographical regions and prepared using different extraction methods [1–4].

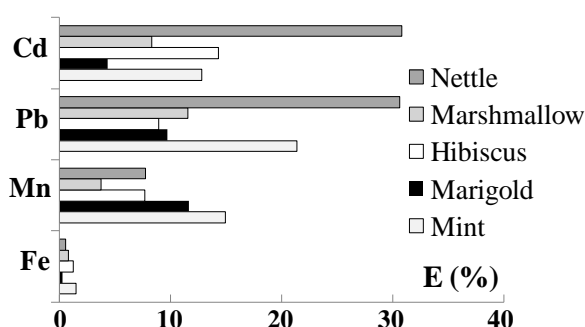


**Figure 1.**  
Extraction efficiency  
of heavy metals from  
selected herbs.

## CONCLUSION

When selected herbal drugs are used for beverages preparation, the content of heavy metals Fe, Mn, Pb and Cd in water extracts depends on total metals concentration in dried herbs and significantly different extraction efficiency of metals (0.2 – 30.8%). The heavy metal contents in examined water extracts varied widely in the range 0.02 (Cd) – 23.08 (Mn) mg kg<sup>-1</sup>, respectively. The consumption of selected herbal extracts as beverages, due to low or moderate transfer of Pb and Cd during the extraction process, is not a pose a health risk factor by toxic heavy metals.

**Acknowledgement** The present investigations were supported by the Ministry of Education, Science and Technological Development of the Republic of Serbia, Grants no. 172015.

## REFERENCES

- [1] S. Korfali, M. Mroueh, M. Al-Zein, J. Food Resear., 2013, **2**, 70–82.
- [2] S. Basgel, S. B. Erdemoglu, Sci. Total Envir., 2006, **359**, 82–89.
- [3] K. Pytlakowska et al., Food Chem. 2012, **35**, 494–501.
- [4] S. Ražić, V. Kuntić, Int. J. Food Prop., 2013, **16**, 1–8.
- [5] FAO/WHO Codex Alimentarius Commission: a) CF/8 INF/1, 2014.
- [6] Pravilnik o količinama pesticida, metala i metaloida i drugih supstancija koje se mogu nalaziti u namirnicama, Službeni list SRJ 32/2002.

## IMPACT OF REMOTE SOURCES ON CHROMIUM CONCENTRATIONS IN BELGRADE AND THE RELATED HEALTH RISK

M. Perišić<sup>1</sup>, A. Stojić<sup>1</sup> and S. Stanišić Stojić<sup>2</sup>

<sup>1</sup>*University of Belgrade, Institute of Physics Belgrade, Pregrevica 118, 11000 Belgrade, Serbia (mirjana.perisic@ipb.ac.rs)*  
<sup>2</sup>*Singidunum University, 32 Danijelova St., 11010 Belgrade, Serbia*

### ABSTRACT

In this paper we investigated the impact of transported air pollution on chromium concentrations and estimated the associated population health risk at three different locations in Belgrade area for the period 2011-2013. According to the results, chromium levels were associated with significant carcinogenic risk, especially in the suburban area affected by industrial pollution. The contribution of transported pollution to the observed chromium concentrations was assessed by the use of hybrid multireceptor models, revealing major potential emission sources located in the neighboring countries of SE Europe.

### INTRODUCTION

The levels of air pollutants in Belgrade are higher than in most European cities. The factors associated with poor air quality include the growth in the number of inhabitants, significant number of poorly-maintained vehicles and outdated technologies in all economy sectors, as well as polluted air masses coming from the neighboring industrial countries [1]. According to the results of long-term measurements, the mean annual PM<sub>10</sub> levels in Belgrade ranged from 30.0 to 58.9  $\mu\text{g m}^{-3}$ , with a significant number of EU AQS limit (40  $\mu\text{g m}^{-3}$ ) exceedances [2]. In addition to PM<sub>10</sub> concentrations, chemical composition is also implicated in particles' relative toxicity. For instance, inhalation of chromium-containing aerosols is recognized to induce a wide range of adverse health effects [3]. The emissions from two main anthropogenic Cr sources, coal combustion and metallurgical processes, result in particles of very small diameter ( $< 1 \mu\text{m}$ ) that may be transported over long distances [4]. The aim of this study was to investigate potential remote emission sources contributing to Cr loadings in Belgrade which are reported to be high [5] and to estimate the related human health risk associated with exposure to the observed concentrations.

## EXPERIMENTAL

Chromium concentrations were determined by the use of inductively coupled plasma mass spectrometry (ICP-MS, Agilent 7500) in PM<sub>10</sub> daily samples collected during the period 2011-2013 at three locations in Belgrade (Serbia) using referent Sven Leckel samplers. The sampling procedure and measurements were conducted according to standards EN 12341 and EN 14902, respectively. Two urban sampling sites included Bojanska, located in highly populated residential area of the city central zone, and Trg JNA, exposed to intense traffic, while Veliki Crljeni, situated in the vicinity of the coal mine, was assigned as suburban-industrial type.

The carcinogenic health risk associated with exposure to the observed Cr levels was calculated in accordance with the US EPA health risk model [6]. The obtained parameter, incremental lifetime cancer risk (ILCR), represents an incremental probability of an individual developing cancer over lifetime as a result of exposure to a carcinogenic compound. The acceptable, baseline risk level is considered to be below  $10^{-6}$ , while  $10^{-4}$  is considered as the upper limit and the reason for public health concern [7].

The potential non-local emission sources and their impact on the observed Cr concentrations were analyzed by the use of 72-h air mass trajectories, calculated as described in Perišić et al. [4], and advanced multi-receptor trajectory ensemble models (TEM), including potential source contribution function (PSCF), concentration weighted trajectory (CWT), residence time weighted concentration (RTWC) and simplified quantitative transport bias analysis (sQTBA), all implemented in MetCor statistical software (MetCor v.1.0, revision 30) [8].

## RESULTS AND DISCUSSION

The toxicity of Cr compounds is mainly associated with metal oxidation state. For instance, hexavalent Cr, mainly originating from anthropogenic sources, is the form considered highly carcinogenic. As no information on Cr oxidation state could be obtained, ILCR was calculated based on one seventh of the measured Cr concentrations, as proposed by the US EPA. The results reveal that ILCR was higher than  $10^{-5}$  at all sampling sites, with the maximum value of  $3.74 \times 10^{-5}$ , as estimated for the suburban-industrial site (Figure 1) [5]. Traffic emissions and fuel burning for heating purposes in cold season were recognized as dominant Cr local sources in urban, residential areas, whereas dust resuspension and coal burning had major impact on Cr concentrations at the suburban-industrial site, located in the vicinity of the lignite mine and thermal power plant Kolubara A [5].

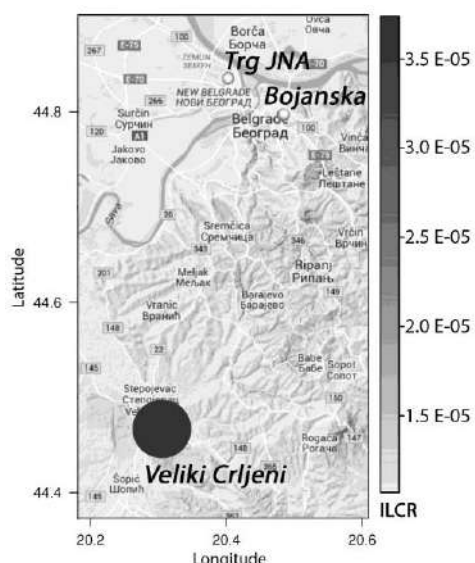


**Figure 1.** Incremental lifetime Cr cancer risk for the period 2011-13.

The prevailing impact of regional sources and sources in Eastern Romania was clearly distinguished by the use of sQTBA.

Nevertheless, air pollution is not only a local and time-limited issue, and our previous studies have confirmed the significant contribution of long-range transport (up to 16%) to locally registered PM<sub>10</sub>[5]. As regards the non-local origin of chromium, the results of multireceptor PSCF model have shown that the potential Cr emission sources were located in NE and SW areas of Belgrade, as well as in the neighboring countries (Figure 2). Additionally, the results of multireceptor CWT and RTWC analysis revealed that the examined sites were influenced by strong Cr emission sources from Eastern Europe, located in the vicinity of the Black Sea.

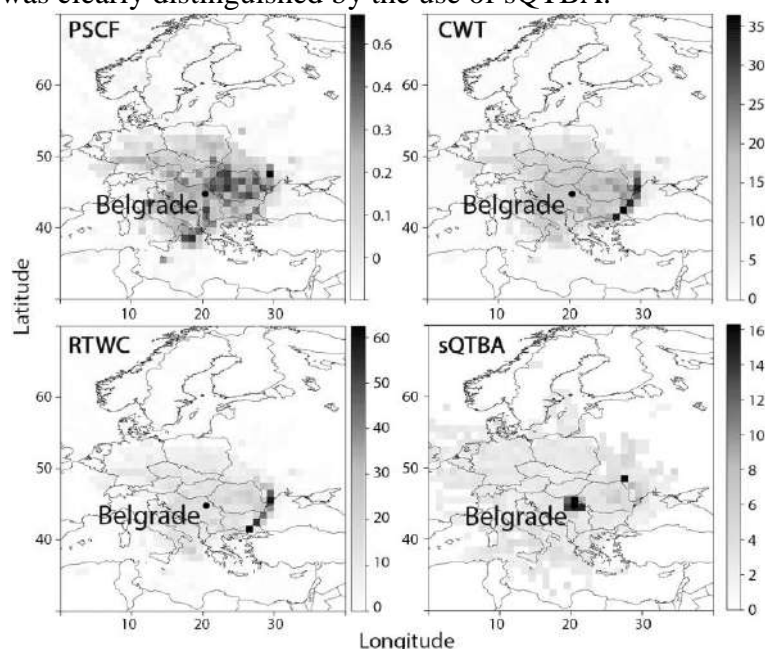


**Figure 2.** Potential Cr sources resolved by the use of multireceptor PSCF (probability), CWT, RTCW and sQTBA [ $\mu\text{g m}^{-3}$ ] for the period 2011-2013.

**CONCLUSION**

Population exposure to chromium compounds in Belgrade is estimated to be associated with high carcinogenic health risk, particularly in the suburban area affected by industrial emissions. According to the results of hybrid multireceptor models, the major potential Cr emission sources were located in NE, E and SW areas of Belgrade, as well as in the neighboring countries.

### ***Acknowledgement***

This paper was realized as part of projects No III43007 and III41011, which were financed by the Ministry of Education, Science and Technological Development of the Republic of Serbia for the period 2011-2016.

### **REFERENCES**

- [1] A.Stojić, S.S.Stojić, I.Reljin, M.Čabarkapa, A.Šoštarić, M.Perišić and Z.Mijić, *Environ Sci Pollut Res.*, 2016, **23**(11), 10722-10732.
- [2] M.Perišić, A. Stojić, S. S.Stojić, A. Šoštarić, Z. Mijić, S. Rajšić, S. Estimation of required PM<sub>10</sub> emission source reduction on the basis of a 10-year period data. *Air Qual, Atmos& Health*, 2015, **8**(4), 379-389.
- [3] S.Langard, M.Costa, in: *Handbook on the toxicology of metals*, Nordberg G (Eds.), 4th edn. Elsevier, London, UK, 2014.
- [4] N.O. Jerome and E. Nieboer, *Chromium in the natural and human environments*. Vol. 20. John Wiley & Sons, 1988.
- [5] M.Perišić, S.Rajšić, A.Šoštarić, Z. Mijić, A.Stojić, *Air Qual, Atmos& Health*, 2016, 1-11. doi:10.1007/s11869-016-0411-6
- [6] United States Environmental Protection Agency (US EPA), *Integrated Risk Information System (IRIS)*, <http://www.epa.gov/iris>, 2013.
- [7] United States Environmental Protection Agency (US EPA), *Methods to Develop Inhalation Cancer Risk Estimates for Chromium and Nickel Compounds*, 2011.
- [8] U.Sofowote, Y.Su, E.Dabek-Zlotorzynska, A.Rastogi, J.Brook, F. Hopke, *Atmos Environ.*, 2015, **108**, 140-150.

## SURVEY OF POTENTIALLY TOXIC ELEMENT POLLUTION OF THE VINEYARD SOIL

T. Milićević<sup>1</sup>, D. Relić<sup>2</sup>, G. Vuković<sup>1</sup>, M. Perišić<sup>1</sup>, D. Majstorović<sup>3</sup>,  
M. Aničić Urošević<sup>1</sup> and A. Popović<sup>2</sup>

<sup>1</sup>*University of Belgrade, Institut of Physics Belgrade, Pregrevica 118, Belgrade, Serbia (tijana.milicevic@ipb.ac.rs)*

<sup>2</sup>*University of Belgrade, Faculty of Chemistry, Studentski trg 12-16, Belgrade, Serbia*

<sup>3</sup>*University of Belgrade, Institut of General and Physical Chemistry, Studentski trg 12/5, Belgrade, Serbia*

### ABSTRACT

In this paper we presented assessment of the potentially toxic elements in the vineyard topsoil (0–5 cm) near the main route in region “Oplenačko vinogorje”. We presented concentrations of potentially toxic elements (Cd, Co, Cr, Cu, Ni, Pb, Sb, V and Zn) and pH values determined in deionized H<sub>2</sub>O, 1 M KCl and 0.01 M CaCl<sub>2</sub>. Concentrations of Cr (89–280 µg g<sup>-1</sup>) and Ni (59–220 µg g<sup>-1</sup>) were determined in values higher than maximum prescribed concentration by regulative. In addition, the high concentration of other elements (Co, Cu, Sb and Zn) points to the necessity of performing more frequently monitoring of potentially toxic elements in the vineyard soil. Significant correlations were obtained between concentrations of Cr–Ni–Sb, but also significant dependence of Zn concentration on pH values was determined.

### INTRODUCTION

Vineyard soil has influences on human health via agricultural production. Foodborne diseases have a significant impact on human health [1]. The increasing release of agrochemicals into the environment has led to growing public concern over the potential accumulation of pollutants (e.g. heavy metals) within agricultural soil.

One of the most important steps in monitoring content of potentially toxic elements in soil is to determine whether the total contents of potentially toxic elements are within the range or over the concentration prescribed by national and international legislation. Therefore, there is a clear interest for monitoring of major and trace elements in agricultural soil, especially those recognized as toxic or carcinogenic.

Soil acidity (key physico-chemical parameter for determine soil bioavailability and mobility fractions) was measured to determine potentially toxic element concentration relation to soil acidity.

The aims of this study were to determine concentrations of potentially toxic elements, their positive correlations and the topsoil acidity (pH).

### EXPERIMENTAL

The “Oplenac” Wine Route is well known region for vine growing and production, 80 km away from Belgrade, a capital of Serbia. The topsoil (0–5 cm) samples were collected during grapevine season of 2015. Twenty-three sampling sites from the vineyard parcels along main route (1<sup>st</sup> parcel x 5 sites, 2<sup>nd</sup> parcel x 2 sites, 3<sup>rd</sup> parcel x 2 sites, 4<sup>th</sup> parcel x 5 sites, 5<sup>th</sup> parcel x 4 sites, 6<sup>th</sup> parcel x 4 sites), and one control sample on the meadow in the vicinity of vineyard parcels.

The soil samples were air dried, grinded in a mortar with a pestleand, and sieved through 2 mm stainless sieve. The hygroscopic moisture of each soil sample was determined at 105°C. The aqua regia digestions were performed in microwave oven (ETHOS 1, Start E Microwave Extraction System, Milestone, Italy) in sealed PTFE vessels using 9 mL HCl and 3 mL HNO<sub>3</sub> for 0.5 g of each soil sample [2,3].

Using inductively coupled plasma optical emission spectrometry (ICP–OES), 25 elements in the soil samples were determined. In this paper we only pay attention to potentially toxic elements (Cd, Co, Cr, Cu, Ni, Pb, Sb, V and Zn) which could have negative consequences for humans and environment.

The pH of soil samples was determined in mixture of (1:5) soil–distilled H<sub>2</sub>O, soil–1M KCl, and soil–0.01M CaCl<sub>2</sub>. Acidity (pH) of soil samples were determined using glass electrode.

For data analysis SPSS software version 21 for Windows and Statistic8 (Stat Soft Inc., Tulsa, OK, USA) were used. Correlation analysis and principal component analysis (PCA) were used to identify specific correlations. Normality of the data was tested by the Kolmogorov–Smirnov test for each element test. Distributions of all determined elements were normal.

### RESULTS AND DISCUSSION

In the vineyard soil samples, determined concentrations of Cr and Ni (Table 1) were above the maximum allowed concentrations proscribed by national Serbian regulative (100 µg g<sup>-1</sup>, 50 µg g<sup>-1</sup>, respectively) [4,5]. The highest correlation coefficients were determining between Cr, Ni and Sb (Cr–Ni: R=0.951, p<0.01; Cr–Sb: R=0.935, p<0.01; Ni–Sb: R=0.887, p<0.01). This indicates that these toxic heavy metals could originate from same

source, probably the nearness traffic route. These elements in the found concentrations could contaminate grapevine and human health in this environment.

Table 1. Descriptive statistic for the element content ( $\mu\text{g g}^{-1}$ ) and pH in soil samples (N=23):

	Mean	Min.	Max.	SD
Cd	2.1	1.9	2.3	0.2
Co	26	21	34	3.4
Cr	150	89	280	40
Cu	51	36	110	15
Ni	110	59	220	37
Pb	21	17	27	3.0
Sb	3.3	2.4	4.7	0.6
V	64	58	71	2.9
Zn	93	69	157	17
pH H <sub>2</sub> O	7.3	6.7	7.9	0.4
pH KCl	6.5	5.2	6.9	0.4
pH CaCl <sub>2</sub>	6.7	5.5	7.1	0.4

Mobility and bioavailability of the elements in soil largely depends on soil acidity. The pH values measured in the soil sample was 5.48–7.06 in 1M KCl, 6.7–7.9 in H<sub>2</sub>O, and 5.5–7.1 in CaCl<sub>2</sub>. According to pH values, these soil samples were moderately acid to neutral, in the soil solution (the most bioavailable fraction) they were neutral to alkaline, and in mineral fraction samples were moderately acid to neutral (Fig 1).

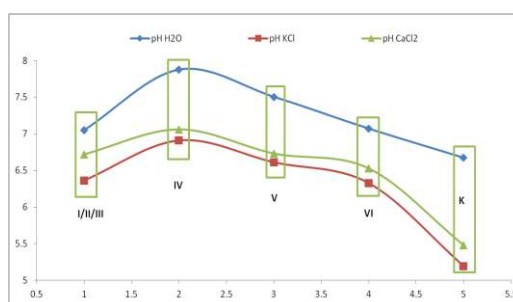
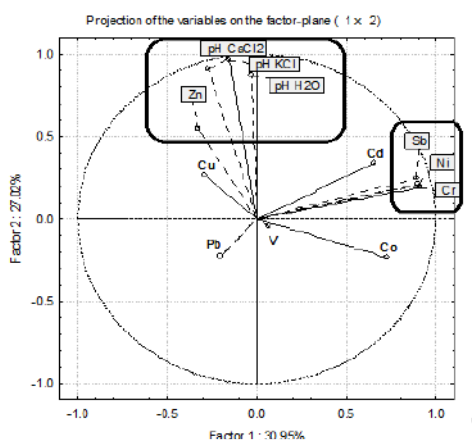


Figure 1. Determined soil pH values in 6 parcels and control location

According to PCA analysis the most correlated concentrations of Cr–Ni–Sb were grouped in the same quadrant. In addition, determined concentrations of Zn were in significant relationship with determined pH values (Fig 2).



**Figure 2.** PCA of the determined elements, and pH values

## CONCLUSION

In addition, according to national regulations and proscribed maximum allow concentrations in soils it could be concluded that beside concentrations of Cr and Ni, monitoring of Co, Cu, Sb and Zn concentrations should be implemented frequently in this vineyard region. In addition, it could be concluded that determined concentration of Zn in these vineyard soil samples widely depends of pH value.

## Acknowledgement

The authors are grateful to the Ministry of Education and Science of the Republic of Serbia (Project No. III 43007, 172001) and to winery "Aleksandrović", Vinča, Topola.

## REFERENCES

- [1] World Health Organization (WHO), [http://www.who.int/topics/food\\_safety/en/](http://www.who.int/topics/food_safety/en/), accessed on 25<sup>th</sup> May, 2016.
- [2] H. Ronkkomaki, R. Poykio, H. Nurmesniemi, K. Popov, E. Merisalu, T. Tuomi, I. Valimaki, *Int. J. Environ. Sci. Technol.*, 2008, **5**, 485 - 494.
- [3] US EPA 3050b Method, Acid digestion of sediments, sledges, and soils, USEPA, Washington, DC, USA, 1996.
- [4] National Regulation, Republic of Serbia 88/2010.
- [5] EU Council Directive 86/278/EEC.

## REMOVAL EFFICIENCY OF SELECTED STEROLS IN WASTEWATER TREATMENT PLANTS IN SERBIA

Z. Jauković<sup>1</sup>, I. Matić Bujagić<sup>2</sup>, S. Grujić<sup>2</sup> and M. Laušević<sup>2</sup>

<sup>1</sup>*University of Belgrade, Innovation Centre of the Faculty of Technology and Metallurgy, Karnegijeva 4, 11000 Belgrade, Serbia.*

*(zpesic@tmf.bg.ac.rs)*

<sup>2</sup>*University of Belgrade, Faculty of Technology and Metallurgy, Karnegijeva 4, 11000 Belgrade, Serbia.*

### ABSTRACT

This paper describes determination of three highly abundant human/animal and plant sterols (coprostanol, cholesterol and  $\beta$ -sitosterol) in influent and effluent samples and their removal rate in two wastewater treatment plants in Serbia. Wastewater samples were prepared using solid-phase extraction and extracts were analyzed by liquid chromatography-linear ion trap-tandem mass spectrometry with atmospheric pressure chemical ionization of analytes. Cholesterol was detected at the highest concentrations in both influent samples at  $44.5 \mu\text{g L}^{-1}$  and  $28.4 \mu\text{g L}^{-1}$ , respectively. Calculated removal efficiencies of two wastewater treatment plants indicate high potential for sterol elimination and removal rate dependence on suspended particles sedimentation and microbial activity in activated sludge treatment.

### INTRODUCTION

Municipal wastewaters are one of the major contributors to the deterioration of the water quality and can have severe impact on human and aquatic organisms' health. Among substances detected at the highest levels in wastewaters are human/animal and plant sterols as products of human metabolism. For this reason, sterols can be used as indicators of environmental pollution originating from human waste. The most important human/animal sterol is coprostanol, produced in digestive tract of humans and animals by microbial reduction of cholesterol [1]. It constitutes 60% of the total sterols present in the human metabolic waste [2]. Another significant sterol present in sewage effluents is cholesterol, which can also originate from additional inputs from non-fecal sources as domestic waste and food leftovers, as well as algae growth in high-nutrient wastewaters [2]. Plant sterols, such as  $\beta$ -sitosterol, are naturally found in oils, cereals, as well as in vegetables and fruits. They are also widely used as supplements in human diet because of their remarkable hypocholesterolemic activity. A limited number

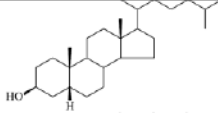
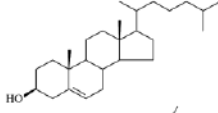
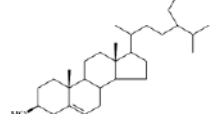
of scientific papers are focused on investigation of sterol removal in wastewater treatment plants (WWTPs) [3, 4]. In these studies, gas chromatography-mass spectrometry (GC-MS) is used for determination of sterol compounds. Additional WWTP influence on environmental quality is utilization of treated wastewater and remaining activated sludge for soil irrigation and fertilization [5].

The aim of this work was to determine selected sterol concentrations in sewage wastewater and to calculate the removal efficiency in two WWTPs. Since the majority of cities in Serbia do not have WWTPs, it is especially important to evaluate treatment plants' impact on quality of the water resources. For this purpose, newly developed liquid chromatography-mass spectrometry (LC-MS) method will be used [6].

### EXPERIMENTAL

High purity (> 99%) analytical standards of coprostanol, cholesterol and  $\beta$ -sitosterol were purchased from Steraloids Inc. (Newport, USA). Important physico-chemical properties of selected sterols are presented in Table 1. All solvents used were LC grade from J.T. Baker or Sigma-Aldrich.

**Table 1.** Common name (IUPAC name), CAS number, chemical structure, molecular weight ( $M_w$ ), water solubility and octanol-water partitioning coefficient ( $\log K_{ow}$ ) of selected sterols.

Common name (IUPAC name)	CAS No.	Chemical structure	$M_w$ (g mol <sup>-1</sup> )	Water solubility (mg L <sup>-1</sup> ) at 25 °C	$\log K_{ow}$
Coprostanol (5 $\beta$ -cholestan- -3 $\beta$ -ol)	360-68-9		388	$3.3 \cdot 10^{-4}$	8.82
Cholesterol (cholest-5-en- -3 $\beta$ -ol)	57-88-5		386	$4.1 \cdot 10^{-4}$	8.74
$\beta$ -Sitosterol (24- -ethylcholest-5- en-3 $\beta$ -ol)	83-46-5		414	$1.3 \cdot 10^{-5}$	9.65

Wastewater samples were collected from two municipal WWTPs in Serbia, with the population equivalents of 35000 (WWTP1) and 8000 (WWTP2). Both plants employ similar conventional treatment processes: primary precipitation treatment coupled with secondary biological activated sludge treatment. Wastewater samples were collected in 4 h time range and composite samples were prepared. They were extracted within 48 h after

collection. Oasis HLB (200 mg/6 mL) solid-phase extraction (SPE) cartridges (Waters, USA) were used for the preparation of wastewater samples. The sample volume of 100 mL, with pH value adjusted to 7.5, was passed through SPE cartridge. Sterols were eluted with 15 mL of methanol; eluate was evaporated to dryness and reconstituted with 0.5 mL of methanol. Surveyor LC system (Thermo Fisher Scientific, Waltham, USA) was used for the separation of analytes on the reverse-phase LiChrospher RP-18 EC column, 250 mm × 4.6 mm i.d. and 5 µm particle size (Cronus, SMI-LabHut Ltd., UK), combined with Zorbax Eclipse® XDB-C18 precolumn, 12.5 mm × 4.6 mm i.d. and 5 µm particle size. The mobile phase consisted of deionized water and methanol. Mass spectra were obtained by LTQ XL (Thermo Fisher Scientific, USA) linear ion trap mass spectrometer. Atmospheric pressure chemical ionization (APCI) technique was used. Extracts were analyzed using previously developed method [7].

## RESULTS AND DISCUSSION

The obtained results are presented in Table 2. It was determined that selected sterols were present at very high concentrations in investigated influent samples. Cholesterol was the most abundant sterol present in sewage wastewater at the levels of 44.5 µg L<sup>-1</sup> and 28.4 µg L<sup>-1</sup>.

**Table 2.** Detected sterol concentrations in influents and effluents, and removal efficiency in two wastewater treatment plants in Serbia.

	Sterols	Concentration±SD (ng L <sup>-1</sup> )		Removal efficiency (%)
		Influent	Effluent	
WWTP1	Coprostanol	3160±180	1170±47	63
	Cholesterol	44535±3096	1025±25	98
	β-Sitosterol	6430±13	2275±108	65
WWTP2	Coprostanol	13060±969	ND	100
	Cholesterol	28435±103	280±16	99
	β-Sitosterol	12335±174	ND	100

Removal rates of sterols in two WWTPs significantly differ. All investigated sterols were completely removed during treatment in WWTP2, whereas WWTP1 was less efficient in sterol elimination, especially in the case of coprostanol (63%) and β-sitosterol (65%). Evidently, the removal efficiency is highly dependent on the activity of microflora in activated sludge treatment as well as the removal of fine particles during the treatment process.

Namely, due to their preference to bind to solid matrices, the removal of sterols can be improved by more efficient removal of suspended particles in treated wastewater [8]. The results have confirmed high importance and crucial impact of municipal wastewater treatment on the quality of the water resources.

## CONCLUSION

The purpose of this study was to determine concentrations of coprostanol, cholesterol and  $\beta$ -sitosterol, as highly abundant sterols in wastewaters, and evaluate their removal efficiency in two WWTPs in Serbia. The results have shown that cholesterol was present at the highest concentration and was completely removed in both WWTPs. It was also determined that removal efficiency of suspended material and activity of microflora in activated sludge treatment have high influence on WWTP performance.

## *Acknowledgement*

This work was financially supported by the Ministry of Education, Science and Technological Development of the Republic of Serbia (Project No. 172007).

## REFERENCES

- [1] Macdonald, V. D. Bokkenheuser, J. Winter, A. M. McLernon, E. H. Mosbach, J. Lipid Res., 1983, **24**, 675-693.
- [2] R. Leeming, A. Ball, N. Ashbolt, P. Nichols, Wat. Res., 30 (1996) 2893-2900.
- [3] V. Furtula, J. Liu, P. Chambers, H. Osachoff, C. Kennedy, J. Harkness, Water Air Soil Pollut., 2012, **223**, 1017-1031.
- [4] M. P. Fernandez, M. G. Ikononou, I. Buchanan, Sci. Total Environ., 2007, **373**, 250-269.
- [5] N. Gottschall, E. Topp, M. Edwards, M. Payne, S. Kleywegt, P. Russell, D. R. Lapen, Chemosphere, 2013, **91**, 275-286.
- [6] I. Matić Bujagić, S. Grujić, Z. Jauković, M. Laušević, Environ. Pollut., 2016, **213**, 76-83.
- [7] I. Matić, S. Grujić, Z. Jauković, M. Laušević, J. Chromatogr. A, 2014, **1364**, 117-127.
- [8] A. Kostamo, J. V. K. Kukkonen, Wat. Res., 2003, **37**, 2813-2820.

*L - Phase Boundaries, Colloids,  
Liquid Crystals,  
Surface-Active Substances*



## STABILITY OF LEAD ETHYL XANTHATE ON GALENA SURFACE

D. R. Vučinić<sup>1</sup> and D. S. Radulović<sup>2</sup>

<sup>1</sup> *University of Belgrade, Faculty of Mining and Geology, Đušina 7, 11000, Belgrade, Serbia. (dvucinic@rgf.bg.ac.rs)*

<sup>2</sup> *Institute for Technology of Nuclear and Other Mineral Raw Materials, Bulevar FranšD'Eperea 86, Belgrade, Serbia*

### ABSTRACT

The stability of lead ethyl xanthate (ethyl xantate ion  $C_2H_5OCS_2^-$ ,  $EX^-$ ) on galena (PbS) surface in an alkaline medium (pH=9-12) was investigated using ATR-IR and UV spectrophotometric methods. The prolonged time of mineral treatment with ethyl xanthate solution up to 4 hours, at pH=9.2, did not affect the surface adsorbed ethyl xanthate. However, within pH range 10-12, the decomposition of surface layer occurs. The ethyl monothiocarbonate ion EMTC<sup>-</sup> (monothiocarbonate  $CO_2S^{2-}$ ) is an intermediate product of lead ethyl xanthate decomposition.

### INTRODUCTION

Much of the research was focused on the action of hydrophobic xanthate-type surfactants ( $ROCS_2M$ ; R = alkyl group;  $M^+ = Na^+, K^+$ ) as flotation reagents (collectors) on sulphide minerals. Different mechanisms have been suggested in literature to explain how xanthates can render hydrophobic the surface of minerals [1,2]. It is generally accepted that galena floats well with K-ethyl xanthate at pH 9 [1-4] due to the formation both forms of lead ethyl xanthate, monolayer of -Pb-EX (-Pb- surface site; chemically adsorbed  $EX^-$ ) and physically adsorbed stoichiometric  $Pb(EX)_2$ , as well as a small amount of ethyl dixanthogen,  $(EX)_2$ .

Several authors have lately suggested the decomposition of lead xanthate in alkaline solutions [5,6].

The purpose of this work was to study the effect of alkaline aqueous solutions (pH=9-12) on the stability of the surface ethylxanthate on galena and degradation kinetics.

### EXPERIMENTAL

Natural galena grains from a StariTrg deposit, Serbia, were manually selected and ground in an agate mortar. The specific surface area of mineral ( $4.00m^2/g$ ) was determined in a Culter Counter Model D Industrial. Chemical analysis

showed that galena contained Pb 85.6% and S 13.7%. Commercial grade potassium ethyl xanthate (KEX) was purified by multiple recrystallization from acetone, and then used as flotation collector (surfactant). Reflection infrared spectra were recorded using a Perkin Elmer Infrared Spectrophotometer with ATR-attachment and Ge crystal. The mineral suspension (0.250 g of the mineral and 0.025 dm<sup>3</sup> of xanthate solution, concentration  $1 \times 10^{-3} \text{ mol dm}^{-3}$ ) was stirred for 15 minutes or 4 hours at pH 9.2, 10.5 and 11.6. After filtration the xanthate-treated galena was washed with distilled water and placed in the Ge reflection element. For UV analysis the ethyl xanthate treated-galena for 15 minutes at pH 9 was filtered, washed and transferred into 15 ml of distilled water, at pH=9.2, 10.5 or 11.6. The concentrations of ethyl xanthate (301 nm) and lead xanthate decomposition product (221 nm) were determined using UV-VIS spectrophotometer UV-1800, Shimadzu.

## RESULTS AND DISCUSSION

The -C-O-C- xanthate band, which appears at about  $1200 \text{ cm}^{-1}$ , was used for determination of the adsorbed form of Pb-ethyl xanthate on galena (Fig.1). The monolayer form of Pb-ethyl xanthate (-Pb-EX; chemically adsorbed  $\text{EX}^-$ ), has a band below  $1200 \text{ cm}^{-1}$ .

The position band above  $1200 \text{ cm}^{-1}$  at pH=9.2 ( Fig.1, a,b) indicates the prevailing presence of the multilayer, physically adsorbed  $\text{Pb}(\text{EX})_2$ . The prolonged contact time did not change the surface layer composition (Fig.1, b).

At pH 10.5, the -Pb-EX is only formed on galena surface (Fig.1, c). A four-hour treatment leads to a decrease of the amount of the chemisorbed  $\text{EX}^-$  (Fig.1, d). When galena was conditioned with KEX 15 min at pH 11.6 the observed absorption bands of  $\text{EX}^-$  were weaker intensities, indicating a small amount of chemisorbed xanthate (Fig.1,e). Surface ethyl xanthate was almost completely decomposed within 4 hours (Fig.1, f) and surface lead hydroxide was detected (Fig.2, a, b).

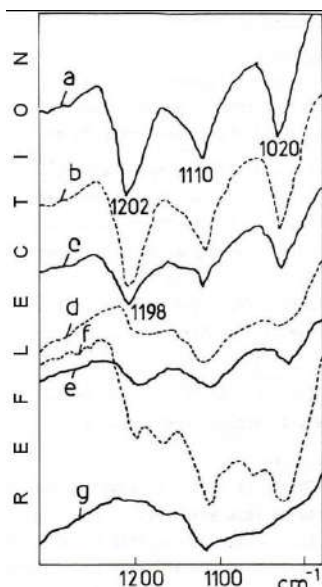


**Figure 1.** IR spectra of KEX treated galena at: pH=9.2, (a) 15 min, (b) 4h; pH=10.5, (c) 15 min, (d) 4 h; pH=11.6, (e) 15 min, (f) 4 h; (g-galena, pH 9.2).

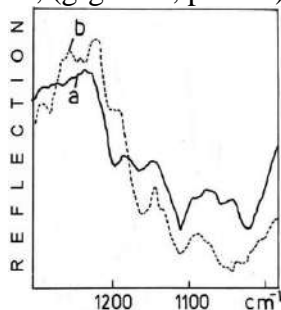


**Figure 2.** IR spectra of: a) KEX treated galena at pH=11.6, 4 h (Fig.1, f); b) Precipitated Pb(OH)<sub>2</sub>.

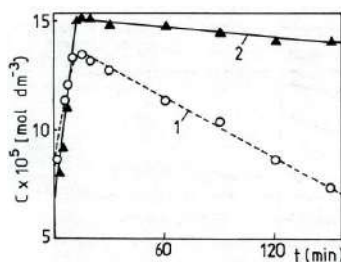


**Figure 3.** EX<sup>-</sup> (1) and EMTC<sup>-</sup> (2) concentrations as a function of time, pH 11.6

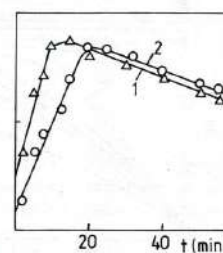


**Figure 4.** EX<sup>-</sup> concentrations at pH 10.5 (2) and 11.6 (1) as a function of time

UV results showed the presence of ethyl xanthate and ethyl monothiocarbonate ions, EMTC<sup>-</sup>, in a high alkaline aqueous solution (pH 10.5 and 11.6) as a decomposition products of surface lead ethyl xanthate (Figs.3 and 4). The rates of EX<sup>-</sup> and EMTC<sup>-</sup> formation were high at the beginning (Fig.3). The EX<sup>-</sup> ion concentration reached its maximum in 15 min at pH 11.6 and in 20 min at pH 10.5 (Fig.4). Further, concentrations of both EX<sup>-</sup> and EMTC<sup>-</sup> ions decreased (Fig.3). These kinetic data can be explained according to the lead xanthate decomposition mechanism proposed by Harris and Finkelstein [5]:



Because the decomposition test was carried in air, ethyl xanthate concentration fell in the reaction with oxygen



Further abstraction of  $\text{EMTC}^-$  from the solution (Fig.3, curve 2) is caused by its decomposition. The ethyl monothiocarbonate ion is obviously an intermediate product of lead ethyl xanthate decomposition.

The surface lead ethyl xanthate at 9.2 is stable. The  $\text{EX}^-$  and  $\text{EMTC}^-$  concentrations in the solution were below  $1 \times 10^{-5} \text{ mol dm}^{-3}$ .

### CONCLUSIONS

The surface ethyl xanthate on galena (chemically and physically adsorbed) is stable within the agitation time of four hours at pH 9.2. The prolonged contact (4 hours) at pH 10.5 leads to a decrease of the amount of the chemisorbed  $\text{EX}^-$ .

When galena was conditioned with  $\text{KEX}^-$  15 min at pH 11.6 the observed absorption bands of  $\text{EX}^-$  were very weak. Surface ethyl xanthate was almost completely decomposed within 4 hours and surface lead hydroxide was detected. The ethyl monothiocarbonate ion is an intermediate product of the ethyl xanthate decomposition. The decomposition rate of surface ethyl xanthate in pH range 10-12 is very high at the beginning.

### *Acknowledgement*

This work was partially supported by the Ministry for Science of the Republic of Serbia (Grants no.33007 and 17010).

### REFERENCES

- [1] J. Leppinen, J. Mielczarski, *Int. J. Miner. Process.*, 1986, **18**, 3-20.
- [2] N. P. Finkelstein, *Int. J. Miner. Process.*, 1997, **52**, 81-120.
- [3] R. Woods, *J. Phys. Chem.*, 1971, **75**, 354-362.
- [4] D. R. Vučinić, P. M. Lazić, A. A. Rosić, *Colloids Surf. A: Physicochem. Eng. Aspects*, 2006, **279**, 96-104.
- [5] P. J. Harris, N. P. Finkelstein, *Int. J. Miner. Process.*, 1975, **2**, 77-100.
- [6] X. Chen, Y. Hu, H. Peng, X. Cao, *J. Cent. South. Univ.*, 2015, **22**, 495-501.

## TIME EVOLUTION OF THE DIFFUSION TIME FOR THE ADSORPTION PROCESS AT THE POTASSIUM ETHYL XANTHATE-CHALCOPYRITE NATURAL MINERAL INTERFACE

D. Todoran<sup>1</sup>, R. Todoran<sup>1</sup>, E. Anitas<sup>2,3</sup> and Zs. Szakacs<sup>1</sup>

<sup>1</sup> *Technical University of ClujNapoca North University Centre of Baia Mare, Department of Economics and Physics, Dr. Victor Babes str., no. 62A, Baia Mare, Maramures, Romania. (szakacs@yaho.com)*

<sup>2</sup> *Joint Institute for Nuclear Research, Dubna, Russian Federation.*

<sup>3</sup> *Horia Hulubei National Institute of Physics and Nuclear Engineering, Bucharest-Magurele, Romania .*

### ABSTRACT

We propose optical reflectance measurements in the theoretical framework of Mandelbrot random walks as a method for the evaluation of the kinetics of adsorption processes. We computed the diffusion time of the adsorption products formed at the interface between the chalcopyrite natural mineral and potassium ethyl xanthate solution. This parameter provides important information regarding the global ion kinetics during interface processes. The continuously measured values of the reflected monochromatic radiation intensity was recorded for 35 minutes, for different solution concentrations and pH values, at a constant temperature. Its time dependence reveals the diffusion properties of the xanthate molecule in the solution, knowing that at the initial state, these molecules were uniformly distributed. Our study leads to the optimization of the industrial froth flotation process, giving insight in the delicate kinetics that are present at the interface level.

### INTRODUCTION

Description of chemisorption and physical adsorption at the interface level involves the characterization of dynamic processes, and is of interest from both theoretical and practical points of view. This study takes into account the different characteristics of the homogenous liquid and the complex structured crystalline solid, at the boundary where the interface is formed.

### THEORY AND EXPERIMENTAL

The theoretical model used in the description of the adsorption processes kinetics at the interface formed between the chalcopyrite natural mineral and K-ethyl xanthate solution is described in [1] and in its references. Its

parameters can be linked directly to experimentally measurable quantities, giving insight into its complex mechanisms: surface diffusion at liquid-solid interface, viscoelastic effects in the fluid phase, exchange between the bulk solution and the solid surface when the surfactant is soluble. In the description of the behavior of an adsorbed molecule one can resort to Mandelbrot random walks [2]. One step in this fractal system, consisting in a desorption, bulk diffusion and then a re-adsorption somewhere else, can be a large Lévy jump or even a Lévy flight. When the exponent of the power law distribution of the step sizes in a fixed period of time is between 1 and 3, the central limit theorem cannot be applied to obtain a Gaussian distribution, leading to Lévy distributions [3].

Studying the dynamic adsorption equilibrium requires taking into account the diffusion of the adsorbed molecule in the liquid solution and the adsorption-desorption rate of the flotation reagent. The system that is formed between the bulk solution and the solid surface can be characterized as a “strongly adsorbing” or a “weakly adsorbing” one. The ratio between the time of an adsorbed molecule to be desorbed  $Q^{-1}$  and the adsorption depth diffusion time  $t_h$  at a certain moment in time permits an evaluation of the evolution trends at a microscopic level, quantifying the above mentioned characteristics. High attractive and retentive properties characterize “strong” systems, the diffusion time  $t_h$  is small and a high number of ions originating from the liquid phase can reach the solid surface. In contrast, when desorption time  $Q^{-1}$  is small, a high number of desorbed ions originate from the solid surface, characterizing a “weak” system, and the diffusion time is much smaller than desorption time. Denoting with  $\Gamma(t)$  the concentration of the adsorbed reagent at a certain moment in time, and with  $\Gamma_{eq}$  the dynamic equilibrium concentration of the adsorbed reagent at the solid

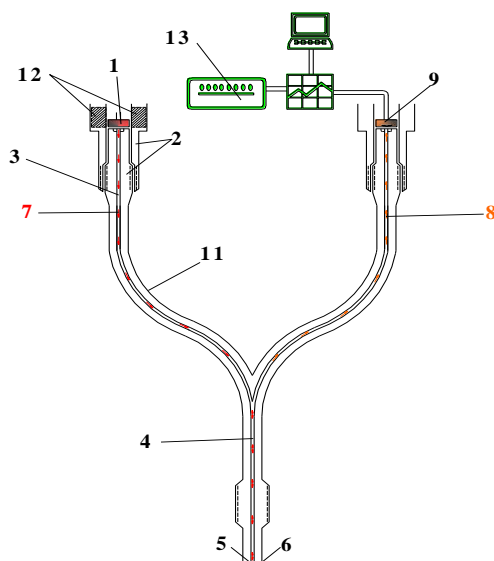


**Figure 1.** Schematic configuration of the experimental setup 1-GaAs laser source; 2-cooler; 3,7,8-optical fiber; 4-the common channel for the optical radiation; 5,6-lenses; 9-photodetector; 10-recording system; 11-Teflon protection; 12-liquid nitrogen cooling system

surface at the end of the adsorption process, the ratio  $\Gamma(t)/\Gamma_{eq}$  is a function of  $(t/t_h)^{1/2}$ .

The chalcopyrite natural mineral's description and preparation was presented in our previous work [4]. The K-ethyl xanthate was purified from a 65% industrial grade one. Its quality was checked before each determination using spectrophotometric measurements in the UV domain. The pH of the solution was fixed using analytical grade HCl and NaOH. The concentrations of the xanthate solutions were: 10 mg/l, 25 mg/l, 50 mg/l, 100 mg/l and 3 g/l for each pH of: 7, 8, 9 and 10. The employed experimental technique permits continuous "in situ" measurements and does not interfere with the evolution of the interface processes. The intensity measurements of the reflected radiation obtained from the investigated interface layer lasted for 38-40 min.

The photon energy of the incident radiation was fixed to 1.431 eV, using a liquid nitrogen cooling system for the GaAs laser ( $\lambda=0.89 \mu\text{m}$ ). The transmittance of the xanthate solution and the reflectance of the mineral was also found to be optimal (above 50%) at this wavelength, without entering deeper in the IR region. A "Y" shaped quartz optical fiber was used as light source and collector [5], its end being fixed 3mm away from the experimental interface.

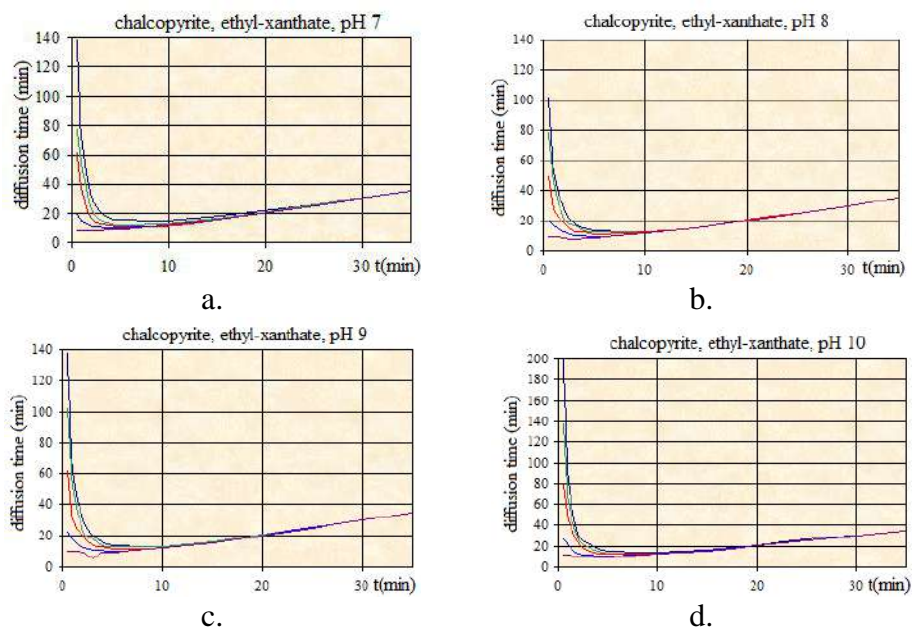


**Figure 2.** Diffusion times for the K-ethyl xanthate on the surface of the chalcopyrite mineral for the pH of (a) 7, (b) 8, (c) 9 and (d) 10. Solution concentrations are: 10mg/l (dark blue), 25mg/l (green), 50mg/l (red), 100mg/l (light blue), 3g/l (lilac)

## RESULTS AND DISCUSSIONS

The characteristic graphs of the diffusion time as a function of time are presented in Figure 2. After a period of 35 min the measured parameter reached a constant value. In each experimental determination, the diffusion time has a fast decreasing speed in the first 4-5min of the adsorption process. A minimum is reached around this moment, followed afterwards by a very slow increase. Thus, the first minutes show a “strongly adsorbing” system. Chalcopyrite is interacting with the nearest xanthate molecules and diffusion time to the interface drops significantly. When the minimum is reached, electrostatic forces at the interface start to block out other flotation reagent molecules and then the system turns to a “weakly adsorbing” one. The fastest time to achieve dynamic equilibrium is for a pH of approximately 8.

## CONCLUSION

Optical “in situ” reflectivity measurement is proposed to determine the kinetics of the evolution of the chalcopyrite natural mineral – K-ethyl xanthate adsorption interface. The diffusion time of the flotation reagent in an aqueous solution is investigated. Dynamic adsorption-desorption equilibrium at the interface level is reached in approximately 35min. The bulk solution – solid surface system can be classified as “strongly adsorbing” for the first 4-5 min, turning afterwards into a system displaying “weakly adsorbing” properties.

### *Acknowledgement*

The authors acknowledge the support from JINR Dubna-TU Cluj-Napoca joint research grants and projects based on the protocol no. 4517-3-16/18.

## REFERENCES

- [1] O. Bychuk, B. O'Shaughnessy, Phys. Rev. Lett., 1995, **71**, 1795.
- [2] B. B. Mandelbrot, The Fractal Geometry of Nature, W.H.Freeman & Co. Ltd., San Francisco, 1982
- [3] M.F. Shlesinger, G.M. Zaslavsky, J. Klafter, Nature, 1993, **363**, 31.
- [4] R. Todoran, D. Todoran, Zs. Szakacs, Russ. J. Phys. Chem. A, 2015 **89**, 2422.
- [5] A. Kikineshi, A. Mishak, A. Sterr, V. Tsigika, 1993, Proceeding of SPIE, **1983**, 462.

## INFLUENCE OF AMINE OXIDE ON ANIONIC SURFACTANTS MIXTURE

S. N. Blagojević<sup>1</sup>, S. M. Blagojević<sup>2</sup> and N. Pejić<sup>2</sup>

<sup>1</sup>*Institute of General and Physical Chemistry, Studentski trg 12/V, Belgrade*

<sup>2</sup>*University of Belgrade – Faculty of Pharmacy, Department of Physical Chemistry and Instrumental Methods, Vojvode Stepe 450, Belgrade, Serbia*

### ABSTRACT

The performances of base anionic surfactants mixture (sodium lauryl ether sulfate (SLES),  $\alpha$ -olefin sulfonates (AOS) and coco betaine (CB)) with nonionic amine oxide (AO) surfactant in various concentration (1–5%), were studied. The parameters measured were critical micelle concentration, CMC, surface tension of particular surfactants mixture,  $\gamma$  and foam volume. The combination of SLES/AOS/CB at ratio 80:15:5 was base surfactants mixture. This study showed that adding of nonionic AO surfactants improved SLES/AOS/CB foaming properties, and the reduction in  $\gamma$  and lowering the CMC. All those indicate that amine oxide surfactant can be used to produce better cleaning products.

### INTRODUCTION

Cleaning in aqueous wash liquor is a complex process involving the interaction of numerous physical and chemical influences. In the broadest sense, washing can be defined as both the removal by water or aqueous surfactant solution of poorly soluble dirt and the dissolution of water [1]. The main ingredients in cleaning liquids are surfactants (surface active agents). They possess both hydrophobic and hydrophilic properties. Because of its dual affinity, surfactants in water based solvents show more or less marked tendency to the spontaneous accumulation in the phase boundary surfaces by reducing the surface tension of the solution, and forming aggregates of molecules (micelles). When a surfactants liquid that have sufficient amount of surfactant is dissolved in water, several bulk solution properties are significantly changed. These changes are happened only when some concentration is reached, this concentration is called the critical micelle concentration, CMC, and that is minimum bulk surfactants concentration. Below CMC surfactants structure is mainly solvated monomeric species, but above the CMC micelles are formed. Modern cleaning liquid formulation has a mixture of surfactants, mainly anionic and nonionic. Nonionic surfactants (amine oxides, ethoxylates, etc.) have a lower foaming performance and are

also highly synergistic, owing to their lack of a charged head group [1]. The main expectation of these products is to be good foaming, detergency and wetting, and for estimating the quality of detergent it is important to determine CMC, surface tension and foaming [2]. A study has been conducted to evaluate the influence of various concentrations of nonionic amine oxide surfactant on base anionic (sodium lauryl ether sulfate,  $\alpha$ -olefin sulfonates and coco betaine) surfactants mixture. The CMC values and surface tension of surfactants mixtures were obtained using the conductometric and stalagmometric method whereas foaming mixture properties were determined by standard measurement method.

### EXPERIMENTAL

For determination of performance of nonionic-anionic dishwashing liquids, all commercial chemical raw materials used in this study were obtained from the stated suppliers and used without any further treatment: sodium lauryl ether sulfate (SLES) (Cosmacol AES-70-2-24, Sasol, Italy), sodium  $\alpha$ -olefin sulfonate (AOS) (Hostapur OSB, Clariant, Switzerland), cocamidopropylbetaine (CAB) (Empigen BS/FA, Huntsman, USA) and lauramine oxide (AO) (Empigen OB, Huntsman, USA). Total surfactant concentration was 10 % for all samples. The surfactant mixture solutions were prepared in a 100-mL volumetric flask and then diluted in deionized water ( $18 \text{ M}\Omega \text{ cm}^{-1}$ , Milli Q, Millipore) to the desired concentration. The conductivity measurements were applied to determine the CMC in various surfactant systems combinations. Those measurements were carried out with digital conductivity meter SensION 5 (Hach, USA) with the accuracy  $\pm 0.5\%$ , and with the 51975 conductivity probe that uses the 4-ring method. The conductometric method is based on the finding of a breaking point on the curve with a relation of the concentration and electrical conductivity. The requested value of CMC is the intercept of two linear functions with different slopes and the surfactants mixture CMC was determined by conductometric titration. The surface tension of each mixed surfactants was measured with a Traub stalagmometer (Neubert-Glass, BN-0330-10-208). The surface tension can be determined using drop counting method. Evaluation of foamability of surfactant mixtures was done by foam volume measuring after free flows from 1 m of 0.4 % dishwashing formulations without soil with total volume of 5 L [3]. The reservoir was placed in such a way that the outlet tube was positioned in the centre of the basin at 1 m height.

## RESULTS AND DISCUSSION

In this study, the values of critical micellar concentration and surface tension as well as foam volume of different surfactant formulations were obtained. The CMC values of examined mixtures of surfactants were determined from inflections in plots of specific conductivity ( $\kappa$ ) vs. concentration of surfactant mixture ( $c$ ). The obtained graphical dependence is a curve which consists of two segments (premicellar and postmicellar) each plot shows the single break point. The CMC is obtained from the intersection of the fitting lines of the  $\kappa/c$  plots above and below the break point. In addition to the conventional procedure (William's method [4]), in order to improve the quality of the calculated CMC, the method proposed by Carpena [5] was also used and the results are obtained by Carpena method. Surface tension measurements performed at 23.0 °C for 0.1% water solutions of surfactant mixture. Summarized results for CMC,  $\gamma$  and foam volume are all presented in Table 1.

**Table 1.** The CMC, surface tension and foam volume of various anionic (SLES/AOS/CB) – nonionic (AO) surfactants mixtures

Surfactants mixture	CMC (g L <sup>-1</sup> )	$\gamma$ (mN m <sup>-1</sup> )	Foam volume (mL)
SLES/AOS/CB	0.28	29.2	210
SLES/AOS/CB – 1% AO	0.20	25.0	225
SLES/AOS/CB – 2% AO	0.15	23.4	235
SLES/AOS/CB – 3% AO	0.10	21.0	250
SLES/AOS/CB – 4% AO	0.07	20.0	255
SLES/AOS/CB – 5% AO	0.07	18.7	260

From the results it is obvious that AO surfactants reduced  $\gamma$  and CMC and make better foaming with no drainage, when mixing with anionic surfactants. This suggest a mixed micelle formation between anionic and nonionic surfactants, and all better performances of surfactant mixtures can be attributed to the interaction of hydrophilic and hydrophobic groups, and better mixing on the air–water surface for foaming. The micelle formation and the adsorption on the interface for a single surfactant is a typical property determined by the length of its hydrophobic chain. When amine oxide surfactant are used with anionic surfactants, foaming of the formulations are improved. A synergistic effect is observed, and mixtures have better performance than single surfactants with the same total concentration. Mixtures of anionic and nonionic surfactants show specific behavior because

of significant reduction in the mixture CMC, and that leads to lower surface tension and better foaming.

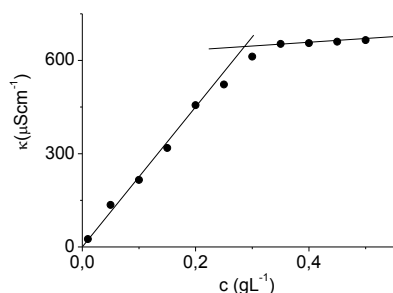


**Figure 1.** The dependence of specific conductivity ( $\kappa$ ) on concentration of surfactant mixture ( $c$ ) for Sles/AOS/CB

It is due to the fact that in mixed micelles, the polar group of the anionic surfactant is located further than the polar group in micelles of a pure anionic surfactant, and therefore, the repulsion energy between the charged groups is smaller, and that is mechanism of influence of AO on reducing surface tension and critical micellar concentration.

## CONCLUSION

Nonionic amine oxide surfactant has a great influence on the critical micellar concentration, surface tension and foaming of anionic surfactant mixtures. Thus, anionic and nonionic mixture of surfactants can be used in a lower concentration. Favorable detergency properties of nonionic surfactants derive largely from the following factors: low critical micelle concentration (CMC = 0.07 g L<sup>-1</sup>), significant reduction of surface tension and improve foaming. However, the low CMC values of nonionic surfactants indicate that they display high detergency performance even at relatively low concentrations.

**Acknowledgement** This work was partially supported by the Ministry for Education, Science and Technological Development of the Republic of Serbia (Grant no. 172015).

## REFERENCES

- [1] J. Falbe, Surfactants in consumer products, Springer, Berlin, 1987.
- [2] C. Nitsch, G. Huttmann, SOFW J, 2002, **128**, 5, 11–15
- [3] Annual book of ASTM standards, 2015, vol. 15.04, ASTM D1173–07
- [4] R. Williams, J. N. Phillips, K. J. Mysels, Trans. Faraday. Soc., 1955, 51, 728–737.
- [5] P. Carpena, J. Aguiar, P. Bernaola-Galva'n, C. Carnero Ruiz, Langmuir, 2002, **18**, 6054–6058.

## *M - Complex Compounds*



## NEW DINUCLEAR ZINC(II) OCTAAZA MACROCYCLIC COMPLEX: CONDUCTOMETRIC STUDY, SYNTHESIS AND CHARACTERIZATION

M. P. Krstić<sup>1</sup>, S. Jevtić<sup>2</sup>, B. B. Petković<sup>2</sup> and M. Milčić<sup>3</sup>

<sup>1</sup>*Faculty of Veterinary Medicine, University of Belgrade, Bulevar oslobođenja 18, 11000 Belgrade, Serbia (milena@vet.bg.ac.rs)*

<sup>2</sup>*Department of Chemistry, Faculty of Natural Sciences and Mathematics, University of Priština, Lole Ribara 29, 38220 Kosovska Mitrovica, Serbia*

<sup>3</sup>*Faculty of Chemistry, University of Belgrade, Studentski trg 12-16, 11000 Belgrade, Serbia*

### ABSTRACT

The new complex  $[\text{Zn}_2(\text{tpmc})\text{NO}_3](\text{NO}_3)_3 \cdot \text{CH}_3\text{OH}$ , where *tpmc* is *N,N',N'',N'''*-tetrakis(2-pyridylmethyl)-1,4,8,11-tetraazacyclotetradecane, have been synthesized and characterized. The conductometric technique played a guiding role in planning experiment with this large macrocyclic ligand. In IR spectrum sharps are shown coordinated and ionic nitrate ions which are in agreement to proposed formula by elemental analysis. Molar electrical conductivities indicated assumption that the complex is about a 1:3 electrolyte type. The optimized complex structure is obtained by molecular modeling and DFT calculations.

### INTRODUCTION

In recent years, macrocyclic polyamine ligands and their complexes have been attractive due to specific structures and properties, as well as possibility of their application [1]. *N,N',N'',N'''*-tetrakis(2-pyridylmethyl)-1,4,8,11-tetraazacyclotetradecane (*tpmc*) is one of the *cyclam* derivatives with eight nitrogen atoms as possible coordinate places. Until today, *tpmc* complexes with only few metals (mostly with Cu (II) ions) are synthesized, and they have shown different electrochemical properties [2], as well as, antibacterial and cytotoxic activity [3].

The goal of the present investigation is to study the stoichiometry of the complexation of *tpmc* with Zn(II) ions and to find the most convenient solvent for synthesis, by using the conductometric titration. Base on this results, here we report the synthesis, characterization and proposed structure of the first binuclear zinc complex with *tpmc* containing nitrate ligand as a bridging ligand.

## EXPERIMENTAL

*Measurements:* Elemental analysis (C, H, N) was carried out by standard micro methods at the Center of Instrumental Analysis, University of Belgrade. IR spectra (KBr disc technique) were recorded on a Perkin-Elmer FTIR 31725 X spectrophotometer. Molar electrical conductivities of the complex ( $c = 1 \times 10^{-3} \text{ mol/dm}^3$ ) solution in acetonitrile was measured at room temperature using a Jenway 4010 conductometer.

*Conductometric procedure:* The experimental procedure for conductometric titrations was reported in our previous work [2]. The conductance measurements were performed on a digital conductometer WTW model 330i (Germany).

*Preparation of compounds:* N,N',N'',N'''-tetrakis(2-pyridylmethyl)-1,4,8,11-tetraazacyclotetradecane (*tpmc*) was prepared using previously described method [4]. *Synthesis of  $[\text{Zn}_2(\text{tpmc})(\text{NO}_3)](\text{NO}_3)_3 \cdot \text{CH}_3\text{OH}$ :* The ligand (*tpmc*) was suspended in to a mixture methanol:water at 50 °C. To this solution was added a methanol solution of zinc(II)-nitrate hexahydrate and mixture was stirred more than hour at 65 °C and then cooled to room temperature. The white crystals which formed were filtered off and washed with ethanol (yield 129 mg, 53%). The crystals were recrystallized from a mixture of water and ethanol (1:1 v/v). Anal. Calc. for  $\text{C}_{35}\text{H}_{48}\text{N}_{12}\text{O}_{13}\text{Zn}_2$ : C 43.09, H 4.96, N 17.23. Found: C 42.81, H 4.83, N 17.08%. IR (KBr,  $\text{cm}^{-1}$ ): 2868.9  $\nu(\text{CH}_2)$ , 1610  $\nu(\text{Py})$ , 1477.9  $\nu(\text{CH}_2)$ , 1361.4  $\nu(\text{NO}_3)$  and 1021.3  $\text{cm}^{-1}$   $\nu(\text{NO}_3)$ .

*Computational details:* Optimization of the complex was done with DFT method, more specifically B3LYP functional and 6-31G(d,p) basis set. For the zinc atoms lanl2dz basis set was used with effective core potential (ECP) for inner electrons.

## RESULTS AND DISCUSSION

Complexation of *tpmc* with  $\text{Zn}^{2+}$  ions was examined by conductometric titration method in ethanol and methanol solution. Based on previously reported conductometric results [2] in acetonitrile and aqueous solution and obtained results for titration in ethanol and methanol solution (Figure 1), for synthesis was chosen methanol due to distinct breaking point which indicate a formation of a relatively stable 2:1 ( $\text{Zn}:\text{tpmc}$ ) complex.

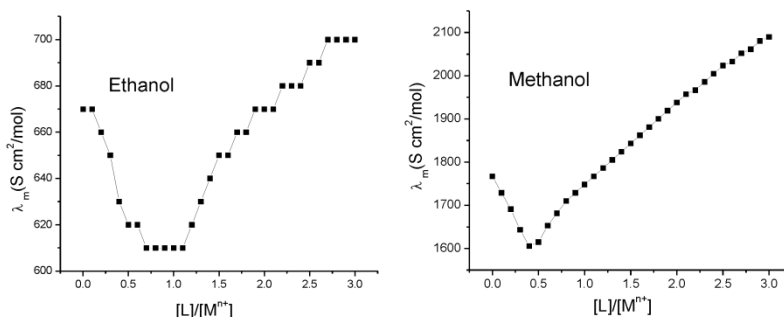


**Figure 1.** Plot of molar conductance,  $\Lambda$ , vs.  $V$  (cm<sup>3</sup> of added ligand) for the binding of  $Zn^{2+}$  by *tpmc* in ethanol and methanol at 20 °C.

The complex was synthesized by the reaction of zinc(II)-nitrate hexahydrate and *tpmc* in 2:1 mole ratio. The results of elemental analysis are consistent with a binuclear structure of the obtained complex with the proposed formula  $[Zn_2(tpmc)NO_3](NO_3)_3 \cdot CH_3OH$ . In the IR spectrum of complex (Fig. 2b), a weak broad band at 2868.9 cm<sup>-1</sup> originates from the stretching vibrations of CH, and two medium bands at 1477.9 and 1445.1 cm<sup>-1</sup> from CH<sub>2</sub> bending vibrations. Sharp band at 1589.4 cm<sup>-1</sup> ascribed to skeletal vibration of the pyridine ring in the spectrum of free *tpmc* (Fig. 2a) is dislocated to 1610.1 cm<sup>-1</sup> upon coordination [3]. Strong broad bands at 1361.4-1295.3 cm<sup>-1</sup> are assigned to coordinated nitrate, while a very strong band at 1021.3 cm<sup>-1</sup> is assigned to ionic nitrate [5].

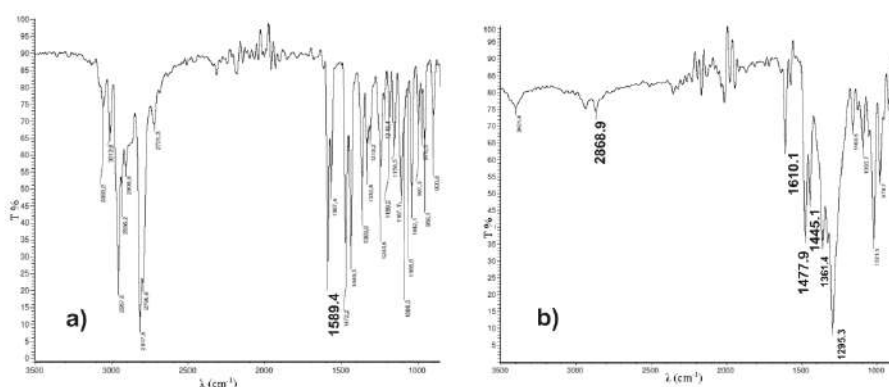


**Figure 2.** IR spectra of a) *tpmc* b)  $[Zn_2(tpmc)NO_3](NO_3)_3 \cdot CH_3OH$ .

DFT calculations and molecular modeling were employed for the optimization of the complex structure (Figure 3).

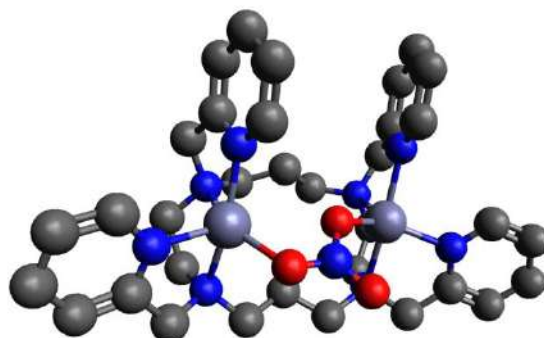


**Figure 3.** Optimized structure of  $[\text{Zn}_2(\text{tpmc})\text{NO}_3]^{3+}$  complex ion. Colors: violet-zinc; red-oxygen; blue-nitrogen; grey-carbon

### CONCLUSION

New binuclear Zn (II) complex with octaazamacrocyclic ligand, *tpmc*, was synthesized, characterized and theoretically optimized structure was proposed. The conductometric technique is convenient for investigation the complex formation between macrocyclic ligands and metallic ions because it provides voluble information for determining the most convenient solvent for synthesis and metal/ligand mole ratio.

### Acknowledgment

Financial support for this study was granted by the Ministry of Science and Technological Development of the Republic of Serbia, Project Number 45022.

### REFERENCES

- [1] T. M. Hunter, I. W. McNae, X. Liang, J. Bella, S. Parson, M. D. Walkinshaw, P. J. Sadler, PNAS, 2005, **102**, 2288.
- [2] B. B. Petković, M. Milčić, D. Stanković, I. Stambolić, D. Manojlović, V. M. Jovanović, S. P. Sovilj, Electrochim. Acta, 2013, **89**, 680.
- [3] G. Vučković, M. Antonijević-Nikolić, S. B. Tanasković, V. Živković-Radovanović, J. Serb. Chem. Soc., 2011, **76**, 719. M. Antonijević-Nikolić, J. Antić-Stanković, S. B. Tanasković, M. J. Korabik, G. Gojgić-Cvijović, G. Vučković, J. Mol. Struct., 2013, **297**, 1054–1055.
- [4] S. Chandrasekhar, W. L. Waltz, L. Prasad, J. W. Quail, Can. J. Chem., 1997, **75**, 1363.
- [5] M. Gaye, F.B. Tamboura, A.S. Sall, Bull. Chem. Soc. Ethiop., 2003, **17**, 27.

## OPTICAL RESPONSE AS FUNCTION OF MIXED COMPLEX FORMATION OF BENZO-CROWN-CONTAINING 4-STYRYLBIPYRIDINE WITH ALKALINE-EARTH AND TRANSITIONAL CATIONS

N. E. Shepel, O. A. Fedorova and Yu. V. Fedorov

*Nesmeyanov Institute of Organoelement Compounds RAS, Vavilova str. 28, 119991, Moscow, Russia. (nick7inc@ineos.ac.ru)*

### ABSTRACT

We studied 15-crown-5 ether mono- and bis(styryl) derivative of 2,2'-bipyridine as a scaffold to construct photoresponsive complexes with  $\text{Cd}^{2+}$ ,  $\text{Zn}^{2+}$ ,  $\text{Hg}^{2+}$ ,  $\text{Co}^{2+}$ ,  $\text{Fe}^{2+}$ ,  $\text{H}^+$ ,  $\text{Ba}^{2+}$ ,  $\text{Ca}^{2+}$  in MeCN. Absorption and emission spectroscopy, 1-D and 2-D  $^1\text{H-NMR}$  spectroscopy and ESI-mass spectrometry were used in our investigation. Optical properties of one dimensional (1D)  $\text{Ca}^{2+}$ -containing and octahedral 3D  $\text{Zn}^{2+}$ -containing complexes with crowned styryl derivatives of 2,2'-bipyridine were described. Bimetallic  $\text{Ca}^{2+}$ ,  $\text{Zn}^{2+}$ -containing complexes possess well-defined structures and particular optical characteristics. Properties of the zinc polypyridyl complexes are modified by intermolecular interactions between the crown ether center and the metal ions, so they are potentially useful in the preparation of chemical sensors

### INTRODUCTION

Bipyridines and their derivatives are of particular interest because they are employed as chelating ligands in catalysis [1], coordination and supramolecular chemistry [2], molecular electronics and optoelectronic devices [3]. The study of interactions between sulfur analogues of thiacycrown ethers containing sulfur atoms directly attached to the 2,2'-bipyridine rings and various inorganic or organic substrates were analyzed in [4]. Besides the well-known complexation of metal ions, the  $\text{C}_2$ -symmetric 2,2'-bipyridine crown ethers have been designed recently for the enantiomeric recognition of amino acid derivatives and chiral organic ammonium salts [5]. Coordination chemistry is a powerful tool for building 3D arrangements. Bipyridyl ligands are excellent building blocks for the construction of octahedral ( $\text{Fe}^{2+}$ ,  $\text{Ru}^{2+}$ ,  $\text{Ni}^{2+}$ ,  $\text{Zn}^{2+}$ ) [6] or pseudo-tetrahedral ( $\text{Cu}^+$ ,  $\text{Ag}^+$ ,  $\text{Zn}^{2+}$ ) [7] complexes.

Two binding centers of different nature in ligands **1** and **2** (Fig. 1) exhibit specific affinity to different metal cations. The crown ether moieties prefer

to bind with alkaline and alkaline-earth metal cations resulting in hypsochromic shift of long wavelength absorption band. On the contrary bipyridine moiety binds with transition metal ions leading to bathochromic shift of long wavelength absorption band.

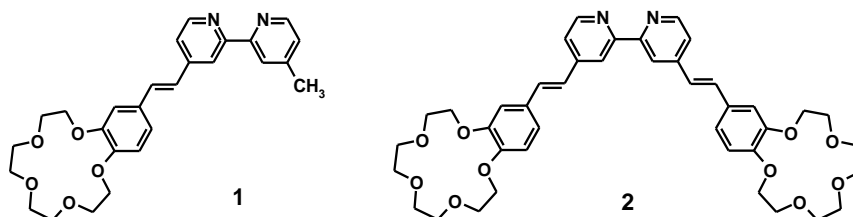


**Figure 1.** Structure of *mono-* and *bis-* crown-containing 4-styryl bipyridine.

## EXPERIMENTAL

It was found that **1** and **2** form with  $\text{Zn}^{2+}$ ,  $\text{Cd}^{2+}$ ,  $\text{Co}^{2+}$ ,  $\text{Hg}^{2+}$ ,  $\text{Fe}^{2+}$  ions mainly cell-type complex due to metal ion coordination via bipyridine moiety with  $\text{Lig}_3 \cdot (\text{M}^{2+})_1$  stoichiometry (for  $\text{Zn}^{2+}$ ,  $\text{Cd}^{2+}$  and  $\text{Co}^{2+}$  ions) and with  $\text{Lig}_2 \cdot (\text{M}^{2+})_1$  stoichiometry (for  $\text{Hg}^{2+}$  and  $\text{Fe}^{2+}$  ions). The presence of two coordination centers of different nature in **1** facilitates mixed complex formation when both of two types cations: transitional and alkaline-earth (e.g.  $\text{Zn}^{2+}$  and  $\text{Ca}^{2+}$ ) cations are presented in a solution at the same time.

At first, the complex  $\mathbf{1}_3 \cdot (\text{Zn}^{2+})_1$  was prepared and its composition confirmed by UV-Vis spectroscopy (Fig. 2, curve 2). The addition of  $\text{Ca}(\text{ClO}_4)_2$  to the complex  $\mathbf{1}_3 \cdot (\text{Zn}^{2+})_3$  causes the formation of  $(\text{Ca}^{2+})_1 \cdot \mathbf{1}_3 \cdot (\text{Zn}^{2+})_1$  at first (Fig. 2, curve 3), but on increasing  $[\text{Ca}^{2+}]$  up to 100 excess, the formation of the complexes with increasing content of  $\text{Ca}^{2+}$  can be supposed on the basis of the appearance of a novel band shifted relative to one of previous complex (Fig. 2, curve 4). Electrospray ionization mass spectrometry (ESI-MS) provides direct and straightforward access to accurate determination of complex

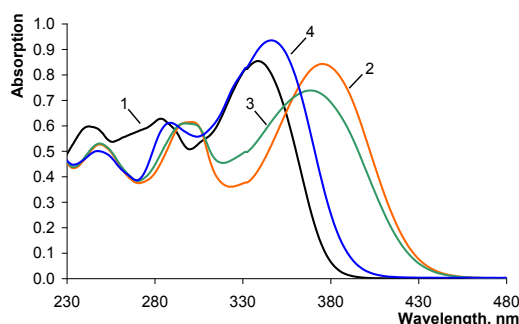


**Figure 2.** Absorption spectra of **1** as free ligand (**1**) and its complexes  $\mathbf{1}_3 \cdot (\text{Zn}^{2+})$  (**2**),  $(\text{Ca}^{2+})_1 \cdot \mathbf{1}_3 \cdot (\text{Zn}^{2+})$  (**3**) and  $(\text{Ca}^{2+})_2 \cdot \mathbf{1}_2 \cdot (\text{Zn}^{2+})$  (**4**) in  $\text{CH}_3\text{CN}$  calculated from spectrophotometric titration data.

compositions in CH<sub>3</sub>CN solutions containing different **1** : **metal ion** ratios. NMR spectroscopy also provides additional data for the analysis.

## RESULTS AND DISCUSSION

The formation of complexes (Ca<sup>2+</sup>)<sub>2</sub>·**1**<sub>3</sub>·(Zn<sup>2+</sup>)<sub>1</sub> and (Ca<sup>2+</sup>)<sub>3</sub>·**1**<sub>3</sub>·(Zn<sup>2+</sup>)<sub>1</sub> as far as (Ca<sup>2+</sup>)<sub>2</sub>·**1**<sub>2</sub>·(Zn<sup>2+</sup>)<sub>1</sub> could be expected. The stability constants evaluation from spectrophotometric titration data looks extremely difficult in this case due to the presence of multiple complexes in solution at the same time. On fitting spectrophotometric titration data we limited the number of mixed complexes taking into account by two with minimal and maximal Ca<sup>2+</sup> content. The first one was (Ca<sup>2+</sup>)<sub>1</sub>·**1**<sub>3</sub>·(Zn<sup>2+</sup>)<sub>1</sub> and the second one was (Ca<sup>2+</sup>)<sub>3</sub>·**1**<sub>3</sub>·(Zn<sup>2+</sup>)<sub>1</sub> or (Ca<sup>2+</sup>)<sub>2</sub>·**1**<sub>2</sub>·(Zn<sup>2+</sup>)<sub>1</sub>.

The best fit was obtained for scheme included (Ca<sup>2+</sup>)<sub>1</sub>·**1**<sub>3</sub>·(Zn<sup>2+</sup>)<sub>1</sub> and (Ca<sup>2+</sup>)<sub>2</sub>·**1**<sub>2</sub>·(Zn<sup>2+</sup>)<sub>1</sub>. The stability constants of mixed complexes calculated from spectrophotometric titration data are presented in Table 1.

The initial ligand *E-1* and its complexes can be subjected to the reversible reaction of *E-Z*-isomerization. The quantum yields of the samples were calculated. For the complex (*E-1*)<sub>3</sub>·(Zn<sup>2+</sup>)<sub>1</sub> the photoisomerization was not observed. Monoionic Zn<sup>2+</sup> – complexes demonstrate quenching of fluorescence (Table 1). The possible explanation could be that the Zn<sup>2+</sup>-complexes is LMCT process occurring from lone pair of oxygen atoms in 15-crown-5 moiety to the Zn<sup>2+</sup> cation capsulated by heterocyclic residues. The addition of the Ca<sup>2+</sup> cations causes the formation of complexes with macrocyclic cavity through the coordination with oxygen heteroatoms. This does the LMCT process to be impossible. In heteroionic Zn<sup>2+</sup>, Ca<sup>2+</sup> – complex the relaxation processes different from LMCT become possible.

**Table 1.** Stability constants of complexes of **1** and **2** with Ca<sup>2+</sup> and Zn<sup>2+</sup> cations and steady-state fluorescence quantum yields (CH<sub>3</sub>CN, 25°C, λ<sub>excit.</sub>=300 nm).

Ligand or complex	Stability const. (lgK)	λ <sub>max</sub> <sup>fl</sup> (nm)	φ <sub>fl</sub> × 10 <sup>-2</sup>
<b>1</b>		444	6.0
<b>1</b> ·Ca <sup>2+</sup>	5.37±0.04	400, 477	2.6
<b>1</b> ·(Ca <sup>2+</sup> ) <sub>2</sub>	8.31±0.03	475	4.2
<b>1</b> <sub>3</sub> ·Zn <sup>2+</sup>	19.6±0.4	577	1.0
Ca <sup>2+</sup> · <b>1</b> <sub>3</sub> ·Zn <sup>2+</sup>	24.3±0.1	493	3.4
(Ca <sup>2+</sup> ) <sub>2</sub> · <b>1</b> <sub>2</sub> ·Zn <sup>2+</sup>	21.4±0.1	493	6.8
<b>2</b>		447	8.2
<b>2</b> ·Ca <sup>2+</sup>	6.7±0.4	437	2.4
<b>2</b> ·(Ca <sup>2+</sup> ) <sub>2</sub>	11.2±0.4	406	3.1
<b>2</b> <sub>3</sub> ·Zn <sup>2+</sup>	21.4±0.4	559	0.3
Ca <sup>2+</sup> · <b>2</b> <sub>3</sub> ·Zn <sup>2+</sup>	25.26±0.02	533	2.9
(Ca <sup>2+</sup> ) <sub>2</sub> · <b>2</b> <sub>2</sub> ·Zn <sup>2+</sup>	21.28±0.06	519	3.5

Thus, *E-Z*- photoisomerization of  $(\text{Ca}^{2+})\cdot(\text{E-1})_3\cdot(\text{Zn}^{2+})_1$  proceeds with high enough quantum yields in both directions. The fluorescence intensity of  $\mathbf{1}_3\cdot(\text{Zn}^{2+})_1$  centered at 577 nm was hypsochromically shifted, and it increased significantly upon the formation of heteroionic  $\text{Zn}^{2+}$ ,  $\text{Ca}^{2+}$ -complex. Similar changes of fluorescence were observed in the case of complexes of ligand 2.

## CONCLUSION

Absorbance and fluorescence maxima of ligands can be shifted to the long wavelength region by addition of  $\text{Zn}^{2+}$  cations as a result of the coordination with heterocyclic residues of three ligands. Receptors provide the shift of LAB to short wavelength region while binding of  $\text{Ca}^{2+}$  through macrocycle moiety. In addition, characteristic fluorescence responses of  $\mathbf{1}_3\cdot(\text{Zn}^{2+})_1$  and  $\mathbf{2}_3\cdot(\text{Zn}^{2+})_1$  upon the addition of  $\text{Ca}^{2+}$  leading to the inhibition of LMCT process can be detected by naked eye in an organic solution. Thus, the complexes  $\text{L}_3\cdot(\text{Zn}^{2+})_1$  can be considered as fluorescent probes for metal ions able to coordinate with crown ether moiety. Therefore, the binding of metal ions with crown ether of  $\text{L}_3\cdot(\text{Zn}^{2+})_1$  particles induced not only emission enhancement but also an emission shift due to the binary inhibition effect of the LMCT and ICT mechanisms. What is more, we believe that the present 2,2'-bipyridine scaffold is quite useful for the construction of various types of receptors by introducing different recognition sites at 4- and 4'-positions.

## Acknowledgement

This work was supported by RSF (Russian Science Foundation, project No 16-13-10226).

## REFERENCES

- [1] G. Chelucci, R. P. Thummel, *Chem. Rev.*, 2002, **102**, 3129.
- [2] J.-M. Lehn, *Supramolecular Chemistry. Concepts and Perspectives*, VCH: Weinheim, 1995.
- [3] D. Pomeranc, V. Heitz, J.-C. Chambrom, J.-P. Savage, *J. Am. Chem. Soc.*, 2001, **123**, 12215.
- [4] C.-F. Chow, B.K.W. Chiu, M.H.W. Lam, W.-Y. Wong, *J. Am. Chem. Soc.*, 2003, **125**, 7802.
- [5] A. A. Marti, C. A. Puckett, J. Dyer, N. Stevens, S. Jockusch, J. Ju, J. K. Barton, N.J. Turro, *J. Am. Chem. Soc.*, 2007, **129**, 8680.
- [6] H. D. Batey, A.C. Whitwood, A.-K. Duhme-Klair, *Inorg. Chem.*, 2007, **46**, 6516.
- [7] B. C. Tzeng, Y.C. Huang, G. H. Lee, *Inorg. Chem. Commun.*, 2008, **11**, 557.

## PREPARATION AND STUDY OF AZAMACROCYCLIC Cu(II) AMINOCARBOXYLATE COMPLEXES

M. Antonijević Nikolić<sup>1</sup>, S. B. Tanasković<sup>2</sup> and V. Živković Radovanović<sup>3</sup>

<sup>1</sup>Higher Technological School of Professional Studies, 15000 Šabac, Serbia

<sup>2</sup>Faculty of Pharmacy, University of Belgrade,

Vojvode Stepe 450, 11000 Belgrade, Serbia

<sup>3</sup>Faculty of Chemistry, University of Belgrade, P.O.Box 118, 11158, Serbia

### ABSTRACT

New cationic complexes of Cu(II) with bridged aminocarboxylates: glycine and alanine, as well as octaazamacrocyclic ligand (*N,N',N'',N'''*-tetrakis(2-pyridylmethyl)-1,4,8,11-tetraazacyclotetradecane), tpmc, general formula [Cu<sub>2</sub>(L)tpmc](ClO<sub>4</sub>)<sub>4</sub>·Y, (**1**): L=glycine, Y=2H<sub>2</sub>O and (**2**): L=alanine, Y=CH<sub>3</sub>CN were synthesized. The composition of the complexes has been assumed on the basis of the molar electrical conductivity and elemental analysis (C, H, N). Characterization of the complexes was performed by UV/Vis and FTIR spectroscopy and the preliminary results of the X-ray analysis. In both complexes is assumed binuclear structure of the complex cation, where Cu(II) ions from the same tpmc unit connected via OCO group. The amino group remains uncoordinated.

### INTRODUCTION

A great number of mono-, bi- and tetranuclear mixed-ligand Cu(II) and Co(II) complexes containing pendant tpmc (*N,N',N'',N'''*-tetrakis(2-pyridylmethyl)-1,4,8,11-tetraazacyclotetradecane) and one or two additional ligands of various types were described. Carboxylate group as bridged ligand is present in several metalloenzymes. Transition metals could coordinate with aminocarboxylato ligands on variety modes. In the most described complexes, aminocarboxylato ligands are bonded in one of many modes using N: as N-monodentate; N,O- bonded as chelate in mononuclear complexes or bridging ligand between two metallic centers. In some binuclear complexes one or both oxygens are included in coordination but -NH<sub>2</sub> group rested uncoordinated: unsymmetrically, symmetrically or in a combined chelate-bridged way. In binuclear Co(II)tpmc complexes glycine, *N*-methylglycine, *N,N*-dimethylglycine, (*S*)-alanine, (*S*)-aminobutyric acid,  $\alpha$ -aminoisobutyric acid,  $\beta$ -aminoisobutyric acid,  $\beta$ -aminobutyric acid and (*S*)-phenylalanine, aminocarboxylate anions are coordinated through COO group [1, 2]. In these complexes tpmc adopted a boat conformation with an

*exo* coordination mode. Now, we prepared analogous mixed ligand Cu(II) complexes with tpmc and additional glycinate and alaninate ligands and determined their structure.

## EXPERIMENTAL

### Preparation

Ligand tpmc and complex  $[\text{Cu}_2\text{tpmc}](\text{ClO}_4)_4$  were prepared according to the literature procedure [3,4].

### General procedure

Complexes with general formula  $[\text{Cu}_2(\text{L})\text{tpmc}](\text{ClO}_4)_4 \cdot \text{Y}$ , (**1**): L=glycine, Y=2H<sub>2</sub>O and (**2**): L=alanine, Y=CH<sub>3</sub>CN were obtained by reaction  $[\text{Cu}_2\text{tpmc}](\text{ClO}_4)_4$  (0,18 mmol) with corresponding amino acids (0,28 mmol) in mixture CH<sub>3</sub>CN/H<sub>2</sub>O under reflux about 3 h on the 80°C in molar ratio 1:1,5. pH of the aqueous solution of amino acid before adding to the reaction mixture was adjusted to pH= 6 with 0.1 M NaOH. Blue reaction solution was cooled to room temperature and left in the fridge. After a few days blue microcrystalline products are separated by filtration.

$[\text{Cu}_2(\text{gly})\text{tpmc}](\text{ClO}_4)_4 \cdot 2\text{H}_2\text{O}$ , Yield 78 %. Anal. Found C 36.30; H 4.73; N 10.66. Calcd. for C<sub>36</sub>H<sub>53</sub>O<sub>20</sub>N<sub>9</sub>Cu<sub>2</sub>Cl<sub>4</sub> (FW = 1200.88) C 36.00; H 4.45; N 10.49. Solubility (t=20±2 °C) wellsoluble in CH<sub>3</sub>CN, DMSO, (CH<sub>3</sub>)<sub>2</sub>CO, H<sub>2</sub>O and DMF, insoluble in EtOH and CH<sub>3</sub>OH.

$[\text{Cu}_2(\text{ala})\text{tpmc}](\text{ClO}_4)_4 \cdot \text{CH}_3\text{CN}$ , Yield 81 %. Anal. Found C 37.10; H 5.00; N 11.58. Calcd. for C<sub>37</sub>H<sub>54</sub>O<sub>18</sub>N<sub>10</sub>Cu<sub>2</sub>Cl<sub>4</sub> (FW = 1195.86) C 37.16; H 4.55; N 11.71. Solubility (t=20±2 °C) wellsoluble in CH<sub>3</sub>CN, DMSO, (CH<sub>3</sub>)<sub>2</sub>CO and DMF, insoluble in EtOH, CH<sub>3</sub>OH and H<sub>2</sub>O.

## RESULTS AND DISCUSSION

The composition of the complexes is determined on the basis of elemental analysis and electrical conductivity. They corresponded to binuclear complexes. The conductivity of the complexes corresponds to the data from the literature for the type of electrolyte 1:4 [4]. The electronic spectra of both complexes corresponds to the position of the absorption maxima d-d transitions for one unpaired electron (Table 1). By comparing the spectra of other electronic Cu(II) carboxylato complex, it was assumed that the aminocarboxylate coordinated over the carboxyl groups. This maximum position corresponds to the chromophore CuN<sub>4</sub>O. The values of extinction are in accordance with the size of the complexes. In IR spectra (ATR technique) of both complexes the following bands were found: ~1610 cm<sup>-1</sup> from skeletal vibrations of the pyridine (sharp), ~1100 cm<sup>-1</sup> from  $\nu(\text{ClO}_4^-)$  (intensive) and at 630 cm<sup>-1</sup> from  $\delta(\text{ClO}_4^-)$  (medium) and at 3441 for the  $\nu(\text{O-H})$  from crystal water in A (medium). In the spectra of the complexes

there is a band around  $470\text{ cm}^{-1}$  which originates from  $\nu(\text{C-N})$  and a band about  $420\text{ cm}^{-1}$  from  $\nu(\text{Cu-O})$ . The comparison of the spectra of the complexes and corresponding amino acids in the range  $1670\text{--}1300\text{ cm}^{-1}$ , where  $\nu_{\text{asym}}(\text{OCO}^-)$  and  $\nu_{\text{sym}}(\text{OCO}^-)$  appear, is given in Table 2.

**Table 1.** Electronic spectral data for the complexes and molar electrical conductivity

complex	$\lambda_{\text{max}}$ [nm]	$\epsilon$ [ $\text{dm}^3\text{mol}^{-1}\text{cm}^{-1}$ ]	$\Lambda_{\text{M}}$ [ $\text{Scm}^2\text{mol}^{-1}$ ] (electrolyte type)
$[\text{Cu}_2\text{tpmc}](\text{ClO}_4)_4$ [4]	670	312	510 (1:4)
$[\text{Cu}_2(\text{gly})\text{tpmc}](\text{ClO}_4)_4 \cdot 2\text{H}_2\text{O}$	645	396	558(1:4)
$[\text{Cu}_2(\text{ala})\text{tpmc}](\text{ClO}_4) \cdot \text{CH}_3\text{CN}$	648	393	570 (1:4)

**Table 2.** IR spectral data of  $\nu(\text{OCO}^-)$  for the free amino acids and their complexes

complex	$\nu_{\text{asym}}$	$\nu_{\text{sym}}$	$\Delta\nu$
$[\text{Cu}_2(\text{gly})\text{tpmc}](\text{ClO}_4)_4 \cdot 2\text{H}_2\text{O}$	1585	1412	173
glycine	1594	1413	181
$[\text{Cu}_2(\text{ala})\text{tpmc}](\text{ClO}_4) \cdot \text{CH}_3\text{CN}$	1572	1382	190
alanine	1592	1412	180

The change of the  $\Delta\nu$  value ( $\nu_{\text{asym}} - \nu_{\text{sym}}$ ) of the complex in comparison with the value for the aminocarboxylate ligand confirms that the ligand is coordinated to the metal through  $\text{COO}^-$  group. It is obvious that  $\nu_{\text{asym}}$  and  $\nu_{\text{sym}}$  are shifted toward lower values in comparison with the corresponding aminocarboxylate ligands, which is the case when  $\text{COO}^-$  participates in coordination is achieved through both oxygens [1,2]. In complexes, both oxygens of  $\text{COO}^-$  are engaged in coordination thus forming a bridge between two Cu(II) from the same tpmc unit (Fig. 1).

Actually, the results of preliminary X-ray structure analysis showed that aminocarboxylate act as bridge ligands with  $\text{COO}^-$  group bridging two Cu atoms. In the binuclear complexes each copper(II) ion is pentacoordinated with four N atoms (two from pyridyl groups and two from cyclam) and O atom from the aminocarboxylate ligand (Figure 1).

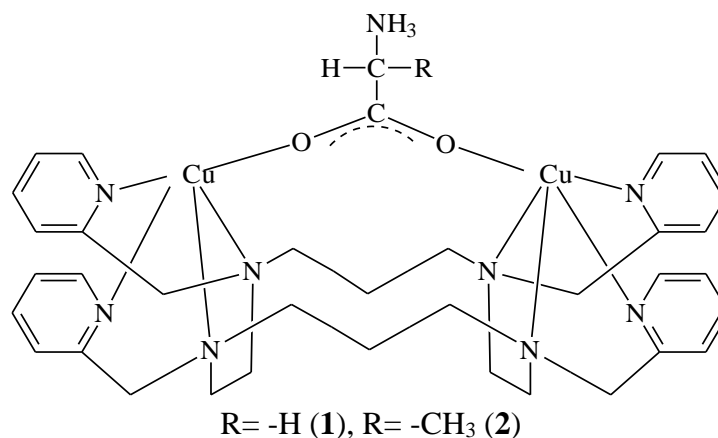


**Figure 1.** Suggested structure of the complex cation  $[\text{Cu}_2(\text{L})\text{tpmc}]^{4+}$ , L=glicine (1) or alanine (2)

### CONCLUSION

Two binuclear Cu(II) complexes with octaazamacrocyclic ligand (tpmc) and glycine or alanine were isolated in pure state. Their composition and geometries were assumed based on elemental analysis, electrical conductivity and spectral properties, as well as by the preliminary results of the X-ray analysis. For complexes the same exo coordination of each Cu(II) ion with azamacrocyclic ligand engaging two pyridine N and two cyclam's N atoms, and O,O'-bonded COO<sup>-</sup> group from bridged amino acids is proposed. Amino group of the amino acids not participate in the coordination of metal ions.

### Acknowledgement

We gratefully acknowledge to the Ministry of Education and Science of the Republic of Serbia (Project No. 172014).

### REFERENCES

- [1] G. Vučković, D. Opsenica, S. P. Sovilj, D. Poleti, M. Avramov-Ivić, *J. Coord. Chem.*, 1997, **42**, 241-251; b) G. Vučković, D. Opsenica, S. P. Sovilj, D. Poleti, *J. Coord. Chem.*, 1999, **47**, 331-339
- [2] G. Vučković, S. B. Tanasković, M. Antonijević-Nikolić, V. M. Živković Radovanović, G. Gojgić-Cvijović, *J. Serb. Chem. Soc.*, 2009, **74**, 629-640
- [3] S. Chandrasekhar, W. L. Waltz, L. Prasad, J. W. Quail, *Can. J. Chem.*, 1997, **75**, 1363-1374
- [4] E. Asato, H. Toftlund, S. Kida, M. Mikuriya, K. S. Murray, *Inorg. Chim. Acta*, 1989, **165**, 207-214.

## PREPARATION AND STUDY OF TWO NEW MIXED LIGAND Co(II) COMPLEXES

S. B. Tanasković<sup>1</sup>, M. Antonijević Nikolić<sup>2</sup>, B. Dražić<sup>1</sup>  
and V. Živković Radovanović<sup>3</sup>

<sup>1</sup> Faculty of Pharmacy, University of Belgrade, Vojvode Stepe 450, 11000  
Belgrade, Serbia

<sup>2</sup> Higher Technological School of Professional Studies, 15000 Šabac, Serbia

<sup>3</sup> Faculty of Chemistry, University of Belgrade, P.O.Box 118, 11158, Serbia

### ABSTRACT

A new complexes with general formula  $[\text{Co}_2(\text{X})_2\text{tpmc}](\text{BF}_4)_2 \cdot \text{Y}$  ( $\text{X} = \text{F}^-$ ,  $\text{Y} = \text{CH}_3\text{CN}$ ;  $\text{X} = \text{Br}^-$ ,  $\text{Y} = \text{H}_2\text{O}$ ;  $\text{tpmc} = N,N',N'',N'''$ - tetrakis(2-pyridylmethyl)-1,4,8,11-tetraazacyclotetradecane), were isolated and their composition were proposed by: elemental analysis (C, H, N), molar conductivity, UV/Vis and FTIR spectroscopy. Then, we compared synthesized complexes with early described chloro analogous. In both complexes proposed *chair* conformation of macrocycle. Complexes were also preliminary assayed toward some microorganisms together with the ligands, starting simple salts and solvents as test substances. In some cases certain antimicrobial activity of the complexes was detected.

### INTRODUCTION

Polyazamacrocyclic ligands and their metal complexes are an attractive field of investigation due to their numerous unusual structural and biological properties. Some of the models for the active centers of metalloenzymes, show potentially are bioactive and could be used as drugs, catalysts etc.

Mixed ligand Co(II) complexes with octadentate ligand with 2-pyridylmethyl groups as pendant arms, *tpmc* (Fig. 1) and various monodentate or helate ligands were intensively studied [1]. Although the majority of these compounds was air stable and for many of them *chair* conformation was proposed, it was difficult to isolate the suitable single crystals. Up to now the X-ray analysis was performed for only two of them:  $\mu$ -oxalato complex having *tpmc* in boat conformation [1b] and  $[\text{Co}_2(\text{Cl})_2\text{tpmc}](\text{BF}_4)_2$  complex with macrocycle in *chair* conformation [2]. The geometry around each Co(II) in the second complex is distorted trigonal bipyramide formed by two cyclam nitrogen atoms and two nitrogens from pyridyl groups (*exo* coordination). The fifth coordination site is occupied by chloro anion. Continuing these investigations, here we report the preparation

of fluoro and bromo analogous and some of their physical and chemical properties.

### EXPERIMENTAL

Ligand *tpmc* was prepared and purified as described in the literature [3]. The other chemicals:  $\text{CoF}_2$ ,  $\text{CoBr}_2$  and  $\text{NaBF}_4$  as *p.a.* commercial products were provided by Sigma Aldrich, USA.

*General procedure for synthesis two new complexes:*

#### $[\text{Co}_2(\text{X})_2\text{tpmc}](\text{BF}_4)_2 \cdot \text{Y}$ :

(complex A:

$\text{X} = \text{F}^-$ ,  $\text{Y} = \text{CH}_3\text{CN}$ ;

complex B:

$\text{X} = \text{Br}^-$ ,  $\text{Y} = \text{H}_2\text{O}$ ),

$\text{CoF}_2/\text{CoBr}_2$  (0.048g/  
0.109g, 0.5mmol) were dissolved in minimum amount of  $\text{CH}_3\text{OH}$  and after that, a suspension of *tpmc* (0.141g, 0.25 mmol) in  $\text{CH}_3\text{OH}$  was added.

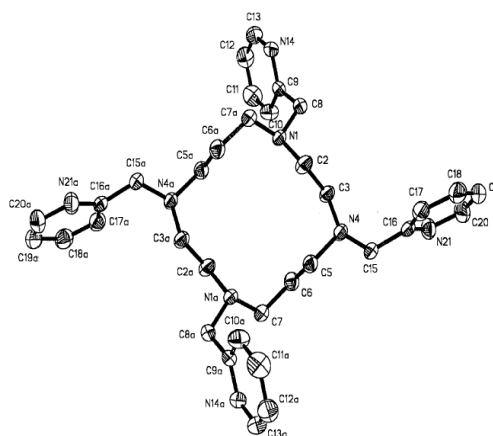


**Figure 1.** Structure of octaazamacrocyclic ligand *tpmc*

Reaction mixture was continuously stirred and refluxed on water bath ( $80^\circ\text{C}$ ) for the next 2 hours, concentrated to 1/4 of initial volume and left in refrigerator overnight. Microcrystalline product was separated by suction, dried at room temperature, washed properly with small portions of cold water, and the procedure is repeated until pure product is obtained (checked using microscope).

**Complex A:**  $[\text{Co}_2(\text{F})_2\text{tpmc}](\text{BF}_4)_2 \cdot \text{CH}_3\text{CN}$ . Yield: 48%; Anal. Calcd. for  $\text{C}_{36}\text{H}_{47}\text{N}_9\text{Co}_2\text{B}_2\text{F}_{10}$  (FW = 935.306): C, 46.23; H, 5.07; N, 13.48. Found: C, 46.63; H, 5.17; N, 13.11.

**Complex B:**  $[\text{Co}_2(\text{Br})_2\text{tpmc}](\text{BF}_4)_2 \cdot \text{H}_2\text{O}$ . Yield: 73%; Anal. Calcd. for  $\text{C}_{34}\text{H}_{46}\text{N}_8\text{Co}_2\text{Br}_2\text{B}_2\text{F}_8$  (FW = 1034.052): C, 39.49; H, 4.48; N, 10.84. Found: C, 39.16; H, 4.62; N, 10.74.

*Analytical methods:* Elemental analyses were performed by standard methods in the Centre for instrumental analyses ICTM in Belgrade. Electronic absorption spectra of complex solution in  $\text{CH}_3\text{CN}$  ( $c=1 \cdot 10^{-3}$  mol/dm<sup>3</sup>) were recorded on GBC UV/Vis spectrophotometer Cintra 20. IR spectra were recorded on NICOLET 6700 FTIR (ATR technique) in the range  $400\text{-}4000\text{cm}^{-1}$ . Molar conductivities were measured on conductometer

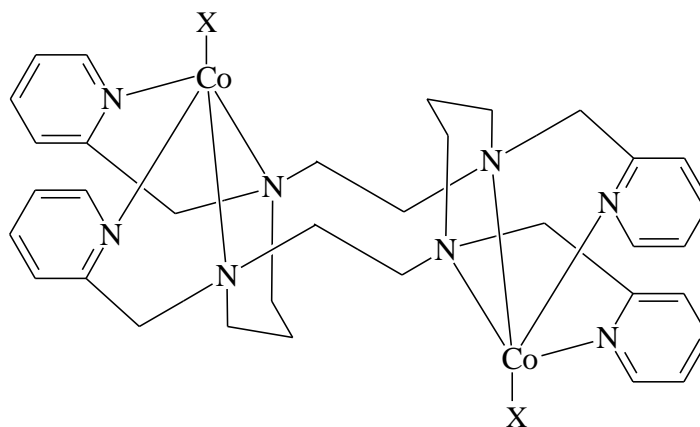
HANNA instruments HI 8820N (at  $20 \pm 2^\circ\text{C}$ ) in  $\text{CH}_3\text{CN}$  ( $c=1 \cdot 10^{-3}$  mol/dm<sup>3</sup>).

## RESULTS AND DISCUSSION

The compounds A and B are partially soluble in DMSO and  $\text{CH}_3\text{CN}$ , but insoluble in  $\text{CH}_3\text{OH}$ ,  $\text{C}_2\text{H}_5\text{OH}$  and cold distilled water. The complexes were stable up to  $260^\circ\text{C}$ . Molar electrical conductivity in  $\text{CH}_3\text{CN}$  of  $265 \text{ Scm}^2\text{mol}^{-1}$  is in agreement with a 1:2 electrolyte type (literature range is  $220\text{-}300 \text{ Scm}^2\text{mol}^{-1}$ ) [4].

UV/Vis spectrum of complexes  $[\text{Co}_2(\text{F})_2\text{tpmc}](\text{BF}_4)_2 \cdot \text{CH}_3\text{CN}$  and  $[\text{Co}_2(\text{Br})_2\text{tpmc}](\text{BF}_4)_2 \cdot \text{H}_2\text{O}$  in  $\text{CH}_3\text{CN}$  is typical for a high-spin Co(II) complexes exhibiting maxima at 483 nm ( $\epsilon=119 \text{ dm}^3\text{mol}^{-1} \text{ cm}^{-1}$ ), 549 nm ( $\epsilon=143 \text{ dm}^3\text{mol}^{-1} \text{ cm}^{-1}$ ) and 589 nm ( $\epsilon=138 \text{ dm}^3\text{mol}^{-1} \text{ cm}^{-1}$ ). The absorption maximum for CT transitions is at  $\sim 220\text{-}225 \text{ nm}$  ( $\epsilon=5500\text{-}6700 \text{ dm}^3\text{mol}^{-1} \text{ cm}^{-1}$ ) [5a].

The IR spectrum of the complexes display characteristic bands ( $\text{cm}^{-1}$ ):  $\nu(\text{C-H})$  at 2952 (medium),  $\nu(\text{BF}_4^-)$  at 1072 (strong, sharp); skeletal pyridine vibration from tpmc at 1605 (strong) suggesting coordination of tpmc and the presence of  $\text{BF}_4^-$  as counter ion [5b]. From all presented data and using models the more probable geometry for both prepared complexes are shown in Scheme 1.



**Scheme 1.** Proposed geometry of the complex cation  $[\text{Co}_2(\text{X})_2\text{tpmc}]^{2+}$  ( $\text{X} = \text{F}^-, \text{Br}^-$ )

Both complexes, all ligands and solvents were preliminary also tested against some Gram(+) bacteria, in DMSO/ $\text{H}_2\text{O}$  and certain bacteriostatic activity is detected in both cases.

## CONCLUSION

In this paper two new binuclear cationic Co(II) complexes with octaazamacrocyclic ligand tpmc and F<sup>-</sup>/Br<sup>-</sup> anions were prepared in good yield. Their composition and geometries were assumed based on elemental analysis, electrical conductivity and spectral properties, as well as by comparison with data of related complex previously published. For complexes the same exo coordination of each Co(II) ion with azamacrocyclic ligand engaging two pyridine N and two cyclam's N atoms, and F<sup>-</sup>/Br<sup>-</sup> in trans position is proposed. Selective antibacterial activity towards Gram(+) bacteria for the complexes was also detected.

## Acknowledgement

This work was partially supported by the Ministry for Science of the Republic of Serbia (Grants no. 172014).

## REFERENCES

- [1] a) H. Harada, M. Kodera, G. Vučković, N. Matsumoto, S. Kida, *Inorg. Chem.* 1991, **30**, 1190-1194; b) S. P. Sovilj, G. Vučković, K. B. Babić-Samardžija, N. Matsumoto, V. J. Jovanović, J. Mroziński, *Synth. React. Inorg. Met.-Org.Chem.* 1999, **29**, 785-803 c) G. Vučković, M. T. Šumar, I.D. Brčeski, V. M. Leovac, D.S. Mitić, *J. Serb. Chem. Soc.* 1999, **64** (3), 191-198; d) G. Vučković, V. Stanić, S. P. Sovilj, M. Antonijević-Nikolić, J. Mroziński, *J. Serb. Chem. Soc.* 2005, **70**(8-9), 1121-1129.
- [2] G. Vučković, S. B. Tanasković, U. Rychlewska, D. D. Radanović, J. Mroziński, M. Korabik, *J. Mol. Struct.*, 2007, **827**, 80-87
- [3] S-G. Kang, S-J. Kim, *Bull. Korean. Chem. Soc.*, 2003, **24**, 269-273
- [4] W. J. Geary, *Coord. Chem. Rev.*, 1971, **7**, 81-122
- [5] a) B. P. Lever, *Inorganic Electronic Spectroscopy*, 2<sup>nd</sup> ed., Elsevier, Amsterdam, 1984; b) K. Nakamoto, *Infrared and Raman Spectra of Inorganic and Coordination Compounds, Part B*, 5<sup>th</sup> ed. Wiley and Sons, New York.

*N - General Physical Chemistry*



## 4D COMPUTER MODEL OF THE Fe-Ni-Co-S T-x-y-z DIAGRAM. PREDICTION OF THE SUBSYSTEM Fe-Ni-Co-FeS-NiS-CoS LIQUIDUS

V. Lutsyk<sup>1,2</sup> and V. Vorob'eva<sup>1</sup>

<sup>1</sup>*Institute of Physical Materials Science,  
6 Sakhyanova st., 670047 Ulan-Ude, Russia (vluts@ipms.bscnet.ru)*  
<sup>2</sup>*Buryat State University, 24a Smolin st., 670000 Ulan-Ude, Russia*

### ABSTRACT

New approach to design and analysis of the quaternary systems phase diagrams is proposed. The four-dimensional computer model of the Fe-Ni-Co-FeS-NiS-CoS subsystem T-x-y-z diagram is represented.

### INTRODUCTION

Design of the 3-dimensional (3D) computer model of ternary system includes two stages [1]. First the analysis of the T-x-y diagram geometric structure is depicted in the form of some template. Coordinates of the template invariant points are given taking into account a temperature row so as to most clearly show the diagram geometric structure. The uni- and invariant states scheme in both table and graphic form is used. As a result, the T-x-y diagram prototype is obtained, it becomes clear with its aid all special features, both the structures diagram (up to quantity and type of all surfaces and phase regions [2]), and the processes of crystallization. Furthermore, the 3D model helps to find errors in the interpretation of experimental data through the diagram [3,4]. Then experimental data are input, and the curvature of curves and surfaces is learned more precisely, and prototype is converted into the real system model.

Approaches to the 4D T-x-y-z diagrams computer models construction are analogous. The bi-, uni- and invariant states scheme in the tabular form is written on the ternary systems geometry base. Then it is designed in the graphic form and becomes the basis for the T-x-y-z diagram prototype. Preliminary conclusion about possible invariant transformations in the quaternary system is done from the scheme. Several versions of 4D model 4D are constructed in the case of different treatment of the phase reactions in the scheme types. It can possible to make final conclusion occurs after the experiment results analysis. The bi-, uni- and invariant states scheme gives also the detailed description of the T-x-y-z diagram geometric structure: - the contour of each hypersurface; - the list of phase regions. As a result, the

4D computer model of the T-x-y-z diagram prototype is obtained. The comparison of model and experimental isothermal sections is produced for the transfer of prototype into the real system model.

The system Fe-Ni-Co-S phase diagram, as the Fe-Ni-Cu-S [5-7], is the basis of the majority of the compositions of the metallic sulfide half-products of the pyrometallurgical processing of the sulfide and oxidized nickel and nickel-cuprum, nickel-cobalt ores.

### TERNARY SYSTEMS

In all boundary ternary systems with iron the polymorphous transfer between two high-temperature allotropic forms  $\delta$ -Fe and  $\gamma$ -Fe (A and A1) occurs according to eutectic type metatectic reaction  $\delta$ -Fe $\rightarrow\gamma$ -Fe+L (A $\rightarrow$ L+A1). Since there are the continuous rows of solid solutions are formed (in the systems Fe-Ni and Fe-Co – with the minimum, correspondingly,  $m_{A1B}$  or  $m_{A1C}$ ) in the systems Fe-Ni=A-B, Fe-Co=A-C, Ni-Co=B-C, that liquidus (and solidus) in the system Fe-Ni-Co T-x-y diagram consists of the surfaces of primary crystallization of the high-temperature polymorphous modification of iron  $\delta$ -Fe=A and the solid solution of its another modification  $\gamma$ -Fe=A1 with nickel and cobalt.

Another ternary systems are considered as the subsystems Fe-Ni-FeS-NiS=A-B-R1-R2, Fe-Co-FeS-CoS=A-C-R1-R4, Ni-Co-NiS-CoS=B-C-R2-R5, where monosulfides form the continuous rows of the solid solutions R1(R2), R1(R5) and R2(R4).

The reaction Q1: L+R1(R2) $\rightarrow$ A1(B)+R3 with R1(R2), A1(B), R1(R3) (with the incongruently melting compound Ni<sub>3</sub>S<sub>2</sub>=R3) solid solutions has a place in the subsystem Fe-Ni-FeS-NiS=A-B-R1-R2 at 789°C.

Eutectic E: L $\rightarrow$ A2(C)+R1(R2)+R3 and quasi-peritectic Q2: L+A1(C) $\rightarrow$ A2(C)+R1(R2), Q3: L+A1(C) $\rightarrow$ A2(C)+R3 reactions are discovered in the subsystem Fe-Co-FeS-CoS=A-C-R1-R2-C, where A1(C) and A2(C) are solid solutions of iron modifications  $\gamma$ -Fe=A1,  $\alpha$ -Fe=A2 with cobalt, Co<sub>4</sub>S<sub>3</sub>=R5 is the incongruently melting compound. The temperature of ternary eutectic is 850°C, and temperatures of Q2, Q3 reactions are not thus far known. Temperature coordinate of the maximum point  $e_1$  in the curve Q2Q3, corresponding to the reaction A1(C) $\rightarrow$ L+A2(C), is 981°C.

Quasi-peritectic reactions Q4: L+R2(R4) $\rightarrow$ R3+R5 and Q5: L+R5 $\rightarrow$ R3+B(C) are in the subsystem Ni-Co-NiS-CoS=B-C-R2-R4. The temperature of first reaction is  $T_1 < 806^\circ\text{C}$ , and of second is  $T_2 < 637^\circ\text{C}$ . The precise values of these temperatures are not thus far established and their values are undertaken approximately for 3D (4D) the computer models.

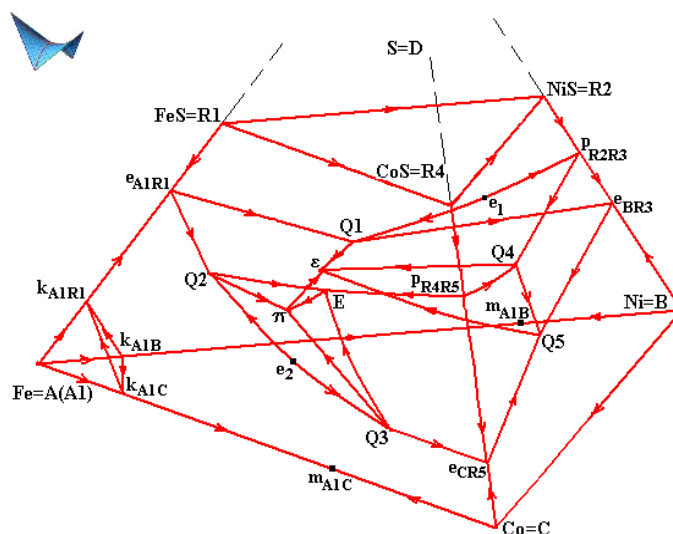
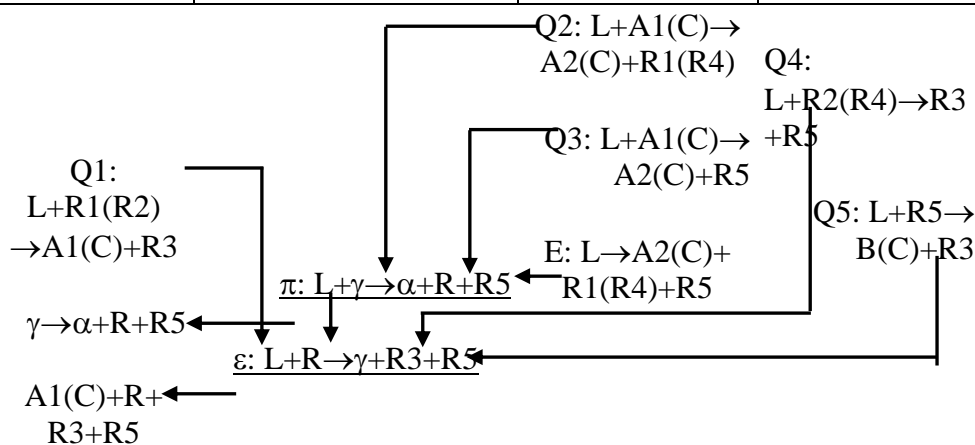


**Figure 1.** Prediction of the subsystem Fe-Ni-Co-FeS-NiS-CoS=A-B-C-R1-R2-R4 liquidus hypersurfaces by the phase reactions scheme (Table 1.)

**Table 1.** Assumed phase reactions scheme of the subsystem Fe-Ni-Co-FeS-NiS-CoS=A-B-C-R1-R2-R4 liquidus (Figure 1)

Fe-Ni-FeS-NiS =A-B-R1-R2	Fe-Ni-Co-FeS-NiS-CoS= A-B-C-R1-R2-R4	Fe-Co-FeS-CoS= A-C-R1-R4	Ni-Co-NiS-CoS= B-C-R2-R4
-----------------------------	---	-----------------------------	-----------------------------



\* Принятые обозначения: R1(R2), R1(R4), R2(R4)=R; A1(B), A1(C), B(C)= $\gamma$ ; A2(C)= $\alpha$ , R3=Ni<sub>3</sub>S<sub>2</sub>, R5=Co<sub>4</sub>S<sub>3</sub>

**QUATERNARY SYSTEM**

Possible liquidus of subsystem Fe-Ni-Co-FeS-NiS-CoS consists of primary crystallization hypersurfaces of the compound Ni<sub>3</sub>S<sub>2</sub>=R3 and solid solutions

on the base of polymorphous modifications of iron  $\gamma$ -Fe(Ni, Co)= $\gamma$ (A1, B, C) and  $\alpha$ -Fe(Ni, Co)= $\alpha$ (A2, B, C), compounds FeS, NiS, CoS = R<sub>i</sub> (R1, R2, R4) and Co<sub>4</sub>S<sub>3</sub>=R5, and also - high-temperature alloropy  $\delta$ -Fe=A. In phase reaction scheme the invariant transformations  $\pi$ : L+ $\gamma$ → $\alpha$ +R+R5 and  $\varepsilon$ : L+R→ $\gamma$ +R3+R5 are assumed (Table 1). It doesn't contradict [7], where R1, R2 and R4 are considered with the stoicheometry 9:8. The prototype (Figure 1) will be transformed after further experimental investigation into the 4D computer model of T-x-y-z diagram for the real subsystem.

## RESULTS AND DISCUSSION

The prototype of the Fe-Ni-Co-FeS-NiS-CoS subsystem T-x-y-z diagram has been constructed. It is assumed on the basis of the phase reactions scheme and the ternary systems data that two invariant transformations are possible in the quaternary subsystem: quasi-peritectic and eutectic.

## CONCLUSION

New approach to the preliminary analysis and further prediction of the quaternary systems phase diagrams structure is demonstrated with the example of the Fe-Ni-Co-FeS-NiS-CoS subsystem. It is possible, according to the extended phase reactions scheme, to determine quantity and type of hypersurfaces and phase regions, to design the 4D prototype of the T-x-y-z diagram, which after additional experiments can be transformed into the real system computer model.

### *Acknowledgement*

This work has been performed under the program of fundamental research SB RAS (project 0336-2014-0003) and was partially supported by the Russian Foundation for Basic Research (projects 14-08-00453, 15-43-04304).

## REFERENCES

- [1] V. I. Lutsyk and V. P. Vorob'eva, *Therm. Anal. Calorim.*, 2010, **101**, 25-31.
- [2] V. I. Lutsyk and V. P. Vorob'eva, *Rus. J. Inorgan. Chem.*, 2016, **61**, 188-207.
- [3] V. I. Lutsyk and V. P. Vorob'eva, *Rus. J. Phys. Chem.*, 2015, **89**, 1715-1722.
- [4] V. Lutsyk, V. Vorob'eva and S. Shodorova, *12<sup>th</sup> Int. Conf. Fund. & Applied Aspects of Phys. Chem., Proc. Vol. 1, Belgrade, Serbia, 2014*, 97-100.
- [5] V. I. Lutsyk, V. P. Vorob'eva and A. M. Zyryanov, *Metal. & Mater. Eng. Cong. of South-East Europe, Belgrade, Serbia, 2015*, 125-129.
- [6] V. Lutsyk, V. Vorob'eva, S. Shodorova and A. Zyryanov, *46<sup>th</sup> Int. October Conf. on Mining and Metallurgy Proc., Bor, Serbia, 2014*, 144-147.
- [7] A. Kitakaze and A. Sugaki, *The Canadian Mineralogist*, 2004, **42**, 17-42.

## ASSEMBLING OF 3D MODELS FOR T-X-Y DIAGRAMS ON THE BOUNDARY OF SYSTEM LiF-PuF<sub>3</sub>-KF-RbF

V. Lutsyk<sup>1,2</sup> and A. Zelenaya<sup>2</sup>

<sup>1</sup>*Institute of Physical Materials Science,  
6 Sahyanova st., 670047 Ulan-Ude, Russia (vluts@ipms.bscnet.ru)*  
<sup>2</sup>*Buryat State University, 24a Smolin st., 670000 Ulan-Ude, Russia*

### ABSTRACT

Computer models of T-x-y diagrams for the systems LiF-KF-RbF, LiF-PuF<sub>3</sub>-KF, LiF-PuF<sub>3</sub>-RbF and KF-PuF<sub>3</sub>-RbF have been elaborated. A detailed description of their geometric structure was made. It allowed to carry out the prediction of liquidus hypersurfaces within T-x-y-z diagram for the system LiF-PuF<sub>3</sub>-KF-RbF.

### INTRODUCTION

System LiF-PuF<sub>3</sub>-KF-RbF and its bounding ternary systems can be the base for fuel compositions for the Molten Salt Reactor [1], although systems LiF-{KF,RbF} are described as the candidate molten salt coolants for the Advanced High-Temperature Reactor. The development of spatial models of T-x-y diagrams permits to use them as a tool for their comprehensive investigation, including the construction of vertical and horizontal sections, the analysis of crystallization paths, the obtaining of data about the microconstituents of concentration fields with different dimensions [2-3]. These models also allow to identify the wrong interpretation of T-x-y diagrams geometry (for example, at experimental study) and to find the contradictions in sections, as well as to consider the different variants of phase diagrams with ambiguous description or the deficit of experimental data. The data about structure of T-x-y diagrams of systems LiF-KF-RbF, LiF-PuF<sub>3</sub>-KF, LiF-PuF<sub>3</sub>-RbF and KF-PuF<sub>3</sub>-RbF is the base for the schema of phase reactions for LiF-KF-PuF<sub>3</sub>-RbF system, which can be used to forecast the liquidus hypersurfaces peculiarities.

### MODELS OF T-X-Y DIAGRAM OF SYSTEM LiF-KF-RbF

There are two variants of models of T-x-y diagrams for system LiF-KF-RbF (A-B-C), because it hasn't the definite description. In the first case, the system doesn't contain the invariant ternary points and the liquidus consists of two surfaces [4] (Fig. 1a). At that, the presence of binary compound

$R=LiRbF_2$  decomposing in the solid phase complicates the structure of T-x-y diagram. In the second case, it was suggested the formation of the ternary eutectic point and the fold from the binary system KF-RbF (Fig. 1b).

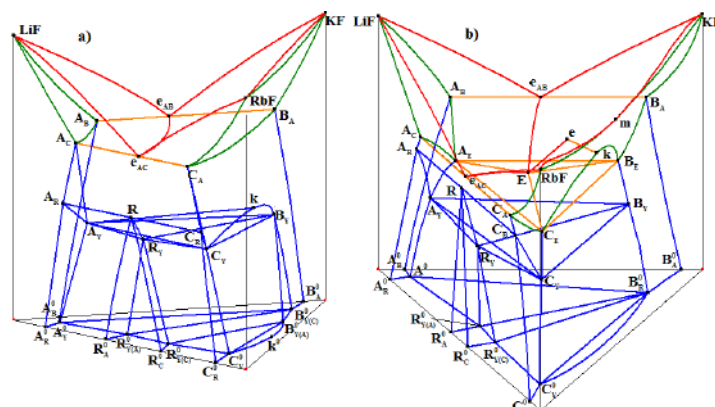


**Figure 1.** Variants of T-x-y diagram for LiF-KF-RbF system

**MODELS OF T-X-Y DIAGRAMS OF SYSTEMS LiF-PuF<sub>3</sub>-KF AND LiF-PuF<sub>3</sub>-RbF**

T-x-y diagrams LiF-PuF<sub>3</sub>-MF (M=K,Rb) have the same topology of liquidus (Fig. 2). They have quasi-peritectic transformation  $L_Q+PuF_3 \rightarrow LiF+R_1$  (825 K, 841 K) and two eutectic ones  $L_{E1} \rightarrow LiF+R_1+R_2$  (786 K, 741 K) and  $L_{E2} \rightarrow LiF+MF+R_2$  (749 K, 713 K) [1], where R1 and R2 have the same stoichiometry in lithium and potassium systems. Monovariant liquidus line  $E_1E_2$  contains the maximum  $e_{max}$ . Binary systems MF-PuF<sub>3</sub> include one incongruently  $R_1=MPuF_4$  and one congruently  $R_2=M_3PuF_6$  melting compounds.

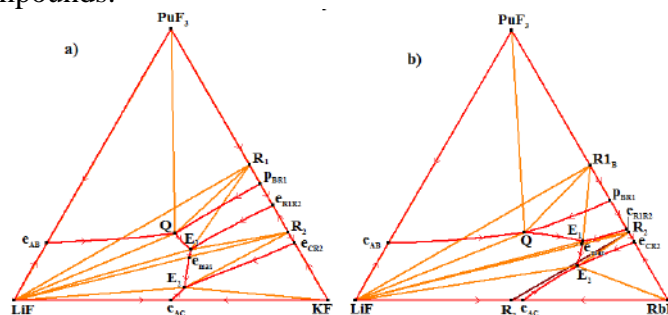


**Figure 2.** XY projection of LiF-PuF<sub>3</sub>-KF and LiF-PuF<sub>3</sub>-RbF T-x-y diagrams

However, the system LiF-PuF<sub>3</sub>-RbF is complicated by the compound  $R_3=LiRbF_2$  decomposing in the solid phase. Both models of T-x-y diagrams

were constructed using a single template, but T-x-y diagram of system LiF-PuF<sub>3</sub>-RbF is added by the surfaces and phase regions corresponding to the compound R<sub>3</sub>. Computer model of system LiF-PuF<sub>3</sub>-KF contains 5 liquidus surfaces, 20 ruled surfaces, 3 horizontal complexes at the temperatures of invariant points E<sub>1</sub>, E<sub>2</sub> and Q (Fig. 2a). Otherwise, 3 ruled surfaces and horizontal plane corresponding to the decomposition of compound R<sub>3</sub> supplement the structure of T-x-y diagram LiF-PuF<sub>3</sub>-RbF (Fig. 2b).

**MODEL OF T-X-Y DIAGRAM OF SYSTEM KF-PuF<sub>3</sub>-RbF**

Binary systems KF-PuF<sub>3</sub> and PuF<sub>3</sub>-RbF have the same topology and contain one incongruently (R<sub>1</sub>=RbPuF<sub>4</sub>, R<sub>3</sub>=KPuF<sub>4</sub>) and one congruently (R<sub>2</sub>=Rb<sub>3</sub>PuF<sub>6</sub>, R<sub>4</sub>=K<sub>3</sub>PuF<sub>6</sub>) melting compounds, correspondingly. Binary system KF-RbF includes the continuous ranges of solid solution with minimum. Ternary system is characterized by two eutectic transformations L<sub>E1</sub>→R<sub>1</sub>+R<sub>3</sub>+R<sub>4</sub> (713 K), L<sub>E2</sub>→KF(RbF)+R<sub>1</sub>+R<sub>4</sub> (714 K) and two quasi-peritectic ones L<sub>Q1</sub>+PuF<sub>3</sub>→R<sub>2</sub>+R<sub>3</sub> (826 K), L<sub>Q2</sub>+R<sub>2</sub>→R<sub>1</sub>+R<sub>3</sub> (758 K) [1].

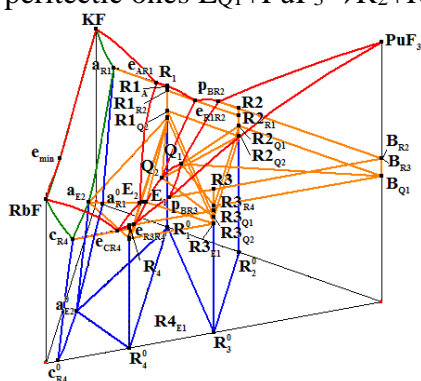


**Figure 3.** 3D model of T-x-y diagram of system KF-PuF<sub>3</sub>-RbF

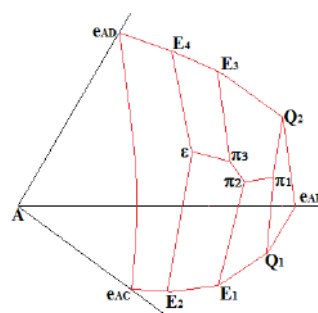


**Figure 4.** Hypersurface of liquidus A(LiF)

Since there are continuous ranges of solid solutions KF(RbF), then the corresponding solidus and solvus surfaces don't degenerate. As a result, 3D model of T-x-y diagram of system KF-PuF<sub>3</sub>-RbF (A-B-C) contains 6 liquidus, 1 solidus, 2 solvus, 31 ruled surface and 4 horizontal complex at temperatures of invariant points E<sub>1</sub>, E<sub>2</sub>, Q<sub>1</sub> and Q<sub>2</sub> (Fig. 3a).

**FORECAST OF STRUCTURE OF HYPERSURFACES LIQUIDUS FOR SYSTEM LiF-PuF<sub>3</sub>-KF-RbF (A-B-C-D)**

The schema of mono- and invariant equilibria (Table 1) were developed on the basis of data about the structure of bounding ternary systems, where the ternary system A-C-D (LiF-KF-RbF) hasn't the invariant transformations. It is assumed that the T-x-y-z diagram can include one eutectic and three quasi-peritectic quaternary points and seven liquidus hypersurfaces (Fig. 3b). Coordinates of the invariant points may be determined by the tie-lines method [5] on the basis of vertical sections obtained by the DTA methods.

**Table 1.** Schema of phase reactions.

A-B-C	A-B-C-D	A-B-D	B-C-D
Q <sub>1</sub> : L+B→A+R <sub>1</sub>		Q <sub>2</sub> : L+B→A+R <sub>3</sub>	
		E <sub>7</sub> : L→A+R <sub>3</sub> +R <sub>4</sub>	Q <sub>3</sub> : L+B→R <sub>1</sub> +R <sub>3</sub>
B+A+R <sub>1</sub> +R <sub>3</sub> ← π <sub>1</sub> : L+B→A+R <sub>1</sub> +R <sub>3</sub>		E <sub>4</sub> : L→A+C(D)+R <sub>4</sub>	Q <sub>4</sub> : L+R <sub>1</sub> →R <sub>2</sub> +R <sub>3</sub>
E <sub>1</sub> : L→A+R <sub>1</sub> +R <sub>2</sub>	L+B→A+R <sub>1</sub> +R <sub>3</sub>		E <sub>5</sub> : L→R <sub>2</sub> +R <sub>3</sub> +R <sub>4</sub>
A+R <sub>1</sub> +R <sub>2</sub> +R <sub>3</sub>	L+A+R <sub>1</sub> +R <sub>4</sub>		E <sub>6</sub> : L→C(D)+R <sub>2</sub> +R <sub>4</sub>
E <sub>2</sub> : L→A+C+R <sub>2</sub>	π <sub>2</sub> : L+R <sub>1</sub> →A+R <sub>2</sub> +R <sub>3</sub>		
A+R <sub>2</sub> +R <sub>3</sub> +R <sub>4</sub>	L+A+R <sub>2</sub> +R <sub>4</sub>		
	π <sub>3</sub> : L+R <sub>3</sub> →A+R <sub>2</sub> +R <sub>4</sub>		
A+C+R <sub>2</sub> +R <sub>4</sub>	L+A+R <sub>2</sub> +R <sub>4</sub>		
A+C+R <sub>2</sub> +R <sub>4</sub>	ε: L→A+C+R <sub>2</sub> +R <sub>4</sub>		

**CONCLUSION**

Models of T-x-y diagrams on boundary of system LiF-PuF<sub>3</sub>-KF-RbF were elaborated and the prediction of liquidus hypersurfaces structure was made.

**Acknowledgement**

This work has been performed under the program of fundamental research SB RAS (0336-2014-0003) and was partially supported by the Russian Foundation for Basic Research (14-08-00453, 15-43-04304).

**REFERENCES**

[1] O. Beneš and R. J. M. Konings, J. Nucl. Mater., 2008, **377**, 449–457.  
 [2] V. Lutsyk, A. Zelenaya, E. Nasrulin and A. Zyryanov, 12<sup>th</sup> Int. Conf. Fund. & Applied Aspects of Phys. Chem., Proc. Vol. 1, Belgrade, Serbia, 2014, 105-108.  
 [3] V. I. Lutsyk, A. E. Zelenaya and A. M. Zyryanov, Metal. & Mater. Eng. Cong. of South-East Europe, 2015, Belgrade, Serbia, 2015, 139-143.  
 [4] E. P. Dergunov, Doklady Akad. Nauk USSR, 1947, **58**, 1369-1372.  
 [5] V. I. Lutsyk and A. E. Zelenaya, Solid State Sci., 2012, **14**, 1604–1608.

## PROTOTYPING OF T-X-Y DIAGRAMS OF SYSTEMS $\text{TiO}_2\text{-ZrO}_2\text{-(Al}_2\text{O}_3\text{,SiO}_2\text{)}$

V. Lutsyk <sup>1,2</sup> and A. Zelenaya <sup>2</sup>

<sup>1</sup>*Institute of Physical Materials Science,*

*6 Sahyanova st., 670047 Ulan-Ude, Russia (vluts@ipms.bscnet.ru)*

<sup>2</sup>*Buryat State University, 24a Smolin st., 670000 Ulan-Ude, Russia*

### ABSTRACT

Peculiarities of topological structure of systems  $\text{TiO}_2\text{-ZrO}_2\text{-Al}_2\text{O}_3$  and  $\text{TiO}_2\text{-ZrO}_2\text{-SiO}_2$  associated with ambiguous description of binary systems and liquidus surfaces were analyzed. The computer prototypes of T-x-y diagrams were elaborated. List of surfaces and phase regions were proposed.

### INTRODUCTION

Computer prototypes can be developed for the phase diagrams of systems having the ambiguous or incorrect description. Such prototypes reproduce the assumed structure, as well as they can simplify or correct the controversial or sophisticated fragments of phase diagrams. Basis for the assembling of computer model are experimental or thermodynamically calculated data concerning the new compounds thermal properties, phase regions boundaries in the binary systems and liquidus surfaces curvature. Thus, the elaborated prototypes can be changed or supplemented as new experimental data will appear [1]. Let's consider systems  $\text{TiO}_2\text{-ZrO}_2\text{-(Al}_2\text{O}_3\text{,SiO}_2\text{)}$  as commonly used materials in the membrane techniques.

### PROTOTYPE OF T-X-Y DIAGRAM OF SYSTEM $\text{TiO}_2\text{-ZrO}_2\text{-Al}_2\text{O}_3$

There are differences in the description of binary systems  $\text{TiO}_2\text{-Al}_2\text{O}_3$  and  $\text{ZrO}_2\text{-TiO}_2$ .

In the system  $\text{TiO}_2\text{-Al}_2\text{O}_3$  there is an incongruently melting compound  $\text{Al}_2\text{O}_3\cdot\text{TiO}_2$  ( $R_2$ ). The character of its existence is defined variously. The authors of [2, p. 123] suggested that the considered compound is the compound of constant composition and exist in the entire temperature range. Whereas the compound  $\text{Al}_2\text{O}_3\cdot\text{TiO}_2$  with variable composition and decomposing to 1553K is presented in [3, p. 502-526]. Similar diagram is shown in [4], but with the compound of constant composition.

The description of system  $\text{ZrO}_2\text{-TiO}_2$  is complicated by the presence of polymorphic modification by component  $\text{ZrO}_2$ . Nevertheless, experimental

[5-6] and calculated [7-8] data confirm the formation of incongruently melting compound  $ZrO_2 \cdot TiO_2$  ( $R_1$ ).

There are also contradictions in the description of liquidus surfaces. The authors of [2, p. 262] demonstrate the projection of liquidus surfaces with three invariant points: two eutectic points ( $E_1$ ,  $E_2$ ) and one quasiperitectic point ( $Q$ ). The monovariant liquidus line connecting one of eutectic ( $E_2$ ) and quasiperitectic ( $Q$ ) points contains the maximum point, which is located on the quasi-binary section  $ZrO_2$ - $R_2$  (Figure 1). At the same time, the point, which is characterized as a quasiperitectic one, is arranged inside the simplex  $ZrO_2$ - $R_1$ - $R_2$ . However, the point with such arrangement can be identified as only eutectic point. For saving its quasiperitectic character, the composition of point should be shifted in the simplex  $TiO_2$ - $R_1$ - $R_2$ .

Liquidus surface obtained by thermodynamic calculation method [9] has the same configuration, but differ in the arrangement of invariant points. Quasiperitectic point arranges in the simplex  $ZrO_2$ - $R_1$ - $R_2$ , two other ternary points are within the simplex  $TiO_2$ - $R_1$ - $R_2$ . In addition, the surface corresponding to the polymorphism of component  $ZrO_2$  is given.

As a result, at the construction of prototype of T-x-y diagram for system  $TiO_2$ - $ZrO_2$ - $Al_2O_3$  (A-B-C) the polymorphism of component  $ZrO_2$  was not considered, and it was suggested that compound  $R_2$  exists in the entire temperature range. Variant [2] of liquidus surfaces structure was used, with the shifting of quasiperitectic point in the simplex  $TiO_2$ - $R_1$ - $R_2$  (Figure 1).

So the prototype of T-x-y diagram of system  $TiO_2$ - $ZrO_2$ - $Al_2O_3$  is characterized by three invariant transformations:  $L_Q + ZrO_2 \rightarrow R_1 + R_2$ ,  $L_{E_1} \rightarrow TiO_2 + R_1 + R_2$ ,  $L_{E_2} \rightarrow ZrO_2 + Al_2O_3 + R_2$  ( $R_1 = ZrO_2 \cdot TiO_2$ ,  $R_2 = Al_2O_3 \cdot TiO_2$ ).

Model of T-x-y diagram includes 5 liquidus surfaces, 20 ruled surfaces, 3 horizontal complexes at the temperatures of invariant points ( $E_1$ ,  $E_2$ ,  $Q$ ), 7 two-phase regions ( $L+A$ ,  $L+B$ ,  $L+C$ ,  $L+R_1$ ,  $L+R_2$ ,  $B+R_1$ ,  $R_1+R_2$ ), 10 three-phase regions ( $L+A+R_1$ ,  $L+A+R_2$ ,  $L+B+R_1$ ,  $L+B+R_2$ ,  $L+B+C$ ,  $L+C+R_2$ ,  $L+R_1+R_2$ ,  $A+R_1+R_2$ ,  $B+R_1+R_2$ ,  $B+C+R_2$ ). Phase regions  $B+R_1$ ,  $R_1+R_2$  are degenerated in two vertical planes.

**PROTOTYPE OF T-X-Y DIAGRAM OF SYSTEM  $TiO_2$ - $ZrO_2$ - $SiO_2$**

The system  $ZrO_2$ - $SiO_2$ - $TiO_2$  is

characterized by presence of liquid

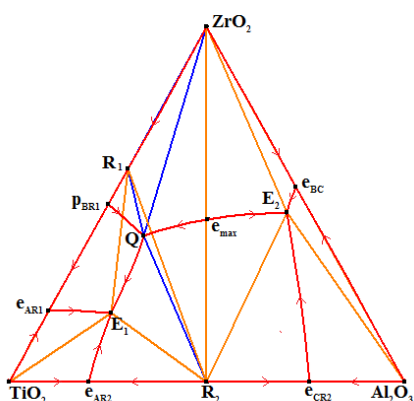


**Figure 1.** Prototype of T-x-y diagram for systems  $TiO_2$ - $ZrO_2$ - $Al_2O_3$

immiscibility in two binary systems  $\text{TiO}_2\text{-SiO}_2$  and  $\text{ZrO}_2\text{-SiO}_2$  [2]. The system  $\text{ZrO}_2\text{-SiO}_2$  has the compound decomposed without melt  $\text{R}_2=\text{ZrO}_2\cdot\text{SiO}_2$ .

According [10], there are two ternary points in the system  $\text{TiO}_2\text{-ZrO}_2\text{-SiO}_2$ . One of them is described as eutectic point and the type of second point is not determined. The presented phase diagram is not included the surface corresponding to the polymorphic modification of component  $\text{ZrO}_2$  and the region of liquid immiscibility from binary system  $\text{ZrO}_2\text{-SiO}_2$ .

At the construction of T-x-y diagram prototype for system  $\text{TiO}_2\text{-ZrO}_2\text{-SiO}_2$  (A-B-C), we not considered the polymorphism of component  $\text{ZrO}_2$ , but taken into account the liquid immiscibility in both binary systems  $\text{TiO}_2\text{-SiO}_2$  and  $\text{ZrO}_2\text{-SiO}_2$ . It was suggested that the ternary system is characterized by eutectic ( $\text{L}_E \rightarrow \text{TiO}_2 + \text{SiO}_2 + \text{R}_1$ ) and quasiperitectic ( $\text{L}_Q + \text{ZrO}_2 \rightarrow \text{SiO}_2 + \text{R}_1$ ) transformations ( $\text{R}_1 = \text{ZrO}_2 \cdot \text{TiO}_2$ ,  $\text{R}_2 = \text{ZrO}_2 \cdot \text{SiO}_2$ ).

Model of T-x-y diagram (Figure 2) is formed by 2 surfaces of liquid immiscibility, 4 liquidus surfaces, 20 ruled surfaces, 2 horizontal complexes at temperatures invariant points (E, Q) and the horizontal plane corresponding to the decomposition beginning of compounds R2. T-x-y diagram include 8 two-phase regions ( $\text{L}_1 + \text{L}_2$ ,  $\text{L}_3 + \text{L}_4$ , L+A, L+B, L+C, L+R1, C+R1, R1+R2), 11 three-phase regions ( $\text{L}_1 + \text{L}_2 + \text{A}$ ,  $\text{L}_3 + \text{L}_4 + \text{B}$ , L+A+C, L+A+R1, L+B+C, L+B+R1, L+C+R1, A+C+R1, B+C+R1, B+R1+R2, C+R1+R2). Phase regions C+R1, R1+R2 are degenerated in the vertical planes. Three-phase regions B+R1+R2 and C+R1+R2 are the result of appearance of compound R2 in solid phase.

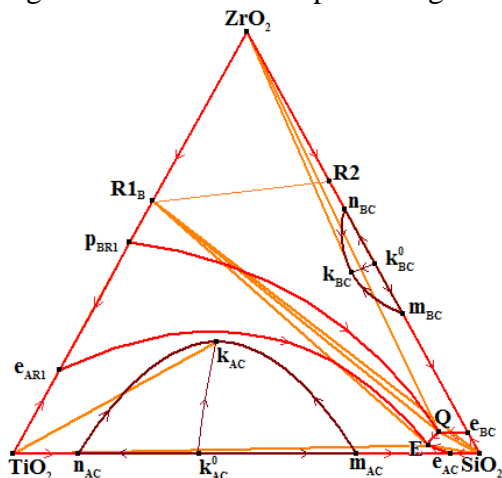


**Figure 2.** Prototype of T-x-y diagram for system  $\text{TiO}_2\text{-ZrO}_2\text{-SiO}_2$

Liquidus surface of  $\text{SiO}_2$  is arranged close to the vertex of Gibbs triangle and has small field. Therefore, for a better understanding of the structure of

T-x-y diagram and the decoding of horizontal and vertical sections, it is appropriate to construct the prototype, in which the binary and ternary points are expanded with saving of T-x-y diagram topological structure.

**CONCLUSION**

Topological features of the systems  $\text{TiO}_2\text{-ZrO}_2\text{-Al}_2\text{O}_3$  ( $\text{SiO}_2$ ) were considered and the prototypes of T-x-y diagrams were elaborated with reconstruction of full geometric structure. Obtained computer models can be compared with available experimental or thermodynamically calculated T-x-y diagrams. In addition, they can be used as the templates for constructions of other oxide systems and for the T-x-y-z diagram  $\text{TiO}_2\text{-ZrO}_2\text{-Al}_2\text{O}_3\text{-SiO}_2$  assembling.

**Acknowledgement**

This work has been performed under the program of fundamental research SB RAS (project 0336-2014-0003) and was partially supported by the Russian Foundation for Basic Research (projects 14-08-00453, 15-43-04304).

**REFERENCES**

- [1] V. I. Lutsyk, V. P. Vorob'eva, A. E. Zelenaya, *Solid State Phenomena*, 2015, **230**, 51-54
- [2] E. M. Levin, C. R. Robbins, H. F. McMurdie, *Phase diagrams for ceramists*, American Ceramic Society, Ohio, 1964.
- [3] *Sintering of Ceramics - New Emerging Techniques*, Arunachalam Lakshmanan (Eds), InTech, 2012.
- [4] A. Serkan, *Journal of Ceramic Processing Research*, 2011, **12**, 21-25.
- [5] A. S. Berezhnoy, *Multicomponent oxide system*, Sciences view, Kiev, 1970. (In Russian)
- [6] A. V. Shevchenko, L. M. Lopato, I. M. Mayster, O. S. Gorbunov, *Russian Journal of Inorganic Chemistry*, 1980, **25**, 2496-2499. (In Russian)
- [7] [http://www.crct.polymtl.ca/fact/phase\\_diagram.php?file=Ti-Zr-O\\_TiO2-ZrO2.jpg&dir=FToxid](http://www.crct.polymtl.ca/fact/phase_diagram.php?file=Ti-Zr-O_TiO2-ZrO2.jpg&dir=FToxid).
- [8] T. A. Schaedler, O. Fabrichnaya, C. G. Levi, *Journal of the European Ceramic Society*, 2008, **28**, 2509–2520.
- [9] [http://www.crct.polymtl.ca/fact/phase\\_diagram.php?file=Al-Ti-Zr-O\\_Al2O3-TiO2-ZrO2\\_liquidus-projection.jpg&dir=FToxid](http://www.crct.polymtl.ca/fact/phase_diagram.php?file=Al-Ti-Zr-O_Al2O3-TiO2-ZrO2_liquidus-projection.jpg&dir=FToxid).
- [10] N. A. Toropov, V. P. Bazarkovsky, V. V. Lapshin et al, *Diagrams of Silicate Systems*, vol. 3 Ternary Silicate Systems, Nauka, Leningrad, 1972 (In Russian).

## QSPR MODELING OF THE SETSCHENOW CONSTANT OF ORGANIC COMPOUNDS BASED ON MONTE CARLO METHOD

Ž. Mitić<sup>1</sup>, A. Veselinović<sup>1</sup>, J. Veselinović<sup>1</sup>, M. Nikolić<sup>2</sup> and G. M. Nikolić<sup>1</sup>

<sup>1</sup>*Faculty of Medicine, University of Niš, RS-18000 Niš, Serbia  
(zak\_chem2001@yahoo.com)*

<sup>2</sup>*Faculty of Sciences and Mathematics, University of Niš, RS-18000 Niš, Serbia*

### ABSTRACT

Quantitative structure – property relationships (QSPRs) for the Setschenow constants are build using calculated Monte Carlo optimization method with optimal descriptors based on SMILES notation. These models are prepared in accordance with the OECD principles. Dataset was split in one split and in training and test set. The predictability of proposed QSPR models for an external test is estimated and for the best model statistical quality is calculated with following characteristics  $r^2 = 0.9609$ ,  $q^2 = 0.9592$ ,  $s = 0.017$  for training and  $r^2 = 0.9417$ ,  $q^2 = 0.9262$ ,  $s = 0.017$ . The definition of the domain of applicability and the mechanistic interpretation for these models are discussed.

### INTRODUCTION

Very important parameter in the fields of chemical processes and reactions, environmental hazard assessment and pharmaceutical design is the aqueous solubility of organic compounds. Transport, release, absorption and tissue distribution of pharmaceuticals are strongly affected by the aqueous solubility [1]. The solubility of organic compounds in water can increase or decrease, in the presence of strong electrolyte salts depending on the polarity of both the solute and the salts. Aqueous solutions of salt as NaCl increases the “squeezing out” effect of water on nonpolar solutes, since polarity of water is increased. The numerical data on the Setschenow Constant is useful and important information from point of view of ecology and pharmacology [2,3]. Although there are several experimental methods available to define the Setchenow constant they are costly and time-consuming [4]. Quantitative structure – property relationships (QSPRs) are a cheminformatics tools to predict various endpoints [5,6]. Simplified molecular input-line entry system (SMILES) in QSPR analysis has been gained in recent years, for building appropriate one-variable models

calculated with application of Monte Carlo optimization method with very good predictability of the SMILES-descriptor based models [7-9]. The aim of this work is the estimation of predictive potential of QSPR models for the Setschenow constants build with application of Monte Carlo method and calculated using CORAL software.

### EXPERIMENTAL

The numerical data on the Setschenow constants were taken from literature [3]. The molecular structure of compounds is represented by SMILES generated with the ACD/ChemSketch program ([www.acdlabs.com](http://www.acdlabs.com)). Three splits into the sub-training, calibration, test, and validation sets were examined. All SMILES based descriptors are considered in this research. For all QSPR models development CORAL software (<http://www.insilico.eu/coral/>) was used.

### RESULTS AND DISCUSSION

Table 1. contains statistical characteristics of QSPR models for the Setschenow constants calculated with the CORAL software and represented by the general formula according to of one-variable models. Fig 1. represents best calculated model graphically, where  $Ac(\text{expr.})$  and  $Ac(\text{calc.})$  are experimental and calculated values for studied endpoint. From presented data can be concluded that build QSPR models have very good predictive potential since statistical parameters are very satisfactory. The best statistical quality for all splits takes place for split 1 in which threshold is equal to 1 and  $N_{\text{epoch}}$  is equal to 13. Developed QSPR model can be represented with following equation:

$$\text{Endpoint} = 0.0397 (\pm 0.0003) + 0.0041 \times \text{DCW}(1,13) \quad (1)$$

DCW represents optimal and it is calculated according to Eq 2:

$$\text{DCW}(\text{Threshold}, N_{\text{epoch}}) = \sum \text{CW}(\text{Sk}) + \sum \text{CW}(\text{SSk}) + \sum \text{CW}(\text{SSSk}) + \text{CW}(\text{NOSP}) + \text{CW}(\text{HALO}) + \text{CW}(\text{BOND}) + \text{CW}(\text{PAIR}) \quad (2)$$

where Sk, SSk, and SSSk, are fragments of SMILES strings which contain one-, two-, and three SMILES atoms respectively. SMILES atoms is one symbol or two symbols which cannot be examined separately, e.g. 'Cl', 'Br', etc. The NOSP is descriptor calculated with SMILES according to presence (absence) in the molecule of nitrogen, oxygen, sulfur, and phosphorus. The HALO is descriptor calculated according to presence (absence) in the molecular structure fluorine, chlorine, bromine, and iodine. The BOND is descriptor calculated according to presence (absence) double,

triple, and stereo chemical (i.e. presence / absence in SMILES symbol '=', '#', and '@', respectively) bonds, and PAIR is descriptor calculated with taking into account all possible combines of above SMILES attributes [7]. The CW(X) is correlation weight for an above described SMILES attribute (i.e. Sk, SSk, SSSk, NOSP, HALO, BOND, and PAIR). Treshold and  $N_{\text{epoch}}$  are parameters related to Monte Carlo optimization procedure.

**Table 1.** Statistical quality of the best calculated QSPR model

	<b>n</b>	<b>r<sup>2</sup></b>	<b>q<sup>2</sup></b>	<b>s</b>	<b>MAE</b>	<b>F</b>
Training	79	0.9609	0.9592	0.017	0.011	1894
Test	22	0.9417	0.9262	0.024	0.019	323

n – Number of molecules in set; r<sup>2</sup> – correlation coefficient; q<sup>2</sup> – cross-validated correlation coefficient; s – standard error of estimation; MAE – mean absolute error; F – Fischer F-ratio

The statistical characteristics of model for the Setschenow constant suggested in the literature are the following: n = 101, r<sup>2</sup> = 0.7717, s = 0.0410; n=30, r<sup>2</sup>=0.764; n=30, r<sup>2</sup>=0.8888 (Artificial neuron networks); n=30, r<sup>2</sup>=0.894 (Multiple linear regression); and n=30, r<sup>2</sup>=0.752 (Super vector machine). Thus, statistical quality of the CORAL models is comparable with the quality of models suggested in the literature [2,3,10].

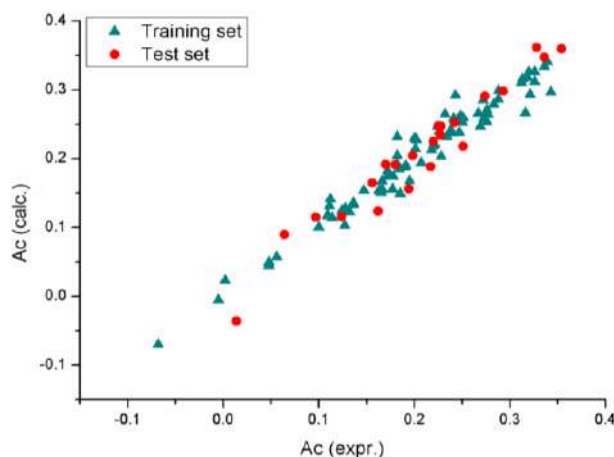


**Figure 1.** Graphical representation of the best calculated QSPR model.

The domain of applicability for suggested model is defined according to the principle: all molecular features should take place in the structured training set (i.e. the sub-training together with the calibration sets). Thus, suggested approach takes into account OECD principles.

Structural features extracted from SMILES which are stable promoters of increase or vice versa decrease of the Setschenow constants are carbon atom and fragments associates two and three carbon atoms are promoter of the Setschenow constants increase; whereas branching, double bonds and presence of two cycles (rings) are promoters of the Setschenow constants decrease.

## CONCLUSION

The suggested modeling process for the Setschenow Constant is based on the representation of the molecular structure by SMILES, SMILES-based descriptors. Using Monte Carlo optimization process the CORAL software was capable to be an efficient tool to build up a robust model. The described QSPR models for the Setschenow constant are quite good. These models are calculated in accordance with the OECD and REACH recommendations.

## Acknowledgement

This work was supported by the Ministry for Science of the Republic of Serbia (Grant **III 41017**; <http://vihos.masfak.ni.ac.rs/site/>).

## REFERENCES

- [1] N. Ni, M. M. El-Sayed, T. Sanghvi, S. H. Yalkowsky, *Journal of Pharmaceutical Sciences*, 2000, **89**(12), 1620–1625.
- [2] Y. Li, Q. Hu, C. Zhong, *Industrial & Engineering Chemistry Research*, 2004, **43**(15), 4465–4468.
- [3] J. Xu, L. Wang, L. Wang, X. Shen, W. Xu, *Journal of Computational Chemistry*, 2011, **32**, 3241–3252.
- [4] M. T. O. Jonker, B. Muijs, *Chemosphere* 2010, 80(3), 223–227.
- [5] T. Le, V.C. Epa, F.R. Burden, D.A. Winkler, *Chemical Reviews*, 2012, **112**(5), 2889–2919.
- [6] P. Liu, W. Long, *International Journal of Molecular Sciences*, 2009, **10**(5), 1978–1998.
- [7] A.M. Veselinović, J.B. Veselinović, J.V. Živković, G.M. Nikolić, *Current Topics in Medicinal Chemistry*, 2015, **15**(18), 1768–1779.
- [8] A.A. Toropov, A.P. Toropova, D.V. Mukhamedzhanova, I. Gutman, *Indian Journal of Chemistry - Section A Inorganic, Physical, Theoretical and Analytical Chemistry*, 2005, **44**(8), 1545–1552.
- [9] A.A. Toropov, E. Benfenati, *Current Drug Discovery Technologies*, 2007, **4**(2), 77–116.
- [10] N. Ni, S.H. Yalkowsky, *International Journal of Pharmaceutics*, 2003, **254**(2), 167–172.

*O - Pharmaceutical Physical Chemistry*



## ACID-BASE EQUILIBRIA AND SOLUBILITY OF VERAPAMIL

M. Popović<sup>1</sup>, G. Popović<sup>2</sup> and M. Stojadinović<sup>2</sup>

<sup>1</sup>*Department of Pharmaceutical Chemistry,  
(majap@pharmacy.bg.ac.rs)*

<sup>2</sup>*Department of General and Inorganic Chemistry, Faculty of Pharmacy,  
University of Belgrade, Vojvode Stepe 450,  
11000 Belgrade, Serbia*

### ABSTRACT

The intrinsic solubility –  $S_0$  (only the neutral form is present in the solution) and pH-dependent solubility -  $S$  (heterogeneous system of neutral and ionized forms) of verapamil were determined spectrophotometrically. Based on solubility data  $pK_a$  value 9.15 of verapamil was indirectly obtained.

### INTRODUCTION

Verapamil belongs to a class of calcium channel blockers applied in the treatment of cardiac arrhythmias, angina pectoris and hypertension. Because to the presence of single ionizable group, aliphatic tertiary amine, verapamil represents a weak base (Figure 1) and exhibits pH-dependent aqueous solubility [1].

In solutions of weak electrolytes there is an equilibrium between molecular and ionized forms with different physico-chemical properties. The most important physico-chemical parameters that affect the liberation and the absorption processes of drugs are solubility and  $pK_a$  value. Comprehensive

understanding of these parameters is necessary for the development of novel drug delivery systems, improvement of existing pharmaceutical formulations, and for the choice of the optimal experimental conditions in drug analysis[2].

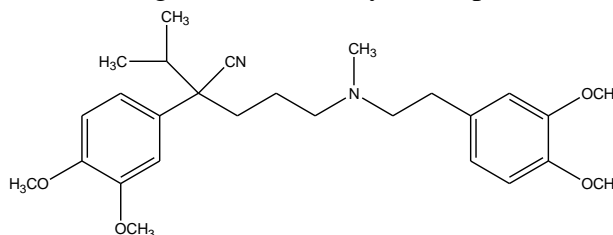


**Figure 1.** Chemical structure of verapamil.

### EXPERIMENTAL

Spectrophotometric measurements were carried out on the UV-Vis spectrophotometer Cintra 20 (GBC, Australia). Automatic titrator 798 MPT

Titrimetric (Metrohm, Switzerland) with a combined electrode LL unitrode Pt 1000 (Metrohm, Switzerland) was used for potentiometric measurements. Verapamil hydrochloride was kindly donated from Medicines and Medical Devices Agency of Serbia (Belgrade, Serbia). All solutions were prepared in double distilled water. Standard solutions of HCl and carbonate-free NaOH were standardized potentiometrically.

Saturated solutions of verapamil (pH 7.8 to 12) were prepared by treating verapamil hydrochloride (0.25 mg/mL) in 0.1 mol/L NaCl solution with 0.1 mol/L NaOH. Suspensions were thermostated at 25°C with occasional stirring for 24 h, then filtered through 0.22 µm membrane filter. After a specified dilution of the filtrate, concentration of verapamil was determined spectrophotometrically at 230 nm.

## RESULTS AND DISCUSSION

From the chemical point of view verapamil represents the monoprotic base and its molecular form is poorly soluble in water. In a saturated aqueous solution of verapamil between the solid phase ( $B_s$ ) and a solution the following equilibria is established:



where  $S_0$  is the intrinsic solubility (solubility of molecular form) of verapamil.

The total solubility ( $S$ ) of verapamil is equal to the sum of the concentrations of the molecular form ( $B$ ) and of the protonated form ( $BH^+$ ):

$$S = [B] + [BH^+] \quad (3)$$

Combining equations (1) – (3) gives the equation:

$$S = S_0 + K_{s1}[H^+] \quad (4)$$

where the constant  $K_{s1}$  can be replaced by relation that connects verapamil acidity constant ( $K_a$ ) and constants in a heterogeneous system:

$$K_a = \frac{[B][H^+]}{[BH^+]} = \frac{K_{s0}}{K_{s1}} \quad (5)$$

to give the following equation:

$$\underbrace{S}_y = S_0 + \frac{S_0}{K_a} \underbrace{[H^+]_x} \quad (6)$$

Equation (6) represents linear dependence of the total solubility ( $S$ ) on  $[H^+]$ . Based on pairs  $S$ - $[H^+]$  it is possible to determine the intrinsic solubility ( $S_0$ ) and the  $K_a$  value. For very poorly soluble compound, such as verapamil, the ordinate intercept ( $S_0$ ) is often within a statistical error. Reliable results

for  $S_0$  of verapamil can be obtained by determining the solubility at  $\text{pH} > (\text{p}K_a + 2)$ , Table 1.

**Table 1.** The intrinsic verapamil solubility at 25°C.

pH	$S_0$ (mol/L)
11.5	$4.24 \times 10^{-5}$
11.7	$2.60 \times 10^{-5}$
11.9	$4.23 \times 10^{-5}$
12.0	$6.20 \times 10^{-5}$
12.2	$5.26 \times 10^{-5}$
Average	$4.51 \times 10^{-5}$

**Table 2.** pH-dependent verapamil solubility at 25°C.

pH	S (mol/L)
8.41	$2.22 \times 10^{-4}$
8.62	$1.46 \times 10^{-4}$
8.84	$8.76 \times 10^{-5}$
8.88	$7.06 \times 10^{-5}$
9.09	$5.57 \times 10^{-5}$

Tables 1 and 2 show the results of determination of the intrinsic solubility ( $S_0$ ) and a pH-dependent solubility of verapamil. Figure 2 shows linear dependence of verapamil solubility (S) on  $[\text{H}^+]$  in a pH interval from 8.41 to 9.09.

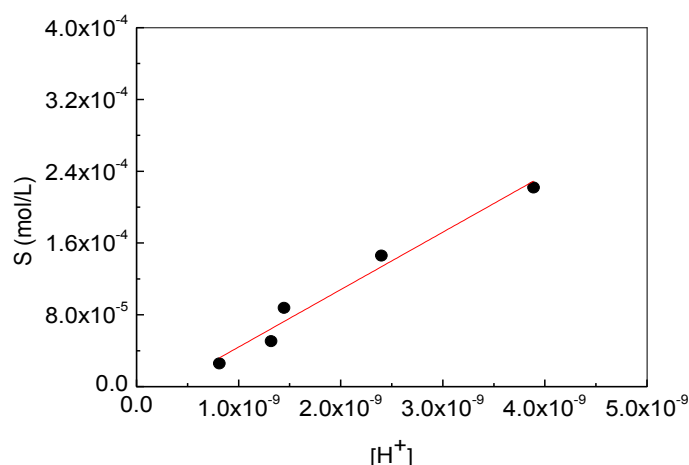


**Figure 2.** Linear dependence of verapamil solubility (S) on  $[\text{H}^+]$ , eq. (6).

Based on the slope of the curve on Figure 2 ( $6.40 \times 10^4$ ) and the intrinsic solubility ( $S_0 = 4.51 \times 10^{-5}$ ), acidity constant of verapamil  $K_a = 7.05 \times 10^{-10}$  ( $\text{p}K_a$  9.15) has been obtained.

The most frequently applied methods for the determination of ionization constants in aqueous solution, potentiometric and spectrophotometric, are not applicable in the case of verapamil. Potentiometry could not be applied due to the low solubility of verapamil, and spectrophotometry due to very small differences in the absorption spectra of molecular and ionized

forms (Figure 3). The few published data show that the  $pK_a$  value of verapamil (8.63, 8.72, 9.07) is determined exclusively by using a cosolvent system [3].

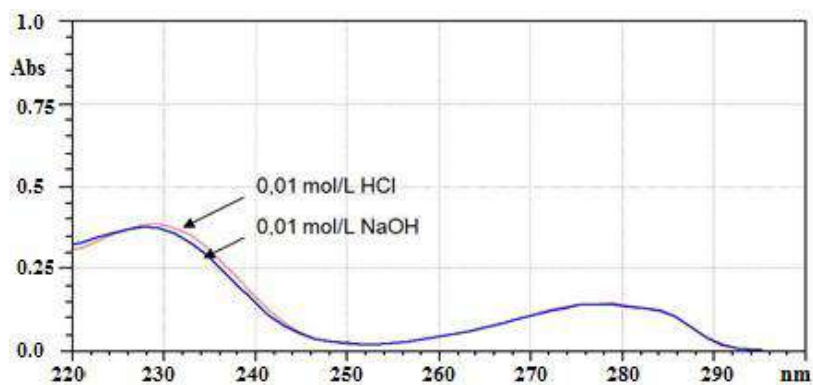


**Figure 3.** UV spectra of verapamil in 0.01 mol/L HCl (ionized form) and 0.01 mol/L NaOH (molecular form).

## CONCLUSION

The intrinsic solubility and pH-dependent solubility of verapamil are determined. Based on the solubility data the  $pK_a$  value of the verapamil is indirectly determined. Obtained data are of great importance for the improvement of analytical procedures, pharmaceutical formulations, and evaluation of the pharmacological behavior of verapamil.

## Acknowledgement

This work was supported by the Ministry of Education, Science and Technological Development of the Republic of Serbia, Contract No. 172033.

## REFERENCES

- [1] Lemke T. L., Williams D. A., Roche V. F., Zito S. W., Foye's Principles of Medicinal Chemistry, Lippincott Williams & Wilkins: Philadelphia, 2013.
- [2] Avdeef A. Absorption and Drug Development: Solubility, Permeability, and Charge State. John Wiley & Sons, New Jersey, 2012.
- [3] Völgyi G., Ruiz R., Box K., Comer J., Bosch E., Takács-Novák K., Anal. Chim. Acta, 2007, **583**, 418-428.

## THEORETICAL STUDY OF IONIZATION OF SARTANSIN AQUEOUS MEDIA

M. Popović<sup>1</sup>, G. Popović<sup>2</sup>, K. Nikolić<sup>1</sup>, M. Grujić<sup>1</sup> and D. Agbaba<sup>1</sup>

<sup>1</sup>*Department of Pharmaceutical Chemistry,  
(majap@pharmacy.bg.ac.rs)*

<sup>2</sup>*Department of General and Inorganic Chemistry,  
University of Belgrade-Faculty of Pharmacy, Vojvode Stepe 450,  
11000 Belgrade, Serbia*

### ABSTRACT

In this study the order of ionization in the molecules of irbesartan, losartan, and valsartan has been investigated. Irbesartan and losartan are ampholytes, valsartan is diacid with close values of ionization constants. In order to get better insight in the overlapped protolytic equilibria of sartans theoretical study was performed. Energy calculation of the optimized structures of equilibrium forms was performed at the B3LYP/6-31G (d,p) level of the Density Functional Theory (DFT). Results of theoretical study confirmed prediction that in all examined compounds higher  $pK_a$  values can be attributed to the ionization of tetrazole.

### INTRODUCTION

Angiotensin II Receptor Blockers (ARB), also known as sartans, are used in the treatment of hypertension, cardiac insufficiency, myocardial infarction, and diabetic nephropathy. Not only the conformation of the sartans active form is important for pharmacological activity but also their ionization state in physiological conditions that can affect partitioning between plasma and biomembranes [1]. Irbesartan and losartan are ampholytes with one acidic (tetrazole ring) and one basic center (imidazole ring), while the valsartan is diprotic acid (carboxylic group and tetrazole ring) (Figure 1). The  $pK_a$  values of examined sartans were determined potentiometrically:  $pK_{a1}$  3.88 and  $pK_{a2}$  4.55 for irbesartan;  $pK_{a1}$  3.27 and  $pK_{a2}$  4.60 for losartan;  $pK_{a1}$  3.79 and  $pK_{a2}$  4.55 for valsartan [2]. Ionization processes include equilibrium forms that can differ in physico-chemical properties. In order to estimate the extent of ionization at any given pH value it is necessary to assign the  $pK_a$  values to corresponding ionizable centers. The main aim of theoretical study was to obtain a better insight in the overlapped protolytic equilibria and properties of sartans equilibrium forms.

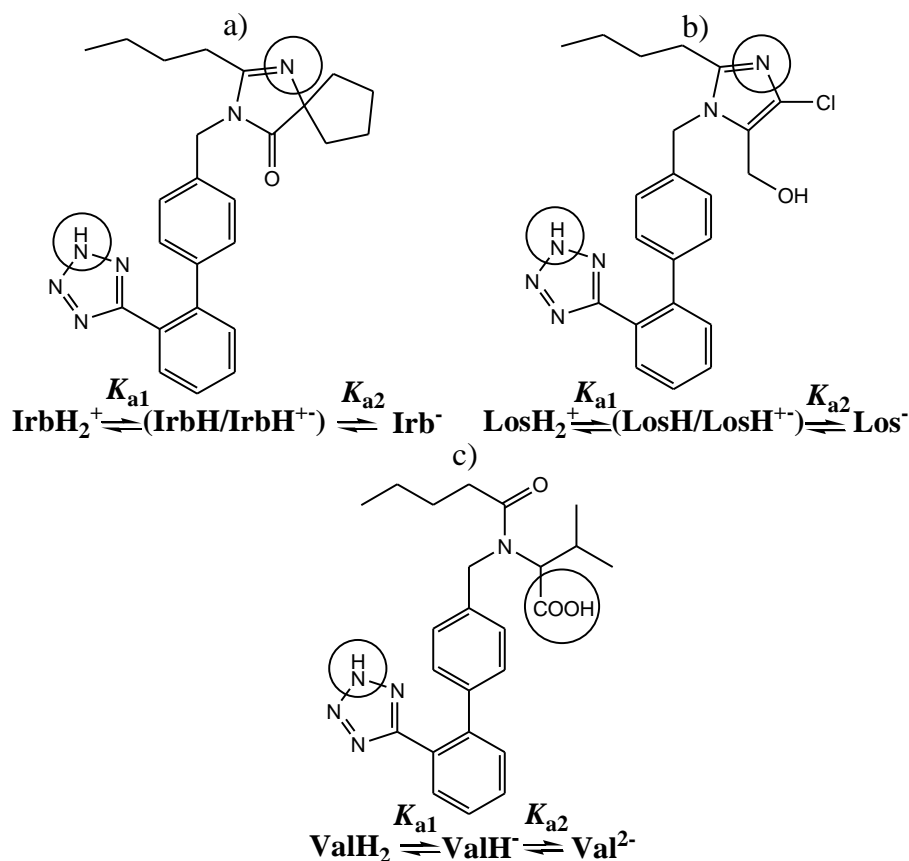


**Figure 1.** Ionization profiles of a) irbesartan, b) losartan, c) valsartan. Equilibrium forms: cationic ( $\text{IrbH}^+$ ,  $\text{LosH}^+$ ), molecular ( $\text{IrbH}$ ,  $\text{LosH}$ ,  $\text{ValH}_2$ ), zwitterionic ( $\text{IrbH}^+$ ,  $\text{LosH}^+$ ), monoanionic ( $\text{Irb}^-$ ,  $\text{Los}^-$ ,  $\text{ValH}^-$ ), dianionic ( $\text{Val}^{2-}$ ).

## EXPERIMENTAL

Chemical structures of each equilibrium form of examined sartans that can exist in solution were built in ChemBioDraw Ultra 13.0 program and copied to ChemBio3D Ultra 13.0 program in order to create their 3D-models. Irbesartan and losartan are ampholytes which may exist in four equilibrium forms in a solution (cationic, anionic, zwitterionic, and molecule), while the valsartan is diacid with three equilibrium forms (molecular, monoanionic, and dianionic). Geometry optimizations of each of the eleven equilibrium forms were performed at the B3LYP/6-31G (d,p) level of the DFT[3, 4] in the gas phase using the Gaussian 09 program [5]. Optimized molecular

models were used for all further calculations. The PCM [6] in the B3LYP/6-31G (d,p)<sup>water</sup> basis set [3, 4] was applied to compute the electronic descriptors, energies of the highest occupied and the lowest unoccupied molecular orbital ( $E_{\text{HOMO}}$  and  $E_{\text{LUMO}}$ ), chemical potential ( $\mu$ ), electronegativity ( $\chi$ ), hardness ( $\eta$ ), global softness ( $S$ ), electrophilicity index ( $\omega$ ), dipole moment, and charges [7].

## RESULTS AND DISCUSSION

Potentiometrically determined  $pK_a$  values of examined sartans are very close which point out to overlapped protolytic equilibria. Order of ionization can be predicted based on the analysis of chemical structure only in case of valsartan (lower  $pK_a$  value of carboxylic group than tetrazole). Irbesartan and losartan contain imidazole ring as a basic center with  $pK_a$  value lower than the  $pK_a$  of tetrazole as an acidic center.

**Table 1.** SCF energies of sartans calculated at B3LYP/6-31G(d,p) level of DFT. Energies are given in hartrees. (Equilibrium forms are explained on Figure 1).

Sartan	Form	SCF <sub>Gas</sub>	SCF <sub>PCM</sub>	$\Delta$ SCF
Irbesartan	IrbH	-1373.29323	-1373.31279	-0.01956
	IrbH <sup>+-</sup>	-1373.29353	-1373.29109	0.00244
	Irb <sup>-</sup>	-1372.74810	-1372.83809	-0.08755
	IrbH <sub>2</sub> <sup>+</sup>	-1373.69218	-1373.77253	-0.08035
Losartan	LosH	-1716.12055	-1716.14021	-0.01966
	LosH <sup>+-</sup>	-1716.11971	-1716.12615	-0.00644
	Los <sup>-</sup>	-1715.58099	-1715.66139	-0.08040
	LosH <sub>2</sub> <sup>+</sup>	-1716.52008	-1716.59122	-0.07114
Valsartan	ValH <sub>2</sub>	-1431.48628	-1431.509456	-0.023176
	ValH <sup>-</sup>	-1430.93597	-1431.027103	-0.091133
	Val <sup>2-</sup>	-1430.32750	-1430.552276	-0.224776

Energy calculation of the optimised molecular models was performed at the B3LYP/6-31G (d,p) [3] level of the DFT [4] in a gas phase and in water solution. The energies of optimised molecular models were computed by applying self-consistent field method (SCF) for transfer the molecules from gas (SCF<sub>Gas</sub>) to aqueous phase (SCF<sub>PCM</sub>) [8] and differences between the energies were calculated ( $\Delta$ SCF = SCF<sub>Gas</sub> - SCF<sub>PCM</sub>) and listed in Table 1.

Value  $\Delta$ SCF is higher for anionic forms of losartan and irbesartan in relation to their corresponding cationic forms, as well as for dianionic

valsartan form compared to its monoanionic form. Larger  $\Delta\text{SCF}$  values were observed for anions formed by deprotonation of tetrazole ( $\text{Irb}^-$ ,  $\text{Los}^-$ ,  $\text{Val}^{2-}$ ) which indicate that more energy is required for ionization of tetrazole in comparison to the ionization of the imidazole and carboxyl group. Based on these results,  $\text{p}K_{\text{a}2}$  values (4.55, 4.60, 4.55) can be attributed to the tetrazole ring of irbesartan, losartan and valsartan, respectively. Accordingly,  $\text{p}K_{\text{a}1}$  values (3.88, 3.27, 3.79) correspond to imidazole ring of irbesartan, imidazole of losartan, and carboxylic group of valsartan, respectively. In case of ampholytes in which  $\text{p}K_{\text{a}}$  of acidic group is greater than the  $\text{p}K_{\text{a}}$  of the basic group is expected that in a solution molecular form is dominant in a relation to zwitterionic.

## CONCLUSION

Experimentally determined  $\text{p}K_{\text{a}}$  values of irbesartan, losartan, and valsartan have been attributed to the corresponding ionizable groups based on results obtained in theoretical study. Defining the ionization of sartans can help with determination of the equilibrium form which is required for achieving a better bioavailability as well as with more accurately explanation of the mechanism of interaction between sartans and their target site of action.

## Acknowledgement

This work was supported by the Ministry of Education, Science and Technological Development of the Republic of Serbia, Contract No. 172033.

## REFERENCES

- [1] Lemke T. L., Williams D. A., Roche V. F., Zito S. W., Foye's Principles of Medicinal Chemistry, Lippincott Williams & Wilkins, 2013.
- [2] Grujic M., Popovic M., Popovic G., Nikolic K., Agbaba D., Protolytic equilibria of sartans in micellar solutions of differently charged surfactants. Accepted for publication in J. Pharm. Sci.
- [3] Becke A. D., J. Chem. Phys., 1993, **98**, 5648-52.
- [4] Lee C., Yang W., Parr R. G., Phys. Rev. B., 1988, **37**, 785.
- [5] Gaussian 09, Revision D.01, Frisch M. J. et al.
- [6] Cossi M., Scalmani G., Rega N., Barone V., J. Chem. Phys., 2002, **117**, 43-54.
- [7] Fleming I., Molecular orbitals and organic chemical reactions. Wiley-VCH: Weinheim, Germany, 2009.
- [8] Floris F. M., Filippi C., Amovilli C., J. Chem. Phys. 2012, **137**, 075102.

## THE EFFECT OF NONIONIC SURFACTANTS ON VERAPAMIL SOLUBILITY

M. Popović<sup>1</sup>, G. Popović<sup>2</sup>, E. Škrijelj<sup>2</sup> and A. Tomić<sup>2</sup>

<sup>1</sup>*Department of Pharmaceutical Chemistry,  
(majap@pharmacy.bg.ac.rs)*

<sup>2</sup>*Department of General and Inorganic Chemistry, Faculty of Pharmacy,  
University of Belgrade, Vojvode Stepe 450, 11000 Belgrade, Serbia*

### ABSTRACT

The intrinsic solubility –  $S_0$  (only the neutral form is present in the solution) of verapamil were investigated in the presence of nonionic micelles (Brij 35 and TX-100) and in surfactant free media. Brij 35 micelles caused the increase in verapamil solubility. The phase separation was observed in solution of TX-100 in the presence of verapamil which points out to specific interactions between verapamil and this surfactant.

### INTRODUCTION

Verapamil belongs to a class of calcium channel blockers applied in the treatment of cardiac arrhythmias, angina pectoris and hypertension. Because to the presence of aliphatic tertiary amine, verapamil represents a weak base [1].

Solubility is one of the most important physico-chemical parameters that affect permeability and absorption of drugs. Solubility is directly related to drug lipophilicity and can be used for its prediction. The knowledge of compound solubility plays a major role in development of pharmaceutical dosage forms. During the transport to the target site of action the drugs have to cross the cell membranes and interact with biomolecules of different polarity and charge. Potential interactions under physiological conditions can affect solubility profile which could differ in relation to aqueous solution. Micellar solutions of surfactants have been used as the biomembrane mimetic systems [2] which act to increase the solubility of poorly soluble drugs. The aim of this study was to investigate the intrinsic solubility of verapamil in micellar solutions of nonionic surfactants (4-octylphenol polyethoxylate - Triton X-100 (TX-100) and Polyoxyethylene lauryl ether - Brij 35) as biomembrane mimetic systems.

## EXPERIMENTAL

Spectrophotometric measurements were carried out on the UV-Vis spectrophotometer Cintra 20 (GBC, Australia). Automatic titrator 798 MPT Titrino (Metrohm, Switzerland) with a combined electrode LL unitrode Pt 1000 (Metrohm, Switzerland) was used for potentiometric measurements. Verapamil hydrochloride was kindly donated from Medicines and Medical Devices Agency of Serbia (Belgrade, Serbia). The nonionic surfactants 4-octylphenol polyethoxylate - TX-100 (Acros Organic) and polyoxyethylene (23) lauryl ether - Brij 35 (Sigma–Aldrich, Germany) were used for the preparation of micellar solutions. All solutions were prepared in double distilled water. Standard solutions of HCl and carbonate-free NaOH were standardized potentiometrically.

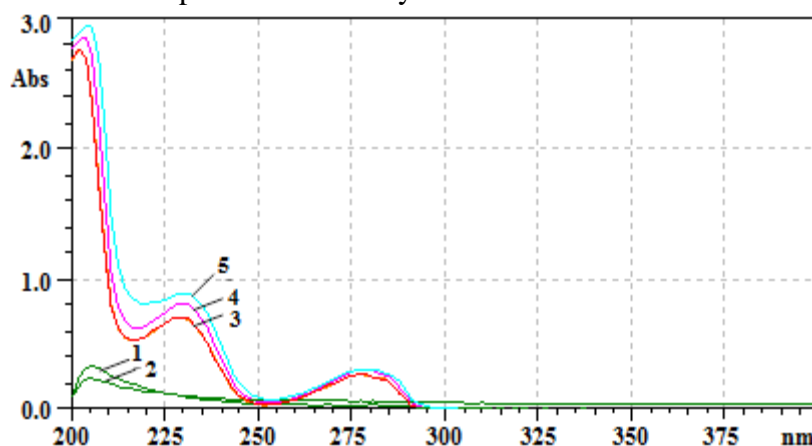


**Figure 1.** Absorption spectra: 1 –Brij 35 ( $10^{-2}$  mol/L); 2– Brij 35 ( $5 \times 10^{-3}$  mol/L); 3– verapamil  $5 \times 10^{-5}$  mol/L; 4– verapamil ( $5 \times 10^{-5}$  mol/L) in the presence of Brij 35 ( $10^{-4}$  mol/L); 5– verapamil ( $5 \times 10^{-5}$  mol/L) in the presence of Brij 35 ( $10^{-3}$  mol/L); Solutions are prepared in 0.01 mol/L HCl.

Saturated solutions of verapamil (pH 11.5 to 12.5) were prepared by treating verapamil hydrochloride solution (0.25 mg/mL) in the presence of micellar solution of surfactants, TX-100 and Brij 35, with 0.1 mol/L NaOH. Suspensions were thermostated at  $25^{\circ}\text{C}$  with occasional stirring for 24 h, then filtered through  $0.22 \mu\text{m}$  membrane filter. Concentration of verapamil in filtrate was determined spectrophotometrically at 280 nm.

## RESULTS AND DISCUSSION

The intrinsic solubility of verapamil (pH > 11.5) is determined in the presence of  $10^{-3}$  mol/L Brij 35 (Table 1). Previously obtained intrinsic

solubility  $S_0$  of verapamil in surfactant free media is  $4.51 \times 10^{-5}$  mol/L. The influence of

verapamil on micelles formation is disabled by selecting the concentration of surfactants much higher than the critical micellar concentration (cmc). Figure 1 shows the absorption spectra of verapamil and Brij 35 separately and of verapamil in the presence of Brij 35. The absorption spectra indicate that the absorbance of the Brij 35 in concentrations less than  $10^{-3}$  mol/L can be neglected at a wavelengths exceeding 280 nm.

**Table 1.** The intrinsic solubility of verapamil determined in the presence of Brij 35 at 25°C.

pH	S (mol/L)
11.5	$2.60 \times 10^{-3}$
11.7	$2.98 \times 10^{-3}$
11.9	$2.71 \times 10^{-3}$
12.0	$2.76 \times 10^{-3}$
Average	$2.76 \times 10^{-3}$

The intrinsic solubility of verapamil is increased in the presence of  $10^{-3}$  mol/L Brij 35 approximately 60 times.

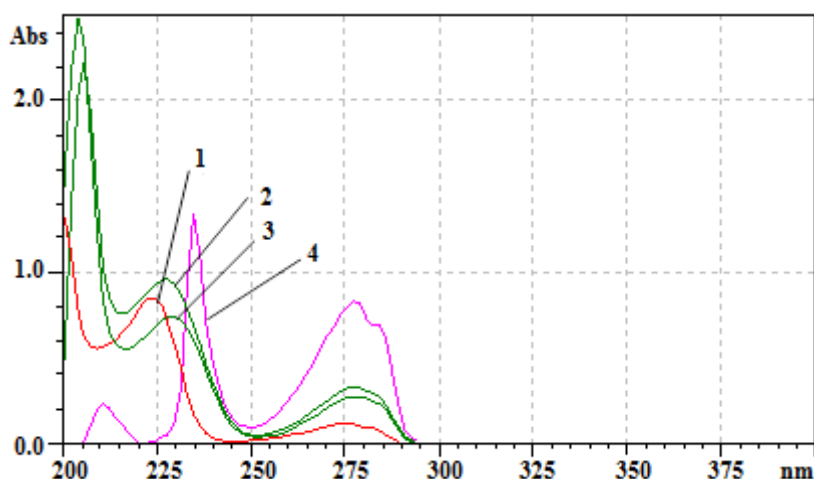


**Figure 2.** Absorption spectra: 1 – TX-100 ( $10^{-4}$  mol/L); 2– verapamil  $5 \times 10^{-5}$  mol/L; 3 – verapamil ( $5 \times 10^{-5}$  mol/L) in the presence of TX-100 ( $10^{-4}$  mol/L); 4– verapamil ( $5 \times 10^{-5}$  mol/L) in the presence of TX-100 ( $10^{-3}$  mol/L); Solutions are prepared in 0.01 mol/L HCl.

Figure 2 shows the absorption spectra of verapamil ( $5 \times 10^{-5}$  mol/L), TX-100 ( $10^{-4}$  mol/L), and verapamil in the presence of  $10^{-3}$  mol/L and  $10^{-4}$  mol/L TX-100. The solution of verapamil in the presence of  $10^{-3}$  mol/L TX-100 has completely rearranged absorption spectra as compared to both verapamil and TX-100.

During the determination of the verapamil solubility in the presence of TX-100, phase separation of the micellar solution ("cloud point" phenomenon) was observed. This phase separation prevented the spectrophotometric determination of verapamil solubility, but point to specific interactions between verapamil and TX-100, which will be the subject of further investigations.

### CONCLUSION

Obtained results point to significant solubility increase of verapamil (about 60 times) in a  $10^{-3}$  mol/L solution of Brij 35. The presence of verapamil led to the phase separation in the micellar solution of TX-100 which indicates a specific interaction between verapamil and this surfactant.

### *Acknowledgement*

This work was supported by the Ministry of Education, Science and Technological Development of the Republic of Serbia, Contract No. 172033.

### REFERENCES

- [1] Lemke T. L., Williams D. A., Roche V. F., Zito S. W., Foye's Principles of Medicinal Chemistry, Lippincott Williams & Wilkins: Philadelphia, 2013.
- [2] Fendler, J. H. Chem. Rev. 1987, 87, 877–899.

## CHITOSAN'S DEGREE OF DEACETYLATION - VOLUMETRIC AND FTIR-ATR DETERMINATION

B. Marković<sup>1</sup>, M. Jankov<sup>2</sup>, I. Popović<sup>2</sup>, B. Ivković<sup>1</sup> and  
K. Karljiković-Rajić<sup>2</sup>

<sup>1</sup>*Department of Pharmaceutical chemistry (bojan@pharmacy.bg.ac.rs)*

<sup>2</sup>*Department of Analytical chemistry, University of Belgrade Faculty of  
Pharmacy, Vojvode Stepe 450, 11221 Belgrade, Serbia.*

### ABSTRACT

The degree of deacetylation (DDA%) of chitosan is essential for its pharmaceutical and biomedical applications. The acid-base back titration method with bromphenol blue provided accurate DDA values of 93.22% (comparable with derivative spectrophotometry 93.04%), and 86.68% for chitosan's samples of different molecular weight. FTIR spectroscopy with ATR technique offered only approximate and lower DDA values of 85.15% and 75.48%, respectively. FTIR spectra indicated the evidence of peak in the band of stretching vibrations of amide C=O for chitosan's sample with higher degree of acetylation (DA%).

### INTRODUCTION

Chitosan is a linear copolymer of  $\beta$ -(1-4) linked 2-acetamido-2-deoxy- $\beta$ -D-glucopyranose and 2-amino-2-deoxy- $\beta$ -D-glucopyranose. Its parent polymer chitin is widely distributed in nature and the main commercial sources of chitin are the shell waste of shrimps, lobsters and crabs. Chitosan (obtained by partial deacetylation of chitin) is a versatile semi-synthetic polymer used in pharmaceutical and biomedical applications, such as drugs delivery systems with modified release; wound-healing products; tissue engineering etc. [1]. Chitosan is readily soluble in dilute acidic solutions below pH 6.0 due to the quaternization of the amine groups becoming a water-soluble cationic polyelectrolyte. The soluble-insoluble transition between chitosan as corresponding salt and chitosan as the base occurs at its pKa value around pH between 6 and 6.5. The pKa value is highly dependent on the degree of N-deacetylation - degree of deacetylation (abbreviations DDA or DD). Chitosan is obtained by the thermochemical deacetylation in the presence of alkali, and the conditions used for deacetylation controls chitosan's molecular weight ( $M_w$ ) and DDA, and those directly affect the physicochemical and biological properties of chitosan.

The aim of this research was to study the possible application of acid-base back titration method for DDA(%) determination for two chitosan's samples of different  $M_w$  and to evaluate the accordance with previously determined DDA value applying derivative spectrophotometry [2] for chitosan hydrochloride prepared from sample with higher  $M_w$ . In addition it was of interest to estimate the relevance of FTIR-ATR technique for calculation of degree of acetylation (DA).

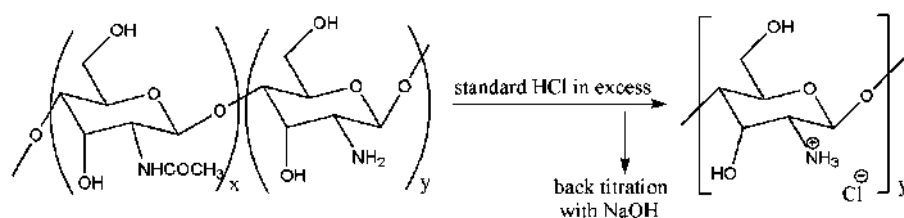
### EXPERIMENTAL

Two samples of chitosan, with different  $M_w$ , were analyzed: Sample 1  $M_r=100-300$  kDa (CNNew Jersey) and Sample 2  $M_r=50-190$  kDa (Sigma Aldrich). Standard solutions of hydrochloric acid ( $c_1=0.09062M$ ,  $c_2=0.08893M$ ) and sodium hydroxide ( $c=0.10058M$ ) were used in acid-base back titration method, for chitosan as base. Suitability of four acid-base indicators, with denoted pH intervals was evaluated: methyl orange-MO (3.1-4.4), bromphenol blue-BPB (3.0-4.6), congo red-CR (3.0-5.0), dimethyl yellow-DY (2.9-4.0). Accurately weighted amount (0.1 g) of each chitosan's sample was transferred into titration flask and 30.00 mL of standard hydrochloric acid solution was added to dissolve samples during 10-15 min on magnetic stirrer. After addition of acid-base indicator the excess of acid was titrated with standard solution of sodium hydroxide. FTIR spectra (Diamond ATR devices technique) were recorded on Nicolet iS10 Thermo-Scientific USA, in the range  $4000$  to  $650$   $cm^{-1}$  with following parameters: scan number 16, resolution  $4$   $cm^{-1}$  and data interval  $0.482$   $cm^{-1}$ .

### RESULTS AND DISCUSSION

Sweidan el al [3] proposed the reaction for DDA determination of chitosan hydrochloride, applying direct acid-base titration with sodium hydroxide solution. The selection of acid-base indicator for back-titration was carried out on chitosan's sample 1. The usage of MO was found inadequate due to difficult end point detection from red to orange. The identical problem was obtained with CO and DY.

Determination of DDA for chitosan as base, by back acid-base titration can be presented with following scheme:



The most appropriate indicator was BPB with obvious color change from yellow to green. The calculated DDA values (Table 1.) obtained according to Zhang et al. [4].

**Table 1.** DDA values of chitosan samples determined applying classical acid-base back titration

Chitosan	Sample 1 (n=9) with MO	Sample 1 (n=7) with MO	Sample 1 (n=7) with BPB	Sample 2 (n=6) with BPB
DDA%	91.04	91.28	93.22	86.68
Sd	3.07	2.51	1.61	0.39
RSD(%)	3.37	2.75	1.73	0.45

The DDA values obtained with indicator MO were lower in comparison with 93.04% determined for chitosan hydrochloride (from sample 1) using derivative spectrophotometry [2], with high RSD(%) values. The average DDA value for sample 1 with indicator BPB (93.22%) was in good accordance with 93.04% with acceptable RSD(%). For sample 2 significantly lower value of 86.68% was calculated, as expected for chitosan of lower molecular weight.

From FTIR spectra the degree of acetylation (DA) was calculated via:

$$DA(\%) = \frac{A_{1655}}{A_{3450}} \times 100 / 1.33$$

from the intensity band absorbance ratio corresponding to stretching vibrations of amide C=O (1680–1630 cm<sup>-1</sup>) and hydroxy O–H group (≈ 3400 cm<sup>-1</sup>). The factor of 1.33 represents the ratio of A<sub>1655</sub>/A<sub>3450</sub> for fully N-acetylated chitosan. The recorded frequencies were 1647 cm<sup>-1</sup> (for sample 1) and 1651 cm<sup>-1</sup> (for sample 2) and for both samples 3355 cm<sup>-1</sup>. The calculated DA values were 14.85% (for sample 1) and 24.52% (for sample 2) with corresponding DDA values of 85.15% and 75.48%, respectively. The obtained values are significantly lower in comparison to DDA determined applying acid-base back titration method for both samples indicating that utilizing ATR technique only approximate DDA values can be calculated. FTIR spectra noticeably distinguished two chitosan's samples since the band for amide C=O for sample 1 was recorded only as the shoulder while for sample 2 with higher DA(%) it was the band with clearly visible peak.

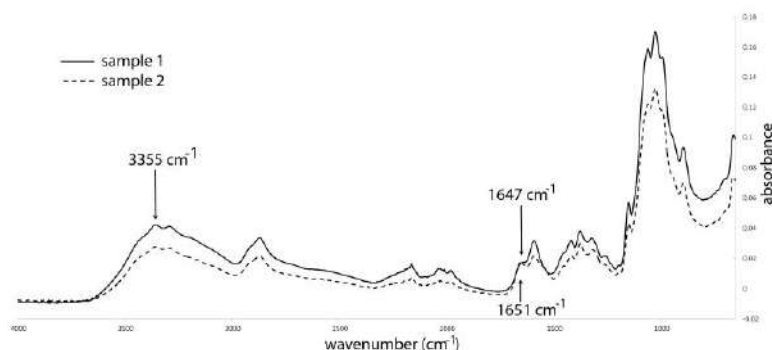


**Figure 1.** FTIR spectra for chitosan's sample 1-solid line and sample 2- broken line

## CONCLUSION

The DDA(%) values of chitosan obtained by classical acid-base back titration using bromphenol blue provided comparable results with derivative spectrophotometric method. FTIR spectroscopy with ATR technique offered only approximate DA(%) values indicating the necessity of KBr technique or evaluation of different wave numbers.

## Acknowledgement

This work was partially supported by the Ministry for Education, Science and Technological Development of the Republic of Serbia (Project no. TR34031).

## REFERENCES

- [1] Younes, M. Rinaudo, Mar. Drugs, 2015, **13**, 1133-1174.
- [2] B. Marković, J. Ignjatović, M. Vujadinović, V. Savić, S. Vladimirov, K. Karljiković-Rajić, Spectrochim. Acta Part A, 2015, **150**, 792-798.
- [3] K. Sweidan, A-M. Jaber, N. Al-jbour, R. Obaidat, M. Al-Remawi, A. Badwan, J. Excipients and Food Chem., 2011, **2**, 16-25.
- [4] A-J. Zhang, Q-L. Qin, H. Zhang, H-T. Wang, X. Li, L. Miao, Y-J. Wu, Czech. J. Food Sci., 2011, **29**, 616-623.

## A NEW COLORED SUBSTRATE FOR SCREENING OF BETA-GLUCANASES-DEGRADING MICROORGANISMS

D. M. Jakovljević<sup>1</sup>, A. N. Đurić<sup>2</sup>, B. D. Kekez<sup>2</sup>, G. Đ. Gojgić-Cvijović<sup>1</sup>,  
V. P. Beškosi<sup>1,2</sup> and M. M. Vrvic<sup>1,2</sup>

<sup>1</sup>*ICH<sub>TM</sub> – Department of Chemistry, University of Belgrade, Njegoševa 12,  
P.O. Box 473, 11000 Belgrade, Serbia (djakovlj@chem.bg.ac.rs)*

<sup>2</sup>*Faculty of Chemistry, University of Belgrade, Studentski trg 12-16,  
P.O. Box 51, 11158 Belgrade, Serbia*

### ABSTRACT

Novel chromogenic macromolecular substrate was synthesized by covalently coupling of branched  $\beta$ -glucan isolated from the cell-wall of baker's yeast *S. cerevisiae* with anthraquinone reactive dye Remazol Brilliant Blue R (RBBR).

New material could potentially have many applications, i.e. for evaluation of endo- and exo-1,3/1,6 glucanases or for screening of  $\beta$ -glucan-degrading microorganisms.

### INTRODUCTION

One of the most studied  $\beta$ -glucan from the microbial origin is the  $\beta$ -glucan isolated from the cell wall of yeast *Saccharomyces cerevisiae*. The basic structural characteristic of this polysaccharide is the main linear backbone consisting of (1,3)-linked  $\beta$ -glucopyranose units. Some of these residues

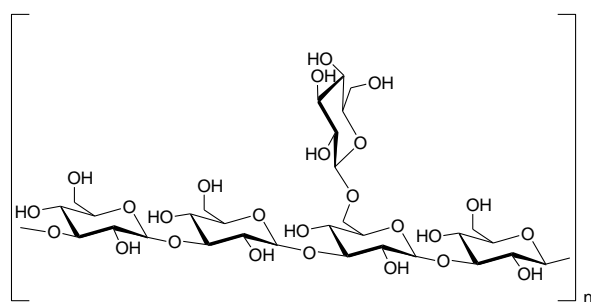


**Figure 1.** Structure of  $\beta$ -glucan

are substituted through O-6 position with single  $\beta$ -glucopyranosyl units, as shown in Figure 1. [1,2]. It is known that glucan from *Saccharomyces cerevisiae* show varied biological activity: immunomodulatory properties, antioxidant effects and protective effect of the aging of cells [3]. Its non-

digestibility and, in some degree, fermentation by intestinal microbial flora affects to be considered as a prebiotic [4].

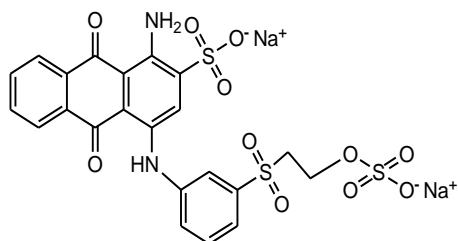


**Figure 2.** Remazol Brilliant Blue R

Reactive dye Remazol Brilliant Blue R (Fig. 2) belongs to the class of anthraquinone dyes that have wide commercial application [5]. Ethylsulfonate group of RBBR in alkaline conditions forms vinyl sulfonate group which undergo addition with carbon nucleophiles of polysaccharide.

The aim of this work was to synthesize and characterize a new polymeric material obtained by covalently coupling of branched  $\beta$ -glucan isolated from the cell wall of baker's yeast *S. cerevisiae* and reactive dye Remazol Brilliant Blue R. This material can be used as potential colored macromolecular substrate for specific assays for selective determination of endo- and exo-1,3/1,6- $\beta$ -glucanases or for screening of  $\beta$ -glucanases-forming microorganisms.

## EXPERIMENTAL

$\beta$ -glucan used in this work was isolated from the cell-wall of active dry baker's yeast (*Saccharomyces cerevisiae*) commercial product made by Fermentation Industry "Alltech-Fermin", Senta, Serbia and purified by repetitive alkaline/acid treatment [1,2]. Other reagents and solvents were purchased from commercial sources and used as supplied.  $\beta$ -D-glucan was stained with RBBR following the procedure of Khalikova nad Usanov with some modifications [6]. The RBBR dyeaqueous solution (0.2 g/6.0 mL) was added dropwise to a vigorously mixed suspension of  $\beta$ -glucan in water (0.5 g/ 40 mL) at 60°C (magnetic stirrer). After 30 min of stirring, 5.5 g of NaCl was added, and mixing was continued for next hour. The mixture was then alkalized with NaOH (0.5 g/10 mL of water) and the reaction mixture was heated to 80°C. Anhydrous  $\text{Na}_2\text{CO}_3$  (0.5 g) was added, and extensive stirring was continued for 2 h at 80°C. After cooling, the stained product was centrifuged (3000 rpm, 10 min) and washed with a 96% ethanol. The colored substrate was resuspended in distilled water, dialyzed and lyophilized. Resulting product was insoluble in distilled water, but was soluble in DMSO after autoclaving. Characterization of samples was performed by FT-IR spectra in ATR mode on Thermo Nicolet 6700 FT-IR Spectrophotometer (500-4000  $\text{cm}^{-1}$ ). UV-VIS spectra were recorded on Shimadzu UV-1280 Spectrophotometer. Elemental analyses were performed on automated analyzer Vario EL III CHNS/O from Elementar Co.

## RESULTS AND DISCUSSION

The biopolymeric colored substrate was synthesized by coupling reaction of  $\beta$ -glucan isolated from the cell-wall of baker's yeast *S. cerevisiae* with reactive dye RBBR. FT-IR spectrum of pure  $\beta$ -glucan contained a strong broad absorption at 3000–3500  $\text{cm}^{-1}$  corresponding to  $\nu$  (OH), the peaks at 2950–2850  $\text{cm}^{-1}$  attributable to ( $\nu$ CH/CH<sub>2</sub>), two partially overlapped absorptions at 1024 and 1048  $\text{cm}^{-1}$  arising to ring and (C–OH) side group stretching, and the peak at 890  $\text{cm}^{-1}$  assigned to the  $\beta$ -glycosidic (C1–H) deformation mode. However, in the FT-IR spectrum of  $\beta$ -glucan-dye derivative (Fig. 3.) typical absorptions at 670–870  $\text{cm}^{-1}$  ( $\gamma$  C–H), 1650–1450  $\text{cm}^{-1}$  ( $\nu$  C=C of aromatic), 1530  $\text{cm}^{-1}$  and 1380  $\text{cm}^{-1}$  ( $\nu$  C–N), 1037  $\text{cm}^{-1}$  and 1120  $\text{cm}^{-1}$  ( $\nu$  S=O) indicate the presence of anthraquinone ring, C–N and S=O vibrations, as a result of the modification of  $\beta$ -glucan with RBBR.

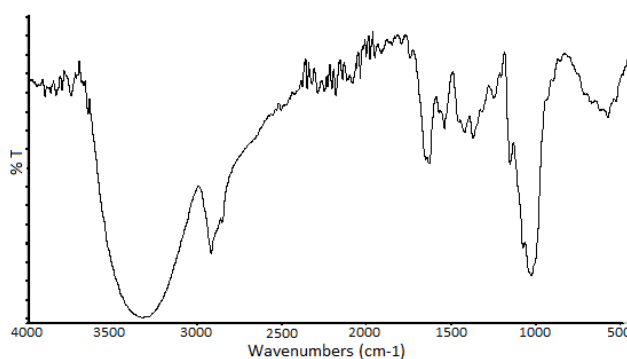


**Figure 3.** FT-IR spectrum of covalently coupled  $\beta$ -glucan-RBBR

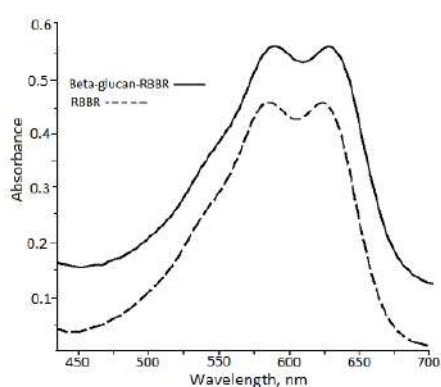


**Figure 4.** UV-VIS spectra of RBBR and  $\beta$ -glucan-RBBR derivative

The elemental analysis of  $\beta$ -glucan yields: C, 44.4; H, 6.2. The obtained values C and H for glucan are in accordance with the values of neutral glycans. In coupled product the content of RBBR is reflected by the increase of nitrogen content after reaction of  $\beta$ -glucan with dye. The elemental analysis of  $\beta$ -glucan-RBBR yields: C, 46.3; H, 6.7; N, 0.6. UV-VIS spectra (region 450–700 nm) of RBBR and synthesized substrate were shown in Fig.4. The free RBBR ( $1.6 \times 10^{-4}$  mM/mL) in DMSO showed two absorption maxima at 585 nm and 625 nm. The spectrum

of  $\beta$ -glucan coupled with RBBR showed a sameshape of the spectrum, with maxima slightly blue-shifted (up to 5 nm) compared to the RBBR, which indicates that contribution to the UV-VIS spectrum of synthesized stained biopolymer comes from the anthraquinone segments. This is in accordance with previously published data [6].

### CONCLUSION

The synthesis of new colored polymeric substrate was performed by covalent coupling of the branched  $\beta$ -glucan isolated from the cell-wall of *S. cerevisiae* with reactive anthraquinone dye Remazol Brilliant Blue R. The coupled derivative was characterized by elemental analysis, FT-IR and UV-VIS data. Synthesized material can be used as potential colored macromolecular substrate for screening of  $\beta$ -glucanases-degrading microorganisms.

### Acknowledgement

This work was supported by the Ministry of Education and Science of the Republic of Serbiathrough Project III 43004.

### REFERENCES

- [1] B.A. Stone, A.E. Clarke, Chemistry and Biology of (1,3)- $\beta$ -Glucans, La Trobe University Press, Australia, 1992, pp. 47–49.
- [2] D. Zlatković, D. Jakovljević, Dj. Zeković, M.M. Vrvic, J. Serb. Chem. Soc. 2003, **68**, 805-809.
- [3] Đ. Zeković, S. Kwiatkowski, M.M. Vrvic, D. Jakovljević, C.A. Moran, Crit Rev. Biotechnol. 2005, **25**, 205-230.
- [4] O.B. Laugier, S.D. Spasić, V. Mandić D. Jakovljević, M.M. Vrvic, Int. J. Food Sci. Technol. 2012, **47**, 369-375.
- [5] C. Fleischmann, M. Lievenbrück, H. Ritter, Polymers, 2015, **7**, 717–746.
- [6] E.F. Khalikova, N.G. Usanov, Appl. Biochem. Microb. 2002, **38**, 89–93.

## SYNTHESIS OF NOVEL PIMARICIN INULIN CONJUGATE

D. M. Jakovljević<sup>1</sup>, B. D. Kekez<sup>2</sup>, A. N. Đurić<sup>2</sup>, G. Đ. Gojgić-Cvijović<sup>1</sup>,  
V. P. Beškoski<sup>1,2</sup> and M. M. Vrvic<sup>1,2</sup>

<sup>1</sup>*ICH<sub>TM</sub> - Department of Chemistry, University of Belgrade, Njegoševa 12,  
P.O. Box 473, 11000 Belgrade, Serbia (djakovlj@chem.bg.ac.rs)*

<sup>2</sup>*Faculty of Chemistry, University of Belgrade, Studentski trg 12-16,  
P.O. Box 51, 11158 Belgrade, Serbia*

### ABSTRACT

Soluble inulin pimaricin conjugate have been synthesized by coupling of aldehyde-*functionalized* polysaccharide inulin with a water-insoluble tetraene macrocyclic membrane-active antifungal antibiotic pimaricin. The synthesized product was soluble in water and characterized by UV-VIS and <sup>1</sup>HNMR spectroscopic data.

### INTRODUCTION

Reactions of covalent coupling of various aldehyde-*functionalized* polysaccharides with biological active compounds has successfully been applied for decades. [1]. The polyaldehyde polymers obtained by periodate oxidation of polysaccharides, *via* reactive -CHO groups can easily bond amine-containing drugs, such as polyene antibiotics, through the Schiff base linkages thus enhancing the water solubility of insoluble drugs and therefore their availability and functionality.

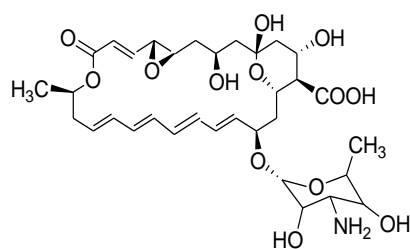


**Figure 1.**  
Structure of pimaricin

Pimaricin is a polyene macrolide antibiotic produced by *Streptomyces natalensis*. It consists of a large lactone ring which is linked to a mycosamine moiety, a deoxyamino-sugar, by a glycosidic bond (Fig.1.) Pimaricin is a potent antifungal compound which specifically inhibits the growth of mold and yeast, and is mostly used in the food industry as a natural preservative and in medicine [2]. However, its insolubility in water limits its wider application.

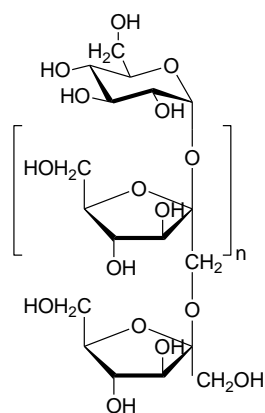


**Figure 2.** Inulin

Inulin is a soluble polysaccharide belonging to a heterogeneous group of carbohydrates known as fructans. This polymer consists of chain-terminating glucosyl moieties on nonreducing end, and a repetitive fructosyl moiety which are linked by  $\beta$ -(2,1) glycosidic bonds (Fig. 2). Due to its excellent features: non-toxicity, water solubility and non-digestibility inulin and its partial hydrolysis products, oligofructose, are used in many areas: in the food industry, pharmacy, medicine [3]. Since the application of pimaricin is rather limited because of its insolubility in aqueous media the goal of the present work was to synthesize a conjugate of this

antibiotic by covalent coupling with aldehyde-*functionalized* inulin in order to increase solubility of the antifungal compound. Water soluble conjugate was characterized by UV-Vis and  $^1\text{H}$ NMR data.

## EXPERIMENTAL

Oxidation of inulin to polyaldehyde derivative was performed following a procedure reported by Tabandeh and Aminlari [4]. Aldehyde functionalized inulin (40 mg) and pimaricin (40 mg) were coupled in borate buffer (pH 8.0) in the dark, with continuous stirring, at 30 °C, during 24 h. Resulting conjugate was precipitated by 96% ethanol (three volumes). After centrifugation, procedure of dissolving in water (5 mL) and precipitation with ethanol was repeated for three times. The conjugate was additionally purified by *gel filtration* on *Sephadex* G-10 using distilled water as an *eluent* and lyophilized (Christ Alpha 2-4 LD plus).  $^1\text{H}$  NMR spectra were recorded on a Varian Gemini 2000 (200 MHz). UV-VIS spectra were measured on Shimadzu UV-1280 spectrophotometer.

## RESULTS AND DISCUSSION

Synthesis of periodate oxidized inulin-pimaricin conjugates was achieved by coupling reaction between aldehyde groups of oxidized polysaccharide and amine group of the antibiotic. Coupling reaction was monitored by UV-Vis and  $^1\text{H}$ NMR spectroscopy. It is known that native and oxidized glycans do not have absorptions in UV-Vis range of 250-400 nm [5]. However, after coupling reaction with tetraene macrolide, spectrum of synthesized conjugate (Fig. 3) shows characteristic absorptions ( $\lambda_{\text{max}}$  291, 304, and 319 nm) slightly red shifted (up to 3 nm) in relation to pimaricin, as shown in Figure 3[6]. This is probably *due* to interchain interactions on the electronic

structure of synthesized conjugate. Based on this, it can be concluded that aldehyde-*functionalized* inulin was successfully coupled with  $-NH_2$  group of antibiotic.

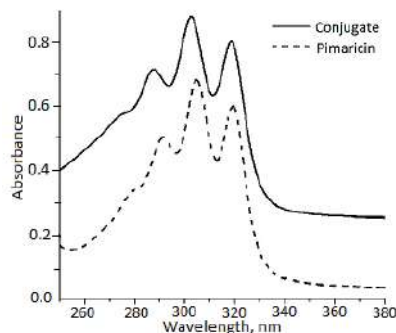


**Figure 3.** UV spectra of pimaricin and inulin-pimaricin conjugate

$^1H$  NMR spectrum of synthesized conjugate (Fig. 4) showed characteristic peaks of  $^1H$  protons of oxidized inulin, as well as peaks of pimaricin. It can be concluded that some signals related to inulin: H-1 anomeric protons of the glucose residues (5.4–5.0 ppm), protons from the  $-OH$  groups of the fructosyl residues (4.9–4.2) and signals of the carbon protons of fructosyl units (3.7–2.5) are overlapped with some peaks characteristic of the

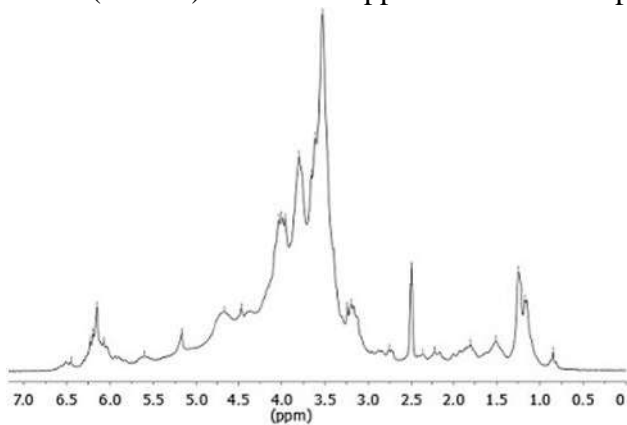


**Figure 4.**  $^1H$ NMR spectrum of inulin-pimaricin conjugate

pimaricin: polyol segment and part of signals of hemiketal six-membered ring (4.50–3.0) [7,8]. Except these overlapping signals, the part of the spectrum related to the polyene region of the antibiotic, and some signals of monosaccharide residues of inulin, are specifically evidenced.

In the  $^1H$ NMR spectrum of conjugate chemical shifts characteristic for the polyene regions (5.50–6.51 ppm) of pimaricin was clearly distinguished, as well as methylene region (2.50–1.40) and methyl groups of this antibiotic (1.24–0.85) [8].

## CONCLUSION

The macromolecular conjugate was synthesized by coupling reaction between aldehyde-*functionalized* polysaccharide inulin and *tetraene* macrolide antibiotic pimaricin. The *obtained product* was characterized by UV-Vis and <sup>1</sup>HNMR data. This novel product potentially could have a great use in food industry as a result of improved drug solubility in water.

## Acknowledgement

This work was supported by the Ministry of Education and Science of the Republic of Serbia through Project III 43004.

## REFERENCES

- [1] R. D. Astronomo, D. R. Burton, *Nature, Reviews Drug Discovery* 2010, **9**, 308-324.
- [2] J. F. Aparicio, E. G. Barreales, T. D. Payero, C. M. Vicente, A. de Pedro, J. Santos-Aberturas, *Appl. Microbiol. Biotechnol.* 2016, **100**, 61–78.
- [3] A.C. Apolinário, B.P.G. Damasceno, N.E.M. Beltrão, A. Pessoa, A. Converti, J.A. da Silva, *Carbohydr. Polym.* 2014, **101**, 368–378.
- [4] M. R. Tabandeh, M. Aminlari, *J. Biotechnol.* 2009, **141**, 189–195.
- [5] S. N. Drobchenko, L. S. Isaeva-Ivanova, A. R. Kleiner, A. V. Lomakin, A. R. Kolker, V. A. Noskin, *Carbohydr. Res.* 1993, **241**, 189-199
- [6] K. Dornberger, D. Voigt, W. Ihn, J. Vokoun, H. Thrum, *Tetrahedron*, 1976, **32**, 3069-3073.
- [7] T. Barclay, M. Ginić-Marković, M.R. Johnston, P. Cooper, N. Petrovsky *Carbohydr. Res.* 2012, **352**, 117–125.
- [8] O. Ceder, B. Hansson, *Tetrahedron*, 1977, **33**, 2703-2714.

## LINEAR SOLVATION ENERGY RELATIONSHIP STUDY OF SELECTED IMIDAZOLINE RECEPTOR LIGANDSON $\alpha$ 1-ACID GLYCOPROTEIN COLUMN

S. Filipić, D. Ružić, J. Vučićević, K. Nikolić and D. Agbaba

*University of Belgrade, Faculty of Pharmacy, Department of  
Pharmaceutical Chemistry, Vojvode Stepe 450, 11000 Belgrade, Serbia  
(druzic@pharmacy.bg.ac.rs)*

### ABSTRACT

The retention properties of 22 selected imidazoline receptor ligands were studied by high-performance liquid chromatography on  $\alpha$ 1-acid glycoprotein (AGP) column using 2-propanol as organic additive and Sørensen phosphate buffer (pH 7.0). Linear solvation energy relationships (LSER) were built using isocratic retention factors-  $\log k_5$ ,  $\log k_8$ ,  $\log k_{10}$ ,  $\log k_{12}$ ,  $\log k_{15}$  obtained for (5, 8, 10, 12, 15)% of 2-propanol in mobile phase, respectively and extrapolated  $\log K_w$  values as dependant variables. Independent variables (Abraham descriptors) for LSER analysis were calculated by ACD/i-Lab software. LSER analysis indicated on McGowan volume, hydrogen bond basicity and excess molar refraction as the most important parameters for all isocratic retention factors and  $\log K_w$  values of 22 selected imidazoline receptor ligands.

### INTRODUCTION

Human serum albumin (HSA) and  $\alpha$ 1-acid glycoprotein (AGP) are the most common proteins of blood that are responsible for drug binding [1]. It is well described that isoelectric point of AGP ( $pI=2,7$ ) at physiological conditions is lower than for HSA. AGP shows significant affinity to basic and neutral drugs. Pathological processes like malignant disease, infection, other inflammatory diseases change the affinity and extent of AGP, therefore the variability of pharmacokinetic profile of basic and neutral drug can be recognized [2].

The pharmacological effect of selected imidazoline derivatives is based on modulation of imidazoline and alpha adrenergic receptors. These drugs such as centrally antihypertensives, diuretics (amiloride) and nasal decongestives (xylometazoline, oxymetazoline) [3].

Early research showed that lipophilicity index of selected drugs is not the only parameter that correlates with protein binding [4]. Based on previous investigation, we extended this approach with linear solvation energy

relationships (LSER) study. The retention of 22 imidazoline receptor ligands on AGP column was examined under different chromatographic conditions (obtained under different percentages of 2-propanol in mobilephase - 5, 8, 10, 12, 15%, respectively). Imidazoline receptor ligands in this study have similar basic properties, thus it is expected that these compounds have affinity to serum AGP.

### EXPERIMENTAL

The group of 22 selected imidazoline derivatives were purchased from Sigma–Aldrich, St. Louis, MO, USA as hydrochloride salts (Clonidine, moxonidine, guanfacine, brimonidine, efaroxan, idazoxan, rilmenidine, harman, harmine, tizanidine, xylometazoline, tetrahydrozoline, oxymetazoline, antazoline, phentolamine, benazoline, cirazoline, detomidine, metformin, and RX 821002) or provided by Zdravlje-Actavis, Leskovac, Serbia (trimazoline) and Galenika, Belgrade, Serbia (amiloride).

Methanol (J.T. Baker, Deventer, Netherlands) and 2-propanol (Sigma–Aldrich, St. Louis, MO, USA) of HPLC grade and deionized water (TKA water purification system, Niederelbert, Germany) were used throughout this study.

The HPLC analysis was performed on a Dionex Ultimate 3000 system (Thermo Fisher Scientific, Germering, Germany) equipped with autosampler, Dionex Ultimate 3000 quaternary pump, and photodiode array detector. The retention behaviour of selected compounds were examined on CHIRALPAK®AGP column 100 mm × 2 mm I.D. packed with  $\alpha_1$ -acid glycoproteinchemically bound to silica particles size of 5  $\mu\text{m}$  (DAICEL CORPORATION, France). The mobile phases flow rate was set to 0.2 mL/min and temperature to 25 °C. The UV detection was performed at 225 nm.

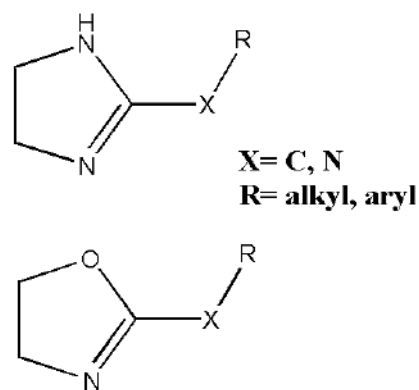


**Figure 1.** General structure of imidazolinereceptor ligands

**RESULTS AND DISCUSSION**

Isocratic retention factors ( $\log k$ ) calculated for different percentage of organic additive in mobile phase (from 5% to 15%) were linearly extrapolated to the lipophilicity index corresponding to 100% of buffered eluent ( $\log K_w$ ), following the Eq.1:

$$\log k = - S\phi + \log k_w \tag{1}$$

where  $\phi$  is the organic solvent fraction, and  $S$  is the slope of the regression curve.

The most accepted representation of the linear solvation energy relationship (LSER) model, proposed by Abraham, is described by Eq 2:

$$\log k = c + eE + sS + aA + bB + vV \tag{2}$$

$E$  - Excessivemolarrefraction,  $S$  - Polarity/polarizability,  $A$  - Hydrogen bond acidity,  $B$  - Hydrogen bond basicity,  $V$  - McGowan Volume

Since electrostatic interactions or ionization effects are not parameterized, positive and negative charged fractions, as  $F^+$  and  $F^-$  have been calculated at pH 7.4. These additional parameters are included in Eq.3. in order to investigate the contribution of charge state in biomimetic retention of imidazolinereceptor ligands.

$$\log k = c + eE + sS + aA + bB + vV + f^+F^+ \tag{3}$$

Coefficients  $c, e, s, a, b, v$  and  $f^+$  are derived by stepwise multiple linear regression (MLR) analysis. Coefficients with  $p < 0.05$  were determined as statistically significant and included in final equations (Eq. 4-9)

The significant coefficients ( $c, e, s, a, b, v$  and  $f^+$ ) of the Abraham's parameters and statistical results presented in Table 1. From the data can be concluded:

**Table. Linear Solvation Energy Relationship Equations**

Eq.	$\log k$	$a$	$b$	$s$	$e$	$v$	Intercept	$f^+$	$r$	$r^2$	SE	$p$
4	$\log K_w$		$-0.492 \pm 0.148$		$0.384 \pm 0.181$	$0.749 \pm 0.177$	$0.567 \pm 0.316$	$-0.007 \pm 0.001$	0.881	0.776	0.206	$2 \cdot 10^{-5}$
5	$\log k_5$		$-0.464 \pm 0.117$		$0.208 \pm 0.101$	$0.626 \pm 0.155$	$0.325 \pm 0.283$	$-0.004 \pm 0.001$	0.853	0.728	0.184	$3 \cdot 10^{-5}$
6	$\log k_6$	$0.379 \pm 0.241$	$-0.521 \pm 0.143$		$0.234 \pm 0.097$	$0.451 \pm 0.146$	$0.294 \pm 0.268$	$-0.002 \pm 0.001$	0.836	0.699	0.173	0.00031
7	$\log k_{10}$	$0.414 \pm 0.246$	$-0.471 \pm 0.146$		$0.235 \pm 0.099$	$0.406 \pm 0.149$	$0.192 \pm 0.273$		0.803	0.645	0.176	0.00123
8	$\log k_{12}$	$0.473 \pm 0.236$	$-0.511 \pm 0.142$			$0.363 \pm 0.137$	$0.134 \pm 0.275$		0.773	0.598	0.180	0.00117
9	$\log k_{15}$		$-0.400 \pm 0.164$			$0.354 \pm 0.163$	$-0.057 \pm 0.325$		0.685	0.469	0.209	0.0132

$r$  - correlation coefficient,  $r^2$  - adjusted for degrees of freedom, SE - standard error of the fit

1. Retention on AGP is mainly guided by McGowan volume, which  $v$ -coefficients show positive influence on retention behavior in all examined systems. Positive signs of coefficients of  $V$  parameters indicates on favourable interactions of bulky analytes with solvated AGP.

2. In all equations  $b$ -coefficients of Abraham basicity show negative influence on retention behavior, which indicates more intensively interaction of the neutral solutes with water/2-propanol then with solvated AGP.

3. Significant positive  $a$ -coefficient of Abraham's acidity parameters in equations ( $\log k_8$ ,  $\log k_{10}$ , and  $\log k_{12}$ , LSER equations 6-8) indicated on influence of 2-propanol in concentration of 8 – 12% on hydrogen bond donating ability of solutes. The results indicate that bond donating groups of the analytes intensify interactions with AGP in this range of organic solvent fraction.

4. The positive  $e$ - and  $v$ - coefficients in our chromatography systems shown that increasing molar refractivity  $E$  and McGowan volume  $V$  facilitate partitioning of solute from mobile phase to stationary phase. This behaviour is explained with more easily formed cavities in solvated AGP phase.

5. The  $f$ -coefficient of  $F^+$  parameter showed very modest influence ( $f$  : -0.007-0.002) on retention behavior of analytes in range of organic solvent fraction (0-8%). These results could be explained with very similar basicity and very narrow pKa interval of the analytes.

## CONCLUSION

By designed LSER study of 22 selected imidazoline receptor ligands, Abraham's descriptors indicated on basicity, McGowan volume and excess molar refractivity of solutes as the most significant parameters for all AGP chromatographic retention factors and  $\log K_w$  values. Described molecular factors represent valuable starting point for further development and prediction of biopharmaceutical properties of imidazoline derivatives.

## Acknowledgement

This work was supported by the Ministry of Science and Technological Development of the Republic of Serbia, Contract No. 172033.

We kindly acknowledge European COST Actions CA15135 and CM1207.

## REFERENCES

- [1] T. Ghafourian, Z. Amin, *Bio. Impacts*, 2013, **3**, 21–27.
- [2] T. Hocheplied, F.G. Berger, H. Baumann, C. Libert, *Cytokine Growth Factor Rev.* 2003, **14**, 25–34
- [3] P. Bousquet, J. Feldman, *Drugs*, 1999, **58**, 799–812.
- [4] F. D. M. Perhourc, A. Radouane, L. Labat, B. Bannwarth, *Pharm. Res.* 1995, **12**, 1535–1538.

## OPTIMIZATION AND VALIDATION OF A HYDROPHILIC INTERACTION LIQUID CHROMATOGRAPHY METHOD FOR DETERMINATION OF MOXONIDINE AND ITS IMPURITIES

S. Filipić, M. Elek, M. Popović, D. Ružić, K. Nikolić and D. Agbaba

*Department of Pharmaceutical Chemistry, Faculty of Pharmacy, University of Belgrade, Vojvode Stepe 450, 11000 Belgrade, Serbia*

### ABSTRACT

Fast and simple hydrophilic interactions liquid chromatography method was developed and validated for the analysis of moxonidine and its impurities in pharmaceutical dosage form. The separation was performed on Zorbax RX-SIL column (250 mm x 4.6 mm, 5  $\mu$ m) using mixture of acetonitrile and 40 mM ammonium-formiat buffer (pH 2.8) in ratio 80:20 (v/v) as mobile phase at flow rate of 1 mL/min, detection at 255 nm and temperature of 25 °C. Under the selected chromatographic conditions separation and analysis of five examined compounds in the mixture is enable within 12 minutes. The validation criteria for selectivity, linearity ( $r \geq 0.9976$ ), accuracy (*recovery*: 93.66 %-114.08 %), precision (RSD: 0.56%-2.55%) and robustness of the method were fulfilled. The obtained values of the limit of detection and quantification revealed that the method can be used for determination of impurities levels below 0.1%.

### INTRODUCTION

Moxonidine belongs to the second generation of centrally acting antihypertensive drug that exhibits high binding affinity for I<sub>1</sub>-imidazoline receptor and minor activity at  $\alpha_2$ -adrenoceptors. It is used in therapy as antihypertensive as well as to improve metabolic profile of patients with hypertension and the type 2 diabetes, or with an impaired glucose tolerance [1]. The European Pharmacopoeia lists 4 related substances of moxonidine (A, B, C and D) (Figure 1.) and prescribes their determination by high performance liquid chromatography using octylsilyl silica gel as stationary phase and the ion-pair reagents as a component of the mobile phase. Because moxonidine and its impurities possess basic character, they are completely ionized in an acid medium. In order to avoid application of ion-pair reagents hydrophilic interaction chromatography (HILIC) which allows the analysis of charged compounds could be also applied. HILIC is

described as a useful alternative to reversed-phase chromatography and in the HILIC mode, an aqueous–organic mobile phase is used with a polar stationary phase to provide normal-phase retention behavior. Silica and amino columns with aqueous–acetonitrile mobile phases offer potential for use in the HILIC [2].

## EXPERIMENTAL

**Moxonidine**, 4-chloro-*N*-(imidazolidin-2-ylidene)-6-methoxy-2-methylpyrimidin-5-amine; **Impurity A**, 4,6-dichloro-*N*-(imidazolidin-2-ylidene)-2-methylpyrimidin-5-amine (6-chloromoxonidine); **Impurity B**, *N*-

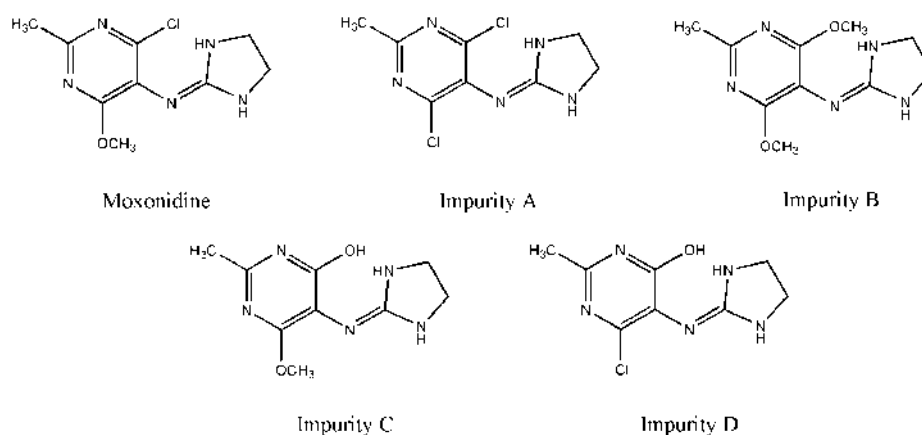


**Figure 1.** Chemical structure of moxonidine and its impurities

(imidazolidin-2-ylidene)-4,6-dimethoxy-2-methylpyrimidin-5-amine (4-methoxymoxonidine); **Impurity C**, 5-[(imidazolidin-2-ylidene)amino]-6-methoxy-2-methylpyrimidin-4-ol (4-hydroxymoxonidine); and **Impurity D**, 6-chloro-5-[(imidazolidin-2-ylidene)amino]-2-methylpyrimidin-4-ol (6-desmethoxymoxonidine) were obtained from Chemagis (Bnei Brak, Israel) (Figure 1.). The Moxogamma<sup>®</sup> 0.4 mg film tablets were manufactured by Worwag Pharma (Böblingen, Germany).

All experiments were performed on the Agilent Technologies 1200HPLC system using Zorbax RX-SIL, 250 mm x 4.6 mm, 5 μm column as stationary phase and mixture of acetonitrile and ammonium-formate buffer as a mobile phase. The acetonitrile content (70% to 80%), pH of the aqueous phase (2.8 to 4.2) and concentration of ammonium formate in aqueous phase (20 mM to 60 mM) were optimized according to the matrix of central composite design obtained by Design-Expert 7.0.0 program (Stat-Ease, Minneapolis, MN, USA). Investigation of the influence of the examined factors on the retention behavior of the tested compounds was carried out by means of the soft independent modeling of class analogy SIMCA P+ 12.0 program.

## RESULTS AND DISCUSSION

Moxonidine and its impurities are compounds with similar polarity (calculated logP values spread in the range 1.57 for the most polar impurity C to 2.49 for impurity A which has the most pronounced lipophilic properties due to the presence of 2 chlorine atoms), thus separation of such compounds in a short period of time is a challenge for analysts. In order to select the chromatographic factors which will be examined during the optimization process a few preliminary experiments have been performed in which content of acetonitrile, pH and the concentration of the buffer, column temperature and flow rate were altered. Based on preliminary results it is observed that retention behavior of examined compounds was most affected by the components of mobile phase such as content of acetonitrile, pH and the concentration of the buffer which were further screened in CCD (Central Composite Design). During method optimization retention factors of analyzed compounds and resolution between critical peak pairs (A/B and C/D) were followed as responses. According to created PLS (Partial Least Squares) models the factors with the significant influence on resolution were identified. The optimal separation conditions were achieved using mobile phases consisting of acetonitrile : 40 mM buffer pH 2.8 (80:20 v/v) (T=25 °C, F =1 mL/min,  $\lambda$ =255 nm) which provide a total analysis time of 12 minutes. Under the selected chromatographic conditions validation of the method was conducted in accordance with ICH guidelines in order to ensure adequate selectivity, linearity, accuracy, precision and robustness. No interference of tablet formulation was observed using the developed chromatographic method which confirms good selectivity of the method. The linearity was evaluated by analyzing nine working solution of impurities over the concentration range 0.0375-0.6  $\mu\text{g mL}^{-1}$  for impurities A and B, and 0.075-1.2  $\mu\text{g mL}^{-1}$  for impurities C and D while in case of moxonidine examination was performed in concentration range 0.05-0.15  $\mu\text{g mL}^{-1}$ . The obtained correlation coefficients 0.9992, 0.9991, 0.9976, 0.9982 and 0.9976 for moxonidine and impurities A, B, C, and D respectively indicated high linearity over the examined concentration range. The assessment of method precision was done by calculating relative standard deviation (RSD): moxonidine (0.56%), impurity A (2.55%), impurity B (1.99%), impurity C (2.01%) and impurity D (2.19%). The obtained values fulfilled the required criteria (RSD 2% for active ingredients, and 10% for impurities C and D, and 15% for impurities A and B [2]). The accuracy of the proposed method was evaluated according to the obtained recovery values (concentration levels of 80%, 100% and 120% of target concentration for moxonidine, and LOQ, 100% and 120% of each

mpurity target concentration) which were in the range 93.66%-101.73%. Experimentally determined values of limit of detection were  $0.011 \mu\text{g mL}^{-1}$  for impurities A and B, and  $0.022 \mu\text{g mL}^{-1}$  for impurities C and D, while values of limit of quantification were  $0.0375 \mu\text{g mL}^{-1}$  for impurities A and B, and  $0.075 \mu\text{g mL}^{-1}$  for impurities C and D. No observable effects on resolution between moxonidine and its impurities was perceived during small variations of working conditions, showing that the proposed method is robustness. The validated method was successfully applied for the analysis of moxonidine purity in available moxonidine tablets (Moxogamma<sup>®</sup> 0.4 mg), Figure 2. The obtained results (97.5 % for content of moxonidine, 0.68 % for impurity C, 0.87% for impurity D, and below LOQ values for impurities A and B) were in accordance with manufacture specification (impurities A i B below 0.5%, and impurities C and D below 1%).

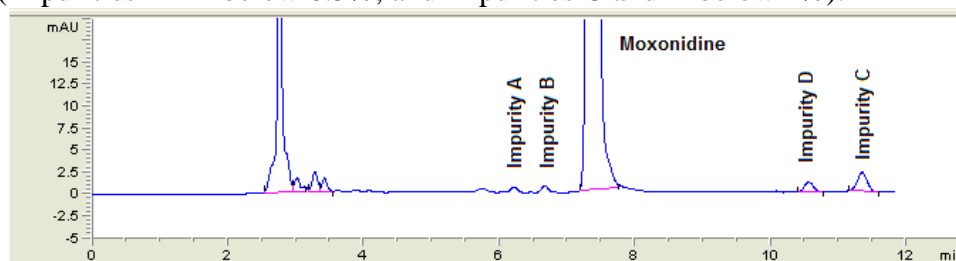


**Figure 2.** The representative chromatogram of sample solution

## CONCLUSION

According to the obtained results the proposed method can be used as fast, simple and reliable for determination of moxonidine and its four impurities in pharmaceutical dosage forms.

## Acknowledgement

This work was partially supported by the Ministry for Science of the Republic of Serbia (Grants no. 172033) and Cost Action CA15135.

## REFERENCES

- [1] C. Fenton, G. M. Keating, A. K. Lyseng-Williamson, *Drugs* 2006, **66**, 477- 496.
- [2] B. A. Olsen, *Journal of Chromatography A* 2001, **913**, 113-122.
- [3] J. B. Crowther, *Validation of pharmaceutical test methods*, in: S. Ahuja, S. Scypin-ski (Eds.), *Handbook of Modern Pharmaceutical Analysis*, Academic Press, New York, 2001, 415–443.

## ELECTROCHEMICAL BEHAVIOR AND DETERMINATION OF SULFAQUINOXALINE AT GLASSY CARBON ELECTRODE

J. Pantić<sup>1</sup>, M. M. Aleksić<sup>1</sup>, V. Kapetanović<sup>2</sup>, and D. Ružić<sup>3</sup>

*University of Belgrade, Faculty of Pharmacy, Departments of <sup>1</sup>Physical Chemistry and Instrumental Methods, <sup>2</sup>Analytical Chemistry, and <sup>3</sup>Pharmaceutical Chemistry, Vojvode Stepe 450, 11000 Belgrade, Serbia (mara@pharmacy.bg.ac.rs)*

### ABSTRACT

Electrochemical behavior of sulfaquinoxaline (SQN) was investigated using cyclic (CV) and differential pulse voltammetry (DPV) at glassy carbon electrode (GCE). CV was applied to investigate the effect of the supporting electrolyte pH on the SQN oxidation. In the pH range 2.0 – 10.0, the best current response was obtained at pH 7.0 in phosphate buffer. Results indicated that SQN is oxidized in irreversible process. DPV method was optimized, and the linear dependence of peak current vs. SQN concentration was obtained in the range  $3 \times 10^{-6}$ – $5 \times 10^{-5}$  molL<sup>-1</sup>, with limits of detection and quantification of  $1.53 \times 10^{-6}$  molL<sup>-1</sup> and  $5.10 \times 10^{-6}$  molL<sup>-1</sup>, respectively.

### INTRODUCTION

The sulfonamide drugs (“sulfas”) had been discovered primarily as antibacterial agents and later on, their efficacy had been shown to extend to protozoan parasites. Sulfaquinoxaline was found to be a superior agent against sporozoan parasite, *Eimeria* spp., the causative agent of coccidiosis in domestic chickens [1]. Different methods such as liquid chromatography with ultraviolet detection [2], high performance liquid chromatography (HPLC) coupled to a mass spectrometer (MS) [3], and a new HPLC method that is based on zwitterionic hydrophilic interaction liquid chromatography (ZIC-HILIC) coupled with ultraviolet detection [4] were used to determine SQN. Electrochemical reduction of SQN at mercury electrode was reported [5] and used for its determination in veterinary preparations. There is no literature report about the oxidation of SQN. The aim of this work was to investigate SQN oxidation properties at GCE and to optimize DPV method for its determination.

## EXPERIMENTAL

The voltammetric measurements were performed with  $\mu$ Autolab analyzer (EcoChemie, Utrecht, TheNetherlands). Three-electrode system was employed with GCE working electrode, Ag/AgCl reference and Pt-auxiliary electrode. Before each experiment the GCE was manually polished using the aqueous slurry of  $\text{Al}_2\text{O}_3$  powder (particle size  $0.05\mu\text{m}$ ) on a smooth polishing pad and sonicated in absolute ethanol. Chloride, acetate, phosphate and ammonia buffers were used as supporting electrolytes. An appropriate volume of supporting electrolyte of different pHs was placed in electrochemical cell, de-aerated for 15 minutes with high purity nitrogen and SQN stock solution ( $c_0=2\times 10^{-3}\text{ molL}^{-1}$ ) was added to make its final concentration of  $1\times 10^{-4}\text{ molL}^{-1}$  for CV and  $1\times 10^{-5}\text{ molL}^{-1}$  for DPV. The cyclic voltammograms were recorded at scan rate of  $100\text{ mVs}^{-1}$ . Parameters for DPV were: potential pulse width 50ms, pulse amplitude 75mV and step potential  $5\text{mVs}^{-1}$ . All experiments were performed at  $24 \pm 1^\circ\text{C}$ .

## RESULTS AND DISCUSSION

The oxidation of  $1\times 10^{-4}\text{ molL}^{-1}$  solution of SQN at GCE was preliminary studied in acetate buffer pH 3.5 by cyclic voltammetry. Cyclic voltammograms were obtained in repeated scans starting from 0 V towards +1.25 V and reversing to negative potential limit -1.2 V at a scan rate  $100\text{ mVs}^{-1}$ . On the first positive-going scan (Fig. 1, grey line) one anodic peak (I) was obtained at  $E_{pI} = 0.98\text{ V}$  and on the second scan (Fig. 1, black line) another anodic peak (II) was obtained at  $E_{pII} = 0.5\text{ V}$ . Changing the scan direction both anodic peaks were obtained (Fig. 2.) in the first scan. Peak II is probably due to oxidation of the SQN reduction product formed at the surface of GCE at negative potential values.

These results correspond to already established redox mechanism of C=N quinoxaline core group [6]. There are no peaks at

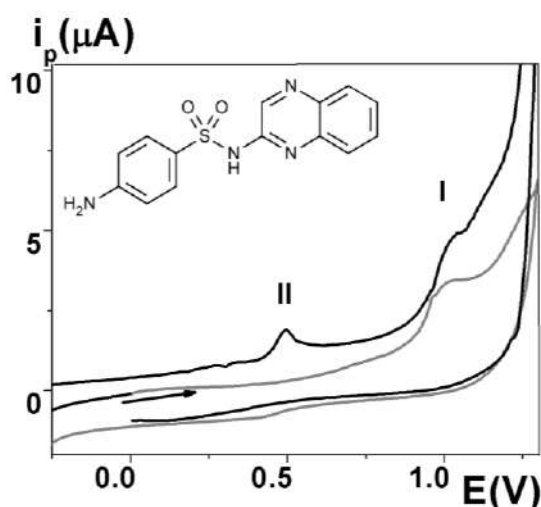


**Figure 1.** CV of  $1\times 10^{-4}\text{ molL}^{-1}$  SQN in two successive scans: — first scan, — second scan ( $v = 100\text{ mVs}^{-1}$ )  
Attached: SQN structure

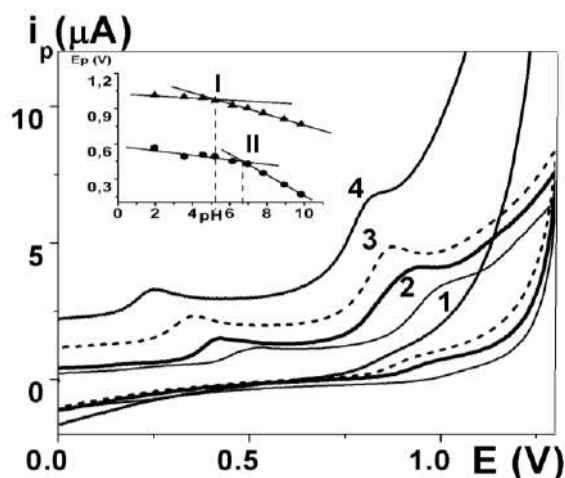


**Figure 2.** CV of  $1 \times 10^{-4} \text{ molL}^{-1}$  SQN at different pH values: 1 – pH 4.6; 2 – pH 6.1; 3 – pH 7.8; 4 – pH 8.9; (scan rate  $100 \text{ mVs}^{-1}$ )

Attached: Influence of the pH on SQN CV peaks potential, I ( $\blacktriangle$ ) and II ( $\bullet$ )

$\text{pKa(I)} \sim 5.2$  and  $\text{pKa(II)} \sim 6.7$ . First value corresponds to literature data ( $\text{pKa} = 5.1$  for sulfonamide nitrogen [7]).

This result indicates that oxidation of nitrogen in sulfonamide group is responsible for peak I and that it could be used for further research and SQN determination. Another  $\text{pKa}$  value corresponds to  $\text{pKa}$  of nitrogen in dihydro derivate of quinoxaline. It is assumed that this derivative is result of the oxidation of SQN reduction product [6].

For peak I the best current response was obtained at pH 7.0 in phosphate buffer. DPV method was optimized by varying important operation parameters, and the best obtained values were: potential pulse width 50ms, pulse amplitude 75mV and scan rate  $5 \text{ mVs}^{-1}$ .

The linear dependence of peak current vs. SQN concentration was obtained in the range  $3 \times 10^{-6} - 5 \times 10^{-5} \text{ molL}^{-1}$ , under optimal conditions, and expressed by the equation  $i_p (\mu\text{A}) = 0.510 \times c (10^{-5} \text{ molL}^{-1}) - 0.139$  ( $r = 0.9984$ ,  $\text{SD} = 0.026 \mu\text{A}$ ), with  $\text{LOD} = 1.53 \times 10^{-6} \text{ molL}^{-1}$  and  $\text{LOQ} = 5.10 \times 10^{-6} \text{ molL}^{-1}$ .

SQN represents one of two active components in veterinary medicine NEOCOCCYN WSP. According to our preliminary results another active component, amprolium hydrochloride, is not electrochemically active under

reverse part of scan indicating that processes corresponding to peaks I and II are irreversible.

Anodic peaks I and II are present in the pH range from 2.0 up to 10.0 at positive potentials. The influence of the pH on these peaks potential resulted in the shift to the less positive potentials with increasing of pH and that  $\text{H}^+$  ions are included in

the electron transfer process. Observing  $E_p$  vs. pH dependence, both peaks show two linear segments. According to their intersection, experimental  $\text{pKa}$  values were determined:

the conditions used for SQN determination, and therefore the proposed DPV method at GCE can be used to determine SQN in this veterinary medicine.

### CONCLUSION

An extensive study of SQN electrochemical behavior at GCE was done by applying CV and DPV. It is confirmed that oxidation of nitrogen from sulfonamide group is irreversible, pH dependent process. From  $E_{pvs}$ . pH relation, experimental pKa values were obtained. The selective/specific DPV method at GCE without pretreatment will be optimized for SQN determination in veterinary medicine NEOCOCCYN WSP, which contains amprolium hydrochloride, as active component too.

### Acknowledgement

This work was supported by the Ministry of Education, Science, and Technological Development of the Republic of Serbia, Grant no. 172033.

### REFERENCES

- [1] W. C. Campbell, The Journal of Parasitology, 2008, **94**, 934-945.
- [2] J. J. BerzasNevado, G. Castaneda Penalvo, F.J. Guzman Bernardo, Journal of Chromatography A, 2000, **870**, 169–177.
- [3] T. A. M. Msagati, M. M. Nindi, Talanta, 2004, **64**, 87–100.
- [4] M. Ghanem, S. Abu-Lafi, R. Karaman, H Hallak, Pharmaceut Anal Acta, 2012, **3**(7), 1-5.
- [5] J. J. Berzas, J. Rodriguez, J. M. Lemus, G. Castaiieda, AnalyticaChimicaActa, 1993, **273**, 369-375.
- [6] M. M. Aleksić, V. Radulović, D. Agbaba, V. Kapetanović, ElectrochimicaActa, 2013, **106**, 75– 81.
- [7] SPARC; pKa/property server. Ver 3. Jan, 2006. <http://ibmlc2.chem.uga.edu/sparc/>

## VALIDATION OF DIRECT RP-HPLC METHOD FOR DETERMINATION OF CICLOPIROX OLAMINE

S. Agbaba, B. Ivković, M. Crevar Sakač and Z. Vujić

*Department of Pharmaceutical Chemistry, Faculty of Pharmacy, University of Belgrade, Vojvode Stepe 450, Belgrade-Serbia.*

*(blucic@pharmacy.bg.ac.rs)*

### ABSTRACT

High performance liquid chromatography (HPLC) has been used for the determination of cixlopirox olamine in cream. Determination was carried out on a Zorbax SB-CN (150 x 4.6 mm, 3.5 $\mu$ m) column using mixture of anhydrous acetic acid, acetonitrile and 0,96gL<sup>-1</sup>Disodium EDTA water solution (0.2 : 300 : 700 V/V/V ) as the mobile phase and UV detection at 298 nm. The method has been validated with respect to its specificity, linearity, precision, accuracy and robustness. Under the described conditions, a method shows linearity over the concentration range 0.07 – 0.13 mgmL<sup>-1</sup> (r=0.999).It was proved good precision (RSD < 2%), accuracy (Recovery in the range 98-102%) and robustness.

### INTRODUCTION

Ciclopirox olamine (CO) (Fig. 1)is a substituted antimycotic pyridone, widely used as an antifungal substance in pharmaceutical preparations as well as an antiseborrheic agent in cosmetics for topical dermatologic treatment of superficial mycoses. It is most useful against *Tinea versicolor*. It is sold under many brand names worldwide. In contrast to the azoles and other antimycotic drugs, the mechanism of action of ciclopirox is poorly understood.<sup>[3]</sup>Its mechanism of action is anticipated to involve chelation with polyvalent metal ions such as Fe<sup>3+</sup> and Al<sup>3+</sup> and inhibition of the metal-dependent enzymes within fungal cells [1-2]. Many analytical methods of ciclopirox quantitative determination in pharmaceutical preparations and biological fluids, such as,<http://dx.doi.org/10.1039/c4ay01421a><http://pubs.rsc.org/en/journals/journal/AY><http://pubs.rsc.org/en/journals/journal/AY?issueid=AY006019> electrophoretic capillary techniques [3], HPLC [4], polarographic [5], amperometry [6] have been reported in the literature on the subject. Ciclopirox cannot be directly quantied by HPLC or reverse phase chromatography, because of strong complexation of its N-hydroxylpyridone group with residues of the metal cations on the stationary phases of HPLC

columns. Therefore, it is necessary to use pre-column derivatization methods to eliminate the chelating effect by the cyclopirox N-hydroxyl group methylation. This paper describes a simple directly RP HPLC method without pre-column derivatization. Thus a fast, economical and simple method is performed on the *Zorbax SB-CN* (150 x 4.6 mm, 3.5  $\mu$ m) column and EDTA as mobile phase additive. The proposed methods were successfully applied for cyclopirox olamine determination in topical pharmaceutical preparations (cream and unguentum).

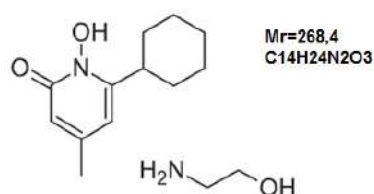


**Figure 1.** Chemical structure of cyclopirox olamine.

## EXPERIMENTAL

All used reagents were of the analytical grade. The mobile phase and the solvents were prepared using acetonitrile (*Lab Scan*, Ireland), acetic acid (*Carlo Erba*, Italy), disodium EDTA (Sigma, Germany) and HPLC grade water.

**Chromatographic conditions:** The isocratic HPLC method was developed using *Zorbax SB-CN* (150 x 4.6 mm, 3.5  $\mu$ m) chromatographic column with mobile phase containing a mixture of anhydrous acetic acid, acetonitrile and 0.96g/L disodium EDTA in the water (0.2 : 300 : 700 V/V/V) respectively. The flow rate of the mobile phase was 1.5 mLmin<sup>-1</sup>. The column temperature was maintained at 35°C and the eluted compound were monitored at the wavelength of 298 nm. Mixture of acetonitrile : mobile phase in the ratio 20 : 80 (V/V) was used as solvent.

**Solutions:** A standard stock solution of CO was prepared in the solvent with to obtain the concentration of 1 mgmL<sup>-1</sup>. The specificity of the method was proved by preparing placebo, standard (0.1 mgmL<sup>-1</sup> CO) and sample solutions. Placebo solution: a quantity of placebo cream equal to 10 mg (about 1g) of CO is accurately weighed and dissolved in a 100 ml volumetric flask with solvent and filled to volume with solvent. The solution is sonicated for 15 minutes. To evaluate the linearity of the method, five solutions of CO in the concentration range from the 0.07 to 0.13 mg mL<sup>-1</sup> were prepared in the solvent using the appropriate standard solutions. The accuracy of the method was proved by preparing three series of solutions containing appropriate placebo and CO in three levels: low level 80% (0,08 mgmL<sup>-1</sup>), medium level 100% (0.1 mgmL<sup>-1</sup>) and high level 120% (0.12 gmL<sup>-1</sup>). To prove the precision of the method, six identical sample solutions

were prepared. The concentration of CO in the prepared sample solutions was  $0.1 \text{ mgmL}^{-1}$ . Sample solutions: weighed about 1.0 g cream into a 100 ml volumetric flask, add 70 ml of the solvent and agitated in an ultrasonic bath for 15 minutes. Allowed to stand for a few minutes at room temperature, the make up the volume with solvent, and then centrifuged for 5 minutes at 2000 rpm. The supernatant was filtered through a PTFE membrane filter of 0.45  $\mu\text{m}$ . Prepare these six solutions.

## RESULTS AND DISCUSSION

The proposed method was validated as per ICH guideline. The following validation characteristics were addressed: suitability, specificity, precision, linearity, accuracy, and robustness.

System suitability (SST) was checked for the conformance of suitability and reproducibility of chromatographic system for analysis. The acceptance criteria were basis of USP (capacity factor  $1 < k' < 10$ , tailing factor (T)  $< 2.0$  and theoretical plate (N)  $\leq 3000$ ). All critical parameters tested met the acceptance criteria [ $k' = 5.14$ , T = 1.4 and %RSD = 0.02]. Specificity study to establish the interference of placebo was conducted. Study was performed on Placebo (Placebo contains excipients without CO). Chromatogram of placebo had shown no peaks at the retention time of CO, indicating that the excipients used in the formulation do not interfere with the estimation of CO. Linearity test solutions were prepared by diluting the stock solutions to the required concentrations by covering the range from 0.07 to 0.13 mg/mL of CO. Calibration curves were plotted between the responses of peak versus analyte concentrations. The correlation coefficient obtained was greater than 0.999. The above result shows that an excellent correlation existed between peak area and concentration of CO.

**Table 1.** The parameters of the regression analysis

concentration range (mg/ml)	$y = ax+b$	r	$R^2$	$t_b$	* $t_{tab}$
0.07 – 0.13	$y=18856x+229.65$	0.9990	0.9926	2.41	2.78

The precision of method was verified by repeatability and intermediate precision at target concentration level (0.1 mg/mL). Repeatability was checked by injecting six individual preparations of sample solutions. The intermediate precision of the method was also evaluated using different analyst and different instrument and performing the analysis on different days. The % RSD for the result of CO in was within 0.64% and in intermediate precision study was within 1.18% which confirms the good precision of the method. Accuracy of the method was evaluated in triplicate

using three concentrations levels (80%, 100% and 120%) and confirmed by calculated recovery values (98.23% to 101.14%). To determine the robustness of the developed method, experimental conditions were deliberately altered and SST parameters for CO were recorded. The variables evaluated during the robustness testing were: composition of the mobile phase, column temperature and flow rate. The obtained results have shown that the method is robust for experimental variation of composition of the mobile phase and column temperature, but it is not robust for the change of the flow rate. Recovery value lies in the proper range of from 95% to 105%, RSD does not deviate by more than  $\pm 5\%$  (RSD=2.22%). To check the application of the method ciclopiroxolamine cream (1%) was used. Sample was analyzed six times as and results are found content of CO in the satisfactory (0.96%)

## CONCLUSION

The simple, fast, economic reverse-phase HPLC method was developed and validated for routine analysis of CO in pharmaceutical forms as well as to check the stability of the CO.

## Acknowledgement

This work was partially supported by the Ministry for Science of the Republic of Serbia (Grants no.172041).

## REFERENCES

- [1] Williams D., Lewke T.; Foye's Principles of Medicinal Chemistry, sixth edition; Lippincott Williams & Wilkins, 2007, 1717-1740.
- [2] Martidale The Complete Drug Reference, 36<sup>th</sup> edition; Pharmaceutical Press, 2009, 517-551.
- [3] Felix F.S., Lago C.L., Angnes L.; Determination of ciclopirox olamine in pharmaceutical products by capillary electrophoresis with capacitively coupled contactless conductivity detection; Electrophoresis, 2011, **32**, 900–905.
- [4] Gagliardi L., Multari G., Cavazzutti G., De Orsi D., Tonelli D.; HPLC Determination of Ciclopirox, Octopirox, and Pyrithiones in Pharmaceuticals and Antidandruff Preparations; Journal of Liquid Chromatography & Related Technologies, 1998, **21**, 2365-2373.
- [5] Ibrahim F., El-Enany N.; Anodic polarographic determination of ciclopirox olamine in pure and certain pharmaceutical preparations; Journal of Pharmaceutical and Biomedical Analysis, 2003, **32**, 353 -/359.
- [6] Ferreira L.M.C., Felix F.S., Angnes L.; Fast Determination of Ciclopirox in Pharmaceutical Products by Amperometry in Flow and Batch Injection Systems; Electroanalysis, 2012, **24**, 961–966.

## PHYSICOCHEMICAL PROPERTIES OF BIOLOGICALLY ACTIVE SUBSTANCES

A. S. Shipilova<sup>1</sup>, A. V. Knyazev<sup>1</sup>, E. V. Gusarova<sup>1</sup>, S. S. Knyazeva<sup>1</sup>,  
V. N. Emel'yanenko<sup>2</sup> and S.P. Verevkin<sup>2</sup>

<sup>1</sup>*Chemistry Department, Lobachevsky State University of Nizhni Novgorod  
Gagarin Av. 23/2, 603950, Nizhni Novgorod, Russia (28\_stasy@bk.ru)*

<sup>2</sup>*Department of Physical Chemistry, University of Rostock, Dr-Lorenz-Weg  
1, D-18059 Rostock, Germany*

### ABSTRACT

The temperature dependences of heat capacity of B<sub>2</sub>, B<sub>3</sub>, B<sub>9</sub> and B<sub>12</sub> have been measured for the first time in the range from 5 to 350 K by precision adiabatic vacuum calorimetry. The experimental data were used to calculate standard thermodynamic functions for the range from 0 to 350 K. Enthalpies of combustion of the B<sub>2</sub>, B<sub>9</sub>, B<sub>12</sub>, prednisolone, hydrocortisone acetate were measured for the first time using high-precision combustion calorimeter. The standard molar enthalpies of formation in the crystalline state at 298.15 K were derived from the combustion experiments. Received values of standard enthalpies and entropies of formation were used to calculate the standard Gibbs functions of formation at 298 K by Gibbs–Helmholtz equation. The thermodynamic analysis of reactions involving nicotinic acid and the acylation reaction of hydrocortisone into hydrocortisone acetate were made.

### INTRODUCTION

Throughout a person's life a complex stream of biologically active substances constantly flows through his body. There are two main currents of this stream, the large one consists of food substances, and the smaller of medicines. They introduce into the body not only substance and energy but also structural information. Biologically active substances must be distinguished according to whether they are beneficial or harmful to the human body. Useful biologically active substances, which contain an adequate volume of structural information, are extremely important in preserving health, and maintaining energy and creative potential [1]. Vitamins and hormones are the most important useful biologically active substances. Vitamins are vital nutrients involved in multiple biological reactions. Due to high turnover rates and biological activities, vitamin supplies are essential for the appropriate functioning of immune cells.

Moreover, accumulating evidence has revealed that vitamins exhibit specific functions in the control of selected immune cells. Thus, excessive or insufficient intake of vitamins leads to impaired immune responses and consequently results in the development of immune diseases or a high susceptibility to infection. Steroid hormones are essential for the proper function of most organ systems in vertebrates. These hormones affect virtually every tissue and organ in the human body and play major roles in the development, differentiation, and homeostasis of normal individuals. They mediate a wide variety of vital physiological functions ranging from antiinflammatory agents to regulating events during pregnancy [1].

The goals of this work include calorimetric determination of the temperature dependences of the heat capacity of riboflavin, nicotinic acid, folic acid dihydrate and cyanocobalamin from 5 to 350 K, definition the energies and enthalpies of combustion of riboflavin, nicotinic acid, folic acid dihydrate, cyanocobalamin, prednisolone, hydrocortisone acetate and calculation of the standard thermodynamic functions.

### EXPERIMENTAL

Vitamins and hormones were purchased from Fluka. For phases identification, an X-ray diffraction patterns of the tested substances were recorded on a Shimadzu X-ray diffractometer XRD-6000 in the  $2\theta$  range from  $5^\circ$  to  $60^\circ$ . The X-ray data and estimated impurity content (0.1 wt %) in the substance led us to conclude that the samples studied were an individual crystalline compounds. The calorimeter design and the operation procedure were described earlier [2]. The calorimeter was tested by measuring the heat capacity of high-purity copper and reference samples of synthetic corundum and K-2 benzoic acid. To measure the heat capacity of the studied substances ( $B_2$ ,  $B_3$ ,  $B_9$ ,  $B_{12}$ ) in the range from 5 to 350 K a BKT-3.0 automatic precision adiabatic vacuum calorimeter with discrete heating was used. The analysis of the results showed that measurement error of the heat capacity of the substance at helium temperatures was within  $\pm 2\%$ , then it decreased to  $\pm 0.5\%$  as the temperature was rising to 40 K, and was equal to  $\pm 0.2\%$  at  $T > 40$  K. The energies of combustion,  $\Delta_c U$ , of the studied substances were measured in a calorimeter (V-08) with a static bomb and an isothermal shield. The calorimeter design, the procedure of measuring the energies of combustion and the results of calibration and testing are given elsewhere [2].

### RESULTS AND DISCUSSION

The heat capacities of  $B_2$ ,  $B_3$ ,  $B_9$  and  $B_{12}$  in the range from 5 to 350 K were measured [3-6]. Experimental values of the all substance were obtained in

two series of experiments. The experimental data were used to calculate standard thermodynamic functions, namely the heat capacity, enthalpy  $H^\circ(T) - H^\circ(0)$ , entropy  $S^\circ(T) - S^\circ(0)$  and Gibbs energy  $G^\circ(T) - H^\circ(0)$ , for the range from 0 to 350 K. The experimental points were fitted by means of the least-squares method and polynomial equations of versus temperature have been obtained. The heat capacity for all substances gradually increases with rising temperature and does not show any peculiarities. The absolute entropies of compounds and the corresponding simple substances were used to calculate the standard entropies of formation of the compounds under study at 298.15 K.

**Table 1.** The values of the fractal dimensions D and Debye characteristic temperatures

Vitamin (compound)	D	$\theta_D$ , K
B <sub>2</sub> (C <sub>17</sub> H <sub>20</sub> N <sub>4</sub> O <sub>6</sub> )	2.0	83.0
B <sub>3</sub> (C <sub>5</sub> H <sub>4</sub> N-COOH)	2.2	108.7
B <sub>9</sub> (C <sub>19</sub> H <sub>19</sub> N <sub>7</sub> O <sub>6</sub> ·2H <sub>2</sub> O)	2.0	95.5
B <sub>12</sub> (C <sub>63</sub> H <sub>89</sub> CoN <sub>14</sub> O <sub>14</sub> P)	1.8	55.0

From the experimental values in the range 20–40K the value of the fractal dimension D of the tested substances were evaluated. According to the fractal theory of the heat capacity, D is the most important parameter that specifies the character of heterodynamics of the substance structure. The D-values point to the layer structure of compounds (Table 1).

**Table 2.** Thermodynamic characteristics of formation of substances

Compound	$-\Delta_f H^\circ(298)$ (kJ/mol)	$-\Delta_f S^\circ(298)$ (J/(mol·K))	$-\Delta_f G^\circ(298)$ (kJ/mol)
Riboflavin	1432 ± 13	1961 ± 3	847 ± 14
Nicotinic acid	344.9±0.9	503±3	195 ± 2
Folic acid dihydrate	1821.0 ± 5.7	2515.5 ± 9.5	1071 ± 6
Cyanocobalamin	5017± 15	7281 ± 5	2846 ± 15
Prednisolone	1020.6 ± 7.6	-	-
Hydrocortisone acetate	1307.0 ± 11.6	-	-

In a calorimeter with a static bomb and an isothermal shield, the energies of combustion of the riboflavin, folic acid dihydrate, cyanocobalamin, prednisolone and hydrocortisone acetate have been measured at 298.15 K. The enthalpies of combustion  $\Delta_c H^\circ$  and the thermodynamic parameters of formation  $\Delta_f H^\circ$ ,  $\Delta_f S^\circ$ ,  $\Delta_f G^\circ$  of the studied substances from simple

substances at  $T = 298.15$  K and  $p = 0.1$  MPa have been calculated. The enthalpy of formation of nicotinic acid was experimentally determined in J. Bickerton's *et al.* work [7].

Received values of standard enthalpies and entropies of formation were used to calculate the standard Gibbs function of formation at 298K by Gibbs–Helmholtz equation (Table 2). The standard thermodynamic functions can be used for optimization of methods of synthesis, as well as for validation of theoretical and empirical methods for prediction of thermodynamic properties.

## CONCLUSION

The general aim of these investigations was to report the results of the thermodynamic study of B vitamins and steroid hormones. The heat capacities of studied substance are measured over a wide temperature range from, the thermodynamic functions are calculated and the fractal dimensions  $D$  are evaluated. Thermochemical parameters of formation are determined by combining the data obtained by using combustion calorimetry and heat capacity measurements.

## Acknowledgement

The work was performed with the financial support of the Russian Foundation of Basic Research (Project Number 16-03-00288).

## REFERENCES

- [1] I. Brekhman, Man and Biologically Active Substances, 1980
- [2] B. V. Lebedev, E.G. Kiparisova, Russ. J. Phys. Chem., 1996, **70**, 1253–1259.
- [3] A. V. Knyazev, I.A. Letyanina, A. S. Plesovskikh, N.N. Smirnova, S.S. Knyazeva, Thermochemica Acta, 2014, **575**, 12–16.
- [4] A. V. Knyazev, N. N. Smirnova, A. S. Plesovskikh, A.N. Shushunov, S. S. Knyazeva, Thermochemica Acta, 2014, **582**, 35–39.
- [5] A. V. Knyazev, N. N. Smirnova, A. S. Shipilova, A. N. Shushunov, E.V. Gusarova, S. S. Knyazeva, Thermochemica Acta, 2015, **604**, 115–121.
- [6] A. V. Knyazev, V. N. Emel'yanenko, A. S. Shipilova, M.I. Lelet, E.V. Gusarova, S. S. Knyazeva, S. P. Verevkin, Journal of Chemical Thermodynamics, 2016, **100**, 185-190.
- [7] J. Bickerton, G. Pilcher, G .Al-Takhin, , J. Chem. Thermodyn., 1984, **16**, 373-378.

## MULTI-STEP SYNTHESIS OF 5'-PROTECTED 5-CYANATO-2'-DEOXYURIDINE

M. Sosnowska

<sup>1</sup> *Laboratory of Biological Sensitizers, Department of Physical Chemistry, Faculty of Chemistry, University of Gdansk, Wita Stwosza 63, 80-308 Gdansk, Poland.  
(marta.sosnowska@ug.edu.pl)*

### ABSTRACT

Modified pyrimidines seem to be especially well suited for radiotherapy, since DNA is a main target of such treatments. Some uracil analogues can be used by a cell for biosynthesis of DNA almost as easily, as thymine. 5-Substituted halogen nucleobases, notably 5-bromouracil, are among the most widely studied groups of sensitizing compounds. Although 5-bromo-2'-deoxyuridine (5-BrdU) possesses a significant radiosensitizing power *in vitro*, clinical studies did not confirm any advantages of radiotherapy employing 5BrdU. This situation prompts a continuous search for efficient radiosensitizers. In the following sections, we present the first report on chemical synthesis of protected 5-cyano-2'-deoxyuridine. This novel compound was prepared by the reaction of 5'-protected 5-hydroxy-2'-deoxyuridine with cyanogen bromide in solution, in the presence of a base.

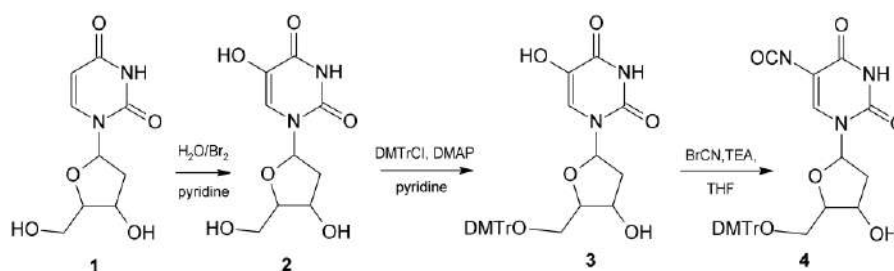
### INTRODUCTION

The growing number of cancer diagnoses calls for an intensive search for new anticancer therapeutics. One possible way to resolve this problem is to improve the efficacy of radiotherapy by employing radiosensitizing substances during the ionizing radiation treatment.

The halogen derivatives of nucleobases, notably 5-bromouracil (5-BrU), are among the most widely studied groups of sensitizing compounds. Moreover, the *in vitro* 5-BrU labeled cells are from 2 to 3 times more radiosensitive than the non-labeled ones [1]. This is because 5-bromouracil (BrU) is a molecule with high affinity towards electrons, prone to the so-called dissociative electron attachment (DEA), the process that leads to a reactive uracil-5-yl radical *via* the unstable 5-bromouracil anion [2]. Thus, solvated electrons, the reducing counterparts of hydroxyl radicals become a damaging factor of the BrdU labeled DNA, although they are inactive toward native DNA, especially when it comes to the strand breaks [3].

Although 5-bromo-2'-deoxyuridine (BrdU) effectively radiosensitizes cell lines *in vitro*, one of the most extensive phase III clinical trials proved no increased survival related to the 5-BrdU administration in radiotherapy for various tumors cancer. Taking this into the account, we performed quantum chemical studies and propose 5-cyanatouracil (5-OCNU) as a potential new DNA radiosensitizer [4].

The C5-substituted uridines are an important class of pyrimidine nucleoside derivatives that have received substantial attention for the decades now. To the best of our knowledge, the synthesis of uracil analogues containing the cyanate functional group has not been reported so far. Consequently, we present the first report on chemical synthesis of the 5'-protected 5-cyano-2'-deoxyuridine. This novel compound was prepared by the reaction of the hydroxyl substituted 5-hydroxy-2'-deoxyuridine with cyanogen bromide in solution and in the presence of a base.



**Scheme 1.** Preparation of 5'-*O*-(4,4'-dimethoxytrityl)-5-cyano-2'-deoxyuridine.

## EXPERIMENTAL

The main goal of the synthesis strategy was to convert a 5-hydroxy functional group into cyanato group. In this work, we described the strategy for synthesis of the 5'-protected 5-OCNdU. The first step involved conversion of 2'-deoxyuridine(dU) to 5-hydroxy-2'-deoxyuridine (5-OHdU) *via* bromination in an aqueous solution [5]. A round-bottom flask was charged with dU and distilled water. Bromine was added dropwise with stirring, until obtaining a permanent yellow colour. To remove an excess of bromine, the solution was stirred until it became clear. Pyridine was then added to the flask at 0°C, and stirring was continued for 1.5 h. Product 2 was subjected to column chromatography (8% MeOH/CH<sub>2</sub>Cl<sub>2</sub>). The second step of synthesis involved protection of 5'-dihydroxyl groups with the 4,4'-dimethoxytrityl (DMTr) group. To a stirred solution of compound 2 and 4-(dimethylamino)pyridine (DMAP) (12 mol %) in pyridine, 4,4'-dimethoxytrityl chloride (DMTrCl) (150 mol %) was added. After 1.5 h at room temperature, an additional amount DMTrCl (90 mol %) was added.

After 3 h, the solvent was removed in vacuum, and the residue was redissolved in dichloromethane and washed with  $\text{NaHCO}_3$  and  $\text{NaCl}$ . The organic solution was dried ( $\text{Na}_2\text{SO}_4$ ), filtered and concentrated [6]. The target 5'-protected 5-OCNdU (compound 4) was obtained by reaction of 3 with bromide cyanogen ( $\text{BrCN}$ ) and triethylamine ( $\text{TEA}$ ) in tetrahydrofuran ( $\text{THF}$ ). A two-necked flask was filled with a solution of the 5'-protected 5-OHdU (4) and  $\text{BrCN}$  in  $\text{THF}$ , and cooled down to  $0^\circ\text{C}$ .  $\text{TEA}$  was introduced dropwise to a mixture of 3 and cyanogen bromide under the argon atmosphere. After 3 hours, the solution was concentrated by rotatory evaporation. Product 4 was subsequently purified by column chromatography (10%  $\text{MeOH}/\text{CH}_2\text{Cl}_2$ ). For all synthesized compounds, the ESI mass spectra were obtained on a High Resolution MS TripleTOF 5600+ system with a DuoSpray<sup>TM</sup> Source (SCIEX) in the positive ion mode. The data were obtained using the software of Analyst TF<sup>TM</sup> 1.5.1.

## RESULTS AND DISCUSSION

We report a three-step synthesis of 5'-protected 5-cyano-2'-deoxyuridine (5-OCNdU), starting with a readily available dU. The first step involved conversion of dU to 5-OH-dU. After selective monotritylation of 5'-hydroxyl, reaction with  $\text{BrCN}/\text{TEA}$  gave suitable product, i.e., 5'-DMTr-5-OCNdU. By using 1 equiv of  $\text{BrCN}$ , reaction was again limited to the 5-position. The lack of the reaction at the 3'-hydroxyl is attributed to the phenolic character of the 5-hydroxy group, making it more reactive than 3'-secondary alcohol. The analysis of 5'-DMTr-5-OHdU by MS indicated the  $[\text{M}+1]^+$  value of  $m/z$  547.1, which confirmed protection of 5'-hydroxyl with the DMTr group (Fig. 1A). The  $[\text{M}+1]^+$  value of  $m/z$  571.1 (Fig. 1B) corresponds with the desired product and it proves formation of 5'-DMTr-5-OCNdU.

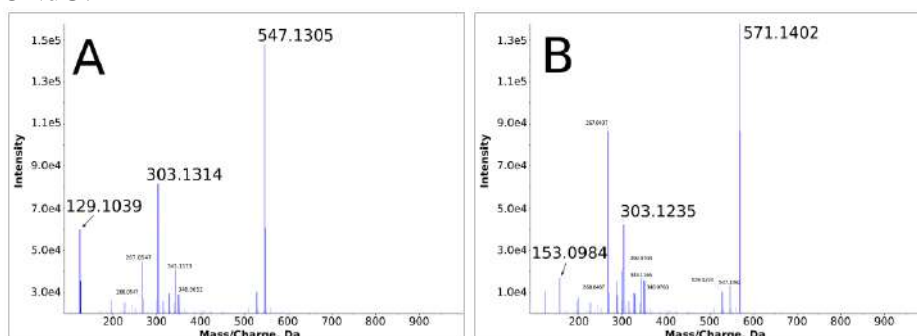


**Figure 1.** TOF-MS analysis of **A)** 5'-O-DMT-5-hydroxy-2'-deoxyuridine (the ion at 547.1305  $m/z$ ) and **B)** 5'-O-DMT-5-cyano-2'-deoxyuridine (the ion at 571.1402  $m/z$ ).

## CONCLUSION

Modified nucleosides are powerful tools in nucleic acid research and their synthesis has become an important aspect of bioorganic and medicinal chemistry. Moreover, modified nucleosides are extensively investigated due to their potential activity as DNA sensitizers. Consequently, an improved and shortened synthesis of modified nucleosides from readily available precursors is of considerable interest. However, nucleosides are challenging the synthetic substrates as they contain several functionalized groups that must be chemically differentiated for a successful transformation. Therefore, multi-step synthesis frequently requires introduction of protective groups and their subsequent removal.

## *Acknowledgement*

This work was supported by the Polish National Science Center (NCN) under the Grant No. 2014/14/A/ST4/00405 (J.R.) and BMN Grant No. 538-8227-B087-15/16 (M.S.).

## REFERENCES

- [1] D. Brust, J. Feden, J. Farnsworth, C. Amir, W. C. Broaddus, K. Valerie. *Can. Gene Ther.*, 2000, **7**, 778–788.
- [2] L. Chomicz L, J. Rak, P. Storonik. *J. Phys. Chem. B*, 2012, **116**, 5612-5619.
- [3] B. D. Michael, P. O'Neill. *Science*, 2000, **287**, 1603.
- [4] L. Chomicz, M. Zdrowowicz, F. Kasprzykowski, J. Rak, A. Buonaugurio, Y. Wang, K. H. Bowen. *J. Phys. Chem. Lett.*, 2013, **4**, 2853-2857.
- [5] E. G. Podrebarac, C. C. Cheng in *Synthetic Procedures In Nucleic Acid Chemistry*, **1**, 1171-1176.
- [6] J. Fujimoto, L. Tran, L. C. Sowers. *Chem. Res. Toxicol.*, 1997, **10**, 1254-1258.
- [7] S. Cui, Y-H. Kim, C-H. Jin, S. K. Kim, M. Rhee, O-S. Kwon, B. J. Moon. *BMB reports*, 2009, 373-379.

## THE APPLICATION OF CALCIUM CHANNEL BLOCKER'S MOLECULAR DESCRIPTORS IN EVALUATION OF THEIR ORAL BIOAVAILABILITY

J. Odović<sup>1</sup>, J. Trbojević<sup>2</sup>, J. Trbojević-Stanković<sup>3</sup> and R. Jelić<sup>2</sup>

<sup>1</sup>*Department of Analytical Chemistry, University of Belgrade-Faculty of Pharmacy, Serbia, (jodovic@pharmacy.bg.ac.rs )*

<sup>2</sup>*Faculty of Medicinal Science, University of Kragujevac, Serbia;*

<sup>3</sup>*School of Medicine, University of Belgrade, Serbia;*

### ABSTRACT

In this study, nine calcium channel blockers were investigated to evaluate relationship between their oral bioavailability data, collected from relevant literature and several molecular descriptors calculated using different software packages. The relationship between computed molecular descriptors and oral bioavailability data were initially investigated using simple linear regression analysis showing correlations with  $R^2 < 0.6$ . In continuation, multiple linear regression analysis was applied to access higher correlation of calcium channel blockers' oral bioavailability data with their molecular properties, the lipophilicity and one additional, calculated molecular descriptor. The best correlations with  $R^2 = 0.783$  were established between calcium channel blockers' oral bioavailability and their lipophilicity data (mllogP) with application of acidity descriptor (pKa) as additional independent variable.

### INTRODUCTION

The hypertension is a world widespread disease. Calcium channel blockers (CCBs) or calcium antagonists are among the most widely applied drugs in cardiovascular medicine. CCBs can be applied not only in hypertension but also in angina pectoris, post myocardial infarction, supraventricular dysrhythmias, hypertrophic cardiomyopathy [1].

According to their structural and functional distinctions CCBs can be subdivided to: dihydropyridine, phenylalkylamine and benzothiazepine derivatives. Most of CCBs, with exception of amlodipine (64-90%) and nifedipine (45-70%), have relatively low (5-35%) oral bioavailability (BA) because of extensive first - pass metabolism. Half - life is relatively short (shorter than 12 hours) with exception is amlodipine which has a longer half - life, longer than 40 hours [1].

In our recently published paper we investigated correlation between molecular properties of selected group of angiotensin II receptor antagonist and their oral bioavailability data [2] as well as the effect of CCBs' molecular properties on their route of elimination [3]. In continuation, the aim of this study was to correlate different molecular properties of nine CCBs (amlodipine, felodipine, isradipine, nicardipine, nifedipine, nimodipine, nisoldipine, verapamil and diltiazem) and to evaluate their oral bioavailability.

## EXPERIMENTAL

### *The investigated drugs*

In this study nine most often prescribed CCBs were investigated: **1.** amlodipine; **2.** felodipine; **3.** isradipine; **4.** nicardipine; **5.** nifedipine; **6.** nimodipine; **7.** nisoldipine; **8.** verapamil and **9.** diltiazem.

### *The calculations*

The CCBs lipophilicity descriptors, different  $\log P$  values ( $A\log P_s$ ,  $AC\log P$ ,  $AB/\log P$ ,  $m\log P$ ,  $A\log P$ ,  $M\log P$ ,  $KOWWIN\log P$ ,  $XLOGP2$ ,  $XLOGP3$ ), as well as their aqueous solubility data ( $\log S$ ) were calculated using software package, Virtual Computational Chemistry Laboratory [4], while software package Molinspiration Depiction Software [5] was used for the calculation of electronic descriptor - polar surface area (PSA); constitutional parameter - molecular weight (Mw) and geometric descriptor - volume value (Vol). The software package DrugBank [6] was used for calculation CCBs acidity descriptors  $pK_a$ . The oral bioavailability data of investigated CCBs were obtained from the relevant literature [1].

Statistical analysis of the regressions was performed using Microsoft Excel 2003 and Origin 7.0 PRO (Origin Lab Corporation, USA).

## RESULTS AND DISCUSSION

The oral bioavailability is one of the most important drug's pharmacologic properties. It is a subcategory of absorption and represents the fraction of orally administered drugs' dose that reaches the systemic circulation. High oral bioavailability reduces the amount of the administered drug necessary to achieve a desired pharmacological effect and therefore can reduce the risk of side-effects and toxicity, while poor oral bioavailability can result in low efficacy and lead to unpredictable response to a drug.

Drugs physical properties (hydrophobicity, acidity, solubility, molecular mass, volume and polar surface area) or drugs formulation, the age and gender of the patients and dosing scheme also exert important influence on drugs' BA.

In this research nine CCBs were studied in order to evaluate correlation between their oral bioavailability data obtained from relevant literature and calculated molecular descriptors using simple or multiple linear regression analysis. According to the data available from the literature, the degree of CCBs' oral bioavailability varies from 5% for nosoldipine to around 80% (64% to 90%) for amlodipine.

In the first step of this study, the correlations between CCBs oral bioavailability data obtained from relevant literature and calculated descriptors were investigated using simple linear regression. Oral bioavailability data and CCBs molecular descriptors - Vol, Mw, PSA, pKa and log*S* showed low correlations ( $R^2 < 0.30$ ). Also the majority of lipophilicity descriptors provided correlations with coefficients  $R^2$  lower than 0.40. Only for lipophilicity descriptors *milogP* and KOWWINlog*P* better correlations were obtained ( $R^2 = 0.570$  and  $R^2 = 0.542$  respectively).

Following, in the next stage of the study, the relationship between CCBs oral bioavailability data and two different molecular descriptors were investigated using multiple linear regression (MLR). The *milogP* values was chosen as the first independent variable since they showed best correlations with CCBs oral bioavailability. The values of Mw, Vol, pKa and PSA were chosen as possible second independent variables. Values of aqueous solubility data, log*S* values, couldn't be used as the second independent variable since it's correlation with *milogP* values provide  $R^2$  around 0.40.

Following correlations were established between oral bioavailability data collected from literature and those predicted, applying lipophilicity descriptor, *milogP* and molecular weight (Eq.1.) or volume (Eq.2.):

$$BA_{\text{pred}}(\%) = -28.80(\pm 7.25)\text{milog}P + 0.26(\pm 0.14)\text{Mw} + 39.38(\pm 15.92) \quad \text{Eq. 1.}$$

$n = 9; R^2 = 0.725; \text{S.D.} = 14.470; F = 7.903;$

$$BA_{\text{pred}}(\%) = -26.80(\pm 7.68)\text{milog}P + 0.17(\pm 0.12)\text{Vol} + 77.05(\pm 42.40) \quad \text{Eq. 2.}$$

$n = 9; R^2 = 0.671; \text{S.D.} = 15.831; F = 6.109.$

The established correlations can be considered as good as proposed by Asuero et al. [7].

However the best correlation, with acceptable P values, was obtained using MLR analysis with application of *milogP* and pKa as independent variables (Eq. 3.):

$$BA_{\text{pred}}(\%) = -20.45(\pm 5.63)\text{milog}P + 5.78(\pm 2.39)\text{pKa} + 73.87(\pm 29.57) \quad \text{Eq. 3.}$$

$n = 9; R^2 = 0.783; \text{S.D.} = 12.86; F = 10.80$

The application of PSA as second variable provided relatively poor correlation ( $R^2 = 0.590$ ). The CCBs calculated molecular descriptors, bioavailability data collected from relevant literature as well as those predicted using MLR are presented at Table 1.

**Table 1.** The CCBs calculated molecular descriptors [4-6]; BA data (1) collected from relevant literature; predicted from (2)  $\text{milog}P$  and Mw; (3)  $\text{milog}P$  and Vol values; (4)  $\text{milog}P$  and pKa values

CCBs	$\text{milog}P$	pKa	Mw	Vol	BA(1)	BA(2)	BA(3)	BA(4)
1.	2.58	9.45	409	364	77	73	69	76
2.	4.80	5.39	384	323	15	3	3	7
3.	3.81	5.33	371	330	20	27	30	27
4.	5.00	8.18	480	437	35	22	16	19
5.	3.07	5.33	346	303	58	42	45	42
6.	4.10	5.41	418	379	13	31	31	21
7.	4.19	5.32	388	353	5	21	24	19
8.	4.55	9.68	455	454	27	28	31	37
9.	3.34	8.18	415	378	50	53	51	53

The calculated values of Mw as well as Vol, presented in Table 1, were already used in our previously published paper [3] for investigation of CCBs' molecular properties effect on route of elimination.

## CONCLUSION

The correlations that were found in presented study confirmed molecular properties, especially lipophilicity and acidity but also molecular weight and volume, as essential for drugs oral bioavailability. Obtained correlations could be regarded as new, additional, *in silico* approach appropriate for evaluating oral bioavailability for investigated group of CCBs.

## REFERENCES

- [1] T.L. Lemke, D.A. Williams, (eds) The Foye's Principles of Medicinal Chemistry, 7<sup>th</sup> ed. Lippincott Williams & Wilkins, Philadelphia, 2013.
- [2] J. Trbojević, J. Odović, J. Trbojević-Stanković, D. Nešić, R. Jelić, Arch Biol Sci., 2016; "in press".
- [3] J. Trbojević-Stanković, J. Odović, R. Jelić, D. Nešić, B. Stojimirović Arch Biol Sci., 2015, **67**(3): 801-6
- [4] IV. Tetko, Virtual Computational Chemistry Laboratory. Available from URL: [www.vcclab.org](http://www.vcclab.org)
- [5] Molinspiration software or free molecular property calculation services. Available from URL: [www.molinspiration.com](http://www.molinspiration.com)
- [6] DrugBank. Available from URL: [www.drugbank.ca](http://www.drugbank.ca)
- [7] A.G. Asuero, A.Sayago, A.G. Gonzalez, Anal. Chem., 2006, **36**, 41-59.

## PREDICTION OF GASTROINTESTINAL ABSORPTION OF NOVEL $\beta$ -HYDROXY- $\beta$ -ARYLALKANOIC ACIDS BY USE OF BIOPARTITIONING MICELLAR CHROMATOGRAPHY

V. Dobričić, J. Savić, S. Vladimirov and J. Brborić

*Department of Pharmaceutical Chemistry, University of Belgrade - Faculty of Pharmacy, Vojvode Stepe 450, 11000 Belgrade, Serbia.  
(vladimir@pharmacy.bg.ac.rs)*

### ABSTRACT

Biopartitioning micellar chromatography (BMC) was used to predict gastrointestinal absorption of thirteen  $\beta$ -hydroxy- $\beta$ -arylpropanoic acids (HAA) with potential anti-inflammatory activity and results were compared to ibuprofen (IBU). All examined HAA exhibit lower retention factor,  $k$  and expected gastrointestinal absorption than IBU. Derivatives of HAA with the highest values of  $k$  are those denoted as 1C, 2APTF, 2C, 2AMTF and 1B (Table 1). In order to identify molecular descriptors with the highest influence on  $k$  as well as to create models which could be used for the design of novel HAA with improved gastrointestinal absorption, quantitative structure-retention relationship analysis was performed. Multiple linear regression model (MLR( $k$ )) was selected and molecular descriptors that form this model were interpreted.

### INTRODUCTION

Nonsteroidal anti-inflammatory drugs (NSAIDs) represent a large class of structurally different compounds [1]. Although NSAIDs are among the oldest drugs, the discovery of novel derivatives with anti-inflammatory activity is still a great challenge due to the fact that these drugs can produce significant side effects.

Thirteen  $\beta$ -hydroxy- $\beta$ -arylalkanoic acids (HAA) were synthesized using previously reported modification of Reformatsky reaction [2] and their anti-inflammatory activity was evaluated.

The aim of this study was to predict gastrointestinal absorption of synthesized HAA and ibuprofen using biopartitioning micellar chromatography (BMC) and to perform quantitative structure-retention relationship (QSRR) analysis, which could be used for the design of novel compounds with improved gastrointestinal absorption.

## EXPERIMENTAL

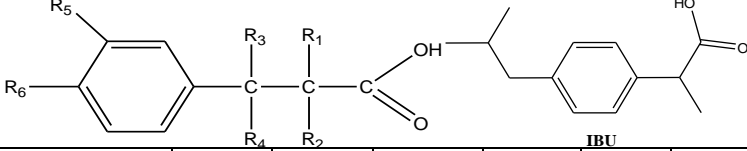
Gastrointestinal absorption of tested compounds was predicted by use of BMC [3] on a Dionex Ultimate 3000 chromatograph (Thermo Fisher Scientific, Germering, Germany) equipped with quaternary pump, autosampler and DAD detector. The chosen column was Zorbax Extend-C18 (150 mm × 4.6 mm, 5 μm particle size). The mobile phase consisted of aqueous phase (40 mM solution of Brij35 in 7 mM disodium hydrogen phosphate) and acetonitrile (80:20, v/v). pH of the mobile phase was adjusted to 5.5 using phosphoric acid. The column temperature was adjusted to 36.5 °C and the flow rate was 1 mL min<sup>-1</sup>. The UV detection was performed at 210 nm. Stock standard solutions of all tested compounds were prepared in methanol. Subsequently, these solutions were diluted with the mobile phase to obtain working solutions (about 0.05 mg mL<sup>-1</sup>). Working solutions were injected in triplicates and retention factors (*k*) were calculated (solution of KI in the mobile phase was used for the determination of column dead time).

More than 4500 molecular descriptors were initially calculated in Dragon 6.0 software (<http://www.taletе.mi.it/>). After the intercorrelation analysis, 254 molecular descriptors were retained and used for further Artificial Neural Networks (ANN) and Multiple Linear Regression (MLR) analysis. Final selection of descriptors was performed by use of forward stepwise MLR (F to enter was 25 and F to remove was 10). Finally, three variables with the highest influence on *k*, i.e. descriptors nBM and P\_VSA\_logP\_8 as well as Eta\_L index, were selected and used for the creation of MLR(*k*) and ANN(*k*) models.

## RESULTS AND DISCUSSION

Chemical structures and retention factors of IBU and HAA are all presented in Table 1. All tested HAA have lower *k* and expected gastrointestinal absorption than IBU. HAA with the highest values of *k* are 1C, 2APTF, 2C, 2AMTF and 1B.

Quantitative structure-retention relationship (QSRR) analysis of these results was performed in order to identify molecular descriptors with the highest influence on *k* and ANN(*k*) and MLR(*k*) models were created. Quality of these models was evaluated by analysis of calculated statistical parameters: RMSEE (root mean squared error of estimation),

**Table 1.** Chemical structures and retention factors of tested compounds


Compound	R <sub>1</sub>	R <sub>2</sub>	R <sub>3</sub>	R <sub>4</sub>	R <sub>5</sub>	R <sub>6</sub>	<i>k</i>
<b>1A</b>	-H	-H	-CH <sub>3</sub>	-OH	-H	-C <sub>6</sub> H <sub>5</sub>	3.27±0.01
<b>1B</b>	-H	-CH <sub>3</sub>	-CH <sub>3</sub>	-OH	-H	-C <sub>6</sub> H <sub>5</sub>	4.81±0.00
<b>1C</b>	-CH <sub>3</sub>	-CH <sub>3</sub>	-CH <sub>3</sub>	-OH	-H	-C <sub>6</sub> H <sub>5</sub>	7.26±0.01
<b>2A</b>	-H	-H	-CH <sub>3</sub>	-OH	-H	-C <sub>6</sub> H <sub>5</sub>	1.61±0.01
<b>2B</b>	-H	-CH <sub>3</sub>	-CH <sub>3</sub>	-OH	-H	-C <sub>6</sub> H <sub>5</sub>	2.87±0.01
<b>2C</b>	-CH <sub>3</sub>	-CH <sub>3</sub>	-CH <sub>3</sub>	-OH	-H	-C <sub>6</sub> H <sub>5</sub>	5.21±0.00
<b>2APN</b>	-H	-H	-C <sub>6</sub> H <sub>5</sub>	-OH	-H	-NO <sub>2</sub>	0.00±0.00
<b>2APTF</b>	-H	-H	-C <sub>6</sub> H <sub>5</sub>	-OH	-H	-CF <sub>3</sub>	5.42±0.01
<b>2APH</b>	-H	-H	-C <sub>6</sub> H <sub>5</sub>	-OH	-H	Cl	4.04±0.00
<b>2APM</b>	-H	-H	-C <sub>6</sub> H <sub>5</sub>	-OH	-H	-CH <sub>3</sub>	2.98±0.05
<b>2AMTF</b>	-H	-H	-C <sub>6</sub> H <sub>5</sub>	-OH	-CF <sub>3</sub>	-H	4.98±0.01
<b>2AMH</b>	-H	-H	-C <sub>6</sub> H <sub>5</sub>	-OH	-Cl	-H	4.00±0.02
<b>2AMM</b>	-H	-H	-C <sub>6</sub> H <sub>5</sub>	-OH	- CH <sub>3</sub>	-H	2.80±0.04
<b>IBU</b>							18.92±0.13

RMSEP (root mean squared error of prediction),  $Q^2$  (cross-validated squared correlation coefficient),  $r$  (correlation between observed and predicted values of test set),  $R^2_{pred}$  (an external validation parameter),  $R^2$  (the squared correlation coefficient), F parameter (ratio between regression and residual variances) and p value (significance of F parameter). Both models have low RMSEE (<0.30) and RMSEP (<0.72), high  $r$  ( $\geq 0.98$ ), as well as  $Q^2$  and  $R^2_{pred}$  higher than 0.5. MLR( $k$ ) model has higher  $Q^2$  value (0.99) than ANN( $k$ ) (0.73) and its predictive capability could be considered higher. Therefore, it was selected as optimal and will be used for the design of novel HAA with higher  $k$  and improved gastrointestinal absorption. Regression equation of this model is:  $k = (18.19 \pm 1.47) - (2.44 \pm 0.06) \cdot nBM + (0.04 \pm 0.01) \cdot P\_VSA\_LogP\_8 + (4.02 \pm 0.28) \cdot \text{Eta\_L}$ .

Descriptor nBM (number of multiple bonds) belongs to constitutional indices and has negative influence on  $k$ . Compound with the highest value of this descriptor is APN, whereas lowest value has IBU. Therefore, elimination of phenyl rings or their replacement with saturated rings should

increase  $k$ . The calculated descriptor P\_VSA\_LogP\_8 belongs to P\_VSA-like descriptors and represents P\_VSA-like on LogP, bin 8 [4]. P\_VSA descriptors are defined as the amount of van der Waals surface area (VSA) having a property P in a certain range [5]. This descriptor has positive influence on  $k$  and compounds with highest value of this descriptor are 2APN, 2APH and 2AMH. Eta\_L belongs to ETA (Extended Topochemical Atom) indices. ETA indices are defined as topological indices derived from the H-depleted molecular graph where a vertex is considered to be comprised of a core and a valence electronic environment [6]. Eta\_L is defined analogously to the composite ETA index, but considers only contributions from pairs of bonded atoms. Eta\_L has positive influence on  $k$  and derivatives with the highest values of this descriptor are 1B, 1C, 2C and 2APTF.

## CONCLUSION

Gastrointestinal absorption of thirteen novel  $\beta$ -hydroxy- $\beta$ -arylalkanoic acids (HAA) was predicted by use of biopartitioning micellar chromatography. All tested HAA have lower  $k$  than ibuprofen and derivatives with the highest values of  $k$  are 1C, 2APTF, 2C, 2AMTF and 1B. Quantitative structure-retention relationship analysis was performed and MLR( $k$ ) was selected as an optimal model that could be used for the design of novel HAA with improved gastrointestinal absorption.

## Acknowledgement

This work was supported by the Ministry of Education, Science and Technological development of the Republic of Serbia (Grant no. 172041).

## REFERENCES

- [1] P. Rao, E. Knaus, J. Pharm. Pharmaceut. Sci., 2008, **11**, 81-110.
- [2] S. Dilber, Ž. Žižak, T. Stanojković, Z. Juranić, B. Drakulić, I. Juranić, Int. J. Mol. Sci., 2007, **8**, 214-228.
- [3] M. Molero-Monfort, L. Escuder-Gilabert, R. M. Villanueva-Camanãs, S. Sagrado, M. J. Medina-Hernández J. Chrom. B, 2001, **753**, 225-236.
- [4] [http://www.taletе.mi.it/products/dragon\\_molecular\\_descriptor\\_list.pdf](http://www.taletе.mi.it/products/dragon_molecular_descriptor_list.pdf)
- [5] P. Labute, J. Mol. Graph. Model., 2000, **18**, 464-477.
- [6] K. Roy, G. Ghosh, Internet Electron. J. Mol. Des., 2003, **2**, 599-620.

*P - Education, History*



## MICHAEL PUPIN AND PHYSICAL CHEMISTRY

N. I. Potkonjak

*Chemical Dynamics Laboratory, Vinča Institute of Nuclear Sciences,  
University of Belgrade, P.O. Box 522, 11001 Belgrade, Serbia  
(npotkonjak@vin.bg.ac.rs)*

### ABSTRACT

Michael Pupin is a great Serbian-American inventor, professor and scientist; best known for his huge contributions to the development of modern telecommunication and X-ray imaging. Less is known that his doctoral dissertation falls within a scope of physical chemistry. Pupin's doctoral dissertation, entitled *Osmotic pressure and his relationship to free energy* was conducted under the mentorship of Helmholtz; can be considered as a pioneer theoretical research in a particular field of physical chemistry, chemical thermodynamics. Aim of this study is to draw public attention on the contribution of the celebrated Pupin to physical chemistry

### FROM EUROPEAN SCHOOLS TO COLUMBIA COLLEGE

Mihajlo Pupin, Anglicized as Michael Idvorsky Pupin was born on October 9<sup>th</sup>, 1854, Idvor, Military frontier of the Austria Empire (now in Republic of Serbia) – died March 12<sup>th</sup>, 1935, New York, USA [1]. His formal education has begun in the village primary school of Idvor. Since he demonstrated marked mental energy and capacity, his secondary education has continued in Pančevo and Prague. During school days in Prague, Pupin met František Ladislav Rieger (1818-1903) and František Palacký (1798-1876); as he wrote "the great apostles of Panslavism and of nationalism of in Bohemia" [2]. Torn between personal aspiration toward higher education and social phenomena of nationalistic enthusiasm resulted in less than average grades. Pupin admits "I never during my whole year's stay in Prague sent a report home on my school work, because I never did more than just enough to prevent my dropping to the lower grade" [2].

Death of his father, mother's insistence to continue his education despite newly created situation and Rieger's advice to leave nationalistic engagement and devoted himself to the higher education, have done major influence on his firm decision to leave Europe, and go to USA. In this endeavor, Pupin was all alone. In order to cover transpiration expenses, he sold his books, watch, clothes. Pupin has left Europe on March 12<sup>th</sup>, 1874 in an immigrant ship. There on the ship, in order to survive coldness, Pupin

has applied the second law of thermodynamics instinctively and unknowingly (*the transfer of heat goes from the hot object to the cold object*). Namely, in order to survive coldness he placed himself alongside to the warm smoke-stack. He wrote, "If it had not been for the warm smoke-stack I should have died of cold" [2].

Due to his intellectual skills, Pupin successfully passed rigorous immigrant cross-examination, and entered the States. During next five years, he was forced to earn for his living, mostly throughout hard labor. Spare time, was reserved for self-education and education at night classes of the Cooper Union. On the last week of September 1879, he took entrance examination at *the Columbia Collage in the city of New York* [2]. He was so brilliant at examination that he managed to enroll at Columbia Collage, released from all tuition fees.

### **FROM COLUMBIA COLLAGE TO EUROPEAN UNIVERSITIES**

His collage career begins in autumn 1879, at the Columbia Collage. As freshmen, Pupin has won first prize in competitive examination in Greek and mathematics. During sophomore year, Pupin has established himself as an excellent wrestler and boxer. Parallel with that, another Pupin's virtue was reviled, that is the ability for qualitative tutoring (coaching) of students who failed in their collage examinations (Greek, Latin, mathematics). He was so good in this, that he earned reputation as a doctor for *lame duck* [2]. These were the first steps in his future successful academic career. Pupin has graduated in 1883, under the mentorship of Lewis Morris Rutherford (1816-1892), and became *Bachelor of Art*. Being a great student, he was appointed as the first to hold a John Tyndall Fellowship. This fellowship was established due to donation of John Tyndall (1820-1893.) to the Columbia Collage.

Pupin has continued his education on the University of Cambridge (1883-1885). There he began studies in mathematical physics under the precept or ship of Edward Routh (1831-1907). Under Routh he obtained mastery of dynamical methods [3]. During postgraduate studies at Cambridge, Pupin has become especially interested in research work of Michael Faraday (1791-1867), James Clerk Maxwell (1831-1879) and Herman von Helmholtz (1821-1894).

Eager to study experimental physics, Pupin obtained permission to continue postgraduate studies at Friedrich Wilhelms University in Berlin. He attended the course on experimental physics given by Helmholtz, and also lectures on the theory of electricity and magnetism given by Gustav Kirchhoff (1824-1887). Pupin has written: "A new physical science was attracting much attention in Germany at that time, the science of physical

chemistry" [2]. He became interested for *this new science*, realizing that research of Josiah Willard Gibbs (1839-1903), from the Yale University, was far ahead if it is compared with achievements obtained by "the alleged German fathers of this new science" [2]. Helmholtz and Pupin had agreed that "It was clean-cut little discovery" [2]. Helmholtz had encouraged Pupin to investigate these findings in more details, suggesting that he might find material for research leading to doctoral dissertation. As Pupin writes "I embraced the suggestion and started an experimental research, at the same time studying the theories of Gibbs, Helmholtz, and other authorities, mostly German, on physical chemistry" [2].

### **PROMOTIONAL EXAM AT FREDRICH WILHELM UNIVERSITY**

Prior to public defense of dissertation, Pupin has taken promotional oral exam on July 15<sup>th</sup> 1889, members of the Commission were Helmholtz, physicist August Kundt (1839-1894), mathematician Lazarus Fuchs (1833-1902) and philosopher Eduard Zeller (1814-1908). The exam was a combination of oral exposition on views regarding three theses (selected by a candidate) and the discussion. As stated by Pupin, in its autobiography [2]: "The three theses which, according to old German custom, every candidate seeking promotion to the dignity of a doctor of philosophy must frame and defend publicly are given here, in order to show my final mental attitude which was formulated by my scientific studies in Europe.

- I. Institutions in Physics in the preparatory schools should be as much as possible a practice one.
- II. The Thermodynamics methods of Gibbs, von Helmholtz, and Plank form most reliable foundation for the study of those physical processes which we cannot analyze by ordinary dynamics.
- III. The Electromagnetic Theory of Light deserves more attention that it has received so far in university lecture".

First thesis came from realization that during his graduated studies on the Columbia College and postgraduate studies at the Cambridge University he receives no practical experience in physical laboratory. Further Pupin admits [2]: "I had no knowledge of physics acquired from my own conscious efforts in a physical laboratory". Consequently, Pupin skeptically claims that, "this was the real secret of my inability to understand Maxwell's physics; I longed for work in a real physical laboratory ...". This thesis was also inspired by a Frederick Bernard (1809-1889), the president of Columbia College, who recognized that "young student in America at that time lacked a knowledge of visible things and not information about them – knowledge acquired by the learner's own conscious efforts, not crammed

into his mind in set forms of words out of books" [2]. During his first address to Helmholtz, Pupin informs professor that he never had an opportunity to work in a physical laboratory. Helmholtz suggested that Pupin "should make up this deficiency as soon as possible" claiming that "a few experiments successfully carried out usually lead to results more important than all mathematical theories" [2].

Second thesis, as Pupin writes "summed up my admiration for the new science of physical chemistry first started by our own Josiah Willard Gibbs (1839-1903)" [2]. This tribute came from Pupin's great respect for Gibbs's work in a field of physical chemistry.

Third thesis is dedicated to the Farady-Maxwell electromagnetic science. To understand reason-way, one must have in mind that Pupin has studied Farady's and Maxwell's work well, and had become their huge admirer. Circumstantially, Pupin was present at a historically important event, which occurred at the end of 1887, during the meeting of Physical Society of Berlin (today's German Physical Society). There, Helmholtz solemnly announced that his former student, and at that time professor Heinrich Hertz (1857-1894) conclusively proved the existence of electromagnetic waves, verifying Farady-Maxwell electromagnetic theory. Impact of this discovery was so powerful on Pupin that it paved a way of his future scientific interests.

### OVERVIEW OF DOCTORAL DISSERTATION

The title of Pupin's doctoral dissertation is *Osmotic pressure and his relationship to free energy* (in original *Der osmotische Druck und seine Beziehung zur freien Energie*) [4]. Mentor of the dissertation was Helmholtz. Public defense was conducted on July 20<sup>th</sup> 1889. As opponents on public defense, following colleagues are cited on the frontal page: physicist August Raps (1865-1920), PhD candidate Arthur Webster (1863-1923) and PhD candidate Vladimir Michelson (1860-1927), Fig. 1. Webster and Pupin were colleagues from Ph.D. studies, and are among founders of American Physical Society (1899).

The dissertation is written in German, on 42 pages, and divided into eight sections: I Introduction, II History, III Concept of the free energy, IV General characteristics of the free energy of salt solutions, V Heat of Dilution, VI Osmotic pressure and its importance, VII Free energy of diluted salt solutions, VIII. Considerations about the internal constitution of a salt solution. Additionally, Thesis and Biography are presented at the last pages of dissertation. [4]

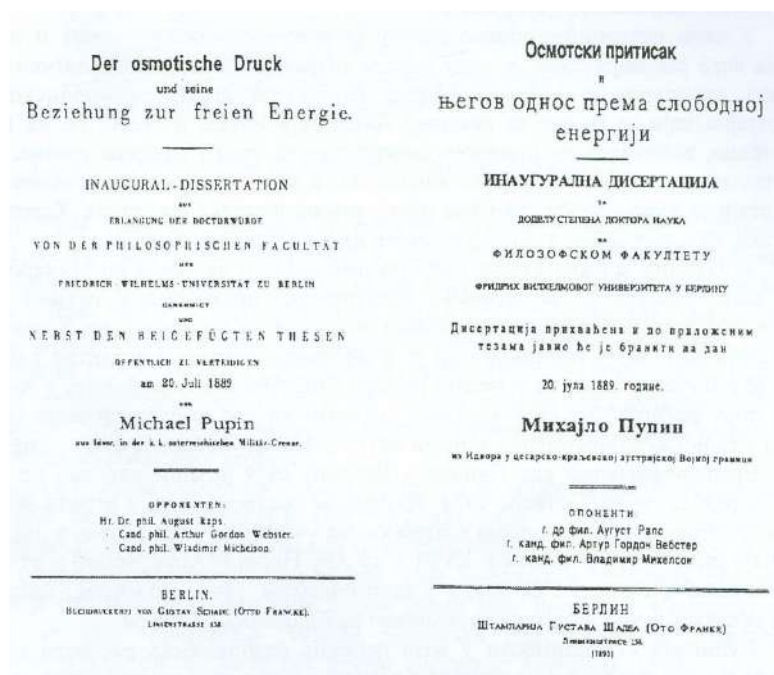


**Figure 1.** Front page of Pupin's doctoral dissertation [4].

In the first section, *Introduction*, Pupin elaborates the aim of dissertation; that is to theoretically derive some characteristic related to the composition of salt solutions from the features of the Helmholtz free energy ( $F$ ), which is the thermodynamic function of the state. Two studies are cited in this section. Helmholtz's paperwork from 1882, entitled *On the Thermodynamics of Chemical Processes*, in which the concept of the free energy is defined; and Wilhem Pfeffer's report from 1877, which concerns investigation on the osmotic pressure (II).

In the next section, *History*, Pupin quotes several scientific papers of importance. Kirchhoff's work from 1858, which considers theoretical investigation of some features of salt solution (mainly heat of dissolution), from the thermodynamic viewpoint. Gibbs's paper from 1875-1878, (entitled *On the equilibrium of heterogeneous substances*), in which analogy between some features of ideal gases and diluted salt solutions is given. Due to complex mathematical language, which outcome from his eager for more general conclusions, this work was incomprehensible by most of chemist and thus avoided. François Massie's (1832-1896) work from 1876, who also had studied the concept of the free energy. Pierre Duhem's (1861-1916) book from 1886; in which applied methods of Massie, Gibbs and Helmholtz are presented. Max Plank's (1858-1947) work on the features of highly

dissolute salt solution, observed from the principles of the increasing entropy of the spontaneous processes. Studies of Wilhelm Ostwald (1853-1932), Jacobus van't Hoff (1852-1911) and Svante Arrhenius (1859-1927), editors of the first scientific journal specialized for physical chemistry *Zeitschrift fur Physikalische Chemie* (first issued in 1887). These three scientists are considered as founders of modern physical chemistry. Wather Nernst's (1864-1941) work also published in *Zeitschrift fur Physikalische Chemie*.

Quality of presented literature in the dissertation proves that Pupin has manage to gather all important articles and books, which either explicitly or implicitly elaborates problematic of modern aspects in the chemical thermodynamics of salt solutions. Today, when we are looking at these articles, and the authors, we consider them as a part of chemical thermodynamics history. Being their contemporaries, one must think of Pupin as a privileged man, who have work on his dissertation in a decade when history of the chemical thermodynamics, thereby physical chemistry was made.

In the third section, *Concept of the free energy*, Pupin mathematically defines the free energy from the first and the second low of thermodynamics [4]:

$$dQ = dU + \sum P_{\alpha} dp_{\alpha} \quad (1)$$

$$dQ = \Theta dS \quad (2)$$

$Q$  denotes the heat,  $U$  denotes the internal energy,  $p_{\alpha}$  denotes parameters defining the state of the body and  $P_{\alpha}$  denotes the force by which system opposes to the internal modification of system represented by  $p_{\alpha}$ ,  $\Theta$  denotes the absolute temperature and  $S$  denotes the entropy. By coupling above equations, and presented them in the form where  $S$  and  $P_{\alpha}$  are unambiguous functions determined by  $\Theta$  and  $p_{\alpha}$ , he obtained [4]:

$$P_{\alpha} = -\frac{\partial}{\partial p_{\alpha}}(U - \Theta S) = -\frac{\partial F}{\partial p_{\alpha}} \quad (3)$$

$U - \Theta S$  is defined as Helmholze free energy ( $F$ ). Thereupon, he showed that  $dF \geq 0$  is sufficient condition for thermodynamic equilibrium. Notation that used in the dissertation is typical for Helmholtz's marking method [5].

In next section, *General characteristics of the free energy of salt solutions*, Pupin mathematically shows that [4]:

$$\frac{\partial}{\partial h} \left( -\frac{\partial F}{\partial w} \right) > 0 \quad (4)$$

w denotes mass of salt solution, h denotes ration w/s, were s denotes mass of salt. He concludes that the force, equation (4), by which salt solution attracts solvent (water) must be negative, also. Hence, the force, by which salt solution attracts ions of salt, declines with concentration, becoming zero when salt solution becomes saturated.

In the section *Heat of Dilution*, he establishes relation between the heat of dissolution and the free energy. By considering changes of the free energy with increasing dilution, he was able to show an analogy between equations which show that both the gas pressure of ideal gases and the osmotic pressure of diluted salt solution are proportional on absolute temperature.

In the last section, *Osmotic pressure and its importance*, Pupin deals with phenomenon of osmotic pressure, giving precisions mathematics explanation of this phenomena and description of experiments according to which it was possible to obtained equation which extract analogy between ideal gas and diluted salt solution [4]:

$$\Pi V = \alpha s \Theta \quad (5)$$

$\Pi$  denotes the osmotic pressure,  $V$  denotes the volume,  $\alpha$  denotes constant which depends on the nature of salt and  $s$  denotes mass of salt.



**Figure 2.** Picture of Michael Idvorky Pupin take around 1890.

## CONCLUSION

Doctoral dissertation of Michael Idvorsky Pupin entitled *Osmotic pressure and his relationship to free energy*, represents theoretical investigation in the field of chemical thermodynamics. Conducted under mentorship of

Helmholtz, this dissertation was publicly defended on July 20<sup>th</sup> 1889, just two years after appearance of the first scientific journal specialized for physical chemistry *Zeitschrift für Physikalische Chemie* (first issued in 1887). Physicochemical community has paid practically no attention on this doctoral dissertation. It remains to be seen whether this study will provoke constructive analysis and criticism regarding scientific importance of Pupin's doctoral dissertation.

### ***Acknowledgement***

This work was supported by the Ministry of Education, Science and Technological Development of the Republic of Serbia (Grants no. 172015). The author would like to thank Mrs. Aleksandra Ninković Tašić for her generous support.

### **REFERENCES**

- [1] K. Snježana, *Život i doprinos Mihajla I. Pupina fizici i hemiji*, Diplomski rad, Univerzitet u Novom Sadu, Prirodno-Matematički fakultet, Departman za fiziku, Novi Sad, 2006. (in Serbian)
- [2] M. I. Pupin, *From Immigrant to Inventor*, Charles Scribner's Sons, New York, 1925.
- [3] A. P. Wills, *Science*, 1935, **81**, 475-479.
- [4] M. I. Pupin, *Der osmotische Druck und seine Beziehung zur freien Energie*, Inaugural Dissertation, Frederich Wilhelm Univerzität zur Berlin, Berlin, 1889 (in German). M. I. Pupin, *Monografije, Osmotski pritisak i njegov odnos prema slobodnoj energiji*, Zavod za udžbenike i nastavna sredstva, Beograd, 1997, (Serbian translation).
- [5] S. Bordoni, *The European Physical Journal H*, 2013, **38**, 617-660.

## USING ANALOGIES TO DETERMINE STUDENTS MISUNDERSTANDINGS RELATED TO SOME CHEMICAL CONCEPTS

N. Azizoglu

*Balikesir University, Faculty of Education, Chemistry Education Department, 10100 Balikesir, Turkey. (nursen@balikesir.edu.tr)*

### ABSTRACT

This study aimed to determine the students' misunderstandings about some chemistry concepts by using the process of analogical mapping. The sample of the study consisted of 26 third year students from undergraduate chemistry education program. In line with the study objectives a worksheet prepared by the researcher was administered to 26 third year pre-service teachers. The worksheet included analogies related to covalent bond formation, collision theory, indicators, compounds and atomic spectrums. The students' mappings were examined and the non-scientific information related to chemistry concepts expressed by the students has been identified. The answers were analyzed qualitatively; the students' answers were presented in frequency tables.

### INTRODUCTION

In recent years, analogy has been seen as one of the most important tool in the teaching-learning process of science related concepts [1-4]. Analogies allow new materials, particularly abstract concepts, to be more easily assimilated with students' prior knowledge, enabling them to develop a more scientific understanding of the concept [5]. An analogy is an effective teaching tool that lets creating similarities for a variety of purposes such as solving problems, constructing arguments or creating explanations.

An *analogy* is a comparison between two domains of knowledge. The familiar domain is referred to as an analog domain; the domain that needs to be learned is referred to as a target domain. Analogy can be expressed as "X is like Y" [6]. For instance, the structure of the atom is like the solar system. The more familiar the solar system forms the analog domain and the structure of the atom represents the target concept. The analogy compares the similar features of the analog with target domains and the process drawing similarities between analog and target is called *mapping* [7]. The aim of an analogy is to transfer a system of relationships from a familiar domain to one that is less familiar [8].

It must be apparent that analogies are representation of target and not the target itself, as students often take it to be. Thus, mapping similarities and differences between analog and target becomes most important [3, 9]. In an analogy, if the analog and target concepts do not completely overlap with each other, students can learn to form concepts incorrectly and make some mistakes [2].

Some studies emphasized benefits of using analogies during the classroom instruction [3, 7]. However, other studies also indicated that analogy can be double-edged sword leading to alternative conceptions [10]. Moreover, ill constructed analogies can encourage growth of alternative conceptions [6, 11].

This study aimed to determine the students' misunderstandings about some chemistry concepts by using the process of analogical mapping. In line with the study purpose a worksheet prepared by the researcher was administered to 26 third year pre-service teachers from an undergraduate chemistry education program. The worksheet included analogies related to covalent bond formation, collision theory, indicators, compounds and atomic spectrums. The used analogies were taken from chemistry textbooks. The analogs and targets used in this study were 1) covalent bond formation-tag of war game, 2) collision theory-from flirting to marriage, 3) indicators-x ray machine, 4) formation of compounds-formation of words from letters, and 5) atomic spectrums-fingerprints. An example of an analogy included in the worksheet was given in Figure 1.

<i>"Indicators work like x-ray machine"</i>	
Consider the above given analogy; write the similarities and differences between the indicator and the x-ray machine in details as much as possible.	
Similarities	Differences
1.....	1.....

**Figure 1.** The appearance of the "indicators – x-ray machine" analogy on the worksheet

The students' mappings were examined and the non-scientific information related to chemistry concepts expressed by the students has been identified. The scientifically incorrect phrases were presented in a frequency table.

## RESULTS AND DISCUSSION

The students' answers were analyzed and phrases including scientifically incorrect knowledge were written, counted and displayed in a frequency table. A summary of the students' misunderstandings determined through analogical mapping is given in Table 1. (f is the number of students expressing the given misunderstanding).

**Table 1.** Students' misunderstandings found in their analogical mappings.

Concept	Misunderstanding	f
Covalent bond formation	The atoms by sharing electrons <u>help each other to become stable...</u>	9
Collision theory	Marriage occurs between two people; <u>no more than two atoms collide...</u>	18
Indicators	Indicators detect whether <u>the substance is acid or base...</u>	21
Formation of compounds	Two words can join to form a new word, <u>but compounds are formed by elements only not by compounds.</u>	11
Atomic spectrums	Isotope atoms have <u>identical atomic spectrums.</u>	23

As shown in Table 1, students have misunderstandings related to the five chemistry concepts. Nine of the students think that the electron sharing in the formation of the covalent bond occurs because the atoms help each other to become stable. They did not mention about the octet rule, the electronegativity of the atoms, polarity of the bonds, etc. The collision theory is another concept that students have misunderstandings; the students do not know that more than two atoms can collide. The analogy led students to incorrect interpretations by giving the analog of marriage. Similarly, indicators were depicted as tools that help to detect acids or bases. This is partially true but there are also solutions, which are not pure substances, where we can use indicators. Students, also have misunderstandings about the formation of compounds. They think that just elements combine to form compounds and ignored the fact that two compounds can also combine to form a new compound for example,  $\text{NH}_3(\text{g})$  and  $\text{HNO}_3(\text{g})$  form  $\text{NH}_4\text{NO}_3(\text{s})$ . The great number of students ( $n=23$ ) thought that isotope atoms have identical atomic spectrums. The fact that the fingerprints of the twins are different was overlooked by the students. Simply the almost identical

appearance of the twins led students think about the identical atomic spectrums of the isotope atoms.

### CONCLUSION

In this study the analogical mapping process was used successfully in determining the students' misunderstandings about the selected chemistry concepts. Even though the students are familiar with the analogs of marriage and fingerprints, the analogs were found to be misleading in the mapping process.

Research showed that specific conditions must be met for analogies to be of use, rather than harm to students. Exclusively showing analogies or having students read them from a text is not enough to help learning processes [7, 9]. In order to be of use of analogies, students must see that the analogy finally breaks down and is no longer adequate as a representation of the target. In this way, the use of analogies can facilitate the conceptual changes [12] and the analogy can stand as an effective tool in constructing relations between concepts [13].

### REFERENCES

- [1] D.E. Brown, *Journal of Research in Science Teaching*, 1993, **30**, 1273-1290.
- [2] J. Clement, *Journal of Research in Science Teaching*, 1993, **30**, 241-1257.
- [3] Z. R. Dagher, *Journal of Research in Science Teaching*, 1995, **32**, 259-270.
- [4] R. B. Thiele, D. F. Treagust, *Instructional Science*, 1994, **22**, 61-74.
- [5] D. F. Treagust, A. G. Harrison, G. J. Venville, *Journal of Science Education*, 1998, **9**, 85-101.
- [6] P. J., Aubusson, A. G., Harrison, S. M. Ritchie in: *Metaphor and analogy in science education*, P. J. Aubusson, A. G. Harrison, S. M. Ritchie (Eds.) Dordrecht, The Netherlands: Springer, 2006.
- [7] R. Duit, *Science Education*, 1991, **75**, 649-672.
- [8] L. Mason, P. Sorzio, *European Journal of Psychology of Education*, 1996, **11**, 3-23.
- [9] C. Sutton, *Journal of Research in Science Teaching*, 1993, **31**, 1215-1227.
- [10] S. Glynn, *Science Teacher*, 1995, **62**, 24-27.
- [11] A. G. Harrison, D. F. Treagust, *International Journal of Science Education*, 2000, **22**, 1011-1026.
- [12] Z. R. Dagher, *Science Education*, 1994, **78**, 601-614.
- [13] D.A. Stepich, T.J. Newby, *Instructional Science*, 1988, **17**, 129-144.

## **PROJECT BASED LEARNING IN A LABORATORY SAFETY PRACTICES COURSE: REDUCING THE LABORATORY ANXIETY**

N. Azizoglu

*Balikesir University, Faculty of Education, Chemistry Education Department, 10100 Balikesir, Turkey. (nursen@balikesir.edu.tr)*

### **ABSTRACT**

In this study, the effect of project based learning (PBL) instruction on sophomore pre-service chemistry teachers' laboratory anxiety in a course named Laboratory Safety Practices (LSP) was examined. The sample of the study consisted of 18 sophomore students from undergraduate chemistry education program. The pre-service teachers taking the LSP course were instructed using PBL approach. A questionnaire involving four-open ended questions on the laboratory anxiety was administered two times to the students, at the beginning and at the end of the semester. The students were asked to express their feelings about the level of anxiety when they are working in a chemistry laboratory. The answers were analyzed qualitatively; the students' answers were read, coded, counted and presented as frequency table. During 12 weeks the sophomore pre-service teachers worked on and completed 6 different projects. The results showed that PBL has some effects on students' laboratory anxiety.

### **INTRODUCTION**

The PBL approach is a model that organizes learning around projects that can be applied to an entire education system or program, at an individual or core set of courses [1]. Project Based Learning Approach focuses on the learning ability of students by establishing their own knowledge through their experiences. It realizes that by giving responsibility to the learners on defining problems, searching for solutions, managing searches, analyzing data, choosing information, integrating the chosen information and correlating the new information with the old ones [2].

This study aimed to determine whether project based learning (PBL) reduces pre-service chemistry teachers' laboratory anxiety, in a course named Laboratory Safety Practices. The sample of the study consisted of 18 sophomore students from undergraduate chemistry teachers program. In the first year of the program the students work in a general chemistry laboratory only. When they pass to the second year of the program the students began

to work in two different courses of chemistry laboratory: the one is the Analytical chemistry laboratory and the other is the Inorganic chemistry laboratory. The LSP is one of the second-year courses of the chemistry education program. The sophomores taking the Laboratory Safety Practices course were instructed using PBL. The PBL implemented course lasted 12 weeks, with three hours per week.

A questionnaire was constructed to determine pre-service teachers' laboratory anxiety level. It was composed of four-open ended questions on the laboratory anxiety. The students were asked to express their feelings about the level of anxiety (by indicating high, medium or low) 1) when they are working with chemicals in the laboratory, 2) when they are working individually or in groups, 3) when they have to complete the work (the experiments) on time, 4) when they are preparing the experiment report at the end of the laboratory session. The questionnaire was administered to the students at the beginning of the study as pre-test. The same questions were administered at the end of the semester as post-test by asking the effect of the projects performed during the course on the aforementioned anxiety levels. The answers were analyzed qualitatively; the students' answers were read, coded, counted and presented as frequency table.

During the 12 weeks the sophomore pre-service teachers worked on and completed 6 different projects. The content of the projects and time allowed for each were as follow:

1) Meaning of the labels – the task requires creating a label for a chemical; 1 week.

2) How chemicals affect human health? – the task requires preparing a leaflet containing information about toxicity and hazards of the chemicals, and safe usage; 1 week.

3) Storage of chemicals – the task requires developing a systematic for storing the chemicals; 1 week.

4) Laboratory waste disposal – the task requires preparing a poster that describes the procedures for disposal of chemical waste in a laboratory; 1 week.

5) First aid practice in laboratory – the task requires preparing a video about first aid intervention of a specific injury (electric shock, poisoning, bleeding, burns, etc.); 1 week.

6) How should the design of a safe laboratory be? – the task requires making a scale model of a safe laboratory; 2 weeks.

Before starting each project in the first week the topics were explained to the students in face to face lessons through lecturing and then detailed instruction for the each project was given. The students were divided into

groups that worked together to the end of the course. Every second week the groups presented their works in class. In total of 12 weeks the course ended.

## RESULTS AND DISCUSSION

The results showed the change in the students' level of anxiety after the PBL. Table 1 shows the analyses results of the students answers. The frequency (f), points to the number of students giving the particular answer.

**Table 1.** Students' anxiety levels before and after PBL.

Question	Anxiety level before PBL	f	Anxiety level after PBL	f
#1	Low	3	Low	6
	Medium	5	Medium	9
	High	10	High	3
#2	Low	5	Low	8
	Medium	9	Medium	7
	High	4	High	3
#3	Low	10	Low	11
	Medium	5	Medium	5
	High	3	High	2
#4	Low	6	Low	7
	Medium	6	Medium	5
	High	4	High	4

The qualitative comparison of the frequencies indicates that some changes occurred in students' anxiety levels. The great change occurred in the number of the students indicating high level of anxiety related to working with chemicals. This result may be encountered because of the project which required gathering information about the hazards of the chemicals. There was also a decrease in the number of students with high anxiety when working in groups and when managing time. The least change occurred in the anxiety level when preparing the report.

The PBL had an effect on students' anxiety because through PBL students obtained information about various topics related to laboratory safety, they took more responsibility in preparing the reports, they had to work cooperatively and presented the works on time.

**CONCLUSION**

Focusing on the results, the study was able to arrive with some conclusions that students' anxiety decreases after undergoing both PBL and lecture.

**REFERENCES**

- [1] C. Magno, J. A. Lajom, J. R. Regodon, "Global Project-Based Learning Forum and Exhibition" Shu-Te University, Kaohsiung, Taiwan, 2005.
- [2] D. Diffily, Gifted Children Today Magazine., **25**, Summer 2002.

## ABRAM IOFFE AND HIS FRIENDS WICH CONTRIBUTED MODERNIZATION OF PHYSICAL CHEMISTRY

T. Halasi<sup>1</sup>, S. Kalamković<sup>2</sup>, M. Milkos<sup>1</sup> and J. Mandić<sup>1</sup>

<sup>1</sup>*Faculty of Science, Department of Chemistry, Biochemistry and Environmental Protection, Methods of Teaching Chemistry, History of Chemistry, University of Novi Sad, Trg Dositeja Obradovića 3, 21000 Novi Sad, Serbia. (tibor.halasi@dh.uns.ac.rs)*

<sup>2</sup>*Primary School „Prva vojvođanska brigada”, Seljačkih buna 51a, 21000 Novi Sad, Serbia*

### ABSTRACT

Abram Ioffe (1880 - 1960), prominent Russian/Soviet physicist, was the “father of Soviet physics”, founder of many physics institutes in Russia, and was a teacher of the best scientists in the country. The world-famous scientists from his school are: P. Kapitsa, I. Kurchatov, L. Landau, N. Semenov, M. Bronstein, A. Alexandrov and many other. Ioffe was the author of numerous papers, textbooks and monographs on subjects that range from theoretical, historical, and philosophical concepts, to the practical applications of science in everyday life.

### BIOGRAPHY

Abram Fedorovich/Fyodorovich Ioffe (*Абра́м Фёдорович Ио́ффе, Аврахам Файвиш-Израилевич*) was born in October 29<sup>th</sup> 1880 in Romny (Ромні) and died in October 14<sup>th</sup> 1960 in Leningrad. He was a prominent Russian/Soviet physicist (Fig. 1). Ioffe was the oldest of five children in a Jewish family. His parents were Fedor Vasilevich (*Файвиш Фёдор Васильевич Иоффе*) and Rahel Abramovna Veinstein - Ioffe (*Рахель Абрамовна Вайнштейн*) (Fig. 2).

He start to read at the age of three and one year later, he was able to write. The level of education at the basic boy's school was very poor because most of the teaching staff was consisted of religious state officials. In Ioffe's words, the essence of his school education was to simply knowing, but not to be understood.[1]



**Figure 1.** Abram Ioffe (1880 - 1960) [1] **Figure 2.** Ioffe's parents [2]

Ioffe graduated at the Saint Petersburg Institute of Technology (1902). He began his scientific career in Munich. He worked as a doctoral student in the laboratory of Wilhelm Conrad Röntgen (1845 - 1923). Ioffe's original intent was to study the nature of odor and its effect on human sense of smell, a subject that had fascinated him even since childhood.

In 1908 Ioffe was married with Vera Andreevna Kravtsova (*Иоффе Вера Андреевна Кравцова*, 1881, Liganka Bogu - 1948, Leningrad), a dentist (Fig. 3). Together they had a daughter, Valentina. Valentina (*Валентина Абрамовна Иоффе*, 1910 - 1985) grew up and followed the footsteps of her father earning a PhD in physics (Fig. 4).



**Figure 3.** Vera Andreevna Kravtsova - Ioffe (1881 - 1948) [3]

**Figure 4.** Valentina Abramovna Ioffe (1910 - 1985) [4]

**Figure 5.** Anna Echeistova (1905 - 1988)

However, later Ioffe was married for the second time with his former student Anna Echeistova (Анна Васильевна Ячейстова-Иоффе, 1905 - 1988), who later worked alongside him and was his most ardent supporter for the rest of his life (Fig. 5).

Ioffe died in his office on October 14<sup>th</sup>, 1960, leaving a great legacy behind. After his death, the institute that he had helped found and under whose directorship it had long remained, was renamed the Leningradski Fiziko-Tekhnicheskii Institut imeni A. F. Ioffe. Nickname of Ioffe: "the red professor" has been taken by the Communist ideas of Marxism, "father of semiconductors", "Papa Ioffe".

### **BIBLIOGRAPHY**

Ioffe studies the elastic and photoelectrical properties of crystals continued, ionic conductors of crystals, explained the reasons of their durability, determined how even small components obscure the qualities of crystals and suggested effective methods of their purification, until 1914. Ioffe was also among the founders of the X-ray and Radiology Institute in Petrograd (1918), later transformed into the Leningrad Physical-Technical Institute (1923) [5]. He organized a system of education combining academic study with practical work in research laboratories. As a result of his activities a system of physical-technical institutes was created, with institutions operating in Kharkov, Sverdlovsk, Tomsk, and other provincial centers. Although Ioffe's main field was the physics of dielectrics. He initiated a program for the study of semiconductor physics (in the late 1920s) and nuclear physics (in 1932). He confirmed the existence of an electron, measured its charge and proved the quantum nature of light and statistical character of the photoelectric effect [6] [7]. Ioffe received many other honors in his country and abroad. In 1920, he was elected as an ordinary member of the Russian Academy of Sciences. From 1945 to 1952, he was a member of the Academy's Presidium. In 1928, he had been elected as a corresponding member of the German Academy of Sciences in Berlin. In 1929, he was an honorary member of the American Academy of Arts and Sciences. Ioffe was a member of several other academies, including the venerable Accademia Nazionale dei Lincei in Rome, the Gottinger Academy and the National Academy of Sciences of India. For many years, he was a member of the Solvay Committee. In 1957, he served as vice president of the International Union for Pure and Applied Physics [8].

**IOFFE'S COOPERATORS**

J. G. Dorfman (1898 - 1974), I. K. Kikoin (1908 - 1984), Y. I. Frenkel (1894 - 1952), P. Kapitsa (1894 - 1984), I. Kurchatov (1903 - 1960), L. Landau (1908 - 1968), N. Semenov (1896 - 1986), M. Bronstein (1906 - 1938), A. Alexandrov (1903 - 1994) and many others [9].

**CONCLUSION**

Ioffe was the “Father of Soviet physics”. He did a lot of quality work.

**REFERENCES**

- [1] O. Prodan, *Prominent Russians: Abram Ioffe*, [http:// russiapedia.rt.com](http://russiapedia.rt.com) [December, 22, 2015].
- [2] Т. М. Чернощекова, *Абрам Федорович Иоффе*, Пособие для учащихся, Москва: Просвещение, 1983.
- [3] Л. А. Шилов, *Абрам Федорович Иоффе, История Российской национальной библиотеки. Российская национальная библиотека, Юбилей РНБ, Сотрудники РНБ - деятели науки и культуры Биографический словарь*, 1-4. [http://www.nlr.ru/nlr\\_history/persons/info.php?id=1008](http://www.nlr.ru/nlr_history/persons/info.php?id=1008) [January, 28, 2016]
- [4] R. R. Andronenko, S. I. Andronenko, In memory of Valentina Abramovna Ioffe (to the 100th anniversary of her birth), *Glass Physics and Chemistry*, 2011, **37(1)**, 115-116.
- [5] K. Kikoin, Ioffe, Abram Fedorovich, *The YIVO Encyclopedia of Jews in Eastern Europe*, 2010. [[http://www.yivoencyclopedia.org/article.aspx/Ioffe\\_Abram\\_Fedorovich](http://www.yivoencyclopedia.org/article.aspx/Ioffe_Abram_Fedorovich), December, 23, 2015],
- [6] V. I. Frenkel, Abram Fedorovich Ioffe, *Soviet Physics-Uspekhi*, 1980, **23(9)**, 531.
- [7] A. F. Ioffe, *Vstrechi s fizikami*, 2nd ed, Leningrad, 1983.
- [8] Biography Resource Center, Gale and K. G. Saur, <http://library.crimea.edu/enciklopedia/persons/09/ioffe/3.html>, [January, 29, 2016],
- [9] А. Иоффе, *Краткая еврейская энциклопедия*, изданной в Иерусалиме в 1976 - 2005, КЕЭ, том **3**, 793–794.

## NICHOLAS EMANUEL MARKOWITZ

T. Halasi<sup>1</sup>, S. Kalamkovic<sup>2</sup> and M. Segedinac<sup>1</sup>

<sup>1</sup>*Faculty of Science, Department of Chemistry, Biochemistry and Environmental Protection, Methods of Teaching Chemistry, History of Chemistry, University of Novi Sad, Trg Dositeja Obradovića 3, 21000 Novi Sad, Serbia. (tibor.halasi@dh.uns.ac.rs)*

<sup>2</sup>*Primary School „Prva vojvođanska brigada”, Seljačkih buna 51a, 21000 Novi Sad, Serbia*

### ABSTRACT

It will be given an overview of the biography and bibliography data on Soviet physical chemist Emanuel Nicholas Markowitz.

### BIOGRAPHY

Nicholas Emanuel Markowitz (*Никола́й Ма́ркович Эмануэ́ль*) was a famous Soviet physical chemist (Fig. 1). He was born in the village of Tim Kursk (Тим Курской), now Timsk district of Kursk region. Markowitz studied at the Physical-Technical Faculty of the Leningrad, Polytechnic Institute between 1930 and 1932, and he specialized in the Department of Chemical Physics. In 1938 he became a PhD student of Leningrad Institute of Chemical Physics under the supervision of Nicholas Semenov (*Никола́й Никола́евич Семёнов*). In 1941 he was drafted into the Red Army. In November 1941 he was demobilized to participate in scientific work on defense projects and returned to the Institute, which was evacuated to Kazan. In 1942 he defended his thesis. In 1949 he obtained his Doctorate. In 1958 the scientist was elected as a corresponding member of Soviet Academy of Sciences, and was upgraded to academic title in 1966 [1].

Eminent scientist died in the village of Chernogolovka (Черноголовка), Moscow region, on December 8, 1984. He was buried at Novodevichy Cemetery in Moscow (station number 10) (Fig. 2).

### BIBLIOGRAPHY

Emanuel's career began after graduating from high school. He started dealing with kinetics and mechanisms of chemical reactions from when he was a student. He was dedicated to kinetics of slow degenerate branching chain reaction of hydrogen sulfide oxidation. Then he was involved in the processes in complex chemical systems and transformation of molecules with complex structure, such as gas-phase oxidation of aldehydes. He and

his colleagues studied the specific role of hydrogen bromide in oxidation reactions of hydrocarbons in the presence of HBr. Their opening was possible with a new mechanism of homogeneous catalysis gas (chemical induction), which they have confirmed by many other initiating additives (chlorine, nitric oxide, nitrosyl chloride). He won the Emanuel won Bach Prize in 1948., for his works. Later, Emanuel researched gas-phase oxidation of hydrocarbons and other chemical substances with changing: temperature, pressure, composition, introduction of catalysts and inhibitors - during process [3].



**Figure 1.** Nicholas Emanuel Markowitz (1915 - 1984)

**Figure 2.** Gravestone of N. E. Markowitz (Семенов Сергей Евгеньевич, 2014-09-14)

Since the mid-50s in work, the study of the kinetics and mechanism of chain reactions of oxidation of organic compounds in the liquid phase is increasingly important. In his laboratory he studied mechanisms of various inhibitors, as well as homogenous and heterogenous catalysts of complex chain reactions. These processes have important practical significance as one of the most promising methods of obtaining many chemical products. As a result of the extensive series of studies in the Institute of Chemical Physics and the Moscow University (Department of Chemical Kinetics, where Emanuel worked since its foundation) theory of chain liquid-phase oxidation of organic compounds was created and experimentally substantiated. On the basis of theoretical and experimental work a number of original methods of obtaining important oxidation products have been proposed. The researcher found how to apply hydrocarbon oxidation reactions in petroleum chemistry of different classes: alkanes, alkenes, arylacetylenes, polyenes, and others. Emanuel suggested a new technique for transferring gas-phase reactions into low-temperature liquid phase

oxidation, which maximized yield of valuable products. For example, Emanuel developed the protocol for butane oxidation under temperatures and pressures, close to critical, and the results were acetic acid, methyl ethyl ketone and ethyl acetate. In 1958, for a series of studies of the properties and characteristics of chain reactions, Emanuel was awarded with the Lenin Prize.

Emanuel also studied inhibitors and contributed a lot to practical application of the theory - aging retardation of combustibles and lubricants, rotting of fats and pharmaceuticals, etc.

He proposed a number of new and effective ways to stimulate the slow chemical reactions due to short-term exposure at the initial time of the reaction of compounds to increase the rate of chain (the so-called initial impetus "chain avalanche").

Another important work of Markowitz was studying the dissolution and stabilization of polymers on the molecular level. The scientist suggested testing techniques for various stabilizing agents and quantitative criteria of polymer resistance to decomposition. Laboratory of professor Emanuel performed research in kinetics of biological processes (clinical oncology, in particular) and tested efficiency of various anti-tumor agents.



**Figure 3.** Prof. Nicholas N. Semenov, Prof. Nicholas M. Emanuel, Prof. G. E. Zaikov, Prof. Guenter Wagner (foto 1976) (Pearce, 2004). [2]

In 1970s the scientist discovered the phenomenon of intensification of free-radical processes at the initial stage of tumor formation. Emanuel and his group found several anti-tumor agents and studied the role of free radicals in radiation injury, as well as showed protective effect of inhibitors of free-radical reactions [2].

It proposed a series of mathematical relationships quantitatively describing these curves, and found a universal equation for a generalized description of kinetic curves of different types.

Emanuel carried on education and training of scientific personnel for most of his work. It has always been popular not only among students but

also among the staff of the Faculty of Chemistry. Among the students who have been taught by Markowitz, there are more than 300 candidates of science, 50 doctors and several members of the Academy of Sciences of the USSR [4]

### FAMOUS MONOGRAPH

- Intermediates complex gas reactions (1946)
- The oxidation of cyclohexane (1962)
- Inhibition of oxidation of fats (1964)
- The chain reaction of oxidation of hydrocarbons (1965)
- Kinetics of experimental tumor processes (1977)
- Nitrosomethylurea (1978)
- Chemical physics of aging and stabilization of polymers (1982)

### CONCLUSION

Emanuel was so extensive that the enumeration of all the organizations and councils, in which he participated, will be very long.

### *Acknowledgement*

The authors wish to thank Ministry of Education and Sciences advance of the Republic of Serbia for financial support this work.

### REFERENCES

- [1] Академик Николай Маркович Эмануэль: *Очерки. Воспоминания. Избранные статьи и письма*, Москва: Наука, 2000, (Ученые России. Очерки, воспоминания, материалы), ISBN 5-02-004354-0.
- [2] E. M. Pearce, Polymers in Europe, Professor Gennady Efremovich Zaikov: Half a Century in Science, *Polymer News*, 2004, **29** (11), 352-354.
- [3] И. В. Березин, В. И. Найдич В., Ученый, учитель, человек. К 70-летию со дня рождения академика Н. М. Эмануэля, Вестник АН СССР, 1985, No. 11, 120.
- [4] И. В. Березин, В. И. Найдич, Николай Маркович Эмануэль, Биография на сайте химического факультета МГУ, <http://www.chem.msu.su/rus/history/acad/emmanuel.html> [December, 10, 2015].

## WALTHER HERMANN NERNST AND THIRD LAW OF THERMODYNAMIC

T. Halasi<sup>1</sup> and S. Kalamkovic<sup>2</sup>

<sup>1</sup>*Faculty of Science, Department of Chemistry, Biochemistry and Environmental Protection, Methods of Teaching Chemistry, History of Chemistry, University of Novi Sad, Trg Dositeja Obradovića 3, 21000 Novi Sad, Serbia. (tibor.halasi@dh.uns.ac.rs)*

<sup>2</sup>*Primary School „Prva vojvođanska brigada”, Seljačkih buna 51a, 21000 Novi Sad, Serbia*

### ABSTRACT

Walther Hermann Nernst (1864 - 1941) was a German physicist. Nernst helped to establish the modern field of physical chemistry and contributed to electrochemistry, thermodynamics and solid state physics. He is known for developing the *Nernst Equation*. In the 1920 Nernst won the Nobel Prize in chemistry for his theories behind the calculation of chemical affinity as embodied in the *Third Law of Thermodynamics*.

### BIOGRAPHY

Nernst was born in Briesen in West Prussia on June 25<sup>th</sup>, 1864, as son of Gustav Nernst (1827 - 1888) and Otilie Nerger (1833 - 1876).[1] Nernst had three sisters and one brother (Fig. 1).[2]



**Figure 1.** Nernst's Family and Car.



**Figure 2.** Nernst, Emma and they children.

Nernst went to elementary school at Graudenz and then studied physics and mathematics of Zürich, Berlin, Graz and Würzburg. Nernst received his doctorate in 1887. Nernst's hobbies included hunting and fishing. Nernst also invented an electric piano *Neo-Bechstein-Flügel* in 1930. which was

never successfully marketed. The piano used electromagnetic pickups to produce electronically modified and amplified sound in the same way as an electric guitar.[3] Emma Lohmeyer was Nernst's wife, and they had two sons and three daughters (Fig. 2). Nernst was a vocal critic of Adolf Hitler and Nazism. His three daughters married Jewish men.

Nernst died of a heart attack on November 18, 1941, at his home at Zibelle, Oberlausitz, near the German-Polish border. He buried near Max Planck (1858 - 1947), Otto Hahn (1879 - 1968) and Max von Laue (1879 - 1960).[4]

### BIBLIOGRAPHY

After graduation, Nernst became an assistant to Friedrich Wilhelm Ostwald (*Фридрих Вильгельм Оствальд*, 1853 - 1932). With his colleagues at the University of Leipzig, Jacobus Henricus van't Hoff (1852 - 1911) and Svante August Arrhenius (1859 - 1927), was establishing the foundations of a new theoretical and experimental field of inquiry within chemistry and suggested setting fire to unused coal seams to increase the global temperature. After some work at Leipzig, Nernst founded the *Institute of Physical Chemistry and Electrochemistry* at Göttingen. Nernst invented, in 1897 an electric lamp, using an incandescent ceramic rod. His invention, known as the *Nernst lamp*, was the successor to the carbon lamp of Edison (*Thomas Alva Edison*, 1847 - 1931) and the precursor to the tungsten incandescent lamp of his student Irving Langmuir (1881 - 1957). In 1889, Nernst addressed another fundamental problem in solution chemistry: precipitation. At the same age, he arrived at his well-known equations which described the concentration dependence of the potential difference of galvanic cells, such as batteries, and were of both great theoretical and practical importance. Nernst started with the investigation of the diffusion of electrolytes in one solution. By combining this with Helmholtz's law, which related thermodynamics to the emf of electrochemical cells, and van't Hoff's equation, which related chemical equilibria to thermodynamics, Nernst derived his second equation for galvanic cells. He wrote a mathematical equation, *Nernst equation*, which relates the electric potential of the ions to various properties of the cell. Nernst had devised methods for determining the pH value of a solution, an expression relating the solution's hydrogen-ion concentration in 1903. He also formulated several significant theories, such as those on the electrostriction of ions, the diffusion layer at electrodes, and the solubility product. That mathematical expression is now known as the solubility product, a special case of the ionization constant for slightly soluble substances. Between 1905 and 1914, Nernst designed a number of ingenious instruments, such as a hydrogen liquefier,



**Figure 3.** M. Planck, W. Nernst, A. Einstein, R. A. Millikan, M. Laue.

thermometers, and calorimeters. In 1911, with Max Planck, Nernst was the main organizer of *The First Solvay Conference in Brussels* (Fig 3).

After studying photochemistry (1918), he proposed the atomic chain reaction theory. His theory is closely related to the natural process of Nuclear Fission ( $\text{Cl}_2 \rightarrow 2\text{Cl}$ ;  $\text{Cl} + \text{H}_2 \rightarrow \text{HCl} + \text{H}$ ;  $\text{H} + \text{Cl}_2 \rightarrow \text{HCl} + \text{Cl}\dots$ ). Nernst was director of the *Institute of Physical Chemistry* at Berlin from

1924. to 1933. His device, a solid-body radiator with a filament of rare-earth oxides, that would later be known as the Nernst glower, is important in the field of infrared spectroscopy. Continuous ohmic heating of the filament results in conduction. The glower operates best in wavelengths from 2 to 14  $\mu\text{m}$ . [5] Walther Nernst's fundamental contributions to electrochemistry, the theory of solutions, thermodynamics, solid state chemistry and photochemistry are recorded in a series of monographs, and in his many papers to learned societies, etc. The famous book: *Theoretische Chemie vom Standpunkte der Avogadro'schen Regel und der Thermodynamik* (Theoretical chemistry from the standpoint of Avogadro's rule and thermodynamics) (1893); *Einführung in die mathematische Behandlung der Naturwissenschaften* (Introduction to the mathematical study of the natural sciences) with Arthur Moritz Schönflies (1853 - 1928); *Die theoretischen und experimentellen Grundlagen des neuen Wärmesatzes* (The New Heat Theorem, 1926) (1918). [6] Nernst became one of the earliest wholehearted supporters of Einstein and quantum mechanics [7]

### THIRD LAW OF THERMODYNAMIC

Nernst researched osmotic pressure and electrochemistry. In 1906, he established what he referred to as his *New Heat Theorem*, later known as the *Third Law of Thermodynamics*. This is the work for which he is best remembered, as it provided a means of determining free energies of chemical reactions from heat measurements. Theodore William Richards (1868 - 1928) claimed Nernst had stolen the idea from him. [5] Based on the *first two laws of thermodynamics* and *Van't Hoff's Equation*, chemical equilibria depended on the free reaction enthalpy  $\Delta G$ , which was a function of both the reaction enthalpy  $\Delta H$  and the reaction entropy  $\Delta S$  according to the Gibbs-Helmholtz equation: The problem was that, although enthalpy

values could be calculated from thermal measurements, entropy values required data at the absolute zero of temperature, which was practically inaccessible. According to a later formulation, it stated that all entropy changes approach zero at the absolute zero. All perfect crystalline compounds were taken as zero at the absolute zero. The theorem was soon applied to industrial problems, including calculations in ammonia synthesis. This theorem implies the impossibility of attaining absolute zero, since as a system approaches absolute zero, the further extraction of energy from that system becomes more and more difficult. Modern science has attained temperatures less than a billionth of a degree above absolute zero, but absolute zero itself can never be reached. Nernst hypothesized that, as they approach absolute zero, the two curves  $F$  and  $H$  become asymptotically tangent to each other - that is to say, in the vicinity of absolute zero,  $\Delta F - \Delta H \rightarrow 0$  (the difference approaches zero). From this form of the Gibbs-Helmholtz equation, it was then possible to calculate the integration constant on the basis of calorimetric measurements carried out in the laboratory.<sup>[4]</sup>

## CONCLUSION

Walther Nernst was one of the geniuses of early twentieth-century German chemistry, a man with a prodigious curiosity about every new development in the physical sciences. Nernst made numerous important contributions to physical chemistry and was a great contributor to the organization of German science.

## Acknowledgement

The authors wish to thank Ministry of Education and Sciences advance of the Republic of Serbia for financial support this work.

## REFERENCES

- [1] D. K. Barkan, *Walther Nernst and the transition to modern physical science*, Cambridge: Cambridge University Press, ISBN 052144456X, 1998.
- [2] H. G. Bartel, Nernst, Walther, in *Neue Deutsche Biographie*, 1999, **19**, 66-68.
- [3] Walther Hermann Nernst, Foundation Nobel Prize. Retrieved 25 April 2012.
- [4] Walter Nernst Biography.nobelprize.org
- [5] H. G. Bartel, R. P. Huebener, *Walther Nernst. Pioneer of Physics and of Chemistry*, Singapore: World Scientific, ISBN 981-256-560-4, 2007.
- [6] J. R. Partington, The Nernst Memorial Lecture, in *Journal of the American Chemical Society*, 1953, 2853-2872.
- [7] A. Einstein, The Work and Personality of Walther Nernst, in *Scientific Monthly*, February, 1942, 195-196.

*Q - Food Physical Chemistry*



## RELATIONS BETWEEN FREE ENERGY AND GRAIN COMPOSITION OF SWEET MAIZE FROM ECOLOGICAL PRODUCTION

V. Dragičević<sup>1</sup>, B. Janošević<sup>2</sup>, M. Simić<sup>1</sup>, M. Brankov<sup>1</sup>, J. Mesarović<sup>1</sup>  
and Ž. Dolijanović<sup>2</sup>

<sup>1</sup>*Maize Research Institute "Zemun Polje", Slobodana Bajića 1, 11185  
Zemun Polje, Serbia. (vdragicevic@mrizp.rs)*

<sup>2</sup>*University of Belgrade, Faculty of Agriculture Nemanjina 6,  
11080 Zemun, Serbia*

### ABSTRACT

The aim of this study was to investigate the influence of different cover crops, in combination with microbiological fertilizer on variability of main kernel components: proteins, starch and oil and their relation with different water types: free, bulk and chemically bound water (present in the form of Gibbs free energy) as factors which contribute to kernel nutritional quality. Applied cover crops and microbiological fertilizer expressed variable effect on content of starch, oil and particularly of proteins. Free energy of free water was negatively correlated with protein and starch and positive with oil in sweet maize kernel, indicating its significance in accumulation of all three examined components. Leguminous cover crops were important for protein accumulation in grain, together with decrease in available sorption sites and decrease in endergonic reactions, what could in result contribute to the increased nutritional quality of produced kernel.

### INTRODUCTION

Food that originates from ecological and so organic production is characterised by higher nutritional value, it is richer in minerals, vitamins and other phytonutrients [1]. Important source of nutrients and energy in maize based food systems is given to sweet maize [2]. It is mainly consumed fresh or processed, but opposite to other types of maize, it is harvesting in milky, i.e. technological maturity (lesser dry substance concentration), when many nutrients are highly digestible.

From this point of view it is important to examine relations between applied cropping practices and nutritional value of produced crops. Many strategies have been involved in ecological production with aim to maintain soil fertility and parallel, to enable maximal utilization of environment with savings in inputs. These strategies imply application of organic and

microbiological fertilizers, intercrops, cover crops, etc. Some studies describe reaction of sweet maize to application of organic fertilizers [3], as well as preceding crops [4,5], which influence not only growth and yielding capacity, but also kernel composition.

The objective of this study was to investigate the influence of different cover crops in combination with microbiological fertilizer on variability of main kernel components: proteins, starch and oil and their relation with different water types: free, bulk and chemically bound water, as factors which contributes to kernel nutritional quality.

### EXPERIMENTAL

A field experiment was carried out over 2014/15, at the Experimental Field of Maize Research Institute in Zemun Polje (44°52'N 20°20'E). The experiment was established as a block design with four replications with winter cover crops as treatment: T1 - common vetch (*Vicia sativa*L.), T2 - winter oats, (*Avena sativa* L.), T3 - fodder kale (*Brassica oleracea* (L.) *convar. acephala*), T4 - field pea (*Pisum sativum*L.) + winter oats, T5 - dead organic mulch, T6 - common vetch + winter oats, T7 - field pea and T8 - classical variant, uncovered during the winter.

The cover crops were sown at the end of October or in early November. Green mass of the cover crops were incorporated in the soil in early May. After that bio-fertilizer – Uniker (containing proteolytic and cellulolytic bacteria) was applied to accelerate mineralization of cover crops, which was followed by sweet maize (ZPSC 421*su*) sowing.

The kernels were harvested at the stage of milk maturity (end of August). The content of protein, starch and oil in grain was determined after drying in ventilation dryer at 80 °C, on infrared analyser (Infraneo, Chopin Technologies, France). The difference between fresh and dry mass (after drying at 60 °C, 105 °C and 130 °C) referred to contents of free, bulk and chemically bound water, calculated by free energy by sorption isotherm [6]:

$$\Delta G = -RT \ln(a_w)$$

where  $a_w$  is the relative water content achieved after drying at T (60, 105 and 130 °C), R is the gas constant (8.3145 J mol<sup>-1</sup> K<sup>-1</sup>) and  $\Delta G$  is differential free energy. The experimental data were statistically processed by standard deviation and correlation (Pearson coefficients).

### RESULTS AND DISCUSSION

According to results presented in Tab. 1, the highest variation in examined kernel constituents was in oil content (15.8%), while the lowest variation was in starch content (3.7%). Among tested treatments, the highest protein content was in T4 treatment, followed by T1 and T7, what could be

explained by the positive response of sweet maize to nitrogen enrichment caused by leguminous plants present in those treatments [4, 5]. The highest starch content was in T5 and the other treatments with non-leguminous cover crops [5]. The highest oil content was in T3 treatment. Other than that, free energy values ( $\Delta G$  60°C) varied in the widest range among all examined parameters (31.1%) and  $\Delta G$  105°C varied in the lowest degree (6.4%). Since free energy presents the work necessary to make the sorption sites available, and so the higher the moisture content is, the number of available sites are lower [1], results in this research indicate that the lowest available sites are present for  $\Delta G$  60°C averagely. Similar trend was observed for T1 treatment, where the lowest values of all three free energy parameters were noticed. The highest values of  $\Delta G$  60°C and  $\Delta G$  105°C were in T2 and the highest value of  $\Delta G$  130°C was in T7 treatment, indicating higher availability of sorption sites, as well as domination of endergonic reactions.

**Table 1.** The influence of different cover crops in combination with Uniker to variation on main composition and free energy in sweet maize grain

Treatm.	Protein (%)	Starch (%)	Oil (%)	$\Delta G$ 60°C (J mol <sup>-1</sup> )	$\Delta G$ 105°C (J mol <sup>-1</sup> )	$\Delta G$ 130°C (J mol <sup>-1</sup> )
T1	11.16	62.2	5.2	0.60	9.38	7.08
T2	10.04	60.6	6.7	1.16	10.43	8.87
T3	10.87	59.7	6.8	0.92	10.07	8.91
T4	11.64	61.7	6.1	0.94	9.53	8.81
T5	10.27	63.4	6.5	0.82	9.94	8.35
T6	11.33	60.0	6.2	0.86	9.92	8.27
T7	11.36	58.7	6.6	0.88	9.45	9.02
T8	11.36	61.3	5.3	0.82	9.70	8.63
CV%	8.8	3.7	15.8	31.2	6.4	16.6

The significant and negative correlation was observable between protein content and  $\Delta G$  60°C and  $\Delta G$  105°C (Tab. 2), as well as between starch content and  $\Delta G$  60°C and  $\Delta G$  130°C, pointing that increase in content of polymers such protein and starch correspond with decrease in available sites for free and bound water sorption, as well as lowering of endergonic reactions [7, 8]. Oil correlated positively with all three examined free energy parameters, indicating importance of all three water types for their accumulation, as well as increase in available sites for all three types of water.

**Table 2.** The correlation between free energy and main grain constituents

	Protein (%)	Starch (%)	Oil (%)
$\Delta G$ 60°C	-0.428*	-0.371*	0.703*
$\Delta G$ 105°C	-0.778*	-0.085	0.597*
$\Delta G$ 130°C	-0.067	-0.521*	0.682*

\*The significant values at the level of significance of 0.05

## CONCLUSION

The combination of different cover crops and microbiological fertilizer expressed variable effect not only on accumulation of main kernel components (nutrients), but also on desorption properties of free, bulk and bound water. Free energy of free water was negative correlated with protein and starch and positive with oil in sweet maize kernel, indicating its importance in accumulation of all three components. Leguminous cover crops were important for protein accumulation, together with decrease in available sorption sites and decrease in endergonic reactions, what could in result contribute to the increased nutritional quality of produced kernel.

## Acknowledgement

This work was supported by the Ministry of Education, Science and Technological Development of the Republic of Serbia (Grant no. TR-31037).

## REFERENCES

- [1] V. Worthington, J. Alter. Complement. Med., 2004, **7**, 161-173.
- [2] G. G. Graham, D.V. Glover, G. Lopez de Romaña, E. Morales, MacLean W. C. Jr., J. Nutr., 1980, **110**, 1061-9.
- [3] C. Lazcano, P. Revilla, R. A. Malvar, J. Domínguez J. Sci. Food Agric., 2011, **91**, 1244–1253.
- [4] T. Griffin, M. Liebman, J. Jemison, Agron. J., 2000, **92**, 144-151.
- [5] L. Idikut, M. Boga, A.I. Atalay, S. N. Kara, A. Kamalak J Anim. Vet. Adv., 2009, **8**, 1979-1981.
- [6] W. Q. Sun, in: Desiccation and Survival in Plants: Drying Without Dying, Black M. & Pritchard H. W. (Ed.), CABI Publishing, New York, USA, 2002, 47-91.
- [7] Y. N. Nkolo Meze'e, N. J. Ngamveng, S. Bardet, Thermochim. Acta, 2008, **468**, 1–5.
- [8] G. H. H. de Oliveira, P. C. Corrêa, E. F. Araújo, D.S.M. Valente, F. M. Botelho, Internat. J. Food Sci. Technol., 2010, **45**, 546–554.

## **DnBP EXTRACTION OPTIMIZATION IN GC-MS DETERMINATION**

T. Anđelković<sup>1</sup>, D. Anđelković<sup>1</sup>, I. Kostić<sup>1</sup>, H. Kocić<sup>2</sup> and G. Kocić<sup>2</sup>

<sup>1</sup> *University of Niš, Faculty of Science and Mathematics,  
Višegradska 33, 18000 Niš, Serbia. (tatjanaan@gmail.com)*

<sup>2</sup> *University of Niš, Faculty of Medicine, Boulevard Zorana Đinđića 81,  
18000 Niš*

### **ABSTRACT**

In this study, three different extraction solvent combinations for di-*n*-butylphthalate (DnBP) determination in milk samples were compared. Combinations of methanol, ethanol and acetonitrile with hexane were investigated. DnBP determination was carried out by gas chromatography – mass spectrometry (GC-MS). Effects of solvent extraction were studied by spiking known amount of DnBP standard solution in concentration range 0.25 to 1.25 mg L<sup>-1</sup>. Obtained results indicate that extraction method which included ethanol/hexane combination of solvents showed the best recovery for all spiked concentrations of DnBP (29.90%). The lowest recovery was obtained for acetonitrile/hexane combination (20.39%).

### **INTRODUCTION**

Phthalates are used as plasticizers in polymeric materials to increase their physical properties, flexibility and softness. Most of packaging materials are made of polymeric material that contain phthalates and they can migrate from packaging because phthalates are not physically bonded to plastics.[1] The most used phthalates in polymers of food packaging materials are di-(ethylhexyl) phthalate (DEHP) and DBP.[2, 3]

These phthalates are listed as endocrine disruptors and they metabolize to bioactive phthalate monoesters. [4] Milk is a major source of nutrition for infants and children, and because of that the presence of DnBP and DEHP in milk is of increasing interest. [5]

Techniques such as solvent extraction and solid phase extraction are used to clean up and concentrate milk samples before analysis. It is very important to find appropriate solvent or combination of few solvents to obtain high recovery. [6]

## EXPERIMENTAL

*DnBP* standard, dibutyl adipate (DBA), acetonitrile and hexane were purchased from Sigma Aldrich, USA. Methanol and ethanol were purchased from Baker, USA. All used solvents were HPLC grade and screened to determine the phthalate background.

All sample and standard manipulation was done avoiding any contact with plastic equipment. Amounts of *DnBP* and DBA standard were accurately weighted out by analytical balance with precision at  $\pm 0.0001$  g (Kern, Germany) and stock solutions were prepared by hexane diluting. Stock and working standards were in fridge.

Milk samples with 2.8% milk fat content were purchased from local supermarket (Niš, Serbia). Effects of solvent extraction were studied by spiking known amount of *DnBP* standard solution in concentration range from 0.25 to 1.25 mg L<sup>-1</sup> in samples before extraction steps. A volume of 10 mL milk sample was put in a polypropylene centrifuge tube and 30 mL of methanol was added. Mixture was treated under ultrasonic conditions for 30 min and centrifuged for 10 min at 4000 rpm. After this step, 20 mL of supernatant was transferred into clean polypropylene tube, 10 mL of hexane was added and mixture was shaken and centrifuged once more by the same conditions. Hexane layer was analyzed by GC-MS. All spiked samples and blank sample were analyzed in three replicates. These procedure was repeated for two other solvents, acetonitrile and ethanol, instead of methanol.

Analysis was carried out by gas chromatography coupled to mass spectrometer (Hewlett Packard 6890 series GC System with autosampler connected with Agilent 5973 Mass Selective Detector (Electron Ionization MSD-EI, single quadrupole). The separation was achieved with 30 m  $\times$  0.25 mm  $\times$  0.25  $\mu$ m a non-polar AGILENT DB-5MS column coated with 5% phenyl, 95% dimethylpolysiloxane. The MSD was used in the single ion-monitoring (SIM) mode. The identification of target compounds was based on the relative retention time, the presence of target ions and their relative abundance. The most abundant ion  $m/z$  149 was chosen for quantification of DBP. Ion  $m/z$  185 was chosen as representative ion of DBA internal standard. The dwell time was 100 ms.

## RESULTS AND DISCUSSION

All quantification was performed by an external calibration method based on response ratios between internal standard and DBP. Calibration curve of *DnBP* standard series was obtained by standard solutions in a concentration range of 0.25 to 10  $\mu$ g mL<sup>-1</sup> and calibration curve showed linearity with correlation coefficient  $> 0.99$ .

Recovery values were calculated for all investigated systems. Mean values of recovery obtained by using three different combination of extraction solvents are given in Table.

DnBP concentration correlation between hexane extract and milk matrix is showed in Figure.

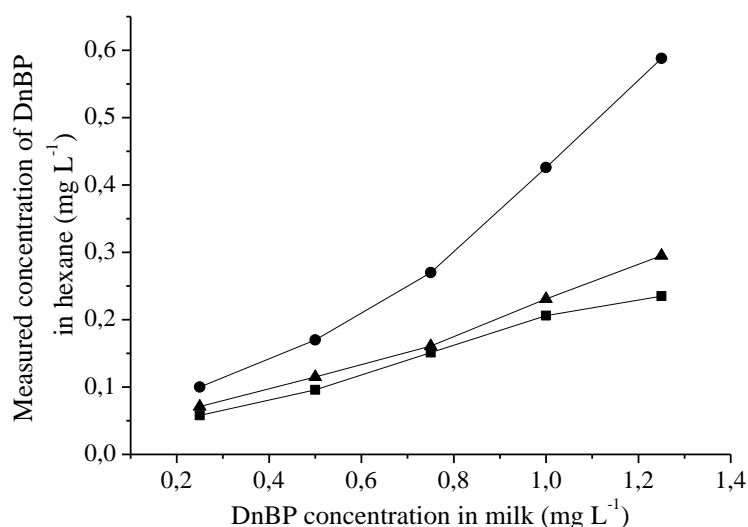


**Figure 1.** DnBP concentration correlation between hexane and milk matrix: (■) – Methanol/hexane; (●) – Ethanol/hexane; (▲) – Acetonitrile/hexane

**Table 1.** Recovery for spiked samples obtained by extraction with methanol, ethanol and acetonitrile

Used solvent	Methanol	Ethanol	Acetonitrile
Spiked concentration (mg L <sup>-1</sup> )	Recovery (%)		
0.25	28.40	29.73	23.20
0.50	23.07	25.54	19.20
0.75	21.51	27.00	20.18
1.00	23.13	31.96	20.57
1.25	23.60	35.27	18.80
Mean value of recovery (%)	23.94	29.90	20.39

Obtained results indicate that extraction method which included ethanol/hexane combination of solvents showed the highest recovery for all

spiked concentrations of DnBP. Also, the lowest recovery was obtained for extraction by acetonitrile/hexane combination of solvents.

Although values of recovery for all tested spike concentrations within applied method showed similar values, there is no established trend between the increase of spiked concentrations and obtained recovery values.

### CONCLUSION

The effectiveness of solvent combination on DnBP extraction in milk samples was investigated. Applied combination ethanol/hexane showed the best recovery value (29.90%) while acetonitrile/hexane combination showed the lowest effectiveness (20.39%).

### *Acknowledgement*

This work was partially supported by the Ministry for Education, Science and Technological Development of the Republic of Serbia (Grant no. TR 31060).

### REFERENCES

- [1] Z. Li, F. Xue, L. Xu, C. Peng, H. Kuang, T. Ding, C. Xu, C. Sheng, Y. Gong, L. Wang, *J. Chromatogr. Sci.*, 2011, **49**, 338-343.
- [2] H. Shen, *Talanta*, 2005, **66**, 734-739.
- [3] J. Hubinger, *J. Cosmet. Sci.*, 2010, **61**, 457-465.
- [4] D. Koniecki, R. Wang, R. Moody, J. Zhu, *Environ. Res.*, 2011, **111**, 329-336.
- [5] G. Mortensen, K. Main, A-M. Andersson, H. Leffers, N. Skakkebak, *Anal. Bioanal. Chem.*, 2005, **382**, 1084-1092.
- [6] J. Zhu, S. Phillips, X-L. Cao in: *Handbook of Dairy Foods Analysis*, Chapter 37, L. Nollet, F. Toldra (Eds.), CRC Press, New York, 2010.

## MILK FAT CONTENT INFLUENCE ON PHTHALATE DETERMINATION

D. Anđelković<sup>1</sup>, T. Anđelković<sup>1</sup>, I. Kostić<sup>1</sup>, H. Kocić<sup>2</sup> and G. Kocić<sup>2</sup>

<sup>1</sup> *University of Niš, Faculty of Science and Mathematics,*

*Višegradska 33, 18000 Niš, Serbia. (darko.andjel@outlook.com)*

<sup>2</sup> *University of Niš, Faculty of Medicine, Boulevard Zorana Đinđića 81, 18000 Niš*

### ABSTRACT

In this study, milk fat content influence on phthalate determination was investigated. Investigated milk samples contained fat in following amounts (%): 0.5, 1.5, 2.8, 3.2 and 3.5. Used method included extraction with acetonitrile and hexane, and centrifugation. The effects of matrix were studied by spiking milk samples with known amount of phthalates standard solution in concentration range 0.25 to 1.25 mg L<sup>-1</sup> before extraction steps. Obtained results indicate that there is no correlation between fat content and phthalate recovery determined by used method in used milk fat content range. The lowest recovery was obtained for dimethylphthalate (DMP) in samples with the lowest fat content (0.5%). The highest recovery was obtained for di(2-ethylhexyl)phthalate (DEHP) from the same milk samples. In general, in all investigated milk samples, DMP showed the lowest recoveries, while in the case of other investigated phthalates, there is no established trend.

### INTRODUCTION

Phthalates are nonvolatile chemical substances used as additives for plastic materials in order to increase flexibility and softness of plastic material.[1, 2] Due to their widespread use phthalates can be found in many consumer products, such as cosmetics, clothing, medical equipment, food and food packaging, *etc.* and humans can be exposed to phthalates by different routes: ingestion, inhalation and dermal absorption. Human exposure to phthalates is mainly caused via food ingestion.[3, 4] Food can be contaminated by the contact with food packaging containing phthalates because phthalates do not form stable bonds with plastics, and they can release into surrounding media. Phthalates have lipophilic nature and tend to leak in oil or fat-containing food.[1, 5] In recent years, phthalates have attracted huge public attention because these compounds are listed as suspected endocrine

disruptors or mutagens, which can have adverse effects on human health even at low levels.[6]

Milk and milk products can be contaminated during the preparation and packaged processes. Milk is a complex matrix consisting of proteins and different amounts of fat, and phthalates can be bound to matrix constituents with different affinity due to their different chain lengths. The tolerable daily intake (TDI) values established by the European Food Safety Authority (EFSA) panel are: 0.05 mg/kg/day for DEHP; 0.5 mg/kg/day for benzylbutyl phthalate (BBP) and 0.01 mg/kg/day for di-*n*-butyl phthalate (DnBP).[6, 7]

### EXPERIMENTAL

DMP, DnBP, BzBP, DEHP, dibutyl adipate (DBA), acetonitrile and hexane were purchased from Sigma Aldrich, USA. Solvents were HPLC grade and screened to determine the phthalate background. Stock solution of each standard was prepared by hexane diluting of phthalate standard amounts and DBA standard that were accurately weighted out by analytical balance with precision at  $\pm 0.0001$  g (Kern, Germany) and stored at 4 °C. Working standard solutions were at the concentration range from 0.25 to 10  $\mu\text{g mL}^{-1}$ . DBA was used as internal standard at concentration 1  $\mu\text{g mL}^{-1}$ .

To avoid phthalates contamination, all glassware used in this study was soaked and washed with acetone, rinsed with hexane and dried at 120 °C for 4 h. After cleaning, glassware was sealed with aluminum foil and stored in a clean environment to avoid adsorption of phthalates from the air.

Milk samples were purchased from local supermarkets (Niš) and all samples were open at the same time in the same place. Five different types of milk were investigated. Fat content in these samples were (%): 0.5, 1.5, 2.8, 3.2 and 3.5. The effects of matrix were studied by spiking samples with known amount of phthalates standard solution in concentration range 0.25 to 1.25  $\text{mg L}^{-1}$  before extraction steps. All spiked samples and blank sample were analysed in three replicates.

A volume of 10 mL milk sample was put in a polypropylene centrifuge tube and 30 mL of acetonitrile was added. Mixture was shaken vigorously for 1 min and centrifuged 10 min at 4000 rpm. After this step, 20 mL of supernatant was transferred into clean polypropylene tube, 20 mL of hexane was added and mixture was shaken and centrifuged once more by the same conditions. Hexane layer was analyzed by GC-MS. All spiked samples and blank sample were analyzed in three replicates.

Analysis was carried out by gas chromatography coupled to mass spectrometer (Hewlett Packard 6890 series GC System with autosampler connected with Agilent 5973 Mass Selective Detector (Electron Ionization MSD-EI, single

quadrupole). The separation was achieved with  $30\text{ m} \times 0.25\text{ mm} \times 0.25\text{ }\mu\text{m}$  a non-polar AGILENT DB-5MS column coated with 5% phenyl, 95% dimethylpolysiloxane. The MSD was used in the single ion-monitoring (SIM) mode. The identification of target compounds was based on the relative retention time, the presence of target ions and their relative abundance. The most abundant ion  $m/z$  149 was chosen for quantification of *DnBP*, *BBP* and *DEHP*, while ion  $m/z$  165 was chosen for *DMP* quantification. Ion  $m/z$  185 was chosen as representative ion of *DBA* internal standard. The dwell time was 100 ms.

## RESULTS AND DISCUSSION

Calibration curves of standard series were obtained by standard solutions in a concentration range of 0.25 to 10  $\mu\text{g/mL}$ . All calibration curves were linear with correlation coefficients  $> 0.99$ .

Phthalate concentration correlation between hexane extract and milk matrix were obtained by hexane extracts of spiked samples in a concentration range of 0.25 to 1.25  $\text{mg L}^{-1}$ . Obtained calibration curves for milk sample with 2.8% fat content is shown in the Figure 1.

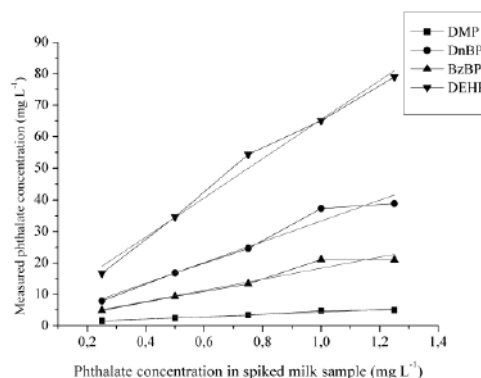


**Figure 1.** Calibration curves of *DMP*, *DnBP*, *BBP* and *DEHP* obtained from spiked milk samples with 2.8% milk fat content

Recovery values were calculated for all investigated samples. Obtained mean values of recovery for all investigated phthalates are given in Table 1.

Obtained results indicate that there is no correlation between fat content and phthalate recovery determined by used method. The lowest recovery was obtained for *DMP* from samples with the lowest fat content (0.5%). The highest recovery was obtain from the same milk samples by investigation of *DEHP*. By compering obtained values of recovery for two other investigated phthalates, *DnBP* and *BBP*, it can be concluded that *DnBP* showed better recovery for all investigated samples, but without established trend between investigated types of milk.

**Table 1.** Recovery of 4 phthalates in 5 different commercial milk samples for 5 different spike concentrations

Fate content (%)	0.5	1.5	2.8	3.2	3.8
Phthalate	Recovery (%)				
DMP	3.39	6.24	3.60	5.08	4.73
DnBP	33.32	50.44	20.39	34.97	31.52
BBP	18.76	20.00	10.63	15.67	12.58
DEHP	67.39	35.62	45.82	33.96	43.20

In general, from all investigated samples, DMP showed the lowest recovery while in case of other investigated phthalates, there is no established trend.

## CONCLUSION

Fat content influence on phthalate determination was investigated. Results showed that there is no correlation between fat content and obtained recoveries. DMP showed the lowest recovery in all investigated samples while the highest recovery value was not established for any of other investigated phthalates.

## Acknowledgement

This work was partially supported by the Ministry of Education, Science and Technological Development of the Republic of Serbia (Grant no. TR 31060).

## REFERENCES

- [1] Z. Guo, S. Wang, D. Wei, M. Wang, H. Zhang, P. Gai, J. Duan, *Meat Sci.*, 2010, **84**, 484-490.
- [2] E. Fasano, F. Bono-Blay, T. Cirillo, P. Montuori, S. Lacorte, *Food Control*, 2012, **27**, 132-138.
- [3] C. Guerranti, I. Sbordoni, E. L. Fsnello, F. Borghini, *Microchemical Journal*, 2013, **107**, 178-181.
- [4] P. Kueseng, P. Thavarungkul, P. Kanatharana, *J. Environ. Sci. Health. Part B*, 2007, **42**, 569-576.
- [5] T. Fierens, M. Van Holderbeke, H. Willems, S. De Henauw, I. Sioen, *Environment International*, 2013, **51**, 1-7.
- [6] S. Keresztes, E. Tatar, Z. Czegeny, G. Zaray, V. G. Mihucz, *Sci. Total Environ.*, 2013, **458-460**, 451-458.
- [7] D. Balafas, K.J Shaw, F.B Whitfield, *Food Chemistry*, 1999, **65**, 279-287.

## THE INFLUENCE OF FATTY ACIDS CONTENT ON CRYSTALLIZATION PROCESS OF BLACKBERRY AND RASPBERRY SEED OILS

D. Micić, S. Ostojić, M. Simonović and B. Simonović

<sup>1</sup> *University of Belgrade, Institute of General and Physical Chemistry, Studentski trg 12-14, 11000 Belgrade, Serbia. (micic83@gmail.com)*

### ABSTRACT

Differential scanning calorimetry (DSC) technique is used to investigate the impact of fatty acids content in blackberry (*R. fruticosus* L., Čačak Thornless cultivar) and raspberry (*Rubus idaeus* L., Willamette cultivar) seed oils on crystallization process of these berry seed oils. Raspberry seed oil crystallizes at a lower temperature (for about 5 °C) compared to the crystallization temperature of blackberry seed oil. The reason for this lies in a higher content of linolenic acid (18:3) in the raspberry than in blackberry seed oil.

### INTRODUCTION

Fats are highly abundant compounds in nature and are widely used in food and other consumer products [1]. Their behavior heavily influences the microstructure and physical properties of these products. The crystallization behavior of fats and lipids has two major industrial implications: (a) processing of the products made of fat crystals, such as chocolate, margarine and shortening, whipping cream, etc., and (b) separation of specific fats and lipids materials from natural resources [1].

Edible oils and fats mainly consist of a multi-component mix of triacylglycerols (TAGs) with a small amount of other minor components. A TAG is a triester of glycerol with three fatty acid molecules. The physical behavior of TAGs influences the physical properties of fat-based products, such as appearance, texture, plasticity, morphology, and rheology [2]. The aim of this paper is to investigate the impact of fatty acids content in blackberry and raspberry seed oils on crystallization process of these berry seed oils by means of differential scanning calorimetry (DSC).

### EXPERIMENTAL

Blackberry (*R. fruticosus* L., Čačak Thornless cultivar) and raspberry (*Rubus idaeus* L., Willamette cultivar) were obtained from the Fruit Research Institute, Čačak, Serbia. Fresh berries were frozen at -20 °C and

stored for one month until processing. Berry seeds were obtained by fruit pulp cold-pressing. Examined oils were obtained by extraction from milled raspberry and blackberry seeds using hexane (Sigma–Aldrich, Missouri, USA) as described in literature[3]. The oil was stored at  $-20\text{ }^{\circ}\text{C}$  until analysis. All chemicals and reagents used were of the highest purity (p.a.). Fatty acids percentage contribution (% w/w) in berry seed oils was determined in our previous work [4]: blackberry seed oil – (16:0) palmitic 3.65, (18:0) stearic 2.27, (18:1) oleic 12.53, (18:2) linoleic 66.33 and (18:3) linolenic acid 14.62 % w/w; raspberry seed oil – (16:0) palmitic 3.47, (18:0) stearic 1.06, (18:1) oleic 11.55, (18:2) linoleic 55.29 and (18:3) linolenic acid 27.80 % w/w. Pure fatty acids (palmitic stearic, oleic, linoleic and linolenic) were purchased from Sigma–Aldrich (Missouri, USA) and their purity was  $>99\%$  according to the manufacturer's specification.

Crystallization process of raspberry and blackberry seed oils and pure fatty acids is studied on TA Instruments DSC Q1000, Differential Scanning Calorimeter (Delaware, USA), with TA Universal analysis 2000 software, under air flow of 50 ml/min. Samples of berry seed oils and pure fatty acids were placed in open aluminum pans and into the equipment's sample chamber, and their mass was  $3.0 \pm 0.3$  mg. DSC scans of analyzed samples were conducted in a temperature range of 80 to  $-90\text{ }^{\circ}\text{C}$  with cooling rate of  $2\text{ }^{\circ}\text{C}/\text{min}$ . Characteristic temperatures of crystallization process were determined from DSC curves: onset temperature ( $T_{\text{on,c}}$ ), offset temperature ( $T_{\text{off,c}}$ ) (as the intersection of the extrapolated baseline and the tangent line of the crystallization peak), and the peak temperature ( $T_{\text{p,c}}$ ) (temperatures of a maximum heat flow) between  $T_{\text{on,c}}$  and  $T_{\text{off,c}}$ . The crystallization enthalpies ( $\Delta H_c$ ) of both berry seed oils and pure fatty acids were obtained by the integration of the crystallization DSC peaks (the linear baseline function integration).

All DSC experiments and measurements were performed in triplicate and the values are presented as mean values  $\pm$  SD. All data ( $T_{\text{on,c}}$ ,  $T_{\text{p,c}}$  and  $T_{\text{off,c}}$ ) were statistically analyzed by one-way analysis of variance (ANOVA) with the STATISTICA 10.0® (StatSoft Inc., Tulsa, OK, USA) software. Tukey's HSD test was applied to determine significant differences between means, at a level of  $p < 0.05$ .

## RESULTS AND DISCUSSION

In Table 1. obtained characteristic crystallization temperatures ( $T_{\text{on,c}}$ ,  $T_{\text{p,c}}$  and  $T_{\text{off,c}}$ ) and enthalpies ( $\Delta H_c$ ) of berry seed oils and pure fatty acids are presented. On the basis of a post-hoc Tukey's HSD test it has been shown that among all the analyzed samples there is a statistically significant difference in terms of their characteristic temperatures and enthalpies of

crystallization. This is an indication that the crystallization process of berry seed oils is influenced by the structure of the fatty acids and composition of the oil (percentage contribution of individual fatty acids).

**Table 1.** Characteristic crystallization temperatures ( $T_{on,c}$ ,  $T_{off,c}$  and  $T_{p,c}$ ) and enthalpies( $\Delta H$ ) of berry seed oils and pure fatty acids.

Sample	$T_{on,c}$ (°C)	$T_{p,c}$ (°C)	$T_{off,c}$ (°C)	$\Delta H_c$ (J/g)
Linolenic	-21.18±0.13 <sup>d</sup>	-21.82±0.19 <sup>c</sup>	-23.17±0.07 <sup>c</sup>	-130.2±1.1 <sup>g</sup>
Linoleic	-22.15±0.20 <sup>c</sup>	-22.55±0.13 <sup>g</sup>	-24.00±0.18 <sup>d</sup>	-151.6±0.9 <sup>f</sup>
Oleic	1.97±0.02 <sup>e</sup>	1.53±0.01 <sup>d</sup>	0.41±0.01 <sup>e</sup>	-181.4±1.2 <sup>c</sup>
Stearic	66.57±0.52 <sup>g</sup>	66.40±0.41 <sup>f</sup>	64.64±0.15 <sup>g</sup>	-415.6±4.3 <sup>e</sup>
Palmitic	60.28±0.36 <sup>f</sup>	60.16±0.57 <sup>e</sup>	58.59±0.55 <sup>f</sup>	-358.8±1.9 <sup>d</sup>
Blackberry seed oil	-57.02±1.01 <sup>a</sup>	-61.36±0.53 <sup>a</sup>	-66.57±1.18 <sup>a</sup>	-29.0±2.1 <sup>a</sup>
Raspberry seed oil	-60.56±0.98 <sup>b</sup>	-66.32±0.84 <sup>b</sup>	-73.40±1.11 <sup>b</sup>	-25.1 ±2.5 <sup>b</sup>

The results are presented as mean±SD; different letter in superscript within the same column indicate significant differences ( $p < 0.05$ ), according to Tukey's test, number of repetitions:  $n=3$ .

On the Fig. 1, the dependence of temperatures,  $T_{p,c}$ , (A) and enthalpies,  $\Delta H_c$ , (B) of crystallization as a function of the type of fatty acids and berry seed oils was shown. It can be seen that the saturated fatty acids have higher values of temperatures and enthalpies of crystallization compared to these values of unsaturated fatty acids. Also, it can be seen that with increasing number of double bonds in the molecule of unsaturated fatty acid their temperatures and enthalpies of crystallization decrease. Namely, crystal formation depends on the linearity of the fatty acid molecules. The double bond in the cis-position breaks the linear structure of the fatty acid chain, and according to that the fatty acid molecules are more difficult to pack in the crystal lattice[5].

Raspberry seed oil crystallizes at a lower temperature ( $T_{p,c}$ ) (for about 5 °C) compared to the crystallization temperature of blackberry seed oil. The reason for this lies in a higher content of linolenic acid (18:3) in the raspberry than in blackberry seed oil. The more double-bonds present in the fatty acid molecules, the more complicated shape of the TAG molecule will be [5]. This will affect the crystallization process of oils.

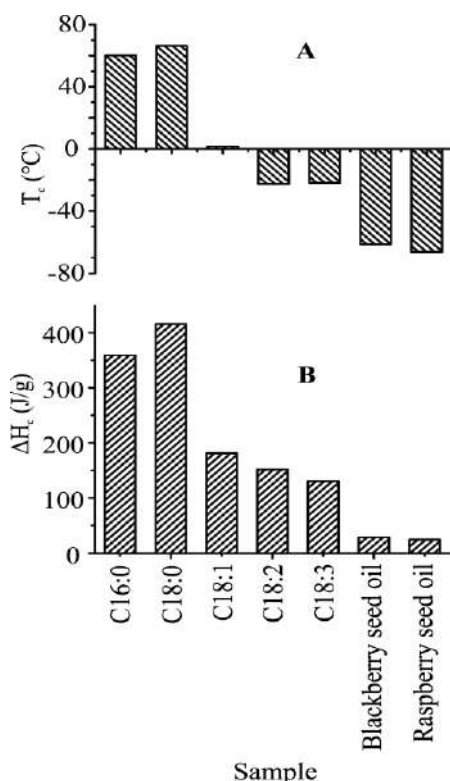


**Figure 1.** Dependence of temperatures  $-T_{p,c}$  (A) and enthalpies  $-\Delta H_c$  (B) of crystallization as a function of the type of fatty acids and berry seed oils.

## CONCLUSION

The saturated fatty acids have higher values of temperatures and enthalpies of crystallization compared to these values of unsaturated fatty acids. Crystal formation depends on the linearity of the fatty acid molecules. Raspberry seed oil crystallizes at a lower temperature ( $T_{p,c}$ ) (for about 5 °C) compared to the crystallization temperature of blackberry seed oil. The reason for this lies in a higher content of linolenic acid in raspberry seed oil. The more double-bonds present in the fatty acid molecules, the more complicated shape of the TAGs molecule will be, and according to that TAG molecules are more difficult to pack in the crystal lattice.

## Acknowledgement

This work was partially supported by the Ministry for Science of the Republic of Serbia (Grants no. 31093).

## REFERENCES

- [1] K. Sato, Chem. Eng. Sci., 2001, **56**, 2255–2265.
- [2] C. Himawan, V.M. Starov, A.G.F. Stapley, Adv. Colloid Interface Sci., 2006, **122**, 3–33.
- [3] B. D. Oomah, S. Ladet, D. V. Godfrey, J. Liang, B. Girard, Food Chem., 2000, **69**, 187–193.
- [4] D. Micić, S. Ostojić, M. Simonović, G. Krstić, L. Pezo, B. Simonović, Thermochim. Acta, 2015, **601**, 39–44.
- [5] I. Tolstorebrov, T.M. Eikevik, M. Bantle, Food Res. Int., 2014, **58**, 132–140.

## HERBAL EXTRACTS AND WINE AS NATURAL PRESERVATIVES AGAINST FOODBORN BACTERIA

M. D. Pavlović<sup>1</sup>, S. Brnjos<sup>2</sup>, T. Stević<sup>3</sup>, B. Nikolić<sup>2</sup>, J. Knežević-Vukčević<sup>2</sup>,  
and D. Mitić Čulafić<sup>2</sup>

<sup>1</sup>University of Belgrade, Institute of General and physical Chemistry,  
Studentski trg 12/V, 11000 Belgrade, Serbia,  
(mirjanapavlovic200@gmail.com)

<sup>2</sup>University of Belgrade, Faculty of Biology, Institute of Microbiology,  
Studentski trg 12-16, 11000 Belgrade, Serbia

<sup>3</sup>Institute for medicinal and plant research "Dr Josif Pančić", Tadeuša  
Koščuška 11000 Belgrade, Serbia

### ABSTRACT

The aim of this work was to investigate the antibacterial effect of combination of ethanolic herbal extracts and red wine against *Listeria monocytogenes*, *Staphylococcus aureus* and *Escherichia coli*, using commercial fresh pork meat as a food model. Red wine (Merlot, Serbia) and ethanolic herbal extracts had shown strong additive effects, causing cellular death and inhibition of bacterial growth at 37°C and at 20°C respectively. Clarifications only slightly diminish the antibacterial effect of wine. The wine and ethanolic herbal extracts, as natural preservatives, could be used as safe and effective antibacterial marinades to extend the shelf life of meat up to 96 h of storage on 20°C.

### INTRODUCTION

Microorganisms are the mayor cause of meat spoilage, producing dangerous products and changes of sensory properties. *Listeria monocytogenes* can survive refrigeration temperature [1] or combination of low pH, low water activity (*A<sub>w</sub>*), sodium chloride and sodium nitrate in meat products [2] and is a particular food safety concern. *Staphylococcus aureus* growing may be inhibited at refrigeration temperatures (8 °C) by appropriately lowering the pH and *A<sub>w</sub>* levels, but it produces a heat stable enterotoxin when allowed to grow for several hours in meat [3]. *Escherichia coli*, the primary pathogen on meat products, could cause serial health problems. The antimicrobial activity of various herbal ethanolic extracts, as replacement for synthetic food preservatives, was found against common meat spoilage and pathogenic bacteria at 20°C and at 4°C in both individual extracts and their combinations in modified atmosphere packed fresh or cooked pork [4].

Wine and spices-based marinades possess strong antibacterial activity [5]. Different components of herbal extracts and wine have been proposed to contribute to antibacterial activity [4], [1]. Some authors emphasize the role of phenolic compounds [1] while accentuate to the other constituents of wine, such as organic acids, ethanol or pH [6]. The main objective of this study was to explore antibacterial effect of combinations of red wine, clarified red wine, ethanolic herbal extracts and ethanol. Combinations giving additive or synergetic effects were tested on commercial fresh pork meat inoculated with *L.monocytogenes* and *S. aureus*.

### EXPERIMENTAL

**Bacterial Strains:** The following bacterial strains were used: *Staphylococcus aureus* ATCC 25923, *Listeria monocytogenes* 19111 and *Echerichia coli* 8739. Bacteria were cultivated at 37°C in appropriate culture media and adjusted to concentration of  $1.0 \times 10^6$  cfu/ml. **Samples:** Herbal extracts in 40% ethanol were obtained from Institute for medicinal and plant research "Dr JosifPančić". Serbian red wine Merlot was obtained from local market. Clarified wine, stripped from phenolic compounds by active carbon, was used as control. The minimal inhibitory and bactericidal concentrations (MIC and MBC) were determined using 96-well microtiter plates [7]. Samples were dissolved in MHB medium with bacterial inoculum of  $1 \times 10^4$  cfu/ml. **Antibacterial activity on pork meat model system:** Lean pork meat was obtained from a local market. A mass of 5g of meat was aseptically placed in polystyrene bottles and 10 ml isotonic solution with combinations of herbal extracts and wine was added [1]. Samples were inoculated at final concentration of  $1 \times 10^5$  cfu/ml of *Staphylococcus aureus* ATCC 25923, *Listeria monocytogenes* 19111 and incubated at 20°C for 96h. Controls were carried out with uninoculated samples.

### RESULTS AND DISCUSSION

Ethanolic herbal extracts showed various degrees of inhibition against Gram-positive bacteria: *L. monocytogenes* and *S. aureus* at 37°C, while 40% ethanol had no activity in MIC and MBC assays *E. coli* (Gram-negative) was resistant (data not shown). The sensitivity difference between two groups of bacteria was previously observed in treatments with ethanolic plant extracts [4], [7] and could be explained by the fact that Gram-negative bacteria possess an outer membrane and a unique periplasmic space not found in Gram-positive bacteria. Red wine inhibited growth of *S. aureus*, while *E. coli* and *L. monocytogenes* were resistant. Low antibacterial activity of clarified wine on *S. aureus* indicate that phenolic compounds contribute to the antibacterial activity of wine, Table 1.

**Table 1.** Antibacterial activity of herbal extracts and wine on Gram-positive bacteria in microdilution method (MIC and MBC are in mg/ml) at 37°C.

Antimicrobial agents (ethanolic herbal extracts, wine, antibiotics)	Test bacteria			
	<i>L. monocytogenes</i>		<i>S. aureus</i>	
	MIC	MBC	MIC	MBC
sage	5	10	2.5	5
mint	-	-	20	40
cumin	-	-	20	40
basil	20	40	10	20
sage, mint, cumin (herbs)	10	20	5	10
sage, mint	10	20	5	10
sage, cumin	10	20	10	20
mint, cumin	-	-	10	20
clarified wine	-	-	20	40
wine	-	-	10	20
streptomycin	0.0625	0.125	0.0625	0.125
rifampicin	ND	ND	0.05	0.10

Herbal extracts in 40% ethanol were adjusted at the concentration of 200 mg/ml. Red wine (14.5 % ethanol) was clarified using activated carbon. Streptomycin and rifampicin (1mg/ml) were used as positive controls. Abbreviations: MIC, minimal inhibitory concentration; MBC, minimal bactericidal concentration, ND, not done.

**Table 2.** Antibacterial activity of mixed herbal extracts and wine against mesophilic aerobic bacteria, *L. monocytogenes* and *S. aureus* at 20°C.

Test	Herbal extracts/wine	Time			
		0h	24h	48h	96h
Mesophilic aerobic bacteria (uninoculated) (cfu/ml)	control	$0.9 \times 10^2$	$3.7 \times 10^9 \pm 2 \times 10^7$	$1.7 \times 10^8 \pm 7.5 \times 10^7$	$1.2 \times 10^8 \pm 1 \times 10^7$
	wine	$0.9 \times 10^2$	0	0	0
	herbs	$0.9 \times 10^2$	0	0	0
	herbs, wine	$0.9 \times 10^2$	0	0	0
<i>L. monocytogenes</i> (cfu/ml)	control	$1 \times 10^5$	$3.3 \times 10^7 \pm 1.4 \times 10^6$	$1.1 \times 10^6 \pm 1.5 \times 10^5$	$5.6 \times 10^6 \pm 6.5 \times 10^5$
	wine	$1 \times 10^5$	0	$6 \times 10^5 \pm 3 \times 10^4$	0
	herbs	$1 \times 10^5$	0	0	0
	herbs, wine	$1 \times 10^5$	0	0	0
<i>S. aureus</i> (cfu/ml)	control	$1 \times 10^5$	$4.3 \times 10^7 \pm 1.4 \times 10^6$	$2.4 \times 10^7 \pm 2.4 \times 10^6$	0
	wine	$1 \times 10^5$	0	0	$2.4 \times 10^7 \pm 5 \times 10^6$
	herbs	$1 \times 10^5$	0	$6 \times 10^5 \pm 3 \times 10^4$	0
	herbs, wine	$1 \times 10^5$	0	0	0

Treatment of pork meat, inoculated with *L. monocytogenes* and *S. aureus*, with combinations of ethanolic herbal extracts from sage, mint and cumin, alone or with wine, had shown strong additive effects, inhibiting growth of *L. monocytogenes*, *S. aureus* and mesophilic aerobic bacteria at 20°C, Table 2.

### CONCLUSION

Ethanolic herbal extracts and red wine inhibited growth of Gram-positive bacteria: *Listeria monocytogenes* and *Staphylococcus aureus* in culture media at 37°C, while Gram-negative bacteria *E. coli* was resistant. Using commercial pork meat as a food model, combinations of herbal extracts, alone or with wine, had shown strong additive effects, causing growth inhibition of *L. monocytogenes*, *S. aureus* and mesophilic aerobic bacteria at 20°C.

### Acknowledgement

This work was partially supported by the Ministry for Science of the Republic of Serbia (Grant no. 31055).

### REFERENCES

- [1] M. J. Rodríguez-Vaquero, P. A. Aredes-Fernández, M. C. Manca de Nadra, Food Technol. Biotechnol., 2013, **51**, 376–382.
- [2] J. L. Johnson, M. P. Doyle, R. G. Cassenes, J. L. Schoeni, Appl. Environ. Microbiol., 1988, **54**, 497-501.
- [3] A. Valero, F. Pérez-Rodríguez, E. Carrasco, J. M. Fuentes-Alventosa, R. M. García-Gimeno, G. Zurera, Int. J. Food Microbiol., 2009, **133**, 186-194.
- [4] H. Zhang, B. Kong, Y. L. Xiong, X. Sun, Meat Science, 2009, **81**, 686-692.
- [5] M. Friedman, P. R. Henika, C.E. Levin, R. E. Mandrell, J. Food Science, 2007, **72**, M207-M213.
- [6] N. Boban, M. Tonkic, D. Budimir, D. Modun, D. Sutlovic, V. Punda-Polic, M. Boban, J. Food Science, 2010, **75**, M322-M326.
- [7] I. T. Karabegović, P. V. Vukosavljević, M. M. Novaković, S. Ž. Gorjanović, A. M. Džamić, M. L. Lazić, Dig. J. Nanomater. Biostruct., 2012, **7**, 1587-1598.

## THERMAL BEHAVIOR OF GRANNY SMITH APPLE WITH DIFFERENT WATER CONTENT

S. Ostojić, S. Zlatanović, D. Micić and O. Kovačević

<sup>1</sup> *Institute of General and Physical Chemistry, University of Belgrade  
Studentski trg 12/V, 11000 Belgrade, Serbia. (sostojic@iofh.bg.ac.rs)*

### ABSTRACT

Thermal behavior of fresh and conventionally dried apple, with different moisture content, was studied by Differential Scanning Calorimetry (DSC). The glass transition temperature ( $T_g$ ) was determined from the DSC curves. Since much of the water was linked to the solid matrix, samples with low moisture content showed the glass transition.  $T_g$  increased with decreasing moisture content.  $T_g$  increased from  $-57.0^\circ\text{C}$  to  $-6.8^\circ\text{C}$  when the moisture content decreased from 58% to 9%.

### INTRODUCTION

Low moisture foods can be considered as solid solutions whose components have been caught in a glassy, solid-like state as a result of water removal. Dehydrated, low-moisture and frozen foods are typically in an amorphous metastable state which is very sensitive to changes in moisture content and temperature. It has been postulated that the mobility of food sugars and proteins increases with temperature near  $T_g$  of the dry food matrix [1, 2]. Increases in concentration of plasticizing agent (water) cause a decrease in  $T_g$ , resulting of facilitated time and temperature dependent physical and chemical changes that are responsible for quality losses during food processing and storage [1,2,3]. The importance of  $T_g$  of amorphous food materials for processing and storage stability has been recognized and emphasized by many researchers and a wide range of potential food applications of the glass transition phenomenon have been identified [4]. Two main alternatives exist to avoid glass-rubber transitions and associated structural collapse to depress processing or storage temperature and /or to add a  $T_g$ -depressing agent to increase the glass transition temperature of the food material [1, 2]. Water activity ( $a_w$ ) and glass transition temperature ( $T_g$ ) provide valuable information on the effects of water content on water availability in foods and on the physical state of food solids [2]. Biological materials are rigid and brittle below the glass transition temperature. The physical state of foodstuffs is very stable below the glass transition temperature because compounds involved in deterioration reactions take

many months or even years to diffuse over molecular distances, and approach each other to react [2]. Water molecules become kinetically immobilized within the concentrated phase, thus being unable to support or participate in the reactions causing deterioration [2].

The objective of the present study was to define thermal transition behavior of fresh and conventionally dried apple (Granny Smith cultivar) with different moisture content, considering glass transition.

### EXPERIMENTAL

Apple (Granny Smith cultivar) slices have been conventionally dried at temperature of 50°C. Samples for drying experiments were apple cylinders (40 mm diameter, 5-7 mm height) that were cut perpendicular to the main axis of the fruit using a knife. The seed lodge was retained and seeds were mechanically removed. During the process of drying the samples with different water content has been taken. Moisture contents were determined according to the SRPS EN 12145:2005. Water activity ( $a_w$ ) has been determined by  $a_w$  meter Testo 650. A differential scanning calorimeter (DSC, Q1000, TA Instruments, New Castle, DE) was used to perform DSC experiments. Samples of fresh and dried Granny Smith apple, 2-4 mg, (moisture content 9.6-85.0%), in aluminum pans, were cooled from 20 °C to -90 °C, equilibrated for 5 min and scanned initially from -90°C to 350°C at a heating rate of 5°C/min. DSC scans were evaluated for: onset temperature of glass transition ( $T_{g \text{ onset}}$ ), glass transition ( $T_g$ ) temperature, end temperature of glass transition ( $T_{\text{end}}$ ), change of specific heat capacity across the glass transition ( $\Delta C_p$ ), peak temperatures of ice melting ( $T_m$ ,  $T_p$ ), and enthalpy of ice melting ( $\Delta H_m$ ), using TA Advantage, Version 4.5A software.

### RESULTS AND DISCUSSION

On the Fig 1. DSC curves are shown obtained for fresh apple and for dried apples with different moisture content. The DSC thermograms presented two main thermal events between -60°C and 20°C: the glass transition phenomenon and the melting transition of ice which can be observed only for the sample of fresh apple, characteristic for apple samples with high and moderate water content [5] (Fig 1). In the temperature range from 20°C to 250°C several thermal events take place: water evaporation in the temperature region from 90°C to 160°C for fresh apple samples, and transition characteristic for apple samples with lowered water content corresponds to thermal transition of the release of the humidity (final drying) between 20 and 150 °C, the degradation of the pectin matrix between 190 -270 °C and the degradation of the cellulose network between

250 and 350 °C [6], followed by process of sample total thermal degradation [7].

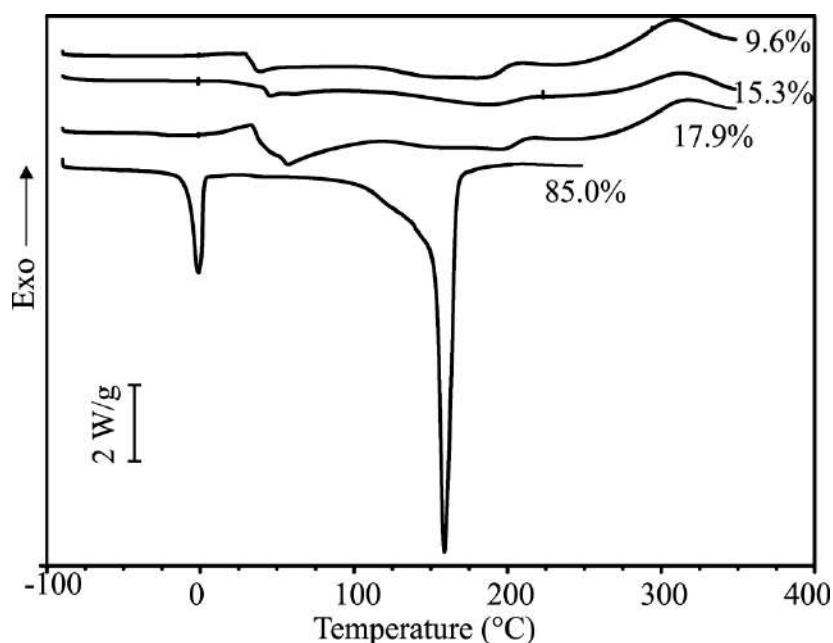


**Figure 1.** DSC curves obtained for fresh apple and for dried apples with different moisture content.

**Table 1.** Water content, glass transition temperatures, melting point and water activity of dried apple with freezable and unfreezable water.

Moisture (%)	$T_{\text{onset}}$ (°C)	$T_g$ (°C)	$T_{\text{end}}$ (°C)	$\Delta C_p$ (J/g)	Ice melting $T_p$ (°C)	$a_w$
85.0±1.0	-57.6±1.1	-57.0±0.5	-52.3±1.0	0.516±0.020	-7.38±0.20	0.91
17.8±1.0	-33.3±2.0	-28.3±0.7	22.35±2.1	0.698±0.010	-	0.50
15.3±1.2	-24.6±1.8	-21.1±0.7	-18.23±1.6	0.087±0.015	-	0.38
9.6±1.0	-15.1±2.1	-6.80±0.9	-6.45±1.9	0.170±0.017	-	0.30

In the Table 1. results are presented obtained for fresh and dried apple considering water content, glass transition temperatures, melting point and water activity. Obtained results for water activity ( $a_w$ ) and glass transition temperature ( $T_g$ ) presented on the Table 1. are in agreement to literature [1,3,5,6]. For samples with lower moisture content there is no melting of water and no transition (Table 1. Fig. 1). For each sample a second order

transition can be observed, with a transition temperature that increases with decreasing water content which is in agreement to the literature [1,3,5,6]. From results obtained, it can be seen that the strong dependence of the  $T_g$  and water content of dried apples, it can be deduced that water acts as a plasticizer by reducing the glass transition temperature of the pectic substances [5,6]. Values for  $\Delta C_p$  are in agreement to in literature found  $\Delta C_p$  values of apple tissue with different water content [1,8].

### CONCLUSION

Thermal behavior of conventionally dried apples (Granny Smith cultivar) with different water content and activities have been defined. From results obtained, it can be concluded that  $T_g$  decreases with increasing moisture content. Water acts as a plasticizer by reducing the glass transition temperature of the pectic substances. During the process of drying the new fruit matrix has been formed. From obtained thermal characteristic of newly formed fruit matrix the process of fruit drying can be enhanced with the aim of creating food product with improved and wished characteristics.

### *Acknowledgement*

This work was partially supported by the Ministry for Science of the Republic of Serbia (Grants no. 31055 and 31093).

### REFERENCES

- [1] J. M. del Valle, T. R. M. Cuadros, J. M. Aguilera, Food Research International, 1998, **31**, No. 3, 191-204.
- [2] Y. H. Roos, Thermal Analysis Journal of Thermal Analysis and Calorimetry, 2003, **71**, 197–203.
- [3] M.M. Sa<sup>l</sup>, A.M. Figueiredo, A.M. Sereno, Thermochemica Acta, 1999, **329**, 31-38.
- [4] Qi-L. Shia, Y. Zhaob, H-H. Chenc, Z-J. Li, C-H. Xuea, Thermochemica Acta, 2009, **493**, 55–60.
- [5] G. Barra, P. Di Matteo, V. Vittoria, L. Sesti Osseo, A. Cesàro J. Therm. Anal. Cal., 2000, **61**, 351-362.
- [6] R. Godeck · H. Kunzek · R. Kabbert, Eur Food Res Technol, 2001, **213**, 395–404.
- [7] K. A. Athmaselvi, C. Kumar, M. Balasubramanian, Ishita Roy Journal of Food Processing, 2014, **2014**, 1-10.
- [8] V. Mykhailyk, N. Lebovka Journal of Food Engineering, 2014, **123**, 32–35

## GLASS TRANSITION OF PORK *Longissimus dorsi*

S. Ostojčić<sup>1</sup>, D. Micić<sup>1</sup>, B. Simonović<sup>1</sup> and Lj. Lević<sup>2</sup>

<sup>1</sup> Institute of General and Physical Chemistry, University of Belgrade  
Studentski trg 12/V, 11000 Belgrade, Serbia. (sostojic@iofh.bg.ac.rs)

<sup>2</sup> University of Novi Sad, Faculty of Technology, Bulevar Cara Lazara 1,  
21000 Novi Sad, Serbia

### ABSTRACT

Fresh pork meat *Longissimus dorsi* has been analysed by Differential Scanning Calorimetry DSC and Thermogravimetric analysis (TGA). Glass transition ( $T_g$ ) of the pork meat *Longissimus dorsi* has been determined by Differential Scanning Calorimetry (DSC). The obtained value of glass transition was  $T_g = -53.9 \pm 1.0$  °C and obtained heat capacity of glass transition was  $\Delta C_p = 0.089$  J/g. Thermal stability of fresh pork meat *Longissimus dorsi* has been characterized by TGA.

### INTRODUCTION

Glass transitions can occur in frozen meat at temperatures below the freezing point of the aqueous phase resulting in immobilized solutes at temperatures below the glass transition temperature,  $T_g$ . Storage of meat at temperatures below  $T_g$  has wide implications since all reactions that depend on the mobility of molecules are hindered in the highly viscous glass formed. Ice recrystallization, oxidative deterioration and all enzymatic processes are prevented, in theory leading to infinite storage stability (Hansen et al 2003).

There is no abundant literature data obtained for the glass transition ( $T_g$ ) of fresh meat. Most literature data obtained for the glass transition ( $T_g$ ) of fresh meat were found to be at low temperatures. For example, for beef  $T_g$  value is in the temperature range of -40°C to -60°C [1]. Values found for the glass transition temperature of fresh veal, were  $T_g = -60$ °C obtained by Rasmussen [2],  $T_g = -40$  °C obtained by Simatos [2]. Levin and Slade [3] have found  $T_g$  for veal  $T_g > -5$  °C. Brake and Fennema [2] determined glass transition of fresh veal at -12 °C ( $T_g = -12$  °C). It has been found for fresh fish meat, that the glass transition temperatures were also in low temperature range between -83 °C and -53 °C [4,5,6]. Glass transition of tuna meat was found to be between -71 °C and -68 °C Inue Ishikawa [7]. There were less literature data for the glass transition temperature ( $T_g$ ) obtained for pork meat.

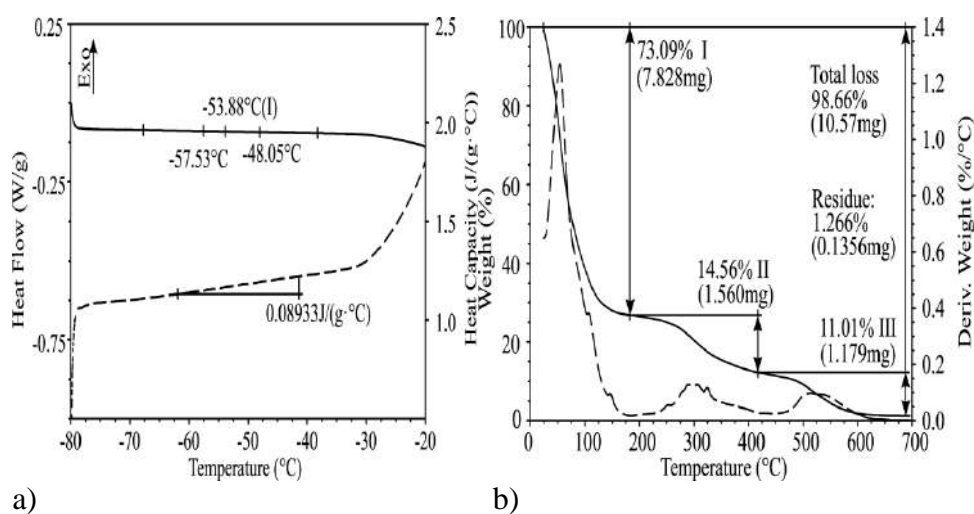
The aim of this work was to obtain the glass transition temperature of pork muscle *Longissimus dorsi* by thermal analysis method Differential scanning calorimetry (DSC).

### EXPERIMENTAL

Pork meat, *L. dorsi* muscle, was purchased from a local supermarket. A differential scanning calorimeter (DSC, Q1000, TA Instruments, New Castle, DE) was used to perform DSC experiments. Pork meat samples (7–11 mg) were subjected to heating, in hermetically sealed Al pans, in the temperature range from -90 °C to 150 °C, with controlled heating rate  $Hr= 5$  °C/min, under the N<sub>2</sub> purge flow of 50 ml/min. The water content was estimated by Thermogravimetric analysis (TGA). TGA measurements were performed on TGA Q 500, (TA Instruments, New Castle, DE) under N<sub>2</sub> purge flow of 60 ml/min, in temperature range from 25 °C to 900 °C, and heating rate  $Hr= 5$  °C/min. Each thermogram was analysed by TA Advantage Universal analysis 2000 software to obtain the glass transition parameters (onset,  $T_{onset}$ ; midpoint,  $T_g$ ; final  $T_{end}$ ,) for the onset, mid and end of transition, and also to obtain the percentage of mass loss from TGA curves. The water activity ( $a_w$ ) has been determined by thermoanalytical techniques as previously described by de Silva et al [8]. Three replicates were used for selected samples (water content).

### RESULTS AND DISCUSSION

Glass transitions are observed as changes in the heat capacity often leading to only a very small jump of the heat flow curve. The glass transition is an important process observed in a large variety of inorganic, organic, and polymeric substances. If a melt is cooled fast enough to outrun nucleation it solidifies without crystallization by forming the amorphous solid called glass [9]. The formation of protein glasses is associated with very low changes in heat capacity often making these changes very difficult to observe. The DSC curve obtained for pork muscle *L. dorsi* is presented on Fig.1. The glass transition temperature obtained in this work was found at  $T_g= -53.9\pm 1.0$  °C and heat capacity  $\Delta C_p= 0.089\pm 0.010$  J/g. Hansen et al [5] were studying the mobile phase solute in a frozen pork meat (*Longissimus dorsi*) using electron spin resonance spectroscopy (EPR) and provided evidence for the existence of the glass transition temperature at -55 °C, which is very close to result obtained for glass transition temperature for fresh pork meat (*Longissimus dorsi*) in our work  $T_g = -53.9\pm 1.0$  °C.



a) b)  
**Figure 1.** a) DSC curve with obtained glass transition temperature ( $T_g$ ) for pork muscle *L. dorsi*: -heat flow - - heat capacity ( $C_p$ ). b) TG (-) and dTG (- -) curves of fresh pork muscle *L. dorsi*.

It is known that in the water system (fresh meat contains about 75% water Fig. 1.b)) phenomena of the glass transition is possible at temperatures below the crystallization temperature [10,11,12], and that glass transition ( $T_g$ ) depends on the concentration of the solute present in the freeze-concentrated phase [7]. As seen from a physicochemical standpoint, it can be concluded that the appearance of the glass transition in fresh meat exclusively depends on the thermal treatment conditions of meat that enable maximum concentration at a freezing temperature.

Changes caused in that way induced a formation of different structure which lead to a reorganization of the material and appearance of the glass [8,13]. Determination of the glass transition in materials with high water content is a complex process, which require certain experimental conditions characteristic for certain types of materials [14]. It was found that at an appropriate annealing procedure in a narrow temperature range between the glass transition temperature and the melting temperature leads to delayed, deferred crystallization [14], which was achieved in this work.

## CONCLUSION

The thermal treatment of sample induced structural changes which led to formation of  $T_g$ . Obtained  $T_g$  value highly correlate to literature data, concerning the temperature of transition and to heat capacity change. It was shown that that existence of glass transition nearly correlate with the conditions of the thermal treatment of meat that enable maximum

concentration at a freezing temperature. These conditions have been achieved in this work.

### ***Acknowledgement***

This work was partially supported by the Ministry for Science of the Republic of Serbia (Grants no. 31055 and 31093).

### **REFERENCES**

- [1] A.Akkose, N. Aktas, *Meat Science*, 2008, **80**, 875–878.
- [2] N. C. Brake, O.R. Fennema, *Journal of Food Science* 1999, **64**, 1, 10-15.
- [3] L. Slade, H. Levine, 1995, *Adv. Food Nutr. Res.*, **38**,103-269.
- [4] I. Tolstorebrov, T.M. Eikevik, M. Bantle, *Food Research International* 2014, **55**, 303–310.
- [5] E. Hansen, M. L. Andersen, L. H. Skibsted, *Meat Science*, 2003, **63**, 63–67.
- [6] V. Orlien, J. Risbo, M.L. Andersen, L.H. Skibsted L. H., *J. Agric. Food Chem.*, 2003, **51**. 211-217.
- [7] C. Inoue, M. Ishikawa, 1997, *J. Food Sci.*, **62**, 496-499.
- [8] V. M. da Silva, L. A. Silva., J. B de Andrade., M.C da Cunha Veloso., G. Vieira Santos, *Quím. Nova*, 2008, **31**, 901-905.
- [9] S. Vyazovkin, 2016, *Phys. Chem. Chem. Phys. in press*, DOI: 10.1039/c6cp02491b
- [10] M.A. Ruiz-Cabrera, S.J. Schmidt, *Journal of Food Engineering*, 2015, **146**, 36–43.
- [11] S. Ogawa, S. Osanai, 2012, *Glass Transition Behavior of Aqueous Solution of Sugar-Based Surfactants, Supercooling*, Prof. Peter Wilson (Ed.), ISBN: 978-953-51-0113-0, InTech, Available from: <http://www.intechopen.com/books/supercooling/glass-transition-behavior-of-aqueous-solution-of-sugar-basedsurfactants>
- [12] T. Suzuki, F. Franks, *J. Chem. Soc. Faraday Trans.*, 1993, **89**, 3283–3288.
- [13] M.S. Rahman., S. Kasapis, N. Guizani, O.S. Al-Amri, *Journal of Food Engineering*, 2003, **57** 321–326.
- [14] J-H. Zhao, F-L. Xin, H-W. Wen, Xiao, Y-Y Ni., *Journal of Food Engineering*, 2015, **157**, 49–56.

*R - Physico-Chemical Analysis*



## SYNTHESIS OF 5-THIOCYANATO-2'-DEOXYURIDINE 5'-TRIPHOSPHATE

P. Spisz, M. Zdrowowicz and J. Rak

*University of Gdańsk, Faculty of Chemistry, Biological Sensitizers  
Laboratory, Wita Stwosza 63, 80-308 Gdańsk, Poland*

### ABSTRACT

Radiotherapy is the most common modality employed in the treatment of cancer disease. However, native DNA is insensitive to one of the main products of water radiolysis – solvated electrons. Hence, in order to increase the efficacy of radiotherapy one should employ a radiosensitizer along with ionizing radiation (IR). Some modified nucleosides possess features that make them potential sensitizers of DNA damage. Quite recently we have demonstrated that 5-thiocyanato-2-deoxyuridine (SCNdU) belongs to such class of compounds. The aim of the current study is to examine radiosensitizing properties of SCNdU in the DNA context. For this purpose it is necessary to synthesize the 5'-triphosphate 5-thiocyanato-2'-deoxyuridine (SCNdUTP). The required triphosphate of SCNdU is obtained in the reaction of dUTP with chlorothiocyanogen (KSCN) in acetic acid (CH<sub>3</sub>COOH).

### INTRODUCTION

Radiotherapy is the most common modality employed in the treatment of cancer. Indeed, about 50% of cancer patients are irradiated with ionizing radiation in some point of their anticancer treatment. In order to increase the efficacy of radiotherapy one should employ a radiosensitizer, i.e. a compound sensitizing DNA of cancer cells to IR. This should lead to the reduction of the radiation dose necessary to kill cancer cells. [1]

Some modified nucleosides have features which make them promising radiosensitizers. An interaction between X-rays or UV radiation and a nucleoside analogue incorporated into DNA produces various types of damage to DNA leading ultimately to lethal effects in the labelled cells. [2] One of the modified nucleosides demonstrating radiosensitizing properties is SCNdU. The results published recently by our team have shown that this uridine analogue is a potential DNA sensitizer.  $\gamma$ -Irradiation of aqueous solutions containing SCNdU leads to the formation of the 5-U• radical which can cause DNA breaks, if SCNdU is incorporated in to the

biopolymer as well as to the generation of the U-5-S• radical that can form a DNA-protein crosslink..[2]

In order to test radiosensitizing property of 5-SCNdU in DNA context, one has to transform the nucleoside into the respective triphosphate. In this form, SCNdU can be incorporated into DNA with the help of PCR or other protocol employing a suitable DNA polymerase.

## **EXPERIMENTAL**

### **Synthesis of SCNdUTP**

A 50 mL double-necked flask with mechanical stirrer was filled with an ice-cold solution of Cl<sub>2</sub> (0.77 g, 10.74 mmol) in dry acetic acid (25 mL, this solution was prepared by passing Cl<sub>2</sub> through a CaCl<sub>2</sub> trap connected to flask). In the next step, KSCN (1.26 g, 13.17 mmol) was added. The prepared solution was stirred for 1.5 hours at room temperature. Then 5-triphosphate 2'-deoxyuridine (20 mg, 0.28 mmol) was added to the solution and stirring was continued for 2.5 hours at room temperature. Before the end of the reaction (about 30 min), 0.5 mL of cyclohexene was added. Finally, the solution was evaporated to dryness under vacuum.

### **Purification of SCNdUTP**

The residue was dissolved in water. The aqueous solution was purified with a preparative HPLC (DGU-20A<sub>5R</sub>) equipped with a UV detector (SPD-M20A) set to 254 nm, on the Gemini (Phenomenex) reverse-phase C18 column (10 mm x 250 mm, 5 mm in particle size and 110 Å in pore size). The linear gradient of 0-40% B in 20 min at the flow rate of 4 mL min<sup>-1</sup> was used; phase A: 20 mM TEAA in water, phase B: 50% acetonitrile and 20 mM TEAA in water.

### **LC-MS conditions**

LC-MS analyses were performed on a TripleTOF 5600+ System (AB SCIEX) coupled with a UHPLC Nexera X2 (Shimadzu). The separation was carried out on a Phenomenex Kineteks 2.6u C18 (150x2.10 mm, 100 Å) column. The linear gradient of 0-40% B in 10 min at the flow rate of 0.4 mL min<sup>-1</sup> was used; phase A: 20 mM TEAA in water, phase B: 50% acetonitrile and 20mM TEAA in water. The injected volume was equal to 10 µL. MS operation parameters: declustering potential (DP): -90 V, curtain gas (CUR): 25 PSI, nebulizer gas (GS1): 30 PSI, heating gas (GS2): 30PSI, ion spray voltage floating (ISVF): -4000 V, m/z: 350-700.

## RESULTS AND DISCUSSION

The carried out synthesis gave triphosphate 5-thiocyanato-2'-deoxyuridine as one of the two main products (see Figure 1). The side product turned out to be tetraphosphate 5-thiocyanato-2'-deoxyuridine. Our results were confirmed by the HPLC and MS analyses (see Figures 1 and 2).

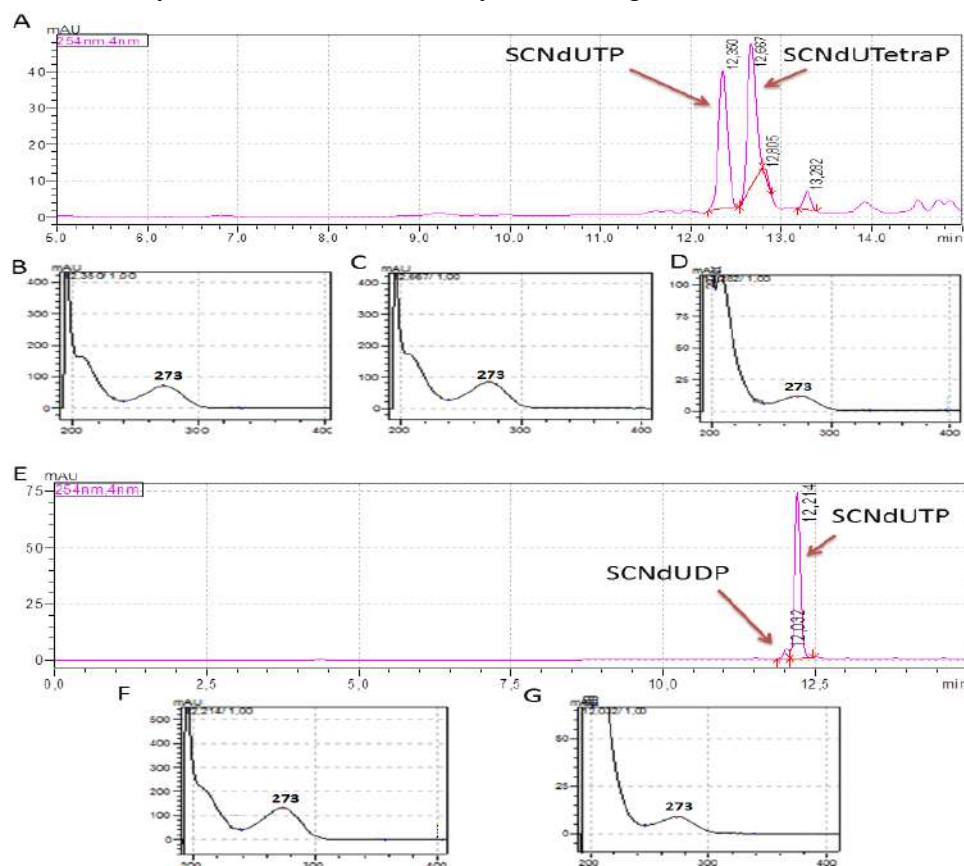


**Figure 1.** HPLC analysis of SCNdUTP before purification (A). UV spectra of signals 12,350 min (B), 12,667 min (C), 13,282 min (D), respectively. HPLC analysis of SCNdUTP after purification (E). UV spectra of signals 12,032 min (F), 12,214 min (G), respectively.

## CONCLUSION

The synthesis of triphosphate of 5-thiocyanato-2'-deoxyuridine is the first step in the studies of radiosensitizing properties of SCNdU. The modified nucleoside triphosphate will be used for synthesis of the labeled DNA by means of PCR or DNA replication by polymerase accepting modified nucleotides.

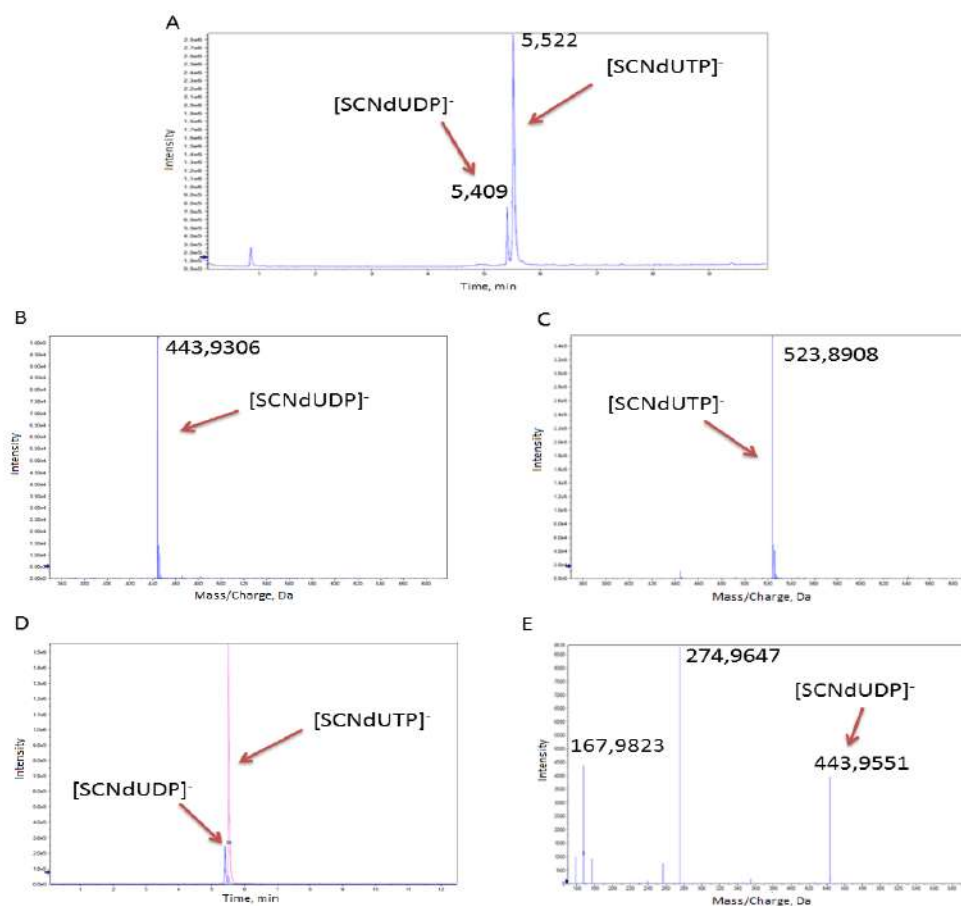


**Figure 2.** TIC for a sample after purification (A). MS spectrum of SCNdUDP in negative mode (B). MS spectrum of SCNdUTP in negative mode (C). Extracted ion chromatogram of SCNdUTP (D). MS/MS spectrum of SCNdUTP (E).

### **Acknowledgement**

This work was supported by the Polish National Science Centre under Grant No. 2014/14/A/ST4/00405 (J.R.) and BMN no. 538-8227-B088-15 and 538-8227-B088-16 (P.S.).

### **REFERENCE**

- [1] J. Rak, L. Chomicz, J. Wicz, K. Westphal, M. Zdrowowicz, P. Wityk, Ł. Golon. *J. Phys. Chem. B*, 2015, **119** (26), 8227-8238.
- [2] M. Zdrowowicz, L. Chomicz, M. Żyndul, P. Wityk, J. Rak, T. J. Wiegand, M. D. Sevilla. *PCCP*, 2015, **17** (26), 16907-16916.

*Author index*



## INDEX

Abazović N. D.	545, 549, 553	Blagojević S. M.	343, 731, 757
Adnađević B.	239, 255, 263	Blagojević S. N.	343, 757
Agbaba D.	801, 821, 825	Blagojević V. A.	123, 127
Agbaba S.	833	Blokhina A. G.	605
Ahrenkiel S. P.	391, 545	Bogdanova Y.	175, 179, 633
Ajduković M.	247, 371, 375	Bogdanović U.	391, 653
Aleksić J.	83, 99, 103	Bojić A. Lj.	715, 719
Aleksić M. M.	383, 829	Bondžić A.	451
Alexandrova S.	319	Bondžić B. P.	79, 83, 123
Amić A.	71	Borić I.	731
Andronache C.	569	Bošnjaković-Pavlović N.	243
Anđelković D.	499, 889, 893	Božić D.	475
Anđelković T.	449, 889, 893	Božinovski D. M.	467
Aničić Urošević M.	739	Brankov M.	855
Anić S.	335, 343, 347	Brborić J.	383, 849
Anitas E.	753	Brnjos S.	901
Antonijević-Nikolić M.	657	Brothers E. N.	467
Antonov S.	179	Bubanja I. N.	259, 335, 347
Azizoglu A.	111, 115, 139	Budimir M..	653
Azizoğlu A. A.	87, 91	Budinski-Simendić J.	677, 681, 685
Azizoglu N.	863, 867	Bueno J. M. C.	185
Bačić G.	491	Bugarski B. M.	75
Baidakov K. V.	609	Bulanov E. N.	605, 609
Bajuk-Bogdanović D.	577	Burmas B.	649
Banković P.	247, 251, 371	Bystrzejewski M.	215, 541, 525
Baranac-Stojanović M.	83, 99, 103	Cakić M.	581
Bedilo A. F.	187	Cakić S.	685
Begović N.	597, 601	Carević M.V.	545, 549, 553
Belić M. R.	467	Çarıkcı S.	87, 91
Beljanski M. V.	463	Chernikova E.	175, 633
Beškoski V. P.	661, 813, 817	Chomicz-Mańka L.	135

## INDEX

Christoforidis A. K	367	Dojčinović B.	251
Ciganovic J.	561	Dolijanović Ž.	885
Ciui B.	358	Dolzhikova V.	633
Craig T.	15	Dondur V.	577
Crevar Sakač M.	833	Dostanić J.	219, 645
Cricenti A.	15	Dragičević V.	885
Cristea C.	358	Dragović S.	707
Cvetković N.	263	Drakulić D.	107, 455
Cvetković T.	499	Dražić B.	775
Čolović M.	243, 451	Dyjak S.	541
Čomor M.I	545, 549, 553	Džambaski Z.	83, 99, 103
Čučulović A. A	691	Đokić-Stojanović D. R.	159
Čudina O.	383	Đorđević B. S.	159
Čupić Ž.	323, 335, 343	Đorđević N.	435, 439, 443
Ćirić-Marjanović G.	391, 623	Đorović J.	71
Ćujić M.	707	Đuričić T.	727
Daković A.	699	Đurić A. N.	813, 817
Damyanova S.	185	Ekmešćić B. M.	637, 641, 645
Danilova M.	211	Elek M.	825
Dapčević A.	235	Emel'yanenko V. N.	837
Denisov D.	301	Erceg T.	681
Dermentzis K.I.	367	Erić N.	731
Dimić D.	131, 143, 431	Exarchos T.	411
Dimitrić Marković J.	131, 143, 431	Fedorov Y. V.	767
Dimitrijević S.	653	Fedorova O. A	767
Dimitrijević S. B.	163	Filipić S.	821, 825
Dimitrijević S. P.	163	Filipović D.	435, 439, 443
Dimitrijević T.	379	Filipović N.	411, 601
Dimitrijević V. D.	715, 719	Finney K. L. N. A	3
Dobričić V.	383, 849	Fleischer M.	25
Dobrota A. S.	29	Florea A.	358

## INDEX

Friedrich B.	510	Incerti S.	447
Fritea L.	358	Ingham J.	15
Fronczak M.	215	Ivanda M.	585
Fuchs E. C.	357	Ivanović-Šašić A.	335, 343, 375
Gabrovska M.	223	Ivković B.	475, 809, 833
Gáspár V.	37	Jakovljević D. M.	661, 813, 817
Gavrilov N. M.	29	Jakovljević J. K.	521
Gergorić M.	649	Janči T.	585
Godziek A.	327	Janicki V.	585
Gojgić-Cvijović G.Đ.	661, 813, 817	Jankov M.	809
Gorjanović S.	167, 171	Janković D. Lj.	641
Gotić M.	585	Janković I. A.	549
Govedarica O.	677, 681, 685	Janković M.	677, 681, 685
Grbić B.	613	Janković M. M.	695
Grinvald I.	155	Janković Mandić Lj.	707
Grković I.	455	Janković-Častvan I.	235
Grubišić S.	475	Janošević B.	885
Grujić M.	801	Jauković Z.	743
Grujić S.	743	Jelenković B.	593
Gusarova E. V.	837	Jelić R.	845
Guševac Stojanović I.	455	Jeremić S.	131
Gutić S.	29	Jerosimić S.	107
Hadžibrahimović M.	395	Jevtić S.	763
Halasi T.	871, 875, 879	Jovančić P.	657
Hall M. B.	467	Jovanovic J. M.	319
Holeljajtner-Antunović I.	577	Jovanović J.	239, 255, 673
Horvat A.	435	Jovanović D.	227, 251, 375
Horváth D.	308	Jovanović M.	491
Hosu O.	358	Jovanović S.	557
Ignjatović N.	581	Jovanović V.	557
Ilić I.	251	Jović A.	577

## INDEX

Jović-Jovičić N.	247, 251, 371	Korshak K. S.	605
Kačarević–Popović Z.	403, 589	Kortz U.	451, 508
Kalagaev I.	155	Kostić I.	499, 889, 893
Kalamković S.	871, 875, 879	Kostina J.	175, 179, 633
Kalijadis A.	235	Kovacević B.	167, 171
Kalska-Szostko B.	517	Kovačević O.	167, 171, 905
Kapetanović V.	829	Kowalik M.	541
Kapustin R.	155	Kowalska K.	495
Karaman M.	471	Kowalska T.	293, 327
Karljiković-Rajić K.	809	Kožuh S.	573
Kawecka A.	495	Kragović M.	699
Kekez B.	661	Krajewska M.	215
Kekez B. D.	813, 817	Kraljić Roković M.	573, 649
Keta O.	447	Krasheninnikova O.V.	609
Kiciński W.	541	Krstić D.	243, 451
Kijevčanin M.	75	Krstić J.	403, 589
Kılıç T.	87, 91	Krstić J.B.	223
Kiss I. Z.	37	Krstić M. P.	379, 763
Kleotka U.	517	Krstić N. S.	715, 719
Knežević-Vukčević J.	901	Krzyminski K.	495
Knyazev A. V.	605, 609, 837	Kuzmanović D.	379
Knyazeva S.S.	609, 837	Kuzmanović M. M.	49, 147
Kocić G.	889, 893	Ladenkov I. V.	605
Kocić H.	889, 893	Laušević M.	231, 235, 743
Kojić K.	119	Laušević Z.	235
Kolar-Anić Lj.	335, 343, 351	Lelet M. I.	605
Komshina M. E.	609	Lente G.	199
Konstantinović S. S.	159	Lević Lj.	909
Konstantinović Z.	521	Lončarević D.	223, 645
Korokin V. Zn.	605	Luce M.	15
Korolev Yu.	179	Lutsyk V.	779, 783, 787

## INDEX

Ly Thi H. G.	23	Matavulj P.	561
Ljubek G.	573	Matić Bujagić I.	743
Maciejowska A.	327	Medvedev J. J.	207
Maćešić S.	263, 277	Mentus S.	29,387,399, 565
Majstorović D.	565, 731, 739	Mesarović J.	885
Maksimović J. P.	347	Mészáros-Szécsényi M.	191
Makurat S.	135	Mijin D.	231
Malešević A. S.	601	Mikac L.	585
Maletić M.	235	Miladinović J.	617
Malinović B. N.	727	Miladinović Z.	617
Malkov S. N.	463	Milčić M.	763
Mandic J.	871	Milenković D.	131, 143, 431
Manojlovic V.	319	Milenković M.	475
Manojlović D.	703	Miletić A.	685
Marinkovic F.	673	Miličević A.	57
Marinković A.	231	Miličević T.	739
Marinković D.	227	Milikić J.	403
Marinović S.	247, 251, 371	Milkos M.	871
Marinović-Cincović M.	557	Milojević-Rakić M.	577
Marković B.	809	Milojković J.	699
Marković D. M.	703	Milošević Z.	411
Marković G.	557	Milošević I. R.	703
Marković J. P.	637	Milovanović M.	107
Marković M.	699	Milutinović-Nikolić A.	247, 251, 371
Marković S.	219, 645	Miljanić Š.	403
Marković S. D	67, 71	Minić D. M.	127, 597, 601
Marković V. M.	323, 351	Mishakov I.V	187
Marković Z.	131, 143, 431	Mitić M.	107
Marmanis D. I.	367	Mitić N. S.	463
Martin D. S.	15	Mitić Ž.	581, 791
Martinović J.	455	MitićĆulafić D.	901

## INDEX

Mitrić M.	391, 521, 653	Pantelić D.	583
Mitrić T.	537	Pantić J.	383, 829
Mitrović N.	455, 597	Pantić T.	163
Mojović Z.	371, 375, 537	Pantović M. R.	75, 665, 669
Momčilović M.	49, 561	Papan J.	597
Mudrinić T.	247, 371, 375	Parac-Vogt T. N.	23
Murić B.	593	Parker D.	3
Muzika F.	301, 311, 331	Parker J.	302
Najman S.	581	Parodi O.	411
Nastasović A. B.	637, 641	Pastor F.	395
Nedić Vasiljević B.	247, 577	Pašti I.	29, 391
Nekoei A. R.	95	PAT S.	151
Nikolic D.	411	Pavelkić V. M.	75, 665, 669
Nikolic Z. S.	529, 533	Pavličević J.	677
Nikolić B.	901	Pavlović D.	499
Nikolić G. M.	791	Pavlović M. D.	463, 901
Nikolić K.	801, 821, 825	Pavlović M. M.	75, 665, 669
Nikolić M.	791	Pavlović S.	223
Nikolić R. S.	715, 719	Pavlović-Lažetić G. M.	463
Nikolić Z.	339	Pejić N.	757
Nikolova D.	223	Pelosi W.	411
Novakovic K.	302	Pergal M. V.	645, 657
Novaković T.	537, 553	Perić I.	435, 439, 443
Nwosu J. C.	302	Perić Ivanagić P.	573
Odović J.	845	Perišić M.	711, 735, 739
Olechno E.	541	Petković A.	699
Ortenzi M.	15	Petković B. B.	379, 557, 763
Ostojić S.	897, 905, 909	Petković M.	163
Ostrovskii N.	191	Petković V.	447
Özer Sağır Z.	87, 91	Petrović I.	447
Pagnacco M.	347, 387, 695	Petrović J.	699

## INDEX

Petrović J.	707	Rakić V. M.	549
Petrović S.	613	Randelović D. V.	641
Petrović Z.	71	Ranković D. P.	147
Petuchov A.	155	Raos N.	57
Plutalova A.	175, 633	Rašović A.	79, 123, 126
Ponomareva K.	331	Relić D.	739
Popa A.	577	Ristić I.	685
Popovic M.	797, 801, 805	Ristić-Fira A.	447
Popovic Z.	507	Rogers N. J.	3
Popović A.	739	Roglić G.	703
Popović G.	797, 801, 805	Rožić Lj.	613
Popović I.	809	Ruzić D.	821, 825, 829
Potkonjak N. I.	339, 347, 855	Ružić D.	821, 825, 829
Potkonjak T. N.	339	Saboni A.	319
Příbyl M.	301	Sajewicz M.	293, 327
Pylinina A.	211	Samaržija-Jovanović S.	557
Quanten T.	23	Sandić Z. P.	637
Racolta D.	569	Săndulescu R.	358
Radenković M.	723	Sap A.	23
Radetić T.	521	Sarap N.	695
Radičević R.	681	Satuła D.	517
Radić N.	611	Saveljić I.	411
Radić R.	723	Savić J.	849
Radisavljević L.	399	Savić T. D.	545, 549, 553
Radišić M.	231	Savić-Šević S.	593
Radojković V.	301, 315	Savović J.	49, 561
Radonjić V.	233	Savović J. J.	147
Radosavljević A.	589	Savushkin I. A.	609
Radulović D. S.	749	Scherbina A.	633
Rajčić B.	163	Schmitz G.	285
Rak J.	459, 479, 915	Schreiber I.	301, 311, 315, 331

## INDEX

---

Schreiberová L.	301, 311, 331	Stanković A.	219
Segedinac M.	875	Stanković B.	255, 673
Semenok D. V.	207	Stanković D.	379
Senanayake P. K.	3	Stanković I.	483, 487
Senćanski J.	565, 695, 731	Stanković I. M.	467
Senćanski M.	475	Stanković M.	223, 227
Shapagin A.	633	Stanković M. N.	715, 719
Shepel N. E.	767	Stanojević A.	323, 351
Shinagawa K.	533	Stanojlović M.	435
Shipilova A. S.	837	Stasić J.	561
Shuvarakova E. I	187	Stefanović I. S.	637, 641, 645
Siggel-King M. R. F.	15	Stergiopoulos D.K.	367
Sikorski A.	495	Stevanović Hedrih K.R	38
Silina N. E.	605	Stevanović K.	259
Simić M.	885	Stević T.	901
Simonović M.	897	Stoiljković M.	49, 521, 653
Simović B.	897, 909	Stojadinović M.	797
Sinadinović-Fišer S.	677, 681, 685	Stojadinović S.	219, 613
Skaf M.	483	Stojanovic M. M.	419
Skorodumova N. V.	29	Stojanović J.	75, 699
Smirnova L. A.	605	Stojanović M.	79, 99, 103
Sopčić S.	649	Stojanović S.	581
Sosnowska M.	841	Stojić A.	711, 735
Spasic A. M	319	Stojković-Simatović I.	565
Spasojević J.	589	Stolić A.	581
Spasojević-de Biré A.	243	Stopic S.	510
Spirin I.	155	Stoševski I.	403
Spisz P.	915	Strachowski P.	525, 541
Stanisavljev D.	259	Stroobants K.	23
Stanisavljević A.	435, 439, 443	Surla R.	597
Stanišić Stojić S.	711, 735	Suručić Lj. T.	637

## INDEX

Sužnjević D.	395	Trtica M.	49
Syrov E. V.	609	Uskoković D.	219
Szabo E.	269	Vasić M. M.	597, 601
Szakacs Zs.	753	Vasić V.	243, 451
Šaponjić Z.	521	Vasilčić R.	613
Šarić M.	649	Vasiljević D.	593
Šećerov B.	491	Vasiljević-Radović D.	645, 657
Škapin S.	219, 653	Vdovykh L.	179
Škrijelj E.	805	Vedyagin A. A.	187
Šljukić B.	403	Veličković S.	107, 163
Talik E.	327	Veljković F.	107, 163, 455
Tanasković S. B.	771, 775	Veljković V. B.	139
Tanišli M.	151	Verevkin S. P.	837
Taşal E.	151	Veselinović A.	581, 791
Teofilović V.	677	Veselinović D. S.	691
Tertiš M.	358	Veselinović J.	581, 791
Tešanović K.	471	Veselinović Lj.	219
Todoran D.	753	Vidaček S.	585
Todoran R.	753	Vladimirov S.	383, 849
Todorović N.	435, 439, 443	Vodnik V.	391, 653
Todorović Z. B.	159	Vojinović N.	447
Tolić Lj.	231	Vorob'eva V.	779
Tomašević A.	231	Vorotyntsev I.	155
Tomić A.	805	Vranješ M.	521
Tomovska R.	624	Vrvić M. M.	661, 813, 817
Tošović J.	67	Vučičević J.	821
Tóth Á.	308	Vučinić D. R.	749
Trajanović M.	581	Vujić Z.	475, 833
Trbojević J.	845	Vujković M.	387, 399, 565
Trbojević-Stanković J.	845	Vukadinović A. A.	641
Troter D.Z.	159	Vukčević M.	235

## INDEX

---

Vukić N.	681
Vukojević V.	5, 323, 351
Vuković G.	739
Vuković Z.	613
Weightman P.	15
Westphal K.	479
Wityk P.	459
Xu X.	243
Yagodovskii V.	211
Yildiz C. B.	63, 111, 139
Zakrzewska J.	395, 471, 617
Zarić M.	455
Zarić M. M.	75, 665, 669
Zarić S.	467, 487
Zdravković S.	420
Zdrowowicz M.	915
Zelenaya A.	783, 787
Zlatanović S.	167, 171, 905
Zlatković M. Z.	159
Zorc H.	585
Živić M.	395
Živković- Radovanović V.	657, 771, 775
Živković S.	49, 561
Žižić M.	395, 471
Žunič V.	653

544(082)  
66.017/.018(082)  
502/504(082)  
663/664:658.56(082)  
615.31:547(082)

INTERNATIONAL Conference on Fundamental and Applied Aspects of Physical Chemistry (13 ; 2016 ; Beograd)

Physical Chemistry 2016 : proceedings. Vol. 2 / 13th International Conference on Fundamental and Applied Aspects of Physical Chemistry, Belgrade, 26-30 September 2016 ; [editors Željko Čupić and Slobodan Anić]. - Belgrade : Society of Physical Chemists of Serbia, 2016 (Belgrade : Jovan). - IV, 507-930 str. : ilustr. ; 24 cm

Tiraž 200. - Bibliografija uz svaki rad.

ISBN 978-86-82475-33-0

1. Society of Physical Chemists of Serbia (Beograd)

а) Физичка хемија - Зборници б) Наука о материјалима - Зборници с) Животна средина - Заштита - Зборници д) Животне намирнице - Контрола квалитета - Зборници е) Фармацеутска хемија - Зборници  
COBISS.SR-ID 225802508

08. 09. 2016

